Published in Journals: GeoHazards, Land,
Remote Sensing, Sustainability and Water

Topic Reprint

Natural Hazards and Disaster Risks Reduction

Volume III

Edited by
Stefano Morelli, Veronica Pazzi and Mirko Francioni

mdpi.com/topics

MDPI

Natural Hazards and Disaster Risks Reduction—Volume III

Natural Hazards and Disaster Risks Reduction—Volume III

Editors

Stefano Morelli
Veronica Pazzi
Mirko Francioni

MDPI

Basel • Beijing • Wuhan • Barcelona • Belgrade • Novi Sad • Cluj • Manchester

Editors

Stefano Morelli
University of Urbino "Carlo Bo"
Urbino
Italy

Veronica Pazzi
University of Firenze
Firenze
Italy

Mirko Francioni
University of Urbino "Carlo Bo"
Urbino
Italy

Editorial Office
MDPI
St. Alban-Anlage 66
4052 Basel, Switzerland

This is a reprint of articles from the Topic published online in the open access journals *GeoHazards* (ISSN 2624-795X), *Land* (ISSN 2073-445X), *Remote Sensing* (ISSN 2072-4292), *Sustainability* (ISSN 2071-1050), and *Water* (ISSN 2073-4441) (available at: https://www.mdpi.com/topics/Natural_Hazards_Disaster_Risks_Reduction).

For citation purposes, cite each article independently as indicated on the article page online and as indicated below:

Lastname, A.A.; Lastname, B.B. Article Title. *Journal Name* **Year**, *Volume Number*, Page Range.

Volume III
ISBN 978-3-7258-0325-5 (Hbk)
ISBN 978-3-7258-0326-2 (PDF)
doi.org/10.3390/books978-3-7258-0326-2

Set
ISBN 978-3-7258-0319-4 (Hbk)
ISBN 978-3-7258-0320-0 (PDF)

Contents

About the Editors

Stefano Morelli

Stefano Morelli has been a professor at the Department of Pure and Applied Sciences (DiSPeA) of the University of Urbino in Physical Geography and Geomorphology since 2021. Previously, from 2005 to 2021, he carried out research activities at the Department of Earth Sciences of the University of Florence, where he was a fixed-term Researcher in Engineering Geology (2016–2019), a short-term Research Fellow (2005–2008) and a Research Assistant (2008–2016 and 2016–2109). He obtained a research doctorate in Geomorphology in 2010. His interests include the geomorphological evolution of river environments and methods for characterizing hydraulic risk in order to improve knowledge of the most effective methodologies and technologies to implement a national monitoring system. At the same time, his interests are oriented toward the protection, safeguarding and sustainable management of natural and anthropic territories and cultural heritage from slope instability risks via the synergistic use of new technologies and traditional methods. His main experiences in this research field relate to his participation in national and international projects (EU-founded and others) on landslides and slope stability analysis under both ordinary and emergency conditions. In particular, he has applied his experience in developing areas of the world, in some UNESCO sites, in national initiatives with the Italian Civil Protection system and in activities dealing with the improvement of resilience for populations threatened by harmful geological events. He is a permanent member of the Editorial Board of Geoenvironmental Disasters as an Editor. He has participated in some Special Issues as Lead Guest Editor, and he is the author or co-author of 40 peer-reviewed international publications (SCOPUS), several book chapters and conference proceedings in the field of geo-hydrological natural hazards (100 works from Scholar sources).

Veronica Pazzi

Veronica Pazzi received her M.Sc. degree in Environmental Engineering (with a thesis on geophysical methods applied to geo-archaeological problems) and her Ph.D. degree in Civil and Environmental Engineering (with a thesis on geophysical methods applied to environmental problems) from the University of Firenze (Florence, Italy) in 2007 and 2011, respectively. From 2011 to 2021, she was a Postdoctoral Researcher at the Department of Earth Sciences at the University of Florence. She also collaborates with the Centre for the Civil Protection of the University of Firenze, a Centre of Competence of the National Department of Civil Protection of the Italian Government for geo-hydrological hazards. From 2021 to 2024, she was a Researcher at the University of Trieste. Since 2024, she has been an Associate Professor in Applied Geophysics at the University of Firenze. Her research interests are focused on the many aspects of engineering geology and applied seismology. These mainly include geophysical investigations, especially electrical resistivity and passive seismic methods, applied to slope instability and the characterization of local seismic effects. Moreover, her field of application is in the development of methods for hazard, vulnerability, risk, and resilience assessment, with special attention to buildings and cultural heritage sites. She is a member of the SEG, EAGE, EGU, IAEG Italian Section, AIGEO and AIGA societies. She is the Editor of *NHESS*, *Landslides*, the *International Journal of Disaster Risk Reduction* and the *International Journal of Geophysics*, as well as many Special Issues in different journals. She has authored about 50 papers (source SCOPUS) and is a reviewer for many international peer-reviewed journals. Since 2022, she has been the Scientific Officer of the EGU NH3—Landslides and Avalanches subdivision.

Mirko Francioni

Mirko Francioni is a professor of Engineering Geology at the University of Urbino, Carlo Bo (Italy). His research mainly involves the combined use of remote sensing, GIS and numerical simulations for the study of natural and engineering slopes. During his academic career, he received his Ph.D. in Engineering Geology at the University of Siena. After obtaining his Ph.D., he worked in Canada (Simon Fraser University) as a post-doctoral researcher, in the UK as a lecturer (University of Exeter) and in Italy as a research fellow and senior researcher (University of Chieti and University of Urbino, respectively). Over the course of these years, he developed new methods for the use of remote sensing/GIS data for conventional and numerical slope analyses. He has participated in several international projects in Africa, Canada, the UK and Italy. Mirko has been the PI of two national (at the University of Exeter and the University of Urbino) and one international project (at the University of Urbino). He has collaborated and performed field work with many universities around the world and has also worked as a consultant for geological engineering and exploration companies in Canada and Italy. He currently serves on the scientific committee of the Italian Association of Engineering Geology and Environment. In 2018, he was appointed as an Honorary Lecturer in Mining Engineering at the University of Exeter, and in the same year, he was awarded by the American Association of Environmental and Engineering Geologists (AEG) with a Publication Award (the best paper from the last four issues of Environmental and Engineering Geoscience). In 2020, Mirko received the Italian National Scientific Habilitation for full professorship.

Preface

This reprint is the third of three volumes that collect articles on the topic of Natural Hazards and Disaster Risks Reduction. Some papers focus on aspects related to the different phases of the risk cycle. Other papers deal with the issues, seismic hazards and natural hazards of very different types (e.g., surface deformation, volcanic activity, dust storms, etc.) with an approach focused on single or multiple hazards. However, all of them paint an important picture of the progress of hazard studies and continuous risk management efforts. Climate change and human actions play a central role in the papers' discussions. The material within this work serves as a valuable collection for scholars involved in comprehending the discussed phenomena and seeking specialized solutions. Furthermore, given its practical attributes, it also provides support for technicians in public administration dedicated to enhancing security in regions affected by these natural adversities striving for sustainable development.

Stefano Morelli, Veronica Pazzi, and Mirko Francioni
Editors

sustainability

MDPI

Article

Correlation between Building Damages and Losses with the Microzonation Map of Mataram—Case Study: Lombok Earthquake 2018, Indonesia

Bambang Setyogroho [1,*], Dicky Muslim [2,*], Muhammad Suwongso Sadewo [3], Ghazi Oktavidi Muslim [2], Safri Burhanuddin [4] and Hendarmawan Hendarmawan [1,*]

1 School of Postgraduate, University of Padjadjaran, Bandung 40132, Indonesia
2 Faculty of Geological Engineering, University of Padjadjaran, Bandung 40132, Indonesia; ghazi17001@mail.unpad.ac.id
3 Research Fellow of Geological Engineering, Faculty of Earth Sciences and Technology, Bandung Institute of Technology, Bandung 40116, Indonesia; dewongs.geo07@gmail.com
4 Coordinating Ministry of Maritime and Investment, Jakarta 10340, Indonesia; safribur@gmail.com
* Correspondence: bambang17003@mail.unpad.ac.id (B.S.); d.muslim@unpad.ac.id (D.M.); hendarmawan@unpad.ac.id (H.H.)

Abstract: The high intensity of the earthquake on Lombok Island on 5 August 2018, with a magnitude of 7.0 Mb, caused material losses experienced by the affected residential areas. The Indonesian Geological Agency in 2015 published a microzonation map that mapped zones prone to earthquake shocks to mitigate disasters. This study aimed to compare the level of damage and loss in residential areas due to earthquakes in Mataram City with earthquake-prone zones using a microzonation map. The correlation between damage and loss value of residentials with microzonation maps was evaluated using the overlay method. The results showed that the level of damage and the value of the loss of houses in the high disaster-prone zone (red zone) showed the highest loss value. In comparison, the level of losses in the moderate disaster-prone zone (yellow zone) and light disaster-prone zone (blue zone) on the microzonation map shows a low and lower loss value. This study concludes that the microzonation map helps determine the damage zone and the level of disaster vulnerability caused by the earthquake hazard.

Keywords: microzonation; earthquake; level of damage and loss; disaster vulnerability

Citation: Setyogroho, B.; Muslim, D.; Sadewo, M.S.; Muslim, G.O.; Burhanuddin, S.; Hendarmawan, H. Correlation between Building Damages and Losses with the Microzonation Map of Mataram—Case Study: Lombok Earthquake 2018, Indonesia. *Sustainability* **2022**, *14*, 2028. https://doi.org/10.3390/ su14042028

Academic Editors: Stefano Morelli, Veronica Pazzi and Mirko Francioni

Received: 20 January 2022
Accepted: 7 February 2022
Published: 10 February 2022

Publisher's Note: MDPI stays neutral with regard to jurisdictional claims in published maps and institutional affiliations.

1. Introduction

The location of Indonesia in the collision zone causes frequent natural disasters. Earthquakes are one of such disasters caused by tectonic activities. The dynamic interaction of numerous tectonic plates in eastern Indonesia causes high seismicity rates, which resulted in catastrophic damaging earthquake sequences on Lombok Island in 2018 [1–3]. Based on the National Disaster Management Agency (BNPB) records, from the beginning of 2017 to June 2018, there have been 4006 disasters in Indonesia, with 30 tectonic earthquakes on Lombok Island occurring in August 2018 with a magnitude of 5.9–6.9. The earthquake in Lombok claimed at least 481 lives and caused an economic loss of US$ 514,000,000 as of 17 August 2018 [4]. These financial losses are caused mainly by damage to infrastructure and buildings.

Natural disasters are a significant concern in Mataram City. A natural disaster is an unanticipated event or set of circumstances that endanger and disrupts people's lives and livelihoods as a result of natural causes, both by natural factors and/or non-natural factors and human factors, resulting in fatalities, environmental damages, property losses, and psychological impacts [5]. Examples of natural catastrophes include floods, tsunamis, earthquakes, and landslides [6,7]. After the earthquake disaster in Lombok in August 2018, the damage level of the Municipality of Mataram ranked fourth out of six regencies

in Lombok with a total loss of US$ 69,008,289. The tremendous damage and loss to the settlement sector reached a value of US$ 34,907,209, damage to the housing subsector reached US$ 32,500,610, and other losses, including cleaning of debris, worth US$ 1,600,470 [4].

Earthquakes are the vibrations or shocks that occur on the surface of the Earth caused by the collisions between the tectonic plates, active fault zones, volcanic eruption activity, and rock debris. Lombok Island is located north of the subduction zone, where the Indo/Australian Plate collides and subducts below the Eurasian Plate with a convergence rate of 44–68 mm/yr [8].

It is crucial to distinguish between risk and vulnerability. Seismic risk is the risk of damage and consequential loss to a particular structure or collection of structures over a specific period. The anticipated losses from all degrees of hazard severity are included in risk, taking their occurrence probability into account, whereas the vulnerability of an element is generally specified for a specific hazard severity level. Seismic vulnerability analysis in urban environments focuses mainly on building structural, geological, and geographical information directly related to potential human and economic losses in the case of a seismic episode [9]. On the other side, Lombok Island is locked between two active faults, the Flores back arc thrust on the north with a convergence rate of ca. 9.9 mm/yr and the normal fault of Sumbawa with a rate of 0.5 mm/yr [10]. Those faults influenced the earthquake events in Lombok Island (Figure 1).

The earthquake with the greatest strength occurred on 19 August 2018, with a magnitude of 6.9 Mb, and the epicenter at a radius of 30 km NE of East Lombok. At the same time, five other earthquakes occurred with a magnitude of 4.9 Mb–5.7 Mb, whose shaking intensities were scattered in several areas in the island of Lombok, with the distribution shown in Figure 2. The earthquake on the island of Lombok, taking place in July–August 2018, had negative impacts, such as fatalities, damages, and material losses. From January through October 2018, there were 98 earthquakes with a magnitude ranging from 4.1 Mb–6.9 Mb. The depth of the earthquake sources was between 5.7 km–121.9 km [11]; the earthquakes that occurred were dominated in the NW–NE region of the island of Lombok.

The microzonation map of Mataram City from the Geological Agency (2015) is used as an estimated vulnerability zoning model. The map is used as a basis to prepare a zonation map by using the microtremor. Bertelli and Omori were the first to discover microtremors in 1909, while Guttenberg was the first to introduce engineering uses of microtremors [12,13]. Microtremor measurements are valuable for assessing seismic threats in the near-surface substructure [14,15]. Microtremor (or ambient vibration) methods analyze the mechanical qualities of the Earth's subsurface, particularly seismic velocities, by measuring background seismic noise. Seismic noise is the constant vibration of the Earth's surface caused by a combination of the low-frequency (less than 1 Hz) natural phenomena (earthquakes, wind, tides, rivers, rain, variations in atmospheric pressure) and high-frequency (greater than 1 Hz) human activities [16,17]. Idriss and Boulanger [18] showed that damage to building structures due to earthquake intensity of ground shocks during an earthquake was significantly influenced by local geological and soil conditions. The microzonation divides or classifies areas of zones that have relatively similar potential shocks and disasters. Their engineering characteristics have local effects. Hard rock sites will experience a low shock intensity, while soft soil will experience a high shock intensity [19–22].

The purpose of this research was to determine the accuracy of the microzonation map against actual building losses and damage when the Lombok earthquake in 2018 occurred. The high accuracy of microzonation maps is perfect for development plans such as urban planning and financial risk transfer strategies. The burden of the state budget will be reduced in the future if disaster impact mitigation using the prediction of microzonation maps goes well; in turn, it will also reduce casualties and material losses.

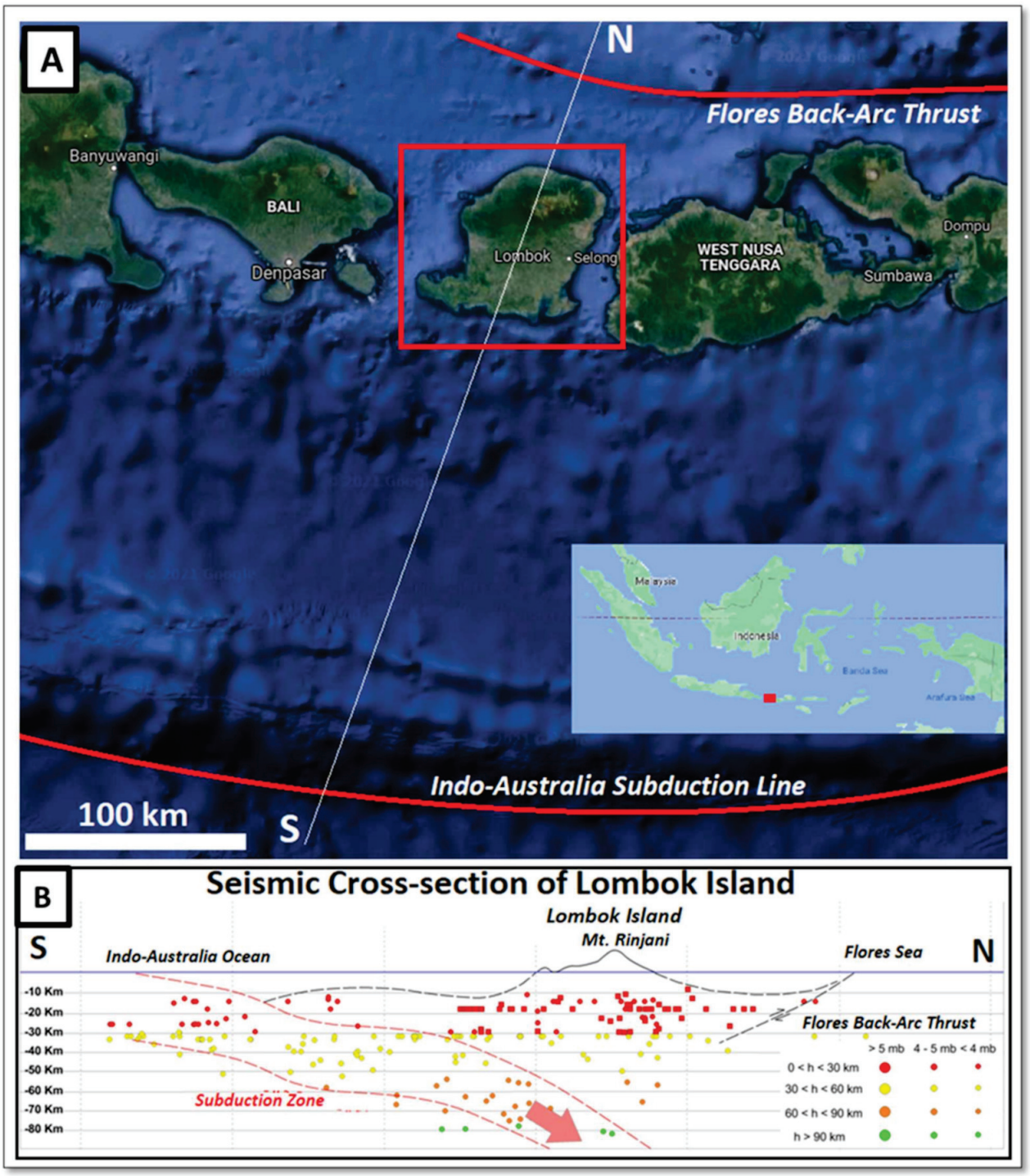

Figure 1. (**A**) Map view of Lombok Island (Google Maps). (**B**) Cross-section of Lombok Island [10].

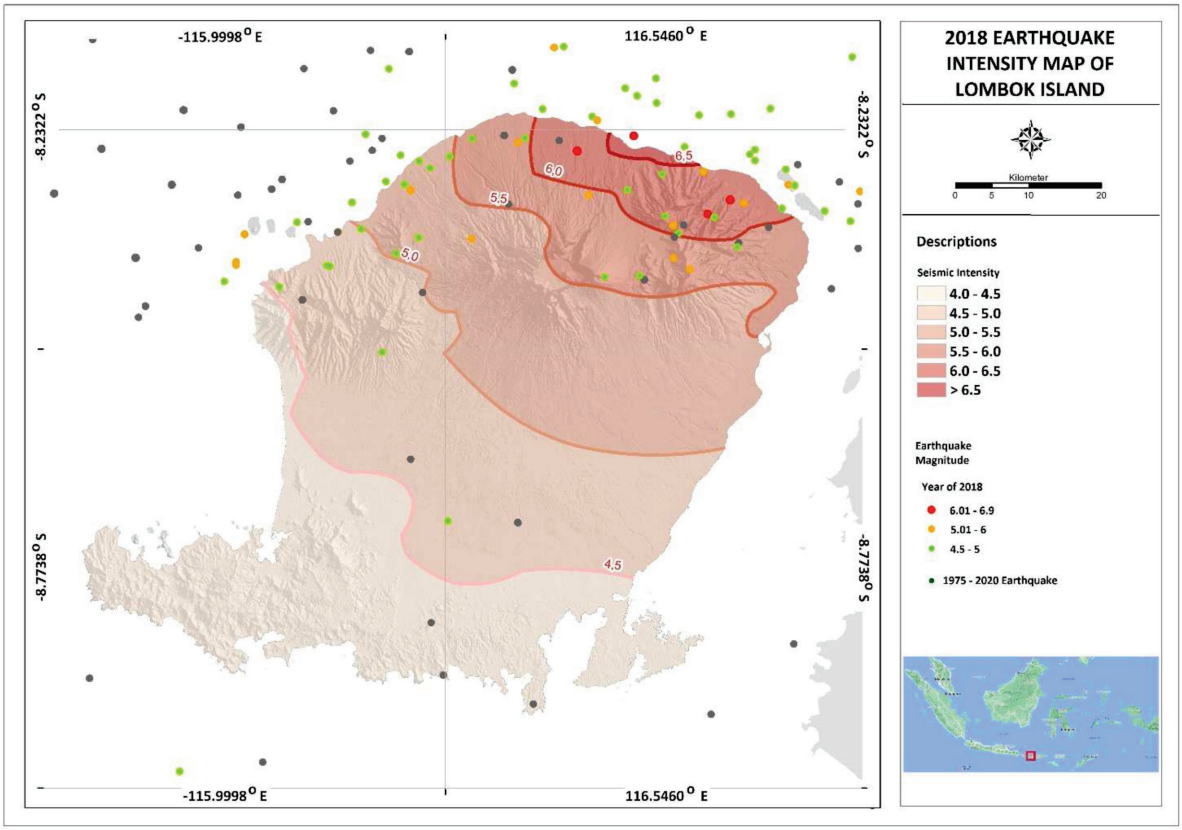

Figure 2. Distribution and intensity map of the Lombok Island Earthquakes, January–October 2018 (Epicenter coordinate based on USGS).

2. Materials and Methods

The availability of microzonation maps is one of the factors that makes Mataram City a research area, with well-collected data on losses and damages to buildings after the 2018 Lombok earthquake. The city of Mataram has six districts, such as the Ampenan District, Sekarbela District, Selaparang District, Mataram District, Cakranegara District, and Sandubaya District. All districts have different values of loss and deterioration to the buildings and their microzonation areas.

2.1. Study Area

Mataram is a land relatively flat, undulating topography, with a slope of 0–2% covering an area of 3.216 hectares and a bumpy area with a slope of more than 2–14% surrounding an area of 2.909 hectares. The altitude of Mataram City is approximately 0–50 m above sea level. These conditions indicate that most of the city is a plain area. The western part of the city is occupied by the flat-sloping area while the eastern has rather high-bumpy relief. The overlay area, with flat physiography, has two conflicting implications. First, flat areas have positive values, namely the construction of infrastructure and facilities which physically have fewer technical obstacles, and the development funding is relatively cheaper. Second, a flat area with an altitude almost parallel to the sea level has terrible implications, including flood-prone areas.

Based on the Geological map of Lombok sheet West Nusa Tenggara [23], three rock formations are covering the research area: Kalikupang Formation (Tqp), Kalibabak Formation (Tqb), and Lekopiko Formation (Qvl) that consists of volcanic rocks, sedimentary rocks, and intrusive rocks whose ages range from Tertiary to Quaternary. The engineering geological map of the Lombok Island, Mataram, lays on the geological unit of the Alluvium deposit (Al), consisting of the river, coastal, and swamp deposits, composed of silty sand, sandy silt, and loose sand [24]. Sedimentary swamp comprises sandy silt, silty clay, black to

grey color, fine-medium grained, very soft-firm, medium to high porosity. River sediment consists of sandy silt to silty clay and loose sand, brownish yellow-brown. It contains gravel, fine-medium-grained, very soft–dense, low to moderate plasticity, 3.50–6.50 m thick. Coastal deposits are black to grey sand, fine-grained, high porosity, containing shells. The engineering geological constraints or geological disasters prone are floods, abrasions, and tsunamis.

2.2. Damage and Loss Due to the Mataram Earthquake in August 2018

The earthquakes hit Mataram City, impacting six districts, including Ampenan, Sekarbela, Selaparang, Mataram, Cakranegara, and Sandubaya. The first earthquake occurred on 5 August 2018, with a magnitude of 7 Mb at 19.46 CIT (Central Indonesian Time). The coordinates of the epicenter of the earthquakes are 8.37° S, 116.48° E, about 27 km NE. The depth of the quake is around 15 km. The aftershock that caused considerable damage in Mataram was on August 9, 2018, at 13.25 CIT, with a magnitude 6.2 Mb located at 8.36° S–116.22° E, 27 km NE of Mataram with a depth of 12 km. On 19 August 2018, the next earthquake occurred at 22.56 CIT, located 75 km NE of Mataram with the magnitude V-VI of MMI (Modified Mercalli Intensity) [4].

The impacts of the Lombok earthquakes caused damages and losses in various sectors such as residential, infrastructure, social, economic, and cross-sectoral, which have disrupted public activities and services in the affected areas based on the data from the Post-Natural Disaster Reconstruction and Rehabilitation Action Plan. This natural disaster caused total damage and loss of 69,008,289 US$. The tremendous damage and loss occurred in some sectors comprising the residential sector amounted to 34,905,750 US$; the social sector amounted to 25,335,416 US$; the cross-sector amounted to 7,023,475 US$; the productive economic industries amounted to 1,743,648 US$.

The amount or pattern of building damage caused by the earthquake that impacted Mataram demonstrates the pattern's conformance with the microzonation map. The proportion of building damage by the district is depicted in Figure 3. The Sekarbela district (21.66 percent) and Ampenan (19.76 percent) have suffered the worst damage, while the Mataram district (8.75 percent), Selaparang (8.75 percent), and Sandubaya (7.76 percent) have sustained minor damage. The Cakranegara district in the blue zone is the least affected (1.7 percent).

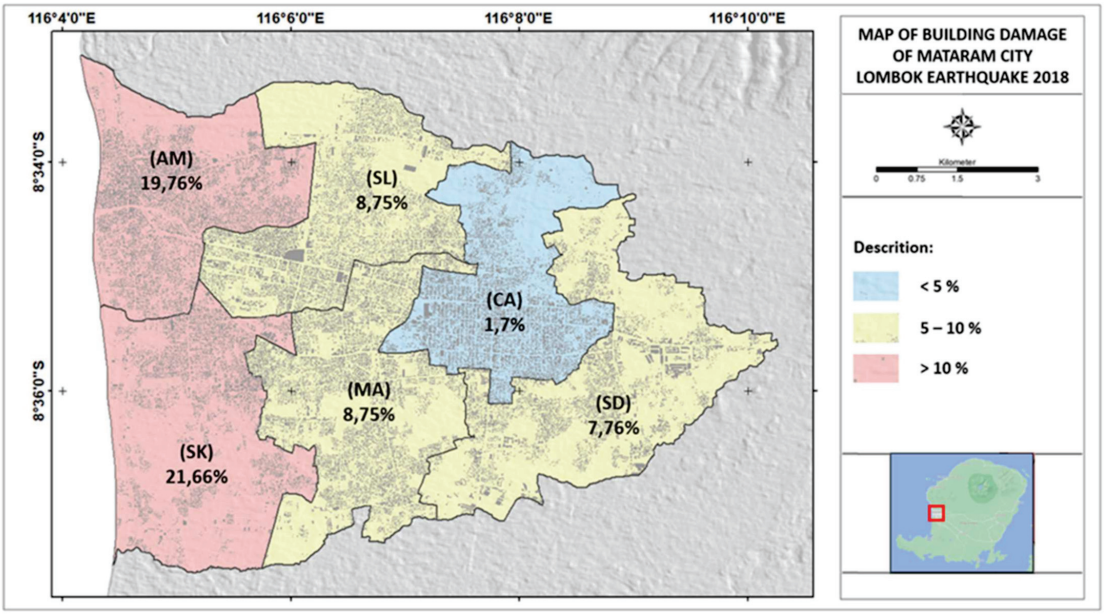

Figure 3. Buildings Damaged Map by the 2018 Lombok Earthquake in Mataram City.

2.3. Microzonation Map

The Potential Earthquake Ground Shaking Hazard Map (Microzonation) Mataram City, West Nusa Tenggara Province, produces three types of zones, namely red, yellow and blue zones (Figure 4). The red zone indicates that the area has a relatively high level of shaking with the morphology of volcanic fluvial plains. The yellow zone means that the area has a fairly medium level of shock in volcanic fluvial plains. The blue one indicates that the area has a relatively low level of shock with the morphology of the undulating volcanic plain of volcanoes. Regional zones on the Microzonation Map of Mataram involve four seismic microzonation parameters, which are dominant periods, soft sediment thickness, average rock/soil amplification, and soil rock site classification.

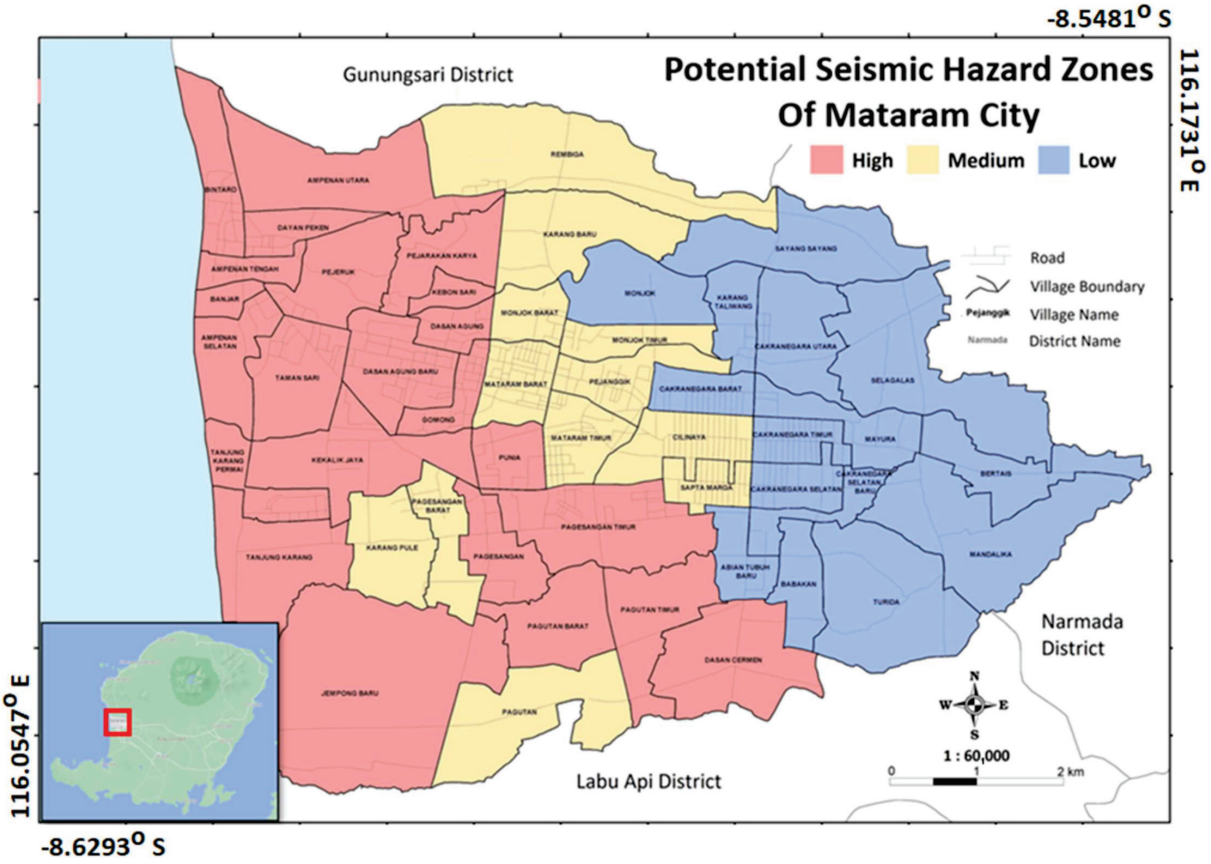

Figure 4. Microzonation Map of Mataram City (Modified from Geological Agency).

The red zone has the characteristics of a dominant period of more than 0.5 s, a soft sediment thickness of more than 30 m, an average amplification ranging from 1.9 to 2.3, and a site class of soft to medium soil. While the yellow zone has the characteristics of a dominant period ranging from 0.25 to 0.5 s, a thickness of soft sediment ranging from 10 to 30 m, an average amplification ranging from 1.6 to 1.9, and a medium soil site class. Finally, the blue zone has the characteristics of a dominant period of less than 0.25 s, a thickness of soft sediment below 10 m and amplification below 1.6, and a hard soil site class.

After generating three types of zones based on the level of shock on the Earthquake Potential Map (Microzonation) of Mataram City, West Nusa Tenggara Province, these zones can be developed based on disaster mitigation recommendations for safer development.

The red zone has a relatively high level of shock. Therefore, this area is not recommended to construct houses or critical and emergency (IV) facilities. However, once facility (IV) has been built, it needs to be reviewed with special geological studies, site investigations, and specialized foundation designs. The yellow zone with a relatively moderate level of shock is recommended for medium-risk (II) facilities built in this zone. The construction

of medium-risk (II) facilities must comply with the provisions of the local building code. The blue zone, which has a relatively low level of shock, is recommended to build facilities in building categories I, II, III, and IV (Table 1).

Table 1. Matrix of potential earthquake hazard of Mataram City (Modified from Geological Agency, 2015).

Potential Seismic Hazard Zone	Landform	Land Use	Recommendations
High Potential Seismic Hazard Zone	Fluvio Volcanic Plan	Public services 70%, Settlement 50% Plantation 60%, Industrial area 100% Defense and security 50%, Agricultural area 60 %	▪ Essential and emergency facilities (IV) should not be built in this zone. ▪ Existent facilities (IV) should be re-evaluated. Retro-fitting of facilities (IV) should be performed. ▪ Require special geological studies, site investigations and special foundation designs. ▪ Low-risk facilities (I) can be built in this zone.
Medium Potential Seismic Hazard Zone	Fluvio Volcanic Plain	Public services 15%, Settlement 30%, Plantation 25%, Defense and security 30%, Agricultural area 20%	▪ Medium-risk facilities (I, II) can be built in this zone. ▪ Enact and adopt building code regulations that adequately represent the seismic hazards. (I, II)
Low Potential Seismic Hazard Zone	Undulating Fluvio Volcanic Plain	Public services 15%, Settlement 20% Plantation 15%, Defense and security 20%, Agricultural area 20%	▪ Facilities (I, II, III and IV) can be built in this zone. ▪ City development is recommended in this zone.

Note: (Facilities I: low risk, such as agriculture, livestock, warehouse, fishery; Facilities II: Medium Risk, such as housing, apartment, office buildings, markets, factories; Facilities III: High Risk, such as stadium, cinemas, medical facilities, prisons; Facilities IV: Essential Facilities, such as hospitals, monumental buildings, schools, energy generation center, public facilities for emergencies.)

According to the microzonation map, it has been found that each district has a zonation of the potential hazardous ground shocks that differ according to the distribution of soil and rocks characteristics. The largest red zone coverages are respectively in Sekarbela (SK), Ampenan (AM), Mataram MA), Selaparang (SL), Sandubaya (SD) and Cakranegara (CA). The results of microzonation research are directly proportional to the damage and losses that occur. These facts are summarized in Table 1, where it has been found that the Sekarbela (SK) district, with the most significant red zone of 88.52%, experienced enormous damage and loss. Meanwhile, the Cakranegara (CA) district, which has the largest blue zone of 85.37%, experienced the slightest damage and loss.

2.4. Worksteps

The Geographic information system is a computer-based information system that focuses on the geography of an area, which can be used and designed to compile, manipulate, process, display, and analyze data that have spatial information. The relation between equal intervals, natural breaks, manual and statistical examination, all of which are GIS-default operations, are the most common mathematical approaches for data classification [25].

The GIS-based data for the land-use suitability analysis has been used in various situations, including geological favorability [26–28]. Simple processes, such as laying a road map over a map of local wetlands, or more complex processes, such as multiplying and adding map characteristics of different values to calculate averages and correlations, can be represented by these outputs. This process could be a visual action at its most basic level, but analytical activities require combining one or more data layers [29–32].

The superimposed research was conducted by correlating the Earthquake Hazard Potential (Microzonation) map of Mataram City, West Nusa Tenggara Province, with data on

damage and losses in each district in Mataram Municipality, based on the BNPB report [4]. The comparison of the two data aimed to determine the correlation between both data is either directly or inversely proportional, or even irregular way. The comparisons were also made on the residential area data from each district obtained from the digitization results of Google Earth satellite imagery. It was performed because the variable density of residential could affect the value of losses caused by earthquake disasters.

This research uses the weighted overlay GIS method (Figure 5). The weighted overlay method analyses spatial data using the overlay technique of several raster maps related to the factors that affect the vulnerability assessment of a problem. Weighted Overlay can combine various inputs in a grid map [33]. This method solves problems with many criteria, such as optimal site selection or suitability modeling.

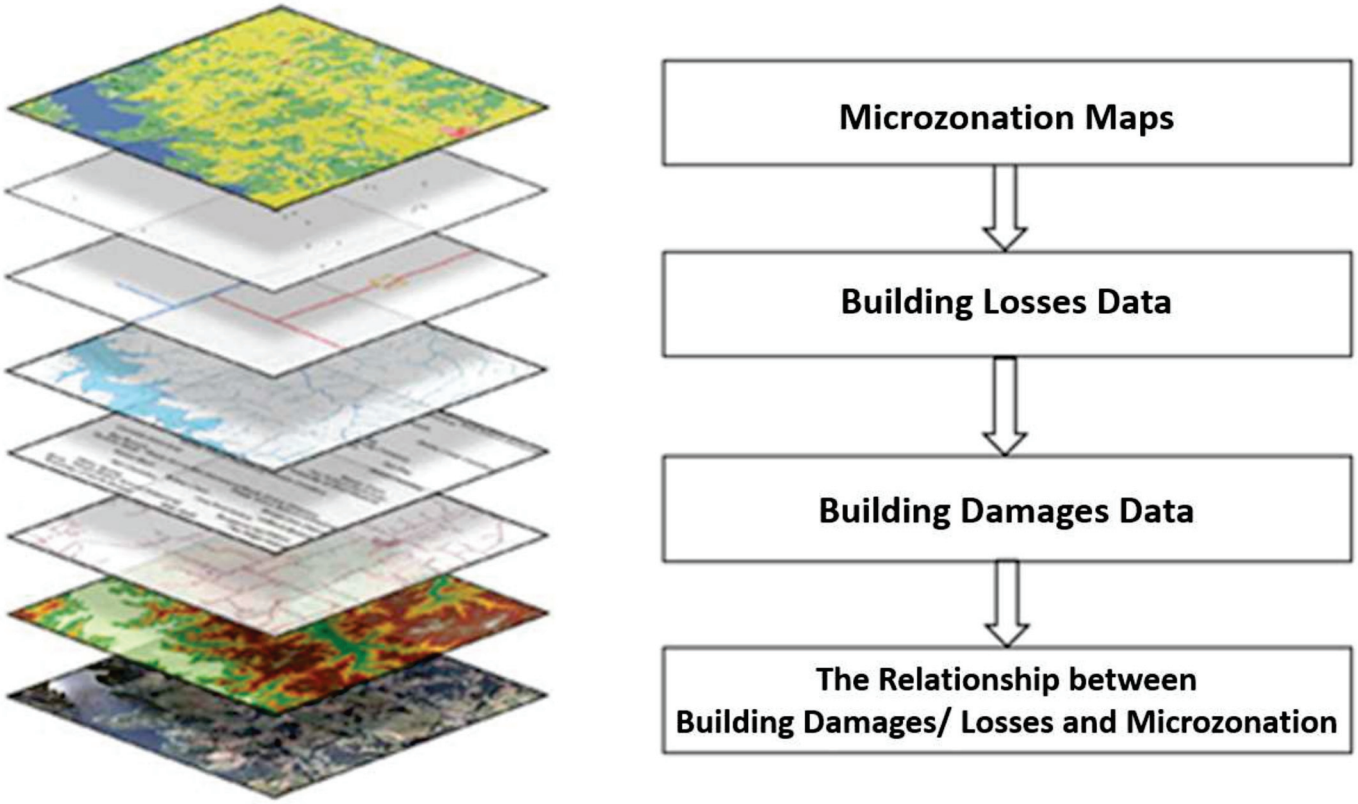

Figure 5. Illustration of overlay method in this research.

Applying the latter approach to the case of the loss and damage data values and the microzonation map units above (Figure 6), the average element values can be obtained using Equation (1) [26]:

$$Zi = \frac{\sum_{j=1}^{n} \partial ij.zj}{\sum_{j=1}^{n} \partial ij} \quad (1)$$

where are:

i = microzonation units
j = loss damage data values
z = variable in the source zones
∂ij = overlapping target zone

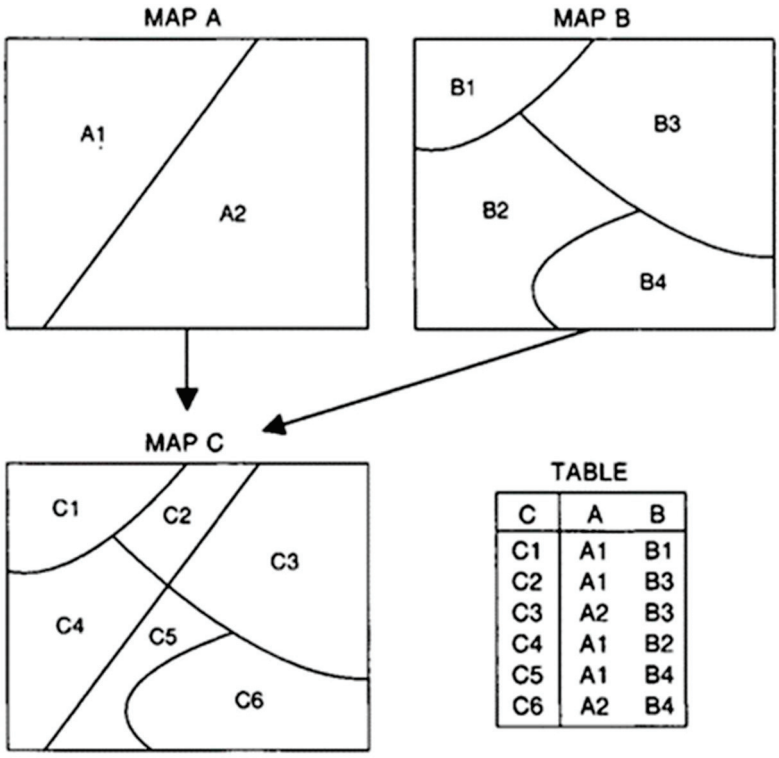

Figure 6. Overlay of two polygon maps, producing a new set of polygons common to both maps. The polygons in C are not linked to the polygons of maps A and B in a polygon attribute Table 2.

3. Results

The level of damage to buildings after the Lombok earthquake (Table 2), adapted from the Mataram city redevelopment action plan in 2018, shows the number of damaged houses in each district in Mataram City. The highest level of damage is in the Ampenan (AM) district, where as many as 4773 units are dominated by light (3162 units), moderate (957 units) and severe (654 units) damage; Second, the number of houses damaged in the Sekarbela district was 3774 units, consisting of 1540 units heavily damaged, moderately damaged (944 units) and lightly damaged (1290 units); Selaparang district contained 1972 damaged houses, dominated by light (1399 units), moderate (495 units), heavily (78 units) damaged; in Mataram Regency, the number of houses damaged was 1467 houses, consisting of lightly (1101 units), moderately (267 units) and heavily (99 units) damaged; Furthermore, the Sandubaya district suffered damage as many as 1211 housing units, consisting of lightly (1096 units), moderately (96 units) and heavily (19) damaged units; Finally, Cakranegara Regency suffered damage as many as 270 houses, with light (246 units), moderate (18 units) and six houses heavily damaged.

The value of losses due to house damage is calculated based on the standard value of the level of damage due to the Lombok earthquake (Table 3), where total loss (100%) is US$ 6320; heavily damaged (80%) worth US$ 5056; moderate damage (50%) worth US$ 3160; and Low (20%) at $1264. Then the value of the loss for each district (Table 4) is the highest loss suffered by Sekarbela (SK) of US$ 12,399,840, the second loss of Ampenan (AM) US$ 10,327,512, followed by Selaparang (SL) of US$ 3,726,904; Mataram (MA) suffered a loss of US$ 2,735,928; Sandubaya (SA) of US$ 1,784,768 and the last is Cakranegara (CA) of US$ 398,160.

Table 2. Level of buildings damages after the earthquake per district in Mataram City (adapted from Mataram City redevelopment action plan, BNPB).

No	District	Damage Data (Units)			
		Heavy	Moderate	Light	Total
1	Ampenan (AM)	654	957	3.162	4.773
2	Cakranegara (CA)	6	18	246	270
3	Mataram (MA)	99	267	1.101	1.467
4	Selaparang (SL)	78	495	1.399	1.972
5	Sandubuya (SD)	19	96	1.096	1.211
6	Sekarbela (SK)	1.540	944	1.290	3.774
	Total	2.396	2.777	8.294	13.467

Table 3. Standard budget for house rehabilitation based on level of damage (BNPB).

Total Loss	High	Moderate	Low
100%	80%	50%	20%
US$ 6320	US$ 5056	US$ 3160	US$ 1264

Table 4. Value of losses after the earthquake per district in Mataram City.

No	District	Value of Damage (US$)			
		Heavy	Moderate	Light	Total
1	Ampenan (AM)	3,306,624	3,024,120	3,996,768	10,327,512
2	Cakranegara (CA)	30,336	56,880	310,944	398,160
3	Mataram (MA)	500,544	843,720	1,391,664	2,735,928
4	Selaparang (SL)	394,368	1,564,200	1,768,336	3,726,904
5	Sandubuya (SD)	96,064	303,360	1,385,344	1,784,768
6	Sekarbela (SK)	7,786,260	2,983,040	1,630,560	12,399,840
Total		12,114,176	8,775,320	10,483,616	31,373,112

The loss rating and dominance of the red zone reflect a pattern of conformity based on the magnitude of losses caused by the earthquake (Table 5). The ranking of earthquake losses is directly related to the prevalence of the red zone distribution in the districts of Sekarbela (SK) and Ampenan (AM). It implied that areas with red zone domination post-earthquake would also suffer significant losses. Based on the rating of the loss value compared to the level of the vulnerability zone (red), it shows the suitability of the pattern. The value of losses due to the earthquake is directly proportional to the dominance of the red zone distribution in the Sekarbela and Ampenan districts. These show that post-earthquake, subdistricts with high red zone dominance will also have high losses.

Table 5. Comparative tables of regional microzonation and damage-loss data.

District	Rank (Damages and Losses)			Zone (%) (Microzonation)		
	Population	Damage	Loss	Red	Yellow	Blue
Sekarbela (SK)	5	2	1	88.52	11.48	0
Ampenan (AM)	4	1	2	79.81	20.19	0
Mataram (MA)	3	4	4	67.01	32.99	0
Selaparang (SL)	1	3	3	33.04	55.14	11.82
Sindubaya (SD)	2	5	5	17.36	0	82.64
Cakranegara (CA)	6	6	6	0	14.63	85.37

4. Discussion

The research area has a thickness of soft rock (volcanic fluvial deposits) which causes earthquake waves to be trapped and amplified, explaining the higher degree of damage. The distribution of damage from the earthquake on Lombok Island was irregular. The study shows that the microzonation map helps determine the damage zone and level of disaster vulnerability due to the earthquake hazards. Earthquake hazard microzonation mapping is an essential tool for land use planning in infrastructure development and mitigation strategies. It provides easy-to-read charts and maps, making it easier for governing bodies to make decisions. It is highly recommended that microzonation studies support urban planning development, residential areas, and areas of people's economic activities in disaster-safe areas.

Microzonation studies over large areas can support urban development plans and designs. This study can mitigate potentially earthquake-prone areas by recording the physical properties of rocks in static conditions so that determining the designation of an area can be more manageable. This research is relatively inexpensive, easy, and suitable for developing and utilizing regions. The blue zone area must be designated for housing, buildings, and areas for community economic activities. While the yellow zone is suitable for developing community activities such as workshops and carpentry, locations included in the red zone allocates as a buffer area for environmental conservation that is reforested by governance programs to reduce carbon emissions.

The level of damage to areas that caused significant losses is dominant in the red zone, although the highest population is not in the areas where the loss rate is high. Local governments should reform land usage and distribution following the disastrous Lombok earthquake.

Based on the comparison between the level of building damage and the value of the loss, it concluded that although the number of damaged houses in the Ampenan district is the highest (4773 units) worth US$ 10,327,512, the loss value is still below that of the Sekarbela district (3774 units), but the loss value is US$ 12,399,840. The number of houses with severe damage dominates the number of damaged in Sekarbela (1540 units), while the value of losses in other districts is proportional to the level of damage. The high level of loss in Sekarbela, caused by the dominance of the number of heavily damaged houses being more than Ampenan.

Future development planning may be more successful in site selection for important infrastructure investment decisions with a scientific understanding of each earthquake hazard level [34,35]. During the 2018–2020 timeframe, 61.000 homes were built for earthquake victims, ranging from mildly damaged to badly damaged homes, while 225.000 buildings were constructed for public amenities and social functions, and millions of dollars were spent to recover the damage [36]. Risk transfer is a strategy to cope with the effects of natural disasters. Natural disasters are unforeseeable, unpredictable phenomena that can have a devastating impact on the population, wreaking havoc on infrastructure and causing enormous human and economic losses [5]. An alternative to risk transfer is disaster insurance, especially earthquake insurance. Earthquake insurance is essential to recover from earthquake disasters and protect from the associated financial losses [37,38].

5. Conclusions

Its location in the collision zone causes frequent natural disasters in Indonesia. Earthquakes are one of such disasters caused by tectonic activities. The dynamic interaction of numerous tectonic plates in eastern Indonesia causes high seismicity rates, which resulted in catastrophic damaging earthquake sequences on Lombok Island in 2018. The research area in the present study has a thickness of the soft rock (volcanic fluvial deposits), causing earthquake waves to be trapped and amplified, which explains the higher level of damage. The distribution of damage caused by the earthquake on the island of Lombok is irregular. Therefore, it can be concluded that mapping hazard zones based on microzonation are directly proportional to the damage and losses caused by the earthquake. In other words, areas included in the red zone are the most vulnerable to damage and losses. In other words, areas included in the red zone are the most vulnerable to damage and losses.

Microzonation research is a valuable tool for mapping potential earthquake threats in a particular area, making research more detailed and accurate. In addition, it is essential to conduct regional tectonic research and its influence on local geological structures that impact Tertiary bedrock covered by Quaternary volcanic rock from the eruption of Mount Rinjani. It is suggested that local government improve the "building code" rules when applying for building permits.

Based on the findings of this study, it is also suggested that additional models be investigated to predict the amount of seismic activity, such as the Markov Chain model, which has been applied to the Algerian region [39]. As a result, the seismic activity can be observed using multiple models to gain a more comprehensive understanding. Meanwhile, since this region is located in a steep area, land use for forests and farmland does not require considerable consideration due to the earthquakes. As a result, substantial consideration must be given to slope stability, building structures, and available types of settlement materials [40].

Author Contributions: B.S. performed manuscript writing, sampling, measurements, data analysis, and summarized conclusions of this research. D.M. supervised writing, organizing structure of the manuscript, and morphotectonic and neotectonic data analysis. M.S.S. performed data sampling and acquisition. G.O.M. (B.Sc., junior researcher, geomorphologist) performed data measurement. S.B. supervised data analysis. H.H. supervised data analysis. All authors have read and agreed to the published version of the manuscript.

Funding: This research received no external funding.

Institutional Review Board Statement: Not applicable.

Informed Consent Statement: Not applicable.

Data Availability Statement: The original data come from Authors and references from Geological Agency and BNPB.

Acknowledgments: The authors would like to express their gratitude to the Coordinating Ministry of Maritime and Investment and the Ministry of Finance of Indonesia for their support in this research.

Conflicts of Interest: This research is purely performed to complete doctoral studies. The author declares no conflict of interest.

References

1. Lüschen, E.; Müller, C.; Kopp, H.; Engels, M.; Lutz, R.; Planert, L.; Shulgin, A.; Djajadihardja, Y.S. Structure, evolution and tectonic activity of the eastern Sunda forearc, Indonesia, from marine seismic investigations. *Tectonophysics* **2011**, *508*, 6–21. [CrossRef]
2. Ramdani, F.; Setiani, P.; Setiawati, D.A. Analysis of sequence earthquakes of Lombok Island, Indonesia. *Prog. Disaster Sci.* **2019**, *4*, 100046. [CrossRef]
3. Supendi, P.; Nugraha, A.D.; Widiyantoro, S.; Pesicek, J.D.; Thurber, C.H.; Abdullah, C.I.; Daryono, D.; Wiyono, S.H.; Shiddiqi, H.A.; Rosalia, S. Relocated aftershocks and background seismicity in eastern Indonesia shed light on the 2018 Lombok and Palu earthquake sequences. *Geophys. J. Int.* **2020**, *221*, 1845–1855. [CrossRef]
4. BNPB. *Action Plan for Post-Earthquake Rehabilitation and Reconstruction in 2018–2019*; National Disaster Management Agency (BNPB): New Delhi, India, 2018.

5. Hidalgo, J.; Baez, A.A. Natural Disasters. *Crit. Care Clin.* **2019**, *35*, 591–607. [CrossRef] [PubMed]
6. Hidayat, E.; Muslim, D.; Zakaria, Z.; Permana, H.; Wibowo, D.A. Tectonic geomorphology of the Karangsambung area, central Java, Indonesia. *Rud. Geol. Naft. Zb.* **2021**, *36*, 85–105. [CrossRef]
7. Koulali, A.; Susilo, S.; McClusky, S.; Meilano, I.; Cummins, P.; Tregoning, P.; Lister, G.; Efendi, J.; Syafi'I, M.A. Crustal strain partitioning and the associated earthquake hazard in the eastern Sunda-Banda Arc. *Geophys. Res. Lett.* **2016**, *43*, 1943–1949. [CrossRef]
8. DeMets, C.; Calais, E.; Merkouriev, S. Reconciling geodetic and geological estimates of recent plate motion across the Southwest Indian Ridge. *Geophys. J. Int.* **2017**, *208*, 118–133. [CrossRef]
9. Sarris, C.; Loupasakis, P.; Soupios, V.; Trigkas, F. Vallianatos, Earthquake vulnerability and seismic risk assessment of urban areas in high seismic regions: Application to Chania City, Crete Island, Greece. *Nat. Hazards* **2010**, *54*, 395–412. [CrossRef]
10. Geological Agency. *Microzonation Potential Earthquake Hazard Assessment Map of Mataram City, West Nusa Tenggara Province*; Geological Agency Ministry of Energy and Mineral Resources: Bandung, Indonesia, 2015.
11. USGS. Available online: https://earthquake.usgs.gov/earthquakes/map (accessed on 5 January 2022).
12. Kanai, K.; Tanaka, T.; Osada, K. Measurement of the Micro-tremor 1. *Bull. Earthq. Res. Inst. Univ. Tokyo* **1954**, *32*, 199–209.
13. Nakamura, Y. Clear identification of fundamental idea of Nakamura's technique and its applications. In Proceedings of the XII World Conference Earthquake Engineerin, Auckland, New Zealand, 30 January–4 February 2000. Paper no 2656.
14. Khalili, M.; Mirzakurdeh, A.V. Fault detection using microtremor data (HVSR-based approach) and electrical resistivity survey. *J. Rock Mech. Geotech. Eng.* **2019**, *11*, 400–408. [CrossRef]
15. Soehaimi, A.; Muslim, D.; Kamawan, I.; Negara, R.S. Microzonation of the Liwa city on the great sumatera active fault and giant ranau volcanic complex in south sumatera, Indonesia. In *Engineering Geology for Society and Territory*; Springer: Cham, Switzerland, 2015; Volume 5. [CrossRef]
16. Molnar, S.; Cassidy, J.F.; Castellaro, S.; Cornou, C.; Crow, H.; Hunter, J.A.; Matsushima, S.; Sánchez-Sesma, F.J.; Yong, A. Application of Microtremor Horizontal-to-Vertical Spectral Ratio (MHVSR) Analysis for Site Characterization: State of the Art. *Surv. Geophys.* **2018**, *39*, 613–631. [CrossRef]
17. Syahbana, A.J.; Iqbal, P.; Irsyam, M.; Asrurifak, M.; Hendriyawan, H. Smoothed gridded seismicity effect for land-use development, case study: Kalimantan Island, Indonesia. *Rud. Geol. Naft. Zb.* **2021**, *36*, 115. [CrossRef]
18. Idriss, I.M.; Boulanger, R.W. *Soil Liquefaction During Earthquakes*; EERI Publication, Monograph MNO-12; Earthquake Engineering Research Institute: Oakland, New Zeland, 2008.
19. Ibs-von Seht, M.; Wohlenberg, J. Seismic noise spectra used to map thickness of soft sediments. In Proceedings of the 58th EAEG Meeting, Amsterdam, The Netherlands, 7 June 1996. [CrossRef]
20. Seht, M.I.V.; Wohlenberg, J. Microtremor Measurements Used to Map Thickness of Soft Sediments. *Bull. Seismol. Soc. Am.* **1999**, *89*, 250–259. [CrossRef]
21. Tuladhar, R.; Yamazaki, F.; Warnitchai, P.; Saita, J. Seismic microzonation of the greater Bangkok area using microtremor observations. *Earthq. Eng. Struct. Dyn.* **2004**, *33*, 211–225. [CrossRef]
22. Yulianur, A.; Saidi, T.; Setiawan, B.; Sugianto, S.; Rusdi, M.; Affan, M. Microtremor datasets at liquefaction site of Petobo, Central Sulawesi-Indonesia. *Data Brief* **2020**, *30*, 105554. [CrossRef]
23. Mangga, S.; Atmawinata, S.; Hermanto, B.; Setyogroho, B.; Amin, T.C. *Geological Map of The Lombok Sheet, West Nusa Tenggara*; Geological Research and Development Centre: Bandung, Indonesia, 1994.
24. Sugiyanto, P.T.; Wafid, M. *Engineering Geological Map of The Lombok Island, West Nusa Tenggara*; Geological Agency: Bandung, Indonesia, 2014.
25. Jena, R.; Pradhan, B.; Beydoun, G. Earthquake vulnerability assessment in Northern Sumatra province by using a multi-criteria decision-making model. *Int. J. Disaster Risk Reduct.* **2020**, *46*, 101518. [CrossRef]
26. Bonham-Carter, G. Geographic information systems for geoscientists: Modelling with GIS. *Comput. Methods Geosci.* **2014**, *13*, 398.
27. Janssen, R.; Rietveld, P. *Multicriteria Analysis and Geographical Information Systems: An Application to Agricultural Land Use in the Netherlands*; Geographical Information Systems for Urban and Regional Planning, Kluwer: Dordrecht, Netherlands, 1990. [CrossRef]
28. Keller, C.P. Geographic information systems for geoscientists: Modelling with GIS. *Comput. Geosci.* **1995**, *21*. [CrossRef]
29. Malczewski, J. GIS-based land-use suitability analysis: A critical overview. *Prog. Plan.* **2004**, *62*, 3–65. [CrossRef]
30. Pereira, J.M.C.; Duckstein, L. A multiple criteria decision-making approach to gis-based land suitability evaluation. *Int. J. Geogr. Inf. Syst.* **1993**, *7*, 407–424. [CrossRef]
31. Yenigun, K.; Ecer, R. Overlay mapping trend analysis technique and its application in Euphrates Basin, Turkey. *Meteorol. Appl.* **2013**, *20*, 427–438. [CrossRef]
32. Yesilnacar, M.I.; Cetin, H. An environmental geomorphologic approach to site selection for hazardous wastes. *Environ. Geol.* **2008**, *55*, 1659–1671. [CrossRef]
33. Thomas, C.F. An Introduction to Geographic Information Systems. In *Libraries*; CRC Press: London, UK, 2019. [CrossRef]
34. Sekac, T.; Jana, S.K.; Pal, I.; Pal, D.K. GIS Based Evaluation in Earthquake Hazard Microzonation—A Case Study of Madang and Morobe Province, Papua New Guinea. *Int. J. Adv. Eng. Res. Sci.* **2016**, *3*, 236817. [CrossRef]
35. Skoufias, E. Economic crises and natural disasters: Coping strategies and policy implications. *World Dev.* **2003**, *31*, 1087–1102. [CrossRef]

36. Mardialina, M.; Munir, A.M. Disaster Recovery in Social Aspect: Evidence from Lombok Earthquake 2018. In Proceedings of the 6th International Conference on Education & Social Sciences (ICESS 2021), Java, Indonesia, 31 July 2021. [CrossRef]
37. Goda, K.; Wilhelm, K.; Ren, J. Relationships between earthquake insurance take-up rates and seismic risk indicators for Canadian households. *Int. J. Disaster Risk Reduct.* **2020**, *50*, 101754. [CrossRef]
38. King, A.; Middleton, D.; Brown, C.; Johnston, D.; Johal, S. Insurance: Its role in recovery from the 2010-2011 Canterbury Earthquake sequence. *Earthq. Spectra* **2014**, *30*, 475–491. [CrossRef]
39. Dahmoune, B.; Mansour, H. Algerian northwestern seismic hazard evaluation based on the markov model. *Rud. Geol. Naft. Zb.* **2019**, *34*, 113–125. [CrossRef]
40. Munirwansyah; Irsyam, M.; Munirwan, R.P.; Yunita, H.; Zulfan, U.M. Geotechnical approach for occupational safety risk analysis of critical slope in open pit mining as implication for earthquake hazard. *IOP Conf. Ser. Mater. Sci. Eng.* **2018**, *352*, 012035. [CrossRef]

sustainability

MDPI

Article

Impact of Urbanization on Seismic Risk: A Study Based on Remote Sensing Data

Liqiang An [1,2,*] and Jingfa Zhang [3]

[1] Key Laboratory of Earthquake Engineering and Engineering Vibration, China Earthquake Administration, Institute of Engineering Mechanics, China Earthquake Administration, Harbin 150080, China
[2] Emergency Information Center, Tianjin Earthquake Agency, Tianjin 300201, China
[3] Key Laboratory of Emergency Satellite Engineering and Application, Ministry of Emergency Management, Beijing 100124, China; zhangjingfa@hotmail.com
* Correspondence: an-liqiang@hotmail.com

Abstract: The management of seismic risk is an important aspect of social development. However, urbanization has led to an increase in disaster-bearing bodies, making it more difficult to reduce seismic risk. To understand the changes in seismic risk associated with urbanization and then adjust the risk management strategy, remote-sensing technology is necessary. By identifying the types of earthquake-bearing bodies, it is possible to estimate the seismic risk and then determine the changes. For this purpose, this study proposes a set of algorithms that combine deep-learning models with object-oriented image classification and extract building information using multisource remote sensing data. Following this, the area of the building is estimated, the vulnerability is determined, and, lastly, the economic and social impacts of an earthquake are determined based on the corresponding ground motion level and fragility function. Our study contributes to the understanding of changes in seismic risk caused by urbanization processes and offers a practical reference for updating seismic risk management, as well as a methodological framework to evaluate the effectiveness of seismic policies. Experimental results indicate that the proposed model is capable of effectively capturing buildings' information. Through verification, the overall accuracy of the classification of vulnerability types reaches 86.77%. Furthermore, this study calculates social and economic losses of the core area of Tianjin Baodi District in 2011, 2012, 2014, 2016, 2018, 2020, and 2021, obtaining changes in seismic risk in the study area. The result shows that for rare earthquakes at night, although the death rate decreased from 2.29% to 0.66%, the possible death toll seems unchanged, due to the increase in population.

Keywords: remote sensing; earthquakes; exposure evaluation; risk assessment; vulnerability assessment; seismic risk management; Tianjin Baodi; China

Citation: An, L.; Zhang, J. Impact of Urbanization on Seismic Risk: A Study Based on Remote Sensing Data. *Sustainability* **2022**, *14*, 6132. https://doi.org/10.3390/su14106132

Academic Editors: Stefano Morelli, Veronica Pazzi and Mirko Francioni

Received: 5 April 2022
Accepted: 17 May 2022
Published: 18 May 2022

1. Introduction

Urbanization refers to the transformation of rural populations into urban populations, the migration of rural people into cities and people no longer working in agriculture [1]. Towns and cities are formed and increase in size with this process. In recent decades, industrialization and modernization have accelerated the process of urbanization, and, as a result, the proportion of the urban population has been increasing worldwide, notably in China. China's urbanization rate has increased steadily over the last decades. In 1950, 13% of people in China lived in cities. By 2010, the urban share of the population had grown to 45% [2]. The Seventh Population Census of China, conducted in 2020, showed that about 63.9 % of the total population lived in cities in 2020.

However, as urbanization continues, the accumulation of the urban population and wealth will directly increase the risk of disaster and pose challenges for disaster mitigation [3–5].

For China, earthquakes are the most damaging of all natural disasters. Over the past decade, more than 50% of deaths from natural disasters in China were caused by earthquakes [6]. As a consequence of the influence of the Pacific Rim and Eurasian seismic belts, China has the most frequent continental earthquakes in the world and faces a significant risk of earthquake disasters [7,8]. Additionally, statistical data show that 41% of large Chinese cities, 33% of prefecture-level cities, and 30% of county-level towns are located in earthquake-prone areas [9].

With the rapid development that has occurred in recent years, China's earthquake disaster mitigation strategy has paid more attention to pre-disaster prevention [10]. This is consistent with the Sendai Framework's focus on disaster preparedness and its emphasis on understanding disaster risk, strengthening disaster risk governance, managing disaster risk, and strengthening preparedness for an effective response [11]. Considering the changes in seismic risk associated with urbanization is critical in improving seismic risk management capabilities and the mitigation of seismic risk [12].

Generally, the seismic risk analysis models used by organizations or institutions around the world, such as The Global Earthquake Model (GEM) [13] and the Federal Emergency Management Agency (FEMA) [14], involve the quantification of three main components, namely hazard, exposure, and vulnerability [15]. Assuming that seismic hazard remains stable in the near future, then the seismic risk is primarily affected by changes in disaster-bearing bodies and their vulnerability.

Furthermore, because social and economic losses due to earthquake disasters are mainly determined by the destruction of structures, it is worth paying closer attention to changes in the building stock.

In recent years, remote sensing technology has become widely used in seismic risk assessment and management due to its ability to obtain large-scale geospatial information quickly and effectively [16]. The international Group on Earth Observations put forward the idea of estimating the seismic vulnerability of buildings through remote sensing data in the work task of 2009–2011. Polli et al. [17] and Zhai Yongmei [18], respectively, proposed earthquake disaster risk estimation workflows based on remote sensing images in 2009. Initially, researchers focused on distinguishing building types based on their height and shape and how to extract geometric properties from remote sensing data about building shapes using remote sensing [19,20]. To improve the accuracy of exposure information extraction, combining statistical data, ground surveys, street views, and digital surface models with proxies obtained from remote sensing data has become a popular approach [20–29]. As well as this, to gather data for the risk assessment of historic monuments, the Wireless Sensors Network (WSN) system is paramount [30–32].

Most of the intelligent analysis algorithms that were developed as a result of the continuous evolution of computer vision tasks, from image-level understanding to pixel-level understanding, were developed to solve the problem of extracting information from remote sensing data.

Traditional feature learning methods often rely on creating features based on specific expertise and therefore often show reduced reusability. In addition, sophisticated methods may be required to handle irregular or complex data [33]. In contrast, deep learning methods learn deep features from the data themselves, which means expertise is not required, and the results based on deep features are much better than shallow methods. In visual recognition, convolutional neural networks outperform other deep learning models [34]. In principle, a CNN is a network that usually consists of many layers of operations, such as convolution, pooling, nonlinear activation functions, and normalizing, that can be divided into a feature extractor and a multilayer perceptron (MLP) [35]. In 2012, Alexnet [36] refreshed people's understanding of CNN. Then, the VGG frame [37] and Resnet model [38] were successively proposed. For semantic segmentation, Fully Convolutional Networks (FCNs), based on VGG and first proposed in 2015 [39], were the first to realize end-to-end segmentation. Several other models, including U-net [40], SegNet [41], PSPNet [42], DeepLab [43–45], and Mask R-CNN [46], are also capable of accurate segmentation, which

is commonly used in remote sensing classification [47–50].Overall, although the research on urbanization process analysis [51–58] and seismic risk assessment [17–29] using remote sensing data has achieved many results, the specific research does not address the changes in seismic risk caused by urbanization and the connection between the two. Accordingly, there is no established methodology within the field of remote sensing applications for understanding the seismic risk associated with urbanization.

Therefore, in this paper, a practical method of observing the changes in seismic risk under urbanization based on remote sensing data is proposed. The objectives of this study are as follows: (i) To improve the remote sensing data analysis method for earthquake bearing-body detection by integrating deep learning semantic segmentation and ensemble learning classification. (ii) To propose a comprehensive workflow for identifying seismic risk change under urbanization processes using remote sensing data. The remainder of this paper is organized as follows: Section 2 provides an overview of the study area and its materials. A method for identifying structural vulnerabilities that integrates object-oriented classification and deep-learning-based segmentation is described as well. Section 3 presents the experimental results in the study area. Section 4 discusses improvements and future directions. A comprehensive summary is given in Section 5.

2. Materials and Methods

2.1. Study Area

Figure 1 shows the study area of this article: the central area of the District Baodi, Tianjin, China, with an approximate population of more than 200,000 people and an area of 35 km^2, located at 39°43′ N,117°18′ E [59].

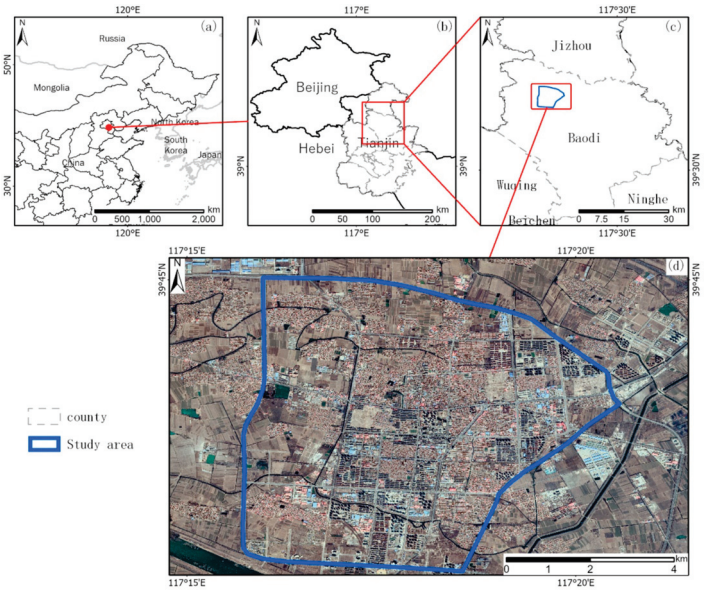

Figure 1. (**a**) Location of the study area in China. (**b**) Baodi District of Tianjin. (**c**) Location of the study area in Baodi. (**d**) Satellite map of the study area.

Tianjin is in the central part of the North China Plain. The city is a port city and the only megacity in China to have experienced a major earthquake in recent decades. Tianjin's District Baodi is a short drive from Beijing, Tangshan City, and the Tianjin downtown area [59]. The agriculture, industry, and tourism here have flourished over the past few decades, and the district has grown from a village to a county, then to a district [60]. However, the district is at risk of earthquakes. Throughout its history, District Baodi has been affected by many major earthquakes, including those of magnitude 7.8 in 1976 Tangshan and 8 in 1679 Sanhe-Pinggu [8]. These earthquakes caused extensive damage to Baodi, and the earthquake intensity was as high as VIII CSIS (China seismic intensity scale) in most areas [61]. An east-west fault in the region, the Baodi fault, shows evidence

of activity in the Quaternary [62]. Over the last ten years, District Baodi was affected by three earthquakes that measured magnitude 3.7, magnitude 4.0, and magnitude 3.3, on 14 January 2005, 18 June 2012, and 26 August 2012, respectively [8].

2.2. Data Sources

In this study, very high resolution (VHR) images, as well as medium-resolution images were collected. They are mainly from Gaofen-2 and Sentinel-2 sensors. ALOS-1 and WorldView-1 satellite data and Google Earth imagery were used as supplements in the years 2011, 2012, and 2014, as Gaofen-2 and Sentinel-2 satellites were not available over these years. At the same time, the census data and statistical yearbook data of the corresponding years were also collected, and the WorldPop [63] data were used as a reference for the spatial distribution of the population. Table 1 shows the information from the data source.

Table 1. Source of datasets.

Dataset	Source	Spatial Resolution	Time Scale
GF-1/6	China Center For Resources Satellite Data and Application http://36.112.130.153:7777/DSSPlatform/index.html (accessed on 9 March 2022)	2 m/8 m	2014–2020
GF-2		1 m/4 m	2016–2021
ZY-3		2 m/6 m	2012–2016
Sentinel 2	https://scihub.copernicus.eu/ (accessed on 9 March 2022)	10 m	2015–2021
Point of interest	https://lbsyun.baidu.com/ (accessed on 9 March 2022)	-	2018, 2020
Questionnaire	Field survey	-	2019
Statistical Yearbook	http://stats.tj.gov.cn/ (accessed on 9 March 2022)	-	2011–2021
Census data	http://stats.tj.gov.cn/ (accessed on 9 March 2022)	-	2010, 2020, 2021

In addition, four separate datasets were built for the four main tasks in this study: (i) footprint segmentation of single buildings, (ii) shadow segmentation of single buildings, (iii) rural building groups, and (iv) vulnerability classification of single buildings. Three of the datasets were instance segmentation datasets, and one was a multi-feature classification dataset.

Based on VHR satellite imagery and ground surveys located approximately 50 km from the study area, we produced data in shapefile format for 62,185 buildings. As shown in Figure 2, the footprint of a building is highly detailed. Building property information is given in the form of vulnerability type, usage, and floor numbers. Using ArcGIS Pro, we turned these data into a dataset that can be used as a basis for training building instance segmentation models, as well as for building vulnerability classification models.

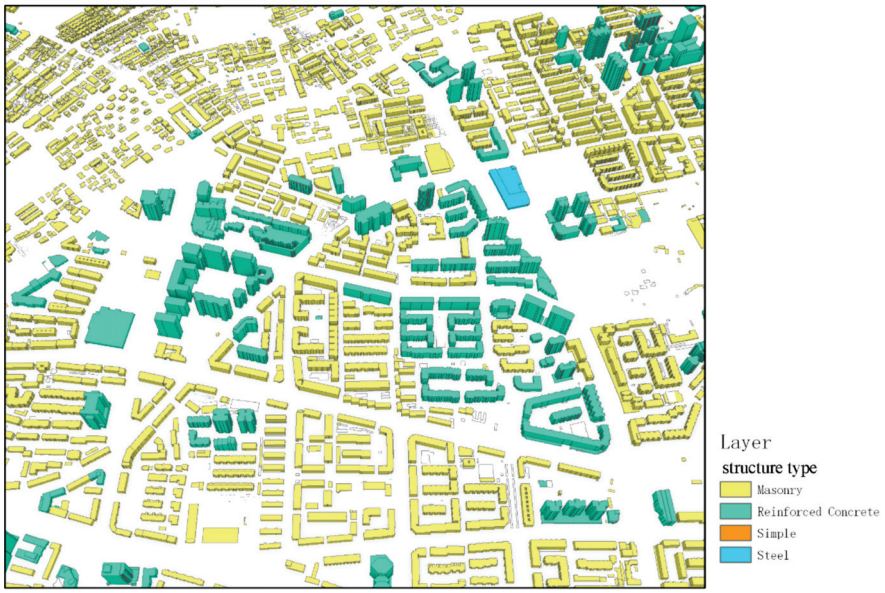

Figure 2. 3D visualization of single building datasets.

Additionally, 720 samples of rural building groups were derived from Sentinel 2 data, and shadow contours of 3250 buildings from GF2. Figure 3 illustrates an example of the instance segmentation dataset.

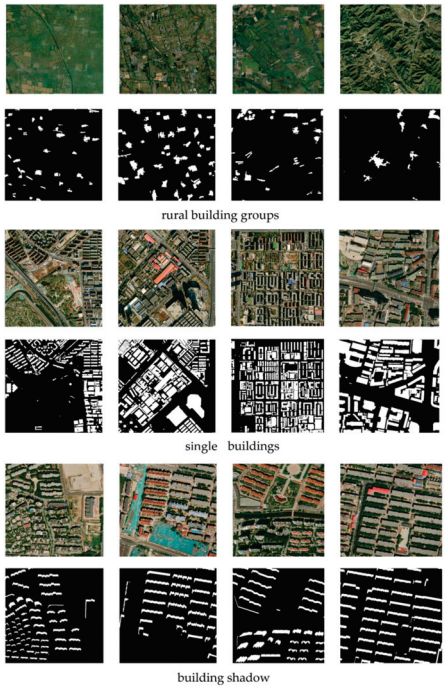

Figure 3. Example of the instance segmentation dataset.

To verify the final results, this study conducted a field survey in the study area during 2019–2020, collected a sample of 823 buildings, as shown in Figure 4, and created a sample of building structures by utilizing Baidu Maps API libraries.

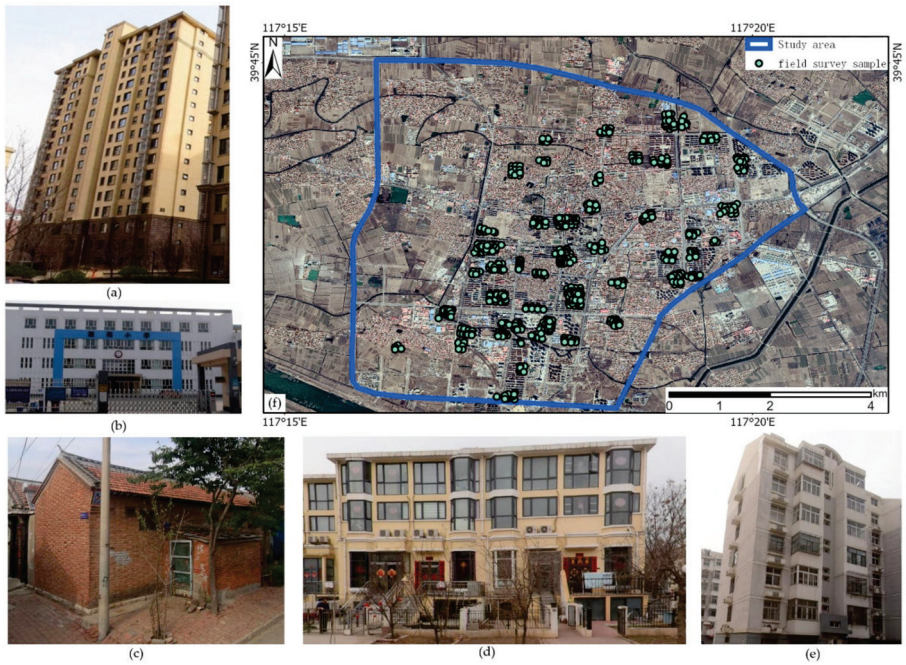

Figure 4. Field survey samples and examples of structure types: (**a**) shear wall structure (dwelling), (**b**) RC structure (hospital), (**c**) brick wood (dwelling), (**d**) RC structure (dwelling), (**e**) confined masonry (dwelling), (**f**) field survey samples.

2.3. Overall Workflow

In this section, the proposed workflow is described in detail. The seismic risk assessment process involves the quantification of three major input components, namely, seismic hazard intensity, exposure, and vulnerability [15].

Our understanding of the change in seismic risk resulting from urbanization relies on the assumption that the seismic hazard remains relatively stable; thus, the change in seismic risk is due to changes in the hazard-bearing body. When a disaster occurs involving an earthquake, social and economic losses are determined by the destruction of buildings. This form of structural change is the focus of our study. The primary role of remote sensing data in this study is to extract building information from images taken over several years. Object-oriented classification and deep-learning-based instance segmentation are integrated into the pipeline to efficiently accomplish this task.

As shown in Figure 5, the overall workflow includes four main parts. Part 1: Building object segmentation and feature extraction. The footprints of single buildings and rural building groups are extracted from high- and medium-resolution imagery, respectively. The image feature extraction is carried out with the building's footprint as the object unit. Part 2: Calculating the proxies in each object unit, according to the extracted object features, and then conducting vulnerability classification to obtain the disaster-bearing body dataset. Part 3: Calculating structural losses and the resulting economic and population losses at three ground motion intensity levels. Finally, repeat the above work for different years to obtain the results regarding changes in seismic risk during the urbanization process. In addition, to extract the building footprint and features and the vulnerability classification of the structure, multiple machine learning classifiers need to be pre-trained. This part can be regarded as Part 0 of the whole process.

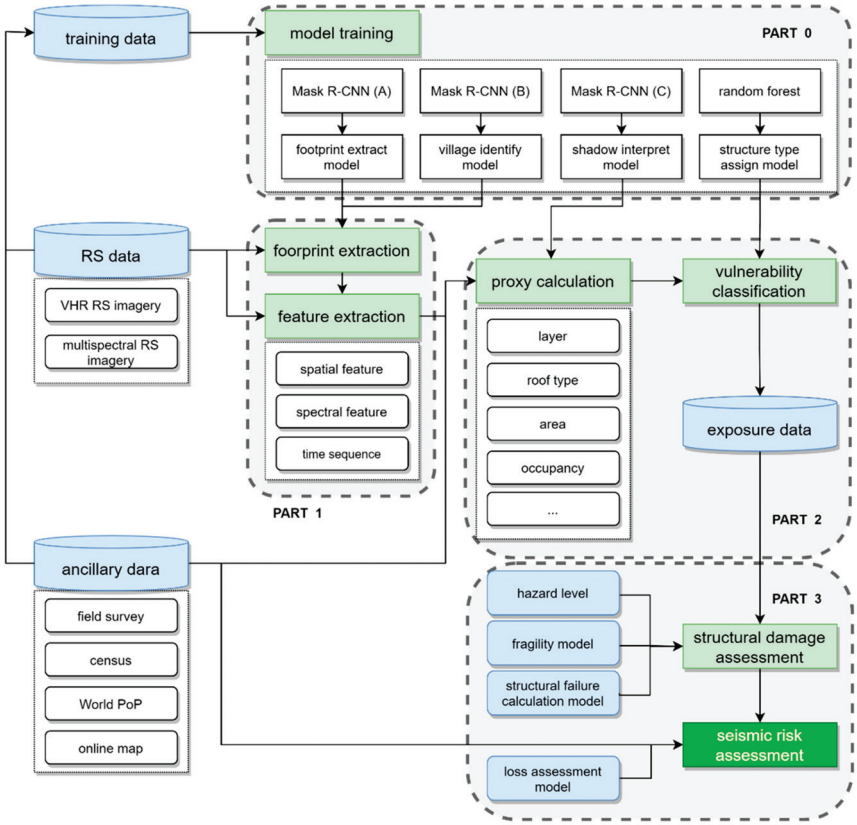

Figure 5. The overall workflow consists of four major sections: part 0 to pre-train the segmentation and classification models, part 1 to extract image features, part 2 to classify structural vulnerability, and part 3, a seismic risk assessment.

2.4. Building Feature Extraction

The acquisition of building parameters is probably the most time-consuming, tedious, and expensive part of each seismic risk assessment [64]. In this study, three BMask R-CNN classifiers were trained to extract footprints from single buildings and rural building groups, respectively. The footprints of single buildings are taken as object units for multi-feature extraction. The footprint of rural building groups can be directly applied to the classification of vulnerability and the calculation of inventory, according to the survey data.

The third BMask R-CNN classifier extracts the shadows of single buildings to calculate the height and number of floors. Other information on single buildings is extracted by eCognition v9.3, Trimble, CA, USA. A pretrained random forest classifier is used for structure vulnerability classification.

2.4.1. Mask R-CNN Framework

Mask R-CNN is a flexible object instance segmentation framework that efficiently detects objects in an image while simultaneously generating a high-quality segmentation mask for each instance [46]. Based on Faster R-CNN [65] and Fast R-CNN [66], Mask R-CNN adds a branch to predict an object mask while preserving the branch for bounding box recognition, thereby achieving pixel-level instance segmentation. Since Mask R-CNN is easy to generalize to other tasks, it has been widely adopted in remote sensing object classification. As shown in Figure 6, the original network structure of MASK R-CNN includes several components. The multiscale feature maps are extracted from the input image through the backbone part based on ResNet and the feature pyramid network (FPN). These features are shared by the RPN part and the RoIAlign layer. The feature map fed to the RPN is further extracted to generate candidate ROIs. After filtering, the obtained feature maps are used as proposals. The feature maps from the backbone part and the RPN part are properly aligned with the input based on bilinear interpolation [46] through the RoIAlign layer. Finally, the aligned feature map enters two branches in the head part: one is a fully convolutional mask prediction branch, and the other branch is divided into two sub-branches for class prediction and bounding box regression [67].

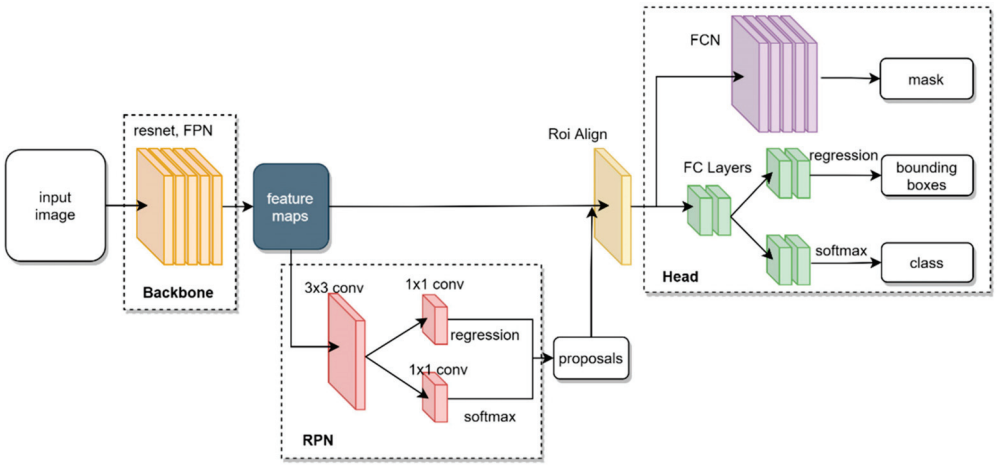

Figure 6. Structure and main components of Mask R-CNN framework [46].

2.4.2. BMask R-CNN Framework

When performing pixel-level instance segmentation based on Mask R-CNN, predictions are made based on the local information. Although large receptive fields are obtained through the deep framework, which helps to extract features and improve the accuracy of classification, the information details, such as the shape information of the object, are still elusive.

To solve the problem of coarseness and indistinctness in the prediction output, Cheng, T.H. et al. [68] proposed a boundary-preserving Mask R-CNN to exploit boundary information and guide more precise mask prediction.

By adopting boundary features and boundary prediction, BMask R-CNN optimizes the mask head in Mask R-CNN, as illustrated in Figure 7. The new mask head is called the boundary-preserving mask head.

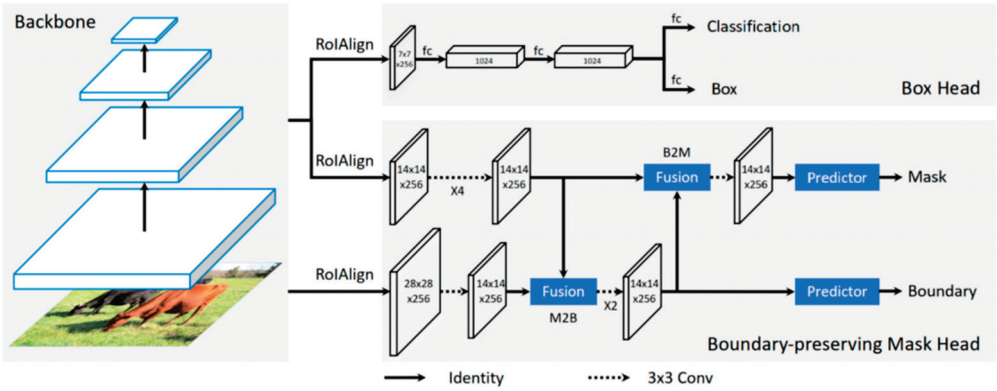

Figure 7. The overall architecture of boundary-preserving Mask R-CNN (BMask R-CNN). The dotted arrow denotes 3 × 3 convolutions, and the solid arrow denotes identity connection unless there is a specified annotation in the boundary-preserving mask head. "×4/×2" denotes a stack of four/two consecutive convs [68].

Boundary-preserving mask heads synchronously learn object boundaries and masks. First, features from the mask sub-network can provide high-level semantic information for learning boundaries. Then, after obtaining the boundaries, the shape information and abundant location information in boundary features can help to achieve more precise mask predictions [68].

Since a boundary learning head branch is added to the multiple Mask R-CNN tasks, the loss function of the model also needs to accordingly increase a component. Here, ref. [68] proposes a combination of dice loss [69] and binary cross-entropy to optimize the boundary learning

$$L_b\left(p_b, y_b\right) = L_{Dice}\left(p_b, y_b\right) + \lambda L_{BCE}\left(p_b, y_b\right) \tag{1}$$

in which $L_{BCE}\left(p_b, y_b\right)$ is binary cross-entropy loss, with λ as a hyperparameter to adjust the weight. p_b and y_b representing the predicted boundary for a particular category and the corresponding boundary ground truth, respectively.

The Dice coefficient is used to measure the spatial overlap or similarities between the two sets. Here, the consistency between the predicted boundary and the corresponding boundary ground truth is compared. Since Dice loss is insensitive to the number of foreground/background pixels, it alleviates the class-imbalance problem. The calculation formula of Dice loss is as follows:

$$L_{Dice}(p_b,\ y_b) = 1 - \frac{2\sum_i^{H\times W} p_b^i y_b^i + \epsilon}{\sum_i^{H\times W}\left(p_b^i\right)^2 + \sum_i^{H\times W}\left(y_b^i\right)^2 + \epsilon} \tag{2}$$

where H and W are the height and width of the predicted boundary map, respectively; i denotes the i-th pixel, and ϵ is a smooth term to avoid zero division.

Finally, after adding a boundary-preserving branch to Mask R-CNN, the combined multi-task learning loss functions are as follows:

$$L = L_{cls} + L_{box} + L_{mask} + L_b \tag{3}$$

where L_{cls}, L_{box}, and L_{mask} represent the loss of classification, localization, and segmentation mask, respectively, which are identical to those in [46].

2.4.3. Post-Processing of Building Footprint

After obtaining the footprints of single buildings and rural building groups from high-resolution and medium-resolution images, respectively, the post-processing of both results must be performed. This mainly includes the following processes:

(i) Eliminating non-structural misclassification by setting an area threshold;
(ii) Intersecting single buildings and building groups, keeping single buildings in the rural building group, and eliminating redundancy in the two output footprints;
(iii) Calculating the actual building area of the rural building group.

In a typical rural residential setting in the study area, a class of simple structures with intact roofs often causes buildings to be misclassified. A good example of this is shown in Figure 8, where the roofs indicated in the red frame generally correspond to actual buildings, whereas other roofs may be simple structures or serve only as shelter from the sun and rain. To estimate the total amount of rural buildings, we apply the empirical formula based on the ratio of the total land area of the rural buildings group to the total area of the rural buildings.

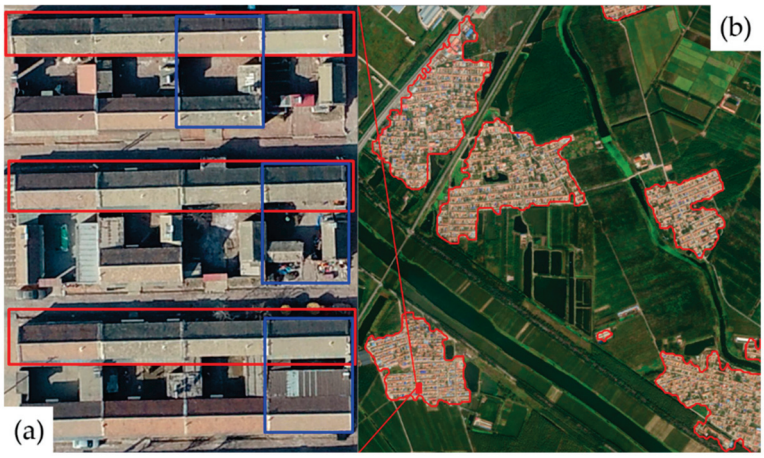

Figure 8. (**a**) Blue boxes indicate a single household, while red boxes indicate buildings to be counted; (**b**) red outline indicates rural building groups.

For our study area, the relationship between the group area of rural buildings and the number of households is as follows:

$$\text{group area} = 652.77\ \text{m}^2 \times \text{number of households} + 1.4366\ \text{m}^2 \quad (4)$$

Further, according to the average floor area of each household, the building stock to be counted can be obtained.

2.4.4. Estimating Floor Numbers

The height of a building is an effective way of assessing its seismic capacity and is essential to the calculation of its area [16]. This can be extracted by applying the shadow length of the building structure in the high-resolution optical image [18–20,27], SAR image imaging geometric characteristics [18], LiDAR data [27], or DSM data [25–27]. Since high-resolution LiDAR data and DSM data were not obtained in this study, the number of floors in the building was inferred from the building shadows in the GF-2 data.

As illustrated in Figure 9, taking a regular building model as an example, according to the angle of solar irradiation and the angle of satellite observation, the geometric relationship between the building and its own shadow mainly presents two situations [70]. When

the sun and the satellite are located on the same side of the building, the building itself partially occludes its own shadow. When the satellite and the sun are located on both sides of the building, the shadow of the building can be fully exposed to the viewing direction.

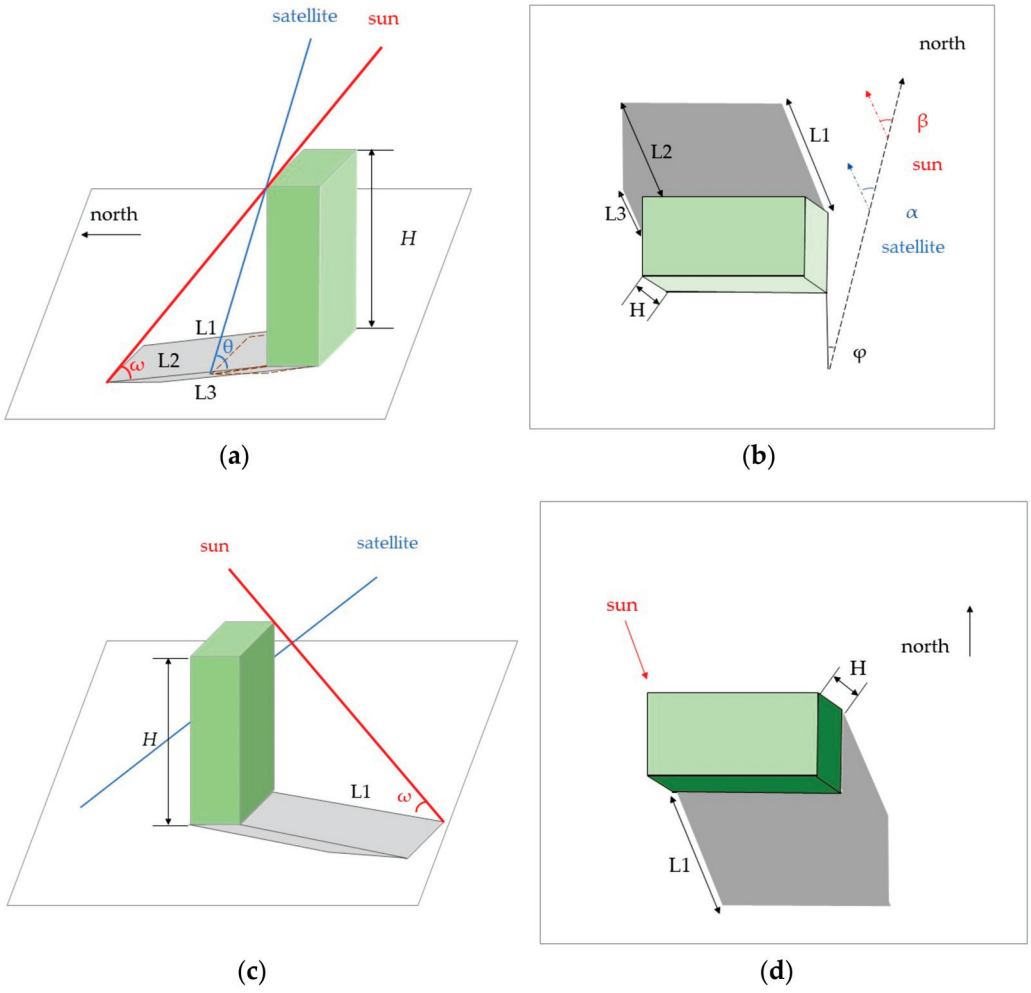

Figure 9. Building shadow geometry; the red and blue lines indicate the line-of-sight directions of the sun and satellites, respectively: (**a**) side view of satellite and sun on the same side; (**b**) top view of satellite and sun on the same side; (**c**) side view of satellite and sun on different sides; (**d**) top view of satellite and sun on different sides.

According to the basic trigonometric function principle, the formula to calculate the height of the building in two different cases can be obtained [70]:

$$H = L_1 \, tan \, \omega \tag{5}$$

here, H represents the height of the building, L_1 represents the length of the unobstructed shadow, and ω is the sun elevation angle. Considering the situation where the shadow is occluded when the sun and the satellite are on the same side, it is necessary to infer H according to L_2 and L_3, as follows:

$$H = L_2 \frac{tan \, \omega tan\theta \cos(\beta - \varphi)}{tan\theta \cos(\beta - \varphi) - tan\omega \cos(\alpha - \varphi)} \tag{6}$$

$$H = L_3 \frac{tan\omega tan\theta \sin(\beta - \varphi)}{tan\theta \sin(\beta - \varphi) - tan\omega sin(\alpha - \varphi)} \tag{7}$$

where θ is the altitude angle of the satellite, α is the azimuth of the satellite, β is the azimuth of the sun, and φ is the azimuth of the building. The computational difficulty is significantly simpler when the satellites and the sun are on different sides of the building.

2.4.5. Occupancy and Population Disaggregation

We assume that the change in the POI of functional facilities is stable and that the increase or decrease in POI in each year is purely dependent on the existence of buildings. Based on the POI obtained in 2018 and 2020, the POI information has been assigned to the building through spatial analysis. By 2020, there were 110 medical institutions of various types, 63 educational institutions at all levels, 24 shopping malls, 39 enterprises exceeding their designated sizes, and 238 manufacturing companies found in the research area.

Samples from the on-site investigation were used to count the density of people in various buildings. These were divided into daytime and nighttime counts.

Table 2 represents the Indoor Population Density of different occupancy (people per square meter).

Table 2. Indoor Population Density of different occupancies (people per square meter).

Occupancy	Office	Factory	Business	Education	Medical	Residency	Other
Day	0.03	0.01	0.09	0.52	0.3	0.01	0.03
Night	0.001	0	0	0.12	0.1	0.033	0.001

2.5. Vulnerability Classification

Based on footprints of single buildings, object feature extraction was carried out in eCognition [71]. Then, a pretrained Random Forest (RF) [72] classifier was adopted to classify the vulnerability type of buildings. The selected features are shown in Table 3.

Table 3. Selected Features.

Type	Features	Data
Extend	Area, length, length/width, width, border length	VHR image
Shape	Asymmetry, compactness, density, elliptic fit, rectangular fit, main direction, shape index, roundness	
Texture	GLCM (homogeneity, contrast, dissimilarity, entropy, Ang. 2nd moment, mean, Std.Dev.)	Multi-Spectral Data
Layer Values	mean, standard deviation, HSI transformation	

2.6. Loss Assessment

In this study, approaches to loss assessment are based on structural damage. Moreover, this study aims to determine the number of deaths and direct losses due to structural damage caused by ground motions. Explicitly addressing the damage and loss caused by secondary disasters such as surface fault rupture, landslides, soil liquefaction, fire, etc., as well as damage to infrastructures such as bridges and roads, is outside the scope of this paper.

2.6.1. Structural Damage

Structural damage assessment based on vulnerability analysis is the basis for quantifying economic loss and casualty. The vulnerability of structures that are exposed to earthquake loading expresses the likelihood of the occurrence of certain damage levels caused by seismic action [15].

Furthermore, the fragility model can be assumed to be a reliable measurement of damage to a respective set of buildings with similar structural taxonomy of dynamic behavior.

Building damage states are divided into five levels, which are intact, slightly damaged, moderately damaged, severely damaged, or collapsed, according to the damage to structural members or the entire structure. The division points of five kinds of failures correspond to the four limit state divisions of the structure in turn, and those from LS1 to

LS4 gradually become more serious. The fragility model relates building response to seismic demand inputs and follows the lognormal assumption [73], as given by Equation (8), which refers to the conditional probability of various limit states of the structure under different earthquakes.

$$F(x, \mu, \sigma) = P(LS \mid x) = \Phi((\ln(x/\mu))/\sigma) \quad (8)$$

here, Φ is a standard normal cumulative distribution function and x denotes seismic motion intensity, which is taken as peak ground acceleration (PGA). Parameters μ and σ are the fragility model median and standard deviation of ln (x). Table 4 presents the parameters of the fragility model used for different structural typologies in this study.

Table 4. Fragility model parameters.

Typology	LS1		LS2		LS3		LS4		Source
	μ	σ	μ	σ	μ	σ	μ	σ	
Brick wood	0.2997	0.093	0.2005	0.1397	0.216	0.2175	0.2228	0.2837	[74]
Confined masonry	0.139	0.845	0.292	0.709	0.510	0.608	1.372	0.828	[75]
Reinforced concrete	0.267	0.785	0.540	0.548	0.841	0.506	1.629	0.558	[75]
shear wall	0.130	0.170	0.150	0.240	0.20	0.470	0.250	0.810	[76]
Bottom RC	0.122	0.2	0.145	0.2	0.213	0.2	0.461	0.2	[75]

According to the parameters of LSs (s = 1, 2, 3, 4), Equation (8) calculates the probability that the structure will reach LSs. Then, the probability of each DSi (i = 0, 1, 2, 3, 4) of the seismic intensity can be calculated:

$$P_{DS0} = 1 - P(LS_1 \mid x) \quad (9)$$

$$P_{DS1} = P(LS_1 \mid x) - P(LS_2 \mid x) \quad (10)$$

$$P_{DS2} = P(LS_2 \mid x) - P(LS_3 \mid x) \quad (11)$$

$$P_{DS3} = P(LS_3 \mid x) - P(LS_4 \mid x) \quad (12)$$

$$P_{DS4} = P(LS_4 \mid x) \quad (13)$$

Based on the hazard level of the study area, we calculated the loss at three different levels of ground motion intensity. The three ground motion levels correspond to rare earthquakes, moderate earthquakes, and frequent earthquakes, respectively. The probability of exceedance during 50 years is 2–3%, 10%, and 63%, respectively.

2.6.2. Economic Loss

In this paper, the method used to calculate direct economic loss according to the damage state, loss ratio, and replacement price refers to the provisions of China Code GB/T 18208.4-2011 (Seismic Field Work Part IV: Disaster Direct Loss Assessment) [77]. According to this code, the formula proposed in this study for the calculation of direct earthquake economic loss for H types of structures is as follows:

(1) The direct economic loss L_A of H building structure types and D damage levels in a certain area is calculated as follows:

$$L_A = \sum_H \sum_D P_h A_d R_d \quad (14)$$

A_d denotes the total area of the h-type structure with damage stated; R_d is the loss ratio when the h-type structure has a damage state of d; and P_h is the replacement price of the h-type structure.

(2) The direct economic loss L_B of the indoor property is calculated as:

$$L_B = \sum_H \sum_D P_h A_d R_d \quad (15)$$

where T_d is the ratio of the indoor property loss when the damage level of the h-type structure is d; P_h is the replacement unit price of the h-type structure; and μ_1 is the ratio of the indoor property value of the building structure to the structural replacement price.

(3) The direct economic loss L_C of decoration damage is calculated as follows:

$$L_C = \sum_H \sum_D \gamma_1 \gamma_2 \gamma_3 Q_h A_d S_d \quad (16)$$

S_d denotes the decoration loss ratio when the damage level of the *h*-type structure is *d*; Q_h denotes the decoration price of the *h*-type structure; γ_1 represents the correction factor, considering the difference in economic development levels; γ_2 represents the correction factor considering building occupancy; and γ_3 represents the proportion of high-level decoration. γ_1 and γ_2 values are specified in [77].

2.6.3. Social Loss

In this study, death and injury calculations were carried out according to the relationship between the damage state of the house and the casualty rate of people, without distinguishing between structure types; the calculation formula is as follows:

$$N_d = \sum_D \rho A_d RD_d \quad (17)$$

$$N_I = \sum_D \rho A_d RI_d \quad (18)$$

N_d and N_I denote the numbers of dead people and injured people, RD_d and RI_d represent the death and injury rate of people under different damage levels, A_d is the area of the building structure under the damage level, and ρ is the density of people in the room. The fatality rate values used in this study are listed in Table 5.

Table 5. Casualty rates of different damage states.

Casualty Rate	Moderate Damage	Severely Damaged	Destroyed
Death Rate	0.001%	0.5%	3%
Injury Rate	10%	15%	30%

2.7. Evaluation Indicators

The performance of the proposed algorithms was assessed using six metrics, namely, IoU, precision, recall, F1-score for segmentation tasks, and Overall Accuracy and Kappa coefficients for vulnerability classification.

$$IoU = \frac{TP}{TP + FP + FN} \quad (19)$$

$$Precision = \frac{TP}{TP + FP} \quad (20)$$

$$Recall = \frac{TP}{TP + FN} \quad (21)$$

$$F1 = \frac{2 * percision * recall}{percision * recall} \quad (22)$$

$$\text{Overall Accuracy} = \frac{TP + TN}{TP + TN + FP + FN} \quad (23)$$

$$Kappa = \frac{P_0 - P_e}{1 - P_e} \quad (24)$$

where TP is the value of the true positives, FP is the value of the false positives, TN is the value of the true negatives, and FN is the value of the false negatives. P_0 is the relative observed agreement among raters. P_e is the hypothetical probability of chance agreement [78].

3. Results

In this section, the results obtained by applying the workflow and method mentioned in Section 3 to the study area in Section 2 are presented. The results of the extraction of disaster-bearing body information and the estimation of seismic risk will be described, as well as the evaluation of the outputs.

3.1. Building Information Extraction Result

The building segmentation of the study area data is performed by the BMask-RCNN model presented in Section 3. Table 6 shows the extraction accuracy of single buildings and rural building groups. In terms of IoU, precision, recall, and F1 score, rural group buildings exhibit a lower extraction accuracy than single buildings. Extraction examples of single buildings and rural group buildings are presented in Figures 10 and 11. The results show a small number of errors and missing records.

Table 6. Extraction Accuracy Evaluation.

Buildings	IoU	Precision	Recall	F1 Score
Rural building group	0.792079	0.898876	0.869565	0.883978
Single buildings	0.855615	0.924855	0.91954	0.92219

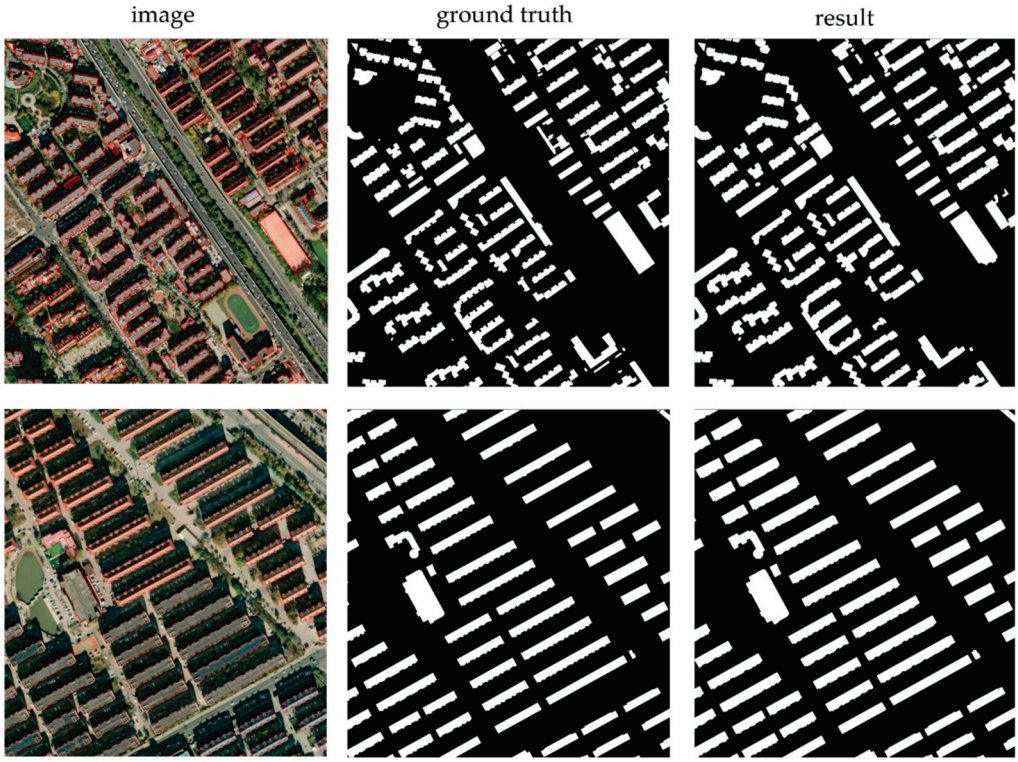

Figure 10. Example of single building extraction results.

The accuracy of height and floor estimation is shown in Figure 12a,b. An excellent linear fitting relationship exists between the height estimate and the real value, and the error of the height estimate is within one meter. The difference between the estimated number of floors and the actual number of floors may be as large as three stories, and the error for from 5- to 10-story buildings is larger.

According to field sampling data, the Overall Accuracy for the building vulnerability classification reached 86.77%, and the Kappa coefficient was 0.6538. Figure 13 shows the distribution of building structures over different years. In Figure 13, the brick–wood

structures represented by the color red are gradually disappearing in the study area. In the extraction results for 2011, 2012, and 2014, brick–wood structures occupied the largest portion of the study area. According to the extraction results, only a few brick–wood structures survived in 2016.

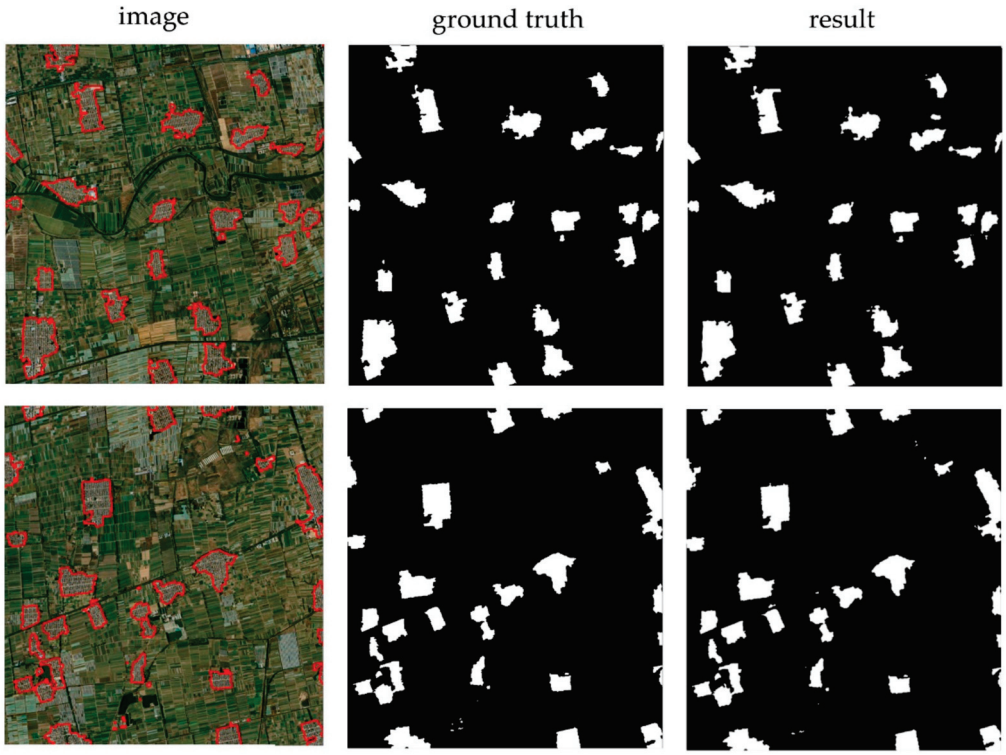

Figure 11. Example of the rural building group.

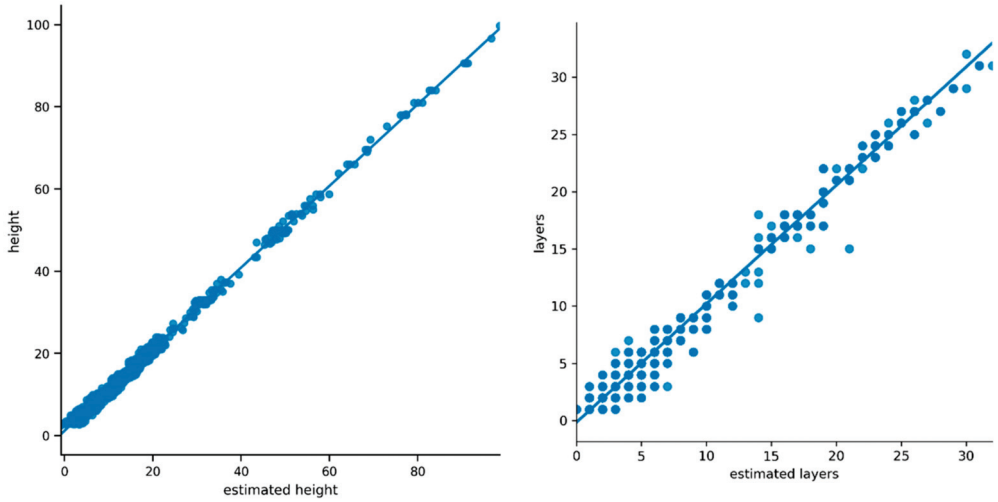

Figure 12. Accuracy of height and floor estimation: (**a**) height and floor estimation; (**b**) layers estimation.

However, the shear wall structures indicated in blue have been increasing since 2016. Meanwhile, brick–wood structures are being replaced with shear wall structures in this process.

Nevertheless, the overall pattern at the center of the study area has not changed dramatically, and the road between building blocks remains generally unchanged. This

area of buildings remains unchanged and includes many functional facilities, including schools, hospitals, malls, offices, etc.

Figure 13. Distribution of building footprints over different years in the study area.

Furthermore, based on the above results, the construction area of various structures in different years can be estimated. In 2020, the construction area of shear wall structure buildings reached 15 times that of the area in 2011, from 0.842 km^2 to 12.643 square km^2. The proportion changed from 9.22% to 64.66%. Figure 14 illustrates how the area of each structure type changes over the years of this study. From 2011 to 2014, the construction area of various types of buildings remained stable, while the area for shear wall structures steadily increased. The construction area of brick wood buildings dramatically declined in 2016. However, the shear wall structure continued to grow into 2018 and saw a surge in 2020.

Grids are used to estimate the density of the building area. Figure 15 was made by applying a 200 × 200 m grid. Comparing Figures 13 and 14, Figure 15 also illustrates that, after experiencing a plateau in 2011, 2012, and 2014, the results in 2016 and 2018 show the disappearance of low-density building areas. Meanwhile, the results for 2020 and

2021 demonstrate the emergence of high-density building areas near the boundary of the study area.

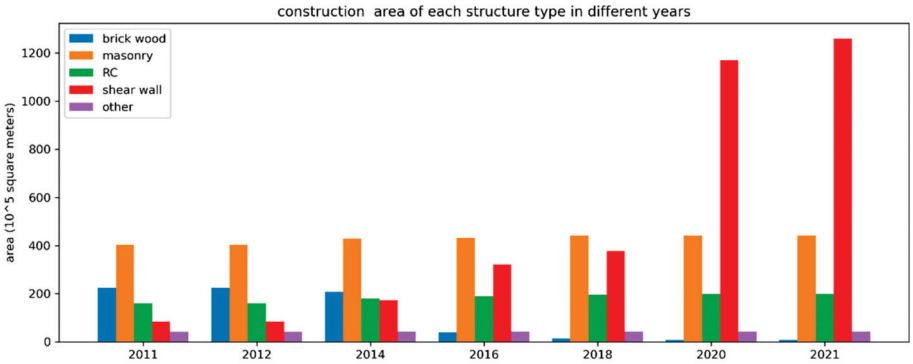

Figure 14. Construction area of buildings in different years.

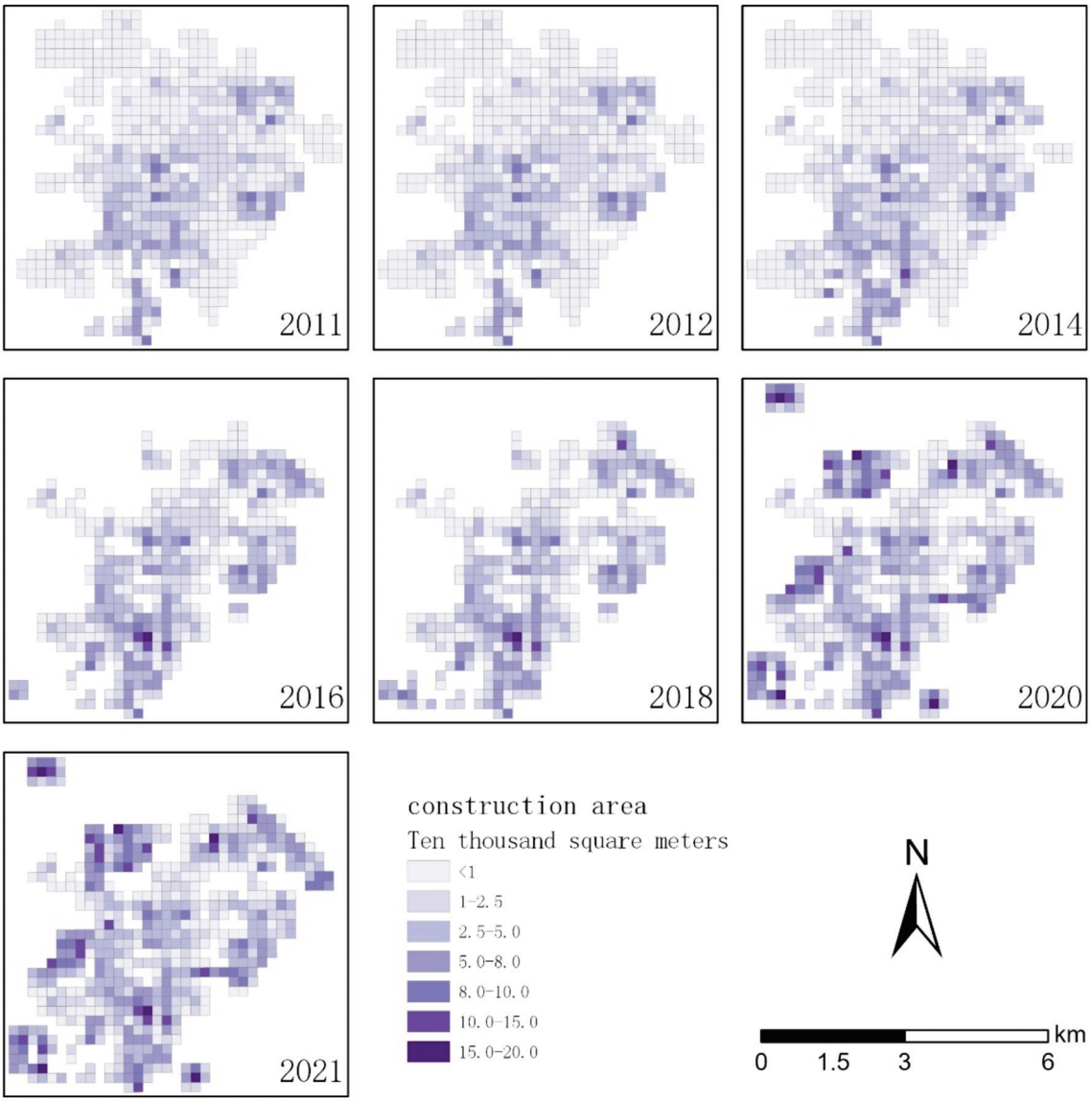

Figure 15. Construction area over different years in the study area, in a 200 m grid.

Table 7 shows the estimated total population for each year.

Table 7. Estimated total population.

Year	2011	2012	2014	2016	2018	2020	2021
Day	240,344	240,260	258,043	268,555	274,613	360,118	369,280
Night	203,244	203,182	233,786	230,443	241,556	477,837	505,323

3.2. Estimation of Seismic Risk Changes

Based on the methods outlined in Section 3 and the results presented in Section 3.1, estimates of losses under different ground motion levels, including direct losses in economic terms and deaths due to seismic activity during night and daytime, were further obtained for the study area. Table 8 provides a summary of the losses.

Table 8. Estimated economic and social losses.

Level	Year	2011	2012	2014	2016	2018	2020	2021
Rare	Eco loss (billion RMB)	57.7964	57.7817	61.1094	54.6339	54.8115	66.6552	68.0225
	Night death toll	4662	4660	4762	3421	3270	3348	3362
	Day death toll	4526	4524	4658	4371	4355	4480	4484
Moderate	Eco loss (billion RMB)	40.8394	40.8280	42.8254	36.9838	36.8194	43.3709	44.1346
	Night death toll	1896	1895	1939	1437	1384	1388	1390
	Day death toll	1630	1629	1670	1540	1530	1554	1555
Frequent	Eco loss (billion RMB)	8.0140	8.0123	8.7140	8.4178	8.6097	11.8013	12.1698
	Night death toll	40	40	43	44	45	45	45
	Day death toll	35	35	37	37	37	37	37

Figure 16 illustrates the trend in earthquake losses over many years based on different levels of ground motion intensity. The estimated results of losses include death tolls when earthquakes occur during the daytime as well as at night, as well as a death toll per 10,000 people when earthquakes occur at night. A direct economic loss is also incurred.

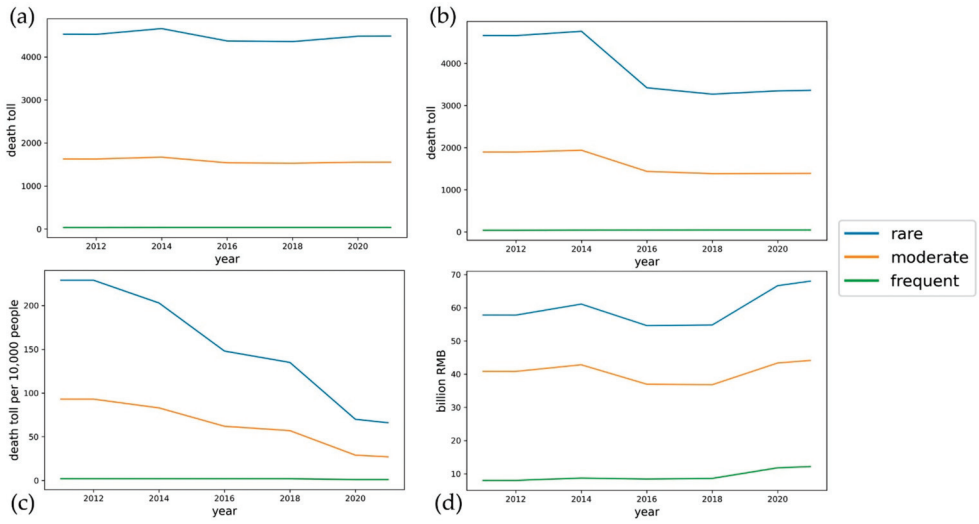

Figure 16. Variation trend of loss under different ground-motion intensity levels. The blue, orange and green lines represent rare earthquakes, moderate earthquakes, and frequent earthquakes, respectively: (**a**) estimated death toll when an earthquake occurs during daytime, (**b**) estimated death toll when the earthquake occurs at night, (**c**) estimated death toll per 10k people when an earthquake occurs at night, (**d**) estimated direct economic loss.

In general, for frequent earthquakes, there was little change in losses from 2011 to 2021, except for an increase in direct economic losses after 2018. In terms of loss estimates

from moderate earthquakes, as well as those from rare earthquakes, the trends were almost identical in recent years.

Firstly, it should be noted that the number of deaths caused by earthquakes occurs during the day and night, with one obvious trend being that the results in 2016 decreased compared with those before 2014 and began increasing thereafter. Additionally, after 2016, the death toll when the earthquake occurred at night was much lower than the death toll when it occurred during the day. A rare earthquake occurring at night will cause 1300 fewer deaths in 2021 than it did in 2011, which represents a reduction of one-third. Second, the death rate has declined from 2011 to 2021. For example, the death rate per 10,000 people resulting from a rare earthquake declined from 229 in 2011 to 66 in 2021. It can be said that the death rate decreased from 2.29% to 0.66%. Similarly, the death rate for every 10,000 people affected by the moderate earthquake declined from 93 to 27.

Third, the economic losses showed a slight upward trend between 2011 and 2014 and began to decline in 2016. There was an inflection point in 2018, and economic losses began to rise after that year.

Figure 17 demonstrates the death toll of a rare earthquake that occurred at night. According to the results of the death toll estimation, the spatialized results for 2011 to 2014 indicate that this stage is mainly characterized by lower values uniformly distributed within space. In the 2016 and 2018 results, some low-value areas disappeared, while the original high-value areas remained. Additionally, the results for 2020 and 2021 indicate several increasing potential deaths.

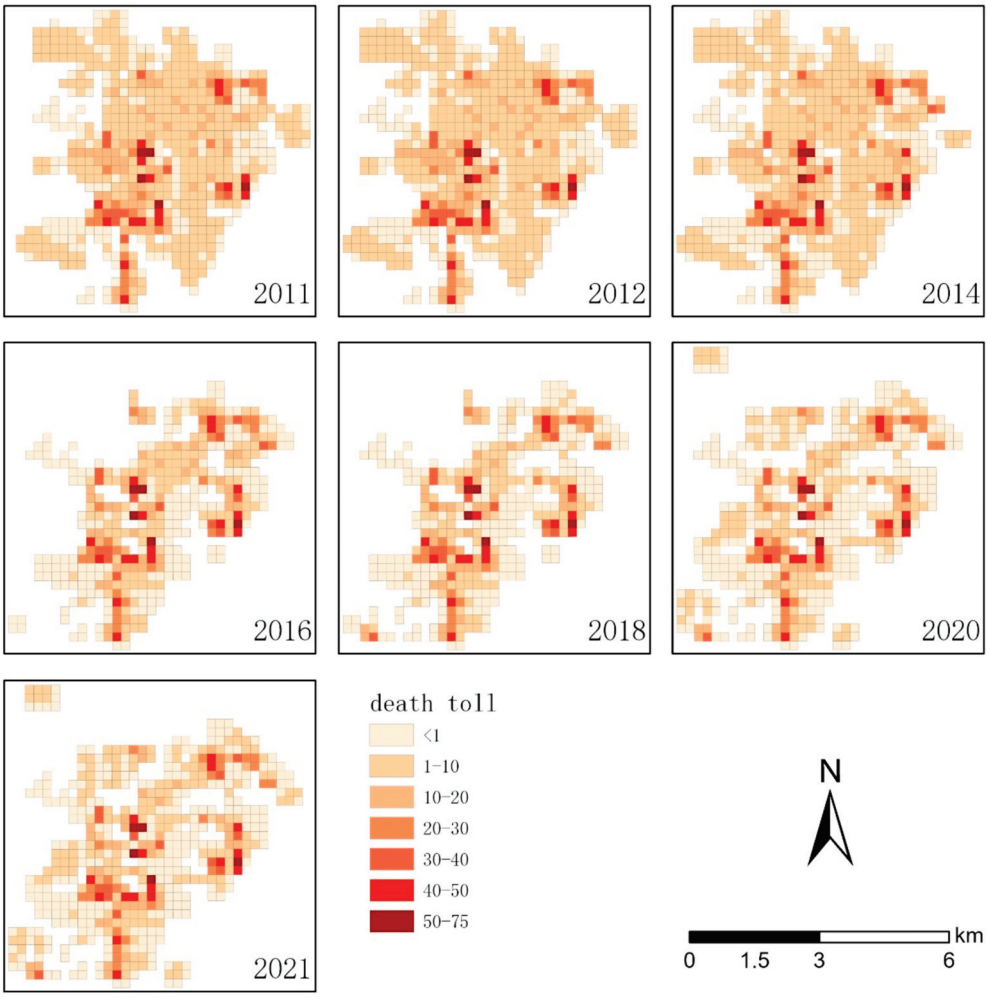

Figure 17. Spatial distribution of population deaths caused by rare earthquakes occurring at night, in a 200 m grid.

4. Discussion

In this paper, we describe a new task regarding the perception of changes in seismic risk due to urbanization, based on remote sensing data. By applying multi-source remote sensing image data for different years and combining auxiliary information, we were able to monitor the earthquake-bearing body changes within the study area as the urbanization process continued and subsequently estimate seismic risk changes. Our work is based on the assumption that the seismic hazard remains relatively stationary over ten years.

Building structure information was extracted using the improved Mask R-CNN instance segmentation model, and the random forest classification algorithm was applied after instance segmentation to obtain a classification result. Furthermore, a method of earthquake disaster loss assessment was used to calculate the societal and economic losses over different years based on the three earthquake intensity levels.

First, building object types were divided into single buildings and rural building groups. Based on the BMask R-CNN model, we obtained relatively reliable results for both building object types.

Several factors affect the extraction accuracy of single buildings:

The shadows cast by tall buildings and tall plants block the view of the buildings; these are the major reasons for misclassifications. Additionally, some low buildings that blend into the background environment are not identified. A third reason is that we use annotated data with very fine edges and an edge-preserving model to construct a finer outline of the building geometry. However, since the sample data have such a large number of edges, it is still challenging to achieve the same level of building segmentation.

Factors that influence building segmentation accuracy in rural areas include:

In some cases, the plastic sheds surrounding rural buildings are similar in color, tone, and geometric size to the buildings, which confuses their classification. As in single buildings, some backgrounds, such as barren land, cause misclassifications and omissions. Moreover, some independent buildings are also incorrectly classified as rural group buildings.

A redundant processing operation is carried out at the intersection between rural group buildings and single buildings, based on the results of the single building extraction.

Although the results for estimations of the height of the building are relatively accurate, there is a certain amount of variance in the estimation of the number of floors of the building. This can be attributed to several factors: (i) There is a wide range of story heights in factory buildings with a single floor, ranging from 3 m to 10 m. (ii) Additionally, classifications of building use types do not always reflect the attributes of each specific building use. An example would be a university campus, which contains a wide variety of buildings, all of which are classified as one occupation, or a gymnasium that may be in a high-rise, one-story structure. Furthermore, the height of the teaching building in schools is often higher than that of the office. (iii) The third point is that the top floor of some buildings has a decorative roof, and the number of floors is rounded off incorrectly.

Confusion between structures primarily exists among confined masonry, reinforced concrete, and shear wall structures. This is particularly true for low-rise dwellings, which usually have a variety of structural types and a close geometrical arrangement. Since high-rise buildings are commonly shear wall structures, the number of stories plays an important role in improving their classification accuracy.

As seen from the result, there has been a significant change in the building stock within the study area from 2011 to 2021. This change could be attributed to several factors. First, the gross floor area of buildings decelerated between 2014 and 2016 but subsequently grew rapidly. A second characteristic of the change in building types is the decreased number of brick wood structures, followed by a significant rise in the number of shear wall structures, while other types of buildings continue to steadily change. Moreover, most of the buildings that were reduced or added were residential. Third, the renewal of buildings occurs in a variety of areas throughout the city, from the center to the edge.

The above analysis results are consistent with the period of demolition and reconstruction in this area in the past. According to the statistical yearbook of the Baodi District,

the district launched a relocation and reconstruction project in October 2015, involving 25,000 households and 66,000 residents, with an investment of 43.3 billion RMB yuan (approximately 6551 million EURO). A total of 35 urban villages and 21 dormitories were demolished in 2016, and, in 2020, 35 replacement communities were built, which are currently in operation.

In this study, the calculation to estimate building area change was based on the extraction of the building's footprint, the estimation of the number of floors, and the classification of building types. Additionally, a change in the building use is implied. This is a major difference from previous methods of monitoring urbanization expansion by identifying impervious layers. We also consider this to be a fundamental issue in our research, and it forms the basis for the determination of variations in specific earthquake losses.

There are still some limitations in our study that need to be acknowledged. During remote sensing analysis, first, we adopted a large private dataset to train the image segmentation model and classification model, which is a time-consuming procedure that needs to be performed carefully. This localized dataset has proven to be indispensable in our research. Second, even though high-rise buildings and one-story rural dwellings are classified with high accuracy, building structure type confusion exists among confined masonry and reinforced concrete.

In calculations of population and economic losses, no earthquake simulation would enable the results to be verified, as in the case of [79]. This means that the results of the calculation presented in this paper are only theoretically reliable. Second, since the study area is relatively small, we perform calculations by setting a consistent PGA value rather than using the conventional seismic hazard model [80,81].

In future work, we will study transfer learning techniques to reduce the dependence on sample size and examine the attention module. We will also study the subdivision of the vulnerability function, as well as the spatialization of population data based on remote sensing.

5. Conclusions

Identifying and mastering the changes in earthquake risk due to urbanization is crucial to effectively adjust countermeasures to reduce earthquake losses and execute earthquake emergency preparedness in a targeted manner. To achieve this goal, we propose an integrated workflow incorporating deep learning and ensemble learning methods for remote sensing image analysis. As an example, the urbanization process of the Baodi core area in Tianjin was studied using remote sensing images taken in recent years. The type of building and changes in building area were analyzed from the extracted building information, and the economic and social losses resulting from these changes were calculated at three ground-motion intensity levels. Yet, the seismic loss calculation was made based on certain parameters; additional factors such as geology, soil type, distance from the seismogenic fault, seismic wave propagation, and secondary hazards were not taken into consideration.

According to our research, the study area has changed from a county seat to a dormitory town of a big city as a result of urbanization. In the study area, the development of commercial real estate eliminated low-quality housing and nearly doubled the number of people that could be accommodated, but the growth rate of functional infrastructure was relatively low.

New residential buildings have resulted in a reduction in the rate of night-time earthquake deaths in this area. The spatial distribution of the probability of a fatality also changes accordingly. However, there is a possibility that the number of deaths caused by rare earthquakes may not significantly decrease, given the dramatic increase in population. This may be overlooked in the context of urbanization.

Earth observation data complement ground-collected data and play a pivotal role in risk assessment and reduction [82]. Moreover, our study demonstrates that remote sensing data can be a valuable resource to observe changes in seismic risk as a result of urbanization. Although there are still some areas for improvement, the method based on remote sensing

data can be used as a tool for updating seismic risk management plans and urban planning in other parts of China in the future.

Author Contributions: Conceptualization, L.A. and J.Z.; methodology, L.A. writing—original draft preparation, L.A.; visualization, L.A.; supervision, J.Z.; funding acquisition, L.A. and J.Z. All authors have read and agreed to the published version of the manuscript.

Funding: This research was funded by the National Natural Science Foundation of China, grant number 41874059 and Tianjin Science and Technology Program Key R&D Project, grant number 20YFZCSN01010 and National Institute of Natural Hazards, grant number No. ZDJ2017-29.

Institutional Review Board Statement: Not applicable.

Informed Consent Statement: Not applicable.

Data Availability Statement: Not applicable.

Acknowledgments: The authors would like to thank Tianjin Earthquake Disaster Prevention Center for organizing the questionnaire and the reviewers for helpful comments.

Conflicts of Interest: The authors declare no conflict of interest.

References

1. Urbanization. Available online: https://en.wikipedia.org/wiki/Urbanization (accessed on 24 March 2022).
2. What Should We Understand about Urbanization in China? YALE INSIGHT. 2013. Available online: https://insights.som.yale.edu/insights/what-should-we-understand-about-urbanization-in-china (accessed on 7 March 2022).
3. Urbanization and Disaster Risks. Spotlightnepal. Available online: https://www.spotlightnepal.com/2016/01/02/urbanization-and-disaster-risks/ (accessed on 28 April 2022).
4. Feng, B.; Zhang, Y.; Bourke, R. Urbanization impacts on flood risks based on urban growth data and coupled flood models. *Nat. Hazards* **2021**, *106*, 613–627. [CrossRef]
5. Global Assessment Report on Disaster Risk Reduction 2015. Available online: https://www.preventionweb.net/english/hyogo/gar/2015/en/home/download.html (accessed on 28 April 2022).
6. Earthquakes are the Most Damaging of all Natural Disasters. Available online: https://www.163.com/dy/article/DUSSDFLN0514R9P4.html (accessed on 28 April 2022).
7. Chen, Y.; Qi, C. Earthquakes and Seismic Hazard in China. In *Science Progress in China*; Science Press: Beijing, China, 2003; pp. 387–400. [CrossRef]
8. China National Earthquake Data Center. Available online: https://data.earthquake.cn/ (accessed on 28 April 2022).
9. In Fact, 41% of the Big Cities in China Are in Earthquake-Prone Zone. Available online: https://www.bilibili.com/video/BV1HF411z7Td?share_source=copy_web (accessed on 24 March 2022).
10. Wu, J. The direction and path of earthquake disaster risk prevention and control. *Overv. Disaster Prev.* **2021**, *119*, 28–31. (In Chinese)
11. Sendai Framework for Disaster Risk Reduction 2015–2030. Available online: https://www.unisdr.org/files/43291_sendaiframeworkfordrren.pdf (accessed on 24 March 2022).
12. Boughazi, K.; Rebouh, S.; Aiche, M.; Harkat, N. Seismic Risk, and Urbanization: The Notion of Prevention. Case of the City of Algiers. *Procedia Econ. Financ.* **2014**, *18*, 544–551. [CrossRef]
13. Vitor, S.; Helen, C.; Marco, P.; Damiano, M.; Rui, P. Development of the OpenQuake engine, the Global Earthquake Model's open-source software for seismic risk assessment. *Nat. Hazards* **2014**, *72*, 1409–1427.
14. Federal Emergency Management Agency (FEMA)-National Institute of Building Sciences (NIBS). *Earthquake Loss Estimation Methodology—HAZUS97*; Technical Manual; Federal Emergency Management Agency: Washington, DC, USA, 1970.
15. Hosseinpour, V.; Saeidi, A.; Nollet, M.-J.; Nastev, M. Seismic loss estimation software: A comprehensive review of risk assessment steps, software development, and limitations. *Eng. Struct.* **2021**, *32*, 111866. [CrossRef]
16. Ghaffarian, S.; Kerle, N.; Filatova, T. Remote Sensing-Based Proxies for Urban Disaster Risk Management and Resilience: A Review. *Remote Sens.* **2018**, *10*, 1760. [CrossRef]
17. Polli, D.; Dell'Acqua, F.; Gamba, P. First steps towards a framework for earth observation (EO)-based seismic vulnerability evaluation. *Environ. Semeiot.* **2009**, *2*, 16–30. [CrossRef]
18. Zhai, Y.M. Research on the Application of High-Resolution Remote Sensing Images in Prediction and Rapid Evaluation of Urban Earthquake Damage. Ph.D. Thesis, Tongji University, Shanghai, China, 2009. (In Chinese)
19. Borzi, B.; Dell'Acqua, F.; Faravelli, M.; Gamba, P.; Lisini, G.; Onida, M.; Polli, D. Vulnerability study on a large industrial area using satellite remotely sensed images. *Bull. Earthq. Eng.* **2011**, *9*, 675–690.
20. Polli, D.; Dell'Acqua, F. Fusion of optical and SAR data for seismic vulnerability mapping of buildings. In *Optical Remote Sensing*; Springer: Berlin/Heidelberg, Germany, 2011; pp. 329–341.

21. Wang, H.F.; Zhai, Y.M.; Chen, X. Rapid Prediction of Earthquake Disaster of Buildings Based on Remote Sensing Images. *North China Earthq. Sci.* **2010**, *28*, 45–47. (In Chinese)
22. Zhao, Q.; Zhai, Y.G.; Li, T.Z. Study on Application of High-Resolution Remote Sensing Images in Rapid Prediction of Earthquake Disaster in Urban Area. *J. Catastrophol.* **2012**, *27*, 72–76. (In Chinese)
23. Ma, J.J.; Feng, Q.M.; Zhou, H.Y. Method for predicting earthquake damage of housing building groups based on image explanation. *J. Nat. Disasters* **2013**, *3*, 62–67. (In Chinese) [CrossRef]
24. Pittore, M.; Wieland, M. Toward a rapid probabilistic seismic vulnerability assessment using satellite and ground-based remote sensing. *Nat. Hazards* **2013**, *68*, 115–145. [CrossRef]
25. Matsuoka, M.; Miura, H.; Midorikawa, S.; Estrada, M. Extraction of urban information for seismic hazard and risk assessment in Lima, Peru using satellite imagery. *J. Disaster Res.* **2013**, *8*, 328–345.
26. Matsuoka, M.; Mito, S.; Midorikawa, S.; Miura, H.; Quiroz, L.G.; Maruyama, Y.; Estrada, M. Development of building inventory data and earthquake damage estimation in Lima, Peru for future earthquakes. *J. Disaster Res.* **2014**, *9*, 1032–1041. [CrossRef]
27. Geiß, C.; Taubenboeck, H.; Tyagunov, S.; Tisch, A.; Post, J.; Lakes, T. Assessment of seismic building vulnerability from space. *Earthq. Spectra* **2014**, *30*, 1553–1583. [CrossRef]
28. Wieland, M.; Pittore, M.; Parola, S.; Begaliev, U.; Yasunov, P.; Tyagunov, S.; Moldobekov, B.; Saidiy, S.; Ilyasov, I.; Abakanov, T. A multiscale exposure model for seismic risk assessment in Central Asia. *Seismol. Res. Lett.* **2014**, *86*, 210–222. [CrossRef]
29. Riedel, I.; Guéguen, P.; Dalla, M.M.; Pathier, E.; Leduc, T.; Chanussot, J. Seismic vulnerability assessment of urban environments in moderate-to-low seismic hazard regions using association rule learning and support vector machine methods. *Nat. Hazards* **2015**, *76*, 1111–1141. [CrossRef]
30. Abruzzese, D.; Angelaccio, M.; Giuliano, R.; Miccoli, L.; Vari, A. Monitoring and vibration risk assessment in cultural heritage via Wireless Sensors Network. In Proceedings of the 2nd Conference on Human System Interactions, Catania, Italy, 21–23 May 2009. [CrossRef]
31. Ceriotti, M.; Mottola, L.; Picco, G.P.; Murphy, A.L.; Guna, S.; Corra, M.; Pozzi, M.; Zonta, D.; Zanon, P. Monitoring heritage buildings with wireless sensor networks: The Torre Aquila deployment. In Proceedings of the International Conference on Information Processing in Sensor Networks, San Francisco, CA, USA, 13–16 April 2009; pp. 277–288.
32. Gaudiosi, G.; Alessio, G.; Nappi, R.; Noviello, V.; Spiga, E.; Porfido, S. Evaluation of Damages to the Architectural Heritage of Naples as a Result of the Strongest Earthquakes of the Southern Apennines. *Appl. Sci.* **2020**, *10*, 6880. [CrossRef]
33. Ball, J.; Anderson, D.; Chan, C.S.A. Comprehensive Survey of Deep Learning in Remote Sensing: Theories, Tools, and Challenges for the Community. *J. Appl. Remote Sens.* **2017**, *11*, 042609. [CrossRef]
34. LeCun, Y.; Bottou, L.; Bengio, Y.; Haffner, P. Gradient-Based Learning Applied to Document Recognition. *Proc. IEEE* **1998**, *86*, 2278–2324. [CrossRef]
35. Zhang, L.; Zhang, L.; Du, B. Deep Learning for Remote Sensing Data: A Technical Tutorial on the State of the Art. *IEEE Geosci. Remote Sens. Mag.* **2016**, *4*, 22–40. [CrossRef]
36. Krizhevsky, A.; Sutskever, I.; Hinton, G. ImageNet Classification with Deep Convolutional Neural Networks. *Communications of the ACM.* **2017**, *60*, 84–90. [CrossRef]
37. Simonyan, K.; Zisserman, A. Very deep convolutional networks for large-scale image recognition. In Proceedings of the 3rd International Conference Learn Represent ICLR, San Diego, CA, USA, 7–9 May 2015; pp. 1–14. [CrossRef]
38. He, K.; Zhang, X.; Ren, S.; Sun, J. Deep Residual Learning for Image Recognition. In Proceedings of the 2016 IEEE Conference on Computer Vision and Pattern Recognition (CVPR), Las Vegas, NV, USA, 27–30 June 2016; pp. 770–778. [CrossRef]
39. Long, J.; Shelhamer, E.; Darrell, T. Fully convolutional networks for semantic segmentation. In Proceedings of the IEEE Conference on Computer Vision and Pattern Recognition 2015, Boston, MA, USA, 7–12 June 2015; pp. 3431–3440.
40. Ronneberger, O.; Fischer, P.; Brox, T. U-Net: Convolutional Networks for Biomedical Image Segmentation. In *Medical Image Computing and Computer-Assisted Intervention*; Springer: Cham, Switzerland, 2015; pp. 234–241.
41. Badrinarayanan, V.; Kendall, A.; Cipolla, R. SegNet: A Deep Convolutional Encoder-Decoder Architecture for Image Segmentation. *IEEE Trans. Pattern Anal. Mach. Intell.* **2017**, *39*, 2481–2495. [CrossRef]
42. Zhao, H.; Shi, J.; Qi, X.; Wang, X.; Jia, J. Pyramid Scene Parsing Network. In Proceedings of the IEEE Conference on Computer Vision and Pattern Recognition 2017, Honolulu, HI, USA, 21–26 July 2017.
43. Chen, L.C.; Papandreou, G.; Kokkinos, I.; Murphy, K.; Yuille, A.L. Deeplab:Semantic Image Segmentation with Deep Convolutional Nets, Atrous Convolution, and Fully Connected CRFs. *IEEE Trans. Pattern Anal. Mach. Intell.* **2018**, *40*, 834–848. [CrossRef]
44. Chen, L.C.; Papandreou, G.; Schroff, F.; Adam, H. Rethinking Atrous Convolution for Semantic Image Segmentation. *arXiv* **2017**, arXiv:1706.05587.
45. Chen, L.-C.; Zhu, Y.-K.; Papandreou, G. Encoder-Decoder with Atrous Separable Convolution for Semantic Image Segmentation. In Proceedings of the European Conference on Computer Vision (ECCV), Munich, Germany, 8–14 September 2018.
46. Kaiming, H.; Gkioxari, G.; Dollár, P.; Girshick, R. Mask R-CNN. Computer Vision and Pattern Recognition(cs.CV). *arXiv* **2018**, arXiv:1703.06870v3.
47. Zhan, Y.; Liu, W.; Maruyama, Y. Damaged Building Extraction Using Modified Mask R-CNN Model Using Post-Event Aerial Images of the 2016 Kumamoto Earthquake. *Remote Sens.* **2022**, *14*, 1002. [CrossRef]

48. Altaweel, M.; Khelifi, A.; Li, Z.; Squitieri, A.; Basmaji, T.; Ghazal, M. Automated Archaeological Feature Detection Using Deep Learning on Optical UAV Imagery: Preliminary Results. *Remote Sens.* **2022**, *14*, 553. [CrossRef]
49. Wang, Y.; Li, S.; Teng, F.; Lin, Y.; Wang, M.; Cai, H. Improved Mask R-CNN for Rural Building Roof Type Recognition from UAV High-Resolution Images: A Case Study in Hunan Province, China. *Remote Sens.* **2022**, *14*, 265. [CrossRef]
50. Yu, K.; Hao, Z.; Post, C.J.; Mikhailova, E.A.; Lin, L.; Zhao, G.; Tian, S.; Liu, J. Comparison of Classical Methods and Mask R-CNN for Automatic Tree Detection and Mapping Using UAV Imagery. *Remote Sens.* **2022**, *14*, 295. [CrossRef]
51. Liu, H.; Gong, P.; Wang, J.; Clinton, N.; Bai, Y.; Liang, S. Annual Dynamics of Global Land Cover and its Long-term Changes from 1982 to 2015. *Earth Syst. Sci. Data* **2020**, *12*, 1217–1243.
52. Gong, P.; Li, X.C.; Zhang, W. 40-Year (1978–2017) human settlement changes in China reflected by impervious surfaces from satellite remote sensing. *Sci. Bull.* **2019**, *64*, 756–763. [CrossRef]
53. Yang, J.; Huang, X. The 30 m annual land cover dataset and its dynamics in China from 1990 to 2019. *Earth Syst. Sci. Data* **2021**, *13*, 3907–3925. [CrossRef]
54. Gruenhagen, L.; Juergens, C. Multitemporal Change Detection Analysis in an Urbanized Environment Based upon Sentinel-1 Data. *Remote Sens.* **2022**, *14*, 1043. [CrossRef]
55. Daudt, R.C.; Le Saux, B.; Boulch, A.; Gousseau, Y. Urban change detection for multispectral earth observation using convolutional neural networks. In Proceedings of the IGARSS 2018—2018 IEEE International Geoscience and Remote Sensing Symposium, Valencia, Spain, 22–27 July 2018; pp. 2115–2118.
56. Huang, X.; Cao, Y.; Li, J. An automatic change detection method for monitoring newly constructed building areas using time-series multi-view high-resolution optical satellite images. *Remote Sens. Environ.* **2020**, *244*, 111802.
57. Du, P.; Hou, X.; Xu, H. Dynamic Expansion of Urban Land in China's Coastal Zone since 2000. *Remote Sens.* **2022**, *14*, 916. [CrossRef]
58. Huang, X.; Wen, D.; Li, J.; Qin, R. Multi-level monitoring of subtle urban changes for the megacities of China using high-resolution multi-view satellite imagery. *Remote Sens. Environ.* **2017**, *196*, 56–75.
59. Statistical Yearbook of District Baodi. 2021. Available online: http://stats.tj.gov.cn/ (accessed on 9 March 2022). (In Chinese)
60. He, Y.J. Study on Pattern of Tianjin Urbanization Since 1990. Ph.D. Thesis, Tianjin University, Tianjin, China, 2012. (In Chinese).
61. Liu, J.W.; Wang, Z.M.; Xie, F.R. Seismic hazard and risk assessments for Beijing-Tianjin-Tangshan area, China. *Chin. J. Geophys.* **2010**, *53*, 318–325. (In Chinese) [CrossRef]
62. Zhang, H.; Xu, K.; Wang, H.; Pan, Z.; Zhuan, S.P.; Zhang, Y.Q.; Li, Q.Z.; Bu, L.; Shi, G.Y.; Zhang, J.L. Study on the Activity of Baodi Fault Since Late Pleistocene in the Northern Margin of North China Basin. *J. Geod. Geodyn.* **2021**, *41*, 1169–1176, 1188. (In Chinese)
63. WorldPop. Available online: https://www.worldpop.org/project/categories?id=3 (accessed on 24 March 2022).
64. Dunbar, P.K.; Bilham, R.G.; Laituri, M.J. Earthquake loss estimation for India based on macroeconomic indicators. In *Risk Science and Sustainability*; Springer: Dordrecht, Netherlands, 2003; pp. 163–180.
65. Shaoqing, R.; Kaiming, H.; Ross, G.; Jian, S. Faster R-CNN: Towards Real-Time Object Detection with Region Proposal Networks. *IEEE Trans. Pattern Anal. Mach. Intell.* **2017**, *39*, 1137–1149. [CrossRef]
66. Ross., G. Fast R-CNN. In Proceedings of the 2015 IEEE International Conference on Computer Vision (ICCV), Washington, DC, USA, 7–13 December 2015; pp. 1440–1448. [CrossRef]
67. Mask-Rcnn. Available online: https://ztlevi.github.io/Gitbook_Machine_Learning_Questions/cv/two-stage-detector/mask-rcnn.html (accessed on 24 March 2022).
68. Cheng, T.; Wang, X.; Huang, L.; Liu, W. Boundary-preserving Mask R-CNN. In *Computer Vision—ECCV 2020*; Springer: Cham, Switzerland, 2020. [CrossRef]
69. Milletari, F.; Navab, N.; Ahmadi, S. V-net: Fully convolutional neural networks for volumetric medical image segmentation. In Proceedings of the 2016 Fourth International Conference on 3D Vision (3DV), Stanford, CA, USA, 25–28 October 2016; pp. 565–571.
70. Chen, C.; Yang, Z.Y.; Shi, X.L.; Shang, Y. Inversion of urban building height based on Google Earth remote sensing images. *Bull. Surv. Mapp.* **2020**, *1*, 90–101. (In Chinese) [CrossRef]
71. Ecognition. Available online: https://geospatial.trimble.com/products-and-solutions/trimble-ecognition (accessed on 24 March 2022).
72. Breiman, L. Random Forests. *Mach. Learn.* **2001**, *45*, 5–32. [CrossRef]
73. Shinozuka, M.; Feng, M.Q.; Lee, J.; Naganuma, T. Statistical Analysis of Fragility Curves. *J. Eng. Mech.-Asce.* **2000**, *126*, 1224–1231. [CrossRef]
74. Yao, X.Q. Analysis of Tianjin Rural Residential Vulnerability and Seismic Capacity Distribution. Ph.D. Thesis, Institute of Engineering Mechanics, China Earthquake Administration, Harbin, China, 2016. (In Chinese)
75. Xin, D.; Daniell, J.E.; Wenzel, F. State of the art of fragility analysis for major building types in China with implications for intensity-PGA relationships. *Nat. Hazards Earth Syst. Sci. Discuss.* **2018**, 1–34. [CrossRef]
76. Cui, M.Z.; Wang, C.K.; Chen, C.H.; Pan, Y.H.; Xiong, Y.H.; Ren, C.C. Seismic fragility analysis on existing high-rise shear-wall structure based on incremental dynamic analysis. *Build. Sci.* **2021**, *37*, 151–157. [CrossRef]
77. China Earthquake Administration. *GB/T18208.4-2011*; Post-Earthquake Field Works—Part 4: Assessment of Direct Loss; Earthquake Press: Beijing, China, 2011.
78. Kappa_Coefficient. Available online: https://www.tutorialspoint.com/statistics/cohen_kappa_coefficient.htm (accessed on 24 March 2022).

79. Wyss, M.; Rosset, P. Near-Real-Time Loss Estimates for Future Italian Earthquakes Based on the M6.9 Irpinia Example. *Geosciences* **2020**, *10*, 165. [CrossRef]
80. Van Houtte, C.; Abbott, E. OpenQuake Implementation of the Canterbury Seismic Hazard Model. *Seismol. Res. Lett.* **2019**, *90*, 2227–2235. [CrossRef]
81. Feliciano, D.; Arroyo, O.; Cabrera, T.; Contreras, D.; Valcárcel Torres, J.A.; Gómez Zapata, J.C. Seismic risk scenarios for the residential buildings in the Sabana Centro province in Colombia. *Nat. Hazards Earth Syst. Sci.* 2022. (*in review*). [CrossRef]
82. Global Assessment Report on Disaster Risk Reduction 2022. Available online: https://www.undrr.org/publication/global-assessment-report-disaster-risk-reduction-2022 (accessed on 28 April 2022).

sustainability

MDPI

Article

Multi-Hazard Emergency Response for Geological Hazards Amid the Evolving COVID-19 Pandemic: Good Practices and Lessons Learned from Earthquake Disaster Management in Greece

Spyridon Mavroulis [1,*], Maria Mavrouli [2], Asimina Kourou [3], Thekla Thoma [3] and Efthymis Lekkas [1,3]

[1] Department of Dynamic Tectonic Applied Geology, Faculty of Geology and Geoenvironment, School of Sciences, National and Kapodistrian University of Athens, Panepistimiopolis Zografou, 15784 Athens, Greece; elekkas@geol.uoa.gr
[2] Department of Microbiology, Medical School, National and Kapodistrian University of Athens, 11527 Athens, Greece; mmavrouli@med.uoa.gr
[3] Earthquake Planning and Protection Organization, 15451 Athens, Greece; akourou@oasp.gr (A.K.); thomathekla@oasp.gr (T.T.)
* Correspondence: smavroulis@geol.uoa.gr

Abstract: Since the beginning of 2020, the COVID-19 pandemic has caused unprecedented global disruption with considerable impact on human activities. However, natural hazards and related disasters do not wait for SARS-CoV-2 to vanish, resulting in the emergence of many conflicting issues between earthquake emergency response actions and pandemic mitigation measures. In this study, these conflicting issues are highlighted through the cases of four earthquakes that struck Greece at different phases of the pandemic. The earthquake effects on the local population and on the natural environment and building stock form ideal conditions for local COVID-19 outbreaks in earthquake-affected communities. However, the implementation of response actions and mitigation measures in light of a multi-hazard approach to disaster risk reduction and disaster risk management has led not only to the maintenance of pre-existing low viral load in the earthquake-affected areas, but in some cases even to their reduction. This fact suggests that the applied measures are good practice and an important lesson for improving disaster management in the future. Taking into account the aforementioned, a series of actions are proposed for the effective management of the impact of a geological hazard in the midst of an evolving biological hazard with epidemiological characteristics similar to the COVID-19 pandemic.

Keywords: earthquake emergency; COVID-19 pandemic; hazard interaction; compound emergencies; multi-hazard management; emergency shelters

Citation: Mavroulis, S.; Mavrouli, M.; Kourou, A.; Thoma, T.; Lekkas, E. Multi-Hazard Emergency Response for Geological Hazards Amid the Evolving COVID-19 Pandemic: Good Practices and Lessons Learned from Earthquake Disaster Management in Greece. *Sustainability* **2022**, *14*, 8486. https://doi.org/10.3390/su14148486

Academic Editors: Stefano Morelli, Veronica Pazzi and Mirko Francioni

Received: 12 June 2022
Accepted: 6 July 2022
Published: 11 July 2022

1. Introduction

The single-hazard approach is widely used by most countries worldwide in disaster management and disaster risk reduction (DRR) because hazards are considered and managed as isolated and independent phenomena. However, in some cases, different types of hazards overlap and interact in the following ways: (i) natural hazards causing one or more hazard events; (ii) human activities causing natural hazards; (iii) human activities exacerbating natural hazard triggering; (iv) networks of hazard interactions (cascades) forming; and (v) the concurrence of two (or more) hazard events are all examples of human activities triggering natural hazards [1,2].

Gill and Malamund [1] studied how natural hazards, including earthquakes, tsunamis, volcanic eruptions, landslides, floods, fires, and extreme weather events, among others, interact. They were able to identify 90 interactions between 21 natural hazards. It is impressive how the number of interactions can be increased if we add different types

of hazards, such as biological as well as human-made hazards and related disasters and crises. Through this synergy of phenomena and impact, we can imagine how many more challenges, incompatibilities and contrasts can arise when disasters from different hazards occur in parallel.

Since March 2020, when the World Health Organization declared a global pandemic caused by the rapid worldwide spread of severe acute respiratory syndrome coronavirus 2 (SARS-CoV-2) infection [3], the last type of such interaction between biological and natural hazards has become a common occurrence. Since then, many countries have been negatively impacted by natural hazards (earthquakes, floods, fires, hurricanes, and other phenomena) and related disasters [4–7], all while attempting to address and mitigate an evolving biological hazard: the COVID-19 pandemic. It is the most important biological hazard that humanity has recently been called to face, as to date (12 June 2022) SARS-CoV-2 has infected 535,125,479 individuals and has claimed the lives of 6,309,209 people (COVID-19 Dashboard at Johns Hopkins University (JHU); https://coronavirus.jhu.edu/map.html, accessed on 12 June 2022). Furthermore, the COVID-19 pandemic has impacted the daily lives of billions of people and has raised many concerns about community exposure, vulnerability, and preparedness. When this evolving biological hazard collides with natural hazards that do not pause for a virus, these issues become even more complicated. Among other complications, the scientific community and disaster risk management authorities are debating the hierarchy of hazards, which can be used to resolve conflicting issues when two (or more) hazards occur simultaneously. Important questions arise to do with the most effective way of responding to competing hazards, and the most efficient disaster management and DRR policies that are incompatible with pandemic mitigation measures. These strategies and policies must be adapted and new innovative multi-hazard approaches should be adopted to reduce individual and community vulnerability.

Many such issues arose during the collision of earthquake-related geological hazards and the evolving pandemic. Many earthquake emergency response actions were incompatible with the pandemic mitigation measures. This fact was highlighted in Greece after the occurrence of large and destructive earthquakes from early 2020. It is important to note that Greece, located in the Eastern Mediterranean region, is characterized by high seismicity [8,9], ranking it first in Europe and sixth in the world among seismic active countries. This high seismicity comprises frequent strong earthquakes [8,9] with a significant impact on the local population, the natural environment, and the building stock, e.g., [10,11]. This is attributed to the occurrence and activation of seismogenic structures, mainly related to the subduction of the Eastern Mediterranean plate beneath the Aegean one along the Hellenic Trench and to major onshore and offshore seismic faults along the margins of neotectonic macrostructures, e.g., [12,13]. Typical examples of such events, which occurred in different waves of the pandemic in Greece and will be examined in the context of this research, are as follows (Figures 1 and 2):

1. The Mw = 5.7 Epirus (northwestern Greece) earthquake generated on 21 March 2020 at the beginning of the first pandemic wave and two days before the installation of a strict nationwide lockdown strategy;
2. The Mw = 7.0 Samos earthquake generated on 30 October 2020 during the second pandemic wave and 7 days before the installation of a strict nationwide lockdown strategy for the second time in Greece;
3. The Mw = 6.3 Thessaly earthquake that occurred on 3 March 2021 during the third pandemic wave;
4. The Mw = 6.0 Crete earthquake that occurred on 27 September 2021 during the fourth pandemic wave.

Regarding the seismotectonic setting of the aforementioned earthquake-affected areas, the main source of the Mw = 5.7 Epirus earthquake was located on the Margariti thrust fault, within the frontal area of the Ionian fold and the thrust belt of the Hellenic orogen [14]; the Mw = 7.0 2020 Samos earthquake epicenter was located along the southern marginal fault of the North Ikaria Basin [15]; the Mw = 6.3 2021 Thessaly earthquake epicenter was located

along the margins of the Tyrnavos Basin [16]; and the Mw = 6.0 2021 Crete earthquake was strongly related to the NNE–SSW-striking W-dipping faults of the Kasteli fault zone located along the eastern margin of the Neogene to Quaternary Heraklion Basin [17].

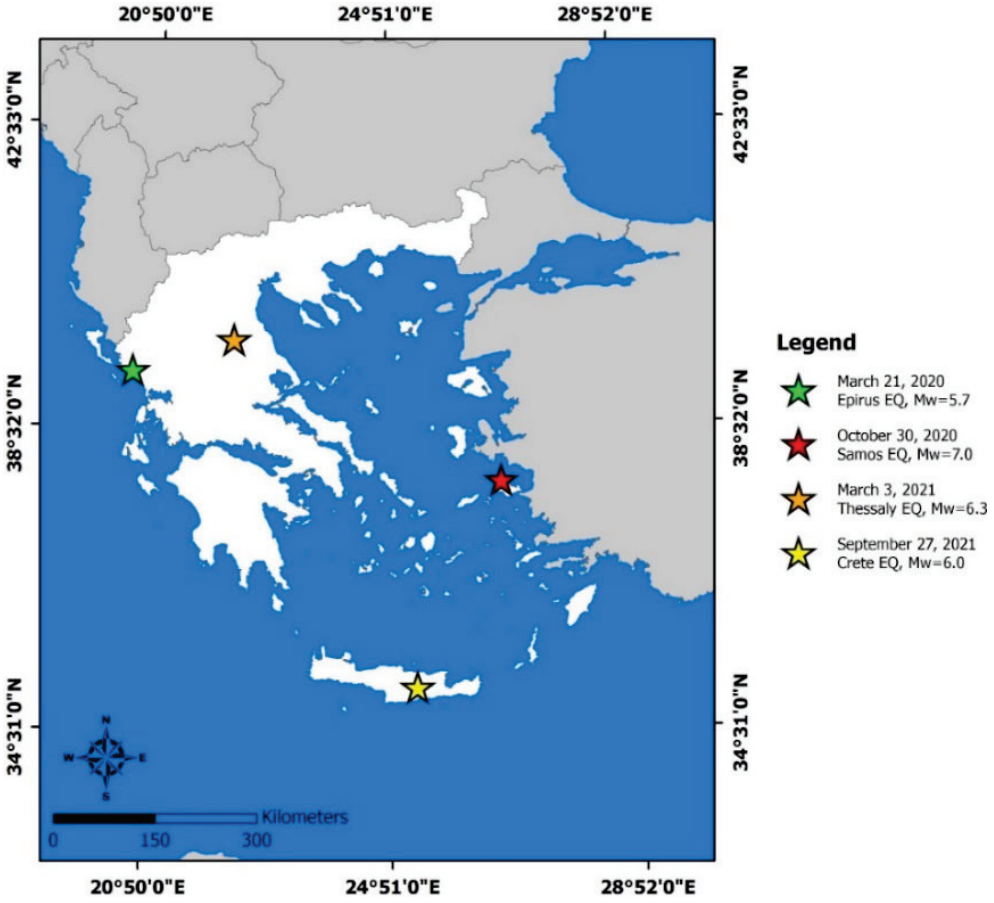

Figure 1. The epicenters of the studied earthquakes in Epirus, Samos, Thessaly, and Crete. They were all generated in different waves of the COVID-19 pandemic in Greece.

Regarding the impact on the local population of Greece, these earthquakes resulted in limited human losses (two fatalities from the Samos earthquake, one from the Thessaly earthquake, and one from the Crete earthquake) attributed to the partial or total collapse of unreinforced masonry structures. The reported losses could be characterized as minimal, considering the extensive structural and non-structural damage observed especially in old unreinforced buildings with load-bearing walls (Ref. [18] for the Samos earthquake; Ref. [19] for the Thessaly earthquake). It is significant to note that the Samos seismic event was the largest in Europe and Turkey and the most fatal worldwide amid the first year of the COVID-19 pandemic evolution, if we also consider the 117 fatalities reported in Izmir city attributed to the partial or total collapse of buildings with reinforced concrete frames and infill walls [17].

Regarding the earthquake environmental effects, the Epirus earthquake triggered rockfalls and river water turbidity in the earthquake-affected area. The Samos earthquake induced primary effects comprising coseismic uplift and surface ruptures and secondary phenomena including slope failures, ground cracks, liquefaction phenomena and hydrological anomalies and the largest tsunami in Greece since 1956 [20]. The Thessaly earthquake triggered extended liquefaction phenomena in recent deposits in the riverbeds of the earthquake-affected area [19]. The Crete earthquake generated mainly rockfalls and slides, as well as ground cracks within or close to landslide zones.

Taking into account the new adverse conditions that have emerged in the field of disaster risk reduction and management, this paper aims to (Figure 3):

1. Highlight the contradictory issues that arose in the emergency response to the aforementioned earthquakes during different phases of the evolving COVID-19 pandemic that did not exist in the pre-pandemic period;
2. Share the practices used during the emergency response;
3. Present the approaches that need to be adapted and adopted during emergency response to earthquakes not only amid the current pandemic but also when geological hazards collide with evolving biological hazards.

Furthermore, in the earthquake-affected regions of Epirus, Samos, Thessaly, and Crete, an analysis of the COVID-19 pandemic's evolution is carried out (Figure 3). The goal of this post-event analysis is to determine the impact of the earthquake on the pandemic's progression in the affected areas, as well as to evaluate the effectiveness of the actions taken in the early hours and days of the emergency response phase.

In this context, a brief description of the Civil Protection framework in Greece is given, with emphasis on the existing general plan for the emergency response and immediate management of the earthquake impact and effects (Figure 3). Particular emphasis is placed on the single-hazard nature of this plan. The absence of a plan that takes into account the interactions between geological and biological hazards is also highlighted. In addition, reference is made to the COVID-19 pandemic mitigation strategies and measures implemented during the last two years in Greece.

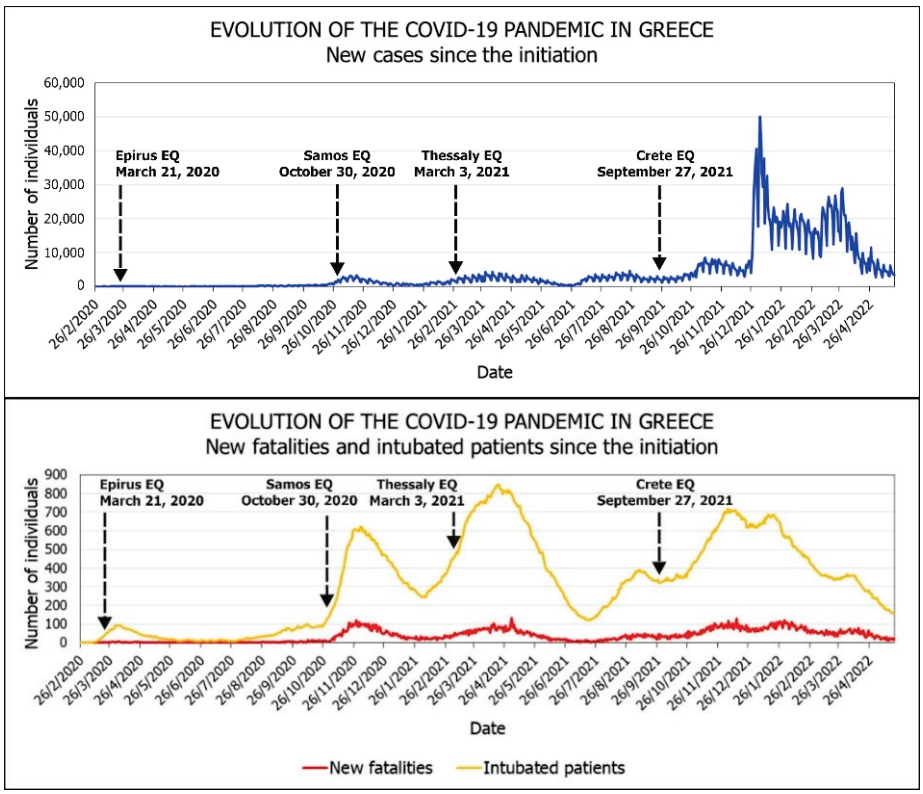

Figure 2. The laboratory-confirmed daily-reported COVID-19 cases, intubated patients and fatalities in Greece from the pandemic onset in February 2020 until late April 2022 based on the daily reports of the National Public Health Organization (NPHO) of Greece. The studied earthquakes of Epirus, Samos, Thessaly, and Crete are also presented.

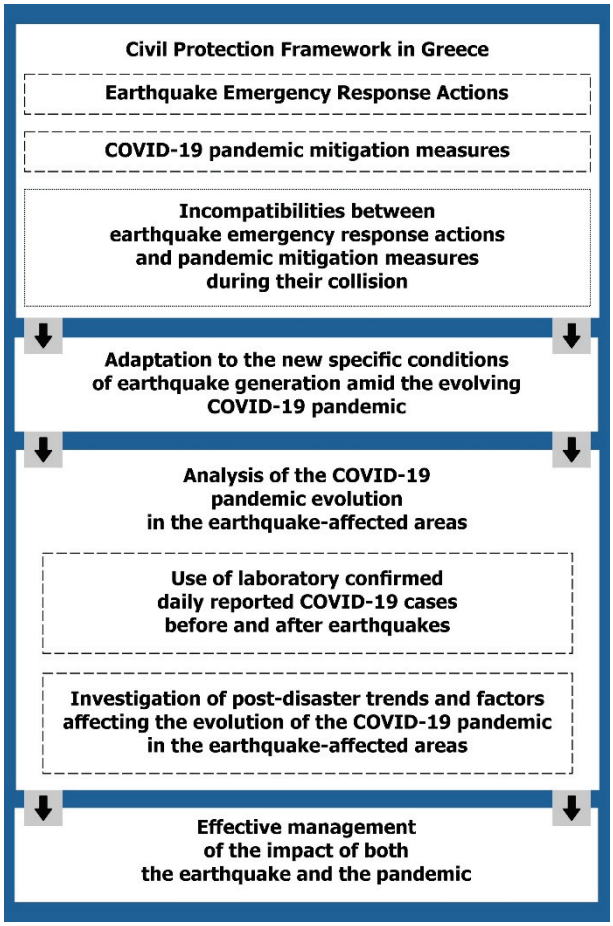

Figure 3. Flow chart showing the approach followed in the present study.

2. Civil Protection Framework in Greece

In late February 2020, the pandemic came knocking on Greece's door. The general plans for dealing with emergencies and managing the consequences of each hazard were also released at the same time. The General Secretariat for Civil Protection (GSCP) announced the formulation of the "Enceladus" earthquake plan, the "Dardanos" flood plan, the "Iolaos" forest fire plan, the "Talos" plan for volcanic activity in the Santorini complex (Aegean Sea), the "Voreas" plan for snowfall and frost, and the "Heraclitus" plan for large-scale technological accidents, all of which are publicly available online at the GSCP site (https://www.civilprotection.gr/en, accessed on 10 May 2022).

In terms of earthquakes, the "Enceladus" plan aims to provide an immediate and coordinated response from authorities at the national, regional, and local levels in order to effectively respond to earthquake effects and manage them. The most significant flaw or omission identified in the aforementioned is the lack of a general plan for dealing with emergencies and managing the consequences of biological hazards. This gap, in the case of the COVID-19 pandemic, was filled by the prevention measures against SARS-CoV-2 issued by the Ministry of Health (https://www.moh.gov.gr/articles/health/dieythynsh-dhmosias-ygieinhs/metra-prolhpshs-enanti-koronoioy-sars-cov-2/, accessed on 10 May 2022) from 28 February 2020 and the information material and specialized instructions of the National Public Health Organization (NPHO) (https://eody.gov.gr/en/covid-19/, accessed on 10 May 2022) from early February 2020 until the present. These bodies are in constant contact with the European Center for Disease Prevention and Control (ECDC) and the World Health Organization (WHO) to ensure that prevention measures, information materials, and specialized instructions are kept up to date, taking into account the pandemic's evolution in Greece. The analysis of these plans also reveals that the existing

plans use a single-hazard approach to assessing hazard potential, in which hazards are treated as separate and unrelated events.

What happens, however, if a disaster induced by a natural hazard strikes in the midst of the COVID-19 pandemic in Greece? Unfortunately, no plans exist to consider potential interactions between natural and biological hazards. This is due to the fact that the pandemic is a constantly evolving biological hazard that poses unprecedented challenges and threats to all, including citizens and governments, patients, and health systems around the world, putting public health and many other aspects of daily life and human activities at risk. The COVID-19 pandemic has evolved into a rapidly changing emergency, with data and measures constantly changing across Europe and around the world, affecting people at all levels.

3. COVID-19 Pandemic Mitigation in Greece

On 26 February 2020, the first confirmed case of SARS-CoV-2 infection in Greece was reported. Since then, the Greek government and authorities involved in the COVID-19 pandemic management in Greece have taken precautionary measures to limit the spread of the novel virus in the community and the pandemic's effects on public health. Mavroulis et al. [6] present the measures taken during the first and second waves of the COVID-19 pandemic in Greece. During the first wave of the pandemic, Greece implemented a strict nationwide lockdown strategy on 23 March 2020, which was extended until 4 May 2020. The emergency COVID-19 restrictive measures were gradually deescalated as of 4 May, with the gradual reopening of retail businesses, commercial stores, educational and religious activities, the lifting of travel restrictions across the country, and the gradual lifting of national and international restrictions.

All daily activity resumptions and restrictions were accompanied by the majority of the population's continued protective measures. These included hygiene and social distancing measures, restrictions on the maximum number of people allowed indoors and outdoors, and guidelines for the use of masks and disposable gloves, both optional and mandatory on occasion. Furthermore, authorities involved in COVID-19 pandemic management, such as the Ministry of Health, the NPHO, and the GSCP, imposed COVID-19 and SARS-CoV-2 transmission prevention measures, taking into account all updated scientific data on the pandemic's evolution in Greece and around the world.

Despite the measures taken, the number of COVID-19 cases increased, and a second wave of the pandemic began in Greece in early August, with a more aggressive course than the first, according to daily reports of laboratory-confirmed COVID-19 cases, ICU patients, and fatalities [21]. By mid-September 2020, the number of cases had surpassed the first wave's peak, and the number of ICU patients and fatalities had surpassed those of April 2020 when a nationwide lockdown was imposed. On 20 October, an upward trend in cases began, peaking on 12 November with 3316 daily reported COVID-19 cases [21]. There was a corresponding increase in the number of fatalities, which peaked on 28 November with 121 casualties [21]. In December and January, there was a gradual decrease in daily COVID-19 cases, ICU patients, and casualties. These figures never recovered to pre-October 2020 levels. This means that the virus was prevalent in the community and that an increase in cases could occur at any time.

The main measures implemented by the government and the involved authorities to limit the spread of the novel virus in the community during the second wave of the COVID-19 pandemic in Greece were local-scale restrictive measures, such as local-scale lockdowns in large cities, towns, and settlements, as well as a second national-scale lockdown, which began on 7 November 2020. The earthquake on Samos struck on 30 October, just days before the second national-scale lockdown.

The main guidelines announced by the involved authorities for preventing SARS-CoV-2 transmission, from the start of the pandemic in Greece on 26 February 2020 until the second wave, included personal hygiene measures, cleaning and disinfecting areas, surfaces, and items, restricting contact, and avoiding gatherings and overcrowding indoors and

outdoors. The announced guidelines included hygiene measures in health-related businesses, hygiene rules for public transportation, protection measures in sports facilities, educational units, workplaces, elderly care units, health units, health service units, and the country's entrance gates, as well as temporary reception and accommodation facilities for refugees seeking asylum and unaccompanied minors and youths, and public infrastructure protection measures.

Personal hygiene guidelines and advice comprised the following actions in order to reduce the infection risk:

- Keeping hands away from the eyes, nose, and mouth;
- Avoiding sharing personal items;
- Covering the mouth and nose with a tissue, sleeve or flexed elbow when coughing or sneezing and throwing the tissue into a closed bin after use;
- Regular hand washing with liquid soap and water for at least 20 s and careful hand drying with disposable paper towels;
- Using alcohol-based hand sanitizer containing at least 70% alcohol;

The cleaning and disinfection guidelines comprised:

- Systematic and adequate ventilation of all areas with complete and frequent air renewal;
- Frequent cleaning of commonly used smooth surfaces (e.g., knobs, handles, handrails or railings, taps, etc.) with common cleaners and disinfectants;
- The use of appropriate protective equipment (gloves and work uniform) during cleaning and disinfection;
- Cleaning objects and surfaces of which a person who showed symptoms of SARS-CoV-2 infection had come into contact.

Physical social contacts were reduced by keeping a distance of at least 1.5 to 2 m and avoiding contact with people who had infection symptoms (shaking hands, hugs, and kissing), avoiding gatherings and overcrowding, reducing contact with people who belonged to vulnerable groups, and minimizing group activities and non-essential movements.

Since the second wave in Greece, the implementation of vaccines—initially for health workers and very high-risk population groups and then for all other age groups of the population—and the subsequent administration of antiviral drugs to patients with COVID-19 infection have been useful tools for halting the pandemic and limiting its negative consequences on public health and all sectors of human activity. However, the imposition or withdrawal of these pandemic containment measures—even after the arrival of vaccines and medicines—is carried out according to the burden that the pandemic occasionally places on the national health system.

4. Earthquake Emergency Response Actions, Incompatibilities with the COVID-19 Pandemic Mitigation Measures, and Adaptation for Dealing with Both Earthquake and Pandemic Effects

Following the aforementioned earthquakes, the Greek government launched a massive resource mobilization effort to aid the affected population. For disaster management, public authorities from all levels of government, Civil Protection agencies and security and armed forces, are mobilized. The main actions taken by agencies during the response to an earthquake disaster can be divided into 11 categories [6,19,22]:

1. Initial earthquake notification;
2. First assessment of the impact, followed by mobilization of and coordination by the Civil Protection authorities;
3. Civil Protection guidelines through emergency communications services;
4. Search and rescue (SAR) operations, first-aid administration and medical care;
5. Mobilization and contribution of volunteers;
6. Set up of emergency shelters;
7. Provision of emergency supplies and donations;
8. Psychological support for the affected population;

9. Raising awareness and education for protective measures to successfully deal with the continuous aftershock sequence;
10. Post-earthquake hazard mitigation and building inspections;
11. Immediate financial relief measures.

The emergency response actions for the mobilization, intervention, and management of earthquake effects had never been tested before in the context of another crisis that posed an additional risk to public health and, thus, human life. In the pre-pandemic period, this sequence of actions would be completely unconcerned. With the earthquakes in Epirus, Samos, Thessaly, and Crete, the local population and Civil Protection authorities were confronted with unprecedented circumstances, including considerable earthquake-triggered effects and the ongoing threat of the COVID-19 pandemic. During the COVID-19 pandemic, many conflicting issues arose from the start of the emergency response, owing to the fact that the majority of emergency actions were incompatible with the pandemic mitigation measures that had been implemented. This is due to the fact that, from the first moments after an earthquake, emergency response actions and people's reactions involve or require the gathering of a large number of people in one location for an extended period of time, the interaction of locals with rescue teams, volunteer teams, and disaster management staff, as well as the unintentional violation of many basic hygiene rules (e.g., regular hand washing, surface disinfection). During the pandemic, these actions may result in clusters of SARS-CoV-2 infection cases within the affected area, hampering emergency response and slowing the recovery process.

To overcome the incompatibilities between earthquake emergency response actions and pandemic mitigation measures, earthquake emergency response actions were adapted to the unprecedented conditions of the parallel occurrence of geological and biological hazards. These adaptations were made in light of a multi-hazard approach at all stages of the earthquake emergency response, starting from the initial mobilization of the Civil Protection authorities up to the conduction of awareness and education activities for the protection of the local population during the continuous aftershock sequence.

The staff of the Civil Protection authorities, who contributed to the earthquake disasters' management, came mostly from other areas with different infection rates and different degrees of public health emergency and risk for SARS-CoV-2 infection. Regarding the implementation of self-protection measures and the protection of the local population by the Civil Protection staff that participated in the emergency management in the earthquake-affected areas, the main adaptations included the mandatory use of masks outdoors and the frequent use of antiseptics, keeping physical distance from the local population, and the disinfection of equipment and tools used by many people. These measures were strictly used especially in actions that required interaction and closer contact with the local population, such as SAR operations, the assessment of building damage, as well as the provision of basic necessities and emergency supplies to the affected residents.

The adaptations for avoiding overcrowding and maintaining physical distancing in emergency shelters comprised the use of a large number of different types of shelters (Figure 4). A typical example of this approach is the emergency shelters used in the 2020 Samos earthquake-affected area. Many homeless and affected people were accommodated in hotel rooms and tourist accommodation facilities. This measure ensured not only the maintenance of physical distance between the affected people, but also the avoidance of overcrowding in outdoor emergency shelters. This solution was possible because the earthquake occurred during the autumn when the tourist traffic in Samos was low, resulting in empty or closed hotels in the earthquake-affected areas. The accommodation of homeless and severely affected people in the unaffected houses of relatives and friends also aided the maintenance of physical distance.

Figure 4. Several types of emergency shelters for the immediate housing of people in need after an earthquake which were used at the Damassi (Thessaly) camp (**a**) after the 3 March 2021 Thessaly earthquake. They comprised (**b**) camper vans, (**c**) tents, and (**d**) temporary container-type structures in the same area. Amid the pandemic, the use of many different types of shelters contributed to the avoidance of overcrowding in camps and the maintenance of physical distance in order to limit the spread of the novel virus in the earthquake-affected community.

The same approach of using a large number of different types of emergency shelters was applied in the case of the 2021 Thessaly earthquake, which occurred a few months later during the third pandemic wave. The Civil Protection authorities used outdoor emergency shelters, hotel rooms and tourist facilities, camper vans, and temporary container-type facilities (Figure 4) as well as accommodation in the houses of relatives and friends. In this way, it was possible to ensure a certain amount of space between groups and individuals who camped in outdoor emergency shelters, which before the pandemic usually housed the majority of earthquake-affected people.

During the collection and distribution of essentials, and especially during the distribution of meals to the affected people, volunteers used personal protective equipment at all stages of the process (Figure 5a–c). As for the daily meals, these were most often prepared in packet form (Figure 5c,d) for further distribution to the affected people.

Regarding the post-earthquake building inspections, information activities were carried out for civil engineering teams outdoors or in closed spaces with adequate ventilation in the earthquake-affected areas. The appropriate physical distances between the participants were effectively maintained. For example, these activities were held either outdoors, such as in the central square of the Town Hall of Eastern Samos in the capital city of the homonymous municipality, or in large indoor spaces, such as indoor sports facilities with large spaces, ensuring the maintenance of physical distance and adequate ventilation, which ensured the safety of the participants during these briefings (Figure 6). In the case of the Thessaly earthquake, the briefings were held in open spaces in the most-affected settlements. In the case of the Crete earthquake, these briefings were held in the courtyard of the 2nd Primary School of Arkalochori town, where the operational center had been established by the Civil Protection authorities (Figure 6).

Figure 5. Typical views of the distribution of relief supplies: (**a**) in the operational center in the Town Hall Square of the Eastern Samos municipality; (**b**,**c**) in the earthquake camp in Damassi (Thessaly); and (**d**) in the earthquake camp at the exhibition center of the earthquake-affected town of Arkalochori on Crete Island. The distribution of relief supplies was adapted to the new conditions formed by the pandemic. Civil Protection personnel, members of the armed forces and voluntary groups used personal protective equipment at every stage of the preparation and distribution of supplies (**c**), and the meals were served packed (**c**,**d**).

Figure 6. Information activities for building inspections on the affected island took place in indoor sports facilities after the 2020 Samos earthquake.

Moreover, building-damage documentation centers were set up outdoors. In these centers, especially during the first hours and days of the emergency phase, it was impossible to implement the measures of physical distancing due to the fact that many residents gathered to report building and property damage. In this case, the use of masks and hand sanitizers was vital. Thus, personal protective equipment supplies were available not only for the affected people but also for the involved personnel.

Coordination meetings of the Civil Protection authorities involved in disaster management took place during the emergency response, with the aim to assess the situation and organize, coordinate and implement further actions. These meetings were conducted in specially designed outdoor sites, which provided not only protection from large aftershocks, but also comfort in maintaining physical distance (Figure 7). In these areas, all personal protective measures including masks, hand sanitizers and disposable gloves when neces-

sary, were available for both the affected people and the Civil Protection staff. In addition, food supplies including bottled water and packaged food were also immediately available and distributed to those in need by complying with all precautions against COVID-19.

Figure 7. (**a**,**b**) The coordination operation center after the 2020 Samos earthquake was set up outdoors with spatial arrangement adapted to the pandemic mitigation measures. (**c**,**d**) The same approach was applied in the case of the Arkalochori (Crete) earthquake. The coordination operation center was also set up outdoors in the courtyard of a school, providing space for maintaining physical distance and avoiding overcrowding.

In Samos, the operations coordination center was set up shortly after the earthquake occurrence in the square in front of the Eastern Samos Municipality building in Vathy (Figure 7a,b). There were seats placed at appropriate distances and personal protective equipment supplies available for all involved when it was not possible to maintain distance. The use of masks was mandatory. In Crete, the operations coordination center was set up shortly after the earthquake occurrence in a courtyard of a primary school (Figure 7c,d) located at the town most affected by the main shock on 27 September 2021.

Regarding raising awareness and education activities for the local population, seminars were held by the Earthquake Planning and Protection Organization of Greece for certain targeted population groups in all earthquake-affected areas in Epirus, Samos, Thessaly and Crete. These seminars were not held indoors, but outdoors (Figure 8), where all the protection measures against the pandemic could be applied. The provided information included training and guidelines for protection during the aftershock period against both possible large aftershocks and the further transmission of the novel virus.

Regarding psychological support for the earthquake-affected people, it was provided to everyone who was experiencing significant psychological stress by the regional and local authorities and voluntary organizations acting in the earthquake-affected Samos, always in excellent cooperation. In order to apply social distancing practices and to avoid overcrowding during sessions, the psychological support was usually provided after making an appointment for in-person counseling, while remote communication via teleconference or videoconference was also available. In the case of in-person meetings, wearing masks and keeping the appropriate physical distance was mandatory both indoors and outdoors.

Table 1 summarizes the main actions taken during the first hours and days of the emergency response that were incompatible with pandemic mitigation measures, as well as the adaptations made in order to effectively deal with both the earthquakes and the pandemic.

Figure 8. Awareness-raising and educational activities were conducted by the staff of the Earthquake Planning and Protection Organization of Greece in the earthquake-affected Samos. Amid the pandemic, the activities were held outdoors with participants using personal protective equipment (mask, gloves and antiseptics). (**a**–**d**) Views from workshops for the directors of primary and secondary schools in Vathy town located at the northeastern part of Samos Island.

Table 1. Earthquake emergency response actions, incompatibilities with the pandemic mitigation measures, and adaptations for the effective management of both the earthquakes and the pandemic.

Earthquake Emergency Response Actions in the Pre-Pandemic Period	Pandemic Mitigation Measures and Incompatibilities with Earthquake Emergency Response Actions	Adaptations for the Effective Management of both Earthquakes and the Pandemic
Mobilization of Civil Protection Authorities		
Civil Protection staff should be on time in the earthquake-affected area.	It is prohibited to move, by any means, outside the boundaries of an area with a larger viral load and higher infection rate. It is prohibited to visit an area with larger viral load and higher infection rate.	Two exclusive flights operated by Civil Protection transported all required personnel a few hours after the earthquake. All the necessary safety measures were taken during the flight (masks throughout the whole journey, one person sitting in each seat row, hand sanitizer).
		Application of preventive measures comprising mandatory mask wearing, hand washing and maintaining physical distance during interactions between the local population and authorities.
Coordination of the Civil Protection Authorities		
Coordination meetings take place usually indoors in unaffected buildings with the staff involved in disaster management.	Gathering many people indoors for several hours should be avoided.	Set up of Emergency Operations Centers outdoors, with seats placed at appropriate distances, personal protective equipment supplies available for all involved, mandatory use of face masks.

Table 1. *Cont.*

Earthquake Emergency Response Actions in the Pre-Pandemic Period	Pandemic Mitigation Measures and Incompatibilities with Earthquake Emergency Response Actions	Adaptations for the Effective Management of both Earthquakes and the Pandemic
SAR Operations		
SAR operations require close and frequent contact not only with the affected local population and local authorities, but also with other rescue teams and volunteers.	Rescuers should maintain the appropriate physical distancing.	Mandatory use of masks indoors and outdoors, frequent use of antiseptics, keeping physical distance from the local population and disinfection of equipment and tools used by many rescuers.
The special equipment can be used by many members of rescue teams.	The use and exchange of items, tools and equipment and the frequent use of surfaces and spaces by many individuals carries the risk of transmitting the novel virus.	
Set up of Emergency Shelters		
Overcrowding and coexistence of many people in emergency shelters over a long period of time.	The accommodated people should maintain physical distancing.	Use of different types of emergency shelters. Outdoor camps, accommodation in hotel rooms, tourist accommodation facilities and unaffected houses of relatives and friends. Personal protective equipment supplies available for all involved in all shelters.
High mobility usually observed in emergency shelters during the first hours and days of the emergency.		
Mobilization and Contribution of Volunteers		
Volunteers not only from the affected area, but from every corner of the country rush to the affected area and provide support.	It is prohibited to move, by any means, outside the boundaries of an area with a larger viral load and higher infection rate. It is prohibited to visit an area with larger viral load and higher infection rate.	Mandatory use of masks indoors and outdoors, frequent use of antiseptics, keeping physical distance from the local population and disinfection of items, tools and equipment.
Volunteers distribute humanitarian aid gathered from various sources.	The distribution of items, tools and equipment and the frequent use of surfaces and spaces by many individuals carries the risk of transmitting the novel virus.	
Volunteers distribute meals to affected people where necessary.		
Voluntary teams and their members come into close contact with many people and for many hours in the affected area.	Volunteers should maintain the appropriate physical distancing.	
Provision of Emergency Supplies and Donations		
People from around the country and worldwide are mobilized in order to donate essential emergency supplies to the affected population.	The whole process, from the collection of emergency supplies to their final distribution to the affected population, involves risks for the public health attributed to touching undisinfected items and surfaces.	Mandatory use of masks indoors and outdoors, frequent use of antiseptics, keeping physical distance from the local population and disinfection of items, tools and equipment.

Table 1. *Cont.*

Earthquake Emergency Response Actions in the Pre-Pandemic Period	Pandemic Mitigation Measures and Incompatibilities with Earthquake Emergency Response Actions	Adaptations for the Effective Management of both Earthquakes and the Pandemic
Post-earthquake Hazard Mitigation and Building Inspections		
Evacuation of the affected population from several heavily affected areas.	Residents and Civil Protection staff should maintain the appropriate physical distancing	The involved Civil Protection staff applied necessary individual preventive measures for their safety and the protection of the affected community (mandatory use of masks, regular hand washing, and maintaining physical distance).
Civil engineers inspect buildings during the emergency response. This action requires interaction with homeowners.		Information activities were carried out for participants in civil engineering teams in open or closed spaces with adequate ventilation. Civil engineers applied necessary individual preventive measures for their safety and the protection of the affected community (mandatory use of masks, regular hand washing, and maintaining physical distance). Building damage documentation centers were set up in open spaces.
Psychological Support for the Affected Population		
Psychological support and counseling sessions are carried out in person and indoors.	These sessions pose a risk of spreading the virus among participants and then in the community.	Remote communication via teleconference or videoconference was available. In the case of in-person meetings, mandatory mask-wearing and keeping appropriate physical distance both indoors and outdoors
Awareness-raising and Education Activities on the Earthquake Effects and Protective Measures		
Seminars take place indoors in educational facilities, properly designed to accommodate many people for many hours.	Gathering of many people indoors for several hours should be avoided.	Outdoors seminars in safe places away from the adverse effects of possible aftershocks and easy application of pandemic mitigation measures comprising mainly maintaining of physical distance.
		Transmission of information through the loudspeakers of police patrol vehicles, calling on the people to comply with the pandemic prevention measures.

5. The Evolution of the COVID-19 Pandemic in the Earthquake-Affected Areas

The findings of the study on the pandemic's post-disaster evolution during the first weeks of emergency response and recovery in earthquake-affected areas are presented in this section. They are based on laboratory-confirmed and daily-recorded COVID-19 cases in earthquake-affected regional units derived from the NPHO's COVID-19 epidemiological surveillance daily reports. These reports are freely available online on the NPHO's website (http://eody.gov.gr/epidimiologika-statistika-dedomena/ektheseis-covid-19/, accessed on 30 January 2022).

Regional units are the smallest local government organizations for which daily case numbers are announced in Greece and include the affected areas based on the above data and the available sources of daily COVID-19 cases. As a result, we used data from the above source in our research for the following regional units (Figure 9):

- The Arta, Thesprotia, Ioannina, and Preveza regional units of the Epirus region, which were affected by the Epirus earthquake;

- The Samos, Ikaria and Chios regional units of the North Aegean region, which were affected by the Samos earthquake;
- The Karditsa, Larissa, Magnesia and Trikala regional units of the Thessaly region, which were affected by the Thessaly earthquake;
- The Heraklion regional unit of the Crete region, which was affected by the earthquake on 27 September 2021.

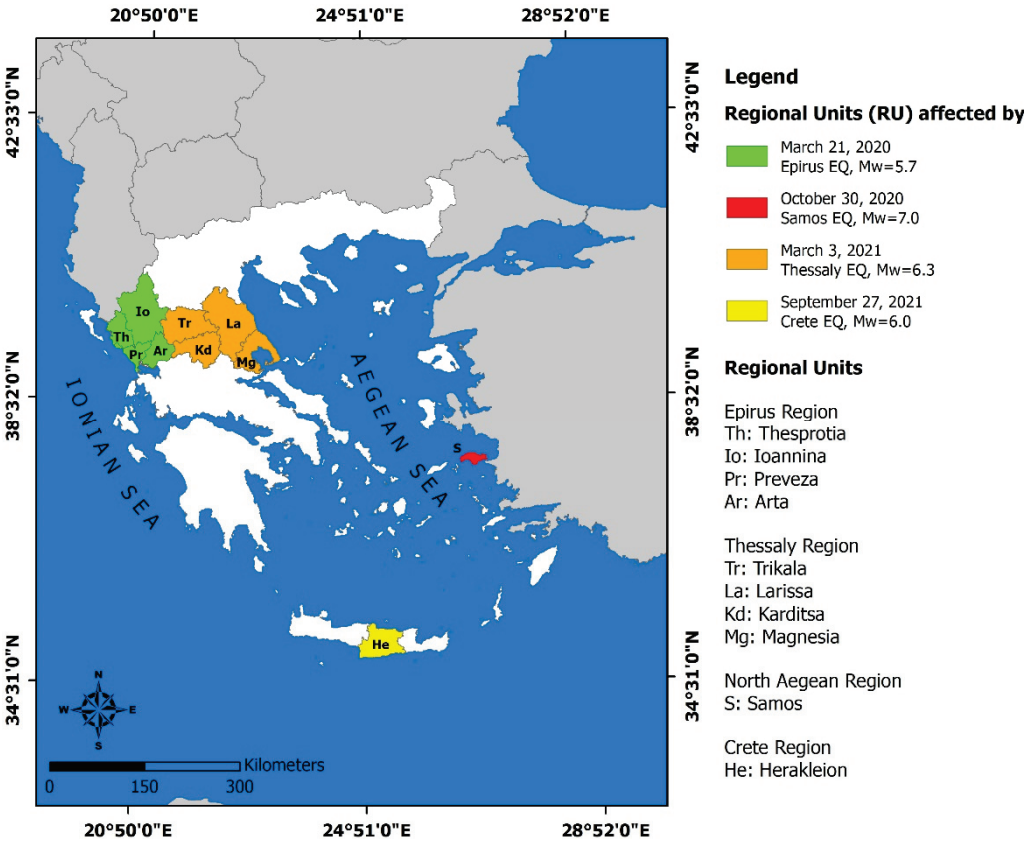

Figure 9. The earthquake-affected regional units in Greece during the COVID-19 pandemic.

Mavroulis et al. [6] used the same methodology to investigate post-disaster trends and factors affecting the evolution of the COVID-19 pandemic in areas affected by geological and hydrometeorological hazards in Greece. In particular, it was taken into account that the estimated incubation period of SARS-CoV-2 ranges from 2 to 14 days (median incubation time: 5 days) [23,24] and that SARS-CoV-2 can be detected by the polymerase chain reaction (PCR) test in infected patients up to 21 days after the onset of symptoms [25,26]. As a result, COVID-19 cases reported 5 days after disasters could be attributed to disaster-related adverse effects. Mavroulis et al. [6] suggested that it was appropriate to track the number of daily confirmed cases in the 7 days (1 week) leading up to the disaster to determine the pre-existing viral load and infection rate in each affected area.

Taking into account all the aforementioned data, the number of daily COVID-19 cases in the present study was tracked:

- From 14 March to 11 April 2020 for the Epirus earthquake generated on 21 March 2020 (Figure 10);
- From 23 October to 21 November 2020 for the Samos earthquake generated on 30 October 2020 (Figure 11);
- From 24 February to 24 March 2021 for the Thessaly earthquake generated on 3 March 2021 (Figure 12);
- From 20 September to 10 October 2021 for the Crete earthquake generated on 27 September 2021 (Figure 13).

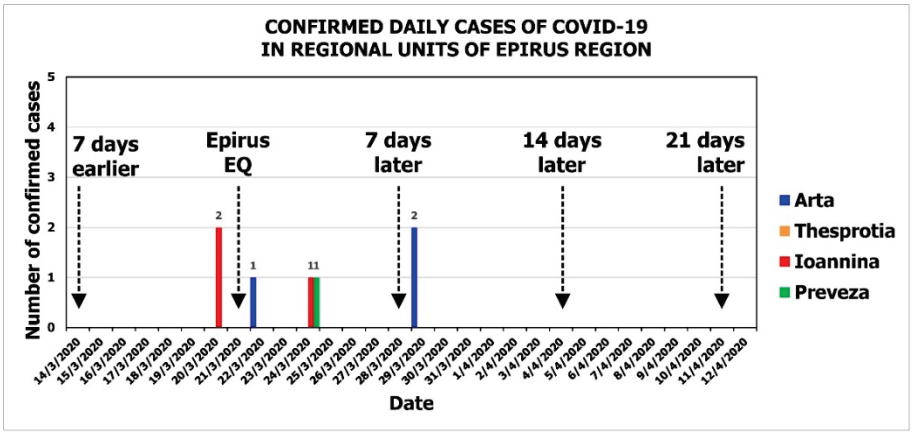

Figure 10. The evolution of COVID-19 cases in the earthquake-affected regional units of the Epirus region before and after the occurrence of the 21 March 2020 Epirus earthquake. The laboratory-confirmed, daily-recorded COVID-19 cases are from the NPHO's COVID-19 epidemiological surveillance daily reports [21] covering the period from 14 March to 12 April 2020.

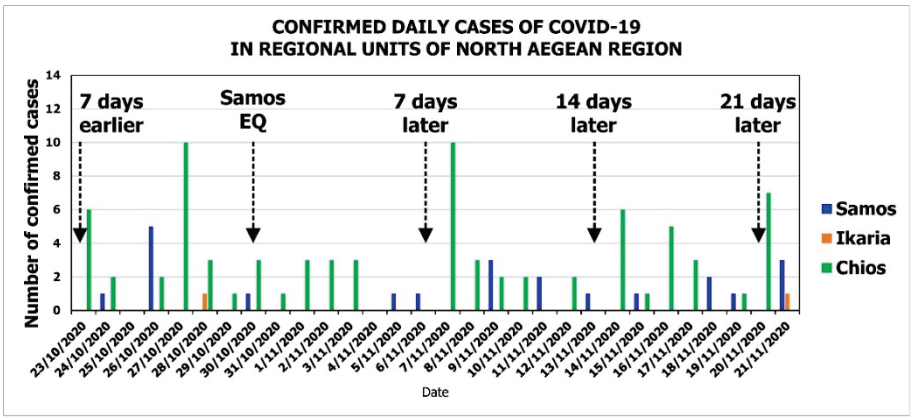

Figure 11. The evolution of COVID-19 cases in the earthquake-affected regional units of the North Aegean region before and after the occurrence of the 30 October 2020 Samos earthquake. The laboratory-confirmed, daily-recorded COVID-19 cases are from the NPHO's COVID-19 epidemiological surveillance daily reports [21] covering the period from 23 October to 21 November 2020.

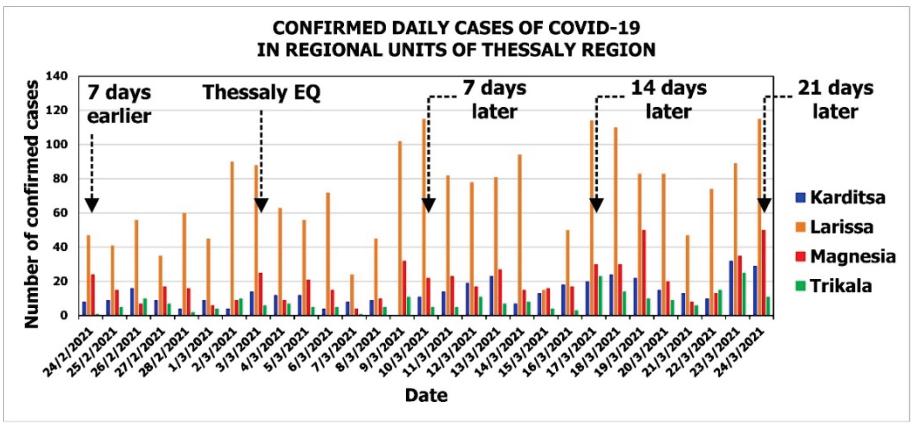

Figure 12. The evolution of COVID-19 cases in the earthquake-affected regional units of the Thessaly region before and after the occurrence of the 3 March 2021 earthquake. The laboratory-confirmed, daily-recorded COVID-19 cases are from the NPHO's COVID-19 epidemiological surveillance daily reports [27] covering the period from 24 February to 24 March 2021.

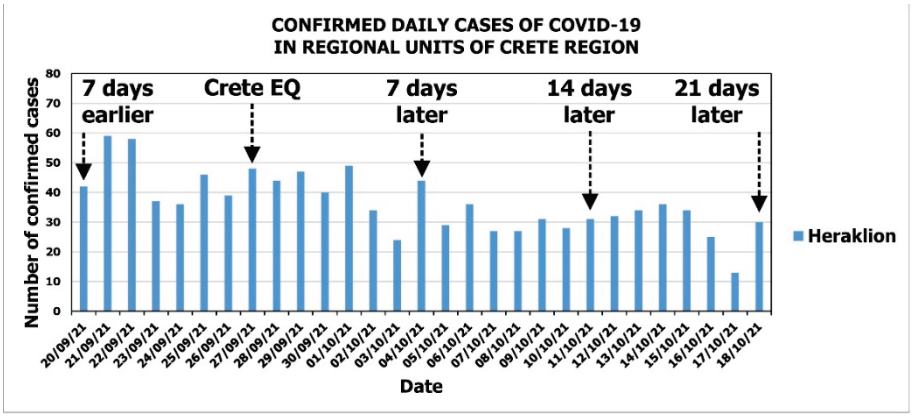

Figure 13. The evolution of COVID-19 cases in the earthquake-affected regional units of the Crete region before and after the occurrence of the 27 September 2021 Arkalochori earthquake. The laboratory-confirmed, daily-recorded COVID-19 cases are from the NPHO's COVID-19 epidemiological surveillance daily reports [27] covering the period from 20 September to 18 October 2021.

According to the following graphs of the laboratory-confirmed and daily-recorded COVID-19 cases (Figures 10–13), it is concluded that no considerable increase in the number of COVID-19 cases was detected in the selected post-disaster period for the earthquake-affected regional units of Epirus, North Aegean, Thessaly or Crete.

In disaster-affected areas around the world, a similar post-disaster trend in the evolution of the pandemic has been observed, including not only earthquakes but also hydrometeorological hazards such as floods and hurricanes. Silva and Paul [5] mention the M = 6.0 earthquake near Khoy (Iran) on 23 February 2020, the M = 5.3 Zagreb (Croatia) earthquake on 22 March 2020, the M = 5.7 Magna earthquake in Utah, and the earthquake swarm that hit Puerto Rico's southern region in early 2020.

In the case of the earthquake in Iran, the first confirmed COVID-19 case was reported a few days before the event, which could indicate that some cases already existed in the earthquake-affected area, that there were no COVID-19 cases in the affected province prior to the seismic event, and that there were less than 40 cases in the 14 days following the event. Silva and Paul [5] assumed that even if the earthquake's impact increased the virus's transmissibility, there were insufficient cases to cause an outbreak.

According to the Croatian Institute of Public Health, 87 COVID-19 cases were noted in the most affected city of Zagreb before the earthquake, and 206 COVID-19 cases were noted in the entire country. In the two weeks that followed, 337 cases were reported in Zagreb. Based on Peitl et al. [28] and Civljak et al. [29], COVID-19 testing was disrupted for hours in hospitals of the earthquake-affected areas, while people left their homes due to widespread unrest and compromised physical distancing measures. The rise in COVID-19 cases could be attributed to the earthquake's potential disruption of safety measures [5]. They did not, however, mention any other factors that could have contributed to the significant increase in cases in Croatia following the earthquake.

After the M = 5.7 Magna earthquake in Utah and the earthquake swarm that hit the southern region of Puerto Rico in early 2020, no significant increase in the number of COVID-19 cases was found, as was the case in Iran. Insufficient pre-existing COVID-19 cases with low potential to trigger an outbreak during the post-disaster period were held responsible for this post-disaster trend [5].

Mavroulis et al. [6] studied how the COVID-19 pandemic evolved in areas affected by disasters caused by hydrometeorological hazards in 2020, such as the Evia flood on August 9 and the Ianos medicane on September 19. They used publicly available laboratory-confirmed daily-recorded COVID-19 cases in disaster-affected areas for post-processing in selected pre- and post-disaster periods, including one week before the earthquake and three weeks after the earthquake, respectively. Only after the Ianos medicane there was an

increase in reported COVID-19 cases in the post-disaster period. After the Evia flood, there was no change in the number of cases.

Mavroulis et al. [6] referred to a number of factors related to the pandemic's evolution, as well as disasters and their management plans, which may have influenced the post-disaster evolution of cases. The pre-existing viral load and infection rate in the affected areas, the severity of the disaster effects, and the measures adopted for the effective disaster management of compound emergencies were all shown to have the potential to influence the pandemic's post-disaster evolution in disaster-affected areas.

In conclusion, the post-disaster evolution of COVID-19 in disaster-affected areas is strongly linked to:

1. The pre-disaster viral load and infection rate in the earthquake-affected areas;
2. The demographic characteristics of the earthquake-affected areas, comprising their population density and spatial distribution;
3. The intensity of the generated earthquakes and the triggered effects on public health (casualties and injured people), on nature (primary and secondary earthquake environmental effects) and on building stock (damage to buildings and infrastructures);
4. The need for immediate evacuation without the assistance of emergency responders;
5. The number of evacuees;
6. The number of people involved in managing the disaster during the immediate response phase;
7. The restrictions on movement and access to the affected area before and after the disaster for mitigating pandemic;
8. The level of training and preparedness of the responders and authorities involved in the disaster management;
9. The effectiveness of the measures adopted and amended by the responders and the authorities involved in disaster management.

Taking into account the results of the analysis of the post-earthquake evolution of the pandemic in the earthquake-affected areas and the factors with which this evolution is closely linked, we can argue that these measures—applied by the Civil Protection authorities during the emergency phase and during the preparation of the immediate response actions, with all the adjustments to the new conditions of the parallel occurrence of earthquakes and the pandemic—can be considered effective in limiting the spread of the pandemic in earthquake-affected communities. There was no increase in any of the examined and analyzed cases under consideration in terms of the number of cases during the post-earthquake period.

At this point, it should be mentioned that these cases may be considered as ideal, as there was no increase in viral load and no increase in infection rate or infection outbreak in the earthquake-affected communities during the pre-earthquake period. However, even in these cases of pre-existing low viral load and low infection rates, the measures adapted to the new specific conditions of the simultaneous occurrence of earthquakes and the pandemic can be characterized as beneficial and effective, as they helped to maintain the low viral load in the post-earthquake period, and in some cases to further reduce it. In any case, they did not lead to an increase in viral load in the earthquake-affected communities.

In view of the latter finding, it can be said that strict compliance with the above adapted measures would have beneficial effects, even in more unfavorable conditions formed by the parallel occurrence of these hazards. Of course, in any case of a parallel occurrence of geological and biological hazards which requires the application of emergency measures to manage the impact on the local population, the applied measures should always be tailored to the type and characteristics of the natural hazard, the epidemiological characteristics, the physiographic and demographic characteristics of the affected area, the characteristics of the affected population and, most importantly, the conditions created by the synergy and the interaction of the aforementioned factors.

6. Proposal of Multi-Hazard Measures for Managing Earthquake Disasters Amid a Pandemic

Based on the good practices and lessons learned from the immediate response of the Civil Protection services for the management of earthquake emergencies in Greece during the pandemic, in this section we share multi-hazard approaches that must be adopted and applied during earthquake emergency responses not only during the current pandemic, but also during future biological hazards with similar characteristics.

The proposed approach constitutes a combination of the aforementioned measures with similar measures that have been applied so far to effectively manage the impact of concurrent crises formed by the simultaneous occurrence of natural and biological hazards, including earthquakes and floods amid the pandemic (e.g., [4,30–32]), and aims to effectively deal with the adverse conditions created when disasters and crises collide to improve disaster management and preparedness in the future.

These approaches comprise:

- Measures for first responders and staff involved in the emergency response phase and increasing the type and number of emergency shelters to limit transmission risk among the affected population;
- Pandemic mitigation measures for accommodated staff and visitors in emergency shelters;
- Administrative and engineering controls in emergency shelters, including changes to facility layouts and supply distribution practices;
- The designation of isolation facilities to separate suspected cases;
- Remote psychological support.

The proposed measures are summarized in Table 2.

Table 2. Multi-hazard measures during the emergency response phase amid the pandemic.

	Proposed Measures during the Emergency Response Phase Amid an Evolving Biological Hazard
Measures for first responders and staff involved in the emergency response phase	• Screening for infectious disease before being transferred to the disaster-affected area; • Rapid diagnostic tests for COVID-19 detection before engaging in emergency response operations and activities; • Regular assessment of the clinical condition of the staff; • Regular screening of temperature during operations; • Mandatory use of mask indoors and outdoors; • Regular hand washing with soap and clean water or the regular use of alcohol-based hand sanitizer; • Covering the mouth and nose with a tissue, sleeve or flexed elbow when coughing or sneezing and throwing tissue into closed bin after use; • Regular disinfection of equipment and surfaces heavily used and often touched; • Maintaining physical distance; • Avoiding places of overcrowding; • Seeking immediate medical care in cases of infection symptoms among the staff; • Activation of an emergency response plan in the case of the detection of infection symptoms among the disaster-affected population; • Isolation of members of teams and staff of Civil Protection authorities who have even mild symptoms or who are expecting test results and have mild symptoms, or who do not have symptoms but have been in contact with a confirmed case.
Avoidance of overcrowding in emergency shelters	• Increasing the number of emergency shelters of the same type; • Using different facility types as emergency shelters.

Table 2. *Cont.*

Proposed Measures during the Emergency Response Phase Amid an Evolving Biological Hazard		
Mitigation measures in emergency shelters	Measures for the staff of the emergency shelters	• Minimum staff needed for the shelter operation; • Screening for symptoms by the medical staff of the shelter; • Training for the detection and reporting of symptoms, infection prevention and control within the facility; • Training for applying pandemic mitigation measures within the emergency shelter; • Using face masks while staying in the emergency shelter, especially during interaction with the disaster-affected people; • Regular hand washing with soap and clean water or the regular use of alcohol-based hand sanitizer; • Using disposable gloves; • Implementing all appropriate measures for the management of a person living in the shelter and suffering infection; • Immediate evaluation of accommodated people by responsible medical staff; • Maintaining an appropriate physical distance between all people in the shelter, including staff, disaster-affected people and visitors.
	Measures for the visitors of the emergency shelters	• Screening temperature before entering emergency shelters; • Using face masks throughout their visit to the emergency shelter; • Maintaining appropriate physical distance; • Regular hand washing with soap or alcohol-based hand sanitizer; • Avoiding visiting when feeling ill or if they have symptoms of infection;
Administrative and engineering controls in emergency shelters	Modification of facility layouts	• Configuration of the emergency shelter spaces in order to maintain physical distance between the affected people: ○ Individual rooms; ○ Separate areas; ○ Large facilities; ○ Guidance for spacing.
	Modification of food distribution practices	• Shelter equipped with adequate handwashing stations with clean water, soap and disposable towels or alcohol-based hand sanitizer for use prior to entering food lines; • Packaged meals prepared and served by staff wearing masks and disposable gloves throughout the preparation and serving of meals; • Each family should consume meals in places that have been predetermined, maintaining physical distance; • Individual and disposable serving items; • Continuous and regular cleaning and disinfection of the used surfaces.
	Restriction of mixing between groups	• Limiting interaction of families with other groups of residents and staff; • Avoiding sharing emergency supplies; • Restriction of entrance to non-essential visitors; • Restriction of entrance to volunteers; • Restriction of mass gatherings; • Designation of outdoor spaces for religious services and communal meetings.
	Designation of isolation facilities to separate suspected cases	• Facilities equipped with beds, oxygen cylinders and equipment for monitoring temperature and oxygen levels; • Access to health assessment, medical care and counseling for the isolated person if needed.

7. Discussion

Many of these measures were proposed and implemented during the emergency response phase after earthquakes generated in the early stages of the pandemic. In this phase, the conditions were unprecedented and difficult for all involved in managing the effects of the pandemic and in dealing with the parallel occurrence of disasters induced by geological and biological hazards. However, the measures were effective as they were reverently applied by the majority of the affected population. Furthermore, their implementation was strictly monitored by Public Health organizations and Civil Protection authorities. It is significant to note that, in the early stages of the pandemic, effective medical means to combat COVID-19 infection and disease, such as antiviral drugs and COVID-19 vaccines, were either non-existent or under development.

After 2 years of the pandemic—marked on the one hand by numerous human losses worldwide, but on the other hand by the discoveries of COVID-19 vaccines and antiviral drugs and extensive vaccination coverage in a large part of the world—it can be said that strict compliance with the above adapted measures would have beneficial effects, even in more unfavorable conditions formed by the parallel occurrence of these hazards. These harsh conditions could be attributed either to single events or to a synergy of events and triggering factors. Characteristic examples of such events and factors could include the occurrence of earthquakes during the winter period, the triggering of earthquake environmental effects and building damage in densely populated urban areas, the creation of large numbers of displaced residents in need of immediate accommodation in emergency shelters and camps, and increased viral load and infection rate resulting in COVID-19 outbreaks and clusters in the pre-disaster period in the areas of interest.

In the case of the relaxation of control measures and a subsequent increase in viral load and infection rate, the majority of these measures should be reapplied at least for the disaster-affected areas, and necessarily for all affected residents and participants in the emergency response zones, among whom interaction cannot be avoided.

8. Conclusions

The COVID-19 pandemic has caused unprecedented global disruption. The disease and the resulting mitigation measures have brought societies and many public services to a halt. Such disruptions also have an impact on disaster risk reduction and disaster risk management. Earthquakes, on the other hand, do not wait for the virus to vanish. From the initiation of the pandemic, earthquakes have struck many countries around the world. One of them was Greece.

The earthquake in Epirus (northwestern Greece) occurred on 21 March 2020, at the start of the country's first wave of the pandemic and two days before the imposition of the first national lockdown. The Samos earthquake occurred on 30 October 2020, just before the peak of the second wave of the pandemic in the country and 7 days before the imposition of the second national lockdown. In 2021, two destructive earthquakes struck Greece: the Thessaly earthquake on 3 March, during the third pandemic wave, and the Crete earthquake on 27 September, during the fourth pandemic wave.

Considering Greece's single-hazard management plans, the multi-hazard approach needed to manage geological hazards (earthquakes and related phenomena) in the midst of an evolving biological hazard (COVID-19 pandemic) has been a challenge for all involved in the scientific community and for Civil Protection personnel. This challenge arose from the fact that many actions, particularly during the first hours of the emergency response, required direct communication, contact, and interaction with the disaster-affected population. SAR operations, the establishment of emergency shelters following the disaster, the contribution of volunteer teams, the distribution of emergency supplies, post-event building inspections, hazard mitigation during the emergency response phase, psychological support, and awareness and education activities during the aftershock period were all included in these actions.

New approaches were used to carry out all of these actions in the case of the earthquakes studied in Greece since the initiation of the COVID-19 pandemic. The main focus of these approaches was on individuals and the community and taking preventive measures against the spread of the novel virus, particularly by maintaining physical distance and avoiding overcrowding, as well as proper mask use and hand hygiene. Considering the post-disaster trend of daily cases and the pandemic's evolution in the affected regional units, it is possible to conclude that the multi-hazard approach to managing the negative effects of the earthquakes and subsequent seismic effects amid the evolving pandemic in the earthquake-affected areas was effective. As a result, we regard the actions taken by the relevant authorities as good practices and important lessons learned for the management of natural hazards and related disasters in the context of an evolving biological hazard.

The synergy of several factors and the characteristics of the affected areas and those affected resulted in this effectiveness. The epidemiological characteristics of the affected areas, such as the low viral load and infection rate in the affected communities, the demographics of the affected areas, such as the low population density, the sparse distribution of residential areas in the affected regional units, and the accessibility to the areas during the emergency phase, as well as the implementation of pandemic mitigation measures, were among these factors.

We propose an approach that could significantly contribute to the safety of staff and affected people in various phases of emergency response after an earthquake disaster amid the evolving pandemic, keeping in mind the lessons learned from the emergency response for the studied earthquakes' management. Individual and collective protection measures for emergency responders and staff before and during their involvement in the affected area, measures to reduce the risk of transmitting the virus to the affected community, and measures to limit the spread of the virus inside shelters are all part of this strategy.

This strategy can be used not only in the event of a destructive earthquake during a pandemic, but also whenever a disaster caused by a natural hazard has a significant impact on the built environment, particularly buildings and infrastructure, necessitating the establishment of emergency shelters until normalcy is restored. It can also be used in seismically similar areas with similar building vulnerability and susceptibility to earthquake-triggered effects. The evolving pandemic and its consequences may exacerbate the effects on public health and lengthen the time it takes to restore normalcy in affected areas if individual and collective pandemic mitigation measures are not followed during an emergency.

The simultaneous occurrence of a natural disaster and an evolving biological hazard (a pandemic) exposes the shortcomings of single-hazard approaches to disaster management and emphasizes the need for a multi-hazard strategy. Every phase of the disaster management cycle, specifically mitigation, preparedness, response, and recovery, should use a multi-hazard strategy. Despite the difficulty of comprehending the interactions between different types of hazards and multi-hazard assessments, the adaptation of general risk management plans and the adoption of multi-hazard approaches involving multi-stakeholder participation are critical, as the frequency and severity of extreme events rise due to the interaction of several factors and the collision of disasters and crises. National, regional, and local government bodies, as well as volunteer teams and the armed forces, should collaborate with scientists who specialize in natural and technological hazards, related disasters, and all types of crises in order to provide the Civil Protection authorities with more knowledge, experience, and expertise. Innovative technology services and tools to support the Civil Protection mission are important results of scientific and operational synergy.

Despite the ongoing mass vaccination campaigns, it is possible that virus transmission will remain high in the coming months. To avoid a resurgence of the pandemic, it is critical for stakeholders and decision-makers to ensure that disaster management approaches take this risk into account. Multiple ongoing disasters and crises are extremely difficult to manage, but adopting the best practices that have emerged in this field is critical.

Author Contributions: Conceptualization, S.M. and M.M.; methodology, S.M. and M.M.; investigation, S.M. and M.M.; resources, M.M.; writing—original draft preparation, S.M. and M.M.; writing—review and editing, S.M., M.M., A.K., T.T. and E.L.; visualization, S.M.; supervision, S.M.; funding acquisition, M.M. All authors have read and agreed to the published version of the manuscript.

Funding: This research received no external funding.

Institutional Review Board Statement: Not applicable.

Informed Consent Statement: Not applicable.

Data Availability Statement: Not applicable.

Acknowledgments: We would like to thank three anonymous reviewers for their constructive comments that helped improve the clarity, the scientific soundness and the overall merit of this work. Figures 1 and 9 were prepared using the ArcGIS 10.7 (ESRI) software. The graphs in Figures 2 and 10–13 were prepared using Excel Spreadsheet Software (Microsoft). Figures 3–8 were prepared with CorelDRAW Essentials 2021 (CorelDRAW).

Conflicts of Interest: The authors declare no conflict of interest.

References

1. Gill, J.C.; Malamud, B.D. Reviewing and visualizing the interactions of natural hazards. *Rev. Geophys.* **2014**, *52*, 680–722. [CrossRef]
2. Gill, J.C.; Malamud, B.D. Hazard interactions and interaction networks (cascades) within multi-hazard methodologies. *Earth Syst. Dyn.* **2016**, *7*, 659–679. [CrossRef]
3. WHO (World Health Organization). Coronavirus Disease 2019 (COVID-19) Situation Report-51. Available online: https://www.who.int/docs/default-source/coronaviruse/situation-reports/20200311-sitrep-51-covid-19.pdf?sfvrsn=1ba62e57_10U43T (accessed on 30 April 2022).
4. Ishiwatari, M.; Koike, T.; Hiroki, K.; Toda, T.; Katsube, T. Managing disasters amid COVID-19 pandemic: Approaches of response to flood disasters. *Prog. Disaster Sci.* **2020**, *6*, 100096. [CrossRef] [PubMed]
5. Silva, V.; Paul, N. Potential impact of earthquakes during the 2020 COVID-19 pandemic. *Earthq. Spectra* **2021**, *37*, 73–94. [CrossRef]
6. Mavroulis, S.; Mavrouli, M.; Lekkas, E. Geological and hydrometeorological hazards and related disasters amid COVID-19 pandemic in Greece: Post-disaster trends and factors affecting the COVID-19 evolution in affected areas. *Saf. Sci.* **2021**, *138*, 105236. [CrossRef] [PubMed]
7. Simonovic, S.P.; Kundzewicz, Z.W.; Wright, N. Floods and the COVID-19 pandemic—A new double hazard problem. *WIREs Water* **2021**, *8*, e1509. [CrossRef]
8. Stucchi, M.; Rovida, A.; Capera, A.A.G.; Alexandre, P.; Camelbeeck, T.; Demircioglu, M.B.; Gasperini, P.; Kouskouna, V.; Musson, R.M.W.; Radulian, M.; et al. The SHARE European earthquake catalogue (SHEEC) 1000–1899. *J. Seismol.* **2013**, *17*, 523–544. [CrossRef]
9. Makropoulos, K.; Kaviris, G.; Kouskouna, V. An updated and extended earthquake catalogue for Greece and adjacent areas since 1900. *Nat. Hazards Earth Syst. Sci.* **2012**, *12*, 1425–1430. [CrossRef]
10. Papazachos, B.; Papazachou, K. *The Earthquakes of Greece*; Ziti Publications: Thessaloniki, Greece, 2003; p. 286.
11. Ambraseys, N. *Earthquakes in the Mediterranean and Middle East: A Multidisciplinary Study of Seismicity up to 1900*; Cambridge University Press: Cambridge, UK, 2009; p. 970.
12. Mariolakos, I.; Papanikolaou, D. The neogene basins of the Aegean arc from the paleogeographic and the geodynamic point of view. In Proceedings of the International Symposium on the Hellenic Arc and Trench (HEAT), Athens, Greece, 8–10 April 1981; Volume 1, pp. 383–399.
13. Mariolakos, I.; Papanikolaou, D. Deformation pattern and relation between deformation and seismicity in the Hellenic arc. *Bull. Geol. Soc. Greece* **1987**, *19*, 59–76.
14. Valkaniotis, S.; Briole, P.; Ganas, A.; Elias, P.; Kapetanidis, V.; Tsironi, V.; Fokaefs, A.; Partheniou, H.; Paschos, P. The Mw = 5.6 Kanallaki earthquake of 21 March 2020 in west Epirus, Greece: Reverse fault model from InSAR data and seismotectonic implications for Apulia-Eurasia collision. *Geosciences* **2020**, *10*, 454. [CrossRef]
15. Ganas, A.; Athens, N.O.O.; Elias, P.; Briole, P.; Tsironi, V.; Valkaniotis, S.; Escartin, J.; Karasante, I.; Efstathiou, E.; De Paris, N.S. Fault responsible for Samos earthquake identified. *Temblor* **2020**. [CrossRef]
16. Karakostas, V.; Papazachos, C.; Papadimitriou, E.; Foumelis, M.; Kiratzi, A.; Pikridas, C.; Kostoglou, A.; Kkallas, C.; Chatzis, N.; Bitharis, S.; et al. The March 2021 Tyrnavos, central Greece, doublet (Mw6.3 and Mw6.0): Aftershock relocation, faulting details, coseismic slip and deformation. *Bull. Geol. Soc. Greece* **2021**, *58*, 131–178. [CrossRef]
17. Mavroulis, S.; Kranis, H.; Lozios, S.; Argyropoulos, I.; Vassilakis, E.; Soukis, K.; Skourtsos, E.; Lekkas, E.; Carydis, P. The impact of the September 27, 2021, Mw=6.0 Arkalochori (Central Crete, Greece) earthquake on the natural environment and the building stock. In Proceedings of the EGU General Assembly 2022, Vienna, Austria, 23–27 May 2022. [CrossRef]

18. Vadaloukas, G.; Vintzilaiou, E.; Ganas, A.; Giarlelis, C.; Ziotopoulou, K.; Theodoulidis, N.; Karasante, H.; Margaris, V.; Mylonakis, G.; Papachristidis, A.; et al. *Samos Earthquake, October 30, 2020*; Preliminary Report; Hellenic Society for Earthquake Engineering: Athens, Greece, 2020; p. 65.
19. Mavroulis, S.; Mavrouli, M.; Carydis, P.; Agorastos, K.; Lekkas, E. The March 2021 Thessaly earthquakes and their impact through the prism of a multi-hazard approach in disaster management. *Bull. Geol. Soc. Greece* **2021**, *58*, 1–36. [CrossRef]
20. Mavroulis, S.; Triantafyllou, I.; Karavias, A.; Gogou, M.; Katsetsiadou, K.-N.; Lekkas, E.; Papadopoulos, G.; Parcharidis, I. Primary and secondary environmental effects triggered by the 30 October 2020, Mw = 7.0, Samos (Eastern Aegean Sea, Greece) earthquake based on post-event field surveys and InSAR analysis. *Appl. Sci.* **2021**, *11*, 3281. [CrossRef]
21. National Public Health Organization. 2020 COVID-19 Daily Reports. Available online: https://eody.gov.gr/category/covid-19/?yeararchive=2020 (accessed on 30 January 2022).
22. Mavroulis, S.; Ilgac, M.; Tunçağ, M.; Lekkas, E.; Püskülcü, S.; Kourou, A.; Sextos, A.; Mavrouli, M.; Can, G.; Thoma, T.; et al. Emergency response, intervention, and societal recovery in Greece and Turkey after the 30th October 2020, MW = 7.0, Samos (Aegean Sea) earthquake. *Bull. Earthq. Eng.* **2022**, 1–23. [CrossRef]
23. Lauer, S.A.; Grantz, K.H.; Bi, Q.; Jones, F.K.; Zheng, Q.; Meredith, H.R.; Azman, A.S.; Reich, N.G.; Lessler, J. The incubation period of coronavirus disease 2019 (COVID-19) from publicly reported confirmed cases: Estimation and application. *Ann. Intern. Med.* **2020**, *172*, 577–582. [CrossRef]
24. WHO (World Health Organization). Coronaviruses Disease (COVID-19). Available online: https://www.who.int/emergencies/diseases/novel-coronavirus-2019/question-and-answers-hub/q-a-detail/coronavirus-disease-covid-19 (accessed on 30 April 2022).
25. La Scola, B.; Le Bideau, M.; Andreani, J.; Hoang, V.T.; Grimaldier, C.; Colson, P.; Gautret, P.; Raoult, D. Viral RNA load as determined by cell culture as a management tool for discharge of SARS-CoV-2 patients from infectious disease wards. *Eur. J. Clin. Microbiol.* **2020**, *39*, 1059–1061. [CrossRef]
26. Garmendia, J.G.; Arcos, M.R.; Almodóvar, A.B.; Caballero, M.C.; Amigo, V.J.; Martino, M.S. Detección viraly respuesta serológica en pacientes críticos intubados con SARS-CoV-2. Implicaciones para retirada de aislamiento. [Viral detection and serological response in critically ill patients with SARS-CoV-2. Implications for isolation withdrawal]. *Med. Intensiv.* **2020**, *44*, 586–588. [CrossRef]
27. National Public Health Organization. 2021 COVID-19 Daily Reports. Available online: https://eody.gov.gr/epidimiologika-statistika-dedomena/imerisies-ektheseis-covid-19/ektheseis-covid-19/ (accessed on 30 January 2022).
28. Peitl, V.; Zatezalo, V.G.; Karlović, D. Mental health issues and psychological crisis interventions during the COVID-19 pandemic and earthquakes in Croatia. *Arch. Psychiatry Res.* **2020**, *56*, 193–198. [CrossRef]
29. Čivljak, R.; Markotić, A.; Capak, K. Earthquake in the time of COVID-19: The story from Croatia (CroVID-20). *J. Glob. Health* **2020**, *10*, 010349. [CrossRef]
30. Francis, B.; Rizal, A.J.; Sabki, Z.A.; Sulaiman, A.H. Remote Psychological First Aid (rPFA) in the time of COVID-19: A preliminary report of the Malaysian experience. *Asian J. Psychiatry* **2020**, *54*, 102240. [CrossRef] [PubMed]
31. Sakamoto, M.; Sasaki, D.; Ono, Y.; Makino, Y.; Kodama, E.N. Implementation of evacuation measures during natural disasters under conditions of the novel coronavirus (COVID-19) pandemic based on a review of previous responses to complex disasters in Japan. *Prog. Disaster Sci.* **2020**, *8*, 100127. [CrossRef] [PubMed]
32. Potutan, G.; Arakida, M. Evolving disaster response practices during COVID-19 pandemic. *Int. J. Environ. Res. Public Health* **2021**, *18*, 3137. [CrossRef] [PubMed]

remote sensing

MDPI

Article

Interseismic Fault Coupling and Slip Rate Deficit on the Central and Southern Segments of the Tanlu Fault Zone Based on Anhui CORS Measurements

Tingye Tao †, Hao Chen †, Shuiping Li *, Xiaochuan Qu and Yongchao Zhu

College of Civil Engineering, Hefei University of Technology, Hefei 230009, China; taotingye@hfut.edu.cn (T.T.); haochen@mail.hfut.edu.cn (H.C.); qqxxcc@hfut.edu.cn (X.Q.); yczhu@hfut.edu.cn (Y.Z.)

* Correspondence: lishuiping@hfut.edu.cn; Tel.: +86-1582-717-2250

† These authors contributed equally to this work.

Abstract: The Tanlu fault zone, extending over 2400 km from South China to Russia, is one of the most conspicuous tectonic elements in eastern Asia. In this study, we processed the Global Positioning System (GPS) measurements of Anhui Continuously Operating Reference System (AHCORS) between January 2013 and June 2018 to derive a high-precision velocity field in the central and southern segments of the Tanlu fault zone. We integrated the AHCORS data with those publicly available for geodetic imaging of the interseismic coupling and slip rate deficit distribution in the central and southern segments of the Tanlu fault zone. This work aims at a better understanding of strain accumulation and future seismic hazard in the Tanlu fault zone. The result indicates lateral variation of coupling distribution along the strike of the Tanlu fault zone. The northern segment of the Tanlu fault zone has a larger slip rate deficit and a deeper locking depth than the southern segment. Then, we analyzed three velocity profiles across the fault. The result suggests that the central and southern segments of the Tanlu fault zone are characterized by right-lateral strike-slip (0.29–0.44 mm/y) with compression components (0.35–0.76 mm/y). Finally, we estimated strain rates using the least-squares collocation method. The result shows that the dilatation rates concentrate in the region where the principal strain rates are very large. The interface of extension and compression is always accompanied by sudden change of direction of principal strain rates. Especially, in the north of Anhui, the dilatation rate is largest, reaching $3.780 \times 10^{-8}/a$. Our study suggests that the seismic risk in the northern segment of the Tanlu fault zone remains very high for its strong strain accumulation and the lack of historical large earthquakes.

Keywords: Anhui CORS; velocity field; fault coupling; slip rate deficit; strain rates

Citation: Tao, T.; Chen, H.; Li, S.; Qu, X.; Zhu, Y. Interseismic Fault Coupling and Slip Rate Deficit on the Central and Southern Segments of the Tanlu Fault Zone Based on Anhui CORS Measurements. *Remote Sens.* **2022**, *14*, 1093. https://doi.org/10.3390/rs14051093

Academic Editors: Mirko Francioni, Stefano Morelli and Veronica Pazzi

Received: 19 January 2022
Accepted: 18 February 2022
Published: 23 February 2022

1. Introduction

Tanlu fault zone, which is mainly characterized by right-lateral strike-slip and reverse components, is one of the largest fault zones in eastern China [1,2]. It runs from Heilongjiang Province in the north to the shore of the Yangtze River, Hubei Province, in the south, totaling 2400 km. The Tanlu fault zone crosses multiple tectonic blocks from north to south and its internal structure is complex. Many earthquakes with magnitudes larger than M_s 5.0 have occurred in the Tanlu fault zone since the Quaternary [3]. For instance, in 1668, an M_s 8.5 earthquake occurred in Tancheng, located on the Yishu fault of the central segment of the Tanlu fault zone, resulting in huge casualties and property losses [4,5]. Additionally, the Tanlu fault zone has also been influenced by the far-field post-seismic effects of many large earthquakes during the past decades, such as the 2008 Wenchuan M_s 8.0 earthquake and the 2011 M_w 9.0 Tohoku, Japan Earthquake [6–8]. The future seismic risk for this densely populated region is still not very clear due to the lack of a detailed study of the crustal deformation and strain accumulation in the Tanlu fault zone. The seismogenic potential on the Tanlu fault zone is largely dominated by the mechanical

properties on the fault interface, in which the coupling ratio (also inferred as locking degree) and slip rate deficit are two vital indicators that can shed light on the strain buildup on fault interfaces. Many previous studies have explored the interseismic coupling and estimated the slip rate deficit on a series of active faults using the Global Positioning System (GPS) and Interferometric Synthetic Aperture Radar (InSAR) measurements [9–11]. For instance, Zhao et al. (2017) inverted the fault locking and fault slip deficit in the main Himalaya thrust fault [12]. They have shown that the maximal magnitude and the rupture extents of large earthquakes on a fault can be well constrained by the spatial distribution of interseismic coupling. Therefore, a refined coupling image for the Tanlu fault zone could help us to assess the strain buildup and future earthquake hazard in this region.

The characteristics of crustal movement and strain accumulation of the Tanlu fault zone have been constrained by geodetic surveying; most of them are GPS observations [13–15]. Recently, Li et al. (2020) used the two periods of GPS horizontal velocity field in the north China between 1999–2017 to invert the fault locking and slip rate deficit of the Tanlu fault zone, by utilizing the back-slip dislocation model, and compared the differences between two periods [16]. They found that the 2011 Tohoku M_W 9.0 earthquake played a vital role in alleviating the strain accumulation of the Tanlu fault zone. Li et al. (2016) inverted the fault locking and slip rate deficit of the Tanlu fault zone by using GPS horizontal velocity of 2009–2014 in North China and verified that different reference frames have little impact on the inversion results [7]. They suggested that the locking depth in the northern end of the Tanlu fault zone is nearly 27 km depth, while the locking depth reaches 32 km in the central segment and then it decreases to only 5 km in the southern end of the Tanlu fault zone, exhibiting lateral variation of fault locking along the strike of the Tanlu fault zone.

It can be inferred that the first-order characteristics of the fault activity and strain buildup on the Tanlu fault zone have been constrained by previous geodetic surveying. However, we still found that fault slip and interseismic coupling distribution on each segment of the Tanlu fault zone revealed by different studies show significant discrepancies. We attributed them to various timescales of GPS data and different parameter settings in the modeling. Additionally, the spatial resolution of interseismic coupling image on the Tanlu fault zone remains low due to the lack of near-field GPS observation. With the completion of the Anhui Continuously Operating Reference System (AHCORS) in 2011 and upgrading in 2016, there are more than 50 AHCORS stations throughout the Anhui Province. Most of these stations are located in the near-field of the central and southern segments of the Tanlu fault zone, providing a valuable chance for us to further study the motion characteristics and strain accumulation in the Tanlu fault zone. In this paper, we processed GPS data of 50 AHCORS stations from January 2013 to June 2018 with time period of nearly 6 years. In combination with the data of Crustal Movement Observation Network of China (CMONOC) between 1999–2016 computed by Wang (2020) [17], we obtained a complete velocity field of the central and southern segments of the Tanlu fault zone. This new velocity field is then employed to invert for the fault locking and slip rate deficit on the central and southern segments of the Tanlu fault zone. Finally, we discussed the characteristics of the fault slip according to two-dimensional velocity analysis. We also analyzed the strain accumulation based on the least-squares collocation method, which has the advantage that the higher the density of the site distribution, the higher the accuracy. Our work provides useful constraints on the fault slip motion and sheds new light on the seismic hazard of the central and southern segments of the Tanlu fault zone.

The rest of the paper is organized as follows. In Section 2, the tectonic setting of the study region is described. In Section 3, datasets, methodology, and fault geometry are presented. Section 4 demonstrates the results of fault coupling ratios, fault slip rate deficit, and velocity profiles. Section 5 discusses how to use checkboard tests to assess the spatial resolution of the fault coupling ratios, comparison with previous studies, strain characteristics, and implication for seismic hazard.

2. Tectonic Setting

The Tanlu fault zone represents a NE-trending continental-scale strike-slip fault zone with high levels of seismicity in East China and records the evolutionary history of plate interactions in East Asia during Mesozoic and Cenozoic times [18]. The Tanlu fault zone is commonly interpreted to have generated due to the collision between the North China block and Yangtze Plate from the middle Triassic [19]. After that, the fault zone was transformed to an extensional structure by the Cretaceous–Paleocene that controlled several grabens filled by Cretaceous volcanic rocks and terrestrial clasts [20]. In terms of geographical location, the Tanlu fault zone is always divided into three segments, that are the northern segment in northeast China, the central segment in the Bohai Bay, and the southern segment from Shandong Province to Anhui Province. The central and southern segments of the Tanlu fault zone, which act as the boundary faults that separate the North China block from the Subei basin and the Sulu belt, experienced a complex deformation characterized by Mesozoic sinistral and Cenozoic dextral motions. The rock types across the fault zone change abruptly from Archean to Paleoproterozoic high-grade metamorphic basement rocks in the North China block to ultra-high-pressure metamorphic rocks and Mesozoic granites in the Sulu belt [21]. The fault outcrops along the central and southern segments of the Tanlu fault zone are diffusely distributed. The central segment of the Tanlu fault zone is composed of five subparallel faults [20]. The fault activities of these faults remain controversial. Both reverse and dextral slips have been proposed to explain the Quaternary activities of these subparallel faults [20,22]. Many large earthquakes have occurred in this segment, such as the 1668 Tancheng Ms 8.5 earthquake and the 1969 Mw 7.4 Bohai earthquake, suggesting that the central segment is still an active earthquake zone [23]. In contrast, the fault activity of the southern segment of the Tanlu fault zone is much weaker than the central segment, consistent with the weak seismic activity of the southern segment [22].

3. Data and Methods

3.1. Data Processing

The GPS data we collected are mainly from AHCORS between January 2013 and June 2018. Figure 1 shows the spatial distribution of AHCORS stations. All the GPS data are processed using the GAMIT/GLOBK software (Ver.10.7) with a double-difference approach to generate daily solutions [24]. In the processing, we eliminated the GPS stations with data integrity less than 90 percent. More than nine International GNSS Service (IGS) stations around the Chinese mainland are adopted in the processing.

In the detailed processing strategy, we adopt the Vienna Mapping Function 1 (VMF1) to correct the tropospheric delay, and a zenith wet delay parameter is estimated every 2 h [25]. The most recent global ocean tide model (Finite Element Solutions 2004, FES2004) is used to correct the station displacements induced by ocean tides [26]. The detailed geophysical models and parameter settings used in the processing are listed in Table 1.

The specific processing is as follows. Firstly, GAMIT is used to obtain daily solutions that are loosely constrained for station coordinates and satellite orbits. Secondly, the global H files released by Scripps Orbits and Permanent Array Center (SOPAC) are used for network adjustment. Finally, the velocity field of AHCORS stations in the International Terrestrial Reference Frame 2008 (ITRF2008) can be obtained through coordinate frame transformation. For the convenience of tectonic interpretation, we transformed the horizontal velocity field from ITRF2008 to a stable Eurasia frame using Euler vectors for the Eurasian plate proposed by Wang et al. (2020) (-0.087, -0.514, and 0.741 mas/a) [17], and the velocity field is listed in Table 2. Figure 2 displays the horizontal velocity field on the central and southern segments of the Tanlu fault zone and its surrounding areas under the Eurasia reference frame, including the velocity field of AHCORS calculated by ourselves and the velocity field of CMONOC. Generally, the velocity of AHCORS stations coincides well with the velocity of CMONOC stations, and our AHCORS stations show higher precision thanks to the longer observation time.

Table 1. Data processing strategy.

Data Processing Strategy	Option
Sampling interval	set sint = '30'
Number of epochs	set nepc = '2880'
Start time for processing	set stime = '0 0'
Choice of Experiment	RELAX.
Type of Analysis	1-ITER
Choice of Observable	LC_AUTCLN
Zenith Delay Estimation	Y
Met obs source	GPT 50
DMap	VMF1
WMap	VMF1
Use otl.grid	Y
Use atml.grid	Y
Use atl.grid	Y

Table 2. Site velocity solution.

Station	Ve_I [a]	Ve_E [b]	dVe [c]	Vn_I [d]	Vn_E [e]	dVn [f]
AQSS	33.831	7.488	0.234	−10.813	−1.414	0.168
AQYX	33.672	7.353	0.166	−11.961	−2.509	0.120
BZGY	34.786	8.504	0.161	−9.981	−0.568	0.155
BZLX	34.122	7.830	0.148	−10.666	−1.254	0.127
BZMC	33.767	7.509	0.157	−11.812	−2.325	0.143
CHCH	33.850	7.669	0.155	−12.460	−2.677	0.104
CHJU	33.475	7.249	0.152	−12.544	−2.890	0.105
CZDY	33.518	7.346	0.136	−11.340	−1.590	0.110
CZLA	33.876	7.769	0.150	−12.224	−2.311	0.120
CZMG	33.769	7.632	0.153	−12.219	−2.400	0.130
CZQJ	33.485	7.358	0.149	−11.351	−1.465	0.128
CZQY	36.731	10.539	0.204	−11.237	−1.446	0.129
CZST	34.930	8.702	0.175	−12.303	−2.595	0.128
CZTC	33.338	7.294	0.149	−11.851	−1.808	0.128
CZZT	35.710	9.424	0.205	−12.047	−2.490	0.097
FYFN	33.736	7.380	0.147	−11.544	−2.265	0.120
FYFY	34.555	8.217	0.141	−10.189	−0.879	0.121
FYJS	35.317	8.953	0.147	−10.143	−0.924	0.119
FYLQ	34.635	8.261	0.155	−9.803	−0.595	0.125
FYTH	32.688	6.348	0.141	−11.228	−1.939	0.113
FYYS	32.883	6.583	0.158	−9.438	−0.014	0.115
HFCF	33.092	6.871	0.161	−11.345	−1.712	0.124
HFFD	34.026	7.820	0.170	−11.239	−1.535	0.138
HSHS	33.885	7.713	0.176	−11.645	−1.793	0.130
HSQM	32.905	6.693	0.174	−11.953	−2.196	0.123
LAHS	33.551	7.237	0.164	−11.113	−1.666	0.130
LALA	33.863	7.569	0.145	−10.967	−1.480	0.099
MASM	33.091	6.979	0.156	−11.844	−1.899	0.133
SZDS	34.521	8.285	0.140	−14.830	−5.385	0.122
SZSX	32.867	6.741	0.156	−10.695	−0.902	0.143
SZXX	33.922	7.736	0.159	−12.062	−2.473	0.125
XCGD	33.422	7.372	0.167	−12.799	−2.664	0.127
XCJD	33.703	7.566	0.167	−9.387	0.553	0.125
XCJN	33.578	7.434	0.172	−12.919	−3.008	0.125
XCJX	33.686	7.551	0.178	−11.446	−1.494	0.128
XCLX	34.776	8.710	0.164	−12.279	−2.195	0.121
XCNG	34.176	8.082	0.181	−12.847	−2.809	0.130

[a] East components under ITRF2008 reference frame. [b] East components under Eurasian plate. [c] East velocity uncertainties. [d] North components under ITRF2008 reference frame. [e] North components under Eurasian plate. [f] North velocity uncertainties.

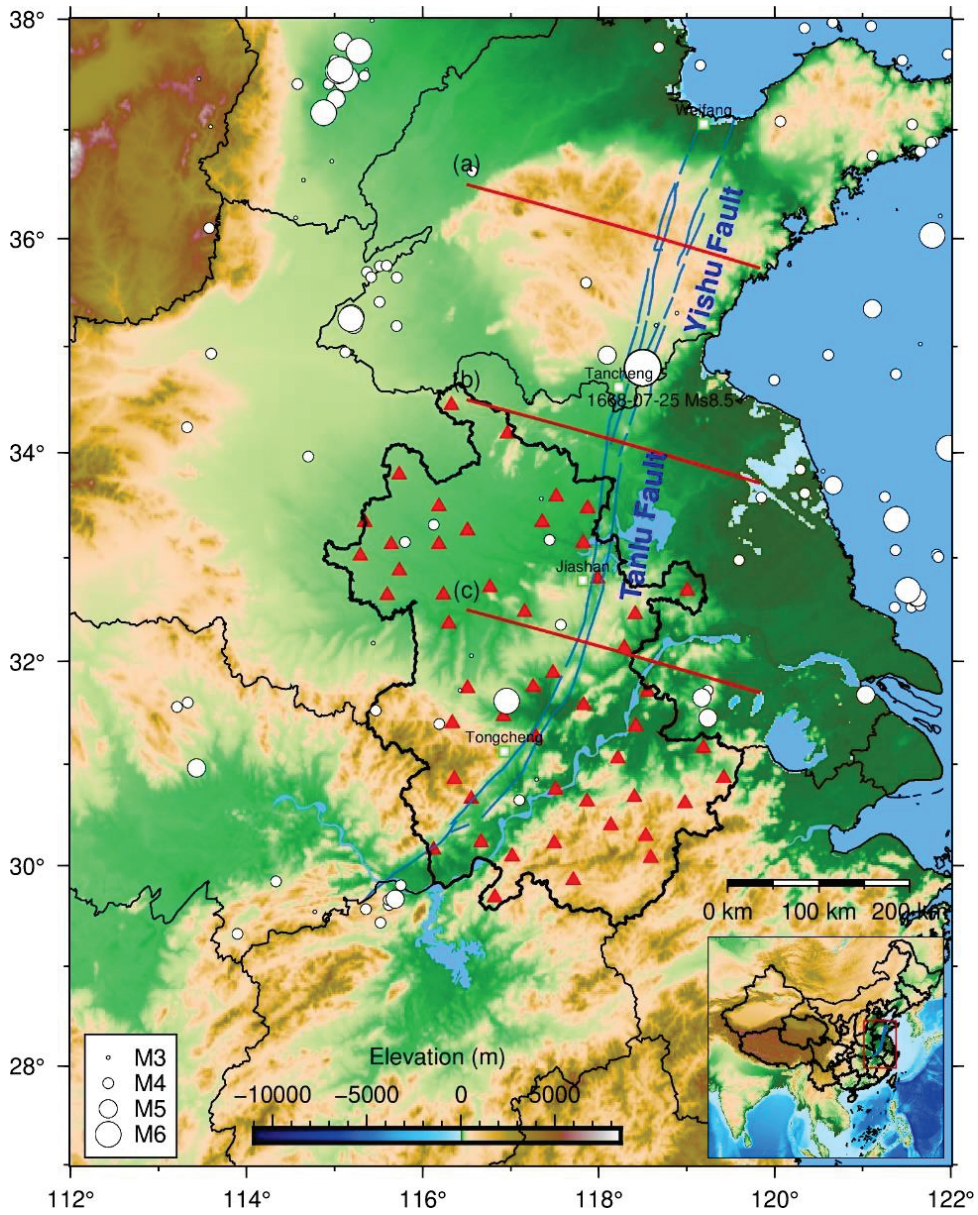

Figure 1. Distribution map of Anhui CORS stations. The red triangles are where the Anhui CORS stations are located. White circles show earthquakes with $3.0 \leq M_s \leq 8.5$ from 1 January 1900 to 31 December 2020 (https://earthquake.usgs.gov, accessed on 14 December 2021). The largest white circle is an M_s 8.5 earthquake that struck Tancheng on 25 July 1668. The blue broken line represents the central and southern segments of the Tanlu fault zone, and the Yishu fault zone is a part of the Tanlu fault zone in Shandong Province. The three red lines labeled by (**a**–**c**) represent the locations of three velocity profiles across the Tanlu fault zone.

3.2. Modeling Approach

In this study, we adopted the Fortran-based DEFNODE software [27,28] for the inversion. The DEFNODE software has been widely used to invert the interseismic block rotation, fault locking, and slip deficit in the northwestern U.S., Pacific Northwest, and southern Cascadia [29–31].

The DEFNODE program assumes that the movement of the points in the blocks are the sum of the surface elastic deformation caused by the block rotation, the uniform strain rates within blocks, and slip deficit at the block boundary due to fault locking. Constrained by GPS vector, surface uplifts, earthquake slip vector, spreading rates, or other data, we

can use grid searches or simulated annealing technique to estimate fault coupling ratios, fault slip rates, and Euler pole at the block boundary. McCaffrey (2002) [32] proposed the expression if there are no uniform strain rates within blocks:

$$V_i(X) = \sum_{b=1}^{B} H(X \in \Delta_b)[{}_R\Omega_b] \cdot i - \sum_{k=1}^{F} \sum_{n=1}^{N_k} \sum_{j=1}^{2} \Phi_{nk} G_{ij}(X, X_{nk}) \left[{}_h\Omega_f \times X_{nk} \right] \cdot j \qquad (1)$$

Where X is the position of GPS stations, B is the number of blocks, Δ_b is the area range of block B ($H = 1$ if the station is within the range of block B, otherwise $H = 0$), i is the unit vector in the i direction, and ${}_R\Omega_b$ is the Euler rotation pole of block B with respect to the reference frame. ${}_h\Omega_f = {}_R\Omega_b - {}_f\Omega_R$ is the Euler vector of footwall block f relative to the hanging wall block, F is the number of faults, N_k is the number of nodes for fault k, j is the unit vector of direction j on the fault surface, Φ_{nk} is the fault coupling ratio of node n on fault k, and X_{nk} is the position of node n on fault k. For $G_{ij}(X, X_{nk})$, it represents the response function of the velocity of surface point X in the direction of i generated by unit slip in the j direction at node X_{nk} on the fault. V is velocity, and the unit of V is in millimeters per year.

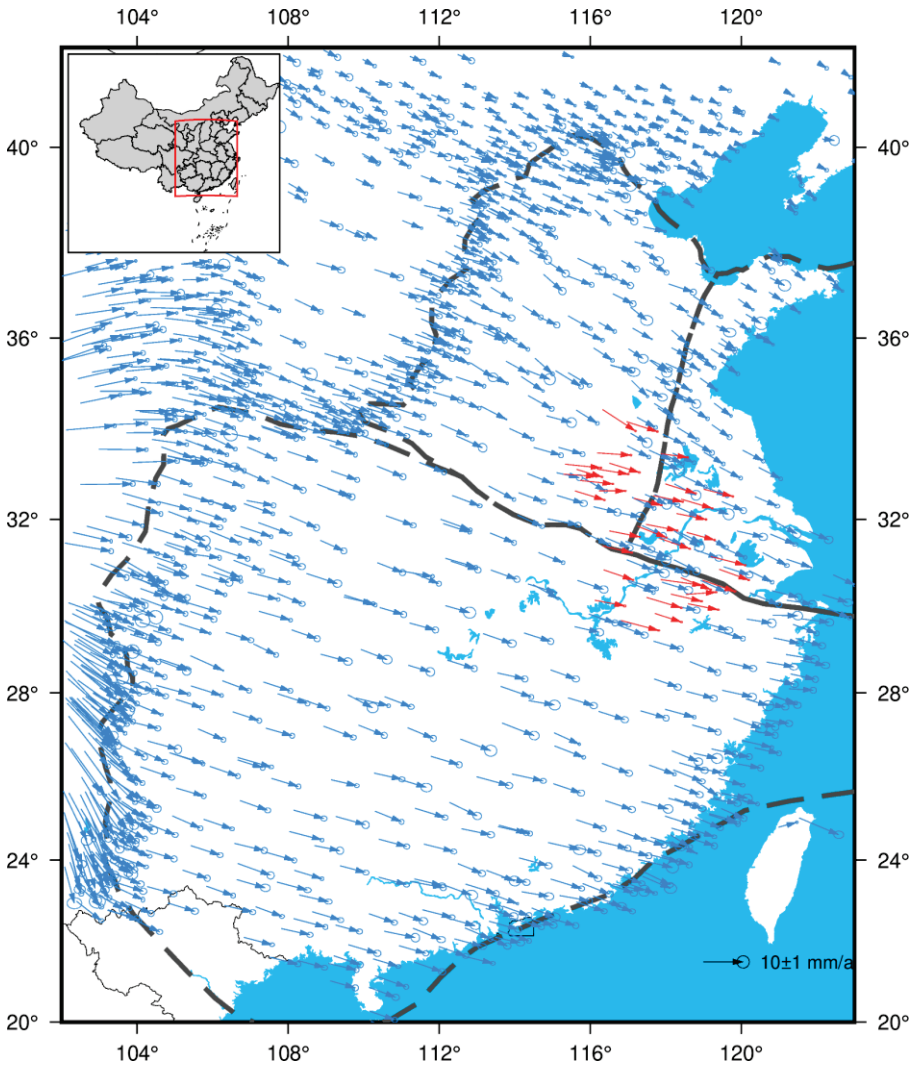

Figure 2. GPS velocity field with respect to Eurasian plate. Blue and red arrows represent the velocity field of CMONOC and AHCORS, respectively. The areas surrounded by dashed line are North China block, Ludong block, and South China block. Error ellipses represent 70% confidence.

If uniform strain exists in the block, the strain rate can be calculated by using Formula (2) given by Savage et al. [33]. In this case, the model is obtained by adding Formula (1) to Formula (2). The velocity caused by the internal strain in the block can be written as

$$\begin{bmatrix} V_\lambda \\ V_\theta \end{bmatrix} = \begin{bmatrix} R\sin\theta_0\Delta\lambda & R\Delta\theta & 0 \\ 0 & R\sin\theta_0\Delta\lambda & R\Delta\theta \end{bmatrix} \begin{bmatrix} \dot{\varepsilon_\lambda} \\ \dot{\varepsilon_{\lambda\theta}} \\ \dot{\varepsilon_\theta} \end{bmatrix} \quad (2)$$

where λ and θ correspond to the colongitude and colatitude, respectively, while the $\Delta\lambda$ and $\Delta\theta$ are the colongitude and colatitude differences between the measuring point and the regional geometric center. R is the mean radius of the regional geometric center and θ_0 is the colatitude of the regional geometric center. V and $\dot{\varepsilon}$ are the velocity component and strain rate component, respectively.

After the GPS horizontal velocity field of a certain region is solved, grid searches or simulated annealing method are then used to invert the fault coupling ratios and slip rate deficit. The coupling ratio is defined as a value between 0 and 1. A value of 1 indicates that the fault patch is fully locked and a value of 0 means that the fault patch is freely creeping. A value between 0 and 1 suggests that the fault is partly locked. The quality of parameter fitting can be evaluated using the reduced χ^2 statistic which is defined as follows [32]:

$$\chi_n^2 = [\sum_{i=1}^{n}\left(\frac{r_i}{f\sigma_i}\right)^2]/dof \quad (3)$$

where n is the number of observed data and r_i is the residual of observed data. For f, it represents the error weight factor, which is generally between 1 and 5 [34]. σ_i is the standard deviation and dof is the degrees of freedom.

In order to obtain a set of optimal solutions, we need to adjust the size of f repeatedly during inversion to make $\chi_n^2 \approx 1$, so that the model is able to simulate the observed data accurately.

3.3. Block Definition and Fault Geometry

According to the geological and geodetic information, Zhang et al. [35] delimited active blocks in China. As a result, our research area is bounded by the central and southern segments of the Tanlu fault zone and divided into three parts: North China block, Ludong block, and South China block. In the inversion process, we assumed that the South China block is an internally stable rigid block, while there is uniform strain in the North China block and Ludong block [2]. The central and southern segments of the Tanlu fault zone have a strike of SSW, a downdip of NW, and the dip angle is fixed at 65° [36]. The fault plane is composed of fifteen nodes along the strike, and the average distance between nodes is about 50 km. Meanwhile, the setting of nodes along the downdip is based on the research results of Li et al. [16]. According to the results of earthquake relocation [7], the depth of earthquakes in the central and southern segments of the Tanlu fault zone are mostly within 30 km, and only a few earthquakes exceed 30 km. Therefore, eight independent nodes are set along the downdip direction, with the depth of 0.1 km, 5 km, 10 km, 15 km, 20 km, 25 km, 30 km, and 35 km. At present, no studies show that there is creeping in the shallow of the central and southern segments of the Tanlu fault zone. Accordingly, a strong constraint with fault coupling ratios of 1.0 is added to the nodes at 0.1 km and 5 km [32], and it is assumed that only free slip exists below 35 km. The coupling ratios of the fault between 0.1–35 km decrease monotonically along the downdip.

4. Results

4.1. Fault Coupling Ratios

According to the parameter settings above, we utilized the velocity field data of AHCORS and CMONOC to obtain our optimal coupling model. For the preferred model, when the sigma scaling factor f of its horizontal velocity field data is taken as 2.754, χ_n^2 is just equal to 1.000 (the number of observations is 1290, the degree of freedom is 1212). Figure 3 depicts the comparison between observed and predicted GPS velocity field and the velocity residuals for the optimal model. The mean residual of the north and east components is −0.223 and 0.058 mm/y, respectively. This indicates that the fitting result of the model is precise.

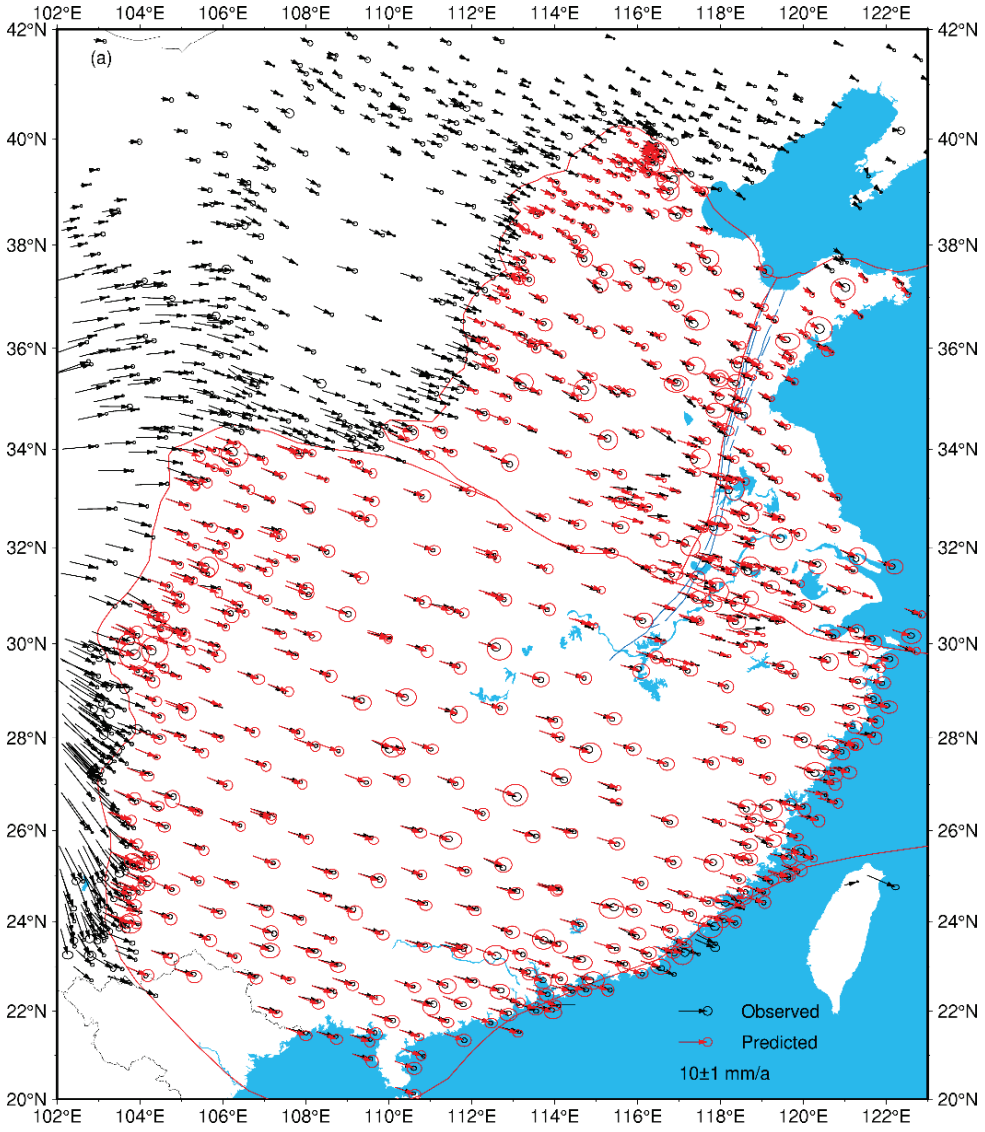

Figure 3. *Cont.*

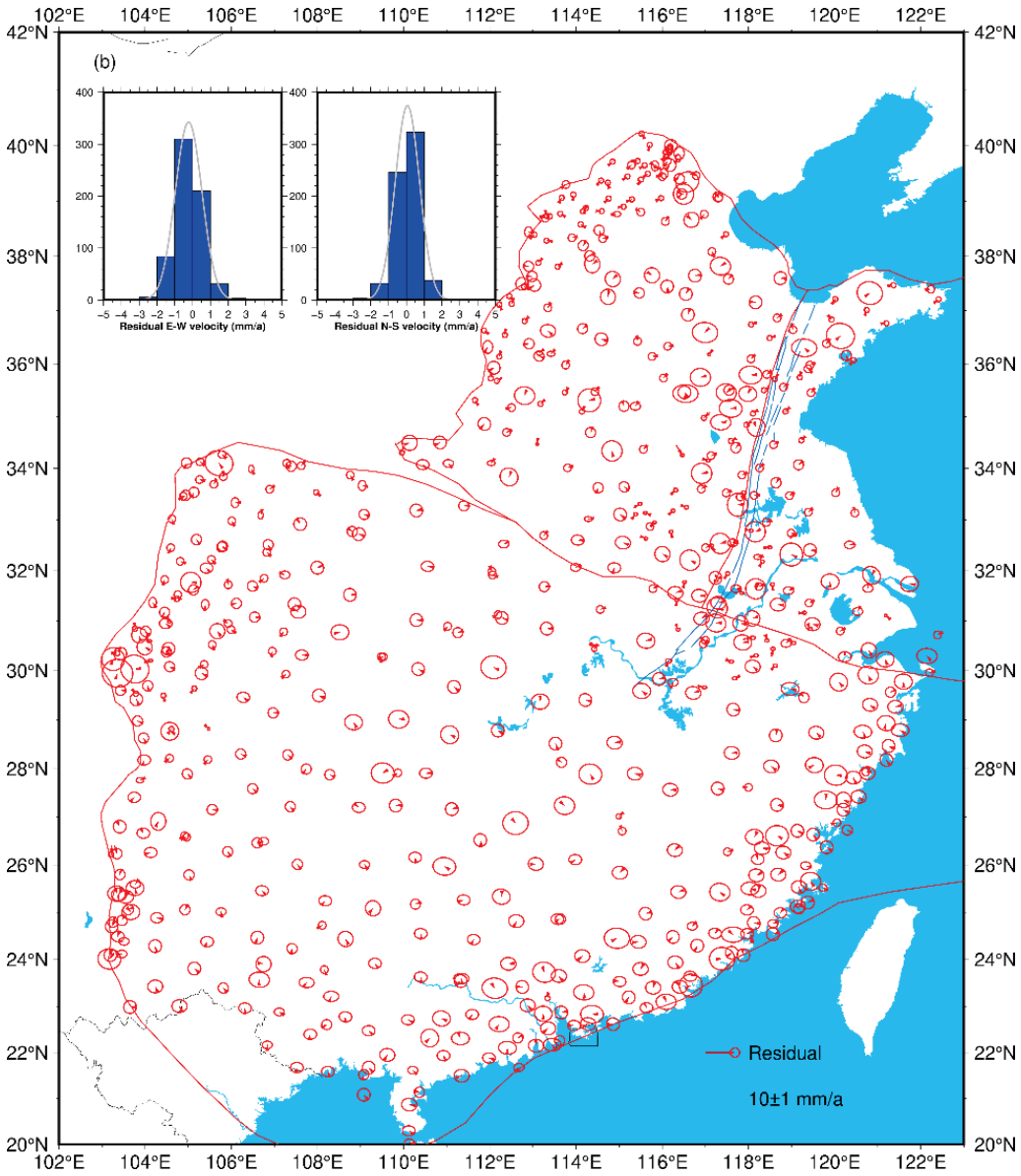

Figure 3. Comparison between observed and predicted GPS velocity field (**a**). Black and red arrows are observed velocity and predicted velocity, respectively. GPS velocity residuals distribution for the optimal model (**b**). The images in the upper left corner are the statistical histogram of residuals of the east components and north components, respectively.

The fault coupling distribution on the central and southern segments of the Tanlu fault zone is shown in Figure 4. For the convenience of analysis, the whole fault is divided into three parts from north to south: the Weifang–Tancheng segment, the Tancheng–Jiashan segment, and the Jiashan–Tongcheng segment. They are all located in eastern China, and most places are plains and hills. From Figure 4, lateral variation of coupling distribution can be found along the strike of the Tanlu fault zone. The Weifang–Tancheng segment is in a state of high coupling 26 km below the surface, with coupling ratios above 0.8. Along the downdip, the coupling ratios decrease with the increase of depth. The coupling ratios of 26–30 km change from high coupling to medium coupling, and the coupling ratios are about 0.6. Along the downdip, from 30 km to 35 km, the fault changes from strong coupling to freely creeping. As for the Tancheng–Jiashan segment, its locking depth is 5 km below the surface, which is much shallower than that of the Weifang–Tancheng segment. The vicinity of Tancheng at the north end is in a fully coupling state within the uppermost

26 km below the surface. The epicenter of the 1663 Tancheng M_S 8.5 earthquake is close to this region. The lower edge of the source fault is determined to be about 32 km depth [37], coinciding well with the strong coupling area. For the Jiashan–Tongcheng segment, its middle and north sections are in a medium coupling state. The middle section especially is still in a strong coupling state 25 km below the surface; however, the south section is freely creeping below the depth of 10 km. Generally, compared with the southern segment of the Tanlu fault zone, the northern segment has a higher coupling degree and a deeper locking depth, which means that the strain accumulation in the northern segment is more rapid.

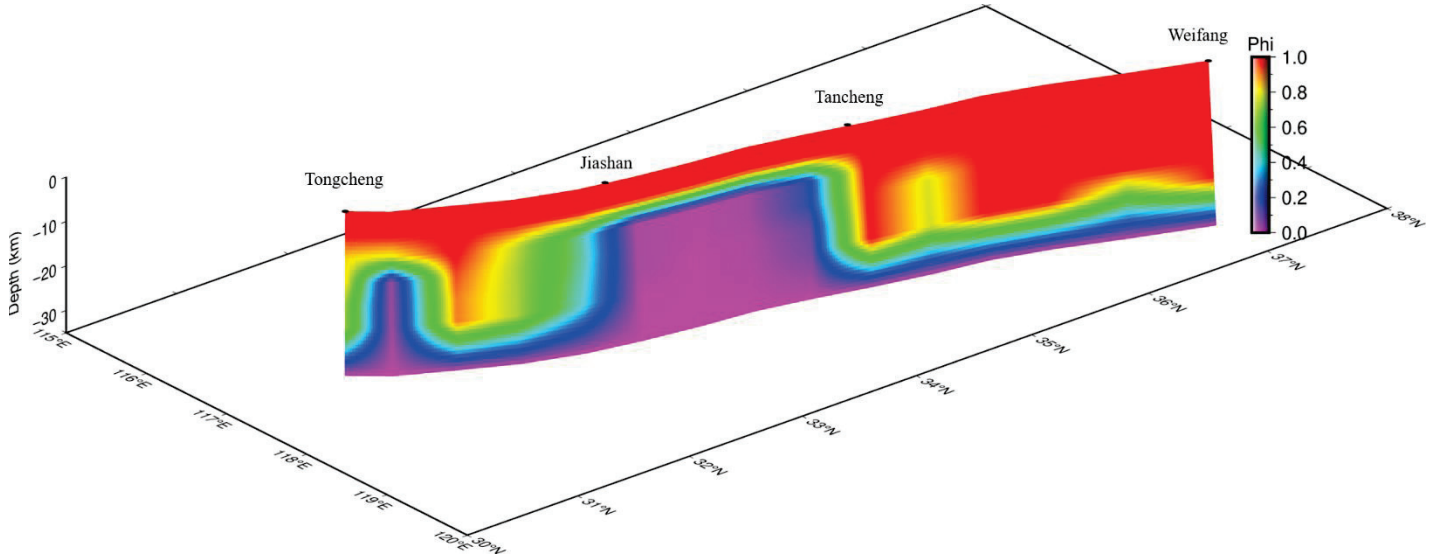

Figure 4. The three-dimensional (3D) spatial distribution of coupling ratios of the optimal model inverted by AHCORS and CMONOC velocity field. Purple to red indicates the fault coupling coefficient. The red places indicate that the fault is fully locked, and the purple places mean that the fault is freely creeping; other colors suggest that the fault is partly locked.

4.2. Fault Slip Rate Deficit

Figure 5 shows the slip rate deficit of the optimal model on the central and southern segments of the Tanlu fault zone. In Figure 5, the 3D spatial distribution of slip rate deficit is similar to coupling ratios. For the Weifang–Tancheng segment, the slip rate deficit is the largest within 30 km below the surface, ranging from 0.8 to 1.6 mm/a. For the Tancheng–Jiashan segment, the slip rate deficit gradually decreases from north to south, and the rate is between 0.6–1.0 mm/a. As for the Jiashan–Tongcheng segment, the slip rate deficit is between 0.2–0.5 mm/a.

Fault slip rate deficit is calculated by multiplying the slip rate by the coupling coefficient. For the central and southern segments of the Tanlu fault zone, we can conclude, by combining the coupling ratios in Figure 4, that although the segments are fully coupled within 5 km underground, the slip rate deficit at the north is larger than that at the south, indicating that the slip rate at the north is larger. This result is consistent with the conclusion of Guo et al. (2011), that the slip rate of Tanlu fault zone gradually decreases from north to south (1.24–1.06 mm/a) [38].

4.3. Velocity Profiles Analysis

It is a conventional method to analyze the relative motion between blocks by GPS velocity profiles across the fault. As shown in Figure 1, we have made three profiles from north to south along the Tanlu fault zone. To facilitate the distinction, we represented them as profile a, profile b, and profile c from north to south, and the velocity profile results are shown in Figure 6. Through the profiles, it is clearer to see some features of the velocity field. For the velocity component parallel to the profile lines, when the slope of the red line

is positive, it indicates extension, while when the slope is negative, it indicates compression. Meanwhile, as for the velocity component perpendicular to the profile lines, positive slopes of blue lines mean left-lateral. On the contrary, negative slopes are right-lateral [28,30,39].

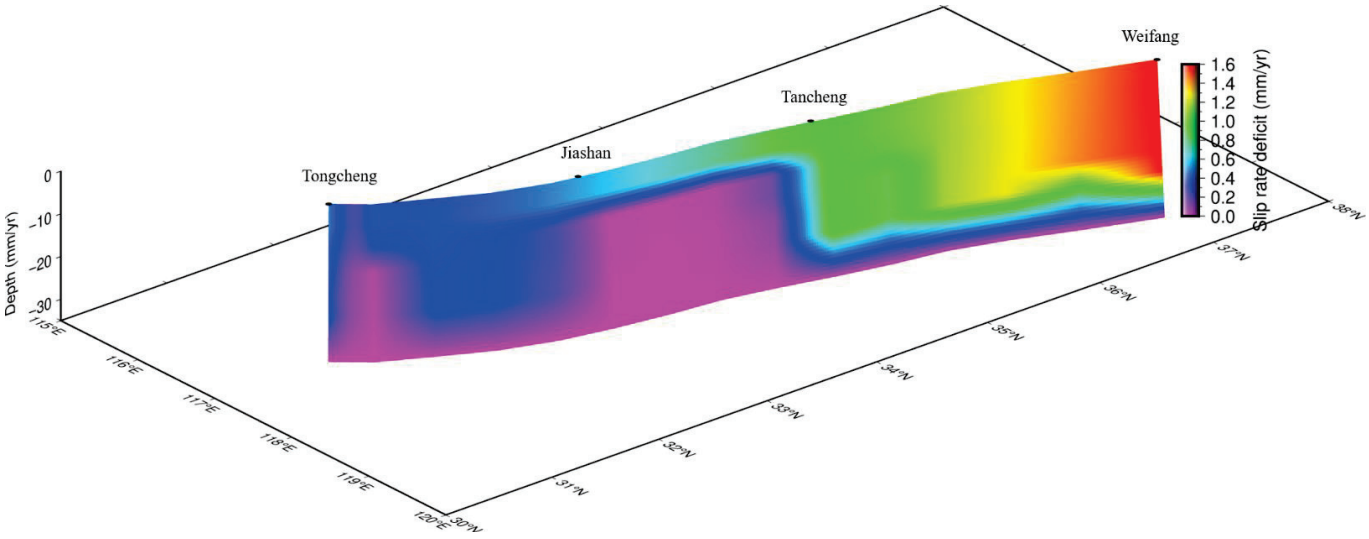

Figure 5. The 3D spatial distribution of slip rate deficit of the optimal model inverted by AHCORS and CMONOC velocity field (mm/a). Purple to red indicates the slip rate deficit. The red places indicate the slip rate deficit is large, and the purple places mean that there is no slip rate deficit.

In Figure 6, we compare the observed (points) and calculated (lines) GPS velocity and found that there are a few misfits between observed and calculated velocity results from longer distance to the profiles. However, on the whole, the fitting result is quite accurate. From the profiles, the velocity parallel to the profile lines and perpendicular to the profile lines changes slightly when passing through the fault; it is continuous without any obvious step, indicating that the fault cannot slip freely and is still locked. At the same time, the velocities of profile a, profile b, and profile c, whether parallel or perpendicular to the profile lines, show a gentle negative slope. We also derived the slip rates and root mean square error of the Tanlu fault by calculating the velocity of the profiles, as shown in Table 3. Generally, the velocity parallel to the profiles is between −0.76 and −0.35 mm/a, and the velocity perpendicular to the profiles is between −0.44 and −0.29 mm/a. Hence, it proves that the fault among the profiles is right-lateral and compressive, and the compression component gradually decreases from north to south. From geological studies, Li et al. (2019) suggested that the kinematic characteristics of the Tanlu fault zone are right-lateral and thrust [40], which is consistent with our result.

Table 3. Slip rates on the central and southern segments of the Tanlu fault zone (left-lateral with tension is positive).

Segment	Velocity Parallel to the Profiles/RMSE (mm·a^{-1})	Velocity Perpendicular to the Profiles/RMSE (mm·a^{-1})
a	−0.76/0.16	−0.44/0.22
b	−0.57/0.11	−0.40/0.15
c	−0.35/0.16	−0.29/0.17

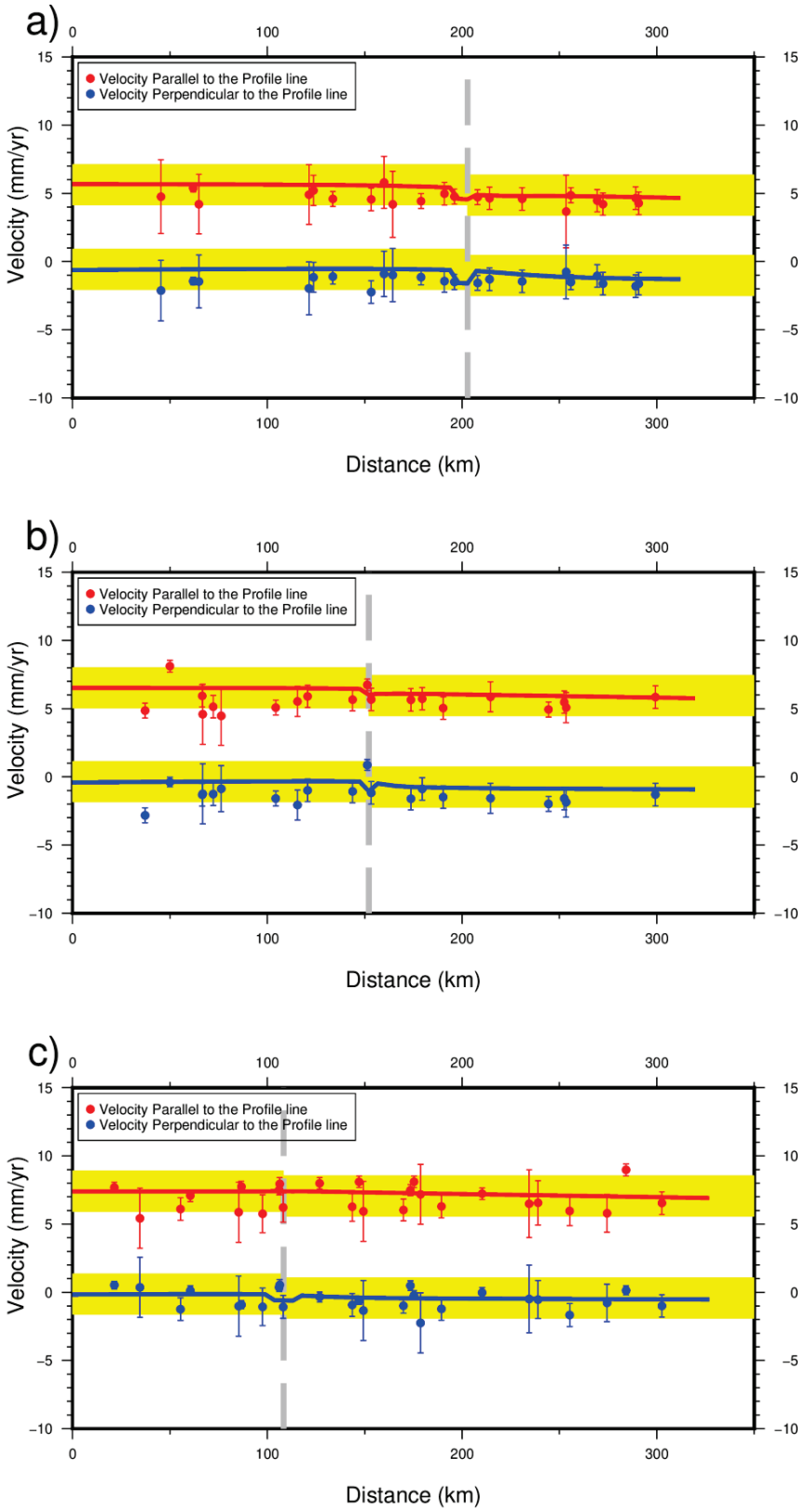

Figure 6. GPS velocity profiles from north to south (**a**–**c**). The length of the profiles is less than 350 km, and the width is 160 km. The red points and lines represent the observed and calculated GPS velocity parallel to the profile lines, respectively. The blue points and lines represent the observed and calculated GPS velocity perpendicular to the profile lines. The gray dashed line represents the Tanlu fault zone, and the median value of the yellow rectangle is the average of the velocities.

5. Discussion

5.1. Checkboard Tests

We conducted a series of checkboard tests to determine the minimum distance along the strike of the coupling ratios that the GPS velocity field can resolve. First, in the forward modeling, we input the rotation parameters of the blocks to estimate the velocity of each station, and then added the Gaussian noise to obtain a new velocity field. Finally, we used the synthetic velocity field to invert the coupling ratios of the fault and compared it with the forward modeling result [41,42], as shown in Figure 7. We compared the cases where the distance between nodes along the strike is 50–70 km and found that when the distance between nodes is 60 km and 70 km, the input information cannot be recovered well, especially at the depth of 20 km below the surface. In Figure 7f, while the distance between nodes is 50 km, most grid cells are recovered well except for a small part, which may be caused by inhomogeneous distribution of velocity field. As a result, we chose 50 km as the minimum distance between adjacent nodes. From the spatial resolution of the coupling ratios, we can conclude that in order to obtain the optimal inversion results, we need to consider the GPS velocity density.

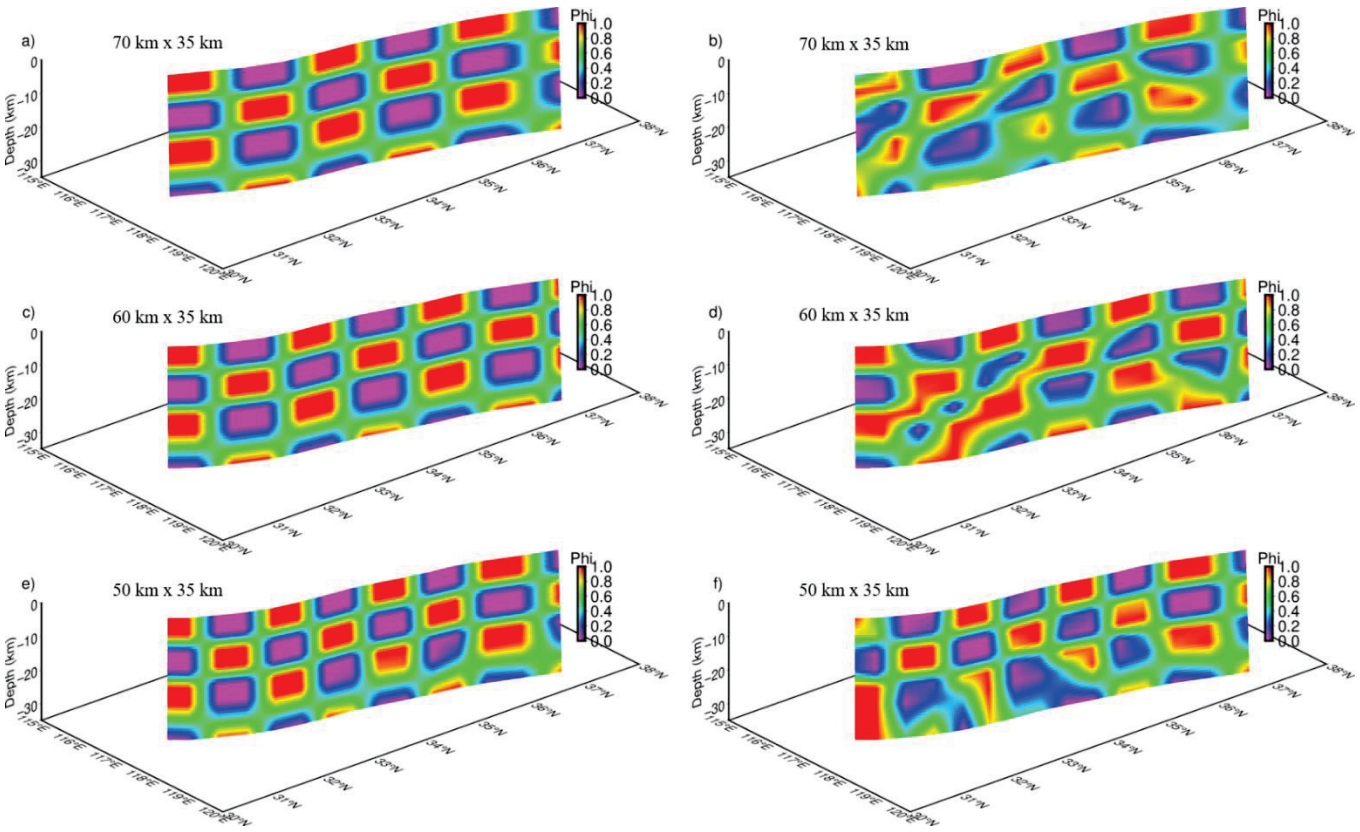

Figure 7. Resolution tests for coupling ratios inverted by different distances between adjacent fault nodes. Figures on the left (**a**,**c**,**e**) are 3D distribution of coupling ratios for forward modeling, and on the right (**b**,**d**,**f**) are recovered 3D distribution of coupling ratios using the same inversion strategy.

5.2. Comparison with Previous Studies

In order to explore whether near-field data will affect the inversion results of the model, we used only CMONOC velocity field to invert the distribution of fault coupling ratios and slip rate deficit, as shown in Figure 8. Comparing the results of this inversion with the results integrating the near-field data of AHCORS, we found that the fault coupling ratios and slip rate deficit are quite similar. In the Tancheng–Jiashan segment, both of them are in a state of strong coupling 26 km below the surface, and the difference mainly lies in the

Tancheng–Jiashan and the Jiashan–Tongcheng segments, which also exactly corresponds to the position of AHCORS velocity field. In the Tancheng–Jiashan segment, the locking depth of the inversion result for the optimal model is relatively shallower than that of this result. In the Jiashan–Tongcheng segment, the inversion result of the optimal model is strongly locked in the middle section, and the depth can reach 25 km, which is not reflected in this inversion. As for slip rate deficit, except for the Jiashan–Tongcheng segment, other parts are basically the same. Compared with the results of Li et al. (2020) [16], the main difference is also shown in the south of Tancheng. As a result, we believe that this is caused by the integration of near-field data, which significantly affects the inversion results.

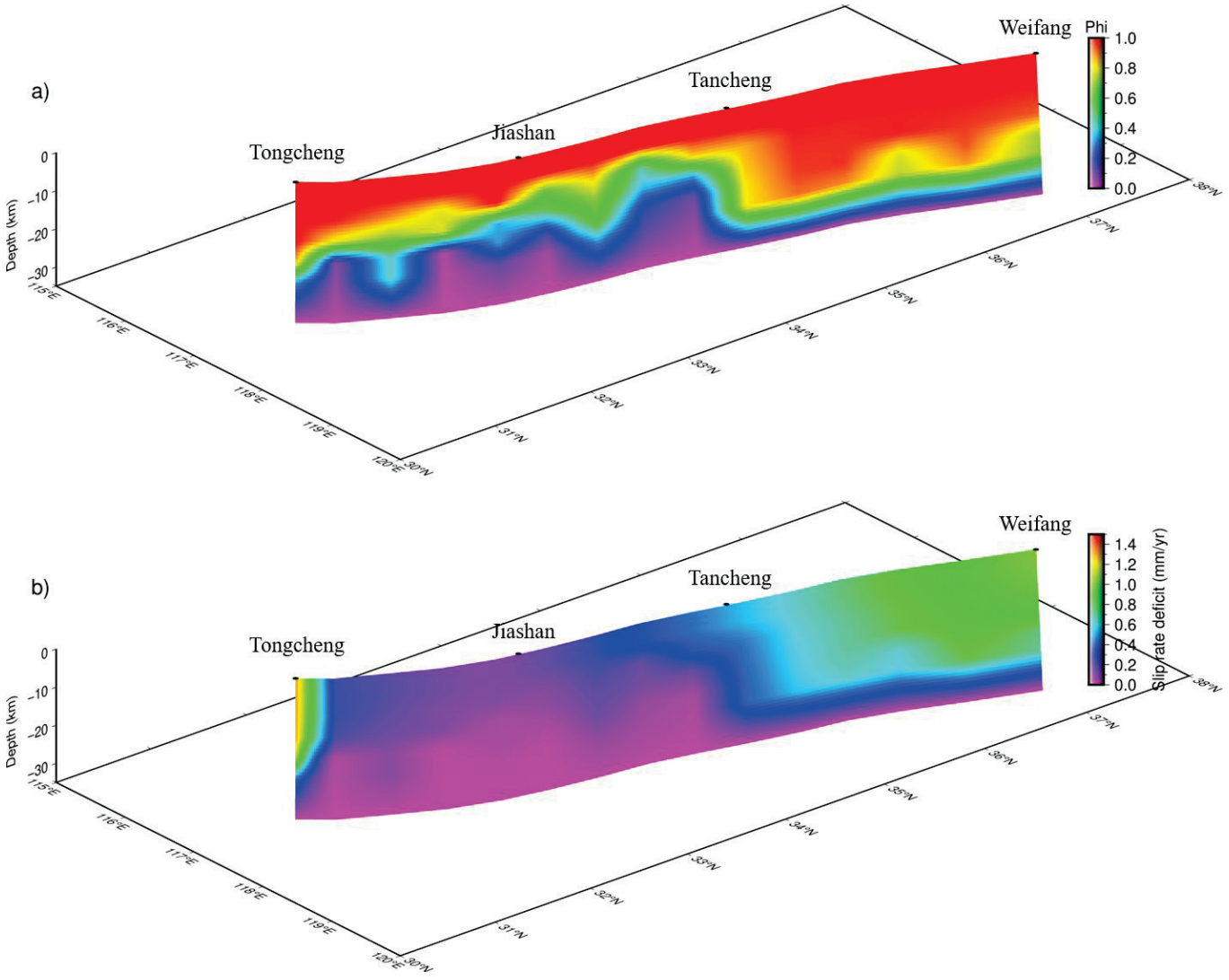

Figure 8. The 3D spatial distribution of coupling ratios inverted only by CMONOC velocity field (**a**). The 3D spatial distribution of slip rate deficit inverted only by CMONOC velocity field (**b**). The values in the northern segment are mostly larger than those in the southern segment.

5.3. Strain Characteristics

The inconsistency of spatial distribution of the GPS horizontal velocity field is a direct reflection of crustal deformation. Different reference frame will lead to a large difference in velocity field; however, the strain rates are not related to the reference datum, and it is one of the crucial indicators to describe regional surface deformation directly [43–45].

Taking GPS horizontal velocity field as constraints, we used DEFNODE to invert the coupling ratios and slip rate deficit of the Tanlu fault zone. Next, we utilized GPS

horizontal velocity field to calculate regional strain rates, to describe surface deformation characteristics and fault activity. In this paper, we chose the horizontal velocity field from 245 stations including CMONOC and AHCORS in the longitude and latitude range of 113° E–122° E and 27° N–38° N, and calculated the principal strain rates, dilatation rates, and maximum shear strain rates of the central and southern segments of the Tanlu fault zone and surrounding areas using least-squares collocation method. The horizontal strain rates are shown in Figure 9.

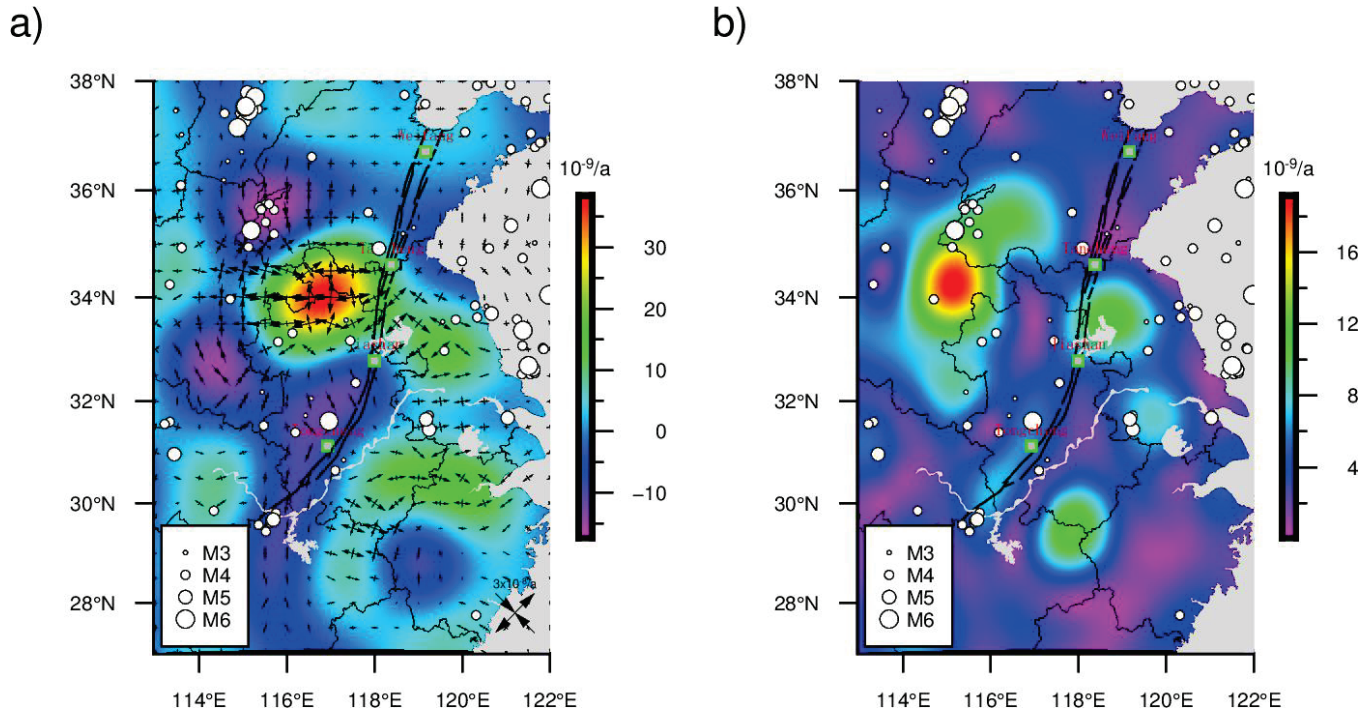

Figure 9. Strain rates on the central and southern segments of the Tanlu fault zone. (**a**) Principal strain rates and dilatation rates. Principle strain rates are shown as vector pairs and dilatation rates are shown in background color. Positive dilatation rates show extension, while negative show compression. (**b**) Maximum shear strain rates. White circles show earthquakes with $3.0 \leq M_s \leq 8.5$ from 1 January 1900 to 31 December 2020.

In Figure 9a, the principal strain rates near the Weifang–Tancheng segment of the Tanlu fault zone are almost zero. The Tancheng–Jiashan segment corresponds to the high-value area of the principal strain rates. Bounded by the Tanlu fault zone, the west side shows a nearly E–W and N–S extension, while the east side is a NE–SW or NW–SE extension. The principal strain rates of Jiashan–Tongcheng are relatively small, and the east side is dominated by approximately E–W extension, and the west side is nearly N–S compression. For dilatation rates, the maximum value appears on the west side of the Tancheng–Jiashan segment, which is 3.78×10^{-8}/a. It is in the north of Anhui Province, where shallow groundwater has been exploited for a long time. Additionally, there are abundant coal resources here, and years of mining have contributed to the subsidence of the area. Therefore, we believe that it is likely to be caused by human activities, which should attract public attention.

In Figure 9b, it can be recognized that the maximum shear strain rates in the central and southern segments of the Tanlu Fault zone are smaller than those on both sides of the Tancheng–Jiashan segment and the east of the southern segment of Tongcheng. Generally, the maximum shear strain rates in the central segment of the Tanlu fault zone are much larger than the southern segment, consistent with the geological results indicating that the activity of the southern segment is weaker than the central segment [22].

5.4. Implication for Future Seismic Hazard

Generally, we believe that the occurrence of an earthquake is a process of continuous strain accumulation. When the accumulation reaches the limitation, it will break through the stable state, resulting in sudden rupture of the fault zone [46–48]. Therefore, for the fault zone with high coupling ratios and deep locking depth, this means the accumulation of strain rates, and it is more likely to have a large earthquake in the future. At the same time, slip rate deficit is also an important indicator of the rate of strain accumulation on active faults [49]. Therefore, we have reason to pay attention to the places with high coupling ratios, deep locking depth, and high slip rate deficit or abnormal strain rates on the surface.

For the central and southern segments of the Tanlu fault zone, according to the spatial distribution of coupling ratios, we could find that the Tancheng–Weifang segment is in a state of high coupling 26 km below the surface, with coupling ratios above 0.8. In this segment, there are only two major earthquakes above M_S 8.0, occurring in Anqiu in 70 BC and Tancheng in 1668. Notably, the focal depth of the 1663 Tancheng M_s 8.5 earthquake is 32 km, which is deeper than the strong coupling depth of 26 km based on our inversion result. It indicates that the locking depth was at least 32 km before the earthquake, and the locking degree has not returned to its previous state, which may be the reason why there has been no earthquake with a magnitude lager than M_s 8.5 in this region so far. From geological studies, Li et al. (2019) considered that the age of the latest paleoseismic event was about $12.8 + 4.0/-3.7$ ka through paleoseismic trough and AMS $-$ ^{14}C dating method [40]. As a consequence, the recurrence interval of long-period large earthquakes is the main feature of Late Quaternary activity in the central and southern segments of Tanlu fault zone. In general, the fault coupling ratios and slip rate deficit of the northern segment are larger than those of the southern segment, which indicates that the northern segment is more prone to generate large earthquakes. Although it has been more than 350 years since the 1668 Tancheng earthquake, the Weifang–Tancheng segment still deserves our attention.

For the distribution of the strain rates, the area with large principal strain rates also corresponds to the high-value area of the dilatation rates, and the interface area between extension and compression is always accompanied by a sudden change in the direction of the principal strain rates. The places where the strain rates are abnormal may have potential for disaster. They provide an important reference for us to prevent seismic hazard.

6. Conclusions

Using the data of AHCORS and CMONOC stations, we inverted the coupling ratios, slip rate deficit, and velocity profiles by DEFNODE on the central and southern segments of the Tanlu fault zone. We found that slip rate deficit and locking depth in the north is higher and deeper than that in the south and it is more likely to produce strain accumulation. In particular, the locking degree of the Tancheng has not been restored to the state before the 1668 Tancheng earthquake, so its adjacent region has not experienced a large earthquake for a long time. Based on geological studies and historical large earthquakes, it can be seen that the Tanlu fault zone is characterized by long-period recurrence interval of large earthquakes. By comparing the coupling ratios and slip rate deficit, the fault shows that it has high coupling ratios within 5 km under the surface; however, the slip rate deficit in the north is larger. Hence, the slip rate in the north is also larger than that in the south. Subsequently, we analyzed three velocity profiles across the fault zone. The result shows that the velocity parallel to the profiles is between -0.76 and -0.35 mm/a, and the velocity perpendicular to the profiles is between -0.44 and -0.29 mm/a, which indicates that the fault is right-lateral strike-slip and compressive. Finally, we used least-squares collocation to calculate the strain rates. The results suggest that where the principal strain rates are large, the value of dilatation rates will also be large. The interface of extension and compression is always accompanied by sudden change of direction of principal strain rates. These places with abnormal strain rates have the potential for disaster.

While we used AHCORS data to obtain a high-precision velocity field on the central and southern segments of the Tanlu fault zone, the measurements of the AHCORS, as is

known, could be affected by various types of uncertainties and inaccuracies that arise from different causes. It would be necessary to evaluate the fuzziness [50] and jumps of data [51], which play an important role in estimating trends and forecasting in the future work. At the same time, we believe that the setting of fault geometry can be further improved, such as setting different dip angles at different depths of the fault. Additionally, only GPS data were used to invert the coupling pattern of the Tanlu fault zone in this study. In the future, a refined coupling model jointly constrained by multisource data (e.g., InSAR and GPS data) could help us to better understand the strain accumulation and seismic risk in the Tanlu fault zone.

Author Contributions: Conceptualization, H.C., T.T. and S.L.; methodology, H.C. and S.L.; software, H.C.; validation, H.C. and T.T.; formal analysis, H.C.; investigation, H.C.; resources, H.C.; data curation, H.C.; writing—original draft preparation, H.C.; writing—review and editing, H.C., T.T. and S.L.; visualization, H.C.; supervision, X.Q. and Y.Z.; project administration, T.T.; funding acquisition, T.T. All authors have read and agreed to the published version of the manuscript.

Funding: This work is funded by Open Research Fund Program of Hunan Province Key Laboratory of Safe Mining Techniques of Coal Mines (Hunan University of Science and Technology) under Grant E22015, and also supported by the Natural Science Foundation of Anhui Province, China under Grant 1808085MD105. This work is supported by the National Natural Science Foundation of China under Grant 42004001.

Acknowledgments: We are grateful to the Anhui Bureau of Surveying and Mapping for providing the raw GNSS observation data. We sincerely thank Min Wang for publishing the velocity field data of CMONOC.

Conflicts of Interest: The authors declare no conflict of interest.

Abbreviations

The following abbreviations are used in this manuscript:

GPS	Global Positioning System
InSAR	Interferometric synthetic aperture radar
AHCORS	Anhui Continuously Operating Reference System
CMONOC	Crustal Movement Observation Network of China
IGS	International GNSS Service
VMF1	Vienna Mapping Function 1
FES2004	Finite 79 Element Solutions 2004
SOPAC	Scripps Orbits and Permanent Array Center
ITRF2008	International Terrestrial Reference Frame 2008
3D	Three-dimensional

References

1. Fang, Z.; Ding, M.; Ji, F.; Xiang, H. Geological analysis of the seismicity in the Tancheng-Lujiang fault zone, East China. *Seismol. Geol.* **1980**, *2*, 39–45.
2. Zhang, P.; Gan, W.; Shen, Z.; Wang, M. A coupling model of rigid-block movement and continuous deformation: Patterns of the present-day formation of China's continent and its vicinity. *Acta Geol. Sin.* **2005**, *79*, 748–756.
3. Wu, D.; Zhang, Y.; Fang, Z.; Zhang, S. On the activity of the Tancheng-Lujiang fault zone in China. *Seismol. Geol.* **1981**, *3*, 15–26.
4. Li, J.; Chao, H.; Cui, Z.; Zhao, Q. Seismic fault of the 1668 Tacheng earthquake (M = $8\frac{1}{2}$) and its fracture mechanism. *Seismol. Geol.* **1994**, *16*, 229–237.
5. Gao, W.; Zheng, L. Active fault segmentation and the identification of potential seismic zones along the Tanlu fault. *Earthq. Res. China* **1991**, *7*, 87–91. (In Chinese)
6. Wang, M.; Li, Q.; Wang, F.; Wang, Y.; Shi, H.; Zhang, P.; Shen, Z. Far-field coseismic displacements associated with the 2011 Tohoku-oki earthquake in Japan observed by Global Positioning System. *Chin. Sci. Bull.* **2011**, *56*, 2419–2424. [CrossRef]
7. Li, Y.; Shan, X.; Song, X.; Jiang, Y.; Gan, W.; Qu, C.; Wang, Z. Fault locking and slip rate deficit on the middle and southern segment of the Tancheng-Lujia fault inverted from GPS data. *Chin. J. Geophys.* **2016**, *59*, 4022–4034. (In Chinese)
8. Meng, G.; Su, X.; Wu, W.; Nikolay, S.; Takahashi, H.; Ohzono, M.; Gerasimenko, M. Crustal deformation of Northeastern China following the 2011 Mw 9.0 Tohoku, Japan earthquake estimated from GPS observations: Strain heterogeneity and seismicity. *Remote Sens.* **2019**, *11*, 3029. [CrossRef]

9. Li, S.; Wang, Q.; Yang, S.; Qiao, X.; Nie, Z.; Zou, R.; Ding, K.; He, P.; Chen, G. Geodetic imaging mega-thrust coupling beneath the Himalaya. *Tectonophysics* **2018**, *747–748*, 225–238. [CrossRef]
10. Liu, C.; Ji, L.; Zhu, L.; Zhao, C. InSAR-Constrained interseismic deformation and potential seismogenic asperities on the Altyn Tagh fault at 91.5–95° E, northern Tibetan plateau. *Remote Sens.* **2018**, *10*, 943. [CrossRef]
11. Qiao, X.; Qu, C.; Shan, X.; Zhao, D.; Liu, L. Interseismic slip and coupling along the Haiyuan fault zone constrained by InSAR and GPS measurements. *Remote Sens.* **2021**, *13*, 3333. [CrossRef]
12. Zhao, J.; Jiang, Z.; Niu, A.; Wu, Y.; Zhan, W.; Wei, W. Characteristics of fault locking and fault slip deficit in the main Himalaya thrust fault. *Geomat. Inf. Sci. Wuhan Univ.* **2017**, *42*, 1756–1764.
13. Guo, L.; Ying, F. Primary study on horizontal deformation and tectonic activity using GPS results in northern part of North China. *Earthq. Res. China* **1998**, *14*, 11–19. (In Chinese)
14. Xu, C.; Li, Z.; Wang, H. The temporal and spatial variation characteristics of crustal deformation of active tectonic blocks in north China. *J. Geod. Geodyn.* **2002**, *22*, 33–40. (In Chinese)
15. Wang, W.; Yang, S.; Wang, Q. Crustal block rotations in Chinese mainland revealed by GPS measurements. *Earthq. Sci.* **2009**, *22*, 639–649. [CrossRef]
16. Li, L.; Li, Y.; Zhang, F.; Chen, C.; Yin, H.; Jia, Y. Faults blocking characteristics and seismic hazard analysis in the middle and southern segments of the Tanlu Faults Zone. *Acta Geol. Sin.* **2020**, *94*, 467–479.
17. Wang, M.; Shen, Z. Present-day crustal deformation of continental China derived from GPS and its tectonic implications. *J. Geophys. Res.* **2020**, *125*, e2019JB018774. [CrossRef]
18. Huang, L.; Liu, C.; Kusky, T. Cenozoic evolution of the Tan-Lu Fault Zone (East China)-constrained from seismic data. *Gondwana Res.* **2015**, *28*, 1079–1095. [CrossRef]
19. Jiang, R.; Cao, K.; Zeng, J.; Liu, K.; Li, C.; Wang, A.; Yu, J.; Peng, B.; Lao, J.; Zhao, L. Late Cenozoic tectonic evolution of the southern segment of the Tan-Lu fault zone, Eastern China. *J. Asian Earth Sci.* **2019**, *182*, 103932.1–103932.19. [CrossRef]
20. Liu, B.; Zhu, G.; Zhai, M.; Gu, C.; Liu, S. Quaternary faulting of the Jiangsu part of the Tan-Lu Fault Zone, East China: Evidence from field investigations and OSL dating. *J. Asian Earth Sci.* **2015**, *114*, 89–102. [CrossRef]
21. Gilder, A.; Leloup, H.; Courtillot, V.; Chen, Y.; Coe, R.; Zhao, X.; Xiao, W.; Halim, N.; Cogné, J.; Zhu, R. Tectonic evolution of the Tancheng-Lujiang (Tan-Lu) fault via Middle Triassic to Early Cenozoic paleomagnetic data. *J. Geophys. Res.* **1999**, *104*, 365–375. [CrossRef]
22. Tang, Y.; Shen, Z.; Lin, A.; Zhang, J. Extending of the Tancheng-Lujiang fault zone at the Anhui section and its neotectonic activity. *Seismol. Geol.* **1988**, *2*, 48–52.
23. Zhu, G.; Hu, W.; Song, L.; Liu, B. Quaternary activity along the Tan-Lu fault zone in the Bohai Bay, East China: Evidence from seismic profiles. *J. Asian Earth Sci.* **2015**, *114*, 5–17. [CrossRef]
24. Herring, T.; King, R.; McClusky, S. *Documentation of the MIT GPS Analysis Software: GAMIT Release 10.4*; Massachusetts Institute of Technology: Cambridge, MA, USA, 2010.
25. Boehm, J.; Werl, B.; Schuh, H. Troposphere mapping functions for GPS and very-long baseline interferometry from European centre for medium-range weather forecasts operational analysis data. *J. Geophys. Res.* **2006**, *111*, 1–9. [CrossRef]
26. Lyard, F.; Lefevre, F.; Letellier, T.; Francis, O. Modeling the Global Ocean Tides: Modern insights from FES2004. *Ocean. Dyn.* **2006**, *56*, 394–415. [CrossRef]
27. McCaffrey, R. Block kinematics of the Pacific–North America plate boundary in the southwestern US from inversion of GPS, seismological, and geologic data. *J. Geophys. Res.* **2005**, *110*, B07401.
28. McCaffrey, R.; Qamar, A.; King, R.; Wells, R.; Khazaradze, G.; Williams, C.; Stevens, C.; Vollick, J.; Zwick, P. Fault locking, block rotation and crustal deformation in the Pacific Northwest. *Geophys. J. Int.* **2007**, *169*, 1315–1340. [CrossRef]
29. McCaffrey, R.; Long, M.; Goldfinger, C.; Zwick, P.; Nabelek, J.; Johnson, C.; Smith, C. Rotation and plate locking at the southern Cascadia subduction zone. *Geophys. Res. Lett.* **2000**, *27*, 3117–3120. [CrossRef]
30. McCaffrey, R.; King, R.; Payne, S.; Lancaster, M. Active tectonics of northwestern U.S. inferred from GPS-derived surface velocities. *J. Geophys. Res.* **2013**, *118*, 709–723. [CrossRef]
31. Manaker, D.; Calais, E.; Freed, A.; Ali, S.; Przybylski, P.; Mattioli, G.; Jansma, P.; Prépetit, C.; de Chabalier, J. Interseismic plate coupling and strain partitioning in the Northeastern Caribbean. *Geophys. J. Int.* **2008**, *174*, 889–903. [CrossRef]
32. McCaffrey, R. Crustal Block Rotations and Plate Coupling. *Plate Boundary Zones.* **2002**, *30*, 101–122.
33. Savage, J.; Gan, W.; Svarc, J. Strain accumulation and rotation in the Eastern California Shear Zone. *J. Geophys. Res.* **2001**, *106*, 21995–22007. [CrossRef]
34. Mao, A.; Harrison, C.; Dixon, T. Noise in GPS coordinate time series. *J. Geophys. Res.* **1999**, *104*, 2797–2816. [CrossRef]
35. Zhang, P.; Deng, Q.; Zhang, G.; Ma, J.; Gan, W.; Min, W.; Mao, F.; Wang, Q. Active tectonic blocks and strong earthquakes in the continent of China. *Sci. China* **2003**, *46*, 13–24.
36. Deng, Q. *China Active Tectonic Map (1:4,000,000)*; Seismological Press: Beijing, China, 2007. (In Chinese)
37. Zhou, C.; Diao, G.; Geng, J.; Li, Y.; Xu, P.; Hu, X.; Feng, X.; Li, D. 3-D characteristics inversion of hypocenter fault-plane of the 1668 Tancheng great earthquake. *Prog. Geophys.* **2013**, *28*, 2814–2824. (In Chinese)
38. Guo, L.; Bo, W.; Yang, G.; Guo, H. Characteristics of horizontal deformation-strain field in north China from 1999 to 2009. *J. Geod. Geodyn.* **2011**, *31*, 15–19. (In Chinese)

39. Payne, S.; McCaffrey, R.; King, R.; Kattenhorn, S. A new interpretation of deformation rates in the Snake River Plain and adjacent basin and range regions based on GPS measurements. *Geophys. J. Int.* **2012**, *189*, 101–122. [CrossRef]
40. Li, K.; Xu, X.; Wei, L.; Wang, Q.; Shu, P. Evidence of long recurrence times and low slip rate along the 1668 Tancheng earthquake fault. *Chin. Sci. Bull.* **2019**, *64*, 1168–1178. [CrossRef]
41. Li, S.; Tao, T.; Gao, F.; Qu, X.; Wang, Q. Interseismic coupling beneath the Sikkim-Bhutan Himalaya constrained by GPS measurements and its implication for strain segmentation and seismic activity. *Remote Sens.* **2020**, *12*, 2202. [CrossRef]
42. Li, Y.; Hao, M.; Song, S.; Zhu, L.; Cui, D.; Zhuang, W.; Yang, F.; Wang, Q. Interseismic fault slip deficit and coupling distribution on the Anninghe-Zemuhe-Daliangshan-Xiaojiang fault zone, southeastern Tibetan Plateau, based on GPS measurements. *J. Asian Earth Sci.* **2021**, *219*, 104899. [CrossRef]
43. Poyraz, F. Determining the strain upon the eastern section of the North Anatolian zone (NAFZ). *Arab. J. Geosci.* **2015**, *8*, 1787–1799. [CrossRef]
44. Pearson, C.; Snay, R. Strain partitioning along the western margin of North America. *J. Struct. Geol.* **2014**, *64*, 67–78. [CrossRef]
45. Craig, T.; Calais, E. Strain accumulation in the New Madrid and Wabash Valley Seismic Zones from 14 years of continuous GPS observation. *J. Geophys. Res.* **2014**, *119*, 9110–9129. [CrossRef]
46. Scholz, C. *The Mechanics of Earthquakes and Faulting*; Cambridge University Press: Cambridge, UK, 2002; 225p.
47. Scholz, C. Earthquakes and friction laws. *Nature* **1998**, *391*, 37–42. [CrossRef]
48. Zhang, P. Beware of slowly slipping faults. *Nature* **2013**, *6*, 323–324. [CrossRef]
49. Li, Y.; Shan, X.; Qu, C.; Wang, Z. Fault locking and slip rate deficit of the Haiyuan-Liupanshan fault zone in the northeastern margin of the Tibetan Plateau. *J. Geodyn.* **2016**, *102*, 47–57. [CrossRef]
50. Versaci, M.; Angiulli, G.; Barba, P.; Morabito, F. Joint use of eddy current imaging and fuzzy similarities to assess the integrity of steel plates. *Open Phys.* **2020**, *18*, 230–240. [CrossRef]
51. Ghaderpour, E. JUST: MATLAB and python software for change detection and time series analysis. *GPS Solut.* **2021**, *25*, 85. [CrossRef]

remote sensing

MDPI

Article

Pre-Seismic Temporal Integrated Anomalies from Multiparametric Remote Sensing Data

Zhonghu Jiao * and Xinjian Shan

State Key Laboratory of Earthquake Dynamics, Institute of Geology, China Earthquake Administration, Beijing 100029, China; xjshan@ies.ac.cn
* Correspondence: jzh@ies.ac.cn

Abstract: Pre-seismic anomalies have the potential to indicate imminent strong earthquakes in the short to medium terms. However, an improved understanding of the statistical significance between anomalies and earthquakes is required to develop operational forecasting systems. We developed a temporal integrated anomaly (TIA) method to obtain the temporal trends of multiparametric anomalies derived from the Atmospheric Infrared Sounder (AIRS) product before earthquakes. A total of 169 global earthquakes that occurred from 2006 to 2020 and had magnitudes of $\geq$7.0 and focal depths of $\leq$70 km were used to test this new method in a retrospective manner. In addition, 169 synthetic earthquakes were randomly generated to demonstrate the suppression capacity of the TIA method for false alarms. We identified four different TIA trends according to the temporal characteristics of positive and negative TIAs. Long-term correlation analyses show that the recognition ability was 12.4–28.4% higher for true earthquakes than for synthetic earthquakes (i.e., higher than that of a random guess). Incorporating 2–5 kinds of TIAs offered the best chance of recognizing imminent shocks, highlighting the importance of multiparameter anomalies. Although the TIA trend characteristics before the earthquakes were not unique, we identified certain unexplained pre-seismic phenomena within the remote sensing data. The results provide new insight into the relationships between pre-seismic anomalies and earthquakes; moreover, the recognition ability of the proposed approach exceeds that of random guessing.

Keywords: earthquake anomaly; multiparametric anomalies; thermal infrared remote sensing

Citation: Jiao, Z.; Shan, X. Pre-Seismic Temporal Integrated Anomalies from Multiparametric Remote Sensing Data. *Remote Sens.* **2022**, *14*, 2343. https://doi.org/10.3390/rs14102343

Academic Editors: Stefano Morelli, Veronica Pazzi and Mirko Francioni

Received: 13 April 2022
Accepted: 10 May 2022
Published: 12 May 2022

Publisher's Note: MDPI stays neutral with regard to jurisdictional claims in published maps and institutional affiliations.

1. Introduction

Earthquakes and their associated disasters are major hazards around the world. Accurately predicting earthquakes would give communities more time to prepare [1,2]; however, despite decades of research, earthquake prediction remains an open question [2–7]. Utilizing pre-seismic anomalies in remote sensing data has become a research focus owing to the continuous development of space-based remote sensing technologies that provide various geophysical parameters from the top of the atmosphere (TOA) to the Earth's surface [8,9]. However, current anomaly detection methods fail to meet the requirements of operational earthquake forecasting systems [10,11]. In particular, improved pre-seismic anomaly recognition is fundamental to advancing short-to-medium term earthquake forecasting based on remote sensing data.

Precursory signals are most significant in epicentral areas and close by, and their possible correlation with earthquake preparation phases is the basis of earthquake forecasts. By monitoring tectonic activity using remote sensing technologies in seismically active areas, we can further our scientific understanding of pre-seismic diagnostic variation [12,13]. An earthquake is a dynamic process that involves the transition of mechanical energy, electromagnetic radiation, and thermal effects [14]. Thus, many physical pre-seismic parameters have been used to analyze the anomalous signals of earthquake events during preparation phases [2,15–19]. Remote sensing data offer a variety of geophysical and

geochemical parameters, and thereby provide abundant data for pre-seismic anomaly detection [8,20]. Moreover, remotely sensed data derived from satellite platforms are of high spatial and temporal resolution, take global measurements, generate rigorously validated data products, are easily accessed, and have broad community applications. Therefore, observable parameters have the potential to indicate the spatial extent, time window, and magnitude of an imminent event at different time scales with various degrees of probability. As such, remote sensing is the principal means of gathering and discerning pre-seismic anomalous information to prepare for potentially destructive earthquakes.

The earthquake preparation phase involves complex nucleation and non-linear faulting processes, and a variety of geophysical parameters have been considered for pre-seismic anomaly analysis [15,21]. Promising correlations between pre-seismic anomalies and strong earthquakes have been reported [4,8,9,15,20,22,23]. Surface temperature is a widely used parameter to detect earthquake-related thermal effects, with anomalous changes of ± 10 K being reported before earthquakes [24–26]. Near-surface air temperature is strongly related to surface temperature, and significant anomalies of air temperature have been observed prior to large earthquakes because of degassing and air ionization along the fault system [27,28]. Column water vapor, which can be accurately estimated from remote sensing data, shows anomalous changes in epicentral areas, possibly related to ascending fluids and surface latent heat flux [29,30]. Outgoing longwave radiation (OLR) at the TOA is another candidate precursor for predicting earthquakes [31]. OLR anomalies represent the overall thermal effects from the clouds, atmosphere, and Earth's surface, all of which are impacted by seismogenic activity; large variations of >10 W/m^2 have been reported prior to earthquakes [32,33]. Finally, multi-parametric analyses have been carried out with the aim of improving correlations between pre-seismic anomalies and imminent shocks [30,33,34].

However, despite some promising advances, in practice, earthquake forecasting results indicate the low statistical significance of these precursors. As a result, forecasts suffer from a high rate of false alarms when using remotely sensed land surface temperatures [11], while the false alarm rate can be effectively suppressed using seismic catalog data based on the natural time analysis approach [23]. Surface and atmospheric anomalies can have different effects. The impacts of short-term meteorological disturbances and anthropogenic interferences are difficult to eliminate. As such, anomaly detection methods require improved knowledge of pre-seismic anomalous characteristics in both the spatial and temporal domains to improve the forecasting ability.

Pre-seismic anomalies are influenced by topography, land cover, meteorology, and deep tectonic features. Observable information that is drawn from deep strata only accounts for a small proportion of most dominant features. Therefore, it is difficult to eliminate the influence of non-tectonic factors on thermal infrared radiation and to extract weak signals (i.e., pre-seismic anomalies) from strong noise backgrounds that reflect both natural processes and anthropogenic activities. Meanwhile, the pre-seismic phase before a significant earthquake is important for identifying anomalous signals. Therefore, we developed a pre-earthquake temporal integrated anomaly (TIA) method to describe the overall anomalous variation in a specified period (from days to months). The foreshocks before strong earthquakes are accompanied by a significant nucleation process [35] and exhibit intensive enhancement with a power law [36–38]. This will affect the occurrence and evolution of pre-seismic anomalies to a certain extent. By using the TIA, the influence of the weakness, transience, and discontinuity of the anomaly was reduced to highlight the overall change over a specific period. Then, the cumulative temporal trend of the TIA was used to identify the intensive enhancement of seismic-related anomalies in different time periods. Moreover, multiparametric TIAs were analyzed to inspect their feasibility for improving earthquake forecasting ability.

2. Data

2.1. Atmospheric Infrared Sounder (AIRS) Product

Hyperspectral infrared data make it possible to retrieve surface and atmospheric properties into various geophysical parameters [39]. Since 2002, the AIRS on the Aqua satellite has measured thermal infrared radiation emitted from the Earth's surface and atmosphere in a three-dimensional structure on a global scale twice a day. In this study, we used the Aqua/AIRS L3 Daily Standard Physical Retrieval (AIRS-only) V7.0 (AIRS3STD) product with 1-degree spatial resolution from descending (nighttime) orbits to estimate pre-seismic anomalies, including skin temperature (ST; K), near-surface air temperature (AT; K), total integrated column water vapor burden (CWV; kg/m^2), OLR (W/m^2), and clear-sky OLR (COLR; W/m^2). These parameters measure information at different vertical levels from the surface to the TOA and reflect the process of thermal radiative energy, which can be affected by seismic-related anomalous interference. Using nighttime remote sensing data minimizes the effect of solar radiation and improves the reliability of pre-seismic anomalies [40,41]. The AIRS data from 2002 to 2020 were used for pre-seismic anomalies.

2.2. Global Earthquake Events

A total of 169 earthquakes representing the most significant seismic events of recent years were collected from the USGS Earthquake Hazards Program (Figure 1). The earthquakes were divided into inland, oceanic, and coastal for comparison, wherein most earthquakes belonged to the coastal class. In addition, to validate the forecasting effectiveness of TIA, 169 synthetic earthquakes were randomly generated based on three criteria: (1) within $\pm 75^{\circ}$ latitudes; (2) occurring between 2006 and 2020; and (3) for day t and position p, we built a spatiotemporal cube of 11×11 pixels around p as the spatial dimension, within which a day ranged between $t - 60$ and $t + 90$ as the time dimension, and if no $M \geq 5.5$ earthquakes occurred within this cube, it was reserved. Randomly generated earthquakes were iteratively produced to check these restrictions, and we collected the first 169 valid events. The synthetic events were more widely dispersed compared with the true earthquakes in earthquake-prone regions (Figure 1a, light gray areas). This was due to the random generation mechanism; compared with the true earthquakes, a higher proportion of the synthetic earthquakes were in the ocean and inland classes; therefore, the number of synthetic coastal earthquakes was very small compared with that of the true earthquakes. As shown in Figure 1b, the temporal distribution of synthetic earthquakes was similar to that of true earthquakes, and their interoccurrence time presented similar statistical characteristics in Figure 1c, which indicates the rationality of the randomly generated synthetic earthquakes.

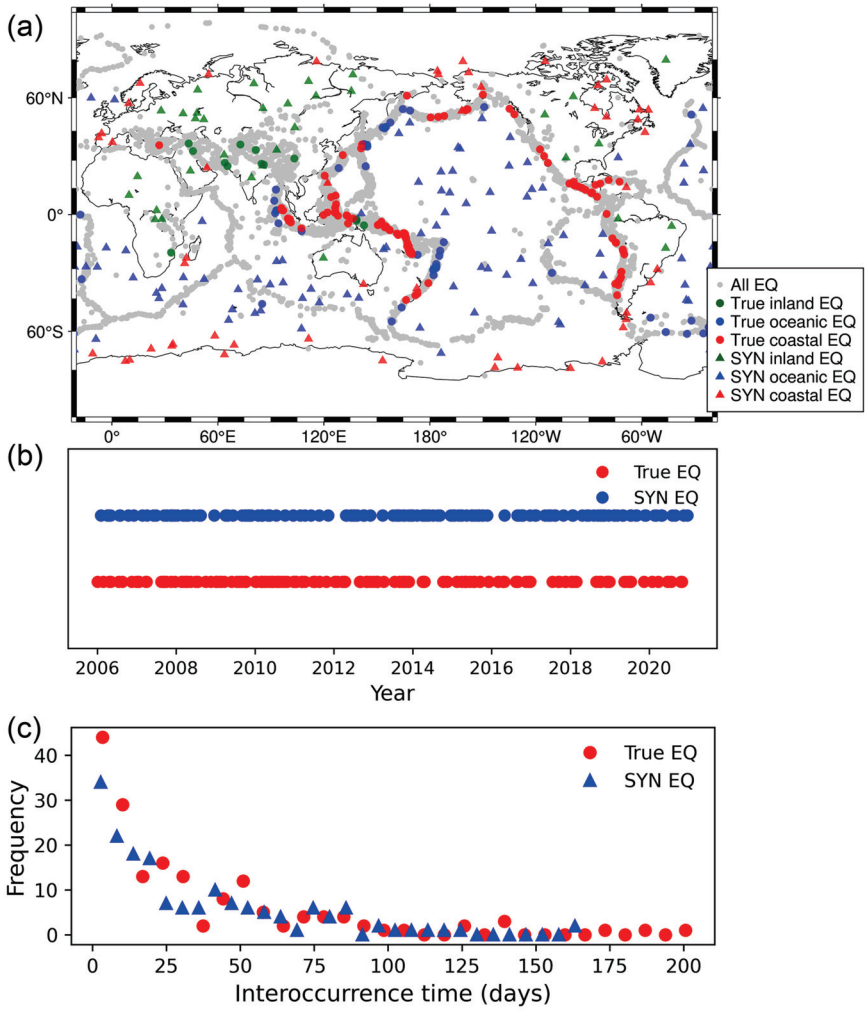

Figure 1. Characteristics of 169 global earthquakes (EQ) and 169 synthetic (SYN) earthquakes with magnitudes ≥7 and focal depths ≤70 km from 2006 to 2020. (**a**) Spatial distribution of both true and SYN EQs. The gray circles denote global 15,646 earthquakes with magnitudes ≥5.5 and focal depths ≤70 km from 1980 to 2020, representing global active seismic regions. (**b**) Temporal characteristics of EQ occurrences. (**c**) Statistics of interoccurrence time of both true and SYN EQs.

3. Methods

3.1. Pre-Seismic Anomaly Detection

A simple and yet widely used anomaly detection method was used to calculate the initial anomalous values from five surface and atmospheric parameters. The Z-Score (ZS) method is defined as the multiple of standard deviation (STD) between measured and mean values [42], and its mathematical formula is:

$$\mathrm{ZS}(x,y,t) = \frac{v(x,y,t) - \mu(x,y)}{\delta(x,y)}, \tag{1}$$

where $v(x,y,t)$ is the pixel value at position (x,y) and at time t, $\mu(x,y)$ is the average of the reference field for the same or similar period in multiple years, and $\delta(x,y)$ is the standard deviation of the reference field.

The daily reference field for each geophysical parameter is essential for calculating anomalies on a robust basis. A time series-based reference field synthesis method was developed to filter outliers in order to improve stability. A dataset of one parameter (e.g., ST) at the same location on the same day during historical years was collected from AIRS3STD data. Negative outliers were removed by retaining only samples with a negative

deviation from the mean value of the dataset less than n times STD, where n is a scaling coefficient of 3. Next, samples with a deviation from the mean value greater than n times STD were regarded as positive outliers and were excluded from the dataset. These two steps were executed for each pixel within the study area, and finally, a daily reference field image was created to represent the long-term average status on that specific day. The 11-day moving window approach was applied to generate daily reference field according to aforementioned method. For example, the reference field for 6 January 2010 was calculated using AIRS data from 1 January to 11 January for each year from 2002 to 2010, representing a 9-year average.

Anomalies calculated by any anomaly detection methods are based on mathematical formula and observation data. A correlation between anomalies and seismogenic conditions is not guaranteed. Moreover, real pre-seismic anomalous signals triggered by earthquakes remain unclear. Therefore, recognition criteria were proposed based on empirical evidence in order to refine anomalies and make them as close as possible to the true situation in terms of spatial and temporal correlations [43]. In a $5^\circ \times 5^\circ$ spatial window surrounding a central pixel (a total of 25 pixels), if pixels had absolute anomaly values of $\geq$2 (i.e., valid pixels), and the average absolute anomaly value from these valid pixels was $\geq$2.5, the anomaly value at the central pixel was considered valid and was retained for subsequent analyses.

3.2. Definition of TIA

The TIA of a pixel is a weighted average calculated from daily anomaly values within a specific time interval (from several days to months). Two types of TIAs were calculated using positive and negative anomalies (e.g., warming and cooling anomalies for temperature) derived from the ZS method for each selected parameter. Daily anomalies were weighted by a given integration function with a temporal distance from the time of earthquake occurrence used as the input. The integration function significantly affects the value of temporally integrated anomalies. Thus, three functions were used to analyze their differences and feasibility in detecting multiparametric anomalies prior to an earthquake. The constant (CST) weighted integration function is an arithmetic mean method using all selected daily anomaly values. Its formula is as follows:

$$\overline{\mathrm{TIA}}_{\mathrm{CST}} = \frac{\sum_{t=1}^{n} \Theta A_t}{\sum_{t=1}^{n} \frac{\Theta}{n}}, \tag{2}$$

where t is the temporal distance relative to the day of an earthquake, which is set to zero; n is the number of days used in the calculation; Θ is a flag with 1 for valid A_t and 0 for invalid A_t; and A_t is the valid anomaly value at day t, which was first calculated by Equation (1), and then filtered according to the recognition criteria in Section 3.1.

Generally, anomaly magnitudes measured closer to the time of an earthquake are more significant. Nevertheless, a TIA with constant weighted integration cannot denote this temporal characteristic. Hence, using two additional methods, we assigned different weights to anomaly points for each day of the integration interval. The Gaussian distribution is widely used to describe a normal distribution in statistics and to define the Gaussian filter in signal processing. The distribution of a Gaussian function is suitable for situations where anomalies occurring closer to the occurrence day have a higher weight. The Gaussian (GAU) weighted integration function was calculated as follows:

$$\overline{\mathrm{TIA}}_{\mathrm{GAU}} = \frac{\sum_{t=0}^{n} \Theta \frac{1}{\sigma\sqrt{2\pi}} e^{\frac{-(t-\mu)^2}{2\sigma^2}} \cdot A_t}{\sum_{t=0}^{n} \Theta \frac{1}{\sigma\sqrt{2\pi}} e^{\frac{-(t-\mu)^2}{2\sigma^2}}}, \tag{3}$$

where μ is set to 0, and σ is the STD that controls the width of the shape of the Gaussian function. The other integration function was the Laplace (LAP) distribution, which

has a steeper distribution, causing the weight assigned to anomaly values to vary more significantly. LAP is calculated as follows:

$$\overline{\mathrm{TIA}}_{\mathrm{LAP}} = \frac{\sum_{t=0}^{n} \frac{\Theta}{2\sigma} e^{\frac{-|t-\mu|}{\sigma}} \cdot A_t}{\sum_{t=0}^{n} \frac{\Theta}{2\sigma} e^{\frac{-|t-\mu|}{\sigma}}}, \quad (4)$$

where μ is set to 0, t is a positive value of zero to n, and σ is the STD of the distribution.

In general, the closer the timing of an anomaly to the time of an earthquake, the greater the weight value for the GAU and LAP, but not for the CST (Figure 2). Among them, the largest weight is from the LAP function in the first few days. If the anomalies for some days are invalid, the corresponding weights of the integration functions are set to zero and the change of the sum of weights reallocates the relative weights, causing different relative weights among different functions. The TIA was calculated using 5×5 window data around the epicenter pixel, where valid positive/negative anomalies were used to calculate positive/negative TIAs (PTIA and NTIA, respectively). The temporal range for predicting impending earthquakes was from 60 days before until the day of the earthquake itself. Note that a longer anomaly window could capture more anomaly counts for anomalies with short durations; however, it would also record more irrelevant anomalies, resulting in higher uncertainties.

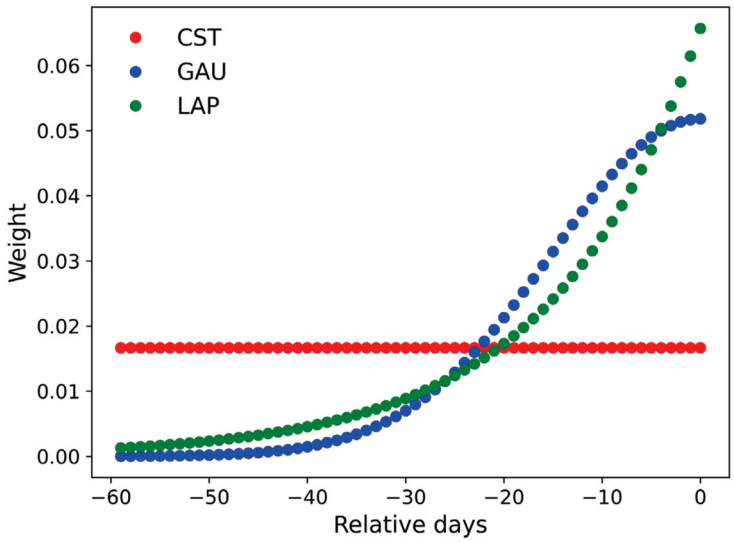

Figure 2. Constant (CST), Gaussian (GAU), and Laplace (LAP) weight integration functions used in the temporal integrated anomaly (TIA) calculation within a 60-day interval. In the LAP and GAU functions, μ is set to 0 and σ is 15. The red, blue, and green dots denote GAU, LAP, and CST weight integration functions, respectively.

4. Results

4.1. Trend Characteristics of Multiparametric TIA

The time series of pre-seismic anomalies of different geophysical parameters used in this study was first obtained within 60 days prior to a true or synthetic earthquake. The TIA for each parameter was calculated with different time intervals according to the method described in Section 3.2, and then the calculated TIA values were plotted in a cumulative manner (Figure 3a). For example, the ST TIA value for the 10th day was calculated using data from 0 to 10 days before the earthquake. Thus, the time series indicates the temporal evolution characteristics of pre-seismic anomalies. When anomalies were observed in multiple parameters, a pre-seismic anomaly was identified, and an alarm warned that an $M \geq 7$ earthquake would likely take place within the $5^\circ \times 5^\circ$ grid within the next few days (Table 1). We identified four different TIA trends, especially for the first ~30 days prior to

the events. For one earthquake, five parameters could present different TIA trends, even when some parameters had no anomalous variation.

Table 1. Fundamental forecasting parameters of pre-seismic anomalies in retrospective analyses according to the trend characteristics of multiparametric TIA.

Parameters	Values
Time range	<10 days
Spatial extent	5° × 5° around the epicenter (equivalent of a circle with the radius of ~275 km)
Magnitude	≥7

Type 1: PTIA and NTIA decrease rapidly before the earthquake with negative anomalies dominating the area near the epicenter (e.g., significant temperature reduction effects) (see ST, AT, CWV, and COLR TIAs in Figure 3). Prior to the 2011 M9.1 Great Tohoku Earthquake, significant crust uplift was detected along with the full southward alignment of Global Positioning System (GPS) azimuths [19], which may have led to cold water upwelling from the seafloor. Meanwhile, in a well 155 km northwest of the epicenter, anomalous decreases in groundwater level and temperature were observed starting 3 months before the earthquake due to possible pre-seismic crustal deformation [44]. These observations could explain negative anomaly phenomena. Similar phenomena can also be observed for inland earthquakes. Significant cooling phenomena along the Himalayas prior to the 2015 Mw 7.9 Nepal earthquake have been reported, and stress relaxation is suggested as a possible explanation [24].

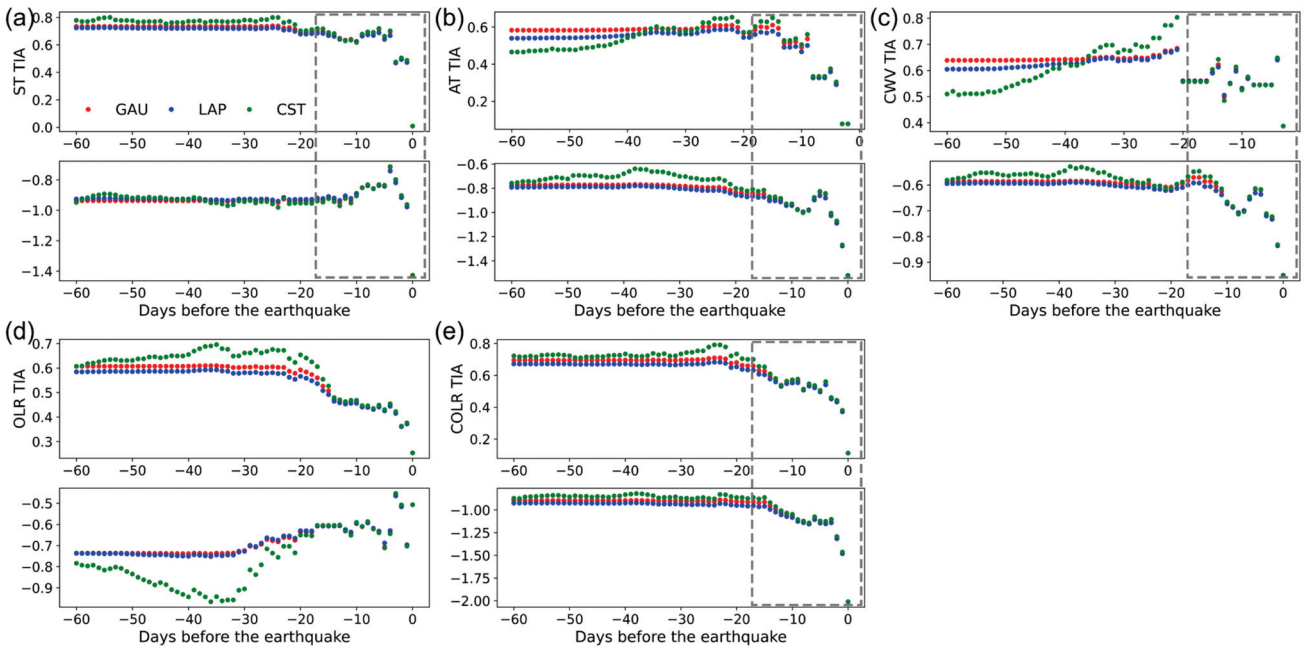

Figure 3. Trend characteristics for multiparametric temporal integrated anomalies (TIAs) before the 2011 M9.1 Great Tohoku Earthquake, Japan, demonstrating enhanced negative TIAs close to earthquake occurrence. (**a**) Skin temperature (ST) TIA; (**b**) air temperature (AT) TIA; (**c**) total integrated column water vapor burden (CWV) TIA; (**d**) outgoing longwave radiation (OLR) TIA; (**e**) clear-sky OLR (COLR) TIA. The two subfigures for each anomaly show the positive and negative TIAs, respectively. Negative days at the abscissa denote the days before the earthquake. The gray dashed frame indicates the TIA trend characteristics. The red, blue, and green dots denote Gaussian (GAU), Laplace (LAP), and Constant (CST) weight integration functions, respectively.

Type 2: PTIA and NTIA increase rapidly before the earthquake with positive anomalies dominating the area near the epicenter (e.g., significant warming effects) (see AT, CWV, OLR, and COLR TIAs in Figure 4). This phenomenon has been reported by many studies; that is, anomalous increases in diverse parameters prior to earthquakes [15].

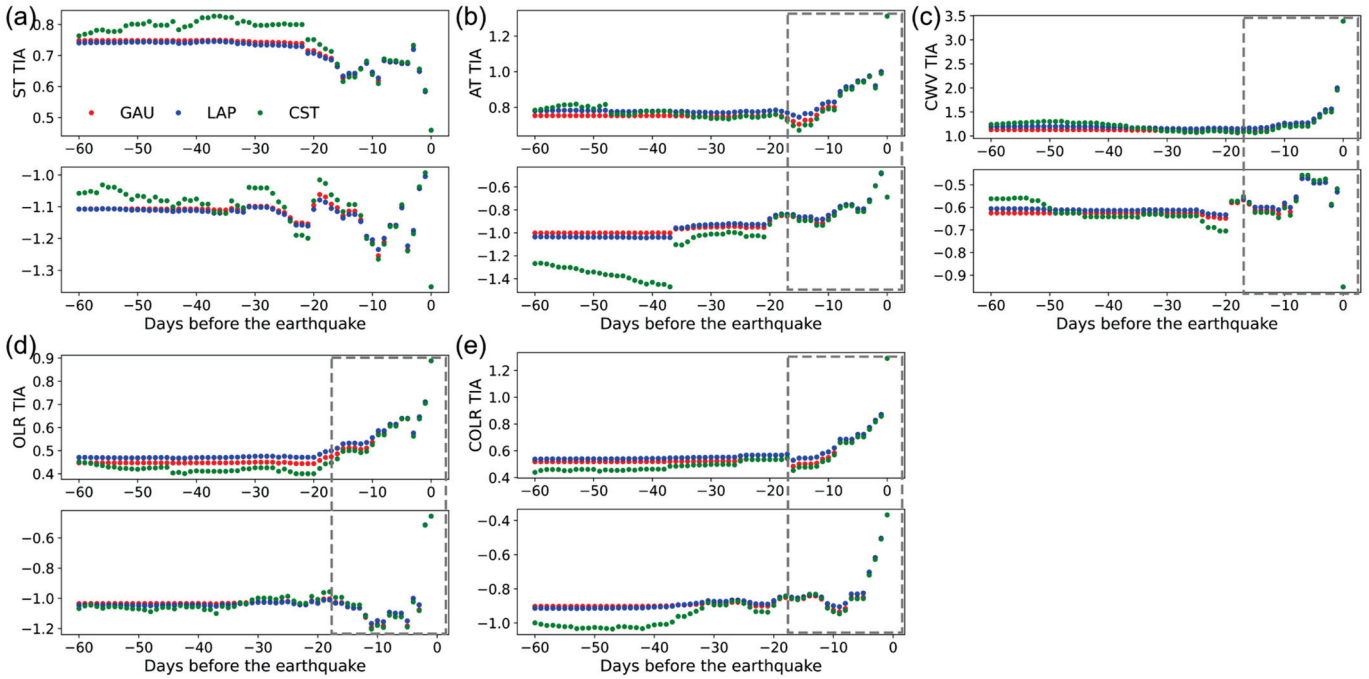

Figure 4. Trend characteristics for multiparametric temporal integrated anomalies (TIAs) before the 2009 M7.7 Papua earthquake, Indonesia, demonstrating enhanced positive TIAs close to earthquake occurrence. (**a**) Skin temperature (ST) TIA; (**b**) air temperature (AT) TIA; (**c**) total integrated column water vapor burden (CWV) TIA; (**d**) outgoing longwave radiation (OLR) TIA; (**e**) clear-sky OLR (COLR) TIA. The two subfigures for each anomaly show the positive and negative TIAs, respectively. Negative days at the abscissa denote the days before the earthquake. The gray dashed frame indicates the TIA trend characteristics. The red, blue, and green dots denote Gaussian (GAU), Laplace (LAP), and Constant (CST) weight integration functions, respectively.

Type 3: PTIA increases and NTIA decreases rapidly before the earthquake, with both positive and negative anomalies apparent in the area near the epicenter before the earthquake (see ST, AT, OLR, and COLR TIAs in Figure 5). This bidirectional trend indicates strongly anomalous perturbation around the epicenter [45].

Type 4: Similar to Type 3, with either PTIA or NTIA reaching a peak and then rapidly disappearing within several days following the strong earthquakes (Figure 6). This delayed phenomenon was observed for only a small percentage of the tested earthquakes.

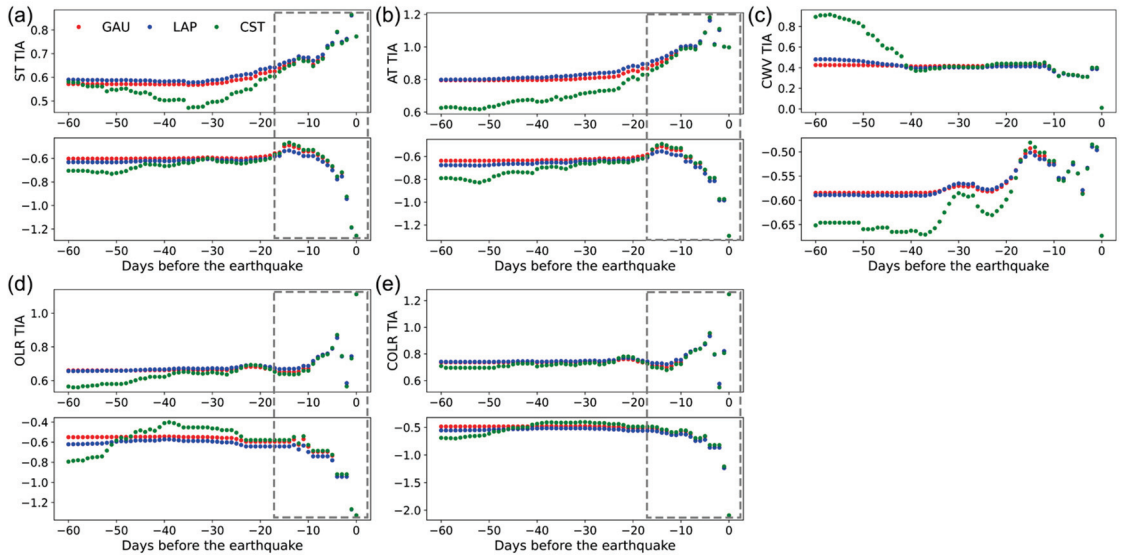

Figure 5. Trend characteristics for multiparametric temporal integrated anomalies (TIAs) before the 2013 M7.7 Awaran earthquake, Pakistan, demonstrating simultaneously enhanced positive & negative TIAs close to earthquake occurrence. (**a**) Skin temperature (ST) TIA; (**b**) air temperature (AT) TIA; (**c**) total integrated column water vapor burden (CWV) TIA; (**d**) outgoing longwave radiation (OLR) TIA; (**e**) clear-sky OLR (COLR) TIA. The two subfigures for each anomaly show the positive and negative TIAs, respectively. Negative days at the abscissa denote the days before the earthquake. The gray dashed frame indicates the TIA trend characteristics. The red, blue, and green dots denote Gaussian (GAU), Laplace (LAP), and Constant (CST) weight integration functions, respectively.

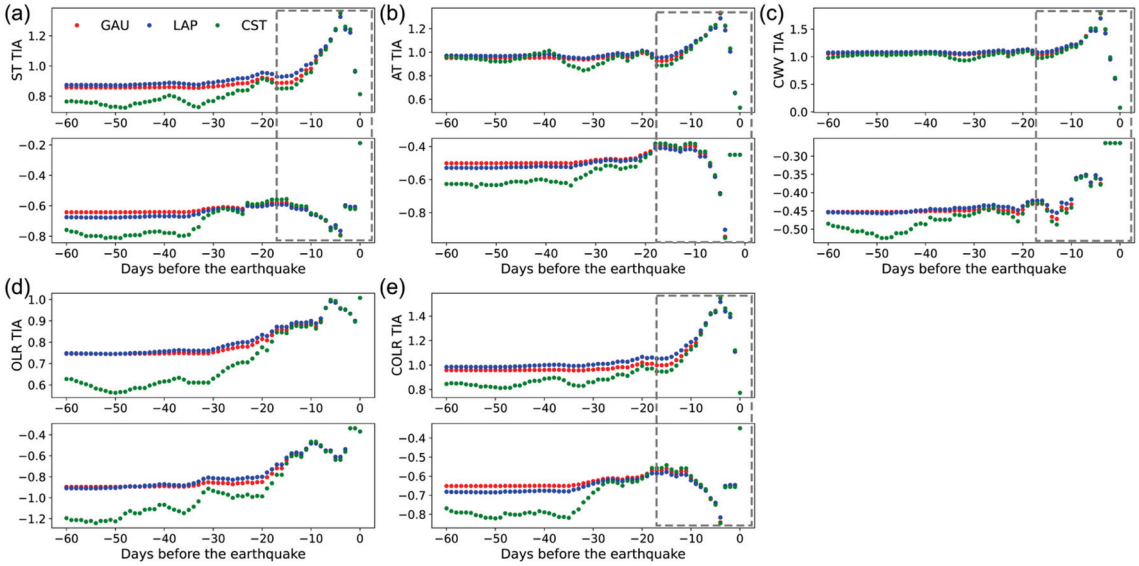

Figure 6. Trend characteristics for multiparametric temporal integrated anomalies (TIAs) before the 2015 M7.2 Murghob earthquake, Tajikistan, demonstrating enhanced positive/negative TIAs close to earthquake occurrence. (**a**) Skin temperature (ST) TIA; (**b**) air temperature (AT) TIA; (**c**) total integrated column water vapor burden (CWV) TIA; (**d**) outgoing longwave radiation (OLR) TIA; (**e**) clear-sky OLR (COLR) TIA. The two subfigures for each anomaly show the positive and negative TIAs, respectively. Negative days at the abscissa denote the days before the earthquake. The gray dashed frame indicates the TIA trend characteristics. The red, blue, and green dots denote Gaussian (GAU), Laplace (LAP), and Constant (CST) weight integration functions, respectively.

4.2. Comparison between True and Synthetic Earthquake TIAs

A higher rate of earthquake alarms was triggered for true earthquakes compared with synthetic earthquakes, and the rates decreased from 93.5% to 0% and from 85.2% to 0% as the number of TIA parameters increased for true and synthetic earthquakes, respectively (Figure 7a). The optimal number of parameters was found to be 2–5, for which the recognition ability for true earthquakes was 12.4–28.4% higher than that for synthetic earthquakes; when >6 TIA parameters were used, the rate of earthquake recognition dropped significantly for both true and synthetic events. In total, we identified 627 TIA for true earthquakes and 430 TIA for synthetic earthquakes. The different TIA types were similar between the true and synthetic earthquakes (Figure 7b,c). For true earthquakes, the NTIAs of ST, AT, CWV, and COLR had slightly more counts; for the synthetic earthquakes, the PTIAs of AT and CWV, and NTIA of COLR had slightly more counts. This suggests that NTIAs tend to correlate with true earthquakes, while PTIAs correlate with synthetic earthquakes. This is consistent with the results of past studies in which significant negative anomalies were confirmed around epicenters [24,45]. For true earthquakes, positive and negative TIAs of AT and CWV had the highest recognition counts (>15); for synthetic earthquakes, positive and negative TIAs of ST and AT had the highest recognition counts (>20) (Figure 7d,e). The TIA trend characteristics before earthquake occurrence were not unique; however, the data revealed certain unexplained anomalous phenomena.

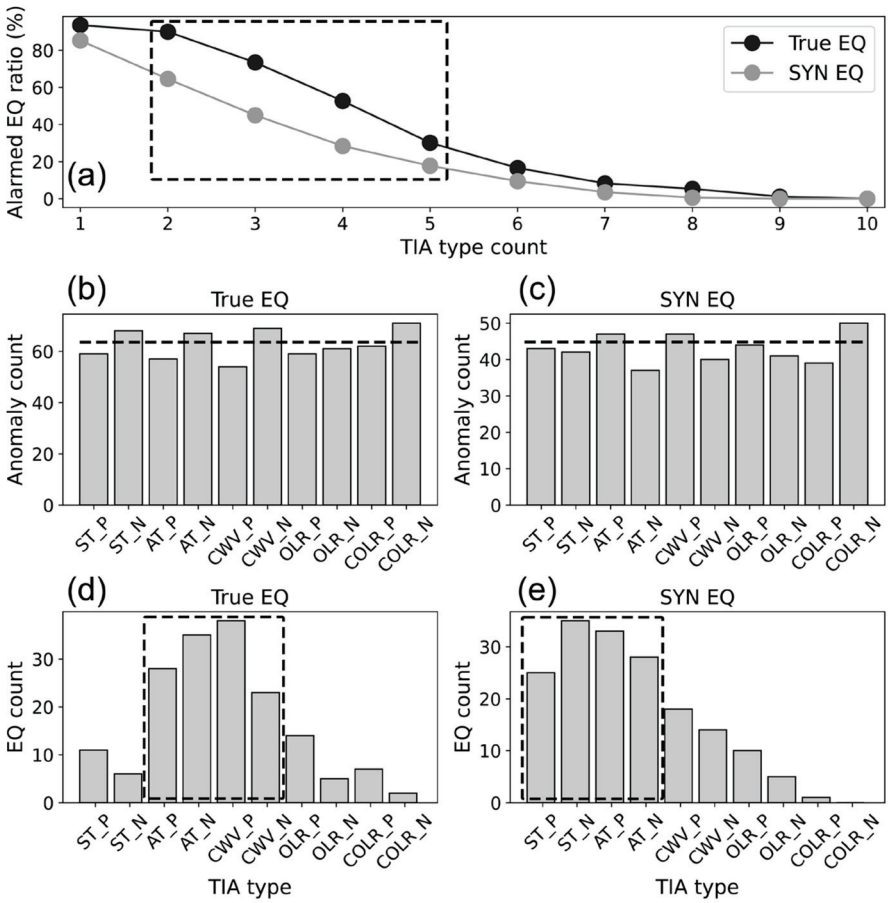

Figure 7. Statistical results of multiparametric temporal integrated anomaly (TIA) trends for true and synthetic (SYN) earthquakes (EQ). (**a**) Alarmed earthquake ratios as a function of TIA type counts for TIAs based on 5 parameters multiplied by 2 types of positive or negative anomalies; anomaly counts of different TIA types for (**b**) true and (**c**) synthetic earthquakes; "P"/"N" before the underscore denotes positive or negative TIA (e.g., ST_P is positive skin temperature TIA); earthquake counts of different TIA types for (**d**) true and (**e**) synthetic earthquakes.

Positive/negative anomalies could have one of four combinations: (1) neither positive nor negative TIA, (2) only positive TIA, (3) only negative TIA, and (4) both positive and negative TIAs. For each geophysical parameter, the likelihood of identifying pre-seismic anomalies was higher for true earthquakes than for synthetic earthquakes (Figure 8). More specifically, synthetic earthquakes had more no-TIA situations, and the counts of the other three combinations were less than those of the true earthquakes. While we identified a small number of exceptions for the AT and CWV TIAs, these results confirm that TIAs for all parameters can identify pre-seismic anomalous signals to some extent (Figure 7). As such, the proposed approach has good potential for predicting future earthquakes. Remote sensing observations from space-borne platforms contain seismogenic information that is subtle and transient compared with the strong background signals from natural processes and anthropogenic activities. As a result, most precursory parameters also had high missed detection and false alarm rates. Moreover, when the false alarm rate was suppressed, the accuracy rate also decreased [45]. The TIA provides the potential to improve forecast accuracy.

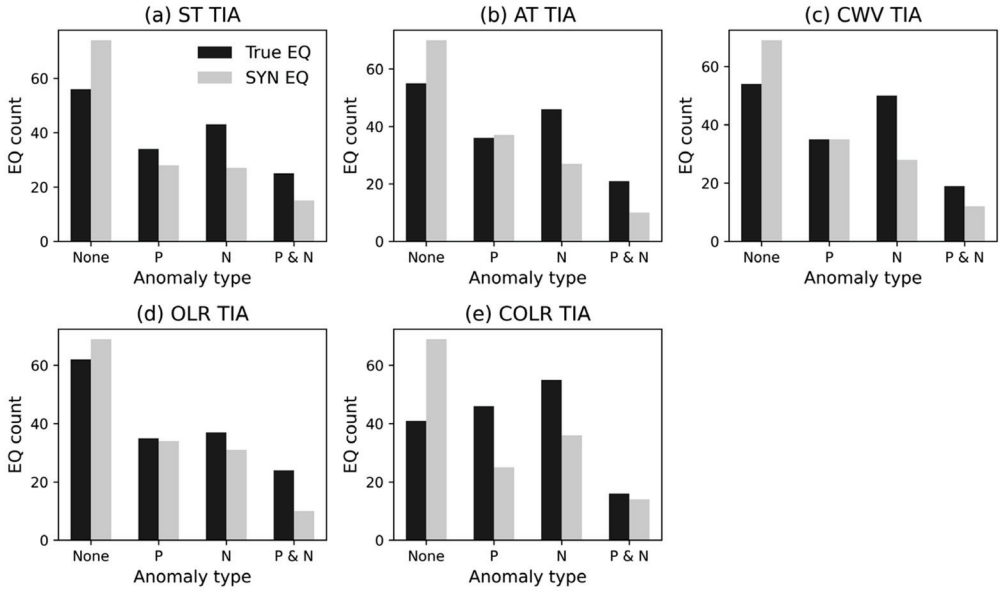

Figure 8. Statistical results of temporal integrated anomalies (TIAs) for each geophysical parameter. (**a**) Skin temperature (ST) TIA; (**b**) air temperature (AT) TIA; (**c**) total integrated column water vapor burden (CWV) TIA; (**d**) outgoing longwave radiation (OLR) TIA; (**e**) clear-sky OLR (COLR) TIA. 'None' denotes neither positive nor negative TIA; P denotes only positive TIA; N denotes only negative TIA; and P & N denotes synchronous positive and negative TIAs.

4.3. Statistical Analysis Based on Earthquake Locations

Earthquake location influences anomaly characteristics owing to different underlying surfaces and medium properties. For true earthquakes, coastal earthquakes were the most common (109), and inland earthquakes were the least common (13; Figure 9). OLR and CWV NTIAs recognized more inland earthquakes but with higher missed earthquakes (Figure 9a). COLR TIA had a strong ability to recognize oceanic earthquakes with both positive and negative anomalies. Similar patterns were observed for coastal and oceanic earthquakes (Figure 9c). The synchronous positive and negative TIAs always had poor recognition ability for oceanic and coastal earthquakes. Land cover affects the spatial distributions of diverse parameters, leading to high spatial heterogeneity, while seawater has high thermal inertia, which changes thermal radiative transfer from the seabed to the sea surface [8]. For instance, CWV increased after the 2001 Gujarat earthquake, for which the epicenter was beneath the sea [29]. Significantly reduced sea surface temperatures have

been observed prior to some earthquakes and may be related to the upwelling of cold water from the ocean floor [46].

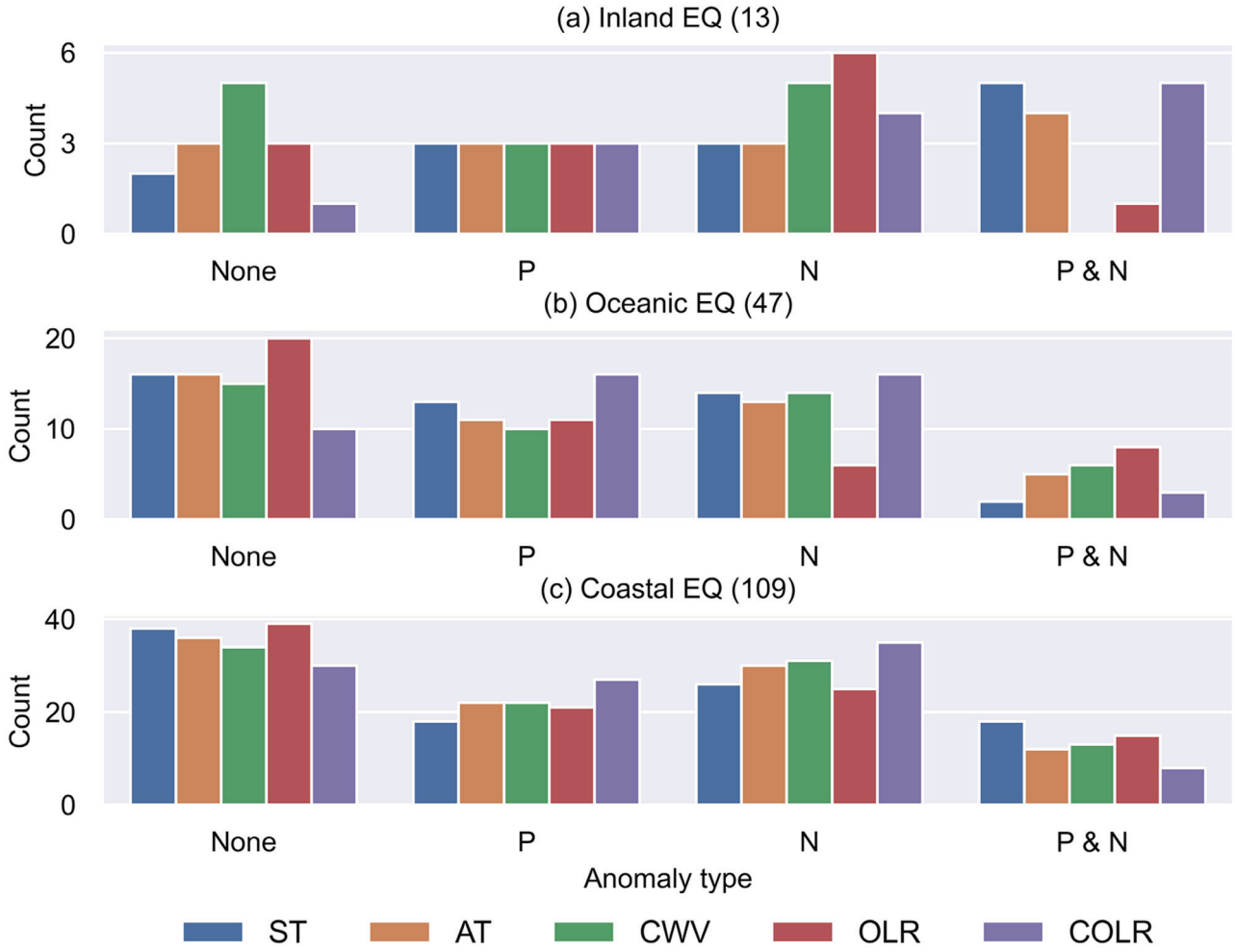

Figure 9. Statistical results of multiparameter temporal integrated anomalies (TIAs) for (**a**) inland, (**b**) oceanic, and (**c**) coastal earthquakes (EQ). ST, skin temperature; AT, air temperature; CWV, total integrated column water vapor burden; OLR, outgoing longwave radiation; COLR, clear-sky OLR.

Figure 10 shows the spatial distributions of recognition and non-recognition earthquakes. The recognized rates were higher near earthquake-prone regions (light gray areas). Therefore, the proposed method provides insight into the apparent statistical significance between anomaly phenomena and earthquakes and has a forecasting ability that exceeds that of random guessing. Our results clearly demonstrate that seismically active regions are the most appropriate for testing methods to forecast earthquakes (e.g., in Japan; [32,43]).

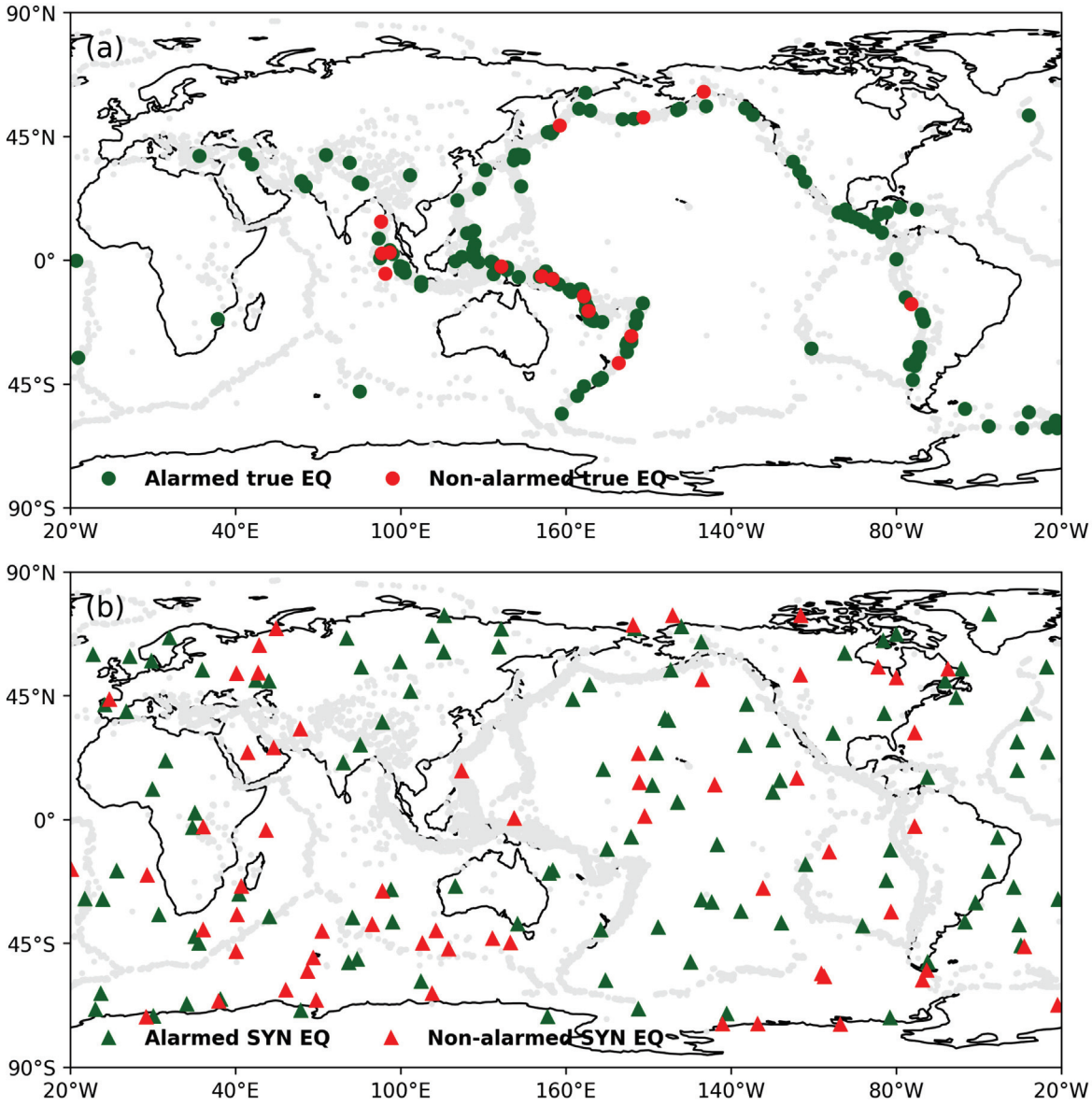

Figure 10. Map of alarmed (temporal integrated anomaly [TIA] counts $\geq$ 2) and not alarmed earthquakes for both (**a**) true and (**b**) synthetic (SYN) events.

4.4. Statistical Analysis Based on Earthquake Focal Mechanisms

Focal mechanisms were obtained from the GEOFON data center of the GFZ German Research Centre [47]. Focal mechanism solutions, which were only available for 94 of the 169 earthquakes (mostly those after 2011), were classified into strike-slip, normal, and thrust. If more than one type existed for a given earthquake, the major component was chosen. For normal earthquakes in Figure 11a, ST PTIA and OLR/COLR NTIAs showed the best recognition ability. Thrust earthquakes were the most numerous (49 events) and were most commonly associated with NTIAs (Figure 11b). For strike-slip earthquakes, synchronous positive and negative TIAs (particularly OLR/COLR TIAs) had better recognition ability than they did for the other earthquake types. Overall, negative anomalies were the most prevalent phenomena for all earthquake types (Figure 9; [45]).

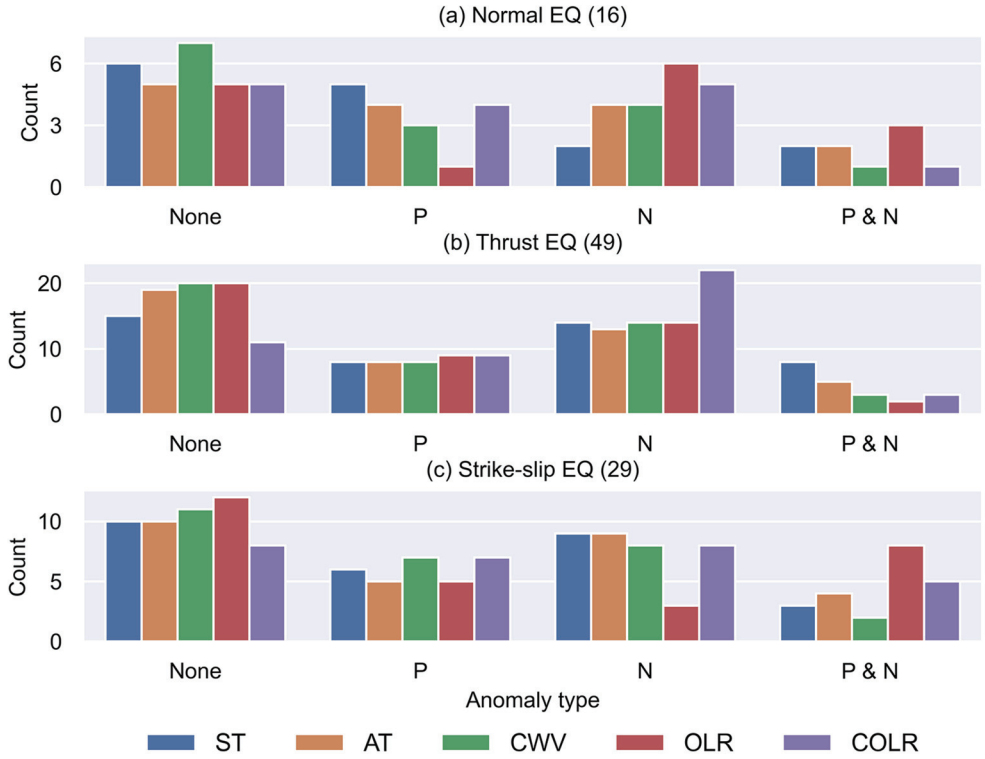

Figure 11. Statistical results of multiparameter temporal integrated anomalies (TIAs) for (**a**) normal, (**b**) thrust, and (**c**) strike-slip earthquakes (EQ). ST, skin temperature; AT, air temperature; CWV, total integrated column water vapor burden; OLR, outgoing longwave radiation; COLR, clear-sky OLR.

5. Discussion

5.1. Implications for Earthquake Forecasts

The prediction of earthquakes has been recognized as a global problem [10]. Earthquakes are rapid energy release processes that must produce various anomalous phenomena with respect to normal reference signals [4,19]. The basic assumptions are: (1) the bigger the earthquake, the more obvious the anomalous signals; and (2) the shorter the interval until the earthquake, the clearer the anomalous signals. TIA trend characteristics were observed for both true and synthetic earthquakes; as such, earthquake alarms based on the proposed method come with significant uncertainties. This is a prevalent issue that impedes operational earthquake forecasting. Anomaly detection methods have good performance for retrospective correlation analysis (i.e., high accuracy and low missed detection rates); however, earthquake forecasting based on prospective statistics in seismically active regions has low forecasting capacity [45].

Despite the optimism of some researchers, routine and accurate earthquake forecasting remains a challenge [48]. Therefore, new approaches (e.g., artificial intelligence) need to be developed and verified [21]. The extension of natural time analysis to remote sensing data is also an important aspect, based on the success of this approach, in the detection of precursory phenomena of seismicity, surface displacements, Earth's magnetic field, and seismic electric signals prior to the strong earthquakes [7,19]. Combining multiple data sources offers the potential to refine the detection of anomalous phenomena [4,15], as confirmed by our results. Therefore, short-term earthquake forecasting models that combine multiple data streams are deemed to be the most promising approach [43]. Moreover, a robust and quantitative evaluation of anomaly detection methods is needed to gain new insights into the feasibility of earthquake forecasts. By constructing a uniform baseline using historical observation data and earthquake catalogs in retrospective and prospective ways [45], we will be better able to compare various approaches and parameters, offering

the potential to develop models for integrating precursors and anomaly detection methods for operational earthquake forecasting.

5.2. Underlying Geophysical Mechanisms of Pre-Seismic Anomalies

The findings derived from rock experiments offer an experimental basis for relating temperature anomalies to variations in crustal stress fields and tectonic activities from remote sensing observations [49–52]. Elastic energy continuously accumulates in the rock mass during earthquake preparation. Both theoretical calculations and laboratory measurements indicate that temperature variations are related to the quantity of volume strain measured under elastic stress conditions for solid materials. The thermal elastic coefficient of roughly 1 mK/MPa is proportional to the principal stress [50,53]. When the volume strain increases due to compression, the temperature also rises, while it will decline in the tensile state. Accompanying thermal effects caused by the change in the strain levels of the deformation field are likely associated with surface temperature, which can be retrieved from thermal infrared (TIR) measurements [54]. TIR radiation field (e.g., ST, AT, and OLR) derived from satellite observations serves as a feasible physical parameter related to regional overall stress fields to some extent in this research field [55].

Fault deformation is always local and mostly deep below the ground surface. However, multiparametric anomalies are widespread and regional at the seismogenic zones. The geophysical mechanism of how the heating derived from fault deformation transfers to the ground surface or the atmosphere is a key point. The thermal conductivity, thermal inertia, and time constant of the thermal diffusion of rocks are the controlling factors for transmitting the Joule temperature to the TIR radiation field. The low heat conductivity of rocks delays the transfer of increased temperatures caused by fault deformation at the scales of months to years, even decades. This is inconsistent with the satellite observation. In p-hole theory [56–60], however, mechanical stresses between rocks lead to the activation of peroxy defects deep in the Earth's crust. These peroxy defects release electronic charge carriers, electrons e' and holes $h^{\bullet}$. The $h^{\bullet}$ have the remarkable ability to flow out into and through the surrounding rocks that are less stressed or unstressed and to propagate rapidly to the distant regions. When the $h^{\bullet}$ arrive on the Earth's surface, they lead to a series of follow-up reactions. The exothermal recombination of $h^{\bullet}$ on the Earth's surface leads to a stimulated TIR emission, another source of thermal radiation other than Joule temperature, which could be received by satellite sensors.

This work illustrates the extensive TIR measurements that can be derived from a satellite platform. It is worth noting that multiparametric anomalies may reflect the fault activities of tectonically active regions that do not always correspond to an impending earthquake, as the anomaly is not a sufficient condition. Various non-seismic factors affect TIR radiation changes and anomalous features [8], and the triggering of an earthquake is also influenced by intricate geologic conditions, tectonic movements, and dynamic processes.

6. Conclusions

The short-term (days or weeks) pre-seismic period is a critical phase during which stress accumulation becomes stronger and corresponding precursory responses (e.g., ST) likely increase in amplitude. We developed a TIA method to obtain the temporal trend of multiparametric anomalies derived from AIRS products before earthquakes; four types of TIA trends were identified. A total of 169 global earthquakes with magnitudes of $\geq$7.0 were used to test this new method in a retrospective manner. In addition, we generated 169 synthetic earthquakes to test the suppression capacity of anomaly detection in tectonically non-active areas. A time series-based anomaly removal method was developed to generate the reference fields of ZS methods. Long-term correlation analyses showed that recognition ability was 12.4–28.4% higher for true earthquakes than for synthetic earthquakes (i.e., higher than that of a random guess). TIA incorporating 2–5 parameters was optimal for recognizing the earthquakes, indicating that multiparametric anomalies can provide complementary information to improve statistical significance. Our results confirm the

appearance of TIA in spatiotemporal correspondence with forthcoming earthquakes, and some unexplained anomalous signals around epicentral areas were observed. A greater understanding of geophysical mechanisms and the development of new anomaly detection methods would strengthen the uniqueness of pre-seismic anomalous phenomena.

Author Contributions: Conceptualization, Z.J.; methodology, Z.J.; writing—original draft preparation, Z.J.; writing—review and editing, Z.J. and X.S. All authors have read and agreed to the published version of the manuscript.

Funding: This research was funded by the National Key Research and Development Program of China, grant number 2019YFC1509202; National Nonprofit Fundamental Research Grant of Institute of Geology, China Earthquake Administration, grant number IGCEA2002; the China Seismic Experimental Site Project, grant number 2018CSES0205; and the Scientific Research Project of the Shanghai Science and Technology Commission, grant number 14231202600.

Data Availability Statement: AIRS AIRS3STD data are available from the GES DISC at https://disc.gsfc.nasa.gov/datasets/AIRS3STD_7.0/summary (accessed on 10 April 2022). Earthquake catalog data are available from the USGS at https://www.usgs.gov/natural-hazards/earthquake-hazards (accessed on 10 April 2022). Seismic data were obtained from the GEOFON data centre of the GFZ German Research Centre for Geosciences at https://geofon.gfz-potsdam.de (accessed on 10 April 2022).

Conflicts of Interest: The authors declare no conflict of interest.

References

1. Geller, R.J. Earthquake prediction: A critical review. *Geophys. J. Int.* **1997**, *131*, 425–450. [CrossRef]
2. Uyeda, S.; Nagao, T.; Kamogawa, M. Short-term earthquake prediction: Current status of seismo-electromagnetics. *Tectonophysics* **2009**, *470*, 205–213. [CrossRef]
3. Bormann, P. From Earthquake Prediction Research to Time-Variable Seismic Hazard Assessment Applications. *Pure Appl. Geophys.* **2010**, *168*, 329–366. [CrossRef]
4. De Santis, A.; De Franceschi, G.; Spogli, L.; Perrone, L.; Alfonsi, L.; Qamili, E.; Cianchini, G.; Di Giovambattista, R.; Salvi, S.; Filippi, E.; et al. Geospace perturbations induced by the Earth: The state of the art and future trends. *Phys. Chem. Earth Parts A/B/C* **2015**, *85–86*, 17–33. [CrossRef]
5. Uyeda, S.; Kamogawa, M. The Prediction of Two Large Earthquakes in Greece. *Eos Trans. Am. Geophys. Union* **2008**, *89*, 363. [CrossRef]
6. Huang, Q. Seismicity Pattern Changes Prior to the 2008 Ms7.3 Yutian Earthquake. *Entropy* **2019**, *21*, 118. [CrossRef]
7. Varotsos, P.A.; Sarlis, N.V.; Skordas, E.S. Self-organized criticality and earthquake predictability: A long-standing question in the light of natural time analysis. *Europhys. Lett.* **2020**, *132*, 29001. [CrossRef]
8. Jiao, Z.-H.; Zhao, J.; Shan, X. Pre-seismic anomalies from optical satellite observations: A review. *Nat. Hazards Earth Syst. Sci.* **2018**, *18*, 1013–1036. [CrossRef]
9. Tronin, A.A. Remote sensing and earthquakes: A review. *Phys. Chem. Earth Parts A/B/C* **2006**, *31*, 138–142. [CrossRef]
10. Bakun, W.H.; Aagaard, B.; Dost, B.; Ellsworth, W.L.; Hardebeck, J.L.; Harris, R.A.; Ji, C.; Johnston, M.J.; Langbein, J.; Lienkaemper, J.J.; et al. Implications for prediction and hazard assessment from the 2004 Parkfield earthquake. *Nature* **2005**, *437*, 969–974. [CrossRef]
11. Pavlidou, E.; van der Meijde, M.; van der Werff, H.; Hecker, C. Time Series Analysis of Land Surface Temperatures in 20 Earthquake Cases Worldwide. *Remote Sens.* **2018**, *11*, 61. [CrossRef]
12. Tronin, A.A. Satellite thermal survey—A new tool for the study of seismoactive regions. *Int. J. Remote Sens.* **1996**, *17*, 1439–1455. [CrossRef]
13. Saraf, A.K.; Rawat, V.; Banerjee, P.; Choudhury, S.; Panda, S.K.; Dasgupta, S.; Das, J.D. Satellite detection of earthquake thermal infrared precursors in Iran. *Nat. Hazards* **2008**, *47*, 119–135. [CrossRef]
14. Bhardwaj, A.; Singh, S.; Sam, L.; Bhardwaj, A.; Martín-Torres, F.J.; Singh, A.; Kumar, R. MODIS-based estimates of strong snow surface temperature anomaly related to high altitude earthquakes of 2015. *Remote Sens. Environ.* **2017**, *188*, 1–8. [CrossRef]
15. Cicerone, R.D.; Ebel, J.E.; Britton, J. A systematic compilation of earthquake precursors. *Tectonophysics* **2009**, *476*, 371–396. [CrossRef]
16. Sun, K.; Shan, X.; Ouzounov, D.; Shen, X.; Jing, F. Analyzing long wave radiation data associated with the 2015 Nepal earthquakes based on Multi-orbit satellite observations. *Chin. J. Geophys.* **2017**, *60*, 3457–3465.
17. Varotsos, P.; Lazaridou, M. Latest aspects of earthquake prediction in Greece based on seismic electric signals. *Tectonophysics* **1991**, *188*, 321–347. [CrossRef]
18. Varotsos, P. *The Physics of Seismic Electric Signals*; TerraPub: Tokyo, Japan, 2005; p. 338.

19. Varotsos, P.A.; Sarlis, N.V.; Skordas, E.S. Phenomena preceding major earthquakes interconnected through a physical model. *Ann. Geophys.* **2019**, *37*, 315–324. [CrossRef]
20. Tronin, A.A. Satellite remote sensing in seismology. A review. *Remote Sens.* **2010**, *2*, 124–150. [CrossRef]
21. Kato, A.; Ben-Zion, Y. The generation of large earthquakes. *Nat. Rev. Earth Environ.* **2020**, *2*, 26–39. [CrossRef]
22. Bhardwaj, A.; Singh, S.; Sam, L.; Joshi, P.K.; Bhardwaj, A.; Martín-Torres, F.J.; Kumar, R. A review on remotely sensed land surface temperature anomaly as an earthquake precursor. *Int. J. Appl. Earth Obs. Geoinf.* **2017**, *63*, 158–166. [CrossRef]
23. Sarlis, N.V.; Skordas, E.S.; Christopoulos, S.-R.G.; Varotsos, P.A. Natural Time Analysis: The Area under the Receiver Operating Characteristic Curve of the Order Parameter Fluctuations Minima Preceding Major Earthquakes. *Entropy* **2020**, *22*, 583. [CrossRef] [PubMed]
24. Chen, S.; Liu, P.; Feng, T.; Wang, D.; Jiao, Z.; Chen, L.; Xu, Z.; Zhang, G. Exploring Changes in Land Surface Temperature Possibly Associated with Earthquake: Case of the April 2015 Nepal Mw 7.9 Earthquake. *Entropy* **2020**, *22*, 377. [CrossRef]
25. Khalili, M.; Alavi Panah, S.K.; Abdollahi Eskandar, S.S. Using Robust Satellite Technique (RST) to determine thermal anomalies before a strong earthquake: A case study of the Saravan earthquake (April 16th, 2013, MW = 7.8, Iran). *J. Asian Earth Sci.* **2019**, *173*, 70–78. [CrossRef]
26. Zoran, M. MODIS and NOAA-AVHRR l and surface temperature data detect a thermal anomaly preceding the 11 March 2011 Tohoku earthquake. *Int. J. Remote Sens.* **2012**, *33*, 6805–6817. [CrossRef]
27. Mahmood, I. Anomalous variations of air temperature prior to earthquakes. *Geocarto Int.* **2019**, *36*, 1396–1408. [CrossRef]
28. Pulinets, S.A.; Dunajecka, M.A. Specific variations of air temperature and relative humidity around the time of Michoacan earthquake M8.1 Sept. 19, 1985 as a possible indicator of interaction between tectonic plates. *Tectonophysics* **2007**, *431*, 221–230. [CrossRef]
29. Dey, S.; Sarkar, S.; Singh, R.P. Anomalous changes in column water vapor after Gujarat earthquake. *Adv. Space Res.* **2004**, *33*, 274–278. [CrossRef]
30. Piscini, A.; De Santis, A.; Marchetti, D.; Cianchini, G. A Multi-parametric Climatological Approach to Study the 2016 Amatrice–Norcia (Central Italy) Earthquake Preparatory Phase. *Pure Appl. Geophys.* **2017**, *174*, 3673–3688. [CrossRef]
31. Mahmood, I.; Iqbal, M.F.; Shahzad, M.I.; Qaiser, S. Investigation of atmospheric anomalies associated with Kashmir and Awaran Earthquakes. *J. Atmos. Sol.-Terr. Phys.* **2017**, *154*, 75–85. [CrossRef]
32. Shah, M.; Aibar, A.C.; Tariq, M.A.; Ahmed, J.; Ahmed, A. Possible ionosphere and atmosphere precursory analysis related to Mw > 6.0 earthquakes in Japan. *Remote Sens. Environ.* **2020**, *239*, 111620. [CrossRef]
33. Venkatanathan, N.; Yang, Y.-C.; Lyu, J. Observation of abnormal thermal and infrasound signals prior to the earthquakes: A study on Bonin Island earthquake M7.8 (May 30, 2015). *Environ. Earth Sci.* **2017**, *76*, 228. [CrossRef]
34. Marchetti, D.; De Santis, A.; Shen, X.; Campuzano, S.A.; Perrone, L.; Piscini, A.; Di Giovambattista, R.; Jin, S.; Ippolito, A.; Cianchini, G.; et al. Possible Lithosphere-Atmosphere-Ionosphere Coupling effects prior to the 2018 Mw = 7.5 Indonesia earthquake from seismic, atmospheric and ionospheric data. *J. Asian Earth Sci.* **2020**, *188*, 104097. [CrossRef]
35. McGuire, J.J.; Boettcher, M.S.; Jordan, T.H. Foreshock sequences and short-term earthquake predictability on East Pacific Rise transform faults. *Nature* **2005**, *434*, 457–461. [CrossRef]
36. Lippiello, E.; Marzocchi, W.; de Arcangelis, L.; Godano, C. Spatial organization of foreshocks as a tool to forecast large earthquakes. *Sci. Rep.* **2012**, *2*, 846. [CrossRef]
37. Derode, B.; Madariaga, R.; Campos, J. Seismic rate variations prior to the 2010 Maule, Chile MW 8.8 giant megathrust earthquake. *Sci. Rep.* **2021**, *11*, 2705. [CrossRef]
38. Bouchon, M.; Durand, V.; Marsan, D.; Karabulut, H.; Schmittbuhl, J. The long precursory phase of most large interplate earthquakes. *Nat. Geosci.* **2013**, *6*, 299–302. [CrossRef]
39. Susskind, J.; Blaisdell, J.M.; Iredell, L. Improved methodology for surface and atmospheric soundings, error estimates, and quality control procedures: The atmospheric infrared sounder science team version-6 retrieval algorithm. *APPRES* **2014**, *8*, 084994. [CrossRef]
40. Zhu, C.; Jiao, Z.-H.; Shan, X.; Zhang, G.; Li, Y. Land Surface Temperature Variation Following the 2017 Mw 7.3 Iran Earthquake. *Remote Sens.* **2019**, *11*, 2411. [CrossRef]
41. Zhao, W.; He, J.; Yin, G.; Wen, F.; Wu, H. Spatiotemporal Variability in Land Surface Temperature Over the Mountainous Region Affected by the 2008 Wenchuan Earthquake From 2000 to 2017. *J. Geophys. Res. Atmos.* **2019**, *124*, 1975–1991. [CrossRef]
42. Ouzounov, D.; Pulinets, S.; Romanov, A.; Romanov, A.; Tsybulya, K.; Davidenko, D.; Kafatos, M.; Taylor, P. Atmosphere-ionosphere response to the M9 Tohoku earthquake revealed by multi-instrument space-borne and ground observations: Preliminary results. *Earthq. Sci.* **2011**, *24*, 557–564. [CrossRef]
43. Genzano, N.; Filizzola, C.; Hattori, K.; Pergola, N.; Tramutoli, V. Statistical Correlation Analysis Between Thermal Infrared Anomalies Observed From MTSATs and Large Earthquakes Occurred in Japan (2005–2015). *J. Geophys. Res. Solid Earth* **2021**, *126*, e2020JB020108. [CrossRef]
44. Orihara, Y.; Kamogawa, M.; Nagao, T. Preseismic changes of the level and temperature of confined groundwater related to the 2011 Tohoku Earthquake. *Sci. Rep.* **2014**, *4*, 6907. [CrossRef] [PubMed]
45. Jiao, Z.-H.; Shan, X. Statistical framework for the evaluation of earthquake forecasting: A case study based on satellite surface temperature anomalies. *J. Asian Earth Sci.* **2021**, *211*, 104710. [CrossRef]

46. Ouzounov, D.; Bryant, N.; Logan, T.; Pulinets, S.; Taylor, P. Satellite thermal IR phenomena associated with some of the major earthquakes in 1999–2003. *Phys. Chem. Earth Parts A/B/C* **2006**, *31*, 154–163. [CrossRef]
47. Quinteros, J.; Strollo, A.; Evans, P.L.; Hanka, W.; Heinloo, A.; Hemmleb, S.; Hillmann, L.; Jaeckel, K.-H.; Kind, R.; Saul, J.; et al. The GEOFON Program in 2020. *Seismol. Res. Lett.* **2021**, *92*, 1610–1622. [CrossRef]
48. Allen, C.R. Responsibilities in earthquake prediction: To the Seismological Society of America, delivered in Edmonton, Alberta, May 12, 1976. *Bull. Seismol. Soc. Am.* **1976**, *66*, 2069–2074. [CrossRef]
49. Huang, J.; Liu, S.; Ni, Q.; Mao, W.; Gao, X. Experimental Study of Extracting Weak Infrared Signals of Rock Induced by Cyclic Loading under the Strong Interference Background. *Appl. Sci.* **2018**, *8*, 1458. [CrossRef]
50. Chen, S.; Liu, P.; Guo, Y.; Liu, L.; Ma, J. An experiment on temperature variations in sandstone during biaxial loading. *Phys. Chem. Earth Parts A/B/C* **2015**, *85–86*, 3–8. [CrossRef]
51. Ren, Y.; Ma, J.; Liu, P.; Chen, S. Experimental Study of Thermal Field Evolution in the Short-Impending Stage Before Earthquakes. *Pure Appl. Geophys.* **2017**, *175*, 2527–2539. [CrossRef]
52. Wu, L.; Liu, S.; Wu, Y.; Wang, C. Precursors for rock fracturing and failure—Part I: IRR image abnormalities. *Int. J. Rock Mech. Min. Sci.* **2006**, *43*, 473–482. [CrossRef]
53. Chen, S.; Liu, L.; Liu, P.; Ma, J.; Chen, G. Theoretical and experimental study on relationship between stress-strain and temperature variation. *Sci. China Ser. D Earth Sci.* **2009**, *52*, 1825. [CrossRef]
54. Ren, Y.-Q.; Liu, P.-X.; Ma, J.; Chen, S.-Y. An Experimental Study on Evolution of the Thermal Field of En Echelon Faults During the Meta-Instability Stage. *Chin. J. Geophys.* **2013**, *56*, 612–622.
55. Ma, J.; Sherman, S.I.; Guo, Y. Identification of meta-instable stress state based on experimental study of evolution of the temperature field during stick-slip instability on a 5° bending fault. *Sci. China Earth Sci.* **2012**, *55*, 869–881.
56. Piroddi, L.; Ranieri, G.; Freund, F.; Trogu, A. Geology, tectonics and topography underlined by L'Aquila earthquake TIR precursors. *Geophys. J. Int.* **2014**, *197*, 1532–1536. [CrossRef]
57. Freund, F. Pre-earthquake signals: Underlying physical processes. *J. Asian Earth Sci.* **2011**, *41*, 383–400. [CrossRef]
58. Freund, F. Toward a unified solid state theory for pre-earthquake signals. *Acta Geophys.* **2010**, *58*, 719–766. [CrossRef]
59. Freund, F.; Kulahci, I.G.; Cyr, G.; Ling, J.; Winnick, M.; Tregloan-Reed, J.; Freund, M.M. Air ionization at rock surfaces and pre-earthquake signals. *J. Atmos. Sol.-Terr. Phys.* **2009**, *71*, 1824–1834. [CrossRef]
60. Freund, F. Pre-earthquake signals—Part I: Deviatoric stresses turn rocks into a source of electric currents. *Nat. Hazards Earth Syst. Sci.* **2007**, *7*, 535–541. [CrossRef]

GeoHazards

MDPI

Article

Correlation Dimension in Sumatra Island Based on Active Fault, Earthquake Data, and Estimated Horizontal Crustal Strain to Evaluate Seismic Hazard Functions (SHF)

Wahyu Triyoso [1,*], David P. Sahara [1], Dina A. Sarsito [2], Danny H. Natawidjaja [3] and Sigit Sukmono [1]

[1] Faculty of Mining and Petroleum Engineering, Bandung Institute of Technology, Bandung 40132, Indonesia; dave.sahara@gmail.com (D.P.S.); sukmono1507@gmail.com (S.S.)
[2] Faculty of Earth Sciences and Technology ITB, Bandung Institute of Technology, Bandung 40132, Indonesia; dina.sarsito@gmail.com
[3] National Research and Innovation Agency (BRIN), Jakarta 10340, Indonesia; danny.hilman@gmail.com
* Correspondence: wahyu@geoph.itb.ac.id or wtriyoso@gmail.com; Tel.: +62-812-147-1417

Abstract: This study intends to evaluate the possible correlation between the correlation dimension (D_C) and the seismic moment rate for different late Quaternary active fault data, shallow crustal earthquakes, and GPS on the island of Sumatra Probabilistic Seismic Hazard Analysis (PSHA). The seismicity smoothing was applied to estimate the D_C of active faults (D_F) and earthquake data (D_E) and then to correlate that with the b-value, which will be used to identify seismic hazard functions (SHF) along with the Sumatra Fault Zone (SFZ). The seismicity based on GPS data was calculated by the seismic moment rate that is estimated based on pre-seismic horizontal surface displacement data. The correlation between D_F, D_E, and the b-value was analyzed, and a reasonable correlation between the two seismotectonic parameters, D_F-b, and D_E-b, respectively, could be found. The relatively high D_C coincides with the high seismic moment rate model derived from the pre-seismic GPS data. Furthermore, the SHF curve of total probability of exceedance versus the mean of each observation point's peak ground acceleration (PGA) shows that the relatively high correlation dimension coincides with the high SHF. The results of this study might be very beneficial for seismic mitigation in the future.

Keywords: correlation dimension; active fault; earthquake; b-value; GPS; seismic moment rate; seismic hazard function

Citation: Triyoso, W.; Sahara, D.P.; Sarsito, D.A.; Natawidjaja, D.H.; Sukmono, S. Correlation Dimension in Sumatra Island Based on Active Fault, Earthquake Data, and Estimated Horizontal Crustal Strain to Evaluate Seismic Hazard Functions (SHF). *GeoHazards* **2022**, *3*, 227–241. https://doi.org/10.3390/geohazards3020012

Academic Editors: Stefano Morelli, Veronica Pazzi and Mirko Francioni

Received: 6 January 2022
Accepted: 19 April 2022
Published: 22 April 2022

1. Introduction

Sumatra Island, Indonesia, is located in the convergent plate zone. It accounts for the high concurrent rate and the oblique NE-ward geometry between the subduction of the Indian–Australian Plates and the overriding southeastern Eurasian Plate [1–3]. This high convergence rate causes Sumatra Island to have many earthquakes annually, implying a high-stress level. The five most significant earthquakes support the large historical catalog of shallow earthquakes along the Sumatran megathrust over the last 250 years, $M_w \geq 8.0$. As explained by references [3,4], the active fault on Sumatra Island has been termed the 1700 km long Sumatran Fault Zone (SFZ). The Sumatran seismotectonic map depicting the Sumatran Subduction Zone, SFZ, and plot of the historical shallow large earthquake data can be seen in Figure 1. Consistent with [1,5], the dominant right-lateral shear fault zone accommodates most of the parallel components of the convergence of the sloping plate between the Indian-Australian and the Sunda Plates and has an average slip rate of ~15–16 mm per annum along some of its length [6–8]. The Sumatra Fault Zone (SFZ) within the mainland of Sumatra suggests that the released megathrust strain directly influences it.

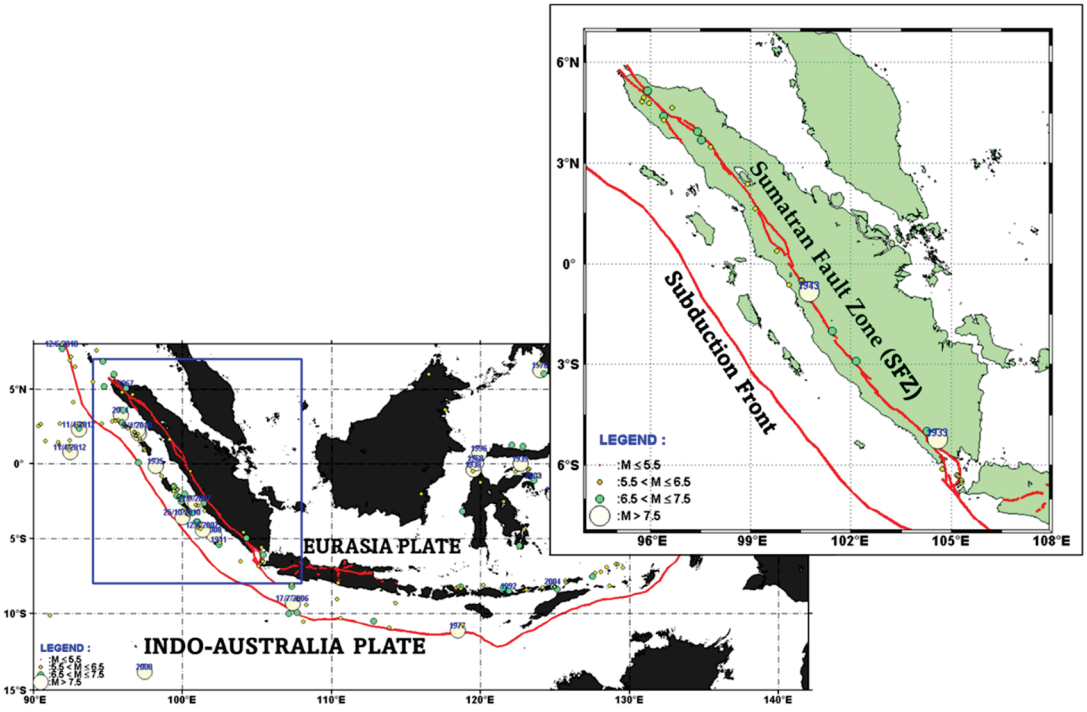

Figure 1. The Sumatran seismotectonic map depicting the Sumatran Subduction Zone and Sumatran Fault Zone (SFZ) overlays with the historical shallow large earthquake data of 1925–2014 with a magnitude (M_w) larger than or equal to 6.0. Historical earthquake data are based on Ref. [9].

McCloskey et al. [10] pointed out the effect of change in stress due to the 2004 Sumatra-Andaman earthquake on the adjacent rupture zone in the Nias segment, which was eventually quaked in March 2005 northern part of the SFZ, which has not yet produced M7 onshore earthquake. Qiu et al. [11] and Cattin et al. [12] suggest that there exists the effect of megathrust earthquakes on the SFZ. Sumatra Island was chosen as a master model because of the large body of complete historical earthquake and active fault data of the Northwestern Sunda Arc that can be found there.

Based on the previous study [13], late quaternary active faults in seismic hazard assessments allowed us to capture the recurrence of large magnitude events and, therefore, increase the reliability of the Probabilistic Seismic Hazard Analysis (PSHA). From a seismic hazard point of view, the first step would be to identify a potentially active fault and then evaluate the earthquake rate that each fault might generate. Swan et al. [14] and others [15,16] proposed the various features of the potential factors controlling the location and length of failure (i.e., rules for segmentation). Meng et al. [17] found that the largest strike-slip and intraplate earthquake ever recorded offshore Sumatra has resulted from the combination of deep extent, high-stress drop, and rupture of multiple faults. Using geometrical constraints to identify persistent segment boundaries (where most or all of a propagating rupture is arrested event after event) provided an important framework for quantifying fault-based PSHA [18–20].

Sieh and Natawidjaja [3] and others [7,8,21] acknowledge that the Sumatran Fault is very segmented. The SFZ has often been divided into 12–19 segments separated by a ~3 to 12 km wide stepover [3], limiting the break area that will break in one event [22,23]. Burton and Hall [21] studied clustering by applying k-means analysis along the SFZ using shallow earthquake data with a strike-slip mechanism. Burton and Hall [21] suggested that about 16 clusters partition the seismicity, and eight significant segments dominate the SFZ. The results of Burton and Hall [21] may improve the previous seismic hazard study [7,24] from the viewpoint of the probabilistic method.

According to Mandelbrot [25], fractal analysis can be used to describe the geometry of objects naturally. Many shreds of evidence of phenomena in space-time, such as

seismicity, can be characterized and interpreted by fractal models using power laws (e.g., Refs. [26–35]).

Studies on the possible correlation between earthquake seismicity and the distribution of active faults are limited. Sukmono et al. [30,31] studied the fractal geometry of the Sumatran active fault system, the data used were active fault data, and the correlation with the earthquake seismicity was not discussed very clearly. Pailoplee and Choowong [34] studied the earthquake frequency-magnitude distribution and fractal dimension; however, they only focused on using the earthquake catalog data. In this study, we use integrated data of active fault, shallow earthquake catalog, and the GPS to understand better the possible correlation between an earthquake and active fault seismicity based on the correlation dimension (D_C) and its correlation with the b-value to estimate the seismic hazard.

Based on previous study results, the b-value in time and space can be related to the phenomenon of stress levels before the occurrence of a large earthquake in a seismotectonic area [26,28,32,33]. Wyss et al. [36] acknowledge that the application of earthquake statistics, frequency-magnitude distribution (FMD) [37], and the correlation dimension (D_C) may be a convenient approach for understanding local seismotectonic activities. Both the b-values of FMD and D_C values are significantly and directly associated with the stress and earthquake phenomena. Pailoplee and Choowong [34] studied the FMD and D_C in mainland Southeast Asia, and their results suggest that the northern part of Sumatra Island has a high-stress level.

Moreover, Bayrak and Ozturk [38] show that a low b-value is closely related to high stress and strain loading. Therefore, it implies that we can expect to find a low b-value area coinciding with a high seismic moment rate; thus, characterizing a correlation between the D_C values and the b-value could help better understand the possible seismic hazards by identifying earthquake hazard functions (SHF). Furthermore, it might be very beneficial for earthquake mitigation efforts, as these areas could be interpreted as having high-stress levels.

Triyoso et al. [39,40] applied the least-square prediction method (LSC) over the entire gridded area using pre-seismic GPS data. Their purpose was to estimate the horizontal surface displacement in each grid or cell of the coastal area of Sumatra Island. The horizontal crustal strain was calculated using the horizontal surface displacement estimated by LSC in the entire study area of each cell. Furthermore, the horizontal crustal strain was used as the input to calculate the seismic moment rate [41–44]. The stress level could then be characterized based on the seismic moment rate; thus, it is possible to better correlate the D_C values and the b-values with the seismic moment rate to understand the stress level [35,45].

This study aims to find the relationship between seismic b-values and the correlation dimension (D_C) based on Sumatran Island's earthquake and active fault data. Since relatively high Dc is often directly associated with the stress level and earthquake phenomena [34,35,45], finding seismic hazard function (SHF) with high Dc at several observation points will be interpreted as areas with high-stress levels; thus, characterizing a correlation between the Dc value and the b-value could help better understand the possible seismic hazard.

The SHF is calculated based on an integrated seismic model of the earthquake catalog, active fault data, and the estimated seismic moment rate. These are taken into consideration to understand better the possible hazard that might occur. The analysis of seismic moments around Sumatra Island refers to references [39,40], in which the approximation made by reference [41] and others, such as Refs. [42–44], was adopted.

This study evaluated the correlation dimension for data from the late Quaternary active fault and the shallow crustal earthquakes. First, the correlation between $D_{F,}$ $D_{E,}$ and the b-value was analyzed using a cross-plot and then compared with the seismic moment rate to estimate the SHF. In addition, the algorithm of the seismic smoothing based on the previous study [39,46,47] is used to estimate the correlation dimension, as it is supposed to obtain a more robust result.

2. Data and Methods

The data utilized in this study are supported by Natawidjaja and Triyoso [7] and others [8,9,39,48]. Pre-seismic GPS data refer to Ref. [49] and others [2,6,50–54]. The earthquake seismic data used in this study are based on earthquake data with a magnitude of $M_w \geq 4.7$ and a maximum depth of 50 km selected from 1963 to 2020 (Figure 2A). This study adopts the 5 km starting locking depth and 20 km of the seismogenic thickness or 25 km of the maximum seismogenic depth by referring to Ref. [39]; thus, the maximum depth of earthquake catalog of 50 km or twice the maximum seismogenic depth is used. Seismic zoning is based on the modified clustering of Burton and Hall [21]. The active fault data are based on the newly revised results of the PuSGeN Team [48] for the Updated Indonesia Seismic Hazard Map with new slip rates from recent geological and geodetical (GPS) studies [8,48]. Based on previous studies [47], the MATLAB subroutine is used to realize seismology and geological data modeling. The FORTRAN and MATLAB subroutine based on Refs. [39,40] is used in the case of the GPS data. Mapping and plotting tools are developed using MATLAB subroutine based on previous studies [39,40,47]. The summarizing data used in this study can be found in the Supplementary Materials. They are shallow earthquake catalog data, the boundary zone based on Ref. [20], the grid in MAT file format LSQR 152 GPS data, and active fault data of SFZ.

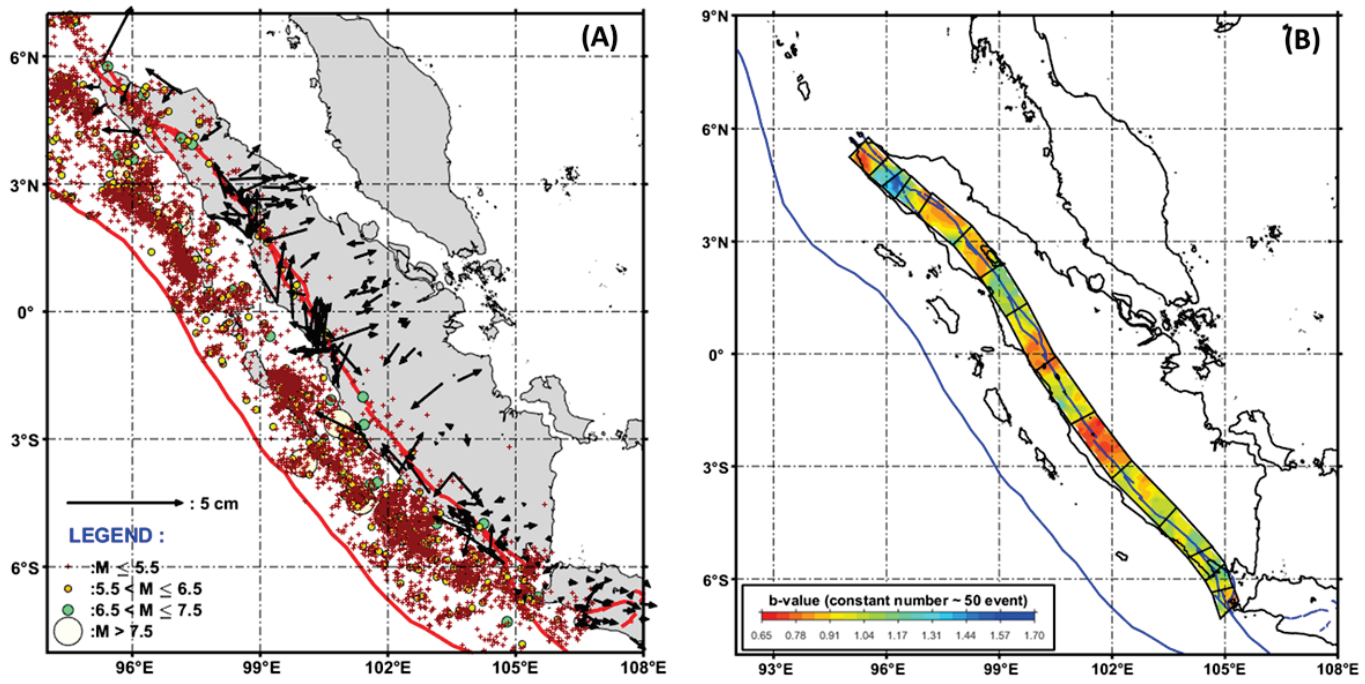

Figure 2. The shallow earthquake catalog data from 1963 to 2020 with the magnitude of Mw $\geq$ 4.7 and a maximum depth of 50 km [9] of 1963–2016 and the GCMT catalog of 2017–2020, the active fault, and pre-seismic GPS data (**A**). The b-value map overlays with the 15 zones area (**B**). The b-value is estimated based on the maximum likelihood (2) using a constant number of 50 events on each grid.

2.1. Earthquake Frequency-Magnitude Distribution (FMD)

Frequency-magnitude distribution (FMD) is usually parameterized by using the Gutenberg-Richter (G-R) power-law relationship [37]; such a frequency-magnitude relationship is as follows:

$$\log_{10} N(M) = a - b(M - M_c) \quad (1)$$

where N(M) is the number of earthquakes with a magnitude greater than or equal to M_c (magnitude completeness or minimum magnitude), a is a constant, and b describes the slope of the size distribution of events. It is proportional to the productivity of the seismic volume or the rate of earthquake production.

The b-value is an important statistical parameter and is correlated with the possible size of the scaling properties of seismicity. Generally, b-values are in the range of 0.3 to 2.0, depending on different regions. According to Ref. [55], the average b-value on a regional scale is usually equal to 1. Lower b-values are often interpreted as possible regions that are subjected to higher applied shear stress after the mainshock. In contrast, areas having higher b-values are areas that have experienced slip. Based on the previous study, high b-values are often found in areas with increased geological complexity, indicating multi-fracture areas. The critical findings of an earlier study [38] show that a low b-value is closely related to the low degree of heterogeneity of the cracked medium, enormous stress and strain, high deformation rates, large faults, and thus, seismic moment rates. The most robust method for calculating the b-value is maximum likelihood [56]. The formula can be written as follows:

$$\mathrm{b} = \frac{\log_{10}(\mathrm{e})}{\left(\overline{\mathrm{M}} - \mathrm{M}_c + 0.05\right)} \tag{2}$$

where $\overline{\mathrm{M}}$ is the average magnitude value greater or equal to M_c, and M_c is the minimum magnitude or the magnitude completeness. The 0.05 in Equation (2) is a correction constant [38]. The standard deviation of the b-value with 95% of the confidence limit can be estimated based on the equation suggested by Ref. [56] as $\approx (1.96\mathrm{b}/\sqrt{\mathrm{n}})$, where n is the number of earthquakes used to estimate the b-value of each zone.

2.2. Correlation Dimension (Dc) of Earthquake and Active Fault Data

In the chaos theory [57], the correlation dimension (D_C) is a measure of the dimension of the space occupied by a set of random points. It is often referred to as a type of fractal dimension. Using a two-point correlation dimension (D_C), the spatial and temporal distribution patterns of fault and earthquake seismicity were shown to be fractal [32–36]. Analysis of the correlation dimension is a powerful tool for quantifying a geometrical object of self-similarity, following Ref. [57], which defined D_C and correlation sum $\mathrm{C}_{(\mathrm{r})}$, as follows:

$$\mathrm{D}_c = \lim_{r \to \infty} \left(\frac{\log \mathrm{C}_{(\mathrm{r})}}{\log(\mathrm{r})} \right) \tag{3}$$

in which $\mathrm{C}_{(\mathrm{r})}$ is the correlation function, r is the distance between two epicenters, and supposing N is the number of pairs of events separated by distance R < r. If the epicenter distribution has a fractal structure, the following relationship would be obtained:

$$\mathrm{C}(\mathrm{r}) = \left(\frac{2\mathrm{N}_{\mathrm{R}<\mathrm{r}}}{\mathrm{N}(\mathrm{N}-1)} \right) \tag{4}$$

$$\mathrm{C}(\mathrm{r}) \ \sim \ \mathrm{r}^{\mathrm{D_c}} \tag{5}$$

where D_C is the fractal dimension (more strictly, the correlation dimension). Distance r between two earthquakes could be calculated (in degrees) using:

$$\mathrm{r} = \cos^{-1}\left(\cos\theta_{\mathrm{i}}\cos\theta_{\mathrm{j}} + \ \sin\theta_{\mathrm{i}}\,\sin\theta_{\mathrm{j}}\cos\left(\phi_{\mathrm{i}} - \phi_{\mathrm{j}}\right)\right) \tag{6}$$

where (θ_{i},ϕ_{i}) and (θ_{j},ϕ_{j}) are the latitudes and longitudes of the *i*th and *j*th events, respectively [26]. In this study, the algorithm of the box counting [58] is adopted to estimate Dc, in which the binary image of the object is successively divided into finer equivalent sub-regions (4, 16, 64, and more) by the ratio (r = 2, 4, 8, and so on) on both horizontal and vertical axis, respectively. Following the box counting algorithm, in which the object pixel value is represented by logical 1 and the background pixel value is represented by logical 0, then the Equation (3) could be written as follows,

$$\mathrm{D}_c = \lim_{r \to \infty} \left(\frac{\log \mathrm{N}_{(\mathrm{r})}}{\log(\mathrm{r})} \right) \tag{7}$$

in which $N_{(r)}$ is the number of the same size squared sub-regions containing one or more pixels of value 1.

By plotting log r and log $N_{(r)}$, the fractal dimension, D_C, could be obtained from the slope of the graph's line of least squares (LLS).

2.3. Seismicity Smoothing

In keeping with the previous study, the seismicity smoothing algorithm using the Gaussian function approach, for example, was implemented [23,39,46,47]. To realize the seismic smoothing algorithm, we first gridded the study area, then counted the number (n_i) of earthquake events with a magnitude greater than or equal to the reference (M_{ref}) in each cell or grid. The counting result of n_i represents the maximum likelihood estimate of 10^a or A-value for earthquakes with a magnitude larger than or equal to M_{ref} in each cell [59]. The n_i values in each cell were then smoothed spatially by applying a Gaussian function. The correlation distance c was used during smoothing. The following equation obtained the smoothed value in each cell:

$$\widetilde{n}_i = \frac{\sum_j n_i e^{\frac{-\Delta_{ij}^2}{c^2}}}{\sum_j e^{\frac{-\Delta_{ij}^2}{c^2}}} \quad (8)$$

in which $\tilde{n}_i$ is normalized and addressed to preserve the total number of events, Δ_{ij} is the distance between the i-th and j-th cells, and c is the correlation distance. In Equation (7), the sum is taken from cell j within a distance of 3c from cell i. When applying seismicity smoothing in this study, a correlation distance of 50 km was used to estimate the A-value.

To derive the correlation dimension based on shallow earthquake data, denoted by D_E, in this study, we first apply the seismicity algorithm using a distance correlation of 25 km. The D_E is then estimated by application of the box-counting algorithm using (7).

2.4. Active Fault Modeling

To derive the correlation dimension based on active fault data, denoted by D_F, in this study, we first create the synthetic epicenter of an earthquake using fault distribution data. The synthetic catalog algorithm is based on Refs. [47,60]. First, the fault earthquake epicenter positions were distributed uniformly along with the active fault positions, with each interval at a distance range of about 5 to 10 km. Subsequent synthetic epicenter distribution data were smoothed with a distance correlation of 10 km. The D_F is then estimated by application of the box counting algorithm using (7).

Furthermore, fault seismicity, or the A-values for active fault data, were modeled by integrating shallow earthquake data from Ref. [9] of the ($M_w \geq 4.7$, $H \leq 50$ km from 1963 to 2016) and GCMT catalog from 2017 to 2020 around the active fault zone and the synthetic catalog data model. For shallow earthquake data around the active fault zone and the synthetic catalog data model, we followed Ref. [60] by applying the seismic smoothing algorithm based on [46] and using a correlation distance of 50 km and 25 km. The integration between the two models was done by weighting the A-value model from the earthquake catalog with normalized smoothed seismicity obtained from active fault data.

2.5. Geodetic Modeling

To obtain the geodetic modeling data, we assumed that the horizontal displacement field of each observation point over the entire seismogenic depth is homogeneous and isotropic. Furthermore, the horizontal displacement components of u and v are in E-W N-S directions. Therefore, an assumption is needed to determine which signals of u and v are not correlated [61,62]. The study area was gridded into 10 km $\times$ 10 km cell sizes to estimate the surface strain rate based on GPS data. Basing our procedures on previous studies [39,40], we calculated the horizontal crustal strain rate of each cell by applying the LSC method. In keeping with previous studies around the Sumatra Islands [39,40], we applied the least-square prediction method, which uses the horizontal surface displacement data to

estimate the horizontal surface displacement of each cell in the study area. Furthermore, the horizontal crustal strain was used as the input to estimate the seismic moments around Sumatra Island. The following equation to calculate the scalar moment was adopted using the formulation done by Refs. [41–44]:

$$\dot{M}_0 = 2\mu HA \max(|e_1|, |e_2|) \quad (9)$$

where μ is the rigidity, H is the seismogenic thickness, A is the unit area, and e_1 and e_2 are the principal strain rates.

Finally, the annual seismicity rate model around the SFZ is estimated based on the integrated annual A-value of the earthquake and active fault data as described in Section 2.4 and is weighted by the normalized seismic moment rate based on GPS data. This annual seismicity rate model is then used to estimate seismic hazards.

2.6. Seismicity Rate Model: Earthquake Rate Formulation

In reference to Refs. [39,40,60], the rate of earthquake occurrence with a magnitude above or equal to magnitude completeness as the magnitude reference (M_{ref}) could be expressed as:

$$v_i(\geq M_{ref}) \approx \frac{N_i}{T} \quad (10)$$

where N_i is the number of earthquakes with a magnitude greater than or equal to magnitude completeness ($\geq M_c$), T is the period of observation, and v_i, based on Ref. [60]'s research, represents the likelihood of the A-value (10^a) of the earthquake with a magnitude greater than or equal to the reference magnitude (M_{ref}). The M_{ref} could be greater than or equal to M_c.

Furthermore, by substituting 10^a of Equation (9) in the frequency-magnitude of the Guttenberg–Richter equation [37], the following equation is obtained:

$$v_i(\geq m) \approx \frac{\widetilde{n}_i(\geq M_{ref})}{Tb\ln(10)} 10^{-bm}\left(1 - 10^{-b(m-M_{max})}\right) \quad (11)$$

where $n_i(\geq M_{ref})$ is the estimated number of earthquakes above or equal to magnitude completeness, T is a period of observation, and b is the b-value.

The annual seismic rate model around the SFZ is used to estimate seismic hazards based on the result as described in Section 2.5.

2.7. Seismic Hazard Function (SHF) Estimation: Ground Motion Prediction Equation (GMPE) and Probability Exceedance (PE)

In reference to Refs. [39,40,60], the probability of exceedance (PE) of the annual earthquake rate with magnitudes greater than or equal to M_c, which can be converted into the estimated ground motion (PGA) using Ground Motion Prediction Equation (GMPE) at point of observation, can be expressed as:

$$P(a \geq a_o) = P_k(m \geq m(a_o, R_k)) = 1 - e^{(-v_i(\geq m(a_o, R_k)))} \quad (12)$$

where P_k ($m \geq m(a_o, R_k)$) is the annual PE of earthquakes in the kth cell, $m(a_o, R_k)$ is the magnitude in the k^{th} source cell that could produce an estimated PGA of a_o or larger at the observation point, and R_k is the distance between the site and the source cell. The calculation of the SHF parameter is based on [60]. The function $m(a_o, R_k)$ is estimated based on the GMPE relation. The GMPE used is based on the results of [7], in which the GMPE of Ref. [63] is used. In this study, the GMPE of Ref. [63] is updated with the GMPE of [64]. The total PE distribution of PGA at the site was estimated based on a given radius of the influences of the surrounding source cells, which can be expressed as:

$$P(a \geq a_o) = 1 - \prod P_k(m \geq m(a_o, R_k)) \quad (13)$$

By substituting the GMPE in (13), we can obtain the annual PE of the particular PGA or PGV as follows:

$$P(a \geq a_o) = 1 - \prod e^{(-v_i(\geq m(a_o,R_k)))} = 1 - e^{-\Sigma v_i(\geq m(a_o,R_k))} \quad (14)$$

Furthermore, for a given time duration T, the PE could be estimated as follows:

$$P(a \geq a_o) = 1 - \prod e^{(-Tv_i(\geq m(a_o,R_k)))} = 1 - e^{-\Sigma Tv_i(\geq m(a_o,R_k))} \quad (15)$$

Thus, each grid's annual PE of specified ground motion is calculated using (14). Then, for a given time duration of T, the PE of a given value of the ground motion is computed using Equation (15).

3. Result and Discussion

The motivation of this study is to determine the relationship between seismic b-values and the correlation dimension (D_C) based on earthquake and active fault data in the Sumatra Islands. The purpose of using both the shallow earthquake catalog data and the active faults to estimate the correlation dimension (D_E and D_F) is to find a better correlation with the b-value, which will be used to identify earthquake hazard functions (SHF) as a function of D_C along with SFZ. The SHF is calculated based on an integrated seismic model of the earthquake catalog, active fault data, and the estimated seismic moment rate. These are addressed to produce an annual seismic rate model based on the combined data sources for probabilistic seismic hazard analysis. In addition, the pre-seismic GPS data are used to estimate the seismic moment rate model based on the estimated horizontal crustal strain. The estimation of the seismic moment around the Sumatra Islands refers to Refs. [39,40], in which the approximation made by Ref. [41] and others, such as Refs. [42–44], was adopted.

The shallow earthquake catalog data from 1963 to 2020 with $M_w \geq 4.7$ and a maximum depth of 50 km [9] of 1963–2016 and GCMT catalog of 2017–2020, the active fault and pre-seismic GPS data are used in this study (Figure 2A). The active fault data are based on the newly revised [9] and recent studies [8,48]. The pre-seismic GPS data are based on [2,6,49–54]. The zonation based on the clustering study of [21] is adopted for estimating D_C and the b-value. In this study, about 15 zones around SFZ are used by following their suggestion [21] to merge the zonations 15^{th} and 16^{th}.

First, to estimate the b-value, we grid the study area based on 15 zones around the SFZ by 10 km $\times$ 10 km. Furthermore, the b-value is calculated based on the maximum likelihood (2) using a constant number of 50 events on each grid. The result can be found in Figure 2B.

Based on the result of Figure 2B, the mean b-value of each zone is calculated, and the D_E and D_F are estimated using (7) based on the box-counting algorithm. Furthermore, the cross plotting between D_E or D_F with the mean b-value is constructed. The result can be seen in Figure 3A. In this study, the purpose of evaluating both D_E and D_F is to find a better correlation between the correlation dimension and the b-value utilized to estimate the SHF of the SFZ or the sites in the SFZ selected zone.

The correlation between D_F, D_E, and the b-value was then evaluated by referring to the previous studies [34,35,38] in which linear regression was applied. Based on Figure 3A, a reasonable correlation between two seismotectonic parameters, D_F-b, and D_E-b, for Sumatra Island can be found. It appears that the relationship of D_F-b seems better compared to D_E-b. It is probably related to the certainty of the distribution of the geometry data. The surface break of the late quaternary active fault is better than the distribution of the epicenter of the earthquake data. Next, to better understand the focal mechanism of the GCMT earthquake catalog in the depth range of 10 to 50 km around the SFZ depicts the strike-slip with a right lateral mechanism, as shown in Figure 3B.

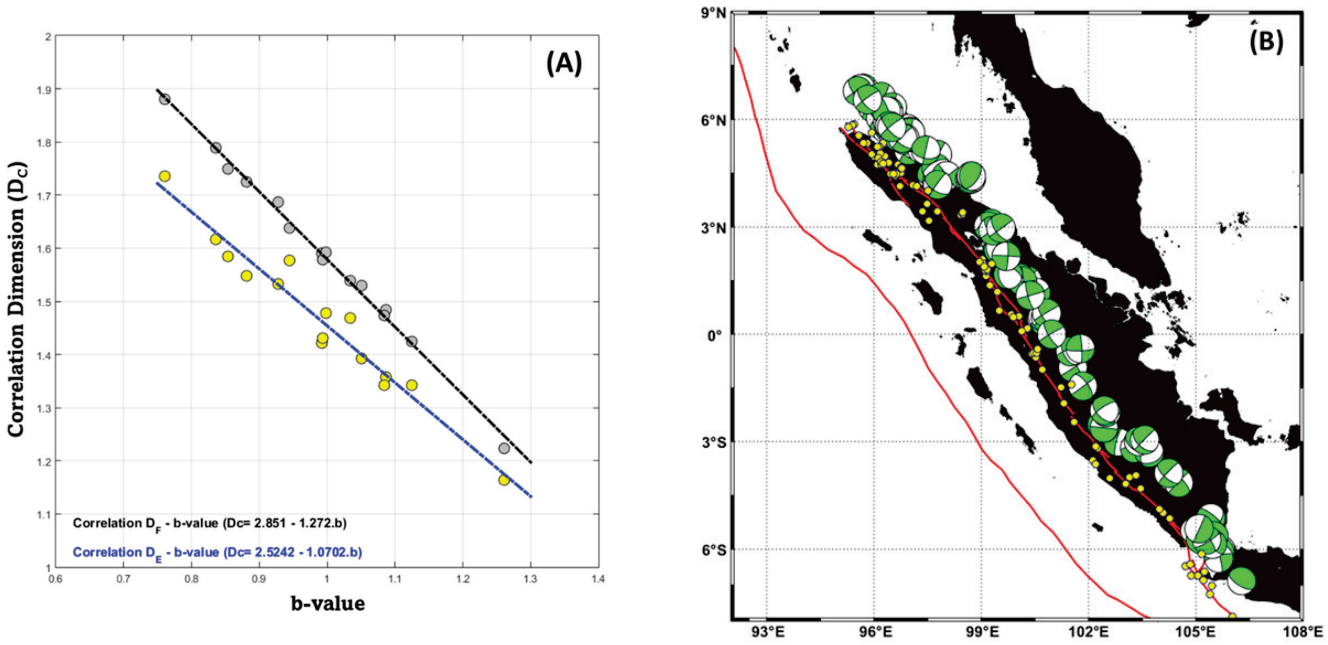

Figure 3. The cross-plot D_F, D_E, and the mean b-values are estimated based on the 15 zones (**A**). The focal mechanism plot is based on the GCMT catalog of shallow earthquake data for earthquakes at depths less than or equal to 50 km with a magnitude larger than or equal to 4.7 in the earthquake period between January 1976 to December 2020 [65,66] (**B**).

The next step calculates the D_F over the entire area of the 15 zones using the equation $D_F = 2.851 - 1.272b$ with the input of the b-value map of Figure 2B. The result can be found in Figure 4A. Figure 4A shows the map of the estimated D_F overlay with the historical large earthquake catalog around the SFZ. The relatively high D_C coincides with the historical data of the large earthquakes with a maximum depth of less than 50 km from 1925 to 2014. To enhance the contrast of DF, we then constructed the map of D_F subtracted by the mean of D_F over the entire area of the 15 zones. Furthermore, we selected about ten sites to evaluate the SHF. The result can be found in Figure 4B. Referring to Figure 4B, relatively high D_C (D_C > the mean of D_F) is distributed along zone 1, zone 5, zone 6, zone 8, zone 10, and part of zone 11; most of the previous historical large earthquakes are found.

The reliable annual seismicity rate model needs to be constructed to estimate the SHF on each site we selected. To assess the reliability of the annual seismicity rate model in this study is developed by integrating shallow earthquake catalog, active fault, and the pre-seismic GPS data. The summarized workflow in this study based on Sections 2.3–2.6 could be described as follows. First, we smoothed the shallow earthquake catalog data around the study area using a 50 km correlation distance. Next, the synthetic catalog data model based on active fault data are smoothed using a correlation distance of 25 km. The integration between the two models was done by weighting the A-value model from the earthquake catalog with normalized smoothed seismicity obtained from active fault data. Furthermore, the shallow crustal dynamic data are incorporated in this study by following [39]; it is used GPS data.

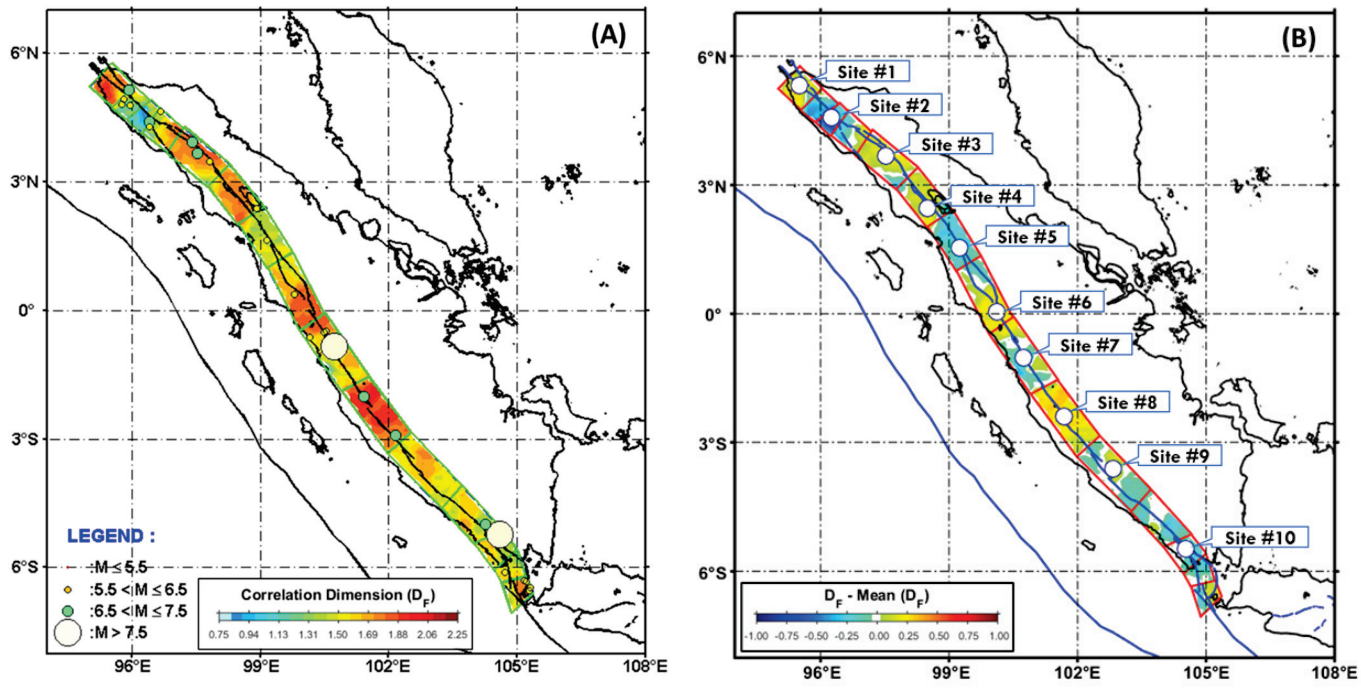

Figure 4. The map of D_F overlay with the historical earthquake catalog with the $M_w \geq 6.0$ around the SFZ (**A**). D_F is calculated using equation $D_F = 2.851 - 1.272b$ with the input of the b-value map of Figure 2B. The map of (D_F—mean of D_F) over the entire clustered zone boundary of Burton and Hall [21] and selected about ten sites to evaluate the SHF starting from the North-West to South-East (**B**). The relatively high D_C coincides with the historical shallow large earthquakes data of Ref. [9] from 1925 to 2014.

The algorithm for constructing the model using the GPS data are as follows. First, we developed the seismic moment rate is based on Sumatran Island's horizontal crustal strain model. In this step, the least-square prediction method [39,40,47,61,62,67] was applied to calculate the horizontal crustal strain based on each cell's horizontal surface displacement estimation over the entire study area. Furthermore, each cell's seismic moment could be calculated using Equation (8) [41–44]. We assumed the rigidity (μ) and the seismogenic thickness (H) to be 3.4×10^{11} dyne·cm^{-2} and 20 km, respectively [39,40]. The result of the seismic moment rate model can be found in Figure 4A. Figure 4A shows that the areas with relatively high correlation dimensions (D_F) coincide with high seismic moment loading rates, implying high tectonic stress loading that could pose the risk of producing significant earthquake hazards. The result of this study is aligned with the previous study [34,35]; however, the advantage result of this study is that we could understand the correlation between the high D_C with the possible present-day strain loading since we incorporate the present-day shallow crustal movement data. It is suggested that the algorithm of this study is applicable in the other active tectonic area as far as the data are available.

Finally, the annual seismicity rate model around the SFZ is estimated based on the integrated annual A-value of an earthquake and active fault data as described in Section 2.4 and is weighted by the normalized seismic moment rate based on GPS data as is shown in Figure 5A. The result can be found in Figure 5B. Figure 5B shows the annual seismicity rate model that we propose as the most reliable model to estimate seismic hazards along SFZ. In addition, the model is suggested to have a better certainty in geometrical source and rate distribution.

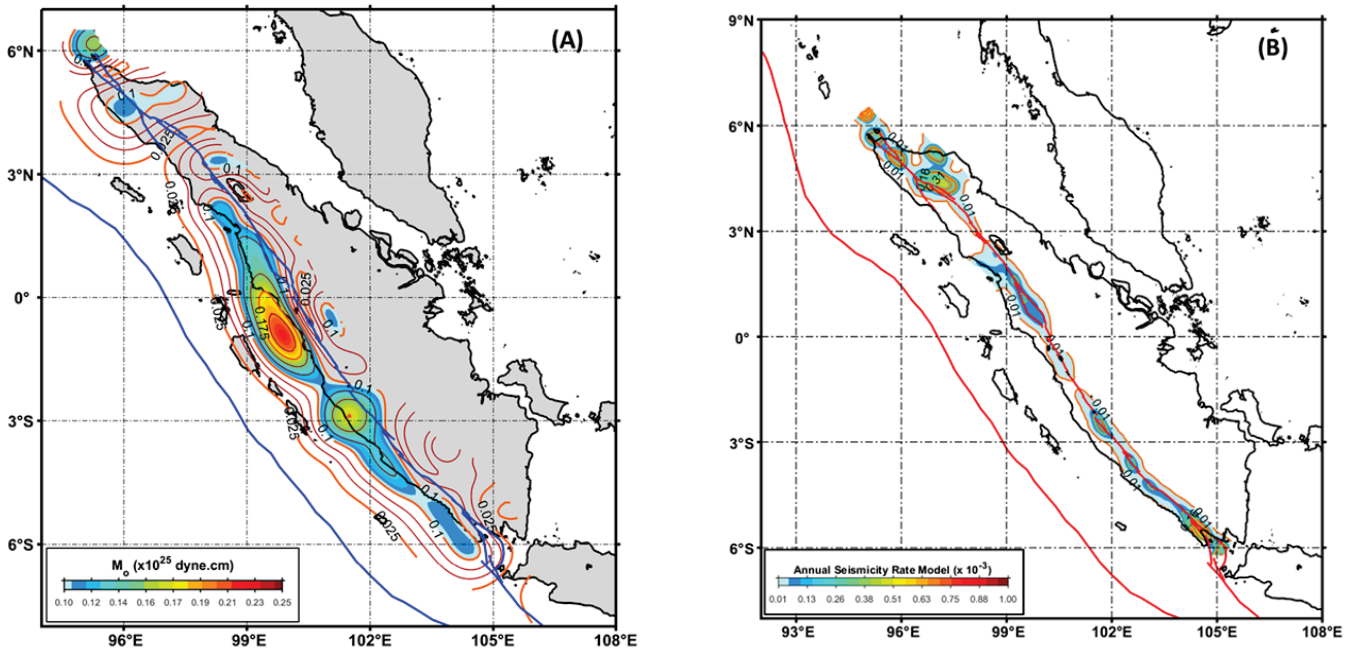

Figure 5. The estimated seismic moment rate is based on the horizontal crustal strain model around Sumatra Island (**A**). The annual seismic rate model for the SHF calculation was constructed based on the seismic smoothing of the earthquake catalog weighted by the normalized fault seismic model and the normalized seismic moment rate model based on the GPS data (**B**).

Furthermore, the SHF curve of the total probability of exceedance versus the mean of the peak ground acceleration of each observation point (sites #1 to #10) was constructed using the maximum radius distance of about 100 km with a magnitude range of 6.0–8.0. Since seismicity smoothing was used, the point source model was applied, and the source depth was placed at about half of the seismogenic thickness (about 20 km), with the starting locking depth being 5 km [39]; thus, a source depth of 15 km was used. The period of the SHF evaluation was set at about 50 years. The result of the SHF curve can be seen in Figure 6A,B. Another critical finding in this study is that the relatively high correlation dimension coincides with a high SHF curve, and it could be summarized that the areas with a relatively high correlation dimension (D_F) overlap with high seismic moment loading rates, which may imply high tectonic stress loading that could pose the risk of producing significant earthquake hazards in the future.

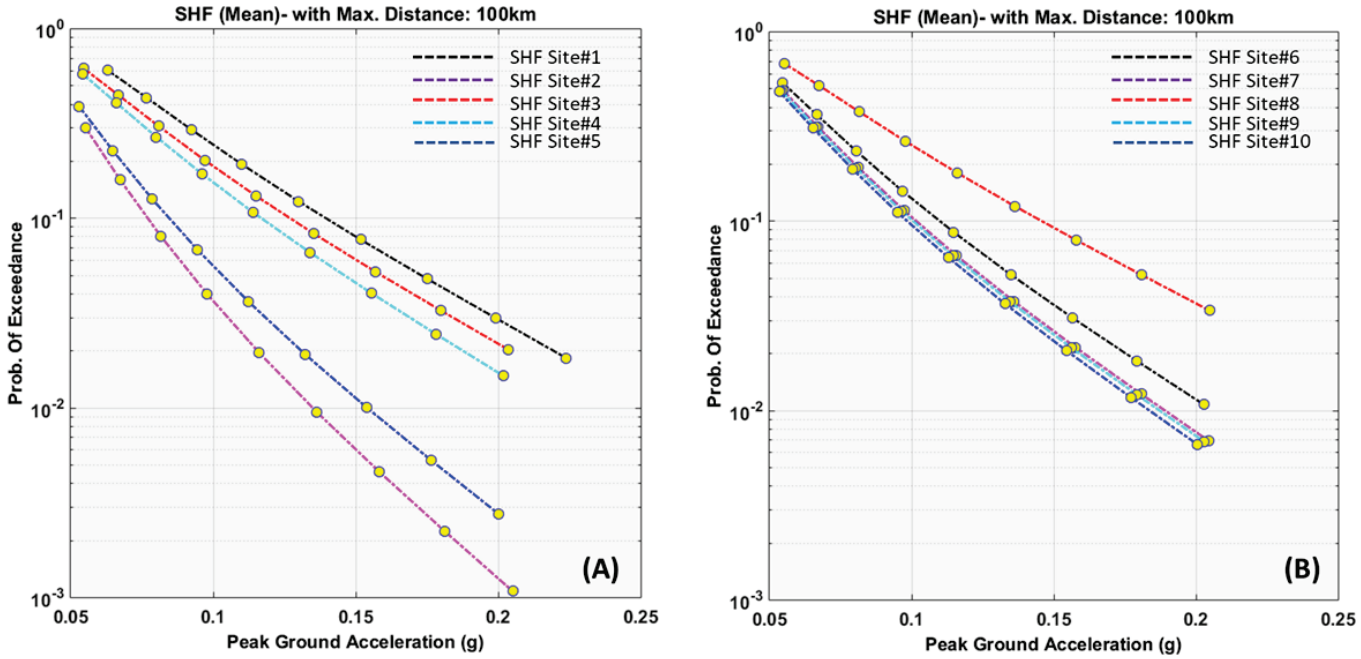

Figure 6. The graphs show the SHF curve of each observation point (**A**,**B**). The SHF curve of total probability of exceedance versus the mean of the peak ground acceleration of each observation point (sites #1 to #10) was constructed using the maximum radius distance of about 100 km with a magnitude range of 6.0–8.0. The source depth was set at half of the seismogenic thickness, which was about 20 km, and the starting locking depth of 5 km was used; thus, 15 km of the source depth was used. The period of the SHF evaluation was set at about 50 years.

4. Conclusions

This study could characterize a reasonable correlation between two seismotectonic parameters, D_F-b and DE-b, for Sumatra Island, especially around SFZ. The relationships are D_F-b and D_E-b, respectively ($D_F = 2.851 - 1.272b$) and ($D_E = 2.5242 - 1.0702b$). It is found that the relationship of D_F-b seems better compared to D_E-b. The result leads to the fundamental understanding that the certainty of the source geometry distribution based on the surface break of the late quaternary active fault is better than the distribution of the epicenter of the earthquake data.

The correlation dimension map in this study concludes that the relatively high D_C coincides with the historical data of large earthquakes from 1925 to 2014. The most critical finding in this study is that the areas with relatively high D_C coincide with high seismic moment loading rates, implying high tectonic stress loading that could pose the risk of producing significant earthquake hazards in the future. The advantage of this study compared to the previous research is that we could understand the correlation between the high D_C with the possible present-day strain loading since we incorporate the present-day shallow crustal dynamic data.

In this study, we have proposed the algorithm to construct the most reliable annual seismicity rate model along the SFZ. The model is estimated based on the integrated annual A-value of the shallow earthquake, active fault, and seismic moment rate derived from the GPS data. We suggest that the annual seismicity rate model tends to have better certainty in geometrical source and rate distribution.

Another critical finding of this study leads us to conclude that the relatively high correlation dimension coincides with a high SHF curve. Therefore, it could be summarized that the areas with relatively high D_C overlap with high seismic moment loading rates, which may imply high tectonic stress loading that could pose the risk of producing significant earthquake hazards in the future. This study also led us to the understanding that the

high correlation dimension is closely related to the possibility of high seismic hazards in the future.

Supplementary Materials: The following supporting information can be downloaded at: https://www.mdpi.com/article/10.3390/geohazards3020012/s1, They contain shallow earthquake catalog data (combined of PUSGEN catalog of 1963–2016 and GCMT catalog of 2017–2020), estimated b-value based on a constant number of 50 events, the boundary zone based on Ref. [21], and grid in MAT file format, LSQR GPS data, active fault data of SFZ and other materials related to the estimation results in this manuscript.

Author Contributions: W.T. developed the main idea and algorithm, analysed, and prepared the figures and the manuscript. D.A.S. helped to collect the GPS data based on several manuscripts. D.P.S. and S.S. helped in the manuscript preparation and discussion. Finally, D.H.N. helped support the most recent active fault data of Sumatra Island and in the discussion. All authors have read and agreed to the published version of the manuscript.

Funding: Funding was supported in part by the Institute of Research and Community Services (LPPM), Bandung Institute of Technology (ITB), Indonesia.

Institutional Review Board Statement: Not applicable.

Informed Consent Statement: Not Applicable.

Data Availability Statement: The authors declare that the materials and data used in this manuscript will be made available promptly to the Editorial Board Members and Referees upon request. The earthquake catalog and historical data are based on the PUSGEN2017 [9] and GCMT of 2017 to 2020 catalog, public domain data. The active fault data are based on the newly revised PUSGEN 2017 and recent studies [8,48]. The pre-seismic GPS data are based on the studies of [2,49–54].

Acknowledgments: The authors wish to thank the Global Geophysics Group and the Faculty of Mining and Petroleum Engineering, Bandung Institute of Technology, for their help in publishing this paper.

Conflicts of Interest: The authors declare that they have no competing interests.

References

1. Fitch, T.J. Plate convergence, transcurrent faults, and internal deformation adjacent to southeast Asia and the western Pacific. *J. Geophys. Res.* **1972**, *77*, 4432–4460. [CrossRef]
2. Prawirodirdjo, L.; McCaffrey, R.; Chadwell, C.D.; Bock, Y.; Subarya, C. Geodetic observations of an earthquake cycle at the Sumatra subduction zone: Role of interseismic strain segmentation. *J. Geophys. Res. Solid Earth* **2010**, *115*, B03414. [CrossRef]
3. Sieh, K.; Natawidjaja, D.H. Neotectonics of the Sumatran fault, Indonesia. *J. Geophys. Res.* **2000**, *105*, 28295–28326. [CrossRef]
4. Genrich, J.F.; Bock, Y.; McCaffrey, R.; Prawirodirdjo, L.; Stevens, C.W.; Puntodewo, S.S.O. Distribution of slip at the northern Sumatran fault system. *J. Geophys. Res.* **2000**, *105*, 28327–28341. [CrossRef]
5. McCaffrey, R. Slip vectors and stretching of the Sumatran forearc. *Geology* **1991**, *19*, 881–884. [CrossRef]
6. Bradley, K.E.; Feng, L.; Hill, E.M.; Natawidjaja, D.H.; Sieh, K. Implications of the diffuse deformation of the Indian Ocean lithosphere for slip partitioning of oblique plate convergence in Sumatra. *J Geophys. Res. Solid Earth* **2017**, *122*, 572–591. [CrossRef]
7. Natawidjaja, D.H.; Triyoso, W. The Sumatran fault zone—From source to hazard. *J. Earthq. Tsunami* **2007**, *1*, 21–47. [CrossRef]
8. Natawidjaja, D.H. Updating active fault maps and slip rates along the Sumatran Fault Zone, Indonesia. *IOP. Conf. Ser. Earth Environ. Sci.* **2018**, *118*, 012001. [CrossRef]
9. Tim Pusat Studi Gempa Nasional-2017 (The 2017 PuSGen). *Peta Sumber dan Bahaya Gempa Indonesia Tahun 2017*; Kementrian Pekerjaan Umum dan Perumahan Rakyat: Jakarta, Indonesia, 2017. (In Indonesian)
10. McCloskey, J.T.; Nalbant, S.S.; Steacy, S. Earthquake risk from co-seismic stress. *Nature* **2005**, *434*, 291. [CrossRef]
11. Qiu, Q.; Chan, C.-H. Coulomb stress perturbation after great earthquakes in the Sumatran subduction zone: Potential impacts in the surrounding region. *J. Southeast Asian Earth Sci.* **2019**, *180*, 103869. [CrossRef]
12. Cattin, R.; Chamot-Rooke, N.; Pubellier, M.; Rabaute, A.; Delescluse, M.; Vigny, C.; Fleitout, L.; Dubernet, P. Stress change and effective friction coefficient along the Sumatra-Andaman-Sagaing fault system after the 26 December 2004 (M_w= 9.2) and the 28 March 2005 (M_w= 8.7) earthquakes. *Geochem. Geophys. Geosystems* **2009**, *10*, 1–22. [CrossRef]
13. Visini, F.; Valentini, A.; Chartier, T.; Scotti, O.; Pace, B. Computational Tools for Relaxing the Fault Segmentation in Probabilistic Seismic Hazard Modelling in Complex Fault Systems. *Pure Appl. Geophys.* **2019**, *177*, 1855–1877. [CrossRef]
14. Swan, F.H.; Schwartz, D.P.; Cluff, L.S. Recurrence of moderate to large magnitude earthquakes produced by surface faulting on the Wasatch Fault Zone, Utah. *Bull. Seismol. Soc. Am.* **1980**, *70*, 1431–1462.

15. Schwartz, D.P.; Coppersmith, K.J. Fault behavior and characteristic earthquakes: Examples from the Wasatch and San Andreas Fault Zones. *J. Geophys. Res. Earth Surf.* **1984**, *89*, 5681–5698. [CrossRef]
16. King, G.; Nabelek, J. Role of fault bends in the initiation and termination of earthquake rupture. *Science* **1985**, *228*, 984–987. [CrossRef] [PubMed]
17. Meng, L.; Ampuero, J.P.; Stock, J.; Duputel, Z.; Luo, Y.; Tsai, V.C. Earthquake in a Maze: Compressional Rupture Branching During the 2012 M_w 8.6 Sumatra Earthquake. *Science* **2012**, *337*, 724–726. [CrossRef]
18. Field, E.H.; Dawson, T.E.; Felzer, K.R.; Frankel, A.D.; Gupta, V.; Jordan, T.H.; Parsons, T.; Petersen, M.D.; Stein, R.S.; Weldon, R.J.; et al. Uniform California Earthquake Rupture Forecast, Version 2 (UCERF 2). *Bull. Seism. Soc. Am.* **2009**, *99*, 2053–2107. [CrossRef]
19. Stirling, M.; McVerry, G.; Gerstenberger, M.; Litchfield, N.; Van Dissen, R.; Berryman, K.; Barnes, P.; Wallace, L.; Villamor, P.; Langridge, R.; et al. National Seismic Hazard Model for New Zealand: 2010 Update. *Bull. Seism. Soc. Am.* **2012**, *102*, 1514–1542. [CrossRef]
20. Peruzza, L.; Pace, B.; Visini, F. Fault-based earthquake rupture forecast in Central Italy: Remarks after the L'Aquila Mw 6.3 Event. *Bull. Seism. Soc. Am.* **2011**, *101*, 404–412. [CrossRef]
21. Burton, P.W.; Hall, T.R. Segmentation of the Sumatran fault. *Geophys. Res. Lett.* **2014**, *41*, 4149–4158. [CrossRef]
22. Segall, P.; Pollard, D.D. Mechanics of discontinuous faults. *J. Geophys. Res.* **1980**, *85*, 4337–4350. [CrossRef]
23. Wesnousky, S.G. Predicting the endpoints of earthquake ruptures. *Nature* **2006**, *444*, 358–360. [CrossRef] [PubMed]
24. Petersen, M.D.; Dewey, J.; Hartzell, S.; Mueller, C.; Harmsen, S.; Frankel, A.; Rukstales, K. Probabilistic seismic hazard analysis for Sumatra, Indonesia and across the Southern Malaysian Peninsula. *Tectonophysics* **2004**, *390*, 141–158. [CrossRef]
25. Mandelbrot, B.B. *The Fractal Geometry of Nature*; Freeman Press: San Francisco, CA, USA, 1982.
26. Hirata, T. Correlation between the b-value and the fractal dimension of earthquakes. *J. Geophys. Res.* **1989**, *94*, 7507–7514. [CrossRef]
27. Henderson, J.; Main, I.G.; Meredith, P.G.; Sammonds, P.R. The evolution of seismicity-observation, experiment, and a fracture—Mechanical interpretation. *J. Struct. Geol.* **1992**, *14*, 905–913. [CrossRef]
28. Öncel, A.O.; Alptekin, Ö.; Main, I. Temporal variations of the fractal properties of seismicity in the western part of the north Anatolian fault zone: Possible artifacts due to improvements in station coverage. *Nonlinear Process. Geophys.* **1995**, *2*, 147–157. [CrossRef]
29. Oncel, A.O.; Wilson, T. Anomalous seismicity preceding the 1999 Izmit event, NW Turkey. *Geophys. J. Int.* **2007**, *169*, 259–270. [CrossRef]
30. Sukmono, S.; Zen, M.T.; Kadir, W.G.A.; Hendrajaya, L.; Santoso, D.; Dubois, J. Fractal pattern of the Sumatra fault seismicity and its possible application to earthquake prediction. *Bull. Seismol. Soc. Am.* **1997**, *87*, 1685–1690. [CrossRef]
31. Sukmono, S.; Zen, M.T.; Kadir, W.G.A.; Hendrajaya, L.; Santoso, D.; Dubois, J. Fractal geometry of the Sumatra active fault system and its geodynamical implications. *J. Geodyn.* **1996**, *22*, 1–9. [CrossRef]
32. Caneva, A.; Smirnov, V. Using the Fractal Dimension of Earthquake Distributions and Slope of the Recurrence Curve to Forecast Earthquakes in Colombia. *Earth Sci. Res. J.* **2004**, *8*, 3–9.
33. Roy, S.; Ghosh, U.; Hazra, S.; Kayal, J.R. Fractal dimension and b-value mapping in the Andaman-Sumatra subduction zone. *Nat. Hazards* **2011**, *57*, 27–37. [CrossRef]
34. Pailoplee, S.; Choowong, M. Earthquake frequency-magnitude distribution and fractal dimension in mainland Southeast Asia. *Earth Planets Space* **2014**, *66*, 8. [CrossRef]
35. Goebell, T.H.W.; Kwiatek, G.; Becker, T.W.; Brodsky, E.E.; Dresen, G. What allows seismic events to grow big?: Insights from b-value and fault roughness analysis in laboratory stick-slip experiments. *Geology* **2017**, *45*, 815–818. [CrossRef]
36. Wyss, M.; Sammis, C.G.; Nadeau, R.M.; Wiemer, S. Fractal Dimension and b-Value on Creeping and Locked Patches of the San Andreas Fault near Parkfield, California. *Bull. Seism. Soc. Am.* **2004**, *94*, 410–421. [CrossRef]
37. Gutenberg, R.; Richter, C.F. Frequency of earthquakes in California. *Bull. Seism. Soc. Am.* **1944**, *34*, 185–188. [CrossRef]
38. Bayrak, Y.; Ozturk, S. Spatial and temporal variations of the aftershock sequences of the 1999 İzmit and Düzce earthquakes. *Earth Planets Space* **2004**, *56*, 933–944. [CrossRef]
39. Triyoso, W.; Suwondo, A.; Yudistira, T.; Sahara, D.P. Seismic Hazard Function (SHF) study of coastal sources of Sumatra Island: SHF evaluation of Padang and Bengkulu cities. *Geosci. Lett.* **2020**, *7*, 1–7. [CrossRef]
40. Triyoso, W.; Sahara, D.P. Seismic hazard function mapping using estimated horizontal crustal strain off West Coast Northern Sumatra. *Front. Earth Sci.* **2021**, *9*, 1–11. [CrossRef]
41. Ward, S.N. A multidisciplinary approach to seismic hazard in southern California. *Bull. Seism. Soc. Am.* **1994**, *84*, 1293–1309. [CrossRef]
42. Molnar, P. Earthquake recurrence intervals and plate tectonics. *Bull. Seism. Soc. Am.* **1979**, *69*, 115–133. [CrossRef]
43. Savage, J.C.; Simpson, R.W. Surface strain accumulation and the seismic moment tensor. *Bull. Seism. Soc. Am.* **1997**, *87*, 1345–1353. [CrossRef]
44. Field, E.H.; Jackson, D.D.; Dolan, J.F. A mutually consistent seismic-hazard source model for southern California. *Bull. Seism. Soc. Am.* **1999**, *89*, 559–578.
45. Scholz, C.H. The frequency-magnitude relation of microfracturing in rock and its relation to earthquakes. *Bull. Seism. Soc. Am.* **1968**, *58*, 399–415. [CrossRef]

46. Frankel, A. Mapping Seismic Hazard in the Central and Eastern United States. *Seism. Res. Lett.* **1995**, *66*, 8–21.
47. Triyoso, W.; Shimazaki, K. Testing various seismic potential models for hazard estimation against a historical earthquake catalog in Japan. *Earth Planets Space* **2012**, *64*, 673–681. [CrossRef]
48. Natawidjaja, D.H.; Bradley, K.; Daryono, M.R.; Aribowo, S.; Herrin, J. Late Quaternary eruption of the Ranau Caldera and new geological slip rates of the Sumatran Fault Zone in Southern Sumatra, Indonesia. *Geosci. Lett.* **2017**, *4*, 21. [CrossRef]
49. Bird, P. An updated digital model of plate boundaries. *Geochem. Geophys. Geosyst.* **2003**, *4*, 1027. [CrossRef]
50. Chlieh, M.; Avouac, J.-P.; Hjorleifsdottir, V.; Song, T.-R.A.; Ji, C.; Sieh, K.; Sladen, A.; Hebert, H.; Prawirodirdjo, L.; Bock, Y.; et al. Coseismic Slip and Afterslip of the Great Mw 9.15 Sumatra-Andaman Earthquake of 2004. *Bull. Seism. Soc. Am.* **2007**, *97*, S152–S173. [CrossRef]
51. Shearer, P.; Bürgmann, R. Lessons Learned from the 2004 Sumatra-Andaman Megathrust Rupture. *Annu. Rev. Earth Planet. Sci.* **2010**, *38*, 103–131. [CrossRef]
52. Susilo; Meilano, I.; Abidin, H.Z.; Sapie, B.; Efendi, J.; Wijanarto, A.B. Preliminary Results of Indonesian Strain Map Based on Geodetic Measuremnts. *AIP Conf. Proc.* **2016**, *1730*, 040004. [CrossRef]
53. Khaerani, D.; Meilano, I.; Sarsito, D.A.; Susilo, D. Deformation of West Sumatra Due to the 2016 Earthquake (M7.8) Based on Continuous GPS Data. In Proceedings of the 2018 IEEE Asia-Pacific Conference on Geoscience, Electronics and Remote Sensing Technology (AGERS), Jakarta, Indonesia, 18–19 September 2018.
54. Qiu, Q.; Feng, L.; Hermawan, I.; Hill, E.M. Coseismic and Postseismic Slip of the 2005 Mw 8.6 Nias-Simeulue Earthquake: Spatial Overlap and Localized Viscoelastic Flow. *J. Geophys. Res. Solid Earth* **2019**, *124*, 7445–7460. [CrossRef]
55. Frohlich, C.; Davis, S. Teleseismic b-values: Or, much ado about 1.0. *J. Geophys. Res.* **1993**, *98*, 631–644. [CrossRef]
56. Aki, K. Maximum likelihood estimate of b in the formula log N = a bM and its confidence limits. *Bull. Earthq. Res. Inst. Tokyo Univ.* **1965**, *43*, 237–239.
57. Grassberger, P.; Procaccia, I. Measuring the strangeness of strange attractors. *Physica* **1983**, *D9*, 189–208.
58. Popescu, A.L.; Popescu, D.; Ionescu, R.T.; Angelescu, N.; Romeo Cojocaru, R. Efficient fractal method for texture classification. In Proceedings of the 2nd International Conference on Systems and Computer Science (ICSCS), Villeneuve d'Ascq, France, 26–27 August 2013. [CrossRef]
59. Bender, B. Maximum likelihood estimation of b values for magnitude grouped data. *Bull. Seism. Soc. Am.* **1983**, *73*, 831–851. [CrossRef]
60. Triyoso, W.; Suwondo, A.; Naibaho, Z.Y.X. Earthquake Potential Hazard Analysis of Palembang City, Sumatra Island. Indones. *J. Geosci.* **2020**, *8*, 1–9. [CrossRef]
61. El-Fiky, G.S.A.; Kato, T. Continuous distribution of the horizontal strain in the Tohoku district, Japan, predicted by least-squares collocation. *Geodynamics* **1999**, *27*, 213–236. [CrossRef]
62. El-Fiky, G.S.; Kato, T.; Oware, E.N. Crustal deformation and interplate coupling in the Shikoku district, Japan, as seen from continuous GPS observation. *Tectonophysics* **1999**, *314*, 387–399. [CrossRef]
63. Fukushima, Y.; Tanaka, T. Reply to T. Masuda and M. Ohtake's "Comment on 'A new attenuation relation for peak horizontal acceleration of strong earthquake ground motion in Japan'". *Bull. Seism. Soc. Am.* **1992**, *82*, 523. [CrossRef]
64. Fukushima, Y.; Tanaka, H. The revision of "A new attenuation relation for peak horizontal acceleration of strong earthquake ground motion in Japan". *Abstr. Seismol. Soc. Jpn.* **1992**, *B18*, 116. (In Japanese)
65. Dziewonski, A.M.; Chou, T.-A.; Woodhouse, J.H. Determination of earthquake source parameters from waveform data for studies of global and regional seismicity. *J. Geophys. Res. Earth Surf.* **1981**, *86*, 2825–2852. [CrossRef]
66. Ekström, G.; Nettles, M.; Dziewoński, A. The global CMT project 2004–2010: Centroid-moment tensors for 13,017 earthquakes. *Phys. Earth Planet. Inter.* **2012**, *200–201*, 1–9. [CrossRef]
67. Kato, T.; El-Fiky, G.S.; Oware, E.N.; Miyazaki, S. Crustal strains in the Japanese Islands as deduced from dense GPS array. *Geophys. Res. Lett.* **1998**, *25*, 3445–3448. [CrossRef]

water

MDPI

Article

Numerical Simulation of Fluid Pore Pressure Diffusion and Its Mechanical Effects during Wenchuan Aftershocks

Tao Chen [1,2,*], Yaowei Liu [2,*] and Guomeng Zhang [2]

[1] Shandong Provincial Key Laboratory of Depositional Mineralization & Sedimentary Minerals, College of Earth Science and Engineering, Shandong University of Science and Technology, Qingdao 266590, China
[2] National Institute of Natural Hazards, Ministry of Emergency Management of China, Beijing 100085, China; guomeng_zhang@163.com
* Correspondence: chentao9330@gmail.com (T.C.); liuyw20080512@126.com (Y.L.)

Abstract: The Ms 8.0 Wenchuan earthquake occurred on 12 May 2008, in the Sichuan Province of China, and it was accompanied by a series of strong aftershocks. The mechanisms contributing to the triggering of the Wenchuan aftershocks have attracted international attention. In this paper, based on previous analysis of spatiotemporal distribution of aftershocks regarding pore pressure diffusion of deep fluid, we established a three-dimensional hydraulic–mechanical coupling model and investigated the influence of fluid migration and its mechanical effects in the Longmenshan fault zone by using FLAC3D software. We obtained the characteristics of the pore pressure diffusion and fault reactivation within 70 days in an area NA. The results show that the pore pressure significantly increases up to 80 MPa during fluid intrusion into the fault plane. The pore pressure increase along the fault dip is greater than that along the fault strike, with a maximum difference of 3.18 MPa. The increase in pore pressure along the fault reduces the effective stress and leads to fault reactivation. The evolution of the fault reactivation area calculated in the model is compared with the spatiotemporal characteristics of the aftershocks. This study is meaningful for furthering the understanding of the role of deep fluids in fault dynamics and aftershocks triggering.

Keywords: numerical simulation; pore pressure; hydraulic–mechanical coupling; spatiotemporal distribution of aftershocks

Citation: Chen, T.; Liu, Y.; Zhang, G. Numerical Simulation of Fluid Pore Pressure Diffusion and Its Mechanical Effects during Wenchuan Aftershocks. *Water* **2022**, *14*, 952. https://doi.org/10.3390/w14060952

Academic Editors: Stefano Morelli, Veronica Pazzi and Mirko Francioni

Received: 17 February 2022
Accepted: 10 March 2022
Published: 18 March 2022

1. Introduction

Earthquakes are often accompanied by changes in the physical properties, chemical compositions, and other aspects of deep fluids [1–5]. The stress changes caused by a mainshock can cause the diffusion of trapped fluids along a seismogenic fault, thereby reducing the effective stresses and leading to further rock failure and triggering aftershocks [6,7]. Geophysical inversions show that some earthquakes are located in areas containing fluids or with high pore pressures, such as the 1995 Kobe earthquake [8], the 2001 Bhuj earthquake [9] and the 1938 Kutcharo earthquake [10] in Japan, and the 2009 L'Aquila earthquake in Italy [11]. Furthermore, there is much evidence to support that the spatiotemporal distribution of some aftershocks may be driven by the migration of fluid [12], including aftershocks of the 1992 Landers earthquake in the United States [13], the 1995 Antofagasta aftershocks in northern Chile [14], the 1997 Umbra–Marche aftershocks in Italy [6], the 2004 Sumatra aftershocks [15], and the aftershocks that occurred in 2014 in the West Bohemia/Vogtland region [16].

The Ms 8.0 Wenchuan earthquake is one of the largest disasters in China in recent years. The mechanisms related to its triggering have been the focus of international attention and have become an attractive field. Some scholars suggest that the occurrence of the Wenchuan earthquake is related to the filling of the Zipingpu reservoir, e.g., [17–19]. Ge et al. [17] calculated stress changes caused by the filling of the Zipingpu reservoir at the depth of the Wenchuan hypocenter and found that its filling could cause an earthquake to

occur earlier than it otherwise would have. Lei et al. [18] analyzed the relationship between reservoir-induced stress changes and seismicity near the reservoir. They found that the filling of the Zipingpu reservoir caused Coulomb stress changes up to 0.05 MPa at 10 km depth along the central fault of the Longmenshan fault zone, which could have contributed to the Wenchuan earthquake. Sun et al. [19] used a three-dimensional porous elastic model to estimate that filling the Zipingpu reservoir increased Coulomb stresses by 1 kPa at the depth of the Wenchuan earthquake hypocenter. Although there is not yet a consensus on whether the Wenchuan earthquake was triggered by the filling of the Zipingpu reservoir [20], these studies show that even small stress changes caused by fluids can lead to the acceleration of seismicity. However, compared with surface reservoir impoundment, the stress changes caused by deep fluid migration may be greater at the depth of the earthquake hypocenter [21–23]. Many scholars have demonstrated the possibility that deep fluid may exist in the Longmenshan fault zone using geophysical and geochemical methods [24–27]. Liu et al. [1] analyzed the Wenchuan aftershock spatiotemporal distributions by pore pressure diffusion mechanics and suggest that the movement of deep fluid may trigger aftershocks in the Longmenshan fault zone (Figure 1). However, it was mainly studied from the point of view of hydraulic dynamics without considering the mechanical process. It is necessary to further discuss the role of deep fluid migration in the triggering of the Wenchuan aftershocks by considering a coupled hydraulic–mechanical model.

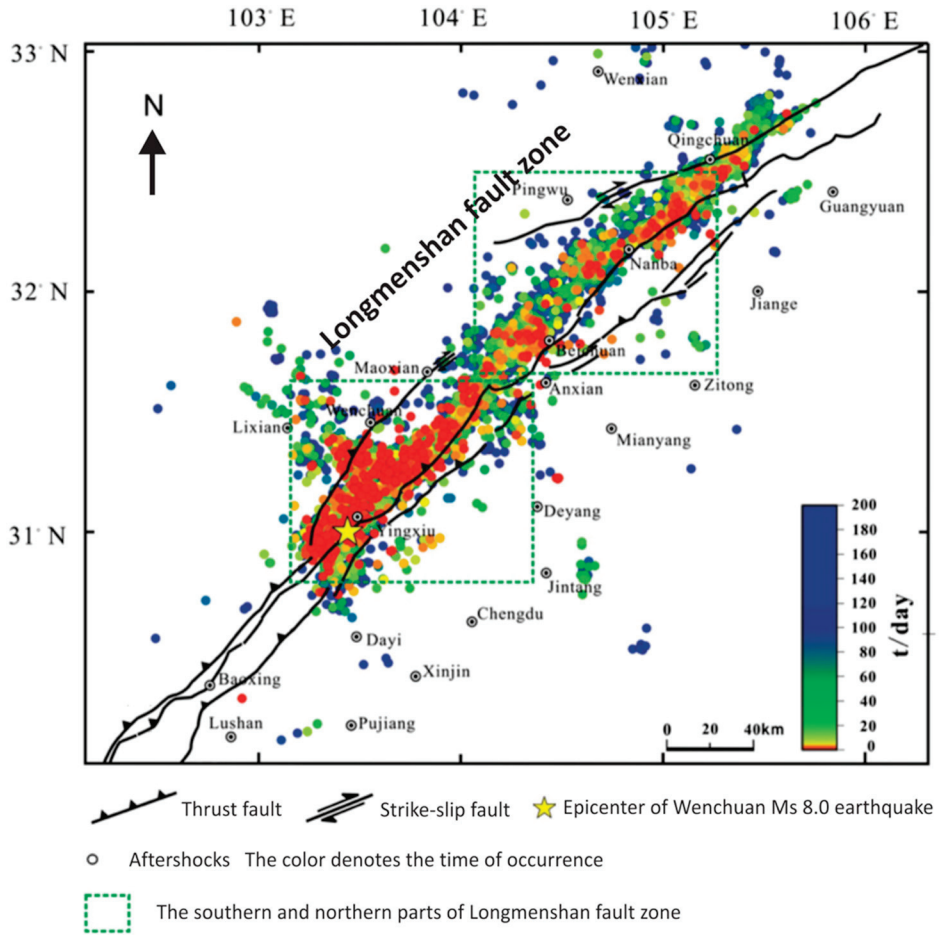

Figure 1. Spatiotemporal distributions of aftershocks [1]. Reproduced with permission from Liu et al., Tectonophysics; published by Elsevier, 2014, with Number 5270230803519.

In this study, based on the analysis of spatiotemporal distribution of Wenchuan aftershocks [1], we build a three-dimensional hydraulic–mechanical coupling model for investigating the process of deep-fluid diffusion along the fault and calculated its mechani-

cal effects on fault reactivation using FLAC3D software. The calculated fault reactivation area is compared with the spatial and temporal distribution of Wenchuan aftershocks. The results provide an insight into the role of pore pressure diffusion in triggering aftershocks and the relationship between deep fluids and the seismogenic process.

2. Study Area

Based on focal mechanisms and distribution of hypocenters of the Wenchuan aftershocks and the Longmenshan fault zone structure [28], there are some areas containing similar types of seismicity along the Longmenshan fault zone. Because the focal mechanisms of the aftershocks are similar in such areas, it is likely that they have the same triggering mechanisms [29], that is, the pore pressure diffusion of trapped deep fluid which is initiated by stress changes caused by the mainshock [6], as observed in aftershocks related to fluid migration elsewhere [11].

Pore pressure diffusion is one of the main methods of analyzing the spatiotemporal distribution of earthquakes and extracting information on fluids involved in earthquakes, e.g., [7,30–32]. If the first earthquake in an earthquake sequence is considered as a fluid intrusion point, then if the distance between the first earthquake and its aftershocks (r) gradually increases with time (t), these points will follow an envelope line in an r–t plot. The emergence of an envelope line demonstrates that the earthquakes are triggered mainly by the diffusion of pore pressure, which can be used to estimate hydraulic diffusivity, D [7]:

$$r = \sqrt{4\pi D t} \tag{1}$$

Liu et al. [1] analyzed the spatiotemporal distribution of aftershocks for the areas with the similar focal mechanisms and concentrated hypocenters and evaluated the hydraulic diffusivities for such areas along the Longmenshan fault zone. An area NA is located in the north of the Longmenshan fault zone (Figure 2a). Considering the aftershocks triggered by pore pressure diffusion may have multiple stages [1], the aftershocks within 70 days in the area NA are analyzed (Figure 2b). The spatiotemporal distribution of the aftershocks in the NA area is plotted on the r–t plot (Figure 2c) and the M–t plot (Figure 2d). The aftershocks in the area NA (Figure 2a) are more in line with an envelope shape in r–t space (Figure 2c) than other areas and suggest that the aftershocks in the area NA were mainly triggered by pore pressure diffusion. The hydraulic diffusivity D was estimated roughly to be 1.8 m^2/s from the envelope line, with a corresponding permeability of $k = 3.7 \times 10^{-15}$ m^2 [14]. The estimated value is reasonable compared to the seismogenic fault rock permeability [33]. Therefore, we select the area NA as the study area here and establish a three-dimensional hydraulic–mechanical coupling model based on the previous work.

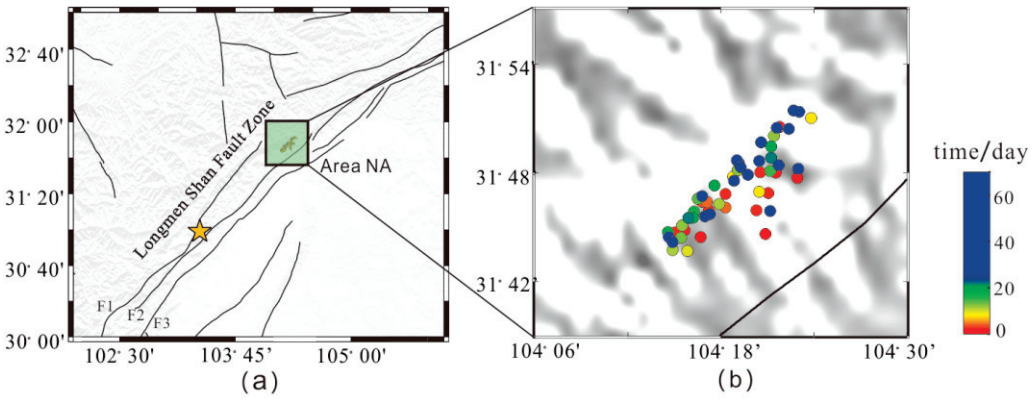

Figure 2. *Cont.*

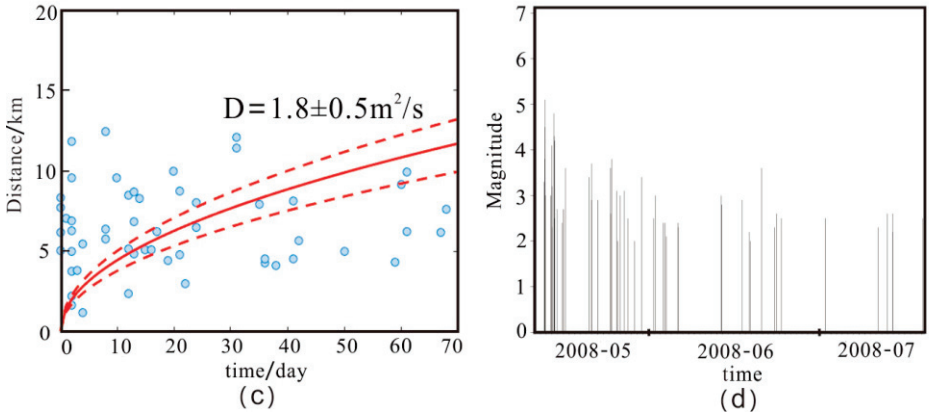

Figure 2. (**a**) The area NA. The star denotes the location of the Wenchuan mainshock, the solid black lines denote faults, F1 denotes the back fault, F2 denotes the central fault, and F3 denotes the piedmont fault (Deng et al., 2003). (**b**) Spatiotemporal distribution of aftershocks in the area NA. The grey color represents the topography of the area. (**c**) The *r*–*t* plot for the area NA. The red lines are the envelope lines for different hydraulic diffusivities D and the blue circles denote aftershocks. (**d**) The M–*t* plot for the area NA.

3. Method

The fault rock was treated as an equivalent porous medium in the hydraulic–mechanical coupling model. The migration of fluid in a porous medium obeys Darcy's law [34], and the rock stresses obey the Terzaghi effective stress principle [35]. The equations for calculating pore pressure and stress changes are briefly described below.

3.1. The Mathematical Model

Based on Darcy's law and mass conservation, the fluid flow in the fault and rock matrix can be expressed by [3]:

$$\frac{\partial(\phi\rho S)}{\partial t} = \nabla\cdot[\rho k(\nabla P - \rho g \nabla z)] + \rho Q, \tag{2}$$

in which ϕ is the porosity, ρ is the fluid density, kg/m^3, S is the saturation, k is the permeability, m^2, P is the pore pressure, Pa, and Q is the source term, m^3/s.

Assuming that the rock is an isotropic elastic medium in the fault, the stress state influenced by the fluid can be represented by the Terzaghi effective stress principle:

$$\sigma' = \sigma - \alpha P, \tag{3}$$

where σ' is the effective stress, Pa, σ is the total stress, Pa, and α is the Biot coefficient.

Fault reactivation occurs when the difference between the maximum and minimum principal stresses is sufficiently large [36]:

$$\frac{\sigma_1'}{\sigma_3'} = \frac{\sigma_1 - \alpha P}{\sigma_3 - \alpha P} \le q = \left[\left(\mu_s^2 + 1\right)^{1/2} + \mu_s\right]^2, \tag{4}$$

where σ_1 and σ_3 are the maximum and minimum principal stresses, respectively, σ_1' and σ_3' are the maximum and minimum effective stresses, respectively, μ_s is static friction coefficient of the rock, and q is the limiting stress difference. When the stress ratio exceeds q, fault reactivation will occur. The mathematical model was solved with the finite difference method by using the software FLAC3D [37]. Compared to the finite element method, the finite difference method is computationally efficient for both meshing and solving the numerical model.

3.2. The Numerical Model

According to the location of the area NA and its fault structure [28,38], we established a 30 km × 30 km × 10 km geological model (Figure 3a). The model includes a fault with a dip of approximately 60° and a thickness of approximately 100 m, corresponding to the high-angle reverse fault of Longmenshan fault zone [25]. Considering that nearly 90% of the aftershocks are distributed shallower than 10 km depth in the area NA, it is assumed that the middle point of the fault in the Y-direction at 10 km depth is the fluid intrusion point (Figure 3b). We should note that the location of the "intrusion point" is chosen based on the mechanism of fluid-induced aftershocks (Liu et al., 2014) and the temporal–spatial distribution of aftershocks in the area NA. From the point of view of the triggering mechanism, it is assumed that there were many areas with trapped fluid along the Longmenshan fault zone before the Wenchuan earthquake, and when the main shock occurred, the changed crustal stress causes the trapped fluid in such zones to diffuse upward. Accordingly, the main shock provides the geomechanical condition of the first occurrence of aftershocks, whereas the zone of the trapped fluid, i.e., the existence of fluid, determines the location of the "intrusion point" of the area. For the studied area NA, considering the seep characteristic of deep fluid, we infer that the "intrusion point" is the middle point in the Y-direction at 10 km depth. We should note that due to the heterogeneity of the subsurface rocks, the inferred "intrusion point" may not be rigorously in the bottom middle of the area, whereas it is a proper one, regarding the above mechanism and the limited data about the geological aspect of this area. Thus, the model includes a three-dimensional rock matrix (impermeable) and fault (permeable). From the point of view of engineering geology, the rock matrix and large fractures (fault) constitute the rock mass. Properties of the rock matrix and fault for the model are presented in Table 1 [33,36].

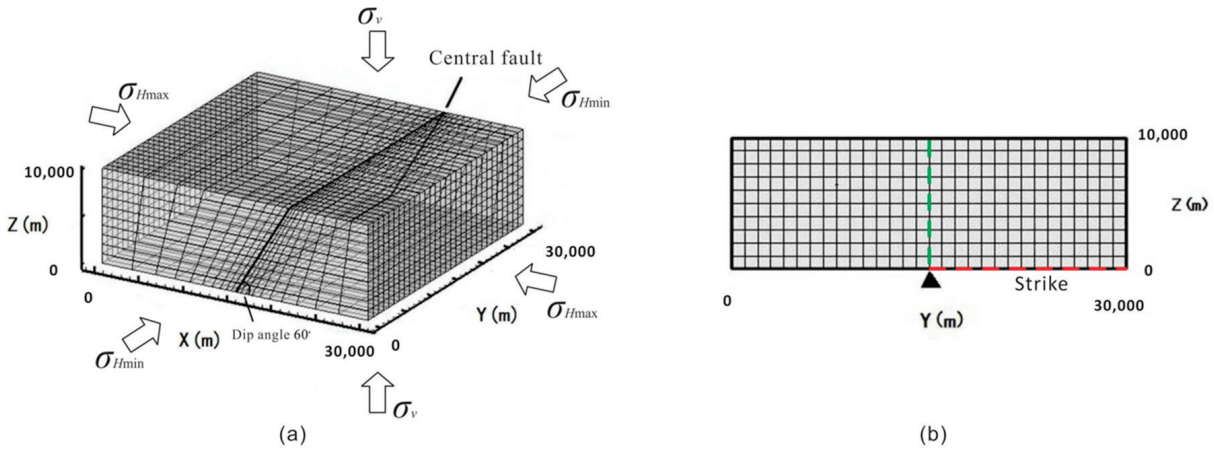

Figure 3. The model geometry and meshes used in the study. (**a**) A 3D view of the grid. (**b**) Plane view of the fault zone in the Y–Z plane. The triangle denotes the fluid intrusion point.

Table 1. Parameters for the rock matrix, fault, and fluid for the numerical model.

Properties	Rock Matrix	Fault
Bulk modulus (Pa)	4.667×10^{10}	2.800×10^{10}
Shear modulus (Pa)	2.890×10^{10}	1.646×10^{10}
Rock density (kg/m^3)	2600	2600
Fluid density (kg/m^3)	N/A	1000
Static friction coefficient	N/A	0.6
Fluid modulus (Pa)	N/A	2.2×10^{10}
Permeability (m^2)	N/A	3.7×10^{-15}
Biot coefficient	N/A	1.00
Porosity	N/A	0.05

3.3. Initial and Boundary Conditions

As Longmenshan fault zone belongs to a reverse fault, which is the result of horizontal compression, the maximum principal stress is in a direction perpendicular to the fault strike in the model. Stress measurements at some places along the Longmenshan fault zone prior to the Wenchuan earthquake show that the horizontal stress (σ_H) was greater than the vertical stress (σ_v) and that $\sigma_H = 1.35 \sim 2.1\sigma_v$ [39]. We set the initial stress conditions for the model based on the measured stresses and the stress characteristics for reverse faulting and assume hydrostatic pressure for the fluid. The stress and hydrostatic pressure increase linearly with depth.

The maximum principal stress is perpendicular to the fault strike in the horizontal plane, and it is also the maximum horizontal stress $\sigma_{H\max}$, MPa, which can be expressed by [39]:

$$\sigma_{H\max} = 6.5 + 0.0494H \tag{5}$$

The intermediate principal stress is in the strike direction of the fault, i.e., the minimum horizontal stress $\sigma_{H\min}$, MPa, can be expressed by the following [39]:

$$\sigma_{H\min} = 4.9 + 0.039H \tag{6}$$

The minimum principal stress is vertical stress σ_v, MPa, which can be expressed by [39]:

$$\sigma_v = \rho_r g H \times 10^{-6}, \tag{7}$$

and the pore pressure, MPa, is assumed as hydrostatic initially [3]:

$$P = 0.01H, \tag{8}$$

where H is the depth, m, ρ_r is the rock density, kg/m^3 and g is the gravitational acceleration of 10 m/s^2.

Considering that stress accumulates relatively slowly compared to stress changes due to pore pressure diffusion, it is assumed that the stress changes caused by tectonic activity were unchanged during the study period. Therefore, the stress boundary conditions are consistent with the initial conditions. The stresses along boundaries perpendicular to the fault were represented by Equation (5), the stresses along boundaries parallel to the fault were represented by Equation (6), and the stresses at the upper and lower boundaries were 0 MPa and 260 MPa, respectively.

Determining the source term of deep fluid and pore pressure in the fault is difficult in the study of fluid dynamics in seismic processes. Although some scholars have studied fluid migration and pore pressure in the Longmenshan fault zone [24], there is little knowledge of the physical parameters of fluids in the fault zone during the Wenchuan earthquake. For the fluid diffusion model in Equation (2), the source term should be specified, whereas, to the best of our knowledge, it is hard to measure at the depth of 10 km. The source term, Q, was 0.15 m^3/s for the Matsushiro earthquake swarm [40], but the magnitude of Wenchuan earthquake was much higher than those of the Matsushiro earthquakes. Hence, the source term is assumed as 1.5 m^3/s in our model.

4. Results

The intrusion of the fluid increases the pore pressure in the fault plane, which reduces the effective stress in a rock and causes failure when it is sufficiently large. Here, we first calculate the increased pore pressure in the fault plane within 70 days. Then the reduced effective stress due to the pore pressure diffusion is analyzed. Last, we estimate the fault reactivation area based on the calculated effective stress state.

4.1. Pore Pressure Increases Caused by the Fluid Intrusion

The fluid flow Equation (1) is solved numerically for investigating the characteristics of pore pressure diffusion within the fault. The gradual increase in pore pressure in the

fault plane due to fluid intrusion is shown in Figure 4. The area of elevated pore pressure expands gradually along the fault dip and strike directions. The pore pressure in the fault plane increases up to 80 MPa during the fluid intrusion.

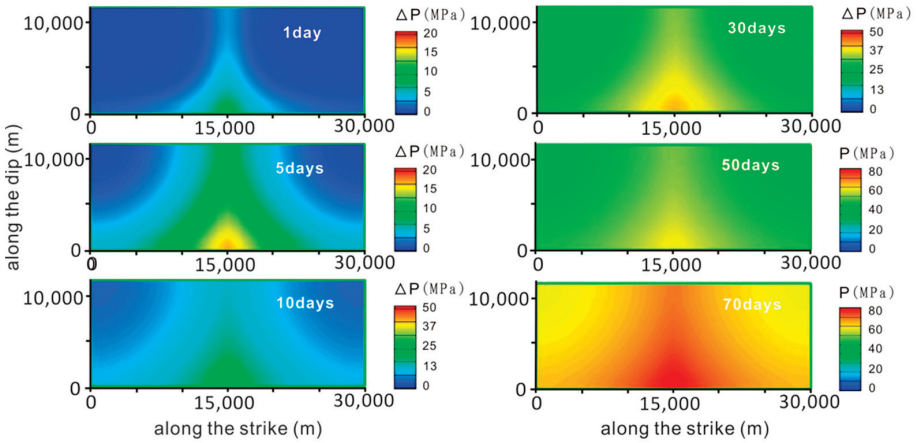

Figure 4. The distribution of increasing pore pressure at different times during the fluid intrusion.

The increases in pore pressures ΔP along the strike (the red dashed line in Figure 3b) and dip (the green dashed line in Figure 3b) differ from each other (Figure 5). It shows that the increase in pore pressure along the dip is greater than along the strike, and the difference increases with distance from the intrusion point and over time, reaching a maximum of 3.18 MPa at 70 days. ΔP decays from the intrusion point over 70 days with an averaged decay gradient of 0.8 MPa/km and 1.1 MPa/km along the dip and strike direction, respectively. This suggests that the range of the increased pore pressure along the dip is bigger than along the strike regarding the fluid intrusion point in this model. According to the Terzaghi effective stress principle, the difference in the increase in pore pressure in the two directions causes stress changes correspondingly. Therefore, it is necessary to further calculate the crustal stress changes caused by the fluid intrusion.

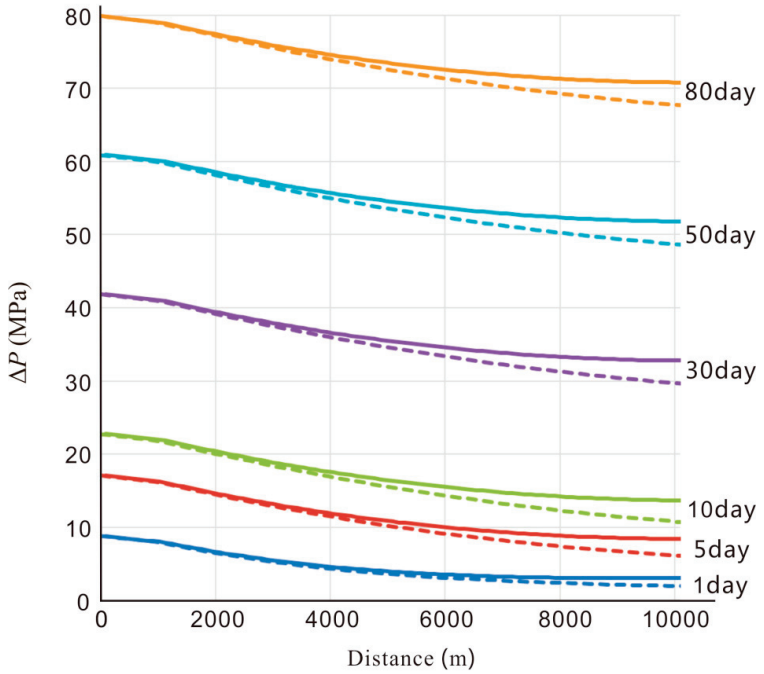

Figure 5. The increases of pore pressure along the dip (solid line) and strike (dashed line) from the intrusion point in the fault plane.

4.2. Changes in Maximum Horizontal Stress and Vertical Stress Caused by Fluid Intrusion

The reduction of the effective stress caused by the increase in pore pressure along the fault zone is one of the main mechanisms to explain earthquake triggering [3]. The failure of rock is related to the difference between the maximum and minimum principal stresses, as shown in Equation (4) [41]. For a reverse fault, the maximum and the minimum principal stresses correspond to the maximum horizontal stress $\sigma_{H\max}$ and the vertical stress σ_v (Figure 3a), respectively. Therefore, we calculated the effective stress in the X- and Z-directions, $\sigma'_{H\max}$ and σ'_v, considering the increased pore pressure (ΔP) using Equation (3). The effective stresses in the X- and Z-directions during fluid intrusion are shown in Figure 6a,b, respectively. It shows that the effective stress gradually decreases over time in both directions.

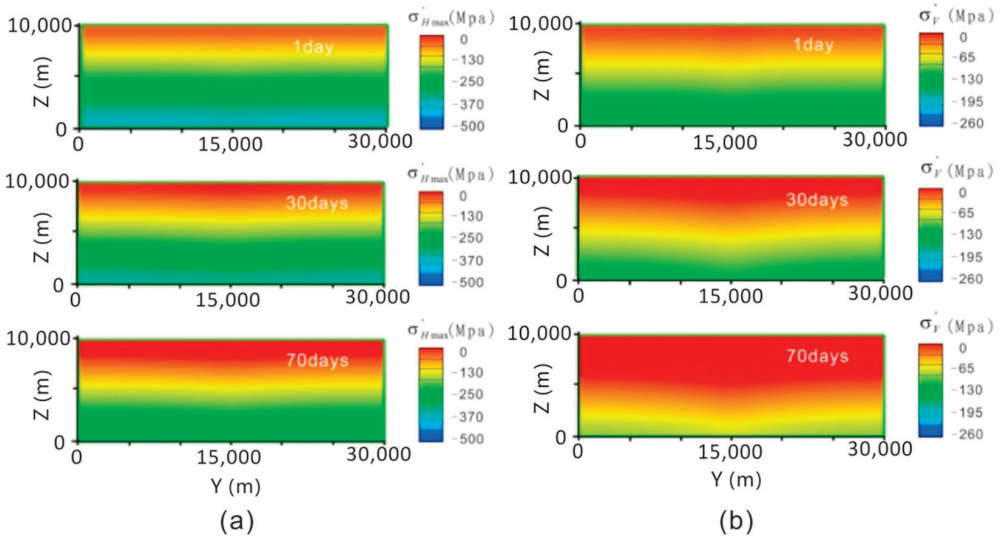

Figure 6. The distribution of effective stress (**a**) in the X-direction $\sigma'_{H\max}$; (**b**) in the Z-direction σ'_v during the fluid intrusion.

4.3. Fault Reactivation Caused by Fluid Intrusion

Fault reactivation occurs after rock failure, and it is then followed by earthquakes [40,41]. Calculating the fault reactivation area caused by fluid intrusion is helpful in analyzing the spatiotemporal distribution of aftershocks triggered by pore pressure diffusion. Based on the effective stresses calculated above, we can estimate the fault reactivation area using Equation (4).

Fault reactivation will occur when the ratio of the effective stresses in the X- and Z-directions exceed the limiting stress difference q shown in Equation (4), which is influenced by the static friction coefficient μ_s. For the Longmenshan fault zone, q is 3.13 when μ_s is assumed to be 0.6 [39]. The ratio of the effective stress in the X- and Z-directions at 10 days, 25 days, and 70 days are shown in Figure 7, where the red area indicates where the fault may reactivate. It suggests that fault reactivation area expands gradually over time in both the X- and Z-directions.

The locations of aftershocks in the area NA for 70 days are plotted in Figure 8a. The spatiotemporal distribution of aftershocks in the area NA shows that most aftershocks locate in the central area initially (red circles) and they expand gradually with time to some extent (blue circles). We should note that computer-aided algorithms would be helpful for a comprehensive analysis of such area/volume in further study. Furthermore, based on the fault reactivation area calculated above (the red area in Figure 7), we delineate the contour of fault reactivation area calculated numerically (Figure 8b). Such comparison of Figure 8a,b provides insights into the correlation between the spatiotemporal distribution of aftershocks and the fault reactivation area.

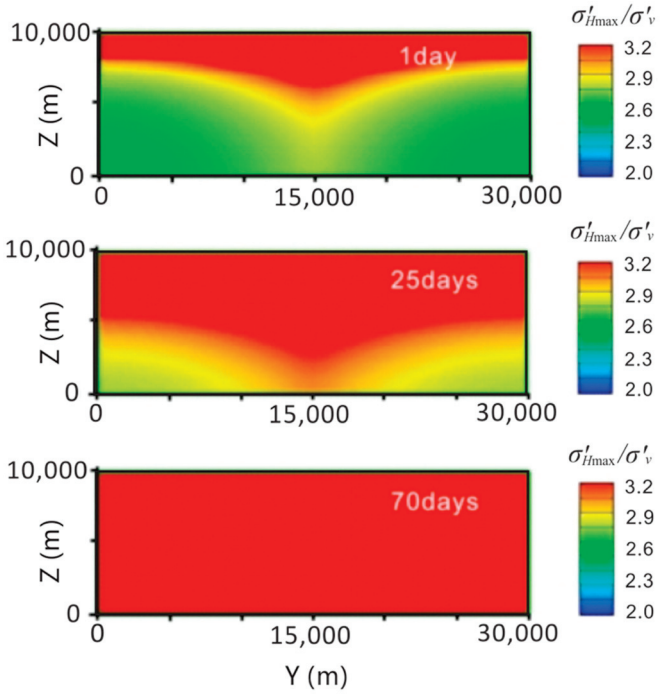

Figure 7. The distribution of the stress ratio σ'_{Hmax}/σ'_v during the fluid intrusion.

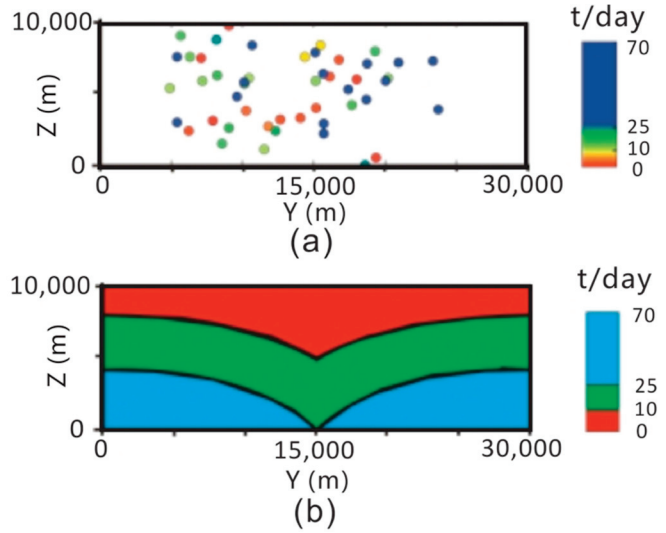

Figure 8. A comparison of the spatiotemporal distribution of aftershocks and the numerical simulation of the fault reactivation area. (**a**) The aftershock distribution at different times. (**b**) The calculated fault reactivation area at different times.

5. Discussion

5.1. Aftershock Triggering Mechanisms and Pore Pressure Diffusion

Based on the results of this study, we suggest that the aftershocks in the area NA are mainly triggered by pore pressure diffusion along the fault. The Longmenshan fault has been very tectonically active since the Cenozoic. It has been under compression due to the collision between the Indian and Eurasian Plates, and the maximum horizontal stress has been increasing until the Wenchuan earthquake, which led to a release of stress. At the same time, there are some studies indicating that deep fluids were likely to exist in the Longmenshan fault zone prior to and during the Wenchuan earthquake. Stress changes generated by the mainshock may lead to the diffusion of fluid trapped along the fault, then

the increased pore pressure caused fault reactivation and triggered aftershocks where the rock stress was at the critical state.

Some aftershocks in the *r–t* plot (Figure 2c) did not follow the envelope line, particularly early in the aftershock sequence. Stress transfer may be the main triggering mechanism of these aftershocks. These aftershocks display burst-like characteristics in *r–t* space [29], but they do not gradually migrate away from the initiation point over time. Although the stress transfer caused by the mainshock may have triggered some aftershocks in the initial stage, pore pressure diffusion may predominate the aftershocks in the area NA afterwards.

Focal mechanism tomography (FMT) is one of the main methods to estimate the excess pore pressure in a source region. Excess pore pressures were in the range of 0~60 MPa for the 2009 L'Aquila earthquake in Italy [11]. In this study, the estimated range of the increase in pore pressure caused by fluid intrusion is 0~80 MPa, which is comparable with the results of the L'Aquila earthquake. In addition, the larger increase in pore pressure along the dip than along the strike is similar to the results of the Matsushiro earthquake [40]. However, in addition to the mechanical aspect, the chemical effect of fluid should also be considered in future research, which may contribute to change the composition of the fluid and rock during fluid migration and hydraulic–mechanical interactions [42].

5.2. Spatiotemporal Distribution of Aftershocks and Pore Pressure Diffusion

In the hydraulic–mechanical coupling model, the evolution of the fault reactivation area calculated is correlated with the spatiotemporal distribution of aftershocks in the area NA. Several investigations of the 1965–1967 Matsushiro earthquake swarm in Japan have also suggested that the migration of deep fluids may have strongly influenced swarm activity [40]. The spatiotemporal distribution of the Matsushiro earthquake swarm is also comparable with the evolution trend of the fault reactivation area in this study [43]. Here, we studied the area NA for analyzing the correlation between the pore pressure diffusion and the aftershocks distribution. Nevertheless, it does not mean that only the aftershocks in the area NA might be related to deep fluid intrusion along the Longmenshan fault zone. This is due to the fact that the geological structure and the focal mechanism of aftershocks are similar in the area NA [29], which indicates that the seismogenic process of the area tends to be uniform. Therefore, the influences of heterogeneous structure and complex stress state along the fault zone on the spatiotemporal distribution of aftershocks have been minimized. However, for analyzing the triggering mechanism of aftershocks and pore pressure diffusion process of fluid intrusion along the whole Longmenshan fault zone, several aspects require further study, as discussed in the following.

First, in the modeling process, we treated fluid as the main factor affecting aftershock activity. However, there may be other important factors, such as the mechanical effect of fault slip, the interaction between aftershocks, or the effect of seismic waves. Additionally, the trapped fluid intrusion area is assumed as a point in the model due to the fact that the dimension of the trapped fluid area is very small compared to the modeling area NA, e.g., [16,44]. However, in the case of the dimension of the modeling area decreasing, the source term might be depicted as a line or other shapes constrained by the geophysical data, which should be explored in the further study. Additionally, the location of the intrusion point and the flow rate of the source term is assumed as constant in this study. We should note that these critical properties may contain uncertainties due to the limitation in the insufficient observation data, which should be further explored. Second, the heterogeneity and anisotropy of rocks and a non-uniform stress distribution along the fault may also affect the spatiotemporal distribution of aftershocks. The permeability of fault rocks affects the fluid migration, which may influence the spatiotemporal distribution of aftershocks [13,45]. Thus, a model with heterogeneous permeability based on upscaling permeability for fractured rocks should be explored in a future study [46]. Furthermore, the sensitivity analysis should be further investigated for such key parameters listed in Table 1, which may have a significant impact on the coupled hydraulic–mechanical model. Third, a different

initial stress state in the model may influence fault reactivation during fluid migration. Advanced methods for calculating crustal stress, e.g., [47], could help in constraining our hydraulic–mechanical model and thus may yield a better match between the real data and model results. Fourth, the model solved the pore-pressure diffusion equation numerically and fault reactivation area analytically, and we noted that recent contributions, e.g., [16,48], built models with coupled fluid–mechanical equations for analyzing the relationship between aftershock and fluid diffusion. Calculation of deformations and displacements should be further studied.

Therefore, it is necessary to further consider the heterogeneity and anisotropy of rocks, the properties of the fluid source, and the related dynamics during aftershocks. Based on the results of scientific drilling in the Wenchuan fault, further research is needed to combine seismology and geochemistry to obtain comprehensive poroelastic parameters and understand their changes along the fault during the aftershock sequence.

5.3. Numerical Aspects of the Model

Considering the Longmenshan fault zone is very large horizontally and the distance between most aftershocks and their initial point (which is located at the bottom-center of the model) is less than 10 km in the studied area (Figure 2c), a rectangle fault plane 30 km × 11.5 km (dip angle 60°, 11.5 = 10/sin(π/3)) is built for eliminating the boundary effect in the horizontal and vertical directions.

The Wenchuan aftershocks were distributed along the Longmenshan fault zone (Figure 1). Especially, the model dimension of the studied area NA is 30 km × 30 km × 10 km, which is still very large and is not feasible for computation when the meshes are very fine. Considering the assumed homogeneous hydraulic properties within the fault plane, which yields more stable results than those of the heterogeneous model, a 1 km × 1 km (30 × 10) grid is assumed. The calculated results in Figures 4 and 5 demonstrate that the change of pore pressure reached the top boundary (i.e., the Earth's surface), which may affect the distribution of pore pressure. In addition, for demonstrating the stability and reliability of the numerical models, sensitivity analyses of mesh and model size have been conducted (Figure 9). It is shown that either refining the grid block of 0.75 km × 0.77 km (40 × 13) for the fault plane (green color) or enlarging the model dimension of 30 km × 40 km × 10 km (blue color), the calculated pore pressures at 30 days are very close regarding the numerical model used in the previous study (red color). The relative errors are roughly evaluated, and are below 6%.

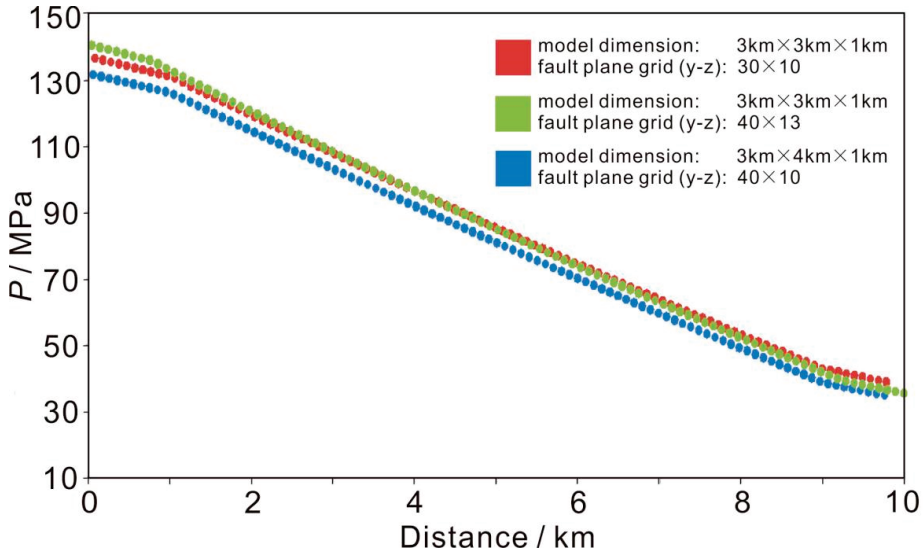

Figure 9. Pore pressure along the dip from the intrusion point in the fault plane for varied model and grid dimensions.

6. Conclusions

Based on previous studies of the Wenchuan earthquake and the spatiotemporal distribution of aftershocks with respect to pore pressure diffusion of deep fluids, we established a three-dimensional hydraulic–mechanical coupling model to investigate pore pressure diffusion and its mechanical effects in the fault plane using FLAC3D. During fluid intrusion into the fault plane, the pore pressures increase significantly by up to 80 MPa within 70 days in the study area NA. The increase in pore pressure, ΔP, along the fault dip is greater than that along fault strike on the fault plane. During 70 days, ΔP decays from the intrusion point with an averaged gradient of 0.8 MPa/km and 1.1 MPa/km along the dip and strike direction, respectively. The increase in pore pressure on the fault plane reduces the maximum and minimum effective stresses and thus can lead to fault reactivation. The evolution of the fault reactivation area calculated in the model is compared with the spatiotemporal distribution of aftershocks, taking into account the assumed input parameters and measurements of other studies. Our results provide insights for understanding the triggering mechanisms of the Wenchuan aftershocks.

Author Contributions: Conceptualization, Y.L.; methodology, T.C.; investigation, G.Z.; data curation, T.C.; writing—original draft preparation, T.C.; writing—review and editing, Y.L.; supervision, Y.L.; project administration, Y.L.; funding acquisition, Y.L. All authors have read and agreed to the published version of the manuscript.

Funding: This work was funded by the "Wenchuan Earthquake Fault Scientific Drilling" of the National Science and Technology Planning Project, grant number WFSD-10, Natural Science Foundation of Shandong Province, China (ZR2019BD028), Scientific Research Foundation of Shandong University of Science and Technology for Recruited Talents (2019RCJJ004).

Data Availability Statement: The data used to numerical simulations of this study are available from the corresponding author upon.

Acknowledgments: We would like to thank the editor and two anonymous reviewers for their efforts and constructive comments. The data for the model is available upon request from the first author. We thank Duoxing Yang, Xiaolong Sun, and Bin Zhang for fruitful discussions.

Conflicts of Interest: The authors declare no conflict of interest.

References

1. Liu, Y.; Chen, T.; Xie, F.; Du, F.; Yang, D.; Zhang, L.; Xu, L. Analysis of fluid induced aftershocks following the 2008 Wenchuan Ms 8.0 earthquake. *Tectonophysics* **2014**, *619*, 149–158. [CrossRef]
2. Liu, Y.W.; Shi, J. Information characteristics of ground fluid precursor on continental strong earthquakes. *Acta Seismol. Sin.* **2000**, *22*, 102–107. [CrossRef]
3. Wang, C.Y.; Manga, M. *Earthquakes and Water*; Springer: New York, NY, USA, 2009; pp. 1–38.
4. Zhang, Q.; Zeng, J.; Lou, K.; Li, S.; Yang, X.F.; Wu, Z.F.; Gao, X.Q. Seismic response of bacterial community structures at No.10 Spring in Urumqi. *Acta Seismol. Sin.* **2012**, *34*, 706–715.
5. Wang, B.; Liu, Y.; Sun, X.; Ma, Y.; Zhang, L.; Ren, H.; Fang, Z. Hydrogeological and geochemical observations for earthquake prediction research in China: A brief overview. *Pure Appl. Geophys.* **2018**, *175*, 2541–2555. [CrossRef]
6. Miller, S.A.; Collettini, C.; Chiaraluce, L.; Cocco, M.; Barchi, M.; Kaus, B.J. Aftershocks driven by a high-pressure CO_2 source at depth. *Nature* **2004**, *427*, 724. [CrossRef]
7. Parotidis, M.; Shapiro, S.A.; Rothert, E. Evidence for triggering of the Vogtland swarms 2000 by pore pressure diffusion. *J. Geophys. Res. Solid Earth* **2005**, *110*, B05S10. [CrossRef]
8. Zhao, D.; Kanamori, H.; Negishi, H.; Wiens, D. Tomography of the source area of the 1995 Kobe earthquake: Evidence for fluids at the hypocenter? *Science* **1996**, *274*, 1891–1894. [CrossRef]
9. Kayal, J.R.; Zhao, D.; Mishra, O.P.; De, R.; Singh, O.P. The 2001 Bhuj earthquake: Tomographic evidence for fluids at the hypocenter and its implications for rupture nucleation. *Geophys. Res. Lett.* **2002**, *29*, 2152. [CrossRef]
10. Ichihara, H.; Mogi, T.; Hase, H.; Watanabe, T.; Yamaya, Y. Resistivity and density modelling in the 1938 Kutcharo earthquake source area along a large caldera boundary. *Earth Planets Space* **2009**, *61*, 345–356. [CrossRef]
11. Terakawa, T.; Zoporowski, A.; Galvan, B.; Miller, S.A. High-pressure fluid at hypocentral depths in the L′Aquila region inferred from earthquake focal mechanisms. *Geology* **2010**, *38*, 995–998. [CrossRef]
12. Nur, A.; Booker, J.R. Aftershocks caused by pore fluid flow? *Science* **1972**, *175*, 885–887. [CrossRef] [PubMed]

13. Bosl, W.J.; Nur, A. Aftershocks and pore fluid diffusion following the 1992 Landers earthquake. *J. Geophys. Res.* **2002**, *107*, 2366. [CrossRef]
14. Shapiro, S.A.; Patzig, R.; Rothert, E.; Rindschwentner, J. Triggering of seismicity by pore-pressure perturbations: Permeability-related signatures of the phenomenon. In *Thermo-Hydro-Mechanical Coupling in Fractured Rock*; Kümpel, H.J., Ed.; Birkhäuser: Basel, Switzerland, 2003.
15. Waldhauser, F.; Schaff, D.P.; Diehl, T.; Engdahl, E.R. Splay faults imaged by fluid-driven aftershocks of the 2004 Mw 9.2 Sumatra-Andaman earthquake. *Geology* **2012**, *40*, 243–246. [CrossRef]
16. Heinze, T.; Hamidi, S.; Galvan, B.; Miller, S.A. Numerical simulation of the 2008 West-Bohemian earthquake swarm. *Tectonophysics* **2017**, *694*, 436–443. [CrossRef]
17. Ge, S.; Liu, M.; Lu, N.; Godt, J.W.; Luo, G. Did the Zipingpu reservoir trigger the 2008 Wenchuan earthquake? *Geophys. Res. Lett.* **2009**, *36*, L20315. [CrossRef]
18. Lei, X.L.; Ma, S.L.; Wen, X.Z.; Su, J.R.; Du, F. Intergated analysis of stress and regional seismicity by surface loading-a case study of Zipingpu reservoir. *Seismol. Geol.* **2008**, *30*, 1046–1064.
19. Sun, Y.J.; Zhang, H.; Dong, S.W.; Zheng, L.; Zhang, B.; Cheng, H.H.; Shi, Y.L. Study on effect of the Zipingpu reservoir on the occurrence of the 2008 Wenchuan earthquake based on a 3D-poroelastic model. *Chin. J. Geophys.* **2012**, *55*, 2353–2361. (In Chinese)
20. Chen, Y. Did the reservoir impoundment trigger the Wenchuan earthquake? *Sci. China Earth Sci.* **2009**, *52*, 431–433. [CrossRef]
21. Du, J.G. The Petrophysical Influenced by Deep Fluid and Its Seismic Geological Significance. Ph.D. Thesis, University of the Chinese Academy of Sciences, Guiyang, China, 2003. (In Chinese)
22. Sibson, R.H. Rupturing in overpressured crust during compressional inversion-the case from NE Honshu, Japan. *Tectonophysics* **2009**, *473*, 404–416. [CrossRef]
23. Du, L.T. The significance of mantle juice (ACOHNS) fluid. *Geotecton. Metallog.* **1989**, *13*, 91–99.
24. Wang, G.Z.; Liu, S.G.; Xu, G.S.; Li, G.R. Characteristics of fluid inclusions in the central Longmenshan nappe. *J. Chengdu Univ. Technol.* **2002**, *29*, 394–398. (In Chinese)
25. Xu, Z.Q.; Li, H.B.; Wu, Z.L. Wenchuan earthquake and scientific drilling. *Acta Geol. Sin.* **2008**, *82*, 1613–1622. (In Chinese)
26. Lei, J.S.; Zhao, D.P.; Su, J.R.; Zhang, G.W.; Li, F. Fine seismic structure under the Longmenshan fault zone and the mechanism of the large Wenchuan earthquake. *Chin. J. Geophys.* **2009**, *52*, 339–345. (In Chinese) [CrossRef]
27. Lin, X.; Dreger, D.; Ge, H.; Xu, P.; Wu, M.; Chiang, A.; Zhao, G.; Yuan, H. Spatial and temporal variations in the moment tensor solutions of the 2008 Wenchuan Earthquake aftershocks and their tectonic implications. *Tectonics* **2018**, *37*, 989–1005. [CrossRef]
28. Tian, Q.J.; Diao, G.L.; Hao, P.; Feng, X.D.; Sun, J. Earthquake geology of the Wenchuan M8.0 mainshock and its aftershocks. *Earthquake* **2009**, *29*, 141–148. (In Chinese)
29. Yukutake, Y.; Ito, H.; Honda, R.; Harada, M.; Tanada, T.; Yoshida, A. Fluid-induced swarm earthquake sequence revealed by precisely determined hypocenters and focal mechanisms in the 2009 activity at Hakone volcano, Japan. *J. Geophys. Res. Solid Earth* **2011**, *116*, B04308. [CrossRef]
30. Liu, Y.W.; Xu, L.Q.; Yang, D.X. Pore pressure diffusion characteristics of Longtan reservoir-induced-earthquake. *Chin. J. Geophys.* **2011**, *54*, 1028–1037. (In Chinese)
31. Chen, T.; Liu, Y.W.; Yang, D.X.; Zhang, L.; Fang, Z.; Xu, L.Q. The role of pore pressure in earthquake triggering and process of swarm earthquakes and aftershocks. *Prog. Geophys.* **2012**, *27*, 2407–2417. (In Chinese)
32. Sun, X.; Yang, P.; Zhang, Z. A study of earthquakes induced by water injection in the Changning salt mine area, SW China. *J. Asian Earth Sci.* **2017**, *136*, 102–109. [CrossRef]
33. Talwani, P.; Chen, L.; Gahalaut, K. Seismogenic permeability, k_s. *J. Geophys. Res. Solid Earth* **2007**, *112*, B07309. [CrossRef]
34. Carslaw, H.S.; Jaeger, J.C. *Conduction of Heat in Solid*; Oxford University Press: New York, NY, USA, 1959.
35. Terzaghi, K. *Erdbaumechanik auf Bodenphysikalischer Grundlage*; Deuticke: Leipzig, Germany, 1925.
36. Jaeger, J.C.; Cook, N.G.W. *Fundamentals of Rock Mechanics*; Methuen: London, UK, 1969.
37. Itasca. *FLAC3D Fast Lagrangian Analysis in Three Dimensions User's Guide*; Itasca Consulting Group: Minneapolis, MN, USA, 2009.
38. Deng, Q.D.; Zhang, P.Z.; Rang, Y.K.; Yang, X.P.; Min, W.; Chen, L.Q. Active tectonics and earthquake activities in China. *Earth Sci. Front.* **2003**, *10*, 66–73.
39. An, Q.M.; Ding, L.F.; Wang, H.Z.; Zhao, S.G. Research of property and actibity of Longmen Mountain fault zone. *J. Geod. Geodyn.* **2004**, *24*, 115–119.
40. Cappa, F.; Rutqvist, J.; Yamamoto, K. Modeling crustal deformation and rupture processes related to upwelling of deep CO_2-rich fluids during the 1965–1967 Matsushiro earthquake swarm in Japan. *J. Geophys. Res. Solid Earth* **2009**, *114*, B10304. [CrossRef]
41. Zhou, Y.F.; Liu, Z.C.; Cao, L.; Zhang, S.L.; Cui, S.B. Mechanical model of tectonic stress on fault movement induced microseism incidents. *Mod. Min.* **2012**, *4*, 20–22. (In Chinese)
42. Gratier, J.P.; Gueydan, F. Deformation in the presence of fluids and mineral reactions: Effect of fracturing and fluid-rocks interaction on seismic cycles. In *The Dynamics of Fault Zones*; Handy, M., Hirth, G., Rice, J., Hovius, N., Friedrich, A., Eds.; MIT Press: Cambridge, MA, USA, 2008; pp. 319–356.
43. Hagiwara, T.; Iwata, T. Summary of the seismographic observation of Matsushiro swarm earthquakes. *Bull. Earthq. Res. Inst. Univ. Tokyo* **1968**, *46*, 485–515. [CrossRef]
44. Hainzl, S.; Fischer, T.; Čermáková, H.; Bachura, M.; Vlček, J. Aftershocks triggered by fluid intrusion: Evidence for the aftershock sequence occurred 2014 in West Bohemia/Vogtland. *J. Geophys. Res. Solid Earth* **2016**, *121*, 2575–2590. [CrossRef]

45. Shi, Z.; Wang, G. Evaluation of the permeability properties of the Xiaojiang Fault Zone using hot springs and water wells. *Geophys. J. Int.* **2017**, *209*, 1526–1533. [CrossRef]
46. Chen, T.; Clauser, C.; Marquart, G.; Willbrand, K.; Hiller, T. Upscaling permeability for three-dimensional fractured porous rocks with the multiple boundary method. *Hydrogeol. J.* **2018**, *26*, 1903–1916. [CrossRef]
47. Zhang, Y.; Zhang, J. Lithology-dependent minimum horizontal stress and in-situ stress estimate. *Tectonophysics* **2017**, *703*, 1–8. [CrossRef]
48. Ucar, E.; Berre, I.; Keilegavlen, E. Three-dimensional numerical modeling of shear stimulation of fractured reservoirs. *J. Geophys. Res. Solid Earth* **2018**, *123*, 3891–3908. [CrossRef]

sustainability

MDPI

Article

Using ARC-D Toolkit for Measuring Community Resilience to Disasters

Muhammad Awfa Islam [1], Musabber Ali Chisty [1,*], Abdullah Fuad [2], Md. Mostafizur Rahman [3], Maliha Muhtasim [1], Syeda Erena Alam Dola [1], Fariha Jahin Biva [1] and Nesar Ahmed Khan [1]

[1] Institute of Disaster Management and Vulnerability Studies, University of Dhaka, Dhaka 1000, Bangladesh; awfaislam@du.ac.bd (M.A.I.); maliha.muhtasim@gmail.com (M.M.); erenaalam@gmail.com (S.E.A.D.); farihajahin03@gmail.com (F.J.B.); arnob.k7715@gmail.com (N.A.K.)
[2] Emergency Response Program, Caritas Bangladesh, Cox's Bazar Office, Dhaka 1217, Bangladesh; abdullahfuad100@gmail.com
[3] Department of Disaster and Human Security Management, Bangladesh University of Professionals, Dhaka 1216, Bangladesh; mostafizur@bup.edu.bd
* Correspondence: musabber.chisty@du.ac.bd

Abstract: Increased levels of resilience will reduce the negative consequences of any disaster and develop the capacities of communities to mitigate future disasters. The main objective of this study was to measure the level of resilience of two different communities in two different study areas and compare the resilience levels in terms of a flood. The study used the Analysis of Resilience of Communities to Disasters (ARC-D) toolkit. The study was conducted in two different areas to compare the level of community resilience. Both quantitative and qualitative methods were used in the study. A structured questionnaire was developed by using the toolkit. Results of the study indicated that communities in study area 1 were more resilient than communities in study area 2. Communities from study area 1 were more aware of their risk(s) and problem(s) and ensured proper strategies and actions to solve problems. On the other hand, communities in study area 2 were less aware of their risk(s). The strategies and actions implemented by the communities of study area 1 focused on the short-term problem(s), which reduced their level of resilience. Measuring resilience is very important in terms of developing disaster risk reduction (DRR) plans and incorporating DRR in the development process in lower-income countries and developing countries. As data scarcity is one of the major issues in developing countries, introducing a community resilience assessment mechanism can be a great help to reduce gaps in the planning and implementation process.

Keywords: community; resilience; measurement; risk; hazard; disaster

Citation: Islam, M.A.; Chisty, M.A.; Fuad, A.; Rahman, M.M.; Muhtasim, M.; Dola, S.E.A.; Biva, F.J.; Khan, N.A. Using ARC-D Toolkit for Measuring Community Resilience to Disasters. *Sustainability* **2022**, *14*, 1758. https://doi.org/10.3390/su14031758

Academic Editors: Stefano Morelli, Veronica Pazzi and Mirko Francioni

Received: 24 December 2021
Accepted: 19 January 2022
Published: 3 February 2022

1. Introduction

Bangladesh is one of the most disaster-prone countries in the world. Bangladesh is situated in the south Asian sub-continent, and due to its unique geographical location, it is always the subject and victim of different kinds of disasters. According to World Risk Index 2019, Bangladesh stood in 10th position in the list of most risky countries around the world [1]. Disasters are almost an annual phenomenon here, that severely render the sustainable and progressive activities of the country. Between 1900 and 2016, ninety major flood events happened in Bangladesh, which cost 52,437 people their lives and almost 32 million people were directly affected [2]. Moreover, poverty, lack of resources, limited preparedness, lack of awareness, and gaps in response mechanisms make the scenario worse. In developing countries, lack of information and data, limited hazard assessment mechanisms, dynamic characteristics of vulnerabilities of the communities, and inadequate knowledge about disaster management also hamper the process of achieving resilience at the community level [3–6].

In the year 2020, floods in the northern part of Bangladesh caused significant destruction. The duration of the 2020 flood was longer than in previous years. Further, the water level was much higher than for regular monsoon floods [7]. Most of the districts in the northern part faced the consequences of the 2020 flood. The government and non-government organizations (NGOs) initiated different projects and programs to support the innocent victims of the flood. Still, they are struggling to adjust to the unfavorable situation as people are not rehabilitated properly following a systematic plan of resilience. After a disaster, recovery activities should focus more on increasing the community's resilience and all other support. The Sendai Framework for Disaster Risk Reduction (SFDRR) 2015–2030 is mainly introduced to make communities more pro-active and initiate action long before the strike of a disaster. All the four priorities of SFDRR are focused to reduce loss of lives, properties, and environment and to make communities resilient.

In English, the word 'resilience' is derived from the Latin words resilire and salire, which stand for leap back, recoil, and spring again. In common words, resilience is said to be the responsiveness of anything in a reflective manner [8]. Resilience can be defined from different disciplines, and there are complexities in developing consensus regarding the definition [8]. In disaster studies, resilience is the ability of any organization to rebound or spring back to normal operations after an event has occurred [8]. Mainly, resilience is seen as a condition or trait or process or outcome that can bend but not break. The system which is capable of bouncing back even grows in the face of an adverse experience [9]. According to [10,11], resilience is related to the capacity of social units to reduce the effects of disasters and continue recovery activities after a disaster to reduce the disruption of social engagements. Furthermore, resilience is known as the ability of individuals to continue working in a given adverse condition [11,12]. Resilience is the level of capacity and resources of any community to organize itself before and during any hazardous event [13]. Resilience is known as the strategy or strength of someone or any society to adapt to face any traumatic situation and continue normal activities. Disaster resilience is related to the disturbance occurring from natural and human phenomenon and community coping capacity. Resilience has been seen as the combination of three criteria: capacity of a system to remain in the same domain but face changes in the system, capacity of a system to reorganize by itself, and capacity of a system to learn and cope with conditions [14]. The basic idea of community resilience is to bounce back to the previous position after any negative life events [15]. Community resilience has been identified in various ways by different researchers. According to [16], community resilience is a condition where the community will bounce forward to address the previous weaknesses and to take measures. It is also coined by [16] that community resilience is a transformational process rather than addressing the strengths of the community. The United Nations Environment Programme (UNEP) took another step to merge resilience with Disaster Risk Reduction (DRR). According to UNEP, through DRR, environments and eco-systems should revitalized to make communities and countries resilient [17]. In the study by [18], community resilience is seen from a public health perspective. As individual resilience is the adaptation strategy after facing an adverse event, community resilience is the ability of the community to sustain in adverse conditions and recover from negative events [18]. It has been identified by [19] that community resilience is not only related to social and natural context within which community lies but also related to the political and economic circumstances.

Community capacity is seen as an ability that will enhance the community's coping capacity after a disaster to manage future disasters [19]. In the work of [20], two major components are identified to define community disaster resilience: emergency adjustment and long-term adaptation capacity. According to [20], community disaster resilience is related to increasing disaster recovery capacity, introducing adjustment to an emergency, and ensuring long-term adaptation after a disaster, eventually reducing community vulnerability. It is also coined here that community disaster resilience is related to the community's social, political, economic, and environmental circumstances [20]. Community resilience is an ongoing process to develop community capacity to prevent or mitigate any stressful incident

and ensure response, recovery, and restoration after an incident [21]. In [22], resilience is indicated as the capacity or ability of communities, cities, or groups to endure hazardous events and recover from such events. Thus, community resilience is the ability of the community to continue functioning during and after a disaster [22]. A study of community disaster resilience [23] defined community disaster resilience as "the capacity or the ability of a community to anticipate, prepare for, respond to, and recover quickly from impacts of disaster". Here, community disaster resilience is related to recovering from hazardous conditions and learning processes to cope with current and future hazards [23]. Community resilience depends on different social values, capacities, social capital, knowledge, expertise, skills, physical assets, relation, economic conditions, and political conditions, reducing vulnerabilities and increasing adaptation capacities [24].

From all these definitions and concepts, it is very clear that community disaster resilience depends on current capacities to endure a hazardous event and develop abilities to adapt to future events without disrupting regular functioning. In this case, it is important to assess the different current social, economic, political, and environmental capacities of the community so that initiatives can be designed to increase the level of resilience. Both short-term responses and long-term efforts should be included. The main objective of this study was to measure the level of resilience of two different communities in two different study areas by using the Analysis of Resilience of Communities to Disasters (ARC-D) toolkit and compare their level of resilience in terms of the flood. The research questions were: to what extent the communities are resilient, and what level of differences are there between the two communities in terms of resilience? Studies explored that making a community resilient is a complex process and it is not easy to define a community that is resilient for all disasters [25]. Thus, assessing the level of resilience of communities for an individual disaster can be effective. This study explicitly focused on floods to assess the resilience level of two different communities. The study used the ARC-D toolkit to showcase the interconnectedness of different components which enable a community to become resilient [26].

2. ARC-D Toolkit

There are different resilience assessment tools that are used to assess the level of resilience from different perspectives. Assessing community resilience is a complex activity. There is no standard tool to measure community resilience. Each tool measures and assesses community resilience with different objectives. It is important to specify why we need to measure community resilience and how we will utilize the results. Tools, such as the Community Disaster Resilience Index (CDRI) [27], Community Disaster Resilience Framework for Iran [28], Community Resilience Score Card [24], Community Resilience framework [29], and Communities Resilience Index [30], are used to measure and analyze community disaster resilience. In this study, we used the Analysis of Resilience of Communities to Disasters (ARC-D) toolkit developed by GOAL [31]. The ARC-D toolkit was developed to measure community resilience under a 10-year project by GOAL [31]. This tool was used in 11 different countries to ensure its credibility, validity, reliability, and applicability. A long research process and testing ensured the proper development of the ARC-D toolkit. There are 30 specific indicators in the ARC-D toolkit to measure community resilience (Table 1). This toolkit is initially derived from the Characteristics of Disaster Resilient Communities guidelines developed by [32]. The main reason for using the ARC-D toolkit in this study was to measure community resilience from a comprehensive perspective. The ARC-D toolkit was designed to assess the multi-dimensional level of community resilience and explore the areas for further development. The ARC-D toolkit not only measures community resilience but also refers to possible actions for the future.

Table 1. ARC-D toolkit resilience components, questions, and measurement scores [31].

Sl. No.	Components	Questions	SFDRR Priority Areas
1	Participatory risk assessment	Has the community carried out a participatory risk assessment (hazard analysis, vulnerability and capacity analysis (VCA), impact analysis), shared the findings, and have human resources capable for conducting and updating this assessment? [31,33]	Priority 1: Understanding disaster risk
2	Scientific risk assessment	Does the community combine local knowledge and perceptions of risk with scientific knowledge, data, and assessment methods? [31,33]	
3	Dissemination of Disaster Risk Reduction (DRR) information	Have community members been exposed to/have participated in DRR specific awareness events (campaigns, discussions, and training) and have improved awareness and practices as a result? [31,33]	
4	Education of children on DRR	Are DRR and recovery knowledge and capacities being passed on to children formally through local schools and informally via oral tradition from one generation to the next? [31,33]	
5	DRR in development planning	Does the community see DRR as an integral part of plans and actions to achieve wider community goals (e.g., poverty alleviation, quality of life)? [31,33]	Priority 2: Strengthening disaster risk governance to manage disaster risk
6	DRR in land use planning	Does community decision-making regarding land use and management take disaster risk into account? [31,33]	
7	Community decision-making	Is the community leadership committed, effective, and accountable? [31,33]	
8	Inclusion of vulnerable groups	Are the vulnerable groups in the community included and represented in community decision-making and management of DRR and recovery? [31,33]	
9	Participation of women	Do women participate in community decision-making and management of DRR and recovery? [31,33]	
10	Rights awareness and advocacy	Is the community aware of its rights, relevant legal mechanisms, and responsible actors for their fulfillment, and does it advocate for these? [31,33]	
11	Partnerships for DRR and recovery	Are there clear, agreed, and stable partnerships between the community and other actors (local authorities, NGOs, businesses, etc.) that provide resources for DRR and recovery? [31,33]	
12	Sustainable environmental management	Does the community adopt sustainable environmental management practices that reduce disaster risk and new risks related to the effects of climate change? [31,33]	Priority 3: Investing in disaster risk reduction for resilience
13	Water security and management	Does the community have access to sufficient quantity and quality of water for domestic needs during disasters? [31,33]	
14	Health access and awareness	Do community members maintain good health in normal times through appropriate awareness and practices (adequate nutrition, hygiene, and health care access)? [31,33]	
15	Secure and sufficient food supply	Does the community have a secure and sufficient food supply during disasters? [31,33]	
16	Hazard-resistant livelihood practices	Does the community employ hazard-resistant livelihood practices for food and income security? [31,33]	
17	Access to market	Are the local market links for products, labor, and services protected against shocks? [31,33]	
18	Access to financial services	Are there affordable and flexible financial services (savings and credit schemes, microfinance), whether formal or informal? [31,33]	
19	Income and asset protection	Are household asset bases (income, savings, and convertible property) sufficiently large and diverse, and protected to ensure reduced vulnerability to disaster? [31,33]	
20	Social protection	Does the community have access to informal and formal social protection schemes that support disaster risk reduction and recovery? [31,33]	
21	Social cohesion and conflict prevention	Is there a sense of peace, security, and effective conflict prevention and mitigation mechanisms, both within the community and with other communities? [31,33]	
22	Critical infrastructure	Are the community's critical infrastructure and basic services resilient to disaster (e.g., located in low-risk areas, using hazard-resistant construction methods, and structural mitigation measures)? [31,33]	
23	Housing	Is the community's housing resilient to disaster (e.g., located in low-risk areas, using hazard-resistant construction methods, and structural mitigation measures)? [31,33]	
24	Contingency and recovery planning	Does the community use communally developed contingency and recovery plans that are widely understood and include measures to protect vulnerable groups? [31,33]	
25	Early warning system	Is there an operational early warning system in the community? [31,33]	
26	Capacity in preparedness, response, and early recovery	Does the community have a trained and operating organization in disaster preparedness, response, and early recovery? [31,33]	

Table 1. Cont.

Sl. No.	Components	Questions	SFDRR Priority Areas
27	Health services in emergencies	Does the community have access to health care facilities and health workers equipped and trained to respond to physical and mental health consequences of disasters, and supported by access to emergency health services, medicines, etc.? [31,33]	Priority 4: Enhancing disaster preparedness for effective response, and to "Build Back Better" in recovery, rehabilitation, and reconstruction
28	Education services in emergencies	Do education services have the capacity to continue operating in emergencies? [31,33]	
29	Emergency infrastructure	Are emergency shelters (purpose-built or modified) accessible to the community and have adequate facilities to meet basic needs for all of the affected population? [31,33]	
30	Leadership and volunteerism in response and recovery	Does the community play a leading role in coordinating preparedness, response, and recovery, reaching all affected people—including the most vulnerable—through organized and trained volunteers? [31,33]	

Measurement Score					
Score	1	2	3	4	5
Description	Minimum resilience	Low resilience	Medium resilience	Approaching resilience	Resilience

3. Data and Method

3.1. Research Approach

The study used a mixed-method approach for collecting and analyzing data. Both qualitative and quantitative methods were used to conduct the study. The quantitative method was focused on the ARC-D tool to measure community resilience. Previous studies showed that this toolkit can be successfully used to measure community resilience in a collective approach [31,33–36]. On the other hand, the qualitative method focused on collecting data on communities' perspectives, beliefs, and practices related to resilience. The quantitative method helps to use different measurements to summarize and quantify results [37]. Through the qualitative method, experiences and practices are recorded to gain a descriptive view related research objective [37]. The study mainly followed the triangulation of methods that ensure the use of more than one method in a study to achieve a more reliable and valid result [37]. Previous community resilience assessment models divided scales in physical, environmental, economic, natural, and social resilience to gain a more in-depth view. However, this study did not follow the process. This can be indicated as a methodological limitation of this study.

3.2. Study Area

Due to the geographical context and physical distribution of rivers, Bangladesh faces flooding regularly every year. The main river systems, which are known as the Ganges, Brahmaputra, and Meghna river systems, bring a huge amount of water from upstream and cause devastating floods in this deltaic area [38]. Rivers in Bangladesh are mainly in the old stage and deposit massive amounts of sediment every year. Due to this reason drainage capacity of the river system is reducing every year [38]. When a massive amount of water passes through the country, it overflows nearby areas and creates devastating floods. This study had chosen two different areas that faced the major impact of the 2020 flood: Sirajganj and Bogura. According to the Need Assessment Working Group 2020 report, approximately 338,455 people were affected by the flood in Sirajganj. On the other hand, according to the same report total of 127,875 people were affected by the flood in Bogura [7]. Throughout the study, areas are referred to as study area 1 = Sirajganj, and study area 2 = Bogura.

3.3. Sample Size and Sampling

There were two study areas (Sirajganj and Bogura). Solvin's 1960 tool was used to select the sample size [39,40]. The formula and sample size are given below (Equation (1)):

$$n = N/\left(1 + N \times e^2\right) \quad (1)$$

where n = sample size, N = total population affected by 2020 flood (Sirajganj = 338,455, Bogura = 127,875) [7], e = margin of error (5%):

$$n = 466330 / \left(1 + 466330 \times (5\%)^2\right)$$

$$n = 399.66$$

A total of 435 respondents were surveyed during the study. After adjusting the missing responses with a 95 percent response rate, 413 responses were transferred for further assessment. After completing the coding and transcription of the data, finally, 410 responses were valid for final analysis. The samples were equally distributed in two study areas (Sirajganj = 205, Bogura = 205).

The study used the snowball sampling technique to select the samples in the study area. Snowball sampling is one of the major non-probability sampling techniques [37,41]. Under the snowball technique, primarily, the samples were selected randomly. After collecting data from a few samples, the respondents were asked to indicate from whom the study should collect the next responses. In this way the respondents who already participated in the study helped to select new samples. A network of samples was developed through this technique. Non-probability sampling techniques help to reach the convenient samples as much as possible [37,42]. The criteria to become a sample in the study were: the respondent must be 15 years old or above, be a permanent member of the study communities, and have faced the impacts of the 2020 flood.

3.4. Data Collection Tool

3.4.1. Quantitative Method

As part of the quantitative approach, a survey tool was used to collect the data. The ARC-D toolkit was followed to develop a structured questionnaire to collect data from the communities (Table 1). The questionnaire was administered by trained data enumerators who translated each question for the respondents and collected the responses. There is a total of 30 components in the ARC-D toolkit. There are specific questions for specific components with a special measurement scale [31]. Responses of questions were collected using a 5-level Likert scale representing 1 = minimum resilience and 5 = full resilience (Table 1). The components of the toolkit are also aligned with the priorities of the Sendai Framework for Disaster Risk Reduction (SFDRR) 2015–2030.

3.4.2. Qualitative Method

The study also used an observation tool as part of the qualitative method. The observation tool helps to gain a broader picture of any field and collect perspective-based information [37]. The main reason behind using a qualitative tool is to gather the information that will support or deny the quantitative findings. Only number-based results are not enough to develop a comprehensive picture of the study communities.

3.5. Data Analysis

Quantitative data were coded and analyzed using IBM SPSS version 25 [43]. The descriptive statistical analysis helped to assess the resilience level. The whole quantitative analysis followed the process from the ARC-D toolkit. Responses of the samples were analyzed, and the mean values were gathered for each component. With the total mean value of each community, the level of resilience was defined. Table 2 shows the scale for assigning community resilience levels according to the ARC-D score [31]. The qualitative data were analyzed based on commonality and differences in the responses. All the common responses were accumulated and discussed with quantitative findings.

Table 2. Community resilience levels [31].

Resilience Level	Score	Description
Very low resilience	30–45	Very limited awareness and knowledge of the problem(s). No action taken [31,33]
Low resilience	46–75	A certain awareness of the problem(s), willingness to act, some actions taken, but actions are fragmented, and solutions are only short term [31,33]
Medium resilience	76–105	Awareness of the problems and long-term actions taken, but not related to a long-term strategy and/or addressing all aspects of the problem(s) [31,33]
Close to resilience	106–135	Long-term actions, in accordance with a predefined strategy, addressing the main aspects of the problem(s), but are inhibited by persistent shortcomings in their implementation [31,33]
Resilience	136–150	Long-term actions are undertaken in accordance with a pre-defined strategy assessing all aspects of the problem(s); they are sustainable and supported by the community [31,33]

3.6. Ethical Considerations

The project proposal and tools were ethically reviewed and approved by the institutional ethical review committee of the Institute of Disaster Management and Vulnerability Studies, University of Dhaka. The committee included both internal and external members. All the respondents participated in the study voluntarily. Prior consent was collected before collecting the data. During the whole study, the research team followed a strong ethical guideline in every stage.

4. Results

4.1. Socio-Demographic Information

Demographic information showed that 55.6 percent of the respondents were male, and 44.4 percent were female. As getting access to women of the household was difficult in the study areas, the number of female respondents is comparatively low. The majority of the respondents were from the 26–35 years age group. Most of the respondents were married and did not have any formal education. The income and expense levels among the respondents were very low. A significant number of respondents depended on peer group-based loans to maintain their families. A low level of income represents a higher level of economic vulnerability (Table 3).

Table 3. Socio-demographic information of the respondents.

Sl. No.	Characteristics	Percent		*p*-Value	Df
		Study Area 1	Study Area 2		
	Sex				
1	Male	28.8	26.8	0.426	1
	Female	21.2	23.2		
	Age				
	<18	2.2	1.7		
	18–25	12.7	11.9		
2	26–35	14.7	14.7	0.002 **	36
	36–45	10.1	12.2		
	>45	10.3	9.5		
	Marital status				
3	Single	5.4	2.7	0.087	2
	Married	44.6	47.3		
	Educational status				
	No formal education	23.9	25.4		
4	Primary level	11.7	16.3	0.024 *	7
	Secondary level	10.7	7.4		
	Higher secondary level and above	3.7	0.9		

Table 3. Cont.

Sl. No.	Characteristics	Percent		*p*-Value	Df
		Study Area 1	Study Area 2		
5	Monthly household expenses (in BDT)			0.001 **	17
	<5000	1.6	2.9		
	5000–10,000	37.1	41.0		
	10,000–20,000	10.0	6.1		
	>20,000	1.3	0.0		
6	Monthly household income (in BDT)			0.000 ***	22
	<5000	0.4	2.5		
	5000–10,000	31.6	40.6		
	10,000–20,000	14.6	6.8		
	>20,000	3.4	0.1		
7	Number of family member(s)			0.001 **	11
	<5	21.0	25.1		
	5–10	27.0	24.8		
	>10	2.0	0.1		

* $p < 0.05$, ** $p < 0.01$, *** $p < 0.001$.

4.2. Community Resilience Level

The following section discusses the results of community resilience measurement activity. In the methodology section, the scoring system and process of collecting data are already discussed. The results in Table 4 are presented to clearly show the comparison of the level of community resilience between the two study areas.

Communities in study area 1 saw disasters as an integral part of their development process. They tried to include disaster-related issues in their development activities. As a result, they have scored a medium level of resilience. On the other hand, communities in study area 2 mostly did not have any idea about how to include disasters in development planning (Table 4). Some of the community members thought about disasters during their livelihood planning. For this reason, they have scored a lower level of resilience. Communities in both study areas were not greatly aware of DRR in land use planning. Due to this, both of the study areas showed low resilience levels in DRR related land use. Community leaders in study area 1 were very proactive related to DRR related activities. The majority of the respondents from study area 1 shared that local leaders work effectively in the pre, during, and post phases of a flood. However, community leaders and political members of study area 2 were not very active in the phases of a flood. Most of the respondents in study area 2 regretted that they did not see that many interventions from community leaders during the recent flood. Both study areas still lag behind in terms of ensuring inclusiveness in the DRR process. Vulnerable groups, especially women, did not receive many opportunities to share their voices in the decision-making platforms. Qualitative data disclosed that limited education and a lower level of income make people more vulnerable to disasters. These vulnerable were socially deprived by other community members. Following this, in both study areas, people were not greatly aware of their rights and legal mechanisms related to DRR. Though communities in study area 1 scored better on the resilience measurement scale, there were still areas for development. Due to the availability of different NGOs in study area 1, the partnership-related resilience was comparatively better in study area 1. However, the communities in study area 2 lagged in partnership-related resources, which hindered their level of resilience. Altogether, study area 1 was in a better position in the governance-related resilience components. Strengthening disaster risk governance is one of the priorities of SFDRR (2015–2030). Ensuring participation of community members in decision-making platforms, building the capacity of local governments, developing a partnership with different organizations, mobilizing resources to vulnerable areas, including at-risk groups in

the planning process, and prioritizing the needs of communities can support strengthening the disaster risk governance.

Table 4. Community resilience level scores [31,33].

Sl. No.	Component	$\bar{x}$		σ		*p*-Value
		Study Area 1	Study Area 2	Study Area 1	Study Area 2	
1	Participatory risk assessment	3.67	1.78	1.032	0.538	
2	Scientific risk assessment	3.50	1.86	1.008	0.570	
3	Dissemination of DRR information	3.24	1.77	1.241	0.509	
4	Education of children on DRR	3.18	1.88	1.241	0.524	
5	DRR in development planning	3.00	1.72	1.122	0.452	
6	DRR in land use planning	2.59	1.92	0.833	0.713	
7	Community decision-making	3.46	1.87	1.319	0.367	
8	Inclusion of vulnerable groups	2.07	1.61	0.918	0.588	
9	Participation of women	2.87	1.56	1.399	0.517	
10	Rights awareness and advocacy	2.91	1.72	1.312	0.520	
11	Partnerships for DRR and recovery	3.31	1.56	1.501	0.497	
12	Sustainable environmental management	2.14	1.79	1.022	0.723	
13	Water security and management	3.92	4.07	0.794	0.671	
14	Health access and awareness	1.91	2.98	1.020	1.014	0.000 ***
15	Secure and sufficient food supply	2.13	1.53	1.050	0.547	
16	Hazard-resistant livelihoods practices	1.84	1.62	0.685	0.579	
17	Access to market	1.61	1.30	0.659	0.458	
18	Access to financial services	2.10	1.66	1.005	0.559	
19	Income and asset protection	1.83	1.58	0.818	0.495	
20	Social protection	2.27	1.65	1.143	0.487	
21	Social cohesion and conflict prevention	3.50	3.66	0.958	0.891	
22	Critical infrastructure	2.13	1.66	0.989	0.474	
23	Housing	2.15	1.50	1.009	0.520	
24	Contingency and recovery planning	2.42	1.60	0.869	0.490	
25	Early warning system	3.41	1.60	1.475	0.566	
26	Capacity in preparedness, response and early recovery	4.08	2.08	0.772	0.527	
27	Health services in emergencies	1.84	1.76	1.078	0.481	
28	Education services in emergencies	1.70	1.55	0.717	0.537	0.005 **
29	Emergency infrastructure	3.55	4.19	1.054	0.519	0.000 ***
30	Leadership and volunteerism in response and recovery	3.29	1.53	1.425	0.573	
	Total Score	81.62	60.56			

** $p < 0.01$, *** $p < 0.001$.

In the participatory risk assessment component, study area 1 scored a medium level of resilience. On the other hand, study area 2 showed a low level of resilience. Following this, study area 1 also showed a medium level of resilience in terms of scientific risk assessment, whereas study area 2 lagged behind. In study area 1, respondents agreed that they had participated in DRR related different training and awareness-raising programs which ensured effective dissemination of DRR information. On the other hand, communities from study area 2 had very little opportunity to participate in DRR information dissemination programs. Furthermore, in study area 1, respondents shared that schools in their communities had formal structures to share DRR related knowledge with children. Whereas children from study area 2 rarely heard about DRR related information in their schools (Table 4). Qualitative data indicated that communities in study area 1 received risk assessment-related training from different non-governmental organizations (NGOs) which were working in their area for a long time. These NGOs organized different awareness-raising programs too. Observation-based data explored that in study area 2, there was almost no intervention related to DRR related knowledge sharing, which ultimately reduced the possibilities of the communities to understand the disaster in their area. If community members become

aware of the risks, they will increase their level of preparedness. One of the first stages to become resilient is identifying the risks. The first priority of SFDRR is also understanding disaster risk. If the communities can assess their risks, they will be able to propose possible preparedness measures too.

Both of the study area communities were not very aware of sustainable environmental management activities (Table 4). However, communities in study area 1 had shown some practices related to environmental management, including specific places in the community for garbage deposition, planting trees near riverbanks to reduce erosion during and after a flood, using modern sanitation systems, and avoiding open defecation, etc. In such a scenario, communities in study area 2 did not have many activities related to sustainable environmental management. These data related to community practices were collected through the qualitative tool. In some components, study area 2 scored better than study area 1. One of them was water security and management. Due to raising the tube wells, communities in study area 2 had access to safe drinking water during the recent flood. Communities in study area 1 were also working to raise their water sources and increase resilience. In components, such as health access and awareness, social cohesion, and conflict prevention, study area 2 showed a better level of resilience than study area 1. Communities in study area 2 were relatively more aware of healthy practices and had better access to healthcare during normal periods than study area 1. Furthermore, communities in study area 2 were more cautious about preventing conflicts. Qualitative data indicated that the community feeling was higher among the respondents of study area 2. In study area 2, community members rush to support each other during a disaster with limited resources. On the other hand, study area 1 had areas to develop related to healthy practices and social cohesion. Other than these several components, study area 1 scored higher than study area 2, including secure and sufficient food supply, hazard-resistant livelihood practices, access to market, access to financial services, income and asset protection, social protection, critical infrastructure, and housing. Qualitative data showed that study area 1 received more resources from both internal (government) and external (NGOs) agencies related to these components, which supported them to score comparatively better than study area 2. Individually, however, study area 1 was lagging behind, and there were areas for improvement. Increasing investment for increasing disaster resilience should be a priority in both study areas. Disaster Risk Reduction (DRR) related investments can come from both governmental and non-governmental agencies. The priority of these investments should be increasing levels of resilience within communities.

Respondents of study area 1 shared that they received training related to contingency and recovery planning (Table 4). Most of the respondents in study area 1 took measures before the monsoon so that they could manage the flood, which was imminent to take place. On the other hand, respondents in study area 2 were not aware of contingency planning. Though they did practice individual preparedness, there was no sign of community-based contingency and recovery planning. In study area 1, respondents had a community-based flood early warning system. An NGO helped them to install a water level measurement scale in the river near the study area. The NGO also provided training to communities about measuring water levels, monitoring and disseminating warnings, and ensuring proper response to the warnings. At the same time, there was no community-based warning system in study area 2. Respondents shared that they learned about the recent flood from radios and from SMS communication from their relatives who faced flooding before them. The absence of a community-based flood warning system increases vulnerability and reduces resilience. It was only in the emergency infrastructure component that study area 2 scored higher than study area 1. There were a large number of flood shelter centers in study area 2 which increased their infrastructure-related resilience. The number of flood shelter centers in study area 1 was comparatively low. Other than this, in components such as capacity in preparedness, education in emergencies, and leadership and volunteerism in response recovery, respondents from study area 1 showed a higher level of resilience than study area 1. Qualitative data explored that external interventions from NGOs were

the main reason for a higher level of community resilience. External interventions helped communities of study area 1 to become more prepared for responding to floods and for recovering effectively. Communities will be more resilient if the level of preparedness is increased for effective response and recovery.

There is a significant relationship between the components and the study areas ($p < 0.001$, $p < 0.01$). The relationship indicates that the level of resilience differs in terms of study areas. Due to physical, economic, social, environmental, cultural, and institutional vulnerabilities, study areas achieved a different level of resilience in each component. The total resilience score of study area 1 was 81.62, and study area 2 was 60.56 (Table 4). According to the community resilience level score (Table 2), the total score of study area 1 represented a medium level of resilience. According to the description, the communities in study area 1 were aware of the problem(s) in their area, and they had taken some sort of long-term action related to the problem(s), but these actions and strategies did not cover all the aspects of the problem(s). Moreover, the strategies implemented to increase the level of resilience in study area 1 were not focused on the long-term perspectives. On the other hand, the total resilience score of the study area represented a low level of resilience. According to the description from Table 2, the communities in study area 1 were aware of the problem(s) to some extent, and there were some actions and strategies to manage those problems. However, these actions were only for short-term solutions to the problems. Results concluded that study area 1 was comparatively more resilient than study area 2.

5. Discussion

The results already indicated the difference in community resilience between the two areas. The study should also reflect the community resilience from the Sendai Framework for Disaster Risk Reduction (SFDRR) 2015–2030 perspective. According to Table 1, the components are related to the four priorities of SFDRR. Figure 1 shows community resilience based on the priorities of SFDRR.

There were four components under priority 1 (Table 1). In understanding disaster risk, study area 1 scored 13.59, whereas study area 2 scored 7.29 (Figure 2). The main reason for the higher resilience level of study area 1 was external interventions. The communities of study area 1 developed partnerships with different NGOs, which increased their capacities to understand the risks. Communities received training and participated in awareness-raising programs organized by the NGOs, which helped them to strengthen their resilience. A completely different picture was seen in study area 2. The communities in study area 2 rarely participated in any risk assessment-related activities. They were aware of the risks in their area by their own traditional knowledge. Moreover, a small number of interventions were seen in study area 2 to raise awareness of disasters such as floods. Disaster-related information was not disseminated at the community level. Formal educational institutions, such as schools, did not have any programs related to DRR. Thus, the level of understanding of disaster risk was low in study area 2. Understanding disasters and sharing information related to disasters are vital components to make communities resilient [44]. Participating in different decision-making platforms and assessment processes is important as these will help communities to understand the risk of disasters and work to reduce risk [28]. Human capital, such as education, knowledge about disasters, and information related to risk, help to implement risk reduction strategies and increase community disaster resilience [23]. This study summarizes that activities, such as training for community members related to DRR, organizing awareness-raising programs, incorporating DRR related knowledge in the formal education system, introducing participatory risk assessment, and including vulnerable groups in assessment, will help communities to understand disaster risks and increase the level of community resilience.

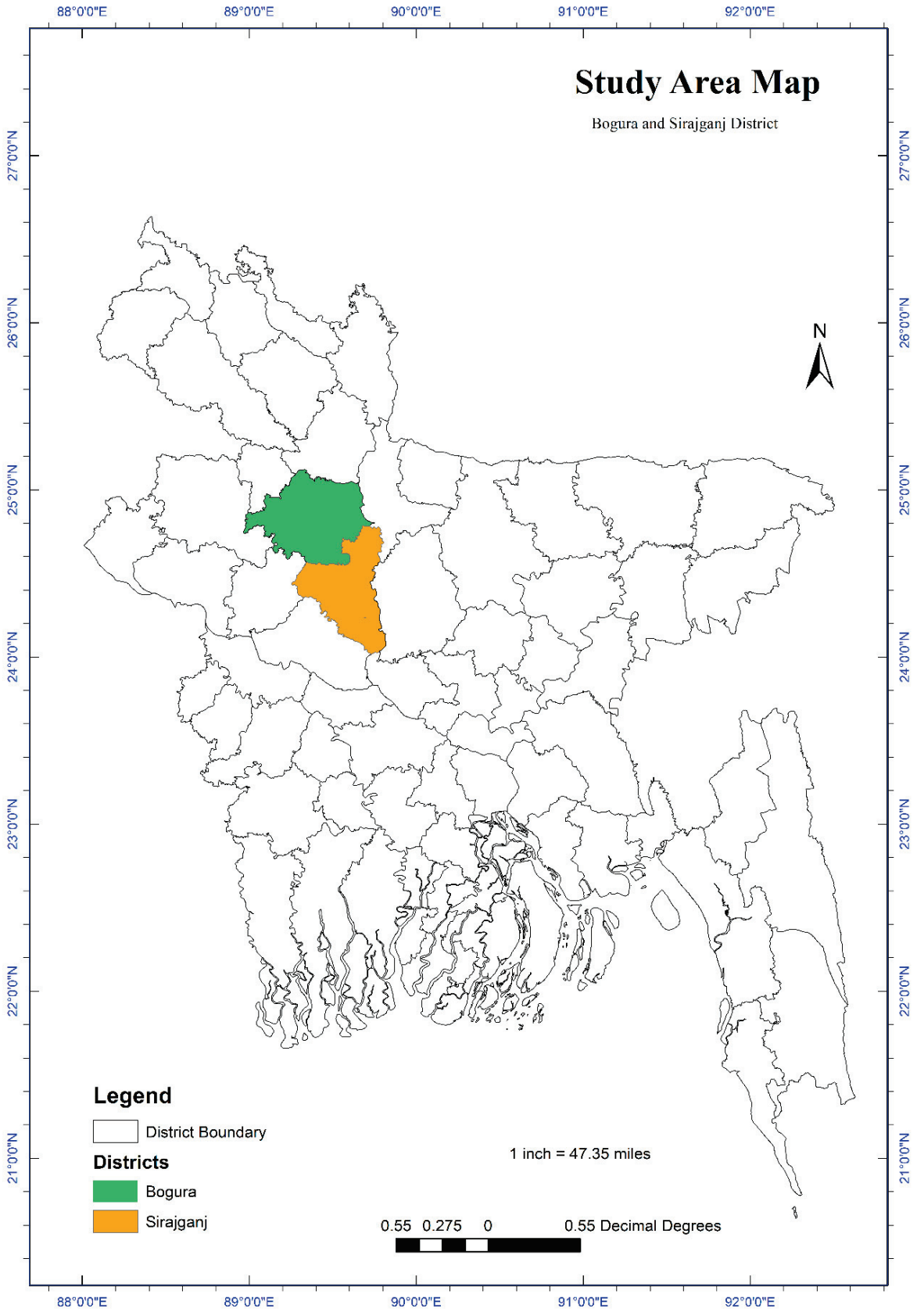

Figure 1. Study area map (source: developed by the study).

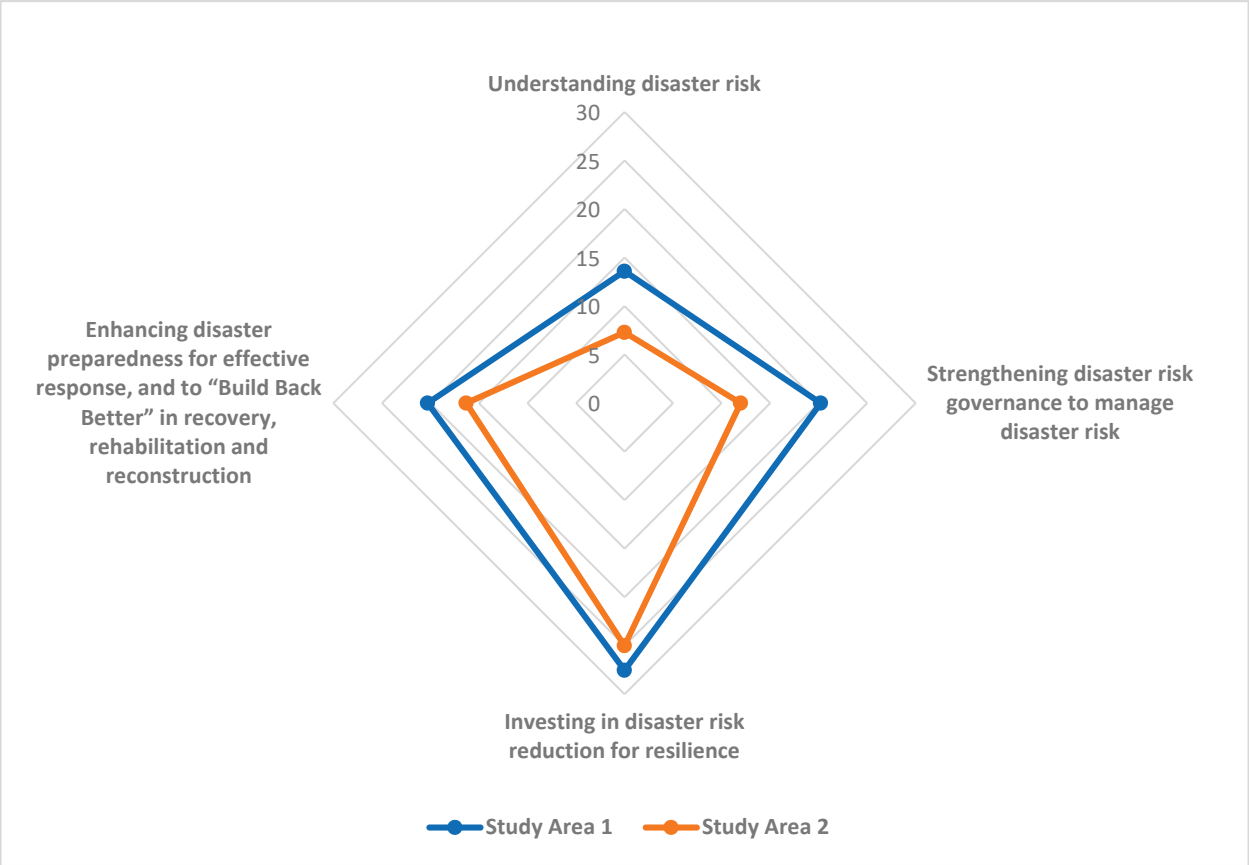

Figure 2. Community Resilience Level (Based on SFDRR Priorities).

Priority 2 had seven components (Table 1). Study area 1 also showed a higher level of resilience in terms of disaster risk governance. The score was 20.21 (Figure 2). Local government and community-based organizations (CBOs) tried to ensure the participation of community members in the decision-making process. Communities in study area 2 were more aware of their rights and responsibilities. Further, women and other vulnerable groups in study area 2 had the opportunity to be included in the DRR process. These reasons supported communities in study area 2 to achieve a higher level of resilience. On the other hand, study area 1 scored 11.96 in disaster risk governance points. The reasons behind the lower level of community resilience were limited access to decision-making platforms, lack of participation of women and other vulnerable groups in DRR activities, ineffective local government agencies, and a lower level of partnership with non-governmental agencies. Studies explored that availability of a strong local government, inclusion of vulnerable populations, equal socio-economic development, and enhancement of community capacities can increase community disaster resilience [30,45,46]. Furthermore, policies that are developed through prioritizing the needs of vulnerable groups can promote community resilience [45]. DRR related training programs for local government agencies can be one of the major interventions to strengthen disaster risk governance. If personnel-related local governments learn about interventions that can reduce disaster risk, they will ensure an inclusive DRR approach. Along with this, it is also important to increase the capacity of at-risk groups. Women, children, persons with disabilities, and elderly people, should be prioritized in DRR planning and programs. Reducing vulnerabilities through strong disaster risk governance will make communities resilient.

In the third priority, communities from both of the study areas scored very closely. The community resilience level of study area 1 was 27.53, and study area 2 was 25.0 (Figure 2). Though both of the study areas scored very closely, the community resilience level was still low. There were 12 components in priority 3 (Table 1). A lower level of

community resilience indicated that there were areas, such as health access during the normal period, access to financial services and markets, social protection, critical infrastructure, housing, and income and asset protection, that needed more interventions. Investing more to reduce disaster risk will also increase community resilience. Previous studies identified the importance of each component to make a community resilient. For instance, social capital and access to economical supports were seen as major variables to improve levels of community resilience [47,48]. Resources, such as social networks, communication infrastructure, transportation, livelihood and employment, economic development, and funding, etc., are seen as capitals which construct the framework to make communities resilient [49,50]. Furthermore, economic stability, equitable income, access to healthcare facilities, availability of critical infrastructure, and sense of community, etc., are also identified as major components to uphold a community as resilient [51–53]. For the study areas, local organizations, national agencies, governmental organizations, international development agencies, and private companies should invest more in these areas to make communities resilient. A developed healthcare system, shock-resistant critical infrastructures, strategies to protect income and assets, inclusive social protection programs, and accessible financial services can increase the level of community resilience. All of these interventions need a higher level of investment.

There were seven components in priority 4 (Table 1). Study area 1 scored 20.29, and study area 2 scored 16.31 in this priority area of SFDRR (Figure 2). Effective disaster preparedness and response depend on several factors, such as contingency planning, education in emergencies, access to health care during emergencies, crisis-related infrastructures such as flood shelter centers, and voluntary activities of different groups. Communities in study area 1 were well ahead in terms of disaster preparedness and recovery planning than communities in study area 1. To enhance the level of preparedness for effective response, government and non-government agencies in study area 2 should come forward. Availability of a recovery plan and business continuity plan, increasing preparedness capacity of communities through training and awareness raising, including exercise and drills in the education system before disasters, improving resources to continue education during disasters and properly managing critical infrastructure such as emergency shelters, etc., will support the process of making communities resilient [54,55]. Involving communities in developing contingency planning can ensure effective response after a disaster and make communities resilient [56]. Furthermore, developing volunteer groups to support vulnerable populations during emergencies will amplify the level of community disaster resilience [57]. The idea of resilience is related to the idea of 'build back better'. Community resilience depends on the capacity of the community, which helps to absorb any shock and cope with the new condition. After any disaster, communities should focus on building their capacity to cope with similar disasters in the future. The idea of resilience is mainly related to response and recovery. If a community can effectively respond to any disaster and recover from the effects in the shortest period then that community will be identified as resilient. Moreover, recovery-related activities must make the community strong enough to absorb a similar level of shocks in the future.

6. Conclusions

The study used the ARC-D toolkit to measure community resilience in two different areas. In nature, the study followed a comparative analysis style. Both study areas had scopes to enhance their resilience. The results indicated that communities in study area 1 were more resilient than study area 2. The ARC-D toolkit helped not only to measure community resilience but also to show the areas which needed immediate attention. Measuring community resilience is very important in developing DRR plans and incorporating DRR in the development process. If concerned authorities are not aware of the level of resilience of different communities, development plans will not be fruitful. A clearer picture of community resilience can be developed if the community receives the opportunity to share its perspectives related to DRR. Involving communities in every aspect of DRR will

help to create ownership and ensure the sustainability of interventions. Using a tool that involves the community in measuring resilience should be prioritized. The ARC-D toolkit has the efficiency to support concerned authorities by measuring community resilience and providing inputs for future planning. As previous literature explained, successful use of this tool in different contexts, as in this study, will strengthen the appropriateness of this tool to be applicable in developing countries.

Author Contributions: Conceptualization, M.A.I. and M.A.C.; methodology, M.A.C.; software, M.A.C. and A.F.; validation, M.A.C., A.F., M.M.R. and S.E.A.D.; formal analysis, M.A.I., M.A.C., M.M. and F.J.B.; investigation, M.A.C., S.E.A.D., M.M.R., F.J.B. and N.A.K.; resources, M.A.I., M.A.C. and N.A.K.; data curation, M.A.C., A.F., M.M.R., S.E.A.D. and M.M.; writing—original draft preparation, M.A.C., M.M., F.J.B. and N.A.K.; writing—review and editing, M.A.I., M.A.C., M.M.R., S.E.A.D., F.J.B. and N.A.K.; visualization, M.A.C.; supervision, M.A.C.; project administration, M.A.C.; funding acquisition, M.A.I. All authors have read and agreed to the published version of the manuscript.

Funding: The study did not receive any funding.

Institutional Review Board Statement: The study was conducted according to the guidelines of the Declaration of Helsinki and approved by the Ethical Review Committee of the Institute of Disaster Management and Vulnerability Studies, University of Dhaka, Dhaka-1000, Bangladesh (date of Approval: 3 August 2020).

Informed Consent Statement: Informed consent was obtained from all subjects involved in the study.

Data Availability Statement: Data will be shared on a requirement basis.

Acknowledgments: The study acknowledges the support of the University of Dhaka. Furthermore, the study acknowledges the support of all the respondents of the study. Also, the study acknowledges the support of persons who were involved in data collection, data cleaning and digitization, data analysis, and proofreading activities.

Conflicts of Interest: The authors declare no conflict of interest.

References

1. Bündnis Entwicklung Hilft, Ruhr University Bochum—Institute for International Law of Peace and Armed Conflict (IFHV). *World Risk Report 2019—Focus: Water Supply*; Bündnis Entwicklung Hilft, Ruhr University Bochum—Institute for International Law of Peace and Armed Conflict: Berlin/Heidelberg, Germany, 2019; Available online: https://reliefweb.int/sites/reliefweb.int/files/resources/WorldRiskReport-2019_Online_english.pdf (accessed on 2 June 2021).
2. Centre for Research on the Epidemiology of Disasters—CRED. EM-DAT: The Emergency Events Database—Université catholique de Louvain (UCL). Available online: www.emdat.be (accessed on 2 June 2021).
3. Pinos, J.; Quesada-Román, A. Flood Risk-Related Research Trends in Latin America and the Caribbean. *Water* **2021**, *14*, 10. [CrossRef]
4. García-Soriano, D.; Quesada-Román, A.; Zamorano-Orozco, J.J. Geomorphological hazards susceptibility in high-density urban areas: A case study of Mexico City. *J. S. Am. Earth Sci.* **2020**, *102*, 102667. [CrossRef]
5. Quesada-Román, A.; Ballesteros-Cánovas, J.A.; Granados-Bolaños, S.; Birkel, C.; Stoffel, M. Improving regional flood risk assessment using flood frequency and dendrogeomorphic analyses in mountain catchments impacted by tropical cyclones. *Geomorphology* **2021**, *396*, 108000. [CrossRef]
6. Quesada-Román, A.; Castro-Chacón, J.P.; Boraschi, S.F. Geomorphology, land use, and environmental impacts in a densely populated urban catchment of Costa Rica. *J. S. Am. Earth Sci.* **2021**, *112*, 103560. [CrossRef]
7. Needs Assessment Working Group (NAWG). *Bangladesh: Monsoon Floods 2020 Coordinated Preliminary Impact and Needs Assessment*; Needs Assessment Working Group: Dhaka, Bangladesh, 2020; Available online: https://reliefweb.int/sites/reliefweb.int/files/resources/nawg_monsoon_flood_preliminary_impact_and_kin_20200725_final_draft.pdf (accessed on 2 June 2021).
8. Wattie, J.; Masys, A.J. Enabling Resilience: An Examination of High Reliability Organizations and Safety Culture through the Lens of Appreciative Inquiry. In *Disaster Management: Enabling Resilience. Lecture Notes in Social Networks*; Masys, A., Ed.; Springer: Cham, Switzerland, 2015; pp. 157–176. [CrossRef]
9. Southwick, S.M.; Bonanno, G.A.; Masten, A.; Panter-Brick, C.; Yehuda, R. Resilience definitions, theory, and challenges: Interdisciplinary perspectives. *Eur. J. Psychotraumatol.* **2014**, *5*, 25338. [CrossRef]
10. Bruneau, M.; Chang, S.E.; Eguchi, R.T.; Lee, G.C.; O'Rourke, T.D.; Reinhorn, A.M.; Shinozuka, M.; Tierney, K.; Wallace, W.A.; von Winterfeldt, D. A Framework to Quantitatively Assess and Enhance the Seismic Resilience of Communities. *Earthq. Spectra* **2003**, *19*, 733–752. [CrossRef]

11. Bhamra, R.S.; Dani, S.; Burnard, K.J. Resilience: The concept, a literature review and future directions. *Int. J. Prod. Res.* **2011**, *49*, 5375–5393. [CrossRef]
12. Paton, D.; Smith, L.; Violanti, J. Disaster response: Risk, vulnerability and resilience. *Disaster Prev. Manag. Int. J.* **2000**, *9*, 173–180. [CrossRef]
13. Etkin, D. *Disaster Theory: An Interdisciplinary Approach to Concepts and Causes*, 1st ed.; Butterworth-Heinemann Elsevier Ltd: Oxford, UK, 2014; p. 368.
14. Shaw, R.; Sharma, A. (Eds.) *Climate and Disaster Resilience in Cities*; Community, Environment and Disaster Risk Management, Volume 6; Emerald Group Publishing Limited: Bingley, UK, 2011. [CrossRef]
15. Ronan, K.R.; Johnston, D.M. *Promoting Community Resilience in Disasters: The Role for Schools, Youth, and Families*; Springer Science + Business Media, Inc.: New York, NY, USA, 2005; p. 221.
16. Ride, A.; Bretherton, D. Conclusion: Community Resilience in Natural Disasters. In *Community Resilience in Natural Disasters*; Palgrave Macmillan: New York, NY, USA, 2011; pp. 169–193.
17. Nehren, U.; Sudmeier-Rieux, K.; Sandholz, S.; Estrella, M.; Lomarda, M.; Guillén, T. *The Ecosystem-Based Disaster Risk Reduction Case Study and Exercise Source Book*, 1st ed.; Partnership for Environment and Disaster Risk Reduction and Center for Natural Resources and Development: Geneva, Switzerland; Cologne, Germany, 2014.
18. Plough, A.; Fielding, J.E.; Chandra, A.; Williams, M.; Eisenman, D.; Wells, K.B.; Law, G.Y.; Fogleman, S.; Magana, A. Building Community Disaster Resilience: Perspectives From a Large Urban County Department of Public Health. *Am. J. Public Health* **2013**, *103*, 1190–1197. [CrossRef]
19. Joerin, J.; Shaw, R.; Takeuchi, Y.; Krishnamurthy, R. Assessing community resilience to climate-related disasters in Chennai, India. *Int. J. Disaster Risk Reduct.* **2012**, *1*, 44–54. [CrossRef]
20. Chen, L.-C.; Wang, Y.-W. Building community capacity for disaster resilience in Taiwan. *J. Disaster Res.* **2010**, *5*, 138–146. [CrossRef]
21. Chandra, A.; Acosta, J.; Stern, S.; Uscher-Pines, L.; Williams, M.V.; Yeung, D.; Garnett, J.; Meredith, L.S. Definition and Application of Community Resilience. In *Building Community Resilience to Disasters*; RAND Corporation: Santa Monica, CA, USA, 2011; pp. 7–10.
22. National Research Council. *Building Community Disaster Resilience through Private-Public Collaboration*; The National Academies Press: Washington, DC, USA, 2011; p. 142. [CrossRef]
23. Mayunga, J.S. *Understanding and Applying the Concept of Community Disaster Resilience: A Capital-Based Approach*; A draft working paper prepared for the Summer Academy for Social Vulnerability and Resilience Building: Munich, Germany, 22–28 July 2007.
24. Arbon, P.; Steenkamp, M.; Cornell, V.; Cusack, L.; Gebbie, K. Measuring disaster resilience in communities and households: Pragmatic tools developed in Australia. *Int. J. Disaster Resil. Built Environ.* **2016**, *7*, 201–215. [CrossRef]
25. Wisner, B.; Kelman, I. Community Resilience to Disasters. In *International Encyclopedia of the Social & Behavioral Sciences*, 2nd ed.; Wright, J.D., Ed.; Elsevier: Amsterdam, The Netherlands, 2015; pp. 354–360. [CrossRef]
26. Fitzpatrick, T. Community disaster resilience. In *Disasters and Public Health*, 2nd ed.; Clements, B.W., Casani, J.A.P., Eds.; Butterworth-Heinemann: Oxford, UK, 2016; pp. 57–85.
27. Yoon, D.K.; Kang, J.E.; Brody, S.D. A measurement of community disaster resilience in Korea. *J. Environ. Plan. Manag.* **2015**, *59*, 436–460. [CrossRef]
28. Ostadtaghizadeh, A.; Ardalan, A.; Paton, D.; Khankeh, H.; Jabbari, H. Community disaster resilience: A qualitative study on Iranian concepts and indicators. *Nat. Hazards* **2016**, *83*, 1843–1861. [CrossRef]
29. Chandra, A.; Williams, M.; Plough, A.; Stayton, A.; Wells, K.B.; Horta, M.; Tang, J. Getting Actionable About Community Resilience: The Los Angeles County Community Disaster Resilience Project. *Am. J. Public Health* **2013**, *103*, 1181–1189. [CrossRef] [PubMed]
30. Sherrieb, K.; Norris, F.H.; Galea, S. Measuring Capacities for Community Resilience. *Soc. Indic. Res.* **2010**, *99*, 227–247. [CrossRef]
31. Clark-Ginsberg, A.; McCaul, B.; Bremaud, I.; Cáceres, G.; Mpanje, D.; Patel, S.; Patel, R. Practitioner approaches to measuring community resilience: The analysis of the resilience of communities to disasters toolkit. *Int. J. Disaster Risk Reduct.* **2020**, *50*, 101714. [CrossRef] [PubMed]
32. Twigg, J. Characteristics of a Disaster-Resilient Community: A Guidance Note. 2007. Benfield UCL Hazard Research Centre Website. Available online: https://www.preventionweb.net/files/2310_Characteristicsdisasterhighres.pdf (accessed on 2 June 2021).
33. Chisty, M.A.; Rahman, M.; Khan, N.A.; Alam Dola, S.E. Assessing Community Disaster Resilience in Flood-Prone Areas of Bangladesh: From a Gender Lens. *Water* **2022**, *14*, 40. [CrossRef]
34. Fenxia, Z. The community resilience measurement throughout the COVID-19 pandemic and beyond -an empirical study based on data from Shanghai, Wuhan and Chengdu. *Int. J. Disaster Risk Reduct.* **2022**, *67*, 102664. [CrossRef]
35. Cruz, N. Measuring Informal Urban Settlements´ Pathway to Resilience Building. In *Proceedings of the IFoU 2018: Reframing Urban Resilience Implementation: Aligning Sustainability and Resilience, Barcelona, Spain, December 2018*; MDPI: Basel, Switzerland, 2018. [CrossRef]
36. Mehryar, S.; Sasson, I.; Surminski, S. Supporting urban adaptation to climate change: What role can resilience measurement tools play? *Urban Clim.* **2022**, *41*, 101047. [CrossRef]
37. Neuman, W.L. *Social Research Methods: Qualitative and Quantitative Approaches*, 7th ed.; Pearson: Essex, UK, 2009; p. 631.

38. Flood Forecasting & Warning Center; Processing & Flood Forecasting Circle; Bangladesh Water Development Board. Annual Flood Report 2016. Flood Forecasting & Warning Center Website. Available online: http://www.ffwc.gov.bd/images/annual16.pdf (accessed on 2 June 2021).
39. Tejada, J.; Punzalan, J. On the Misuse of Slovin's Formula. *Philipp. Stat.* **2012**, *61*, 129–136.
40. Chakraborty, U.; Bhat, S. The Effects of Credible Online Reviews on Brand Equity Dimensions and Its Consequence on Consumer Behavior. *J. Promot. Manag.* **2018**, *24*, 57–82. [CrossRef]
41. Creswell, J.W.; Clark, V.L.P. *Designing and Conducting Mixed Methods Research*, 3rd ed.; SAGE Publications Inc: Los Angeles, CA, USA, 2017.
42. Sarantakos, S. *Social Research*, 4th ed.; Red Globe Press: London, UK, 2013.
43. *IBM SPSS Statistics*, version 25; Campus licentie; IBM: Armonk, NY, USA, 2018. Available online: https://www.surfspot.nl/ibm-spss-25-statistics.html (accessed on 2 June 2021).
44. Nakamura, H.; Umeki, H.; Kato, T. Importance of communication and knowledge of disasters in community-based disaster-prevention meetings. *Saf. Sci.* **2017**, *99*, 235–243. [CrossRef]
45. Price-Robertson, R.; Knight, K. Natural disasters and community resilience: A framework for support. Child Family Community Australia (CFCA): Canberra, Australia, 2012. Available online: https://aifs.gov.au/cfca/sites/default/files/cfca/pubs/papers/a141862/cfca03.pdf. (accessed on 2 June 2021).
46. Cavaye, J.; Ross, H. Community resilience and community development: What mutual opportunities arise from interactions between the two concepts? *Community Dev.* **2019**, *50*, 181–200. [CrossRef]
47. Cutter, S.; Ash, K.; Emrich, C.T. The geographies of community disaster resilience. *Glob. Environ. Chang.* **2014**, *29*, 65–77. [CrossRef]
48. Chisty, M.A.; Alam Dola, S.E.; Khan, N.A.; Rahman, M. Intersectionality, vulnerability and resilience: Why it is important to review the diversifications within groups at risk to achieve a resilient community. *Contin. Resil. Rev.* **2021**, *3*, 119–131. [CrossRef]
49. Cox, R.S.; Hamlen, M. Community Disaster Resilience and the Rural Resilience Index. *Am. Behav. Sci.* **2014**, *59*, 220–237. [CrossRef]
50. Fekete, A. Critical infrastructure cascading effects. Disaster resilience assessment for floods affecting city of Cologne and Rhein-Erft-Kreis. *J. Flood Risk Manag.* **2020**, *13*, e312600. [CrossRef]
51. Cutter, S.L.; Burton, C.G.; Emrich, C.T. Disaster Resilience Indicators for Benchmarking Baseline Conditions. *J. Homel. Secur. Emerg. Manag.* **2010**, *7*, 1–25. [CrossRef]
52. Gwimbi, P. Linking rural community livelihoods to resilience building in flood risk reduction in Zimbabwe. *Jàmbá J. Disaster Risk Stud.* **2009**, *2*, 80–89. [CrossRef]
53. Cox, R.S.; Perry, K.-M.E. Like a Fish Out of Water: Reconsidering Disaster Recovery and the Role of Place and Social Capital in Community Disaster Resilience. *Am. J. Community Psychol.* **2011**, *48*, 395–411. [CrossRef] [PubMed]
54. Boin, A.; McConnell, A. Preparing for Critical Infrastructure Breakdowns: The Limits of Crisis Management and the Need for Resilience. *J. Contingencies Crisis Manag.* **2007**, *15*, 50–59. [CrossRef]
55. Zavaleta, K.W.; Asirvatham, U.; Callies, B.; Franz, W.B.; Scanlan-Hanson, L.; Molella, R.G. Improving Community Resilience through Disaster Simulation: How Simulation-based Education Augments Emergency Management Exercises. *J. Homel. Secur. Emerg. Manag.* **2018**, *15*, 20180002. [CrossRef]
56. Ohara, M.; Nagumo, N.; Shrestha, B.B.; Sawano, H. Evidence-Based Contingency Planning to Enhance Local Resilience to Flood Disasters. In *Recent Advances in Flood Risk Management*; Abbot, J., Hammond, A., Eds.; IntechOpen: London, UK, 2019; pp. 39–55. [CrossRef]
57. Pfefferbaum, R.L.; Pfefferbaum, B.; Nitiéma, P.; Houston, J.B.; Van Horn, R.L. Assessing Community Resilience: An Application of the Expanded CART Survey Instrument With Affiliated Volunteer Responders. *Am. Behav. Sci.* **2014**, *59*, 181–199. [CrossRef]

sustainability

MDPI

Article

An Assessment of Social Resilience against Natural Hazards through Multi-Criteria Decision Making in Geographical Setting: A Case Study of Sarpol-e Zahab, Iran

Davoud Shahpari Sani [1], Mohammad Taghi Heidari [2], Hossein Tahmasebi Mogaddam [2], Saman Nadizadeh Shorabeh [3], Saman Yousefvand [4], Anahita Karmpour [5] and Jamal Jokar Arsanjani [6,*]

1 Department of Demography, Faculty of Social Sciences, University of Tehran, Tehran 1417935840, Iran; dshahpari@ut.ac.ir
2 Department of Geography, Faculty of Humanities, University of Zanjan, Zanjan 3879145371, Iran; mt.heydari@znu.ac.ir (M.T.H.); tahmasebihossein@znu.ac.ir (H.T.M.)
3 Department of Remote Sensing and GIS, Faculty of Geography, University of Tehran, Tehran 1417935840, Iran; saman.nadizadeh@ut.ac.ir
4 Department of Sociology, Faculty of Social Sciences, University of Tehran, Tehran 1417935840, Iran; samanyousefvand@ut.ac.ir
5 Department of Political & Social Science, Institute of Sociology, Freie Universität Berlin, 14195 Berlin, Germany; anahita1366@zedat.fu-berlin.de
6 Geoinformatics Research Group, Department of Planning and Development, Aalborg University Copenhagen, A.C. Meyers Vænge 15, DK-2450 Copenhagen, Denmark
* Correspondence: jja@plan.aau.dk

Citation: Shahpari Sani, D.; Heidari, M.T.; Tahmasebi Mogaddam, H.; Nadizadeh Shorabeh, S.; Yousefvand, S.; Karmpour, A.; Jokar Arsanjani, J. An Assessment of Social Resilience against Natural Hazards through Multi-Criteria Decision Making in Geographical Setting: A Case Study of Sarpol-e Zahab, Iran. *Sustainability* **2022**, *14*, 8304. https://doi.org/10.3390/su14148304

Academic Editors: Stefano Morelli, Veronica Pazzi and Mirko Francioni

Received: 6 June 2022
Accepted: 5 July 2022
Published: 7 July 2022

Abstract: The aim of this study was to propose an approach for assessing the social resilience of citizens, using a locative multi-criteria decision-making (MCDM) model for an exemplary case study of Sarpol-e Zahab city, Iran. To do so, a set of 10 variables and 28 criteria affecting social resilience were used and their weights were measured using the Analytical Hierarchy Process, which was then inserted into the Weighted Linear Combination (WLC) model for mapping social resilience across our case study. Finally, the accuracy of the generated social resilience map, the correlation coefficient between the results of the WLC model and the accuracy level of the social resilience map were assessed, based on in-situ data collection after conducting a survey. The outcomes revealed that more than 60% of the study area falls into the low social resilience category, categorized as the most vulnerable areas. The correlation coefficient between the WLC model and the social resilience level was 79%, which proves the acceptability of our approach for mapping social resilience of citizens across cities vulnerable to diverse risks. The proposed methodological approach, which focuses on chosen data and presented discussions, borne from this study can be beneficial to a wide range of stakeholders and decision makers in prioritizing resources and efforts to benefit more vulnerable areas and inhabitants.

Keywords: social resilience; natural hazards; locative multi-criteria decision-making (MCDM) model; Sarpol-e Zahab

1. Introduction

According to United Nations estimates, more than 70 percent of the world's population will live in urban areas by 2050 [1]. Due to the population growth in cities, it is of great importance to consider the socio-economic and administrative processes related to the performance of cities, and to evaluate the resilience of residents to natural hazards [2,3]. Cities today have not only taken the path of development, but have also expanded their spatial areas into areas that need physical development against natural hazards to ensure they are ready to accommodate more people [4].

Natural hazards are "disasters that occur suddenly and cause harm to humans and the environment" [5,6]. These hazards can be highly devastating in terms of human lives, assets and infrastructure, and pose major challenges to sustainable urban development [7,8]. Therefore, preparing for these hazards can lead to increased adaptive capacity and sustainable livelihoods for urban communities [9,10]. One of the ways to prepare cities for these risks is to increase *social resilience* [7,11]. Adger [12] defines social resilience as the ability of individuals, groups, and communities/cities to cope with external stresses and environmental disturbances. The goal of this study wa/*s to assess social resilience with a view to finding ways to increase the resilience capacity of communities and strengthen the ability of citizens and urban managers to cope with the impacts of natural hazards [13].

Given the continuous growth of the urban population and its density, as well as the threat of natural hazards, it is of outmost importance to pay attention to, and strengthen, social resilience in cities as the backbone of disaster risk management [14,15]. Considering that natural disasters cause immense social disruption in cities, promoting social resilience as a capability not only helps to maintain the basic performance of cities, but also leads to the improvement and prosperity of cities after disasters [16]. Resilient cities are capable of positively responding to hazards or stresses [17,18]. These cities can also maintain their primary functions as a whole, despite existing tensions, and move towards sustainable development through a cohesive and integrated approach [3,19].

Iran is frequently affected by natural hazards due to its geographical and geological conditions [20,21], as 31.7 percent of the country's territory is exposed to natural hazards, and 70 percent of its population are residing in vulnerable areas [21,22]. Sarpol-e Zahab city has been one of the most affected cities by natural disasters in Iran in recent decades. Statistical and historical studies show that this city has experienced many natural disasters so far. Natural disasters such as earthquakes, floods, droughts, air pollution and dust storms are the main hazards that severely affect this city. Examples of natural disasters that have caused major challenges to the citizens of Sarpol-e Zahab and have, hence, indicated that the building of social resilience against natural hazards is an imperative, include the following: Floods in 1998 and 2007; Earthquakes in 2003, 2014 and 2017, and recent droughts and dust storms (Iran Crisis Management Organization, 2020).

Social resilience is influenced by various criteria with spatial reference, so the use of spatial systems and analysis can be useful in spatial measurement and analysis of social resilience. In addition, the use of spatial multifactor decision-making models can increase the accuracy of measurement. In this paper, GIS-MCDM spatial multi-criteria decision-making models were used to measure the social resilience of the Sarpol-Zahab urban areas. The general purpose of GIS-MCDM techniques is to help decision-making processes towards selecting the most suitable option among existing options. These techniques combine in-situ data and decision makers' priorities, based on decision-making principles [23,24]. Considering the fact that making a right and timely decision can have a substantial effect in choosing suitable options using various criteria, the need for a robust technique that can help various stakeholders is important. The MCDM techniques are effectively used in various studies, such as geothermal sources [25], usage of lands [26,27], migration [28,29], thermal comfort [30], solar energy [31,32] and natural hazards [33–35].

Many studies have been conducted in relation to analysis of resilience and its role in reducing the consequent effects of natural incidents, but previous studies to assess social resilience are descriptive and statistically-based, and the weight of effective metrics and user preferences are not considered. Therefore, to make data-informed decisions, it is necessary to consider various effective criteria in a comprehensive approach. As mentioned earlier, the GIS-MCDM approach can be very useful in this regard. Furthermore, previous studies have not combined GIS and MCDM. Therefore, the main objective of this study was to measure social resilience in Sarpol-e Zahab so as to raise awareness against natural hazards. The results of this study could be very useful and practical for managers and urban planners.

2. Literature Review

The term social resilience, in social systems, was first coined by Adger [12]. Social resilience provides a conceptual framework for measuring community capacity to cope with change and emergencies [36]. A resilient society is able to respond positively to changes or tensions and is able to maintain its core function as a society despite tensions. A particular change can have far-reaching and different consequences in different societies, and different societies will show different degrees of resilience to change. A resilient society not only minimizes the difficulty of overcoming vulnerability, but also implements it through education and adaptation to advance society [37]. According to Bogardi [38], social resilience is measured over time. In particular; how long does it take for a community to respond to an incident, organize itself, and integrate lessons learned before returning to a new practice? The amount of time it takes to escape a hazard not only affects a society's economic presence, but also its social context or the "intermediary" that holds it together. The longer this recovery lasts, the more likely society is to be destroyed as recession ensues and emotional and psychological pressures spread [39].

In recent years, several studies have been conducted on the analysis of social resilience and its role in reducing the effects of natural disasters. Some studies have identified *social harms*, *social capital* and *demographic characteristics* as features characterizing the resilience of societies to natural hazards [11,12,40–42]. Some studies [43,44] also consider *religious beliefs* and values to be effective in creating a sense of calm, hope, and a return to the pre-crisis state. Various studies [12,45–47] also *consider local community capabilities*, *diversity of resources/skills*, *level of awareness and human capital* as resilience requirements against hazards. Various studies [46,48–50] have also pointed out the negative effects of lack of *security* and *social inequality* on the resilience of society to disasters. Most previous attempts to assess social resilience are descriptive and statistically based, and the weight of effective metrics and user preferences are not considered. Moreover, this topic has not been studied visually and from a spatial perspective. Therefore, to make an accurate decision in this regard, it is necessary to consider various effective criteria in a comprehensive approach. As mentioned earlier, the GIS -MCDM approach can be very useful in this regard. Furthermore, previous research has not combined GIS and MCDM. Therefore, the main objective of this study was to measure the social resilience of urban areas in Sarpol-e Zahab with a view to reducing risk against natural hazards, based on multi-criteria decision models. The results of this study could be very useful and practical for managers and urban planners. Effective criteria in social resilience analysis and description of each of them are presented in Table 1.

Table 1. The variables used for assessing social resilience.

Variables	Sub-Variables	Description	References
Demographic Characteristics	Age Structure (population aged under 15 and over 65); Literacy Status; Gender (ratio); Population Density; Immigration; Female-headed households; Occupation Status	Population and its characteristics are among the most important criteria affecting the rate of resilience in a region. In order to achieve a resilient society, special attention should be given to the demographic structure and context of the regions and their changes. Accurate knowledge about the demographic structure of a region before, during and after the occurrence of hazards, is of particular importance.	[11,12,40–42,51–53]
Social harms	Poverty; Addiction; Suicide; Divorce	Social harms disturb relationships between members of the society, cause failures in social relations and lead to inability of society to integrate itself; this can be one of the important factors reducing the resilience of societies against crises.	[12,17,54–57]

Table 1. *Cont.*

Variables	Sub-Variables	Description	References
Social Capital	Social Trust; Social Participation; Social Integrity; Social Awareness; Social Support; Social Networks; Social Relations	Social capital, referring to the social relations of individuals with each other, can have a very positive effect on social resilience and developing security in cities. The greater the amount of social capital in a region, the more resilient that region will be in the course of a crisis.	[12,46,51,58–62]
Religious Beliefs and Values	-	Beliefs are considered as an essential factor in strengthening the social resilience of societies against hazards, having an influential role in creating a sense of calmness, hope and returning to a pre-crisis state.	[43,44,63,64]
The General Capability of Local Community	Sense of Belonging to a Place; Sympathy and Altruism; Cooperation	Membership in the local community is one of the necessities for resilience and an important resource for encouraging community members to be efficiently capable when faced with challenges. With a sense of local community, participation in social networks takes form and capabilities of individuals increase capabilities of the community to use internal resources when encountering crises.	[12,45–47,65,66]
Resources and Skills	-	Resources and skills in a society are positively correlated with social resilience of that society against crises, because they promote the qualities of time and effort spent on planning	[10,12,44,65,67–69]
Social Inequality	-	Inequalities lead a society to mistrustfulness, isolation and lawlessness; strengthening such unfairness leads to forming a kind of anger caused by disparities in individuals. This will affect social ties and break individual and group relationships.	[45,46,50,62,65]
Social Security	Theft; Murder; Individual Conflicts; Group Conflicts	In a society that has maximum security, it will be easily possible to implement knowledge of design and construction related to encountering hazards, through strengthening these features to achieve resilience.	[12,48,49,54]
Human Assets	Public Health; Having Trained and Skilled Workforce	Human assets bring flexibility power, which is one of the principals of resilience. Having a sufficient, skilled and trained workforce is a prerequisite for economic development and capacity building. This means that the more human assets available in society, equals more capacity to develop better resilience.	[11,40,46,62,70–72]
Awareness and ducation	-	The level of public awareness and knowledge about the incidents that might threaten them is very effective in building resilience of society and for proper reaction to the events; thus, greatly reducing the damage inflicted.	[11,47,62,65,66,72,73]

3. Materials and Methods

3.1. Study Area

The city of Sarpol-e Zahab is the center of a county with the same name in Kermanshah province, with an area of 1271 km^2, located between 45°52″ E longitude and 34°24″ latitude, in the western part of Iran, at the end of the slopes of the Zagros heights. According to the 2016 census, conducted by the Statistical Center of Iran (SCI), the city includes 35 urban areas (Figure 1). Regarding population, Sarpol-e Zahab is the third most populated county

in Kermanshah province. According to the latest census (mentioned above), the population of the county was 85,342, 53% of which (45,481) lived in urban areas. According to the official statistics of the Statistical Center of Iran, the city of Sarpol-e Zahab did not fare well in terms of social resilience indicators before the earthquake. A comparison of the average sex ratio, percentage of households headed by women, employment percentage, and literacy rate in the country, and in Sarpol-e Zahab city, shows that Sarpol-e Zahab city was in an unfavorable situation in all these indicators, compared to the country as a whole. In terms of statistics on suicide, divorce rate and unemployment, Sarpol-e Zahab is also in a worse situation than the country average. Being the city with the most unemployment among the country's cities indicates problems, such as addiction, domestic violence, reduction of social capital, etc. The city also ranks first in the country in suicides. In addition, the divorce rate in this city is higher than the national average, which may reduce social skills in this city. In areas where these conditions are evident, disaster prevention issues can no longer be given much importance. Therefore, based on the particular conditions in Sarpol-e-Zahab city, it can be said that the poor responses to the consequences of natural disasters, such as floods and earthquakes, are due to lack of risk management, lack of education, lack of empowerment and, finally, lack of social resilience. Sarpol-e Zahab has been categorized as one of the most disaster-prone cities of Iran, experiencing various natural hazards. According to field observations and reports from urban dwellers and experts from the earthquake-exposed areas of Kermanshah province, the damaged buildings and infrastructure resulting from previous earthquakes are not yet restored and living conditions are still unsuitable. The earthquake in 2017, with a magnitude of 7.3 on the Richter scale, was devastating and caused deaths exceeding 621, along with 9388 people injured and almost 70,000 people becoming homeless. Subsequent events such as torrential rains, lack of adequate emergency and temporary accommodation, the inadequacy of tents against cold and heat, social damage and increasing poverty, and the price of construction materials and labor have aggravated the situation (Iran Crisis Management Organization, 2020).

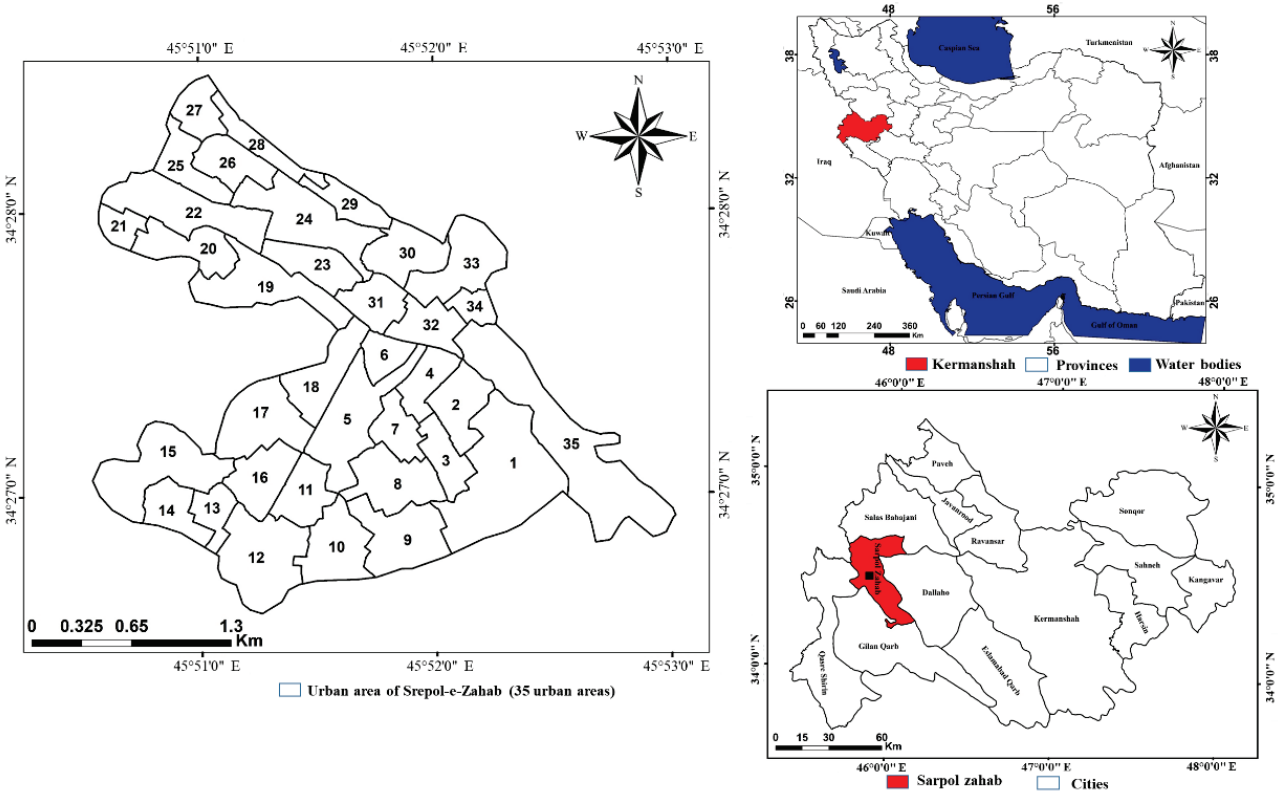

Figure 1. Study area.

3.2. Data Collection

The sources of the data used for each index is presented in Table 2. As is known, some data sources have been obtained using surveys and questionnaires with the support of the Iranian Sociological Association. In order to determine the sample size, we used the framework of the census by the Statistics Center of Iran in 2016. Cochran's Formula was applied to estimate an optimal sample size, which suggested 385 people to include in a random sampling setting.

Table 2. The characteristics of data used in this study.

Row	Data	Format	Source
1	Demographic Characteristics	Vector (polygon)	Civil Registration Organization and Statistics Center of Iran
2	Social harms	Vector (polygon)	National Plan for Family Conversations and Statistics Center of Iran
3	Social Capital	Vector (polygon)	Sarpol-e Zahab Health Center and Statistical Center of Iran
4	Religious Beliefs and Values	Vector (polygon)	Questionnaire
5	The General Capability of Local Community	Vector (polygon)	Questionnaire
6	Resources and Skills	Vector (polygon)	Questionnaire
7	Social Inequality	Vector (polygon)	Questionnaire
8	Social Security	Vector (polygon)	Sar-pol-e Zahab Police Force
9	Human Assets	Vector (polygon)	Questionnaire
10	Awareness and education	Vector (polygon)	Questionnaire

3.3. Overall Method

In Figure 2, the overall flowchart of the proposed methodology is illustrated. In the first step of this proposed approach, the effective social resilience variables were selected and standardized with reference to theoretical literature and previous studies. In the second step, the criteria were weighted based on experts' opinions and an Analytical Hierarchy Processes [28] method. In the third step, using the suggested GIS-MCDM approach and the map of criteria and the resulted weights, the final social resilience map of the target region was prepared. At the end, in the fourth step, the obtained results were assessed.

3.3.1. Variables Selection and Standardization

After reviewing experts' opinions and the literature related to the concept of resilience, a total of 28 sub-indicators embedded within 10 locative variables were selected for making social resilience maps. These selected variables included demographic characteristics, social harms, social capital, religious beliefs and values, general capability of the local community, resources and skills, social inequality, social security, human assets, and level of awareness and education (Table 1).

After the set of variables for assessing social resilience were selected, each index was stored on a locative database as a GIS map. GIS-MCDM requires standardized criterion maps, as evaluating all criteria together requires converting layers into comparable units [74]. In this study, it was, therefore, necessary to standardize the criteria, considering that the data of each index came from different sources, in order for the criteria to be comparable with each other.

As "maximum" values for some variables, and "minimum" values for other variables, have more significance regarding the definition of resilience, in the present study a "maximum–minimum" standardization method was employed. The variables were categorized into two main groups: benefit variables (the variables in which maximum value was of significance) and cost variables (the variables in which minimum value was

of significance). The benefit variables, including demographic characteristics, social capital, religious beliefs and values, general capability of the local community, resources and skills, social security, human capital, and the level of awareness and education were standardized through Equation (1), and the cost variables, including social harms, and social inequality were standardized through Equation (2) (Table 3). For instance, to calculate social capital, the higher the social capital, the higher the level of social resilience. Therefore, the maximum values were more important and, as a result, Equation (2) was adapted, while for the social harms variable, the lower the value of this index, the higher the social resilience. As a result, Equation (1) was applied to create a normal marker.

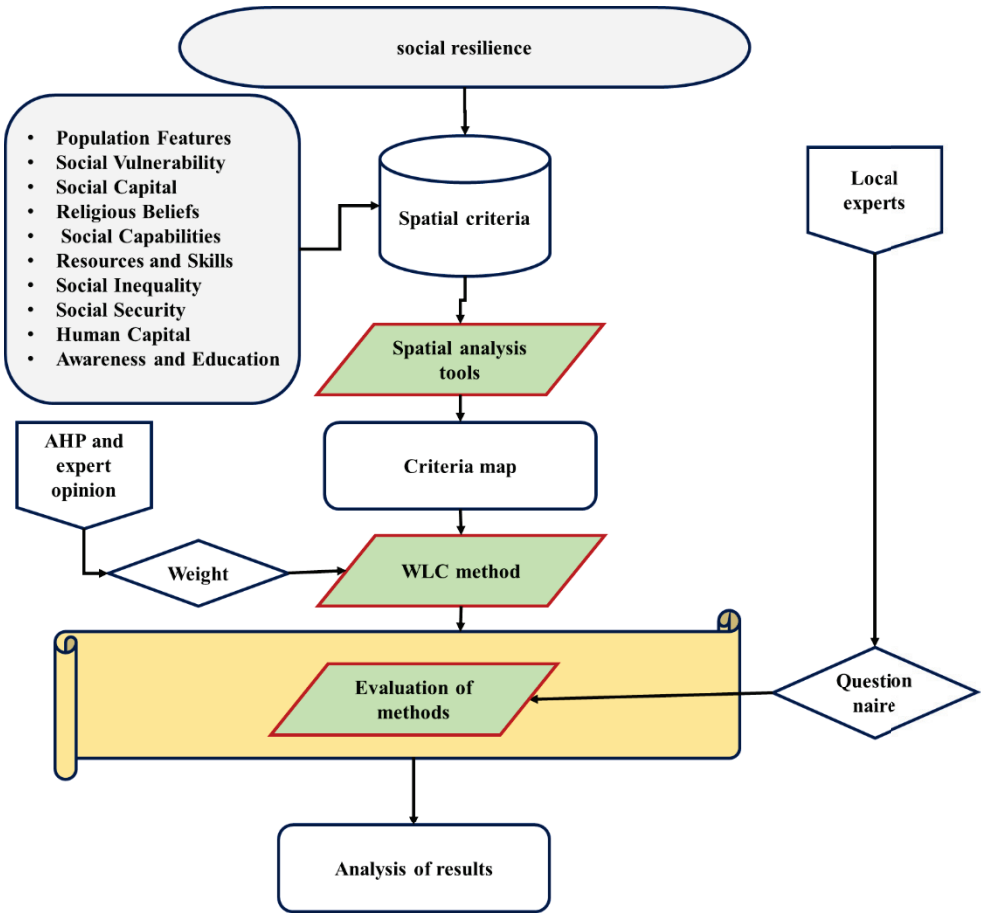

Figure 2. The flowchart of the main steps of the study.

Table 3. The equations used for standardization of social resilience variables.

	Equation	Applied Condition	Standardization Technique
(1)	$n_{ij} = \frac{r_{ij} - r_{min}}{r_{max} - r_{min}}$	Minimum variables	Linear: Maximum-Minimum
(2)	$n_{ij} = \frac{r_{max} - r_{ij}}{r_{max} - r_{min}}$	Maximum variables	

3.3.2. AHP Method

The AHP is one of the most efficient techniques of multi-criteria decision making, which was first suggested by Saaty [75]. A general overview of multi-criteria decision-making methods was conducted by Pohekar and Ramachandran [76] who concluded that, among all weighting techniques, the AHP method was the most popular one. This method is based on pairwise comparisons of criteria and gives managers and decision-makers the possibility of reviewing different strategies [75,77]. This technique is one of the most comprehensive systems designed for decision-making with multiple criteria; because it

provides the possibility of formulation of complicated problems in a hierarchical manner, and also offers the possibility of considering different quantitative and qualitative criteria in the problem [77,78].

The first step in the AHP method, is to construct a hierarchical structure. This is the most crucial step of the hierarchical analysis process, because, in this step, with decomposition of difficult and complicated problems, it becomes possible to transform the problems into simple forms corresponding to human mind and nature [79,80]. At the top of this hierarchy would be the general goal of the problem and on the other layers, the criteria and options. The second step is forming a pairwise comparison matrix. At this stage, elements of each layer in the hierarchy are compared with their corresponding criteria in the higher layers to form pairs, and the pairwise comparison matrix is formed [74]. In order to determine importance and preference in pairwise comparisons, a 1 to 9 range is used (Table 4). The third step is calculating the inconsistency rate. The inconsistency rate clarifies whether the pairwise comparisons have stability and consistency or not. If the value of this rate is lower than 0.1, it is indicative of higher consistency of the matrix, while if the value is above 0.1, there needs to be reconsideration about the pairwise comparison results [81].

Table 4. Weighting variables according to priority in the form of pairwise comparison.

Value	Status of Comparing *i* to *j*	Description
1	Similar Priority	Index *i* ranks similar to index *j* in terms of significance, or there is no priority.
2	A Little Prioritized	Index *i* slightly outranks index *j* in terms of significance.
5	Moderately Prioritized	Index *i* moderately outranks index *j* in terms of significance.
7	Highly Prioritized	Index *i* significantly outranks index *j*.
9	Absolutely Prioritized	Index *i* has absolute priority over index *j*.
2-4-6-8	In-between	These figures indicate "in-between" values; e.g., a value of 8, is higher in priority than 7, but lower than 9 for a given index (*i*).

In this study, using the AHP method and the opinion of 30 experts in the fields of social sciences (sociology, demography, etc.), geography and urban planning, remote sensing and GIS, regional planning and development, and crisis management, the criteria were ranked at different levels relative to each other and according to the degree of their importance at each decision-making level.

3.3.3. Weighted Linear Combination (WLC) Method

There are several methods for analyzing multi-criteria assessments, and the WLC method is one of the most applied and most common ones for preparing suitability maps [82–84]. This technique is also called "the simple collectible weighting method", or "the scoring method", which operates according to mean weight; namely, the relative weight of each criterion measured by experts and the weighting method [28], is multiplied by the value of each pixel [85–87]. Once the final value of each option is determined, the options with the highest values are selected as the appropriate locations for the target [88]. In this study, the WLC model was used to combine different criteria to create the final social resilience index (standard map). In this model, the map of each criterion was multiplied by its own weight (which was determined by experts using the AHP method), and, finally, the sum of all the criteria together was the final result of the WLC model (WLC section,

relationship 3), which resulted in the same map. The ultimate aim in this study was that of assessing social resilience. This method was calculated using Equation (3):

$$A_j = \sum_{j=1}^{n} W_j \times X_j \quad (3)$$

In the above equation, W_j is the relative weight of each criterion/index and X_j is the value of each pixel or location.

3.3.4. Evaluation of the Accuracy of the Proposed Model

The results of multi-criteria decision-making methods are not complete, until their accuracy is evaluated, and in order to ensure the actuality ratio of the prepared map, its accuracy had to be evaluated. In order to evaluate the final map of social resilience obtained from the multi-criteria spatial decision-making system, another questionnaire was designed to represent the current situation, the information of which was collected from the officials of the city administration system and the local government of Sarpol-e Zahab. Based on the combination of information collected from the questionnaires, an urban social resilience map of the city was prepared on the principles of public participation geographic information system (PPGIS). Finally, the correlation coefficient between the social resilience status model, based on the multi-criteria spatial decision-making system, and the social resilience status, based on the questionnaire, were evaluated. The accuracy of the produced map showed the level of confidence in the results of the multi-criteria decision models [89]. Vanolya, et al. [90] used PPGIS results to evaluate the validity of the results of the multi-criteria spatial decision system.

4. Results

In this study, using the AHP model, the final weights for the criteria at each level were calculated and the results are presented in Table 5. According to the experts, social capital (0.23) and social harm (0.19) variables had the greatest influence and religious beliefs and values (0.01) and awareness and education (0.03) variables had the least influence on social resilience.

In order to investigate the locative distribution of the effective criteria on social resilience, each criterion was standardized according to its highest and lowest values. For a more precise review of resilience conditions for the studied region under the locative aspect, the standardized values of the different sub-criteria were calculated for different urban areas. Below, the standardized sub-criteria maps for the study region are shown. Indicator values range from 0 to 1. Values of zero (brown color) represent very low resilience and values of one (blue color) represent very high resilience.

According to the results shown in Figure 3, the demographic parameters influencing social resilience in Sarpol-e Zahab tended to have a lot of locative variances. Regarding literacy status, social resilience of urban areas appeared to be on an optimal level and only three urban areas had unfavorable conditions. As is clear, regarding occupation status, southern areas of the city were not in good conditions, while, compared to other areas, the northwestern parts had better conditions regarding employment. Also, regarding population density, the status of central areas was not good.

The statuses regarding the criteria related to the social harms index are shown in Figure 4, and indicate that, from this regard, Sarpol-e Zahab was not in a good condition. As can be clearly seen, the suicide criterion had a high locative variance throughout the city compared to other criteria; specifically, the southern and southwestern areas were not in good condition, while the northwestern regions were in a better state than the others. Regarding addiction and poverty, in most parts conditions were not suitable.

Table 5. The variables and criteria used for assessing social resilience, and their corresponding weight values.

Variables	Variable–Weight	CR *	Sub-Variables	Criterion Weight	CR	Criterion Type
Demographic Characteristics	0.07	0.004	Age Structure (population aged under 15 and over 65)	0.23	0.002	Minimum
			Literacy Status	0.19		Maximum
			Gender (ratio)	0.11		Maximum
			Population Density	0.28		Minimum
			Immigration	0.04		Minimum
			Female-headed households	0.07		Minimum
			Occupation Status	0.08		Maximum
Social Harms	0.19		Poverty	0.31	0.008	Minimum
			Addiction	0.26		Minimum
			Suicide	0.24		Minimum
			Divorce	0.19		Minimum
Social Capital	0.23		Social Trust	0.18	0.005	Maximum
			Social Participation	0.22		Maximum
			Social Integrity	0.12		Maximum
			Social Awareness	0.09		Maximum
			Social Support	0.08		Maximum
			Social Networks	0.16		Maximum
			Social Relations	0.15		Maximum
Religious Beliefs and Values	0.01		-			Maximum
The General Capability of Local Community	0.05		Sense of Belonging to a Place	0.48	0.004	Maximum
			Sympathy and Altruism	0.13		Maximum
			Cooperation	0.39		Maximum
Resources and Skills	0.09		-		0.001	Maximum
Social Inequality	0.14		-		0.005	Minimum
Social Security	0.11		Theft	0.28	0.005	Minimum
			Murder	0.37		Minimum
			Individual Conflicts	0.14		Minimum
			Group Conflicts	0.21		Minimum
Social Capital	0.08		Public Health	0.68	0.008	Maximum
			Having Trained and Skilled Workforce	0.32		Maximum
Awareness and Education	0.03		-		0.006	Maximum

* Consistency Rate.

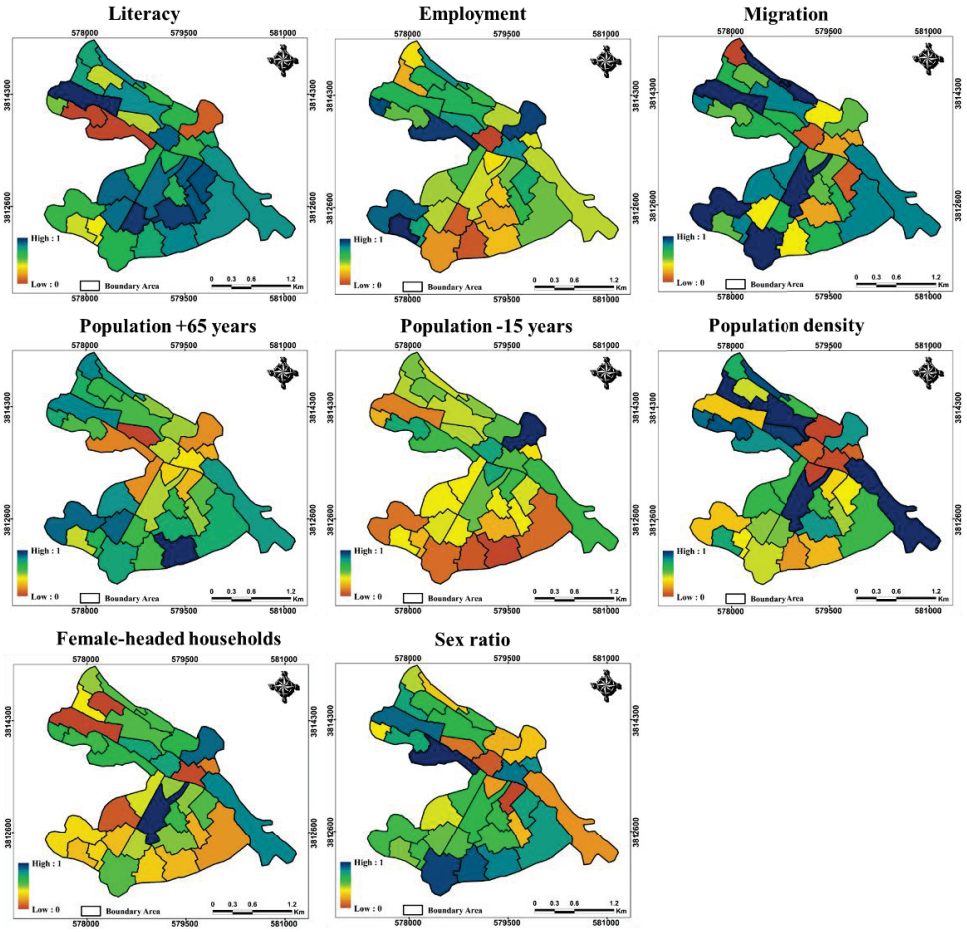

Figure 3. The standardized maps of different criteria related to the demographic index.

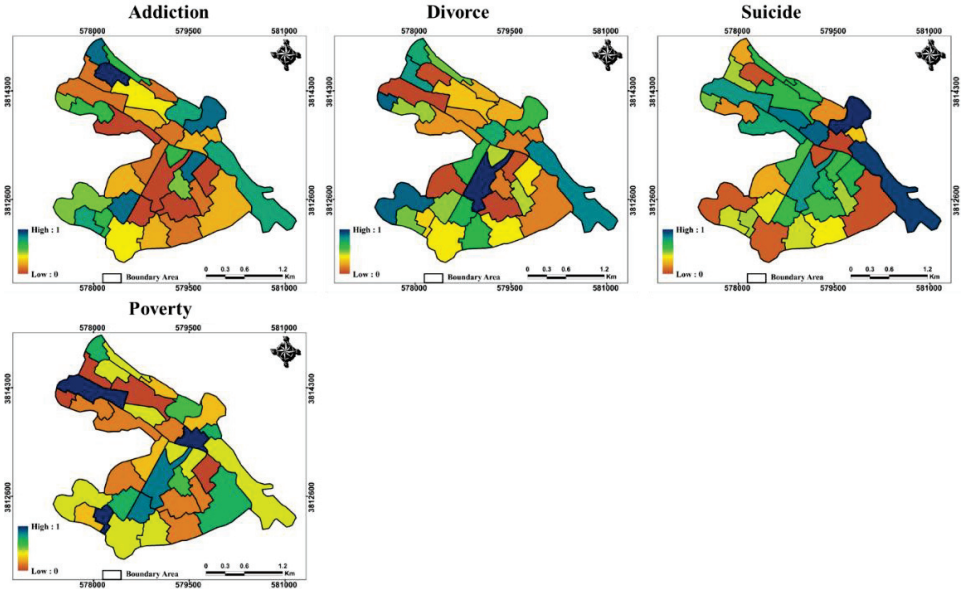

Figure 4. The standardized maps of different criteria related to social harms index.

Figure 5 shows the status of the criteria related to the social capital index. As is observable, regarding social participation, most urban areas were in a favorable status. Furthermore, considering the social integration criterion, most urban areas were in a moderate condition. Among the criteria related to the index of social capital, social trust was not at a good level in most of the urban areas; in other words, the majority of the

urban areas were on a low level in terms of the social trust criterion. Considering social awareness, most of the urban areas were in a moderate status. Besides this, social relations were at moderate and low levels in most of the urban areas.

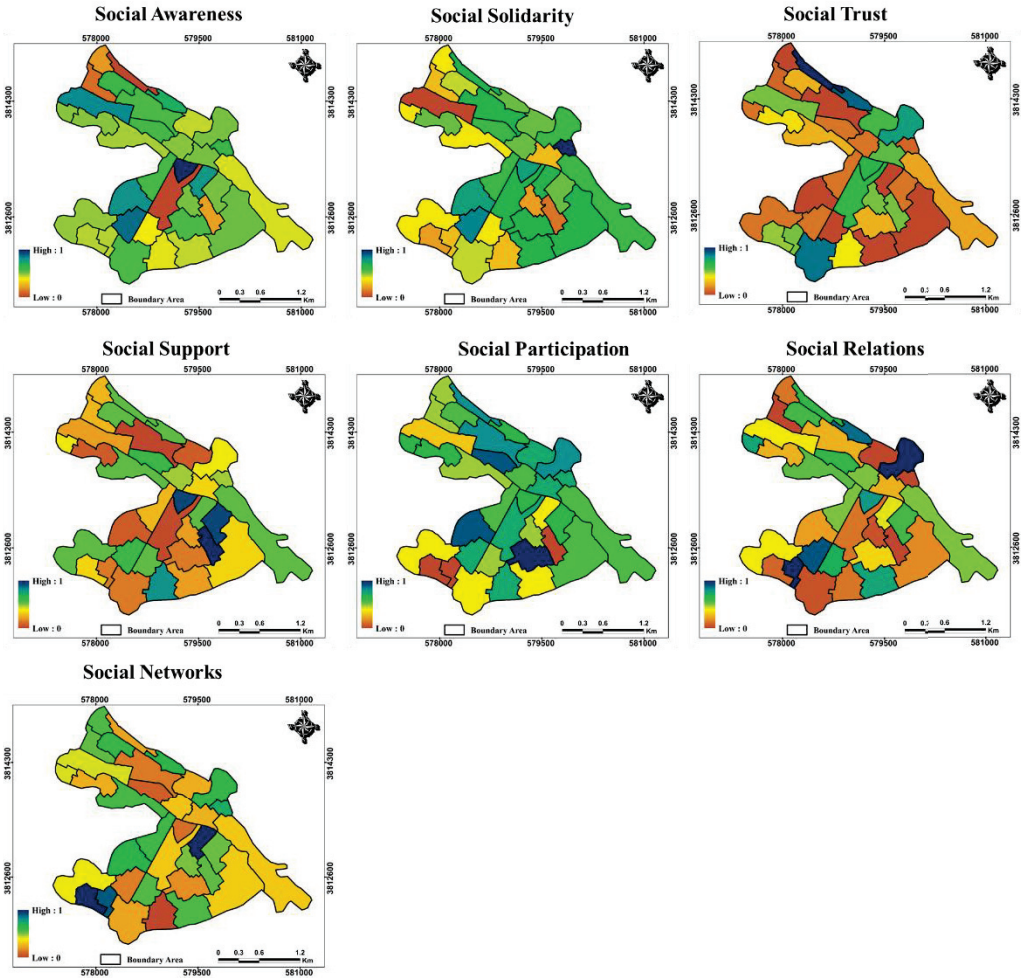

Figure 5. The standardized maps of different criteria related to social capital index.

Figure 6 depicts the status of the religious beliefs index as a significant factor affecting social resilience against various hazards. As is clear from the maps, in this regard, a specific locative pattern was observable throughout the urban areas; the northwestern parts, that are mainly populated by Sunnis, were in an unsuitable state. The central regions, the population of which mostly believe in the Yarsan religion, were in a relatively good state. Additionally, the southeastern parts were in a suitable status, while the southern areas were in unsuitable conditions.

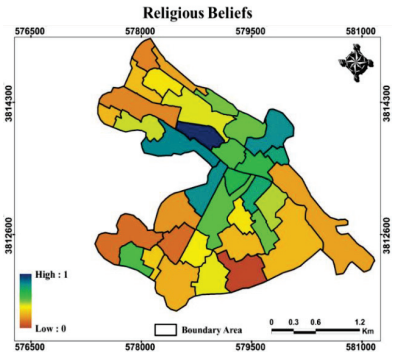

Figure 6. The standardized maps of the criteria related to religious beliefs and values index.

According to the findings depicted in Figure 7, showing the status of the local community capability index, it is observable that there was a certain locative diversity among urban areas in all the criteria. The sense of belonging to place was relatively low in the central areas, medium in the southern areas, high in the southeastern areas, and relatively high in the northwestern areas of the city. Besides this, the sense of empathy and altruism were low in the southern areas, moderate in the northwestern areas, and high in parts of the southeastern areas.

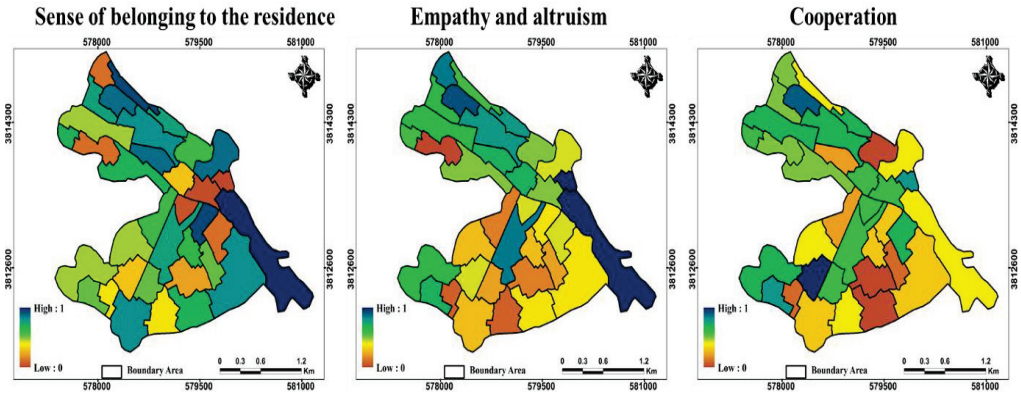

Figure 7. The standardized maps of the criteria related to general capability of local community index.

The results illustrated in Figure 8 show that in terms of the resources and skills index status, except for some areas in the center and northwest, most other urban areas were not in good conditions. As is observable, in this regard, the southern and suburban areas of the city were in unacceptable conditions, and centralization of resources in the central part of the city was higher than in other areas.

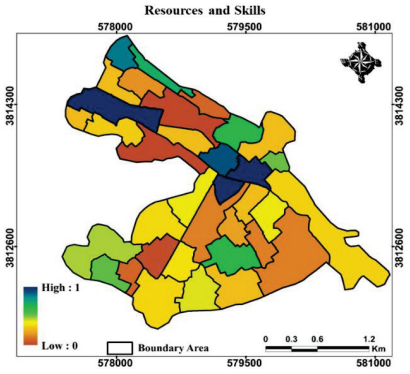

Figure 8. The standardized map of resources and skills index.

The status of the social inequality index presented in Figure 9 shows the imbalance of educational, cultural and social facilities in the private and public sectors of Sarpol-e Zahab. As is observable, the southeastern parts were in better conditions than other urban areas. Most of the governmental centers and organizations are located in this part of the city. The southern, southwestern and northwestern regions (except for one urban area) were not in favorable conditions in this regard.

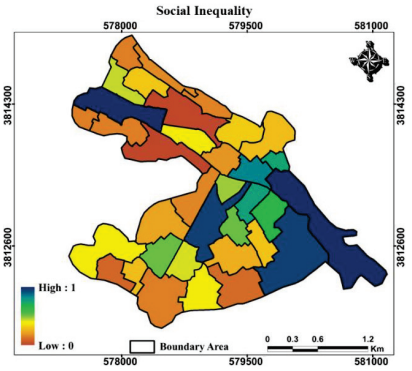

Figure 9. The standardized map of social inequality index.

The findings depicted in Figure 10 show that there is great locative diversity between urban areas in terms of the social security index criterion in Sarpol-e Zahab. As is clear, the murder rate was high in southern and central areas, low in southeastern areas and moderate in northwestern areas. Also, the rate of theft was very high in the southern and central areas of the city, and moderate in the southeastern areas.

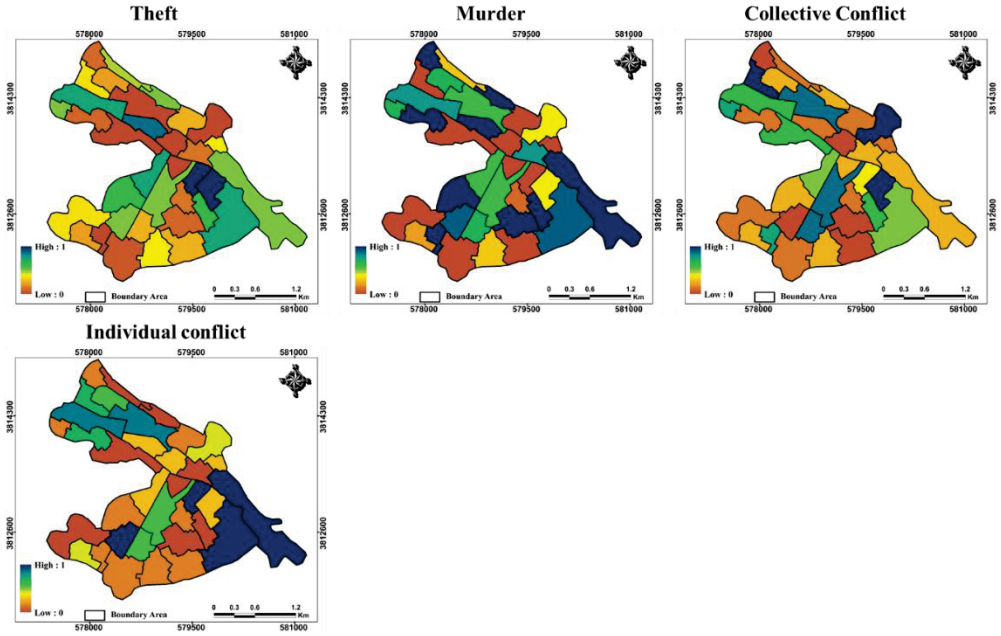

Figure 10. The standardized maps of the criteria related to social security index.

According to the results shown in Figure 11, that are indicative of the conditions of the human assets index criterion, it is clearly observable that, considering population health, there was locative diversity throughout the city. Southern parts were not in good conditions, central regions were in good conditions, southeastern areas were in moderate conditions and northwestern parts were in relatively good conditions. On the other hand, considering the criterion of a trained and skilled workforce, most of the urban areas were not in good conditions.

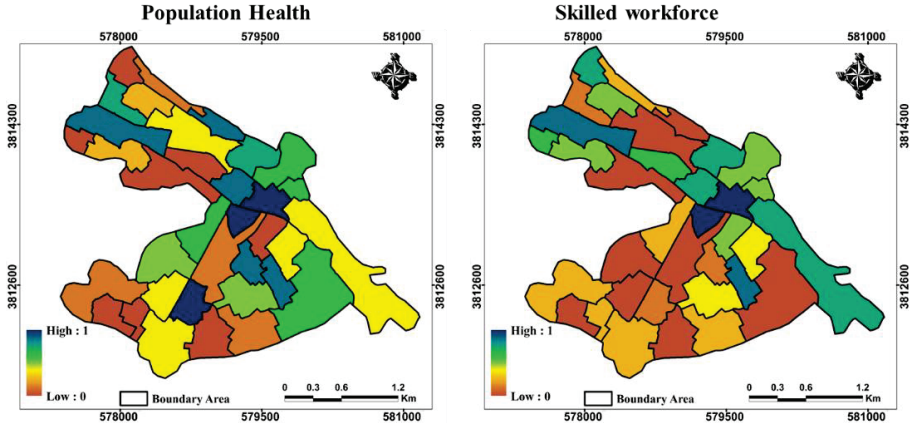

Figure 11. The standardized maps of the criteria related to human assets index.

The status of the urban areas in Sarpol-e Zahab, regarding the awareness and education index, as one of the key variables for social resilience against incidents and shocks, is illustrated in Figure 12; it shows that, in this regard, except for the central areas, most of the other parts were in unfavorable conditions.

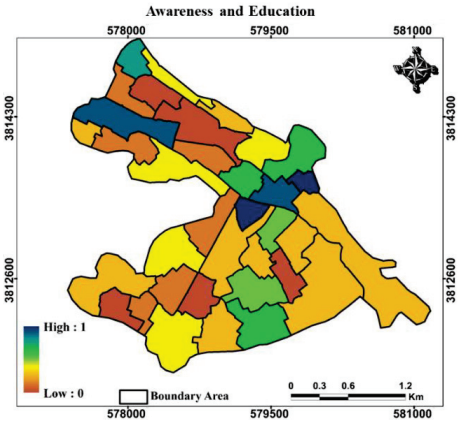

Figure 12. The standardized map of awareness and education index.

4.1. Locative Distribution of the Criteria Affecting Social Resilience

According to the values of the standardized criteria and criteria weights, the decision-making analysis method could be used to create a set of social resilience maps, based on the WLC method. Social resilience maps are prepared on the basis that the weights of the criteria are different for all variables. The values of variables range from 0 to 1. Values of 0 indicate very low resilience and values of 1 indicate very high resilience. The maps of variables were categorized into 5 categories, based on the degree of social resilience: very low (0–0.2), low (0.2–0.4), medium (0.4–0.6), high (0.6–0.8) and very high (0.8–1).

Figure 13 illustrates the extent of the variables, including demographic characteristics, social harms, social capital, religious beliefs and values, general capability of local communities, resources and skills, social inequality, social security, human assets, and awareness and education, on social resilience. Overall, the results indicated a variant locative distribution of the mentioned variables throughout the study region. The status of social capital, as the most significant factor that can promote social resilience of society, generally (country) and specifically (cities), shows that more than 48% of urban areas in the studied region were at a low level and had unfavorable conditions in terms of social resilience. Moreover, the results for social harms of individual urban areas were indicative of a generally low level of social resilience in the city; only 20 percent of the urban areas had high or very high social resilience levels. The status of resources and skills, as another affecting index for social resilience, showed that, except for the central areas and one area

in the northwest, where the level of resilience was high, other areas were in unfavorable conditions regarding social resilience level. The southeastern areas and urban area 22 in the northwest were in a very high level of resilience, in terms of social security and social inequality variables. Generally, it can be claimed that, considering the results of most of the variables, urban areas 35 and 22 were at good levels of social resilience, while the southern areas were at poor levels for most of the variables.

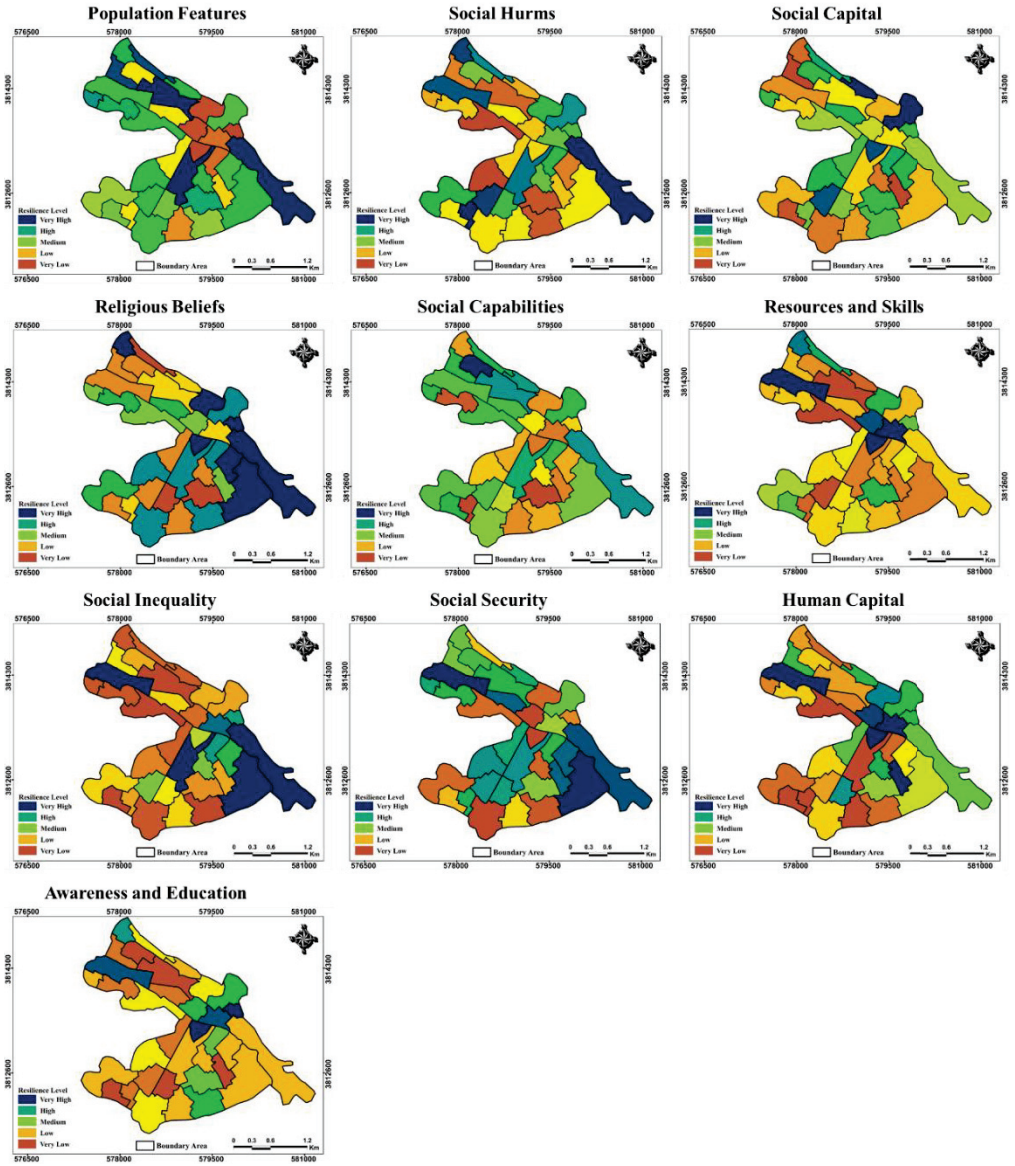

Figure 13. The standardized maps of the variables affecting social resilience.

In Figure 14, the final map of social resilience obtained from the WLC model, based on GIS-MCDM and the diagram of the percentage of social resilience in the urban areas in different classes, is presented. The results indicated that the levels and scope of social resilience were not evenly distributed throughout the city. Almost all areas in the south and southwest were in poor social resilience conditions. The central and eastern areas had better conditions, in terms of social resilience, compared to other districts and urban areas.

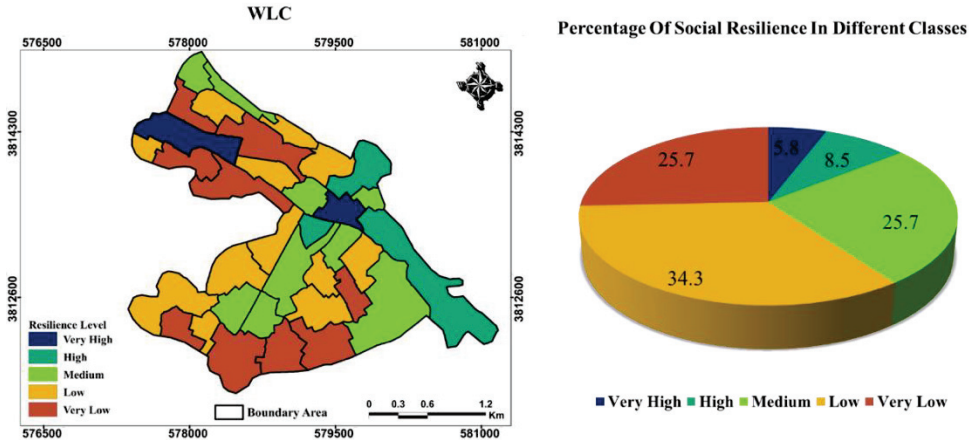

Figure 14. Final social resilience map prepared based on wlc model.

4.2. Accuracy Assessment

In order to assess the accuracy of the final social resilience map, the correlation coefficient between the results of the WLC model and the real-world resilience data from each urban area acquired through the questionnaires, was calculated. The results are presented in Figure 15. The results showed that the correlation coefficient between the WLC model and the level of social resilience was 0.79, which was indicative of the high capability of the proposed WLC model for preparing the locative map of social resilience.

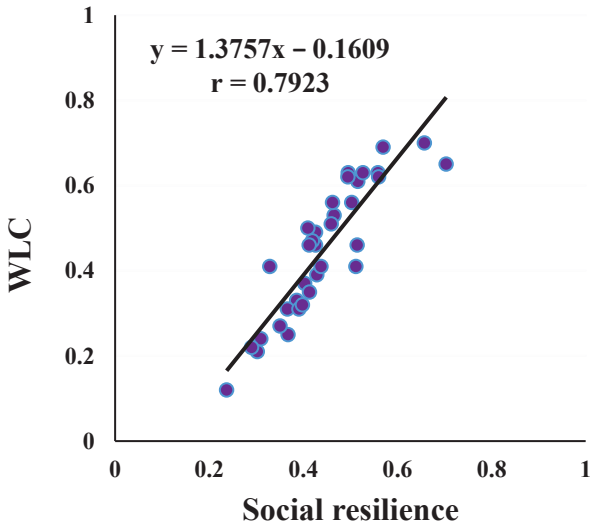

Figure 15. Correlation coefficient between the results of WLC model and real-world social resilience data.

5. Discussion

Facing natural hazards is one of the most important concerns of human communities [91]. Despite developments in encountering these hazards, there are limitations imposed on humans from nature, preventing effective mitigation actions [7]. Social resilience, as one of the effective metrics in the process of crisis management, is a community-based approach to improve the preparedness of urban communities against instabilities resulting from natural hazards [7,18]. In the meantime, identifying the resilient points of a city before, during, and after the occurrence of natural hazards has a great effect on the amount and time of recovery after the occurrence of shocks in every area [41,59–61].

This study was conducted with the aim of measuring the social resilience of Sarpol-e Zahab city against natural hazards. The results showed that most of the urban areas of Sarpol-e Zahab are in an unfavorable situation in terms of social resilience to natural haz-

ards. In most urban areas, the situation is unfavorable in social capital and social damage variables compared to other variables. According to experts, these two variables have the greatest weight in reducing social resilience. In this regard, the research findings are consistent with the results of studies [11,59,60,92,93] shown in a study of Jabareen [92]. In a society where social capital is strong, a return from a damaged state is quick. Peregrine [93], in his study, concluded that social capital can strengthen and expand the area of cohesion and solidarity, sense of responsibility, social participation and awareness of citizens to develop and strengthen social justice in cities (Provide). The results of a study by Cutter, Barnes, Berry, Burton, Evans, Tate and Webb [59] also showed that reducing social vulnerability (poverty, addiction, etc.) and empowering people strengthens social resilience in urban communities. It also showed that, considering social resilience, more than 60% of the studied urban areas were at low to very low levels, 25% were at a moderate level, and nearly 14% at high to very high levels. This was indicative of the low defensive power of the city against shocks and incidents. Evidence on the retrieval rate in all urban areas of Sarpol-e Zahab shows that recovery from the earthquake in 2017 has remained really slow and unchanged in recent years. After almost four years since the incident, most of the urban areas have not dealt properly with the shock and have not returned to their initial states. The occurrence of that incident has affected all aspects of the survivors' lives and has had consequences, such as homelessness, displacement, social dispersions, social discrimination and inequality, poverty and unemployment, violence against women, social rejection, lack of social and psychological security, and various other social problems.

From the viewpoints of the researchers studying resilience of urban communities, the basis of resilience and sustainability of a whole society against natural hazards, lies in the extent of its social resilience [3,94,95]. In this approach, the concepts of public engagement and social development are given deeper and more serious attention; and because this approach includes community-oriented factors, it has a significant impact on reducing vulnerability, and, thus, enhancing the power of defense mechanisms and the resilience of cities against natural hazards [17,59]. Nevertheless, the approach of urban crisis management concerning the encountering of natural hazards in Iran, tends to be more physical and only reinforcement of buildings is taken into consideration, while other aspects of social resilience, such as economic and social aspects, are overlooked. Due to the non-participatory, highly centralized, vertical (top-to-down), and politicized characteristics of the urban management structure in Iran, there is a lack of horizontal convergence and mutual relations among different urban levels, and so, modern approaches of urban management are overlooked. This, along with other issues, is why retrieval after an incident is belated or delayed, thereby turning any natural hazard into a crisis.

Considering the applications and strengths of GIS-MCDM techniques in various decision-making processes relating to natural and human phenomena, this method was used in this study as a proposed method to identify the degree of social resilience of different urban areas and to determine the optimal areas for resilience in Sarpol-e Zahab city. In GIS-MCDM models, areas with high or low resilience can be determined according to the values and weights of the effective criteria. Obviously, the region with high resilience is one that has good conditions in terms of all variables.

The methods of GIS-MCDM consider the user's preferences, manipulate the data, and help decision-makers in complex multi-criteria decision scenarios by combining preferences and data [83]. The WLC method is one of the simplest and most common techniques in GIS-MCDA and was used in this study to identify urban resilient areas to natural hazards. The main advantage of this technique is that it can be implemented very easily in a GIS environment. Moreover, it is easy to understand and intuitively appealing to analysts [96].

6. Conclusions

Today, following the growth of urbanization and increasing natural hazards, investigating and measuring urban resilience to reduce the impact of natural hazards is considered one of the effective and most important factors of urban planning and management. Appro-

priate and accurate knowledge of the characteristics of each urban area, facilitates decision making and planning to monitor natural hazards, use of urban capacity, optimal location and finally management and decision making in urban affairs.

In this study, the level of social resilience in different urban areas of Sarpol-e Zahab city, Iran, was evaluated using local multi-criteria decision-making models with 10 variables and 28 criteria. The results showed that the southern, southwestern and northwestern parts of the city were unsuitable in all criteria (except for one urban area) and the central and southeastern areas had a significant area of medium and suitable rating in terms of flexibility. They were social. Considering that most of the urban areas, 60% of the study area, had very low levels in terms of social resilience, it is suggested that by strengthening communication between people and institutions, enhancing risk awareness, improving environmental quality, increasing the preparedness of people and NGOs, and developing and implementing disaster management plans to support the recovery process, social resilience could be achieved, resulting in improved urban areas.

Our findings indicate the relatively high performance of locative multi-criteria decision-making models for assessing the level of social resilience in highly vulnerable cities. The following limitations were encountered in the course of this study: (a) the strong dependency of the accuracy of the results on the experts' knowledge; (b) the input data were collected from different sources and at heterogenous coordinate systems, resolutions (i.e., spatial or temporal), and data formats (i.e., raster or vector); (c) data redundancy. As per future studies, we suggest considering models with the ability to consider the concept of risk in decision-making, based on Ordered Weight Averaging (OWA) logic for better mapping of optimal areas, in terms of social resilience. Furthermore, the incorporation of fuzzy logic-based models could be very useful, in order to consider uncertainty in measuring urban social resilience.

Author Contributions: Conceptualization, D.S.S.; methodology, D.S.S. and S.N.S.; software, D.S.S.; validation, S.Y., A.K. and M.T.H.; resources, D.S.S.; data curation, D.S.S.; writing—original draft preparation, D.S.S., A.K. and S.N.S.; writing—review and editing, D.S.S., J.J.A. and H.T.M.; visualization, D.S.S.; project administration, D.S.S. and S.N.S. All authors have read and agreed to the published version of the manuscript.

Funding: This research received no external funding.

Informed Consent Statement: Informed consent was obtained from all subjects involved in the study.

Data Availability Statement: Data available on request due to restrictions e.g., privacy or ethical.

Conflicts of Interest: The authors declare that they have no known competing financial interests or personal relationships that could have appeared to influence the work reported in this paper.

References

1. United Nations Department for Economic and Social Affairs. *World Urbanization Prospects 2018*; United Nations Department for Economic and Social Affairs: New York, NY, USA, 2018.
2. Huck, A.; Monstadt, J.; Driessen, P. Building urban and infrastructure resilience through connectivity: An institutional perspective on disaster risk management in Christchurch, New Zealand. *Cities* **2020**, *98*, 102573. [CrossRef]
3. Zhang, X.; Li, H. Urban resilience and urban sustainability: What we know and what do not know? *Cities* **2018**, *72*, 141–148. [CrossRef]
4. Meerow, S.; Newell, J.P. Urban resilience for whom, what, when, where, and why? *Urban Geogr.* **2019**, *40*, 309–329. [CrossRef]
5. White, G.F. *Natural Hazards, Local, National, Global*; Oxford University Press: Oxford, UK, 1974.
6. White, G.F. Natural hazards research. In *Directions in Geography*; Routledge: London, UK, 2019; pp. 193–216.
7. Adger, W.N.; Hodbod, J. Ecological and social resilience. In *Handbook of Sustainable Development*; Edward Elgar Publishing: Cheltenham, UK, 2014.
8. Chen, C.; Xu, L.; Zhao, D.; Xu, T.; Lei, P. A new model for describing the urban resilience considering adaptability, resistance and recovery. *Saf. Sci.* **2020**, *128*, 104756. [CrossRef]
9. Field, C.B.; Barros, V.; Stocker, T.F.; Dahe, Q. *Managing the Risks of Extreme Events and Disasters to Advance Climate Change Adaptation: Special Report of the Intergovernmental Panel on Climate Change*; Cambridge University Press: Cambridge, UK, 2012.
10. Matarrita-Cascante, D.; Trejos, B. Community resilience in resource-dependent communities: A comparative case study. *Environ. Plan. A* **2013**, *45*, 1387–1402. [CrossRef]

11. Saja, A.A.; Goonetilleke, A.; Teo, M.; Ziyath, A.M. A critical review of social resilience assessment frameworks in disaster management. *Int. J. Disaster Risk Reduct.* **2019**, *35*, 101096. [CrossRef]
12. Adger, W.N. Social and ecological resilience: Are they related? *Prog. Hum. Geogr.* **2000**, *24*, 347–364. [CrossRef]
13. Mitchell, T.; Harris, K. *Resilience: A Risk Management Approach*; ODI Background Note; Overseas Development Institute: London, UK, 2012; pp. 1–7.
14. Meerow, S.; Newell, J.P.; Stults, M. Defining urban resilience: A review. *Landsc. Urban Plan.* **2016**, *147*, 38–49. [CrossRef]
15. Shamsuddin, S. Resilience resistance: The challenges and implications of urban resilience implementation. *Cities* **2020**, *103*, 102763. [CrossRef]
16. Brown, A.; Dayal, A.; Rumbaitis Del Rio, C. From practice to theory: Emerging lessons from Asia for building urban climate change resilience. *Environ. Urban.* **2012**, *24*, 531–556. [CrossRef]
17. Maguire, B.; Hagan, P. Disasters and communities: Understanding social resilience. *Aust. J. Emerg. Manag.* **2007**, *22*, 16.
18. Ozel, B.; Mecca, S. Rethinking the role of public spaces for urban resilience: Case study of Eco-village in Cenaia. In Proceedings of the Past Present and Future of Public Space Ð International Conference on Art, Architecture and Urban Design, Bologna, Italy, 25–27 June 2014.
19. Sachdeva, M. Urban Resilience and Urban Sustainability. Master's Thesis, Columbia University, New York, NY, USA, 2016.
20. Fekete, A.; Asadzadeh, A.; Ghafory-Ashtiany, M.; Amini-Hosseini, K.; Hetkämper, C.; Moghadas, M.; Ostadtaghizadeh, A.; Rohr, A.; Kötter, T. Pathways for advancing integrative disaster risk and resilience management in Iran: Needs, challenges and opportunities. *Int. J. Disaster Risk Reduct.* **2020**, *49*, 101635. [CrossRef]
21. Zengir, V.S.; Sobhani, B.; Asghari, S. Monitoring and investigating the possibility of forecasting drought in the western part of Iran. *Arab. J. Geosci.* **2020**, *13*, 1–12.
22. Najafabadi, R.M.; Ramesht, M.H.; Ghazi, I.; Khajedin, S.J.; Seif, A.; Nohegar, A.; Mahdavi, A. Identification of natural hazards and classification of urban areas by TOPSIS model (case study: Bandar Abbas city, Iran). *Geomat. Nat. Hazards Risk* **2016**, *7*, 85–100. [CrossRef]
23. Jelokhani-Niaraki, M. Web 2.0-Based Collaborative Multicriteria Spatial Decision Support System: A Case Study of Human-Computer Interaction Patterns. Ph.D. Thesis, University of Western Ontario, London, ON, Canada, 2013.
24. Mohammadnazari, Z.; Mousapour Mamoudan, M.; Alipour-Vaezi, M.; Aghsami, A.; Jolai, F.; Yazdani, M. Prioritizing post-disaster reconstruction projects using an integrated multi-criteria decision-making approach: A case study. *Buildings* **2022**, *12*, 136. [CrossRef]
25. Yalcin, M.; Gul, F.K. A GIS-based multi criteria decision analysis approach for exploring geothermal resources: Akarcay basin (Afyonkarahisar). *Geothermics* **2017**, *67*, 18–28. [CrossRef]
26. Bacca, E.J.M.; Knight, A.; Trifkovic, M. Optimal land use and distributed generation technology selection via geographic-based multicriteria decision analysis and mixed-integer programming. *Sustain. Cities Soc.* **2020**, *55*, 102055. [CrossRef]
27. Ristić, V.; Maksin, M.; Nenković-Riznić, M.; Basarić, J. Land-use evaluation for sustainable construction in a protected area: A case of Sara mountain national park. *J. Environ. Manag.* **2018**, *206*, 430–445. [CrossRef]
28. Shahpari Sani, D.; Mahmoudian, H. Identifying and prioritizing of the effective factor on the tendency of immigration in abadan city using multi-criteria decision making techniques. *J. Popul. Assoc. Iran* **2019**, *13*, 89–118.
29. Mijani, N.; Shahpari Sani, D.; Dastaran, M.; Karimi Firozjaei, H.; Argany, M.; Mahmoudian, H. Spatial modeling of migration using GIS-based multi-criteria decision analysis: A case study of Iran. *Trans. GIS* **2022**, *26*, 645–668. [CrossRef]
30. Mijani, N.; Alavipanah, S.K.; Hamzeh, S.; Firozjaei, M.K.; Arsanjani, J.J. Modeling thermal comfort in different condition of mind using satellite images: An Ordered Weighted Averaging approach and a case study. *Ecol. Indic.* **2019**, *104*, 1–12. [CrossRef]
31. Firozjaei, M.K.; Nematollahi, O.; Mijani, N.; Shorabeh, S.N.; Firozjaei, H.K.; Toomanian, A. An integrated GIS-based Ordered Weighted Averaging analysis for solar energy evaluation in Iran: Current conditions and future planning. *Renew. Energy* **2019**, *136*, 1130–1146. [CrossRef]
32. Shorabeh, S.N.; Samany, N.N.; Minaei, F.; Firozjaei, H.K.; Homaee, M.; Boloorani, A.D. A decision model based on decision tree and particle swarm optimization algorithms to identify optimal locations for solar power plants construction in Iran. *Renew. Energy* **2022**, *187*, 56–67. [CrossRef]
33. Moghadas, M.; Asadzadeh, A.; Vafeidis, A.; Fekete, A.; Kötter, T. A multi-criteria approach for assessing urban flood resilience in Tehran, Iran. *Int. J. Disaster Risk Reduct.* **2019**, *35*, 101069. [CrossRef]
34. Bertilsson, L.; Wiklund, K.; de Moura Tebaldi, I.; Rezende, O.M.; Veról, A.P.; Miguez, M.G. Urban flood resilience–A multi-criteria index to integrate flood resilience into urban planning. *J. Hydrol.* **2019**, *573*, 970–982. [CrossRef]
35. Karpouza, M.; Chousianitis, K.; Bathrellos, G.D.; Skilodimou, H.D.; Kaviris, G.; Antonarakou, A. Hazard zonation mapping of earthquake-induced secondary effects using spatial multi-criteria analysis. *Nat. Hazards* **2021**, *109*, 637–669. [CrossRef]
36. Bonanno, G.A.; Romero, S.A.; Klein, S.I. The temporal elements of psychological resilience: An integrative framework for the study of individuals, families, and communities. *Psychol. Inq.* **2015**, *26*, 139–169. [CrossRef]
37. Folke, C. Resilience: The emergence of a perspective for social–ecological systems analyses. *Glob. Environ. Chang.* **2006**, *16*, 253–267. [CrossRef]
38. Bogardi, J. Resilience Building: From Knowledge to Action. Introduction to UNU-EHS. Presented at the UNU–EHS Summer Academy, Munich, Germany, 23–30 July 2006.

39. Sapirstein, G. Social resilience: The forgotten dimension of disaster risk reduction. *Jàmbá J. Disaster Risk Stud.* **2006**, *1*, 54–63. [CrossRef]
40. Ainuddin, S.; Routray, J.K. Earthquake hazards and community resilience in Baluchistan. *Nat. Hazards* **2012**, *63*, 909–937. [CrossRef]
41. Cutter, L.; Barnes, L.; Berry, M.; Burton, C.; Evans, E.; Tate, E.; Webb, J. *Community and Regional Resilience to Natural Disasters: Perspective from Hazards, Disasters and Emergency Management*; CARRI Research Report 1; Community and Regional Resilience Institute: Oak Ridge, TN, USA, 2008.
42. Dumenu, W.K.; Obeng, E.A. Climate change and rural communities in Ghana: Social vulnerability, impacts, adaptations and policy implications. *Environ. Sci. Policy* **2016**, *55*, 208–217. [CrossRef]
43. Kulig, J.C.; Hegney, D.; Edge, D.S. Community resiliency and rural nursing: Canadian and Australian perspectives. In *Rural Nursing: Concepts, Theory and Practice*; Springer: New York, NY, USA, 2009; pp. 385–400.
44. Matarrita-Cascante, D.; Trejos, B.; Qin, H.; Joo, D.; Debner, S. Conceptualizing community resilience: Revisiting conceptual distinctions. *Community Dev.* **2017**, *48*, 105–123. [CrossRef]
45. Kuhlicke, C.; Steinführer, A.; Begg, C.; Bianchizza, C.; Bründl, M.; Buchecker, M.; De Marchi, B.; Tarditti, M.D.M.; Höppner, C.; Komac, B. Perspectives on social capacity building for natural hazards: Outlining an emerging field of research and practice in Europe. *Environ. Sci. Policy* **2011**, *14*, 804–814. [CrossRef]
46. Norris, F.H.; Stevens, S.P.; Pfefferbaum, B.; Wyche, K.F.; Pfefferbaum, R.L. Community resilience as a metaphor, theory, set of capacities, and strategy for disaster readiness. *Am. J. Community Psychol.* **2008**, *41*, 127–150. [CrossRef] [PubMed]
47. Twigg, J. Characteristics of a Disaster-Resilient Community: A Guidance Note (Version 2). 2009. Available online: https://discovery.ucl.ac.uk/id/eprint/1346086/1/1346086.pdf (accessed on 5 June 2022).
48. Abesamis, N.P.; Corrigan, C.; Drew, M.; Campbell, S.; Samonte, G. Social Resilience: A Literature Review on Building Resilience into Human Marine Communities in and around MPA Networks. MPA Networks Learning Partnership, Global Conservation Program, USAID. 2006. Available online: http://www.reefresilience.org/pdf/Social_Resilience_Literature_Review.pdf (accessed on 5 June 2022).
49. Ebadollahzadeh, M.S.; Khanloo, N.; Ziyari, K.; Shali, A.V. Prioritization of factors affecting social resilience against natural hazards with emphasis on earthquakes. *Hoviateshahr* **2019**, *13*, 45–58.
50. Voss, M. The vulnerable can't speak. An integrative vulnerability approach to disaster and climate change research. *Behemoth-A J. Civilis.* **2008**, *1*, 39–56. [CrossRef]
51. Saja, A.A.; Teo, M.; Goonetilleke, A.; Ziyath, A.M. An inclusive and adaptive framework for measuring social resilience to disasters. *Int. J. Disaster Risk Reduct.* **2018**, *28*, 862–873. [CrossRef]
52. Moher, D.; Liberati, A.; Tetzlaff, J.; Altman, D.G.; Group, P. Preferred reporting items for systematic reviews and meta-analyses: The PRISMA statement. *PLoS Med.* **2009**, *6*, e1000097. [CrossRef]
53. Godschalk, D. Functions and phases of emergency management. In *Emergency Management: Principles and Practice for Local Government*; ICMA Press: Zurich, Switzerland, 2007; pp. 87–112.
54. Sanders, A.E.; Lim, S.; Sohn, W. Resilience to urban poverty: Theoretical and empirical considerations for population health. *Am. J. Public Health* **2008**, *98*, 1101–1106. [CrossRef]
55. Shaw, D.; Scully, J.; Hart, T. The paradox of social resilience: How cognitive strategies and coping mechanisms attenuate and accentuate resilience. *Glob. Environ. Chang.* **2014**, *25*, 194–203. [CrossRef]
56. Arefi, M. Design for resilient cities: Reflections from a studio. In *Companion to Urban Design*; Routledge: London, UK, 2011; pp. 688–699.
57. Béné, C.; Newsham, A.; Davies, M.; Ulrichs, M.; Godfrey-Wood, R. Resilience, poverty and development. *J. Int. Dev.* **2014**, *26*, 598–623. [CrossRef]
58. Bastaminia, A.; Fakhraie, O.; Alizadeh, M.; Asadi, A.B.; Dastoorpoor, M. Social capital and quality of life among university students of Yasuj, Iran. *Int. J. Soc. Sci. Stud.* **2016**, *4*, 9. [CrossRef]
59. Cutter, S.L.; Barnes, L.; Berry, M.; Burton, C.; Evans, E.; Tate, E.; Webb, J. A place-based model for understanding community resilience to natural disasters. *Glob. Environ. Chang.* **2008**, *18*, 598–606. [CrossRef]
60. Aldrich, D.P.; Meyer, M.A. Social capital and community resilience. *Am. Behav. Sci.* **2015**, *59*, 254–269. [CrossRef]
61. Kimhi, S. Levels of resilience: Associations among individual, community, and national resilience. *J. Health Psychol.* **2016**, *21*, 164–170. [CrossRef]
62. Qasim, S.; Qasim, M.; Shrestha, R.P.; Khan, A.N.; Tun, K.; Ashraf, M. Community resilience to flood hazards in Khyber Pukhthunkhwa province of Pakistan. *Int. J. Disaster Risk Reduct.* **2016**, *18*, 100–106. [CrossRef]
63. Freitag, R.C.; Abramson, D.B.; Chalana, M.; Dixon, M. Whole community resilience: An asset-based approach to enhancing adaptive capacity before a disruption. *J. Am. Plan. Assoc.* **2014**, *80*, 324–335. [CrossRef]
64. Berkes, F.; Ross, H. Community resilience: Toward an integrated approach. *Soc. Nat. Resour.* **2013**, *26*, 5–20. [CrossRef]
65. Ross, H.; Cuthill, M.; Maclean, K.; Jansen, D.; Witt, B. *Understanding, Enhancing and Managing for Social Resilience at the Regional Scale: Opportunities in North Queensland*; Report to the Marine and Tropical Sciences Research Facility; Reef and Rainforest Research Centre Limited: Cairns, Australia, 2010.
66. Cinner, J.; Fuentes, M.M.; Randriamahazo, H. Exploring social resilience in Madagascar's marine protected areas. *Ecol. Soc.* **2009**, *14*, 41. [CrossRef]

67. Magis, K. Community resilience: An indicator of social sustainability. *Soc. Nat. Resour.* **2010**, *23*, 401–416. [CrossRef]
68. Obrist, B.; Pfeiffer, C.; Henley, R. Multi-layered social resilience: A new approach in mitigation research. *Prog. Dev. Stud.* **2010**, *10*, 283–293. [CrossRef]
69. Becker, P. The importance of integrating multiple administrative levels in capacity assessment for disaster risk reduction and climate change adaptation. *Disaster Prev. Manag. Int. J.* **2012**, *21*, 226–233. [CrossRef]
70. Mayunga, J.S. Understanding and applying the concept of community disaster resilience: A capital-based approach. *Summer Acad. Soc. Vulnerability Resil. Build.* **2007**, *1*, 1–16.
71. Morrow, B.H. *Community Resilience: A Social Justice Perspective*; CARRI Research Report; Community and Regional Resilience Initiative: Oak Ridge, TN, USA, 2008.
72. Cutter, S.L.; Burton, C.G.; Emrich, C.T. Disaster resilience indicators for benchmarking baseline conditions. *J. Homel. Secur. Emerg. Manag.* **2010**, *7*, 51. [CrossRef]
73. Keeley, B. *Human Capital: How What You Know Can Shape Your Life*; Danvers, M.A., Ed.; Organization for Economic Co-Operation and Development (OECD): Paris, France, 2007.
74. Boloorani, A.D.; Kazemi, Y.; Sadeghi, A.; Shorabeh, S.N.; Argany, M. Identification of dust sources using long term satellite and climatic data: A case study of Tigris and Euphrates basin. *Atmos. Environ.* **2020**, *224*, 117299. [CrossRef]
75. Saaty, T.L. Axiomatic foundation of the analytic hierarchy process. *Manag. Sci.* **1986**, *32*, 841–855. [CrossRef]
76. Pohekar, S.D.; Ramachandran, M. Application of multi-criteria decision making to sustainable energy planning—A review. *Renew. Sustain. Energy Rev.* **2004**, *8*, 365–381. [CrossRef]
77. Mijani, N.; Samani, N.N. Comparison of fuzzy-based models in landslide hazard mapping. *Int. Arch. Photogramm. Remote Sens. Spat. Inf. Sci.* **2017**, *42*, 407–416. [CrossRef]
78. Saaty, T.L. Decision making with the analytic hierarchy process. *Int. J. Serv. Sci.* **2008**, *1*, 83–98. [CrossRef]
79. Mekonnen, A.D.; Gorsevski, P.V. A web-based participatory GIS (PGIS) for offshore wind farm suitability within Lake Erie, Ohio. *Renew. Sustain. Energy Rev.* **2015**, *41*, 162–177. [CrossRef]
80. Qureshi, S.; Shorabeh, S.N.; Samany, N.N.; Minaei, F.; Homaee, M.; Nickravesh, F.; Firozjaei, M.K.; Arsanjani, J.J. A new integrated approach for municipal landfill siting based on urban physical growth prediction: A case study mashhad metropolis in Iran. *Remote Sens.* **2021**, *13*, 949. [CrossRef]
81. Shorabeh, S.N.; Firozjaei, M.K.; Nematollahi, O.; Firozjaei, H.K.; Jelokhani-Niaraki, M. A risk-based multi-criteria spatial decision analysis for solar power plant site selection in different climates: A case study in Iran. *Renew. Energy* **2019**, *143*, 958–973. [CrossRef]
82. Abdelkarim, A.; Al-Alola, S.S.; Alogayell, H.M.; Mohamed, S.A.; Alkadi, I.I.; Ismail, I.Y. Integration of GIS-based multicriteria decision analysis and analytic hierarchy process to assess flood hazard on the Al-shamal train pathway in Al-Qurayyat region, kingdom of Saudi Arabia. *Water* **2020**, *12*, 1702. [CrossRef]
83. Malczewski, J. *GIS and Multicriteria Decision Analysis*; John Wiley & Sons: Hoboken, NJ, USA, 1999.
84. Shahabi, H.; Keihanfard, S.; Ahmad, B.B.; Amiri, M.J.T. Evaluating Boolean, AHP and WLC methods for the selection of waste landfill sites using GIS and satellite images. *Environ. Earth Sci.* **2014**, *71*, 4221–4233. [CrossRef]
85. Babalola, M.A. Application of GIS-based multi-criteria decision technique in exploration of suitable site options for anaerobic digestion of food and biodegradable waste in Oita City, Japan. *Environments* **2018**, *5*, 77. [CrossRef]
86. Hajizadeh, F.; Poshidehro, M.; Yousefi, E. Scenario-based capability evaluation of ecotourism development—An integrated approach based on WLC, and FUZZY–OWA methods. *Asia Pac. J. Tour. Res.* **2020**, *25*, 627–640. [CrossRef]
87. Tang, Z.; Yi, S.; Wang, C.; Xiao, Y. Incorporating probabilistic approach into local multi-criteria decision analysis for flood susceptibility assessment. *Stoch. Environ. Res. Risk Assess.* **2018**, *32*, 701–714. [CrossRef]
88. Thill, J.-C. *Spatial Multicriteria Decision Making and Analysis: A Geographic Information Sciences Approach*; Routledge: London, UK, 2019.
89. Schlossberg, M.; Shuford, E. Delineating "public" and "participation" in PPGIS. *URISA J.* **2005**, *16*, 15–26.
90. Vanolya, N.M.; Jelokhani-Niaraki, M.; Toomanian, A. Validation of spatial multicriteria decision analysis results using public participation GIS. *Appl. Geogr.* **2019**, *112*, 102061. [CrossRef]
91. Jha, A.K.; Bloch, R.; Lamond, J. *Cities and Flooding: A Guide to Integrated Urban Flood Risk Management for the 21st Century*; The World Bank: Washington, DC, USA, 2012.
92. Jabareen, Y. Planning the resilient city: Concepts and strategies for coping with climate change and environmental risk. *Cities* **2013**, *31*, 220–229. [CrossRef]
93. Peregrine, P.N. Political participation and long-term resilience in pre-Columbian societies. *Disaster Prev. Manag. Int. J.* **2017**, *26*, 314–329. [CrossRef]
94. Beatley, T.; Newman, P. Biophilic cities are sustainable, resilient cities. *Sustainability* **2013**, *5*, 3328–3345. [CrossRef]
95. Windle, G. What is resilience? A review and concept analysis. *Rev. Clin. Gerontol.* **2011**, *21*, 152. [CrossRef]
96. Malczewski, J. On the use of weighted linear combination method in GIS: Common and best practice approaches. *Trans. GIS* **2000**, *4*, 5–22. [CrossRef]

sustainability

MDPI

Article

Breaking the Negative Feedback Loop of Disaster, Conflict, and Fragility: Analyzing Development Aid by Japan and South Korea

Suyeon Lee * and Huck-ju Kwon

Global Development Institute for Public Affairs, Graduate School of Public Administration, Seoul National University, Seoul 08826, Korea
* Correspondence: lee.suyeon@snu.ac.kr

Abstract: Disaster risk reduction (DRR) has become an important element of donor policy, because numerous governments have expressed their commitment to helping countries vulnerable to natural hazards by mainstreaming DRR into their development programs. Meanwhile, countries that are considered fragile, as well as conflict-affected states, have faced a high risk of disasters brought on by natural hazards. However, there has been little research that addresses the complex relationship between disasters, conflict, and fragility in the context of development cooperation. Against this backdrop, this study analyzed the determinants of DRR aid allocation from Japan and South Korea—two East Asian countries that have shown a strong commitment to disaster resilience and peacebuilding—to investigate whether they are responsive to countries experiencing the combined risks of disasters and conflicts and/or fragility. Despite the vulnerable countries being in the most need, the study found that both Japan and Korea's aid allocation has not been influenced much by the concurrence of disasters and conflict. Rather, it has been more driven by the level of a country's climate vulnerability than the level of a country's fragility. This suggests that developing countries facing multiple risks and challenges are at a major disadvantage in terms of the responsiveness of donors toward their needs and vulnerability.

Keywords: development cooperation; climate change; disaster risk reduction (DRR); fragile and conflict-affected states (FCSs); generalized method of moments (GMM); official development assistance (ODA)

Citation: Lee, S.; Kwon, H.-j. Breaking the Negative Feedback Loop of Disaster, Conflict, and Fragility: Analyzing Development Aid by Japan and South Korea. *Sustainability* **2022**, *14*, 10003. https://doi.org/10.3390/su141610003

Academic Editors: Stefano Morelli, Veronica Pazzi and Mirko Francioni

Received: 17 July 2022
Accepted: 10 August 2022
Published: 12 August 2022

1. Introduction

Although climate change affects every country, its effects are distributed differently across the globe. In this study, countries classified as low (with a GNI per capita of USD 1085 or less) and lower-middle income countries (with a GNI per capita between USD 1086–4255) by the World Bank are considered developing countries, while developed countries are high-income economies with a GNI per capita of $13,205 or more. Developing countries are the most impacted by climate change given their large rural population, the pervasiveness of resource-dependent livelihoods, and poverty, as well as their lack of coping capacities to protect themselves against environmental shocks [1,2]. Future climate change effects will be more severe and pervasive, and bring will irreversible impacts on all [3]. Hence, without proper adaptation, people in developing countries are more likely to lose their livelihoods and homes during natural hazards, which would prevent their social mobility out of poverty. Furthermore, the risks associated with climate change are already affecting millions of people around the globe, aggravating already fragile situations, such as poverty and hunger.

In fragile and conflict-affected states (FCSs), there is a greater risk for climate change to cause instability and unrest, posing serious threats to human security [4,5]. This is due to the conditions of fragile and conflict-affected states, including extreme poverty, war, and the process of reconstruction to crises and disasters [6]. As such, these countries lack

the capacities to carry out basic governance functions, leaving their citizens vulnerable to a range of shocks [7–10]. In other words, a state's level of fragility and violent conflict increases people's likelihood to be harmed by natural hazards because it limits their ability to cope with the impact. The occurrence of a natural hazard in FCSs exacerbates existing challenges that people face on a daily basis, heightening sources of tensions, such as weak governance, historical grievances, mobilization, and poverty [11–13]. Put differently, there is a risk of a negative feedback loop emerging, where existing fragility and conflict undermine the ability of a government to manage or mitigate social, economic, political, security, or environmental risks, and this, in turn, potentially exacerbates the conflict itself, further reducing the ability of states to respond and recover from disasters. Within these contexts, climate change considerations must be integrated into peacebuilding and development interventions to promote climate-resilient peacebuilding in FCSs [13,14].

Disaster risk reduction (DRR) is a concept of the practice of "preventing new and reducing existing disaster risk and managing residual risk" [15]. Reducing exposure and vulnerability of people and assets, strengthening buildings and roads, improving forecasting and early warning systems, maintaining adequate emergency shelters, and strict land-use planning are all examples of disaster risk reduction [16]. In short, the omission of these acts can turn natural hazards into a disaster. While DRR has long been recognized as a powerful tool for strengthening resilience and, therefore, achieving sustainable development, DRR has rarely been integrated into development efforts. While several studies [17–19] assessed the environmental impact of overall development aid, there is little research that concentrates almost exclusively on the determinants of DRR aid. In addition, previous research has often only examined development policies focusing on DRR and, thus, studies based on empirical analysis on aid allocation in DRR are rather scarce.

Against this background, this study aims to examine the determinants of Japan and South Korea's aid allocation in relation to DRR. According to Stallings [20], Japan and South Korea share a set of characteristics that differentiate them from Western donors in terms of geographical and sectoral focus, grants and loans profile, and public-private links. The commonalities—including prioritizing economic growth and preference for subsidized loans rather than grant aid, infrastructure-centered programs, and the pursuit of mutual benefits—have created an image of Japan and South Korea's aid as self-serving. Amongst the OECD DAC donors, Japan and South Korea stand out as two of the most widely criticized donor countries based on allegations that they both prioritize national interests over the needs of recipient countries [21–23]. Indeed, what distinguishes them from other Western donors is that for both Japan and South Korea, aid has not been only altruistic, but also about mutual benefits, global recognition, and economic interests [23,24]. Meanwhile, both countries have committed to building disaster resilience in the international community by leading in, namely, DRR and green growth, while also committing to expand efforts for peacebuilding.

The previous literature that looked at Japan's foreign policy tended to focus on Japan's major DRR efforts, policy strategies, and funding trends [23,25,26]. In the case of South Korea, most of the climate literature has examined the process of green growth or SDGs mainstreaming into Korea's development portfolios, but these studies did not make policy connections to DRR despite the shared goals between the field of green growth, climate change adaptation, and DRR [27–29]. To the best of the authors' knowledge, no research has been conducted that compares the two donors' policy rhetoric in relation to DRR aid with their behavior as carried out in this study. The comparative approach allows us to examine the differences and similarities between these donors to provide a broader picture of DRR aid policy.

2. Literature Review

2.1. Disproportionate Risks of Climate Change

From 1990–2018, a total of 3734 disasters related to natural hazards were recorded in the emergency events database (EM-DAT). Figure 1 illustrates the frequency of each disaster

type from 1990 to 2018 in low, lower-middle, and upper-middle-income countries. Over the past 30 years, Asian countries have experienced more disasters than any other region. The cumulative number of disasters for East and South Asia between 1990 and 2018 was 3501, which accounts for 40.1% of the total reported disasters around the world in the same period. Floods occurred more often than any other type, accounting for 46.8% of incidents, followed by storms at 32.7%, and earthquakes at 9.2%. Bangladesh, Pakistan, and Vietnam have faced relentless floods over the past three decades. Because of under-reporting in low- and lower-middle income countries due to the difficulty of tracking disasters, the actual number of incidents in those places is expected to be higher.

As evident in Figure 1, statistics reveal that more than half of the people affected by disasters have lived in a FCS, demonstrating a "deadly interdependence" between conflict, fragility, and disasters [30–32]. In 2018, Somalia experienced deadly flooding, which affected over 700,000 people and, in Nigeria, flooding took 300 lives and impacted nearly 4 million people [33]. Droughts were frequent in many Sub-Saharan African countries, as 37.6% of the total drought incidents occurred in this region from 1990 to 2018 alone; more than 3 million people were affected by drought in Kenya. Additionally, Afghanistan suffered a major drought that impacted 2.2 million people, causing the internal displacement of thousands [34]. According to the UN, the drought in 2018 displaced more Afghans than the conflict between the Taliban and the domestic government [35]. According to a 2020 report by the International Committee of the Red Cross (ICRC), 14 of the 25 countries that are considered to be fragile and conflict-affected states are currently facing environmental degradation and climate change. In summary, the intersections between disasters and conflict and fragility are manifold, and have become a source of massive human suffering and even more instability and conflict in FCSs [36,37]. If the international community is to build resilience and peace across the world, it must understand the negative feedback loop, where existing fragility and conflict raise people's potential to be harmed by natural hazards, which in turn exacerbate the sources of tension and poverty; the international community must work together to confront these interrelated and mutually reinforcing risks [38].

Over the past decade, development research tried to capture the broad spectrum of a possible relationship between disasters and conflicts [5,31,37,39], and several aid projects have been conducted by development agencies to reduce the threats to human well-being from consequences of disasters and conflicts [40,41]. The sustainable development goals (SDGs), launched in 2015, recognize and reaffirm the urgent need to reduce the risk of disasters and promote peace, justice, and inclusion in FCSs. While 'peace' is explicitly mentioned in Goal 16, a peace dimension is found across the SDGs as a whole, and 25 targets in 10 of the 17 SDGs are related to DRR [42]. Indeed, building peace and resilience across the world is the priority. To this end, a more strategic and innovative approach that can break the negative feedback loop of disasters, conflict, and fragility is necessary for development aid to promise a meaningful path forward.

2.2. The Lead-Up to the Appearance of DRR in Development Assistance

Typically, DRR is a combination of measures that reduce exposure and susceptibility to natural hazards by enhancing coping and adaptive capacity [15]. The last two decades have seen intense global actions toward mainstreaming DRR principles in development planning and practices, due to the ongoing disasters in many developing countries. In fact, a series of UN conferences on disaster and climate risk management convened in Japan, namely in Yokohama in 1994, Hyogo in 2005, and Sendai in 2015.

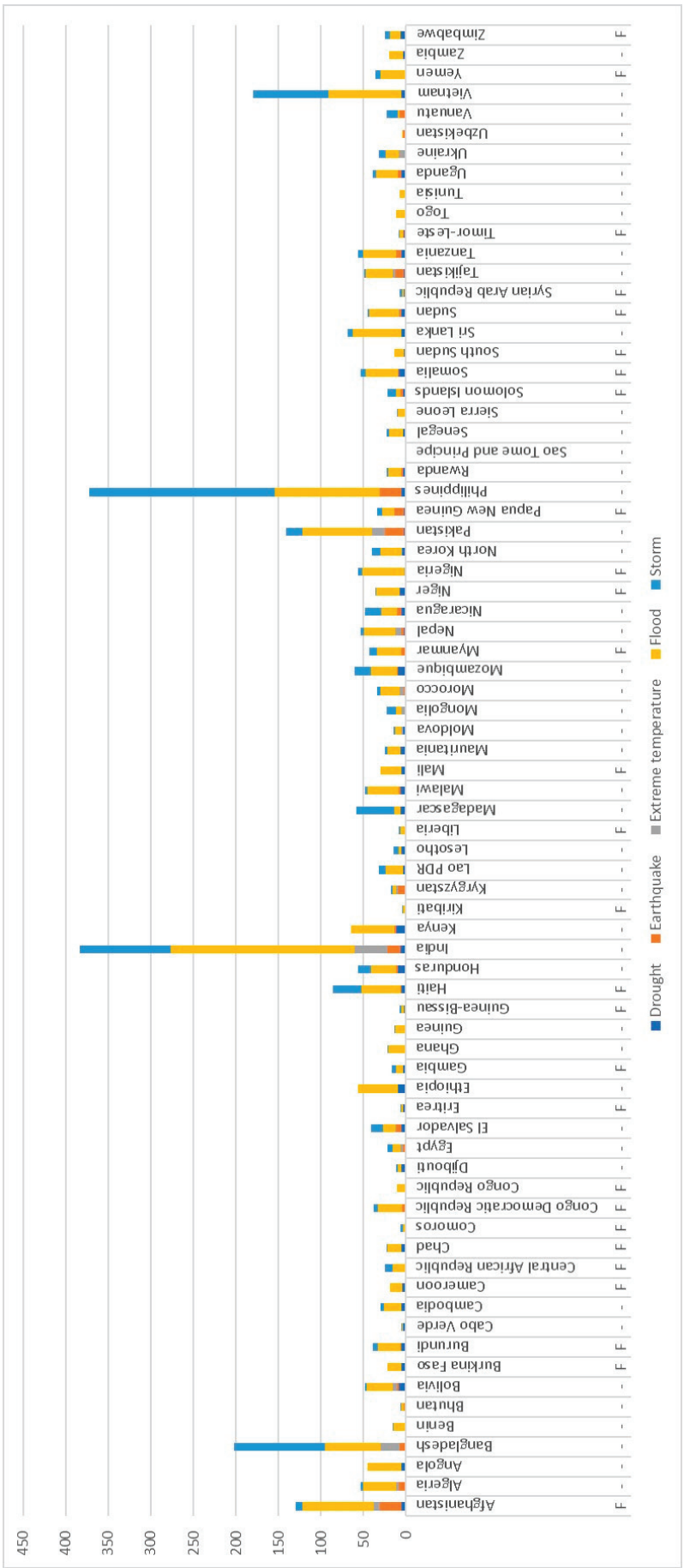

Figure 1. Frequency of disasters in low-income and lower-middle income countries in 1990–2018 (fragile states marked with "F" at the bottom). Note: The author used disaster occurrence data from the emergency events database (EM-DAT) and the World Banks' 2020 harmonized list to specify fragile states.

The Sendai Framework for Disaster Risk Reduction 2015–2030 calls for a strong integration of DRR into development. One of the targets of the Sendai Framework seeks to accomplish the following:

> '*Substantially enhance international cooperation to developing countries through adequate and sustainable support to complement their national actions for implementation of the present Framework by 2030.*' [16]

Nevertheless, the mere ratification of international DRR agreements tells us little about how serious countries are in addressing climate change. To confirm whether their commitment has been converted into action, it is important to examine donor's aid activities and track the exact amount of official development assistance (ODA) invested in DRR.

Many studies that attempted to analyze DDR via ODA reported that the lack of adequate DRR classification and information in the OECD development assistance committee (DAC)'s creditor reporting system (CRS) poses a major bottleneck in estimating the aid flows in DRR or climate-related areas [25,43]. There have been no standardized guidelines for tracking such investments. This is largely due to how DRR has rarely been seen as a stand-alone factor; DRR activities have been commonly included within wider programs and projects, including those related to rural development, food security, health systems, energy production, environmental protection, etc. Due to the cross-cutting nature of DRR, it was hard to quantify the exact amount spent on DRR, and donors were unsure of how to report it; thus, the data on DRR investment has been limited [25,43]. Against this backdrop, in 2018, OECD DAC members agreed to add a new marker called "Disaster Risk Reduction" to the CRS database to easily identify DRR-related ODA. However, scholars have questioned how accurately this marker conveys the true purpose of aid in practice based on the experiences with other environmental markers, namely the "Rio climate" markers [44]. For example, Roberts et al. [45] found that only 25% of projects with Rio markers were actually relevant to climate change, and Michaelowa and Micahelowa [46] and Junghans and Harmeling [47] later came to similar conclusions. Consequently, environmental markers lack reliability as well as validity [44,48].

Because of the newness of the DRR marker in CRS, not all projects have been screened against the DRR marker. As an alternative, this study uses five different sectors to identify DRR aid. While there is no single approach to track and evaluate DRR aid, this study will consider sectors commonly used in other studies [25,43] to evaluate DRR aid, such as (i) "disaster prevention and preparedness", (ii) "reconstruction relief & rehabilitation", (iii) "general environmental protection", (iv) "energy generation and non-renewable sources", and (v) "disaster risk reduction", a subcategory of the multi-sector. Furthermore, "emergency response"—a category under "humanitarian Aid"—may appear directly related to DRR, but it has served multiple purposes, responding to a variety of needs including education, protection, and safety in conflict situations, health, pandemics, post-crisis refugees, etc. [25,49]. For this reason, "Emergency Response" will be omitted from further analysis. The sectoral name in (i), (ii), and (v) makes apparent its relevance to DRR by its name. The "energy generation and renewable resources" sector is included since the replacement of fossil fuels with various sources of renewable energy plays a crucial role in all stages of DRR, especially considering the importance of the energy sector in everyday activities [50]. The "general environment protection" sector is also added to the estimation of DRR aid, given that many development projects classified into this sector are designed with DRR-related intents, such as flood prevention and control, environmental policy, protection of ecosystems and biosphere, and environmental research [43,51]. Furthermore, despite the large number of sectors that may include an element of DRR, Spark's research (2012) found that only three sectors–disaster prevention and preparedness, reconstruction relief and rehabilitation, and general environmental protection accounted for 80% of the entire DRR aid in the fiscal years 2006–2010 [25]. This method is prone to bias and omission, as the selection depends entirely on the sector description. It will be sufficient, however, to explain the recent trend of donors' ODA spending in DRR.

2.3. Japan and Korea's Environmental Initiatives

In 2019, Japan's ODA stood at 15.5 billion USD, making Japan the fourth largest donor in absolute terms (OECD statistics). Being one of the oldest members of the OECD-DAC, Japan has been the only major aid donor not located in Western Europe or North America. On the other hand, South Korea only joined the OECD-DAC in 2010. In 2019, South Korea spent 2.5 billion USD on its ODA, making South Korea the 15th largest donor country (OECD statistics). Although Japan does not select priority partner countries, its recipient countries have been concentrated in the Asia region, with a slow expansion to sub-Saharan Africa in recent years [52]. In the case of South Korea, it has chosen priority countries every five years, allocating a large proportion of its ODA to them. In January 2021, the South Korean government re-selected priority partner countries for the next five years. The new priority partner countries are composed of 11 Asian countries, 8 African countries, 4 Central and South American countries, 2 Middle Eastern countries, and 1 in Oceania [53].

Japan and Korea share very similar developmental approaches. Both have allocated about three-quarters of their total ODA to bilateral ODA over the past decade (OECD statistics). Both countries have been subject to criticism for their self-serving features, including a high proportion of concessional loans and tied aid, often heavily tied to procurement of their own domestic contractors [54–57]. In addition, their aid has primarily focused on the hardware of development (i.e., infrastructure and industrial production) with less concern for the software (i.e., governance and institutions) [58]. In sum, Japan and Korea's ODA have been often regarded as instruments of growth rather than of relief and life-saving assistance.

Nevertheless, both countries deserve serious credit for actively promoting DRR and climate change adaptation, which is referred to as activities that reduce the vulnerability of human and natural systems to the impacts of climate change [59]. As a host country for all three World Conferences on Natural Disasters from 1994 to 2015, Japan has played a leading role in sharing its experience, knowledge, and techniques relating to DRR, and is strongly committed to building a sustainable and resilient international community [60]. Between 1991 and 2010, Japan spent the largest amount of ODA for DRR activities among the DAC donors, disbursing 64% (3.7 billion USD) of the total funding [61]. Furthermore, important synergies exist between the Sendai Framework and Japan's ODA Charter, revised in 2015 for the third time since its initial formulation in 1992. It outlines three basic policies, as follows: (i) contribute to peace and prosperity, (ii) promote human security, and (iii) emphasize self-reliant development and collaboration [62]. Japan's desire for peace, stability, and prosperity in the international community can only be realized when safe and resilient societies are built in developing countries, especially in fragile states. There is overlap in the thematic priorities of Japan's ODA and the Sendai Framework, as both are grounded in "human security" perspectives.

Whereas Japan has been at the forefront of DRR initiatives, South Korea has been at the front of green growth initiatives. In 2005, the concept of "green growth" was pioneered and brought into the discussion by the United Nations Economic and Social Commission for Asia and the Pacific (UNESCAP) during the Fifth Ministerial Conference on Environment and Development (MCED) in Asia and the Pacific held in Seoul, Korea. Regarded as the most appropriate approach for harmonizing economic growth with environmental sustainability, the principles and approaches of green growth attracted significant attention in many countries, and have been incorporated into various DRR activities [63–65].

South Korea is the first country to make green growth a national strategy [64,66]. In response to the 2008 global financial crisis, South Korea adopted "low carbon green growth" as the country's new development vision with the hope of getting the economy back on track. South Korea formulated two major national plans for green growth, as follows: the National Strategy for Green Growth (2009–2050) and the Five-Year Plan (2009–2013). These plans were implemented to ensure that green growth initiatives are pursued in a systematic and organized manner. Around the same time, South Korea launched the East Asia Climate Partnership (EACP), the most significant initiative under "green ODA", and dedicated

200 million USD for 2008–2012 in the form of ODA [67]. Notably, Korea turned its pledge into action to fight climate change and promote green growth. Attempting to establish South Korea as truly a global player, South Korea joined the OECD-DAC in 2010 and pledged to spend 30% of its entire ODA on green projects by 2020, up from 11% in 2007 [68]. Lastly, in the same year, South Korea established the Global Green Growth Institute (GGGI) as a way to extend its green growth strategies into "green ODA", and to share its green growth experience with developing countries [66].

In South Korea, the presidential election takes place every five years, and the new foreign policy agenda set by a new office shapes the direction and strategies of development cooperation policies, often resulting in policy discontinuity and inconsistency [69]. Aid policy in Korea is strongly determined by the type of vision the new president has for the future of the country. The term "green growth"—a slogan that epitomized the national development policies from 2008–2013—has gradually disappeared in South Korea's ODA agenda with the start of a new presidency in 2013, but the concept of green growth—reducing environmental impacts of society while still expanding the economy—remained in the ODA agenda under different names and purposes, such as "sustainable development" and "climate change adaptation" [69,70].

As for security and peacebuilding efforts, Korea pledged to increase its support for FCSs and least-developed countries following the endorsement of the New Deal for Engagement in Fragile States in 2011, which is an international guidance document on supporting FCSs. Specifically, South Korea formulated its own guidelines to support FCSs in 2012, a plan to implement the New Deal in 2015, and the Mid-term Assistance Strategy for Fragile States in 2016. South Korea expressed a strong willingness in recent years to contribute to institutional-building, peacekeeping, and the containment of transborder threats in FCSs.

Such evidence of climate, DRR, and peacebuilding initiatives by Japan and South Korea leads us to the following questions: how responsive are Japan and South Korea to the needs of low-income countries, specifically those experiencing compound risks of disasters and conflict? Are these donors more sensitive to the interplay of disasters and conflict, or are they more influenced by one type of risk over the other? For 50 years, developed countries used ODA as a strategic tool to respond to humanitarian crises. In the name of ODA, developed countries have delivered various forms of assistance including projects, trainings, the dispatch of experts and volunteers, and the import of equipment for development cooperation. Indeed, ODA has been the global standard for measuring donors' responsiveness to the needs of recipient countries, as well as assessing their performance against their pledges. In this study, donors' responsiveness to disaster risk is measured with the actual amount of ODA disbursed with DRR objectives.

As disasters associated with natural hazards could compromise development and peacebuilding efforts in FCS, this study tests a hypothesis regarding an increase in responsiveness by Japan and South Korea to recipient countries with combined risks. The result of this study would answer our main question of whether Japan and Korea have become donors who are sensitive to the needs of developing countries with fragility and high risks of disaster, moving beyond self-interest by turning their pledges to disaster resilience and peacebuilding into real action.

3. Methodology

3.1. Data Description

We used several indicators to explore the determinants of Japan and Korea's bilateral DRR aid. For reference, determinants of DRR aid by OECD-DAC donors as a group have also been looked at, which would help us understand in general whether donors' policies are oriented toward disasters or man-made crises in terms of aid allocation.

As a dependent variable (DV), we used the disbursements of total bilateral ODA, as well as the one of the combined bilateral ODA in five DRR-related sectors. Both are converted to natural logs to account for the skewed distribution. The reason for focusing

on bilateral aid is because most climate aid is bilateral [44,71]. By 2008, bilateral aid represented two-thirds of the 15 million USD categorized as climate aid. According to a study by Victor [72], bilateral environmental aid is over 20 times larger than multilateral climate funds. Additionally, as previously mentioned, our main countries of interest, Japan and Korea, allocate about three-quarters of their total ODA for bilateral ODA. Thus, the bilateral ODA of Japan and Korea, and that of other OECD-DAC donors, is substantively more important and more likely to have discernible effects in the environmental field.

As for the core explanatory variables, we constructed four respective categories (disaster-prone countries, FCS, both, and neither). Countries in the reference category are neither FCSs nor disaster-prone countries, but either low or lower-middle income countries, having a GNI per capita below UDS 4045 based on the World Bank country classification by income level.

As for constructing the dummy variable "FCS", we used the Fragile State Index (FSI). The FSI is based on 12 key political, social, and economic indicators and over 100 sub-indicators. The 12 key risk indicators measure whether conditions with regard to security apparatus, fractionalized elites, group grievance, economic decline, uneven economic development, human flight and brain drain, state legitimacy, public services, human rights and rule of law, demographic pressures, refugees and internally displaced persons, and external intervention, are improving or worsening. developed by a US think tank, the Fund for Peace. Since 2005, the FSI has measured the social, economic, and political pressures facing countries around the world based on a scale of 0–120, with 0 being the lowest intensity (least fragile) and 120 being the highest intensity (most fragile). As a composite index, it is comprised of 12 primary indicators that create a representation of overall fragility and conflict. This is used extensively by government bodies and aid agencies to assess their contributions toward development initiatives [73]. The World Bank and OECD also refer to the FSI when creating their own list of fragile states. From 2016, KOICA, Korea's ODA agency, also began to refer to the FSI to identify countries in need and to select priority fragile states for support, and now uses a cutoff value of 90 in the FSI score [74]. We apply the same rule and consider a country fragile if it has an FSI score greater than or equal to 90.

As for constructing the "disaster-prone countries" dummy variable, we used the Climate Risk Index (CRI). The CRI uses a country's fatalities and economic losses to calculate the impacts on each country. The average ranking in four indicating categories, namely number of deaths, number of deaths per 100,000 inhabitants, sum of losses in USD in purchasing power parity, and losses per unit of gross domestic product, are used to calculate the CRI score. The CRI was developed by a German think tank, GermanWatch. This is one of the leading risk indices, and it is highly cited in scientific domain [75–77] The CRI analyzes to what extent countries have been affected by the impacts of extreme weather events based on four sub-indicators, such as fatalities and economic loss [78]. The higher the CRI score, the more vulnerable the country is to disasters associated with natural hazards. Since the average CRI score for around 180 countries in the period of 1990–2018 was 90, this number was used as a cutoff value to create a dummy variable, namely "disaster-prone countries." In the end, there were a total of 66 low and lower-middle countries in 4 different groups, with 20 in the disaster-prone countries group, 14 in the FCS group, 14 in both, and 18 in neither.

Over the past 20 years, more than 4.4 billion people have been made homeless or injured [79]. According to the 'Lost at home' report by UNICEF, in 2019 alone, 33 million new people became internally displaced by conflict and disasters worldwide, around 25 million of which were due to disasters associated with natural hazards. Given that displacement associated with disasters is one of today's most serious consequences of natural hazards, displacing millions from their home every year, the number of internal displacement cases, provided by the Internal Displacement Monitoring Center (IDMC), is used as an indicator to show the scale and severity of disasters within countries. We did not

put them in same regression model due to the nature of the strong correlation between the number of internal displacement cases and the "disaster-prone countries" dummy variable.

For control variables, we used 11 additional indicators across regression models. They include a population indicator from the UN Population Prospects, as well as fragility and conflict indicators, such as security threat, economic inequality, public services functioning from the Fund for Peace. Macroeconomic indicators, such as GDP per capita, foreign direct investment (FDI), trade openness, and remittances from the World Bank were also used.

Firstly, population is an important predictor of development assistance [24,80–82]. More populous developing countries are expected to be in greater need of development and more likely to receive aid [83] but, at the same time, large population tends to decrease marginal benefits of aid allocation and, thus, aid has been much higher for counties with small populations in relative terms [84]. Secondly, country's income level (GDP per capita) is also an important factor to consider because the material need of recipient countries is measured by the level of income [85]. As countries with low per capita income have a greater need for foreign aid, donors tended to respond negatively to per capita income [86]. Third, there has been a notion that FDI and aid are complementary sources of capital [87]. While the aid allocation sends a signal to firms that donors have trust in local authorities, FDI decision signals the presence of good physical infrastructure in recipient countries to donor countries. We expect countries receiving larger FDI would attract more aid. Fourth, the degree of the recipient country's trade openness has been one of the most frequently used determinants of development finance [83,88]. Trade liberalization policies would enhance competitiveness and send signals to donors of the country's commitment to sound macroeconomic policies. In this study, we expect that donors allocate more aid to reward countries for the good quality of their economic policies, in particular their trade liberalization policies. Lastly, a number of past studies analyzed the relationship between aid and remittances, and found that development aid acts as a complement to remittances [18,89,90]. By improving household capacity to invest in education and healthcare, remittance does improve the recipient country's absorption capacity, the lack of which has been often pointed out as a bottleneck to aid scaling up. Therefore, remittances can in fact lead to an increase in aid. In this study, we expect likewise.

As for proxies for fragility and conflict, security threats to a recipient country, the presence of basic state functions, and inequality within the economy are selected. Security threats refer to the level of danger associated with events, such as bombings, attacks, rebel movements, or terrorism [91]. Public service functioning refers to the presence of basic state functions in terms of providing essential services, such as health, education, water and sanitation, transport infrastructure, etc. The economic inequality indicator refers to structural inequality that is based on identity groups, such as racial, ethnic, or religious inequality. These proxies are carefully chosen based on the key characteristics of fragile states defined by several institutes [6,92–94] that, as follows: (i) fragile states are active in armed conflicts involving the use of weapons, violence, and force; (ii) they have weak governance, ineffective public administration, and rule of law and, therefore, their government cannot or will not provide its core functions to the majority of its people; and (iii) structural inequality is inherent in those states due to extractive institutions, which prevent some people from having economic opportunities to better their lives. Such inequality in return fuels communal tensions and violence, creating the 'vicious cycle'. Indeed, all three indicators appear to be good proxies for describing the conditions of state fragility. The higher the score in each indicator, the worse the country's fragility.

Lastly, we added a couple of regional indicators in regression models on Korea and Japan, such as South and East Asia, and Africa, hoping that our core explanatory variables, fragile states and disaster-prone countries dummy variables, do not spuriously capture the effects of regions since both Korea and Japan tend to favor countries in these two regions in terms of aid allocation. Given that many of these indicators are available from 2008 up to 2018, we conduct a regression analysis based on the 2008–2018 data.

3.2. Methodological Framework

In this study, we use dynamic panel data, meaning that the current behaviors of the dependent variable depend upon past behavior. In addition, some of our explanatory variables are endogenous. For instance, the direction of the causality flow of bilateral ODA to the characteristics of recipient countries remains uncertain.

The quantity of ODA is likely to be endogenous to each recipient country's characteristics. Often, donors are reluctant to interfere in states characterized by low democratic activity, absence of public services, corruption, and a weak legal system [95,96]. There is evidence that poor countries with thorough policies received more financing than equally poor countries with weak economic management and political instability [88]. Besides the situations associated with fragility, countries differ in several ways, such as their colonial history, political regimes, ideologies, religious affiliation, and geographic locations. Failing to take this heterogeneity into account will inevitably produce bias in the results.

Using a lagged dependent variable in panel data regression does come with complications, since lagged dependent variables are correlated with the disturbance term, which is due to unobserved effects, resulting in a bias, particularly in the "small T, large N" context [97]. If individual-level error terms are correlated with the lagged dependent variable to some degree, their coefficients are likely to be biased as well.

The generalized method of moments (GMM) estimators help overcome this problem by utilizing a set of instruments to deal with the potential problem of correlation between the lagged dependent variable and the disturbance term [98]. The Arellano and Bond estimator works by taking the first difference of the regression model to sweep out the individual fixed effect and its associated omitted variable bias; it then uses lagged levels of the dependent variable as instruments for differenced lags of the dependent variable. This is the standard first-difference GMM estimator. A potential weakness in the difference GMM is that the lagged levels are often rather poor instruments for first-differenced variables, and the dependent variable is close to a random walk. Arellano and Bover (1995), and later and Blundell and Bond (1998), identified this weakness and modified the estimator to include lagged levels as well as lagged differences, naming this the system GMM estimator. The introduction of more instruments at both levels and first-differences in the estimation process can dramatically improve efficiency. We will employ the two-step robust option, since it is more efficient than the one-step robust in system GMM [99].

For the possible weaknesses in the estimation results, such as unobserved heterogeneity, endogeneity, autocorrelation, and weak instruments, we conduct the Arellano–Bond AR test for autocorrelation and the Hansen J tests for over-identifying restrictions to provide some evidence of the instruments' validity.

Given the considerations presented above, the GMM is specified as follows:

$$y_{it} = \alpha_1 y_{it-1} + \alpha_2 X\prime_{it} + \beta_1 D_{it} + \beta_2 F_{it} + \beta_3 C_{it} + u_{i,} + \varepsilon_{it}$$

where y_{it} is the dependent variable (DV) which is either log of per capita ODA or DRR aid of country i at time t. Additionally, y_{it-1} is the one-period lagged dependent variable; X'_{it} represents a vector of control variables; the dummy variable D_{it} captures natural hazard vulnerability, taking 1 for environmentally vulnerable states and 0 otherwise; F_{it} is a measure of fragility and conflict, taking 1 for fragile states and 0 otherwise; C_{it} captures the concomitance of natural hazards and conflicts, taking 1 for countries under compound risks and 0 otherwise; $u_{i,}$ is an unobserved country-specific effect; and ε_{it} is the remainder error term that varies over both country and time.

4. Results

4.1. General Trend of DRR Aid over 2006–2019

Between 2006–2019, 86 billion USD of official ODA was reported as DRR, which constituted approximately 5.8% of the total ODA (1.5 trillion USD) spent by the OECD DAC donor countries over the same period. This DRR aid has increased considerably from

2006 to 2010, rising from 3.3 billion to 7.9 billion USD in 2010, but since then the amount has been up and down around 7 billion USD, standing at 7.3 billion USD in 2019. The increase in DRR aid in 2010 may partially be due to the improved reporting of expenditure to DRR, as 21 out of 24 donors began to report their DRR funding from 2010, compared to only 10 in 2006 [25]. Although a new marker, "disaster risk reduction", was added to the CRS reporting format in 2019 for 2018 data, there was no significant change in DRR amount from 2017 to 2018.

The DRR aid has been marginal for all donor countries. Table 1 shows that only two donors, Norway and Germany, have spent more than 10% of their total ODA on DRR between 2006–2019. Seven donors (France, Finland, Denmark, Spain, Japan, New Zealand, Czech Republic, and the UK) have allocated around 5–8% of their budgets, and the remaining donors have allocated below 5%. However, in absolute terms, Japan was the second largest donor to DRR, spending 12 billion USD throughout 2006–2019. Korea's DRR aid has amounted to 4.57%, which is the average percentage for all DAC members in 2006–2019. Overall, data suggest that the majority of OECD donors have not met the wide range of commitments they have made in the DRR framework.

Figure 2. compares the top 10 recipient countries of Japan and Korea with those of OECD-DAC members as a reference. The main recipients of Japan's DRR aid throughout 2006–2019 were Asian countries, with 7 out of 10 being in East and South Asia; none of these countries were FCSs. In the case of South Korea, the composition of the top 10 recipient countries were more diverse, with four East and South Asian countries, two Central American countries, two Sub-Saharan African countries, and one Middle East country; three of these were FCSs (marked with [F] in the figure). However, 6 out of these 10 are Korea's priority partner countries (Vietnam, Mongolia, Lao PDR, Nepal, Indonesia, and Mozambique), meaning they were meant to receive Korea's aid regardless of their state of danger. As for the OECD countries, only one recipient country was a fragile state.

In addition, for both Japan and Korea, a heavy concentration of DRR aid in relatively few countries and perhaps in a small number of projects is found as a pattern. Both countries allocated about 75% of the total DRR aid to their top 10 recipient countries for 2006–2019, whereas OECD-DAC members as a whole allocated about 45% of their total DRR aid to their top 10 recipient countries, meaning that, compared to Japan and Korea, many more high-risk countries shared little funding across many projects. In an exact number figure, 30 countries shared about 75% of the total DRR aid throughout 2006–2019. However, in terms of income classification, only about 18% went to low-income countries, whereas lower-middle income and upper-middle income groups received about 44% and 37% of OECD-DRR aid, respectively. For instance, China, Brazil, and Mexico—classified as upper-middle income countries, received around 6%, 5.1%, and 3.6% of the total DRR aid throughout 2006–2019, respectively, for various types of disasters, which may suggest that, when allocating DRR aid, donors' main priority is recipient countries' exposure to natural hazards alone, ignoring the potential for a far greater risk that may arise from the interplay between natural hazards and poverty, as well as conflict in the recipient country.

Figure 3 shows that none of the five DRR sub-sectors exceeded 5% of the total ODA in 2006–2019. Korea's allocation for reconstruction and rehabilitation and Japan's allocation for general environment protection rose close to 5% immediately following their endorsement the of Hyogo Framework in 2005, but this did not sustain over time. While investment in all DRR sectors was marginal, constituting less than 1% of the total ODA over time, the amount allocated for the sector of energy generation and renewable sources has fluctuated the most for both countries. Overall, there was no sign of sufficient support for DRR from both countries.

Table 1. The OECD-DAC member's total ODA spending towards DRR in 2006-2019 (unit: USD in millions).

OECD-DAC Members	Energy Generation, Renewable Sources (1)	General Environment Protection (2)	Disaster Risk Reduction (3)	Reconstruction Relief & Rehabilitation (4)	Disaster Prevention & Preparedness (5)	Total DRR Funding (a = 1 + 2 + 3 + 4 + 5)	ODA Total (b)	% of DRR in ODA (a/b)
Germany	9235	8212	189	3199	492	21,328	201,190	10.60%
Japan	4521	3824	1356	1605	874	12,180	183,753	6.63%
United States	463	7154	15	1038	1516	10,185	410,941	2.48%
France	2420	7219	108	306	35	10,088	117,424	8.59%
United Kingdom	841	5528	61	790	786	8006	134,267	5.96%
Norway	1120	4860	43	270	280	6575	43,699	15.04%
Sweden	228	1706	51	188	198	2371	48,116	4.93%
Netherlands	496	1093	81	601	22	2292	59,151	3.88%
Spain	786	742	7	415	118	2068	30,718	6.73%
Canada	776	616	50	216	188	1846	42,999	4.29%
Denmark	285	1259	0	159	41	1744	25,580	6.82%
Australia	42	679	18	492	386	1618	39,428	4.10%
Switzerland	115	799	25	172	165	1276	30,994	4.12%
Italy	435	358	12	327	41	1172	24,599	4.77%
Korea	402	285	43	101	87	918	18,470	4.97%
Finland	283	268	5	186	31	773	10,023	7.71%
Belgium	141	266	2	221	77	707	20,944	3.38%
New Zealand	138	43	4	71	57	312	4898	6.38%
Ireland	7	57	3	152	69	289	8202	3.52%
Austria	89	76	5	40	19	229	10,832	2.11%
Portugal	120	21	0	8	1	150	4056	3.69%
Luxembourg	4	21	4	64	35	129	4186	3.08%
Czech Republic	14	6	2	19	3	45	710	6.27%
Greece	4	26	0	2	0	32	1929	1.65%

Table 1. *Cont.*

OECD-DAC Members	Energy Generation, Renewable Sources (1)	General Environment Protection (2)	Disaster Risk Reduction (3)	Reconstruction Relief & Rehabilitation (4)	Disaster Prevention & Preparedness (5)	Total DRR Funding (a = 1 + 2 + 3 + 4 + 5)	ODA Total (b)	% of DRR in ODA (a/b)
Iceland	14	1	0	1	2	17	396	4.30%
Poland	2	5	1	5	2	16	1328	1.17%
Hungary	1	1	0	8	0	10	479	2.07%
Slovenia	1	3	0	1	2	8	245	3.37%
Slovak Republic	0	0	0	2	0	2	169	1.32%

Note: Numbers and letters in parentheses in each column are inserted to show how the total DRR funding in column 7 and % of DRR in ODA in column 9 are calculated.

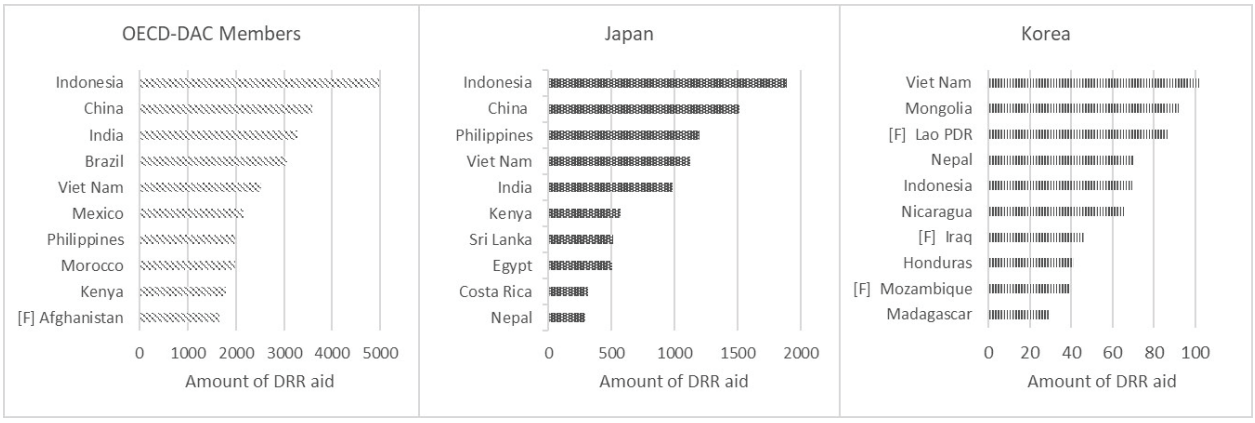

Figure 2. Top 10 DRR recipient countries, 2006–2019 (unit: in USD millions). Note: the author used data from OECD Creditor Reporting System (CRS). Here, [F] indicates fragile states.

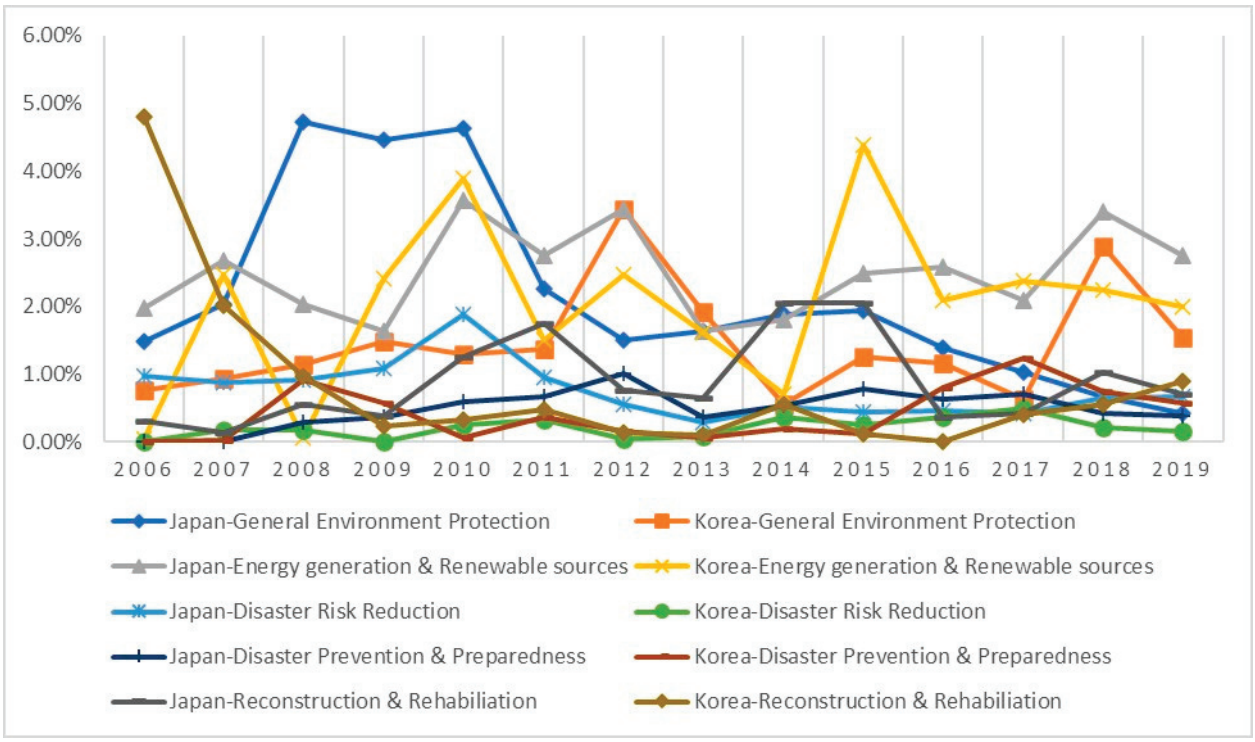

Figure 3. Changes in Japan and Korea's DRR spending as % of total ODA in 2006–2019. Note: author used data from OECD Creditor Reporting System (CRS).

4.2. Empirical Results

Table 2 provides the estimation results for the allocation of both total bilateral ODA and DRR aid. The coefficients for the three dummy categories show a clear-cut pattern. The results in models 3, 7, and 11 show that OECD-DAC donors, Korea, and Japan provided approximately 36%, 11%, and 39% more of DRR aid to disaster-prone countries, respectively, than those low-income countries in the reference group throughout 2008–2018. This indicates that donor states significantly increase their DRR aid with respect to the recipient countries' level of disaster risk, but not to their level of fragility and conflict. This reveals that, at least for utilizing DRR aid, the underlying orientations of donor countries are focused on the recipient country's vulnerability to climate-induced natural hazards rather than being strategically deployed to respond to risks from a combination of disasters, conflict, and fragility. The result that donors do not respond to the DRR needs of

FCSs, could be a reflection of difficulties and challenges in implementing DRR work in FCSs because of violence, social and political instability, weak governance, and a generally unsafe environment [100,101]. Yet, there was no indication that FCSs, nor countries with both frequent conflicts and disasters, receive significantly less aid than those in the reference group.

Given the strong correlation between those dummy groups and their country characteristics, the dummy groups are omitted from models 2, 4, 6, 8, and 10 and, instead, characteristics that describe different dimensions of countries' fragility and conflict are included. As a proxy for vulnerability to natural hazards, internal displacement is included. Korea's aid responsiveness to the recipient country's internal displacement situation was much stronger via its total bilateral ODA. In model 6, a 1% increase in internal displacement cases resulted in a 0.053% increase in the amount of Korea's bilateral ODA but, ironically, such responsiveness disappears in its DRR aid. However, in the case of Japan, internal displacement was an important determinant of its DRR aid. The result of model 12 shows that countries that experienced large internal displacement received larger amounts of DRR aid from Japan. This suggests that Korea's DRR aid may have a specific purpose of strengthening recipient countries' adaptive capacity to climate change, whereas Japan intends to help the victims in post-crisis situations, who are generally poorly assisted by their own government. While recipient countries' internal displacement situation did not have a significant influence on Japan's total bilateral ODA allocation, one must not forget that the amount of Japan' ODA specifically allocated for DRR sectors is significantly larger than that of Korea. For instance, Japan's DRR aid for 2006–2019 was approximately 13 times greater than that of Korea, meaning Japan has spent a significant amount of money for post-crisis situations over the past decade with their DRR aid. Overall, the internal displacement situation is an important factor that influences the ODA budget allocation of bilateral donors.

The population size of the recipient county is included across all models, assuming that larger countries receive more overall aid. While large countries received more DRR aid from Japan and other DAC countries, they received less in terms of overall development assistance, meaning donors are likely to have multiple motivations across different types of aid [102]. The total bilateral aid with multiple objectives may be more likely to be associated with donors' self-interest and, thus, less likely to be used for populous countries where the marginal benefits of aid decrease [84]. However, in the context of DRR aid, donors' altruistic humanitarian motivation tends to play a bigger role because what really matters is helping as many people as possible that are devasted by wars and natural hazards. In case of Korea, population size did not influence its DRR aid allocation.

The most common indicator used in ODA development assistance studies is GDP per capita, which approximates the economic needs of the recipient country's population. The effect of the economic hardship was not strong on Japan and Korea's aid allocation decisions, which is rather surprising since both Japan and Korea have a reputation of favoring countries with growth potential and, thus, growing GDP [24,103]. However, Japan does appear to pursue self-interests in the sense that it has assisted countries with higher FDI. Perhaps such a result can be explained by the fact that institutions and financial systems tend to be better in countries receiving a high level of FDI [104,105] and, thus, more effective use of ODA is guaranteed to some degree. A slight tendency for increased aid for countries with higher FDI and a higher trade share is found for OECD-DAC donors. Both variables are significant at the 0.1 level. This confirms the results of various studies that showed the United Kingdom favored countries that have a high trade share relative to their GDP [58,106].

Table 2. Determinants of bilateral ODA in the period of 2008–2018.

	OECD DAC				South Korea				Japan			
	Bilateral ODA per Capita		DRR Aid		Bilateral ODA per Capita		DRR Aid		Bilateral ODA per Capita		DRR Aid	
	Model 1	Model 2	Model 3	Model 4	Model 5	Model 6	Model 7	Model 8	Model 9	Model 10	Model 11	Model 12
Lagged D.V	0.595 ***	0.523 ***	0.476 ***	0.593 ***	0.999 ***	0.441 ***	0.669 ***	0.743 ***	0.222 *	0.166 **	0.229 **	0.239 **
	(0.076)	(0.151)	(0.0765)	(0.167)	(0.100)	(0.078)	(0.153)	(0.125)	(0.093)	(0.082)	(0.084)	(0.102)
Disaster-prone countries	0.116		0.362 *		0.041		0.113 *		−0.034		0.388 *	
	(0.101)		(0.184)		(0.061)		(0.051)		(0.14)		(0.191)	
FCS	0.085		−0.0948		−0.135		0.007		−0.151		−0.0632	
	(0.109)		(0.169)		(0.495)		(0.031)		(0.141)		(0.123)	
Countries with compound risks	0.141		−0.0730		0.116		0.02		−0.107		0.109	
	(0.176)		(0.177)		(0.479)		(0.046)		(0.153)		(0.190)	
log of cases of internally displaced persons		0.014		0.045 **		0.053 *		−0.002		0.021		0.0604 **
		(0.017)		(0.017)		(0.024)		(0.006)		(0.016)		(0.0216)
log of population	−0.175 ***	−0.180 *	0.309 ***	0.293 **	−0.024	−0.297 *	0.009	0.006	−0.253 ***	−0.242 ***	0.200 ***	0.192 ***
	(0.049)	(0.079)	(0.063)	(0.111)	(0.387)	(0.16)	(0.020)	(0.019)	(0.051)	(0.054)	(0.057)	(0.057)
log of GDP per capita	−0.113	−0.225 *	−0.108	−0.223 **	−0.033	0.043	0.024	−0.051	−0.026	0.049	0.162	−0.057
	(0.07)	(0.099)	(0.090)	(0.083)	(0.032)	(0.145)	(0.031)	(0.032)	(0.131)	(0.104)	(0.0925)	(0.088)
FDI (% of GDP)	0.004		0.0005		0.00005		0.001		0.008 ***		−0.002	
	(0.002)		(0.003)		(0.00011)		(0.003)		(0.002)		(0.003)	
Trade openness (% of GDP)	0.002		0.005 **		−0.0001		0.001		0.002		0.0006	
	(0.001)		(0.002)		(0.049)		(0.0009)		(0.001)		(0.003)	
log of inflow remittances	−0.006		0.007		−0.031		0.0003		−0.003		0.012	
	(0.005)		(0.009)		(0.018)		(0.003)		(0.0075)		(0.009)	
Security threats		−0.097 *		0.030		−0.199 *		−0.012		−0.078 *		0.052
		(0.041)		(0.041)		(0.1002)		(0.012)		(0.04)		(0.042)
Public Services		−0.211		−0.008		−0.087		−0.019		0.108		−0.547
		(0.141)		(0.095)		(0.111)		(0.019)		(0.087)		(0.403)
Economic Inequality		0.020		0.042		−0.037		0.006		−0.079		0.0095
		(0.091)		(0.065)		(0.137)		(0.027)		(0.044)		(0.057)
South and East Asia *					0.004	0.212	0.004	0.0001	0.869 ***	0.661 *	0.993 ***	0.632 ***
					(1.252)	(0.145)	(0.105)	(0.073)	(0.239)	(0.308)	(0.280)	(0.192)
sub-Saharan Africa **					0.859	0.236	−0.075	-0.081	0.109	0.008	−0.0102	−0.130
					(1.183)	(0.256)	(0.058)	(0.052)	(0.208)	(0.151)	(0.252)	(0.141)

Table 2. *Cont.*

	OECD DAC				South Korea				Japan			
	Bilateral ODA per Capita		DRR Aid		Bilateral ODA per Capita		DRR Aid		Bilateral ODA per Capita		DRR Aid	
AR(1)	0.003	0.042	0.000	0.000	0.001	0	0	0.043	0.015	0.027	0.000	0.002
AR(2)	0.132	0.653	0.325	0.739	0.148	0.313	0.463	0.421	0.231	0.462	0.623	0.874
Hansen test of over-identifying restrictions	0.318	0.312	0.543	0.892	0.319	0.516	0.331	0.679	0.164	0.442	0.343	0.607
Observations	500	309	504	313	482	411	504	420	488	412	504	427
Number of groups	60	53	60	53	58	60	60	59	60	61	60	61
Number of instruments	19	28	19	19	21	20	21	19	21	29	21	19

Note: Robust standard errors in parenthesis. *** $p < 0.001$, ** $p < 0.01$, * $p < 0.05$; * South and East Asia countries are as follows: Bangladesh, Bhutan, Cambodia, India, Mongolia, Myanmar, Nepal, Pakistan, Papua New Guinea, Philippines, Solomon Islands, Sri Lanka, Timor-Leste, and Vietnam; ** Sub-Saharan Africa countries are as follows: Angola, Benin, Burkina Faso, Burundi, Cabo Verde, Cameroon, Central African Republic, Chad, Comoros, DR Congo, Congo Republic, Côte d'Ivoire, Eritrea, Ethiopia, Gambia, Ghana, Guinea, Guinea-Bissau, Kenya, Lesotho, Liberia, Madagascar, Malawi, Mauritania, Mozambique, Niger, Nigeria, Rwanda, Senegal, Sierra Leone, Sudan, Tanzania, Togo, Uganda, Zambia, Zimbabwe.

The level of recipient country's trade openness had an effect on neither Japan nor Korea, which does not seem very intuitive, as one would expect that Japan and Korea would provide more aid to countries with stronger commercial ties, counting on forming or strengthening trade partnerships [107,108]. However, this study found no evidence that either Japan or Korea tried to pursue national interests by strategically allocating ODA to countries with higher trade flows.

The estimation results show that OECD donors, Japan, and Korea have been reluctant to support states with higher security threats. The allocation of their total bilateral ODA was lesser for those states. However, no such indication was found with their DRR aid. Such mixed results raise the following question: if development aid in general does not work in countries with high-security threats, why should DRR aid should fare any better? Previous studies on environmental aid may answer this question. For instance, Connolly [109] notes that "donors do not always provide aid in order to solve environmental problems . . . sometimes care more about the appearance of doing something . . . than about finding genuine solutions." This image-focused motivation explains why many of the environmental projects marked with the "Rio marker" were unrelated to climate-related projects, which was found in a study by Michaelowa and Michaelowa [46]. The results of our study reinforce their viewpoint that donors have political motives for linking their aid to environmental markers, simply to show that they are "doing something good".

The regional indicators show that Japan has strongly favored countries in South and East Asia when allocating their bilateral aid, including DRR aid. Countries in South and East Asia received a disproportionate quantity of Japan's ODA compared to the rest of the world during 2008–2019. This is consistent with recent statistics that Japan's ODA is still mainly concentrated in the Asian region [110]. In the case of Korea, its priority ODA partner countries have been more diverse in recent years, beyond its traditional Asian partners [111].

5. Conclusions

The study focused on the role of development aid in breaking the negative feedback loop between disasters, conflict, and fragility. Many studies have shown that disasters and conflicts have occurred alongside one another over the past decades. The nexus of disasters, conflict, and fragility have severely undermined peaceful development and poverty reduction because most the world's poor lives in fragile and conflict-affected states. The effects of climate change will only intensify the situation and bring unintended consequences in the future. Despite this relationship, few studies have evaluated the combined risks from disasters and conflict in the development literature. The literature gap is jarring, given that disasters are also a driver of conflict.

In this context, this study examined how two East Asian donors, Japan and Korea, with reference to OECD-DAC donors as a group, have responded to disasters and conflict in their aid allocation. First, the proportion of DRR aid in the total bilateral aid is found to be small for all donors. Most OECD-DAC members spent less than 5% of development aid on DRR activities. Further, DRR aid, particularly of Korea and Japan, has been heavily concentrated in a few developing countries; this especially holds for those located in Asia. Only a fraction of the aid went to FCSs. Thus, DRR aid has not always reached people in most need.

The GMM estimators showed that neither Japan nor Korea is responsive to the compound risk of disasters and conflict. Both donors are found to have been more influenced by recipient countries' disaster vulnerability than their fragility and conflict, implying that the climate aid policies of both Japan and Korea are more oriented toward building resilience in disaster-prone countries. This answers the main question of the study, namely whether Japan and South Korea have moved beyond their self-serving behaviors and responded more effectively to the development needs of FCSs, despite their characteristics of being dysfunctional, fragile, and high-risk, to help them achieve climate-resilient peacebuilding, thereby lessening their ODA policy orientations toward economic consideration. Unfor-

tunately, there was no such indication that FCSs and countries with compounding risks received more aid from either Japan or Korea.

In the era of climate change, addressing the root causes of disasters is a strategic priority to end extreme poverty and promote growth in developing countries. Yet, this study found that the topics of fragility and conflict, which have the potential to disrupt governance and the implementation of DRR or any other development programs, are barely considered by Japan and Korea in the DRR program design process. Consequently, no matter the size of DRR funding and efficiency of DRR program design, fragility and conflict make operating environments too difficult for DRR strategies and programs. Indeed, the lack of fragility and conflict considerations in DRR program design becomes a contributing factor that reduces the probability of program success.

As noted earlier, DRR programs in both Japan and Korea are conducted in relatively peaceful and stable contexts. Though conflict makes the attainment of DRR outcomes more challenging, it is necessary to offer opportunities to FCSs to advance DRR and help find innovative ways to manage the impacts of natural hazards. It is time to design a DRR roadmap for fragile and conflict situations, train staff accordingly, and have much patience. In the process, it is vital to build synergies between local and scientific knowledge to establish the right policies and procedures, as the other scientific literature has already suggested [112]. This is the only way to break the negative feedback loop between disaster, fragility, and conflict. Now, the question becomes whether Japan and Korea are willing to acknowledge the link between disasters, conflict, and fragility, and if they can act accordingly. We know that the Sendai Framework and SDGs can only be realized in a world of peace, security, and respect for human rights. Japan and Korea have shown a strong commitment to disaster resilience over the past decade, but still need to reflect on the complexities of conflict and disasters and respond to them in a holistic and integrative manner.

Despite the conclusions and implications drawn from the findings, certain limitations of this study must be noted. It is too early to assess the disbursement and recipients of DRR aid, especially regarding Korea's small DRR aid quantity and, more importantly, there is an overall lack of reliable data relating to aid with DRR objectives. Without accurate coding, donors may over-report or under-report their efforts related to DRR and climate change adaptation to varying degrees. As there is no system in place to verify their claims, identifying aid whose core purpose is clearly climate-relevant and, thus, measuring its true impacts, would be exceedingly difficult. Addressing limitations relating to DRR aid data remains a task for all donors to conduct meaningful studies about the development–disaster–conflict nexus.

Furthermore, this study has limited its analysis to Japan and South Korea's bilateral aid. With various innovative financing mechanisms becoming more prominent in funding developing countries to address climate change issues, it would be necessary to compare the aid delivery and effectiveness via different financial mechanisms in the future.

Author Contributions: S.L. conceived the presented idea and wrote the manuscript with support from H.-j.K. All authors discussed the results and contributed to the final manuscript. All authors have read and agreed to the published version of the manuscript.

Funding: This research was supported by the Global Development Institute for Public Affairs (Research Grant 2020), the Graduate School of Public Administration, Seoul National University.

Institutional Review Board Statement: Not applicable.

Informed Consent Statement: Not applicable.

Data Availability Statement: The data that support the findings of this study are available from the corresponding author, upon reasonable request.

Conflicts of Interest: The authors declare no conflict of interest.

References

1. OECD. Climate Change: Helping Poor Countries to Adapt. In *Development Co-Operation Report 2010*; OECD Publishing: Paris, France, 2010; pp. 65–74. [CrossRef]
2. Kraemer, M.; Negrila, L. *Climate Change Is a Global Mega-Trend for Sovereign Risk*; Standard and Poor's Ratings Services LLC: New York, NY, USA, 2014; p. 14.
3. IPCC. *Climate Change 2014: Synthesis Report*; The Core Writing Team, Pachauri, R.K., Meyer, L., Eds.; Intergovernmental Panel on Climate Change: Geneva, Switzerland, 2015; ISBN 978-92-9169-143-2.
4. Cammack, D. *Understanding the Political Economy of Climate Change Is Vital to Tackling It*; Overseas Development Institute: London, UK, 2007.
5. Crawford, A.; Dazé, A.; Hammill, A.; Parry, J.-E.; Zamudio, A.N. *Promoting Climate-Resilient Peacebuilding in Fragile States*; IISD: Winnipeg, MB, Canada; Geneva, Switzerland, 2015; p. 29.
6. OECD. *States of Fragility 2020*; OECD: Paris, France, 2020.
7. Ember, C.R.; Ember, M. Resource Unpredictability, Mistrust, and War: A Cross-Cultural Study. *J. Confl. Resolut.* **1992**, *36*, 242–262. [CrossRef]
8. Olson, R.S.; Drury, A.C. Un-Therapeutic Communities: A Cross-National Analysis of Post-Disaster Political Unrest. *Int. J. Mass Emerg. Disasters* **1997**, *15*, 221–238.
9. OECD. Concepts and Dilemmas of State Building in Fragile Situations: From Fragility to Resilience. *OECD J. Dev.* **2009**, *9*, 61–148. [CrossRef]
10. Gutiérrez-Sanín, F. Evaluating State Performance: A Critical View of State Failure and Fragility Indexes. *Eur. J. Dev. Res.* **2010**, *23*, 20–42. [CrossRef]
11. Brown, O.; Crawford, A. *Assessing the Security Implications of Climate Change for West Africa: Country Case Studies of Ghana and Burkina Faso*; International Institute for Sustainable Development: Winnipeg, MB, Canada, 2009.
12. Yanda, P.; Bronkhorst, S. Climate Change and Conflict: Conflict-Sensitive Climate Change Adaptation in Africa. *Policy & Practice Brief ACCORD* **2011**. Available online: https://www.files.ethz.ch/isn/137666/policy_practice14.pdf (accessed on 26 March 2022).
13. Goulden, M.; Few, R. *Climate Change, Water and Conflict in the Niger River Basin*; USAID: Washington, DC, USA, 2011.
14. Vivekananda, J.; Schilling, J.; Smith, D. Climate resilience in fragile and conflict-affected societies: Concepts and approaches. *Dev. Pract.* **2014**, *24*, 487–501. [CrossRef]
15. UNDRR. Terminology. Available online: https://www.undrr.org/terminology/disaster-risk-reduction (accessed on 26 March 2022).
16. UN. *Sendai Framework for Disaster Risk Reduction 2015–2030*; UNISDR: Geneva, Switzerland, 2015.
17. Copeland, B.R.; Taylor, M.S. Trade, Growth, and the Environment. *J. Econ. Lit.* **2004**, *42*, 7–71. [CrossRef]
18. Arvin, B.M.; Lew, B. Do happiness and foreign aid affect bilateral migrant remittances? *J. Econ. Stud.* **2012**, *39*, 212–230. [CrossRef]
19. Opršal, Z.; Harmáček, J. Is Foreign Aid Responsive to Environmental Needs and Performance of Developing Countries? Case Study of the Czech Republic. *Sustainability* **2019**, *11*, 401. [CrossRef]
20. Stallings, B.; Kim, E.M. South Korea as an Emerging Asian Donor. In *Promoting Development: The Political Economy of East Asian Foreign Aid*; Development Cooperation and Non-Traditional Security in the Asia-Pacific; Palgrave Macmillan: Singapore, 2017; pp. 81–116. ISBN 978-981-10-3164-9.
21. Wajjwalku, S.; Tasarika, E. Thailand: What Makes Recipient Ownership? A Comparative Study of Japanese and Danish Aid to Environmental Conservation. In *Aid Relationships in Asia*; Jerve, A.M., Shimomura, Y., Hansen, A.S., Eds.; Palgrave Macmillan: London, UK, 2008; pp. 209–223. ISBN 978-1-349-28177-0.
22. Kalinowski, T.; Cho, H. Korea's Search for a Global Role between Hard Economic Interests and Soft Power. *Eur. J. Dev. Res.* **2012**, *24*, 242–260. [CrossRef]
23. Tonami, A.; Müller, A.R. Japanese and South Korean Environmental Aid: A Comparative Historical Analysis. *J. Environ. Dev.* **2013**, *23*, 191–219. [CrossRef]
24. Kim, E.M.; Oh, J. Determinants of Foreign Aid: The Case of South Korea. *J. East Asian Stud.* **2012**, *12*, 251–274. [CrossRef]
25. Sparks, D. *Aid Investments in Disaster Risk Reduction-Rhetoric to Action*; Global Humanitarian Assistance: Bristol, UK, 2012.
26. OECD. *Japan-DAC Peer Reviews of Development Co-Operation, 2014*; OECD: Paris, France, 2014; Available online: https://www.oecd.org/dac/peer-reviews/peer-review-japan.htm (accessed on 31 July 2022).
27. Jung, J.; Song, J. Integrating Climate Change into Development Cooperation-Korea's Experience. *Korea Inst. Int. Econ. Policy* **2014**, *10*, 1–6.
28. Kim, Y. Improving Korea's Climate Finance for Developing Countries: Policy Analysis of the Management of Climate-Related Development Finance (CRDF). *J. Int. Dev. Coop.* **2020**, *15*, 141–185. [CrossRef]
29. Yim, H. Incorporating Climate Change Adaptation into Sustainable Development. *J. Int. Dev. Coop.* **2017**, *2017*, 139–171. [CrossRef]
30. UNEP. Natural Resources and Conflict: A Guide for Mediation Practitioners. Available online: http://www.unep.org/resources/report/natural-resources-and-conflict-guide-mediation-practitioners (accessed on 26 March 2022).
31. Peters, K. *When Disasters and Conflict Collide: Uncovering the Truth*; Overseas Development Institute: London, UK, 2018.
32. ICRC. *Annual Report 2020*; International Committee of the Red Cross: Geneva, Switzerland, 2021.

33. Cred Crunch Newsletter, Issue No. 54 (April 2019)—Disasters 2018: Year in Review—World | ReliefWeb. Available online: https://reliefweb.int/report/world/cred-crunch-newsletter-issue-no-54-april-2019-disasters-2018-year-review (accessed on 11 August 2021).
34. BBC News. Afghan Drought 'Displacing More People than Taliban Conflict'. Available online: https://www.bbc.com/news/world-asia-45872897 (accessed on 16 March 2021).
35. OCHA Afghanistan: UN Funds Allocate US$34.6M to Assist 2.2M People Severely Affected by Ongoing Drought. Available online: https://www.unocha.org/story/afghanistan-un-funds-allocate-us346m-assist-22m-people-severely-affected-ongoing-drought (accessed on 16 March 2021).
36. Mitra, S.; Vivekananda, J. *Compounding Risk: Disasters, Fragility and Conflict*; Policy Brief; International Alert: London, UK, 2015.
37. Coulbaly, B.S. *Foresight Africa: Top Priorities for the Continent in 2019*; Brookings Institution: Washington, DC, USA, 2019.
38. GFDRR. *Disasters, Conflict and Fragility: A Joint Agenda*; GFDRR: Washington, DC, USA, 2016.
39. Ferris, E. *Natural Disasters, Conflict, and Human Rights: Tracing the Connections*; Brookings Institution and Universitat Bern: Washington, DC. USA, 2010.
40. UNEP. *Disasters and Conflicts*; United Nations Environment Programme: Geneva, Switzerland, 2010.
41. UNDP. *Disaster-Conflict Interface: Comparative Experiences*; United Nations Development Programme: New York, NY, USA, 2011.
42. UNISDR. *Disaster Risk Reduction and Resilience in the 2030 Agenda for Sustainable Development*; UNISDR: New York, NY, USA, 2015.
43. OECD. DAC Proposal to Establish a Policy Marker for Disaster Risk Reduction (DRR) in the OECD DAC Creditor Reporting System (CRS). 2017.
44. Kono, D.Y.; Montinola, G.R. Foreign Aid and Climate Change Policy: What Can('t) the Data Tell Us? *Aid Impact Eff.* **2019**, *7*, 68–92.
45. Roberts, J.T.; Starr, K.; Jones, T.; Abdel-Fattah, D. *The Reality of Official Climate Aid*; Oxford Institute for Energy Studies: Oxford, UK, 2008.
46. Michaelowa, A.; Michaelowa, K. Coding Error or Statistical Embellishment? The Political Economy of Reporting Climate Aid. *World Dev.* **2011**, *39*, 2010–2020. [CrossRef]
47. Junghans, L.; Harmeling, S. *Different Tales from Different Countries–A First Assessment of the OECD "Adaptation Marker"*; Germanwatch: Bonn, Germany; Berlin, Germany, 2012; p. 24.
48. Weikmans, R.; Roberts, J.T.; Baum, J.; Bustos, M.C.; Durand, A. Assessing the credibility of how climate adaptation aid projects are categorised. *Dev. Pract.* **2017**, *27*, 458–471. [CrossRef]
49. OECD. *Indicative Table to Guide Rio Marking by Sector/Sub-Sector*; OECD: Paris, France, 2016; Available online: https://www.oecd.org/dac/environment-development/Indicative%20table%20to%20guide%20Rio%20marking%20by%20sector.pdf (accessed on 13 October 2020).
50. Flores, A.; Peralta, L. *The Enhancement of Resilience to Disasters and Climate Change in the Caribbean through the Modernization of the Energy Sector*; Studies and Perspectives Series-ECLAC Subregional Headquarters for the Caribbean; Economic Commission for Latin America and the Caribbean (ECLAC): Santiago, Chile, 2020.
51. UNDRR. *United Nations Office for Disaster Risk Reduction. 2020 Annual Report*; United Nations Office for Disaster Risk Reduction: Geneva, Switzerland, 2021.
52. Donor Tracker. ODA Funding Trends-Japan. Available online: https://donortracker.org/country/japan (accessed on 23 March 2021).
53. Government of Republic of Korea. *Re-Selection of ODA Priority Partner Countries*; Government of Republic of Korea: Seoul, Korea, 2021. (In Korean).
54. Kulessa, M. A Western Critique of Japan's Development Aid. In *Europe, Japan and America in the 1990s*; Leuenberger, T., Weinstein, M.E., Eds.; Springer: Berlin/Heidelberg, Germany, 1992; pp. 107–122.
55. Furuoka, F. *International Comparison of Japan's Official Development Assistance (ODA) Policy*; MPRA Paper No. 11899; University Library of Munich: Munich, Germany, 2009.
56. Kim, E.M.; Lee, J.E. Busan and Beyond: South Korea and the Transition from Aid Effectiveness to Development Effectiveness: Busan and Beyond. *J. Int. Dev.* **2013**, *25*, 787–801. [CrossRef]
57. Jung, C.; Cho, W.; Hwang, W. Does Official Development Assistance Promote Foreign Policy Cooperation from its Recipients? The Case of South Korea: ODA and Foreign Policy Cooperation. *Pac. Focus* **2018**, *33*, 83–110. [CrossRef]
58. Rodella-Boitreaud, A.-S.; Wagner, N. *'Natural' Disaster, Conflict and Aid Allocation*; IHEID Working Papers; The Graduate Institute of International Studies: Geneva, Switzerland, 2011.
59. OECD. *OECD DAC Rio Markers for Climate: Handbook*; OECD: Paris, France, 2011; p. 3. Available online: https://www.oecd.org/dac/environment-development/Revised%20climate%20marker%20handbook_FINAL.pdf (accessed on 5 April 2020).
60. JICA. *JICA's Cooperation for Disaster Risk Reduction. Disaster Resilient Society for All*; Japan International Cooperation Agency: Tokyo, Japan, 2016. Available online: https://www.jica.go.jp/english/publications/brochures/c8h0vm0000avs7w2-att/disaster_en.pdf (accessed on 28 August 2020).
61. Kellett, J.; Caravani, A. *Financing Disaster Risk Reduction: A 20 Years Story of International Aid*; GFDRR: Washington, DC, USA; ODI: London, UK, 2013.
62. Ministry of Foreign Affairs of Japan. *MoFA of Japan Cabinet Decision on the Development Cooperation Charter 2015*; Ministry of Foreign Affairs of Japan: Tokyo, Japan. Available online: https://www.mofa.go.jp/files/000067701.pdf (accessed on 18 July 2020).
63. Green Growth Leaders Shaping the Green Growth Economy. Available online: https://sustainabledevelopment.un.org/index.php?page=view&type=400&nr=691&menu=1515 (accessed on 16 March 2021).

64. UNESCAP (Ed.) *Low Carbon Green Growth Roadmap for Asia and the Pacific: Turning Resource Constraints and the Climate Crisis into Economic Growth Opportunities*; UNESCAP: Bangkok, Thailand, 2012; ISBN 978-974-680-329-8.
65. Gupta, A.; Gotmore, S.; Dinakaran, U.; Babu, S. *Green Growth Benefits for Climate and Disaster Resilience: Concerns for Urban and Infrastructure Systems*; National Institute of Disaster, Management (NIDM), Ministry of Home Affairs, Government of India: New Dehli, India; Global Green Growth Institute (GGGI): New Delhi, India, 2019.
66. GGGI. *Korea's Green Growth Experience: Process, Outcomes and Lessons Learned*; Global Green Growth Institute (GGGI): Seoul, Korea, 2015.
67. Tonami, A.; Müller, A.R. *Japanese and South Korean Environmental Aid: What Are Their Life Stories?* Danish Institute for International Studies: Copenhagen, Denmark, 2013.
68. KOICA. *KOICA Annual Report 2010*; KOICA: Seongnam, Korea, 2011.
69. Cho, B. *Park Geun Hye's "Samaeul Diplomacy" Resembles MB's "Resource Diplomacy"*; Pressian: Seoul, Korea, 2015. (In Korean).
70. Ministry of Foreign Affairs. *2016 Diplomatic White Paper*; Ministry of Foreign Affairs: Seoul, Korea, 2016.
71. Arndt, C.; Tarp, F. Aid, Environment and Climate Change. *Rev. Dev. Econ.* **2017**, *21*, 285–303. [CrossRef]
72. Victor, D. *Foreign Aid for Capacity-Building to Address Climate Change*; UNU-WIDER: Helsinki, Finland, 2015.
73. IFAD. Defining and Measuring State Fragility. Available online: https://www.ifad.org/en/web/latest/-/story/defining-and-measuring-state-fragility (accessed on 10 July 2022).
74. KOICA. *KOICA Mid-Term Assistance Strategy for Fragile States 2017–2019*; KOICA: Seongnam, Korea, 2016. (In Korean)
75. Klingelhöfer, D.; Müller, R.; Braun, M.; Brüggmann, D.; Groneberg, D.A. Climate change: Does international research fulfill global demands and necessities? *Environ. Sci. Eur.* **2020**, *32*, 137. [CrossRef] [PubMed]
76. Horton, R.; De Mel, M.; Peters, D.; Lesk, C.; Bartlett, R.; Helsingen, H.; Bader, D.; Capizzi, P.; Martin, S.; Rosenzweig, C. *Assessing Climate Risk in Myanmar: Technical Report*; Center for Climate Systems Research at Columbia University, WWF-US and WWF-Myanmar: New York, NY, USA, 2016.
77. Garschagen, M.; Doshi, D.; Reith, J.; Hagenlocher, M. Global patterns of disaster and climate risk—An analysis of the consistency of leading index-based assessments and their results. *Clim. Chang.* **2021**, *169*, 11. [CrossRef]
78. GermanWatch. Global Climate Risk Index 2020. Available online: https://www.germanwatch.org/en/17307 (accessed on 20 March 2021).
79. Wallemacq, P.; House, R. *Economic Losses, Poverty & Disasters: 1998–2017*; United Nations Office for Disaster Risk Reduction: Geneva, Switzerland, 2018.
80. Furuoka, F. Determinants of China's and Japan's Foreign Aid Allocations in Africa: China's and Japan's Foreign Aid Allocations. *Afr. Dev. Rev.* **2017**, *29*, 376–388. [CrossRef]
81. Martinsen, L.; Ottersen, T.; Dieleman, J.L.; Hessel, P.; Kinge, J.M.; Skirbekk, V. Do less populous countries receive more development assistance for health per capita? Longitudinal evidence for 143 countries, 1990–2014. *BMJ Glob. Health* **2018**, *3*, e000528. [CrossRef] [PubMed]
82. Zengin, H.; Korkmaz, A. Determinants of Turkey's foreign aid behavior. *New Perspect. Turk.* **2019**, *60*, 109–135. [CrossRef]
83. Younas, J. Motivation for bilateral aid allocation: Altruism or trade benefits. *Eur. J. Political Econ.* **2008**, *24*, 661–674. [CrossRef]
84. UNDP. *Towards Human Resilience: Sustaining MDG Progress in an Age of Economic Uncertainty*; United Nations Development Programme Bureau for Development Policy: New York, NY, USA, 2011.
85. In'Airat, M. Aid allocation, selectivity, and the quality of governance. *J. Econ. Finance Adm. Sci.* **2014**, *19*, 63–68. [CrossRef]
86. Bandyopadhyay, S.; Wall, H.J. *The Determinants of Aid in the Post-Cold War Era*; Federal Reserve Bank of St. Louis: St. Louis, MO, USA, 2006; ISBN 0-444-52765-6.
87. Garriga, A.C.; Phillips, B. Foreign Aid as a Signal to Investors: Predicting FDI in Post-Conflict Countries. *J. Confl. Resolut.* **2013**, *58*, 280–306. [CrossRef]
88. Alesina, A.; Dollar, D. Who Gives Foreign Aid to Whom and Why? *J. Econ. Growth* **2000**, *5*, 33–63. [CrossRef]
89. Driffield, N.; Jones, C.M. Impact of FDI, ODA and Migrant Remittances on Economic Growth in Developing Countries: A Systems Approach. *Eur. J. Dev. Res.* **2013**, *25*, 173–196. [CrossRef]
90. Le Goff, M.; Kpodar, K. *IMF Working Paper; Do Remittances Reduce Aid Dependency?* International Monetary Fund: Washington, DC, USA, 2011; Volume 11, p. 31. [CrossRef]
91. The Fund for Peace Fragile States Index. Available online: https://fragilestatesindex.org/indicators/c1/ (accessed on 20 March 2021).
92. ADB. *Working Differently in Fragile and Conflict-Affected Situations: The ADB Experience*; Asian Development Bank: Manila, Philippines, 2012.
93. Kangas, A.; Haider, H.; Fraser, E. *Gender: Topic Guide*; GSDRC: Bermingham, UK, 2014.
94. Corral, P.; Irwin, A.; Krishnan, N.; Mahler, D.G.; Vishwanath, T. *Fragility and Conflict: On the Front Lines of the Fight against Poverty*; World Bank: Washington, DC, USA, 2020.
95. Devarajan, S. Aid and Corruption. Available online: https://blogs.worldbank.org/africacan/aid-and-corruption (accessed on 24 March 2021).
96. Hayman, R. Budget Support and Democracy: A twist in the conditionality tale. *Third World Q.* **2011**, *32*, 673–688. [CrossRef]
97. Nickell, S. Biases in Dynamic Models with Fixed Effects. *Econometrica* **1981**, *49*, 1417–1426. [CrossRef]
98. Arellano, M.; Bond, S. Some Tests of Specification for Panel Data: Monte Carlo Evidence and an Application to Employment Equations. *Rev. Econ. Stud.* **1991**, *58*, 277–297. [CrossRef]

99. Olubusoye, O.; Salisu, A.; Olofin, S. *Applied Panel Data Analysis*; Ibadan University Press: Ibadan, Nigeria, 2016; ISBN 978-978-54045-7-9.
100. Twigg, J. *Disaster Risk Reduction: Good Practice Review 9*; Humanitarian Practice Network: London, UK, 2015.
101. Mena, R. Responding to Socio-Environmental Disasters in High-Intensity Conflict Scenarios: Challenges and Legitimation Strategies. In *Climate Change, Disasters, Sustainability Transition and Peace in the Anthropocene*; Brauch, H.G., Oswald Spring, Ú., Collins, A.E., Serrano Oswald, S.E., Eds.; The Anthropocene: Politik—Economics—Society—Science; Springer International Publishing: Cham, Switzerland, 2019; Volume 25, pp. 27–66. ISBN 978-3-319-97561-0.
102. Civelli, A.; Horowitz, A.W.; Teixeira, A. *A Signal of Altruistic Motivation for Foreign Aid: A Theoretical Model and Empirical Test*; Social Science Research Network: Rochester, NY, USA, 2015.
103. Cooray, N.S.; Shahiduzzaman, M. Determinants of Japanese Aid Allocation: An Econometric Analysis. *Int. Dev. Ser.* **2004**, *4*, 2–19.
104. Harms, P.; Ursprung, H.W. Do civil and political repression really boost foreign direct investments? *Econ. Inq.* **2002**, *40*, 651–663. [CrossRef]
105. Alvi, E.; Senbeta, A. Does foreign aid reduce poverty? *J. Int. Dev.* **2012**, *24*, 955–976. [CrossRef]
106. OECD; World Trade Organization. *Aid for Trade at a Glance 2019: Economic Diversification and Empowerment*; OECD: Paris, France, 2019; ISBN 978-92-64-42951-2.
107. Tuman, J.P.; Strand, J.R. The Role of Mercantilism, Humanitarianism, and Gaiatsu in Japan's ODA Programme in Asia. *Int. Relat. Asia-Pac.* **2006**, *6*, 61–80. [CrossRef]
108. Oh, J.; Song, J. Dual determinants: Aid disbursement and volume, with special reference to Japan. *Asia Pac. Manag. Rev.* **2018**, *23*, 268–277. [CrossRef]
109. Connolly, B. Increments for the Earth: The Politics of Environmental Aid. In *Institutions for Environmental Aid*; The MIT Press: Cambridge, MA, USA, 1996; pp. 327–365.
110. OECD. *OECD Development Co-Operation Peer Reviews: Japan 2020*; OECD Development Co-operation Peer Reviews; OECD: Paris, France, 2020; ISBN 978-92-64-90571-9.
111. OECD. Development Cooperation Profiles 2020: Korea. Available online: https://www.oecd-ilibrary.org/sites/d919ff1a-en/index.html?itemId=/content/component/d919ff1a-en (accessed on 20 March 2021).
112. Gaillard, J.; Mercer, J. From knowledge to action: Bridging gaps in disaster risk reduction. *Prog. Hum. Geogr.* **2012**, *37*, 93–114. [CrossRef]

sustainability

MDPI

Article

Research on a Scheduling Model for Social Emergency Resource Sharing Based on Emergency Contribution Index

Wenqi Cui [1], Xinwu Chen [1], Boyu Liu [1], Qian Hu [1], Miaomiao Ma [1], Xing Xu [2], Zhanyun Feng [2], Jiale Chen [2] and Wei Cui [2,*]

[1] Experimental Teaching Center, Hubei University of Economics, Wuhan 430205, China; w.q.cui@hbue.edu.cn (W.C.); cxw777@hbue.edu.cn (X.C.); liuboyu1983@hbue.edu.cn (B.L.); huqian@hbue.edu.cn (Q.H.); mamiaomiao@hbue.edu.cn (M.M.)

[2] School of Resource and Environmental Engineering, Wuhan University of Technology, Wuhan 430070, China; 276824@whut.edu.cn (X.X.); 276762@whut.edu.cn (Z.F.); chenjl07@whut.edu.cn (J.C.)

* Correspondence: cuiwei@whut.edu.cn; Tel.: +86-136-2860-8563

Abstract: A large number of massive repair machines are urgently necessary for a post-disaster rescue. These machines also need to be operated by professionals, and the demands require the participation of different industries in the whole society since they cannot be met via the national emergency resource storage system. Therefore, the support of extensive emergency resources from different industries across the entire society is needed in the rescue process, that is, social emergency resource sharing. To achieve this sharing, an emergency resource scheduling model should have the ability to allocate resources from the whole society. However, traditional emergency scheduling models have not considered the suppliers' willingness to take part in the scheduling activities and their abilities to supply the resources. To solve the above issues, this paper designs a scheduling model for social emergency resource sharing based on an emergency contribution index (SSERS). The emergency contribution index (ECI) can be used to find the enterprises that not only have the ability to provide efficient emergency resources on time but also have the willingness to participate in emergency rescue. The results show that our model effectively optimizes the basic models to some extent and achieves social emergency resource sharing.

Keywords: emergency resource; social emergency resource sharing; SSERS; emergency contribution index; emergency production capacity; enterprise willingness

Citation: Cui, W.; Chen, X.; Liu, B.; Hu, Q.; Ma, M.; Xu, X.; Feng, Z.; Chen, J.; Cui, W. Research on a Scheduling Model for Social Emergency Resource Sharing Based on Emergency Contribution Index. *Sustainability* **2023**, *15*, 13029. https://doi.org/10.3390/su151713029

Academic Editor: Paulo Santos

Received: 22 July 2023
Revised: 25 August 2023
Accepted: 25 August 2023
Published: 29 August 2023

1. Introduction

The existing emergency resource scheduling models (traditional models) can be mainly divided into two types, i.e., single-objective models and multi-objective models. The single-objective models mainly aim to minimize time [1–4], minimizing distance [5–7], maximizing satisfaction [8–10], etc. The multi-objective models combine the above objectives to find the best solution [11–19]. These models are mainly applicable to the suppliers of daily living materials, such as the national emergency resource reserve system, and they focus more on providing basic emergency materials, such as food and water, to disaster-affected areas in the shortest time and with the lowest costs, but they fail to consider the specific situations in terms of a dynamic and open environment. Large and specialized engineering equipment, such as the graders, road rollers, and pavers required for road repair construction, are not only expensive and require a great deal of storage space, but they also need to be operated by professionals to function, so they are not included in the national reserve system. In this case, the massive resources existing in various industries across the entire society need to be used in the post-disaster emergency process so as to effectively compensate for the lack of national emergency resource reserves, minimize disaster losses, and protect people's lives and property.

In summary, due to the differences between the national reserve system and social emergency resource sharing, i.e., that the suppliers of the social emergency resource sharing come from different industries across the entire society, and their resource abilities and willingness to participate in emergency resource scheduling are quite different, scientific social emergency resource sharing requires emergency resource scheduling to be transformed from a static, closed national emergency resource system to an environment which adapts to a dynamic and open society.

However, in previous research [1–5], the researchers mainly focused on the constraints of the amount of emergency resources, the scheduling time, or the costs, and they did not take production ability and the willingness of the suppliers into account.

In the traditional model [1], each supplier is a national emergency resource reserve base, the types of emergency resources stored are basically the same, and only the distances from the disaster site are different for each. In this case, the only things that need to be considered during emergency resource scheduling are the time and cost of transportation. However, in social emergency resource sharing, things are quite different, and the abilities and willingness of the enterprises providing emergency resources will affect the efficiency of the scheduling. Currently, there are a large number of enterprises that can produce emergency resources from many industries in China, but their supply capacities are different. On the other hand, some enterprises may prioritize pursuing their own interests rather than the common goal of completing an emergency rescue. These differences will affect the efficiency of social emergency resource sharing, but as far as we know, no research has been published on the impacts of enterprises' intrinsic factors (abilities and willingness to provide emergency resources) on social emergency resource sharing.

Briefly, there are two issues that must be addressed in the design of a new model. First, the participants have different abilities to provide emergency resources, and some may not be suitable for social emergency resource sharing. Second, it is difficult to coordinate and efficiently complete emergency resource-sharing operations because of the different interests and demands of the participants.

Therefore, in this paper, an emergency contribution index is introduced into the traditional emergency resource scheduling; it includes two components: emergency production capacity and enterprise willingness. The emergency production capacity of an enterprise is used to reflect its ability to supply various emergency resources, which is characterized by the enterprise's capital information and business scope. The enterprise's willingness can be divided into staff motivation and leadership enthusiasm. The staff motivation is used to reflect the commitment of the staff to the enterprise; the higher the staff motivation is, the greater the production capacity will be. Leadership enthusiasm is used to reflect the willingness of the leaders in an enterprise to participate in emergency resource-sharing activities. It is characterized by the ratio of the enterprise's philanthropy expenditures in the previous year to the total expenditures of that year.

After considering the emergency resources needed and the spatial distance involved, the introduction of the emergency contribution index is helpful in choosing an enterprise that has both strong production capacity and a strong willingness to participate in social emergency resource-sharing activities from among a large number of emergency resource production enterprises, so as to optimize the traditional emergency resource scheduling program.

The innovations of this paper are listed below.

(1) The "Emergency Production Capacity" was innovatively designed and used to quantitatively describe an enterprise's ability to provide emergency resources; thus, it is helpful in choosing enterprises that can provide more suitable emergency resources.
(2) More Powerful Participation Willingness We first designed the "Enterprise Willingness", which can be used as a quantitative evaluation indicator to select enterprises with a strong willingness to participate in social emergency resource scheduling.
(3) SSERS Model In this paper, we proposed the SSERS Model for the first time. On the basis of the traditional multi-objective emergency resource scheduling models that

merely considered the requests of demand-side (scheduling time and costs, etc.), this model takes the supply side into account, i.e., the supply capabilities (emergency production capacity and staff motivation) of emergency resources and the willingness to participate in emergency resource scheduling (leadership enthusiasm). This innovation gives the model the ability to quantitatively describe the capacity and willingness for the first time; thus, the enterprises with stronger supply abilities and willingness to participate in the emergency resource scheduling can be chosen as suppliers of the emergency resources.

The remainder of the paper is organized as follows: Section 2 presents a literature review of previous research on emergency resource scheduling. Section 3 describes the details of the SSERS Model. The experiments and analysis are illustrated in Section 4, and the conclusions are discussed in the final section.

2. Related Works

2.1. The Issues Exist in the Traditional Emergency Resource Scheduling Models

At this stage, some researchers have already studied the multi-object emergency resource dispatch and proposed different models, which can be divided into the following types.

2.1.1. Single Objective Emergency Resource Scheduling

When studying the scheduling plan of emergency resources, different researchers may have different goals. To improve the efficiency of rescue, some researchers chose minimum time as a goal. Hu et al. aimed for minimum time and put forward an emergency resource scheduling model of multi-vehicle types [1]. Yan et al. studied the emergency material scheduling for multi-rescue points under real-time conditions and then used an improved Genetic Algorithm (GA) to realize the dynamic path adjustment [2]. Lu et al. presented a rolling horizon based on real-time relief distribution of a disaster. [3]. Chai et al. defined the rescue route travel time as the sum of free flow travel time and queuing delay time then set the minimum travel time as a goal of the scheduling [4].

Apart from minimum time, other researchers prefer taking the shortest distance. Batmetan et al. calculated the shortest path to be selected by using a multi-objective optimization algorithm for cloud computing task scheduling based on an improved ant colony algorithm in the Lokon volcano [5]. Ferrer et al. built a compromise programming model for multi-criteria optimization in humanitarian last-mile distribution [6]. Vidal et al. established three emergency material scheduling (EMS) models with time windows, which were multi-cycle, multi-distribution center, and disaster point that can only be guaranteed by special vehicles [7].

Furthermore, other researchers took the satisfaction of the demand points in the scheduling as an objective. Das et al. constructed a warehouse location model with the goal of maximum satisfaction [8]. Chen et al. took the satisfaction of the whole disaster area as the objective of emergency resource scheduling and built a model for multi-commodity, multi-supply depots to maximize efficiency [9]. Wang et al. constructed a multi-level emergency material scheduling optimization model for marine disasters by using the cooperative scheduling method to maximize the reliability of material supply [10].

2.1.2. Multi-Objective Emergency Resource Scheduling

Ding et al. proposed an emergency supplies scheduling model based on multi-objectives, then designed the minimum time cost and the shortest route cost model. The results show that the two cost models can serve different scheduling needs and provide efficient scheduling for emergency supplies [11]. Wan et al. established a multi-objective, multi-constraint (EMS) model based on the above-mentioned principle. Subsequently, a hybrid ant colony optimization (HACO) was proposed to solve EMS. The experimental results show that HACO has better performance than other methods [12]. Chi et al. combined two rescue objectives, i.e., time and resource satisfaction, into a timeliness evaluation function,

which provides new insight into the design of objective functions utilized in emergency resource scheduling [13]. Zhou et al. designed a multi-objective optimization model for multi-period dynamic emergency resource scheduling problems. The results show that the model can find a better candidate solution than traditional models [14]. Zhang et al. proposed a three-stage stochastic program model; its objectives were to minimize the time and costs of the scheduling and the number of unsatisfied demands [15]. Cui et al. came up with a post-disaster material transportation model to minimize the time and costs [16]. Wang et al. gave out a two-dimensional and multi-objective emergency resource scheduling model to achieve the shortest time and the lowest costs [17].

Behrooz et al. [18] formulated the Multi-Resource Scheduling and Routing Problem (MRSRP) for emergency relief and developed a solution framework. Results show that the six methods are valid when optimizing the existing solutions. Zhang et al. aimed to conduct a study on a novel dynamic multi-objective location-routing model with split delivery considering practical characteristics. A two-stage optimization model was proposed to address the model's complexity [19]. Xu et al. proposed a plug-in-free three-dimensional spatial fusion scheme based on WebGL rendering technology and developed a visualization system for emergency rescue data fusion [20]. Li et al. developed an emergency resource dispatching model with random demands and optimized the expected total cost [21]. Wang et al. [22] presented a two-stage optimization model of emergency resource storage and scheduling. In the first stage of the model, the objective is to decrease the response time, while in the second stage, the objective turns to optimizing the resource scheduling satisfaction. Chen et al. proposed a co-scheduling model of emergency resources with the goals of minimizing time-consuming, cost, and shedding load [23].

Affected by COVID-19, Sun et al. proposed a multi-resource collaborative scheduling optimization model with the objectives of minimizing the makespan of Quay Crane and transportation energy consumption [24]. Ding et al. [25] put forward an emergency material scheduling model with multiple logistics supply points for multiple demand points. They achieved an optimization on this model by using a multi-objective algorithm based on a genetic algorithm.

The above-mentioned models improved the efficiency of the rescue to some extent. However, most of the above models use the national emergency material reserve base as the source; the materials they reserve are basically the same category, and the bases are only at different distances from the disaster point. As a result, these models only need to consider the time cost when completing the scheduling task. However, the social emergency resource-sharing process has the following differences:

(1) The suppliers of social emergency resource sharing are from different industries; they have different abilities to provide the resources.
(2) Unlike simple emergency material dispatch, social emergency resource sharing often involves professional services in related industries, which includes not only professional equipment but also the support of professional human resources.
(3) The willingness of each enterprise to participate in the social emergency resource sharing is related to the form of the sharing (like paid or unpaid).

Therefore, the particularity of social emergency resource sharing must be incorporated into the model using quantitative indicators.

2.2. The Issues Exist in the Social Emergency Resource Sharing

In terms of the social emergency resource sharing, Zhang et al. established a tripartite evolutionary model of the government, enterprise, and society, explored the influencing factors of realizing government-enterprise cooperation, i.e., income variables, cost variables, initial willingness and stakeholder behaviors [26]. Meng presented an integrated social emergency resource monitoring system to optimize the collection and dispatch of emergency resources. A time-bound multi-layer recruitment network of emergency resources was modeled to maximize the amount of the collected resources and minimize the logistics costs [27]. Olanrewaju et al. proposed to integrate the decision-making of supplier

selection into the preparedness stage in responding to disasters for the timely distribution of relief supplies [28]. Hu et al. presented a two-stage stochastic program model to produce plains, including facility location and inventory, supplier selection, and distribution of relief supplies [29].

The scheduling plan involved in the current research only considers the constraints of the quantity of the emergency materials while ignoring the supply capacity of the suppliers and their subjective willingness to participate in the social emergency resource sharing, which results in the lack of rationality of the emergency resource scheduling plan.

3. Methodology

In this chapter, we propose a scheduling model for social emergency resource sharing with multiple objectives. On the basis of the traditional model, the emergency production capacity and leadership enthusiasm of enterprises are taken into account so that we can choose enterprises with a strong ability to provide emergency resources and a strong willingness to participate in the sharing activities.

3.1. The Emergency Contribution Index of an Enterprise

To choose a better supplier from multiple candidate enterprises, the emergency contribution index (ECI) of an enterprise is defined, which includes two components: Emergency Production Capacity and Enterprise Willingness.

3.1.1. Enterprise Willingness

The Enterprise Willingness consists of two key parts: staff motivation and leadership enthusiasm. They are employed to quantitatively describe the willingness of an enterprise to participate in emergency resource sharing at the levels of employee and leader separately.

(1) Staff Motivation

The staff motivation of an enterprise is an indicator used to evaluate the work motivation of the staff in the enterprise. It is affected by the ratio of the number of insured employees to the size of staff and the ratio of employees' wages to the local average wage. The higher the number of insured employees in an enterprise, the more emphasis the enterprise attaches to employee benefits, thus the higher the enthusiasm of employees for work. The calculative formula is shown below:

$$\omega = (\frac{i}{i_0} + \frac{q}{q_a})/m \quad (1)$$

where ω means the staff motivation of an enterprise, "i" means the insured persons, and "i_0" means the total personnel of the enterprise. So, $\frac{i}{i_0}$ means the ratio of the number of insured persons to the size of personnel. "q" means the average salary of the staff in the enterprise, and "q_a" means the local average salary. So, $\frac{q}{q_a}$ means the ratio of the average salary of the enterprise to the average salary of the city in which the enterprise is located. The "m" means the number of the parameters.

(2) Leadership Enthusiasm

The leadership enthusiasm of an enterprise is an indicator used to evaluate the willingness of the leaders of an enterprise to participate in social emergency resource sharing. It is affected by the amount of charitable donations (including money and items) made by the enterprise in the previous year, the costs of human resources (such as labor cost for emergency resource transportation) in the previous year, and the output value of the previous year. The higher the proportion of an enterprise's social donation in the previous year to its total output value in the previous year, the more emphasis the enterprise's leaders attach to the corporation's social responsibility. When natural disasters or social events

occur, such leaders are often more willing to be active and get involved in the response. The calculative formula is shown below:

$$\theta = \frac{w + y}{v} \tag{2}$$

where θ means the leadership enthusiasm of an enterprise, "w" means the enterprise's value of public donations in the previous year, "y" means the costs incurred by the enterprise in participating in emergency resource-sharing activities, and "v" means the total operating income in the previous year.

3.1.2. Emergency Production Capacity

The emergency production capacity can be used to evaluate the ability to provide emergency resources of an enterprise in the process of social emergency resource sharing. It is related to factors such as the enterprise's operating status, unified social credit code, business scope change records, the ratio of the paid-in capital to the registered capital, and the ratio of the value of emergency resources produced by the enterprise to the total value of all products of the enterprise. These factors are divided into two types: control factors and contribution factors. The calculative formula of emergency production capacity is shown below.

$$\varphi = (b \times s \times r) \times [(\frac{c}{c_0} + \frac{p_e}{p_t})]/n \tag{3}$$

where φ means the emergency production capacity of an enterprise, "b", "s", and "r" are the control factors of the emergency production capacity, which is the business status, business scope change records, and social credit code, respectively. The value of these factors is either 0 or 1, i.e., when an enterprise no longer exists or it changed the business scope before (which does not produce emergency resources anymore), these values of this enterprise will be 0; otherwise, they will be 1. The "$\frac{c}{c_o}$" are contribution factors of the emergency production capacity, it means the ratio of the enterprise's registered capital to paid-in capital and the "$\frac{p_e}{p_t}$" means the ratio of the value of emergency supplies produced to the value of all products of an enterprise. These factors take values between 0 and 1. The "n" means the number of contribution factors; its value is 2 in this paper.

The purpose of introducing this indicator is to compare the enterprises' operating conditions, social credit ratings, registered and paid-in capital, personnel scale, etc., and then to select enterprises with strong supply abilities for emergency resources from a large number of candidate enterprises as suppliers to participate in social emergency resource sharing.

Therefore, emergency production capacity is an indicator that can effectively exclude some small and weak enterprises that are limited by their own conditions and cannot efficiently complete the process of post-disaster rescue.

3.1.3. Emergency Contribution Index

The ECI is an indicator that can comprehensively describe the ability to provide emergency resources and the willingness to participate in emergency resource sharing of an enterprise. The calculative formula is shown below:

$$\text{ECI} = \theta \times \omega \times \varphi \tag{4}$$

where θ means the leadership enthusiasm of an enterprise, ω means the staff motivation of an enterprise, and φ means the emergency production capacity of an enterprise. The three parameters commonly form the ECI. The higher the value of these parameters, the higher the value of ECI, indicating that the enterprise is more capable of providing emergency resources and simultaneously has a stronger willingness to participate in social emergency resource sharing.

3.2. Social Emergency Resource Sharing Scheduling Model Based on ECI

In this section, the ECI is combined into the traditional emergency resource scheduling model, giving it the ability to quantify the production capacities and willingness of the enterprises, thus compensating for the weakness of the traditional model that it only focuses on the demand side.

3.2.1. The SSERS Model

In this section, we will establish a function for analysis with the goal of minimizing total delay time and total cost and then improve it on the basis of the previous studies. The improved scheduling model is shown below.

$$min\sum_{a=1}^{m}\sum_{b=1}^{n}(1-ECI_a)(t_{ab}-t_b+\tau)x_{ab} \tag{5}$$

$$min\sum_{a=1}^{m}\sum_{b=1}^{n}(1-ECI_a)c_{ab}x_{ab} \tag{6}$$

The constraints of the model are shown below:

$$\sum_{a=1}^{m}s_a=\sum_{b=1}^{n}d_b \tag{7}$$

$$\sum_{a=1}^{m}x_{ab}=d_b \tag{8}$$

$$0\le s_a\le s_a{}' \tag{9}$$

$$x_{ab}\ge 0 \tag{10}$$

In the above equations, the $1-ECI_a$ is a selection factor; the higher the ECI, the lower the value of the select factor, and the more suitable it is to participate in social emergency resource sharing. The $(t_{ab}-t_b)$ is the total delay time in transporting emergency resources from the supply point (a) to the demand point (b), x_{ab} is the number of emergency resources that have been transported from the supply point (a) to the demand point (b). c_{ab} is the cost of transporting a unit of emergency resource from the supply point (a) to the demand point (b).

Among the above equations, Equations (5) and (6) are objective functions, which indicate that the total delay time and total economic cost in the emergency resource transportation process are the lowest. Equations (7)–(10) are the restrictions, where Equation (7) means that the total supply of emergency resources should be equal to the total demand. Equation (8) indicates that the total amount of emergency resources shipped from each supply point to the transfer station near the disaster area should be equal to the total demand for the transfer station. Equation (9) means that the emergency resource supply of each supply point cannot exceed the maximum amount it can provide. Equation (10) means that the number of emergency resources transferred from the supply points to the demand point is a non-negative number.

3.2.2. Model Analysis

Compared with the traditional model, a selection factor, 1 − ECI, is added to our model, as shown in Equations (5) and (6). Enterprises with higher ECI have greater production capacity and willingness, and accordingly, their values of 1 − ECI are lower, and thus, the total delay time and total costs will be lower. Therefore, such enterprises are more likely to be selected to participate in social emergency-sharing activities so that the defect of the traditional model of treating all emergency resource suppliers indiscriminately can be solved.

The improved model has the following advantages:

(1) This model can select the enterprises that best provide the emergency resources required by the disaster area in sufficient quantity in the shortest time based on the Emergency Production Capacities. The factors of registered and paid-in capital, size of personnel, and the nature of the enterprises in the emergency production capacity are able to identify larger state-owned enterprises. In addition, the factors of industry and business scope enable the scheduling program to filter equipment wholesale and retail enterprises. The model prefers enterprises that can provide equipment and technical staff at the same time. For example, in the process of road rescue, the model can choose road engineering service enterprises (with professional engineers) instead of enterprises that solely sell machines.

(2) When comprehensively considering emergency production capacity and leadership enthusiasm, the model is able to select enterprises that can not only provide appropriate emergency resources but also have a strong willingness to participate in emergency resource sharing. While analyzing the supply capacity of various supply enterprises using their emergency production capacities, their leadership enthusiasms can be analyzed by calculating the percentage of their charitable donations in the total output in the previous year. This indicator is able to select enterprises with a higher willingness to participate in social emergency resource sharing.

4. Experiments

In 2008, a massive 8.0 magnitude earthquake occurred in Wenchuan County, Sichuan Province in China; the direct economic loss caused by the earthquake was about 845.14 billion RMB, of which the value of damaged roads was about 185 billion RMB [30,31]. In this section, the calculation process and results of the SSERS Model will be shown.

4.1. Introduction of the Experimental Area

This study involves an area in Wenchuan, Sichuan Province. The remote sensing image was taken on 1 July 2008 by Worldview-1 satellite; its spatial resolution is 0.5 m. The latitude and longitude ranges are 31°25′48″ N to 31°31′23″ N and 103°31′34″ E to 103°38′13″ E, respectively. These ranges cover an area of 149.36 square kilometers. The entire research area is shown in Figure 1.

Figure 1. The research area of this study (Wenchuan).

4.2. The Process of the Experiments

In this study, the experiments can be divided into five stages. Figure 2 shows the details of these stages.

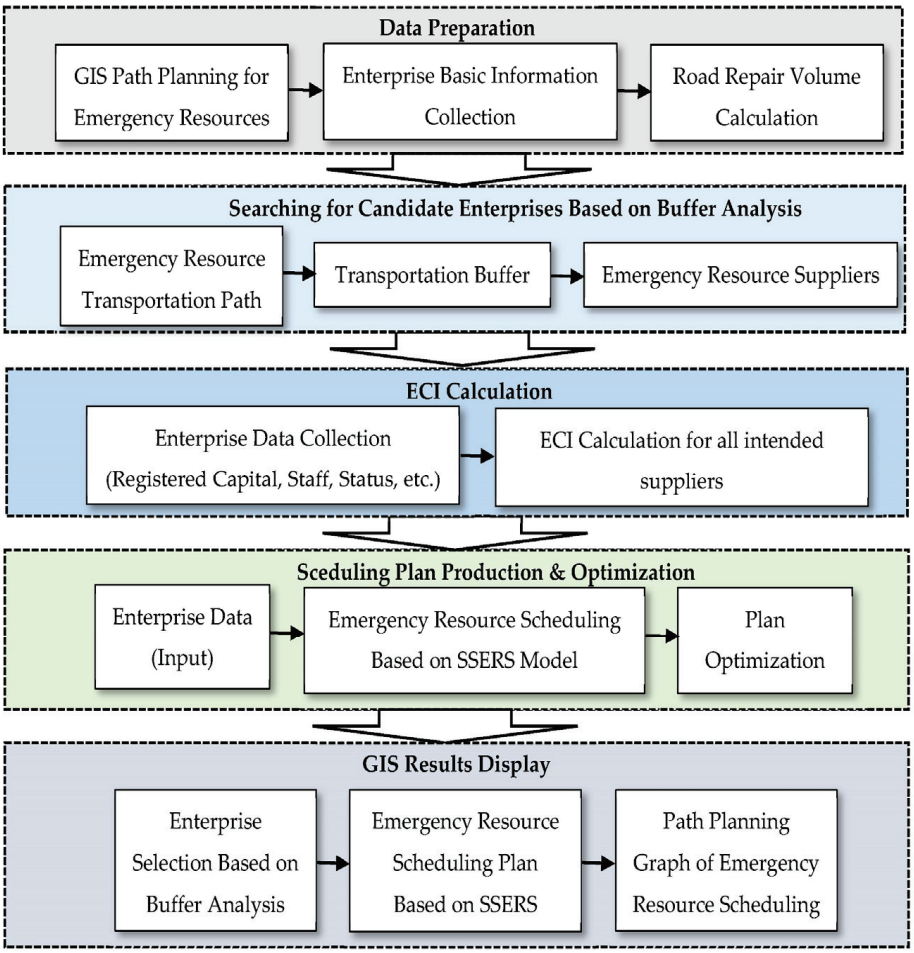

Figure 2. The process of our experiment.

Step 1: Data Preparation. First, a path for emergency resource transportation between the supply points to the disaster-affected area will be planned. Then, the data for road repair volume calculation will be collected, which includes the level of the roads, the construction standards of the roads, the essential materials for road repair, etc. Finally, the total volume for road repair and the number of road repair machinery required to complete the repair project within the specified time will be calculated.

Step 2: Enterprise Initial Selection Based on Buffer Analysis. The beginning city of resource transportation will be determined based on the time and the transportation costs. Then, the enterprises can be initially selected based on the buffer analysis.

Step 3: ECI Calculation. First, the basic information of all the enterprises that passed the initial selection will be collected, which includes operation status, registered capital, number of staff, etc. Then, for the ith supplier (S_i), calculate its ECI_i by using Formula (4).

Step 4: Scheduling Plan Production and Optimization. For every supplier (S_i), we bring its ECI_i into the Formulas (5) and (6), then the emergency resource scheduling plan with S_i can come out.

Step 5: GIS Results Display. Combining the initial enterprise screening based on buffer analysis and the emergency resource scheduling plan based on the SSERS Model, a path planing graph of emergency resource transportation based on GIS will be displayed.

4.3. Emergency Resource Scheduling Based on the SSERS Model

In this section, the 24-h post-disaster road repair is selected as an example; then the SSERS Model will be used to design the road repair equipment scheduling scheme.

(1) **Data Preparation—the Demands of the Volume of Road Reparation**

The demands of road repair equipment are related to the volume of the repair, so the working efficiency of every set of equipment should be determined first, then the total volume of road repair should come out. Based on these parameters, the number of sets of equipment required to complete road repair within the specified time can be derived.

The equipment used to repair such pavement and its efficiency are shown below. The equipment is generally provided in sets. Table 1 shows a set of equipment.

Table 1. Equipment used in road repairment (1 set) Reprinted/adapted with permission from [32].

Types of Equipment	Names of Equipment	Product Ratio (t/h)	Weight (t)	Number	Product Ratio of Every Set of Equipment (t/h)
Mixing equipment	Cement mixing machine	600	30	1	1400
	Sand and soil mixing machine	700	60	1	
	Asphalt mixing machine	280	50	1	
Booth equipment	Cement booth machine	600	28	2	
	Sand and soil booth machine	400	24	1	
	Asphalt booth machine	400	30	1	
Compaction equipment	Vibratory roller		22	2	
	Double-wheel vibratory roller		14	2	
	Double-wheel vibratory roller		12	1	
	Rubber wheel roller		30	1	
	Rubber wheel roller		22	1	
	Rubber wheel roller		12	1	
Loader			8	8	
Grader			20	1	

In this section, the number of sets of road repair equipment needs to be determined, so we designed the following formula.

$$n = \frac{D}{p_s T} \tag{11}$$

where n means the number of sets of equipment required in the road repairment (sets). The "D", which equals to $Atl\rho$, means the total mass of construction materials required in the course of road repairs (t), it is used to indicate the total project of the road repairs. p_s means the product ratio of each set of equipment (t/h), its value is 1400, and T means the total time required in the repairment (h).

The average density of cement and soil is 2.5 t/m^3. As a result, the total mass of materials required in road repair (D) should be:

$$\mathrm{D} = At \times l \times \rho = 198{,}000\ \mathrm{m}^2 \times 0.5\ \mathrm{m} \times 2.5\ \mathrm{t/m}^3 = 247{,}500\ \mathrm{t} \tag{12}$$

In order to complete the road repairs as soon as possible, we design that the repairs need to be finished within 24 h after the earthquake. If the equipment is transported from Chengdu City, the distance between Chengdu and Wenchuan is 128 km, based on the speed of 80 km/h. The transport time should be 1.6 h, so the repair time should be 22.4 h.

In summary, the sets of equipment required in the process of road repairs should be:

$$n = \frac{247{,}500\ \mathrm{t}}{1400\ \mathrm{t/h} \times 22.4\ \mathrm{h}} = 8\mathrm{sets} \tag{13}$$

The above result means that the road repairs need to be finished within 24 h, and the 8 sets of equipment should work simultaneously. That includes 8 of each of the three

types of mixing machines, 16 cement booth machines, a number of sand and soil booth machines, and asphalt booth machines is 8, respectively. Further, 64 loaders and 8 graders are also required.

(2) **Enterprise Initial Selection Based on Buffer Analysis**

The equipment is set to be dispatched from Chengdu; considering the actual situation, the target time is designed to be 2 h, which means the loaders should be transported to Wenchuan within 2 h. Using an average speed of 80 km/h, it takes 1.8 h to reach Wenchuan from Chengdu. The total delay time from Chengdu to Wenchuan is calculated below:

$$T = tab - tb = 1.85 - 2 = -0.15 \quad (14)$$

So, the radius of the buffer will be:

$$R = 80\ km/h \times 0.15 = 12\ km \quad (15)$$

Based on this calculation and the buffer analysis, there are six enterprises that can meet the needs, which are recorded as No. 1–No. 6. The number of loaders shipped from Chengdu to Wenchuan is x_1–x_6. The details of these enterprises are shown below.

The above table shows the basic information of the six enterprises, including the registered and paid-in capitals, numbers of the total and insured staff, the profits of produced emergency resources, the profits of all products of every enterprise, the donations and labor expenses, and their industries.

(3) **ECI Calculation**

The emergency production capacity and leadership enthusiasm of the above enterprises can be calculated based on Equations (1)–(3); the data used in the calculation comes from Table 2. The results are shown in the Table 3. We assume that all the enterprises have no business scope change records, so their values are 1.

Table 2. Details of the six enterprises in Chengdu in 2021.

#	Name of the Enterprise	Registered Capital (RMB)	Paid-in Capital (RMB)	Number of Staff	Insured Staff	Profits of Produced Emergency Resources (RMB)	Profits of All Products (RMB)	Donations and Labor Expenses (RMB)	Industry
1	Chengdu Chenggong Industry	14 million	14 million	500	268	720 million	1.2 billion	633 million	Construction
2	Sichuan Zhonglu Architecture	68 million	50 million	500	206	33 million	152 million	20 million	Construction
3	Sichuan Highway Architecture	30 million	30 million	1000	885	639 million	1.7 billion	729 million	Construction
4	Chengdu Zhongzhi Construction	36 million	36 million	1000	724	1.1 billion	2 billion	780 million	Construction
5	Sichuan No. 1 Construction	6 million	6 million	100	51	52 million	150 million	33 million	Construction
6	ChengduYixin Industry	5 million	5 million	100	57	30 million	102 million	20 million	Retail

Source: https://www.tianyancha.com/company/2314420002, accessed on 12 May 2023.

Table 3. The Values of the Components of ECI of the 6 Enterprises.

Name of Enterprises	Sichuan Highway Architecture	Chengdu Chenggong Industry	Chengdu Zhongzhi Construction	Sichuan No. 1 Construction	Sichuan Zhonglu Architecture	Chengdu Yixin Construction
Emergency Production Capacity	0.8	0.69	0.76	0.68	0.48	0.65
Staff Motivation	0.89	0.54	0.72	0.51	0.41	0.57
Leadership Enthusiasm	0.43	0.53	0.39	0.22	0.13	0.19
ECI	0.26	0.23	0.21	0.08	0.07	0.03

(4) **Scheduling Plan Production and Optimization (Emergency Resource Scheduling Based on SSERS)**

This model adds emergency production capacity and emergency willingness of the enterprises simultaneously on the basis of the traditional model, which can make the scheduling plan more reasonable. The related indicators of the above-mentioned six enterprises are shown below.

When calculating the data, we will first use the traditional model to analyze the scheduling and analyze the irrationality of only considering the restriction of the amount of emergency resources. On the basis of this analysis, the emergency production capacity and leadership enthusiasm of every enterprise will be considered. We will use the same restrictions to compare different scheduling plans, and then the best plan can be developed.

In this example, there is only one demand point for emergency resources (Wenchuan), so the value of "b" is 1. Thus, Equations (3)–(5) will be changed into:

$$min \sum_{a=1}^{m} (1 - ECI_i)(t_{i1} - t_1 + \tau)x_{i1} \tag{16}$$

To make the results more realistic, the restrictions of this model are shown below. $x_1 < 100$, $x_2 < 100$, $x_3 < 100$, $x_4 < 200$, $x_5 < 200$, $x_6 < 200$,

The calculative result is: $x_1 = 4$, $x_2 = 0$, $x_3 = 60$, $x_4 = x_5 = x_6 = 0$.

When considering emergency production capacity and leadership enthusiasm simultaneously, the scheduling plan is shown in Table 4.

Table 4. The scheduling plan of loaders is based on the SSERS Model.

Name of Enterprises	Sichuan Highway Architecture	Chengdu Chenggong Industry	Chengdu Zhongzhi Construction	Sichuan No. 1 Construction	Sichuan Zhonglu Architecture	Chengdu Yixin Industry
ECI	0.26	0.23	0.21	0.08	0.07	0.03
Scheduling Quality (Ton)	60	4	0	0	0	0

(5) **GIS Result Display**

Figure 3 shows the spatial distribution of the six selected enterprises, of which Chengdu Chenggong Industry and Sichuan Highway Industry (shown as blue points) are the two preferred enterprises to participate in the social emergency resource scheduling. The red line in the figure is the transportation path of the emergency resource from the preferred enterprises to Wenchuan based on the SSERS Model.

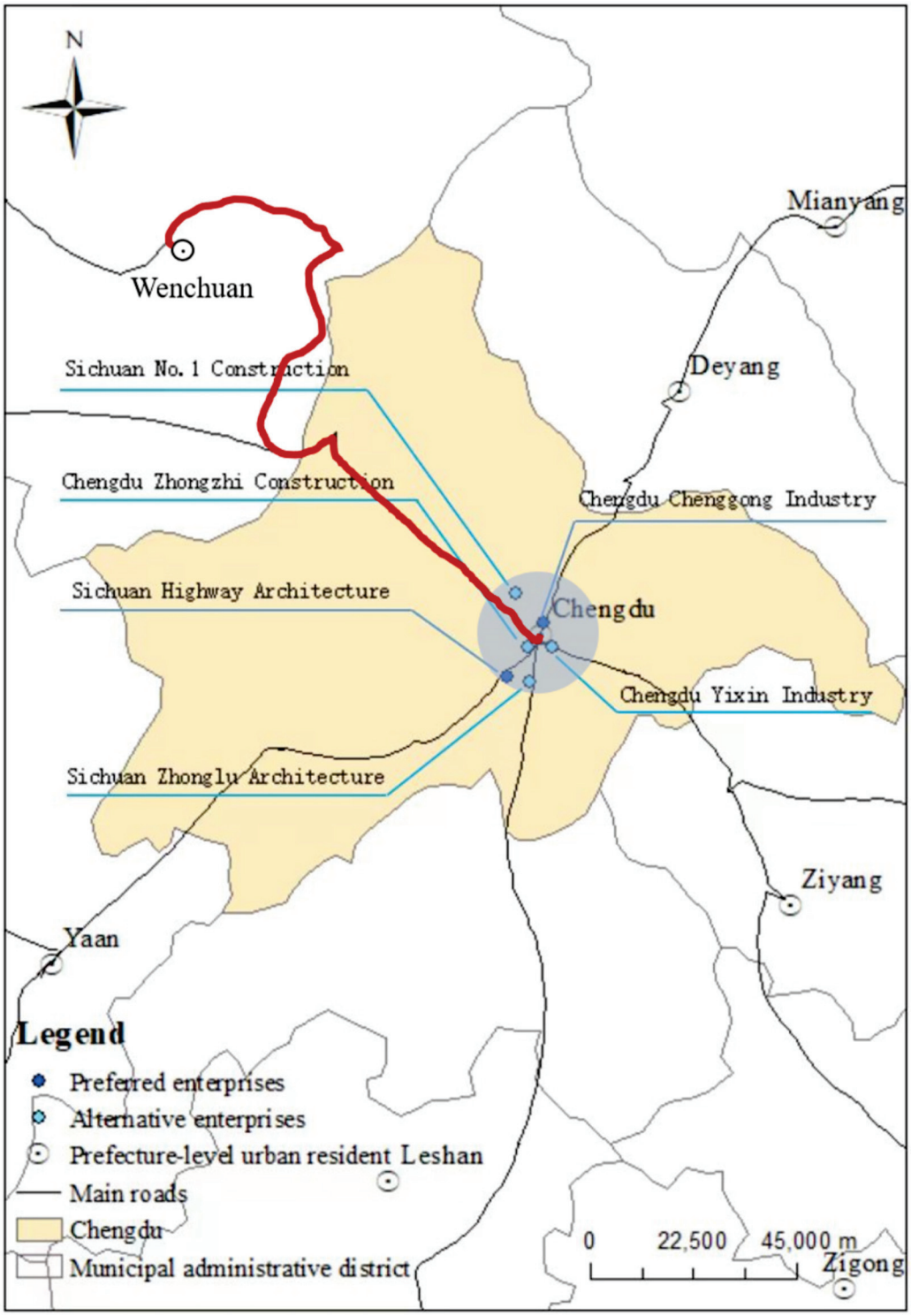

Figure 3. The spatial distribution of the six selected enterprises.

5. Discussion

In this section, the traditional model will be used to design an emergency resource scheduling plan first; then, it will be compared with the plan based on the SSERS Model to testify to the effects of our model.

5.1. Emergency Resource Scheduling Based on the Traditional Model

This model only considers the restrictions of the number of resources and does not take the emergency production capacity and enterprise willingness of the enterprises into account. In the extreme emergency period, the total demand on loaders was 64; the model and its restrictions are shown below.

$$min\sum_{a=1}^{m}\sum_{b=1}^{n}(t_{ab}-t_b)x_{ab} \tag{17}$$

$$min\sum_{a=1}^{m}\sum_{b=1}^{n}c_{ab}x_{ab} \tag{18}$$

The constraints of the model are shown below:

$$\sum_{a=1}^{m}s_a=\sum_{b=1}^{n}d_b \tag{19}$$

$$\sum_{a=1}^{m}x_{ab}=d_b \tag{20}$$

$$0\ \le s_a \le\ s_a{}' \tag{21}$$

$$x_{ab}\ge 0 \tag{22}$$

In the above equations, $(t_{ab}-t_b)$ is the total delay time in transporting emergency resources from the supply point (a) to demand point (b), x_{ab} is the number of emergency resources that have been transported from the supply point (a) to demand point (b). c_{ab} is the cost of transporting a unit of emergency resource from the supply point (a) to the demand point (b).

Among the above equations, (17) and (18) are objective functions, which indicate that the total delay time and total economic cost in the emergency resource transportation process are the lowest. Equations (19)–(22) are the restrictions, where Equation (19) means that the total supply of emergency resources should be equal to the total demand. Equation (20) indicates that the total amount of emergency resources shipped from each supply point to the transfer station near the disaster area should be equal to the total demand for the transfer station. Equation (21) means that the emergency resource supply of each supply point cannot exceed the maximum amount it can provide. Equation (22) means that the number of emergency resources transferred from the supply points to the demand point is a non-negative number.

In this example, there is only one demand point (Wenchuan), so the "b" in Equation (17) equals 1. The Equation used here is:

$$min\sum_{a=1}^{m}(t_{i1}-t_1)x_{i1}$$

The constraints of the model are shown below:

$x_1 < 100$, $x_2 < 100$, $x_3 < 100$, $x_4 < 200$, $x_5 < 200$, $x_6 < 200$,

The calculative result is: $x_1 = x_2 = x_3 = x_4 = x_5 = 0$ and $x_6 = 64$.

When only considering the restriction of the amount, the scheduling plan is shown in Table 5.

Table 5. The scheduling plan of loaders is based on the traditional model.

Name of Enterprises	Sichuan Highway Architecture	Chengdu Chenggong Industry	Chengdu Zhongzhi Construction	Sichuan No. 1 Construction	Sichuan Zhonglu Architecture	Chengdu Yixin Industry
ECI	0.26	0.23	0.21	0.08	0.07	0.03
Scheduling Quality (Ton)	0	0	0	0	0	64

The ECI values of the six enterprises are calculated according to the formula (4), and the data used in the calculation comes from Table 3.

The above result shows that when only considering the restrictions of amount, all 64 loaders would be provided only by Chengdu Blue Eagle Beverage Co., Ltd. (Chengdu, China). However, its ECI value is 0.03, which ranked 6th among the six enterprises.

5.2. A Comparison of the Traditional Model and the SSERS Model

The results of the two models are integrated in Table 6.

Table 6. The results of the two models.

Name of Enterprises	Sichuan Highway Architecture	Chengdu Chenggong Industry	Chengdu Zhongzhi Construction	Sichuan No. 1 Construction	Sichuan Zhonglu Architecture	Chengdu Yixin Industry
ECI	0.26	0.23	0.21	0.08	0.07	0.03
Scheduling Quality (Ton) based on the basic model	0	0	0	0	0	64
Scheduling Quality (Ton) based on the SSERS model	60	4	0	0	0	0

The above results show that when considering the emergency contribution index, 64 of the loaders can be provided by Chengdu Chenggong Co., Ltd. and Sichuan Highway Architecture Co., Ltd.

Sichuan Highway Architecture and Chengdu Chenggong Industry ranked among the top two out of the six enterprises in terms of the ECI (0.26 and 0.23, respectively). These enterprises have the following advantages:

(1) They have a stronger willingness to participate in social emergency resource sharing.

The leadership enthusiasm of the two enterprises is 0.53 and 0.43, respectively, which are ranked in the top two among the six enterprises. This means the enterprises are keen on leadership enthusiasm and have a strong sense of social responsibility. Further, the staff motivation of these enterprises is 0.54 and 0.89, respectively, positioning them at the top among these enterprises, so they have a high value on the enterprise willingness. It means that in these two enterprises, both the leaders and the employees are passionate about social charity work; they are willing to contribute to relief efforts when disasters happen.

(2) They have stronger abilities to provide emergency resources.

The Emergency Production Capacity of the two enterprises is 0.69 and 0.8, respectively, which rank third and first among the six enterprises, which shows that both of them have a relatively strong ability to provide emergency resources. The Sichuan Highway Architecture has the largest number of personnel among the six enterprises, and its registered capital ranks highly, so its emergency production capacity reaches the highest level of 0.8. Further, both enterprises have strong economic strength (registered and paid-in capitals) in the six enterprises, which can strongly guarantee the production of emergency resources.

From the above analysis, it can be seen that both the emergency production capacity and the enterprise willingness of the two enterprises chosen using the SSERS Model are relatively high, which means that they have a strong ability and willingness to provide emergency resources. Regarding the enterprise chosen using the traditional model, the

values of the three indicators, emergency production capacity, staff motivation, and leadership enthusiasm, for the enterprise are 0.65, 0.57, and 0.19, respectively. Among the six candidates, they rank 5th, 3rd, and 5th, respectively, which indicates that the emergency production capacity of the Chengdu Yixin Industry is not very strong; it may not be able to meet the resource demands during the post-disaster emergency rescue operation. On the other hand, the leaders and the staff in this enterprise are not enthusiastic about participating in emergency resource sharing. As a result, its ECI value is only 0.03, which is the lowest of the six candidates. Therefore, compared with the Chengdu Yixin industry, Sichuan Highway Architecture and Chengdu Chonggong Industry are fit for emergency resource sharing.

6. Conclusions

To quantify the supply ability and willingness to participate in social emergency resource sharing, this paper defines the emergency contribution index (ECI) of an enterprise, which includes emergency production capacity and enterprise willingness. Then, we proposed a multi-objective social emergency resource scheduling model based on the emergency contribution index (SSERS). It incorporates the ECI of an enterprise for the first time, addressing the limitations of traditional models that overlook supply-side conditions. As a result, the SSERS realizes the optimization of the social emergency resource scheduling and sharing scheme.

However, the model proposed in this paper still has some limitations: the calculation of Leadership enthusiasm only takes the enterprises' information in the previous year into consideration, and it is disturbed using incomplete information.

Therefore, in the future, it will be necessary to use Big Data for trend analysis to more accurately describe the supply capabilities of emergency resources and the willingness to participate in social emergency resource sharing.

Author Contributions: Data curation, M.M.; Formal analysis, W.C. (Wenqi Cui) and Q.H.; Investigation, B.L.; Methodology, W.C. (Wenqi Cui) and W.C. (Wei Cui); Resources, X.C.; Validation, W.C. (Wei Cui); Writing—original draft, W.C. (Wenqi Cui); Writing—review and editing, X.X., Z.F. and J.C. All authors have read and agreed to the published version of the manuscript.

Funding: This research received no external funding.

Institutional Review Board Statement: Not applicable.

Informed Consent Statement: Not applicable.

Data Availability Statement: Not applicable.

Conflicts of Interest: The authors declare no conflict of interest.

References

1. Hu, F.; Tian, C.; Zhao, M.; Han, X. Research on hierarchical linkage scheduling emergency supplies based on genetic algorithm. *Appl. Res. Comput.* **2017**, *33*, 439–443.
2. Yan, J.; Guo, Y. Unconventional Emergency Aid Delivery Path Optimization Research. *J. Catastr.* **2017**, *31*, 193–200.
3. Lu, C.C.; Ying, K.C.; Chen, H.J. Real-Time Relief Distribution in the Aftermath of a Disaster—A Rolling Horizon Approach. *Transp. Res. E-Log.* **2019**, *93*, 1–20. [CrossRef]
4. Chai, G.; Cao, J.; Huang, W.; Guo, J.O. ptimized Travel Emergency Resource Schuding Using Time Vary Rescue Route Travel Time. *Neurocompting* **2018**, *275*, 1567–1575. [CrossRef]
5. Batmetan, J.; Santoso, A.; Pranowo, A. Multiple-Objective Ant Colony Algorithm for Optimization Disaster Relief Logistics. *Adv. Sci. Lett.* **2017**, *23*, 2344–2347. [CrossRef]
6. Ferrer, J.M.; Martín-Campo, F.J.; Ortuño, M.T.; Pedraza-Martínez, A.J.; Tirado, G.; Vitoriano, B. Multi-Criteria Optimization for Last Mile Distribution of Disaster Relief Aid. *Eur. J Oper. Res.* **2018**, *269*, 201–215. [CrossRef]
7. Vidal, T.; Crainic, T.G.; Gendreau, M.; Prins, C. A Hybrid Genetic Algorithm with Adaptive Diversity Management for a Large Class of Vehicle Routing Problems with Two-Windows. Comput. *Oper. Res.* **2015**, *40*, 475–489.
8. Das, R. Disaster Preparedness for Better Response: Logistics Perspectives. *Int. J. Disast. Risk Reduct.* **2018**, *31*, 153–159. [CrossRef]
9. Chen, L.; Wang, H. Optimal Scheduling Model for Emergency Logistics based on Satisfaction under Lagrge-Scale Emergencies. *China Saf. Sci. J.* **2020**, *20*, 46.

10. Wang, J.; Wang, M. Study on Optimizing of Emergency Resource Scheduling for Maritime Perils. *China Saf. Sci. J.* **2020**, *23*, 166–170.
11. Ding, Z.; Zhao, Z.; Liu, D.; Cao, Y. Multi-Objective Scheduling of Relief Logistics Based on Swarm Intelligence Algorithms and Spatio-Temporal Traffic Flow. *J. Safe Sci. Resil.* **2021**, *2*, 222–229. [CrossRef]
12. Wan, F.; Guo, H.; Li, J.; Gu, M.; Pan, W.; Ying, Y. A Scheduling and Planning Method for Geological Disasters. *Appl. Soft Comput.* **2021**, *111*, 107712. [CrossRef]
13. Chi, H.; Li, J.; Shao, X. Timeliness Evaluation of Emergency Resource Scheduling. *Eur. J. Oper. Res.* **2017**, *258*, 1022–1032. [CrossRef]
14. Zhou, Y.; Liu, J.; Zhang, Y.; Gan, X. A Multi-Objective Evolutionary Algorithm for Multi-Period Dynamic Emergency Resource Sheduling Problems. *Transp. Res. E-Log.* **2017**, *99*, 77–95. [CrossRef]
15. Zhang, J.; Liu, H.; Yu, G.; Ruan, J.; Chan, F.T. A Three-Stage and Multi-Objective Stochastic Programme Model to Improve the Sustainable Rescue Ability by Considering Secondary Disasters in Emergency Logistics. *Comput. Ind. Eng.* **2019**, *135*, 1145–1154. [CrossRef]
16. Cui, S.; Liu, S.; Tang, X.; Zhu, T. Emergency Material Allocation Problem Considering Post-Disaster Impact. In Proceedings of the 8th International Conference on Industrial Technology and Management (ICITM), Cambridge, UK, 2–4 March 2019.
17. Wang, H.; Xu, R. Research on the Optimized Dispatch and Transportation Scheme for Emergency Logistics. *Procedia Comput. Sci.* **2018**, *129*, 208–214. [CrossRef]
18. Bodaghi, B.; Shahparvari, S.; Fadaki, M.; Lau, K.H.; Ekambaram, P.; Chhetri, P. Multi-Resource Scheduling and Routing for Emergency Recovery Operations. *Int. J. Disast. Risk Reduct.* **2020**, *50*, 101780. [CrossRef]
19. Zhang, L.; Lu, J.; Yang, Z. Dynamic Optimization of Emergency Resource Scheduling in a Large-Scale Maritime Oil Spill Accident. *Comput. Ind. Eng.* **2021**, *152*, 107028. [CrossRef]
20. Xu, C.; Song, Y.; Yu, Z.; Zhuang, Z. Multi-Source Detecting Data Fusion Technology for Emergency Rescue. *Comput. Syst. Appl.* **2019**, *101*, 104201.
21. Li, X.; Li, Y. A Model on Emergency Resource Dispatch under Random Demand and Unreliable Transportation. *Syst. Eng. Procedia* **2012**, *5*, 248–253. [CrossRef]
22. Wang, Y.; Fan, J.; Wu, S. Research on the Scheduling Scheme of Resource Storage Locations in Deep-Sea Oil and Gas Exploitation. *J. Petrol. Sci. Eng.* **2023**, *220*, 111214. [CrossRef]
23. Chen, L.; Li, Y.; Chen, Y.; Liu, N.; Li, C.; Zhang, H. Emergency Resource Schduling in Distribution System: From Cyber-Physical-Social System Perspective. *Electr. Pow. Syst. Res.* **2022**, *210*, 108114. [CrossRef]
24. Sun, B.; Zhai, G.; Li, S.; Pei, B. Multi-Resource Collaborative Scheduling Problem of Automated Terminal Considering the AGV Charging Effect under COVID-19. *Ocean Coast. Manag.* **2023**, *232*, 106422. [CrossRef]
25. Ding, Z.; Xu, X.; Jiang, S.; Yan, J.; Han, Y. Emergency Logistics Scheduling with Multiple Supply-Demand Points based on Gery Interval. *J. Safe Sci. Rel.* **2022**, *3*, 179–188.
26. Zhang, M.; Kong, Z. A Tripartite Evolutionary Game Model of Emergency Supplies Joint Reserve among the Government, Enterprise and Society. *Comput. Ind. Eng.* **2022**, *169*, 108132. [CrossRef]
27. Meng, Y. The Optimization and Coordination of Multi-Layer Recruitment Network for Social Emergency Resources. *Comput. Ind. Eng.* **2019**, *130*, 50–61. [CrossRef]
28. Olanrewaju, O.; Dong, Z.; Hu, S. Supplier Selection Decision-Making in Disaster Response. *Comput. Ind. Eng.* **2020**, *143*, 106412. [CrossRef]
29. Hu, S.; Dong, Z. Suppliers Selection and Pre-Positioning Strategy in Humanitarian Relief. *Omega* **2019**, *83*, 287–298. [CrossRef]
30. Chinese National People's Congress Website. The Direct Economic Loss of Wenchuan Earthquake. Available online: http://www.npc.gov.cn/zgrdw/npc/zt/2008-09/05/content_1448390.htm (accessed on 20 November 2022).
31. Cui, W.; He, X.; Yao, M.; Wang, Z.; Li, J.; Hao, Y.; Wu, W.; Zhao, H.; Chen, X.; Cui, W. Landslide Image Captioning Method Based on Semantic Gate and Bi-Temporal LSTM. *ISPRS Int. J. Geo.-Inf.* **2020**, *9*, 194. [CrossRef]
32. Wang, J. Rational Configuration and Methods of Highway Construction Mechanization. *Value Eng.* **2017**, *36*, 3.

water

MDPI

Article

Determining the Risk Level of Heavy Rain Damage by Region in South Korea

Jongsung Kim [1], Donghyun Kim [2], Myungjin Lee [1], Heechan Han [3] and Hung Soo Kim [2,*]

[1] Institute of Water Resources System, Inha University, Incheon 22201, Korea; kjjs0308@naver.com (J.K.); lmj3544@naver.com (M.L.)
[2] Department of Civil Engineering, Inha University, Incheon 22201, Korea; yesdktpdi@naver.com
[3] Blackland Research and Extension Center, Texas A&M AgriLife, Temple, TX 76502, USA; heechan.han@ag.tamu.edu
* Correspondence: sookim@inha.ac.kr; Tel.: +82-10-3441-1038

Abstract: For risk assessment, two methods, quantitative risk assessment and qualitative risk assessment, are used. In this study, we identified the regional risk level for a disaster-prevention plan for an overall area at the national level using qualitative risk assessment. To overcome the limitations of previous studies, a heavy rain damage risk index (HDRI) was proposed by clarifying the framework and using the indicator selection principle. Using historical damage data, we also carried out hierarchical cluster analysis to identify the major damage types that were not considered in previous risk-assessment studies. The result of the risk-level analysis revealed that risk levels are relatively high in some cities in South Korea where heavy rain damage occurs frequently or is severe. Five causes of damage were derived from this study—A: landslides, B: river inundation, C: poor drainage in arable areas, D: rapid water velocity, and E: inundation in urban lowlands. Finally, a prevention project was proposed considering regional risk level and damage type in this study. Our results can be used when macroscopically planning mid- to long-term disaster prevention projects.

Keywords: disaster prevention project; heavy-rain-damage risk index; hierarchical clustering; qualitative risk assessment

Citation: Kim, J.; Kim, D.; Lee, M.; Han, H.; Kim, H.S. Determining the Risk Level of Heavy Rain Damage by Region in South Korea. *Water* **2022**, *14*, 219. https://doi.org/10.3390/w14020219

Academic Editors: Stefano Morelli, Veronica Pazzi and Mirko Francioni

Received: 6 December 2021
Accepted: 8 January 2022
Published: 12 January 2022

1. Introduction

The frequency and magnitude of natural disasters such as localized torrential rain and typhoons caused by climate change are increasing worldwide, and have resulted in massive property damage and casualties [1]. Heavy rainfall damage, which is one of the main types of natural disaster in South Korea, causes over 120 million USD in damage every year in South Korea [2]. Emergency managers in many countries use four phases of disaster management to reduce the damage caused by natural disasters—Phase 1: Mitigation, Phase 2: Preparedness, Phase 3: Response, and Phase 4: Recovery. The mitigation phase is to prevent future emergencies and to take steps to minimize their effects. The preparedness phase is to take actions ahead of time to be ready for an emergency. The response phase is to protect people and property in the wake of an emergency, disaster, or crisis. The recovery phase is to rebuild after a disaster in an effort to return operations back to normal. The mitigation phase is an especially important element that forms the basis of disaster management.

Studies on the mitigation phase are closely related to risk assessment and are divided into quantitative and qualitative risk assessments. Within quantitative risk assessment, flood risk (i.e., inundation depth and area of flooded land) is analyzed based on a physical model, and quantitative loss (i.e., damage of property and fatality) is also identified. Ţîncu, et al. [3] estimated direct flood damage in three scenarios (i.e., residential buildings, infrastructure, agriculture) in the basin of the Trotus River located in Romania. Di et al. [4] proposed a quantitative risk assessment method for the loss of fatality caused by floods.

In this study, we reproduced the 1953 East Coast flood event in England and used several methods, such as "Mortality Function" and "Flood Risk Method to People", for detailed assessments of the subsequent mortality. The quantitative risk assessment method can be used to calculate the cost-benefit ratio through reduced loss when disaster prevention facilities are introduced in a specific area; this method can then be utilized to evaluate the economics of prevention facilities.

For qualitative risk assessment, the integrated index is calculated using statistical indicators reflecting regional characteristics, and the risk level of each region is analyzed. This method can be used to identify the relative level of risk when establishing a disaster prevention plan for the overall area at the national level. Zhang et al. [5] proposed a fourth-grade flood damage risk index (FDRI) that considers the potential flood damage risk, the status of flood damage, flood damage change, degree of social and economic development, and flood damage defense capability. Fekete [6] proposed social flood vulnerability indicators based on factor analysis of flood damage data collected by Germany's Federal Government Statistics Office. Sharma et al. [7] assessed the flood risk in the Kopili River basin of India using flood maps derived from satellite data by overlapping them with GIS data on roads, crops, and buildings. Amira et al. [8] used qualitative flood risk assessment to ascertain the risk of flooding in Jakarta, assigning each indicator a score using the categorical scale method.

In previous research related to qualitative risk assessment, a framework to define flood risk has been heavily emphasized. For example, Lim et al. [9] developed dimension-related indicators for various basins based on the Organization for Economic Cooperation and Development (OECD)'s (2001) P-S-R framework (i.e., the pressure, state, and response framework), and proposed a flood risk index (FRI) that can identify the overall flood risk for any given study area. Within the P-S-R framework [10] used in this study, P refers to a dangerous natural phenomenon or economic loss, S refers to the inventory affected by dangerous natural phenomena, and R refers to the ability to adapt to dangerous natural phenomena; however, the PSR framework cannot consider inventory vulnerability. Anindita et al. [11] performed a spatial assessment of flood risk for coastal areas of Central Java, Indonesia, based on the Intergovernmental Panel on Climate Change (IPCC) framework (i.e., considering nature of hazard, exposure, sensitivity, and adaptive capacity). Each region was divided into five risk levels and mapped using GIS. In the IPCC framework [12], hazard, exposure, and adaptive capacity have the same meaning as pressure, state, and response of the PSR framework; sensitivity refers to the vulnerability of the inventory. The Korea Institute of Civil Engineering and Building Technology (KICT) [13] evaluated qualitative flood risk for Korea using the framework (i.e., considering hazard, exposure, vulnerability, capacity) presented by the United Nations International Strategy for Disaster Reduction (UNISDR). The components of the UNISDR framework [14] are similar in meaning to the IPCC's framework, with the only difference being in words such as vulnerability (sensitivity is used instead) and capacity (adaptive capacity is used instead).

The results of the aforementioned risk assessment may be analyzed differently depending on the selection of indicators. Rygel et al. [15] mentioned that the most important factor in vulnerability assessment is selecting an appropriate indicator, and proposed vulnerability assessment techniques that were selected as indicators using the Pareto-ranking process. Joo et al. [16] stated that disaster management decision-makers may be perplexed by inconsistent results for each methodology of flood risk assessment. To solve this issue, a new method was proposed based on a Bayesian network, designed to support comprehensive judgment by integrating indicators and weights in major previous studies. Kim et al. [17] selected assessment indicators via factor analysis and proposed a heavy rain damage risk index (HDRI). They then presented the results of the risk assessment by classifying it into three risk levels for Gyeonggi-do, South Korea. Birkmann [18] mentioned that because the selection of an indicator is the most important part of process to develop an index, it should be selected through clear principles. In addition, he proposed the concept of a method for qualitative disaster risk assessment.

However, in many previous studies, there is insufficient evidence to support selection on assessment indicators, and the frameworks used in their studies are unclear. Therefore, this study used the UNISDR framework (i.e., hazard, exposure, vulnerability, and capacity), which is judged to be the most clearly distinguished among such frameworks. In addition, a clear selection principle was identified by reviewing the selection principles mentioned in previous studies, after which the assessment indicators were selected.

There are various types of disaster prevention projects related to floods, which are related to the causes of flood damage (river maintenance project: river inundation; erosion control maintenance project: landslide; sewer pipe maintenance project: inland flooding due to poor sewage; drainage pump station project: inland flooding in the region of lower elevation, etc.). However, previous studies did not consider the regional cause of flood damage. As a result, although it was possible to grasp the level of risk in each region, it was not possible to present a disaster-prevention project favorable to the region. To address these limitations, the aim of this study is twofold.

The first aim is to improve the limitations, such as unclear frameworks, the assessment indicator selection of previous qualitative risk assessments; we investigated the assessment indicators and frameworks used in previous studies. The UNISDR's framework (i.e., hazard, exposure, vulnerability, and capacity) was judged the most clearly distinguished among the various frameworks. The assessment indicators used in previous studies were then reconstructed into the UNISDR framework. The second aim is to identify the main causes of damage, by region, that were not considered in previous studies. We also performed hierarchical cluster analysis using historical damage data through a novel approach to the existing methodology. Furthermore, the assessment indicators used in this study were chosen based on six selection principles. Finally, a prevention project suitable depending on the regional damage type was proposed.

2. Theoretical Background (Materials and Methodology)

2.1. Characteristics of the Study Area

In this study, South Korea was selected as the study area. South Korea is divided into nine provinces, i.e., GyeongGi (GG), GangWon (GW), GyeongsangBuk (GB), Gyeongsang-Nam (GN), ChungcheongBuk (CB), ChungcheongNam (CN), JeollaBuk (JB), JeollaNam (JB), and JeJu (JJ), and eight major cities, i.e., Seoul (SO), Incheon (IC), Busan (BS), Daegu (DG), Ulsan (US), Daejeon (DJ), Sejong (SJ), and Gwangju (GJ). These cities and provinces have an average of 14 administrative districts, giving a total of 228 administrative districts. The location and features of the administrative districts of South Korea are summarized in Figure 1 and Table 1. In general, the eight cities have a higher level of regional development than the provinces. Therefore, these cities contain a large number of impervious areas, whereas the provinces contain large portions of permeable areas due to their agricultural system. Despite being a province, Gyeonggi-do has a high level of regional development because it is included in the metropolitan area.

South Korea's main topographical feature is its peninsula, with high elevation in the east and low elevation in the west. This is due to the country's extensive mountain ranges, which are in GW, JB, and GB. Figure 2a shows the elevation of South Korea, where the part marked in red represents the mountain range. Moreover, as shown in Figure 2b, rivers in South Korea are primarily classified into three types: national rivers, local rivers, and small rivers. National rivers are largely divided into four basins: Han, Nakdong, Geum and the Seomjin-Yeongsan. The Han River flows through SO, IC, GG, and GW, the Nakdong River flows through GB, GN, DG, US, the Geum River flows through BS. CB, CN, SJ, and DJ, and JB, JN, and GJ are home to the Seomjin-Yeongsan River. From Figure 2a,b, it can be seen that rivers are less distributed in regions containing mountain ranges. This means that mountain ranges and rivers have opposite characteristics, and therefore, the types of damage caused in each landscape may be different.

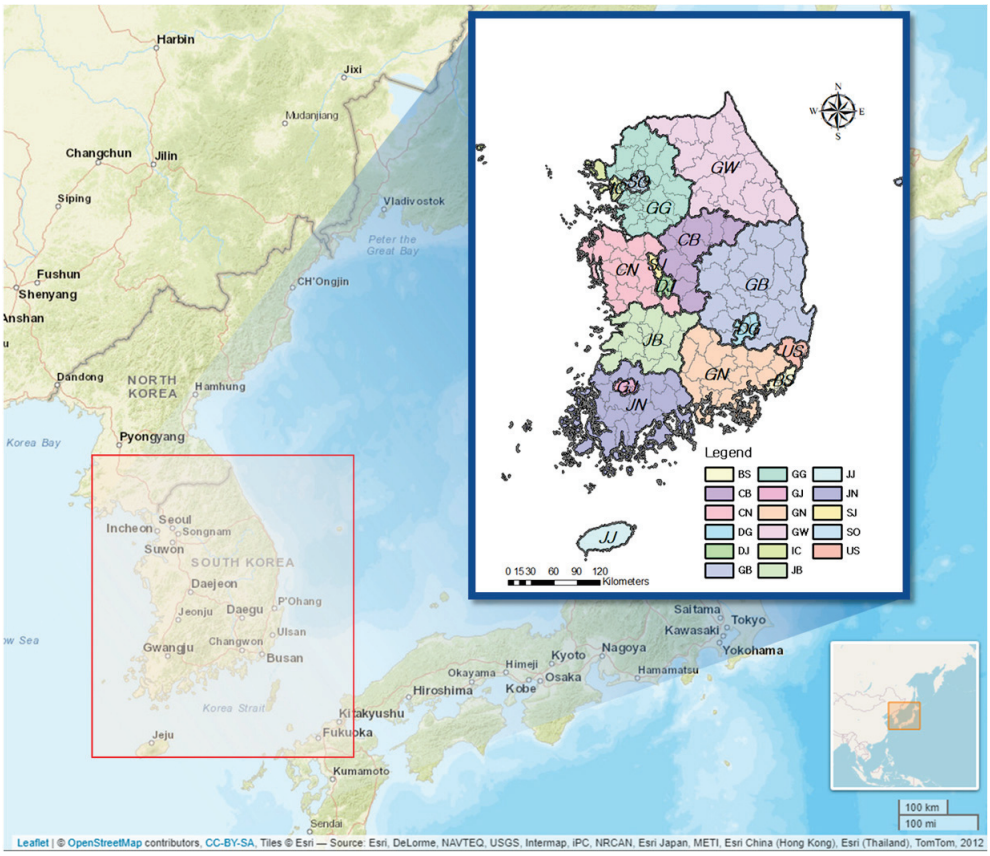

Figure 1. Locations of nine provinces and eight cities in South Korea.

Table 1. Abbreviations for the provinces and cities of South Korea.

Province	Abbreviation	City	Abbreviation
Gyeonggi-do	GG	Seoul	SO
Gangwon-do	GW	Incheon	IC
Gyeongsangbuk-do	GB	Busan	BS
Gyeongsangnam-do	GN	Daegu	DG
Chungcheongbuk-do	CB	Ulsan	US
Chungcheongnam-do	CN	Daejeon	DJ
Jeollabuk-do	JB	Sejong	SJ
Jeollanam-do	JN	Gwangju	GJ
JeJu-do	JJ		

2.2. Qualitative Risk Assessment Method

Risk assessment is a method for evaluating the relative risk level in a region by calculating an integrated index from statistical indicators representing a region's risk levels. Here, an indicator refers to a variable that contains information about a risk level or state, and an index is calculated by aggregating two or more indicators or computing their weights. The procedure for performing heavy rain damage risk assessment is shown in Figure 3.

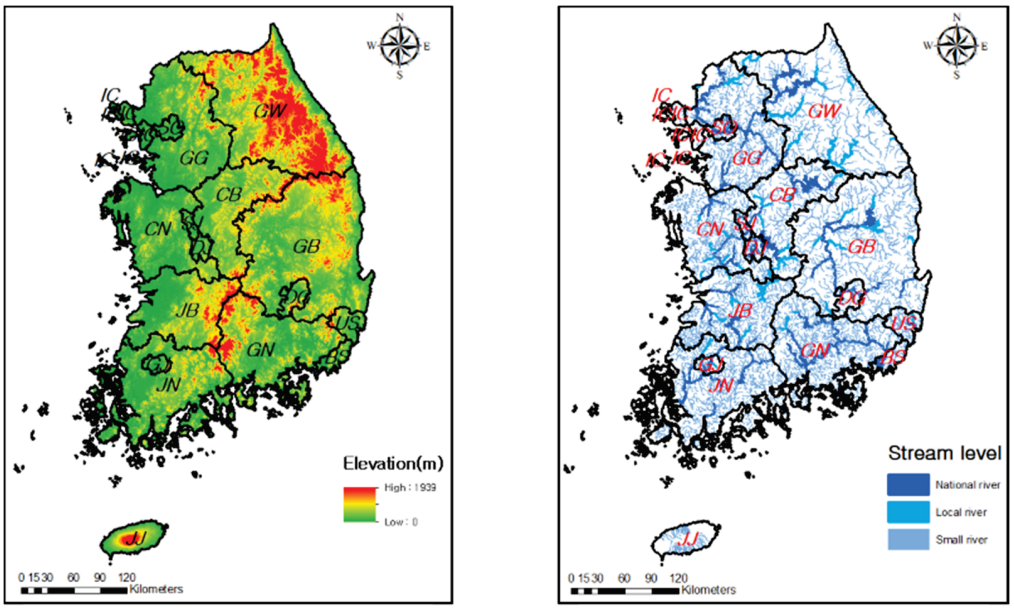

(**a**) The map is elevation distribution (**b**) The map is stream distribution

Figure 2. Elevation and river map in study area.

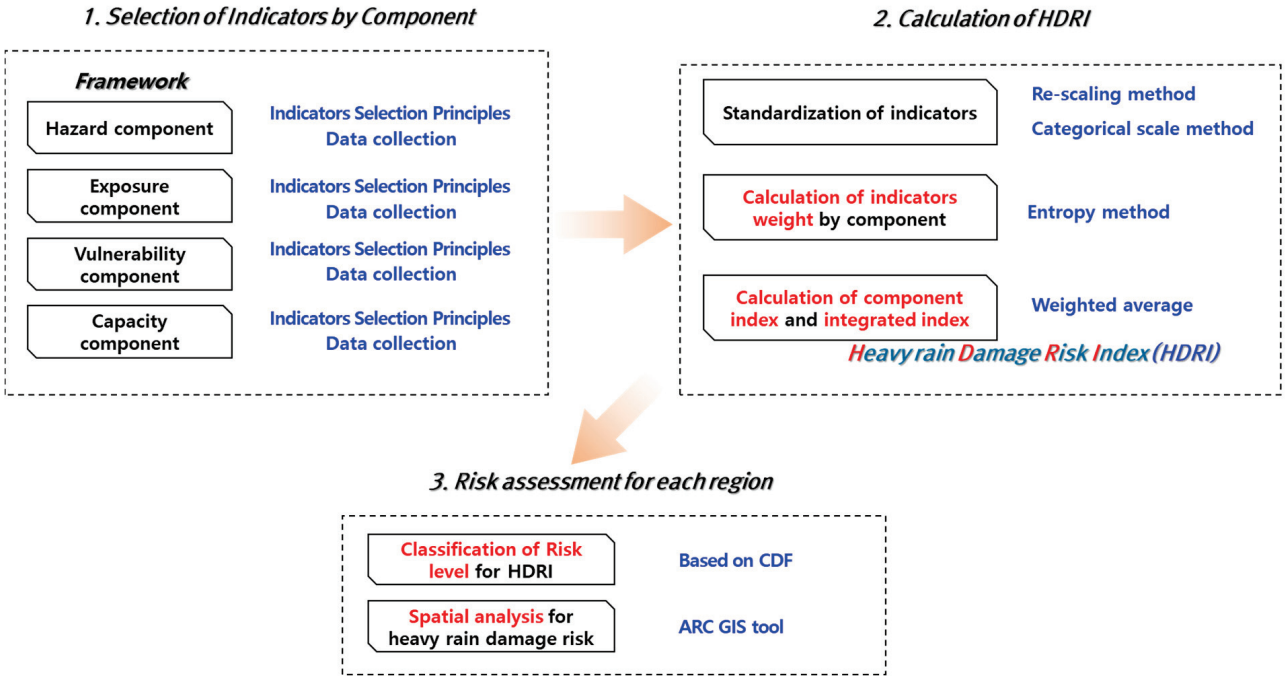

Figure 3. Procedure of heavy rain damage risk assessment.

The first step was to select and collect assessment indicators for the component. The component used the framework suggested by UNISDR, and consisted of hazard, exposure, vulnerability, and capacity. Assessment indicators were selected and collected according to the selection principle. In the second stage, assessment indicators were standardized and calculated for weight of each indicator. Then, the integrated index, defined as the heavy-rain-damage risk index (HDRI) was calculated. In the third step, risk levels were classified for HDRIs by region based on probability distributions. Heavy-rain-damage risk was then analyzed spatially using ARC GIS tool.

The sub-index was calculated corresponding to the indicators and it weight of each component. For example, the Hazard index was integrated through the indicators and weight of hazard component. If the calculations for the four sub-indices, Hazard index, Exposure index, Vulnerability index, and Capacity index were complete, they were integrated as the HDRI.

$$\text{Sub index (SI)} = \sum_{i=1}^{n} I_j \cdot w_j \quad (1)$$

$$\text{HDRI} = \sum_{i=1}^{n} SI_i \cdot w_i = HI \cdot w_H + EI \cdot w_E + VI \cdot w_V + CI \cdot w_C \quad (2)$$

where I_j is jth indicator of corresponding component, w_j is the jth indicator of corresponding component, HI is the Hazard index, w_H is the weight of Hazard index EI is the Exposure index, w_E is the weight of Exposure index, VI is the Vulnerability index, w_V is the weight of Vulnerability index, CI is the Capacity index, and w_C is the weight of the Capacity index.

2.2.1. Principle for Selecting Assessment Indicators

It was confirmed that several principles with similar meanings were repeated in previous studies for indicator selection. [19–21]. The most frequently used and important principles among these were extracted; those six principles are listed in Table 2. The major principles included were correlation, simplicity, quantitative, reliability, redundancy, and ease. The first principle, correlation, was to check whether the meaning of the components was similar; the second principle, simplicity, was to check whether the meanings of individual indicators were easy to understand; the third principle, quantitative, was to check whether an indicator could be quantified numerically; the fourth, validity, was to check whether the conceptual basis of the relevant indicator was clear; the fifth, redundancy, was to check whether there were indicators with overlapping meanings and, finally, ease was to check whether it was easy to continuously collect data.

Table 2. Six principles for selection of indicators [19–21].

Indicator Selection Principles	Abbreviations	Descriptions
Correlation	C	Examines whether the meanings of the components are similar
Simplicity	S	Examines whether the meanings of individual indicators are easy to understand
Quantitative	Q	Examines whether indicators can be quantified numerically
Validity	V	Examines whether the conceptual basis of the relevant indicator is clear
Redundancy	R	Examines whether any of the indicators have overlapping meanings
Ease	E	Examines whether it is easy to continuously collect data

2.2.2. Standardization Method for Assessment Indicators

When calculating an index using an indicator, it is necessary to perform standardization, calculation of weights, and aggregation, because the assessment indicators used to calculate the index are unit- and scale-dependent, thus making direct calculation impossible. Standardization is a method for resolving the issues of deviation and distortion caused by size and unit differences, by converting each evaluation index into a dimensionless value. Typically, rankings, Z-scores, categorical scales, and re-scaling are used as representative standardization methods; in this study, data were standardized using both method re-scaling and categorical scale methods. Generally, the re-scaling method is easy to understand, and the categorical scale method can be used to solve the problem of distortion in given datasets [22]. Table 3 describes the features of the two standardization methods used in this study.

Table 3. Features of standardization methods used in this study [22].

Methods	Equation	Description
Categorical scale	$I_i = \left\{ \begin{array}{c} 0.25, \quad if\ x_i \in \left\{ p^{25th} \right\} percentile \\ 0.5, \quad if\ x_i \in \left\{ p^{50th} - p^{25th} \right\} percentile \\ 0.75, \quad if\ x_i \in \left\{ p^{75th} - p^{50th} \right\} percentile \\ 1.00, \quad if\ \ x_i \in \left\{ p^{100th} - p^{75th} \right\} percentile \end{array} \right\}$	A method of classifying categories by quantile and assigning scores even if the range of specific indicator values is very wide.
	x_i means the value of the ith data, and scores are given according to the range to which the value belongs.	
Re-Scaling	$I_i = \frac{x_i - \min(x)}{\max(x) - \min(x)}$	A transformation method based on the range of indicators. Standardized values are included in the range of 0 to 1.
	x_i means the value of the ith data, and $\max(x)$ and $\min(x)$ represent the maximum and minimum values of the data, respectively.	

2.2.3. Method of Calculating Weights

Assessment indicators have varying degrees of impact depending on the purpose of analysis, and they should be given weights during the process of determining their significance and calculating them as an index. Typically, the analytical hierarchy process (AHP), factor analysis, the Delphi method, and the entropy method are used as weight determination techniques [23–26] This study used the entropy technique, which is a method for calculating objective weights and conducting experiments.

The following procedures were used to calculate the weight of each indicator using the aforementioned entropy method. First, the constructed values of each indicator are organized into a matrix by region, followed by the normalization of the configured attribute information of each indicator. Weight values between the indicators were finally determined after calculating the entropy for each attribute using normalized data. Equations (3)–(7) summarize this process [27].

First, a matrix of attribute information of regional assessment indicators is set up:

$$\mathrm{D} = \begin{bmatrix} x_{11} & \cdots & x_{1n} \\ \vdots & \ddots & \vdots \\ x_{m1} & \cdots & x_{mn} \end{bmatrix} \tag{3}$$

Second, attribute information is normalized using the assessment indicator:

$$p_{ij} = \frac{x_{ij}}{\sum_{i=1}^{m} x_{ij}} (i = 1, 2, \cdots m\ ;\ j = 1, 2, \cdots,\ n) \tag{4}$$

Third, the entropy for each attribute is calculated:

$$E_j = -k \sum_{i=1}^{m} p_{ij} \log p_{ij} \left(\text{Here, } k = \frac{1}{\log m}; j = 1, 2, \cdots, n \right) \tag{5}$$

Fourth, the weight of each assessment indicator was calculated by considering the degree of diversity.

$$\text{Degree of diversity}: \ d_j = 1 - E_j \tag{6}$$

$$\text{Weight}: \ w_j = \frac{d_j}{\sum_{j=1}^{n} d_j} (j = 1,\ 2,\ \cdots, n) \tag{7}$$

where, m is the number of regions, n is the number of indicators, i is the ith region, j is the jth indicator, p_{ij} is the ith and jth normalized assessment indicators, and E_j is the entropy of the jth assessment indicator.

2.3. Hierarchical Cluster Analysis

Cluster analysis is a typical statistical technique that can identify group objects with similar characteristics in given datasets. The two types of cluster analysis are hierarchical and non-hierarchical cluster analysis [28,29]. Hierarchical cluster analysis is a technique for deriving a target cluster by sequentially clustering subjects with a high degree of similarity and gradually combining clusters. Non-hierarchical clustering is a technique for clustering that involves specifying the number of clusters and the initial starting point based on the cluster center [30].

The advantage of hierarchical cluster analysis is that it can perform clustering in a way that the cluster forms a hierarchy without first specifying the number of clusters, after which it identifies the cluster's hierarchical structure using dendrograms [31]. The dendrogram expresses a cluster's hierarchical structure in the form of a tree, and within the hierarchical structure, the lower cluster takes on the form of the upper cluster (Figure 4). In this study, hierarchical cluster analysis was used to cluster groups that were sequentially or hierarchically similar to each other.

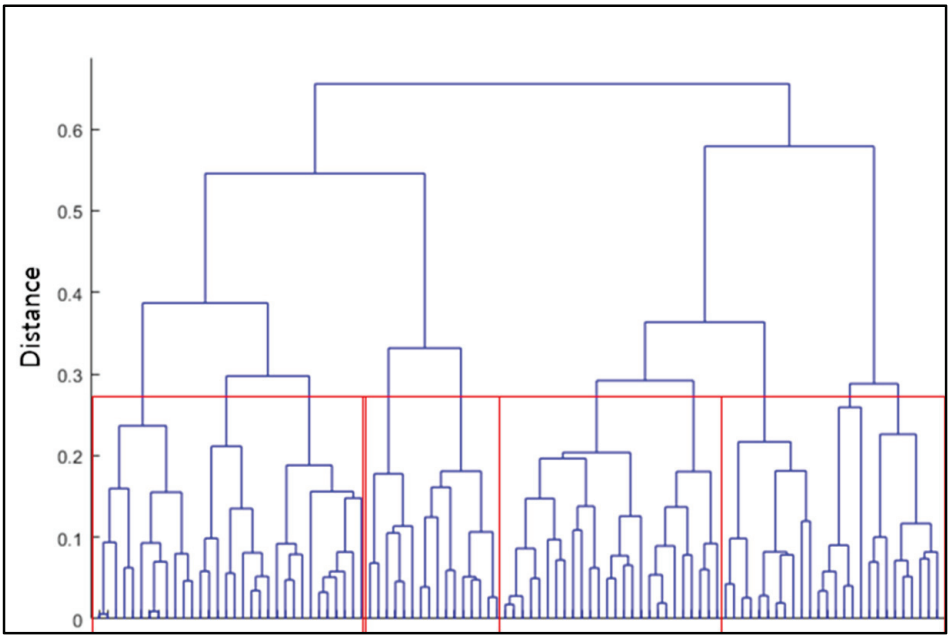

Figure 4. Conceptual diagram of dendrogram [31].

Here, the term "distance" should be used to refer to a metric of regional similarity. There are several methods of defining distance—Euclidean distance, which is the most frequently used, hamming distance, which is used when all variables are categorical, Manhattan distance, and cosine similarity. Since the normalized data was used in this study, the distance was calculated using the Euclidean distance. Equation (8) illustrates the Euclidean distance equation [32].

$$d_{ij} = \left[\sum_{k=1}^{p}\left(x_{ik} - x_{jk}\right)^2\right]^{1/2} \quad (8)$$

where i and j are two objects in p-dimensional space and d_{ij} represents the Euclidean distance, i.e., the shortest direct distance. p is the total number of variables and k is kth variable.

3. Result of Analysis

3.1. Risk Assessment of Heavy Rain Damage

3.1.1. Selection and Construction of Assessment Indicators

In this study, we investigated the assessment indicators and framework used in references [5–18]. The UNISDR framework (hazard, exposure, vulnerability, and capacity) was judged to be the most clearly distinguished among various frameworks and the assessment indicators used in previous studies were reconstructed into the UNISDR framework. The assessment indicators used in this study were chosen based on six selection principles (Table 2). The principles were correlation (C), simplicity (S), quantitative (Q), validity (V), redundancy (R), and ease (E). Table 4 shows the assessment indicators selected through indicator-selection principles.

Table 4. Selection of assessment indicators.

Framework	Components	Potential Assessment Indicators	Indicator Selection Principles						Final Selection
			C	S	Q	V	R	E	
Hazard	Meteorological	Probable rainfall	X	○	○	○	○	○	X
		Number of days of rainfall of 80 mm	○	X	○	○	X	○	X
		Maximum rainfall per day	○	○	○	○	X	○	X
		Maximum rainfall during the duration (24 h)	○	○	○	○	○	○	○ (H1)
		Annual average rainfall	○	○	○	○	○	○	○ (H2)
	Historical Damage	Flood damage	○	○	○	○	○	○	○ (H3)
		Scale of flood damage	○	○	○	○	X	○	X
		Frequency of flood damage	○	○	○	○	○	○	○ (H4)
		Flooded area	○	○	X	X	○	X	X
Exposure	Socio-economic	Total population	○	○	○	○	○	○	○ (E1)
		GRDP	○	○	○	○	○	○	○ (E2)
		Per capita income	○	○	○	○	X	○	X
		Average official land price	○	○	○	○	X	○	X
		Population density	○	○	○	○	X	X	X
	Physical	Number of buildings	○	○	○	○	○	○	○ (E3)
		Infrastructure (road)	○	○	○	○	○	○	○ (E4)
		Slope	X	○	○	○	X	○	X
		River density	○	○	○	○	○	○	○ (E5)
Vulnerability	Social	Vulnerable population	○	○	○	○	○	○	○ (V1)
		Poor population	○	○	○	○	X	X	X
		Infant mortality	○	○	○	○	X	X	X
		TV distribution rate	X	○	○	○	○	X	X
		Number of semi-basement households	○	○	○	○	○	X	X
		Population in flooded areas	○	○	X	X	○	X	X
		Number of households not supplied with electricity	X	○	○	○	X	X	X
	Physical	Area of the lowland area	○	X	○	X	X	X	X
		Runoff curve index	○	○	○	○	○	X	X
		Disaster-prone districts	○	○	○	○	○	○	○ (V2)
		Steep slope	○	○	○	○	○	○	○ (V3)
		Old buildings	○	○	○	○	○	○	○ (V4)

Table 4. *Cont.*

Framework	Components	Potential Assessment Indicators	Indicator Selection Principles						Final Selection
			C	S	Q	V	R	E	
Capacity	Disaster Prevention Capability	Number of disaster prevention facilities	○	○	○	○	○	X	X
		Preventive facilities	○	○	○	○	X	X	X
		Drainage pump station	○	○	○	○	○	○	○ (C1)
		Dam and reservoir	○	○	X	○	○	X	X
		River management personnel	X	○	X	○	○	X	X
		Financial independence	○	○	○	○	○	○	○ (C2)
	Disaster Prevention History	Cumulative disaster prevention budget	○	○	○	○	○	○	○ (C3)
		Promotion of preventive measures	○	○	X	○	X	X	X
		River embankment ratio	X	○	X	X	○	X	X

The hazard-component indicators selected were maximum rainfall during the duration (24 h) (H1), annual average rainfall (H2), flood damage (H3), and flood damage frequency (H4). The exposure component indicators were the total population (E1), the GRDP (gross regional domestic product) (E2), total number of buildings (E3), road facility area (E4), and river density (E5). The vulnerability component indicators were vulnerable populations (V1), disaster-prone districts (V2), steep slopes (V3), and old buildings (V4). Capacity indicators were drainage pump stations (C1), financial independence (C2), and cumulative disaster prevention budgets (C3). All assessment indicators chosen for this study were constructed as of 2019 and as cumulative or average concepts, depending on the nature of the data.

Meteorological data were obtained from the Korea Meteorological Administration (KMA), and damage data were obtained from the Statistical Yearbook of Natural Disaster (SYND) published by the Ministry of the Interior and Safety (MOIS). The total population, GRDP, total number of buildings, and financial independence were obtained from the Korean Statistical Information Service (KOSIS) and data on road area and river density were obtained from the Ministry of Environment (MOE). MOIS collected data on drainage pump stations and investment costs for the disaster prevention budget. In Table 4, a circle means the indicator was selected, and a cross means the indictor was not selected.

3.1.2. Standardization and Calculation of Weights of Assessment Indicators

Since it is advantageous for the visualization of integrated index, the re-scaling method was standardized and used, but the categorical scale method was also considered to minimize distortion caused by extreme values. Statistics of the assessment indicators for standardization are shown in Table 5.

As shown Table 5, the maximum values of H4, V3, and C1 were excessively large in comparison to the average value, and thus, 80% of data did not exceed 0.1. The data mentioned above (H4, V3, and C1) signified that the probability distribution was skewed to the left and the tail was generated far to the right, which means that some data among the total are extreme values. If there is standardization without using the categorical scale method, significant data distortion problems can be caused. To this end, the integrated index was also calculated considering the categorical scale, and the score for each percentile is shown in Table 6.

Table 5. Elementary statistics for assessment indicators.

Assessment Indicators	Re-Scaling		The Percentage of Standardized Value			
	Min	**Max**	**20%**	**40%**	**60%**	**80%**
H1	833.18	1443.75	0.2245	0.3503	0.4490	0.5518
H2	96.43	200.625	0.2906	0.3778	0.4889	0.6391
H3	0	156	0.2321	0.3654	0.4679	0.5923
H4	0	635,553,387	0.0024	0.0065	0.0161	0.0407
E1	16,993	1,194,465	0.0245	0.0709	0.1753	0.3181
E2	431,322	60,407,392	0.0171	0.0446	0.0853	0.1725
E3	2257	180,936	0.1184	0.1718	0.2508	0.3608
E4	0.000421	0.281286	0.0233	0.0346	0.0712	0.1614
E5	0	0.209904	0.0444	0.0712	0.1098	0.1740
V1	7382	258,384	0.0491	0.1038	0.2135	0.3627
V2	0	20	0.0250	0.0500	0.1500	0.3000
V3	0	71.76	0.0002	0.0025	0.0224	0.1015
V4	337	67,767	0.1235	0.1843	0.2463	0.3156
C1	0	283,740	0.0008	0.0016	0.0081	0.0250
C2	0	453,722.3	0.0176	0.0352	0.0851	0.1341
C3	8.5	69.2	0.1081	0.1951	0.2965	0.4870

Table 6. Percentile and score for standardized value.

Percentile	Score	Percentile	Score
$0\% \leq x_i < 20\%$	0.2	$60\% \leq x_i < 80\%$	0.8
$20\% \leq x_i < 40\%$	0.4	$80\% \leq x_i < 100\%$	1.0
$40\% \leq x_i < 60\%$	0.6	-	-

Table 7 summarizes the weights of the assessment indicators and the sub-index. Here, the sub-index means that it is integrated by the indicators of each framework. As shown in Table 7, the Hazard index places a large weight on H4 (accumulated amount of heavy rain damage), showing that previous damage is critical for determining the current risk of heavy rain damage. The Exposure index is distributed more evenly than the hazard, index and the density of river has the most weight. The steep slopes of the Vulnerability index (V3) show that it has the highest weight, whereas the number of disaster-prone districts (V2) has the second-highest weight. In terms of capacity, the drainage pump station's treatment capacity (C1) had the highest weight. As for the weights of the sub-index, the Hazard index had the highest weight for each sub-index and the Capacity index has the second-highest weight.

3.1.3. Definition of the Risk Level of Heavy Rain Damage by Region

Each sub-index was calculated using the weight and assessment indicators corresponding to each component (see Equation (1)). Figure 5 illustrates the spatial distribution map of each sub-index. The Hazard index, Exposure index, and Vulnerability index have positive (+) values which show an increased risk of heavy rain damage, while the Capacity index has a negative $(-)$ value which indicates a decreased risk of heavy rain damage. According to the Hazard index, the frequency of damage was high in GG and the scale of damage was large in GW and JB. It was confirmed that rainfall occurrence characteristics were concentrated in the central and southern coastal regions, and as a result, GW, GG,

JB, and GN have a high Hazard index. The Exposure index consists of indicators that are susceptible to damage from heavy rain, and the more developed a region is, the greater the risk of flooding. Indicators such as population, GRDP, and road density were found to be higher in urban areas such as SO, BS, IC, DG, and GJ. Thus, the Exposure index seemed to be higher in urban areas.

Table 7. Weights of the assessment indicators and sub-index.

Framework	Assessment Indicators	Indicators Weight	Sub-Index Weight
Hazard	H1	0.0043	0.3198
	H2	0.0075	
	H3	0.0867	
	H4	0.9014	
Exposure	E1	0.139	0.1978
	E2	0.1861	
	E3	0.0613	
	E4	0.189	
	E5	0.4245	
Vulnerability	V1	0.123	0.186
	V2	0.2937	
	V3	0.518	
	V4	0.0654	
Capacity	C1	0.7646	0.2963
	C2	0.1983	
	C3	0.0371	

The Vulnerability index was highest in GW, GB, JB, and JN, which are predominantly composed of disaster-prone districts and steep slopes. As shown in the elevation map (Figure 4), there are many areas that are vulnerable to damage from heavy rain distributed along the mountain ranges. In addition, these areas have a high risk of landslide damage. The Capacity index refers to areas with a high density of disaster-prevention facilities, and this index was particularly high in JN, GN, and CN.

The heavy-rain-damage risk index (HDRI) was integrated through Equation (2) using sub-index and weight. Figure 6a shows the probability distribution of HDRI. Since HDRI followed a normal distribution, it was possible to classify the probability values into evenly intervals. This means that some regions have similar probability values and therefore, similar risk levels. The cumulative probability of the HDRI is shown in Figure 6b, and the probability boundaries between Levels 1 and 4 was defined as 0%, 25%, 75%, and 100%. As such, areas at low risk of heavy-rain damage were classified as Level 1, whereas those at high risk were classified as Level 4.

The assessment indicators for flood risk were selected based on the principle, these were weighted averaged and integrated as the HDRI. The heavy-rain-damage risk level was classified based on the probability distribution of the HDRI. Figure 7 illustrates the spatial distribution map of the risk level by region. According to the results of the regional heavy-rain-damage risk assessment presented in Figure 7, the risks were greatest in GD, GG, and JB, while SO, IC, DG, CN, and JD were considered relatively safe.

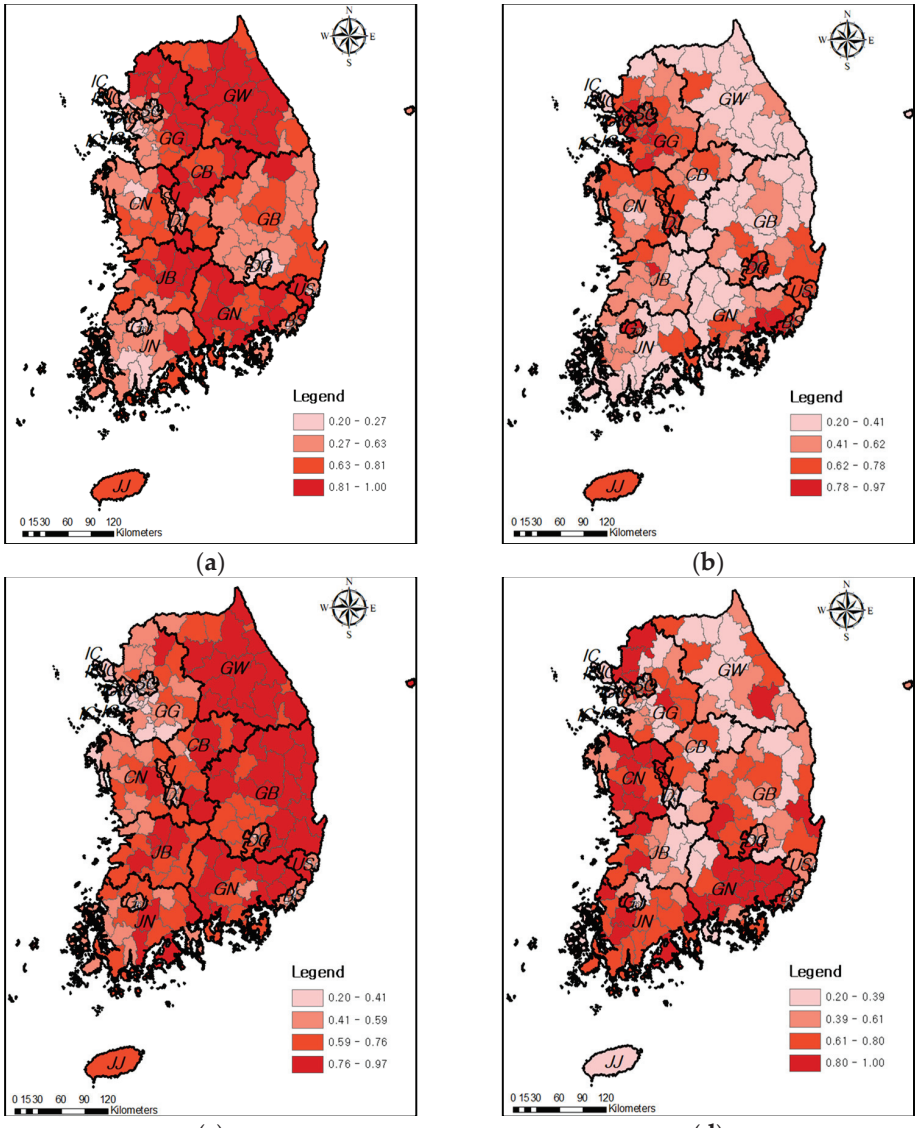

Figure 5. Normalized spatial distribution of each sub–index. (**a**) Hazard index, (**b**) Exposure index, (**c**) Vulnerability index, and (**d**) Capacity index.

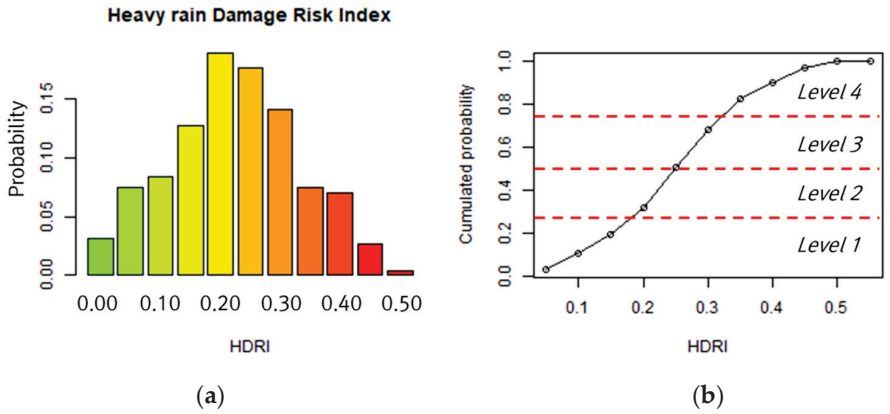

Figure 6. Classification of risk level based on probability distribution. (**a**) PDF of HDRI and (**b**) classification of risk level using CDF.

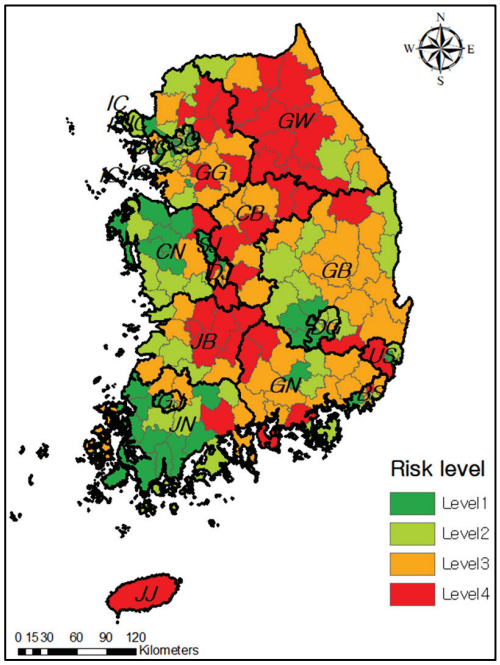

Figure 7. Result of risk assessment.

3.2. Classification of Heavy Rain Damage Types Based on Hierarchical Cluster Analysis

The magnitude of damage that occurs each year in South Korea is aggregated and recorded for a total of 23 facilities: 13 public and 10 private facilities. The study collected data on heavy rain damage from 2003–2019 and analyzed the ratio of major damaged facilities.

As can be seen in Figure 8, more than 30% of damage occurred in streams, 17% in water resource infrastructure, 13% on roads, and 8.9% in erosion-control infrastructure. Furthermore, 5% damage is incurred by arable land, 4% by buildings, and 2% by military facilities; facilities that accounted for less than 1% of damage were not indicated. The primary facilities in South Korea that sustain damage from heavy rains are streams, water resource facilities, roads, erosion control projects, arable land, buildings, and military facilities. In order to identify the type of damage by region according to topographical characteristics, we performed a hierarchical cluster analysis using the regional damage ratios for the seven facilities as variables. As shown Figure 9, damage types were divided into five clusters.

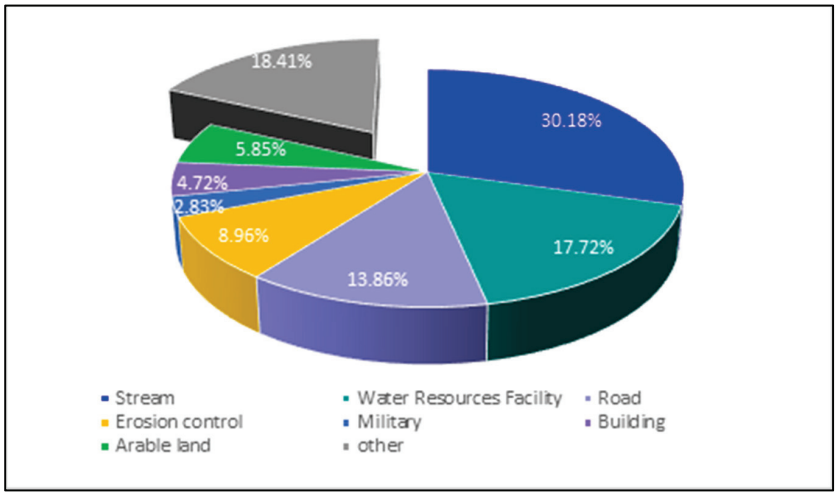

Figure 8. Distribution of facilities affected by heavy rain damage from 2003–2019 in South Korea.

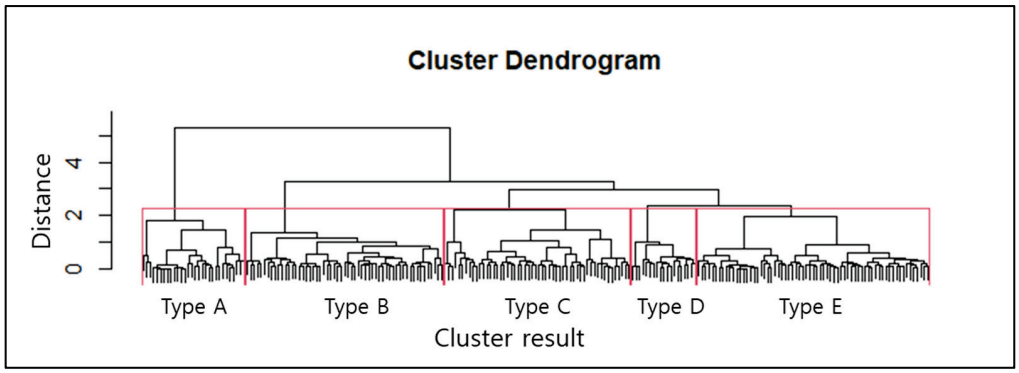

Figure 9. Hierarchical cluster analysis result based on dendrogram.

Based on the findings in Figure 10, the Type A area was identified as the location of the most damage in "erosion control" and "road", and the Type B area had the highest damage ratio in "stream facility" and "road". In addition, the Type C area had a high damage ratio in arable land, Type D area was identified as just "stream facility". Type E area had a high damage ratio for "building". These findings indicate that topographical characteristics and the level of regional development have a significant impact on different types of damage from heavy rainfall.

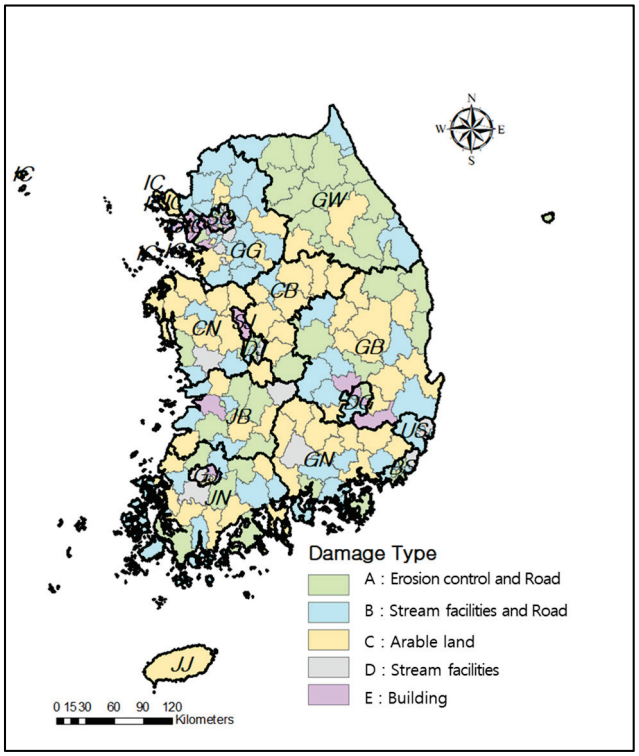

Figure 10. Regional classification of damage type from the analysis.

Considering the damage-type map and topographical characteristics together, Type A was mainly found in mountainous regions of GW, JB, and JN, indicating that the damage in "erosion control" and "road" due to landslides was severe. Damage occurs frequently in the local river in the GG area near the Han River in the case of Type B. Type C was confirmed to be primarily distributed in CN, CB, GN, and GB areas where arable land is located. Type D was confirmed in the GJ and GG areas where damage occurred in "stream facility". Type E was primarily found in city-oriented SO, IC, and DG areas.

Type A affects erosion control facilities and roads due to landslides, and thus, in Type A areas, prevention projects such as erosion facility maintenance and repair projects and road drainage maintenance projects to reduce landslides should be implemented. Type B is a case of damage caused to levee facilities by river inundation, and to road facilities by poor road drainage; thus, a river improvement project that can lower water depth and a road drainage maintenance project that can well release water into drainage should be implemented.

Because Type C can occur due to poor drainage in arable land, prevention projects such as sewer-pipes maintenance projects should be implemented. Type D was a case of damage caused to a stream facility by rapid water velocity and river inundation, and prevention projects such as a river improvement project that can lower the flow velocity and water depth could be implemented. Type E mainly occurred due to inundation of urban area by lowlands areas; thus, prevention projects such as drainage-pump projects that can release the flooded water in lowlands into rivers could be implemented.

3.3. Analysis for Heavy Rain Damage Risk and Damage Type in Each Region

To comprehend the characteristics of heavy rain damage by region, risk level, and damage types classified in the previous section, the two results are evaluated in this section. As shown Figure 11, the risk level is represented by a fill color, and the damage type is represented by an outline color. From the results of this study, GW, JB, CB, and GG areas were identified as having high risk levels. For damage type in these areas, GW and JB were shown to be Type A and C, the GG area was Type B and C, and the CB area was Type C. Considering the causes of damage in these areas, when damage occurs in GW and JB, the scale of damage can be large and caused by landslides, and as the stream density in the GG area is high, damage can be occur frequently. In the CB area, damage are occurred mainly in arable land due to poor drainage by steep slopes. The GB and GN areas are the representative areas shown to be in risk level 3, and the damage type for this area is C.

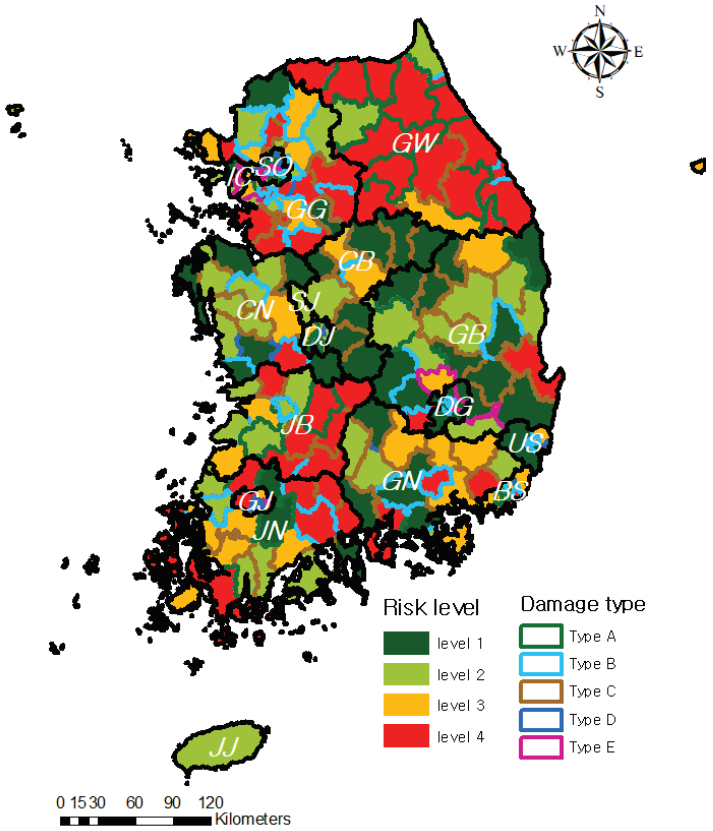

Figure 11. Regional risk level and heavy rain damage types from the analysis.

In addition, urban area such as IC, SO, BS, and GJ were presented Type E and low risk level; west coast area such as JN, CN, and IC also were presented a low risk level. However, even if the risk levels are comparable, the damage type and cause can be different according to the topographic characteristics. Thus, in order to determine the priority and type of appropriate prevention projects, it is necessary to consider the risk level and damage type each region.

4. Discussions and Conclusions

In this study, a method which can identify the types and priorities of disaster prevention projects by considering various regional characteristics was proposed. First, potential assessment indicators for risk assessment were gathered by reviewing previous research cases, and assessment indicators relevant to this study were chosen based on principle for indicator selection. Following that, an integrated index and the risk level were calculated and four grades were identified. Damage types by region were classified into five types using hierarchical cluster analysis and the facility's history of damage in the corresponding region. Finally, the two results were combined to examine the characteristics of heavy-rain damage in each region, and appropriate types and priorities of disaster prevention projects were proposed based on these findings.

The results of the risk-level analysis revealed that the risk level was relatively high in cities such as GW, JB, GG, CB, and JJ, where heavy rain damage occurs frequently or is severe, and relatively low in cities such as JN, CN, IC, and SE. The frequency of damage was found to be low in GW and JB, but the scale was very large; while, the scale was small, but it occurred very frequently in GG. According to the damage type analysis, Type A which mainly consists of landslide damage was primarily found in GW and JB, whereas Type B is river inundation damage and was found in GG. Furthermore, Type C is agricultural land damage which was prevalent in CB, and Type D is stream facility damage by rapid water velocity and was found in GJ, GG. Type E is building damage, which was prevalent in urban areas such as SO, IC, and DG. When analyzing regional characteristics by linking risk level and damage type, there were few cases of damage due to landslides in GW and JB, but most of the damage was significant. Damage occurred primarily in river facilities in GG, and most of the damage was minor, but it occurred frequently. Finally, considering the most dangerous areas in relation to the risk level and damage type, GW and JB areas were identified as requiring an erosion facility maintenance and repair project and a sewer pipes maintenance project; a river improvement project was suggested for the GG area. Furthermore, in CB and JJ, a sewer-pipe maintenance project should ideally be implemented.

We were able to identify the flood cause and to propose the prevention project for each region by analyzing the major damage types that were not considered in previous risk-assessment studies and with risk level. However, since this study is the result of analysis at the national level, it was impossible to identify the specific location at district level where each prevention project was necessary. Therefore, in future research, it will be necessary to derive the specific location via quantitative risk assessment for high-risk areas that were identified in the results of this study.

In this study, a strategy for determining the risk level and type of damage South Korea's entire region was proposed. When developing various types of disaster-prevention project plans from a macroscopic perspective, it is believed that identifying the types of projects and prioritizing them can be of great help in reducing the national budget in terms of time and cost. Therefore, the findings of this study are expected to be used as a method of identifying damage characteristics by region when developing a plan for disaster prevention projects.

Author Contributions: Conceptualization, J.K. and H.S.K.; formal analysis, J.K.; methodology, D.K. and M.L.; supervision, H.S.K. and H.H.; writing—original draft, J.K.; writing—review and editing, J.K. and H.H. All authors have read and agreed to the published version of the manuscript.

Funding: INHA UNIVERSITY Research Grant.

Institutional Review Board Statement: Not applicable.

Informed Consent Statement: Not applicable.

Data Availability Statement: Not applicable.

Acknowledgments: This work was supported by INHA UNIVERSITY Research Grant.

Conflicts of Interest: The authors declare no conflict of interest.

References

1. UNDP. Sendai Framework for Disaster Risk Reduction (2015–2030). Available online: https://www.undrr.org/publication/sendai-framework-disaster-risk-reduction-2015-2030 (accessed on 18 March 2021).
2. Ministry of the Interior and Safety (MOIS). *The Statistical Yearbook of Natural Disaster*; MOIS: Korea, Sejong, 2019.
3. Ţîncu, R.; Zêzere, J.L.; Crăciun, I.; Lazăr, G.; Lazăr, I. Quantitative micro-scale flood risk assessment in a section of the Trotuș River, Romania. *Land Use Policy* **2020**, *95*, 103881. [CrossRef]
4. Di Mauro, M.; De Bruijn, K.M.; Meloni, M. Quantitative methods for estimating flood fatalities: Towards the introduction of loss-of-life estimation in the assessment of flood risk. *Nat. Hazards* **2012**, *63*, 1083–1113. [CrossRef]
5. Zhang, J.; Okada, N.; Tatano, H.; Hayakawa, S. Risk Assessment and Zoning of Flood Damage Caused by Heavy Rainfall in Yamaguchi Prefecture, Japan. *Flood Def.* **2002**, *2002*, 162–169.
6. Fekete, A. Validation of a social Vulnerability index in context to river-floods in Germany. *Nat. Hazards Earth Syst. Sci.* **2009**, *9*, 393–403. [CrossRef]
7. Shivaprasad Sharma, S.V.; Parth Sarathi, R.; Chakravarthi, V.; Srinivasa Rao, G. Flood risk assessment using multi-criteria analysis: A case study from Kopili River Basin, Assam, India. *Geomat. Nat. Hazards Risk* **2017**, *9*, 79–93. [CrossRef]
8. Amira, R.F.; Surjandari, I.; Laoh, E. Jakarta Flood Risk Mapping Using Index-based Approach and Spatial Analysis. In Proceedings of the 2020 International Conference on ICT for Smart Society (ICISS), Bandung, Indonesia, 19–20 November 2020. [CrossRef]
9. Lim, K.S.; Choi, S.J.; Lee, D.R.; Moon, J.W. Development of Flood Risk Index using causal relationships of Flood Indicators. *J. Korean Soc. Civ. Eng.* **2010**, *30*, 61–70.
10. OECD. *OECD Environmental Indicators 2001—Towards Sustainable Development*; OECD: Paris, France, 2001. [CrossRef]
11. Mustika Anindita, R.; Susilowati, I.; Muhammad, F. Flood risk spatial index analysis in the coastal Pekalongan, Central Java, Indonesia. In *E3S Web of Conferences*; EDP Sciences: Les Ulis City, France, 2020; Volume 202, p. 06028.
12. IPCC. *Climate Change 2007: The Physical Science Basis, Contribution of Working Group I to the Fourth Assessment Report of the Intergovernmental Panel on Climate Change*; IPCC: Switzerland, Geneva, 2007.
13. Korea Institute of Civil Engineering and Building Technology. *Construction of Calculation Process and Advancement for Flood Damage Risk Index to Assess Qualitative Risk*; KICT: Ilsan, Korea, 2020.
14. 2009 UNISDR Terminology on Disaster Risk Reduction. Available online: https://www.undrr.org/publication/2009-unisdr-terminology-disaster-risk-reduction (accessed on 18 March 2021).
15. Rygel, L.; O'Sullivan, D.; Yarnal, B. A method for constructing a social Vulnerability index: An Application to Hurricane Storm Surges in a Developed Country. *Mitig. Adapt. Strateg. Glob. Change* **2006**, *11*, 741–764. [CrossRef]
16. Joo, H.; Choi, C.; Kim, J.; Kim, D.; Kim, S.; Kim, H.S. A Bayesian network-based integrated for flood risk assessment (InFRA). *Sustainability* **2019**, *11*, 3733. [CrossRef]
17. Kim, J.S.; Choi, C.H.; Lee, J.S.; Kim, H.S. Damage prediction using heavy rain risk assessment:(1) Estimation of heavy rain damage risk index. *J. Korean Soc. Hazard Mitig.* **2017**, *17*, 361–370. [CrossRef]
18. Birkmann, J. Measuring vulnerability to promote disaster-resilient societies: Conceptual frameworks and definitions. *Meas. Vulnerability Nat. Hazards Disaster Resilient Soc.* **2006**, *1*, 9–54.
19. Choi, H.C.; Sirakaya, E. Sustainability indicators for managing community tourism. *Tour. Manag.* **2006**, *27*, 1274–1289. [CrossRef]
20. Berry, D. *Sustainable Development in the United States: An Experimental Set of Indicators*; Interim Report; US Interagency Working Group on Sustainable Development Indicators: Washington, DC, USA, 1997.
21. Bundesregierung, D. Perspektiven fur Deutschland. *Unsere Strategie fur Eine Nachhaltige Entwicklung*. 2002. Available online: https://www.nachhaltigkeit.info/media/1326188329phpYJ8KrU (accessed on 10 May 2021).
22. Nardo, M.; Saisana, M.; Saltelli, A.; Tarantola, S. Tools for composite indicators building. *Eur. Com. Ispra* **2005**, *15*, 19–20.
23. Forman, E.H.; Gass, S.I. The analytic hierarchy processan exposition. *Oper. Res.* **2001**, *49*, 469–486. [CrossRef]
24. MacCallum, R. A comparison of factor analysis programs in SPSS, BMDP, and SAS. *Psychometrika* **1983**, *48*, 223–231. [CrossRef]
25. Dalkey, N.; Helmer, O. An experimental application of the Delphi method to the use of experts. *Manag. Sci.* **1963**, *9*, 458–467. [CrossRef]
26. Ozkul, S.; Harmancioglu, N.B.; Singh, V.P. Entropy-based assessment of water quality monitoring networks. *J. Hydrol. Eng.* **2000**, *5*, 90–100. [CrossRef]
27. Joo, H.; Kim, S.; Lee, M.; Kim, H. A study on determination of investment priority of flood control considering flood vulnerability. *J. Korean Soc. Hazard Mitig.* **2018**, *18*, 417–429. [CrossRef]

28. Kyoung, M.S.; Kim, S.D.; Kim, B.K.; Kim, H.S. Construction of hydrological drought severity-area-duration curves using cluster analysis. *J. Korean Soc. Civ. Eng.* **2007**, *27*, 267–276.
29. Han, S.M.; Hwang, G.S.; Choe, S.Y.; Park, J.W. A study on classifying algorithm of disaster recovery resources using statistical method. *J. Korean Soc. Hazard Mitig.* **2014**, *14*, 49–58. [CrossRef]
30. Nam, W.H.; Kim, T.; Hong, E.M.; Hayes, M.J.; Svoboda, M.D. Water supply risk assessment of agricultural reservoirs using irrigation vulnerability model and cluster analysis. *J. Korean Soc. Agric. Eng.* **2015**, *57*, 59–67.
31. Pham, D.T.; Afify, A.A. Engineering applications of clustering techniques. In *Intelligent Production Machines and Systems, ScienceDirect*; Elsevier: Amsterdam, The Netherlands, 2006; pp. 326–331. [CrossRef]
32. Son, Y.; Chung, M. Digital Forensics for Android Location Information using Hierarchical Clustering. *J. Inst. Electron. Inf. Eng.* **2014**, *51*, 143–151. [CrossRef]

remote sensing

MDPI

Article

Geo-Environment Vulnerability Assessment of Multiple Geohazards Using VWT-AHP: A Case Study of the Pearl River Delta, China

Peng Huang, Xiaoyu Wu, Chuanming Ma * and Aiguo Zhou

School of Environmental Studies, China University of Geosciences, Wuhan 430000, China
* Correspondence: machuanming@cug.edu.cn; Tel.: +86-027-6788-3159

Abstract: Geohazards pose significant risks to communities and infrastructure, emphasizing the need for accurate susceptibility assessments to guide land-use planning and hazard management. This study presents a comprehensive method that combines Variable Weight Theory (VWT) with Analytic Hierarchy Process (AHP) to assess geo-environment vulnerability based on susceptibility to various geohazards. The method was applied to the Pearl River Delta in China, resulting in the classification of areas into high vulnerability (5961.85 km^2), medium vulnerability (19,227.93 km^2), low vulnerability (14,892.02 km^2), and stable areas (1616.19 km^2). The findings demonstrate improved accuracy and reliability compared to using AHP alone. ROC curve analysis confirms the enhanced performance of the integrated method, highlighting its effectiveness in discerning susceptibility levels and making informed decisions in hazard preparedness and risk reduction. Additionally, this study assessed the risks posed by geohazards to critical infrastructures, roads, and artificial surfaces, while discussing prevention strategies. However, this study acknowledges certain limitations, including the subjective determination of its judgment matrix and data constraints. Future research could explore the integration of alternative methods to enhance the objectivity of factor weighting. In practical applications, this study contributes to the understanding of geo-environment vulnerability assessments, providing insight into the intricate interplay among geological processes, human activities, and disaster resilience.

Keywords: geo-environment vulnerability; geohazard susceptibility; VWT-AHP; Pearl River Delta

Citation: Huang, P.; Wu, X.; Ma, C.; Zhou, A. Geo-Environment Vulnerability Assessment of Multiple Geohazards Using VWT-AHP: A Case Study of the Pearl River Delta, China. *Remote Sens.* **2023**, *15*, 5007. https://doi.org/10.3390/rs15205007

Academic Editors: Francesca Cigna, Stefano Morelli, Veronica Pazzi and Mirko Francioni

Received: 15 September 2023
Revised: 15 October 2023
Accepted: 16 October 2023
Published: 18 October 2023

1. Introduction

Geohazards encompass a range of geological processes occurring on the Earth's surface influenced by interactions among the atmosphere, hydrosphere, and biosphere [1]. Geohazards, notably landslides and debris flows, have caused significant human casualties and property losses, reaching billions of dollars [2,3]. Improving geohazard risk management is a crucial global effort aimed at mitigating the consequences of geohazards [4]. Geo-environment vulnerability assessment is an effective tool for enhancing disaster management. It can assess susceptibility to various geohazards, offering proactive strategies for disaster reduction. Consequently, it can contribute significantly to promoting symbiosis and sustainable development between humanity and the natural environment.

Vulnerability stands as a metric extensively harnessed in the fields of climate change, resource environments, and ecosystems [5–11]. Due to variations in research subjects and disciplinary perspectives, the definition of vulnerability can vary significantly among disciplines [12]. Initially introduced by Margat (1968) [13] in a study on groundwater pollution susceptibility, vulnerability is defined as the ability of groundwater to resist contamination based on hydrogeological conditions. Timmerman (1981) [14] defined vulnerability from the perspective of climate change as the degree to which a system responds unfavorably when subjected to damage. Smit et al. (1999) [15], at the scale of global change, described vulnerability as the extent to which a system is susceptible to harm or injury.

Research in the field of geo-environment vulnerability remains limited, leading to a lack of a universal definition for geo-environment vulnerability. In this study, geo-environment vulnerability is considered the capacity of a geo-environmental system to autonomously regulate and reinstate its structure and functionality amid external disruptions [16]. The magnitude of geo-environment vulnerability depends on the components and configuration of the system, intertwined with the nature and intensity of external perturbations. When the intensity of external disturbances surpasses the system's self-regulatory capacities, latent geo-environment vulnerability transforms into geo-environmental issues or geohazards [17]. Consequently, the susceptibility status of geohazards can characterize geo-environment vulnerability [17]. The impact and duration of geohazards vary, occurring in isolation or conjunction. Thus, conducting vulnerability assessments based on a range of geohazards is essential, rather than relying on the susceptibility to a single type of geohazard [18,19].

Advancements in remote sensing (RS) technology and geographic information systems (GIS) have contributed to the maturity of geo-environment vulnerability assessment techniques. Ma et al. (2019) [17] assessed the geo-environment vulnerability of Beihai, China, based on the susceptibility to landslides, collapses, and sea water intrusion. Ma et al. (2020) [20] assessed the geo-environmental risk in Zhengzhou, China, considering regional crustal stability and 11 types of geohazards and progressive geo-environmental issues. Chang et al. (2022) [21] researched the susceptibility of landslides, collapses, ground subsidence, and debris flows, proposing a multi-hazard vulnerability assessment method. Li et al. (2023) [22] developed an assessment framework for the ecological geo-environment vulnerability of arid and semi-arid cities, focusing on land desertification, soil erosion, and landslides. While these studies have made progress, there is currently no unified quantitative scoring standard, and research on geo-environment vulnerability assessment in large urban clusters is limited [23]. These limitations hinder the ability to balance socio-economic development and effective decision-making for geohazard prevention and control.

Multiple methods exist for assessing susceptibility to geohazards, classified into the following four primary categories: process-based modeling methods, statistical methods, machine learning methods, and knowledge-driven methods [24]. Process-based modeling methods simulate the occurrence processes of geohazards, grounded in physical or mathematical principles and capable of delivering precise susceptibility predictions [25]. However, their applicability to regional-scale studies is limited due to the substantial requirements of detailed field data and extensive computational simulations [26]. Statistical methods, such as Frequency Ratio (FR) [27], Logistic Regression (LR) [28], and Weight of Evidence (WoE) [29], rely on extensive data and statistical analysis, with result accuracy closely associated with statistical assumptions [26]. Machine learning methods, such as Support Vector Machine (SVM) [30], Random Forest (RF) [31], and Artificial Neural Network (ANN) [32], manage multidimensional data and complex linear relationships but may face challenges related to interpretability and data quality [26,33]. Knowledge-driven methods are flexible approaches relying on the judgment of decision-makers or experts based on their knowledge and experience, offering high decision-making efficiency and effectiveness [34]. These methods are adaptable to various spatial and temporal scales and suitable for a wide range of applications. They are particularly valuable when data is limited or unavailable, allowing for assessments even in data-scarce scenarios [35].

Multi-Criteria Decision Analysis (MCDA) is a fundamental knowledge-driven method, recognized as an essential tool for environmental decision-making, enabling the visualization and resolution of competitive decision problems [36–39]. By integrating qualitative and quantitative criteria, MCDA has become a cornerstone in integrated problem-solving solutions [40]. Among the suite of MCDA techniques, the Analytic Hierarchy Process (AHP) emerges as a fitting choice for grappling with intricate issues [41]. AHP is a framework that ascertains the relative significance of factors through pairwise comparisons and expert assessments, harmonizing subjective and objective criteria [42,43]. This method deconstructs complex problems into distinct factors, systematically arranging them in a

hierarchical manner according to their interrelationships, yielding a multi-level analytical structural model [44].

While AHP furnishes unchanging factor weights across varying conditions, the values of these factors exhibit diversity amidst different circumstances. Consequently, AHP falls short in capturing the dynamic fluctuations of factor weights within distinct contexts [45]. The core concept of the Variable Weight Theory (VWT) involves introducing a state-variable weight vector while retaining the stability of factor weights. This theoretical framework comprises three distinctive modes: penalization-based, incentive-based, and a hybrid form combining both penalization and incentive elements [46]. This method guarantees the flexibility of weight adjustments in alignment with varying factor values and specific contextual circumstances, thereby presenting an effective resolution to these complexities [47].

China is significantly impacted by global geohazards, evident from the mounting intensity and frequency of such incidents [48]. In recent times, driven by rapid socio-economic growth and urbanization, the Pearl River Delta, as one of the largest urban clusters in China, has experienced an expansion in geological environmental development and utilization. Characterized by intricate tectonics, extensive karst landscapes, and widespread Quaternary deposits, the area faces natural catastrophes including landslides, collapses, and debris flows, resulting in substantial economic losses [49–52]. Data from the Guangdong Province Disaster Prevention and Reduction Yearbook [53] show that between 1994 and 2009, geohazards caused 276 fatalities, 534 injuries, and economic losses totaling 256.48 million US dollars. Research on the geo-environment vulnerability in the Pearl River Delta primarily focuses on two aspects: geological environmental status assessments and single geohazard susceptibility assessments. Zeng and Liu (2015) [54] conducted an investigation into key geo-environmental issues in the Pearl River Delta, including ground subsidence, sea water intrusion, and waste pollution. The study identified rising sea levels, human activities, and extreme weather events as the primary triggering factors for geohazards. In a separate study, Zhang et al. (2019) [55] employed the AHP method to assess landslide susceptibility. Dou et al. (2008) [56] introduced an innovative automated detection method for karst collapse based on image analysis. Liu et al. (2023) [57] conducted ground subsidence modeling and assessment using remote sensing imagery and geological data. Furthermore, Lin et al. (2019) [58] employed an integrated Bayesian model for modeling sea water intrusion. Presently, there exists a notable dearth of comprehensive assessments regarding geological environmental vulnerability. Given the presence of geohazards, such as landslides, debris flows, ground subsidence, and karst collapses, the assessment of geo-environment vulnerability based on susceptibility to multiple geohazards is crucial for effective prevention and mitigation, ensuring human safety and protecting valuable assets.

Using the AHP method, this study partitioned geo-environment vulnerability into discrete dimensions: landslide and collapse susceptibility, debris flow susceptibility, karst collapse susceptibility, ground subsidence susceptibility, soil erosion susceptibility, and sea water intrusion susceptibility. Comprehensive assessment indicators and classification criteria were delineated for each dimension. Judgment matrices were formulated to establish constant weights of individual indicators. Moreover, a "penalization-incentive" variant of the VWT was adeptly utilized to dynamically adjust the weights of these indicators. By assessing the susceptibility to distinct geohazards, the methodology subsequently defined distinct zones of geo-environment vulnerability. Based on the assessment results and in conjunction with the distribution of land use/land cover (LULC), road, and critical infrastructure, the impact of geohazard susceptibility and geo-environment vulnerability on urban development was discussed. The specific research objectives are as follows:

1. Propose a multi-hazard geological disaster susceptibility assessment system using the VWT-AHP method.
2. Analyze the geo-environment vulnerability in the Pearl River Delta.
3. Provide recommendations for LULC, road, and critical infrastructure planning.

The implications of the findings from this assessment hold substantial pertinence for local governing bodies, providing invaluable insights for the formulation of land use planning and strategies for industrial development.

2. Study Area

Situated in the central-southern expanse of Guangdong Province, China, the Pearl River Delta shares its borders with the South China Sea. Geographically, it spans longitudinally from approximately 112°0′E to 115°24′E and latitudinally from 21°43′N to 23°56′N, encompassing a land area of 41,698 km^2. The region's topography features a central lowland and elevations that ascend in the northwest and east (Figure 1b). A dominant landform is the alluvial plain, with low mountains, hills, and tablelands distributed across the western, northern, and eastern sectors (Figure 1a). The region's hydrology is extensive, characterized by river systems such as the Xi River and Dong River, which emanate from mountainous terrains and discharge into the South China Sea. The climatic conditions prevailing in this study area are warm and humid, with an average annual temperature of 21.9 °C. Monsoonal influences lead to pronounced temporal and spatial variations in precipitation, with a concentrated peak during the summer months. The yearly average precipitation amounts to approximately 1600 mm, with certain mountainous locales experiencing levels ranging from 2000 mm to 2600 mm (Figure 1c).

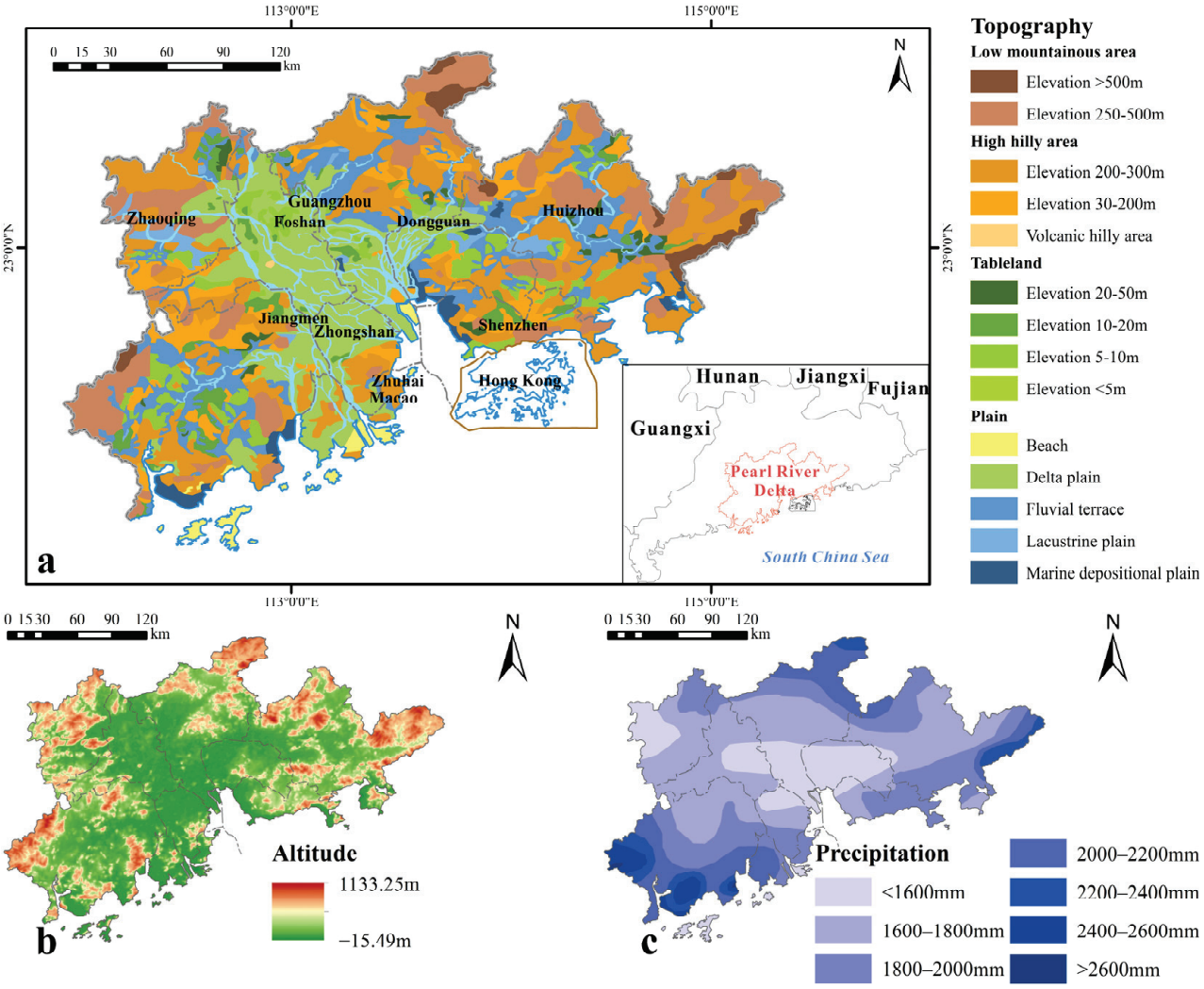

Figure 1. The altitude, precipitation, and topography of the study area. (**a**) Topography, (**b**) Altitude, (**c**) Precipitation.

The study area exhibits a comprehensive and diverse development of geological strata, with extensive distribution patterns. Encompassing a broad spectrum, geological formations range from the ancient, highly metamorphosed rocks of the Mesoproterozoic era to the more recent loose clastic sediments of the Quaternary period. Geological dynamics in this region are primarily characterized by significant, episodic fluctuations in elevation and subsidence, accompanied by differential block movements. The demarcation of boundaries is predominantly dictated by fault lines, while the internal structure is further influenced by the intersection of secondary faults oriented in various directions. Drawing from the attributes, origins, and structural traits of lithological entities, the geological compositions in the study area are classified into six primary categories: unconsolidated soil, intrusive rocks, volcanic rocks, metamorphic rocks, clastic rocks and carbonate rocks (Figure 2). Groundwater predominantly exists within the interstices of loose sediments, fractures within carbonate rocks, and fissures in bedrock.

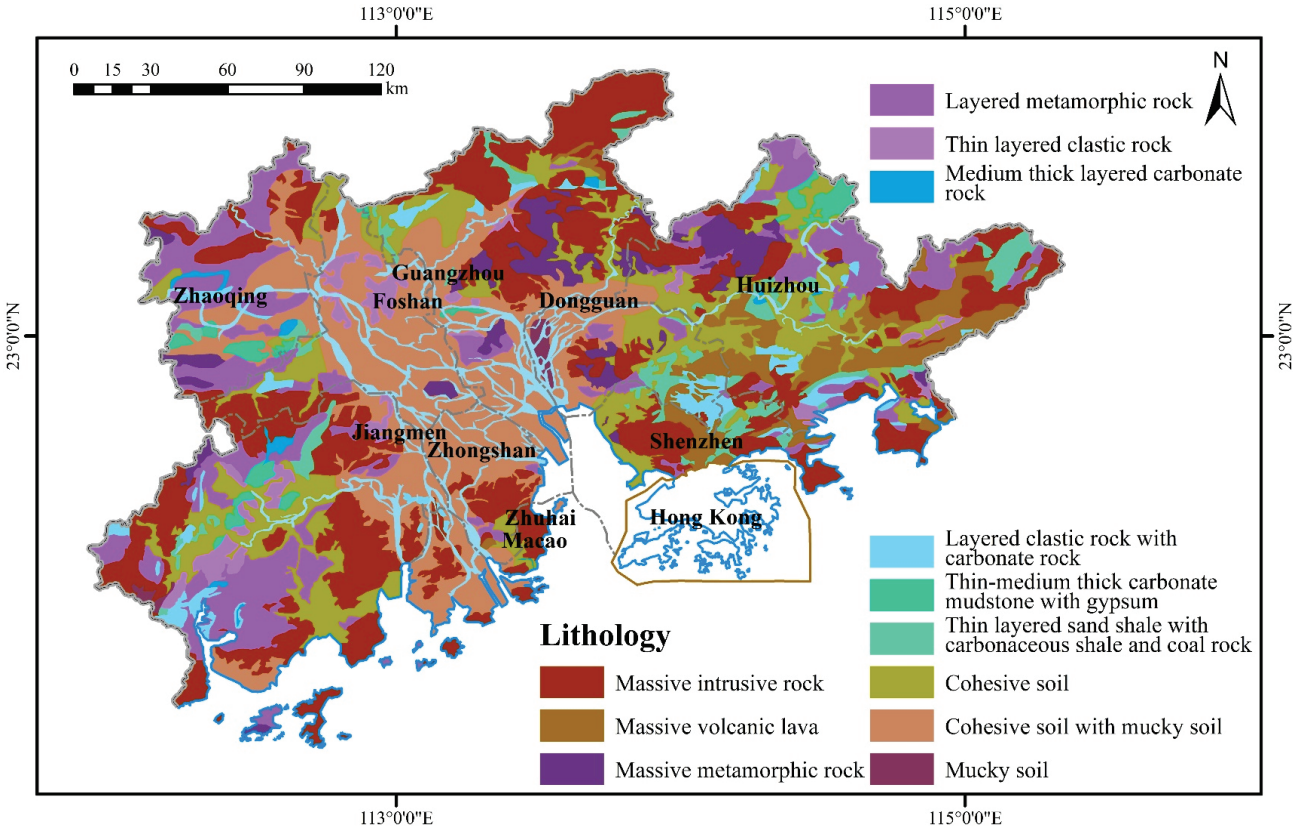

Figure 2. The lithology of the study area.

3. Methods and Materials

3.1. Technical Route

In this study, the assessment of landslide and collapse susceptibility, debris flow susceptibility, karst collapse susceptibility, ground subsidence susceptibility, soil erosion susceptibility, and sea water intrusion susceptibility was carried out utilizing the VWT-AHP method. Furthermore, the assessment of geo-environment vulnerability was conducted by drawing parallels with the principle of the "barrel effect". Based on the assessment results and considering the distribution of LULC, road construction, and critical infrastructure, recommendations for geohazard prevention and mitigation were provided. The flowchart for this study is depicted in Figure 3.

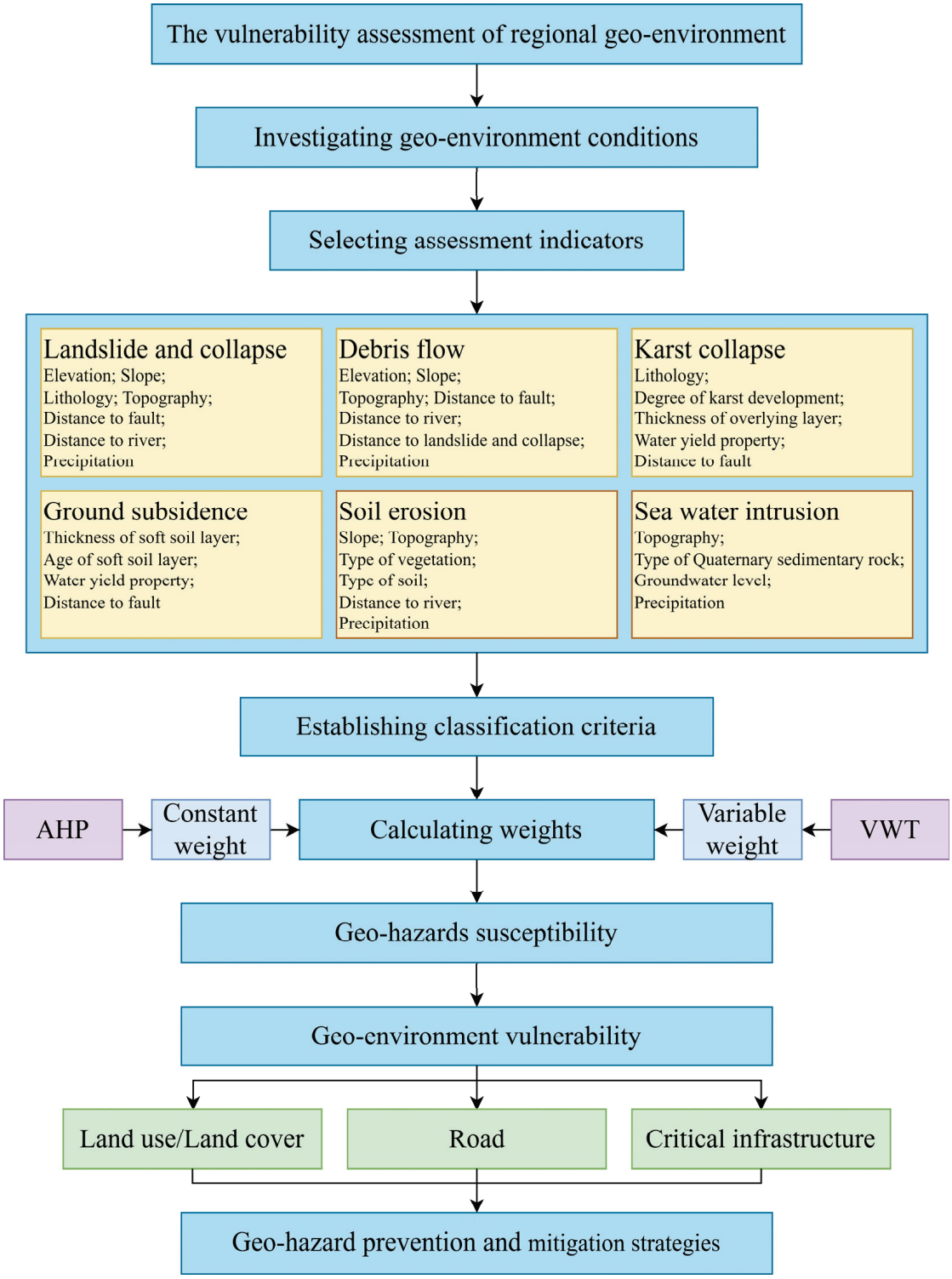

Figure 3. Flowchart of this study.

3.2. Database

3.2.1. Geo-Hazard Inventory

The geological environmental challenges in the study area are predominantly characterized by occurrences of collapses, landslides, debris flows, karst collapses, ground subsidence, and soil erosion, showcasing a widespread distribution (Figure 4). As of 2020, there are 83 locations with landslides and collapses posing a threat to over 100 people, 23 locations with debris flows endangering more than 100 people, and 97 locations expe-

riencing karst collapses. Ground subsidence exceeding 10 cm has been documented in 65 locations. Soil erosion takes the form of a fragmented distribution within the research zone, covering 1.76% of the total study area. Employing a criterion of Total Dissolved Solids (TDS) exceeding 1 g/L, the Pearl River Estuary region experiences a discernible degree of seawater intrusion, affecting approximately 10.87% of the total area. The distribution map of geohazards was provided by the Guangdong Geological Survey Institute.

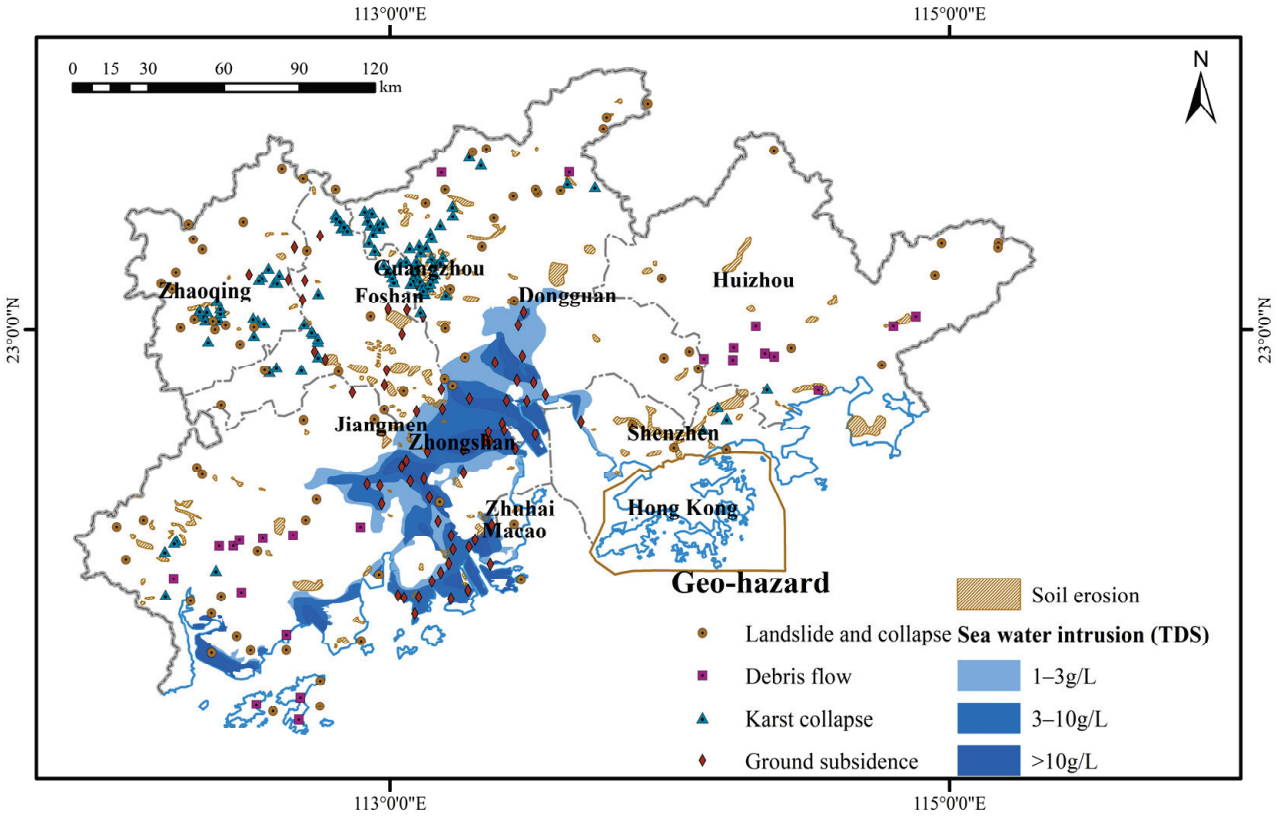

Figure 4. The distribution map of geohazards in the study area.

3.2.2. Assessment Indicators

In this study, a total of 34 factors were selected for assessing the susceptibility to six types of geohazards. Details regarding the data types, resolutions, temporal coverages, and sources of these factors are detailed in Table 1.

Table 1. Data types, resolutions, temporal coverages, and sources of all indicators.

Geohazard Susceptibility	Assessment Indicator	Data Type	Resolution	Temporal Coverage	Source
Landslide and collapse (A_1)	Elevation (B_{11})	TIFF	30 m × 30 m	/	Geospatial Data Cloud [59]
	Slope (B_{12})	TIFF	30 m × 30 m	/	/
	Lithology (B_{13})	Shapefile (Polygon)	/	/	Guangdong Geological Survey Institute
	Topography (B_{14})	Shapefile (Polygon)	/	/	Guangdong Geological Survey Institute
	Distance to fault (B_{15})	Shapefile (Polygon)	/	/	Guangdong Geological Survey Institute
	Distance to river (B_{16})	Shapefile (Polygon)	/	2020	Google Earth
	Precipitation (B_{17})	Shapefile (Polygon)	/	2020	Guangdong Geological Survey Institute

Table 1. *Cont.*

Geohazard Susceptibility	Assessment Indicator	Data Type	Resolution	Temporal Coverage	Source
Debris flow (A_2)	Elevation (B_{21})	TIFF	30 m × 30 m	/	Geospatial Data Cloud [59]
	Slope (B_{22})	TIFF	30 m × 30 m	/	/
	Lithology (B_{23})	Shapefile (Polygon)	/	/	Guangdong Geological Survey Institute
	Topography (B_{24})	Shapefile (Polygon)	/	/	Guangdong Geological Survey Institute
	Distance to fault (B_{25})	Shapefile (Polygon)	/	/	Guangdong Geological Survey Institute
	Distance to river (B_{26})	Shapefile (Polygon)	/	2020	Google Earth
	Distance to landslide and collapse (B_{27})	Shapefile (Polygon)	/	/	Guangdong Geological Survey Institute
	Precipitation(B_{28})	Shapefile (Polygon)	/	2020	Guangdong Geological Survey Institute
Karst collapse (A_3)	Lithology (B_{31})	Shapefile (Polygon)	/	/	Guangdong Geological Survey Institute
	Degree of karst development (B_{32})	Shapefile (Polygon)	/	/	Guangdong Geological Survey Institute
	Thickness of overlying layer (B_{33})	Shapefile (Polygon)	/	/	Guangdong Geological Survey Institute
	Water yield property (B_{34})	Shapefile (Polygon)	/	2020	Guangdong Geological Survey Institute
	Distance to fault (B_{35})	Shapefile (Polygon)	/	/	Guangdong Geological Survey Institute
Ground subsidence (A_4)	Thickness of soft soil layer (B_{41})	Shapefile (Polygon)	/	/	Guangdong Geological Survey Institute
	Age of soft soil layer (B_{42})	Shapefile (Polygon)	/	/	Guangdong Geological Survey Institute
	Water yield property (B_{43})	Shapefile (Polygon)	/	2020	Guangdong Geological Survey Institute
	Distance to fault (B_{44})	Shapefile (Polygon)	/	/	Guangdong Geological Survey Institute
Soil erosion (A_5)	Slope (B_{51})	TIFF	30 m × 30 m	/	/
	Topography (B_{52})	Shapefile (Polygon)	/	/	Guangdong Geological Survey Institute
	Type of vegetation (B_{53})	Shapefile (Polygon)	/	2020	Guangdong Geological Survey Institute
	Type of soil (B_{54})	Shapefile (Polygon)	/	2020	Soil Science Database [60]
	Distance to river (B_{55})	Shapefile (Polygon)	/	2020	Google Earth
	Precipitation (B_{56})	Shapefile (Polygon)	/	2020	Guangdong Geological Survey Institute
Sea water intrusion (A_6)	Topography (B_{61})	Shapefile (Polygon)	/	/	Guangdong Geological Survey Institute
	Type of Quaternary sedimentary rock (B_{62})	Shapefile (Polygon)	/	/	Guangdong Geological Survey Institute
	Groundwater level (B_{63})	TIFF	30 m × 30 m	2020	Guangdong Geological Survey Institute
	Precipitation (B_{64})	Shapefile (Polygon)	/	2020	Guangdong Geological Survey Institute

Landslide and collapse susceptibility. Landslides refer to the downward movement of rock and soil masses along weak surfaces under the influence of gravity, whereas collapses involve the abrupt detachment of soil or rock masses from their parent materials, resulting in vertical descent and potential rolling and accumulation along slopes. Numerous factors trigger landslides and collapses, including heavy precipitation, lithology, seismic activity, geomorphic processes, and human activities [61,62]. These events predominantly occur in mountainous and valley regions, characterized by steep topography and significant elevation differences. Steeper slopes with intense terrain incision are more prone to landslides and collapses due to concentrated stress at steeper angles. Geological factors such as lithology and geological structures play pivotal roles in landslides and collapses. Lithology serves as the fundamental condition determining the possibility of these events, while geological structures influence the

development of fractures within rocks. In regions marked by fault zones and the presence of weak rocks, fissures within rocks lead to structural looseness, reduced shear strength, and diminished resistance to weathering. Greater fissure development and rock fragmentation heighten the likelihood of landslides and collapses. Precipitation is a critical triggering factor, as water infiltrates through rock fractures, eroding and softening the material, promoting further fissure expansion, weakening the mechanical strength of rocks, and simultaneously eroding slope angles, thus forming precipitous faces. In this study, the selected assessment indicators encompassed elevation, slope, lithology, topography, distance to fault, distance to river, and precipitation [63–67]. Slope data was computed using ArcGIS 10.6 based on the elevation data. River data was extracted from remote sensing images and the distance to river was calculated using ArcGIS 10.6 with the Euclidean distance method.

Debris flow susceptibility. Debris flow entails the rapid surging of a mixture comprising water, sediment, rocks, and soil on steep slopes, often triggered by heavy precipitation. They exhibit high speeds, extended propagation distances, and significant destructive potential [68–70]. In regions characterized by intense fissure development, active faulting, and abundant landslides, fragmented rocks constitute the material basis for debris flow occurrence. Precipitation plays a pivotal role as a triggering factor for mudflows, as intense precipitation generates temporary surface runoff that provides the dynamic conditions for mudflow initiation. Debris flows predominantly occur in steep mountainous terrain, where unstable slopes are prone to landslides and collapses, facilitating the rapid accumulation of fragmented rock masses. Debris flows frequently follow river valleys and ravines, which facilitate the convergence of water flow and the transportation of eroded rock–soil material. For this study, the chosen assessment indicators encompassed elevation, slope, lithology, topography, distance to fault, distance to river, distance to landslide and collapse, and precipitation [71–74]. The distance to landslide and collapse was calculated using ArcGIS 10.6 with the Euclidean distance method.

Karst collapse susceptibility. Karst collapse refers to the abrupt sinking and deformation of loose rock–soil material overlaying soluble rock layers with well-developed karst cavities, resulting from the collapse of the terrain. The presence of karst caves is a prerequisite for karst collapse occurrences. The concentration of stress induced by surrounding rock dynamics on the roofs and sidewalls of karst caves impairs their stability. The extent of karst formation, the quantity, and dimensions of karst caves all contribute to heightened susceptibility to karst collapses. Groundwater inflow augments the weight of the cave roof rock mass, coursing through fractures to diminish shear resistance between adjacent rock segments and exacerbate the erosion of soluble rock, thereby intensifying karst development. Greater fragmentation of the soluble rock mass corresponds to more advanced fissuring, rendering it increasingly susceptible to groundwater erosion. This study incorporated a range of assessment indicators for karst collapse susceptibility, including lithology, degree of karst development, thickness of overlying layer, water yield property, and distance to fault [31,75–77].

Ground subsidence susceptibility. Ground subsidence refers to the abrupt or gradual downward movement of the Earth's surface, primarily in the vertical dimension, with minimal lateral shifts [78]. Ground subsidence is frequently instigated by excessive groundwater extraction [79]. A fundamental prerequisite for ground subsidence is the presence of an overlaying stratum of soft soil. The drainage of water from the soft soil results in diminished pore water pressure and amplification of effective stress, leading to the consolidation and densification of the soft soil layer. Crustal movements can also trigger ground subsidence, typically manifesting at a comparably sluggish pace. In this study, the chosen assessment indicators encompassed thickness of soft soil layer, age of soft soil layer, water yield property, and distance to fault [80–83].

Soil erosion susceptibility. Soil erosion is the phenomenon in which soil particles disperse, transport, and submerge under the influence of hydraulic processes and human activities. Climate, topography, land cover, and land use conditions are pivotal factors shaping soil erosion dynamics [84,85]. The physical structure of soil serves as the substrate for soil erosion, with loosely compacted soil structures and reduced viscosity rendering

it more susceptible to erosion caused by water and human actions. Precipitation-induced surface runoff acts as a fundamental driving force behind soil erosion, with higher precipitation intensities leading to increased runoff volumes and escalated erosion potential. Slope gradient stands as a critical determinant in soil erosion resistance, as steeper slopes elevate the propensity of soil mass movement due to gravitational forces, thereby intensifying surface runoff and augmenting erosion risks. Vegetation plays a crucial role in intercepting precipitation, thus mitigating surface runoff intensity. Root systems contribute to water retention and soil compaction, thereby ameliorating the impact of soil erosion. In this study, the selected assessment indicators for soil erosion susceptibility encompassed slope, topography, type of vegetation, type of soil, distance to river, and precipitation [86–88].

Sea water intrusion susceptibility. Sea water intrusion pertains to the process whereby freshwater aquifers undergo salinization due to both natural and human-induced factors [89]. The manifestation of sea water intrusion necessitates the fulfillment of two conditions: the existence of hydraulic conduits and a disparity in hydraulic pressure within the aquifer. In coastal aquifers characterized by porous or fractured substrates, as well as those shaped by karst formations, sea water gains access to the groundwater system through these pathways. As the hydraulic head of sea water surpasses that of the coastal aquifer, driven by this hydraulic gradient, sea water infiltrates the groundwater reservoir via hydraulic connections. The replenishment of groundwater, which potentially leads to an increase in groundwater levels within coastal aquifers, can occur through mechanisms like precipitation-induced infiltration. In this study, the chosen indicators for assessing sea water intrusion susceptibility encompassed topography, type of Quaternary sedimentary rock, groundwater level, and precipitation [90–93].

Each indicator has been assigned ratings of 0.1, 0.3, 0.7, and 0.9 across four ranges. In cases where an indicator is categorized into three ranges, its ratings were adjusted to 0.1, 0.3, and 0.7. The delineation of factor ranges and assignment of ratings are derived from previous studies [94–98]. The ranges and ratings of all indicators are presented in Table 2. The distribution maps of all indicators are available in Figures 5–10.

Table 2. Ranges and ratings of all indicators.

Geohazard Susceptibility	Assessment Indicator	Rating			
		0.9	**0.7**	**0.3**	**0.1**
Landslide and collapse (A_1)	Elevation (B_{11})	>400 m	200–400 m	80–200 m	<80 m
	Slope (B_{12})	>20°	10°–20°	5°–10°	<5°
	Lithology (B_{13})	Metamorphic rock; clastic rock; sand shale	Carbonate rock; carbonate mudstone	Massive rock; massive lava	Mucky soil; cohesive soil
	Topography (B_{14})	Mountainous area; hilly area (>200 m)	Hilly area (<200 m); volcanic hilly area; tableland (>20 m)	Tableland (10–20 m); lacustrine plain	Tableland (<10 m); beach; fluvial plain; marine depositional plain; delta plain
	Distance to fault (B_{15})	<2 km	2–4 km	4–6 km	>6 km
	Distance to river (B_{16})	<0.5 km	0.5–1 km	1–1.5 km	>1.5 km
	Precipitation (B_{17})	>2400 mm	2000–2400 mm	1600–2000 mm	<1600 mm
Debris flow (A_2)	Elevation (B_{21})	>600 m	300–600 m	100–300 m	<100 m
	Slope (B_{22})	>20°	10°–20°	5°–10°	<5°
	Lithology (B_{23})	Mucky soil; cohesive soil	Metamorphic rock; clastic rock; sand shale	Carbonate rock; carbonate mudstone	Massive rock; massive lava
	Topography (B_{24})	Mountainous area; hilly area (>200 m)	Hilly area (<200 m); volcanic hilly area; tableland (>20 m)	Tableland (10–20 m); lacustrine plain	Tableland (<10 m); beach; fluvial plain; marine depositional plain; delta plain
	Distance to fault (B_{25})	<2 km	2–4 km	4–6 km	>6 km
	Distance to river (B_{26})	<0.5 km	0.5–1 km	1–1.5 km	>1.5 km
	Distance to landslide and collapse (B_{27})	<2 km	2–4 km	4–6 km	>6 km
	Precipitation(B_{28})	>2400 mm	2000–2400 mm	1600–2000 mm	<1600 mm

Table 2. *Cont.*

Geohazard Susceptibility	Assessment Indicator	Rating			
		0.9	**0.7**	**0.3**	**0.1**
Karst collapse (A_3)	Lithology (B_{31})	/	Carbonate rock	Argillaceous limestone; sandstone; basalt	Mudstone; shale; silly slate
	Degree of karst development (B_{32})	/	Strong	Moderate	Poor
	Thickness of overlying layer (B_{33})	/	<10 m	10–20 m	>20 m
	Water yield property (B_{34})	/	>1000 m^3/d	100–1000 m^3/d	<100 m^3/d
	Distance to fault (B_{35})	/	<2 km	2–4 km	>4 km
Ground subsidence (A_4)	Thickness of soft soil layer (B_{41})	/	>20 m	10–20 m	<10 m
	Age of soft soil layer (B_{42})	/	Holocene alluvial deposits; Holocene residual deposits	Holocene Dawanzhen Formation; Holocene Mugao Formation	Holocene Guizhou Formation; Upper Pleistocene deposits
	Water yield property (B_{43})	/	>1000 m^3/d	100–1000 m^3/d	<100 m^3/d
	Distance to fault (B_{44})	/	<2 km	2–4 km	>4 km
Soil erosion (A_5)	Slope (B_{51})	>20°	10°–20°	5°–10°	<5°
	Topography (B_{52})	Mountainous area; hilly area (>200 m)	Hilly area (<200 m); volcanic hilly area; tableland (>20 m)	Tableland (10–20 m); lacustrine plain	Tableland (<10 m); beach; fluvial plain; marine depositional plain; delta plain
	Type of vegetation (B_{53})	Sandy land; urban land	Arable land	Grassland; economic forest land; protective forest land	Arbor land; shrub land
	Type of soil (B_{54})	Latosolic red soil	Alluvial soil	Red soil	Paddy soil
	Distance to river (B_{55})	<0.5 km	0.5–1 km	1–1.5 km	>1.5 km
	Precipitation (B_{56})	>2400 mm	2000–2400 mm	1600–2000 mm	<1600 mm
Sea water intrusion (A_6)	Topography (B_{61})	Tableland (<10 m); beach; fluvial plain; marine depositional plain; delta plain	Tableland (10–20 m); lacustrine plain	Hilly area (<200 m); volcanic hilly area; tableland (>20 m)	Mountainous area; hilly area (>200 m)
	Type of Quaternary sedimentary rock (B_{62})	Alluvial sandy clay	Marine clay	Proluvial clay	Bedrock
	Groundwater level (B_{63})	<−2 m	−2–0 m	0–2 m	>2 m
	Precipitation (B_{64})	<1600 mm	1600–2000 mm	2000–2400 mm	>2400 mm

3.2.3. LULC, Road, and Critical Infrastructure

In the study area, there are 13 LULC types (Figure 11). Artificial surfaces are predominantly found in urban areas, particularly in Guangzhou and Shenzhen. The area also includes both paddy fields and dryland and economic crops mainly include banana, citrus, and sugarcane. The mountainous areas exhibit significant variation in vegetation cover, ranging from less than 30% to over 90%. The LULC data for the year 2020 was provided by the Guangdong Geological Survey Institute.

The road network encompasses national highways, provincial roads, and railways, while critical infrastructure comprises facilities related to education, energy, healthcare, and water resources. All data was sourced from OSM (2023) [99].

3.3. Methods

3.3.1. Analytic Hierarchy Process

The AHP, introduced by Saaty (1980) [42], is known for its simplicity in principle and dependable theoretical foundation. Abundant practical cases have demonstrated the significant applicability of AHP in effectively addressing complex multi-objective com-

petitive decision-making problems [100–104]. The AHP generally involves the following three steps:

Step 1: Develop a multi-level hierarchical structure model.

The multi-level hierarchical structure elucidates the interplays among various constituents within complex challenges [105]. Factors are categorized into distinct strata based on their attributes, with each stratum subordinate to higher-level factors and capable of influencing lower-level factors. The identification of factors primarily relies on existing knowledge and expertise.

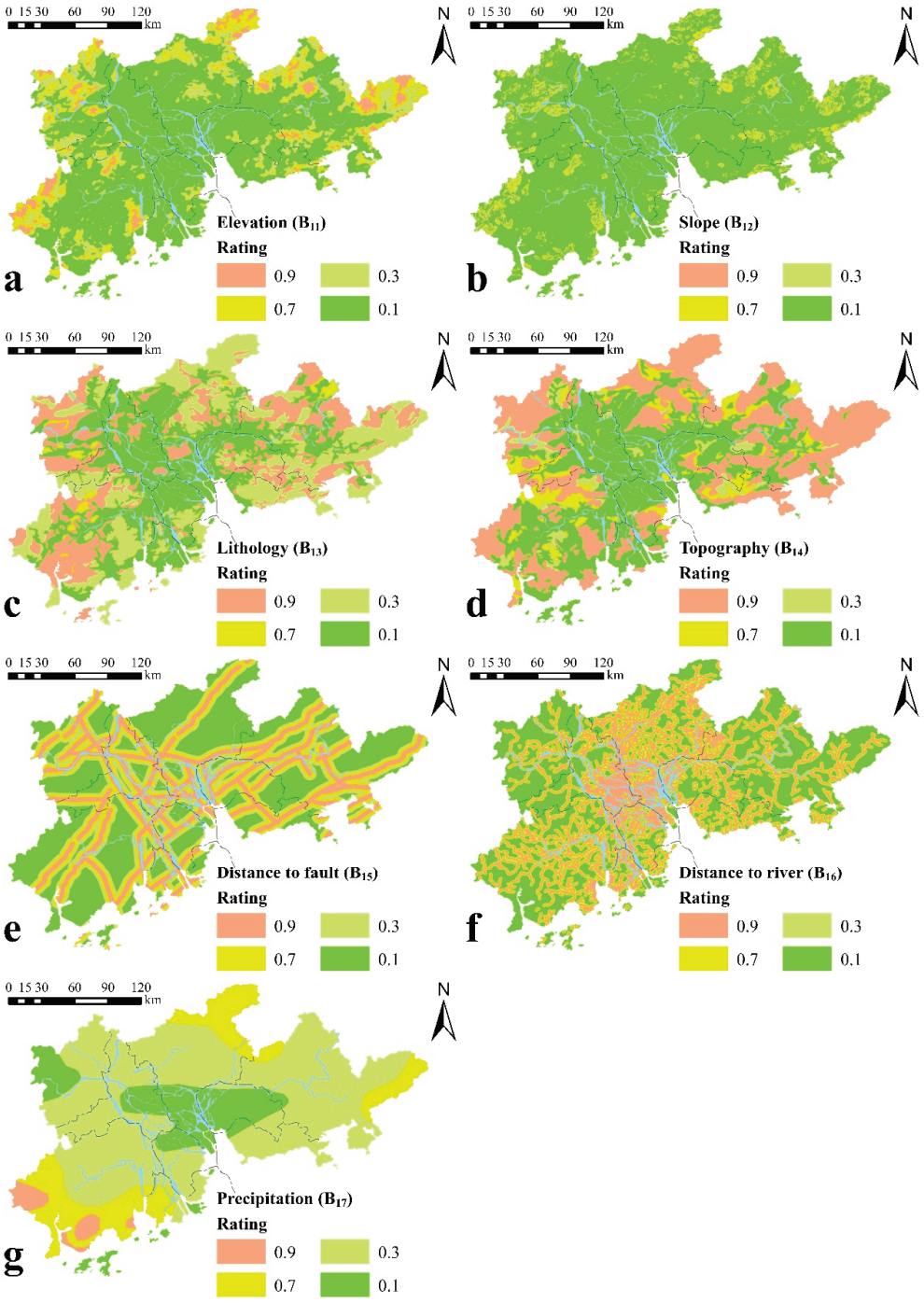

Figure 5. Distribution maps of assessment indicators for landslide and collapse susceptibility. (**a**) Elevation, (**b**) Slope, (**c**) Lithology, (**d**) Topography (**e**), Distance to fault, (**f**) Distance to river, (**g**) Precipitation.

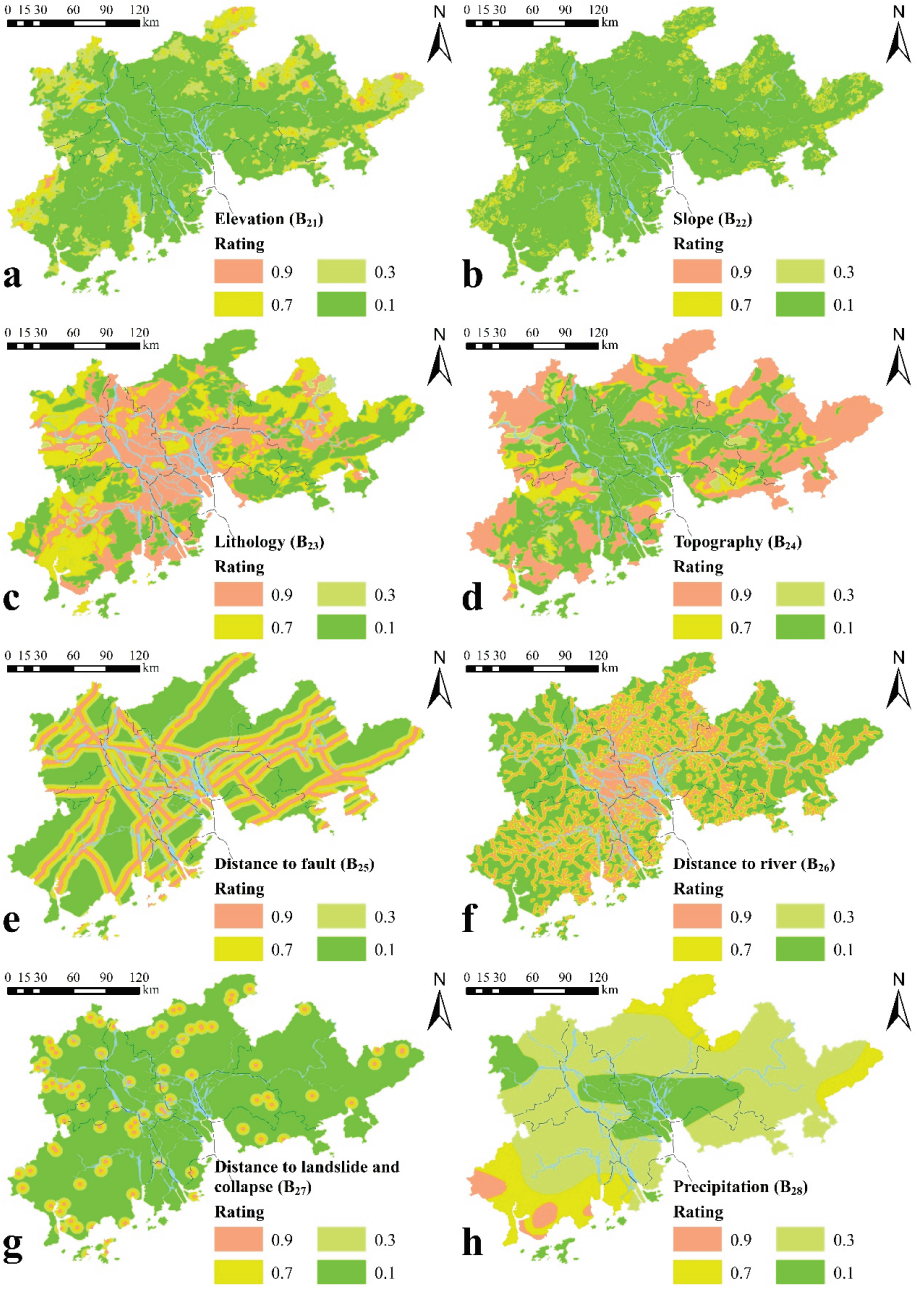

Figure 6. Distribution maps of assessment indicators for debris flow susceptibility. (**a**) Elevation, (**b**) Slope, (**c**) Lithology, (**d**) Topography, (**e**) Distance to fault, (**f**) Distance to river, (**g**) Distance to landslide and collapse, (**h**) Precipitation.

Step 2: Conduct pairwise comparisons of factors and formulate judgment matrices.

Based on the assessments of decision-makers or experts, the relative importance of factors is determined through pairwise comparisons. For these comparisons, a scale from 1 to 9 is used (Table 3). The judgment matrix A, derived from these pairwise comparisons, is used to calculate the weights of each factor. Matrix A is represented in Equation (1). The dimension n of the matrix corresponds to the number of factors.

$$A = \begin{bmatrix} a_{11} & \cdots & a_{1n} \\ \vdots & \ddots & \vdots \\ a_{n1} & \cdots & a_{nn} \end{bmatrix} \quad (1)$$

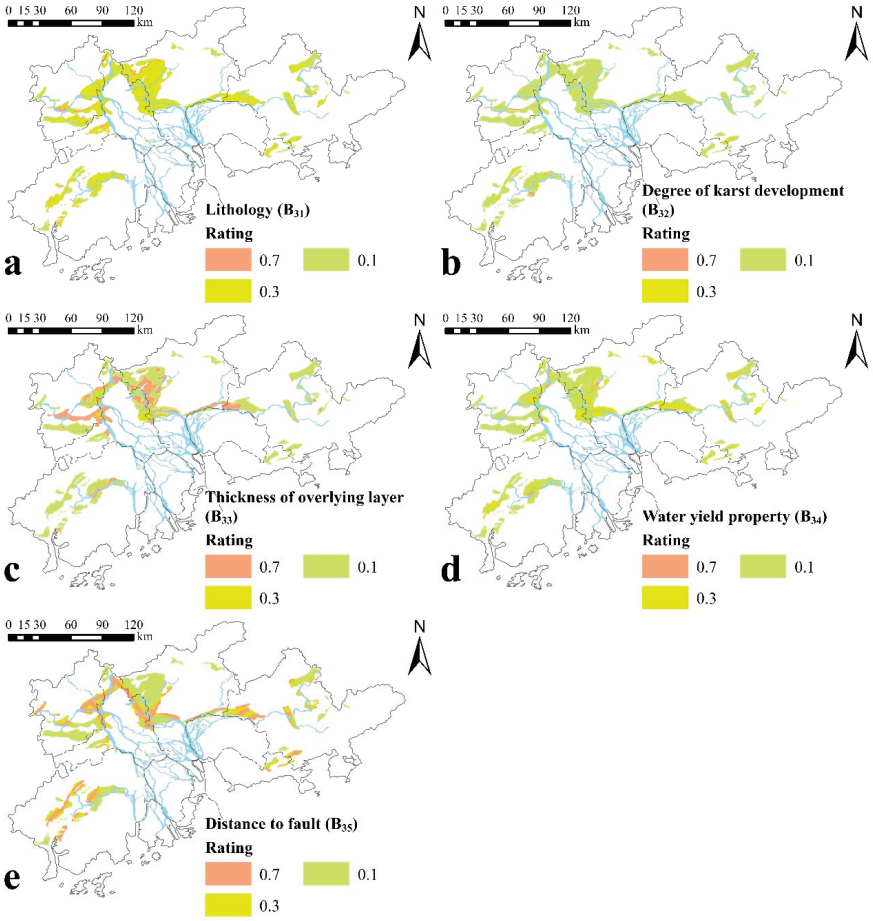

Figure 7. Distribution maps of assessment indicators for karst collapse susceptibility. (**a**) Lithology, (**b**) Degree of karst development, (**c**) Thickness of overlying layer, (**d**) Water yield property, (**e**) Distance to fault.

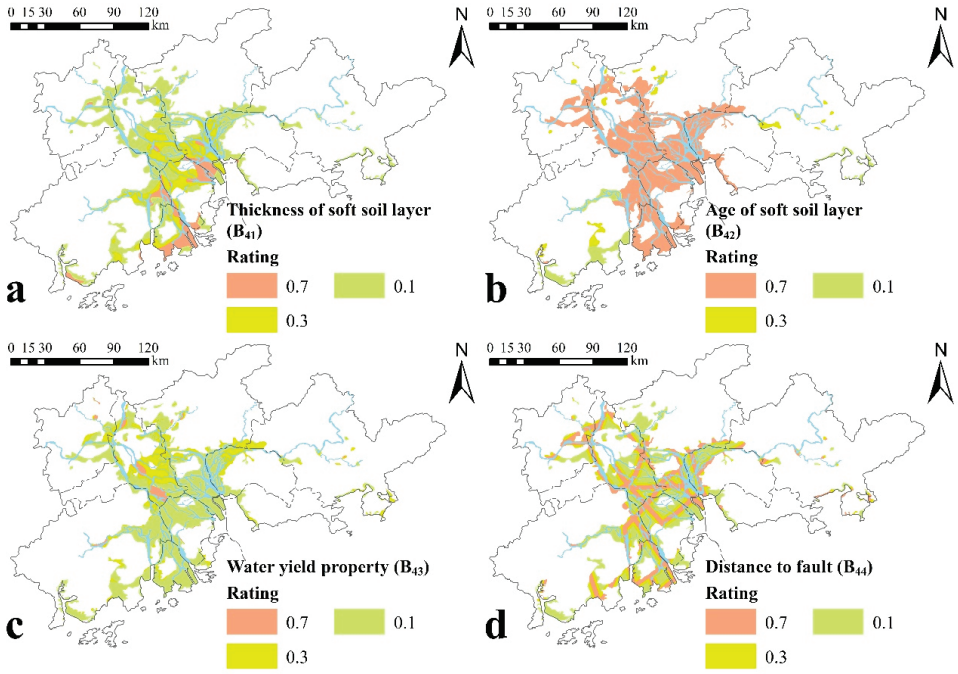

Figure 8. Distribution maps of assessment indicators for ground subsidence susceptibility. (**a**) Thickness of soft soil layer, (**b**) Age of soft soil layer, (**c**) Water yield property, (**d**) Distance to fault.

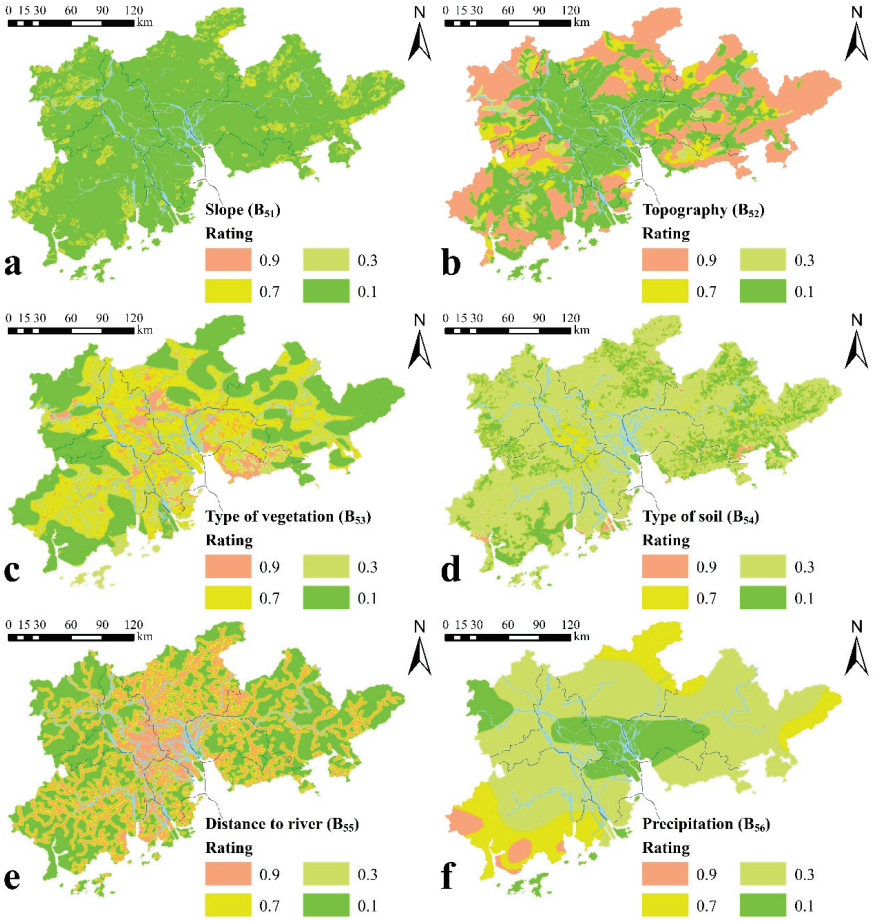

Figure 9. Distribution maps of assessment indicators for soil erosion susceptibility. (**a**) Slope, (**b**) Topography, (**c**) Type of vegetation, (**d**) Type of soil, (**e**) Distance to river, (**f**) Precipitation.

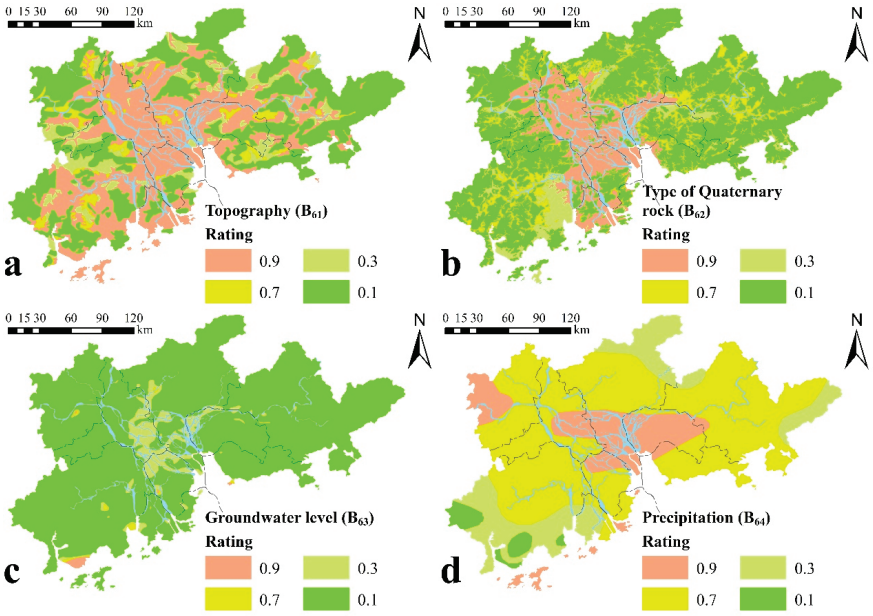

Figure 10. Distribution maps of assessment indicators for sea water intrusion susceptibility. (**a**) Topography, (**b**) Type of Quaternary rock, (**c**) Groundwater level, (**d**) Precipitation.

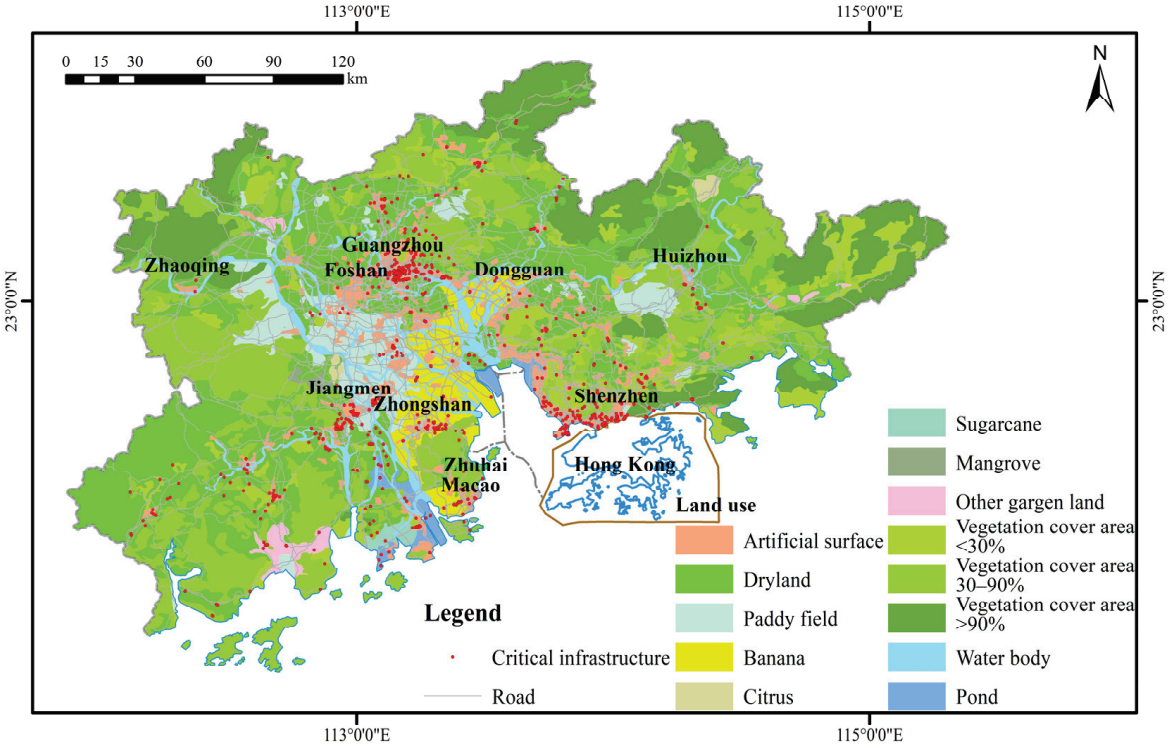

Figure 11. Distribution map of LULC, road construction and critical infrastructure.

Table 3. Pairwise comparison scale for AHP.

Scale	1	3	5	7	9
Importance	Equal	Moderate	Strong	Very strong	Extreme

To reduce significant variations among the elements within the judgment matrix A, a normalization procedure is applied to the matrix elements. The calculation method for normalizing the elements within the matrix is outlined in Equation (2).

$$b_{ij} = \frac{a_{ij}}{\sum_{i=1}^{n} a_{ij}} \tag{2}$$

To calculate the eigenvector corresponding to the maximum eigenvalue, the average of the row elements of the normalized matrix is calculated as described in Equation (3).

$$w_i = \frac{\sum_{j=1}^{n} b_{ij}}{n} \tag{3}$$

The method for calculating the maximum eigenvalue is outlined in Equation (4).

$$\lambda_{max} = \frac{1}{n}\sum_{i=1}^{n} \frac{(Aw)_i}{w_i} \tag{4}$$

Step 3: Determine factor weights and perform consistency checks.

The coherence of pairwise comparisons plays a pivotal role in influencing the precision of decisions made by evaluators. Improved coherence corresponds to more accurate outcomes in these pairwise assessments. When coherence is found to be lacking, a re-examination of the pairwise comparisons among factors becomes imperative. The

procedure for computing the Consistency Index (*CI*), an indicator used to quantify the consistency of the judgment matrix, is explained in Equation (5).

$$CI = \frac{\lambda_{max} - n}{n - 1} \tag{5}$$

To calculate the Consistency Ratio (*CR*), the first step involves establishing the Average Random Consistency Index (*RI*), as guided by the values provided in Table 4.

Table 4. Average Random Consistency Index.

n	**1**	**2**	**3**	**4**	**5**	**6**	**7**	**8**	**9**	**10**
RI	0	0	0.52	0.89	1.11	1.24	1.35	1.40	1.45	1.49

The equation to calculate the *CR*, used for addressing inconsistencies, is provided by Equation (6). A *CR* value less than or equal to 0.10 is considered acceptable for maintaining a reasonable level of consistency.

$$CR = \frac{CI}{RI} \tag{6}$$

3.3.2. Variable Weight Theory

In the context of the AHP, the conventional assumption assumes the constancy of factor weights. However, in practical scenarios, factors with exceptionally high or low values can significantly impact assessment outcomes. To address this issue, this study introduces the VWT, a mechanism that dynamically adjusts the weights of factors based on their values. This adaptation enhances the fidelity of assessment results in representing complex real-world contexts.

The VWT, initially introduced by Wang (1985) [106], has garnered significant attention and application across diverse fields [107–110]. This theory presents a framework that establishes a linkage between weight vectors and state vectors, enabling the adaptation of factor weights by shifts in decision states.

To better reflect the impact of extreme values on indicator weights, this study introduces a "penalization-incentive" variant of the VWT. The definitions of the state variable weight vector and the variable weight vector are provided, along with their corresponding calculation methods presented in Equations (7) and (8), respectively.

$$s_i = \begin{cases} \frac{a-b}{\alpha-\lambda}\lambda ln\frac{\lambda}{x_i} + a & x_j \in (0, \lambda] \\ \frac{b-a}{\alpha-\beta}x_i + \frac{a\alpha-b\lambda}{\alpha-\lambda} & x_j \in (\lambda, \alpha] \\ \frac{a-b}{2(\alpha-\lambda)(\beta-\alpha)}(\beta - x_i)^2 + c & x_j \in (\alpha, \beta] \\ c & x_j \in (\beta, \mu] \\ k(1-\mu)ln\frac{1-\mu}{1-x_i} + c & x_j \in (\mu, 1) \end{cases} \tag{7}$$

$$w_i' = \frac{w_i s_i}{\sum_{i=1}^{n} w_i s_i} \tag{8}$$

In Equations (7) and (8), the symbol x_j represents the rating of the *i*-th indicator, s_i signifies the state variable weight vector corresponding to the *i*-th indicator, w_i denotes the constant weight vector associated with the *i*-th indicator, and w_i' indicates the variable weight vector of the *i*-th indicator. The parameters are subject to the conditions $0 < \lambda < \alpha < \beta < \mu < 1$ and $0 < c < b < a < 1$. In this study, the parameter values were set as follows: $\lambda = 0.2$, $\alpha = 0.4$, $\beta = 0.6$, $\mu = 0.8$, $c = 0.2$, $b = 0.3$, and $a = 0.5$ [111].

Finally, the Comprehensive Index (*CPI*) is determined by Equation (9).

$$CPI = \sum_{i=1}^{n} w_i' x_i \tag{9}$$

3.3.3. Assessment Unit Segmentation

The irregular polygon grid method was used to segment assessment units [112]. Specifically, for each geohazard, the distribution maps of all indicators were superimposed using ArcGIS 10.6 to generate a susceptibility distribution map. Each closed polygon with uniform ratings was treated as an individual assessment unit, thus eliminating rating inconsistencies within the same unit that could introduce errors. The irregular polygons formed by overlaying the susceptibility distribution maps were considered as the assessment units for geo-environment vulnerability assessment. The distribution maps of assessment units are shown in Supplementary Figures S1–S7.

3.3.4. Weight Determination and Comprehensive Index Calculation

Utilizing the AHP method, the constant weights of each indicator were computed, and the VWT was employed to determine the variable weights. Specifically, within each assessment unit, the constant weights for each indicator remained fixed, while the variable weights were dynamically adjusted based on the indicator's rating and Equations (7) and (8).The judgment matrices and the constant weights of each factor are presented in Supplementary Tables S1–S6. The variable weights of each factor are presented in Supplementary Tables S7–S12.

The *CPI* for each assessment unit was calculated following Equation (9) and categorized [113,114]. Based on the classification results, high susceptibility areas, medium susceptibility areas, low susceptibility areas, and stable areas were identified using the Jenks Natural Breaks method [114].

3.3.5. Geo-Environment Vulnerability Assessment

The categorization of geo-environment vulnerability is determined based on the principle of the "barrel effect", considering the susceptibility to all geohazards. Specifically, for each assessment unit, if a high susceptibility area is identified for any type of geohazard, it is designated as a high geo-environment vulnerability area. Conversely, if a medium susceptibility area exists for any geohazard, it is classified as a medium geo-environment vulnerability area. In cases where neither high nor medium susceptibility areas are present for any geohazard, and a low susceptibility area is detected, it is categorized as a low geo-environment vulnerability area. Otherwise, it is classified as a stable area.

4. Results and Discussion

4.1. Geohazard Susceptibility

4.1.1. Landslide and Collapse Susceptibility

The high susceptibility areas are concentrated within three subareas in both the eastern and western sectors, covering a combined area of 3514.68 km^2 (Figure 12). Subarea A is located in the southwestern mountainous and hilly terrain of the study area, characterized by prevalent geological formations such as metamorphic rock, clastic rock, and sand shale, with annual precipitation exceeding 2000 mm. Subarea B is located in the northwestern portion of the study area, exhibiting similar topographical and geological conditions to Subarea A. Nevertheless, the precipitation within this area falls below 2000 mm. Subareas C, D, and E are distributed in the mountainous and hilly areas of the eastern part of the study area. The dominant geological formations include metamorphic rock, clastic rock, sand shale, massive rock, and massive lava. The annual precipitation in these subareas ranges from 1600 mm to 2400 mm. In comparison to the other subareas, Subarea C exhibits a denser river network. The medium susceptibility areas and low susceptibility areas are primarily situated around the high susceptibility areas, covering an area of 9848.89 km^2 and 9688.68 km^2, respectively. The stable areas are extensively distributed across low-altitude tablelands and plains, encompassing an area of 18,645.75 km^2. These areas feature widespread occurrences of mucky soil and cohesive soil, dense river networks, and precipitation predominantly below 1600 mm.

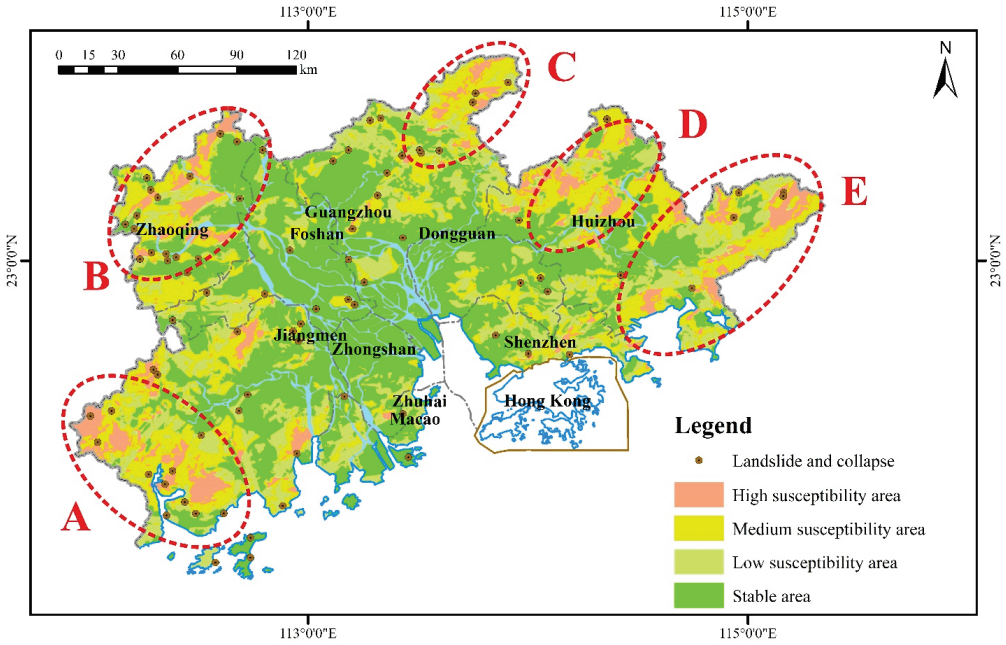

Figure 12. Distribution map of landslide and collapse susceptibility.

4.1.2. Debris Flow Susceptibility

The high and medium susceptibility areas are concentrated in the southwestern part of the study area, characterized by higher elevations and precipitation below 1600 mm, primarily within mountainous and hilly areas (Figure 13). In other parts of the study area, the high susceptibility areas are scattered along faults and river valleys, primarily within areas of fractured rock. The high susceptibility areas cover 480.94 km^2, while the medium susceptibility areas span 3619.66 km^2. The low susceptibility areas are situated around the high susceptibility areas and medium susceptibility areas, as well as along rock fractured areas along faults, covering an area of 26,905.16 km^2. The stable areas are widely distributed in the study area, encompassing low-elevation, flat terrain such as tablelands and plains, with a total area of 10,692.25 km^2.

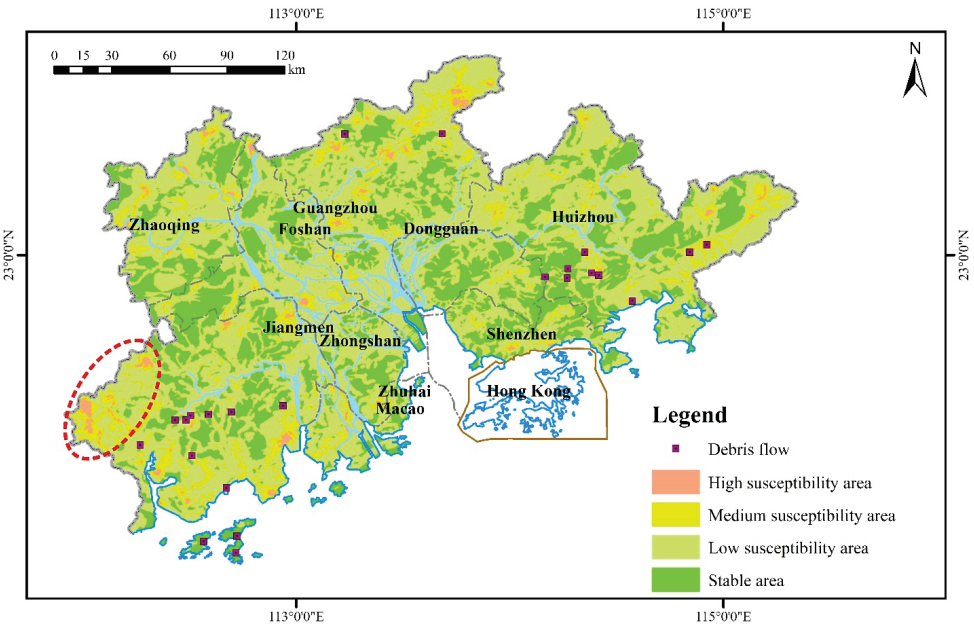

Figure 13. Distribution map of debris flow susceptibility.

4.1.3. Karst Collapse Susceptibility

The high susceptibility areas cover an extent of 484.94 km^2, primarily subdivided into three subareas characterized by dominant rock formations including argillaceous limestone, sandstone, and basalt, with a fragmented geological structure (Figure 14). Subarea A is situated in the southwestern portion of the study area, exhibiting a moderate degree of karst development and a thickness of overlying layer generally exceeding 20 m. Subarea B experiences a poorer degree of karst development, with thickness of overlying layer typically under 20 m. Subarea C, located in the central part of the study area, presents a limited degree of karst development, and the thickness of overlying layer is generally less than 10 m. The medium susceptibility areas are distributed around the high susceptibility areas, covering areas characterized by thickness of overlying layer below 10 m, significant aquifer yields surpassing 100 m^3/d, or prominent fault development. The combined area of these areas totals 2553.61 km^2. The low susceptibility areas are distributed within areas outside the high and medium susceptibility areas, where distributed soluble lava is present, covering an area of 1812.95 km^2. Areas lacking distributed soluble lava are designated as stable areas, covering an expanse of 36,841.23 km^2.

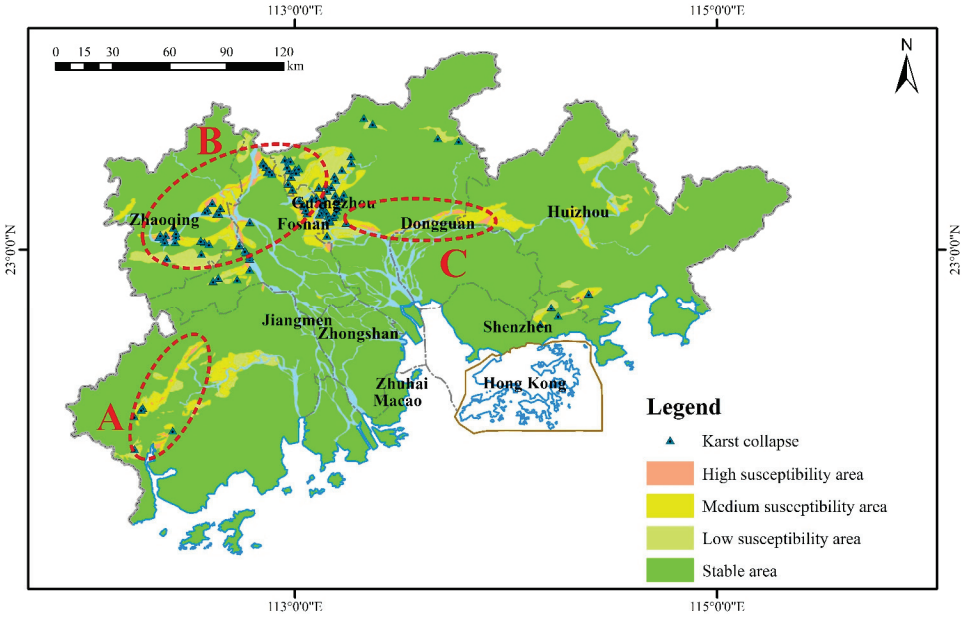

Figure 14. Distribution map of karst collapse susceptibility.

4.1.4. Ground Subsidence Susceptibility

The high susceptibility areas are sparsely distributed in areas with a thickness of soft soil layer exceeding 20 m, fractured geological structures, and aquifer yields less than 100 m^3/d, covering an area of 454.65 km^2 (Figure 15). The medium susceptibility areas are predominantly distributed along faults, characterized by thickness of soft soil layer surpassing 10 m, encompassing an area of 3741.20 km^2. The low susceptibility areas are situated within areas other than the high susceptibility and medium susceptibility areas, where distributed soft soil layers are present, covering a total area of 4468.67 km^2. Areas devoid of distributed soft soil layers are classified as stable areas, covering an area of 36,841.23 km^2.

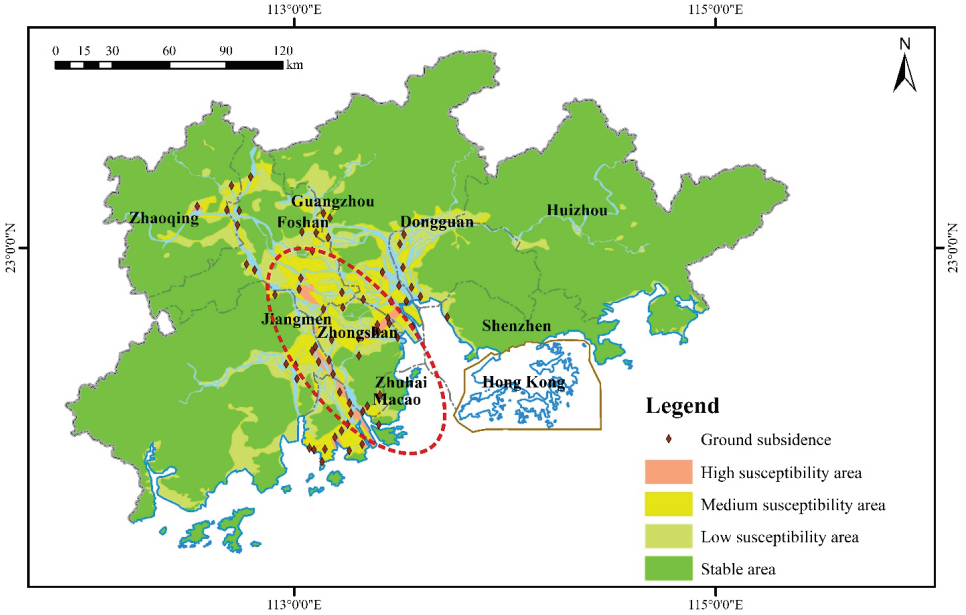

Figure 15. Distribution map of ground subsidence susceptibility.

4.1.5. Soil Erosion Susceptibility

The high susceptibility areas are primarily concentrated in the central part of the study area, with scattered occurrences in other areas, generally associated with sandy terrain or urban land use (Figure 16). These areas are characterized by predominantly alluvial soil, dense river networks, and cover a total area of 344.54 km^2. The medium and low susceptibility areas are widely distributed along riverbanks, characterized by diverse vegetation and soil types. The total area occupied by the medium susceptibility areas is 5526.97 km^2, while the low susceptibility areas encompass an extensive expanse of 22,743.83 km^2. The stable areas are predominantly distributed across arbor lands and shrub lands, characterized by predominant soil types of red soil and paddy soil. These areas are situated at a considerable distance from rivers, covering a total area of 13,081.98 km^2.

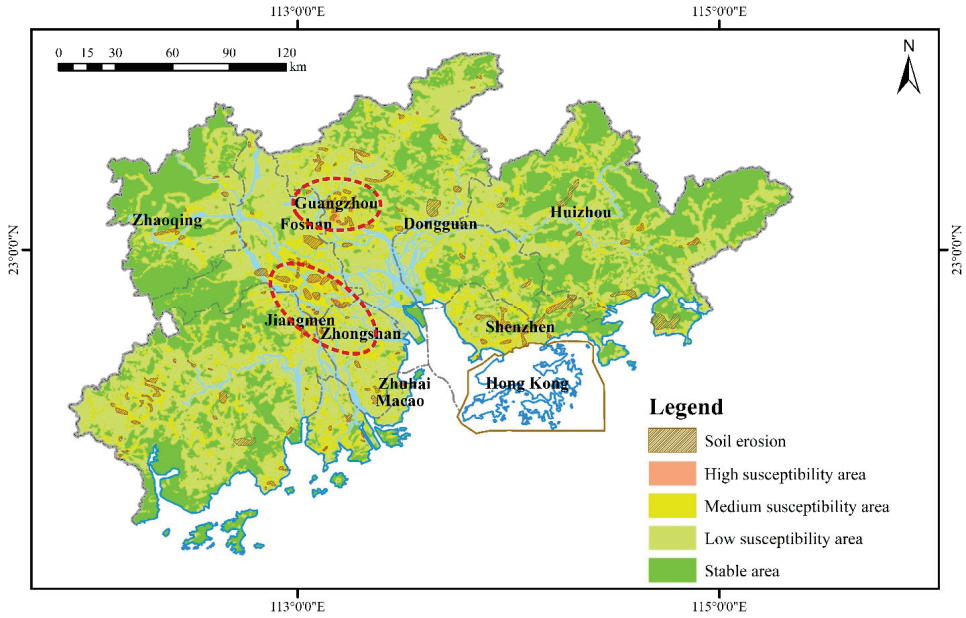

Figure 16. Distribution map of soil erosion susceptibility.

4.1.6. Sea Water Intrusion Susceptibility

The high susceptibility areas can be further subdivided into two subareas, covering a total area of 1095.33 km^2 (Figure 17). Subarea A is located in the southwestern plains of the study area, characterized by widespread distribution of proluvial clay and bedrock. The groundwater level is situated below −2 m, and the annual precipitation surpasses 2000 mm. Subarea B is distributed in the central plains of the study area, characterized by widespread distribution of alluvial sandy clay. The groundwater level typically ranges between 0 m to 2 m, and the annual precipitation is generally less than 2000 mm. The medium susceptibility areas are primarily situated in the plains surrounding the high susceptibility areas. The topographical and geological conditions in these areas are relatively comparable to the high susceptibility areas. The annual precipitation typically falls within the range of 1600 mm to 2000 mm. The cumulative area of these medium susceptibility areas amounts to 4341.74 km^2. The low susceptibility areas are extensively distributed across plains and tablelands, characterized by widespread presence of alluvial sandy clay and marine clay. The groundwater level typically remains above 2 m, while the annual precipitation is less than 2000 mm. The combined area of these low susceptibility areas encompasses 14,123.59 km^2. The stable areas are predominantly situated in the mountainous and hilly areas characterized by extensive distribution of bedrock, covering a total area of 22,136.74 km^2.

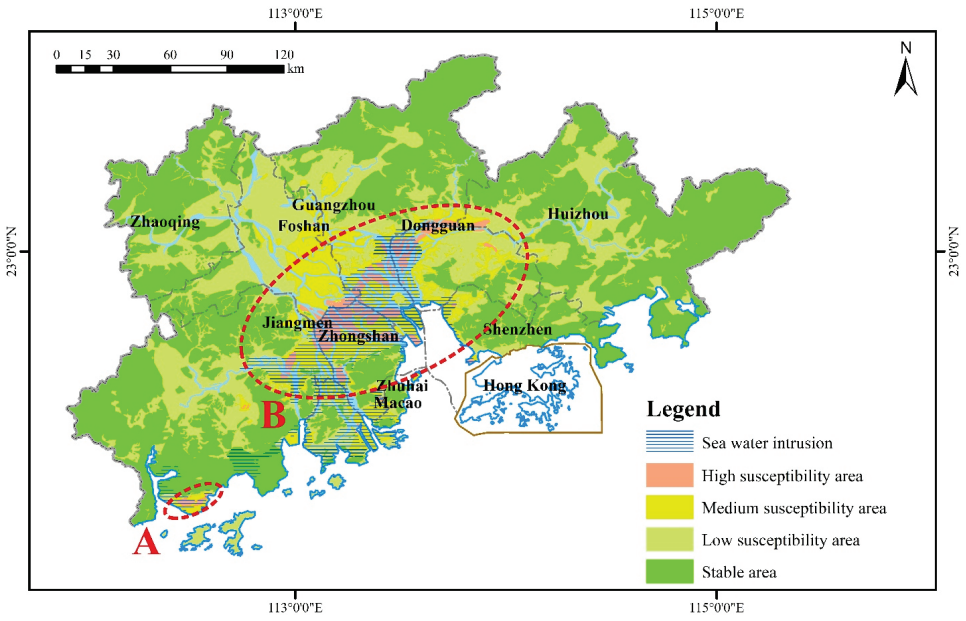

Figure 17. Distribution map of sea water intrusion susceptibility.

4.2. Geo-Environment Vulnerability

The high vulnerability areas are predominantly situated in the southwestern, northwestern, and northeastern mountainous and hilly areas, as well as the central plains of the study area (Figure 18). These areas cover a total area of 5961.85 km^2 and can be further divided into four subareas. Subarea A is situated in the southwestern part of the study area, while Subarea B is located in the northwestern portion. Both subareas exhibit higher susceptibility to landslides, collapses, debris flows, and karst collapses. Subarea C is located in the northwestern section of the study area, exhibiting an elevated susceptibility to landslides, collapses, and debris flows. Subarea D is situated in the central plains of the study area, characterized by a higher susceptibility to karst collapse, ground subsidence, soil erosion, and sea water intrusion. The medium vulnerability areas, low vulnerability areas, and stable areas are interspersed, covering areas of 19,227.93 km^2, 14,892.02 km^2, and 1616.19 km^2, respectively.

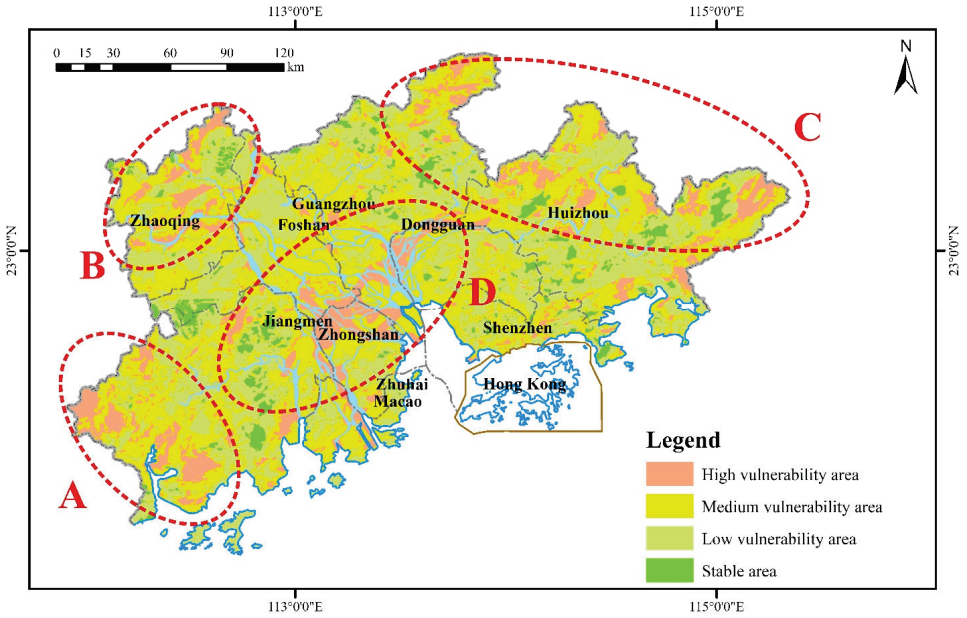

Figure 18. Distribution map of geo-environment vulnerability.

4.3. Accuracy of Assessment Results

In this study, the integration of the AHP and VWT was employed for the assessment of susceptibility to multiple geohazards. In comparison to using only AHP, notable shifts in the weights of factors were observed, resulting in significant changes in the distribution and extent of susceptibility areas (Table 5). The results of geohazard susceptibility assessment should adhere to two sufficiency principles: the density of geohazards gradually increases from stable areas to high susceptibility areas, and the high susceptibility areas occupy a relatively smaller area [115]. Table 5 demonstrates that regardless of whether the VWT-AHP method or the AHP method is employed, the assessment results consistently adhere to the first principle. Except for the susceptibility assessment results for sea water intrusion obtained using the AHP method, all other results also conform to the second principle. It is worth noting that for the same geohazard, the susceptibility assessment results obtained using the VWT-AHP method indicate a higher density of geohazards in the high susceptibility areas compared to the results obtained using the AHP method. A similar trend is observed for the density of geohazards in the medium susceptibility areas for debris flows, ground subsidence, soil erosion, and sea water intrusion.

Table 5. Results of susceptibility assessment of geohazards.

Geohazard	Method	Area	Stable	Low	Medium	High
Landslide and collapse	VWT-AHP	Area (km^2)	18,645.75	9688.68	9848.89	3514.68
		Number of geohazards	3	3	22	56
		Density of geohazards	0.0002	0.0003	0.0022	0.0159
	AHP	Area (km^2)	20,079.53	11,597.94	8076.18	1944.34
		Number of geohazards	8	25	37	13
		Density of geohazards	0.0004	0.0022	0.0046	0.0067
Debris flow	VWT-AHP	Area (km^2)	10,692.25	26,905.16	3619.66	480.94
		Number of geohazards	2	1	11	9
		Density of geohazards	0.0002	0.0000	0.0030	0.0187
	AHP	Area (km^2)	14,253.97	19,483.31	6716.05	1244.67
		Number of geohazards	5	6	9	3
		Density of geohazards	0.0004	0.0003	0.0013	0.0024

Table 5. *Cont.*

Geohazard	Method	Area	Stable	Low	Medium	High
Karst collapse	VWT-AHP	Area (km^2)	36,841.23	1812.95	2553.61	484.94
		Number of geohazards	0	1	39	57
		Density of geohazards	0.0000	0.0006	0.0153	0.1175
	AHP	Area (km^2)	36,841.23	3033.69	1752.37	65.42
		Number of geohazards	0	24	62	11
		Density of geohazards	0.0000	0.0079	0.0354	0.1681
Ground subsidence	VWT-AHP	Area (km^2)	33,007.04	4468.67	3741.2	454.65
		Number of geohazards	0	1	33	31
		Density of geohazards	0.0000	0.0002	0.0088	0.0682
	AHP	Area (km^2)	33,007.04	1109.03	5616.46	1939.02
		Number of geohazards	0	0	25	40
		Density of geohazards	0.0000	0.0000	0.0045	0.0206
Soil erosion	VWT-AHP	Area (km^2)	13,081.98	22,743.83	5526.97	344.54
		Area of geohazards (km^2)	71.96	252.77	627.08	133.84
		Density of geohazards	0.0055	0.0111	0.1135	0.3885
	AHP	Area (km^2)	14,525.31	15,470.48	10,386.07	1315.47
		Area of geohazards (km^2)	81.36	180.78	548.36	275.17
		Density of geohazards	0.0056	0.0117	0.0528	0.2092
Sea water intrusion	VWT-AHP	Area (km^2)	22,136.74	14,123.59	4341.74	1095.33
		Area of geohazards (km^2)	471.08	1277.44	1893.99	889.54
		Density of geohazards	0.0213	0.0904	0.4362	0.8121
	AHP	Area (km^2)	20,285.86	9269.77	8698.65	3443.12
		Area of geohazards (km^2)	196.89	846.61	1875	413.55
		Density of geohazards	0.0097	0.0913	0.2156	0.1201

The Receiver Operating Characteristic (ROC) curve serves as a tool for quantitative analysis to gauge the precision of models, with the Area Under the Curve (AUC) value falling within the range of 0.1 to 1.0 [116,117]. A higher AUC value indicates enhanced model accuracy, with an AUC value of 1.0 signifying optimal accuracy. An AUC value below 0.5 suggests that the model's predictive ability is less precise than random chance. Based on the AUC value, the performance of the assessment model is classified as excellent (0.9–1.0), very good (0.8–0.9), good (0.7–0.8), general (0.6–0.7), or poor (0.5–0.6) [118,119]. The ROC curves illustrating the susceptibility assessment results for different geohazards are shown in Figure 19. The AUC values demonstrate that the utilization of VWT-AHP in assessing the susceptibility of various geohazards consistently yields outcomes categorized as "very good", while the employment of AHP alone results in classifications of "good" or "general". This suggests a reasonable determination of constant weights of each assessment indicator, with the variable weights calculated by VWT more closely aligned with the actual conditions of the study area. For the assessment of geohazard susceptibility, the VWT-AHP model demonstrates higher precision compared to AHP alone.

In addition, a comparison was made with other studies focusing on geohazard susceptibility within the study area. Zhang et al. (2019) [55] conducted landslide susceptibility assessments using the AHP method with ten random samples, resulting in ROC curves with a maximum AUC value of 0.855, a minimum of 0.791, and an average of 0.831. This closely aligns with the AUC value of 0.82 obtained in this study. Lin et al. (2019) [58] employed a Bayesian averaging approach, combining three machine learning models for predicting sea water intrusion susceptibility, achieving a Nash-Sutcliffe Efficiency Coefficient (NSE) of 0.79, indicating a good fit. In this study, an AUC value of 0.81 was achieved, classified as "very good". However, it is essential to acknowledge that comparing the accuracy of results between classification and regression tasks is not straightforward. Liu et al. (2023) [57] investigated ground subsidence in a specific area of the Pearl River Delta using an RF

model, yielding an R^2 of 0.579. In contrast, this study achieved an AUC value of 0.84. Notably, the spatial patterns of ground subsidence susceptibility obtained from the two studies were not significantly different.

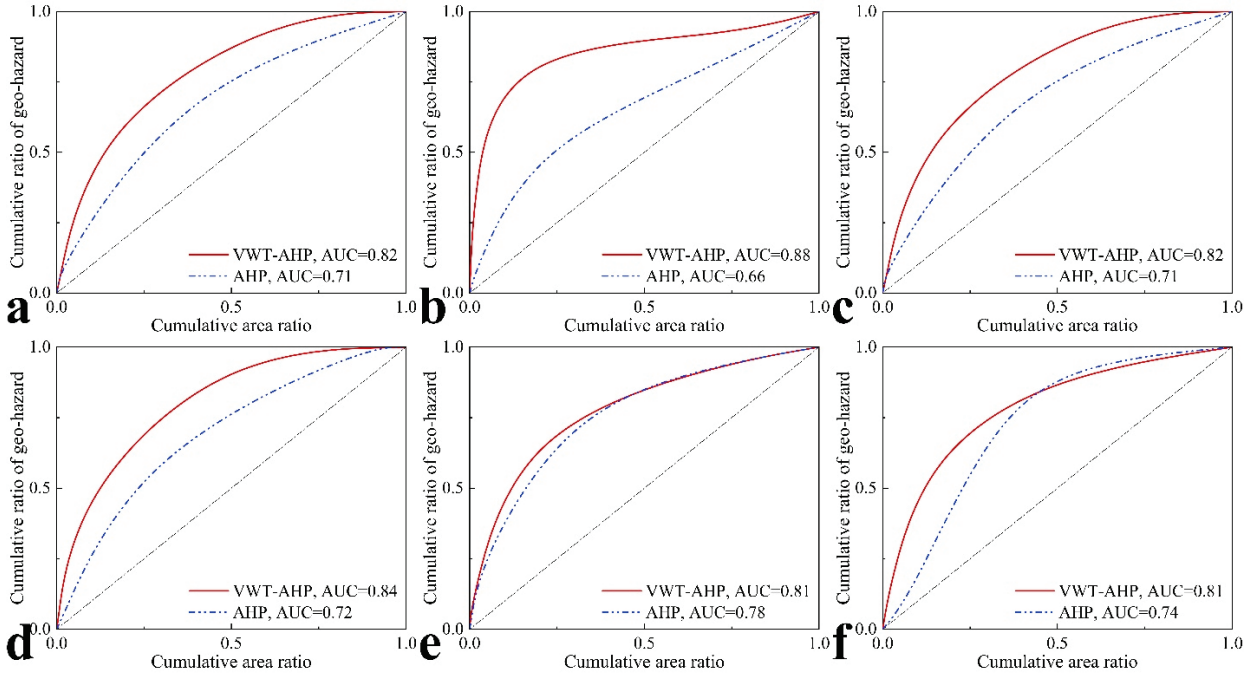

Figure 19. ROC curves of susceptibility assessment results for various geohazards. (**a**) Landslide and collapse, (**b**) Debris flow, (**c**) Karst collapse, (**d**) Ground subsidence, (**e**) Soil erosion, (**f**) Sea water intrusion.

4.4. Single-Indicator Sensitivity Analysis

The single-indicator sensitivity analysis is utilized to assess the spatial importance of each indicator in the assessment of geohazard susceptibility [120]. Higher effective weights indicate a more pronounced importance of factors in the geohazard susceptibility assessment. The calculation method for effective weights is presented in Equation (10).

$$W_i = \frac{x_i \cdot w_i'}{CPI} \tag{10}$$

In Equation (10), the symbol x_j represents the rating of the i-th indicator, w_i' indicates the variable weight vector of the i-th indicator, CPI represents the comprehensive index.

Table 6 presents the maximum, minimum, average, and standard deviation values of the effective weights of each assessment indicator. The effective weights reveal that in the assessment of landslide and collapse susceptibility, topography and lithology are indispensable crucial indicators. For debris flow susceptibility, topography and landform remain highly significant, but the impact of the distance to river should not be disregarded. In the assessment of karst collapse susceptibility, the distance to fault emerges as the paramount indicator, followed by lithology. In the assessment of ground subsidence susceptibility, the age of soft soil layer holds the most significant effective weight. The most significant effective factor for soil erosion susceptibility is the type of vegetation, followed by distance to river and topography. In the assessment of sea water intrusion susceptibility, precipitation holds the highest level of effect, followed by topography and type of Quaternary sedimentary rock.

Table 6. Results of single-indicator sensitivity analysis.

Geohazard Susceptibility	Assessment Indicator	Maximum	Minimum	Average	Standard Deviation
Landslide and collapse (A_1)	Elevation (B_{11})	0.6089	0.0133	0.1004	0.0877
	Slope (B_{12})	0.4058	0.0106	0.0492	0.0371
	Lithology (B_{13})	0.8187	0.0280	0.2413	0.1969
	Topography (B_{14})	0.6304	0.0096	0.1844	0.1407
	Distance to fault (B_{15})	0.6512	0.0100	0.1453	0.1435
	Distance to river (B_{16})	0.4906	0.0059	0.0952	0.0904
	Precipitation (B_{17})	0.8034	0.0218	0.1842	0.1232
Debris flow (A_2)	Elevation (B_{21})	0.3267	0.0063	0.0403	0.0383
	Slope (B_{22})	0.3539	0.0069	0.0318	0.0267
	Lithology (B_{23})	0.6452	0.0112	0.1638	0.1372
	Topography (B_{24})	0.6646	0.0135	0.2371	0.1696
	Distance to fault (B_{25})	0.5780	0.0080	0.1008	0.0990
	Distance to river (B_{26})	0.7111	0.0162	0.1680	0.1411
	Distance to landslide and collapse (B_{27})	0.7722	0.0206	0.0960	0.1028
	Precipitation(B_{28})	0.7722	0.0207	0.1621	0.1123
Karst collapse (A_3)	Lithology (B_{31})	0.7268	0.0603	0.2707	0.1429
	Degree of karst development (B_{32})	0.7268	0.0587	0.1748	0.0946
	Thickness of overlying layer (B_{33})	0.4356	0.0161	0.1288	0.1149
	Water yield property (B_{34})	0.4356	0.0178	0.0852	0.0531
	Distance to fault (B_{35})	0.6833	0.0491	0.3405	0.1852
Ground subsidence (A_4)	Thickness of soft soil layer (B_{41})	0.7917	0.0747	0.1872	0.1114
	Age of soft soil layer (B_{42})	0.7683	0.1054	0.5342	0.1878
	Water yield property (B_{43})	0.4935	0.0203	0.0826	0.0690
	Distance to fault (B_{44})	0.6223	0.0376	0.1960	0.1396
Soil erosion (A_5)	Slope (B_{51})	0.3794	0.0077	0.0398	0.0356
	Topography (B_{52})	0.5837	0.0082	0.1825	0.1612
	Type of vegetation (B_{53})	0.8482	0.0295	0.3052	0.2061
	Type of soil (B_{54})	0.8290	0.0305	0.1728	0.1076
	Distance to river (B_{55})	0.7106	0.0152	0.2072	0.1488
	Precipitation (B_{56})	0.6175	0.0089	0.0925	0.0765
Sea water intrusion (A_6)	Topography (B_{61})	0.6626	0.0155	0.2534	0.1756
	Type of Quaternary sedimentary rock (B_{62})	0.7534	0.0240	0.2046	0.1731
	Groundwater level (B_{63})	0.8753	0.0496	0.1346	0.0829
	Precipitation (B_{64})	0.8054	0.0270	0.4074	0.1521

4.5. Geo-Hazard Prevention Strategies

The distribution of critical infrastructures, roads, and artificial surfaces in various geo-environment vulnerability areas is presented in Figure 20 and Table 7. The distribution in different geohazard susceptibility areas can be found in Figure S8 and Table S13.

Table 7. Distribution of critical infrastructures, roads, and artificial surfaces in different vulnerability areas.

	Stable	Low	Medium	High
Critical infrastructure	8	175	512	102
Road (km)	575.43	10,258.47	16,550.36	3890.09
Artificial surface (km^2)	18.95	447.95	1653.15	359.71

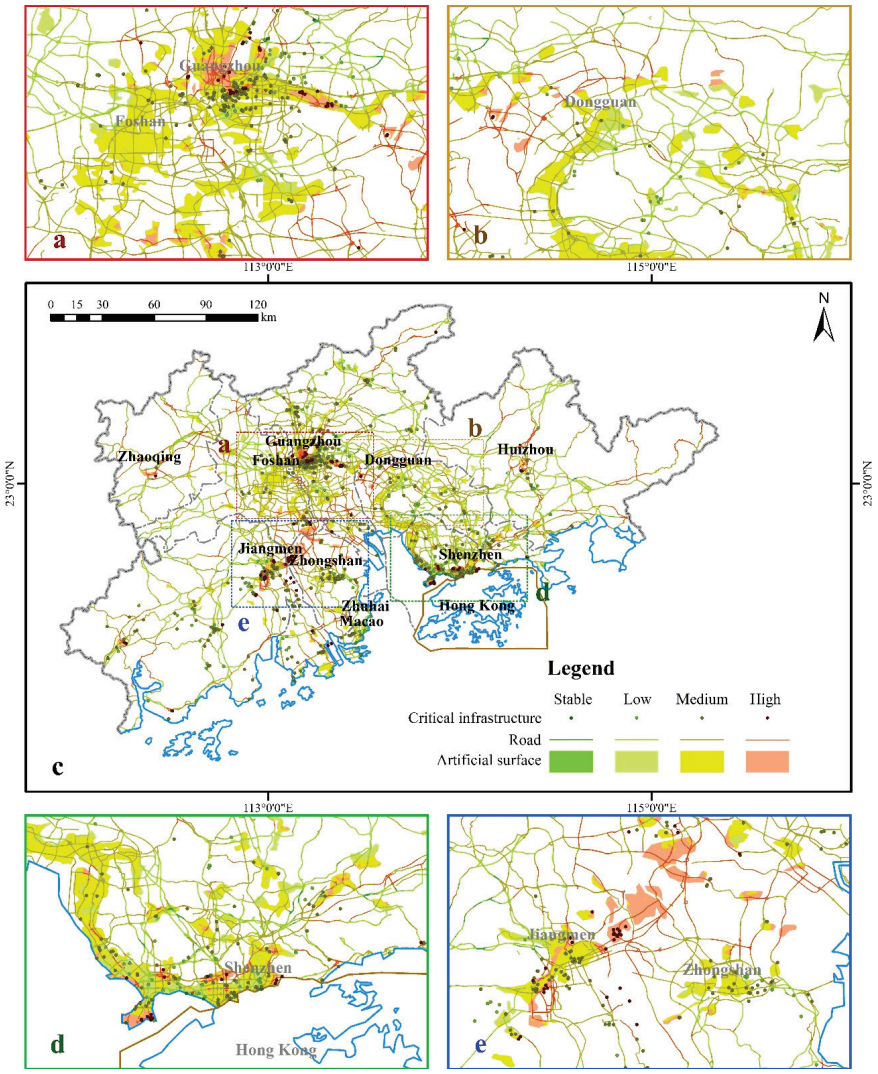

Figure 20. Distribution maps of critical infrastructures, roads, and artificial surfaces in different vulnerability areas. (**a**) Guangzhou and Foshan, (**b**) Dongguan, (**c**) the entire study area, (**d**) Shenzhen, (**e**) Jiangmen and Zhongshan.

The critical infrastructures and artificial surfaces are primarily located in medium and high geo-environment vulnerability areas, particularly in the major cities in the study area (Figure 20). Guangzhou, Shenzhen, and Jiangmen face significant threats from landslides, collapses, and debris flows. When selecting locations for critical infrastructure, it is crucial to avoid faults and hazardous slopes. Simultaneously, identifying potential hazard-prone areas is essential for implementing early protective measures or considering relocation. Karst collapses also pose a threat to Guangzhou and Foshan, mainly due to the widespread distribution of soluble rocks and the thickness of overlying layers. Conducting a comprehensive assessment of karst development and implementing measures such as reinforcement in vulnerable areas is necessary. Foshan and Jiangmen need to address the threat of ground subsidence. New construction should strictly control ground loads, and in areas prone to subsidence attention should be paid to controlling groundwater extraction and implementing groundwater recharge measures if necessary. Soil erosion and sea water intrusion are common challenges faced by all cities. Soil erosion often arises large-scale urban development, extensive agricultural activities, and low vegetation cover. Enhancing vegetation restoration, planning protective forests, and implementing sustainable land management practices are advisable to mitigate soil erosion. Sea water intrusion primarily results from groundwater extraction during urbanization. It is recommended to establish

effective coastal management policies, construct protective structures such as seawalls, and manage groundwater extraction rationally to address sea water intrusion issues.

Over half of the road mileage is situated in medium and high geo-environment vulnerability areas. In urban areas, roads encounter geohazard threats akin to critical infrastructure. In mountainous areas, road construction is mainly impacted by landslides, collapses, and debris flows. Hence, it is essential to identify potential threats during road planning, avoid areas with fractured rock slopes and valleys, and implement protective measures for hazardous slopes.

4.6. Limitation and Future Research

This study is inherently constrained by certain limitations. The availability of data has imposed significant constraints on the selection of indicators for assessing geohazard susceptibility. Notably, the absence of long-term monitoring data for groundwater levels represents a substantial limitation, impeding the acquisition of crucial indicators of susceptibility to ground subsidence and sea water intrusion [121,122]. On the other hand, within the VWT-AHP method, the judgment matrix is established by researchers, introducing a notable element of subjectivity. Even though results with relatively high accuracy have been obtained, to enhance the objectivity and precision of weights, alternative methodologies such as regression models, decision trees, and artificial neural networks could be considered [123–125].

Geohazard susceptibility is a crucial aspect of disaster prevention and management. Nevertheless, the devastating impacts of geohazards are not solely contingent on susceptibility, but also intricately linked to regional economic progress and human activities. The geo-environment vulnerability assessed in this study is rooted in the susceptibility to diverse geohazards. Due to the determination of geo-environment vulnerability based on the principle of the "barrel effect", there is a possibility of an overestimation of vulnerability levels in certain areas. As a result, it serves merely as a fundamental point of reference for the systematic development of strategies in geohazard management and economic growth planning. The alignment of geological circumstances with human activities remains a pivotal concern that local administrations and researchers must conscientiously address.

5. Conclusions

In conclusion, this study successfully demonstrates the methodology of using VWT-AHP for assessing geo-environment vulnerability based on susceptibility to various geohazards. The application of this method resulted in the classification of the Pearl River Delta in China into high vulnerability (5961.85 km^2), medium vulnerability (19,227.93 km^2), low vulnerability (14,892.02 km^2), and stable areas (1616.19 km^2). The ROC curves indicate that the accuracy and reliability of VWT-AHP are significantly improved compared to the standalone use of AHP. Furthermore, the study assessed the threats posed by various geohazards to critical infrastructure, roads, and artificial surfaces, while discussing prevention measures.

However, the study does acknowledge several limitations. The constrained availability of data limited the selection of indicators for assessment, particularly the absence of long-term groundwater level data which impacted the assessment of susceptibility to ground subsidence and sea water intrusion. Furthermore, the subjectivity inherent in the establishment of judgment matrices within VWT-AHP underscores the necessity of exploring alternative methodologies to enhance the objectivity of factor weights.

It is crucial to recognize that geo-environment vulnerability is just one facet of disaster prevention and management. The broader impacts of geohazards are interlinked with regional economic development and human activities. The geo-environment vulnerability identified in this study serves as a crucial reference for informed decision-making in geohazard management and economic planning. Balancing geological considerations with human actions emerges as a critical imperative for local governance.

Supplementary Materials: The following supporting information can be downloaded at: https://www.mdpi.com/article/10.3390/rs15205007/s1. Figure S1: Distribution map of assessment units of landslide and collapse susceptibility; Figure S2: Distribution map of assessment units of debris flow susceptibility; Figure S3: Distribution map of assessment units of karst collapse susceptibility; Figure S4: Distribution map of assessment units of ground subsidence susceptibility; Figure S5: Distribution map of assessment units of soil erosion susceptibility; Figure S6: Distribution map of assessment units of sea water intrusion susceptibility; Figure S7: Distribution map of assessment units of geo-environment vulnerability; Figure S8: Distribution of critical infrastructures, roads, and artificial surfaces in different susceptibility areas; Table S1: Judgment matrix and constant weights of each indicator for landslide and collapse susceptibility; Table S2: Judgment matrix and constant weights of each indicator for debris flow susceptibility; Table S3: Judgment matrix and constant weights of each indicator for karst collapse susceptibility; Table S4: Judgment matrix and constant weights of each indicator for ground subsidence susceptibility; Table S5: Judgment matrix and constant weights of each indicator for soil erosion susceptibility; Table S6: Judgment matrix and constant weights of each indicator for sea water intrusion susceptibility; Table S7: Variable weights of each indicator for landslide and collapse susceptibility; Table S8: Variable weights of each indicator for debris flow susceptibility; Table S9: Variable weights of each indicator for karst collapse susceptibility; Table S10: Variable weights of each indicator for ground subsidence susceptibility; Table S11: Variable weights of each indicator for soil erosion susceptibility; Table S12: Variable weights of each indicator for sea water susceptibility; Table S13: Distribution of critical infrastructures, roads, and artificial surfaces in different susceptibility areas.

Author Contributions: Conceptualization, P.H.; methodology, P.H.; software, P.H.; validation, P.H.; formal analysis, C.M.; investigation, P.H.; resources, X.W.; data curation, X.W.; writing—original draft preparation, P.H.; writing—review and editing, A.Z.; visualization, P.H. and X.W.; supervision, C.M.; project administration, A.Z.; funding acquisition, C.M. All authors have read and agreed to the published version of the manuscript.

Funding: This research was funded by the Fundamental Research Funds for the Central Universities, China University of Geosciences (Wuhan), grant number CUGCJ1822.

Data Availability Statement: The elevation data used in this study are available at https://www.gscloud.cn/ (accessed on 4 July 2023), and other data are available on request from the corresponding author due to privacy restrictions.

Acknowledgments: The authors wish to thank the Guangdong Geological Survey Institute for data curation. The authors also thank Zechen Zhang and Zuo Liu for their assistance in the analysis and visualization. The authors are grateful to the editor and reviewers for their suggestions.

Conflicts of Interest: The authors declare no conflict of interest.

References

1. Zhang, Y.C.; Zhang, F.; Zhang, J.Q.; Guo, E.L.; Liu, X.P.; Tong, Z.J. Research on the Geological Disaster Forecast and Early Warning Model Based on the Optimal Combination Weighing Law and Extension Method: A Case Study in China. *Polish J. Environ. Stud.* **2017**, *26*, 2385–2395. [CrossRef]
2. Metternicht, G.; Hurni, L.; Gogu, R. Remote sensing of landslides: An analysis of the potential contribution to geo-spatial systems for hazard assessment in mountainous environments. *Remote Sens. Environ.* **2005**, *98*, 284–303. [CrossRef]
3. Wang, H.; Qian, G.Q.; Tordesillas, A. Modeling big spatio-temporal geo-hazards data for forecasting by error-correction cointegration and dimension-reduction. *Spatial Stat.* **2020**, *36*, 100432. [CrossRef]
4. Yanar, T.; Kocaman, S.; Gokceoglu, C. Use of Mamdani Fuzzy Algorithm for Multi-Hazard Susceptibility Assessment in a Developing Urban Settlement (Mamak, Ankara, Turkey). *ISPRS Int. J. Geo-Inf.* **2020**, *9*, 114. [CrossRef]
5. Detree, C.; Navarro, J.M.; Font, A.; Gonzalez, M. Species vulnerability under climate change: Study of two sea urchins at their distribution margin. *Sci. Total Environ.* **2020**, *728*, 138850. [CrossRef] [PubMed]
6. Gonzalez, P.; Neilson, R.P.; Lenihan, J.M.; Drapek, R.J. Global patterns in the vulnerability of ecosystems to vegetation shifts due to climate change. *Glob. Ecol. Biogeogr.* **2010**, *19*, 755–768. [CrossRef]
7. He, L.; Shen, J.; Zhang, Y. Ecological vulnerability assessment for ecological conservation and environmental management. *J. Environ. Manag.* **2018**, *206*, 1115–1125. [CrossRef]
8. Marshall, D.J.; Pettersen, A.K.; Bode, M.; White, C.R. Developmental cost theory predicts thermal environment and vulnerability to global warming. *Nat. Ecol. Evol.* **2020**, *4*, 406. [CrossRef]

9. Maru, Y.T.; Smith, M.S.; Sparrow, A.; Pinho, P.F.; Dube, O.P. A linked vulnerability and resilience framework for adaptation pathways in remote disadvantaged communities. *Glob. Environ. Chang.* **2014**, *28*, 337–350. [CrossRef]
10. Stevenazzi, S.; Bonfanti, M.; Masetti, M.; Nghiem, S.V.; Sorichetta, A. A versatile method for groundwater vulnerability projections in future scenarios. *J. Environ. Manag.* **2017**, *187*, 365–374. [CrossRef]
11. Talukdar, S.; Pal, S. Wetland habitat vulnerability of lower Punarbhaba river basin of the uplifted Barind region of Indo-Bangladesh. *Geocarto Int.* **2020**, *35*, 857–886. [CrossRef]
12. Yin, L.Z.; Zhu, J.; Li, W.S.; Wang, J.H. Vulnerability Analysis of Geographical Railway Network under Geological Hazard in China. *ISPRS Int. J. Geo-Inf.* **2022**, *11*, 342. [CrossRef]
13. Margat, J. *Vulnerability of Groundwater to Pollution*; BRGM: Orléans, France, 1968.
14. Timmerman, P. *Vulnerability, Resilience and the Collapse of Society: A Review of Models and Possible Climatic Application*; Institute for Environmental Studies: Toronto, ON, Canada, 1981.
15. Smit, B.; Burton, I.; Klein, R.J.T.; Street, R. The Science of Adaptation: A Framework for Assessment. *Mitig. Adapt. Strateg. Glob. Chang.* **1999**, *4*, 199–213. [CrossRef]
16. Huang, Y.Z. Reserch on the Vulnerability of Geological Environment and Its Countermeasures in Lijiang. Ph.D. Thesis, Kunming University of Science and Technology, Kunming, China, 2010. (In Chinese).
17. Ma, C.M.; Wu, X.Y.; Li, B.; Gao, L.; Li, Q. The vulnerability evaluation of regional geo-environment: A case study in Beihai City, China. *Environ. Earth Sci.* **2019**, *78*, 129. [CrossRef]
18. Arnous, M.O.; Green, D.R. GIS and remote sensing as tools for conducting geo-hazards risk assessment along Gulf of Aqaba coastal zone, Egypt. *J. Coast. Conserv.* **2011**, *15*, 457–475. [CrossRef]
19. Pourghasemi, H.R.; Gayen, A.; Edalat, M.; Zarafshar, M.; Tiefenbacher, J.P. Is multi-hazard mapping effective in assessing natural hazards and integrated watershed management? *Geosci. Front.* **2020**, *11*, 1203–1217. [CrossRef]
20. Ma, C.M.; Yan, W.; Hu, X.J.; Kuang, H. Geo-environment risk assessment in Zhengzhou City, China. *Geomat. Nat. Hazards Risk* **2020**, *11*, 40–70. [CrossRef]
21. Chang, M.; Dou, X.Y.; Tang, L.L.; Xu, H.Z. Risk assessment of multi-disaster in Mining Area of Guizhou, China. *Int. J. Disaster Risk Reduct.* **2022**, *78*, 103128. [CrossRef]
22. Li, P.X.; Wang, B.; Chen, P.; Zhang, Y.L.; Zhao, S.H. Vulnerability assessment of the eco-geo-environment of mining cities in arid and semi-arid areas: A case study from Zhungeer, China. *Ecol. Indic.* **2023**, *152*, 110364. [CrossRef]
23. Jie, M.L.; Ju, N.P.; Zhao, J.J.; Fan, Q.; He, C.Y. Comparative analysis on classification methods of geological disaster susceptibility assessment. *Geomat. Inf. Sci. Wuhan Univ.* **2021**, *45*, 1003–1014. (In Chinese) [CrossRef]
24. Reichenbach, P.; Rossi, M.; Malamud, B.D.; Mihir, M.; Guzzetti, F. A review of statistically-based landslide susceptibility models. *Earth-Sci. Rev.* **2018**, *180*, 60–91. [CrossRef]
25. Wei, H.; Pierre-Yves, H.; Xu, Q.; Theo, V.; Wang, G.H. Experimental Study of Fluidized Landslide. In Proceedings of the 4th World Landslide Forum, Ljubljana, Slovenia, 29 May–2 June 2017; pp. 477–479. [CrossRef]
26. Shano, L.; Raghuvanshi, T.K.; Meten, M. Landslide susceptibility evaluation and hazard zonation techniques—A review. *Geoenviron. Disasters* **2020**, *7*, 18. [CrossRef]
27. Das, G.; Lepcha, K. Application of logistic regression (LR) and frequency ratio (FR) models for landslide susceptibility mapping in Relli Khola river basin of Darjeeling Himalaya, India. *SN Appl. Sci.* **2019**, *1*, 1453. [CrossRef]
28. Papadopoulou-Vrynioti, K.; Bathrellos, G.D.; Skilodimou, H.D.; Kaviris, G.; Makropoulos, K. Karst collapse susceptibility mapping considering peak ground acceleration in a rapidly growing urban area. *Eng. Geol.* **2013**, *158*, 77–88. [CrossRef]
29. Kontoes, C.; Loupasakis, C.; Papoutsis, I.; Alatza, S.; Poyiadji, E.; Ganas, A.; Psychogyiou, C.; Kaskara, M.; Antoniadi, S.; Spanou, N. Landslide Susceptibility Mapping of Central and Western Greece, Combining NGI and WoE Methods, with Remote Sensing and Ground Truth Data. *Land* **2021**, *10*, 402. [CrossRef]
30. Li, Y.M.; Deng, X.L.; Ji, P.K.; Yang, Y.M.; Jiang, W.X.; Zhao, Z.F. Evaluation of Landslide Susceptibility Based on CF-SVM in Nujiang Prefecture. *Int. J. Environ. Res. Public Health* **2022**, *19*, 14248. [CrossRef]
31. Wang, G.L.; Hao, J.Y.; Wen, H.J.; Cao, C. A random forest model of karst ground collapse susceptibility based on factor and parameter coupling optimization. *Geocarto Int.* **2022**, *37*, 15548–15567. [CrossRef]
32. Yu, H.R.; Arabameri, A.; Costache, R.; Craciun, A.; Arora, A. Land subsidence susceptibility assessment using advanced artificial intelligence models. *Geocarto Int.* **2022**, *37*, 18067–18093. [CrossRef]
33. Cui, H.; Ma, C.M.; Tan, X.F.; Chen, H.N.; Hu, B.; Xu, S.M.; Tan, X.Q.; Zhang, Y. Evaluation of Jining mining subsidence susceptibility based on three multiple-criteria decision analysis methods. *Geocarto Int.* **2023**, *38*, 2248069. [CrossRef]
34. Raghuvanshi, T.K.; Ibrahim, J.; Ayalew, D. Slope stability susceptibility evaluation parameter (SSEP) rating scheme—An approach for landslide hazard zonation. *J. Afr. Earth Sci.* **2014**, *99*, 595–612. [CrossRef]
35. Kumar, R.; Dwivedi, S.B.; Gaur, S. A comparative study of machine learning and Fuzzy-AHP technique to groundwater potential mapping in the data-scarce region. *Comput. Geosci.* **2021**, *155*, 104855. [CrossRef]
36. Schey, C.; Krabbe, P.F.M.; Postma, M.J.; Connolly, M.P. Multi-criteria decision analysis (MCDA): Testing a proposed MCDA framework for orphan drugs. *Orphanet J. Rare Dis.* **2017**, *12*, 10. [CrossRef] [PubMed]
37. Lim, K.S.; Lee, D.R. The spatial MCDA approach for evaluating flood damage reduction alternatives. *KSCE J. Civ. Eng.* **2009**, *13*, 359–369. [CrossRef]

38. Tadesse, T.B.; Tefera, S.A. Comparing potential risk of soil erosion using RUSLE and MCDA techniques in Central Ethiopia. *Model. Earth Syst. Environ.* **2021**, *7*, 1713–1725. [CrossRef]
39. Maciol, A.; Rebiasz, B. Multicriteria Decision Analysis (Mcda) Methods in Life Cycle Assessment (Lca). A Comparison of Private Passenger Vehicles. *Oper. Res. Decis.* **2018**, *28*, 5–26. [CrossRef]
40. Tangestani, M.H. Landslide susceptibility mapping using the fuzzy gamma approach in a GIS, Kakan catchment area, southwest Iran. *Aust. J. Earth Sci.* **2004**, *51*, 439–450. [CrossRef]
41. Jabbar, F.K.; Grote, K.; Tucker, R.E. A novel approach for assessing watershed susceptibility using weighted overlay and analytical hierarchy process (AHP) methodology: A case study in Eagle Creek Watershed, USA. *Environ. Sci. Pollut. Res.* **2019**, *26*, 31981–31997. [CrossRef]
42. Saaty, T.L. *The Analytic Hierarchy Process*; McGraw-Hill: New York, NY, USA, 1980.
43. Saaty, T.L. The Modern Science of Multicriteria Decision Making and Its Practical Applications: The AHP/ANP Approach. *Oper. Res.* **2013**, *61*, 1101–1118. [CrossRef]
44. Basu, T.; Pal, S. A GIS-based factor clustering and landslide susceptibility analysis using AHP for Gish River Basin, India. *Environ. Dev. Sustain.* **2020**, *22*, 4787–4819. [CrossRef]
45. Chen, W.; Han, H.X.; Huang, B.; Huang, Q.L.; Fu, X.D. Variable-Weighted Linear Combination Model for Landslide Susceptibility Mapping: Case Study in the Shennongjia Forestry District, China. *ISPRS Int. J. Geo-Inf.* **2017**, *6*, 347. [CrossRef]
46. Shu, B.R.; Bakker, M.M.; Zhang, H.H.; Li, Y.L.; Qin, W.; Carsjens, G.J. Modeling urban expansion by using variable weights logistic cellular automata: A case study of Nanjing, China. *Int. J. Geogr. Inf. Sci.* **2017**, *31*, 1314–1333. [CrossRef]
47. Wu, Q.; Zhao, D.K.; Wang, Y.; Shen, J.J.; Mu, W.P.; Liu, H.L. Method for assessing coal-floor water-inrush risk based on the variable-weight model and unascertained measure theory. *Hydrogeol. J.* **2017**, *25*, 2089–2103. [CrossRef]
48. Hou, J.D.; Lv, J.; Chen, X.; Yu, S.W. China's regional social vulnerability to geological disasters: Evaluation and spatial characteristics analysis. *Nat. Hazards* **2016**, *84*, S97–S111. [CrossRef]
49. Cui, Q.L.; Wu, H.N.; Shen, S.L.; Xu, Y.S.; Ye, G.L. Chinese karst geology and measures to prevent geohazards during shield tunnelling in karst region with caves. *Nat. Hazards* **2015**, *77*, 129–152. [CrossRef]
50. Du, Y.N.; Feng, G.C.; Liu, L.; Fu, H.Q.; Peng, X.; Wen, D.B. Understanding Land Subsidence Along the Coastal Areas of Guangdong, China, by Analyzing Multi-Track MTInSAR Data. *Remote Sens.* **2020**, *12*, 299. [CrossRef]
51. Liu, X.L.; Chen, H.Z. Integrated assessment of ecological risk for multi-hazards in Guangdong province in southeastern China. *Geomat. Nat. Hazards Risk* **2019**, *10*, 2069–2093. [CrossRef]
52. Zhu, Z.Y.; Xie, J.B.; Zhang, J.G.; Liang, H.X.; Qiu, Y.; Xia, Z.; Ling, Q.X.; Lin, J.A.; Zhou, H.Y. Characteristics of geological hazards in South China coastal areas and impact on regional sustainable development. *Int. J. Sustain. Dev. World Ecol.* **2007**, *14*, 421–427. [CrossRef]
53. GPDPRYEC. *Guangdong Province Disaster Prevention and Reduction Yearbook*; South China University of Technology Press: Guangzhou, China, 2010. (In Chinese)
54. Zeng, M.; Liu, F.M. The main geo-environment problems and countermeasure research of the coastal zone of Pearl River Estuary. In *AER—Advances in Engineering Research, 4th International Conference on Sustainable Energy and Environmental Engineering (ICSEEE), Shenzhen, China, 20–21 December 2015*; Atlantis Press: Amsterdam, The Netherlands, 2016; pp. 942–946.
55. Zhang, H.R.; Zhang, G.F.; Jia, Q.W. Integration of Analytical Hierarchy Process and Landslide Susceptibility Index Based Landslide Susceptibility Assessment of the Pearl River Delta Area, China. *IEEE J. Sel. Top. Appl. Earth Obs. Remote Sens.* **2019**, *12*, 4239–4251. [CrossRef]
56. Dou, J.; Zheng, X.Z.; Qian, J.P.; Liu, R.H.; Wu, Q.T. Intelligence Based Automatic Detection and Classification of Ground Collapses Using Object-Based Image Analysis Method: A Case Study in Paitan of Pearl River Delta. In *Geoinformatics 2008 and Joint Conference on GIS and Built Environment—Advanced Spatial Data Models and Analyses*; SPIE: Bellingham, WA, USA, 2008. [CrossRef]
57. Liu, Z.Y.; Ng, A.H.M.; Wang, H.; Chen, J.W.; Du, Z.Y.; Ge, L.L. Land subsidence modeling and assessment in the West Pearl River Delta from combined InSAR time series, land use and geological data. *Int. J. Appl. Earth Obs. Geoinf.* **2023**, *118*, 103228. [CrossRef]
58. Lin, K.R.; Lu, P.Y.; Xu, C.Y.; Yu, X.; Lan, T.; Chen, X.H. Modeling saltwater intrusion using an integrated Bayesian model averaging method in the Pearl River Delta. *J. Hydroinf.* **2019**, *21*, 1147–1162. [CrossRef]
59. Geospatial Data Cloud. Available online: https://www.gscloud.cn/ (accessed on 4 July 2023). (In Chinese)
60. Soil Science Database. Available online: http://vdb3.soil.csdb.cn/ (accessed on 4 July 2023). (In Chinese)
61. Li, Y.Y.; Sheng, Y.F.; Chai, B.; Zhang, W.; Zhang, T.L.; Wang, J.J. Collapse susceptibility assessment using a support vector machine compared with back-propagation and radial basis function neural networks. *Geomat. Nat. Hazards Risk* **2020**, *11*, 510–534. [CrossRef]
62. Psomiadis, E.; Papazachariou, A.; Soulis, K.X.; Alexiou, D.S.; Charalampopoulos, I. Landslide Mapping and Susceptibility Assessment Using Geospatial Analysis and Earth Observation Data. *Land* **2020**, *9*, 133. [CrossRef]
63. Qasimi, A.B.; Isazade, V.; Enayat, E.; Nadry, Z.; Majidi, A.H. Landslide susceptibility mapping in Badakhshan province, Afghanistan: A comparative study of machine learning algorithms. *Geocarto Int.* **2023**, *38*, 2248082. [CrossRef]
64. Pandey, A.; Sarkar, M.S.; Palni, S.; Parashar, D.; Singh, G.; Kaushik, S.; Chandra, N.; Costache, R.; Singh, A.P.; Mishra, A.P.; et al. Multivariate statistical algorithms for landslide susceptibility assessment in Kailash Sacred landscape, Western Himalaya. *Geomat. Nat. Hazards Risk* **2023**, *14*, 2227324. [CrossRef]

65. Basharat, M.; Khan, J.A.; Abdo, H.G.; Almohamad, H. An integrated approach based landslide susceptibility mapping: Case of Muzaffarabad region, Pakistan. *Geomat. Nat. Hazards Risk* **2023**, *14*, 2210255. [CrossRef]
66. Taalab, K.; Cheng, T.; Zhang, Y. Mapping landslide susceptibility and types using Random Forest. *Big Earth Data* **2018**, *2*, 159–178. [CrossRef]
67. Bouzerda, M.; Mehdi, K.; Fadili, A.; Boualla, O. Collapse dolines susceptibility mapping using frequency ratio method and GIS in Sahel-Doukkala, Morocco. *Model. Earth Syst. Environ.* **2020**, *6*, 349–362. [CrossRef]
68. Bregoli, F.; Medina, V.; Chevalier, G.; Hurlimann, M.; Bateman, A. Debris-flow susceptibility assessment at regional scale: Validation on an alpine environment. *Landslides* **2015**, *12*, 437–454. [CrossRef]
69. Cama, M.; Lombardo, L.; Conoscenti, C.; Rotigliano, E. Improving transferability strategies for debris flow susceptibility assessment: Application to the Saponara and Itala catchments (Messina, Italy). *Geomorphology* **2017**, *288*, 52–65. [CrossRef]
70. Kang, S.; Lee, S.R. Debris flow susceptibility assessment based on an empirical approach in the central region of South Korea. *Geomorphology* **2018**, *308*, 1–12. [CrossRef]
71. Shen, C.W.; Lo, W.C.; Chen, C.Y. Evaluating Susceptibility of Debris Flow Hazard using Multivariate Statistical Analysis in Hualien County. *Disaster Adv.* **2012**, *5*, 743–755.
72. Qin, S.W.; Lv, J.F.; Cao, C.; Ma, Z.J.; Hu, X.Y.; Liu, F.; Qiao, S.S.; Dou, Q. Mapping debris flow susceptibility based on watershed unit and grid cell unit: A comparison study. *Geomat. Nat. Hazards Risk* **2019**, *10*, 1648–1666. [CrossRef]
73. Mehmood, Q.; Qing, W.; Chen, J.P.; Yan, J.H.; Ammar, M.; Rahman, G. Nasrullah Susceptibility Assessment of Single Gully Debris Flow Based on AHP and Extension Method. *Civil Eng. J. Tehran* **2021**, *7*, 953–973. [CrossRef]
74. Li, K.; Zhao, J.S.; Lin, Y.L. Debris-flow susceptibility assessment in Dongchuan using stacking ensemble learning including multiple heterogeneous learners with RFE for factor optimization. *Nat. Hazards* **2023**, *118*, 2477–2511. [CrossRef]
75. Zhang, K.; Zheng, W.B.; Liao, Z.Y.; Xie, H.P.; Zhou, C.T.; Chen, S.G.; Zhu, J.B. Risk assessment of ground collapse along tunnels in karst terrain by using an improved extension evaluation method. *Tunnell. Underground Space Technol.* **2022**, *129*, 104669. [CrossRef]
76. Xie, Y.H.; Zhang, B.H.; Liu, Y.X.; Liu, B.C.; Zhang, C.F.; Lin, Y.S. Evaluation of the Karst Collapse Susceptibility of Subgrade Based on the AHP Method of ArcGIS and Prevention Measures: A Case Study of the Quannan Expressway, Section K1379+300-K1471+920. *Water* **2022**, *14*, 1432. [CrossRef]
77. Kim, Y.J.; Nam, B.H.; Shamet, R.; Soliman, M.; Youn, H. Development of Sinkhole Susceptibility Map of East Central Florida. *Nat. Hazards Rev.* **2020**, *21*, 04020035. [CrossRef]
78. Tomas, R.; Romero, R.; Mulas, J.; Marturia, J.J.; Mallorqui, J.J.; Lopez-Sanchez, J.M.; Herrera, G.; Gutierrez, F.; Gonzalez, P.J.; Fernandez, J.; et al. Radar interferometry techniques for the study of ground subsidence phenomena: A review of practical issues through cases in Spain. *Environ. Earth Sci.* **2014**, *71*, 163–181. [CrossRef]
79. Catalao, J.; Nico, G.; Lollino, P.; Conde, V.; Lorusso, G.; Silva, C. Integration of InSAR Analysis and Numerical Modeling for the Assessment of Ground Subsidence in the City of Lisbon, Portugal. *IEEE J. Sel. Top. Appl. Earth Obs. Remote Sens.* **2016**, *9*, 1663–1673. [CrossRef]
80. Bianchini, S.; Solari, L.; Del Soldato, M.; Raspini, F.; Montalti, R.; Ciampalini, A.; Casagli, N. Ground Subsidence Susceptibility (GSS) Mapping in Grosseto Plain (Tuscany, Italy) Based on Satellite InSAR Data Using Frequency Ratio and Fuzzy Logic. *Remote Sens.* **2019**, *11*, 2015. [CrossRef]
81. Lee, S.; Park, I.; Choi, J.K. Spatial Prediction of Ground Subsidence Susceptibility Using an Artificial Neural Network. *Environ. Manage.* **2012**, *49*, 347–358. [CrossRef]
82. Ghasemi, A.; Bahmani, O.; Akhavan, S.; Pourghasemi, H.R. Investigation of land-subsidence phenomenon and aquifer vulnerability using machine models and GIS technique. *Nat. Hazards* **2023**, *118*, 1645–1671. [CrossRef]
83. Mohammadifar, A.; Gholami, H.; Golzari, S. Stacking- and voting-based ensemble deep learning models (SEDL and VEDL) and active learning (AL) for mapping land subsidence. *Environ. Sci. Pollut. Res.* **2023**, *30*, 26580–26595. [CrossRef]
84. Magliulo, P. Assessing the susceptibility to water-induced soil erosion using a geomorphological, bivariate statistics-based approach. *Environ. Earth Sci.* **2012**, *67*, 1801–1820. [CrossRef]
85. Ochoa, P.A.; Fries, A.; Mejia, D.; Burneo, J.I.; Ruiz-Sinoga, J.D.; Cerda, A. Effects of climate, land cover and topography on soil erosion risk in a semiarid basin of the Andes. *Catena* **2016**, *140*, 31–42. [CrossRef]
86. Torra, O.; Hurlimann, M.; Puig-Polo, C.; Moreno-de-las-Heras, M. Assessment of badland susceptibility and its governing factors using a random forest approach. Application to the Upper Llobregat River Basin and Catalonia (Spain). *Environ. Res.* **2023**, *237*, 116901. [CrossRef]
87. Ouallali, A.; Bouhsane, N.; Bouhlassa, S.; Moukhchane, M.; Ayoubi, S.; Aassoumi, H. Rapid magnetic susceptibility measurement as a tracer to assess the erosion-deposition process using tillage homogenization and simple proportional models: A case study in northern of Morocco. *Int. J. Sediment Res.* **2023**, *38*, 739–753. [CrossRef]
88. Aboutaib, F.; Krimissa, S.; Pradhan, B.; Elaloui, A.; Ismaili, M.; Abdelrahman, K.; Eloudi, H.; Ouayah, M.; Ourribane, M.; Namous, M. Evaluating the effectiveness and robustness of machine learning models with varied geo-environmental factors for determining vulnerability to water flow-induced gully erosion. *Front. Environ. Sci.* **2023**, *11*, 1207027. [CrossRef]
89. Klassen, J.; Allen, D.M. Assessing the risk of saltwater intrusion in coastal aquifers. *J. Hydrol.* **2017**, *551*, 730–745. [CrossRef]
90. Kazakis, N.; Busico, G.; Colombani, N.; Mastrocicco, M.; Pavlou, A.; Voudouris, K. GALDIT-SUSI a modified method to account for surface water bodies in the assessment of aquifer vulnerability to seawater intrusion. *J. Environ. Manag.* **2019**, *235*, 257–265. [CrossRef]

91. Sujitha, V.; Purandara, B.K.; Shivapur, A.V.; Davithuraj, J. Assessment of Aquifer Vulnerability Using GALDIT Model–A Case Study. *J. Geol. Soc. India* **2020**, *95*, 507–512. [CrossRef]
92. Bordbar, M.; Khosravi, K.; Murgulet, D.; Tsai, F.T.C.; Golkarian, A. The use of hybrid machine learning models for improving the GALDIT model for coastal aquifer vulnerability mapping. *Environ. Earth Sci.* **2022**, *81*, 402. [CrossRef]
93. Pham, N.Q.; Ta, T.T.; Tran, L.; Nguyen, T.T. Assessment of seawater intrusion vulnerability of coastal aquifers in context of climate change and sea level rise in the central coastal plains, Vietnam. *Environ. Dev. Sustain.* **2023**. [CrossRef]
94. Myronidis, D.; Papageorgiou, C.; Theophanous, S. Landslide susceptibility mapping based on landslide history and analytic hierarchy process (AHP). *Nat. Hazards* **2016**, *81*, 245–263. [CrossRef]
95. Wei, A.H.; Li, D.; Zhou, Y.H.; Deng, Q.; Yan, L.D. A novel combination approach for karst collapse susceptibility assessment using the analytic hierarchy process, catastrophe, and entropy model. *Nat. Hazards* **2021**, *105*, 405–430. [CrossRef]
96. Deros, S.N.M.; Din, N.M.; Norzeli, S.M.; Omar, R.C.; Usman, F.; Hamim, S.A. Land Subsidence Susceptibility Projection for Palembang Slum Area by Complex MCDM-AHP Technique. *J. Eng. Technol. Sci.* **2022**, *54*, 220104. [CrossRef]
97. Vijith, H.; Dodge-Wan, D. Modelling terrain erosion susceptibility of logged and regenerated forested region in northern Borneo through the Analytical Hierarchy Process (AHP) and GIS techniques. *Geoenviron. Disasters* **2019**, *6*, 8. [CrossRef]
98. Saravanan, S.; Pitchaikani, S.; Thambiraja, M.; Sathiyamurthi, S.; Sivakumar, V.; Velusamy, S.; Shanmugamoorthy, M. Comparative assessment of groundwater vulnerability using GIS-based DRASTIC and DRASTIC-AHP for Thoothukudi District, Tamil Nadu India. *Environ. Monit. Assess.* **2023**, *195*, 57. [CrossRef]
99. OpenStreetMap. Available online: https://www.openstreetmap.org/ (accessed on 6 October 2023).
100. Zhang, L.X.; Wang, Y.W.; Zhang, J.K.; Zhang, S.; Guo, Q.L. Rockfall hazard assessment of the slope of Mogao Grottoes, China based on AHP, F-AHP and AHP-TOPSIS. *Environ. Earth Sci.* **2022**, *81*, 377. [CrossRef]
101. Sinha, A.; Nikhil, S.; Ajin, R.S.; Danumah, J.H.; Saha, S.; Costache, R.; Rajaneesh, A.; Sajinkumar, K.S.; Amrutha, K.; Johny, A.; et al. Wildfire Risk Zone Mapping in Contrasting Climatic Conditions: An Approach Employing AHP and F-AHP Models. *Fire* **2023**, *6*, 44. [CrossRef]
102. Lyu, H.M.; Zhou, W.H.; Shen, S.L.; Zhou, A.N. Inundation risk assessment of metro system using AHP and TFN-AHP in Shenzhen. *Sustain. Cities Soc.* **2020**, *56*, 102103. [CrossRef]
103. Biswas, B.; Ghosh, A.; Sailo, B.L. Spring water suitable and vulnerable watershed demarcation using AHP-TOPSIS and AHP-VIKOR models: Study on Aizawl district of North-Eastern hilly state of Mizoram, India. *Environ. Earth Sci.* **2023**, *82*, 80. [CrossRef]
104. Feizi, Z. Efficiency Assessment of AHP and Fuzzy AHP in Suitability Mapping for Artificial Recharging (Case Study: South of Kashan Basin, Isfahan, Iran). In *Sustainable Energy-Water-Environment Nexus in Desert Climates, Proceedings of the First International Conference on Sustainable Energy-Water-Environment Nexus in Desert Climate, Doha, Qatar, 2–5 December 2019*; Springer: Cham, Switzerland, 2022; pp. 59–70. [CrossRef]
105. Unver, S.; Ergenc, I. Safety risk identification and prioritize of forest logging activities using analytic hierarchy process (AHP). *Alex. Eng. J.* **2021**, *60*, 1591–1599. [CrossRef]
106. Wang, P.Z. *Fuzzy Set and Random Set Shadow*; Beijing Normal University Press: Beijing, China, 1985. (In Chinese)
107. Wang, B.; Fan, T.Y.; Liu, M.Q.; Wang, F.Q.; Nie, X.T. Evaluation of management level of water conservancy construction supervision unit based on variable weight fuzzy theory. *Desalin. Water Treat.* **2019**, *152*, 66–74. [CrossRef]
108. Han, F.; Liu, Z.L.; Wang, C.X. Research on a Comfort Evaluation Model for High-Speed Trains Based on Variable Weight Theory. *Appl. Sci.* **2023**, *13*, 3144. [CrossRef]
109. Zeng, Q.; Luo, X.; Yan, F. The pollution scale weighting model in water quality evaluation based on the improved fuzzy variable theory. *Ecol. Indic.* **2022**, *135*, 108562. [CrossRef]
110. Wang, S.; Li, L.P.; Cheng, S.; Liu, Z.H.; Ding, R.S.; You, Q. Model on Improved Variable Weight-Matter Element Theory for Risk Assessment of Water Inrush in Karst Tunnels. *Geotech. Geol. Eng.* **2021**, *39*, 3533–3548. [CrossRef]
111. Ma, C.M.; Li, Y.G.; Li, X.; Gao, L. Evaluation of groundwater sustainable development considering seawater intrusion in Beihai City, China. *Environ. Sci. Pollut. Res.* **2020**, *27*, 4927–4943. [CrossRef]
112. Liu, Y.X.; Zhuo, L.; Pregnolato, M.; Han, D.W. An assessment of statistical interpolation methods suited for gridded rainfall datasets. *Int. J. Climatol.* **2022**, *42*, 2754–2772. [CrossRef]
113. Febrianto, H.; Fariza, A.; Hasim, J.A.N. Urban Flood Risk Mapping Using Analytic Hierarchy Process and Natural Break Classification. In Proceedings of the 5th International Conference on Knowledge Creation and Intelligent Computing (KCIC), Manado, Indonesia, 15–17 November 2016; pp. 148–154.
114. Khamis, N.; Sin, T.C.; Hock, G.C. Segmentation of Residential Customer Load Profile in Peninsular Malaysia using Jenks Natural Breaks. In Proceedings of the 7th IEEE International Conference on Power and Energy (PECon), Kuala Lumpur, Malaysia, 3–4 December 2018; pp. 128–131.
115. Li, B.H.; Liu, K.; Wang, M.; He, Q.; Jiang, Z.Y.; Zhu, W.H.; Qiao, N.N. Global Dynamic Rainfall-Induced Landslide Susceptibility Mapping Using Machine Learning. *Remote Sens.* **2022**, *14*, 5795. [CrossRef]
116. Fawcett, T. An introduction to ROC analysis. *Pattern Recognit. Lett.* **2006**, *27*, 861–874. [CrossRef]
117. Taheri, K.; Missimer, T.M.; Mohseni, H.; Fidelibus, M.D.; Fathollahy, M.; Taheri, M. Enhancing spatial prediction of sinkhole susceptibility by mixed waters geochemistry evaluation: Application of ROC and GIS. *Environ. Earth Sci.* **2021**, *80*, 470. [CrossRef]

118. Liu, G.X.; Zhang, Y.C.; Zhang, J.Q.; Lang, Q.L.; Chen, Y.A.; Wan, Z.Y.; Liu, H.A. Geographic-Information-System-Based Risk Assessment of Flooding in Changchun Urban Rail Transit System. *Remote Sens.* **2023**, *15*, 3533. [CrossRef]
119. Shawky, M.; Hassan, Q.K. Geospatial Modeling Based-Multi-Criteria Decision-Making for Flash Flood Susceptibility Zonation in an Arid Area. *Remote Sens.* **2023**, *15*, 2561. [CrossRef]
120. Huang, P.; Ma, C.M.; Zhou, A.G. Assessment of groundwater sustainable development considering geo-environment stability and ecological environment: A case study in the Pearl River Delta, China. *Environ. Sci. Pollut. Res.* **2022**, *29*, 18010–18035. [CrossRef] [PubMed]
121. Abd-Elhamid, H.F. Investigation and control of seawater intrusion in the Eastern Nile Delta aquifer considering climate change. *Water Sci. Technol. Water Supply* **2017**, *17*, 311–323. [CrossRef]
122. Intui, S.; Inazumi, S.; Soralump, S. Sustainability of Soil/Ground Environment under Changes in Groundwater Level in Bangkok Plain, Thailand. *Sustainability* **2022**, *14*, 10908. [CrossRef]
123. Paulin, G.L.; Pouget, S.; Bursik, M.; Quesada, F.A.; Contreras, T. Comparing landslide susceptibility models in the Rio El Estado watershed on the SW flank of Pico de Orizaba volcano, Mexico. *Nat. Hazards* **2016**, *80*, 127–139. [CrossRef]
124. Tehrany, M.S.; Pradhan, B.; Jebur, M.N. Spatial prediction of flood susceptible areas using rule based decision tree (DT) and a novel ensemble bivariate and multivariate statistical models in GIS. *J. Hydrol.* **2013**, *504*, 69–79. [CrossRef]
125. Moayedi, H.; Mehrabi, M.; Mosallanezhad, M.; Rashid, A.S.A.; Pradhan, B. Modification of landslide susceptibility mapping using optimized PSO-ANN technique. *Eng. Comput.* **2019**, *35*, 967–984. [CrossRef]

sustainability

MDPI

Article

A Multimodal Data Analysis Approach to Social Media during Natural Disasters

Mengna Zhang [1,2], Qisong Huang [3,*] and Hua Liu [4]

[1] School of Management, Guizhou University, Guiyang 550025, China; zhang_mengna1@163.com
[2] Academic Affairs Office, Guizhou University of Finance and Economics, Guiyang 550025, China
[3] Guizhou Minzu University, Guiyang 550025, China
[4] Faculty of Law, Guizhou University, Guiyang 550025, China; liuhua202203@126.com
* Correspondence: qshuang1976@126.com

Abstract: During natural disasters, social media can provide real time or rapid disaster, perception information to help government managers carry out disaster response efforts efficiently. Therefore, it is of great significance to mine social media information accurately. In contrast to previous studies, this study proposes a multimodal data classification model for mining social media information. Using the model, the study employs Late Dirichlet Allocation (LDA) to identify subject information from multimodal data, then, the multimodal data is analyzed by bidirectional encoder representation from transformers (Bert) and visual geometry group 16 (Vgg-16). Text and image data are classified separately, resulting in real mining of topic information during disasters. This study uses Weibo data during the 2021 Henan heavy storm as the research object. Comparing the data with previous experiment results, this study proposes a model that can classify natural disaster topics more accurately. The accuracy of this study is 0.93. Compared with a topic-based event classification model KGE-MMSLDA, the accuracy of this study is improved by 12%. This study results in a real-time understanding of different themed natural disasters to help make informed decisions.

Keywords: multimodal data; LDA; Bert; VGG-16

Citation: Zhang, M.; Huang, Q.; Liu, H. A Multimodal Data Analysis Approach to Social Media during Natural Disasters. *Sustainability* **2022**, *14*, 5536. https://doi.org/10.3390/su14095536

Academic Editors: Stefano Morelli, Veronica Pazzi, Mirko Francioni and Marc A. Rosen

Received: 5 March 2022
Accepted: 28 April 2022
Published: 5 May 2022

Publisher's Note: MDPI stays neutral with regard to jurisdictional claims in published maps and institutional affiliations.

1. Introduction

Flood is a high-frequency natural disaster [1], which occurs worldwide with a profound impact on national and social development [2]. Since the 21st century, with the rapid development in China, flood disaster has caused immeasurable economic losses [3]. According to "the water drought disaster Bulletin of China" during the decade of 2010–2019, the total value of direct financial loss due to flood disasters has exceeded 234.31 billion in the country. Flood disasters occurred in 62% of cities nationwide, and 137 cities experienced more than three episodes of flood disasters. Severe human injuries, economic losses, and traffic are often caused by heavy rainfall because of the clustering of crucial infrastructure such as population, resources, transportation, as well as power disruption.

With the development of information technology, the number of social media users is growing. The research institution We Are Social released the latest global digital reports in 2019. The report shows that the number of global social media users has increased to 3.5 billion. Each user spends one-third of their Internet time on social media every day. After a natural disaster, rescue organizations need to use extensive data in the initial phase as a decision basis to make low-risk decisions quickly [4]. Natural disasters can cause signal interruption, and so obtaining useful data information has become an urgent problem. In the past, due to the lack of data, experts made emergency decisions mainly relying on their knowledge and experience [5]. In recent years, with the rapid development of social networks, experts have found an essential platform for information dissemination [6]. Therefore, after the occurrence of natural disasters, hundreds of millions of people share information on social media, forming a vast amount of data information that could serve

as a basis for making emergency decisions in the literature [7]. Behl et al. proposed that the sudden and urgent nature of emergencies requires crisis managers to remain updated and meet the critical information needs of the public, so that researchers could use social media as a source of information for crisis management [8]. Kitazawa proposed the rapid development and application of social media in crisis communication, the effectiveness of which improved the efficiency of crisis communication, enhanced emergency response methods, reduced the cost of disasters, and increased transparency and democratism in decision-making [9]. The author further proposed that in an emergency event, social media contains a large amount of subject matter, spatiotemporal and other emergency information, by classifying the real-time and massive emergency information, which could identify the subject matter information such as the facts, rescue, and impact of the event, so that it was beneficial to understand the status of the emergency event.

Most previous studies on social media data had focused on a single form of data (e.g., text or visual data). Piatyszek adopted a logistic regression algorithm to classify text data, and detected damage and injuries caused by Sri Lankan flooding; however, the overall accuracy of this classifier was only 0.647 because the subject sample size was too small [10]. Yu used the CNN classifier to classify text data and detect damages caused by hurricanes by using the text data of hurricanes Sandy and Harvey, resulting in relevant recommendations for donation and assistance [11].

To increase precision, we needed to analyze the other modal data while classifying textual information [12]. The analysis of seismic image information, from which human body parts were examined from debris, provided an adequate basis for developing seismic rescue measures, with a precision of 0.8037. Seismic rescue efforts need to obtain geographic location information in addition to accurate image information, an effective combination of both kinds of information to obtain precise information on people trapped in earthquakes. Aznar-Crespo classified disaster social media images into three categories: severe, mild, and no damage, to analyze the effects caused by natural disasters, develop related assistance measures, and mine their corresponding text information, while classifying image information, which could further improve the accuracy of classification [13].

Recently, the form of people's expression views on social media platforms had significantly changed and people prefer diverse expressions, such as text, images, and video, to help multimodal data contain richer information and more accurately describe the natural disaster situation [9]. Therefore, we must establish a model for multimodal data analysis. Multimodal data analysis was a very challenging task [14]. Min constructed a unified cross-media word bag model for both text and image; the model acquired the representation of text and image and used a logistic regression classifier. Through the experiment, the precision of the CBM model, which could analyze both text and image modal data, was 0.80, and the precision of the logistic regression, which could analyze the text data, was 0.76. The experiment results showed that the preparation rate of information classification for analyzing both text and image modal data was 4% higher than the text-based method [15]. Kaplan and Haenlein also used 2CNN structures, which extracted text data features and image data features separately and performed significantly better than existing models that used only text or visual content [16].

In natural disasters, local and international studies have proven that social media data could be applied to real-time monitoring, trending the prediction of disaster events [17]. Disaster-related text data were usually thematically classified, as in the literature [18]. Combined LDA and SVM were used to construct a theme classification model, which divided microblogs related to the typhoon "moranti" into four themes: "early warning information", "disaster information", "irrelevant information", and "rescue information". Ghosh et al. proposed an LDA subject-based event detection model, in which multimodal information was used to increase the number of acquired event descriptions, and the multimodal data were combined into the subject model, which all achieved a classification accuracy of 81% [19]. In addition, Wood et al. designed a system named m-trend, based on tweets containing geographic information [20], to construct and visualize the spatiotempo-

ral variation trends of the display theme as well as explore the trend and spatial distribution law of disaster events [21]. Thematic model analysis of user-developed text information on microblogs generated before and after the onset of a heavy storm in Beijing in 2012 revealed differences in the temporal and spatial distribution of microblogs across themes.

Based on this, this paper proposes a multi-modal data mining method based on theme change, to perceive the development trend of disaster. This study has the following three contributions:

1. This study presents a multimodal system for classifying and processing multimodal data from social media.
2. In this study, the heavy storm disaster topic was more meticulously divided using the Latent Dirichlet Allocation (LDA) theme model, which realizes real-time extraction of information on serious storm disasters from social media.
3. Based on Sina Weibo, a multi-classification model was constructed using convolutional neural networks to extract storm-related disaster information [22], such as weather, traffic, and rescue, from a large number of social media text streams. At the same time, the study visualizes and analyzes different rainstorm disaster themes in terms of relative quantity and spatial attributes as well as explores the time trend of disaster development and spatial distribution characteristics of rainstorm events.

The rest of the paper is organized as follows. In Section 2, we present the working principle of the topic classification model and multi-modal data processing model. In Section 3, we take the Henan rainstorm as the research object, we present the results and discussion of these experiments. In Section 4, we discuss the conclusions and future work.

2. Methods

This study takes heavy rain in Henan in 2021 as an example. Since the night of 17 July 2021, Henan Province had experienced heavy rains. The average rainfall in the province was 73.1 mm. As of noon, 2 August 2021, 150 counties (cities and districts), 1663 townships, and 14,531,600 people were affected. The whole province had organized emergency avoidance for 933,800 people and relocation for 1,470,800 people. Heavy rain resulted in the collapse of 89,001 houses; the area affected by crops was 109.04 Square kilometres, and direct economic loss was 114.269 billion yuan. Sadly, 302 people were killed and 50 people were missing. Therefore, this study combines the Weibo API and web crawler to obtain a total of 28,099 pieces of data from 0:00 on 18 July 2021 to 23:00 on 30 July 2021, using "Henan rainstorm" as the keywords.

This study focuses on automatically locating and mining natural disaster information from images and text data on social media. A real-time classification and positioning model of emergency topics based on social text and images is proposed. The structure diagram of Multimodal data classification is shown in Figure 1. The model consists of the following modules. The data processing module is responsible for data collection and processing. Since the correlation between images and text data is weak, this study treats text and image data separately. The topic mining module is responsible for mining hidden topics. By mining the topic information, we can fully understand emergencies. The topic analysis module is responsible for analyzing text and image data.

2.1. Acquisition and Preprocessing of Data

Weibo is used as the research object; it is a popular social-media platform. In particular, there are thousands of pieces of Weibo data on natural disasters every day. During natural disasters, people report disaster information through Weibo, express their urgent needs, and seek help. As a result, Weibo data have become an important source of data for disaster management. Text, images, and geographic location data can be used to learn more about natural disasters and provide a data basis for natural disaster management.

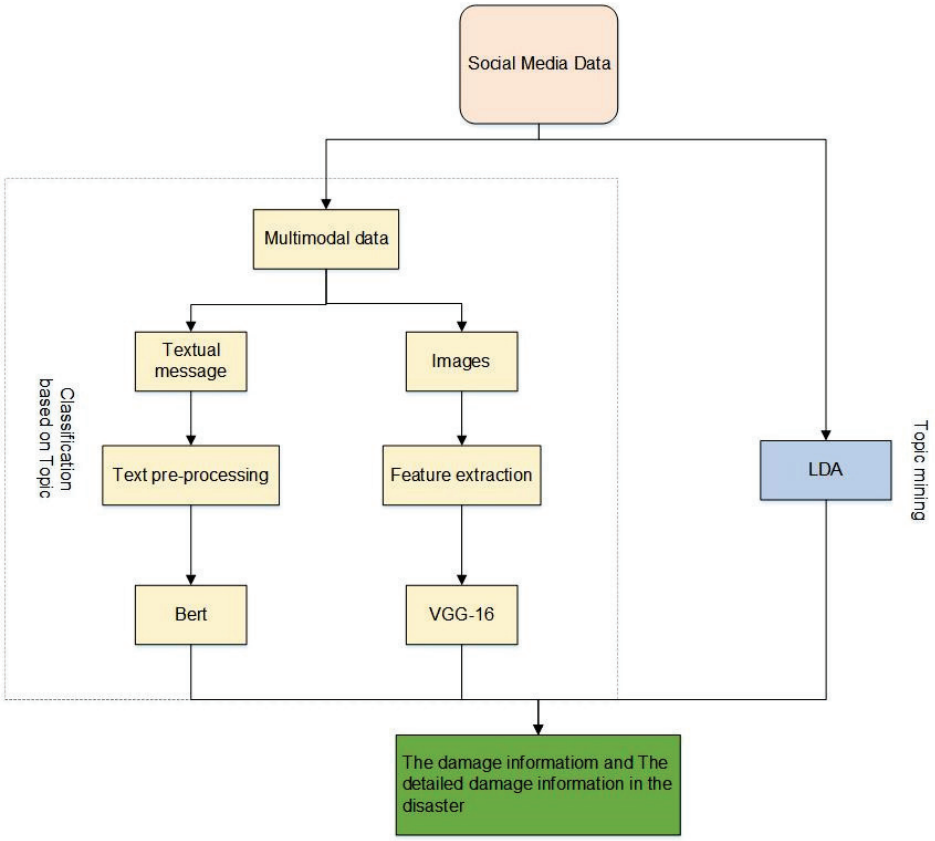

Figure 1. A structure diagram of multimodal data classification.

2.2. Topic Mining

A topic model is an essential tool for data mining on social media and has attracted extensive attention in recent years. Empirical research has found that the release of social data is closely related to the cycle of disaster occurrence, which is usually divided into three stages: pre-disaster preparation, emergency response, and post-disaster recovery. People discuss different topics on social media at different stages. In the early days of a disaster, people discussed content mainly on disaster preparedness and weather warnings. After the disaster, people focused on disaster discussions and emergency rescue. In the later stage of the disaster, people mainly focused on post-disaster recovery and reconstruction. Thus, different themes occurred in different periods.

LDA (Latent Dirichlet Allocation) is the most representative topic model [23]. The LDA model is a typical generative model that is primarily used in text and image processing [24]. Owing to the emergence of the BOW model, it is currently widely used for image labeling. The text uses the LDA model for topic mining of images and text data [25]. The core idea of the LDA model is to regard topics as the probability distribution of text words and different topics corresponding to other text word distributions. In the field of image annotation, we need to extract the low-level features of the image and perform clustering. Then, we use the clustering algorithm to vectorize the low-level features of the image into visual words. Finally, we use the BOW model to convert the image into a set of visual words. The LDA probability graph model is shown in Figure 2. Table 1 lists the symbols used in the model, and their meanings are shown in Figure 2.

2.3. Text Data Classification Model

The use of social media texts for natural disaster assessment can be divided into three areas. First, we must identify whether the tweets are related to rainstorm damage; this is a two-classification task. Second, rainstorm damage was divided into multiple categories

according to the theme; this is a multi-classification task. Finally, we classified the text data according to the theme and generated a damage report.

The process of subject classification is shown in Figure 3. First, we use Bert to build a relational classification model to identify text segments corresponding to two aspects, namely entity tags. Then, we used the predicted relationship and text to build an entity extraction model using Bert, that is, a multi-classification task. We divided each sentence into a three-tuple of description objects, damage descriptions, and damage results. Corresponding to relationships.

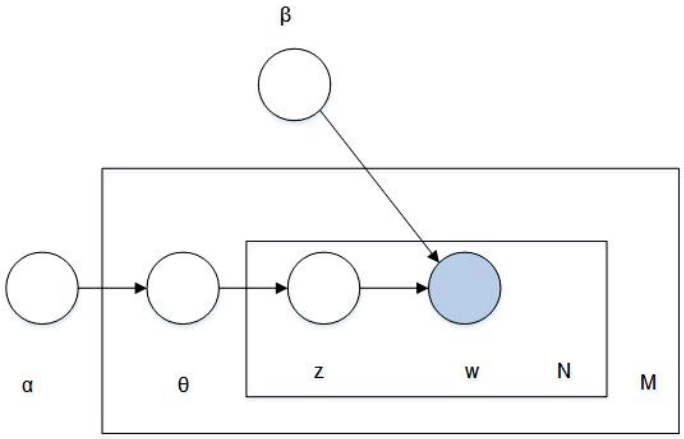

Figure 2. Probabilistic graphical model of LDA model.

Table 1. Symbols and their meanings in Figure 1.

Symbol	Symbolic Meaning	Symbol	Symbolic Meaning
M	Training set size	N	Number of words
α	Model parameters	w	words
z	Potential topic	θ	Theme ratio
β	Model parameters		

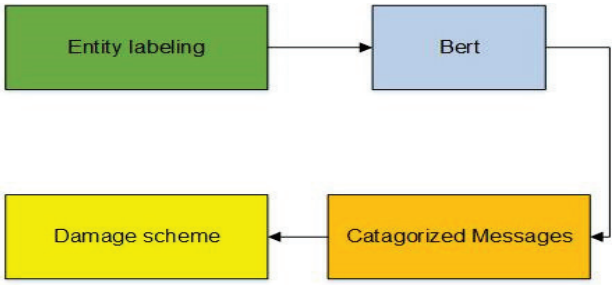

Figure 3. The framework of topic classification.

Bert is a large pre-trained model that shows excellent performance when generating text-entity embeddings [26]. The Bert model improves the performance of text classification through entity embedding, so it can identify tweets and generate corresponding damage reports. Finally, we classify the damage reports into corresponding topics.

2.3.1. Damage Relationship Definition

Topic classification based on social media text data requires identifying tweets with a harmful relationship, which can be abstracted into a triad, with three aspects describing the object. Common victims of heavy rain include roads, people, houses, water, and electricity. The damage description is related to the feature words corresponding to the description object, and the damage result describes the ultimate severity of the damage.

For example, 10,600 houses collapsed; this sentence describes the object as a house, the damage is described as 10,600 houses, and the result of the damage is collapsed. Thus, it is possible to classify the damage reports as corresponding. We can identify whether the tweets are related to the rainstorm based on the damage report, classify the damage report by topic, and, finally, classify the damage report into the corresponding topic.

The word collocation in this paper is based on the Chinese word collocation database SogouR, and we summarize the collocations of the Weibo texts of the rainstorm event. The construction of lexical collocation model in this paper is based on the text statistics of rainstorm events in Weibo, and the data were obtained from the "2017 Rainstorm Disaster Social Media Dataset". We randomly selected 5000 pieces of text information from the rainstorm event, analyzed the grammatical characteristics of the disaster information, and obtained the lexical rules shown in Table 2, thereby obtaining the collocation relationship between the expression description object and the damage result.

Table 2. The lexical rule pattern.

Pattern Rule	Text Word
v-n	Shattered glass everywhere
n-v	The whole village was blown to the ground
a-n	Broken window glass in one place
n-a	The road has been blocked
d-v_i	Soon the community will no longer supply water
v-v_i	About to stop power supply
r-v	Saw him smashed by a tree
v-r	The branch was blown off by the wind just hit him
v_i	Power outage for one day today

Note: v is a verb; n is a noun; a is an adjective; d is an adverb; r is a pronoun; v_i is an intransitive verb.

We present examples of identifying whether a tweet is heavy rain related based on a damage report.

Negative example: Heavy rains in Henan in 2021, the tribute to the cutest man! Tributes to people's younger cousins.

Positive example: The father was washed away by a flood at 2 p.m. on 20 July 2021, at the Sukangcun Shi River, Takayama Town, Xingyang, from south to north and in the direction of the downstream fenggou. His upper body was covered with a white spot under the curve, and the lower body with sports pants.

Although the negative examples mention the heavy rain, they do not contain a detailed description or relevant contents of the damage, so they cannot be regarded as related to heavy rain. The positive examples include a detailed description of the subject's father, and they include a detailed description of the damage in Baohe, Zhonggang Village, Gaoshan Town, and Xingyang City. Therefore, they were regarded as related to heavy rain.

2.3.2. Constructing Word Pairing Rules

In the study, we use the skip-gram to extract feature. Based on lexical rules to extract feature words in a small-scale annotated corpus, the feature words are used to express the object, damage description, or damage result. Then, we put the object, damage description, and damage result together as the original word pair. Based on this, the word vector model and the extended version of "Synonyms Clin" are used to enrich the collocation information of characteristic words, to realize the diversity of Chinese expressions.

In this study, based on the results of subject mining, the original words are defined as six aspects: weather warning, traffic situation, rescue information, disaster information, disaster cause, casualty, and damage. According to these six aspects, a dictionary of description objects and damage results is established, as shown in Table 3.

Table 3. The dictionary of description objects and damage results.

The Object	Damage Description	Damage Result
Weather	Southern North China, Henan	Rainstorm, Moderate to heavy rain, Continuous heavy rainfall
Traffic situation	Railway Line 2, Platform, road	Pause, Adjustment operation, Temporary closure, Blocked
Rescue information	Xiao Pengpeng, Huang xinrui, Genghuang Central Primary School	Lost contact, Lost contact, Bedding
Infrastructure	Civic Center Station, Escalator, College Road, East Coach Station	Service paused, Temporary closure, Sever diplomatic relations
Hazard Factor	Worldwide, Western Pacific Subtropical, Dongfeng	High temperature, High pressure, Rapids
Water or Power Supply	Anyang, Village, Outdoor	Water and power outages, Fetch water

In the field of natural language processing, the word vector model is used to calculate the distance between words. Usually, two words that are close in the distance are also highly correlated, thus realizing the expansion of feature word collocation. The commonly used word vector model contains CBOW (continuous bag of words) and Skip-gram models. For data with less than 100 million words, the performance of the skip-gram model is better [25], therefore, this study uses the skip-gram model to calculate the phase between the relevance of words. The structure of the model is shown in Figure 4. The frontal context information is predicted by the current word W(t) for the etymological sequence in which the word resides.

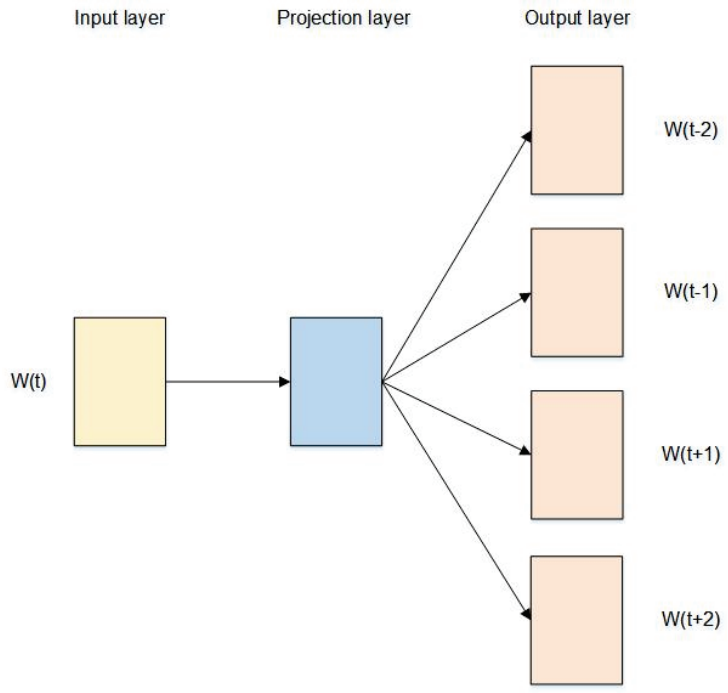

Figure 4. The model structure diagram.

2.4. Image Data Classification Model

Compared with social media text data, images convey information as more objective and valuable. Contrary to a few studies that have utilized graphical data for natural disaster damage assessment, this study uses image and text data for multimodal data analysis, to make damage assessment more objective and accurate.

Image data are processed by converting the image into a digital feature vector, and, then, using the classifier for image classification. The classifiers are responsible for different tasks that define the semantic hierarchy.

In this study, Vgg-16 was used to extract the image features. VGG-16 is a classic CNN network of convolutional neural networks. The VGG-16 convolutional neural network uses the small convolution kernel 3×3 and the largest pooling layer 2×2. The model stacks the convolutional layers several times the number of layers in the standard CNN model. With the maximum pooling layer, the parameters can be reduced, the number of calculations can be reduced, and the model's ability to express nonlinear data can be improved [26].

The structure of the image feature extraction model based on Vgg-16 is illustrated in Figure 5. The input of the Vgg-16 network was fixed in size as 224×224. Opencv is an open-source computer vision library that utilizes the resize function, which uniformly scales the images of the dataset to 224×224, which can be input to the VGG-16 network.

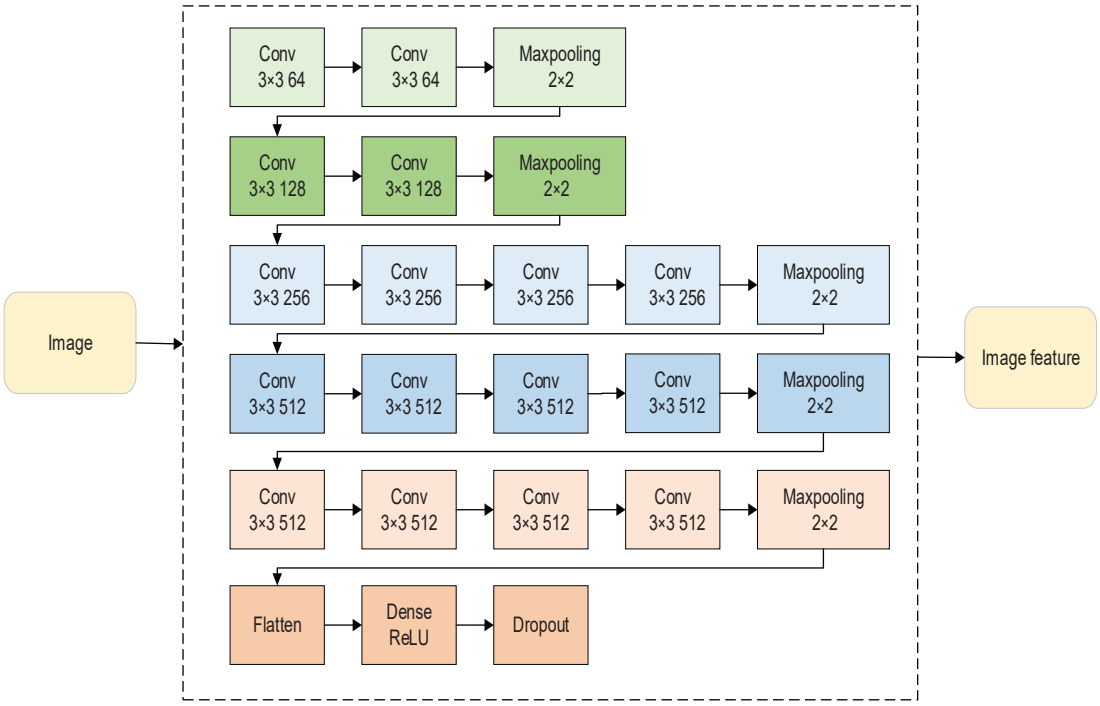

Figure 5. The image feature extraction model structure diagram.

The remaining network structure of the original VGG-16 model is encapsulated in the Keras deep learning library, except for the fully connected layer. To realize the feature-based transfer learning method in the homogeneous space, we choose the VGG-16 model parameters pre-trained by ImageNet as the initial value of the feature extraction model; that is, the weight parameters of VGG-16 is set to "image net". The flattened layer is used to make the multi-dimensional input one-dimensional, and, then, input the one-dimensional vector into the dense layer using ReLu as the activation function. The dropout layer is, finally, added to obtain the image feature extraction model based on VGG-16.

AdaBoost Classifier

In this study, we switched the softmax classifier from the original model of Vgg-16 to an AdaBoost classifier with better classification performance. The working principle of the Adaboost classifier is to train multiple different weak classifiers from a training set and retrain them each time, by combining the last training sample with the new sample to obtain a new classifier, finally forming a stronger classifier for the model classification. The AdaBoost iteration algorithm was divided into three steps.

(1) Initialize the distribution of weights for the training data. If there are N samples, each is given the same weight at the very beginning: $1/N$.

$$D_1 = (w_{11}, w_{12} \cdots w_{i1} \cdots, w_{1N}), w_{i1} = \frac{1}{N}, i = 1, 2, \cdots, N \tag{1}$$

where w_{1i} is the weight of the sample, D_1 is the set of the weights.

(2) Train weak classifiers. In the specific training process, if a sample point has been accurately classified, its weight is reduced in the construction of the next training set; however, if a sample point has not been accurately classified, its weight is increased. Then, the sample set with updated weights is used to train the next classifier, and the entire training process proceeds iteratively in this manner, where $m = 1, 2, \ldots, M$ is used to indicate the number of iterations.

(3) The weak classifiers obtained from each training session were combined into a robust classifier. After the training process of each weak classifier is completed, the weight of the weak classifier is increased with a small classification error rate, to make it play a more significant role in the final classification function and reduce the weak classifier with a significant classification error rate. Weight plays a minor decisive role in the last classification function. In other words, a weak classifier with a low error rate occupies a more significant weight in the final classifier; otherwise, it becomes smaller.

2.5. Emergency Severity Assessment Based on Entropy Method

In this paper, social media related to events are grouped by day, and the entropy method is used to evaluate the severity of emergencies. It is mainly used to judge the degree of dispersion of a certain indicator. The calculation process for assessing the severity of emergencies in this study is as follows:

$$X_i = \frac{v_i - \min_{0 \le i \le n(v_i)}}{\max_{0 \le i \le n(v_i)} - \min_{0 \le i \le n(v_i)}} \tag{2}$$

where X_i is the data after standardized processing, the range of values of i is from 1 to n, and n is the number of samples.

$$p_i = \frac{x_i}{\sum_{i=1}^{n} x_i} \tag{3}$$

where p_i is the proportion of the ith sample value.

$$f_i = -k \sum_{i=1}^{n} p_i \ln(p_i) \tag{4}$$

where f_i is the entropy of the ith indicator, $k = 1/\ln(n)$.

$$d_i = 1 - f_i \tag{5}$$

where d_i is the redundancy of information entropy.

$$W_i = \frac{d_i}{\sum_{i=1}^{n} d_i} \tag{6}$$

where W_i is the weight of indicators.

$$F = \sum_{i=1}^{n} W_i \times X_i \tag{7}$$

where F is the severity of the emergency.

3. Research Result

In this study, we develop the crawler program based on Python and use "Henan rainstorm" as the keywords to obtain a total of 28,099 pieces of data from 0:00 on 18 July 2021 to 23:00 on 30 July 2021. We count the number of social media posts per day during the heavy rains in Henan, and the statistical graph of the number of tweets based on time is shown in Figure 6. Since the night of 17 July 2021, heavy rains began to attract widespread public attention, and on 20 July 2021, the emergency response level was elevated from level IV to level II by the Henan Provincial command on drought resistance, due to the severe prevention situation. According to the statistics in Figure 6, the number of microblogs started to rise significantly on 20 July in response to the increasing severity of the forms of flooding; the mobile communication network of the province was fully restored and the supply of water was restored in most areas starting on 25 July. Thus, the public concern for heavy rains in Henan gradually declined as typhoon "fireworks" on 27 July affected Henan; as a result, the number of microblogs showed an obvious upward trend. Thus, the temporal trend of microblog data largely coincides with the real-time occurrence of the event, suggesting that Sina's original information on microblogs has usage value when a major emergency occurs.

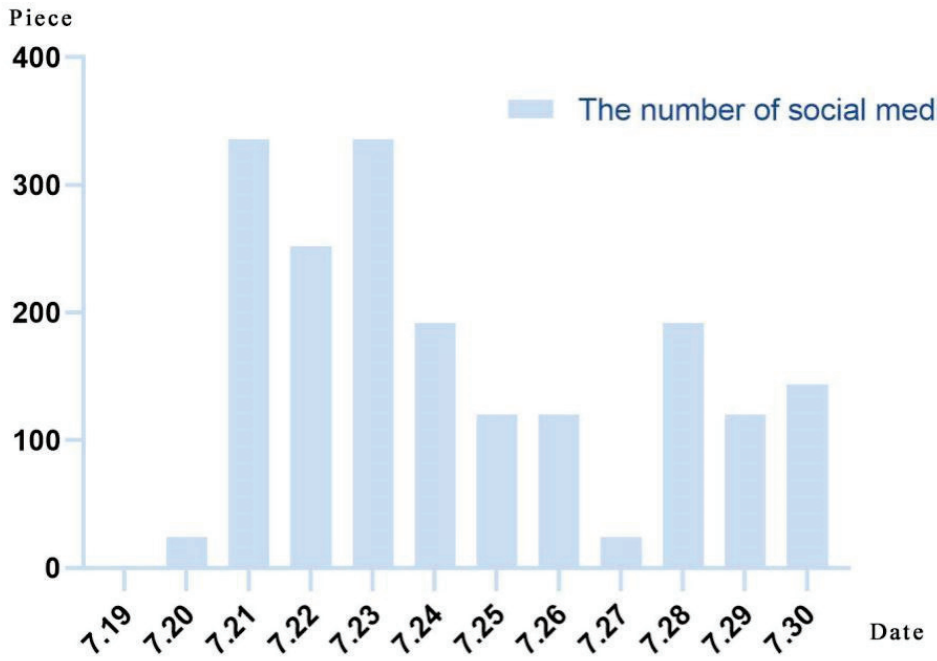

Figure 6. The number of social media.

3.1. Topic Mining

This study extracted 2219 pictures related to the Henan rainstorm from Weibo and randomly selected 20% of the pictures as the test set, with the remaining 80% of the pictures as the training set. The image annotation results obtained using the LDA model are listed in Table 4. The image size was set to 224 × 224 × 3, obtaining an average number of annotated words per picture of 4.5. The average number of annotated images for each annotated word is 58.6. A total of 170 annotated words in the image set and annotated words with fewer annotated images were eliminated, while the remaining 120 words formed the label vocabulary.

In Table 4 deduplication, Chinese word segmentation, stop word removal, and emoji preprocessing were performed on the 25,880 Weibo datasets obtained from Weibo. The vocabulary expression of each Weibo dataset was obtained, and the data were manually labeled to obtain the corresponding Weibo vocabulary collection and emergency themes. To verify the accuracy of the model classification, 20% of the samples were randomly selected as the test set and the remaining 80% were used as the training set. Using the LDA model as the topic classification model, the topic distribution of the sample documents and the

respective feature vocabulary distributions of all the topics were obtained. Some of these themes are shown in Figure 7.

Table 4. The theme extraction of a picture.

Image	Topic Model
	People, umbrella, bicycle, rainstorm, tree
	Houses, tree, flood, people

#Topic4		#Topic17		#Topic18		#Topic27		#Topic29	
Airport	0.021267	Stagnant wat	0.096204	Early warning	0.042271	Rescue	0.077723	Die	0.132123
Hour	0.052066	Drain	0.039654	Rainfall	0.040495	Encounter	0.060422	Victims	0.049918
Stay	0.027527	Serious	0.037401	Area	0.040141	Assault	0.048871	Disaster	0.039559
Subway	0.022227	Transportatio	0.023929	Maximum	0.035745	Come on	0.036526	Confirm	0.034913
Traveler	0.021267	Paralysis	0.018862	Rain	0.023859	Strongest	0.033091	Identity	0.032775
Sit	0.014818	Road section	0.017362	Hour	0.021661	[Microphone]	0.028187	Die	0.032523
Train	0.014723	No	0.016191	Part	0.020818	Unable to	0.027953	People	0.030909
Real	0.014431	Center	0.015243	Predict	0.019912	To	0.027324	Extra large	0.029438
Late	0.014421	Rainwater	0.014202	Reach	0.019417	Fire fighting	0.025341	Lethal	0.023085
Station	0.014053	Road	0.011039	Rainfall	0.019362	Serious	0.024981	To	0.022143
No one	0.013371	Cause	0.013339	Last	0.015673	On site	0.022374	Announce	0.022075
Line	0.011875	Overpass	0.011919	Weather static	0.015664	Begging	0.020939	Disaster	0.021528
Once in a hundred years	0.011562	Pavement	0.011039	Citywide	0.015511	Dispatch	0.019004	Drowning	0.021184
Influence	0.010943	Long	0.009032	Urban area	0.015369	Condition	0.018881	Discover	0.021051
Train	0.010693	Map	0.008984	Orange	0.014722	Go to	0.018615	Happen	0.018821
Bus	0.010651	Expert	0.008719	Blue	0.014547	Suffer	0.018542	Houses	0.018143
Capital Airport	0.010156	Municipal	0.007733	Yellow	0.014382	Trapped	0.017739	List	0.017801
Out of service	0.010138	Report	0.007567	Average	0.013896	Diffusion	0.017288	Deceased	0.014983
Ask	0.009949	Department	0.007351	Mudslide	0.013396	Submerged	0.015447	Collapse	0.014968
Arrive	0.009792	Wish to be happy and prosperous	0.007043	Influence	0.013292	Personnel	0.014372	Electric shock	0.014137
Frequent visitor	0.009504	River	0.006357	Signal	0.013012	Police force	0.013492	Lightning strike	0.013532
. . .		...		...		...		...	

Figure 7. The part of the theme distribution.

Through thematic classification of text data, we finally got 40 thematic categories, as shown in Figure 7. Through lexical analysis of thematic distribution, we merge similar topics manually, such as both topic 29 and topic 33 discussion themes were about the losses and impacts caused by heavy rains in Henan. Therefore, we combined similar themes, and obtained 40 thematic categories combined to get "weather warning", "traffic situation", and six emergency-information-related topics including "rescue information", "disaster information", "disaster cause", and "casualties and losses". The classification of their topics is shown in Table 5.

Table 5. Social media classification scheme.

	Class	Description	Example
1	Weather warning	A warning is given about the change of the weather	According to the latest weather forecast by the Meteorological Bureau, it is expected that there will be heavy rainfall in Zhengzhou from 22 July to 25 July
2	Traffic condition	The traffic obstruction and the damage to vehicles	At 4 p.m. on 20 July 2021, a lot of rain poured into the platform layer of the Huiji District Government Station of Zhengzhou Metro Line 2
3	Rescue information	Provide goods and services needed by victims	On 20 July 2021, Gongyi, Henan was hit by heavy rain, and the Yichuan Condor rescue team rushed to the disaster area overnight for rescue
4	Disaster information	The information about the level and duration of the rainstorm	Continuous heavy rainfall has caused the flooding of roads, subways, and other public facilities in many places in Henan
5	The cause of the disaster	The discussion of the cause of the rainstorm	More rainfall in the north this year the most important reason is the abnormally northerly subtropical high
6	Casualties and damage	Information about casualties or infrastructure damage	Wang Yufeng walked to Sizhuang Village after about 2:40 and lost contact

3.2. Disaster Type Classification as Well as Severity Information

Weibo data were classified according to the subject classification results, which ultimately yielded the natural disaster situation for each region of Henan. Figure 8 presents the number of subject social media during heavy rains in Henan. Figure 9 presents the change in subject microblogs overtime during heavy rains in Henan. As shown in Figures 8 and 9, little attention has been paid to weather warnings during heavy rains, though it began on 19 July. Henan experienced a heavy storm; people started to release weather warning information via Weibo, so the number of Weibo posts with a weather warning on 19 July was significantly more than that of other subjects, and on 27 July the typhoon "fireworks" affected Henan, so the number of microblogs regarding weather warning increased on 27 July. With the development of catastrophes, the number of microblogs regarding disaster information rapidly increased on 19 July. On 24 July, as rainfall declined, people's concerns about disaster information gradually decreased. Heavy rain caused huge damage to Henan; therefore, it can be seen in Figure 8 that people discussed was mainly focused on rescue information and casualty loss. From 20 July, there was an explosion of social media about rescue information and casualty loss. The concern about rescue information, casualties, and loss was much higher than for other topics throughout the storm. On 26 July, as rainfall decreased, concerns about rescue information, casualties, and loss began, and the degree showed a decreasing trend. People's attention to traffic information and the causes of disaster situations during heavy rains was generally low, and there were a few discussions about disaster information and traffic information during the period of storm disaster emergencies from 21 July to 22 July. Therefore, during heavy rains in Henan, people paid more attention to rescue information and the relationship between casualties and loss situations.

When natural disasters occur, we need to focus on the geographical distribution of disaster occurrence and disaster severity. Therefore, we fully mined the geographical location information in Weibo tweets, as shown in Figures 10 and 11, as a regional distribution map of social media as well as a map of social media quantity distribution. As can be seen in Figures 10 and 11, there were relatively more heavy-rain-related Weibo numbers released from the Zhengzhou and Xinxiang regions during the heavy rains in Henan. Second, Hebi, Anyang, and Luoyang released a certain amount of Weibo posts about heavy rain. Figure 12 calculates the damage reporting ratio for all tweets in each city. In the work of Zou et al., the damage reporting ratio is considered as the ratio of disaster-related tweets

to the total number of tweets, which is the damage severity metric: its value range is 0–1. Based on the data contrasted in Figures 10–12, on the one hand, the number of Weibo posts in each area is related to the severity of the rainstorm; on the other hand, it is related to the population density of the city. Zhengzhou is subjected to heavy rains during heavy rainfall. There are heavy rains affecting 10.352 million people, simultaneously, in Zhengzhou. Thus, Zhengzhou released the largest number of microblogs, at the same time that Xinxiang City was severely affected by heavy rains, but the population of Xinxiang was 6.043 million people. Thus, the number of microblogs in Xinxiang with regard to heavy rains is less than that of Zhengzhou. At the same time, Anyang City, Hebi City, and Luoyang City were all seriously affected by heavy rains. However, the population of Anyang City is 5.192 million, that of Luoyang City is 6.69 million, and that of Hebi City is 1.609 million. Therefore, the population of Hebi City is significantly lower than that of Hebi City and Anyang City. Although Hebi City, Anyang City, and Luoyang City have almost the same number of microblogs as rainstorms, it can be inferred that Hebi City is affected more by rainstorms than Anyang City and Luoyang City.

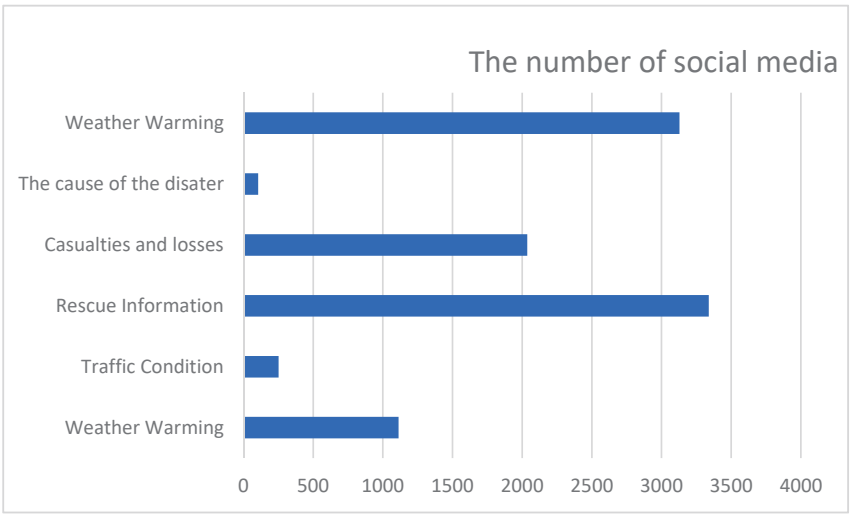

Figure 8. The histogram of natural disaster classification.

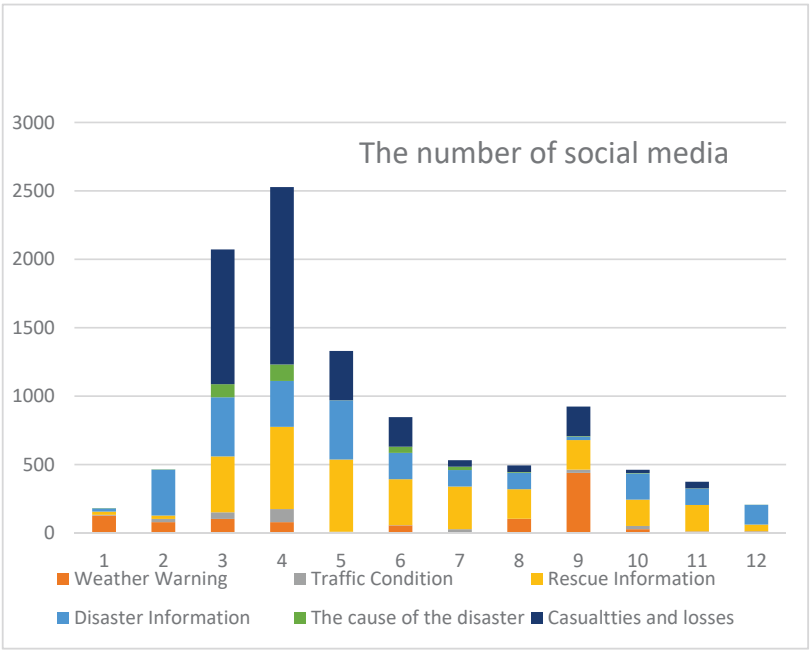

Figure 9. The number of Weibo posts on every topic.

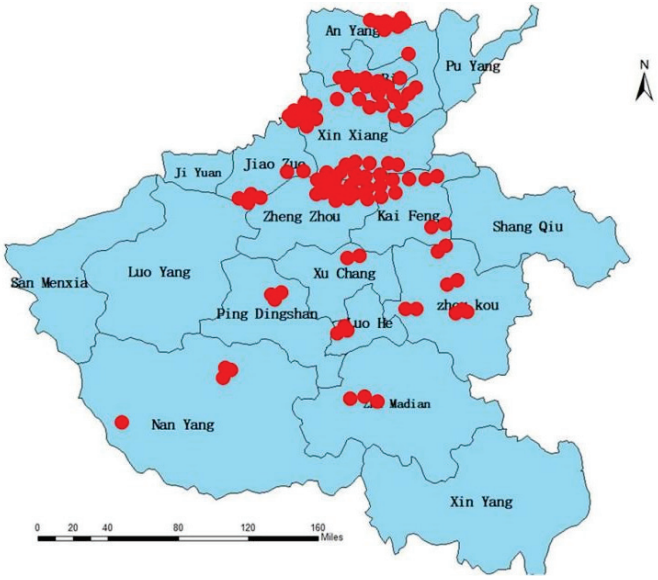

Figure 10. The space distribution map by region.

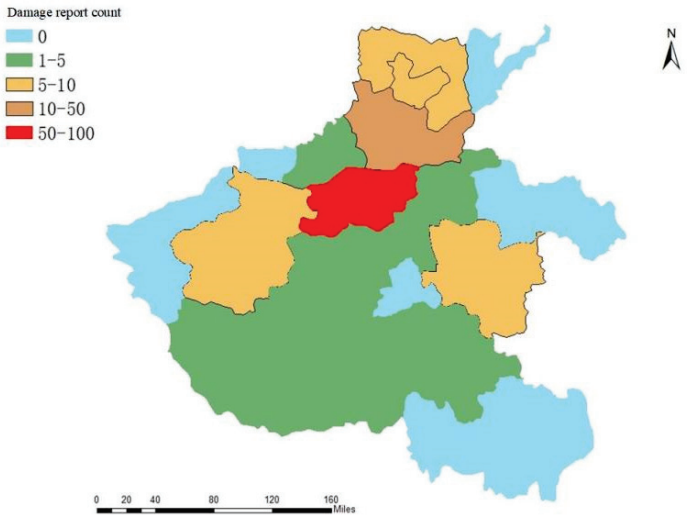

Figure 11. The number of loss reports by region.

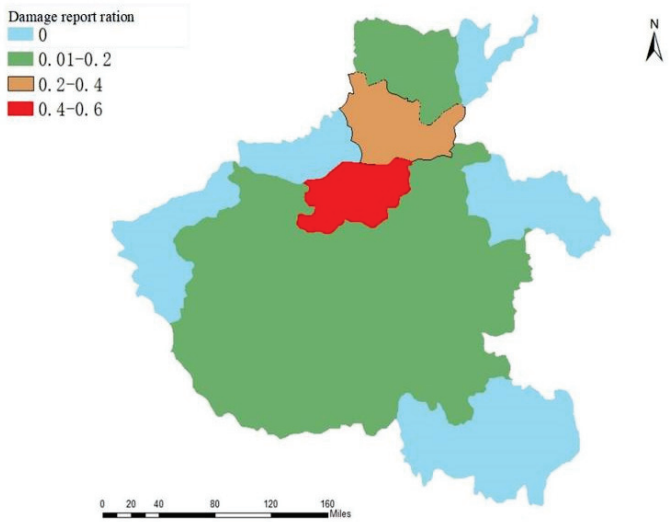

Figure 12. The loss reported rate by region.

Since more attention has been paid to rescue information as well as casualties and loss information during heavy rains, the geographical location of the rescue information as well as casualty and loss information are discussed separately in this paper. Figures 13 and 14 show the regional distribution plots of microblogs, with respect to rescue information during heavy rains, as well as the distribution plots of microblog numbers. Figures 13 and 14 show the microblog area distribution map and the number of microblogs about rescue information during the heavy rain; the number of rescued information microblogs are larger, and there are few discussions about rescue information. The population size of Zhengzhou is 10.352 million, the population size of Xinxiang is 6.043 million, the population size of modification is 6.922 million, the population size of Anyang is 5.19 million, the population size of Zhoukou is 8.8 million, the population size of Zhu median is 6.89 million, and the population of Hebi City is 1.6 million. According to the ratio of the number of microblogs related to rescue information in Figure 15, we can infer that Zhengzhou City, Xinxiang City, Hebi City, and Anyang City are comparable, although the number of microblogs related to rescue information in Hebi City is slightly less than in Anyang City, though the population of Hebi City is significantly less than Anyang City, so the rescue demand in Hebi City is higher than Anyang City; at the same time, Luoyang City, Kaifeng City, Zhoukou City, and Zhumadian City have issued a certain amount of rescue information, and we need to pay attention to the rescue needs of the area.

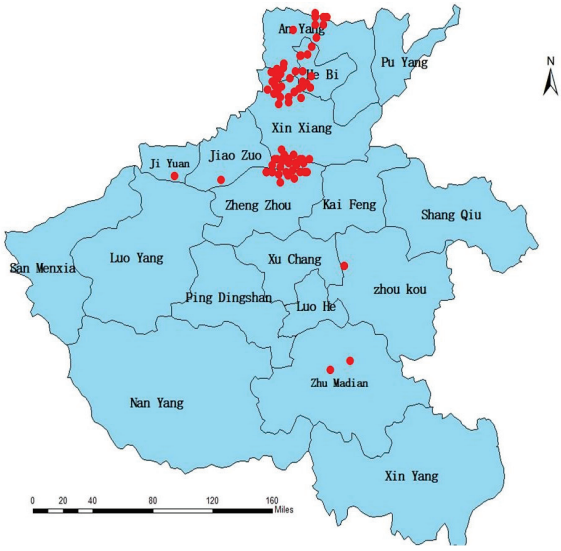

Figure 13. The area distribution map of rescue information.

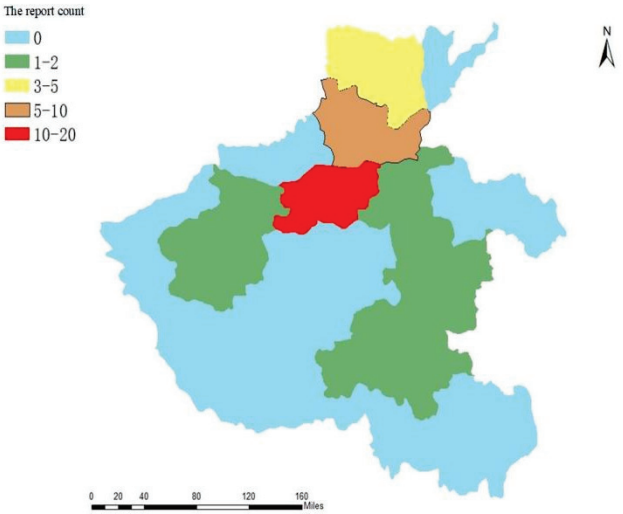

Figure 14. The number distribution map of rescue information.

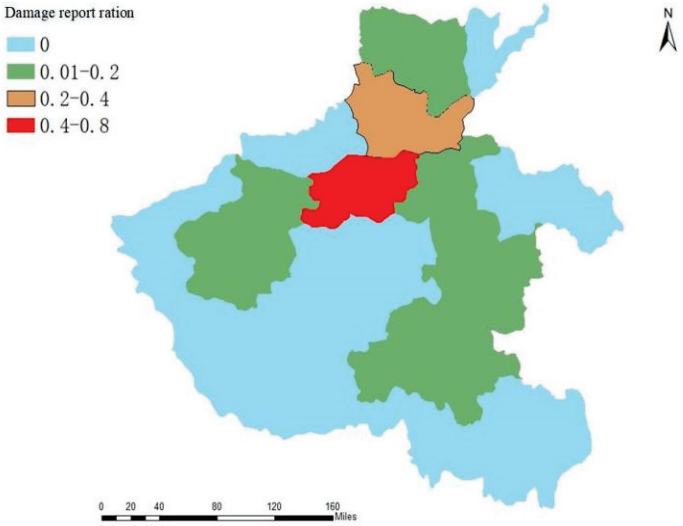

Figure 15. The loss reported rate by region.

Figures 16 and 17 show the Weibo area distribution map regarding casualties and losses during heavy rain and the distribution map of the number of Weibo posts. Figures 16 and 17 show that Weibo posts about casualties and losses are mainly concentrated in the Zhengzhou area, followed by a certain number of Weibo posts in Xinxiang and Zhoukou City, while Hebi and Luoyang also made Weibo posts about casualties and losses. By comparing the casualty and loss ratio chart in Figure 18, we can infer that the Weibo posts of casualties and losses are mainly concentrated in Zhengzhou City because Zhengzhou City experienced a greater impact from heavy rains, and Zhengzhou has a large population. At the same time, Hebi and Anyang had a small number of casualties, and loss microblogs were posted in Zhumadian and Luoyang. It can be seen that the number of casualties and loss microblogs is related to the severity of the heavy rains in each city and the population density. At the same time, compared with the number of rescue information microblogs, the distribution of casualties and losses was more concentrated in Zhengzhou. This is because during heavy rains, people use microblogs to seek help and find missing persons, and such microblogs attract more public attention. A large number of reposts were generated. Therefore, the Weibo location information of casualties and losses is more accurate and concentrated.

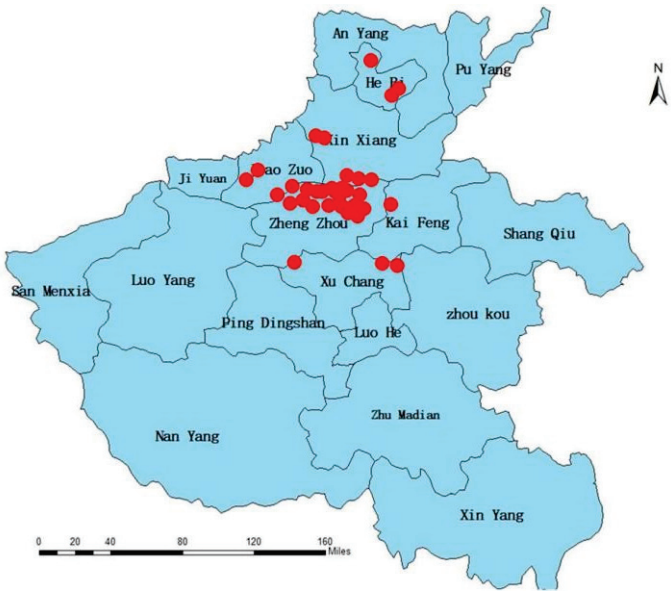

Figure 16. The area distribution map of casualties and losses.

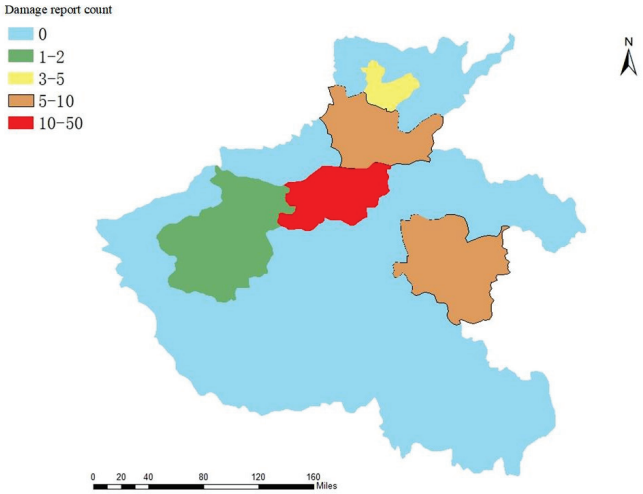

Figure 17. The number distribution map of casualties and losses.

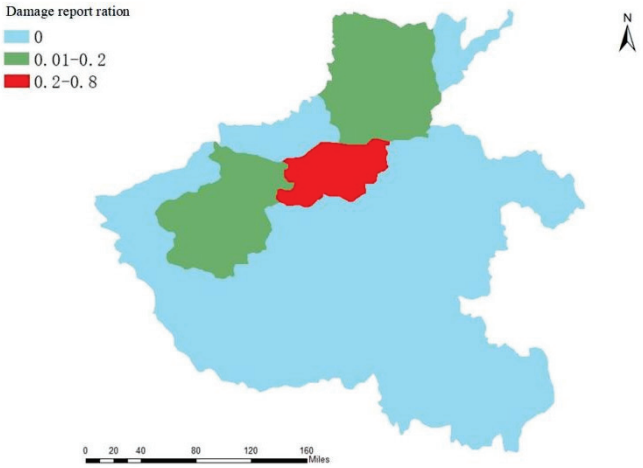

Figure 18. The casualties and losses reported rate by region.

3.3. Evaluating Indicator

Classification performance was evaluated by precision, recall, and F1-score. Three indicators were used to measure the accuracy of the proposed classification method. The accuracy of the calculations for each category is presented in Table 6. From the perspective of accuracy, recall rate, and F1-score, most of them are above 0.8, indicating that most of the disaster themes can be correctly identified, and that the method used in this study has a comparative advantage. A good classification effect exists, but the poor performance of the recall rate of the weather warning category is due to a large amount of weather warning information being misidentified. This may be because of two reasons. On the one hand, the number of Weibo posts related to weather warnings is small; on the other hand, the content of Weibo posts related to weather warnings is relatively complicated and may contain various types of information, resulting in misidentification from the text.

Table 6. The text disaster information accuracy assessment results.

Category	Acc	Rel	F1_Score
Weather warning	0.99	0.07	0.13
Traffic condition	0.97	0.89	0.90
Rescue information	0.95	0.91	0.93
Disaster information	0.88	0.87	0.85
The cause of the disaster	0.98	0.86	0.83
Casualties and losses	0.89	0.89	0.89
Overall	0.93	0.78	0.85

We collect 25,880 tweets from Weibo. We perform the following standard text preprocessing steps: (1) remove the content on Weibo that is not related to the rainstorm in Henan; (2) classify the remaining text by topic; and (3) manually read and mark 3000 texts as training samples for the Bert model.

All images are resized to ($224 \times 224 \times 3$), which is the input size that Vgg-16 needs. In the dataset, 20% of samples are used to evaluate the performance of models, and the remaining 80% of them are used for training.

To prove the effectiveness of the model proposed in this study, we compare the model with several traditional models and several state-of-the-art models on our dataset. In contrast, the classification performance is measured by three indicators: accuracy, recall, and F1-score, which are shown in Table 7. Table 7 displays the performance of all the compared models in three categories: (1) text-based networks: the model is listed in No.1 in the table. The model was designed based on the encoder of bidirectional transformer. They were trained from scratch on our dataset; (2) imaged-based networks: these models are listed from No.2 to No.3 in the table. In our experiment, these models were initialized with weights learned from ImageNet and fine-tuned with our dataset; and (3) multimodal-based networks: these models are listed from No.4 to No.6 in the table, which uses both image and textual information for the model training. These models were also trained entirely on our dataset. The performance of our multimodal network is listed in the last line of the table.

Table 7. Compared with traditional classification models.

	Acc	**Rel**	**F1_Score**
Bert (text only)	0.78	0.79	0.78
Vgg-16 (image only)	0.79	0.80	0.80
Vgg-19 (image only)	0.80	0.81	0.81
CCR [27]	0.81	0.81	0.82
KGE-MMSLDA [28]	0.81	0.82	0.83
EANN [29]	0.84	0.82	0.83
Proposed approach	0.93	0.84	0.85

Based on the testing results in Table 7, we have several observations: (1) our proposed network outperforms the other multimodal based networks; (2) modes that leverage multimodal information perform better than only considering single modal information; and (3) image-based models perform better than text-based models. This is reasonable since image information is more intuitive and clearer.

3.4. The Severity Assessment of Emergencies

According to the description of the entropy method in the research, the study calculates the weights, then, we convert the indicators so that the larger of the F values represents a higher severity. At last, we expand the value of F to 100 times, thus, its range of values is transformed into [0, 100].

According to F values, the study set the severity assessment levels in Table 8.

Table 8. The severity level and warning level.

***F*-Value**	**The Severity Level**	**The Warning Level**
[0, 10]	/	The grey warning
[10, 30]	I	The yellow warning
[30, 60]	II	The orange warning
[60, 100]	III	The red warning

As shown in Table 9 the study judges the severity of the event, it takes the highest value of the event in the whole time period as the final evaluation level. The experiments have shown that the highest score of weather warning is 38, and the corresponding severity level

is II. The highest score of traffic condition is 6, and the corresponding severity level is /. The highest score of rescue information is 73, and the corresponding severity level is III. The highest score of disaster information is 49, and the corresponding severity level is II. The highest score of the cause of the disaster is 19, and the corresponding severity level is I. The highest score of the casualties and losses is 81, and the corresponding severity level is III.

Table 9. Early warning mechanism for emergencies.

The Indicators	The Grey Warning	The Yellow Warning	The Orange Warning	The Red Warning	The Others
Post rate	<100	<300	<500	≥500	— —
Retweet rate	<500	<1000	<3000	≥3000	— —
Comment rate	<1000	<2000	[3000, 6000]	≥6000	Between [2000–3000], to avoid deterioration to amoderate events
Liket rate	<2000	<6000	[8000, 80,000]	≥80,000	Between [6000–8000], to avoid deterioration to amoderate events

When the post rate is less than 100, the retweet rate is less than 500, the comment rate is less than 1000, and the like rate is less than 2000, the event may be in the initial period or recession. However, we need to pay special attention to the double growth of these indicators: if they suddenly increase exponentially, the event is deteriorating.

When the post rate is between [100–300], the retweet rate is between [500–1000], the comment rate is between [1000–2000], and the like rate is between [2000–6000], the event may be in the period of outbreak and spread. At this time, the impact on the severity of emergencies tends to be general, so in order to avoid further deterioration of the incident, the government needs to start the yellow warning in time.

When the post rate is more than 300, the retweet rate is between [1000–3000], the comment rate is between [3000–6000], and the like rate is between [8000–80,000], the event may be in the period of outbreak and spread. At this time, the impact on the severity of emergencies tends to be medium, so the government needs to start the orange warning in time.

When the post rate is more than 500, the retweet rate is more than 3000, the comment rate is more than 6000, and the like rate is more than 80,000, the event may be in the period of outbreak and spread. At this time, the impact on the severity of emergencies tends to be serious, so the government needs to start the red warning in time.

4. Conclusions

In recent years, the acquisition and analysis of disaster information have become key issues for government and scientific research institutions. Social media data can enable officials and victims to be the truth and disseminators of natural disaster information, simultaneously, and social media data have the advantages of real-time and low latency. Therefore, social media has become an important source of natural disaster information. With the development of technology, scholars have optimized the methods for studying natural disaster information.

This study uses a classification model based on LDA and a multi-classification model based on Bert and Vgg-16, which are suitable for short-term social media and other types of disaster events that have caused a large-scale sensation.

In this study, we first used a web crawler combined with the Weibo API to obtain the text and graphic data for subsequent processing and classification. The LDA model was used to classify and identify topics related to emergencies. Based on the data characteristics of text and images, this study constructed a network framework suitable for microblog text and image disaster extraction. After optimization operations, such as control over-fitting and grid-parameter optimization, the accuracy of the model on the test set was improved, and the classification accuracy reached more than 80%. The results of the verification on the newly acquired Henan torrential rain dataset in 2021 further show that the application of the model to disaster information classification has a certain degree of accuracy. Finally,

through the visualization and statistical analysis of the data, it was found that the disaster information is consistent with the actual disaster development stage, which shows that the method proposed in this study is effective in monitoring Henan rainstorm disaster events and can effectively help in official disaster decision-making.

Author Contributions: Conceptualization, Q.H.; methodology, Q.H.; software, M.Z.; validation, M.Z. and H.L.; formal analysis, H.L.; investigation, Q.H.; resources, M.Z.; data curation, M.Z.; writing–original draft preparation, H.L.; writing–review and editing, M.Z.; visualization, Q.H.; supervision, M.Z.; project administration, Q.H.; funding acquisition, Q.H. All authors have read and agreed to the published version of the manuscript.

Funding: This research was funded by National Social Science Foundation of China, grant number 20AZZ006; the Innovation and Entrepreneurship Foundation of Guizhou, grant number S.202110671039; and the Foundation of Guizhou University of Finance and Economics, grant number 2020XQN04.

Institutional Review Board Statement: The studes are not applicable for ethical review and approval for studies not involving humans or animals.

Informed Consent Statement: Not applicable.

Acknowledgments: The authors thanks Qisong Huang for their support during the experiment.

Conflicts of Interest: The authors declare no conflict of interest.

References

1. Abid, F.; Li, C.; Alam, M. Multi-source social media data sentiment analysis using bidirectional recurrent convolutional neural networks. *Comput. Commun.* **2020**, *157*, 102–115. [CrossRef]
2. Basalamah, A.; Rahman, S. An Optimized CNN Model Architecture for Detecting Coronavirus (COVID-19) with X-ray Images. *Comput. Syst. Sci. Eng.* **2022**, *40*, 375–388. [CrossRef]
3. Chen, C.C.; Wang, H.-C. Using community information for natural disaster alerts. *J. Inf. Sci.* **2020**, *46*, 1–15. [CrossRef]
4. Kang, A.; Ren, L.; Hua, C.; Dong, M.; Fang, Z.; Zhu, M. Stakeholders' views towards plastic restriction policy in China: Based on text mining of media text. *Waste Manag.* **2021**, *136*, 36–46. [CrossRef] [PubMed]
5. Xu, N.; Mao, W. A Residual Merged Neutral Network for Multimodal Sentiment Analysis. In Proceedings of the 2017 IEEE 2nd International Conference on Big Data Analysis (ICBDA), Beijing, China, 10–12 March 2017.
6. Kitazawa, K.; Hale, S.A. Social media and early warning systems for natural disasters: A case study of Typhoon Etau in Japan. *Int. J. Disaster Risk Reduct.* **2021**, *52*, 101926. [CrossRef]
7. Nguyen, D.T.; Ofli, F.; Imran, M.; Mitra, P. Damage Assessment from Social Media Imagery Data during Disasters. In Proceedings of the 2017 IEEE/ACM International Conference on Advances in Social Networks Analysis and Mining, Sydney, Australia, 31 July–3 August 2017.
8. Behl, S.; Rao, A.; Aggarwal, S.; Chadha, S.; Pannu, H.S. Twitter for disaster relief through sentiment analysis for COVID-19 and natural hazard crises. *Int. J. Disaster Risk Reduct.* **2021**, *55*, 102101. [CrossRef]
9. Hao, H.; Wang, Y. Leveraging multimodal social media data for rapid disaster damage assessment. *Int. J. Disaster Risk Reduct.* **2020**, *51*, 101760. [CrossRef]
10. Piatyszek, E.; Karagiannis, G.M. A model-based approach for a systematic risk analysis of local flood emergency operation plans: A first step toward a decision support system. *Nat. Hazards* **2012**, *61*, 1443–1462. [CrossRef]
11. Yu, M.; Huang, Q.; Qin, H.; Scheele, C.; Yang, C. Deep learning for real-time social media text classification for situation awareness—Using Hurricanes Sandy, Harvey, and Irma as case studies. *Int. J. Digit. Earth* **2019**, *12*, 1230–1247. [CrossRef]
12. Ghafarian, S.H.; Yazdi, H.S. Identifying crisis-related informative tweets using learning on distributions. *Inf. Process. Manag.* **2020**, *57*, 102145. [CrossRef]
13. Aznar-Crespo, P.; Aledo, A.; Melgarejo-Moreno, J.; Vallejos-Romero, A. Adapting Social Impact Assessment to Flood Risk Management. *Sustainability* **2021**, *13*, 3410. [CrossRef]
14. Kumar, A.; Singh, J.P.; Dwivedi, Y.K.; Rana, N.P. A deep multi-modal neural network for informative Twitter content classification during emergencies. *Ann. Oper. Res.* **2020**. [CrossRef]
15. Wang, M.; Cao, D.; Li, L.; Li, S.; Ji, R. Microblog Sentiment Analysis Based on Cross-media Bag-of-words Model. In Proceedings of the International Conference on Internet Multimedia Computing and Service, Xiamen, China, 10–12 July 2014.
16. Ragini, J.R.; Anand, P.R.; Bhaskar, V. Big data analytics for disaster response and recovery through sentiment analysis. *Int. J. Inf. Manag.* **2018**, *42*, 13–24. [CrossRef]
17. Rasiwasia, N.; Pereira, J.C.; Coviello, E.; Doyle, G.; Lanckriet, G.R.; Levy, R.; Vasconcelos, N. A New Approach to Cross-Modal Multimedia Retrieval. In Proceedings of the 18th ACM International Conference on Multimedia, Firenze, Italy, 25–29 October 2010.
18. Ghosh, S.; Srijith, P.K.; Desarkar, M.S. Using social media for classifying actionable insights in disaster scenario. *Int. J. Adv. Eng. Sci. Appl. Math.* **2017**, *9*, 224–237. [CrossRef]

19. Wood, E.; Sanders, M.; Frazier, T. The practical use of social vulnerability indicators in disaster management. *Int. J. Disaster Risk Reduct.* **2021**, *63*, 102464. [CrossRef]
20. Xu, Z. How emergency managers engage Twitter users during disasters. *Online Inf. Rev.* **2020**, *44*, 933–950. [CrossRef]
21. Yang, T.; Xie, J.; Li, G.; Mou, N.; Chen, C.; Zhao, J.; Liu, Z.; Lin, Z. Traffic Impact Area Detection and Spatiotemporal Influence Assessment for Disaster Reduction Based on Social Media: A Case Study of the 2018 Beijing Rainstorm. *ISPRS Int. J. Geo-Inf.* **2020**, *9*, 136. [CrossRef]
22. Gupta, A.; Katarya, R. PAN-LDA: A latent Dirichlet allocation based novel feature extraction model for COVID-19 data using machine learning. *Comput. Biol. Med.* **2021**, *138*, 104920. [CrossRef]
23. Hung, P.T.; Yamanishi, K. Word2vec Skip-Gram Dimensionality Selection via Sequential Normalized Maximum Likelihood. *Entropy* **2021**, *23*, 997. [CrossRef]
24. Yu, Y.; Lin, H.; Meng, J.; Zhao, Z. Visual and Textual Sentiment Analysis of a Microblog Using Deep Convolutional Neural Networks. *Algorithms* **2016**, *9*, 41. [CrossRef]
25. Qiao, B.; Zou, Z.; Huang, Y.; Fang, K.; Zhu, X.; Chen, Y. A joint model for entity and relation extraction based on BERT. *Neural Comput. Appl.* **2022**, *34*, 3471–3481. [CrossRef]
26. Gao, W.; Li, L.; Zhu, X.; Wang, Y. Detecting Disaster-Related Tweets Via Multimodal Adversarial Neural Network. *IEEE MultiMedia* **2020**, *27*, 28–37. [CrossRef]
27. You, Q.; Luo, J.; Jin, H.; Yang, J. Cross-modality consistent regression for joint visual-textual sentiment analysis of social multimedia. In Proceedings of the Ninth ACM International Conference on Web Search and Data Mining, San Francisco, CA, USA, 22–25 February 2016.
28. Xue, F.; Hong, R.; He, X.; Wang, J.; Qian, S.; Xu, C. Knowledge-Based Topic Model for Multi-Modal Social Event Analysis. *IEEE Trans. Multimedia* **2020**, *22*, 2098–2110. [CrossRef]
29. Wang, Y.; Ma, F.; Jin, Z.; Yuan, Y.; Xun, G.; Jha, K.; Su, L.; Gao, J. EANN: Event Adversarial Neural Networks for Multi-Modal Fake News Detection. In Proceedings of the 24th ACM SIGKDD International Conference on Knowledge Discovery& Data Mining, London, UK, 19–23 August 2018; pp. 849–857.

sustainability

MDPI

Article

Multi-Hazard Meteorological Disaster Risk Assessment for Agriculture Based on Historical Disaster Data in Jilin Province, China

Jiawang Zhang [1], Jianguo Wang [1,*], Shengbo Chen [2], Siqi Tang [1] and Wutao Zhao [1]

[1] College of Earth Sciences, Jilin University, Changchun 130061, China; jwzhang20@mails.jlu.edu.cn (J.Z.); tangsq21@mails.jlu.edu.cn (S.T.); wtzhao21@mails.jlu.edu.cn (W.Z.)
[2] College of Geo-Exploration Science and Technology, Jilin University, Changchun 130026, China; chensb@jlu.edu.cn
* Correspondence: wang_jg@jlu.edu.cn

Abstract: The impact of global climate change is gradually intensifying, and the frequent occurrence of meteorological disasters poses a serious challenge to crop production. Analyzing and evaluating agricultural multi-hazard meteorological disaster risks based on historical disaster data and a summary of disaster occurrences and development patterns are important bases for the effective reduction of natural disaster risks and the regulation of agricultural production. This paper explores the technical system of agricultural multi-hazard meteorological disaster risk assessment and establishes a disaster risk assessment model based on the historical disaster data at the regional level from 1978–2020 in the first national comprehensive natural disaster risk census, carrying out multi-hazard meteorological disaster risk assessments in 18 major grain-producing regions in Jilin province. The empirical evidence shows: (1) drought and flood disasters are the key disasters for agricultural meteorological disaster prevention in Jilin province. Hotspots of drought and flood disasters are widely distributed in the study area, while hail and typhoons are mainly concentrated in the eastern region with a certain regionality. (2) The risk values of the four major meteorological disasters all decreased with the increase of the disaster index. Under the same disaster index, the disaster risk of various disasters in the main grain-producing areas is as follows: drought > flood > typhoon > hail. Under different disaster indices, Jiutai, Nongan, Yitong, Tongyu, and other places all presented high and medium–high risk levels. (3) From the spatial evolution trend, along with the rising disaster index, the risk of multi-hazard meteorological hazards is spatially oriented in a southeastern direction, and the risk level of multi-hazard meteorological hazards in the central part of the study area decreases gradually along with the increasing damage index. In addition, regional agricultural multi-hazard meteorological disaster risk reduction recommendations are made in three aspects: institutional construction, management model, and reduction capacity.

Keywords: historical disasters; multi-hazard meteorological disasters; risk assessment; major grain-producing areas; Jilin province

Citation: Zhang, J.; Wang, J.; Chen, S.; Tang, S.; Zhao, W. Multi-Hazard Meteorological Disaster Risk Assessment for Agriculture Based on Historical Disaster Data in Jilin Province, China. *Sustainability* **2022**, *14*, 7482. https://doi.org/10.3390/su14127482

Academic Editors: Stefano Morelli, Veronica Pazzi and Mirko Francioni

Received: 20 May 2022
Accepted: 17 June 2022
Published: 19 June 2022

1. Introduction

The Sixth Assessment Report of the IPCC, held in August 2021, noted that climate change has affected the occurrence of a number of extreme weather and climate events in all regions of the world [1]. Global warming and urbanization have brought about changes in the intensity and frequency of weather-causing factors and in the exposure of crop-bearing bodies, which have important implications for agricultural production's ability to withstand natural disasters, and the assessment of agricultural multi-hazard disaster risks is important for formulating disaster reduction measures and increasing farmers' income [2–5]. China is one of the countries that is most severely affected by natural disasters in the world due to its vast territory, complex geographical environment, large climate fluctuations, poor

ecological stability, and high frequency and intensity of multiple disaster types. Although agricultural production has gradually declined in the process of economic development due to rapid economic growth, it is undeniable that agriculture plays a major role in ensuring people's living standards and the stable operation of the national economy. Natural disasters pose a major challenge to China's food security. The analysis and evaluation of agricultural multi-hazard meteorological disaster risks based on historical disaster data and the summary of disaster occurrence patterns are important bases for regulating agricultural production and effectively mitigating natural disaster risks. The total grain output of Jilin province in 2021 was 80.784 billion pounds, maintaining the fifth position among all provinces in the national ranking; the grain yield was 941.3 pounds/acres, increasing by 48.7 pounds/acres compared with the previous year. The yield maintained Jilin province's position of fourth place among all provinces in China (http://www.moa.gov.cn/xw/qg/202112/t20211227_6385576.htm, accessed on 5 May 2022). All data reflect that Jilin province's food security production cannot be ignored.

Agricultural production relies on the natural environment for animal and plant growth and is more vulnerable to natural disasters than other industries. In recent years, agricultural disaster risk assessment has been carried out in various large food-producing regions. Kim et al. used the heavy rain damage risk index (HDRI) to analyze flood risk levels in the southern region of Korea, to determine high-risk cities and five causes of damage, and to propose reduction and control programs based on regional risk levels and hazard types [6]. Liu et al. used a comprehensive multi-indicator evaluation method, combined with an entropic information diffusion model, to assess the risk of agricultural droughts and floods in the middle and lower reaches of the Yangtze River, proposing relevant policy recommendations based on the assessment results [7]. Summarizing the past studies, it was found that the agricultural multi-disaster risk assessment mainly focused on single-hazard or single-crop studies, and there were few multi-hazard risk assessments. Furthermore, in terms of the use of historical disaster data, the historical disaster data were mostly based on regional or national assessment units, and there was little guidance for disaster risk assessment and work in small regions.

Since the 21st century, various countries have gradually tried to establish national or regional disaster risk databases, such as the Emergency Disaster Database (EM-DAT) of the National Centre for Research on the Epidemiology of Disasters of the University of Leuven in Belgium, the Natural Disaster Database (Nat-Cat) of the Munich Reinsurance Company in Germany, and the database of the Swiss Reinsurance Company (Sigma), etc. [8–11]. However, these databases are often based on regional or national statistical units, and the spatial distribution of risks is vague and thus cannot accurately guide the local agricultural safety production and disaster reduction work. Moreover, historical disaster information of small-scale regional units often exists in the form of reports, yearbooks, news reports, disaster records, etc. The statistical caliber of disaster indicators varies especially greatly among different departments, making it difficult for disaster reduction departments to effectively collect and use early historical disaster data.

China plans to carry out the first national comprehensive natural disaster risk census in 2020–2022, which is a survey of China's natural disaster risk potential and basic national conditions, and this work is currently under intense progress [12]. The construction of historical disaster surveys and databases is the highlight of the first comprehensive natural disaster risk survey. The Emergency Management Department coordinates the collection of historical disaster archives from 1978 to 2020 by various sectors (e.g., Water, Meteorological, Agricultural). This is the first large-scale and comprehensive risk survey since the founding of the People's Republic of China. This data survey is characterized by a large amount of data with many sectors involved featuring a full range of disaster types. The collected data are of great significance for the future assessment of natural disaster risk and the sustainable development of agriculture in China.

In this study, we used the meteorological disaster data and related historical disaster files from the first comprehensive natural disaster risk census, and used the crop disaster

index to characterize the impact range of each disaster. After combining the historical disaster database of the first comprehensive natural disaster risk census and the actual situation in the main grain-producing areas of Jilin province, the agricultural multi-hazard meteorological hazards in the study area were confirmed. We analyzed and evaluated the risk of agricultural multi-hazard meteorological disasters in the region by constructing an agricultural multi-hazard meteorological disaster risk assessment model, and obtained the risk level and spatial variation of agricultural multi-hazard meteorological hazards under different disaster indices. The study is a useful exploration of the application of natural disaster census data to multi-hazard meteorological disaster risk assessment methods at the county level, and provides a quantitative basis for relevant departments to scientifically formulate disaster reduction and mitigation policies and plans. The main contributions of the article are as follows:

1. Disaster risk identification: confirm the hotspots of various disasters in the study area;
2. Disaster risk analysis: calculate the meteorological disaster risk value of the study area and the weight of a single disaster risk in each region;
3. Disaster risk assessment: determine the multi-hazard risk level and spatial differentiation in the study area;
4. Disaster risk reduction: put forward three suggestions for the reduction of food safety production in the study area.

2. Materials and Methods

2.1. Study Area

Jilin province is located at mid-latitudes on the eastern side of the Eurasian continent (121°38′ E–131°19′ E, 40°52′ N–46°18′ N). It has a land area of about 187,400 km^2. The area is rich in products and is fertile; the main grain crops are corn and rice. It is one of the three major black soil distribution areas in the world. The eastern part of Jilin is the Changbai Mountains, the central part is Song Liao Plain, and the western part is the Horqin Grassland. The terrain is high in the southeast and low in the northwest, with significant differences in geomorphology and obvious spatial differentiation in land use types [13,14]. Climatic conditions are an important factor influencing the layout and structure of food crops. The study area is influenced by the westerly wind circulation and the low-pressure system of Lake Baikal. In terms of seasonal distribution, rapid warming and high insolation rates in spring provide light resources for the early stages of crop production. High temperatures and rain in summer with long daylight hours are favorable for crops to photosynthesize. Autumn has sufficient light, a large temperature difference between day and night, more sunshine, and less rain, which is conducive to nutrient accumulation in food crops. Cold and long winters reduce the occurrence of pests and pesticide use, which is conducive to the rest and recuperation of arable land. There are obvious seasonal variations and regional differences in temperature and precipitation in Jilin province [15–17]. The average winter temperature is below −11 °C, and the average summer temperature is above 23 °C. The frost-free period is 100–160 days, and there is an annual average of 2259–3016 h of sunshine with a sunshine rate of 50–70%. The average annual precipitation is 400–600 mm, with summer exceeding the sum of spring, autumn, and winter, just at the peak of crop development and growth with light, heat, and rain arriving simultaneously; this is a unique advantage for crop cultivation in Jilin province [18–20]. There is an obvious wet to semi-humid to semi-arid transition from the east to the west, and the alluvial plain area covered by sand dunes in the west is a sensitive area for climate change response and an important agricultural production base in China; thus, there is some theoretical significance and practical value to studying the integrated risk law of multi-hazards in the study area. Combining the available data, the article classifies the province's grain yield using the natural intermittent classification method based on the grain yield data of 60 districts in Jilin province in 2020, and finally obtains 18 districts with high and medium–high yield grades as the study area (Figure 1a). The study area is mostly arable land with an arable land cover of 70% (Figure 1b).

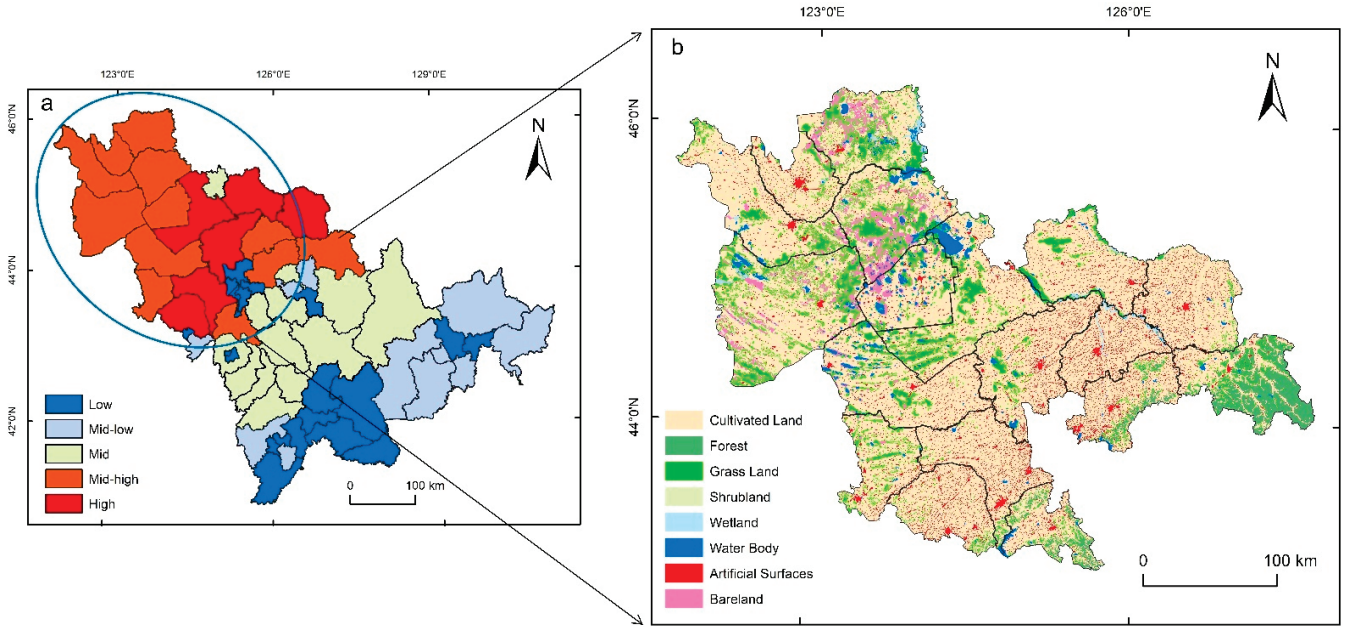

Figure 1. The main grain-producing area of Jilin province, China: (**a**) distribution of grain yield classes in Jilin province (**left**); (**b**) distribution of land use types in the study area (**right**).

2.2. Data Sources

The historical disaster survey of the first national comprehensive natural disaster risk census uses the district as its basic survey unit. Seven types of disasters, namely, drought, flood, typhoon, hail, sandstorm, freezing, and snowstorm, were investigated in the historical disasters from 1978 to 2020. Because of the wide distribution of historical disaster files, non-uniform statistical indicators, and a lack of data precision, the management of historical disaster files has been confusing in various industries. The first national comprehensive natural disaster risk census historical disaster database is the most comprehensive coverage of disaster database construction since the founding of the People's Republic of China, which is of great significance for the subsequent statistics and predictions of natural disaster risk. The data underlying this study were derived from this historical disaster database (https://fxpc.mem.gov.cn/NationalDisastersProject/#/LoginPage, accessed on 14 January 2022). Through the collation and measurement of all survey data, we obtained basic data for the last 43 years. The basic data and the disaster data, such as sown area, crop damage, and house damage, for each disaster type in the past years were obtained. Taking the main grain-producing areas in Jilin province as the basic evaluation unit, the multi-hazard meteorological disaster risk was studied from the perspective of disaster loss, using the crop damage area and annual sown area data of each disaster in the past years, as well as the grain production data in 2020, as the original data. With the help of the disaster index (disaster index = affected area/sown area), which reflects the degree of agricultural disaster, the larger the index is, the greater the impact of the disaster and the higher the crop yield reduction due to the disaster.

The disaster information for seven major disaster types in the study area was extracted from the historical disaster database of the first comprehensive natural disaster risk census. It mainly includes statistics on the average affected area, average demolished area, and frequency of disasters in the main grain-producing areas of Jilin province (Figure 2). In terms of average affected area, drought has the largest disaster area, while floods, typhoons, and freezing have little difference in disaster areas, indicating that the main grain-producing areas in Jilin province are prone to large disaster areas due to drought. The average demolished area refers to the sown area where the crop yield has been reduced by more than 80% compared with the normal year due to the disaster. The average demolished area can reflect the severity of disasters from the side. The average demolished area of four

disasters, namely, drought, flood, hail, and typhoon, exceeds 1000 hm^2, indicating that four disasters have a high degree of impact on agricultural production in Jilin province. In terms of the frequency of disasters in the main grain-producing areas, the frequency of droughts, floods, hail, and typhoons all exceed 50 times, which are high-frequency disasters in the main grain-producing areas of Jilin province. Freezing events and snowstorms are common after November, but the main grain-producing areas in Jilin province have completed harvesting and transferring the crop yield into a warehouse, as well as other tasks, by this time, so the impact on the large area of grain damage is minimal. Similarly, sandstorms tend to occur in March, when crops have not been sown and do not cause serious damage. Grain crops in Jilin province are sown in April and harvested in October. These three disasters (freezing, snowstorm, and sandstorm) do not cause widespread damage. Based on the above analysis, four disasters, namely, drought, flood, hail, and typhoon, were selected as the disasters for our study.

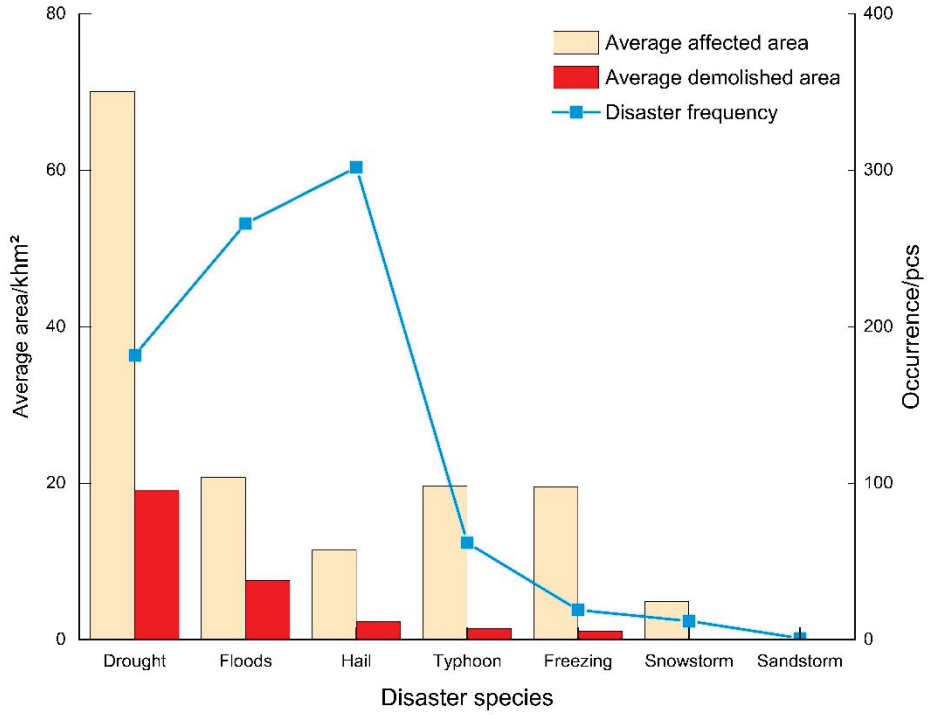

Figure 2. Average affected (demolished) area and frequency of each disaster species in the study area.

From the original data, four disasters affected the main grain-producing areas in Jilin province (Table 1). The average disaster index for drought in Taonan and Qianan in the western region of the study area was greater than 0.5, and the severity of the disaster was more serious compared with other places. Floods and hail occurred with high frequency in the study area but did not cause larger-scale disasters to occur, and the average disaster index was below 0.3. The average disaster index of typhoons in Yitong and Jiutai is relatively high, and the others are at relatively low levels, with certain regional characteristics. In general, there are many kinds of disasters in the main grain-producing areas of Jilin province, and the wide distribution of the affected areas and the multi-hazard meteorological disasters pose a greater threat to the agricultural safety production in the province's main grain-producing areas, which should attract the attention of local governments and experts.

Table 1. Average damage index of four disaster species in the main grain-producing areas.

Evaluation Unit	Drought	Flood	Typhoon	Hail
Jiutai (JT)	0.390631	0.148485	0.235727	0.124041
Nongan (NA)	0.394813	0.116918	0.095588	0.038850
Yushu (YS)	0.343445	0.084944	0.021053	0.043148
Dehui (DH)	0.285873	0.122036	0.194169	0.031608
Gongzhuling (GZL)	0.175963	0.079955	0.066505	0.054757
Shulan (SL)	0.216273	0.070940	0.110332	0.123191
Lishu (LS)	0.302651	0.089038	0.081240	0.069131
Yitong (YT)	0.313006	0.161347	0.370114	0.084881
Shuangliao (SL)	0.300570	0.197455	0.026547	0.046671
Qianguo (QG)	0.346500	0.081293	0.042080	0.059420
Changling (CL)	0.383543	0.098864	0.080606	0.043555
Qianan (QA)	0.532736	0.131110	0.070101	0.044578
Fuyu (FY)	0.160851	0.034925	0.109651	0.020429
Taobei (TB)	0.479668	0.203550	0.026796	0.149567
Zhenlai (ZL)	0.442655	0.293019	0.020543	0.032686
Tongyu (TY)	0.254391	0.228752	0.006609	0.031698
Taonan (TN)	0.576323	0.274184	0.000000	0.084189
Daan (DA)	0.277935	0.123955	0.065271	0.078949

2.3. Methodology

In this study, we arrived at comprehensive disaster risk assessment research results by using historical disaster data over the years to calculate the disaster index of various disasters, and then using the fuzzy mathematical method for small-area and small-sample risk assessment to infer the risk value of disaster risk occurrence under different disaster indices. The risk level of disaster evaluation was classified using the risk recurrence period, and the risk assessment level and spatial distribution of multi-hazard meteorological disasters at the county level were obtained by weighting each disaster type based on the entropy weighting method. The used multi-hazard risk assessment technical route is shown in Figure 3.

For disaster risk identification, the average affected area was used to calculate the local Getis-Ord *Gi** index, and the cold hotspot area of each single disaster species and the dominant disaster species of multi-hazard meteorological hazards in the region were determined. Based on the average affected area of each region, the entropy weight method was used to reflect the amount of information contained in the disasters in the main grain-producing areas so as to obtain the risk assessment weight of each disaster type in each assessment unit.

For the disaster risk analysis, using the agricultural disaster indices of each disaster species, the single sample observations were converted into fuzzy sets by information diffusion coefficients. Meanwhile, a quantitative analysis of regional agricultural multi-hazard meteorological hazards was carried out, and the probability values and risk values of multi-hazards under different disaster indices were calculated for each evaluation unit. In addition, based on the risk values of the disaster risk analysis, the risk recurrence period of each disaster under different disaster indices was calculated, and five risk evaluation levels under different disaster indices were classified according to the actual situation of risk values.

In the disaster risk assessment, the assessment weights in the risk identification stage and the risk evaluation levels in the disaster risk analysis stage were weighted and summed to obtain the risk assessment results of agricultural multi-hazard meteorological hazards for each assessment unit under different disaster indices. In addition, the spatial directionality and predictability of the risk assessment results of agricultural multi-hazard meteorological hazards were studied to obtain their spatial distribution.

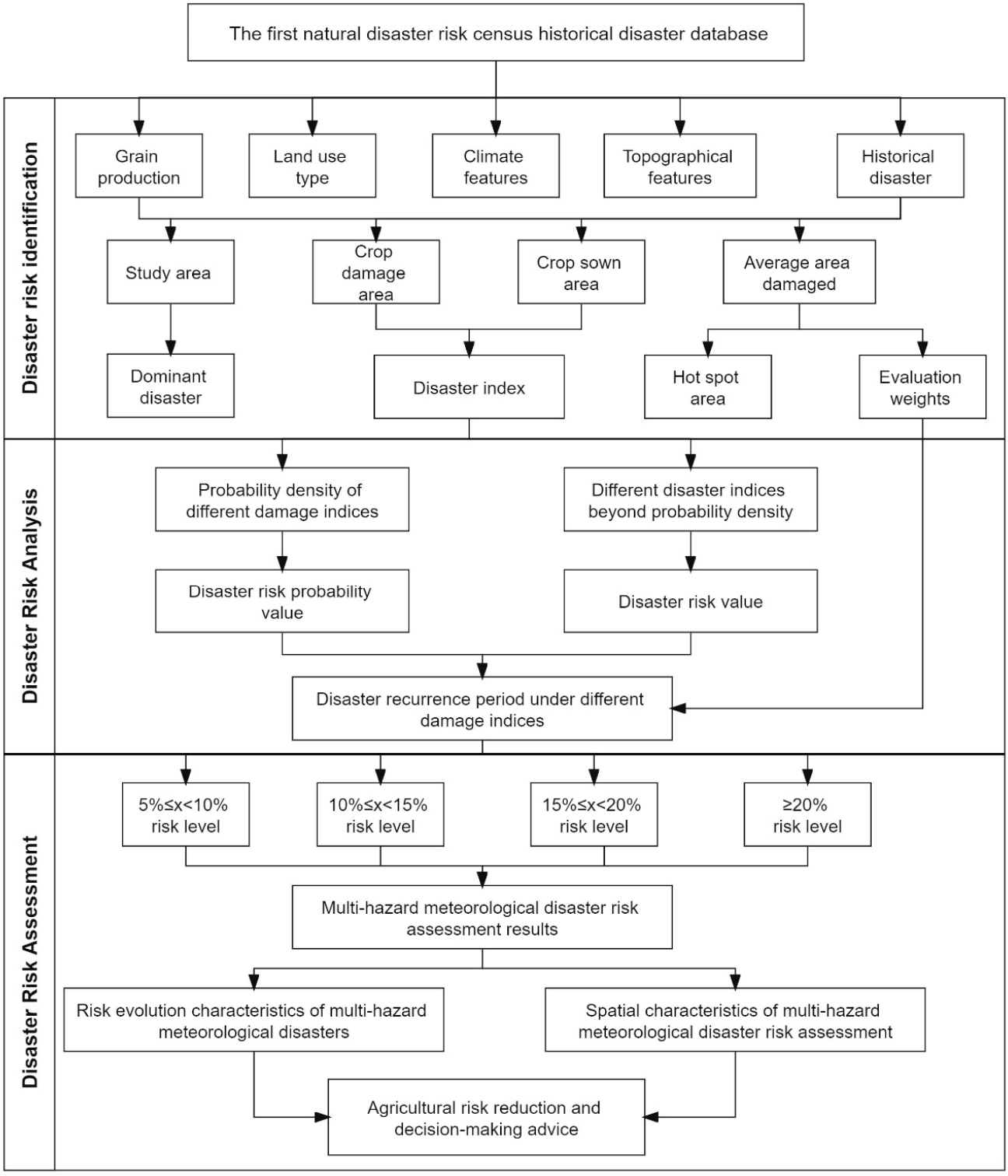

Figure 3. Multi-hazard risk assessment technical route.

2.3.1. Fuzzy Risk Analysis Model

The risk analysis and evaluation of agricultural multi-hazard meteorological disasters was based on the method of fuzzy mathematics to collect the traditional observation sample points in order to solve the problem of insufficient sample data and improve the accuracy of information processing [21–23]. The specific operation steps are as follows:

Assume that $y_1, y_2, \cdots, y_m$ are the actual values (observations) of risk factor indicators (hazard indicators) in year m, and the set of observation samples is:

$$y_j = \{y_1, y_2, \cdots, y_m\} \tag{1}$$

where: y_j—sample observation points; m—total number of sample observations.

Let the universe of y_j (u_i), $u_i(i = 1, 2 \ldots n)$ be the control point of the universe of disaster index:

$$u_i = \{u_1, u_2, \cdots, u_n\} \tag{2}$$

where: u_i—any discrete real value obtained by discretizing at a fixed interval in the interval [0, 1]; n—the total number of discrete points.

The information carried by each single observation sample value y_j is diffused to each member of the indicator domain u_i based on the following equation, the information diffusion equation for y_j:

$$f_j(u_i) = \frac{1}{h\sqrt{2\pi}} e^{\left[-\frac{(y_j - u_i)^2}{2h^2}\right]} \tag{3}$$

where: h—the diffusion coefficient, which is determined according to the number of samples. It is given by the following equation:

$$h = \begin{cases} 0.8146(b-a), \ m = 5 \\ 0.5690(b-a), \ m = 6 \\ 0.4560(b-a), m = 7 \\ 0.3860(b-a), m = 8 \\ 0.3362(b-a), \ m = 9 \\ 0.2986(b-a), \ m = 10 \\ \frac{2.6851(b-a)}{(m-1)}, \ m \geq 11 \end{cases} \tag{4}$$

where: b—the maximum value in the sample set; a—the minimum value in the sample set; m—the number of samples.

If marked:

$$C_j = \sum_{i=1}^{n} f_j(u_i), \ j = 1, 2, \ldots, m \tag{5}$$

then any observation sample y_j becomes a fuzzy set with $\mu_{yj}(u_i)$ as the affiliation function, and the affiliation function of the corresponding fuzzy subset is:

$$\mu_{yj}(u_i) = \frac{f_j(u_i)}{c_j} \tag{6}$$

where: c_j is the sum of $f_j(u_i)$; $\mu_{yj}(u_i)$ is the normalized information distribution of sample y_j. Then, let:

$$\mathrm{Q}(u_i) = \sum_{j=1}^{m} \mu_{yj}(u_i) \tag{7}$$

From the set of observation samples $\{y_1, y_2, \cdots, y_m\}$, it is inferred by information diffusion that if the sample observation can only take one of $\{u_1, u_2, \cdots, u_n\}$, the number of samples with observation u_i is $\mathrm{q}(u_i)$ when all y_j are considered as sample representatives. $\mathrm{Q}(u_i)$ is usually not a positive integer, but must be a number not less than 0.

$$\mathrm{Q} = \sum_{i=1}^{n} \mathrm{q}(u_i) \tag{8}$$

Q is the sum of the number of samples at each u_i point, so theoretically it should be Q = m, but due to the error of numerical calculation, Q is slightly different from m.

$$P(u_i) = \frac{q(u_i)}{Q} \tag{9}$$

$P(u_i)$ is the probability value of the sample falling at u_i, which can be used as a probability estimate. For a single-valued observation sample indicator $y_j = \{y_1, y_2, \cdots, y_m\}$, take y_j as an element u_i in the theoretical domain u. The probability value of exceeding u_i should be:

$$P(u \geq u_i) = \sum_{k=i}^{n} P(u_i) \tag{10}$$

where $P(u_i)$ is the value of the frequency of the sample falling at u_i, which is the value of the probability of exceeding u_i ; $P(u \geq u_i)$ is called the risk value or loss value of the hazard factor.

2.3.2. Entropy Weight Method

The entropy weight method is a mathematical formula that calculates a comprehensive index based on the comprehensive consideration of the information provided by various factors. As an objective comprehensive weight determination method, it mainly determines the weight according to the amount of information that each indicator transmits to decision makers. The entropy weight method can accurately reflect the amount of information contained in the disasters of major grain-producing areas and can solve the problems of a large amount of information and the difficulty of accurate quantification for each index of multi-disaster agricultural risk assessment [24–29].

If the study area has n assessment units, there are m evaluation indicators reflecting its disaster indicators, which are $X_i (i = 1, 2 \ldots m)$, and the statistical values of each evaluation indicator in each county are obtained. Let its matrix be:

$$R' = \left(r'_{ij}\right)_{m \times n} \ (i = 1, 2 \ldots m;\ j = 1, 2 \ldots n) \tag{11}$$

where r'_{ij} is the statistical value of the jth district on the ith index. In order to eliminate the influence of the dimension, the extreme value method is used to standardize the statistical data on R', and the index standardization matrix r_{ij} is obtained:

$$r_{ij} = \frac{r'_{ij} - min_j^{|r'_{ij}|}}{max_j^{|r'_{ij}|} - min_j^{|r'_{ij}|}} \times 10 \tag{12}$$

After normalization, the information entropy of each index can be calculated. The entropy H_i of the ith index can be defined as:

$$H_i = -t \sum_{j=1}^{n} f_{ij} ln_{f_{ij}} \tag{13}$$

In the formula

$$f_{ij} = \frac{r_{ij}}{\sum_{j=1}^{n} r_{ij}},\ t = \frac{1}{lnn} \tag{14}$$

The entropy weight w_i of the ith indicator is as follows:

$$w_i = \frac{1 - H_i}{m - \sum_{i=1}^{m} H_i} \tag{15}$$

2.3.3. Hotspot Analysis

Hotspot and cold spot analysis are performed to delineate the spatial cluster of the average affected area of each single disaster in Jilin province based on the Getis-Ord *Gi** statistic using a fixed distance band in ArcGIS software. The local Getis-Ord *Gi** was used to identify hotspots with statistical significance, and the extremes and hotspots were spatially superimposed to explore the clustering characteristics of each disaster distribution in the study area. The Z-score obtained using ArcGIS software identifies regions that have high or low clustering in space. A larger Z-score indicates a stronger clustering of high values (hot spots), a smaller Z-score indicates a stronger clustering of low values (cold spots), and a Z-score closer to zero indicates no significant spatial clustering [30–33].

The Getis-Ord local statistic is given as:

$$G_i^* = \frac{\sum_{j=1}^{n} w_{i,j}x_j - \overline{x}\sum_{j=1}^{n} w_{i,j}}{S\sqrt{\frac{\left[n\sum_{j=1}^{n} w_{i,j}^2 - \left(\sum_{j=1}^{n} w_{i,j}\right)^2\right]}{n-1}}} \quad (16)$$

where x_j is the attribute value for feature j, $w_{i,j}$ is the spatial weight between features i and j, n is equal to the total number of features, and:

$$\overline{x} = \frac{\sum_{j=1}^{n} x_j}{n} \quad (17)$$

$$S = \sqrt{\frac{\sum_{j=1}^{n} w_j^2}{n} - (\overline{x})^2} \quad (18)$$

The G_i^* statistic is a Z-score, so no further calculations are required.

2.3.4. Ordinary Kriging

Kriging in geostatistics refers to a family of generalized least square regression methods. It helps to estimate the unknown variable values at unobserved locations based on the observed known values at surrounding locations [34,35]. The general expression of the ordinary kriging to estimate missing value of variable Z in space is given by:

$$Z(x_0) = \sum_{i=1}^{n} \lambda_i Z(x_i) \quad (19)$$

where $Z(x_0)$ refers to the estimated missing value of variable Z (multi-hazard risk assessment levels in this study) at desired location x_0; λ_i is the kriging weights associated with the observation at location x_i with respect to x_0; and n indicates the number of observed data points.

3. Results and Discussion

3.1. The Characteristics of Agricultural Multi-Hazard Meteorological Disasters

Grasping the development characteristics of disaster risk is one of the important links for effective disaster reduction and control. The statistical analysis of the affected area of the major meteorological disasters in Jilin province was carried out by combination with the previous statistical data. The purpose of this section is to provide a preliminary understanding of the disaster situation in the region and to provide a reference for the determination of the dominant disaster types later. However, due to the different degrees of retention of historical records, there is missing data for some years.

The drought disaster not only affected a large area of crops, but also affected a wide range; all the major food production areas have been affected by the drought disaster. Nongan and Yushu were seriously affected by the drought, with the average affected area exceeding 100 khm^2 (Figure 4a). The average affected area caused by flood disasters

has decreased compared with drought, and the average affected area of each main grain-producing area is below 40 khm^2; however, the average affected area in Taonan, Tongyu, and Zhenlai is higher compared with other places, which has a certain correlation with the water system, such as Nen Jiang River or Jiao Liu River, in the region (Figure 4b). Typhoon disaster presents a certain regional correlation in the main grain-producing areas of the eastern regions of Jiutai, Nongan, Dehui, Yitong, and other places where the more obvious impact is the focus on regional prevention (Figure 4c). Hail disasters have the least impact on the main grain-producing areas, with an average affected area of 20 khm^2; only Changling and Tongyu are relatively high and need to focus on prevention (Figure 4d). From a comprehensive point of view, among the four hazard disasters studied, drought disasters and flood disasters are the core disasters in the main grain-producing areas of Jilin province and need to be the focus of prevention methods. The average disaster losses of crops from hail and typhoon disasters are relatively lower, but regional hail and typhoon disasters occur frequently, and their resulting regional impacts cannot be ignored.

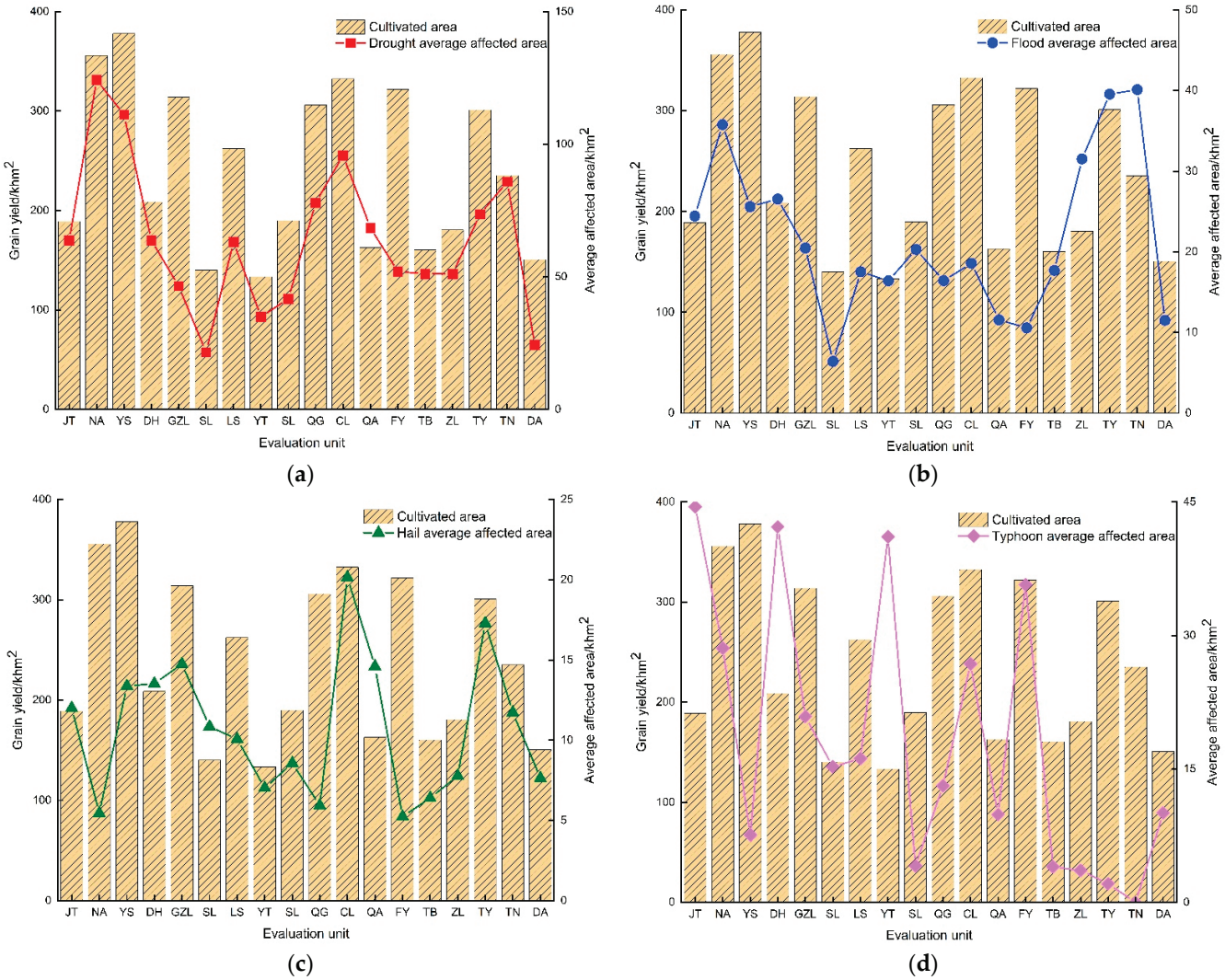

Figure 4. Grain production and average area affected by each disaster in major grain-producing areas ((**a**). Drought; (**b**). Flood; (**c**). Hail; (**d**). Typhoon).

Based on the average disaster area of 18 major grain-producing areas, the local Getis-Ord *Gi** index was used to study the degree of clustering of the spatial distribution of variables, which can respond well to the distribution of cold hotspots on the local spatial area of variables. The distribution of hotspot areas for each disaster was analyzed for 18 major grain-producing areas, and the degree of clustering was expressed according to

the significance Z. The higher and greater that Z was than 0, the tighter the target object's high-value clustering (forming a hotspot); the lower and greater that Z was than 0, the tighter the target object's low-value clustering (forming a cold spot). The hotspot and cold spot are calculated by Formulas (16)–(18). In hotspot analysis, the natural intermittent point method was used to divide the cold hot spot area into five categories, namely, core hot spot area, sub-core hot spot area, transition area, sub-core cold spot area, and core cold spot area. The results show that the hotspot areas for drought hazards are widely distributed in the study area. Qianguo, Nongan, Dehui, and Jiutai are the core hotspot areas of drought disasters, and Taonan and Tongyu, in the western part of the study area, are the sub-core hotspot areas (Figure 5a). Flood disasters are similar to drought disasters, with Taonan and Tongyu as the core hotspot areas and Jiutai and other places in the eastern region as the sub-core hotspot areas (Figure 5b). This means drought and flood disasters are widely distributed and many hotspot areas are affected. Hail disasters present core hotspot areas and sub-core hotspot areas in the five eastern places of study, while Tao Nan is also a hotspot area (Figure 5c). In addition, the hotspot area of typhoon disasters is mainly concentrated in the eastern part of the study area (Figure 5d). This means the distribution of hail and typhoon disasters has a certain regional nature.

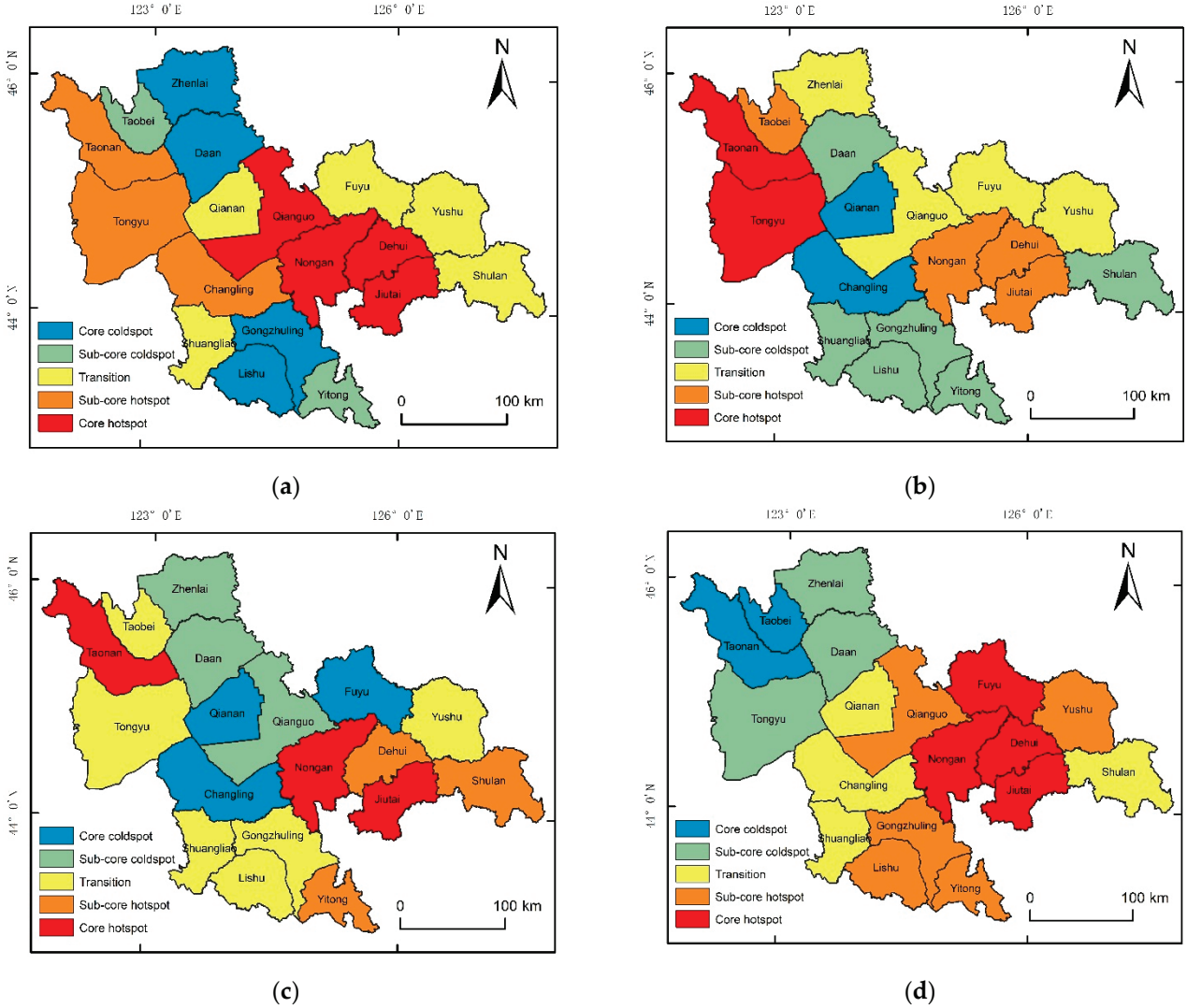

Figure 5. Distribution of each disaster hotspot area in the main grain-producing areas of Jilin province ((**a**). Drought; (**b**). Flood; (**c**). Hail; (**d**). Typhoon).

After standardizing the average area affected in each district, the entropy weights of multi-hazard meteorological hazards were calculated using Formulas (11)–(15) to obtain the weights of four meteorological hazards in 18 major grain-producing regions, and the results are shown in Table 2.

Table 2. Weight of single disaster species in the main grain-producing areas of Jilin province.

Evaluation Unit	Drought	Flood	Hail	Typhoon
Jiutai (JT)	0.11	0.13	0.38	0.39
Nongan (NA)	0.29	0.24	0.19	0.28
Yushu (YS)	0.36	0.22	0.32	0.10
Dehui (DH)	0.16	0.22	0.07	0.55
Gongzhuling (GZL)	0.11	0.18	0.38	0.33
Lishu (LS)	0.19	0.14	0.42	0.25
Yitong (YT)	0.06	0.14	0.12	0.68
Shuangliao (SL)	0.25	0.49	0.09	0.18
Qianguo (QG)	0.30	0.15	0.30	0.24
Changling (CL)	0.30	0.14	0.19	0.37
Qianan (QA)	0.44	0.14	0.11	0.32
Fuyu (FY)	0.18	0.07	0.01	0.73
Taobei (TB)	0.15	0.16	0.61	0.07
Zhenlai (ZL)	0.26	0.63	0.00	0.11
Tongyu (TY)	0.28	0.51	0.18	0.04
Taonan (TN)	0.25	0.38	0.37	0.00
Shulan (SL)	0.00	0.00	0.55	0.45
Daan (DA)	0.04	0.19	0.32	0.46

3.2. Multi-Hazard Meteorological Hazard Risk Analysis in Agriculture

The discrete domain is constructed according to the scope of disaster, the maximum value of the intensity of disaster, and the possible value of disaster; the discrete domain is constructed and the probability of disaster risk under different disaster indices in the main grain-producing areas is obtained according to Formulas (1)–(10). The probability density reflects the probability of the occurrence of major meteorological disasters under different disaster indices in the main grain-producing areas of Jilin province, so that the probability of the occurrence of different disaster levels can be inferred (Figure 6). The results show that the disaster indices of four meteorological disasters span the whole disaster index axis and all have the possibility of large area damage, among which the disaster areas of hail, typhoon, flood, and drought do not exceed 20%, 30%, 50%, and 80% of the total sown area, respectively. The density of exceedance probability can laterally reflect the level of risk of major meteorological disasters in Jilin agriculture under different disaster indices (Figure 7). The results show that the risk values of four major meteorological disasters decrease with the increase of disaster indices, and the disaster risk of each disaster in the main grain-producing areas under the same disaster indices is: drought > flood > typhoon > hail. From the frequency of disasters and the scope of disaster impact, drought disaster is the main natural disaster that harms Jilin province's main natural disaster for grain production.

In order to give managers and decision makers a clearer understanding of the risk level based on the disaster risk values obtained from the fuzzy risk model, and to make the risk assessment results more intuitive, the grading criterion of risk recurrence period (T = 1/P) was used to calculate the risk levels of meteorological hazards under different disaster indices. To facilitate the analysis and evaluation of the spatial distribution characteristics of each meteorological disaster risk in 18 major grain-producing areas in Jilin province, the main meteorological risk assessment grades for 18 major grain-producing areas were developed by combining the actual situation of the main meteorological risk values in each area (Table 3). The multi-hazard meteorological hazard risk assessment levels were divided into five levels of high, medium–high, medium, medium–low, and low under different damage indices, and were assigned 5, 4, 3, 2, and 1, respectively. The classification of disaster risk level is mainly based on the previous research results and the actual situation

of disaster risk value. The high risk implies a short period of occurrence and a high frequency of recurrence of disasters under the same crop damage.

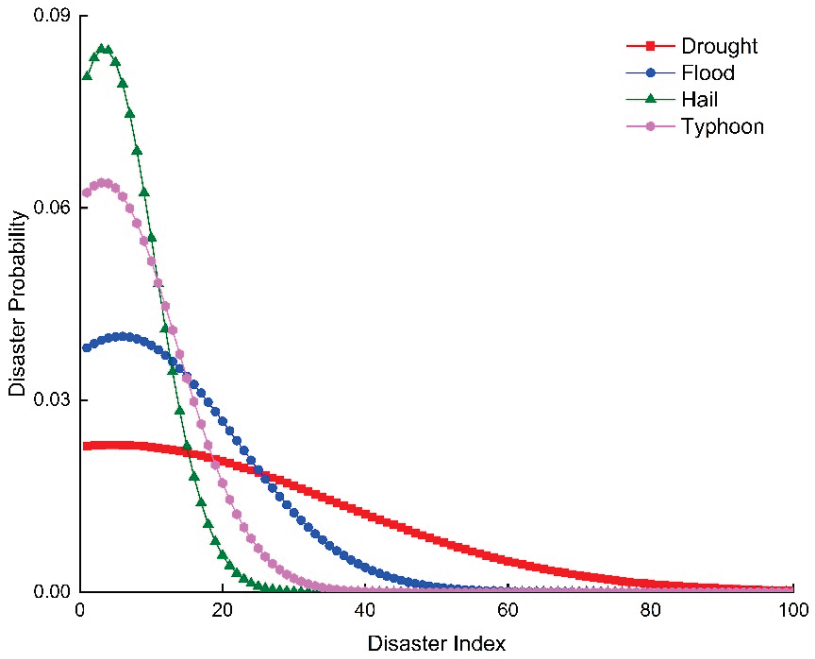

Figure 6. Probability density of multi-hazard meteorological hazards in major grain-producing areas.

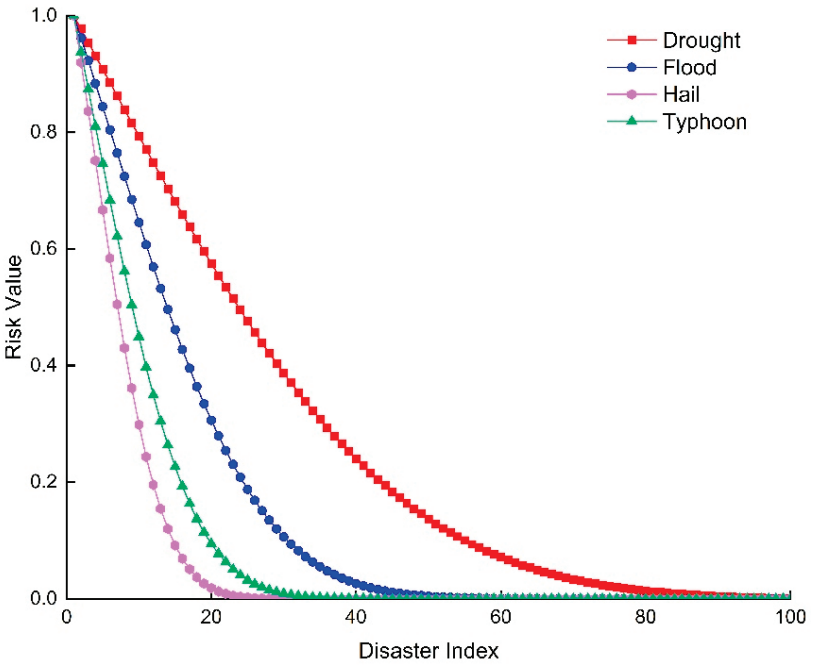

Figure 7. Risk values of multi-hazard meteorological hazards in major grain-producing areas.

Table 3. The main meteorological risk assessment scale of Jilin province.

Disaster Index	High	Medium–High	Medium	Medium–Low	Low
$5\% \leq x < 10\%$	$T = 1$	$1 < T \leq 2$	$2 < T \leq 3$	$3 < T \leq 4$	$T > 4$
$10\% \leq x < 15\%$	$1 < T \leq 2$	$2 < T \leq 3$	$3 < T \leq 4$	$4 < T \leq 6$	$T > 6$
$15\% \leq x < 20\%$	$1 < T \leq 2$	$2 < T \leq 4$	$4 < T \leq 6$	$6 < T \leq 10$	$T > 10$
$\geq 20\%$	$1 < T \leq 2$	$2 < T \leq 5$	$5 < T \leq 10$	$10 < T \leq 20$	$T > 20$

In Table 3, T = 1 means the frequency of disaster occurrence is once a year, $1 < T \leq 2$ means the frequency of disaster occurs once every 1~2 years, T > 4 means the probability of disaster occurrence is greater than once every 4 years, and so on for the rest. According to the above risk analysis model and risk classification criteria, the results of meteorological disaster risk evaluation in 18 major grain-producing areas in Jilin province under different disaster indices are derived.

Overall, under different disaster index conditions, drought and flood are the dominant hazards affecting the 18 major grain-producing areas in Jilin province. The risk level of multi-hazard meteorological hazards is higher in Nongan when the disaster index is $5\% \leq x < 10\%$, and the risk level of multi-hazard meteorological hazards is at a higher level in Jiutai and Yitong when the disaster index is $10\% \leq x < 15\%$ and $15\% \leq x < 20\%$, respectively. As the disaster index rises to $x \geq 20\%$, Jiutai is at high risk of multi-hazard meteorological hazard risk and the probability of a large area of multi-hazard hazard risk is higher.

At the disaster index of $5\% \leq x < 10\%$ (Figure 8), the risk level of drought disaster in each major grain-producing area is at medium–high or high risk, and the risk probability is once every 1~2 years. A flood disaster is a secondary disaster affecting the main grain-producing areas in Jilin province, and the risk level of a flood disaster in each main grain-producing area is in the medium–high- or high-risk area, but it is low in Fuyu City, which is related to the lack of data that may be caused by the change of administrative division in the history of Fuyu. The risk level of hail disasters in each major grain-producing area is at a medium or low risk level, but Yushu and Shulan are at high and medium–high risk levels, showing that the probability of hail disasters in these three places is higher than in other places. The risk level of typhoon disaster in each major grain-producing area has a large difference. Specifically, the risk level of Yushu, Changling, Zhenlai, Tongyu, Changling, Taobei, Taonan, Yushu, and Daan is small, while Jiutai, Nongan, and Dehui are high, which is in line with the actual situation.

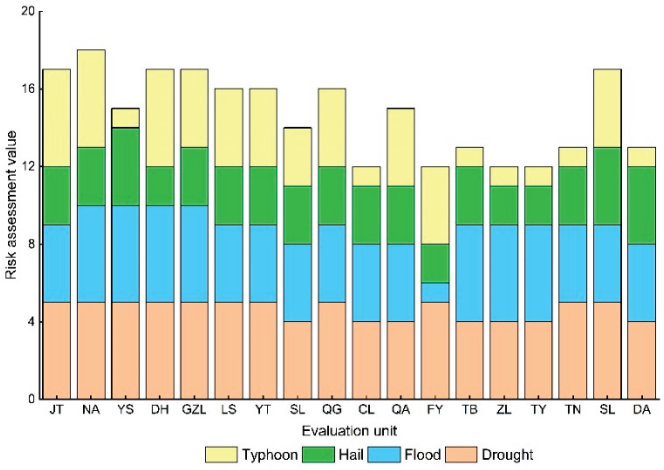

Figure 8. Risk evaluation value of multi-hazard meteorological disasters under the disaster index of $5\% \leq x < 10\%$.

At a disaster index of $10\% \leq x < 15\%$ (Figure 9), there was almost no change in the risk level of drought disaster and flood disaster in each major grain-producing area with a disaster index of $5\% \leq x < 10\%$. The risk level of hail hazards in each major grain-producing area was elevated, and only two areas (Shuangliao and Qianan) had no change in disaster risk level. Typhoon disaster risk is just the opposite of hail disaster risk. The risk level of most areas did not change, but the disaster risk level of Fuyu and Yitong increased to a high level.

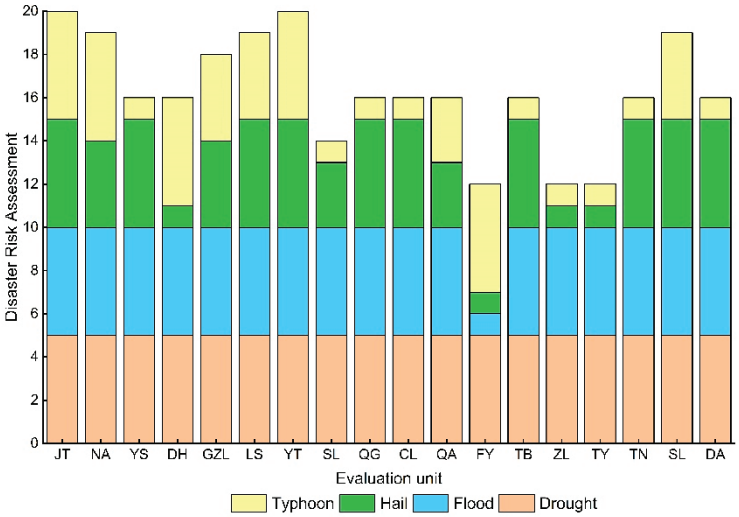

Figure 9. Risk evaluation value of multi-hazard meteorological disasters under the disaster index of $10\% \leq x < 15\%$.

At the disaster index of $15\% \leq x < 20\%$ (Figure 10), the risk of drought disaster was at high risk in all major grain-producing regions. The risk level of flood disaster in all other regions remained unchanged. The risk levels of hail disasters all decreased overall, but Jiutai, Yushu, Yitong, Changling, and Taobei were still at high-risk levels, and the chance of suffering large area damage remained high. There was no big change in the overall probability of typhoon disasters, and the disaster risk levels of Gongzhuling and Qianan have dropped to medium–low and low risk, that is, the recurrence period of typhoon disasters is more than once every 6 years.

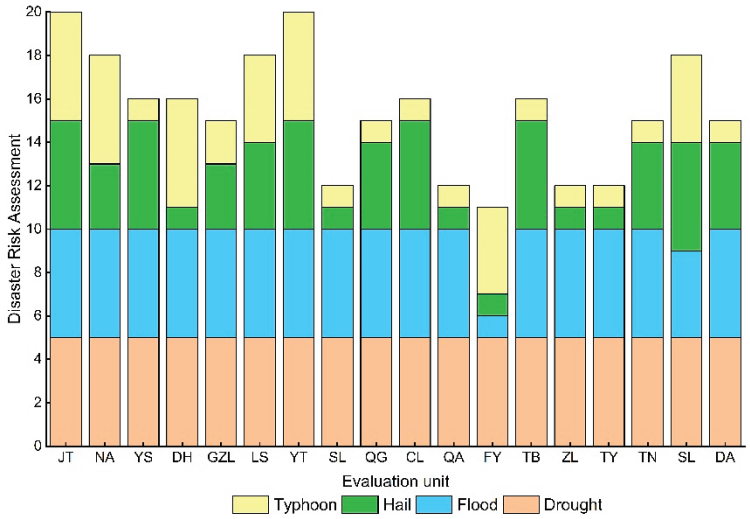

Figure 10. Risk evaluation value of multi-hazard meteorological disasters under the disaster index of $15\% \leq x < 20\%$.

At a disaster index of $x \geq 20\%$ (Figure 11), the risk levels of drought disaster and flood disaster in each major grain-producing area are at high and medium–high risk levels. This indicates that droughts and floods have a serious impact on the main grain-producing areas in Jilin province, with droughts and floods causing more than 20% damage, occurring about once every 5 years. With the rise of the disaster index, the risk level of hail disasters in most areas is at medium risk or below, but Jiutai and Yushu are still at high risk levels, indicating that these two areas have a high chance of being affected by hail disasters and are prone to large areas of hail disasters. The risk level of typhoon disasters appears to be widely different, with relatively high disaster risk in the eastern part of the study

area. Specifically, the risk levels of Jiutai, Nongan, Dehui, Yitong, Fuyu, and Shulan have remained medium–high or high, while other major grain-producing areas are at low risk.

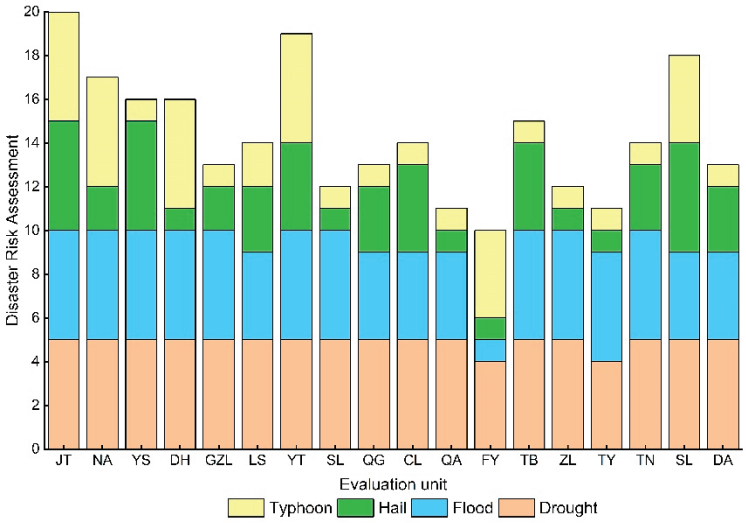

Figure 11. Risk evaluation value of multi-hazard meteorological disasters under the disaster index of $x \geq 20\%$.

3.3. Risk Assessment and Spatial Distribution of Multi-Hazard Meteorological Hazards in Agriculture

After completing the analysis and evaluation of multi-hazard meteorological disaster risk levels in agriculture, the multi-hazard meteorological disaster risk assessment results were weighted and summed with each disaster weight to obtain the multi-hazard meteorological disaster risk assessment results for 18 major grain-producing areas, according to the disaster index, disaster recurrence period, and risk level classification criteria. At the same time, the assessment results were classified into five levels (high, medium–high, medium, medium–low, and low) using the natural interruption point method, and the multi-hazard disaster risk assessment level maps were obtained for 18 major grain-producing areas under different disaster indices. Based on the results of agricultural multi-hazard meteorological disaster risk assessment, the spatial distribution pattern and regional distribution characteristics of agricultural multi-hazard disasters under 18 major grain-producing areas in Jilin province were analyzed.

The disaster risk level in the Yushu, Dehui, Nongan, and Jiutai areas in the eastern part of the study area has been at high and medium–high levels, and the areas at high and medium–high risk are expanding as the disaster index continues to increase. When the disaster index is $5\% \leq x < 10\%$, the southwest side of the study area is a medium-risk area, and the high hail is mainly concentrated on the northeast side of the study area in Nongan and Dehui, both of which are high-risk areas. That is, they suffered from a high frequency of multi-hazard impacts and caused a large area of agricultural losses (Figure 12a). When the disaster index was $10\% \leq x < 15\%$, the high-risk area was expanding. Jiutai, Tongyu, and Lishu were high-risk areas, and the risk level in some areas in the southeast of the region was decreasing (Figure 12b). When the damage index increases to 15%, the risk level in the central part of the study area is medium–low and low risk, i.e., there is a low chance of widespread, high-frequency, and strong damage. Jiutai and Lishu are high-risk areas, and three places in the western part of the study area are in medium–high-risk areas with the feasibility of suffering from large areas and high frequency (Figure 12c). When the disaster index is $x \geq 20\%$, the multi-hazard rating of the main grain-producing areas shows the characteristics of medium–high risk in the western region, low and medium–low risk in the central region, and high and medium–high risk in the eastern region. Among them, the danger of the disaster-causing factors of agricultural multi-hazard species in Dehui, Jiutai, and Lishu cannot be ignored, which are prone to causing large-scale damage and

forming disaster chains, and the task of coping with multi-hazard meteorological disaster prevention is arduous (Figure 12d).

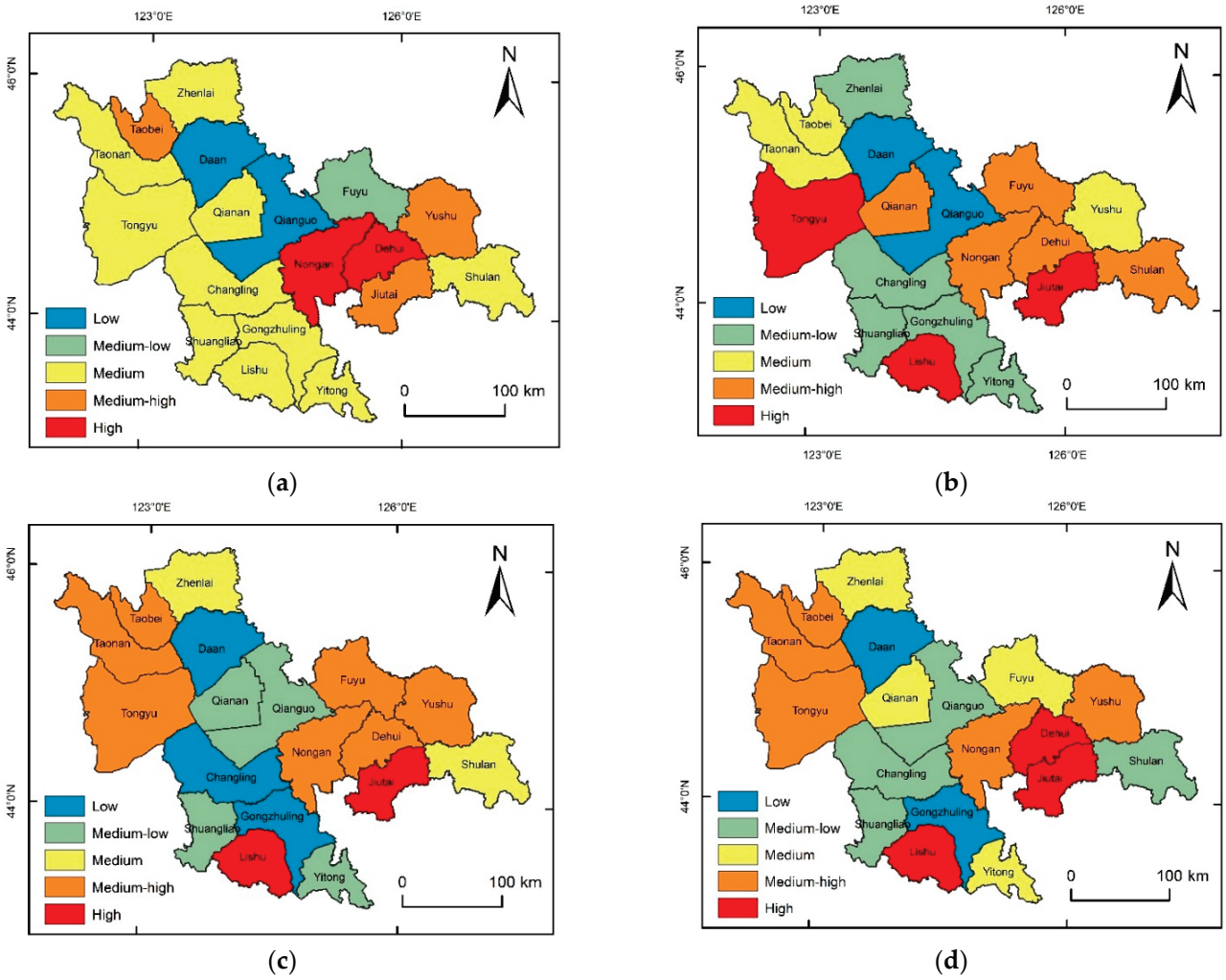

Figure 12. Risk assessment map of multi-hazard meteorological disasters under different disaster indices ((**a**). 5% ≤ x < 10%; (**b**). 10% ≤ x < 15%; (**c**). 15% ≤ x < 20%; (**d**). x ≥ 20%).

An ordinary kriging interpolation method based on variance function theory and structural analysis was used in this study for an unbiased optimal estimation of regionalized variables in a limited area. Specifically, it was used to predict the risk of agricultural multi-hazard meteorological hazards in the study area. The ordinary kriging to estimate the missing value of variable Z is calculated by Formula (19). The results show that the risk of multi-hazard meteorological hazards shows a southeastern direction. At the same time, the multi-hazard meteorological disaster risk level gradually decreases in both the southeast direction and the northwest direction, with the continuous increase of the disaster index. There are high- and medium–high-risk trends of multi-hazard meteorological disasters in Taonan, Taobei, Tongyu, Shulan, Jiutai, Yitong, Yushu, and Dehui. Thus, they are the focus of agricultural multi-hazard meteorological disaster risk prevention.

Specifically, when the disaster index is 5% ≤ x < 10% (Figure 13a), the multi-hazard rank trend in the central part of the study area shows medium–low risk, the multi-hazard rank trend in some districts and counties in the eastern part is high and medium–high risk, and this area is the key area for multi-hazard risk prevention. With the increase of the disaster index to 10% ≤ x < 15% (Figure 13b), the trend of agricultural multi-hazard meteorological disaster risk level develops from the east and west to the middle, and the low-risk area in the middle of the study area expands. Shulan and Yushu may have

more than 10% of their crops affected by multiple hazards. When the damage index is 15% ≤ x < 20% (Figure 13c), the range of low- and medium–low-risk areas is further expanded, and the risk levels in the central part of the study area all show low risk levels, while only some areas in Taonan, Yushu, and Shulan are medium–high risk, and the area covered by low risk is the most extensive at this time. When the disaster index is x ≥ 20% (Figure 13d), the range of medium–high risk is further expanded, and the northeast of the study area and the western part of Taonan and other places present a medium–high-risk grade of agricultural multi-hazard meteorological disaster. Some areas in the northeastern direction suffer from the possibility of a multi-hazard meteorological disaster risk impact and a wide range of impact, which is the focus of regional agricultural prevention.

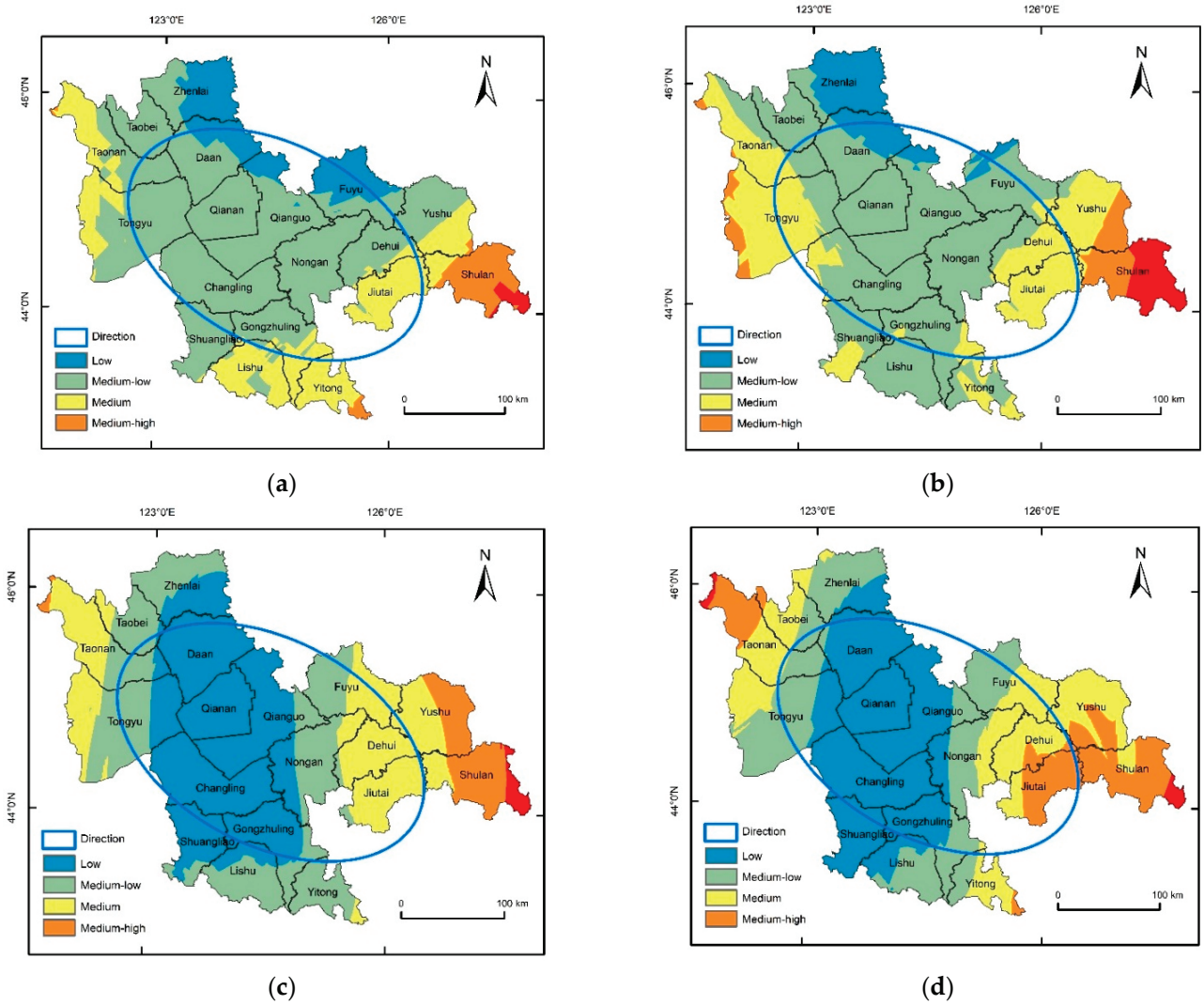

Figure 13. Risk trend of multi-hazard meteorological disasters under different disaster indices ((**a**). 5% ≤ x < 10%; (**b**). 10% ≤ x < 15%; (**c**). 15% ≤ x < 20%; (**d**). x ≥ 20%).

3.4. Agricultural Multi-Hazard Meteorological Disaster Risk Reduction Recommendations

This paper assesses the risk of agricultural multi-hazards using the historical disaster data of the first natural disaster risk census in 18 major grain-producing areas in Jilin province, and obtains the risk of each multi-hazard meteorological disaster, which is an attempt to apply the data from the first natural disaster risk census. From the actual situation of food production areas, we put forward the following recommendations for the reduction of agricultural multi-hazard meteorological disaster risks so they might provide a reference for the reduction and resolution of major disaster risks under the new situation, ensuring the strategic goals of national food security and sustainable development.

3.4.1. Improve Regional Agricultural Multi-Hazard Risk Reduction System Construction

To develop effective agricultural multi-hazard reduction policies according to local conditions, appropriate mechanisms and legal system construction are very important, which is a necessary guarantee to improve the efficiency of disaster mitigation and reduction. Multi-hazard meteorological disaster risk reduction in agriculture involves multiple sectors and regions, with more emphasis on information sharing, horizontal collaboration, and up–down linkage, and it is necessary to strengthen the top design of the central government and make a good overall plan [36–39].

Firstly, accelerate the improvement of the system of multiple coordination mechanisms and real-time emergency plans to provide an all-round institutional guarantee to enhance regional agricultural multi-hazard risk reduction capabilities. Secondly, the government should increase its financial investment in agricultural water conservancy construction and subsidize the construction of small water conservancy projects on collective village farmland [40,41]. Thirdly, the government should increase its investment in agricultural insurance for natural disasters in Jiutai, Tongyu, and other places; moreover, it should increase its investment in rural social security, medical care, and minimum living security as well to improve disaster response capacity. The government could act as a reinsurer against agricultural losses so that it can provide protection for agricultural crop and livestock insurance initiatives, even if local insurers and international reinsurers are unwilling to provide excess-of-loss reinsurance [42]. Overall, combining normal disaster reduction and mitigation with extraordinary emergency disaster relief, enhancing the integration of laws and the whole disaster risk management system, and realizing coordinated operation and comprehensive management of multiple subjects are good strategies for multi-hazard risk reduction.

3.4.2. Optimize Regional Agricultural Multi-Hazard Risk Management Models

The inefficiency of disaster risk management in administrative regions independent of each other often leads to gaps in disaster risk management. In order to further change the idea of "disaster relief over disaster mitigation", a whole-process disaster risk management model should be established. While developing emergency plans, the government should vigorously develop a watershed disaster management network system to form and coordinate a linkage [38,43–45]. From international experience, the United States has formed a triple system of federal, regional, and local emergency response mechanisms; the United Kingdom mobilizes the resources of the whole society to structure the emergency management system [46,47]; and Japan has established a prevention-centered emergency management system [48,49]. The experiences from which you can learn are as follows.

Firstly, in terms of the main body of disaster management, we should include social agricultural companies, agricultural volunteers, and grassroots organizations in the government to improve agricultural disaster mitigation capacity through these experts who are familiar with local agricultural disasters and land conditions so that they can become an important force in disaster mitigation [41,50]. Second, on the mechanism of disaster management, we should strengthen the unified dispatch and management of multi-hazard meteorological disaster risks (especially in several areas of the Nen Jiang and Heilongjiang River Basin), break the mechanism of independent management in each administrative region, realize the rational allocation of resources, and reduce disputes over the impact of disaster risks. Overall, the communication–feedback–supervision working mechanism should be continuously improved for the weak links of natural disaster risk management, especially the coupling aspect of multi-hazards, by insisting on the prevention-oriented methods combined with disaster reduction and relief, and improving the decision-making capacity of risk management.

3.4.3. Strengthened Regional Agricultural Multi-Hazard Risk Reduction Capacity

In the face of the severe and complex situation of major disasters and multi-hazard disaster risks, agricultural multi-hazard risk reduction should be incorporated into the

overall planning of social development to provide support for effectively enhancing the ability of the whole society to reduce major disaster risks. The first national comprehensive natural disaster risk census is also a survey of China's national situation and strength and is a fundamental work to enhance disaster risk reduction capacity, which is of great significance in mapping out the risk base [51–53].

Overall, in terms of proceeding with strengthening the capacity of agricultural production for disaster reduction and mitigation, first, the construction of farmland water conservancy facilities to improve the ability to resist drought and flooding, especially in small watersheds, should be strengthened [54–56]. Second, to strengthen the transformation of low-yielding fields, the "fertile soil project" should be implemented to improve the organic content of farmland and enhance fertilizer supply and water retention capacity, and thus to improve the ability of crops to withstand natural disasters [57,58]. Third, harmful biological early warning systems and disaster forecasting, monitoring, reduction, and control capacity should be strengthened.

Specifically, Nongan, Jiutai, and Yitong should strengthen agricultural drought-prevention systems, concentrating on the establishment of an effective early warning system for agricultural drought reduction and mitigation. In order to improve farmland water conservancy facilities in agricultural production areas, especially small farmland water conservancy facilities in villages and towns, deep ditches should be built, as should more profound ditches for agricultural water storage and farmland drainage to facilitate flood and drought reduction [59–63]. The western part of the study area should strengthen flood and drought control facilities, especially drainage facilities, to focus on construction. In addition to the construction of farmland water conservancy facilities, the resilience of crops themselves should be strengthened. Research and promotion of good crop varieties should be firmly supported. The application of high-quality and flexible crop varieties can improve the disaster resistance of crops. Dehui, Shulan, and Yushu should do a good job of laying and covering hail nets for each crop and should carry out reinforcement work for seedling sheds and breeding bases to reduce the impact of hail disasters on crops.

4. Conclusions

The difficult problem in disaster risk assessment is how to use incomplete information to derive the most accurate evaluation results possible. To this end, this paper proposes a multi-hazard meteorological disaster risk assessment method for agriculture based on historical disaster data, which mainly consists of three aspects: disaster risk identification, disaster risk analysis, and disaster risk assessment. Meanwhile, the authors made a preliminary attempt to conduct a multi-hazard meteorological disaster risk assessment for each major grain-producing area based on historical disaster data from the first national comprehensive natural disaster risk census of 18 major grain-producing areas in Jilin province. The results of the study provide a new idea for the application of historical disaster data at the small-scale area level in the later stage of the disaster risk census results and provide a basis for agricultural safety and disaster prevention and control in the main grain-producing areas. The main conclusions are as follows.

By a comprehensive analysis of the climatic conditions of crop growth in the study area and the disaster damage data in the database, four kinds of disasters, namely, drought, flood, typhoon, and hail, were identified as disasters in the study area. The frequency of drought and flood disasters is high, and the scope of the disasters is large. The core hotspots and sub-core hotspots are Jiutai, Nongan, Dehui, Tongyu, Taonan, and other places, which are the key disasters for agriculture meteorological disaster reduction in the main grain-producing areas of Jilin province. The hail and typhoon disasters are regional, and the core hotspots and sub-core hotspots are mainly in the east of the main grain-producing areas. Attention should be paid to these two disasters in the eastern part of the study area.

Using a fuzzy risk analysis model and the entropy weight method to calculate the meteorological disaster risk value in the study area and the single disaster risk weight in each region, respectively, the risk value of the four major meteorological disasters de-

creases with the increase of the disaster index, and the hazard of each disaster in the main grain-producing areas under the same disaster index is drought > flood > typhoon > hail. When the disaster index is 5% $\leq$ x < 10%, the disaster risk level for Nongan is high, and the comprehensive risk evaluation value rises with the rising disaster index; when 10% $\leq$ x < 15% and 15% $\leq$ x < 20%, Yitong and Jiutai are multi-hazard meteorological disasters at high risk; when the disaster index is increased to x $\geq$ 20%, the risk level of Jiutai multi-hazard meteorological disaster is at an even higher level. The probability of the occurrence of a large area of multi-hazard disaster risk is high.

The risk value of each disaster and the weight of each assessment unit are weighted to obtain the multi-hazard comprehensive risk assessment risk level of each main grain-producing area. The risk assessment results of multi-hazard meteorological hazards showed that Jiutai, Nongan, Yitong, and Tongyu showed high and medium–high risk levels under different disaster indices. There is a wide range of high-frequency, strong disaster situations, and the risk of its multi-hazard-causing factors cannot be ignored. To deal with multi-hazard meteorological disaster prevention tasks is difficult. In addition, the risk of multi-hazard meteorological hazards is spatially oriented to the southeast, and the risk level of multi-hazard meteorological hazards in the central part of the study area is decreases gradually along with the increasing disaster index. Based on the severe and complex disaster risk situation in the study area, especially the complexity and high uncertainty of multi-hazard meteorological disaster risks, suggestions are given on three aspects: improving regional agricultural multi-hazard risk reduction system construction; optimizing regional agricultural multi-hazard risk management models; and strengthening regional agricultural multi-hazard risk reduction capacity, so as to face the severe and complex multi-hazard disaster risk situation.

Shortcomings and prospects: this paper evaluates the multi-hazard meteorological disaster risk of all crops to guide various regions in carrying out regional multi-hazard agricultural safety production and risk prevention. If the crops were further divided into specific food products (such as rice, corn, etc.), and the disaster resistance of each food product was added to the evaluation system, it could more accurately guide the agricultural disaster reduction and mitigation work in each grain-producing area.

Author Contributions: Conceptualization, formal analysis, and methodology, J.Z. and J.W.; investigation and resources, S.C., S.T. and W.Z.; writing—original draft preparation, J.Z.; writing—review and editing, J.W. All authors have read and agreed to the published version of the manuscript.

Funding: The authors gratefully acknowledge the support provided by the Natural Disaster Risk Census Project in Jilin province (JLSZC202002826).

Institutional Review Board Statement: Not applicable.

Informed Consent Statement: Informed consent was obtained from all subjects involved in the study.

Data Availability Statement: Not applicable.

Conflicts of Interest: The authors declare no conflict of interest.

References

1. Climate Change 2021—The Physical Science Basis. Available online: https://www.undrr.org/publication/sendai-framework-disaster-risk-reduction-2015--2030 (accessed on 4 May 2022).
2. Mishra, A.; Bruno, E.; Zilberman, D. Compound natural and human disasters: Managing drought and COVID-19 to sustain global agriculture and food sectors. *Sci. Total Environ.* **2021**, *754*, 142210. [CrossRef] [PubMed]
3. Weerasekara, S.; Wilson, C.; Lee, B.; Hoang, V.-N. Impact of natural disasters on the efficiency of agricultural production: An exemplar from rice farming in Sri Lanka. *Clim. Dev.* **2022**, *14*, 133–146. [CrossRef]
4. Platania, F.; Hernandez, C.T.; Arreola, F. Social media communication during natural disasters and the impact on the agricultural market. *Technol. Forecast. Soc. Change* **2022**, *179*, 121594. [CrossRef]
5. Albris, K.; Lauta, K.C.; Raju, E. Strengthening Governance for Disaster Prevention: The Enhancing Risk Management Capabilities Guidelines. *Int. J. Disaster Risk Reduct.* **2020**, *47*, 101647. [CrossRef]
6. Kim, J.; Kim, D.; Lee, M.; Han, H.; Kim, H.S. Determining the Risk Level of Heavy Rain Damage by Region in South Korea. *Water* **2022**, *14*, 219. [CrossRef]

7. Xiaobing, Y.; Chenliang, L.; Tongzhao, H.; Zhonghui, J. Information diffusion theory-based approach for the risk assessment of meteorological disasters in the Yangtze River Basin. *Nat. Hazards* **2020**, *107*, 2337–2362. [CrossRef]
8. Shen, G.; Hwang, S.N. Spatial–Temporal snapshots of global natural disaster impacts Revealed from EM-DAT for 1900–2015. *Geomat. Nat. Hazards Risk* **2019**, *10*, 912–934. [CrossRef]
9. Floresta, G.; Amata, E.; Barbaraci, C.; Gentile, D.; Turnaturi, R.; Marrazzo, A.; Rescifina, A. A Structure- and Ligand-Based Virtual Screening of a Database of "Small" Marine Natural Products for the Identification of "Blue" Sigma-2 Receptor Ligands. *Mar. Drugs* **2018**, *16*, 384. [CrossRef]
10. Zhi-Yong, L.; Hong-Yan, L.; Huan, Y.; Chang-Jian, Z.; Hui, Y.; Huan-Huan, W.; Xin-Xin, C.; Ya-Wei, Z.; Zhen-Dong, S.; Wen-Chao, L.; et al. Pro54DB: A database for experimentally verified sigma-54 promoters. *Bioinformatics* **2017**, *33*, 467–469. [CrossRef]
11. Welker, C.; Faust, E. Tropical cyclone-related socio-economic losses in the western North Pacific region. *Nat. Hazards Earth Syst. Sci.* **2013**, *13*, 115–124. [CrossRef]
12. The First National Comprehensive Natural Disaster Risk Census. Available online: http://emerinfo.cn/zt/zrzhzhfxpc1/index.htm (accessed on 5 May 2022).
13. Liu, Y.; Tong, L. Spatio-temporal Pattern and Driving Forces of Comprehensive Agricultural Productivity in Jilin Province, China. *Chin. Geogr. Sci.* **2020**, *30*, 493–504. [CrossRef]
14. Zheng, X.; Qin, L.; He, H. Impacts of Climatic and Agricultural Input Factors on the Water Footprint of Crop Production in Jilin Province, China. *Sustainability* **2020**, *12*, 6904. [CrossRef]
15. Li, Q.S.; Willardson, L.S.; Deng, W.; Li, X.J.; Liu, C.J. Crop water deficit estimation and irrigation scheduling in western Jilin province, Northeast China. *Agric. Water Manag.* **2005**, *71*, 47–60. [CrossRef]
16. Li, Y.; Li, Q.; Guo, D.; Liang, S.; Wang, Y. Ecological stoichiometry homeostasis of Leymus chinensis in degraded grassland in western Jilin Province, NE China. *Ecol. Eng.* **2016**, *90*, 387–391. [CrossRef]
17. Xu, L.; Zhang, Q.; Zhang, J.; Zhao, L.; Sun, W.; Jin, Y.-X. Extreme meteorological disaster effects on grain production in Jilin Province, China. *J. Integr. Agric.* **2017**, *16*, 486–496. [CrossRef]
18. Zhang, Y.; Jiang, Y.; Jia, Z.; Qiang, R.; Gao, Q. Identifying the scale-controlling factors of soil organic carbon in the cropland of Jilin Province, China. *Ecol. Indic.* **2022**, *139*, 108921. [CrossRef]
19. Zhang, Z.; Feng, B.; Shuai, J.; Shi, P. ENSO–climate fluctuation–crop yield early warning system—A case study in Jilin and Liaoning Province in Northeast China. *Phys. Chem. Earth Parts A/B/C* **2015**, *87–88*, 10–18. [CrossRef]
20. Zou, T.; Chang, Y.; Chen, P.; Liu, J. Spatial-temporal variations of ecological vulnerability in Jilin Province (China), 2000 to 2018. *Ecol. Indic.* **2021**, *133*, 108429. [CrossRef]
21. Xiaobing, Y.; Xianrui, Y.; Chenliang, L.; Zhonghui, J. Information diffusion-based risk assessment of natural disasters along the Silk Road Economic Belt in China. *J. Clean. Prod.* **2020**, *244*, 118744. [CrossRef]
22. Pan, X.; Huang, C.; Pu, C. Comprehensive disposal plan design & polymerization disaster risk assessment based on information diffusion technology in Fujiang River basin in Sichuan. *Environ. Res.* **2020**, *188*, 109744. [CrossRef]
23. Liu, Y.; You, M.; Zhu, J.; Wang, F.; Ran, R. Integrated risk assessment for agricultural drought and flood disasters based on entropy information diffusion theory in the middle and lower reaches of the Yangtze River, China. *Int. J. Disaster Risk Reduct.* **2019**, *38*, 101194. [CrossRef]
24. Ma, S.; Lyu, S.; Zhang, Y. Weighted clustering-based risk assessment on urban rainstorm and flood disaster. *Urban Clim.* **2021**, *39*, 100974. [CrossRef]
25. Li, Z.; Luo, Z.; Wang, Y.; Fan, G.; Zhang, J. Suitability evaluation system for the shallow geothermal energy implementation in region by Entropy Weight Method and TOPSIS method. *Renew. Energy* **2022**, *184*, 564–576. [CrossRef]
26. Qin, Y.; Guan, K.; Kou, J.; Ma, Y.; Zhou, H.; Zhang, X. Durability evaluation and life prediction of fiber concrete with fly ash based on entropy weight method and grey theory. *Constr. Build. Mater.* **2022**, *327*, 126918. [CrossRef]
27. Sidhu, A.S.; Singh, S.; Kumar, R. Bibliometric analysis of entropy weights method for multi-objective optimization in machining operations. *Mater. Today Proc.* **2022**, *50*, 1248–1255. [CrossRef]
28. Wu, H.-W.; Li, E.-Q.; Sun, Y.-Y.; Dong, B.-T. Research on the operation safety evaluation of urban rail stations based on the improved TOPSIS method and entropy weight method. *J. Rail Transp. Plan. Manag.* **2021**, *20*, 100262. [CrossRef]
29. Zhao, J.; Tian, J.; Meng, F.; Zhang, M.; Wu, Q. Safety assessment method for storage tank farm based on the combination of structure entropy weight method and cloud model. *J. Loss Prev. Process Ind.* **2022**, *75*, 104709. [CrossRef]
30. Guerri, G.; Crisci, A.; Congedo, L.; Munafò, M.; Morabito, M. A functional seasonal thermal hot-spot classification: Focus on industrial sites. *Sci. Total Environ.* **2022**, *806*, 151383. [CrossRef]
31. Kuznetsov, A.; Sadovskaya, V. Spatial variation and hotspot detection of COVID-19 cases in Kazakhstan, 2020. *Spat. Spatio-Temporal Epidemiol.* **2021**, *39*, 100430. [CrossRef] [PubMed]
32. Liu, W.; Ma, L.; Smanov, Z.; Samarkhanov, K.; Abuduwaili, J. Clarifying Soil Texture and Salinity Using Local Spatial Statistics (Getis-Ord *Gi** and Moran's I) in Kazakh–Uzbekistan Border Area, Central Asia. *Agronomy* **2022**, *12*, 332. [CrossRef]
33. Zhang, L.; Tao, Z.; Wang, G. Assessment and determination of earthquake casualty gathering area based on building damage state and spatial characteristics analysis. *Int. J. Disaster Risk Reduct.* **2022**, *67*, 102688. [CrossRef]
34. Yang, Y.; Wang, P.; Brandenberg, S.J. An algorithm for generating spatially correlated random fields using Cholesky decomposition and ordinary kriging. *Comput. Geotech.* **2022**, *147*, 104783. [CrossRef]

35. Zhong, X.; Kealy, A.; Duckham, M. Stream Kriging: Incremental and recursive ordinary Kriging over spatiotemporal data streams. *Comput. Geosci.* **2016**, *90*, 134–143. [CrossRef]
36. Busayo, E.T.; Kalumba, A.M.; Afuye, G.A.; Olusola, A.O.; Ololade, O.O.; Orimoloye, I.R. Rediscovering South Africa: Flood disaster risk management through ecosystem-based adaptation. *Environ. Sustain. Indic.* **2022**, *14*, 100175. [CrossRef]
37. Roopnarine, R.; Eudoxie, G.; Wuddivira, M.N.; Saunders, S.; Lewis, S.; Spencer, R.; Jeffers, C.; Haynes-Bobb, T.; Roberts, C. Capacity building in participatory approaches for hydro-climatic Disaster Risk Management in the Caribbean. *Int. J. Disaster Risk Reduct.* **2021**, *66*, 102592. [CrossRef]
38. Khan, I.; Ali, A.; Waqas, T.; Ullah, S.; Ullah, S.; Shah, A.A.; Imran, S. Investing in disaster relief and recovery: A reactive approach of disaster management in Pakistan. *Int. J. Disaster Risk Reduct.* **2022**, *75*, 102975. [CrossRef]
39. Howland, F.; Francois Le Coq, J. Disaster risk management, or adaptation to climate change? The elaboration of climate policies related to agriculture in Colombia. *Geoforum* **2022**, *131*, 163–172. [CrossRef]
40. Asare-Donkor, N.K.; Ofosu, J.O.; Adimado, A.A. Hydrochemical characteristics of surface water and ecological risk assessment of sediments from settlements within the Birim River basin in Ghana. *Environ. Syst. Res.* **2018**, *7*, 9. [CrossRef]
41. Garrigou, A.; Laurent, C.; Baldi, I.; Berthet, A.; Colosio, C.; Daubas-Letourneux, V.; Galey, L.; Goutille, F.; Jackson Filho, J.M.; Jas, N.; et al. Response from the authors of the article "Critical review of the role of personal protective Equipment (PPE) in the prevention of risks related to agricultural pesticide use" to the letter to the editor from the European crop protection association (ECPA) Occupational and bystander exposure expert group (OBEEG). *Saf. Sci.* **2021**, *138*, 105191. [CrossRef]
42. Alam, A.S.A.F.; Begum, H.; Masud, M.M.; Al-Amin, A.Q.; Filho, W.L. Agriculture insurance for disaster risk reduction: A case study of Malaysia. *Int. J. Disaster Risk Reduct.* **2020**, *47*, 101626. [CrossRef]
43. Guan, X.; Zang, Y.; Meng, Y.; Liu, Y.; Lv, H.; Yan, D. Study on spatiotemporal distribution characteristics of flood and drought disaster impacts on agriculture in China. *Int. J. Disaster Risk Reduct.* **2021**, *64*, 102504. [CrossRef]
44. Wang, X.; Zhang, C.; Wang, C.; Liu, G.; Wang, H. GIS-based for prediction and prevention of environmental geological disaster susceptibility: From a perspective of sustainable development. *Ecotoxicol. Environ. Saf.* **2021**, *226*, 112881. [CrossRef] [PubMed]
45. Zhang, Y.; Qu, H.; Yang, X.; Wang, M.; Qin, N.; Zou, Y. Cropping system optimization for drought prevention and disaster reduction with a risk assessment model in Sichuan Province. *Glob. Ecol. Conserv.* **2020**, *23*, e01095. [CrossRef]
46. Mashi, S.A.; Oghenejabor, O.D.; Inkani, A.I. Disaster risks and management policies and practices in Nigeria: A critical appraisal of the National Emergency Management Agency Act. *Int. J. Disaster Risk Reduct.* **2019**, *33*, 253–265. [CrossRef]
47. Muñoz, V.A.; Carby, B.; Abella, E.C.; Cardona, O.D.; López-Marrero, T.; Marchezini, V.; Meyreles, L.; Olivato, D.; Trajber, R.; Wisner, B. Success, innovation and challenge: School safety and disaster education in South America and the Caribbean. *Int. J. Disaster Risk Reduct.* **2020**, *44*, 101395. [CrossRef]
48. Ba, R.; Deng, Q.; Liu, Y.; Yang, R.; Zhang, H. Multi-hazard disaster scenario method and emergency management for urban resilience by integrating experiment–simulation–field data. *J. Saf. Sci. Resil.* **2021**, *2*, 77–89. [CrossRef]
49. Park, E.-S.; Yoon, D.K. The value of NGOs in disaster management and governance in South Korea and Japan. *Int. J. Disaster Risk Reduct.* **2022**, *69*, 102739. [CrossRef]
50. Garrigou, A.; Laurent, C.; Berthet, A.; Colosio, C.; Jas, N.; Daubas-Letourneux, V.; Jackson Filho, J.M.; Jouzel, J.N.; Samuel, O.; Baldi, I.; et al. Critical review of the role of PPE in the prevention of risks related to agricultural pesticide use. *Saf. Sci.* **2020**, *123*, 104527. [CrossRef]
51. Andriyanto, A.; Hidayati, R.N. Improving collaboration skills among nursing students through disaster preparedness simulation. *Enfermería Clínica* **2021**, *31*, S644–S648. [CrossRef]
52. Qing, C.; Guo, S.; Deng, X.; Xu, D. Farmers' disaster preparedness and quality of life in earthquake-prone areas: The mediating role of risk perception. *Int. J. Disaster Risk Reduct.* **2021**, *59*, 102252. [CrossRef]
53. Kamari, M.; Ham, Y. AI-based risk assessment for construction site disaster preparedness through deep learning-based digital twinning. *Autom. Constr.* **2022**, *134*, 104091. [CrossRef]
54. Cao, Y.; Bai, Y.; Zhang, L. The impact of farmland property rights security on the farmland investment in rural China. *Land Use Policy* **2020**, *97*, 104736. [CrossRef]
55. Pu, G. Achieving agricultural revitalization: Performance of technical innovation inputs in farmland and water conservation facilities. *Alex. Eng. J.* **2022**, *61*, 2851–2858. [CrossRef]
56. Wang, C.; Wang, G.; Feng, Z.; Ji, X.; Li, Q.; Zhang, Z.; Song, D. Strengthen Water Conservancy Construction, Use Water Resources Scientifically, and Develop Modern Agriculture. *Procedia Environ. Sci.* **2011**, *10*, 1595–1600. [CrossRef]
57. Jiang, D.; Zhuang, D.; Fu, J.; Huang, Y.; Wen, K. Bioenergy potential from crop residues in China: Availability and distribution. *Renew. Sustain. Energy Rev.* **2012**, *16*, 1377–1382. [CrossRef]
58. Liu, X.; Zhao, C.; Song, W. Review of the evolution of cultivated land protection policies in the period following China's reform and liberalization. *Land Use Policy* **2017**, *67*, 660–669. [CrossRef]
59. Luo, D.; Ye, L.; Sun, D. Risk evaluation of agricultural drought disaster using a grey cloud clustering model in Henan province, China. *Int. J. Disaster Risk Reduct.* **2020**, *49*, 101759. [CrossRef]
60. Raikes, J.; Smith, T.F.; Baldwin, C.; Henstra, D. The influence of international agreements on disaster risk reduction. *Int. J. Disaster Risk Reduct.* **2022**, *76*, 102999. [CrossRef]

61. Vučetić, M.; Brokešová, Z.; Hudec, M.; Pastoráková, E. Financial literacy and psychological disaster preparedness: Applicability of approach based on fuzzy functional dependencies. *Inf. Processing Manag.* **2022**, *59*, 102848. [CrossRef]
62. Wang, J.-J.; Tsai, N.-Y. Factors affecting elementary and junior high school teachers' behavioral intentions to school disaster preparedness based on the theory of planned behavior. *Int. J. Disaster Risk Reduct.* **2022**, *69*, 102757. [CrossRef]
63. Zaremohzzabieh, Z.; Samah, A.A.; Roslan, S.; Shaffril, H.A.M.; D'Silva, J.L.; Kamarudin, S.; Ahrari, S. Household preparedness for future earthquake disaster risk using an extended theory of planned behavior. *Int. J. Disaster Risk Reduct.* **2021**, *65*, 102533. [CrossRef]

sustainability

MDPI

Article

High-Resolution Hazard Assessment for Tropical Cyclone-Induced Wind and Precipitation: An Analytical Framework and Application

Jiting Tang [1,2,3], Fuyu Hu [4], Yimeng Liu [1,2,3], Weiping Wang [5] and Saini Yang [1,2,3,5,*]

[1] Key Laboratory of Environmental Change and Natural Disaster, Ministry of Education, Beijing Normal University, Beijing 100875, China
[2] State Key Laboratory of Earth Surface Processes and Resource Ecology, Beijing Normal University, Beijing 100875, China
[3] Academy of Disaster Reduction and Emergency Management, Faculty of Geographical Science, Beijing Normal University, Beijing 100875, China
[4] School of International Affairs and Public Administration, Ocean University of China, Qingdao 266100, China
[5] School of National Safety and Emergency Management, Beijing Normal University, Beijing 100875, China
* Correspondence: yangsaini@bnu.edu.cn

Abstract: Intensified tropical cyclones (TCs) threaten the socioeconomic development of coastal cities. The coupling of strong wind and precipitation with the TC process usually amplifies the destructive effects of storms. Currently, an integrated analytical framework for TC hazard assessment at the city level that combines the joint statistical characteristics of multiple TC-induced hazards and local environmental features does not exist. In this study, we developed a novel hazard assessment framework with a high spatiotemporal resolution that includes a fine-tuned K-means algorithm for clustering TC tracks and a Copula model to depict the wind–precipitation joint probability distribution of different TC categories. High-resolution wind and precipitation data were used to conduct an empirical study in Shenzhen, a coastal megacity in Guangdong Province, China. The results show that the probabilities of TC-induced wind speed and precipitation exhibit significant spatial heterogeneity in Shenzhen, which can be explained by the characteristics of TC tracks and terrain environment factors. In general, the hazard intensity of TCs landing from the west side is higher than that from the east side, and the greatest TC intensity appears on the southeast coast of Shenzhen, implying that more disaster prevention efforts are needed. The proposed TC hazard assessment method provides a solid base for highly precise risk assessment at the city level.

Keywords: tropical cyclone; hazard assessment; high resolution; Copula theory; K-means clustering; Shenzhen

Citation: Tang, J.; Hu, F.; Liu, Y.; Wang, W.; Yang, S. High-Resolution Hazard Assessment for Tropical Cyclone-Induced Wind and Precipitation: An Analytical Framework and Application. *Sustainability* **2022**, *14*, 13969. https://doi.org/10.3390/su142113969

Academic Editors: Stefano Morelli, Veronica Pazzi and Mirko Francioni

Received: 16 August 2022
Accepted: 24 October 2022
Published: 27 October 2022

1. Introduction

This past decade has been marked by devastating extreme events, including Hurricane Harvey in 2017, Typhoon Lekima in 2019, and Typhoon Rai in 2021. Climate change has intensified tropical cyclones (TCs), posing a greater threat to life and property along coastal areas [1,2]. With the influence of the anthropogenic rise in greenhouse gases, cyclone track density, power dissipation, and cyclone genesis have shown robust increasing trends over the North Pacific [3,4]. In addition, the development of infrastructure in coastal areas, especially in developing countries, has accelerated. As a result, risks have increased with the urban infrastructures from more severe TCs [5]. TC hazard assessment at a high spatial resolution is an inevitable and fundamental step for risk assessment.

The demand from stakeholders for information on natural hazards has been highlighted in several reports, such as Global Assessment Reports on Disaster Risk Reduction and IPCC SREX. Comprehensive hazard assessment is essential to achieving the Millennium Development Goals, Sustainable Development Goals, and the Sendai framework.

Knowledge of natural hazards is key to developing preventative policies and taking risk-reduction measures. Such information is valuable to stakeholders from the (re)insurance, governance, and spatial planning sectors.

Many empirical models consider that TC hazards vary among different areas, provinces, cities, and even greater regions. However, the spatial or temporal resolution of previous studies has generally been rough, making it difficult to illustrate the hazards of a TC process at the city level. How do TC hazards vary within a city? What factors can explain the variation? In contrast to the extensive studies of inventory exposure to TCs with a high spatiotemporal resolution, these questions have not received adequate attention. High-resolution TC hazard assessment is urgently needed for refined risk analysis and emergency management in coastal cities. For a more accurate impact analysis of TCs, hazard assessments with a high temporal resolution are needed to depict the changes during a TC process. Additionally, hazard assessments with a high spatial resolution are also essential to match the heterogeneously distributed urban infrastructures in cities. Meanwhile, a single factor of TC, such as wind speed, cannot fully reflect the compound impacts of TCs, which usually include strong winds, rainfall, and flooding [6]. Therefore, the combined possibilities of the intensity and frequency of multiple hazards caused by TCs should be considered simultaneously. In addition, the location and direction of TCs affect the scope and distribution pattern of wind and rain in coastal cities [7,8], such that the hazards of different TC categories should be assessed separately.

To address the above issues, we developed a hazard assessment framework with a high spatiotemporal resolution to analyze regional TC hazards. In the framework, TC tracks are clustered by a fine-tuned K-means algorithm, and the wind–precipitation joint probability distribution of different TC categories is depicted by a Copula model. The proposed framework focuses on the short-term wind–rain joint occurrence probability during TC processes and enables subsequent fine-grained risk analysis. To the best of our knowledge, this is the first TC hazard assessment study with such a high temporal and spatial resolution. The outcomes can also be used to plan and schedule disaster preparedness and response operations in urban areas.

The paper is organized as follows. Section 2 reviews previous studies. Section 3 describes the proposed methodological framework, and Section 4 presents a hazard assessment application and results for Shenzhen, China. Thereafter, Sections 5 and 6 present the discussion and conclusions, respectively.

2. Literature Review

This section surveys an extensive set of TC clustering techniques and TC hazard assessment methodologies.

2.1. TC Clustering Techniques

In recent years, many clustering algorithms have been used to categorize TCs based on their features, such as TC tracks, forms, lengths, or intensities, from TC databases, among which tracks (longitudes and latitudes) have been the most widely used. The key for a clustering algorithm is clustering the data into several groups based on some similarity measures such that the total variance among the groups is minimized. The K-means algorithm is a straightforward and widely used partitioning method that seeks to assign each track to one of K groups [9–11]. However, difficulties arise because of the differentiated TC evolution processes, which result in very different point shapes and lengths. The typical K-means algorithm is not suitable for TC tracks of different lengths, and we show that this is a serious shortcoming for TCs. Hu et al. interpolated different tracks to obtain the same length of vectors [12], which added errors. Tian et al. detected interdecadal changes in the genesis of TCs in the western North Pacific based on pHash and K-means cluster analysis [13]. Chand et al. [14] and Samuel et al. [15] used the curve-clustering approach to classify TC tracks. Camargo et al. developed a special probabilistic clustering algorithm that relies on a regression mixture model to cluster TC tracks [16,17]. These techniques

provide a mixture of polynomial regression functions (curves) to fit the geographical shapes of trajectories. The Hausdorff distance is a simple dissimilarity measure and is widely used for comparing point sets [18] and image identifying [19]. The combination of the K-means algorithm and the Hausdorff distance can be a new way to cluster the irregular point sets.

2.2. TC Hazard Assessment

There are two main categories of TC hazard assessment methodologies. The first category consists of comprehensive index constructions, including the weighting, normalization, and mechanism-based methods. The weighting method gives weights to different hazard factors according to their importance, occurrence probability, or hazard intensity [20]. The normalization method normalizes a variety of indices into a single index, which is convenient for comprehensive probability analysis [21,22]. However, in these methods, the relationship among factors is characterized as linear, while it is nonlinear for actual TCs. Some researchers have constructed comprehensive indices based on the physical mechanisms or economic characteristics of TCs, such as Accumulated Cyclone Energy [23], Integrated Kinetic Energy [24], and Carvill Hurricane Index [25]. These comprehensive indices mainly focus on winds and fail to consider other TC-induced hazards (e.g., precipitation).

The other category consists of joint probability models, which construct a joint probability distribution function based on multi-hazard correlations. The Copula theory uses marginal distributions to form a joint distribution. It can solve nonlinear, nonnormal, nonsymmetric, and long-tailed problems. In recent years, this theory has been widely used in multivariate analysis in the fields of extreme value theory [26], financial risk [27], wireless communication [28], drought [29,30], and flood disasters [31,32]. Some researchers have previously constructed the TC-induced wind–rain joint probability distribution function based on Copula theory. However, the data are mainly the maximum or accumulated value of annual statistics [33] or TC events [6,34] from a single meteorological station. Recent studies have used meteorological data from multiple stations to depict the regional difference of hazard intensity [35,36]. These studies have indicated that Copula theory can be an effective tool for TC hazard assessment.

3. Methodological Framework

In this paper, a novel TC hazard assessment framework is proposed and divided into three steps: determination of hazard datasets, analysis of hazard probability, and assessment of regional hazards. The analytical framework of this work is shown in Figure 1.

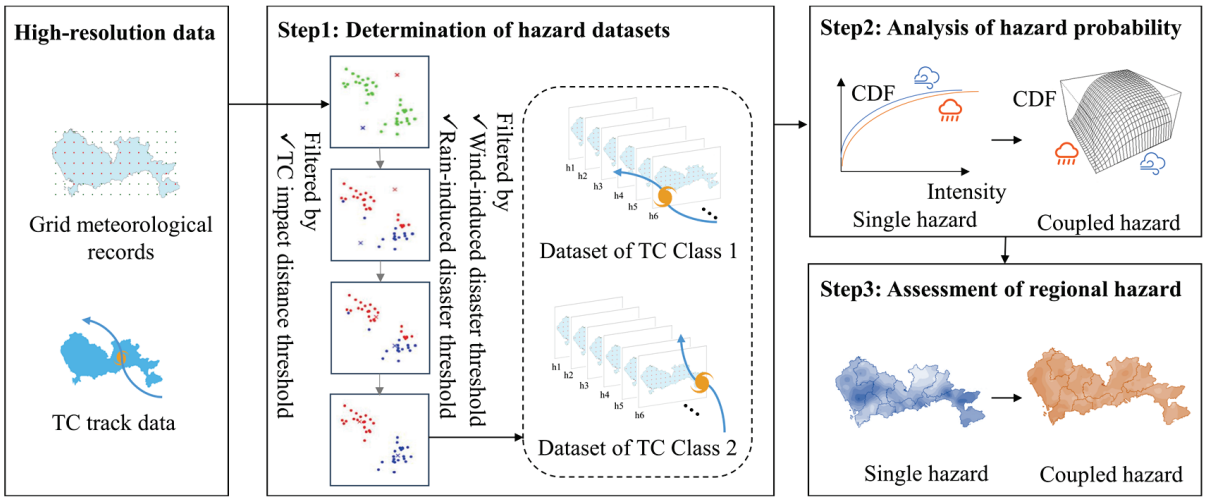

Figure 1. The analytical framework.

3.1. Hazard Datasets

3.1.1. Disaster Thresholds

The proposed framework assesses wind and rain, the two representative TC-induced hazards. Wind and rain have a significant influence on society, as they commonly lead to storm surges, floods, and debris flows. Our goal is to assess the comprehensive hazard intensity of short-term wind or rain exceeding certain thresholds during TC processes. Therefore, we set the distance threshold from the location to the TC center to determine if the wind and rain are induced by the TC and the intensity thresholds to determine if a hazard of a certain intensity will cause damage.

The thresholds used in this study include the TC impact distance threshold, wind-induced disaster threshold, and rain-induced disaster threshold. (1) TCs in the western Pacific Ocean are nearly circular circulation systems, with a typical radius of approximately 200–500 km [37]. Previous studies have shown that rainfall within 5° in longitude-latitude (approximately 500 km) from the TC center can be considered TC-induced rainfall [38], which is also consistent with on-site evidence. Therefore, we used a circle with a radius of 500 km from the TC center as the TC impact distance threshold. (2) According to the national standard of Grade of tropical cyclones https://www.codeofchina.com/standard/GBT19201-2006.html (accessed on 23 October 2022), a tropical depression is defined when the maximum 2 min mean wind speed near the TC center exceeds 10.8 m/s. Therefore, we set 10.8 m/s as the wind-induced disaster threshold. (3) According to the national standard of Grade of precipitation https://www.codeofchina.com/standard/GBT28592-2012.html (accessed on 23 October 2022), the precipitation was divided into seven levels. In this study, we chose the precipitation reaching the storm level (50 mm/24 h) as the rain-induced disaster threshold.

3.1.2. The Fine-Tuned K-Means Algorithm

In a general K-means algorithm, the data are mapped into points in a Euclidean space and clustered into several classes. These classes can be natural groups of variables, data points, or objects similar to one another in terms of some similarity measures. The clustering performance is evaluated by using the sum of squares for the error from each data point to the clustering center, as shown in Equation (1).

$$S_T = \sum_{i=1}^{K} \sum_{e_j \in P_i} \|e_j - c_i\|^2 \quad (1)$$

Here, K is the number of classes; c_i is the clustering center of Class i; P_i is the dataset for Class i; e_j is the location attribute of TC track j (the latitudes and longitudes of TC centers); and $\|e_j - c_i\|$ is the Euclidean distance from e_j to c_i.

The iterative calculation process of K-means is as follows:

(1) Select K TC tracks as the initial clustering center.
(2) Calculate the Euclidean distances from all the tracks to each clustering center and assign them to the nearest class.
(3) Calculate the mean value of all data in each class as the new clustering center.
(4) End if S_T converges or the number of iterations reaches the preset maximum; otherwise, return to Step (2).

K-means cannot accommodate tracks of different lengths [37]. To address this problem, we fine-tuned the distance calculation in the algorithm by changing the Euclidean distance of two points to the Hausdorff distance of two point sets [38]. The Hausdorff distance is defined as follows:

$$H(A, B) = \max[h(A, B),\ h(B, A)] \quad (2)$$

Here,

$$h(A, B) = \max_{a \in A} \min_{b \in B} \|a - b\| \quad (3)$$

$$h(B, A) = \max_{b \in B} \min_{a \in A} \|b - a\| \quad (4)$$

$H(A, B)$ is the bidirectional Hausdorff distance between point sets A and B, $h(A, B)$ is the unidirectional Hausdorff distance from A to B, and correspondingly, $h(B, A)$ is the Hausdorff distance from B to A. $H(A, B)$ is larger than $h(A, B)$ and $h(B, A)$, which measures the maximum mismatch between two point sets. In this study, the K-means clustering algorithm was reconstructed using the Hausdorff distance.

The fine-tuned K-means algorithm used in this study to fit the geographical shape of the trajectories allows the clustering to be posed and accommodates TC tracks of different lengths. The filtered TC tracks might be composed of the longitudes and latitudes of TC centers with different numbers, that is, have different lengths and shapes. The proposed method is more objective and simpler than the mixture K-means method used in previous studies.

We determined the hazard datasets in three steps. First, we filtered out the historical TC tracks by using the TC impact distance threshold. Second, we split the TC tracks according to the fine-tuned K-means clustering algorithm. Third, we filtered the meteorological data by using the wind-induced disaster threshold and rain-induced disaster threshold. Thus, the subsequent hazard analysis was carried out based on the subsets of wind speed and precipitation during the impact of different TC classes.

3.2. Analysis of Hazard Probability

The hazards for different TC classes were analyzed during two stages: single hazard of wind or rain and coupled hazards of wind–rain. Single hazard analysis constructs the probability density function (PDF), which indicates the probability of a hazard with different intensities. The probability distribution of a single hazard is the basis of multi-hazard joint probability analysis, commonly known as the marginal distribution. Then, the cumulative distribution function (CDF) of coupled hazards can be further generated based on the two-dimensional (2D) Copula functions.

Copulas are a family of functions that construct the joint distribution of two or more random variables with an unidentified dependence among the variables [39,40]. The most widely used Copula functions include two categories: Elliptic Copulas and Archimedean Copulas. Elliptic Copulas mainly include Gaussian Copula and t Copula, which are suitable when the marginal distribution obeys the standard normal distribution or Student's T distribution. Archimedean Copulas are obtained by constructing different generator functions, including Clayton Copula, Frank Copula, Gumbel Copula, and Joe Copula (Table 1).

Table 1. Commonly used 2D Archimedean Copulas.

Copulas	$C(u,v;\theta)$	Limiting Condition
Clayton Copula	$\left[\max\left\{u^{-\theta} + v^{-\theta} - 1; 0\right\}\right]^{-1/\theta}$	$\theta \in [-1, \infty]$
Frank Copula	$-\frac{1}{\theta}\log\left[1 + \frac{(\exp(-\theta u)-1)(\exp(-\theta v)-1)}{(\exp(-\theta)-1)}\right]$	$\theta \neq 0$
Gumbel Copula	$\exp\left[-((-\log(u))^{\theta} + \left(-\log(v)\right)^{\theta})^{\frac{1}{\theta}}\right]$	$\theta \in [1, \infty]$
Joe Copula	$1 - \left((1-u)^{\theta} + (1-v)^{\theta} - (1-u)^{\theta} * (1-v)^{\theta}\right)^{\frac{1}{\theta}}$	$\theta \in [1, \infty]$

Here, u and v are the marginal distributions of two variables, θ is the Copula function parameter, and $C(u, v; \theta)$ is the 2D Archimedean Copula.

We constructed a multi-hazard joint probability model based on 2D Copula theory, which was divided into the following four steps:

(1) Determine the marginal distribution of the wind speed and precipitation;
(2) Measure the correlation among the hazards;

(3) Estimate the parameters of Copula functions that may be applicable;
(4) Select the appropriate Copula function to fit the joint distribution. Then, the probability of multiple hazards with different intensities can be calculated.

To choose the marginal distribution and joint distribution in Steps (1) and (4), we first determined if the variable was subject to the fitted distribution type based on the Kolmogorov-Smirnov (K-S) test. Then, we selected the best fitting function based on the Akaike information criterion (AIC) minimum, Bayesian information criteria (BIC) minimum, and log-likelihood (LogLik) maximum principle. The calculation formulas are shown in Equations (5)–(8).

$$AIC = 2k - 2\ln(L(\theta)) \tag{5}$$

$$BIC = kln(n) - 2\ln(L(\theta)) \tag{6}$$

$$L(\theta) = \prod_{i=1}^{m} p(y_i;\theta) \tag{7}$$

$$LogLik(\theta) = lnL(\theta) \tag{8}$$

where y_i is the data sample, and $p(y_i;\theta)$ is the PDF of the fitting function.

According to the single-hazard X occurrence probability $P_{(x)} = P(X \geq x) = 1 - F(x)$, we defined two kinds of double-hazard joint occurrence probability. $P_{\cup(x_1,x_2)}$ indicates the probability of at least one hazard reaching a specific intensity, while $P_{\cap(x_1,x_2)}$ indicates the probability of two hazards reaching a specific intensity simultaneously. The calculation formulas are shown in Equations (9) and (10).

$$P_{\cup(x_1,x_2)} = P(X_1 \geq x_1 \; or \; X_2 \geq x_2) = 1 - F(x_1, x_2) \tag{9}$$

$$P_{\cap(x_1,x_2)} = P(X_1 \geq x_1 \; and \; X_2 \geq x_2) = 1 - F_{X_1}(x_1) - F_{X_2}(x_2) + F(x_1, x_2) \tag{10}$$

where X_1, X_2 are random variables, their respective CDFs are $F_{X_1}(x_1)$ and $F_{X_2}(x_2)$, and the joint CDF of the Copula function is $F(x_1, x_2)$.

In this study, we fitted the marginal distributions of the hourly wind and precipitation data separately and then fitted the joint distribution of the coupled wind and precipitation by Copula theory. Based on the single or coupled hazard fitting results of different subareas, we quantitatively depicted the characteristics of regional hazards.

4. Application and Results

4.1. Study Area and Data Source

Shenzhen, which is an economically developed and densely populated coastal megacity in China, has an area of 1997.47 km^2, a GDP of 2.69 trillion yuan and a permanent population of 13.44 million as of 2019 http://www.sz.gov.cn/en_szgov/aboutsz/profile/content/post_10093130.html (accessed on 23 October 2022), a total road mileage of 8066.1 km, and a civilian car ownership of 3.53 million as of 2020 http://tjnj.gdstats.gov.cn:8080/tjnj/2021/directory/15/html/15-11-0.htm (accessed on 23 October 2022). Shenzhen faces the South China Sea and the Pearl River. It has a subtropical oceanic climate. During summer, Shenzhen is vulnerable to frequent TCs from the western Pacific Ocean. With the development of infrastructure, the TC risk to Shenzhen's transportation system, communication system, and buildings has increased.

Four categories of data were used in this study: (1) the meteorological data of Shenzhen provided by the National Climate Center (NCC), including 10 m wind speed and precipitation data between 1 January 2008 and 31 December 2018 in 39 grid points with resolutions of 0.0625° × 0.0625° and 1 h, respectively http://data.cma.cn/en/?r=data/detail&dataCode=NAFP_CLDAS2.0_NRT (accessed on 23 October 2022); (2) the TC track dataset provided by the NCC, which includes the hourly historical TCs that landed in China from 2008 to 2018. Each record includes the TC ID, year, month, day, time, longitude, and latitude of the TC centers https://tcdata.typhoon.org.cn/en/zjljsjj_sm.html (accessed on 23 October 2022); (3) the 90 m digital elevation model (DEM) of Shenzhen from the NASA SRTM3 dataset https://www.gscloud.cn/ (accessed on 23 October 2022); and (4) the

data of the main rivers and water bodies in Shenzhen from the Resource and Environment Science and Data Center https://www.resdc.cn/DOI/DOI.aspx?DOIID=44 (accessed on 23 October 2022). The meteorological data and TC tracks were used to determine the hazard datasets, and the distribution of the DEM and river/water bodies served as a reference for subsequent causative analysis. Figure 2 shows the geographical location of Shenzhen and the distribution of multisource meteorological environment data.

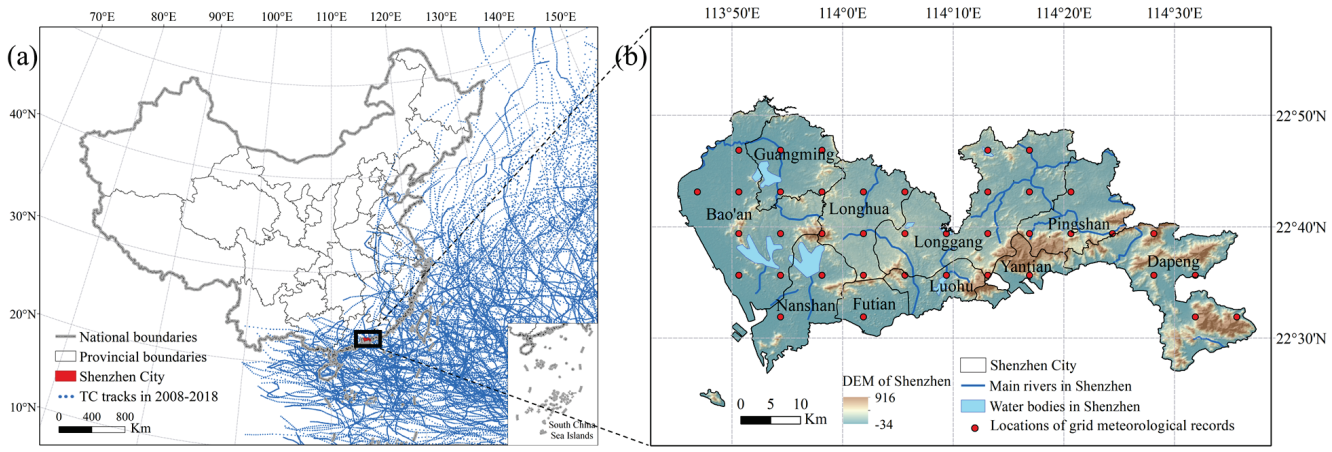

Figure 2. Case study area: Shenzhen. (**a**) The geographical location; (**b**) The distribution of multisource environmental data.

Compared with the annual or TC events in previous studies, the temporal resolution of the hourly data used in this study is considerably enhanced. In meteorological research, one hour is typically acknowledged as a high-precision time unit. When compared to historical weather station observational data utilized for regional hazard studies, the spatial resolution of 0.0625° is significantly more accurate.

4.2. Preprocessing of Hazard Datasets

We filtered out the datasets according to the proposed K-means-based TC track clustering algorithm and three thresholds referred to in Step 1 in Figure 1.

First, for each grid point in Shenzhen, we calculated the distance d from the TC center in all the track records (Figure 2a) to the grid. The grid point was classified as being impacted by TCs at that moment if $d \leq 500$ km. From 2008–2018, 74 TCs affected Shenzhen, with an average duration of 47.89 h. Then, we clustered the TC tracks affecting Shenzhen based on the fine-tuned K-means algorithm. We clustered the TC tracks into two classes, and the maximum number of iterations was 100. Figure 3 shows that the two TC classes can be roughly interpreted as landing from the west side of Shenzhen (Class 1) or the east side (Class 2). Furthermore, we retrieved the hourly wind speed and precipitation data for a grid point if the 24 h cumulative precipitation was greater than 50 mm or the wind speed was greater than 10.8 m/s. Thus, we created TC-induced wind speed and precipitation datasets for 39 grid points and 2 TC classes. Approximately 80–200 samples were recorded per grid point for each TC class. Next, we analyzed the TC hazards from the single variable (wind or precipitation) and coupled variables (joint wind–precipitation).

4.3. Hazard Analysis

In this section, we conducted the analysis of hazard probability referred to Step 2 in Figure 1. First, we found a fit for the CDF of observed wind and precipitation data. Then, we specified the Copula method to fit the joint PDFs and CDFs. Later, we appraised the performance of the hazard assessment.

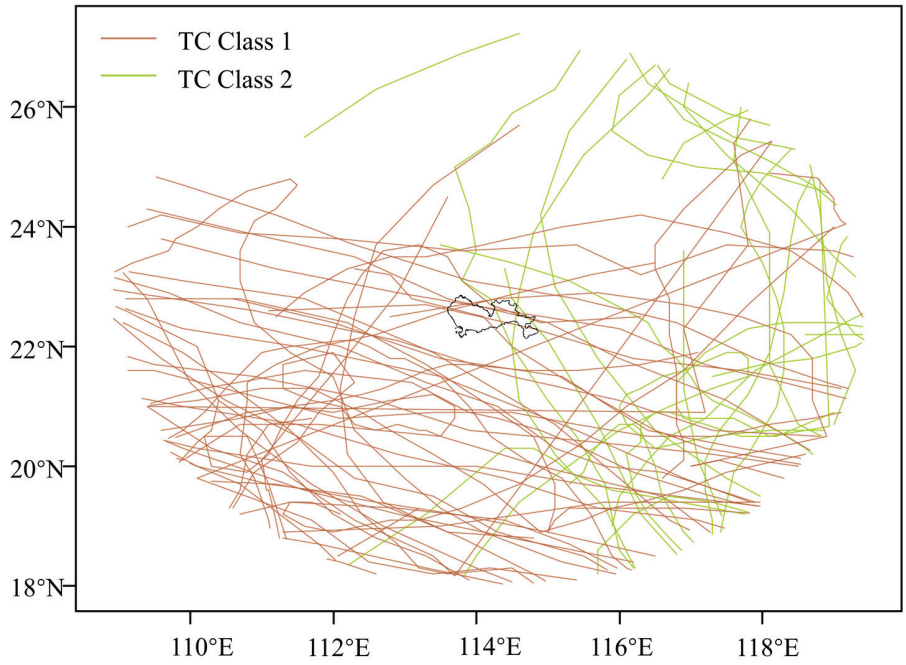

Figure 3. Clustering results of TCs affecting Shenzhen.

4.3.1. Single Hazard Analysis

We randomly picked one grid point (denoted by $\mathcal{A}$) as an example to analyze a single hazard. There were 105 records of grid point $\mathcal{A}$ for TC Class 1 and 143 records for TC Class 2. Referring to existing research results [33–35], we selected the Gumbel, Weibull, Gamma, and lognormal distributions as the theoretical distribution functions to fit the hourly wind and precipitation data separately. We utilized the maximum likelihood estimate (MLE) approach to estimate the parameters. According to the AIC, BIC, and LogLik values, we found that for two TC classes, Gamma distribution was the best marginal distribution to fit the wind speed data (Figure 4a,b), whereas the lognormal distribution was suitable for fitting the precipitation data (Figure 4c,d).

For TC Class 1, the fitting Gamma CDF $F_1(x_1)$ of the wind speed data in $\mathcal{A}$ is

$$F_1(x_1) = \frac{\int 0.50^{2.16} {x_1}^{1.16} \exp(-0.50x_1)}{\Gamma(2.16)dx_1} \tag{11}$$

Here, $\Gamma(x) = \int_0^\infty t^{x-1}e^{-t}dt$ is the Gamma function with recursion, i.e., $\Gamma(x+1) = x\Gamma(x)$.

The fitting lognormal CDF $F_2(x_2)$ of the precipitation in $\mathcal{A}$ is

$$F_2(x_2) = \frac{1}{2} + \frac{1}{2}erf\left[\frac{\ln(x_2) - 1.13}{1.35 * \sqrt{2}}\right] \tag{12}$$

Here, $erf(x) = \frac{2}{\sqrt{\pi}} \int_0^x e^{-y^2}dy$ is the Gaussian error function.

For TC Class 2, the fitting Gamma CDF $F_1(x_1')$ of the wind speed data in $\mathcal{A}$ is

$$F_1(x_1') = \frac{\int 0.60^{3.02} {x_1'}^{2.02} \exp(-0.60x_1')}{\Gamma(3.02)dx_1'} \tag{13}$$

The fitting lognormal CDF $F_2(x_2')$ of the precipitation in $\mathcal{A}$ is

$$F_2(x_2') = \frac{1}{2} + \frac{1}{2}erf\left[\frac{\ln(x_2') - 1.07}{1.40 * \sqrt{2}}\right] \tag{14}$$

Based on Equations (11)–(14), we calculated the corresponding wind speed and precipitation intensities with different probabilities (Table 2) and the probabilities of different wind speeds (Table 3) and precipitations (Table 4) for the two TC classes.

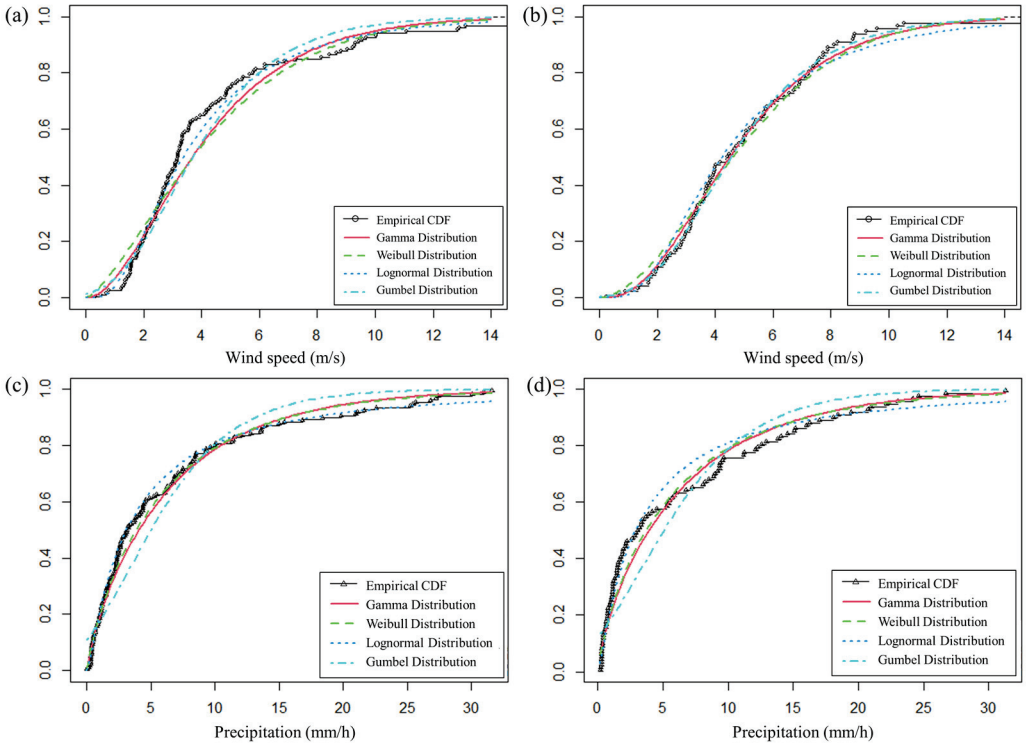

Figure 4. The fitting Cumulative Distribution Function of the hourly wind speed (**a**,**b**) and precipitation (**c**,**d**) in grid point $\mathcal{A}$ for TC Class 1 (**a**,**c**) and Class 2 (**b**,**d**).

Table 2. The wind speeds and precipitations with different probabilities in $\mathcal{A}$.

TC Classes	Class 1		Class 2	
Probability	**Wind Speed (m/s)**	**Precipitation (mm/h)**	**Wind Speed (m/s)**	**Precipitation (mm/h)**
50%	3.67	3.11	4.50	2.92
20%	6.41	9.72	7.18	9.48
10%	8.25	17.64	8.93	17.57
5%	10.00	28.86	10.56	29.23
1%	13.87	72.64	14.08	75.95
0.5%	15.48	101.84	15.53	107.73

In addition, we found that the gamma distribution and lognormal distribution are also good fits for the TC-induced wind speed and precipitation in other grid points in Shenzhen.

4.3.2. Coupled Hazard Analysis

Using grid point $\mathcal{A}$ as an example, the bivariate distribution of hourly wind speed and precipitation is given in Figure 5. The blue line in Figure 5 is the linear regression fit, and the shading along the lines is the confidence interval (95%). There are some points with wind speeds less than 10 m/s and 24 h cumulative precipitation greater than 50 mm. This is consistent with the facts—a typhoon may bring rainfall for several hours, but it is not always windy. At a high temporal resolution, such as one hour, the TC-induced wind and precipitation are not synchronous. The scattered distribution of the wind speed and

precipitation in Figure 5 caught our attention. For TC Class 1, the wind–rain correlation was $P_{west} = 0.13$, passing the significance test of 0.05. The distributions of the hourly wind and rain data were asymmetric and nonnormal, as indicated by the kurtosis values of the wind speed and precipitation, which were 4.65 and 2.17, and their skewness values, which were 2.07 and 1.71, respectively. For TC Class 2, the wind–rain correlation was $P_{east} = 0.17$. The kurtosis values of the wind speed and precipitation were 6.99 and 0.84, and their skewness values were 1.99 and 1.29, respectively. Therefore, we selected Archimedean Copulas to fit the joint probability distribution and estimated the parameters by MLE. We found that the Joe Copula outperformed the other three Copulas in fitting the joint probability of the TC-Class-1-induced wind speed and precipitation in grid point $\mathcal{A}$, but the Clayton Copula performed better for fitting the TC-Class-2-induced wind and precipitation (Table 5). Figure 6 shows the Copula fitting results in grid point $\mathcal{A}$.

Table 3. The probabilities of different wind speeds in $\mathcal{A}$.

Grade of TCs	Wind Speed (m/s)	Wind Scale	Probability (Class 1)	Probability (Class 2)
Tropical depression	10.8–17.1	6–7	0.036	0.045
Tropical storm	17.2–24.4	8–9	0.002	0.002
Severe tropical storm	24.5–32.6	10–11	/	/
Typhoon	32.7–41.4	12–13	/	/
Strong typhoon	41.5–50.9	14–15	/	/
Super typhoon	≥51.0	≥16	/	/

/ indicates that the calculated value is too small, the same below.

Table 4. The probabilities of different precipitations in $\mathcal{A}$.

Grade of Precipitation	Precipitation (mm/h)	Probability (Class 1)	Probability (Class 2)
Light rain	≤2.5	-	-
Moderate rain	2.6–8.0	0.564	0.544
Heavy rain	8.1–15.9	0.243	0.236
Torrential rain	16.0–49.9	0.113	0.112
Heavy downpour	50.0–99.9	0.020	0.021
Rainstorm	≥100.0	0.005	0.006

Table 5. Comparison of AIC, BIC, LogLik results for Copulas in $\mathcal{A}$.

TC Class	Copulas	Fitting θ	AIC	BIC	LogLik
Class 1	Clayton	0.32	−6.96	−4.00	4.48
	Frank	0.88	−0.66	2.31	1.33
	Gumbel	1.15	−5.45	−2.48	3.72
	Joe	**1.26**	**−7.85**	**−4.89**	**4.92**
Class 2	**Clayton**	**0.23**	**−1.02**	**−1.63**	**1.51**
	Frank	0.95	−0.64	2.02	1.32
	Gumbel	1.12	−1.00	−1.65	1.50
	Joe	1.18	−0.67	−1.98	1.34

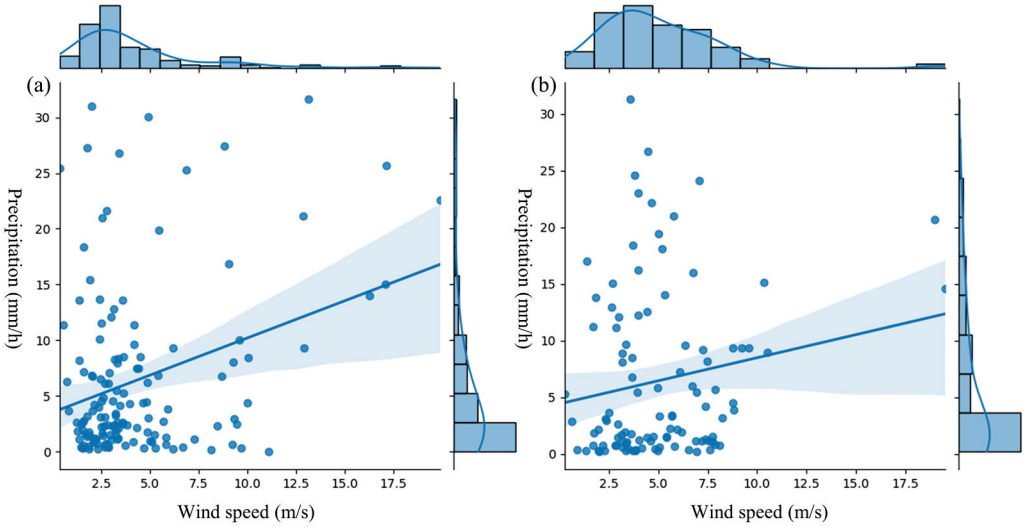

Figure 5. Bivariate distribution of wind speed and precipitation in grid point $\mathcal{A}$ for TC Class 1 (**a**) and Class 2 (**b**). The blue line is the linear regression fit, and the shading along the lines is the confidence interval (95%).

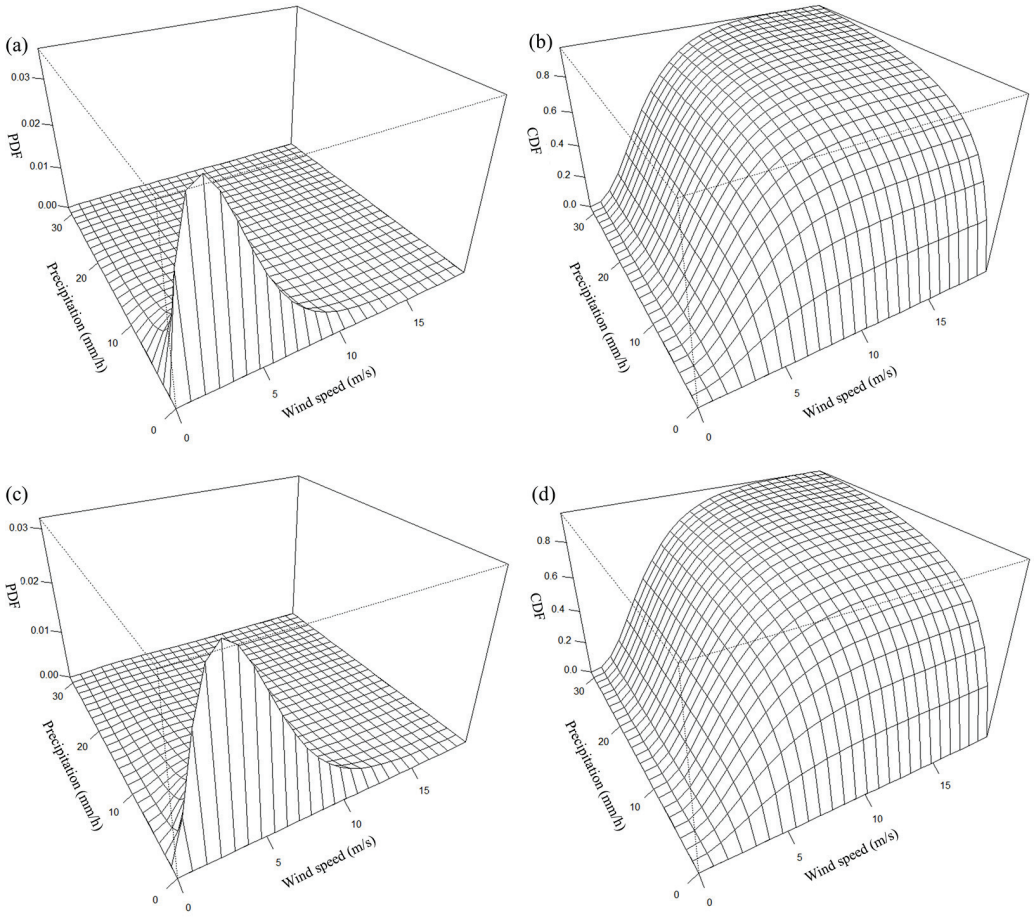

Figure 6. The fitting results of the coupled hazards in $\mathcal{A}$. (**a**) Joe Copula PDF for TC Class 1; (**b**) Joe Copula CDF for TC Class 1; (**c**) Clayton Copula PDF for TC Class 2; (**d**) Clayton Copula CDF for TC Class 2.

Based on the fitting Copula and marginal distribution of two single hazards, we obtained the joint occurrence probability of double hazards in $\mathcal{A}$. When the TC lands in western Shenzhen (Class 1), the probability of the simultaneous occurrence of a rain-

storm and a tropical depression in one hour during the TC process is $P_{\cap(10.8,16.0)} = 0.021$, and the probability of occurrence of a rainstorm or tropical depression in one hour is $P_{\cup(10.8,16.0)} = 0.136$. When the TC lands on the east side (Class 2), $P_{\cap(10.8,16.0)} = 0.017$, $P_{\cup(10.8,16.0)} = 0.125$. That is, for grid point $\mathcal{A}$, the TCs landing on the west side of Shenzhen have a higher intensity than those landing on the east side. The results may help prepare for events that have not yet been observed in the past but nonetheless can be expected in the future.

4.3.3. The Performance of Hazard Assessment

Based on the fitting results above, we calculated descriptive statistics, including the mean value, standard deviation (s_d), coefficient of skewness (c_s), and their relative error (RE, in %) [41], to demonstrate the performance of the hazard assessment (Table 6). Here, the descriptive statistics were calculated by Monte Carlo simulation, which consisted of three steps: (1) generating 5000 random numbers obeying the fitted Copula functions, (2) performing a computation of descriptive statistics using the random numbers, and (3) averaging the results across 10 repetitions to eliminate randomness.

Table 6. The comparison of the fitting results in $\mathcal{A}$.

TC Classes	Statistics	Wind Speed					Precipitation				
		Single Factor Fitting	Coupled Factor Fitting	Empirical Value	RE of Single Factor	RE of Coupled Factor	Single Factor Fitting	Coupled Factor Fitting	Empirical Value	RE of Single Factor	RE of Coupled Factor
Class 1	Mean	4.32	4.31	4.32	0	0	7.72	7.86	6.42	0.20	0.22
	s_d	2.94	2.96	3.50	−0.16	−0.15	16.86	17.69	7.54	1.24	1.35
	c_s	1.36	1.49	2.07	−0.34	−0.28	4.84	4.79	1.71	1.83	1.80
Class 2	Mean	5.04	4.25	5.04	0	−0.16	7.75	7.37	6.48	0.20	0.14
	s_d	2.90	1.35	3.03	−0.04	−0.55	8.35	8.84	7.31	0.14	0.21
	c_s	2.15	2.93	1.99	0.08	0.47	3.05	2.41	1.29	1.36	0.87

Table 6 shows the fitting results of the single and coupled hazards. The descriptive statistics of the single fitting factor were calculated from Equations (11)–(14). The descriptive statistics of the fitting coupled factors were calculated from $C(u, v; \theta)$ of Joe Copula and Clayton Copula in Table 1; here, θ is the bold fitting θ in Table 5, and u, v are taken from Equations (11)–(14). The descriptive statistics of the empirical values were calculated from preprocessed hazard datasets in Section 4.2. Then, we compared the RE of the descriptive statistics between the empirical values and fitting values. Table 6 demonstrates that the hazard assessment performed well because the REs for more than half of the statistics were less than 30%. Comparing the wind speed and precipitation, we found that the fitting REs of the precipitation are larger than those of the wind speed because the wind speed values are mostly concentrated in a smaller range (approximately 0–14 m/s). While the precipitation span is larger (approximately 0–40 mm/h), the extreme precipitation values amplify the bias. Comparing the three statistics, we found that the REs of the mean are small, while the REs of s_d and c_s are large. Because the statistics of the fitting values were generated based on simulation data with randomness, the generated extreme values have a smaller impact on the mean value but a greater impact on s_d and c_s.

It should be noted that the uncertainty of the meteorological gridded data, which are interpolated based on the observational data from the weather stations, affects the goodness of the fitting results.

4.4. The Spatial Heterogeneity of TC Hazards

Based on the analysis results of single and coupled hazard probabilities, we further assessed the regional hazards for specific infrastructure risks referred to in Step 3 in Figure 1. Using road traffic as an example, we analyzed the spatial distribution of TC hazards and identified significant heterogeneity. We set the TC disaster threshold for road traffic based

on the Technical Specification for Highway Travel Information Service as 10 mm/h for the precipitation and 8 m/s for the wind speed.

For the 39 grid points in Shenzhen, we used Gamma distribution to fit the wind speed and a lognormal distribution to fit the precipitation for the two TC classes. Then, we calculated the probability of wind speeds over 8 m/s as P(west_wind) and P(east_wind) and the probability of precipitation over 10 mm/h as P(west_rain) and P(east_rain). Figure 7 displays the spatial distribution.

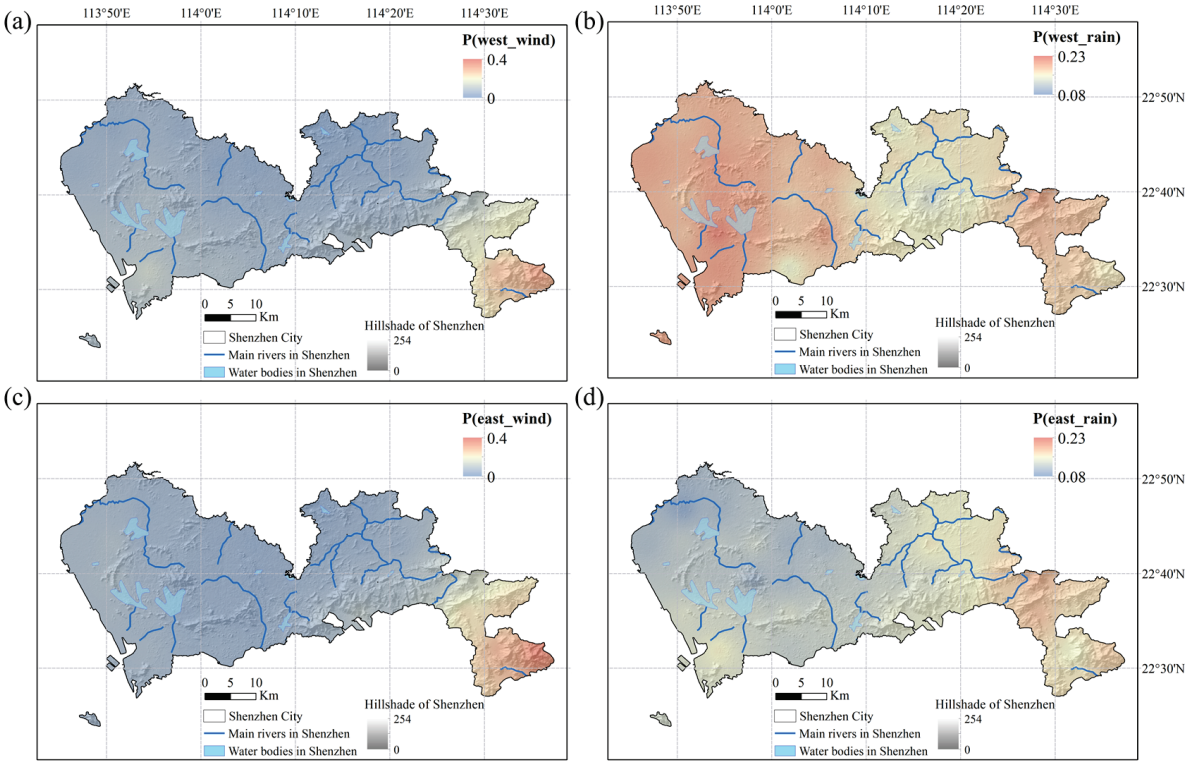

Figure 7. Spatial distribution of the probability of a single hazard for road traffic. (**a**) P(west_wind); (**b**) P(west_rain); (**c**) P(east_wind); (**d**) P(east_rain).

Figure 7a,c demonstrate that the spatial distributions of P(west_wind) and P(east_wind) have a similar pattern regardless of the TC landing location. The east is larger than the west, and the south is larger than the north because the water vapor and surface environment are distinct between the sea and the land, and TCs cause much stronger winds in coastal areas compared to inland areas. In Shenzhen, the TC-induced winds in the west have been significantly weakened due to the blockage of the Pearl River estuary and Hong Kong. The eastern region, particularly Dapeng District, lacks natural barriers and is frequently exposed to severe winds.

Most of western Shenzhen and some of eastern Shenzhen have a higher probability of experiencing rainfall over 10 mm/h when a TC arrives from the west (Figure 7b), whereas small areas of eastern Shenzhen experience rainfall exceeding 10 mm/h when a TC arrives from the east (Figure 7d). This higher probability is due to the terrain and TC tracks. Shenzhen is generally in low hilly areas with mild terraces in between, with a high elevation in the southeast and a low elevation in the northwest. When addressing TCs that are landing from the west, Shenzhen's western plains and rivers promote significant rainfall, which gradually decreases until it hits gentle hills. The southeast mountains would obstruct the flow while facing TCs arriving from the east. As a result, the elevation causes the wind to be weaker and the rainfall to be heavier on the windward sides. Dense air flow lines at the top and sides of the mountains cause the wind to blow faster. As a result, in the

area east of Shenzhen, the likelihood of strong winds would decrease, while the likelihood of heavy rain would change from south to north.

In conclusion, there is a significant spatial difference in the probability of a single hazard affecting road traffic. The most widespread effects of TC-induced rainfall occurred when it arrived from the west. The spatial heterogeneity of TC hazards is influenced by multiple factors of the meteorological environment. These findings validate the necessity and illustrate the importance of high-resolution hazard assessments, especially for accurate urban disaster management.

Repeating the calculation process, we tested the fitting performance of Archimedean Copulas for 39 grid points in Shenzhen. Joe Copula and Clayton Copula fit 27 and 12 grid points, respectively, for TCs landing in western Shenzhen (Class 1). For TCs landing in eastern Shenzhen (Class 2), Clayton Copula had a good fitting performance on the combined probability of 28 grid points, and Joe Copula fit well for 11 grid points. Most of the hourly data in our dataset are on the low side, and Clayton Copula is sensitive to changes at the lower tail of the variables. Joe Copula can describe the intense wind and rain because it is more sensitive to changes in the upper tail of the variable. This higher sensitivity indicates that in some areas, a TC-induced rainfall process may be accompanied by extremely high winds and rainfall. We estimated the two double-hazard joint occurrence probabilities for the two TC classes as P(west_and), P(west_or), P(east_and), and P(east_or) based on the best fitted Copula for each grid. The spatial distributions are given in Figure 8.

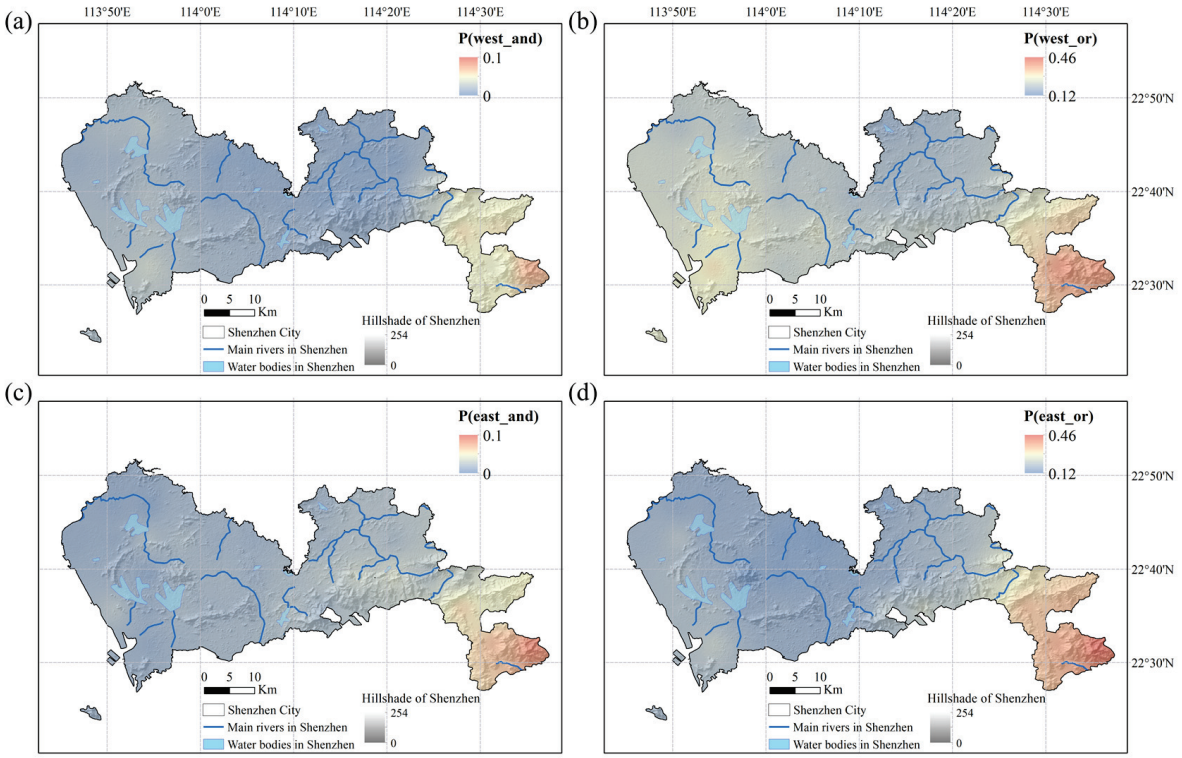

Figure 8. Spatial distribution of the probability of coupled hazards for road traffic. (**a**) P(west_and); (**b**) P(west_or); (**c**) P(east_and); (**d**) P(east_or).

Dapeng District of Shenzhen is the most vulnerable and in need of catastrophe protection, as indicated in Figure 8. When a TC arrives from the west, the probability of at least one hazard affecting road traffic P(west_or) is approximately 12–46%. Comparing the colors of Figure 8b,d, we find that P(west_or) is larger than P(east_or) in most areas of Shenzhen, especially in western Shenzhen. The analysis results of grid point $\mathcal{A}$ show that the wind–rain hazard of TCs arriving from the west is higher than that of TCs arriving from the east, and this finding is also applicable to the other area in Shenzhen.

5. Discussion

The trend in hazard assessment is toward high resolutions for refined risk analysis and emergency management. Figure 5 shows the weak correlation between the hourly wind speed and precipitation during the impact of TCs—this is surprising, but it also makes sense. A typhoon may bring rainfall for several hours, but it is not always windy. At a high temporal resolution, such as one hour, the TC-induced wind and precipitation are not synchronous. In previous studies, a higher correlation has been found by using maximum or cumulative values based on TC events or annual statistics. This finding suggests that we need to consider the time scale differences of TC hazard assessment. Here, we compared the Pearson correlation coefficients of wind and rain over various time scales. Coefficients were used instead of Copulas because Copula fitting results may vary for different time scales. The Pearson correlation coefficient represents the degree of linear correlation between winds and rains. A larger correlation indicates a larger risk of strong winds and heavy rains. Based on the filtered hourly data reaching three thresholds in Section 4.2, we calculated the maximum wind speed and cumulative precipitation for 39 grid points at four time scales, including the hour, rainfall process, TC event, and year. Here, a rainfall process is a set of continuous records with hourly precipitation data greater than 0. We then obtained their Pearson coefficients.

Figure 9 shows a higher and more dispersed correlation when using the cumulative data (rainfall process, TC event, and year scales) than the hourly data. We speculate that the reason is that the temporal accumulation amplifies the compound hazard severity and local spatial heterogeneity. If we evaluate the TC process hazards based on the overall statistics, the higher correlation between multiple hazards would lead to a higher disaster risk. This finding suggests that we need to pay attention to the time scale of TC hazard analysis. For research on the impact of TCs on urban infrastructures that change rapidly, such as urban road transportation, the evolution of a TC process matters. Hazard analysis with a high temporal resolution can help improve the accuracy of determining how TC processes affect urban infrastructures.

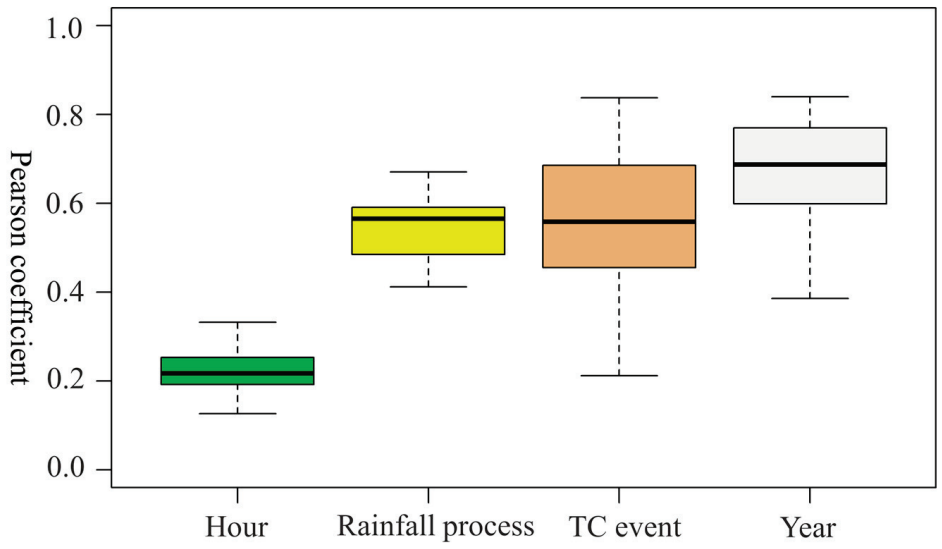

Figure 9. The box plot of wind–rain correlation at different time scales.

From the hazard assessment results based on the high-resolution TC-induced wind rain data in Shenzhen, we found that the probability of the TC-induced wind speed and precipitation displayed a significant spatial heterogeneity, which can be explained by the TC tracks and terrain environment factors. The findings show that the TC hazard assessment results in different regions are customized. However, the proposed framework can be generalized.

6. Conclusions

This study developed a high-resolution framework to assess the regional hazards of wind and rain. This is a key step toward city-scale risk management and infrastructure resilience analysis during TC processes.

The proposed framework was applied to Shenzhen, China. Based on the hazard assessment results, we identified a significant spatial heterogeneity of TC hazards for urban traffic within the city and addressed the importance of high-resolution hazard assessment in urban disaster management. The southeast coast of Shenzhen is the most likely to be affected by TCs, and disaster prevention efforts should be increased. The hazard of TCs arriving from the west is greater than that of TCs arriving from the east, mostly due to the geographical location and terrain environment.

Our framework has the following three advantages: (1) the framework integrates single hazards and coupled hazards at the city level and is combined with joint statistical characteristics of TC hazards and local environmental features; (2) the fine-tuned K-means clustering algorithm provides a simple method to cluster TC tracks of various shapes and lengths and maintains the characteristics of the original data; and (3) the Copula-based joint probability model provides considerable flexibility for additional multiple hazards and can also be expanded to the joint probability distribution of more dimensions.

There are also certain limitations to this study. When studying joint probability based on Copula theory, we need to select the marginal distribution function and joint probability distribution. The outcomes of the joint probability distribution can vary with different models and fitting methods. Discussing the uncertainty of the results in Copula-based hazard analysis is worthwhile. Several extensions to the methodology are anticipated in our future work. We will analyze historical data based on a larger time scale and more dimensions to improve the fitting performance.

Our study can better reveal the interaction between a TC system and the physical environment of Shenzhen. The expected assessment outputs can be used for informed decision making and as a reference for disaster risk reduction.

Author Contributions: Conceptualization, S.Y.; Methodology, J.T. and W.W.; Supervision, S.Y.; Validation, Y.L.; Writing—original draft, J.T.; Writing—review and editing, F.H. and S.Y. All authors have read and agreed to the published version of the manuscript.

Funding: This research was funded by the National Key Research and Development Program of China, grant number 2018YFC1508903; and by the Scientific Research Start-up Funding of Ocean University of China, grant number 862201013145.

Institutional Review Board Statement: Not applicable.

Informed Consent Statement: Not applicable.

Data Availability Statement: Restrictions apply to the availability of these data. Data were obtained from the National Climate Center.

Acknowledgments: Many thanks to reviewers for their valuable suggestions.

Conflicts of Interest: The authors declare no conflict of interest.

References

1. Balaguru, K.; Foltz, G.R.; Leung, L.R.; Emanuel, K.A. Global Warming-Induced Upper-Ocean Freshening and the Intensification of Super Typhoons. *Nat. Commun.* **2016**, *7*, 13670. [CrossRef] [PubMed]
2. Sobel, A.H.; Camargo, S.J.; Hall, T.M.; Lee, C.; Tippett, M.K.; Wing, A.A. Human Influence on Tropical Cyclone Intensity. *Science* **2016**, *353*, 242–246. [CrossRef] [PubMed]
3. Ying, M.; Chen, B.; Wu, G. Climate Trends in Tropical Cyclone-Induced Wind and Precipitation over Mainland China. *Geophys. Res. Lett.* **2011**, *38*, L01702. [CrossRef]
4. Zhang, L.; Karnauskas, K.B.; Donnelly, J.P.; Emanuel, K. Response of the North Pacific Tropical Cyclone Climatology to Global Warming: Application of Dynamical Downscaling to CMIP5 Models. *J. Clim.* **2017**, *30*, 1233–1243. [CrossRef]

5. Chavas, D.; Chen, J. Tropical Cyclones Could Last Longer After Landfall in a Warming World. *Nature* **2020**, *587*, 200–201. [CrossRef]
6. Ye, Y.; Fang, W. Estimation of the Compound Hazard Severity of Tropical Cyclones over Coastal China During 1949–2011 with Copula Function. *Nat. Hazards* **2018**, *93*, 887–903. [CrossRef]
7. Kumar, A.; Nanda, K.R.B.; Krishna, K.O.; Dev, N. On the Relationship between Intensity Changes and Rainfall Distribution in Tropical Cyclones over the North Indian Ocean. *Int. J. Clim.* **2020**, *40*, 2015–2025.
8. Yu, Z.; Wang, Y.; Xu, H. Observed Rainfall Asymmetry in Tropical Cyclones Making Landfall over China. *J. Appl. Meteorol. Clim.* **2015**, *54*, 117–136. [CrossRef]
9. Il, C.; Lm, L. Cluster Analysis of Philippine Tropical Cyclone Climatology: Applications to Forecasting. *J. Climatol. Weather. Forecast.* **2016**, *4*, 1–17.
10. Fang, W.; Zhang, H. Zonation and Scaling of Tropical Cyclone Hazards based on Spatial Clustering for Coastal China. *Nat. Hazards* **2021**, *109*, 1271–1295. [CrossRef]
11. Samuel, S.B.; Savin, S.C.; Suzana, J.C.; Kevin, J.T.; Chris, T.; Harvey, Y. Western North Pacific Tropical Cyclone Tracks in CMIP5 Models: Statistical Assessment Using a Model-Independent Detection and Tracking Scheme. *J. Clim.* **2019**, *32*, 7191–7208.
12. Hu, F.; Yang, S.; Russell, G.T. Resilience-Driven Road Network Retrofit Optimization Subject to Tropical Cyclones Induced Roadside Tree Blowdown. *Int. J. Disast. Risk Sci.* **2021**, *12*, 72–89. [CrossRef]
13. Tian, Y.; Zhou, W.; Wong, W.K. Detecting Interdecadal Change in Western North Pacific Tropical Cyclone Genesis Based on Cluster Analysis Using pHash + Kmeans. *Front. Earth Sci.* **2022**, *9*, 825835. [CrossRef]
14. Chand, S.S.; Walsh, K.J.E. The Influence of the Madden–Julian Oscillation on Tropical Cyclone Activity in the Fiji Region. *J. Clim.* **2010**, *23*, 868–886. [CrossRef]
15. Samuel, S.B.; Savin, S.C.; Kevin, J.T.; Andrew, J.D.; Chris, T.; Harvey, Y. Projections of Southern Hemisphere Tropical Cyclone Track Density Using CMIP5 Models. *Clim. Dynam.* **2019**, *52*, 6065–6079.
16. Camargo, S.J.; Robertson, A.W.; Gaffney, S.J.; Smyth, P.; Ghil, M. Cluster Analysis of Typhoon Tracks. Part I: General Properties. *J. Clim.* **2007**, *20*, 3635–3653. [CrossRef]
17. Camargo, S.J.; Robertson, A.W.; Gaffney, S.J.; Smyth, P.; Ghil, M. Cluster Analysis of Typhoon Tracks. Part II: Large-Scale Circulation and ENSO. *J. Clim.* **2007**, *20*, 3654–3676. [CrossRef]
18. Marosevic, T. The Hausdorff distance between some sets of points. *Math. Commun.* **2018**, *23*, 247–257.
19. Sung, S.; Lee, E.; Shin, B. Prevention of mountain disasters and maintenance of residential area through real-time terrain rendering. *Sustainability* **2021**, *13*, 2950. [CrossRef]
20. Kakareko, G.; Jung, S.; Vanli, O.A.; Tecle, A.; Khemici, O.; Khater, M. Hurricane Loss Analysis Based on the Population-Weighted Index. *Front. Built Environ.* **2017**, *3*, 46. [CrossRef]
21. Chen, W.; Lu, Y.; Sun, S.; Duan, Y.; Leckebusch, G.C. Hazard Footprint-Based Normalization of Economic Losses from Tropical Cyclones in China During 1983–2015. *Int. J. Disast. Risk Sci.* **2018**, *9*, 195–206. [CrossRef]
22. Somnath, B.; Balamurugan, G.; Ranit, C.; Rajib, S. Geographic Variation of Resilience to Landslide Hazard: A Household-based Comparative Studies in Kalimpong Hilly Region, India. *Int. J. Disast. Risk Reduct.* **2020**, *46*, 101456.
23. Roca-Flores, E.; Naumis, G.G. Assessing Statistical Hurricane Risks: Nonlinear Regression and Time-Window Analysis of North Atlantic Annual Accumulated Cyclonic Energy Rank Profile. *Nat. Hazards* **2021**, *108*, 2455–2465. [CrossRef]
24. Bass, B.; Irza, J.N.; Proft, J.; Bedient, P.; Dawson, C. Fidelity of the Integrated Kinetic Energy Factor as an Indicator of Storm Surge Impacts. *Nat. Hazards* **2017**, *85*, 575–595. [CrossRef]
25. Giovanni, M. Hurricane Lifespan Modeling through a Semi-Markov Parametric Approach. *J. Forecast.* **2013**, *32*, 369–384.
26. Jan, B. On the Effect of Long-Range Dependence on Extreme Value Copula Estimation with Fixed Marginals. *Commun. Stat.-Theory Methods* **2016**, *45*, 5590–5618.
27. Wang, H.; Yuan, Y.; Li, Y.; Wang, X. Financial Contagion and Contagion Channels in the Forex Market: A New Approach via the Dynamic Mixture Copula-Extreme Value Theory. *Econ. Model.* **2021**, *94*, 401–414. [CrossRef]
28. Farshad, R.G.; Ghosheh, A.H. Copula Function-based Analysis of Outage Probability and Coverage Region for Wireless Multiple Access Communications with Correlated Fading Channels. *IET Commun.* **2020**, *14*, 1804–1810.
29. Yuan, Y.; Bao, A.; Jiang, P.; Hamdi, R.; Termonia, P.; De Maeyer, P.; Guo, H.; Zheng, G.; Yu, T.; Prishchepov, A.V. Probabilistic Assessment of Vegetation Vulnerability to Drought Stress in Central Asia. *J. Environ. Manag.* **2022**, *310*, 114504. [CrossRef]
30. Seo, J.; Won, J.; Choi, J.; Lee, J.; Kim, S. A Copula Model to Identify the Risk of River Water Temperature Stress for Meteorological Drought. *J. Environ. Manag.* **2022**, *311*, 114861. [CrossRef]
31. Jang, J.; Chang, T. Flood Risk Estimation under the Compound Influence of Rainfall and Tide. *J. Hydrol.* **2022**, *606*, 127446. [CrossRef]
32. Klaho, M.H.; Safavi, H.R.; Golmohammadi, M.H.; Alkntar, M. Comparison between Bivariate and Trivariate Flood Frequency Analysis Using the Archimedean Copula Functions, A Case Study of the Karun River in Iran. *Nat. Hazards* **2022**, *112*, 1589–1610. [CrossRef]
33. Dong, S.; Jiao, C.; Tao, S. Joint Return Probability Analysis of Wind Speed and Rainfall Intensity in Typhoon-Affected Sea Area. *Nat. Hazards* **2017**, *86*, 1193–1205. [CrossRef]
34. Um, M.; Joo, K.; Nam, W.; Heo, J. A Comparative Study to Determine the Optimal Copula Model for the Wind Speed and Precipitation of Typhoons. *Int. J. Clim.* **2017**, *37*, 2051–2062. [CrossRef]

35. Ming, X.; Xu, W.; Li, Y.; Du, J.; Liu, B.; Shi, P. Quantitative Multi-Hazard Risk Assessment with Vulnerability Surface and Hazard Joint Return Period. *Stoch. Environ. Res. Risk A* **2015**, *29*, 35–44. [CrossRef]
36. Meng, C.; Xu, W.; Qiao, Y.; Liao, X.; Qin, L. Quantitative Risk Assessment of Population Affected by Tropical Cyclones Through Joint Consideration of Extreme Precipitation and Strong Wind—A Case Study of Hainan Province. *Earth's Future* **2021**, *9*, e2021EF002365. [CrossRef]
37. Jiang, H.; Zipser, E.J. Contribution of Tropical Cyclones to the Global Precipitation from Eight Seasons of TRMM Data: Regional, Seasonal, and Interannual Variations. *J. Clim.* **2010**, *23*, 1526–1543. [CrossRef]
38. Maiseli, B.J. Hausdorff Distance with Outliers and Noise Resilience Capabilities. *SN Comput. Sci.* **2021**, *2*, 358. [CrossRef]
39. Fernández-Sánchez, J.; Úbeda-Flores, M. Proving Sklar's Theorem Via Zorn's Lemma. *Int. J. Uncertain. Fuzziness Knowl.-Based Syst.* **2018**, *26*, 81–85. [CrossRef]
40. Nadaf, T.; Lotfi, T.; Shateyi, S. Revisiting the Copula-Based Trading Method Using the Laplace Marginal Distribution Function. *Mathematics* **2022**, *10*, 783. [CrossRef]
41. Chen, L.; Singh, V.P.; Guo, S.; Zhou, J.; Zhang, J. Copula-based Method for Multisite Monthly and Daily Streamflow Simulation. *J. Hydrol.* **2015**, *528*, 369–384. [CrossRef]

water

MDPI

Article

The 100-Year Series of Weather-Related Fatalities in the Czech Republic: Interactions of Climate, Environment, and Society

Rudolf Brázdil [1,2,*], Kateřina Chromá [2], Lukáš Dolák [1,2], Pavel Zahradníček [2,3], Jan Řehoř [1,2], Petr Dobrovolný [1,2] and Ladislava Řezníčková [1]

[1] Institute of Geography, Masaryk University, 611 37 Brno, Czech Republic; dolak@sci.muni.cz (L.D.); 433735@mail.muni.cz (J.Ř.); dobro@sci.muni.cz (P.D.); ladkar@sci.muni.cz (L.Ř.)
[2] Global Change Research Institute, Czech Academy of Sciences, 603 00 Brno, Czech Republic; chroma.k@czechglobe.cz (K.C.); zahradnicek.p@czechglobe.cz (P.Z.)
[3] Czech Hydrometeorological Institute, 616 67 Brno, Czech Republic
* Correspondence: brazdil@sci.muni.cz

Abstract: The paper investigates weather-related fatalities over the territory of the Czech Republic in the 100-year period from 1921 to 2020. The unique database, created from documentary evidence (particularly newspapers), includes, for each deadly event, information about the weather event, the fatality itself, and related circumstances. A total of 2729 fatalities were detected during the 100-year period and were associated with various weather categories including frost (38%), convective storms (19%), floods (17%), fog (11%), snow and glaze ice (8%), windstorms (5%), and other inclement weather (2%). A detailed analysis was performed for each individual category. Fatalities occurred throughout the country, with a main maximum in winter (January) and a secondary maximum in summer (July), corresponding to the occurrence of extreme weather. Deaths were mainly interpreted as direct, caused by freezing to death/hypothermia or drowning, and occurred in the afternoon and at night in open countryside or on rivers and water bodies. Males outnumbered females, and adults outnumbered children and the elderly. Hazardous behavior was more frequent than non-hazardous behavior among victims. The information on fatalities and the structure of their characteristics strongly reflects historical milestones of the country, political and socioeconomic changes, as well as changes in lifestyle. Although important weather effects were observed on the deadliest events, the character of the data did not allow for clear evidence of the effects of long-term climate variability.

Keywords: weather-related fatality; fatality characteristics; documentary data; flood; windstorm; convective storm; snow; glaze ice; frost; fog; inclement weather; Czech Republic

Citation: Brázdil, R.; Chromá, K.; Dolák, L.; Zahradníček, P.; Řehoř, J.; Dobrovolný, P.; Řezníčková, L. The 100-Year Series of Weather-Related Fatalities in the Czech Republic: Interactions of Climate, Environment, and Society. *Water* **2023**, *15*, 1965. https://doi.org/10.3390/w15101965

Academic Editors: Stefano Morelli, Veronica Pazzi and Mirko Francioni

Received: 4 May 2023
Revised: 15 May 2023
Accepted: 17 May 2023
Published: 22 May 2023

1. Introduction

Meteorological and hydrological extremes cause great material damage and high numbers of associated injuries and fatalities worldwide every year. In Europe, the period from 1970 to 2019 experienced 1672 disastrous events, with economic damage calculated at US$476.5 billion, attributed particularly to floods (38% and 36%, respectively) and storms (32% and 44%, respectively). Whereas the number of related fatalities achieved 9953 in the three decades between 1970 and 1999, in the two following decades, it rose to 82,919 and 66,566 fatalities, respectively, with an absolutely dominant role of heat waves [1]. For the Czech Republic, the recorded 1619 weather-related fatalities in 1961–2020 represent a lower estimate [2]. According to the European Severe Weather Database (ESWD), selected weather extremes in Central Europe (avalanche, severe wind, tornado, lightning, heavy rain) have been responsible for 799 fatalities in 2010–2020 [3].

Fatalities related to extreme weather are a frequent topic of research, covering different time periods (usually a few decades) and scales (from local over regional to global). Particularly high attention has been devoted to flood fatalities (e.g., [4–8]), sometimes together with landslides (e.g., [9–11]), based on different databases, such as the Euro-Mediterranean

database—FFEM-DB [12,13] or the pan-European database—HANZE [14]. Many papers have also dealt with fatalities related to heat waves (e.g., [15–18]), cold waves (e.g., [19]) or both (e.g., [20,21]). Fatalities during convective storms were analyzed with respect to lightning strikes (e.g., [22–25]) or tornadoes (e.g., [26]). Even daily mortality in connection with drought has also been analyzed [27].

Regarding the Czech Republic, the highest attention has been given not only to heat-wave fatalities (e.g., [28–31]), but also to cold-wave fatalities (e.g., [32,33]). Brázdil et al. [34] evaluated the potential of documentary evidence for studying fatalities of hydrological and meteorological events. The systematic collection of weather-related fatalities was reflected in their analysis for the periods of 2000–2019 [35] and 1961–2020 [2]. Vehicle accidents accompanied by severe weather for the period of 1979–2020 were also investigated separately [36]. Czech flood-related fatalities from 1980 became part of the FFEM-DB [5,13].

The aim of the recent paper is to present a unique 100-year chronology (1921–2020 CE) of weather-related fatalities in the Czech Republic, explaining their spatiotemporal variability and the features/circumstances of related deadly events, taking into account weather/climatic, environmental, and socio-political situations that strongly influence not only the occurrence of these deadly events but also the communication of information about them.

2. Materials and Methods

2.1. Data

2.1.1. The Czech Republic

The Czech Republic (further as CR) was formed on 1 January 1993 following the split of Czechoslovakia into the Czech and Slovak republics. It is located in Central Europe, covering an area of 78,866 km^2. Historically, its territory consisted of Bohemia in the western part and Moravia and southern Silesia in the eastern part (Figure 1a). The territory comprises various geographic units, from lowlands to mountains (Figure 1b), with an average altitude of 390 m a.s.l. (with an altitudinal range from 115 to 1603 m). The mean areal air temperature is 7.6 °C, and the total precipitation is 677 mm (for the period 1921–2020). In the long-term context, in addition to large interannual and interdecadal variability, temperatures have experienced a statistically significant increasing (warming) linear trend (0.21 °C/10 years, $p < 0.01$), whereas precipitation totals have shown a non-significant decreasing trend (−2.2 mm/10 years) (Figure 1c). Based on the Köppen climatic classification, most of the CR belongs to the category of temperate broadleaf deciduous forest (Cfb), whereas the remaining parts are attributed to a boreal climate, particularly Dfb and less Dfc [37].

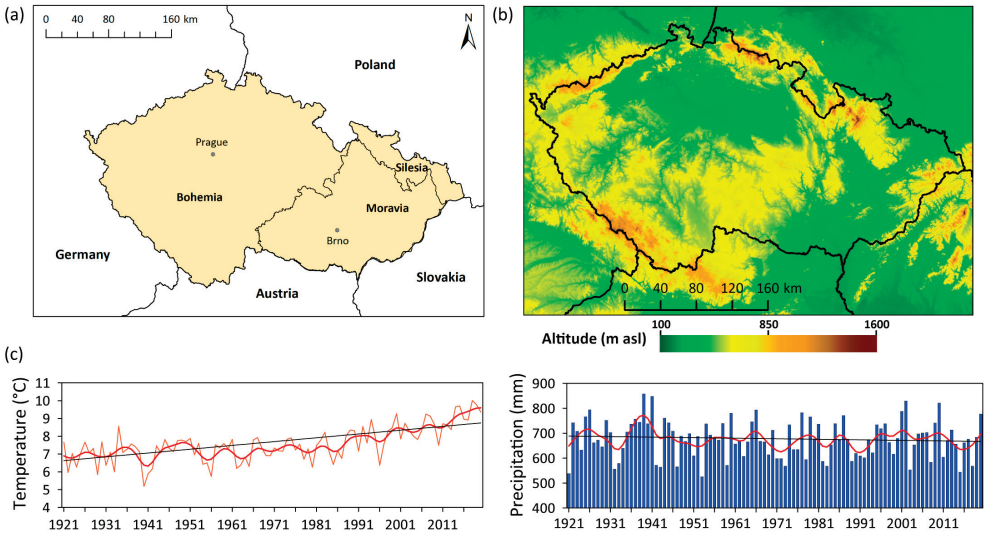

Figure 1. *Cont.*

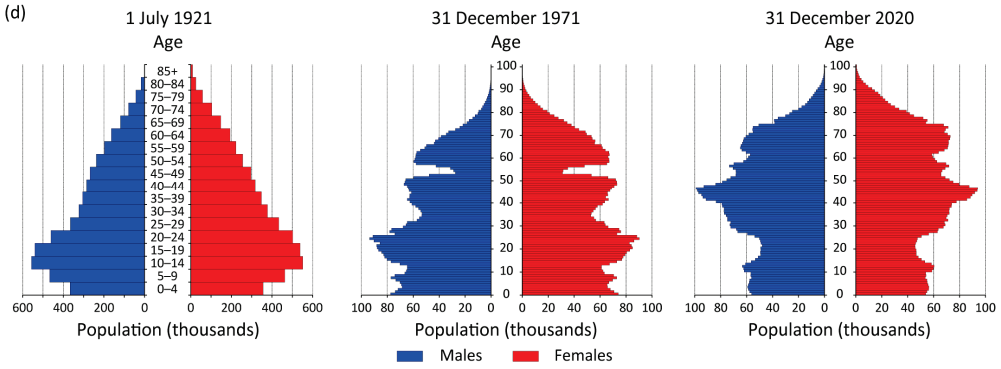

Figure 1. Basic information about the Czech Republic: (**a**) location in Central Europe and historical parts; (**b**) physical-geographic map; (**c**) fluctuations and linear trends in mean areal annual temperatures and precipitation totals in 1921–2020 smoothed by 10-year Gaussian filter (data in [38], extended); (**d**) age pyramids for 1 July 1921, 31 December 1971, and 31 December 2020 (data from [39]).

The number of inhabitants in the CR slightly decreased between 1921 and 1971 (from 9,966,856 to 9,830,602), and then grew until 2020 (10,701,777). The proportion of females decreased from 52.1% to 50.7%. The age proportion was characterized by an aging population (Figure 1d), with the proportion in the 65 years and older category growing from 6.2% in 1921 to 20.2% in 2020, whereas the proportion in the child category (0–14 years) decreased from 27.8% in 1921 to 16.0% in 2020. The proportion of adults (15–64 years) remained relatively stable (66.0%, 66.6%, and 63.8%, respectively). There was also a growing proportion of city dwellers, who comprised 73.1% of the population in 2020 [39].

2.1.2. Fatality Data

Different types of documentary evidence can be used to extract data on fatalities attributed to severe weather, represented particularly by:

(i) Newspapers and magazines

Weather-related fatality reports for the 1921–2020 period were systematically collected from three long-term printed newspapers: *Lidové noviny* 1921–1950, *Rudé právo (Právo)* 1945–2020, and *Svobodné slovo* 1954–1997 (Figure 2). Based on digitized versions of other newspapers, they were non-systematically complemented by reports from *Venkov* and *Národní listy* before 1945 and by *Lidová demokracie*, *Rovnost*, and other local newspapers after 1946. The printed version of *Právo* and its internet archives Novinky.cz were systematically excerpted based on the online monitoring method according to selected keywords for 1991–2020. Since 1998, the additional newspaper internet archive iDNES.cz was also systematically investigated. For example, *Rudé právo* [40] reported a fatal event from 12 February 1975: "*Two boys drowned in the water reservoir at Větřní, the Český Krumlov district* [for the location of places see Figure A1 in Appendix A]. *Nine-year-old Ludvík and his brother, two years younger, rode a bicycle on the ice, which collapsed under them*". During the continuing frosty weather from the beginning of 2010, the newspaper *Právo* [41] reported two fatalities in Prague: "*Police drove out yesterday* [24 January] *at around noon to Makovská street in Prague 6-Řepy, where there was a dead man. "Around one hour later we went to the other* [man], *who was found also dead in the area of a former kindergarten in Radlická street at* [Prague-] *Jinonice", said the police spokesperson Eva Miklíková. From investigations so far it is most probable that they were homeless, and according to the preliminary doctor's report, they died of hypothermia*".

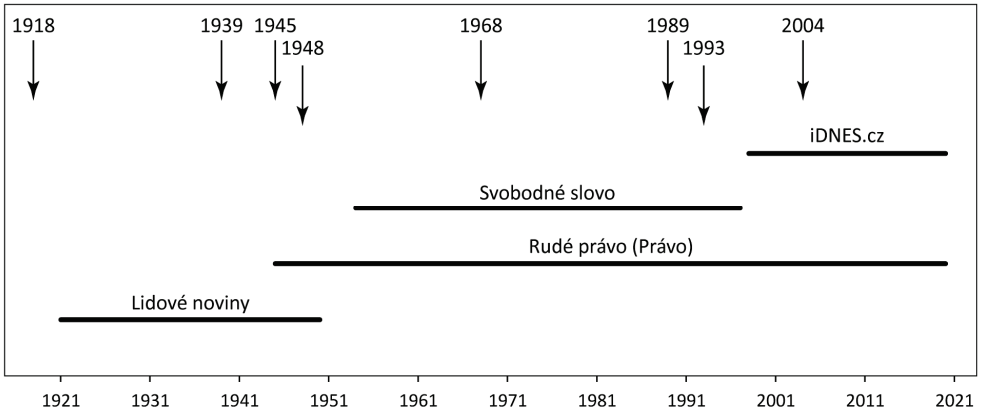

Figure 2. Temporal coverage of basic newspapers used and major historical and socio-political events in the Czech Republic: 1918—establishment of Czechoslovakia, 1939–1945—the Second World War, 1948—communist coup, 1968—"Prague spring", 1989—"velvet revolution", 1993—the Czech Republic establishment, 2004—EU membership.

(ii) Narrative sources

After 1918, keeping chronicles of villages and towns became a broad praxis in Czechoslovakia. In the annual description of the life in a particular settlement, notes about the loss of lives related to severe weather appeared. For example, the memorial book of Karlovice (north Bohemia) reported torrential rain on the night of 29 May 1941 and subsequent flash floods in the broader surroundings that a woman at Loučky and a lieutenant of the governmental army at Turnov drowned during the rescuing work [42]. The chronicle of Radotín (central Moravia) described a tragic event from 15 August 1962 [43]: "*On 15th August in the late afternoon, seven children were bathing in a small pond at Radvanice not far from Přerov. After the sudden onset of a thunderstorm, they looked for shelter and found it in a nearby unfinished waterwork object of the local cooperative farm. Around 1900* [CET—Central European Time], *a lightning strike hit this object, and six children, four boys, and two girls were killed. Only one boy with severe burns survived*".

(iii) Climatological records

In some cases, sheets of climatological observations at the standard meteorological stations of the Czech Hydrometeorological Institute may contain short notes of observers or clippings from newspapers concerning fatalities during observed weather events. For example, the observer at the Polička station (east Bohemia) added on 6 September 1934 that a lightning strike killed the farmer Andrlík at Nedvězí during the raking of hay [44]. The climatological sheet of the Nový Jičín station (the northeast of the CR) reported a thunderstorm with 60.4 mm of precipitation, flash floods in the region, great damage, and two drowning people on 18 August 1958 [45].

(iv) Parliamentary proposals

The Czechoslovak digital parliament library [46] contains proposals from some deputies of the parliament on sets of measures to help people who have been affected by natural disasters (e.g., flash floods). However, fatalities reported there were expressed rather generally, and more detailed information has to be searched elsewhere (e.g., in newspapers). As an example of detailed information, a proposal connected with damaging cloudburst and flash flood on 9 May 1927 in the Třebíč region (southwest Moravia) reported three casualties [47]: " . . . *A torrent of water a meter deep swept away the family of the cooper Štancl when they were returning from the fields; Štancl's wife Antonie and their two small children, aged three and a half and five and a half, were drowned. Their corpses were washed away by the rapid torrent and found only on the morning of the subsequent day* [10 May]".

(v) Professional papers and reports

Information about weather-related fatalities may occur in special reports devoted to extreme events or in professional papers investigating some particular problems. To such papers can be attributed, for example, the study by Polách and Gába [48], who described in detail the history of (flash) floods in the regions of Šumperk and Jeseník in north Moravia, giving also particular attention to their damaging consequences, including fatalities. For example, they mentioned the death of a father and his son in Šumperk-Temenice (north Moravia) on 13 July 1984: they tried to take out a car from a flooded garage after a torrential rain but were killed in the water by electric current from a damaged cable.

(vi) Memorials

Memorials were created to remember particular events and their victims. They usually contain basic information about the event and its date, names of affected people, and also the year of their birth. Frequent are, for example, "memorials of mountain victims" with the list of related fatalities with brief information on how they died (e.g., for the Krkonoše Mts. [49] or for the Jeseníky Mts. [50]) or memorials devoted to the deaths of individual people by lightning strike, flood, freezing to death, aircraft crashes, and other causes. For example, an inscription on the memorial at Třemošná-Záluží (west Bohemia) explains death during a thunderstorm [51]: "*Let this stone remember them who will come after us that on 22 June 1959, between 1500 and 1600* [CET] *in the afternoon, Šustrová Emilie, Marková Anežka, Čechurová Růžena,* [and] *Pešková Jarmila were tragically killed by lightning during a sudden and sharp* [thunder]*storm at this place. Honor to their memory!*" A short description of a particular memorial can be expanded by more detailed chronicles or newspaper reports, as is the case for many such memorials in the region of the Jizerské hory Mts. in North Bohemia [52].

(vii) Internet sources

Great attention on the internet has been devoted to aircraft crashes. In very detailed records of such events involving military or civilian airplanes, based on the results of investigation commission reports, it is possible to distinguish the role of inclement weather patterns in these accidents. This type of information in the CR has been systematically documented since 1918 [53,54]. A similar type of information is available for train accidents [55].

2.2. Methods

2.2.1. Types of Severe Weather

Each deadly event is the result of a combination of different effects and circumstances that ultimately lead to the loss of human life. The course of the weather or the occurrence of some severe weather phenomena, which do not necessarily have characteristics of extremes in the statistical sense, may be one of the driving or contributing factors resulting in deaths. Since we are dealing with fatalities that can be attributed in some way to (severe) weather, the variety of weather circumstances of such fatalities is divided into the following weather categories:

(i) Flood

Fatalities attributed to floods usually occur when people are drowned and swept away by strong water torrents or killed in collapsed buildings or objects. Two types of floods are taken into account. The first type includes floods arising from single-day or multi-day rainfall (rainy floods), sudden melts of deep snow cover (snow floods), and a combination of snow-melt and rainfall, sometimes even accompanied by ice jams on rivers (mixed floods) on larger rivers. The onset of flood-waves in these cases can start relatively slowly, and high-water levels have a longer duration. The second type are flash floods, which have a sudden onset and shorter duration and follow cloudbursts or torrential rain in any area, usually occurring on smaller water streams but not necessarily joining with them.

(ii) Windstorm

Fatalities in this category are associated with strong winds or wind gusts that cause trees or branches to fall, walls to collapse, or buildings or other objects to collapse. Meteorologically, they are associated with windstorms that originate as a result of existing large horizontal pressure gradients. Their duration ranges from a few hours to several days.

(iii) Convective storm

The development of cumulonimbus clouds is associated with several severe phenomena, particularly lightning, strong winds (such as squalls, tornadoes, or downbursts), hailstorms, or downpours. Fatalities attributed to this category are divided into those caused by lightning strikes, strong winds (same deadly reasons as mentioned in point (ii)), and thunderstorms in general (if corresponding effects were not specified in sufficient detail).

(iv) Snow and glaze ice

This category includes fatalities associated with a large amount of snow or the occurrence of glaze ice. Related fatalities in this category are divided into snow-related deaths (e.g., death during the cleaning of streets and roads, removing snow from roofs, accidents while sledding), avalanche-related deaths in mountain regions, and deaths caused by falls on slippery ground due to glaze ice.

(v) Frost

Fatalities in this category are related either to cold spells with severe frosts, when people are freezing to death or dying of hypothermia during the night spent outside buildings or resulting from activities undertaken on insufficiently frozen water bodies (such as ice skating, sliding on ice, or walking across it), with victims subsequently drowning after breaking through the ice.

(vi) Fog

Fatalities in this category are related to situations with significantly decreased visibility caused by water droplets or snow particles in the air. This concerns airplane crashes, particularly during landing in fog or flight in low clouds when pilots lose spatial orientation. Deadly train accidents in dense fog also fall into this category.

(vii) Other inclement weather

This category includes less frequently occurring fatalities that occurred in situations not attributable to any of the preceding six categories, where the reason for deaths related to hot weather (heatwaves), landslides, rime, rain events, or during inclement weather without closer specification.

2.2.2. Database of Fatalities

The Czech database of weather-related fatalities follows the concept presented by Petrucci et al. [5,12] and maintains the same structure with slight changes. This database has been used in two previous papers [2,34] and includes the following information:

(i) date of the fatal accident or event;
(ii) locality (i.e., the place of the fatal accident or event);
(iii) type of weather category (see Section 2.2.1);
(iv) time (hour) of the day when the fatal accident or event occurred (morning 0400–0800 CET, forenoon 0800–1200 CET, afternoon 1200–1800 CET, evening 1800–2200 CET, night 2200–0400 CET);
(v) name of the casualty;
(vi) gender of the casualty (male, female);
(vii) age of the casualty (exact age in years or estimated age: child 0–15 years, adult 16–65 years, elderly 66 years and older);
(viii) cause of death (drowning, falling tree/branch, traffic (vehicle/plane/train) accident, underlying health reason, freezing to death/hypothermia, lightning strike, other reason);

(ix) place of death (river/lake/reservoir/bank, within a building, road, open space in a built-up area, countryside, other places);
(x) type of death (direct—deaths caused by weather phenomena, e.g., drowning due to water torrent or collapse of a building; indirect—deaths during activity related to weather phenomena, e.g., health collapse during saving activities);
(xi) behavior of the casualty or culprit of a deadly event (non-hazardous, hazardous);
(xii) source of information.

Not all data in the above points (i)–(xi) were available or clearly interpretable for each fatality. In such cases, the related information was taken as "unknown".

2.2.3. Statistical Analysis

The database of weather-related fatalities in the CR for the 1921–2020 period was used for all analyses done in this paper. Figures presenting long-term fluctuations in annual frequencies of fatalities, their annual variations, spatial distribution, and selected characteristics that explain basic circumstances joined with fatality events according to Section 2.2.2 were prepared for every particular weather category and all weather categories together. Long-term fluctuations in annual frequencies of fatalities were not complemented by calculations of linear trends, which would be misleading with respect to the temporal distribution of data (see Section 4.1 for more details).

For the 100-year series of temperature and precipitation in Figure 1c, their fluctuations were smoothed by a 10-year Gaussian filter and complemented by linear trends. The non-parametric Theil–Sen method, which is more robust to outliers in time series, was used to estimate parameters of linear trends [56,57]. The significance of linear trends was evaluated by applying the non-parametric Mann–Kendall test [58,59].

3. Results

3.1. Fatalities in Individual Weather Categories

3.1.1. Floods

A total of 471 people died during floods in the CR between 1921 and 2020, of which 194 fatalities (41.2%) were attributed to flash floods. The deadliest event was a rainy flood in early July 1997 in Moravia and Silesia [60], which claimed 61 direct and indirect fatalities (63 fatalities for the entire year of 1997) (Figure 3a). The most tragic flash flood was on 9 June 1970 at Šardice in southern Moravia, where a lignite mine collapsed due to a water torrent, resulting in 34 fatalities ([34]; 52 fatalities for the entire year of 1970). Of several important floods that occurred after 2000, the August 2002 flood in Bohemia [61] claimed 17 fatalities (a total of 22 fatalities in 2002), whereas in other flood years of 2009, 2010, and 2013 [62–64], the number of deaths gradually achieved 16, 19, and 18 fatalities, respectively. In ten other years of the 100-year series, the annual death toll was $\geq$10 fatalities, but in 32 years, no fatalities were recorded. In terms of annual variations, the highest numbers of fatalities occurred in July (28.0% with dominance of floods) and in June (27.6% with dominance of flash floods) (Figure 3b). The spatial distribution of flood fatalities shows, as expected, their concentration around larger rivers, as well as around small water streams (Figure 3c). In the context of the entire country, the fatality region in the northeastern part of the CR is particularly well expressed, as well as other similar regions in South Moravia. Drowning (80.3%), as expected, was identified as the most frequent reason for death, but only 62.0% of fatalities were attributed to the place category "river/lake/reservoir/bank" (14.6% died within collapsing buildings) (Figure 3d,f). Fatalities from floods were mainly direct victims (89.0%) (Figure 3e). Whereas for nearly half of the fatalities the part of the day was not specified, for 22.3% of them, it was in the afternoon (Figure 3g). In other fatality categories, distributions were males 68.2% to females 24.6%, adults 47.8% to children 18.7% and elderly 11.0%, and non-hazardous behavior of victims 49.5% to hazardous 36.1% (Figure 3h–j).

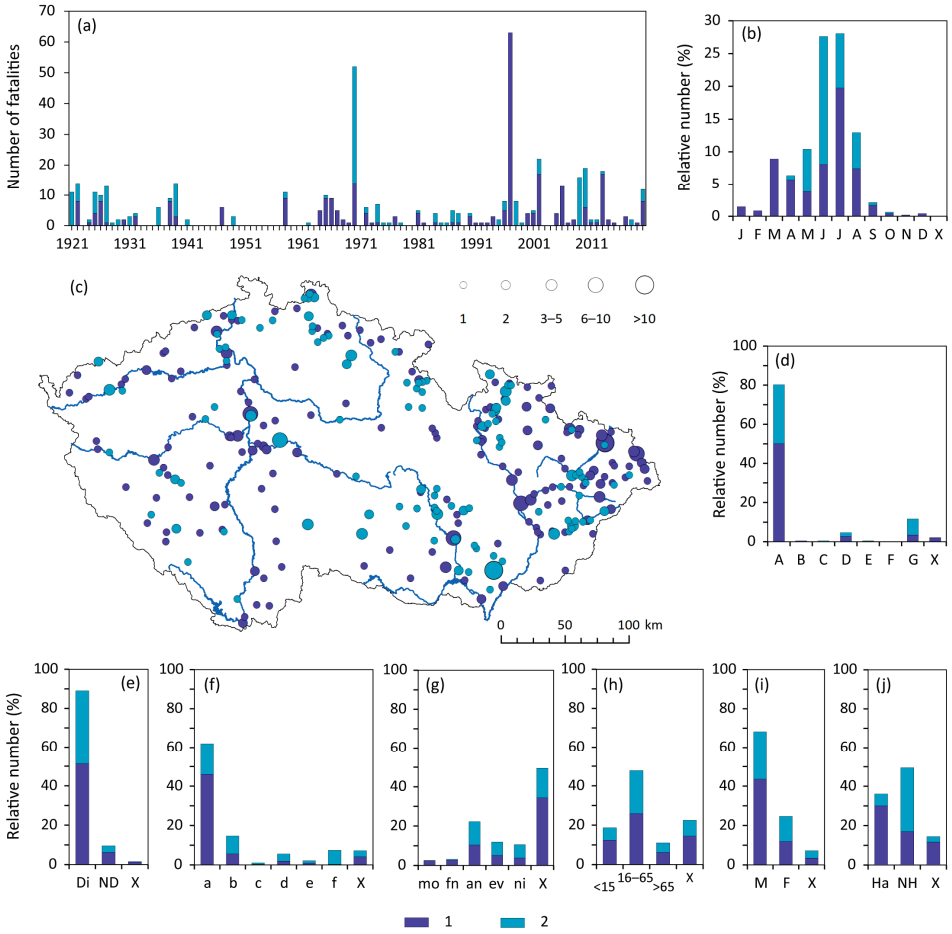

Figure 3. Characteristics of flood-related fatalities in the Czech Republic during the 1921–2020 period (1—flood, 2—flash flood): (**a**) long-term fluctuation; (**b**) annual variation (J—January, F—February, . . . , D—December); (**c**) spatial distribution (15 fatalities lack exact locations); (**d**) cause of death; (**e**) type of fatality; (**f**) place of death; (**g**) part of the day; (**h**) age (years); (**i**) gender; (**j**) behavior. Symbols and abbreviations: A—drowning, B—tree/branch fall, C—traffic (vehicle/plane/train) accident, D—underlying health reason, E—freezing to death/hypothermia, F—lightning strike, G—other reason; Di—direct death, ND—non-direct death; a—river/lake/reservoir/bank, b—within a building, c—road, d—open space in built-up area, e—open countryside, f—other place; mo—morning, fn—forenoon, an—afternoon, ev—evening, ni—night; M—males, F—females; Ha—hazardous behavior, NH—non-hazardous behavior; X—unknown.

3.1.2. Windstorms

A 100-year chronology of deaths associated with windstorms includes 128 fatalities. Whereas one-third of all years had only one or two fatalities, five or more occurred in only eight years (Figure 4a). As for significantly damaging windstorms that affected Central Europe, six fatalities were attributed to the Kyrill storm on 18–19 January 2007 [65] and four to the Herwart storm on 29 October 2017 [66]. The annual variation shows two maxima of fatalities: the primary maximum in March (14.1%), slightly higher than in February (13.3%), and the secondary maximum in November (12.5%), slightly higher than in October (10.9%) (Figure 4b). As for the spatial distribution of windstorm-related fatalities, a rather random distribution of them across the country is characteristic, with some concentration of higher casualties in Prague and its surroundings and, to a lesser extent, also in Brno and its surroundings (Figure 4c). The majority of fatalities (82.0%) were classified as "direct" victims (Figure 4e). People died especially due to falling trees or branches (39.8%), but fatalities in traffic accidents or due to other reasons were also common (21.9% each) (Figure 4d). The place of deaths was mainly open spaces in built-up areas (28.9%) or in

open countryside (27.3%), followed by roads (18.8%) (Figure 4f). One-third of deadly events occurred in the afternoon (34.4%), but for a higher proportion of fatalities (44.5%), the part of the day was not specified (Figure 4g). In other categories of fatalities, males predominated (80.5%, females 17.2%), as did adults (61.7%, but 24.2% unknown), and their behavior was mostly non-hazardous (73.4%, hazardous 23.4%) (Figure 4h–j).

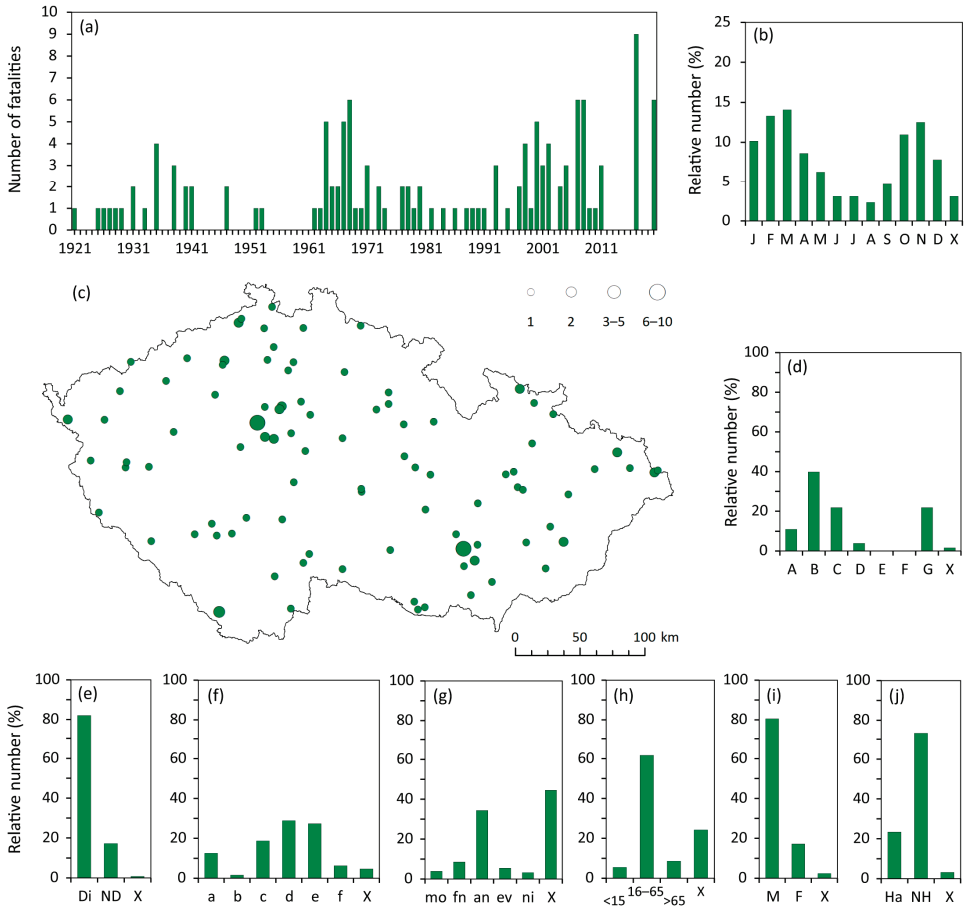

Figure 4. Characteristics of windstorm-related fatalities in the Czech Republic during the 1921–2020 period: (**a**) long-term fluctuation; (**b**) annual variation; (**c**) spatial distribution (four fatalities lack exact locations); (**d**) cause of death; (**e**) type of fatality; (**f**) place of death; (**g**) part of the day; (**h**) age; (**i**) gender; (**j**) behavior. For symbols and abbreviations see Figure 3.

3.1.3. Convective Storms

A total of 530 fatalities occurred during the 1921–2020 period, associated with convective storms. These fatalities were divided into 371 (70.0%) due to lightning, 108 (20.4%) due to strong winds, and the remaining 51 (9.6%) during thunderstorms without further specification. Most fatalities occurred between 1921–1939 (287 fatalities, i.e., 54.2%) and 1962–1972 (84 fatalities, i.e., 15.8%) (Figure 5a). The highest number of fatalities, 48, was recorded in 1929, primarily connected with an extremely damaging convective storm with extreme winds on 4 July [67]. There were 32 fatalities in 1925 and $\geq$20 fatalities in 1927, 1928, 1930, and 1937. A total of 31.1% of fatalities occurred in July, followed by June (24.3%), May (19.6%), and August (17.5%). In these four months combined, 92.5% of fatalities took place (Figure 5b). The spatial distribution of convective storm-related fatalities does not show any systematic features, and appears rather random, despite the existence of some small areas where no deaths were recorded (Figure 5c). "Direct" deaths comprised 84.3% of all fatalities (Figure 5e). The dominant proportion of lightning-related fatalities was reflected in 68.9% of fatalities due to lightning strikes, in open countryside (46.8%) or open spaces within built-up areas (17.9%), and occurring particularly in the afternoon (26.0%,

but for 51.9% of fatalities, the time was unknown) (Figure 5d,f,g). Male fatalities were more than double those of females (63.6% compared to 30.0%), and adults represented the most affected category (41.9%), despite a high proportion of unknown cases (46.0%) (Figure 5h,i). A total of 57.7% of fatalities were attributed to non-hazardous behavior (26.0% hazardous) (Figure 5j).

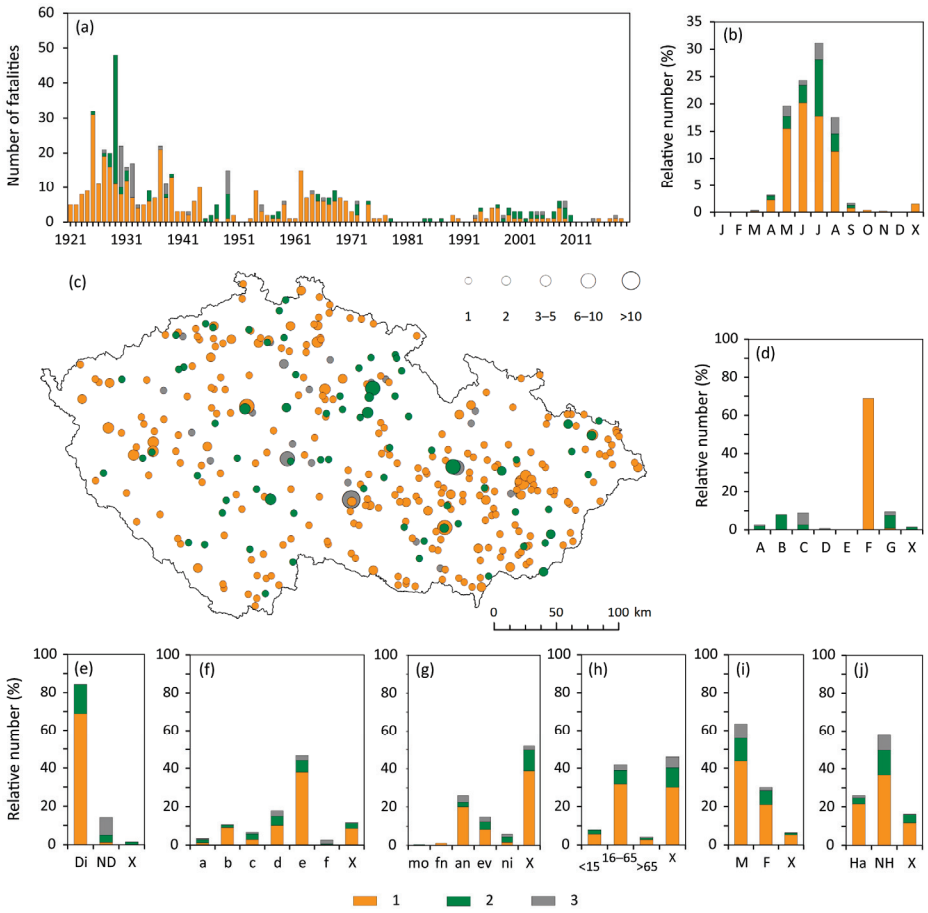

Figure 5. Characteristics of fatalities related to convective storms (1—lightning strike, 2—strong wind, 3—during a thunderstorm) in the Czech Republic during the 1921–2020 period: (**a**) long-term fluctuation; (**b**) annual variation; (**c**) spatial distribution (42 fatalities lack exact locations); (**d**) cause of death; (**e**) type of fatality; (**f**) place of death; (**g**) part of the day; (**h**) age; (**i**) gender; (**j**) behavior. For symbols and abbreviations see Figure 3.

3.1.4. Snow and Glaze Ice

In the period of 1921 to 2020, there were 213 fatalities associated with this category, with 140 fatalities due to snow (65.7%), 41 fatalities due to glaze ice (19.3%), and 32 fatalities due to avalanches (15.0%). A maximum of 31 fatalities was recorded in 1945 (two air crashes in snowstorms [53,54]), despite the end of the Second World War and a general drop in the number of reports in newspapers that year (Figure 6a). In the remaining years, 12 people died in 1929, 9 in 1962 and 2006, and only 1 or 2 fatalities were recorded in 46 years. The annual distribution shows a clear dominance of the months December through March (92.5% combined), with the maximum in January (32.9%), followed by February (31.9%) (Figure 6b). The spatial distribution of fatalities shows a rather irregular pattern, with increased numbers of casualties in the northwestern and northern Bohemia regions. Other clusters are apparent in eastern Bohemia and central Moravia (Figure 6c). As for avalanche-related fatalities, they were limited exclusively to the Krkonoše Mts. in northern Bohemia, the Jeseníky Mts. in the northern part, and the Moravskoslezské Beskydy Mts. in the northeastern part of Moravia and Silesia. Fatalities attributed to

snow and glaze ice were characterized by a higher proportion of indirect deaths (62.4% indirect to 37.6% direct) and comparable hazardous and non-hazardous behavior (50.2% hazardous to 48.4% non-hazardous) (Figure 6e,j). The cause of death was mainly due to other reasons (57.3%), followed by traffic accidents (29.6%) (Figure 6d). People died mainly in open countryside (52.1%), but also in open spaces in built-up areas (18.3%) (Figure 6f). Despite comparable proportions of fatalities in the afternoon and at night (16.0% and 17.4%, respectively), the time of day was not specified for 44.6% of fatalities (Figure 6g). A total of 77.0% of fatalities were male, whereas 18.8% were female (Figure 6h). The number of adult fatalities was comparable to unknown (39.4% to 38.0%), but a relatively high proportion of child deaths occurred (16.9%) (Figure 6i).

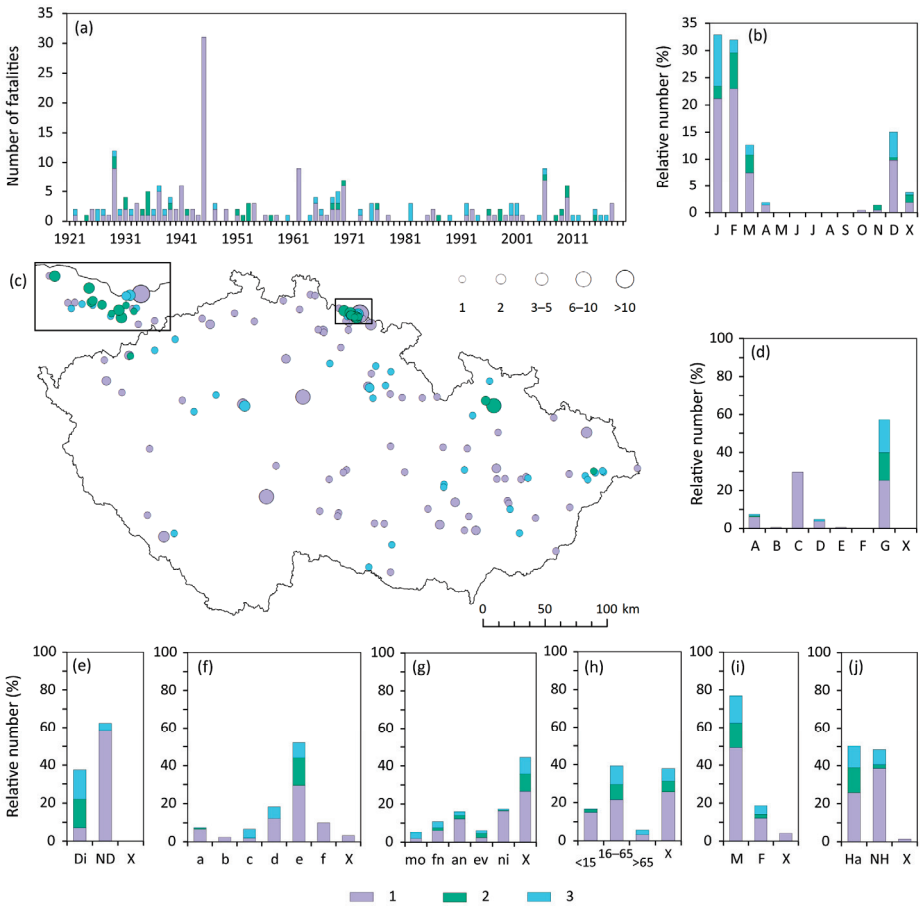

Figure 6. Characteristics of fatalities related to snow and glaze ice (1—snow, 2—avalanche, 3—glaze of ice) in the Czech Republic during the 1921–2020 period: (**a**) long-term fluctuation; (**b**) annual variation; (**c**) spatial distribution (four fatalities lack exact locations); (**d**) cause of death; (**e**) type of fatality; (**f**) place of death; (**g**) part of the day; (**h**) age; (**i**) gender; (**j**) behavior. For symbols and abbreviations see Figure 3.

3.1.5. Frosts

A total of 1031 fatalities in the 1921–2020 period were associated with the frost category, of which 758 fatalities (73.5%) were attributed to cold spells and 273 fatalities (26.5%) to accidents on ice. The maximum of 63 fatalities was recorded in 2010, followed by 44 in 2012 and 43 in 1929 (as a result of the coldest winter of 1928/29 in the past century—e.g., [34,68]) (Figure 7a). The annual distribution shows the highest proportion of fatalities in January (30.8%), followed by February (25.2%) and December (25.0%), i.e., 81.0% combined (Figure 7b). Frost-related fatalities densely cover the entire country with some spots in and around large towns and cities (e.g., Prague, Plzeň, Brno, Olomouc, or Ostrava) (Figure 7c). However, for some relatively larger areas in western and south-east central Bohemia, as

well as in a belt located easterly of the Jeseníky Mts., no such fatalities were found. Nearly all frost fatalities (99.1%) were interpreted as "direct" (Figure 7e). The cause of death in this category has been split between freezing to death/hypothermia (72.8%) and drowning (26.6%) during breaking of ice with people on water bodies (Figure 7d). Nearly equal proportions of fatalities were attributed to three places of death: open spaces in built-up areas (29.1%), open countryside (28.3%), and river/lake/reservoir/bank (28.1%) (Figure 7f). A quarter of frost fatalities occurred during the night (25.3%), but the majority of them were not attributed to any part of the day (60.1%) (Figure 7g). In other fatality characteristics, males prevailed compared to females (78.8% to 17.1%) as well as adults (46.3%, but 24.6% in the child category) (Figure 7h,i). Hazardous behavior of fatalities was dominant compared to non-hazardous fatalities (73.0% to 10.7%) (Figure 7j).

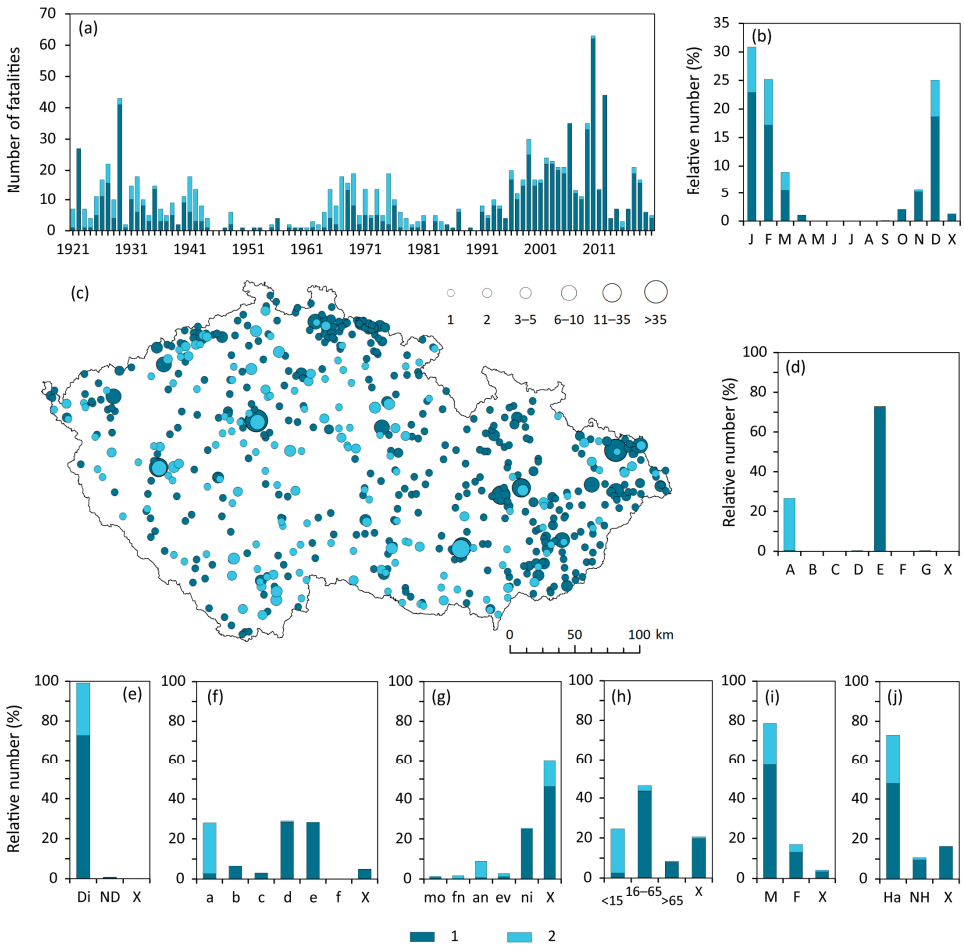

Figure 7. Characteristics of frost-related fatalities (1—cold spell, 2—ice) in the Czech Republic during the 1921–2020 period: (**a**) long-term fluctuation; (**b**) annual variation; (**c**) spatial distribution (19 fatalities lack exact locations); (**d**) cause of death; (**e**) type of fatality; (**f**) place of death; (**g**) part of the day; (**h**) age; (**i**) gender; (**j**) behavior. For symbols and abbreviations see Figure 3.

3.1.6. Fog

A total of 293 fatalities were associated with very poor visibility, i.e., included under fog. This category was represented particularly by deaths during air crashes, involving both military and civilian aircraft. This was connected with a loss of pilot orientation due to poor visibility in dense fog or low clouds, causing uncontrollable aircraft to crash into the ground. The deadliest crash happened on 30 October 1975, at 09:20 CET, when a Yugoslavian McDonnell Douglas DC-9 airplane, preparing to land during fog at the Prague-Ruzyně airport, crashed into the ground in a cottage colony above the River Vltava valley in Prague-Suchdol (Figure 8a). The crash claimed 79 lives and caused 41 injuries

among airplane passengers, mostly Czech tourists returning from holiday, and additionally, an older woman in the cottage colony [69]. Following the 1975 event, two other years, 1945 and 1962, each had 16 fatalities. In 1945, this included eight fatalities of two Soviet military planes, which crashed on 18 July in dense fog while flying to Moscow for a military parade [54]. Another Czech aircraft crashed on 14 December when eight men died (ibid.). In 1962, 13 people died and 29 were seriously injured when an Il-14M airplane, operated by Czechoslovak airlines and flying on 10 October from Košice (Slovakia) to Prague, crashed around 10:00 CET in dense fog on a hill (280 m a.s.l.), 6 km before the intermediate landing at Brno airport [70].

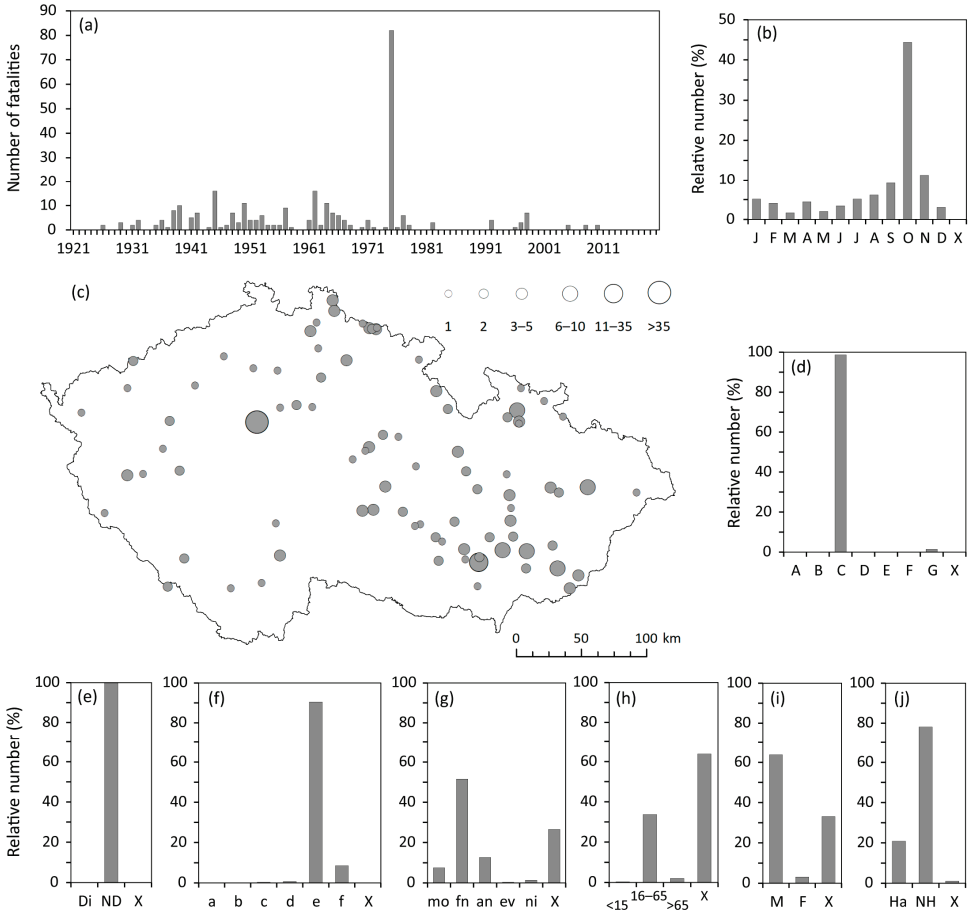

Figure 8. Characteristics of fog-related fatalities in the Czech Republic during the 1921–2020 period: (**a**) long-term fluctuation; (**b**) annual variation; (**c**) spatial distribution; (**d**) cause of death; (**e**) type of fatality; (**f**) place of death; (**g**) part of the day; (**h**) age; (**i**) gender; (**j**) behavior. For symbols and abbreviations see Figure 3.

The above-mentioned major crashes, along with other similar events, influence all other characteristics of fatalities, with a high proportion of unknown cases. In the annual distribution (Figure 8b), proportions of fatalities in autumn months, with the most frequent occurrence of fog during the year, were the highest: October 44.4%, November 11.3%, and September 9.2%. Spatial distribution of fatalities indicates rather places of aircraft crashes close to airports in Prague or Brno (here particularly places located south-easterly from the town) (Figure 8c). The highest proportions of fatalities in other characteristics consist of indirect deaths (100.0%), aircraft and train crashes (98.6%), open countryside (90.4%), forenoon (51.5%), males (63.8%, but 33.1% unknown), adults (33.8%, but 63.8% unknown), and non-hazardous behavior (78.2%) (Figure 8d–j).

3.1.7. Other Inclement Weather

This category includes fatalities that could not be assigned to any of the preceding six weather categories. It includes 63 fatalities attributed to hot weather (41.3%), inclement weather without specification (23.8%), landslides (11.1%), and rime (9.5%). The remaining portion of 14.3% fatalities includes accidents on wet ground during downpour or heavy rain. Fatalities attributed to hot weather appeared particularly after 2000, with a maximum of nine fatalities in June–July 2006. Inclement weather was often reported in the case of airplane accidents. For example, on 30 November 1952, a military airplane transported the print matrix of the communist newspaper *Rudé právo* from Prague to Brno. As the airplane of Czechoslovak airlines did not fly due to bad weather, the military plane crashed into a hill at 20:59 CET during landing, and all five men onboard died [54,71]. Three boys died in a tent on 5 July 1969, at Sivice (easterly from Brno), when a part of a slope with a brick wall collapsed in the morning (after strong rain) [72–74].

3.2. Synthesis of Weather-Related Fatalities

A total of 2729 fatalities associated with severe weather were found in the 1921–2020 period in the CR. The highest annual numbers in this 100-year chronology reflect the deadliest events mentioned already in the individual weather categories: 110 fatalities in 1929, 106 in 1975, 95 in 2010, 86 in 1997, and 72 in 1970 (Figure 9a). Based on individual decades, the highest numbers were recorded in 2001–2010 (450 fatalities, i.e., 16.5%) and 1921–1930 (434, i.e., 15.9%), the lowest in 1951–1960 (106, i.e., 3.9%) and 1981–1990 (73, i.e., 2.7%). Fatality proportions according to individual weather categories were as follows: frosts 37.8%, convective storms 19.4%, floods 17.3%, fog 10.7%, snow and glaze ice 7.8%, windstorms 4.7%, and other inclement weather 2.3%. The annual variation of fatalities shows two maxima: the main maximum in January with 15.5% (winter 40.2%) and the secondary in July with 12.2% (summer 29.3%) (Figure 9b). Spatial distribution of fatalities shows their dense distribution over the country with the higher coverage particularly in the eastern part of the CR, as well as in northwestern, northern, and central Bohemia (Figure 9c). Deaths were interpreted as direct for 77.0% of fatalities and as indirect for 22.4% (Figure 9e). Freezing to death/hypothermia (27.6%) and drowning (25.5%) were the most frequent reasons, followed by traffic accidents (16.3%) and lightning strikes (13.4%) (Figure 9d). People died particularly in open countryside (36.1%), followed by categories river/lake/reservoir/bank (23.2%) and open spaces in built-up areas (19.0%) (Figure 9f). The critical parts of the day were in the afternoon (16.9%) and night (14.3%), but for half of the fatalities (50.9%), corresponding information was missing (Figure 9g). Males accounted for 72.3% of all fatalities, whereas females accounted for 19.4% (Figure 9i). Adults had the highest proportion according to age with 44.7%, but for 32.1% of fatalities, this information remained unknown; more than double the number of deaths occurred in the child category compared to the elderly (16.0% to 7.2%) (Figure 9h). Hazardous behavior in deadly events was higher than non-hazardous behavior (46.9% to 40.7%) (Figure 9j).

Figure 9c characterizes the distribution of fatalities across the territory of the CR according to individual places, whereas Figure 10 shows a summarized distribution of their numbers for the 77 existing districts. The highest number of 244 fatalities (8.9% of all of them) was recorded in the capital, Prague, which has the highest concentration of people (1.335 million in 2020). A lower number of casualties occurred in other large towns (with a population of over 100,000 inhabitants): Ostrava had 74 fatalities (2.7%), Brno had 71 fatalities (2.6%), but when combined with the adjacent Brno-venkov district, there were 141 fatalities (5.2%), and Plzeň had 35 fatalities (1.3%). As for other districts, the Trutnov district in northeast Bohemia recorded the second-highest number of casualties, with 125 (4.6%) fatalities recorded, particularly deaths in the Krkonoše Mts. A greater part of the Bohemian districts had fewer than 20 fatalities. In general, seven other districts in the eastern CR, along with the Brno region and Ostrava, experienced higher numbers of fatalities (more than 50), whereas in Bohemia, it was only the Liberec district in north Bohemia that had a similar number of fatalities (56).

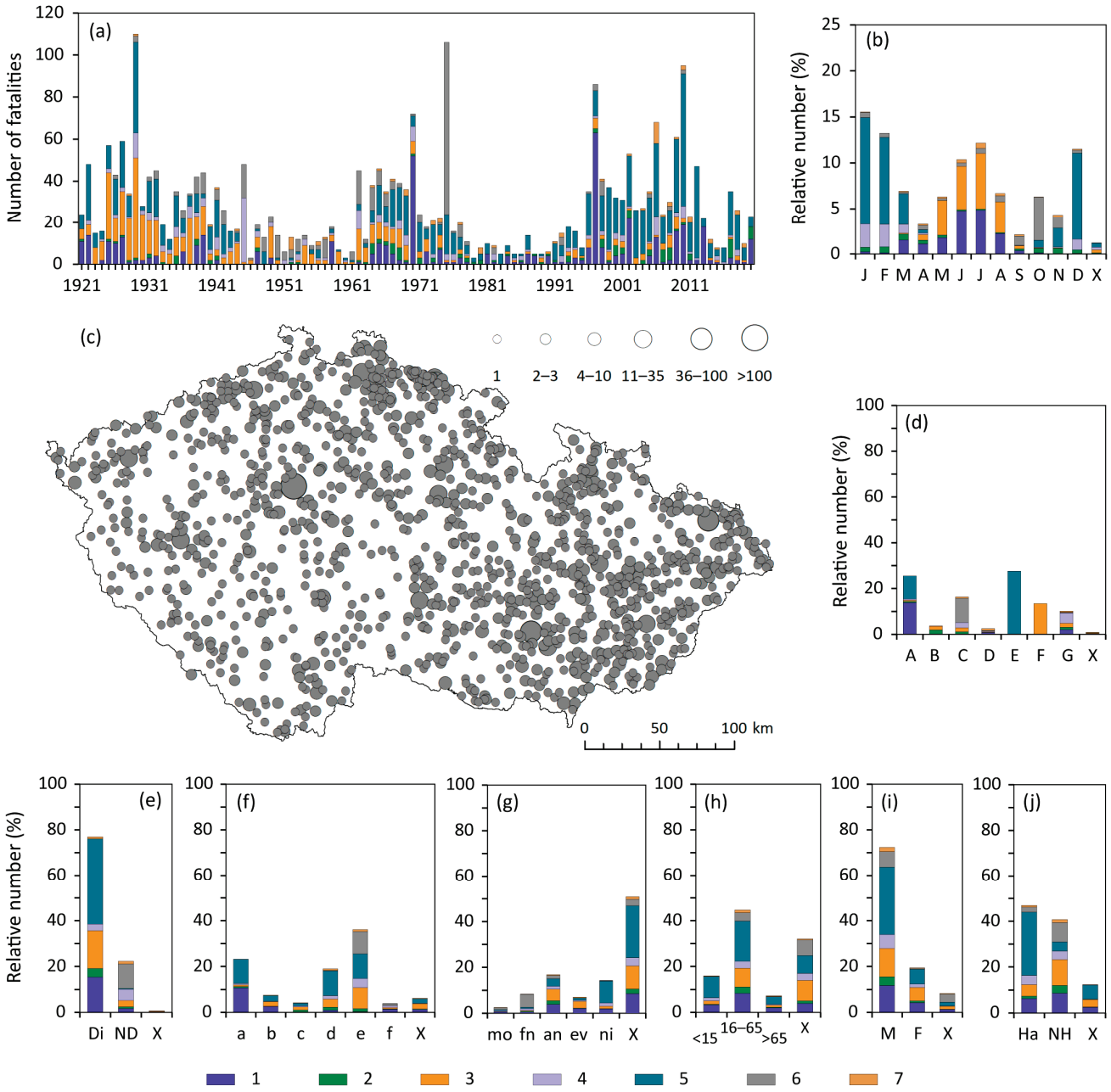

Figure 9. Characteristics of weather-related fatalities (1—flood, 2—windstorm, 3—convective storm, 4—snow and glaze ice, 5—frost, 6—fog, 7—other inclement weather) in the Czech Republic during the 1921–2020 period: (**a**) long-term fluctuation; (**b**) annual variation; (**c**) spatial distribution (88 fatalities lack exact locations); (**d**) cause of death; (**e**) type of fatality; (**f**) place of death; (**g**) part of the day; (**h**) age; (**i**) gender; (**j**) behavior. For symbols and abbreviations see Figure 3.

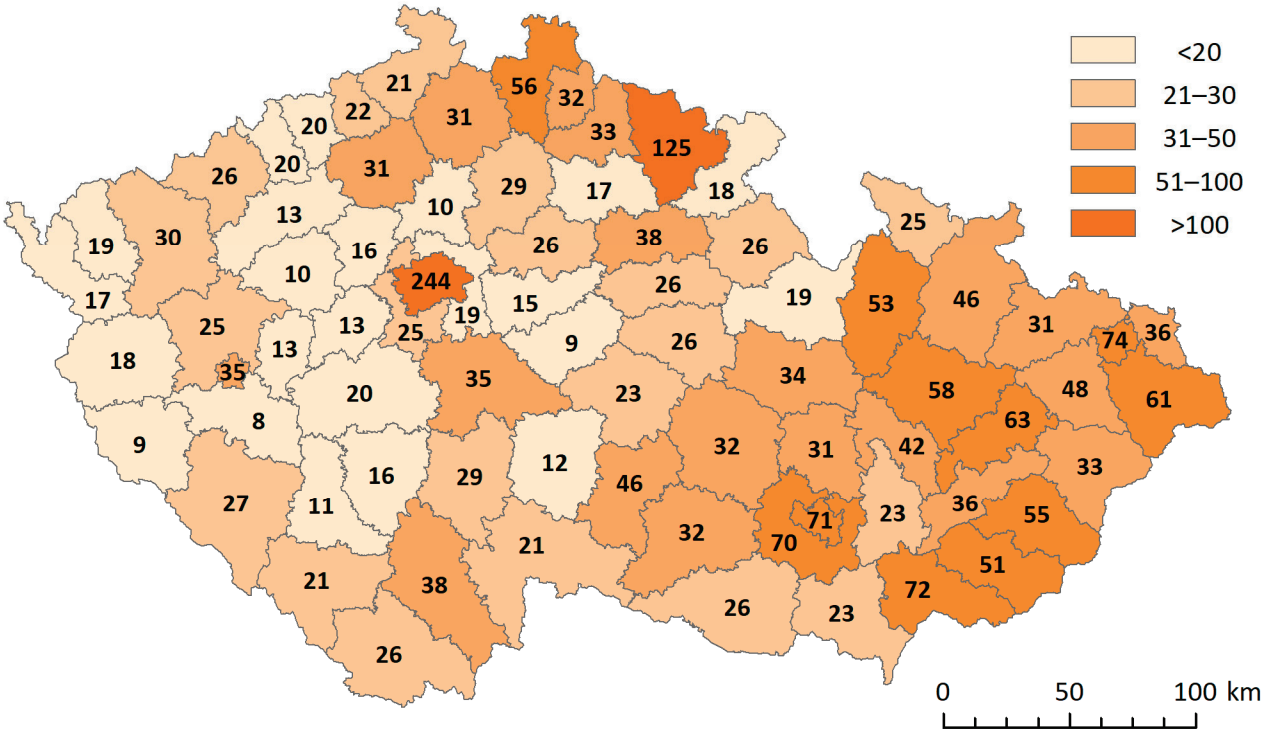

Figure 10. Distribution of weather-related fatalities for the individual districts of the Czech Republic during the period of 1921–2020, expressed in colored intervals and numbers of fatalities.

4. Discussion

4.1. Data Uncertainty

Information on weather-related fatalities from newspapers is often used as the main source of data to create corresponding fatality datasets (e.g., [9,75–80]). Regarding the CR, information on 2435 fatalities (i.e., 89.2% of all of them) comes from this particular source. Despite systematic extractions of reports from three basic newspapers covering long time intervals (*Rudé právo/Právo* for 76 years, *Svobodné slovo* for 44 years, and *Lidové noviny* for 30 years) and their complementing by many other newspapers extracted for several months, the whole year, or a couple of years (see Section 2.1.2, point (i)), fatality reports have been strongly influenced by many other factors, particularly with political, societal, and economic changes in the country.

After the establishment of Czechoslovakia in 1918 (see Figure 2), the media flourished in a democratic society, and information on weather phenomena and related fatalities or injuries received ample attention. Surprisingly, a relatively high level of local information in Czech written media (e.g., *Lidové noviny* or *Venkov*) remained even after the full occupation of Czechoslovakia by Nazis in 1939 (borderland areas, "Sudetenland", were occupied after the signing of the Munich Agreement on 29 September 1938), as well as during the Second World War until 1944. The last year of the war, 1945, was characterized by close war operations, which caused disruptions in newspaper publishing and information flow. After the liberation of Czechoslovakia, some communist newspaper (e.g., *Rudé právo*, *Rovnost*), prohibited during Nazis occupation have been again issued, but some newspapers produced during occupation were stopped and some new ones appeared, which were published for a few years or longer (e.g., *Lidová demokracie*, *Svobodné slovo*). The post-war years in newspapers were particularly focused on dealing with the far-reaching consequences of the war. This democratic development and media freedom were interrupted by the communist coup in 1948 when the country became a part of the Soviet bloc. Newspapers, strongly influenced by communist ideology, "building of socialism" and "cold war" between East and West, reported rather larger weather extremes, but paid less attention to deadly events during these extremes or describing their circumstances. This

trend continued until the early 1960s. The political liberalization afterwards, culminating in the "Prague Spring" in 1968 (which was stopped by Soviet occupation), brought positive changes to the reporting of weather-related injuries and fatalities, but in the late 1970s and 1980s, these reports became less frequent again. The return to a democratic society after the "Velvet Revolution" in 1989 and the establishment of the CR in 1993 were reflected with some delay in an increase in regional or local reports of weather events and their fatalities and injuries. The described facts and circumstances were reflected in three periods that were relatively well-covered by the data analyzed, namely 1921–1944, 1962–1977, and 1996–2020, whereas the years in between, i.e., 1945–1961 and 1978–1995, suffered from a lack of weather-related fatality reports. This uneven temporal information coverage explains why our unique 100-year long fatality chronology is not suitable for the study of any long-term trends.

In addition to the historical milestones and subsequent changes, the media market itself and internal changes in newspapers may have played an important role in reporting weather-related fatalities. Changes in the space devoted to certain kinds of information, the perceived interest of target readers, the political orientation of the newspaper, the reduction in regional editorial staff, different quantities of space given to regional and countrywide reporting, advertising space, competition in reporting, reader fatigue, availability of regional/local news taken from other bodies (e.g., police, press agencies, state and regional administration), etc., could all have had an impact.

Despite the unique character of our 100-year database of weather-related fatalities, it represents a lower estimate of the real numbers. Spatial and temporal non-homogeneity in available data is a typical feature of most analyses based on documentary data (e.g., [34]). For example, the lower number of fatalities in Bohemia compared to Moravia and Silesia in Figure 10 could be partly related to the availability of local newspaper issues. The problem of data non-homogeneity is not solved by other "official" databases such as the Czech Statistical Office (CSO), which, besides its short length (since 1994), is influenced by the subjective evaluation of causes of death by doctors and contains only limited information about fatality characteristics (for a comparison of our and CSO databases in the 2000–2019 period, see [35]).

4.2. Broader Context

The results of the recent article reflect the progress achieved in the study of weather-related fatalities in the past few years. Whereas the first study by Brázdil et al. [34] presented very preliminary results with only 269 fatalities (including vehicle accidents) during the period of 1981–2018 and some methodological considerations related to the use of documentary evidence, the subsequent study for 2000–2019 [35] reported 601 fatalities (excluding vehicle accidents). The extension of our dataset to a 60-year period [2] focused on comparing two "normal" periods, 1961–1990 and 1991–2020, which are typically used in climatology and reported 657 and 962 fatalities, respectively (a total of 1619 fatalities). The recent paper is based on a unique 100-year chronology for the period of 1921–2020, adding 1074 new fatalities before 1961 (part of the fatalities reported in *Lidové noviny* were extracted based on [81,82]) and 36 new fatalities after 1960 (i.e., 40.7% of all fatalities in the 100-year period). Apart from flood fatalities (e.g., [6,8]), there are not many papers analyzing such a broad scale of weather-related fatalities in this long-term context and detailed internal structure (e.g., [83]) as our study.

Section 4.1 demonstrated how past historical milestones, subsequent political changes, and newspaper "politics" could have influenced the availability of weather-related fatality data. However, the frequency and structure of fatalities also reflect other socio-economic changes and changes in lifestyle. During the 100-year period analyzed, there was an important change in the proportion of people working in agriculture, i.e., people who were more frequently exposed to the outdoors and an open landscape; their numbers continuously and strongly declined from the past to the present. In 1930, their number was 2.316 million, but in 1946, it was 1.588 million, in 1961, 0.832 million, in 1981, 0.578

million, in 2001 only 156 thousand, and finally, in 2021, 133 thousand ([84], complemented). The proportion of women decreased between 1930 and 2021 from approximately 59% to 35%. These facts are well reflected in the number of fatalities due to lightning strikes. Of 371 such fatalities, 33.2% of them were recorded in 1921–1930, 22.9% in 1931–1940, and after two clearly underestimated decades, 18.1% in 1961–1970. In the five decades after 1970 until 2020, only 12.9% of all such fatalities were recorded. No doubt, the clear decreasing tendency in these fatalities is also due to the increased use of lightning conductors, vast improvements in medical services, an increase in the availability of immediate emergency help with rapid transport to hospitals, and a broader public awareness of how to behave during a thunderstorm [23,34]. Similarly, well-expressed decreasing lightning-related fatalities were documented, for example, also for the UK [22], Switzerland [83], Western Europe [85], or Romania [25].

Despite the decreasing severity of winter temperature and snow patterns in the CR from 1961 [86], fatalities attributed to cold spells, i.e., due to freezing to death or hypothermia, surprisingly significantly increased after 1990. The following three decades experienced 63.7% of all 758 such fatalities during the past 100 years. This increase can be explained by the important increase in the homeless population after the "Velvet Revolution" in the CR, whereas before 1990, such people were very rare. Despite some possibilities to spend nights with heavy frosts in some special facilities, many homeless people prefer to spend the night outside, often with heavy alcohol consumption. The opposite situation characterizes higher proportions of deaths by drowning during different activities provided on not enough frozen water bodies with a subsequent breaking of ice: from 273 such fatalities, 40.7% of them died in 1921–1950, and 41.4% in 1961–1980. A very high proportion of 83.5% belongs to the child category (0–15 years), which—compared to recent decades—was related to more frequent children's activities outdoors in the past, often without any supervision from parents. It also reflects changes in age pyramids in Figure 1d, demonstrating significantly decreasing proportions of children from 27.8% in 1921 to 16.0% in 2020. However, the results for the CR differ from those obtained for ten countries over the Northern Hemisphere, for which Sharma et al. [87] found increased drownings in ice-covered regions in warmer winters.

Finding stronger relationships between weather-related fatalities and long-term climate variability is more complicated. Although there has been a significant increase in maximum temperatures and frequency of heat waves [88,89], which is well reflected in growing numbers of heat-wave-related fatalities (e.g., [1,18]), the relationship with other weather-related fatalities is not as conclusive.

Of the 277 flood fatalities detected, 48.8% were recorded only between 1996 and 2013. Although 22.7% of these fatalities were a consequence of the July 1997 flood event [60] by itself, the period from 1997 to 2010 in the CR was generally evaluated as flood-rich, compared to relatively flood-poor years from 1966 to 1992 [90]. The years from 1996 to 2013 in the CR are within the 1990–2016 period, which Blöschl et al. [91] identified among the ten most flood-rich periods in Western and Central Europe in the context of the past 500 years. Despite regional variations of none, increasing, or decreasing trends in flood-related fatalities in past decades (e.g., [4,5,92,93], Paprotny et al. [94] reported an increase in annually inundated area and in the number of persons affected for 37 European countries (HANZE database) since 1870, but a substantial decrease in flood fatalities. Similarly, Franzke and Torelló i Sentelles [95] found a significant downward flood fatality trend for Europe in 1960–2019, but an upward trend for worldwide aggregated data.

Regarding fatalities from flash floods in the CR, besides the deadliest year of 1970 (38 fatalities, i.e., 19.6% of all flash flood fatalities), 33.0% of such fatalities occurred in 1921–1940 and 22.7% in 2001–2020. These values show that the past two decades did not experience any particular increase in fatalities related to flash floods in the context of the 100-year series. Terti et al. [96], analyzing 1075 fatalities from flash floods across the United States in 1996–2012, found no clear trend in such events and associated fatalities. Ahmadalipour and Moradkhani [97], extending that period until 2017 with 1399 fatalities

across the contiguous United States, mentioned only that the number of flash flood fatalities did not decrease in the past decades. Vinet et al. [98], analyzing French departments prone to Mediterranean flash floods in 1980–2020, pointed out a decreased mean toll of flood events but an increase in the number of deadly events. Similarly, Diakakis et al. [8], investigating 132 flash floods with $\geq$10 fatalities in 13 countries over the eastern Mediterranean during 1882–2021, found a statistically significant increase in the number of fatalities.

Although 26 fatalities related to hot weather or heat-waves appeared in our database (see Section 3.1.7), such information occurred in newspapers only sporadically. These fatalities have to be derived from another type of data (namely medical data of deaths due to cardiovascular problems) than those we used to create our database. From the many papers dealing with heat-waves in the CR, some quantitative fatality data can be derived. For example, Urban et al. [31], analyzing mortality attributed to heat in Prague during 1982–2019, found the following numbers of excess deaths for the individual decades: 61 fatalities per year in 1982–1989, 43 in 1990–1999, 53 in 2000–2009, and nearly 90 in 2010–2019, while the highest annual value with 271 excess deaths was achieved in 2015. These numbers are significantly exceeding the numbers of fatalities attributed to other weather phenomena in the entire CR as presented in our study.

Despite some specific characteristics of fatalities in the CR for the individual weather categories, some general features can be summarized from their synthesis in Section 3.2. The main maximum appears in the winter months, and the secondary maximum appears in the summer months, which is connected to the climatology of decisive weather extremes. Deaths were interpreted mainly as direct, caused particularly by freezing to death/hypothermia or drowning, happening in the afternoon and night in an open countryside or on rivers and in water bodies. Males prevailed over females, and adults over the categories of children and elderly people. Hazardous behavior of victims or culprits of deadly events was more frequent than non-hazardous behavior. Similar features in fatality characteristics can be found in many similar studies in other countries or regions (e.g., [7,10,12,83,99]). On the other hand, some regionally specific features not typical for fatalities in the CR can appear, such as an important proportion of vehicle fatalities during floods, as documented, for example, for Greece [100], Portugal and Greece [92], Spain [101], or the United States [93].

The fatality database used in the recent paper did not include fatalities during vehicle accidents that occurred during inclement weather conditions (divided into seven categories: fog, onset of rain and light rain, rain, snow and snowfall, glaze of ice and rime, gusty wind, and other inclement weather) which have been analyzed in the earlier studies [2,35,36] and create another database. The exceptions were only a few cases when either the accident took place in a flood or flooded area (e.g., driving in flowing water on the road or accident of a rescue car on the way to flooded area) or was connected with strong winds or thunderstorms (e.g., accidents caused by sudden strong wind gust or crash to a tree uprooted by strong wind on the road). Moreover, compared to the previous study by Brázdil et al. [2], which pointed out 1834 fatalities of vehicle accidents in the CR for the 1961–2020 period connected with any inclement weather, only 60 new such fatalities were found for 1921–1960, which represents a deep underestimation of their real value, particularly before 1961, even though the number of cars and types of roads used was smaller than in the following decades. If any vehicle accidents were mentioned in the extracted newspapers (particularly for any persons considered as "important"), accompanying weather patterns were usually only sporadically reported. For this reason, we skipped this type of analysis for the whole 100-year period. Concerning the reported 60 fatalities before 1961, more than two-thirds of them were attributed to the categories snow and snowfall (35.0%) and fog (33.3%); for glaze of ice, it was 16.7%, and for wet road and rain, it was 15.0%.

5. Conclusions

The analysis of the 100-year chronology (1921–2020) of fatalities attributed to severe weather in the CR allows us to summarize the main results as follows:

(i) The database of weather-related fatalities in the past 100 years was created from different documentary sources, particularly newspapers. By covering a long period and a broad scope of severe weather events, it is a unique dataset in the national and European scales. Despite representing a lower estimate of the real numbers of such fatalities, this database is suitable for the study of spatiotemporal variability of weather-related fatalities, as well as their different special characteristics and features.
(ii) Historical milestones, political and socioeconomic developments, as well as changes in media, significantly influenced the availability of fatality reports related to extreme weather in newspapers. As a result, fatality data are highly underestimated in 1945–1961 and 1978–1995, which makes it difficult to analyze long-term trends and compare them with trends in selected climatological variables.
(iii) An annual average of 27.3 weather-related fatalities per year was attributed to the following weather categories: frosts—cold spells and ice on water bodies (38%); convective storms—lightning strike, strong wind, thunderstorm (19%); floods—including flash floods (17%); fog with bad visibility (11%); snow, avalanches, and glaze ice (8%); windstorms (5%); and other inclement weather not attributable to any preceding categories (2%).
(iv) Despite some differences among individual weather categories, the prevailing characteristics/features of all fatalities were as follows: direct deaths; fatalities mainly caused by freezing to death/hypothermia or drowning, happening in the afternoon and night in an open countryside or on rivers and water bodies; particularly dominant male and adult fatalities; hazardous behavior of victims (or culprits of deadly events) more frequently than non-hazardous.
(v) Detailed knowledge of weather-related fatalities with respect to their spatiotemporal occurrence, structure, and characteristics, with almost half of them classified as hazardous behavior of victims (or culprits of deadly events), offers the possibility to learn from this fatality data to apply appropriate risk communication and contribute to potentially decreasing fatalities (injuries) during extreme weather events.
(vi) Further research on weather-related fatalities in the CR would require their comparison with other official public sources as demographic yearbooks (despite their more generalized data), extension of the period analyzed back to 19th century and the study of fatalities in their broad climatological, environmental, and socioeconomic context in contrast to recent climate change.

Author Contributions: Conceptualization, R.B.; methodology, R.B., P.Z. and P.D.; formal analysis, K.C.; data curation, K.C. and P.Z.; data extraction: R.B., K.C., L.D., P.D., J.Ř. and L.Ř.; software, K.C. and P.Z.; visualization, K.C. and J.Ř.; writing—original draft preparation, R.B.; writing—review and editing, R.B. and K.C. All authors have read and agreed to the published version of the manuscript.

Funding: This research has been supported by the Ministry of Education, Youth and Sports of the Czech Republic for the SustES—Adaptation strategies for sustainable ecosystem services and food security under adverse environmental conditions, project ref. CZ.02.1.01/0.0/0.0/16_019/0000797.

Data Availability Statement: Fatality data from authors database can be made available by the authors upon request.

Acknowledgments: R.B., L.D., P.Z. and P.D. were financially supported by the Ministry of Education, Youth and Sports of the Czech Republic for the SustES—Adaptation strategies for sustainable ecosystem services and food security under adverse environmental conditions, project ref. CZ.02.1.01/0.0/0.0/16_019/0000797. K.C. was supported by the Global Change Research Institute of the Czech Academy of Sciences and J.Ř. by Masaryk University within project ref. MUNI/A/1323/2022. P. Štěpánek (Brno, Czech Republic) is acknowledged for providing us with mean areal temperature and precipitation series for the CR and A. Věžník (Brno, Czech Republic) with statistical data of agriculture. We thank Laughton Chandler (Charleston, SC, USA) for English style corrections.

Conflicts of Interest: The authors declare no conflict of interest.

Appendix A

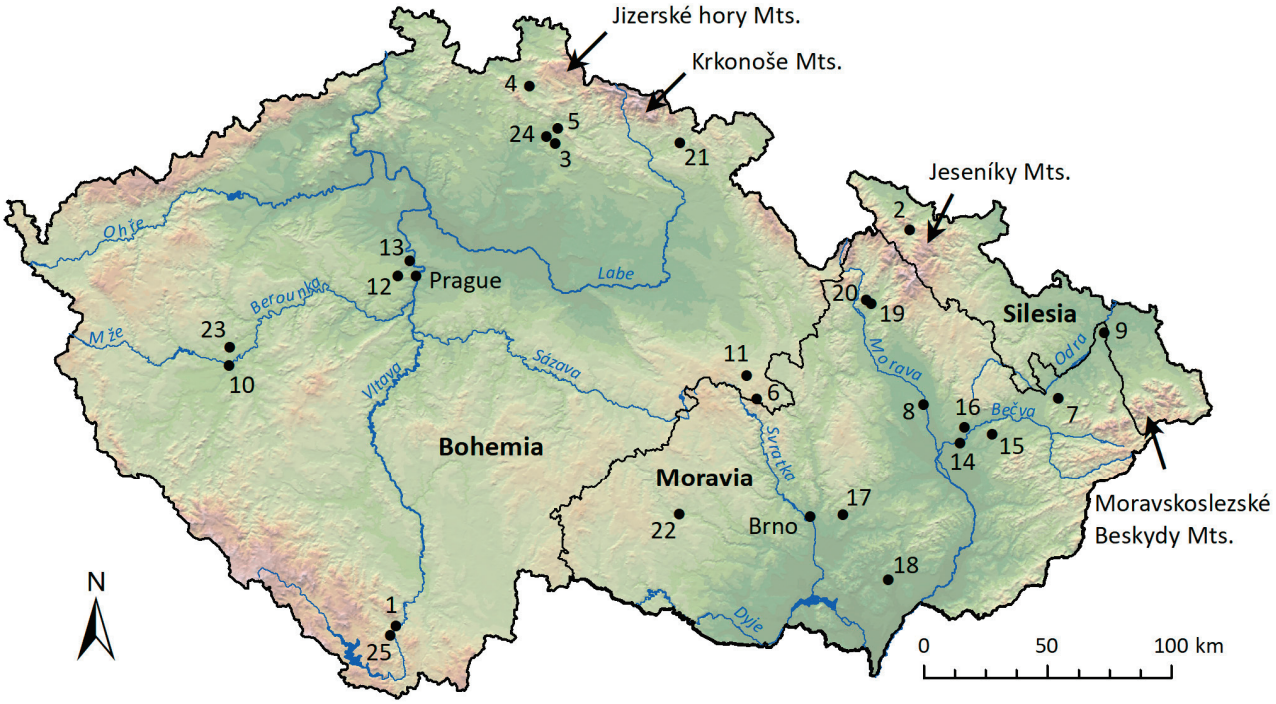

Figure A1. Location of places reported in this study (1—Český Krumlov; 2—Jeseník; 3—Karlovice; 4—Liberec; 5—Loučky; 6—Nedvězí; 7—Nový Jičín; 8—Olomouc; 9—Ostrava; 10—Plzeň; 11—Polička; 12—Prague-Ruzyně; 13—Prague-Suchdol; 14—Přerov; 15—Radotín; 16—Radvanice; 17—Sivice; 18—Šardice; 19—Šumperk; 20—Šumperk-Temenice; 21—Trutnov; 22—Třebíč; 23—Třemošná-Záluží; 24—Turnov; 25—Větřní).

References

1. WMO. *Atlas of Mortality and Economic Losses from Weather, Climate and Water Extremes (1970–2019)*; WMO-No. 1267; World Meteorological Organization: Geneva, Switzerland, 2021.
2. Brázdil, R.; Chromá, K.; Zahradníček, P.; Dobrovolný, P.; Dolák, L.; Řehoř, J.; Řezníčková, L. Changes in weather-related fatalities in the Czech Republic during the 1961–2020 period. *Atmosphere* **2022**, *13*, 688. [CrossRef]
3. Pilorz, W.; Laskowski, I.; Surowiecki, A.; Łupikasza, E. Fatalities related to sudden meteorological events across Central Europe from 2010 to 2020. *Int. J. Disaster. Risk Reduct.* **2023**, *88*, 103622. [CrossRef]
4. Diakakis, M.; Deligiannakis, G. Flood fatalities in Greece: 1970–2010. *J. Flood Risk Manag.* **2017**, *10*, 115–123. [CrossRef]
5. Petrucci, O.; Aceto, L.; Bianchi, C.; Bigot, V.; Brázdil, R.; Pereira, S.; Kahraman, A.; Kiliç, Ö.; Kotroni, V.; Llasat, M.C.; et al. Flood fatalities in Europe, 1980–2018: Variability, features, and lessons to learn. *Water* **2019**, *11*, 1682. [CrossRef]
6. Špitalar, M.; Brilly, M.; Kos, D.; Žiberna, A. Analysis of flood fatalities—Slovenian illustration. *Water* **2020**, *12*, 64. [CrossRef]
7. Petrucci, O. Review article: Factors leading to the occurrence of flood fatalities: A systematic review of research papers published between 2010 and 2020. *Nat. Hazards Earth Syst. Sci.* **2022**, *22*, 71–83. [CrossRef]
8. Diakakis, M.; Papagiannaki, K.; Fouskaris, M. The occurrence of catastrophic multiple-fatality flash floods in the Eastern Mediterranean region. *Water* **2023**, *15*, 119. [CrossRef]
9. Hilker, N.; Badoux, A.; Hegg, C. The Swiss flood and landslide damage database 1972–2007. *Nat. Hazards Earth Syst. Sci.* **2009**, *9*, 913–925. [CrossRef]
10. Salvati, P.; Petrucci, O.; Rossi, M.; Bianchi, C.; Pasqua, A.A.; Guzzetti, F. Gender, age and circumstances analysis of flood and landslide fatalities in Italy. *Sci. Total Environ.* **2018**, *610–611*, 867–879. [CrossRef]
11. Petrucci, O. Landslide fatality occurrence: A systematic review of research published between January 2010 and March 2022. *Sustainability* **2022**, *14*, 9346. [CrossRef]
12. Petrucci, O.; Papagiannaki, K.; Aceto, L.; Boissier, L.; Kotroni, V.; Grimalt, M.; Llasat, M.C.; Llasat-Botija, M.; Rosselló, J.; Pasqua, A.A.; et al. MEFF: The database of MEditerranean Flood Fatalities (1980 to 2015). *J. Flood Risk Manag.* **2019**, *12*, e12461. [CrossRef]
13. Papagiannaki, K.; Petrucci, O.; Diakakis, M.; Kotroni, V.; Aceto, L.; Bianchi, C.; Brázdil, R.; Grimalt Gelabert, M.; Inbar, M.; Kahraman, A.; et al. Developing a large-scale dataset of flood fatalities for territories in the Euro-Mediterranean region, FFEM-DB. *Sci. Data* **2022**, *9*, 166. [CrossRef] [PubMed]

14. Paprotny, D.; Morales-Nápoles, O.; Jonkman, S.N. HANZE: A pan-European database of exposure to natural hazards and damaging historical floods since 1870. *Earth Syst. Sci. Data* **2018**, *10*, 565–581. [CrossRef]
15. Výberči, D.; Švec, M.; Faško, P.; Savinova, H.; Trizna, M.; Mičietova, E. The effects of the 1996–2012 summer heat events on human mortality in Slovakia. *Morav. Geogr. Rep.* **2015**, *23*, 58–70. [CrossRef]
16. Graczyk, D.; Kundzewicz, Z.W.; Choryński, A.; Førland, E.J.; Pińskwar, I.; Szwed, M. Heat-related mortality during hot summers in Polish cities. *Theor. Appl. Climatol.* **2019**, *136*, 1259–1273. [CrossRef]
17. Park, J.; Choi, Y.; Chae, Y. Heatwave impacts on traffic accidents by time-of-day and age of casualties in five urban areas in South Korea. *Urban Clim.* **2021**, *39*, 100917. [CrossRef]
18. Vicedo-Cabrera, A.M.; Scovronick, N.; Sera, F.; Royé, D.; Schneider, R.; Tobias, A.; Astrom, C.; Guo, Y.; Honda, Y.; Hondula, D.M.; et al. The burden of heat-related mortality attributable to recent human-induced climate change. *Nat. Clim. Chang.* **2021**, *11*, 492–500. [CrossRef]
19. Analitis, A.; Katsouyanni, K.; Biggeri, A.; Baccini, M.; Forsberg, B.; Bisanti, L.; Kirchmayer, U.; Ballester, F.; Cadum, E.; Goodman, P.G.; et al. Effects of cold weather on mortality: Results from 15 European cities within the PHEWE Project. *Am. J. Epidemiol.* **2008**, *168*, 1397–1408. [CrossRef]
20. Fonseca-Rodríguez, O.; Sheridan, S.C.; Lundevaller, E.H.; Schumann, B. Effect of extreme hot and cold weather on cause-specific hospitalizations in Sweden: A time series analysis. *Environ. Res.* **2021**, *193*, 110535. [CrossRef]
21. Petkova, E.P.; Dimitrova, L.K.; Sera, F.; Gasparrini, A. Mortality attributable to heat and cold among the elderly in Sofia, Bulgaria. *Int. J. Biometeorol.* **2021**, *65*, 865–872. [CrossRef]
22. Elsom, D.M. Deaths and injuries caused by lightning in the United Kingdom: Analyses of two databases. *Atmos. Res.* **2001**, *56*, 325–334. [CrossRef]
23. Elsom, D.M.; Webb, J.D.C. Deaths and injuries from lightning in the UK, 1988–2012. *Weather* **2014**, *69*, 221–226. [CrossRef]
24. Singh, O.; Singh, J. Lightning fatalities over India: 1979–2011. *Meteorol. Appl.* **2015**, *22*, 770–778. [CrossRef]
25. Antonescu, B.; Cărbunaru, F. Lightning-related fatalities in Romania from 1999 to 2015. *Weather Clim. Soc.* **2018**, *10*, 241–252. [CrossRef]
26. Taszarek, M.; Gromadzki, J. Deadly tornadoes in Poland from 1820 to 2015. *Mon. Weather Rev.* **2017**, *145*, 1221–1243. [CrossRef]
27. Salvador, C.; Nieto, R.; Linares, C.; Díaz, J.; Gimeno, L. Short-term effects of drought on daily mortality in Spain from 2000 to 2009. *Environ. Res.* **2020**, *183*, 109200. [CrossRef]
28. Kyselý, J.; Plavcová, E. Declining impacts of hot spells on mortality in the Czech Republic, 1986–2009: Adaptation to climate change? *Clim. Chang.* **2012**, *113*, 437–453. [CrossRef]
29. Hanzlíková, H.; Plavcová, E.; Kynčl, J.; Kříž, B.; Kyselý, J. Contrasting patterns of hot spell effects on morbidity and mortality for cardiovascular diseases in the Czech Republic, 1994–2009. *Int. J. Biometeorol.* **2015**, *59*, 1673–1684. [CrossRef]
30. Arsenović, D.; Lehnert, M.; Fiedor, D.; Šimáček, P.; Středová, H.; Středa, T.; Savić, S. Heat-waves and mortality in Czech cities: A case study for the summers of 2015 and 2016. *Geogr. Pannonica* **2019**, *23*, 162–172. [CrossRef]
31. Urban, A.; Fonseca-Rodríguez, O.; Di Napoli, C.; Plavcová, E. Temporal changes of heat-attributable mortality in Prague, Czech Republic, over 1982–2019. *Urban. Clim.* **2022**, *44*, 101197. [CrossRef]
32. Kyselý, J.; Pokorná, L.; Kyncl, J.; Kříž, B. Excess cardiovascular mortality associated with cold spells in the Czech Republic. *BMC Public Health* **2009**, *9*, 1–11. [CrossRef] [PubMed]
33. Plavcová, E.; Urban, A. Intensified impacts on mortality due to compound winter extremes in the Czech Republic. *Sci. Total Environ.* **2020**, *746*, 141033. [CrossRef] [PubMed]
34. Brázdil, R.; Chromá, K.; Řehoř, J.; Zahradníček, P.; Dolák, L.; Řezníčková, L.; Dobrovolný, P. Potential of documentary evidence to study fatalities of hydrological and meteorological events in the Czech Republic. *Water* **2019**, *11*, 2014. [CrossRef]
35. Brázdil, R.; Chromá, K.; Dolák, L.; Řehoř, J.; Řezníčková, L.; Zahradníček, P.; Dobrovolný, P. Fatalities associated with the severe weather conditions in the Czech Republic, 2000–2019. *Nat. Hazards Earth Syst. Sci.* **2021**, *21*, 1355–1382. [CrossRef]
36. Brázdil, R.; Chromá, K.; Zahradníček, P.; Dobrovolný, P.; Dolák, L. Weather and traffic accidents in the Czech Republic, 1979–2020. *Theor. Appl. Climatol.* **2022**, *149*, 153–167. [CrossRef]
37. Tolasz, R.; Míková, T.; Valeriánová, A.; Voženílek, V. *Atlas Podnebí Česka (Climate Atlas of Czechia)*; Český Hydrometeorologický ústav, Univerzita Palackého v Olomouci: Praha, Czech Republic, 2007.
38. Brázdil, R.; Bělínová, M.; Dobrovolný, P.; Mikšovský, J.; Pišoft, P.; Řezníčková, L.; Štěpánek, P.; Valášek, H.; Zahradníček, P. *Temperature and Precipitation Fluctuations in the Czech Lands During the Instrumental Period*; Masaryk University: Brno, Czech Republic, 2012.
39. Český Statistický Úřad, Veřejná Databáze (Czech Statistical Office, Public Database). Available online: https://vdb.czso.cz/vdbvo2/faces/en/index.jsf (accessed on 3 April 2023).
40. Bor. Z černé kroniky, Dva chlapci utonuli (From Black Chronicle, Two Boys Drowned). *Rudé Právo*, 14 February 1975, p. 4.
41. Mrazy zabily o víkendu šest lidí (Frosts killed six people during the weekend). *Právo*, 25 January 2010, p. 1.
42. Pamětní kniha obce Karlovice (The Memorial Book of the Karlovice Village). Available online: http://karlovice-sedmihorky.cz/Oobci/Kronika/1941-50.htm#1941 (accessed on 22 September 2022).
43. Obec Radotín, Kronika 1961–1981 (The Radotín Village, The Chronicle 1961–1981). Available online: https://www.obecradotin.cz/kronika-1961-1981 (accessed on 15 September 2022).

44. Český hydrometeorologický ústav, pobočka Hradec Králové. Klimatologický výkaz stanice Polička, září 1934 (Czech Hydrometeorological Institute, Hradec Králové. Climatological sheet of the Polička station, September 1934). *Unpublished work*.
45. Český hydrometeorologický ústav, pobočka Ostrava. Klimatologický výkaz stanice Nový Jičín, srpen 1958 (Czech Hydrometeorological Institute, Ostrava. Climatological sheet of the Nový Jičín station, August 1958). *Unpublished work*.
46. Společná česko-slovenská digitální parlamentní knihovna (Joint Czech and Slovak Digital Parliamentary Library). Available online: http://www.psp.cz/eknih/ (accessed on 10 April 2022).
47. Národní shromáždění československé/Poslanecká sněmovna 1925–1929, tisk 1028 (Czechoslovak National Assembly/Chamber of deputies 1925–1929, Print 1028). Available online: https://www.psp.cz/eknih/1925ns/ps/tisky/t1028_00.htm (accessed on 25 April 2022).
48. Polách, D.; Gába, Z. Historie povodní na šumperském a jesenickém okrese (History of floods in the Šumperk and Jeseník districts). *Sev. Morava* **1998**, *75*, 3–30.
49. Památník obětem hor (Monument to Victims of Mountains). Available online: https://www.krkonose.eu/pamatnik-obetem-hor (accessed on 14 December 2022).
50. Památník obětem hor na Červenohorském sedle. Jména v památníku. (Monument to Victims of Mountains at the Červenohorské Sedlo. Names on the monument). Available online: https://www.pamatnik-obetem-hor.com/plakety-v-pamatniku2/ (accessed on 16 December 2022).
51. Památník čtyř žen usmrcených bleskem severně od Záluží (Memorial of Four Women Killed by Lightning North of Záluží). Available online: https://www.drobnepamatky.cz/node/5697 (accessed on 18 January 2023).
52. Jizerskohorské pomníčky. Seznam pomníčků (Memorials of the Jizerské hory Mts. List of Memorials). Available online: http://jizerpom.wz.cz/ (accessed on 17 June 2022).
53. Letecká badatelna (Air research). Available online: http://www.leteckabadatelna.cz/havarie-a-sestrely (accessed on 11 November 2022).
54. Letecké nehody vojenských strojů České a Československé republiky (Air Crashes of Military Planes of the Czech and Czechoslovak Republics). Available online: https://cs.wikipedia.org/wiki/Letecké_nehody_vojenských_strojů_České_a_Československé_republiky (accessed on 11 November 2022).
55. Seznam železničních nehod v Česku (List of Czech train accidents). Available online: https://cs.wikipedia.org/wiki/Seznam_železničních_nehod_v_Česku (accessed on 10 October 2022).
56. Sen, P.K. Estimates of the regression coefficient based on Kendall's tau. *J. Am. Stat. Assoc.* **1968**, *63*, 1379–1389. [CrossRef]
57. Theil, H. A rank-invariant method of linear and polynomial regression analysis. In *Henri Theil's Contributions to Economics and Econometrics*; Advanced Studies in Theoretical and Applied Econometrics 23; Raj, B., Koerts, J., Eds.; Springer: Dordrecht, The Netherlands, 1992; pp. 345–381. [CrossRef]
58. Mann, H.B. Non-parametric tests against trend. *Econometrica* **1945**, *13*, 163–171. [CrossRef]
59. Kendall, M.G. *Rank Correlation Methods*, 4th ed.; Charles Griffin: London, UK, 1975.
60. Matějíček, J.; Hladný, J. *Povodňová katastrofa 20. století na území České republiky (Flood Disaster of the 20th Century on the Territory of the Czech Republic)*; Ministerstvo Životního Prostředí České Republiky: Praha, Czech Republic, 1999.
61. Hladný, J.; Krátká, M.; Kašpárek, L. *August 2002 Catastrophic Flood in the Czech Republic*; Ministry of the Environment of the Czech Republic: Prague, Czech Republic, 2004.
62. Daňhelka, J.; Kubát, J. *Flash Floods in the Czech Republic in June and July 2009*; Ministry of the Environment of the Czech Republic, Czech Hydrometeorological Institute: Prague, Czech Republic, 2009.
63. Daňhelka, J.; Kubát, J.; Šercl, P. *Povodně v České republice v roce 2010 (Floods in the Czech Republic in 2010)*; Český Hydrometeorologický Ústav: Praha, Czech Republic, 2012.
64. Daňhelka, J.; Kubát, J.; Šercl, P.; Čekal, R. *Floods in the Czech Republic in June 2013*; Czech Hydrometeorological Institute: Prague, Czech Republic, 2014.
65. Hostýnek, J.; Novák, M.; Žák, M. Kyrill a Emma v Česku—Meteorologické příčiny, průběh bouří s hodnocením větrných extrémů (The Kyrill and Emma storms in Czechia—Meteorological causes and the course of the storms, with evaluation of wind extremes). *Meteorol. Zpr.* **2008**, *61*, 65–71.
66. Hujslová, J.; Šimandl, P. Bouře Herwart v Česku (The storm Herwart in Czechia). *Meteorol. Zpr.* **2018**, *71*, 60–63.
67. Brázdil, R.; Stucki, P.; Szabó, M.; Řezníčková, L.; Dolák, L.; Dobrovolný, P.; Tolasz, R.; Kotyza, O.; Chromá, K.; Suchánková, S. Windstorms and forest disturbances in the Czech Lands: 1801–2015. *Agric. Forest Meteorol.* **2018**, *250–251*, 47–63. [CrossRef]
68. Krška, K. Zima 1928/29 v Česku se zřetelem k povaze extrémů a dobové literatuře (Winter 1928/29 in Czechia with respect to the nature of extremes and the period literature). *Meteorol. Zpr.* **2009**, *62*, 5–9.
69. Jsou to jatka, volali zdravotníci. Pád letadla v Suchdole nepřežily desítky lidí (It is Carnage, Declared the Paramedics. Dozens of People Were Killed in a Plane Crash in Suchdol). Available online: https://zdarsky.denik.cz/zpravy-z-ceska/havarie-letadla-v-suchdole.html (accessed on 31 May 2022).
70. V Újezdu u Brna odhalili pomník jedné z nejhorších leteckých katastrof (The Memorial to One of the Largest Plane Disasters Was Unveiled at Újezd u Brna). Available online: https://ct24.ceskatelevize.cz/archiv/1095541-v-ujezdu-u-brna-odhalili-pomnik-jedne-z-nejhorsich-leteckych-katastrof (accessed on 30 June 2022).
71. Letecká badatelna. D-47A, Vřesovice okr. Hodonín, 30.11.1952 (Air research. D-47A, Vřesovice, the Hodonín district, 30 November 1952). Available online: http://www.leteckabadatelna.cz/havarie-a-sestrely/detail/276/ (accessed on 18 November 2022).

72. Z černé kroniky, Spadlá zeď usmrtila tři chlapce (From black chronicle, Collapsed wall killed three boys). *Rudé Právo*, 7 July 1969, p. 2.
73. Ob. Prázdninová tragédie (Holiday tragedy). *Svobodné Slovo*, 7 July 1969, p. 2.
74. Čtk. Zahynuli ve stanu (Lost their lives in a tent). *Lidová Demokracie*, 7 July 1969, p. 3.
75. Llasat, M.C.; Barnolas, M.; Ĺopez, L.; Altava-Ortiz, V. An analysis of the evolution of hydrometeorological extremes in newspapers: The case of Catalonia, 1982–2006. *Nat. Hazards Earth Syst. Sci.* **2009**, *9*, 1201–1212. [CrossRef]
76. Zêzere, J.; Pereira, S.; Tavales, A.; Bateira, C.; Trigo, R.; Quaresma, I.; Santos, P.; Santos, M.; Verde, J. DISASTER: A GIS database on hydro-geomorphologic disasters in Portugal. *Nat. Hazards* **2014**, *72*, 503–532. [CrossRef]
77. Vinet, F.; Boissier, L.; Saint-Martin, C. Flashflood-related mortality in southern France: First results from a new database. In 3rd European Conference on Flood Risk Management (FLOODrisk 2016). *E3S Web Conf.* **2016**, *7*, 06001. [CrossRef]
78. Aceto, L.; Pasqua, A.A.; Petrucci, O. Effects of damaging hydrogeological events on people throughout 15 years in a Mediterranean region. *Adv. Geosci.* **2017**, *44*, 67–77. [CrossRef]
79. Petrucci, O.; Salvati, P.; Aceto, L.; Bianchi, C.; Pasqua, A.A.; Rossi, M.; Guzzetti, F. The vulnerability of people to damaging hydrogeological events in the Calabria Region (Southern Italy). *Int. J. Environ. Res. Public Health* **2018**, *15*, 48. [CrossRef]
80. Grimalt-Gelabert, M.; Rosselló-Geli, J.; Bauzà-Llinàs, J. Flood related mortality in a touristic island: Mallorca (Balearic Islands) 1960–2018. *J. Flood Risk Manag.* **2020**, *13*, e12644. [CrossRef]
81. Bláhová, A. Časoprostorová variabilita hydrometeorologických extrémů v ČR na základě novinových článků, 1941–1960 (Spatiotemporal Variability of Hydrometeorological Extremes in the Czech Republic Based on Newspaper Articles, 1941–1960). Master's Thesis, Masarykova Univerzita, Brno, Czech Republic, 2021.
82. Opatřil, M. Analýza hydrometeorologických extrémů na území ČR na základě novinových článků, 1921–1940 (Analysis of Hydrometeorological Extremes in the Czech Republic Area Based on Newspaper Articles, 1921–1940). Master's Thesis, Masarykova Univerzita, Brno, Czech Republic, 2023.
83. Badoux, A.; Andres, N.; Techel, F.; Hegg, C. Natural hazard fatalities in Switzerland from 1946 to 2015. *Nat. Hazards Earth Syst. Sci.* **2016**, *16*, 2747–2768. [CrossRef]
84. Sálusová, D.; Zavázal, P.; Kovář, J.; Makovičková, J.; Nováková, H.; Švec, J. *České zemědělství očima statistiky (Czech Agriculture from View of Statistics)*; Český Statistický Úřad: Praha, Czech Republic, 2003.
85. Holle, R.L. A summary of recent national-scale lightning fatality studies. *Weather Clim. Soc.* **2016**, *8*, 35–42. [CrossRef]
86. Brázdil, R.; Zahradníček, P.; Chromá, K.; Dobrovolný, P.; Dolák, L.; Řehoř, J.; Zahradník, P. Severity of winters in the Czech Republic during the 1961–2021 period and related environmental impacts and responses. *Int. J. Climatol.* **2023**, *43*, 2820–2842. [CrossRef]
87. Sharma, S.; Blagrave, K.; Watson, S.R.; O'Reilly, C.M.; Batt, R.; Magnuson, J.J.; Clemens, T.; Denfeld, B.A.; Flaim, G.; Hori, Y.; et al. Increased winter drownings in ice-covered regions with warmer winters. *PLoS ONE* **2020**, *15*, e0241222. [CrossRef] [PubMed]
88. Zahradníček, P.; Brázdil, R.; Štěpánek, P.; Trnka, M. Reflections of global warming in trends of temperature characteristics in the Czech Republic, 1961–2019. *Int. J. Climatol.* **2021**, *41*, 1211–1229. [CrossRef]
89. Zahradníček, P.; Brázdil, R.; Řehoř, J.; Lhotka, O.; Dobrovolný, P.; Štěpánek, P.; Trnka, M. Temperature extremes and circulation types in the Czech Republic, 1961–2020. *Int. J. Climatol.* **2022**, *42*, 4808–4829. [CrossRef]
90. Brázdil, R.; Řezníčková, L.; Havlíček, M.; Elleder, L. Floods in the Czech Republic. In *Changes in Flood Risk in Europe*; IAHS Special Publication 10; Kundzewicz, Z.W., Ed.; IAHS Press and CRC Press/Balkema: Wallingford, UK, 2012; pp. 178–198. [CrossRef]
91. Blöschl, G.; Kiss, A.; Viglione, A.; Barriendos, M.; Böhm, O.; Brázdil, R.; Coeur, D.; Demarée, G.; Carmen Llasat, M.; Macdonald, N.; et al. Current European flood-rich period exceptional compared with past 500 years. *Nature* **2020**, *583*, 560–566. [CrossRef] [PubMed]
92. Pereira, S.; Diakakis, M.; Deligiannakis, G.; Zêzere, J.L. Comparing flood mortality in Portugal and Greece (Western and Eastern Mediterranean). *Int. J. Disaster Risk Reduct.* **2017**, *22*, 147–157. [CrossRef]
93. Han, Z.; Sharif, H.O. Analysis of flood fatalities in the United States, 1959–2019. *Water* **2021**, *13*, 1871. [CrossRef]
94. Paprotny, D.; Sebastian, A.; Morales-Nápoles, O.; Jonkman, S.N. Trends in flood losses in Europe over the past 150 years. *Nat. Commun.* **2018**, *9*, 1985. [CrossRef]
95. Franzke, C.L.E.; Torelló i Sentelles, H. Risk of extreme high fatalities due to weather and climate hazards and its connection to large-scale climate variability. *Clim. Chang.* **2020**, *162*, 507–525. [CrossRef]
96. Terti, G.; Ruin, I.; Anquetin, S.; Gourley, J.J. A situation-based analysis of flash flood fatalities in the United States. *Bull Am. Meteorol. Soc.* **2017**, *98*, 333–345. [CrossRef]
97. Ahmadalipour, A.; Moradkhani, H. A data-driven analysis of flash flood hazard, fatalities, and damages over the CONUS during 1996–2017. *J. Hydrol.* **2019**, *578*, 124106. [CrossRef]
98. Vinet, F.; Cherel, J.-P.; Weiss, K.; Lewandowski, M.; Boissier, L. Flood related mortality in the French Mediterranean region (1980–2020). *LHB Hydrosci. J.* **2022**, *108*, 2097022. [CrossRef]
99. Hadjij, I.; Sardou, M.; Missoum, H.; Maouche, S. Flood-related deaths in Northwestern Algeria from 1966 to 2019. *Arab. J. Geosci.* **2021**, *14*, 1923. [CrossRef]

100. Diakakis, M.; Deligiannakis, G. Vehicle-related flood fatalities in Greece. *Environ. Hazards* **2013**, *12*, 278–290. [CrossRef]
101. Enríquez-de-Salamanca, Á. Victims crossing overflowing watercourses with vehicles in Spain. *J. Flood Risk Manag.* **2020**, *13*, e12645. [CrossRef]

remote sensing

MDPI

Article

Spatially Varying Relationships between Land Subsidence and Urbanization: A Case Study in Wuhan, China

Zhengyu Wang [1], Yaolin Liu [1,2,3,*], Yang Zhang [4], Yanfang Liu [1], Baoshun Wang [1] and Guangxia Zhang [1]

[1] School of Resource and Environmental Sciences, Wuhan University, Wuhan 430079, China; wangzhengyu@whu.edu.cn (Z.W.); yfliu610@163.com (Y.L.); wangbaoshun@whu.edu.cn (B.W.); zhangguangxia@whu.edu.cn (G.Z.)
[2] Key Laboratory of Geographic Information System, Ministry of Education, Wuhan University, Wuhan 430079, China
[3] Collaborative Innovation Center for Geospatial Information Technology, Wuhan 430079, China
[4] School of Architecture, Southeast University, Nanjing 210096, China; zhangyang2021@seu.edu.cn
* Correspondence: Yaolin2020adc@126.com

Abstract: Land subsidence has become an increasing global concern over the past few decades due to natural and anthropogenic factors. However, although several studies have examined factors affecting land subsidence in recent years, few have focused on the spatial heterogeneity of relationships between land subsidence and urbanization. In this paper, we adopted the small baseline subset-synthetic aperture radar interferometry (SBAS-InSAR) method using Sentinel-1 radar satellite images to map land subsidence from 2015 to 2018 and characterized its spatial pattern in Wuhan. The bivariate Moran's I index was used to test and visualize the spatial correlations between land subsidence and urbanization. A geographically weighted regression (GWR) model was employed to explore the strengths and directions of impacts of urbanization on land subsidence. Our findings showed that land subsidence was obvious and unevenly distributed in the study area, the annual deformation rate varied from −42.85 mm/year to +29.98 mm/year, and its average value was −1.0 mm/year. A clear spatial pattern for land subsidence in Wuhan was mapped, and several apparent subsidence funnels were primarily located in central urban areas. All urbanization indicators were found to be significantly spatially correlated with land subsidence at different scales. In addition, the GWR model results showed that all urbanization indicators were significantly associated with land subsidence across the whole study area in Wuhan. The results of bivariate Moran's I and GWR results confirmed that the relationships between land subsidence and urbanization spatially varied in Wuhan at multiple spatial scales. Although scale dependence existed in both the bivariate Moran's I and GWR models for land subsidence and urbanization indicators, a "best" spatial scale could not be confirmed because the disturbance of factors varied over different sampling scales. The results can advance the understanding of the relationships between land subsidence and urbanization, and they will provide guidance for subsidence control and sustainable urban planning.

Keywords: SBAS-InSAR; Sentinel-1 images; geographically weighted regression (GWR); bivariate Moran's I; land subsidence; urbanization; spatial non-stationarity

Citation: Wang, Z.; Liu, Y.; Zhang, Y.; Liu, Y.; Wang, B.; Zhang, G. Spatially Varying Relationships between Land Subsidence and Urbanization: A Case Study in Wuhan, China. *Remote Sens.* **2022**, *14*, 291. https://doi.org/10.3390/rs14020291

Academic Editors: Stefano Morelli, Veronica Pazzi and Mirko Francioni

Received: 9 December 2021
Accepted: 6 January 2022
Published: 9 January 2022

1. Introduction

Land subsidence (LS) is the gentle settlement of the ground surface due to the consolidation of compressible sediments or loss of regional earth materials as a result of water exploitation or extraction of oil and gas. Land subsidence is usually observed as a series of geological-environmental hazards, including severe destruction of buildings [1], roads [2], bridges, pipelines [3], railway tracks [4], and metro networks [5], and it increases the risk of urban flooding particularly in coastal regions experiencing sea-level rise [6]. In 1891, land subsidence was first observed in Mexico City while it has been detected and recorded in Shanghai (China) since 1921 [7,8]. Currently, land subsidence occurs mainly in regions with

flat terrains where loose deposits accumulate in river deltas or coastal plains, especially densely populated areas, as well as urban or agricultural areas developed in temperate or arid climates that are characterized by long-term drought [9–11]. Although land subsidence affects 8% of the global terrestrial area, people at risk account for approximately 16% of the total world population comprising approximately 1.2 billion inhabitants [12]. Along with a growing population and the developments in urbanization and industrialization, the exposure of the population to land subsidence is expected to increase by 30% approximately to 1.6 billion inhabitants while predicted potential subsidence areas will increase by only 7% globally; 1596 of 7343 major world cities are predicted to be located in potential subsidence areas by 2040 [13]. Land subsidence is one of the considerable challenges facing the world, and poses a significant threat to the long-term sustainable development of the humankind. Therefore, it is crucial to effectively monitor and map land subsidence in real time [14].

Differential synthetic aperture radar interferometry (D-InSAR) spaceborne-based is a remotely sensed technology that enables investigation of widespread surface deformation across the earth. In contrast to conventional spirit levelling and GPS survey techniques, D-InSAR provides spatially dense displacement measurements that are updated periodically at relatively low cost. Advanced multitemporal InSAR (MT-InSAR) technology such as persistent scatterer interferometry (PS-InSAR) [15,16] and small baseline subset interferometry (SBAS-InSAR) [17,18] can effectively overcome spatial-temporal decorrelations and mitigate atmospheric delay effects, thus allowing the measurement of surface deformation with centimeter and even subcentimeter accuracy at very high spatial resolution [19]. To date, the MT-InSAR method has been widely applied to monitor deformation of the earth's surface [20], including volcanoes and seismic activity [21], landslides [22], glacial motion [23], mining-related subsidence [24], subsidence of urban or peri-urban area [25,26], and even large-scale land deformation nationwide [27].

Wuhan, as the largest city in central China, has recently been a relatively highly populous metropolis. In the last two decades, Wuhan has experienced rapid urbanization and industrialization combined with ongoing construction of high-rise buildings and massive underground space development. At present, a variety of efforts have been made to measure and map land subsidence derived from multisource space-borne remotely sensed data based on the MT-InSAR method in Wuhan, concentrating on wide-coverage urban surface settlement and building structure stability. It can be stated in detail as follows. Zhou monitored the spatial distribution of land subsidence from 2015 to 2016 using Sentinel-1 SAR images [28]. Han and Jiang [29,30] investigated the spatial pattern and temporal evolution characteristics of land subsidence, aiming to reveal the spatiotemporal variations in subsidence and the induction of subsidence. Bai and Zhang [31,32] qualitatively analyzed the relationship between land subsidence and influential factors from the aspects of natural conditions and human activities. In addition, Ding [33] predicted time-series surface subsidence based on long short-term memory (LSTM) model in selected key regions.

The aforementioned works have led to a substantial understanding of the spatial extent, magnitude, and temporal evolution of land deformation and qualitatively explored influential factors in Wuhan. However, local clustering patterns between land subsidence and urbanization have been ignored, and fewer studies have examined the quantitative impact of urbanization on land subsidence in Wuhan, especially for spatially varying relationships between land subsidence and urbanization at different scales. In fact, knowledge of spatially varying relationships is an important prerequisite to protect cities from damage due to surface subsidence. In addition, previous studies have neglected the interactions between land subsidence and its various impact factors, which exhibit scale dependence.

To address the gaps in the existing studies, we first adopted the SBAS-InSAR method using Sentinel-1 radar satellite images to map land subsidence and characterized its spatial pattern in Wuhan. Furthermore, the bivariate Moran's I index was used to test and visualize the spatial correlations between land subsidence and urbanization. In addition, a geographically weighted regression (GWR) model was employed to explore the strengths

and directions of impacts of urbanization on land subsidence. Finally, we discussed scale effects on the spatially varying relationship between land subsidence and urbanization.

2. Study Area

Wuhan is located in the eastern region of the Jiang-Han Plain, with geographical coordinates between latitudes 29°58′ N and 31°22′ N and between longitudes 113°41′ E and 115°05′ E (see Figure 1). The Yangtze River and its largest branch, the Han River, have a confluence in central urban areas of Wuhan, which divides it into three main parts. The overall terrain of Wuhan is flat, with an average altitude of approximately 37 m above sea level. Soft clay layers with high compressibility and low strength are primarily spread along both banks of the Yangtze River in Wuhan. The belts of carbonate rock in Wuhan cover an area of more than 1100 km^2, and they align in a trend with a nearly east–west orientation. Wuhan is in a northern humid subtropical monsoon climate zone, which is characterized by plentiful rainfall and abundant sunshine. The average annual temperature is approximately 16.6 °C and precipitation ranges from 1150 mm to 1450 mm. The rainfall is concentrated mainly in the rainy season from June to August every year, accounting for 41% of the total precipitation.

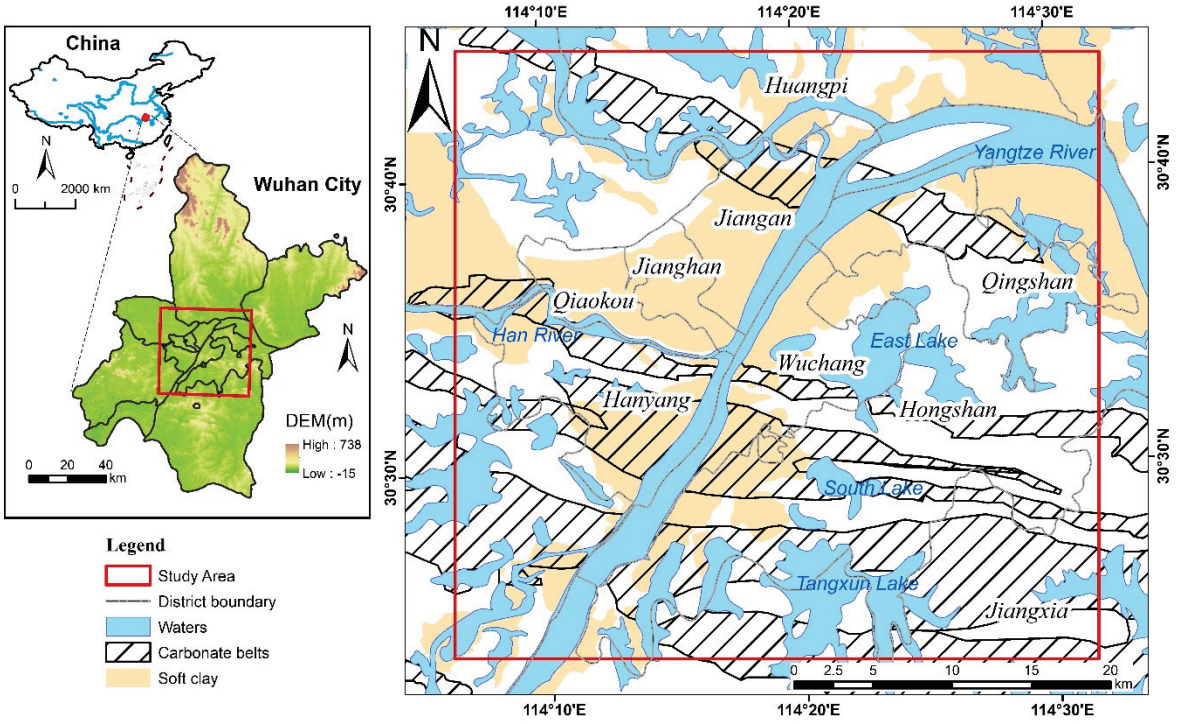

Figure 1. Location of study area and Wuhan city. The study area is represented by the red square. The simplified geological setting of the study area is shown in the right panel.

Wuhan, the capital city of Hubei Province, acts as an important industrial and economic center, cultural and educational base, and comprehensive transportation hub in central China. It covers a total area of 8494 km^2 with permanent residents totaling approximately 11.08 million in 2018. Wuhan has witnessed unprecedented economic development and urban sprawl since the new millennium.The urban built-up area in 2000 was 221.01 km^2, while it reached 812.39 km^2 at the end of 2018, and the average annual urban expansion rate was more than 7%. During the process of horizontal urban growth, a mass of high-rise buildings and underground space development promoted significant urban expansion in the vertical direction, thus resulting in the continuous emergence of the subsidence phenomena in Wuhan.

3. Materials and Methods

3.1. Land Subsidence Extraction

Sentinel-1 mission SAR sensors operate in the C-band (a wavelength of approximately 5.6 cm) and two satellites consisting of Sentinel-1 A/B satellites observe earth's surface globally within 6 days and 12 days for a single satellite. The Sentinel-1 interferometric wide swath mode (IW) provides large swath width of ~250 km images using the novel terrain observation by progressive scans (TOPSAR) imaging technique. The spatial resolutions of the IW mode are less than 20 m and 5 m in the azimuth and range directions (single look), respectively [34]. The Sentinel-1 satellite single look complex (SLC) data for interferometric applications can be accessed freely from European Space Agency (ESA) Copernicus Open Access Hub website (https://scihub.copernicus.eu (accessed on 8 December 2021).

In this work, we used 30 Sentinel-1A SAR images acquired in IW mode with VV (vertical-vertical) polarization between April 2015 and January 2019 to provide an assessment of land subsidence in Wuhan, China. All scenes were acquired along the descending orbits and average value of incidence angle is approximately 41.59°. The SBAS algorithm [17] was employed to process multitemporal IW SLC level-1 data products to derive the land subsidence velocity. A combination of time-series images within thresholds of spatial and temporal baseline (smaller than 148 m and less than 365 days) was selected to generate a connected graph of differential interferograms, which allows maximization of geometric coherence [35]. After the removal of interferometric pairs with low coherence and poor unwrapping, a total of 99 differential interferograms were obtained. The average number of connections per scene is more than 5 to ensure sufficient interconnected redundancy. The flat-earth phase of interferograms can be determined and removed by the precise orbit determination (POD) data provided by the ESA. Shuttle Radar Topographic Mission (SRTM) DEM data with a resolution of 30 m obtained from the U.S. Geological Survey (https://lta.cr.usgs.gov (accessed on 8 December 2021) was used to simulate and eliminate topographic phases and geocode displacement results. We selected 30 stable pixels without displacement located in the study site as ground control points (GCPs) to perform orbital refinement and phase reflattening for interferometric pairs. A multilooking operation with a ratio of 1:4 in the azimuth and range directions was carried out to improve the phase performance of the differential interferograms, and the interferograms were processed with the adaptive Goldstein-Werner filter to further mitigate the effects of speckle noise. Then, phase unwrapping of each interferometric pair was implemented with minimum cost flow (MCF) network and Delaunay 3D method, setting the unwrapping coherence threshold ranging from 0.2 to 0.3 by trial and error. The singular value decomposition (SVD) method was employed to generate the minimum norm least square solution for the unwrapped phase for pixels exhibiting consistently high coherence levels from interferograms and to retrieve the deformation time series. In addition, the atmospheric phase signal and nonlinear displacement component were estimated and subtracted from the displacement time series through a low pass spatial filter combined with a high temporal pass filter. Finally, the line-of-sight (LOS) deformation was transformed into the vertical direction using the radar incident angle assuming that the displacement in the horizontal direction is negligible. Thus, positive values of the deformation rate indicate that the ground is moving upwards in the vertical direction (uplift), whereas negative values mean that the ground is moving downwards in the vertical direction (subsidence). The land subsidence velocity map was extracted using SARScape module version 5.2.1 in the ENVI software environment and is shown in Figure 2.

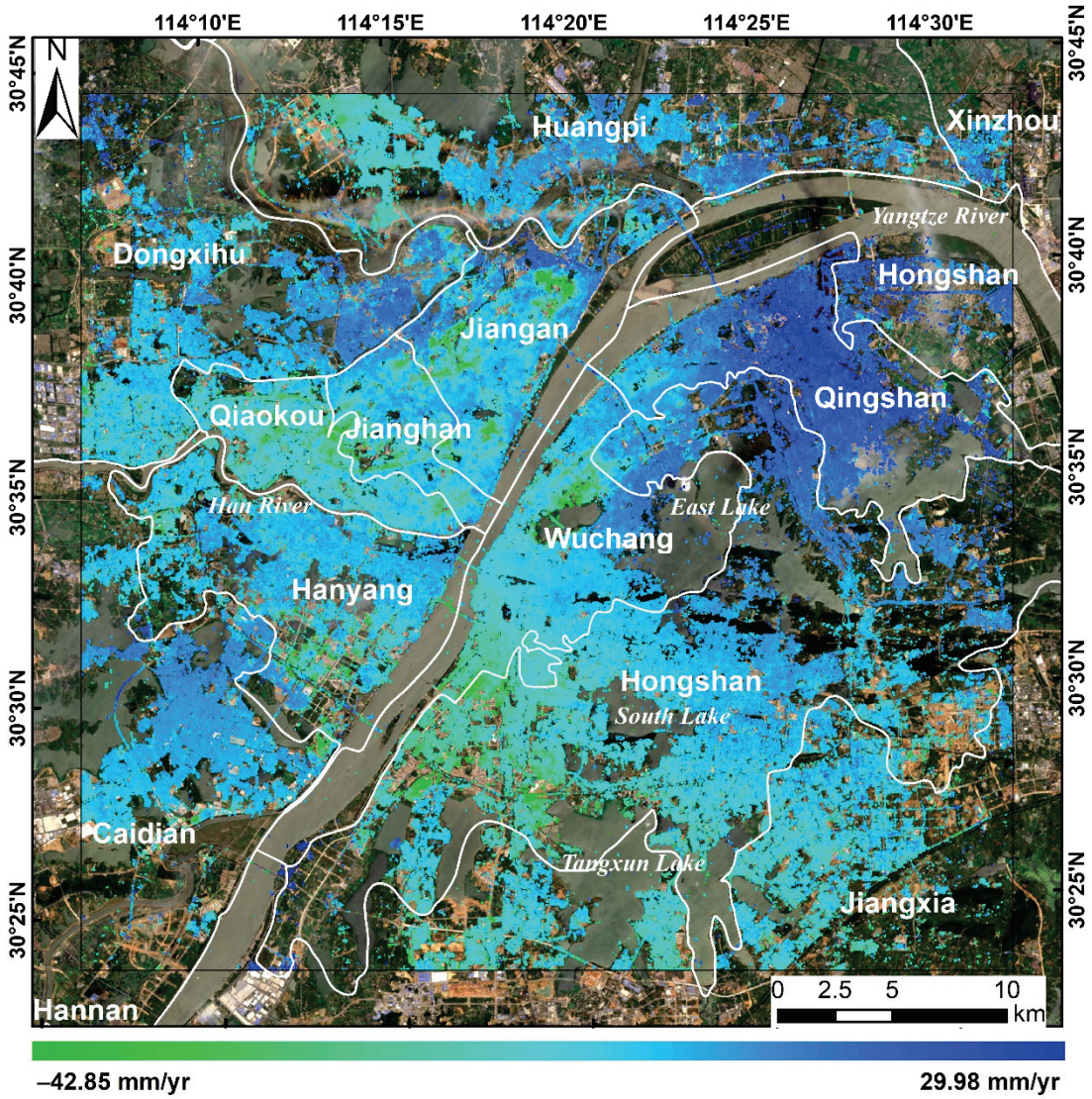

Figure 2. The average land subsidence velocity in the vertical direction from 2015 to 2018 across the study area in Wuhan city using Sentinel-1A SAR images. The Landsat-8 OLI optical image acquired on 27 June 2018 is used as the background.

3.2. Urbanization Metric Quantification

Impervious surfaces, defined as artificial structures that prevent natural infiltration of water into the soil, are considered an indicator of urbanization [36,37]. The impervious surface area (ISA) data were extracted from the global artificial impervious area (GAIA) dataset [38], an annual product in raster format with a 30 × 30 m resolution between 1985 and 2018. The original ISA raster data in 2018 were resampled at a resolution of 500 × 500 m. Building and road network data in vector format were obtained from the Wuhan Nature Resource and Planning Bureau.

Night-time lights generated by anthropogenic activities correlate significantly with numerous urbanization and socioeconomic parameters at regional or global scales, which have been recorded by satellite sensors for a long time. Satellite-based artificial night-time light (NTL) observations provide a unique proxy measure for unveiling urbanization and regional development [39]. Night-time light satellite images are obtained from the extended time series (2000–2018) of global NPP-VIIRS-like night-time light data [40], which has a consistent temporal trend at both global and regional scales. NTL and ISA can be applied to represent the comprehensive degree of urbanization because they both belong to physical quantity.

Numerous high-rise buildings and roads densely concentrated within the limits of plane space transform the natural landscape, which is necessary content and one of the spatial manifestations of urbanization. Buildings and roads parallel the intensity of urbanization, and the changes in landscape characteristics can reflect the degree of human influences on the environment. The building load plays an important factor in land subsidence. The central area of the building group has larger subsidence and the subsidence superimposition effect is obvious [41]. The kernel density method is employed to quantify the component of urbanization related to buildings, called building kernel density (BKD), based on the weight of base areas by the number of floors. Similarly, the line density method is used to estimate the component urbanization related to roads named road line density (RLD), based on the weight of the type and grade of roads.

3.3. Exploratory Spatial Data Analysis

Tobler's first law of geography [42] pointed out that ubiquitous spatial dependence occurs widely in geographical phenomena. Spatial dependency is defined as an effect between the occurrence of a given geographical location and that of surrounding locations. The global and local Moran's I indicators were used to describe the global spatial dependence among variables. The global Moran's I statistic is defined as follows [43]:

$$I_g = \frac{n\sum_{i=1}^{n}\sum_{j=1}^{n} W_{ij}\left(X_i - \overline{X}\right)\left(X_j - \overline{X}\right)}{\sum_{i=1}^{n}\sum_{j=1}^{n} W_{ij}\sum_{i=1}^{n}\left(X_i - \overline{X}\right)^2}, \quad (1)$$

where n is equal to the total number of spatial units in the study area; X_i and X_j are the observed value of the variable for spatial units i and j ($i \neq j$), respectively; $\overline{X}$ denotes the mean of the variable; and W_{ij} is the spatial weight between spatial units i and j defined by the inverse distance method, which is commonly used in row-standardized form. In general, the global Moran's I value ranges from -1 to 1. The Global Moran's I > 0 indicates that similar subsidence values are clustered together (positive spatial autocorrelation), whereas the global Moran's I < 0 indicates that dissimilar subsidence values are clustered together (negative spatial autocorrelation); and when the global Moran's I is zero, no spatial autocorrelation exists.

The local indicator of spatial association (LISA; local Moran's I statistic) measures the degree of spatial autocorrelation in each sample unit. For each spatial unit i, the LISA is calculated as follows [44,45]:

$$I_i = \frac{(n-1)\left(X_i - \overline{X}\right)}{\sum_{j=1,j\neq i}^{n}\left(X_j - \overline{X}\right)^2}\sum_{j=1,j\neq i}^{n} W_{ij}\left(X_j - \overline{X}\right), \quad (2)$$

The LISA index can identify two spatial cluster types: a high-high cluster indicating a high value surrounded by higher value; and a low-low cluster indicating a low subsidence value surrounded by neighbors with lower values. Spatial outliers refer to those values that are significantly different from the values of their neighbors, including low-high (a low value surrounded by high value) and high-low (a high value surrounded by low values) outliers. The Monte Carlo simulation method (999 permutations) was used to test the statistical significance of Moran's I, and significance value for spatial autocorrelation was set at $p < 0.05$. The global Moran's I is regarded as the average LISA value of all spatial units. The land subsidence/uplift clusters were obtained using GeoDa software version 1.12 (GeoDa Press LLC, Chicago, IL, USA) and are shown in Figure 3.

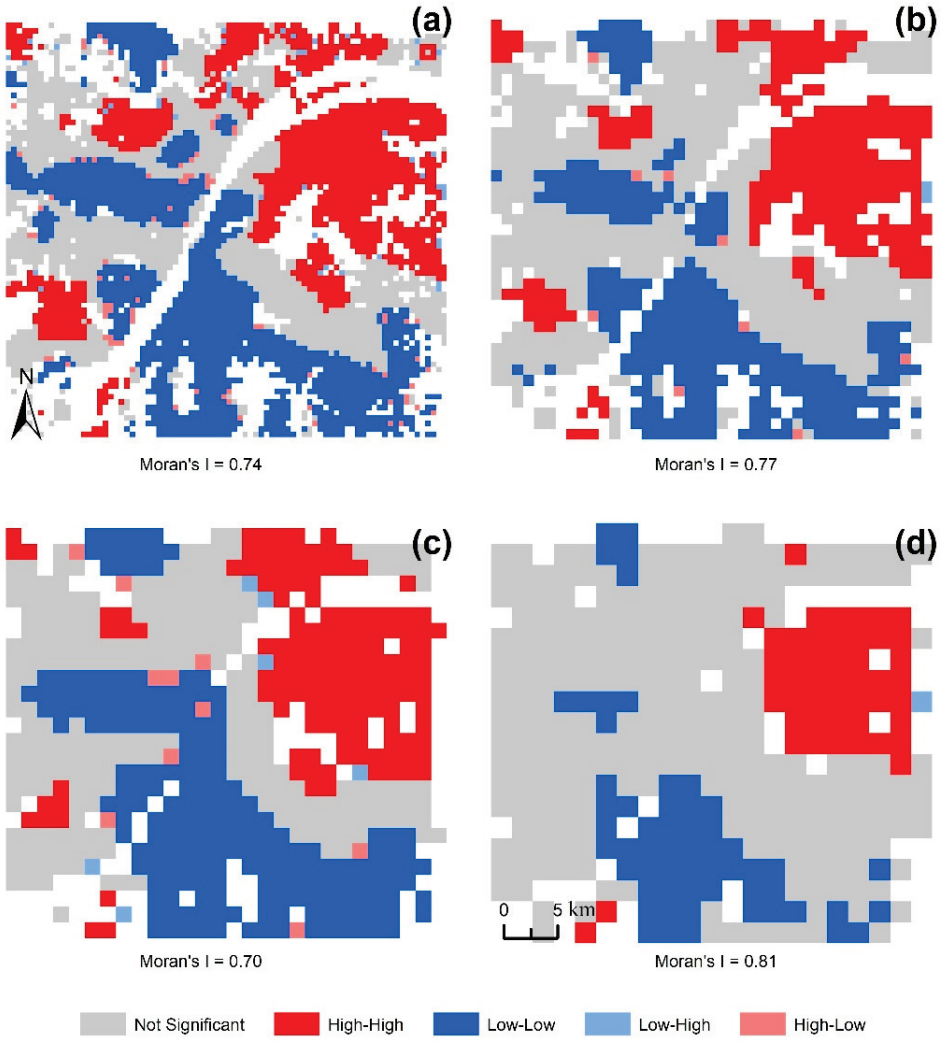

Figure 3. Local indicator of spatial association for land subsidence at block scales of 0.5 km × 0.5 km (**a**), 1 km × 1 km (**b**), 1.5 km × 1.5 km (**c**), and 2 km × 2 km (**d**) across the study area in Wuhan city.

We use the bivariate Moran's I index to measure the spatial association relationships between land subsidence and urbanization. The bivariate global Moran's I can detect whether a cluster or outlier exist in the study area, and bivariate local Moran's I is able to identify the exact location. The bivariate global Moran's I statistic is expressed as follows [46]:

$$I_{lm} = \sum_{p=1}^{n} \sum_{q=1}^{n} W_{pq} z_l^p z_m^q, \quad (3)$$

For each spatial unit p, the bivariate local Moran's I (bivariate LISA) is defined as follows:

$$I_{lm}^p = z_l^p \sum_{q=1}^{n} W_{pq} z_m^q, \quad (4)$$

where n is the total number of spatial units; z_l^p is the standard value of land subsidence in spatial unit p; z_m^q is the standard value of the urbanization metric in spatial unit q; and W_{pq} is the spatial weight between units p and q. The value of bivariate Moran's I ranges between -1 and 1, where a positive value suggests positive spatial correlation and a negative value indicates negative spatial correlation between two variables. When bivariate Moran's I is equal to 0, it signifies a random spatial pattern. In the case of statistical significance, the bivariate local Moran's I index divides the spatial relationship between land subsidence and urbanization in each sample unit into: "High-High (HH)", "Low-Low (LL)", "High-Low

(HL)", and "Low-High (LH)". We used Monte Carlo randomization (9999 permutations) to assess the significance of the bivariate Moran's I. When the test is significant ($p < 0.05$), there is a clustered or dispersed pattern between two variables. The land subsidence/uplift clusters were obtained using GeoDa software version 1.12 (GeoDa Press LLC, Chicago, IL, USA; Anselin, Luc, 2006) and are shown in Figure 3.

3.4. Geographically Weighted Regression Model

GWR is a relatively simple but effective, technique that extends the traditional regression framework for exploring spatial nonstationarity. It allows different relationships to exist at different points in space, such that local rather than global parameters can be estimated. Brunsdon [47] described spatial heterogeneity as a condition where a global regression model cannot describe the relationship between the response variable and explanatory variables because of the variation in characteristics among the observation regions. Global regression models, such as ordinary least squares (OLS), assume constant relationships over space, ignoring the effects of spatial heterogeneity among the observations. The GWR model can capture spatial nonstationarity by allowing the variation in relationships across space, and the model can be defined as follows [48]:

$$y_i = \beta_{i0} + \sum_k \beta_{ik} x_{ik} + \varepsilon_i \tag{5}$$

where y_i represents the value of the dependent variable, β_{i0} is the constant term, x_{ik} is the value of the independent variable k of unit I, β_{ik} is the parameter estimate associated with x_{ik}, and ε_i is the random error. The local estimates for unit i using matrix representation are calculated as follows [47,48]:

$$\hat{\beta}(i) = \left(X^T W(i) X\right)^{-1} X^T W(i) Y, \tag{6}$$

where X is a $(n \times (k+1))$ independent variable matrix, the first column of which represents the intercept term and all of them are set as 1; Y denotes an $n \times 1$ vector of dependent variables; $W(i)$ is an $n \times n$ matrix with the element W_{ij} indicating the spatial weight between units i and j, whose diagonal elements are spatial weights between two units, and the off-diagonal elements are set to zero. To obtain weights, we used the adaptive Gaussian function to define the spatial kernel:

$$W_{ij} = exp\left[-\left(\frac{d_{ij}}{b_i}\right)^2\right], \tag{7}$$

where b_i represents the spatial distance between units i and j, i.e., the bandwidth of unit i, which determines whether the kernel function will be performed.

The selection of bandwidth of spatial kernel function plays a critical role in GWR model performance [49], which is more important than the choice of spatial kernel function itself. In this work, we used the corrected Akaike information criterion (AICc) to determine the appropriate bandwidth of each kernel as it achieves a balance between goodness-of-fit and model complexity. Under the circumstance of GWR, the AICc is expressed as follows:

$$AIC = 2n\, log_e(\hat{\sigma}^2) + n\, log_e(2\pi) + n\left\{\frac{n + tr(S)}{n - 2 - tr(S)}\right\}, \tag{8}$$

where S denotes the hat matrix; $\hat{\sigma}^2$ is defined as the variance in the error term; and $tr(S)$ is the trace of the hat matrix.

4. Results and Discussion

4.1. Spatial Autocorrelations of Land Subsidence

A total of 2,013,600 pixels were ultimately identified as coherent targets (CTs) in the study area, the density of which was 1293 CTs per km^2. In general, CT pixels were more densely distributed in the core of urban areas with plenty of buildings and roads than peri-urban areas. Figure 2 demonstrates the spatial distribution of the CT pixels and the corresponding vertical deformation velocity field map across the study area. During the whole observation period, the annual deformation rate of CT pixels varied from −42.85 mm/year to +29.98 mm/year, and its average value and standard deviation were −1.0 mm/year and 3.86 mm/year, respectively. As shown in Figure 2, obvious heterogeneous land subsidence patterns were detected in Wuhan. The main land subsidence zones were distributed in central built-up areas of Wuhan along the bank of the Yangtze River. Most of the severe subsidence zones were located in Jianghan (JH), Jiangan (JA), Qiaokou (QK), Wuchang (WC), and Hongshan (HS) districts.

The global Moran's I index was calculated to examine the spatial dependence of land subsidence across the whole study area (Figure 3). The value of global Moran's I at the four block scales ranged from 0.70 to 0.81 and passed the significance test at the 99% confidence level, which indicated a significantly positive global spatial autocorrelation of land subsidence across the entire study area. In general, the values of the global Moran's index for land subsidence have an increasing trend with increasing block scale, with the exception of 1.5 km × 1.5 km. The multiscale comparative analysis of the global Moran's I index suggests that the spatial autocorrelation of land subsidence is not an accidental phenomenon dependent on scale.

The LISA index was used to depict the local spatial correlation of land subsidence across the study area (Figure 3). The cluster maps of LISA in Figure 3 exhibit the spatial aggregation state of land subsidence and distinct spatial patterns of the clusters at four block scales. The low-low clusters (serious land subsidence) were mainly concentrated in QK, JH, the south of Hanyang (HY), the southwest of HS, the north of Jiangxia (JX) and WC along the southern bank of the Yangtze River, while the high-high value agglomerations (land uplift) were mostly located north of HS and south of Huangpi (HP) along the Yangtze River. With an increase in block scale, the area of low-value and high-value agglomerations for land subsidence gradually shrank and some clusters disappeared. Nevertheless, the spatial distribution of low-value and high-value agglomerations for land subsidence became more concentrated. The LISA index can accurately delineate the funnel of land subsidence quantitatively. Thus, the multiscale LISA index can help guide corresponding actions at different administrative levels to address the consequences of land subsidence. The small number of spatial outliers (low-high or high-low) for land subsidence at four block scales were sporadically distributed within the study area. The high-low outlier refers to area where a unit with higher subsidence value is surrounded by other comparatively lower subsidence value units, it is likely to develop into an emerging subsiding area in the near future according to Tobler's first law of geography [42].

4.2. Spatial Patterns of Urbanization

As shown in Figure 4, all urbanization indicators (ISA, NTL, BKD and RLD) gradually decrease from the city center to its outer periphery, and their spatial distributions are similar to each other globally. The ratio of the area for ISA across the study area is 44.40%, and the averages of NTL, BKD, and RLD are 16.31 $n \cdot W \cdot cm^{-2} \cdot sr^{-1}$, 523.40, and 14.93, respectively. ISA and NTL are comprehensive indicators of urbanization, while BKD and RLD focus on a single aspect of urbanization. Therefore, the intragroup similarity between ISA and NTL, BKD and RDL is higher than the intergroup similarity in terms of spatial patterns. It is observed that water bodies, which are mainly composed of rivers, lakes, and reservoirs, play a crucial role in shaping the urban expansion of Wuhan according to the spatial distribution of urbanization indicators. In addition, BKD and RLD were both found to exhibit low values compared to the relatively values of high ISA and NTL in the southeastern part of

the study area, which indicated local spatial disparities among urbanization indicators. The urban-rural gradient of NTL and BKD has a significant spatial variation as opposed to ISA and RLD. Although the spatial distribution of RLD is different from that of the original road, RLD also showed an obvious linear distribution characteristic.

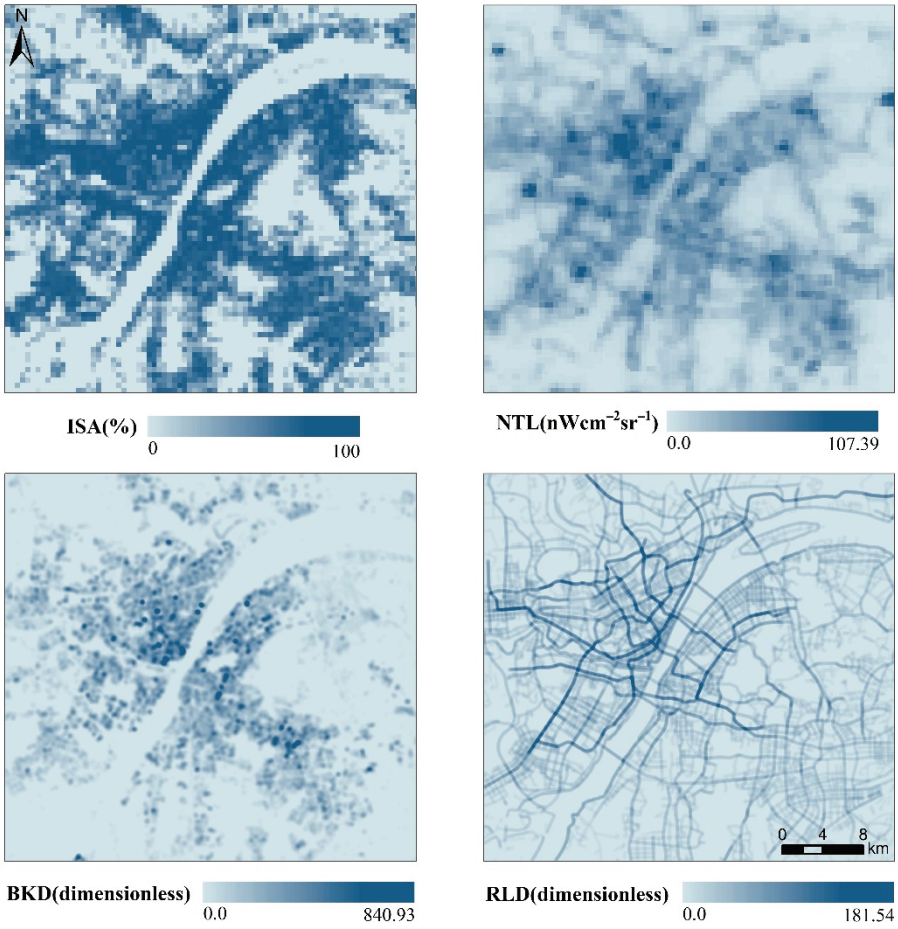

Figure 4. Spatial distribution of urbanization indicators of Wuhan city in 2018. Abbreviations: impervious surface area (ISA); night-time lights (NTL); building kernel density (BKD); road line density (RLD).

4.3. Spatial Associations between Land Subsidence and Urban Development

The values of global bivariate Moran's I at four block scales are less than 0 ($p < 0.01$), indicating significantly negative spatial correlations between the four types of urbanization indicators and surface deformation (Figure 5). That is, overall, urbanization is an important factor leading to land subsidence. However, the degree of negative spatial correlation varied with different urbanization factor types and scales. Among these types, the strongest negative correlation was found between land subsidence and BKD (Moran's I: ranging from −0.1911 to −0.1639), followed by that between land subsidence and NTL (Moran's I: ranging from −0.1793 to −0.1220) and that between land subsidence and RLD (Moran's I: ranging from −0.1224 to −0.0683). The weakest correlation was between land subsidence and ISA (Moran's I: ranging from −0.1121 to −0.0666). The negative spatial correlation between urbanization and land deformation manifested as a gradual increase in the block size.

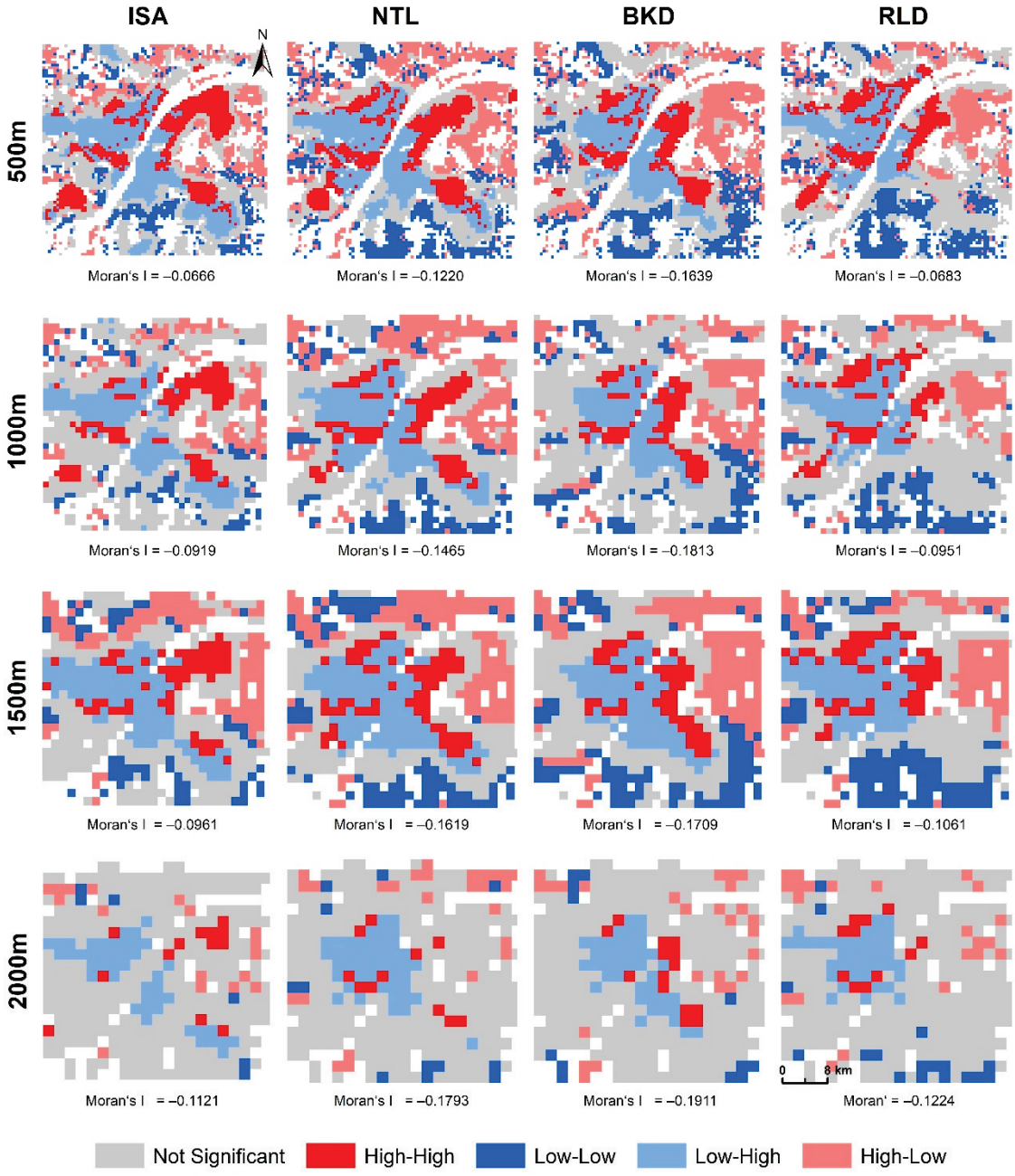

Figure 5. Bivariate local indicators of spatial associations between land subsidence and four kinds of urbanization indicators in Wuhan city at four block scales.

The cluster maps of the bivariate local Moran's I in Figure 5 further illustrate the pattern of spatial heterogeneity in the relationships between land subsidence and urbanization at four block scales. We observed an obvious clustering pattern similarity between the spatial distributions of each of the urbanization indicators and land subsidence in the study area at four block scales. The low-high spatial outliers were mainly concentrated in the urban center of Wuhan, particularly in JA, JH, QK, and WC along the bank of the Yangtze River, and the southwest HS. A low-low cluster was significantly observed in the periphery of the study area, especially in the south HS, north JX. The high-low areas were mostly located across the region clustered in the northeast section of the study area. A high-high cluster was mainly distributed in the transition zone between East Lake and the Yangtze River and Hanyang (HY) district along the bank of the Han River, almost adjacent to the low-high regions. At block scale of 2 km $\times$ 2 km, the number of statistically significant

clusters and their occupied areas both decreased compared to those at other scales in terms of the four types of urbanization indicators. In particular, the other three types of clusters (except for low-high outliers) exhibited drastic declines in the number of clusters and the occupied areas and the low-high cluster appeared to have a concentrated distribution. The degree of global spatial correlation was the highest when low-high outliers became dominant agglomerates because clusters whose bivariate spatial autocorrelation type was opposing no longer canceled each other out. This suggests that the value of local bivariate Moran's I between land subsidence and urbanization indicators depends on the block scale to some degree.

4.4. Impacts of Urbanization on Land Subsidence

To prevent the disturbance of potential multicollinearity on the parameter estimation of the model, each urbanization factor was independently analyzed with the land subsidence indicator in the GWR model due to high correlations existing among the urbanization indicators [50]. Thus, a total of $4 \times 4 = 16$ GWR models were generated and combined with four block scales. The standardized residual values of all GWR models range from −11.0298 to 6.7591 at most; more than 97% is in the range of −2.58–2.58. Therefore, the standardized residual values of all GWR models are randomly distributed at a 95% confidence level. To further examine whether the residuals from GWR models exhibit spatial randomness, a spatial autocorrelation analysis was performed on the residuals to obtain the global Moran's I statistics. As shown in Table 1, in general, low spatial autocorrelations of residuals from the GWR model are detected at the small block scale compared to the large scale, indicating that the variance in land subsidence over the study area is relatively random and exhibits spatial stationarity at the small block scale.

Table 1. Global Moran's I for residuals of GWR models.

Scale	ISA	NTL	BKD	RLD
500 m	0.0570	−0.0377	−0.0623	−0.0581
1000 m	**0.1267**	−0.0309	−0.0711	−0.0038
1500 m	−0.0281	−0.0585	−0.0278	−0.0129
2000 m	**0.1150**	**0.1167**	**0.1268**	0.0216

Notes: Bold numbers denote significance at less than 0.01 level. Abbreviations: impervious surface area (ISA); night-time lights (NTL); building kernel density (BKD); road line density (RLD).

The local parameter estimates of the GWR model indicate the spatially varying relationships between the independent variable and response variable at different locations. The magnitude of the absolute value of the model regression coefficient denotes the degree of impact of an independent variable on land subsidence. In addition, the local adjusted determined coefficient (adjusted R^2) value from the GWR model is used to detect and assess the ability of the explanatory variable to explain the spatial variance in land subsidence, and a higher local adjusted R^2 value means better performance of the model. The ranges of local parameter estimate and adjusted R^2 between land subsidence and urbanization indicators obtained from GWR models are summarized in Table 2. Both positive and negative relationships are identified by local coefficients between urbanization indicators and land subsidence at different block scales, and the average of regression coefficients for NTL (except at the 1500 m scale) is less than 0. The local adjusted R^2 indicated that the urbanization indicators could explain more than 75% of the spatial variance in land subsidence on average at the four block scales (Table 2). In general, the explanatory power of urbanization indicators on land subsidence presents no significant difference from small to large block scales. However, the higher adjusted R^2 suggests that NTL has a stronger ability to explain the land subsidence changes than ISA at different block scales, which indicates that both ISA and NTL are relatively comprehensive indicators measuring the degree of urbanization, although NTL can reflect dynamic human activities and urban vitality better than ISA because artificial lights provide a direct signature of human activity [51].

Table 2. Descriptive statistical summary for GWR models.

Scale	Variable	Coefficient					Adjusted R^2
		Min	Lower Quartile	Mean	Upper Quartile	Max	
500 m	ISA	−0.2393	−0.0058	0.0240	0.0528	0.3389	0.7525
	NTL	−2.2963	−0.1292	−0.0026	0.1413	3.6109	0.7929
	BKD	−32.1901	−0.0593	0.0722	0.1371	39.3492	0.8180
	RLD	−3.1004	−0.0548	0.0295	0.0913	1.9124	0.8205
1000 m	ISA	−0.2357	−0.0332	0.0126	0.0653	0.2151	0.7535
	NTL	−1.4376	−0.1626	−0.0126	0.1586	2.2220	0.8191
	BKD	−13.7699	−0.0816	0.0356	0.1842	6.6497	0.8374
	RLD	−0.7648	−0.0905	0.0389	0.1339	1.5085	0.8019
1500 m	ISA	−0.5730	−0.0766	0.0043	0.1050	0.3629	0.7895
	NTL	−4.4310	−0.1935	0.0129	0.2425	3.4730	0.8667
	BKD	−1.4849	−0.0952	0.1182	0.2601	3.4356	0.7841
	RLD	−0.8631	−0.1476	0.0408	0.2192	2.0384	0.7835
2000 m	ISA	−0.5431	−0.0940	0.0013	0.1154	0.3364	0.7701
	NTL	−1.2506	−0.2347	−0.0581	0.1684	0.9370	0.7805
	BKD	−3.2007	−0.1089	0.0918	0.2867	2.2430	0.7660
	RLD	−1.7809	−0.2026	0.0237	0.2558	1.8308	0.8136

As shown in Figure 6, the explanatory ability of GWR revealed by the local adjusted R^2 varies spatially. In general, GWR exhibits stronger explanatory power in WC, QS, central HS adjacent to East Lake, and northern JX. In contrast, the prediction ability of GWR appears to be lower in JA and around the periphery of the study area. The spatial patterns of coefficients of independent variables for urbanization indicators identified by GWR are clearly shown in Figure 7. In terms of the spatially varying regression coefficients, the directions (positive or negative) and strengths of the relationships between land deformation and urbanization indicators are not constant over the study area at different block scales. This result suggests that homogeneity and heterogeneity in the spatial relationships between land subsidence and urbanization indicators are sensitive to spatial scales. In addition, the spatial patterns of the regression coefficients of urbanization indicators tend to become more similar with increasing block scale. At the 2000 km block scale, negative relationships between urbanization indicators and land surface deformation are detected for JA, JH, QK, and WC along the Yangtze River and south HS, indicating that urban construction and anthropogenic activities resulted in the occurrence of land subsidence.

As shown in Figure 7, the negative values of the regression coefficients from the GWR model concentration region coincide with the distribution of soft soils or carbonate rocks, which have a high degree of urbanization. According to the definitions of urbanization indicators (ISA, NTL, BKD, and RLD), a region with a high degree of urbanization has large dynamic and static loads or is undergoing frequent construction and renewal activities. The urban construction of Wuhan city witnessed a stage of rapid development during the study period. In the construction process, groundwater extraction is required for operations around sites where buildings and subways are constructed. Previous studies have shown that the loss of groundwater results in consolidation of highly compressible soft soils and the dissolution of carbonate rocks, which thereby leads to land subsidence [30]. At the same time, the excavation of a subway tunnel inevitably disturbs the surrounding soil layers, followed by ground settlement. After the completion of project construction, i.e., in the process of building and subway operation, continuous dynamic and static loading act on the foundations of structures such as buildings, subways, and bridges. When the soil layer underneath a structure can no longer support the loading, settlement occurs within the structure and the surrounding area [32,41,52].

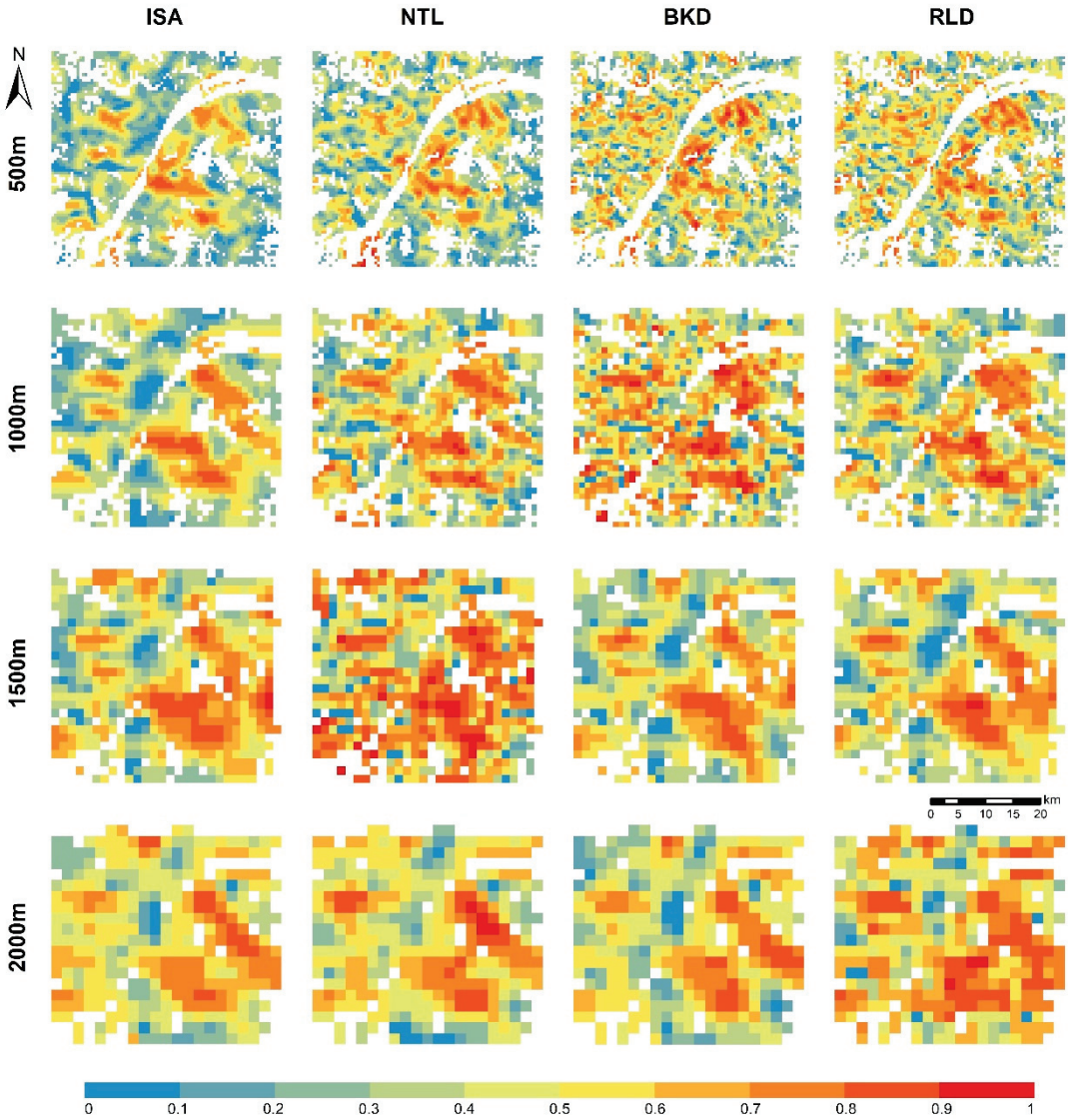

Figure 6. Spatial patterns of local adjusted R^2 obtained from the GWR model for urbanization indicators at four block scales.

In contrast, some unexpected local relationships are also identified by the GWR model. For example, the southeastern and northeastern parts of the study area have concentrations of positive values. The density of deformation monitoring point pixels obtained in peri-urban areas is sparser than that in the center of the city due to dense vegetation and abundant waters. As a result, the land surface deformation monitoring data in the aggregated unit are easily influenced by random errors, and such unexpected results thus appear. Additionally, some omitted unknown variables in the GWR model may also contribute to the unexpected results.

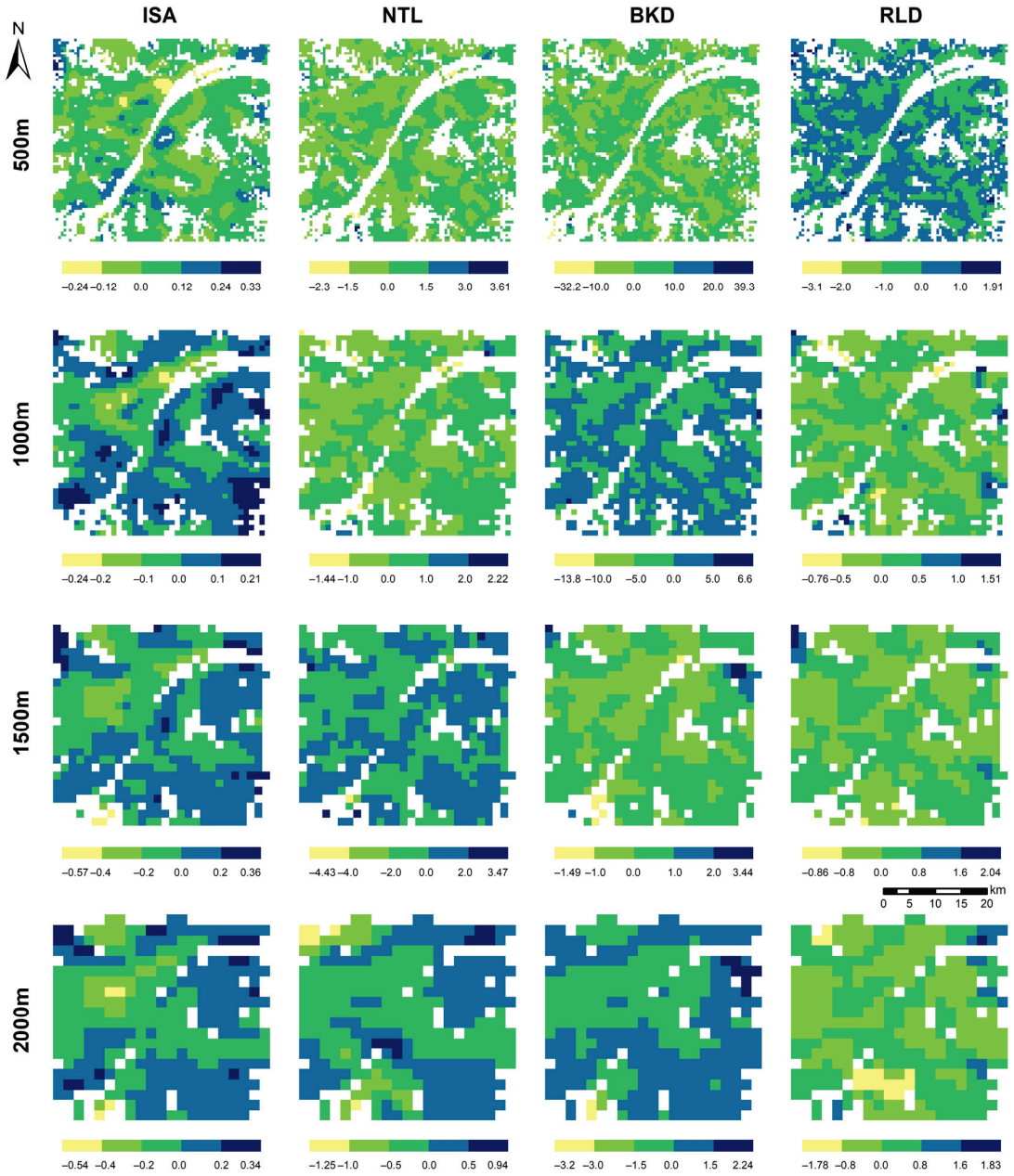

Figure 7. Spatial distribution of regression coefficients between urbanization indicators and land subsidence.

4.5. Scale Effects of Relationships between Land Subsidence and Urbanization

The scale effect refers to smaller units being aggregated into larger units for spatial data, this likely provides inconsistent results [53]. Numerous studies have pointed out that the scale effect has been proven to be ubiquitous in the analysis of geographical phenomena and processes [54–56]. Neglecting the scale effect may lead to uncertainty in the results of spatial analyses and statistics and may even produce false conclusions. Thus, scale effects cannot be overlooked when analyzing the relationship between land subsidence and urbanization. In this work, the global and local bivariate Moran's I (Figure 5), the spatial patterns of the local adjusted R^2 (Figure 6), and the directions and strengths of the identified relationships between land subsidence and urbanization (Figure 7) all varied among the different block scales. In other words, the above results showed that the spatially varying relationship between land subsidence and urbanization was also scale dependent. First, the explanatory ability of the GWR models increased as the block scale increased,

but approximately 20% of the spatial variance in land subsidence remained unexplained even at a block scale of 2 km. The reason for this may be that the larger block size was able to significantly reduce random disturbance for the estimation of land subsidence at the statistical unit due to the effect of spatial filtering. Nevertheless, the spatial autocorrelations of the residuals produced from the GWR models did not change accordingly with the variation in the block scale. Notably, significant positive spatial autocorrelations were found in the GWR model for land subsidence and ISA at the scales of 1.0 km (Moran's I = 0.1267, $p < 0.01$) and 2.0 km (Moran's I = 0.1150, $p < 0.01$), NTL (Moran's I = 0.1167, $p < 0.01$), and BKD (Moran's I = 0.1268, $p < 0.01$) at the 2.0 km scale. This finding indicated that although the results of the GWR model varied with changes in the block scale, certain bias occurred randomly in the calibration due to the interference of other factors that were not considered.

In fact, the interactions between land subsidence and urbanization indicators are very complicated, and thus it is difficult to design an appropriate method to sample spatial data. Therefore, to correctly analyze such interactions, a comparative analysis with multiscale data is very important and necessary. Although it is difficult to recommend the "best" spatial scales for the GWR model because the influences of factors vary over different sampling scales [57], the degrees of fitting for an observation measured by the adjusted R^2 and the spatial autocorrelation of the GWR model residuals should both be considered for the selection of a suitable block scale. In general, the suitable spatial scale in a GWR model should not only effectively prevent the interference of random factors but also reveal locally varying patterns of the identified relationships. Furthermore, the directions (positive or negative) and strengths of the spatial regression coefficients produced for the GWR models also varied across various scales and implied that spatial relationships between land subsidence and urbanization indicators gradually became global and that the spatial stationarity tended to be strong, which was consistent with the spatial resolution effects on the relationships between urban heat islands and their impact factors [58,59].

In this paper, an adaptive Gaussian kernel using the golden section search method was adopted to identify the optimal bandwidth size for a GWR model and mainly focused on the effects of block scale [60]. Future work is needed to consider a comparative analysis with multi-bandwidth models for GWR. In addition, we only analyzed spatially varying relationships between land subsidence and urbanization indicators at four block scales. As a result, it remains unknown whether there is a threshold within which scale effects are significant. It is therefore necessary to conduct a further comparative study of the GWR results obtained for a series of block scales [61].

5. Conclusions

In this study, the land deformation in Wuhan, the largest city in central China, obtained from Sentinel-1 SAR time-series datasets based on the SBAS-InSAR method was presented. We investigated the spatially varying relationships between land subsidence and urbanization in Wuhan by using bivariate Moran's I and GWR models. Our analysis concentrated on a set of empirical results that support the following conclusions. The derived deformation results showed that land subsidence was obvious and unevenly distributed in the study area, the annual deformation rate varies from −42.85 mm/year to +29.98 mm/year, and its average value was −1.0 mm/year. A clear spatial pattern for land subsidence in Wuhan was mapped, and several apparent subsidence funnels identified by the LISA index were primarily located in central urban areas. As indicated by bivariate global and local Moran's I, four types of urbanization indicators ISA, NTL, BKD, and RLD, were found to be significantly spatially correlated with land subsidence at different scales, which implied that the urbanization indicators could have an impact on the land subsidence of its surrounding neighbors. In addition, the GWR model results showed that all urbanization indicators were significantly associated with land subsidence across the whole study area in Wuhan, mainly controlled by the thickness of soft soil, but the relationships were not completely consistent among land subsidence and different urbanization indicators. The results of

bivariate Moran's I and GWR confirmed that the relationships between land subsidence and urbanization varied spatially in Wuhan at multiple spatial scales. Moreover, scale dependence existed both in bivariate Moran's I and GWR models for land subsidence and all urbanization indicators, however, a "best" spatial scale could not be confirmed because the disturbances of factors vary over different sampling scales. We suggest that the results from our study advance the understanding of the spatially varying relationships between land subsidence and urbanization, and it is hoped that they will provide guidance for subsidence control and sustainable urban planning.

Author Contributions: Conceptualization, Z.W.; methodology, Z.W.; software, Y.Z.; validation, Y.L. (Yaolin Liu), Z.W. and Y.Z.; formal analysis, Z.W.; investigation, Z.W., Y.L. (Yanfang Liu) and B.W.; resources, Y.L. (Yanfang Liu) and B.W.; data curation, Y.Z. and Y.L. (Yanfang Liu); writing—original draft preparation, Z.W.; writing—review and editing, Z.W., Y.L. (Yaolin Liu) and Y.Z.; visualization, G.Z.; supervision, Y.L. (Yaolin Liu); project administration, Y.L. (Yaolin Liu); funding acquisition, Y.L. (Yaolin Liu). All authors have read and agreed to the published version of the manuscript.

Funding: This research was jointly funded by the (Grant No. 2017YFB0503601), the China Postdoctoral Science Foundation (2021M700760).

Data Availability Statement: Not applicable.

Acknowledgments: We thank the European Space Agency for its considerable efforts in collecting and distributing the remotely sensed SAR data, and making Sentinel-1 available at no cost out of generosity (https://scihub.copernicus.eu (accessed on 8 December 2021). We also appreciate Tsinghua University for the Finer Resolution Observation and Monitoring of Global Land Cover (FROM-GLC) dataset released to the public for free (http://data.ess.tsinghua.edu.cn (accessed on 8 December 2021). Shuttle Radar Topographic Mission DEM data at 30 m resolution was downloaded for free from U.S. Geological Survey (https://lta.cr.usgs.gov/ (accessed on 28 December 2021)). The extended time series (2000–2018) of night-time light data with a spatial resolution of 15 arcsec (about 500 m) was freely downloaded from Harvard Dataverse website (https://doi.org/10.7910/DVN/YGIVCD (accessed on 8 December 2021). We are deeply grateful to the two anonymous reviewers for valuable and constructive comments that improved the quality of the manuscript significantly.

Conflicts of Interest: The authors declare no conflict of interest.

References

1. Chen, F.; Guo, H.; Ma, P.; Lin, H.; Wang, C.; Ishwaran, N.; Hang, P. Radar interferometry offers new insights into threats to the Angkor site. *Sci. Adv.* **2017**, *3*, e1601284. [CrossRef]
2. Zhao, R.; Li, Z.; Feng, G.; Wang, Q.; Hu, J. Monitoring surface deformation over permafrost with an improved SBAS-InSAR algorithm: With emphasis on climatic factors modeling. *Remote Sens. Environ.* **2016**, *184*, 276–287. [CrossRef]
3. Qu, F.; Zhang, Q.; Lu, Z.; Zhao, C.; Yang, C.; Zhang, J. Land subsidence and ground fissures in Xi'an, China 2005–2012 revealed by multi-band InSAR time-series analysis. *Remote Sens. Environ.* **2014**, *155*, 366–376. [CrossRef]
4. Chen, F.; Lin, H.; Li, Z.; Chen, Q.; Zhou, J. Interaction between permafrost and infrastructure along the Qinghai–Tibet Railway detected via jointly analysis of C- and L-band small baseline SAR interferometry. *Remote Sens. Environ.* **2012**, *123*, 532–540. [CrossRef]
5. Chen, W.; Chen, W.; Gong, H.; Chen, B.; Chen, B.; Liu, K.; Gao, M.; Zhou, C. Spatiotemporal evolution of land subsidence around a subway using InSAR time-series and the entropy method. *Gisci. Remote Sens.* **2017**, *54*, 78–94. [CrossRef]
6. Nicholls, R.J.; Lincke, D.; Hinkel, J.; Brown, S.; Vafeidis, A.T.; Meyssignac, B.; Hanson, S.E.; Merkens, J.; Fang, J. A global analysis of subsidence, relative sea-level change and coastal flood exposure. *Nat. Clim. Chang.* **2021**, *11*, 338–342. [CrossRef]
7. Ye, S.; Luo, Y.; Wu, J.; Yan, X.; Wang, H.; Jiao, X.; Teatini, P. Three-dimensional numerical modeling of land subsidence in Shanghai, China. *Hydrogeol. J.* **2016**, *24*, 695–709. [CrossRef]
8. Yu, H.; Gong, H.; Chen, B.; Liu, K.; Gao, M. Analysis of the influence of groundwater on land subsidence in Beijing based on the geographical weighted regression (GWR) model. *Sci. Total Environ.* **2020**, *738*, 139405. [CrossRef] [PubMed]
9. Higgins, S.A. Review: Advances in delta-subsidence research using satellite methods. *Hydrogeol. J.* **2016**, *24*, 587–600. [CrossRef]
10. Ma, P.; Wang, W.; Zhang, B.; Wang, J.; Shi, G.; Huang, G.; Chen, F.; Jiang, L.; Lin, H. Remotely sensing large- and small-scale ground subsidence: A case study of the Guangdong–Hong Kong–Macao Greater Bay Area of China. *Remote Sens. Environ.* **2019**, *232*, 111282. [CrossRef]
11. Zhang, B.; Wang, R.; Deng, Y.; Ma, P.; Lin, H.; Wang, J. Mapping the Yellow River Delta land subsidence with multitemporal SAR interferometry by exploiting both persistent and distributed scatterers. *ISPRS J. Photogramm.* **2019**, *148*, 157–173. [CrossRef]

12. Dinar, A.; Esteban, E.; Calvo, E.; Herrera, G.; Teatini, P.; Tomás, R.; Li, Y.; Ezquerro, P.; Albiac, J. We lose ground: Global assessment of land subsidence impact extent. *Sci. Total Environ.* **2021**, *786*, 147415. [CrossRef] [PubMed]
13. Herrera-García, G.; Ezquerro, P.; Tomás, R.; Béjar-Pizarro, M.; López-Vinielles, J.; Rossi, M.; Mateos, R.M.; Carreón-Freyre, D.; Lambert, J.; Teatini, P.; et al. Mapping the global threat of land subsidence. *Science* **2021**, *371*, 34–36. [CrossRef]
14. Liu, X.; Wang, Y.; Yan, S.; Shao, Y.; Zhou, H.; Li, Y. Ground subsidence characteristics associated with urbanization in East China analyzed with a Sentinel-1A-based InSAR time series approach. *Bull. Eng. Geol. Environ.* **2019**, *78*, 4003–4015. [CrossRef]
15. Ferretti, A.; Prati, C.; Rocca, F. Nonlinear subsidence rate estimation using permanent scatterers in differential SAR interferometry. *IEEE Trans. Geosci. Remote Sens.* **2000**, *38*, 2202–2212. [CrossRef]
16. Ferretti, A.; Prati, C.; Rocca, F. Permanent Scatterers in SAR Interferometry. *IEEE Trans. Geosci. Remote Sens.* **2001**, *39*, 8–20. [CrossRef]
17. Berardino, P.; Fornaro, G.; Lanari, R.; Sansosti, E. A new algorithm for surface deformation monitoring based on small baseline differential SAR interferograms. *IEEE Trans. Geosci. Remote Sens.* **2002**, *40*, 2375–2383. [CrossRef]
18. Usai, S. A least squares database approach for SAR interferometric data. *IEEE Trans. Geosci. Remote Sens.* **2003**, *41*, 753–760. [CrossRef]
19. Heleno, S.I.N.; Oliveira, L.G.S.; Henriques, M.J.; Falcão, A.P.; Lima, J.N.P.; Cooksley, G.; Ferretti, A.; Fonseca, A.M.; Lobo-Ferreira, J.P.; Fonseca, J.F.B.D. Persistent Scatterers Interferometry detects and measures ground subsidence in Lisbon. *Remote Sens. Environ.* **2011**, *115*, 2152–2167. [CrossRef]
20. Liu, Y.; Liu, J.; Xia, X.; Bi, H.; Huang, H.; Ding, R.; Zhao, L. Land subsidence of the Yellow River Delta in China driven by river sediment compaction. *Sci. Total Environ.* **2021**, *750*, 142165. [CrossRef]
21. Meyer, F.J.; McAlpin, D.B.; Gong, W.; Ajadi, O.; Arko, S.; Webley, P.W.; Dehn, J. Integrating SAR and derived products into operational volcano monitoring and decision support systems. *ISPRS J. Photogramm.* **2015**, *100*, 106–117. [CrossRef]
22. Dong, J.; Zhang, L.; Liao, M.; Gong, J. Improved correction of seasonal tropospheric delay in InSAR observations for landslide deformation monitoring. *Remote Sens. Environ.* **2019**, *233*, 111370. [CrossRef]
23. Necsoiu, M.; Onaca, A.; Wigginton, S.; Urdea, P. Rock glacier dynamics in Southern Carpathian Mountains from high-resolution optical and multi-temporal SAR satellite imagery. *Remote Sens. Environ.* **2016**, *177*, 21–36. [CrossRef]
24. Zhang, Z.; Wang, C.; Tang, Y.; Fu, Q.; Zhang, H. Subsidence monitoring in coal area using time-series InSAR combining persistent scatterers and distributed scatterers. *Int. J. Appl. Earth Obs.* **2015**, *39*, 49–55. [CrossRef]
25. Castellazzi, P.; Arroyo-Domínguez, N.; Martel, R.; Calderhead, A.I.; Normand, J.C.L.; Gárfias, J.; Rivera, A. Land subsidence in major cities of Central Mexico: Interpreting InSAR-derived land subsidence mapping with hydrogeological data. *Int. J. Appl. Earth Obs.* **2016**, *47*, 102–111. [CrossRef]
26. Zuo, J.; Gong, H.; Chen, B.; Liu, K.; Zhou, C.; Ke, Y. Time-Series Evolution Patterns of Land Subsidence in the Eastern Beijing Plain, China. *Remote Sens.* **2019**, *11*, 539. [CrossRef]
27. Costantini, M.; Ferretti, A.; Minati, F.; Falco, S.; Trillo, F.; Colombo, D.; Novali, F.; Malvarosa, F.; Mammone, C.; Vecchioli, F.; et al. Analysis of surface deformations over the whole Italian territory by interferometric processing of ERS, Envisat and COSMO-SkyMed radar data. *Remote Sens. Environ.* **2017**, *202*, 250–275. [CrossRef]
28. Zhou, L.; Guo, J.; Hu, J.; Li, J.; Xu, Y.; Pan, Y.; Shi, M. Wuhan Surface Subsidence Analysis in 2015–2016 Based on Sentinel-1A Data by SBAS-InSAR. *Remote Sens.* **2017**, *9*, 982. [CrossRef]
29. Han, Y.; Zou, J.; Lu, Z.; Qu, F.; Kang, Y.; Li, J. Ground Deformation of Wuhan, China, Revealed by Multi-Temporal InSAR Analysis. *Remote Sens.* **2020**, *12*, 3788. [CrossRef]
30. Jiang, H.; Balz, T.; Cigna, F.; Tapete, D. Land Subsidence in Wuhan Revealed Using a Non-Linear PSInSAR Approach with Long Time Series of COSMO-SkyMed SAR Data. *Remote Sens.* **2021**, *13*, 1256. [CrossRef]
31. Bai, L.; Jiang, L.; Wang, H.; Sun, Q. Spatiotemporal Characterization of Land Subsidence and Uplift (2009–2010) over Wuhan in Central China Revealed by TerraSAR-X InSAR Analysis. *Remote Sens.* **2016**, *8*, 350. [CrossRef]
32. Zhang, Y.; Liu, Y.; Jin, M.; Jing, Y.; Liu, Y.; Liu, Y.; Sun, W.; Wei, J.; Chen, Y. Monitoring Land Subsidence in Wuhan City (China) using the SBAS-InSAR Method with Radarsat-2 Imagery Data. *Sensors* **2019**, *19*, 743. [CrossRef]
33. Ding, Q.; Shao, Z.; Huang, X.; Altan, O.; Zhuang, Q.; Hu, B. Monitoring, analyzing and predicting urban surface subsidence: A case study of Wuhan City, China. *Int. J. Appl. Earth Obs.* **2021**, *102*, 102422. [CrossRef]
34. Torres, R.; Snoeij, P.; Geudtner, D.; Bibby, D.; Davidson, M.; Attema, E.; Potin, P.; Rommen, B.; Floury, N.; Brown, M.; et al. GMES Sentinel-1 mission. *Remote Sens. Environ.* **2012**, *120*, 9–24. [CrossRef]
35. Zebker, H.A.; Villasenor, J. Decorrelation in interferometric radar echoes. *IEEE Trans. Geosci. Remote Sens.* **1992**, *30*, 950–959. [CrossRef]
36. Arnold, C.L.; Gibbons, C.J. Impervious surface coverage—The emergence of a key environmental indicator. *J. Am. Plan. Assoc.* **1996**, *62*, 243–258. [CrossRef]
37. Weng, Q. Remote sensing of impervious surfaces in the urban areas: Requirements, methods, and trends. *Remote Sens. Environ.* **2012**, *117*, 34–49. [CrossRef]
38. Gong, P.; Li, X.; Wang, J.; Bai, Y.; Cheng, B.; Hu, T.; Liu, X.; Xu, B.; Yang, J.; Zhang, W.; et al. Annual maps of global artificial impervious area (GAIA) between 1985 and 2018. *Remote Sens. Environ.* **2020**, *236*, 111510. [CrossRef]
39. Zhao, M.; Zhou, Y.; Li, X.; Cheng, W.; Zhou, C.; Ma, T.; Li, M.; Huang, K. Mapping urban dynamics (1992-2018) in Southeast Asia using consistent nighttime light data from DMSP and VIIRS. *Remote Sens. Environ.* **2020**, *248*, 111980. [CrossRef]

40. Chen, Z.; Yu, B.; Yang, C.; Zhou, Y.; Yao, S.; Qian, X.; Wang, C.; Wu, B.; Wu, J. An extended time series (2000–2018) of global NPP-VIIRS-like nighttime light data from a cross-sensor calibration. *Earth Syst. Sci. Data* **2021**, *13*, 889–906. [CrossRef]
41. Cui, Z.; Yang, J.; Yuan, L. Land subsidence caused by the interaction of high-rise buildings in soft soil areas. *Nat. Hazards* **2015**, *79*, 1199–1217. [CrossRef]
42. Tobler, W.R. A Computer Movie Simulating Urban Growth in the Detroit Region. *Econ. Geography.* **1970**, *46* (Suppl. S1), 234–240. [CrossRef]
43. MORAN, P.A. Notes on continuous stochastic phenomena. *Biometrika* **1950**, *37*, 17–23. [CrossRef]
44. Anselin, L. Local Indicators of Spatial Association:LISA. *Geogr. Anal.* **1995**, *27*, 93–115. [CrossRef]
45. Anselin, L.; Syabri, I.; Kho, Y. GeoDa: An Introduction to Spatial Data Analysis. *Geogr. Anal.* **2006**, *38*, 5–22. [CrossRef]
46. Anselin, L.S.I.S. Visualizing multivariate spatial correlation with dynamically linked windows. In Proceedings of the CSISS Workshop on New Tools for Spatial Data Analysis, Santa Barbara, CA, USA, 10–11 May 2002.
47. Brunsdon, C.; Fotheringham, S.; Charlton, M. Geographically weighted regressionÐmodelling spatial non-stationarity. *Statistician* **1998**, *47*, 432–443.
48. Brunsdon, C.; Fotheringham, A.S.; Charlton, M.E. Geographically Weighted Regression: A Method for Exploring Spatial Nonstationarity. *Geogr. Anal.* **1996**, *28*, 281–298. [CrossRef]
49. Xiao, R.; Su, S.; Wang, J.; Zhang, Z.; Jiang, D.; Wu, J. Local spatial modeling of paddy soil landscape patterns in response to urbanization across the urban agglomeration around Hangzhou Bay, China. *Appl. Geogr.* **2013**, *39*, 158–171. [CrossRef]
50. Tu, J. Spatially varying relationships between land use and water quality across an urbanization gradient explored by geographically weighted regression. *Appl. Geogr.* **2011**, *31*, 376–392. [CrossRef]
51. Levin, N.; Kyba, C.C.M.; Zhang, Q.; De Sánchez Miguel, A.; Román, M.O.; Li, X.; Portnov, B.A.; Molthan, A.L.; Jechow, A.; Miller, S.D.; et al. Remote sensing of night lights: A review and an outlook for the future. *Remote Sens. Environ.* **2020**, *237*, 111443. [CrossRef]
52. Chen, G.; Zhang, Y.; Zeng, R.; Yang, Z.; Chen, X.; Zhao, F.; Meng, X. Detection of Land Subsidence Associated with Land Creation and Rapid Urbanization in the Chinese Loess Plateau Using Time Series InSAR: A Case Study of Lanzhou New District. *Remote Sens.* **2018**, *10*, 270. [CrossRef]
53. Garreton, M.; Sánchez, R. Identifying an optimal analysis level in multiscalar regionalization: A study case of social distress in Greater Santiago. *Comput. Environ. Urban Syst.* **2016**, *56*, 14–24. [CrossRef]
54. Meentemeyer, V. Geographical perspectives of space, time, and scale. *Landsc. Ecol.* **1989**, *3*, 163–173. [CrossRef]
55. Atkinson, P.M.; Tate, N.J. Spatial Scale Problems and Geostatistical Solutions: A Review. *Prof. Geogr.* **2000**, *52*, 607–623. [CrossRef]
56. Šímová, P.; Gdulová, K. Landscape indices behavior: A review of scale effects. *Appl. Geogr.* **2012**, *34*, 385–394. [CrossRef]
57. Du, S.; Wang, Q.; Guo, L. Spatially varying relationships between land-cover change and driving factors at multiple sampling scales. *J. Environ. Manag.* **2014**, *137*, 101–110. [CrossRef]
58. Luo, X.; Peng, Y. Scale Effects of the Relationships between Urban Heat Islands and Impact Factors Based on a Geographically-Weighted Regression Model. *Remote Sens.* **2016**, *8*, 760. [CrossRef]
59. Zhao, H.; Ren, Z.; Tan, J. The Spatial Patterns of Land Surface Temperature and Its Impact Factors: Spatial Non-Stationarity and Scale Effects Based on a Geographically-Weighted Regression Model. *Sustainability* **2018**, *10*, 2242. [CrossRef]
60. Li, C.; Li, F.; Wu, Z.; Cheng, J. Exploring spatially varying and scale-dependent relationships between soil contamination and landscape patterns using geographically weighted regression. *Appl. Geogr.* **2017**, *82*, 101–114. [CrossRef]
61. Su, S.; Xiao, R.; Zhang, Y. Multi-scale analysis of spatially varying relationships between agricultural landscape patterns and urbanization using geographically weighted regression. *Appl. Geogr.* **2012**, *32*, 360–375. [CrossRef]

remote sensing

MDPI

Article

Ground Surface Deformation Analysis Integrating InSAR and GPS Data in the Karstic Terrain of Cheria Basin, Algeria

Loubna Hamdi [1,†], Nabil Defaflia [1,†], Abdelaziz Merghadi [2,3,*,†], Chamssedine Fehdi [3], Ali P. Yunus [4], Jie Dou [5], Quoc Bao Pham [6], Hazem Ghassan Abdo [7,8,9], Hussein Almohamad [10] and Motrih Al-Mutiry [11]

1 Research Laboratory of Sedimentary Environment, Mineral and Water Resources of Eastern Algeria, Echahid Cheikh Larbi Tebessi University−Tebessa, Tébessa 12002, Algeria; loubna.hamdi@univ-tebessa.dz (L.H.); nabil.defaflia@univ-tebessa.dz (N.D.)
2 Applied Research in Engineering Geology, Geotechnic, Water Science & Environment, Université Ferhat Abbas de Sétif, Sétif 19000, Algeria
3 Water and Environment Laboratory, Echahid Cheikh Larbi Tebessi University−Tebessa, Tébessa 12002, Algeria; fehdi.chemseddine@univ-tebessa.dz
4 Department of Earth and Environmental Sciences, Indian Institute of Science Education and Research, Mohali 140306, Punjab, India; yunusp@iisermohali.ac.in
5 Badong National Observation and Research Station of Geohazards, China University of Geosciences, Wuhan 430074, China; doujie@cug.edu.cn
6 Faculty of Natural Sciences, Institute of Earth Sciences, University of Silesia in Katowice, Będzińska Street 60, 41-200 Sosnowiec, Poland; quoc_bao.pham@us.edu.pl
7 Geography Department, Faculty of Arts and Humanities, Tartous University, Tartous P.O. Box 2147, Syria; hazemabdo@tartous-univ.edu.sy
8 Geography Department, Faculty of Arts and Humanities, Damascus University, Damascus P.O. Box 30621, Syria
9 Geography Department, Faculty of Arts and Humanities, Tishreen University, Lattakia P.O. Box 2237, Syria
10 Department of Geography, College of Arabic Language and Social Studies, Qassim University, Buraydah 51452, Saudi Arabia; h.almohamad@qu.edu.sa
11 Department of Geography, College of Arts, Princess Nourah bint Abdulrahman University, Riyadh 11671, Saudi Arabia; mkalmutairy@pnu.edu.sa
* Correspondence: abdelaziz.merghadi@gmail.com or merghadi.abdelaziz@univ-tebessa.dz; Tel.: +213-676735046
† These authors contributed equally to this work.

Citation: Hamdi, L.; Defaflia, N.; Merghadi, A.; Fehdi, C.; Yunus, A.P.; Dou, J.; Pham, Q.B.; Abdo, H.G.; Almohamad, H.; Al-Mutiry, M. Ground Surface Deformation Analysis Integrating InSAR and GPS Data in the Karstic Terrain of Cheria Basin, Algeria. *Remote Sens.* **2023**, *15*, 1486. https://doi.org/10.3390/rs15061486

Academic Editors: Stefano Morelli, Veronica Pazzi and Mirko Francioni

Received: 18 February 2023
Accepted: 28 February 2023
Published: 7 March 2023

Abstract: Karstic terrains are usually dominated by aquifer systems and/or underground cavities. Overexploitation of groundwater in such areas often induces land subsidence and sometimes causes sinkholes. The Cheria basin in Algeria suffers from severe land subsidence issues, and this phenomenon has been increasing in recent years due to population expansion and uncontrolled groundwater exploitation. This work uses GPS data and persistent scatterer interferometry synthetic aperture radar (PS-InSAR) techniques to monitor the land subsidence rate by employing Sentinel-1 satellite data for the period from 2016 to 2022. Our results demonstrate that the Cheria basin experiences both uplift and subsidence in places, with an overall substantial change in the land surface. The total cumulative subsidence over 6 years reached a maximum of 500 mm. Comparison of land deformation between PSI and GPS showed root mean square error (RMSE) values of about 2.83 mm/year, indicating that our analyzed results are satisfactorily reproducing the actual changes. Nonetheless, these results can be used to extract the susceptible zones for vertical ground displacement and evaluate the surface deformation inventory map of the region for reducing damages (e.g., human losses, economic impact, and environmental degradation) that may occur in the future (e.g., sinkholes) and can be further utilized in perspective for a sinkhole early warning system.

Keywords: land subsidence; InSAR; karst; sinkholes; climate change; PS-InSAR

1. Introduction

Groundwater resources are very vulnerable due to natural and anthropogenic impacts, especially in karstic terrains of arid and semi-arid zones, due to increased requirements caused by climate change and population expansion [1,2]. Karst landscapes are considered highly fragile settings that are severely vulnerable to sinkhole formation. Sinkhole landforms are depression areas with subcircular shapes on a surface typically common in carbonate and/or evaporate rocks; these terrains are characterized by minerals that might dissolve in water and are controlled by (1) texture, (2) mechanical strength (i.e., rocks have lower mechanical strength and have faster and higher solubility behavior), and (3) solubility mechanisms, etc. [3]. Typically, water molecules absorb atmospheric carbon dioxide (CO_2) and transform it into carbonic acid (H_2CO_3) in soils, which pushes carbonate minerals into the leaching process. The acidic solution H_2CO_3 filters through the weak areas (joints, faults, and fractures) and involves the formation of underground cavities [4,5].

Land subsidence issues have become increasingly prominent in recent years in many parts of the world. Land subsidence is the lowering of the ground surface elevation due to underground material movement. It occurs due to a complex process controlled by natural or anthropogenic causes or a combination of both effects. Natural causes could be events such as earthquakes, soil compaction, glacial isostatic adjustment, erosion, and sinkhole formation; anthropogenic effects are activities such as the removal of water, oil, natural gas, or mineral resources from the ground by pumping, fracking, or mining activities. Typically, sinkhole collapse happens when the piezometric level goes down. The damage could vary from one region to another and can be affected indirectly by infrastructure presence and population concentrations [5]. Because of urban expansion and climate change issues, sinkhole subsidence geohazards have been reported worldwide, including in Mexico [6], the USA [7], Iran [8], the UAE [9], and Turkey [10].

Subsidence is a common geological hazard and can cause infrastructure damage, ground surface ruptures, increasing flood risk, and adverse socioeconomic impacts on communities. Detecting the spatial extent and monitoring temporal evolution is crucial to determine the causes of subsidence and prevent activities to mitigate the negative effects. Elevation or elevation-change measurements are fundamental to monitoring land subsidence and have been measured by using traditional methods; Global Positioning System (GPS) stations, leveling networks, and recently, satellite InSAR (interferometric synthetic aperture radar) remote sensing are prominent techniques.

In recent years, InSAR has become a powerful remote sensing technique for monitoring global earth changes. Persistent scatterer interferometry synthetic aperture radar (PS-InSAR), which belongs to differential interferometric synthetic aperture radar (DInSAR) groups, is an innovative technology for surface displacement monitoring. These methods are less affected by time and space decoherence and have low-cost advantages and high precision. Phase interferometry contains artifacts that reduce the quality of the interferograms. A small space and temporal baseline of the C-band images were constructed to avoid and minimize errors conserved during the acquisition time of each image [11]. However, it is the contribution of atmospheric conditions such as temperature, vapor content, and pressure that are converted into small-magnitude errors in interferograms [11,12].

The PS-InSAR approach was first realized by Ferretti [13]. The algorithms identify high persistent scatterer (PS) pixels less affected by time and space decoherence, as well as relatively stable pixels, by analysis of their amplitude scintillations in interferogram series and time/frequency characteristics of each phase. This algorithm works better in urban areas with a large number of artificial man-made structures that increase the identification of scatterers. Persistent scatterer interferometry (PSI) uses phase analysis for PS pixel identification proposed by Hooper [14]. This algorithm uses a combination of amplitude dispersion index and phases spatial correlation to identify PS points to produce a time series of deformation using the spatially correlated nature, rather than requiring a known temporal dependence [14].

The present work aims to study the subsidence in a karst semi-arid area that suffers from severe drought and groundwater exploitation problems. Interferometry techniques with large-scale acquisition and high accuracy provide subsidence rates and help to extract and delineate the ground movement changes registered over the study period. The spatiotemporal land deformation distribution identified by exploring InSAR and GPS highlights the serious land subsidence damages that have occurred in arid and semi-arid regions. The findings will help the local authority to improve a strategy for regional deformation and the implementation of inventory maps to avoid human and economic losses.

2. Study Area

The Cheria basin is situated in the southwestern part of Tebessa within the northeast province of Algeria between the latitudes of 35°18′41,62″ and 35°14′51,30″N and longitudes of 7°42′51,40″ and 7°47′34,62″E (Figure 1). The basin is surrounded by mountain ranges with an elevation exceeding 1000 m, with some areas at elevations of up to 1200 m, such as Djebal Achour and Djebal Dokkan in the east; Djebal Zora and Djebal Boukammech in the south; Djebal Troubia and Djebal Tazbent in the north; and Djebal Kamallel and Djebel El Abtine in the west.

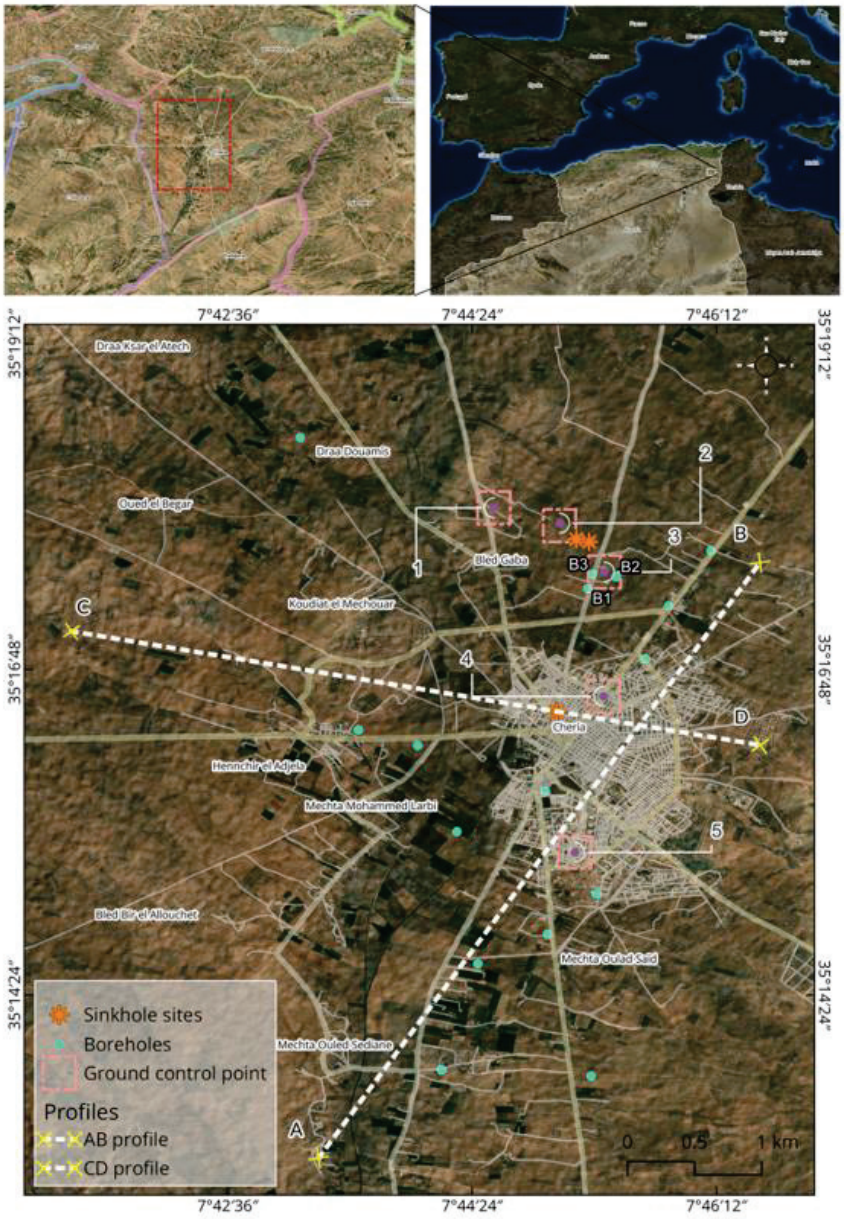

Figure 1. Location map of the study area (background image: Landsat-8 OLI dated 12 September 2022). Orange stars are past sinkhole sites; B1, B2, and B3 are borehole wells where the water level was monitored; pink rectangular boxes are the location of ground control points; and dashed white lines are profiles selected for the analysis of PSI and GPS results.

The local geology consists of lithostratigraphic units that vary from bottom to top by Maastrichtian limestone, Eocene limestone, and Mio-Plio-Quaternary deposits (Figure 2) [15]. The sinkhole studied is a cover-collapse type characterized by Eocene limestone layers covered with Quaternary deposits (gravel, sand, silt, and clay) (see Figure 2). They are mainly synsedimentary subsidence types caused by the dissolution of the karstic bedrock [16]. The tectonic system dissected by conjugation faults is controlled by the local hydrogeographic networks, the NE–SW and the vertical NW–SE diagonal system, and the N–S (Alpine phase) system [17]. The region has a semiarid climate, and the local precipitation is approximately 340–400 mm/year.

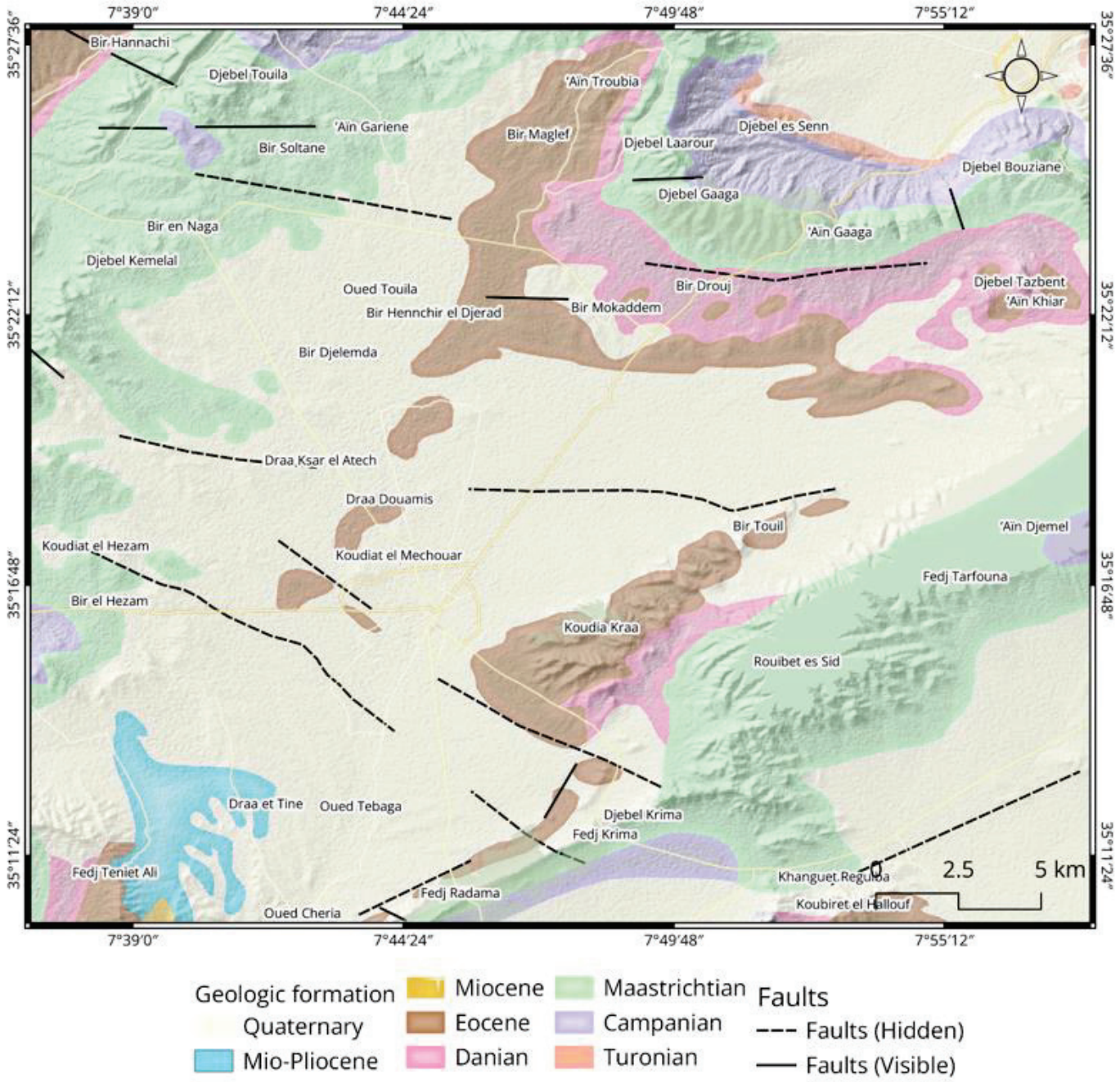

Figure 2. Regional geological map of the study area showing the dominant Quaternary formation and the Maastrichtian and Eocene formations.

The dominant type of sinkhole present in the study region is the cover-collapse sinkhole. Cover-collapse sinkholes are one of the most dangerous types that can collapse in minutes or even seconds, causing disastrous damages. Real damage caused by past sinkhole collapse events is displayed in Figure 3.

Figure 3. Sinkhole example images: (**a**) Draa-Douamis sinkholes 1 and 2 collapsed with a diameter of 66.47 and 24.88 m, respectively (location: see Figure 1—sinkhole sites; date: during 2004); (**b**) example of sinkhole diameter enlargement in surface; (**c**) Harkat Bouziane sinkhole collapsed in the city with a diameter of ~50 m and height of 2 m (location: see Figure 1—sinkhole sites; date: February 2009), destroying infrastructure; and (**d**) damage created by a sinkhole event (i.e., sewer network and roads broken).

3. Data and Methods

In this paper, we focus on investigating the subsidence phenomenon and evolution between specific periods selected based on GPS measurements and PS-InSAR techniques. SAR images were obtained from the Sentinel 1-A and 1-B satellites between 2016 and 2022. The SAR scenes selected for the case study were carefully chosen (e.g., based on good weather, etc.). The study area is mostly bare land with a very low percentage of permanent vegetation, which makes it easier to obtain good SAR scenes. The Sentinel-1 short wavelength is sensitive to vegetation, which leads to serious decorrelated noise due to vegetation changes during the revisiting period of the SAR images. The GPS datasets were measured by a Leica 1200 GNSS system receiver with an ATX1230 antenna and an RTX1250GG receiver.

More information about the satellite image dataset and baseline distribution related to acquisition time is provided in Table 1.

Table 1. Details of the Sentinel-1A and Sentinel-1B data used in this study.

Satellite	Track	Band	Covered Period	Number of Scenes
Sentinel-1A	161	C-band	03 January 2016 to 07 January 2022	50
Sentinel-1B	168	C-band	12 October 2016 to 22 October 2021	50

The phase difference between SAR images consists of measuring the ground difference along the radar line of sight (LOS) direction. The interferometric phase comprises the following contribution in Equation (1):

$$\Phi = \varphi orb\varphi^{orb} + \varphi dem\varphi^{dem} + \varphi unw\varphi^{unw} + \varphi noise\varphi^{noise} + \varphi atm\varphi^{atm} \quad (1)$$

where $\varphi orb\varphi^{orb}$ represents the residual orbit error caused by an inaccurate orbit sensor; $\varphi dem\varphi^{dem}$ is related to the topographic variation enhanced with physical features of the ground surface; $\varphi unw\varphi^{unw}$ is the unwrapping error and the main algorithm process applied to recovering an unambiguous phase and correcting the residual phases (orb, dem, and unw) for accurate high deformation results; $\varphi noise\varphi^{noise}$ is the residual thermal noise effect; and $\varphi atm\varphi^{atm}$ is the atmospheric errors during SAR image acquisition that are influenced by various signals. It is the main artifact source and is generated when the microwave passes through the tropospheric layer (i.e., elevation component due to atmospheric vertical stratification, and turbulent component referring to horizontal changes in water vapor distribution over short time intervals) [11,18].

Data preparation consisted of the creation of single-look master interferograms from the N + 1 single-look complex (SLC) SAR images with the most optimal configuration. All the other images were denoted as slaves and co-registered to generate interferograms. Integration of external DEM SRTM 1 sec data was completed as a topographic reference, and these data were also used to eliminate the topographic effects and geocoding. All preprocessing steps were carried out using Gamma software (20220701) and MATLAB (9.13 R2022b). The flowchart of the overall methodology is presented in Figure 4.

The PSI method processed to find pixels not affected by noise with high phase stability is performed using the following steps:

i. In preliminary analysis loading, persistent scatterer (PS) candidate points are selected as pixels with a value of the amplitude dispersion index (ADI) that is smaller than a threshold.
ii. Estimate phase noise means the atmospheric phase screen (APS) value is contained on each candidate pixel in the interferogram, defined by the spatially correlated phase and uncorrelated terrain errors. For good results, various spatiotemporal filters are used to correct APS and achieve only the deformation part.
iii. Persistent scatterer points are selected according to the atmospheric phase screen (APS) correction parameter and the percentage of random pixels in a scene per density is estimated by application of a probability statistics method.
iv. The PSs selected in the previous step are weeded, removing those that are deemed too noisy due to signal contributions from neighboring ground resolution elements.
v. The wrapped phase of the selected pixels is corrected for a spatially uncorrelated look angle DEM error.
vi. Three-dimensional unwrapping of the above-mentioned corrected phase PS result is used; unwrapping errors are more likely to occur in a longer perpendicular baseline interferogram.
vii. A spatially uncorrelated look angle SCLA error was calculated in step iii and removed in step v; in step vii, a spatial look angle error is calculated which is due almost exclusively to a spatially correlated DEM error (this includes an error in the

DEM itself and incorrect mapping of the DEM into radar coordinates). The master atmosphere and orbit error phase are estimated simultaneously.

viii. Atmospheric filtering and estimation of other spatial correlation error terms are conducted. The results are a data file containing final PS points with a deformation velocity in the precision of mm/year representing the land deformation model of the area of interest [14].

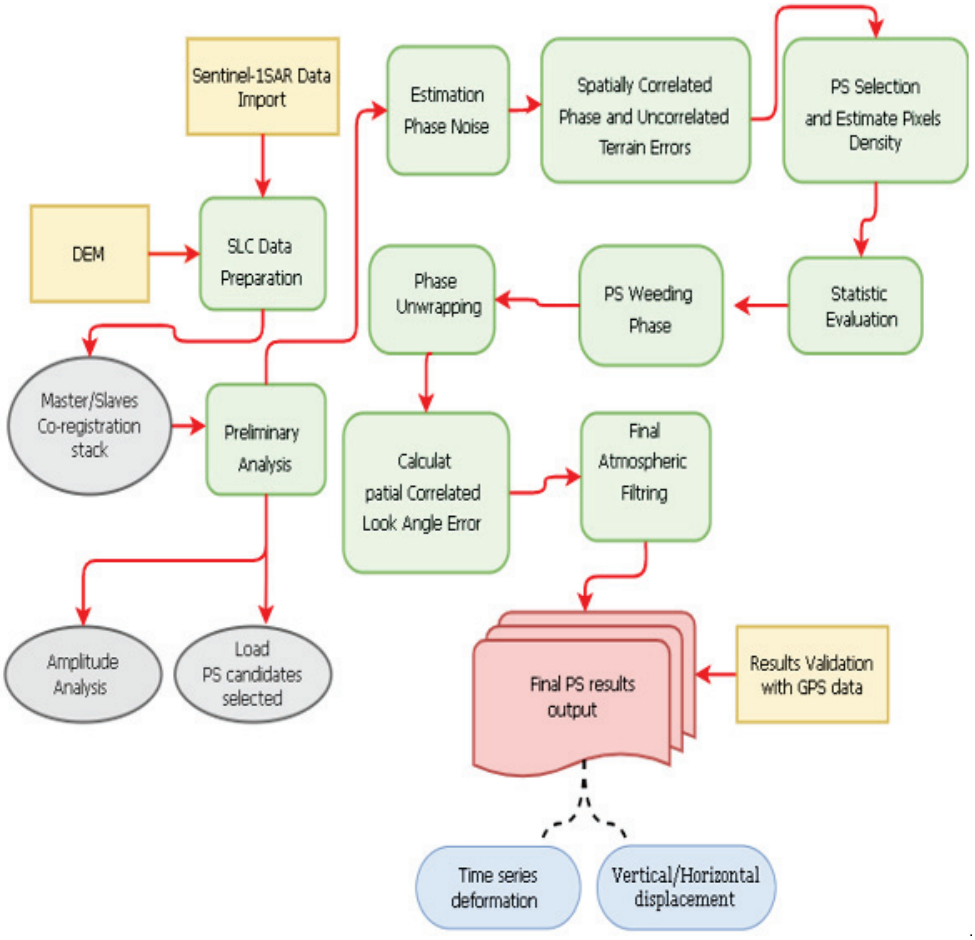

Figure 4. Flowchart depicting the overall methodology adopted in this research.

To compare these measurements with GPS vertical measurements, we transformed SAR measurements recorded along the radar line of sight (LOS) into 3D displacement. The velocity (V_{LOS}) measured can be constructed from SAR image acquisition geometry using Equation (2):

$$V_{LOS} = (cos\theta - sin\theta\ cos\alpha + sin\theta\ sin\alpha) \begin{pmatrix} v_U \\ v_N \\ v_E \end{pmatrix} \quad (2)$$

where θ and α are pixel-based radar incident angles and azimuth angles of the satellite, respectively; v_U, v_N, and v_E represent real vertical north–south direction and west–east direction deformations, respectively. If V_{LOS}^A and V_{LOS}^D are the velocities along the radar line of sight for ascending and descending tracks, Equation (2) can be rewritten into Equation (3):

$$V_{LOS} = \begin{pmatrix} V_{LOS}^A \\ V_{LOS}^D \end{pmatrix} = \begin{bmatrix} cos\theta_A & -cos\alpha\ sin\theta_A & -sin\alpha\ sin\theta_A \\ cos\theta_D & cos\alpha\ sin\theta_D & sin\alpha\ sin\theta_D \end{bmatrix} \begin{pmatrix} v_U \\ v_N \\ v_E \end{pmatrix} \quad (3)$$

To further simplify Equation (3) with three variables, displacements occurring along the north–south direction cannot be measured accurately (almost parallel to the satellite orbit). Assuming that the north–south component projection of the velocity along the LOS radar is negligible for both ascending and descending orbit tracks, in this case, Equation (3) can be approximated and further simplified:

$$V_{LOS} \simeq \begin{pmatrix} V_{LOS}^{A} \\ V_{LOS}^{D} \end{pmatrix} = \begin{bmatrix} cos\theta_A & -cos\alpha\ sin\theta_A \\ cos\theta_D & cos\alpha \sin\theta_D D \end{bmatrix} * \begin{pmatrix} v_U \\ v_E \end{pmatrix} \quad (4)$$

In situ dataset measurements were performed in this region for six years by manually monitoring millimeter surface displacement in this study area (unfortunately, no permanent GPS monitoring station exists). A total of five ground control points (GCP) were selected and used for validation purposes of persistent scatterer results. The GPS observation measurements were obtained with a session length of 30 min for five selected GCP points and 10 min for each of the remaining sites (Profiles AB-CD). The periodic measurements over an extended period are a great approach to flattening the error curve and eliminating outliers and artifacts in GPS measurements [19] (i.e., the same concept used by InSAR time-series analysis). The Geodetic Reference System 1980 (GRS80) was used for the ellipsoidal heights. Furthermore, the geoid model of EGG2008 was used to convert the ellipsoidal heights into orthometric heights.

It is important to keep in mind that GPS measurement can obtain the Earth's surface motion information with high precision and can directly reflect the vertical variation characteristics of the observed object. However, measurements cannot be densely organized on a large scale due to the critical limitations of GPS such as low spatial resolution and high cost and time consumption [20,21]. Therefore, the PSI results were used and validated with five monitored GPS ground control points received during the period of analysis.

Finally, to assess the discrepancy found between PS-InSAR and GPS, root mean square error (RMSE) was used. RMSE is common and is considered an excellent general-purpose error metric that can be used to (1) indicate the absolute fit of the model to the data and (2) provide the average model prediction error in units of the variable of interest; RMSE is a negatively oriented score, which means lower values are better [22–24]. RMSE can be calculated using Equation (5):

$$RMSE = \sqrt{\frac{1}{n}\sum_{i=1}^{n}(\hat{y}_i - y_i)^2} \quad (5)$$

where y_i is the GPS measurements, $\hat{y}_i$ is the PS-InSAR measurements, and n is the number of observations available for analysis.

4. Results

For the deformation monitoring in the study area, we used PS-InSAR in combination with GPS measurements, as described in Section 3. The mean velocity maps of the final geocoded vertical and horizontal displacement generated from Sentinel-1 data are presented in Figure 5. Color ramp distribution of the velocity maps gives a visual preliminary overview of the dominant movement (e.g., subsidence or uplift, east or west). Our results show a vertical mean velocity with a large percentage of negative values compared with positive values, with values ranging between −35.95 and 12.73 mm/year. On the other hand, horizontal mean velocity shows an equal percentage of negative and positive values, with values ranging from −22.98 to 21.85 mm/year. In the vertical mean velocity map, negative rates indicate subsidence and positive rates indicate land uplift, whereas in the horizontal mean velocity map, the negative values indicate deformations in the west direction and positive values indicate deformations in the east direction. It can be seen that the urban areas such as Cheria city are covered totally by negative values, which indicates that the whole city subsides (e.g., a sinkhole collapsed in 2009). However, rural areas with high-density borehole wells register the highest fluctuation of subsidence/uplift

velocity rates (up to −35 mm/year) due to ongoing unsupervised excessive underground water pumping.

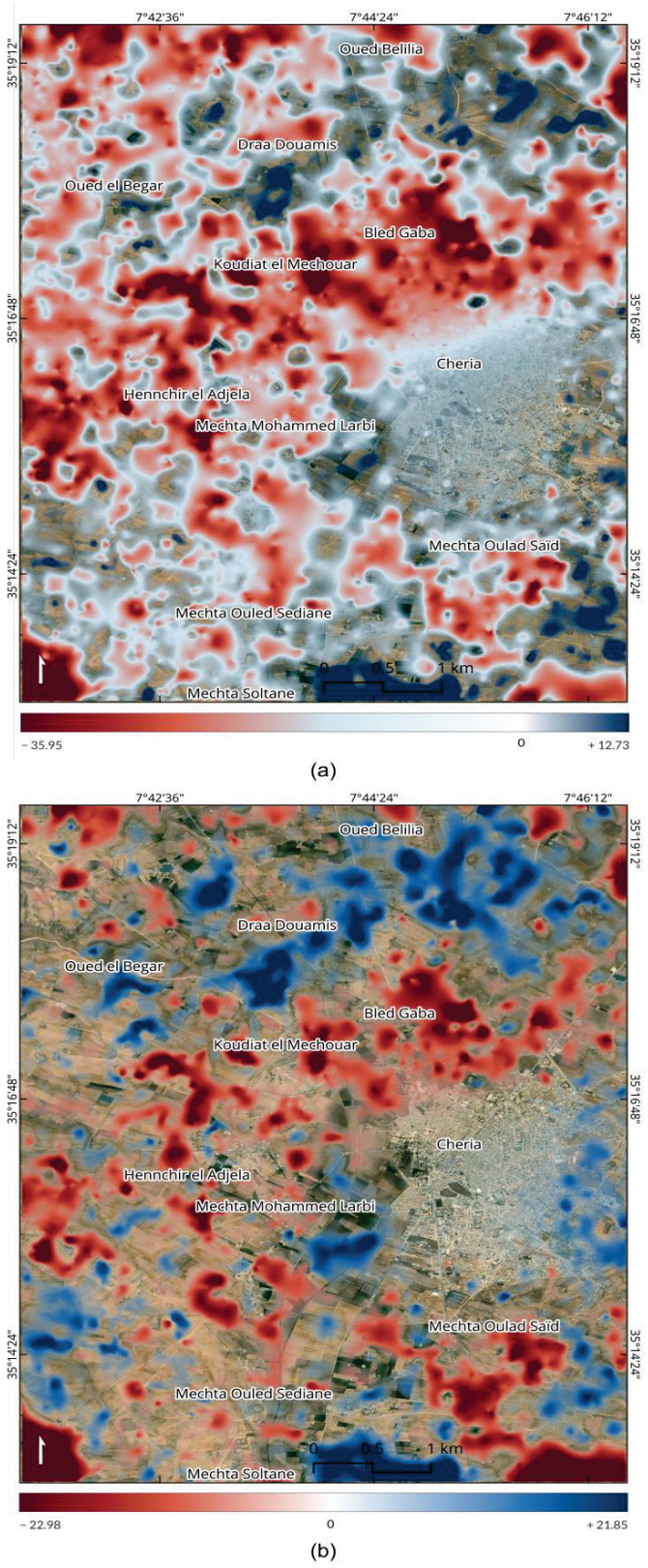

Figure 5. Vertical and horizontal mean velocity map of the study area showing (**a**) vertical mean velocity (up and down directions) and (**b**) horizontal mean velocity (east and west directions). (To enhance the visibility of positive and negative values, values close to 0 were rendered transparent.)

Five GCP points (P1, P2, P3, P4, and P5) were selected for the cumulative analysis of ground movement in the study area during the period between 2016 and 2022 (Figure 6). The analysis of five ground control points illustrates a high rate of vertical movement caused by land subsidence. Overall, the PS-InSAR results are in close agreement with GPS measurements, with a ±3 mm/year difference. Point P1 shows an aggressive land subsidence at the start, reaching values greater than −275 mm, followed by a slow subsidence of approximately 30 mm registered at the end of the observation period. Point P2 (near the sinkhole that collapsed in 2004) shows that progressive land subsidence can reach a value of −200 mm. At P3, the progressive land subsidence reached −140 mm, and at P4, the uplift reached 25 mm, and huge land subsidence was registered at ~−250 mm. For P5, the progressive subsidence reached approximately −265 mm to −275 mm.

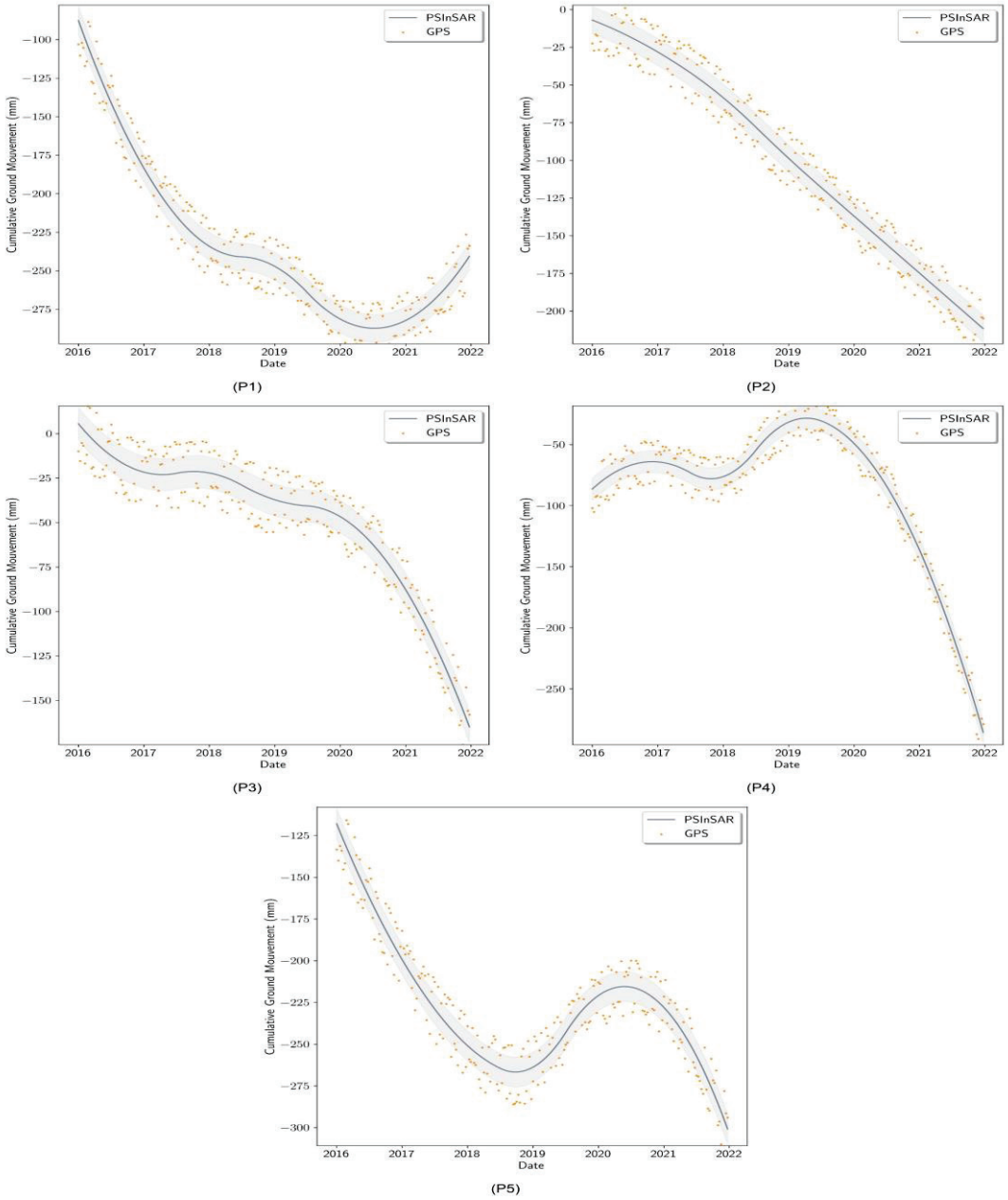

Figure 6. Graphs of the cumulative deformation of the selected points (P1, P2, P3, P4, and P5) from PSI and GPS results used to detect subsidence; the *x*-axis is time, 2016–2022, and the *y*-axis represents the movement of the ground.

To analyze the subsidence trend in the study area, two profiles (AB and CD) with NE–SW and NWW–SEE directions were selected and plotted (see Figure 7). The trend of cumulative vertical and horizontal ground movement profiles during the period of the analysis was visualized to determine the changes in the study area. The fluctuation of the vertical ground movement demonstrates that the study area suffers from a heavy subsidence pattern with a maximum displacement rate ranging between 0 and 350 mm, approximately. For the CD profile, the vertical ground movement shows a varying amount of subsidence where the maximum rates are between −100 and −500 mm.

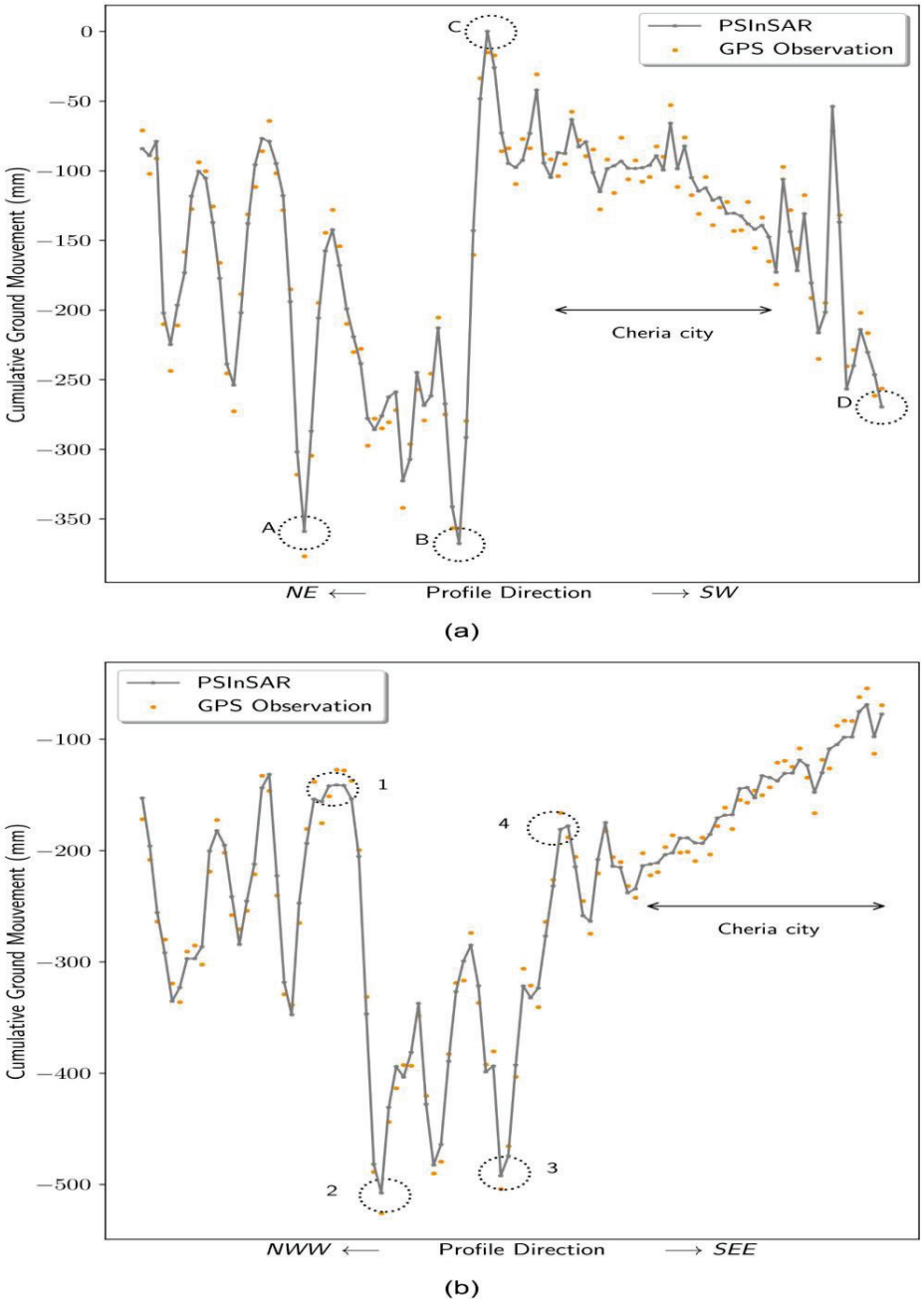

Figure 7. Cumulative vertical ground movement profiles: (**a**) AB and (**b**) CD profiles. The *x*-axis in the figure represents the profile direction along NE–SW and NWW–SEE directions, while the *y*-axis represents the cumulative vertical ground movement (mm). The black circle referring to selected points A, B, C, and D through the AB profile, and 1, 2, 3 and 4 through the CD profile, are also presented in Figure 8.

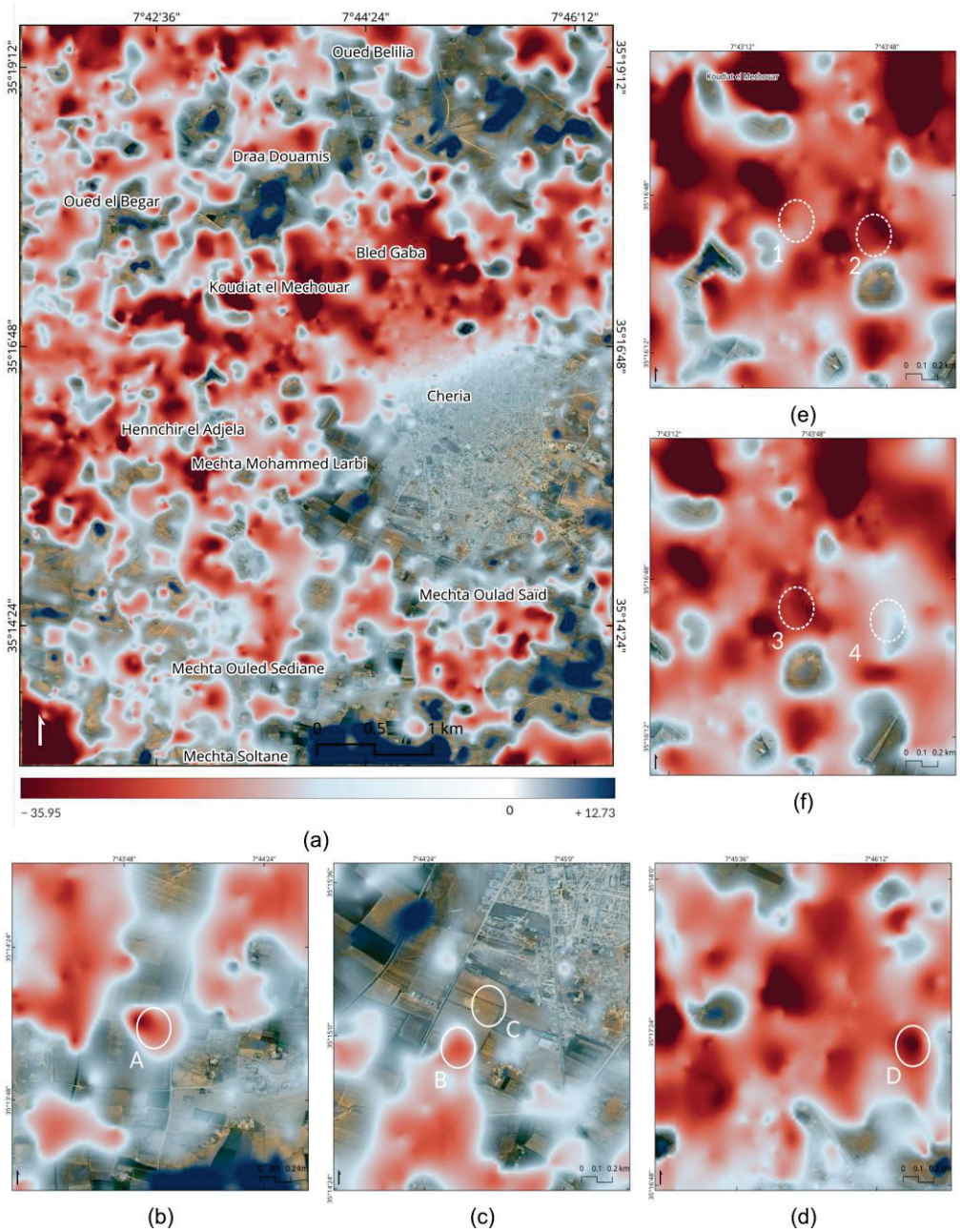

Figure 8. (**a**) Positions and overview of the eight selected sample sites (A, B, C and D through the AB profile, and 1, 2, 3 and 4 through the CD profile) from Figure 7; (**b**–**f**) represent a close-up overview of selected sample sites (i.e., highlighted with white circles).

An overview of eight sites selected from cumulative vertical ground movement profiles is presented in Figure 8, with personalized zoom to monitor the total displacement resulting from over five years of analysis. For further detail, in Figure 8b,c, the selected points A and B represent areas facing serious land subsidence highlighted in the map, with a sub-circular shape of the total value reaching more than −350 mm. In Figure 8c,d, point C is situated near the urban perimeter and is represented on the map by near-zero vertical movements that indicate relatively stable zones. Point D suggests a medium to high land subsidence, with a value reaching −270 mm; while in Figure 8e,f, points 1 and 4 refer to ground subsidence with values between −140 and −170 mm, respectively. On the other hand, points 2 and 3 represent areas with the highest land sinking values registered during

the analysis period, at more than −490 mm. GPS distribution is very similar to the InSAR deformation field.

Our vertical velocities, obtained using the GPS rapid static mode, confirm the subsidence detected with InSAR.

The displacement rates derived from the PS-InSAR and GPS measurements were compared by calculating the root mean square error (RMSE) for vertical and horizontal displacement rates (Table 2). The data are in close agreement, with an accuracy of 2–3 mm/year. RMSE comparison results show 2.8374 mm/year for vertical movement direction and 2.9155 mm/year for horizontal movement direction.

Table 2. Root mean square error (RMSE) values (in mm/year) for InSAR and GPS results.

Comparison	Movement Direction	RMSE (mm/Year)
InSAR vs. GPS	Vertical	2.8374
InSAR vs. GPS	Horizontal	2.9155

5. Discussion

Over the years, a limited focus on InSAR subsidence was given in Algeria, especially to subsidence-related issues in karstic terrains [25]. Here, we compare the map of vertical ground deformation rates generated by PS-InSAR with GPS measurements. The results obtained in this research demonstrate the effectiveness of the monitoring system based on the integration of PS-InSAR data and GPS measurements. Our results (see Figure 5) show that the study area is largely dominated by subsidence and needs continuous monitoring to understand the risks involved. We also noticed remarkable ground uplift at places with deformation ranging between 0 and +12.73 mm/yr. A possible explanation for this anomalous phenomenon could be related to the sudden hydrologic overpressure in the karst networks, seasonal water changes, and groundwater redistribution leading to the natural pressurization of the underground karst flow channels. These water storage losses correlate to flexural unloading [26,27]. Previous research has found that fluid extraction can lead to strain and an increase in pore pressure variations in the sediments [28]. Slow land uplift has been proposed to be connected to increases in pore pressure accompanying groundwater redistribution [29].

The reason behind the high subsidence rates detected in the study area seems to be a combination of multiple factors. The study area has known heavy groundwater exploitation in the last and present century. The main water resource for human supplies and agricultural uses in this area is groundwater. An in situ investigation of the consumption of underground water conducted in 2007 [15] suggests that the average consumption is approximately 22 hm^3/year. The population grew by an average of 3.7%— from 74,129 in 2008 to 96,827 in 2020—in an area of about 267 km^2. Today, the study area suffers from groundwater drawdown due to two major factors: (a) the ongoing unsupervised groundwater exploitation to fulfill the increased water demand, and (b) the severe droughts and soil degradation affecting the area [15]. In scientific literature (e.g., [30,31]), a world map climate classification was published which suggests that the study area is recognized as a hot desert climate type. Global warming in semi-arid regions makes drought more severe and last longer [32], which makes dry regions drier [15]. In the case of the study area, due to the lack of surface water resources needed for sustaining agriculture irrigation, local farmers rely on underground water as the only resource available. The study area is a semi-arid region that suffers from low rainfall precipitations and extreme heat variation. Therefore, there is huge reliance on underground water supplies for Cheria city and adjacent cities. Water pumped from underground mostly goes to: (a) agriculture which uses a huge amount of water in the form of primitive irrigation (see Figure 1, below)—the water used is mostly lost to evaporation, and the remaining water either seeps underground to accelerate the dissolution of karst formation (see Figures 2 and 3) and/or causes the swelling of clayey formations; and (b) the local drinking water network (Cheria city and adjacent cities), and

subsequently to poorly maintained sewer systems (most Algerian cities do not have water treatment facilities) that usually dump water, such as irrigation water, on the surface.

Three boreholes (B1, B2, and B3; see Figure 1 for location) were monitored between 2011 and 2012 (Figure 9). The graphs in Figure 9 show that the water table declined gradually without picking up. This comes with the knowledge that the current status of the underground water table is at its lowest and cannot fulfill human life needs for much longer. In the 1980s, the study area had a water table near the ground surface and even small swamps were documented [15]. Excessive underground water pumping leads to water table decline, compression of soils, and land sinking. In semi-arid regions, the water table declines rack up rapidly. The drinking water crisis explodes with expanding water supply demand. The shortage in water halts agriculture-related activities. The consumption of huge quantities of the already dwindling water reserves creates an underground imbalance due to the extracted water densities that existed in the karst cavities. Therefore, soils covering these surfaces sink massively. This results in a subsidence phenomenon that will transform into sinkholes at any moment, especially in karstic formations. Furthermore, it was noticed that for a lot of sinkhole incidences in the region, the local authorities were not aware of them. Small subsurface circular areas of land sink gradually, and local farmers try to conceal them by adding soil on top in an attempt to stop land degradation and surface sinking. Additionally, local farmers and communities are afraid of land being seized without compensation. Algerian laws issued in 2004 concerning natural hazards do not recognize a lot of hazards such as climate change, heatwaves, land subsidence, etc. In addition to the lack of recognition, these laws were not updated to reflect the results of research reported by the scientific community. Therefore, no compensation was provided to landowners in the form of insurance or aid by local municipalities in the case of sinkhole collapse.

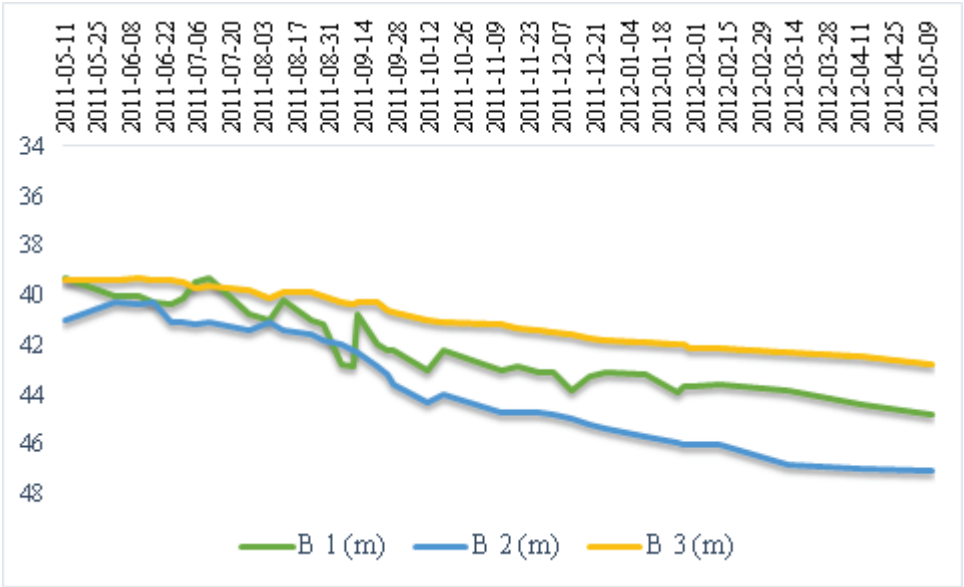

Figure 9. Water changes of three boreholes, B1, B2, and B3, monitored between 2011 and 2012, located in the northern part of the study area (modified after [16]).

Based on the profiles of cumulative vertical ground movement fluctuation in AB and CD, urban areas are affected by continuous minimum rates of land deformation which alternate between slightly up and down variations. On the other hand, rural areas are extremely affected by maximum downward/upward movement deformation rates. This analysis clearly shows that subsidence dominated the study area during the investigation period, and the area surrounding the city experienced high to very high subsidence, while the interior of the city experienced low subsidence. In detail, the rural areas suffer due to dense illegal water boreholes being implemented.

Comparing the GPS measurements with the PS-InSAR results (Table 2 and Figures 6–8) shows satisfying results. PS-InSAR deformation rates are in close agreement with GPS measurements covering the period from 2016 to 2022. The RMSE was less than 3 mm/year. Since RMSE can range from 0 to ∞, there is no absolute good or bad threshold. Therefore, it is recommended to assess RMSE based on the case study and the observation samples available. The obtained RMSE value is great considering the scale of analysis, the budget available, and time consumption. Studies (e.g., [33–40]) have obtained similar RMSEs to this study despite the difference in the processing approach. The obtained RMSEs between GPS and PS-InSAR deformation rates can be improved by enhancing the SAR processing algorithms and GPS measurements.

The comparison of GPS and PS-InSAR goes beyond comparing the deformation values from each method. Precise GPS positions can be used to enhance the deformation accuracy of InSAR images. PS-InSAR and GPS are two different technologies to monitor land surface deformation. Where PS-InSAR can measure changes in elevation over large areas with high accuracy, GPS can only measure elevation changes over small areas because it is time-consuming and requires high-cost equipment. Innovative methods of comparing and integrating GPS and InSAR measurements will facilitate enhanced land deformation mapping and provide a better understanding of subsidence processes.

PS-InSAR has been proven to be a very useful technique for monitoring deformations affecting rural and urban areas and provides information for large-scale and slow surface movement with centimeter to millimeter accuracy for hazards such as ground subsidence, structure collapse, landslides, mining subsidence, etc. Meanwhile, our results successfully demonstrated subsidence phenomena in the study area, but they can be further modified with in situ data analysis and other techniques, such as SBAS or Quasi-PS. It is also suggested that, in the future, a multi-scale (space-based and ground-based) study should be conducted to thoroughly analyze ground subsidence to avoid serious damage in this area. That being said, the applicability of the methodology presented here is subject to two conditions: (1) the availability of InSAR data covering the study region with high coherence; (2) the availability of measurements of some discrete variables highly correlated with InSAR data. In this study, we used GPS to assess the PS-InSAR results. Piezometric data can be also used, but the mathematical relationship with ground deformation is not established yet. The Sentinel-1 satellites, with a short revisit time, provide greater spatial coverage, and temporal sampling provides a great opportunity for developing countries to evaluate and monitor natural hazards with great consistency instead of GPS observation networks, which are very expensive and time-consuming. Our preliminary result from Sentinel-1 data demonstrates that excellent results were achieved over a wide area with the PS-InSAR, which is a key condition in order to apply the proposed methodology.

6. Conclusions

The availability of high-resolution InSAR images from Sentinel-1 datasets for large-scale mapping and monitoring measurements are aimed at detecting millimeter land deformation before and after natural hazard precursors.

The region shows an important ground deformation magnitude that refers to a dangerous state of subsidence that requires local authority attention, especially since there is no possibility for interpreting if there is a relation between the resulting vertical displacements and the existence of underground cavities. These results can be further verified in situ with geophysical tools.

Remote sensing techniques contribute to sinkhole hazard assessments and often predict their occurrence as well as at-risk surfaces before collapse. This implementation provides a crucial database that can be used not only on soil stability monitoring, but also as a natural hazard warning system for potentially catastrophic events. Useful maps can be generated for the Cheria basin to extract and delineate areas susceptible to land subsidence and sinkholes. These maps can alert local authorities to the current situation and reduce future damages.

Author Contributions: Conceptualization, A.M., A.P.Y., J.D. and L.H.; methodology, A.M., L.H. and A.P.Y.; software, A.M. and L.H.; validation, C.F., A.M. and L.H.; formal analysis, L.H., A.M., Q.B.P. and J.D.; investigation, L.H. and N.D.; resources, N.D.; data acquisition and curation, L.H. and A.M.; writing—original draft preparation, L.H.; review and editing, A.M., Q.B.P., A.P.Y., J.D., C.F., N.D., H.G.A., H.A., M.A.-M. and L.H.; visualization, A.M., A.P.Y. and L.H.; supervision, A.M.; project administration, N.D.; funding acquisition, H.G.A., H.A. and M.A.-M. All authors have read and agreed to the published version of the manuscript.

Funding: This project was funded by Princess Nourah bint Abdulrahman University Research Supporting Project Number PNURSP2022R241, Princess Nourah bint Abdulrahman University, Riyadh, Saudi Arabia.

Data Availability Statement: Raw data were generated from European Space Agency. Derived data supporting the findings of this study are available from the corresponding author A.M. on request.

Acknowledgments: The authors would like to thank the European Space Agency for the free available data. We thank the academic editor and the anonymous reviewers for their constructive comments that improve the quality of the paper.

Conflicts of Interest: The authors declare no conflict of interest.

References

1. Oliver, D.M.; Zheng, Y.; Naylor, L.A.; Murtagh, M.; Waldron, S.; Peng, T. How Does Smallholder Farming Practice and Environmental Awareness Vary across Village Communities in the Karst Terrain of Southwest China? *Agric. Ecosyst. Environ.* **2020**, *288*, 106715. [CrossRef]
2. Stevanović, Z.; Stevanović, A.M.; Pekaš, Ž.; Eftimi, R.; Marinović, V. Environmental Flows and Demands for Sustainable Water Use in Protected Karst Areas of the Western Balkans. *Carbonates Evaporites* **2022**, *37*, 3. [CrossRef]
3. Mouici, R.; Baali, F.; Hadji, R.; Boubaya, D.; Audra, P.; Fehdi, C.-É.; Cailhol, D.; Jaillet, S.; Arfib, B. Geophysical, Geotechnical, and Speleologic Assessment for Karst-Sinkhole Collapse Genesis in Cheria Plateau (NE Algeria). *Min. Sci.* **2017**, *24*, 59–71. [CrossRef]
4. Baali, F.; Fehdi, C.; Rouabhia, A.; Mouici, R.; Carlier, E. Hydrochemistry and Isotopic Exploration for a Karstic Aquifer in a Semi-Arid Region: Case of Cheria Plain, Eastern Algeria. *Carbonates Evaporites* **2015**, *30*, 99–107. [CrossRef]
5. Theron, A.; Engelbrecht, J. The Role of Earth Observation, with a Focus on SAR Interferometry, for Sinkhole Hazard Assessment. *Remote Sens.* **2018**, *10*, 1506. [CrossRef]
6. Castellazzi, P.; Arroyo-Domínguez, N.; Martel, R.; Calderhead, A.I.; Normand, J.C.L.; Gárfias, J.; Rivera, A. Land Subsidence in Major Cities of Central Mexico: Interpreting InSAR-Derived Land Subsidence Mapping with Hydrogeological Data. *Int. J. Appl. Earth Obs. Geoinf.* **2016**, *47*, 102–111. [CrossRef]
7. Kuniansky, E.L.; Weary, D.J.; Kaufmann, J.E. The Current Status of Mapping Karst Areas and Availability of Public Sinkhole-Risk Resources in Karst Terrains of the United States. *Hydrogeol. J.* **2016**, *24*, 613–624. [CrossRef]
8. Soldo, B.; Mahmoudi Sivand, S.; Afrasiabian, A.; Đurin, B. Effect of Sinkholes on Groundwater Resources in Arid and Semi-Arid Karst Area in Abarkooh, Iran. *Environments* **2020**, *7*, 26. [CrossRef]
9. Elmahdy, S.I.; Mohamed, M.M.; Ali, T.A.; Abdalla, J.E.-D.; Abouleish, M. Land Subsidence and Sinkholes Susceptibility Mapping and Analysis Using Random Forest and Frequency Ratio Models in Al Ain, UAE. *Geocarto Int.* **2022**, *37*, 315–331. [CrossRef]
10. Orhan, O. Monitoring of Land Subsidence Due to Excessive Groundwater Extraction Using Small Baseline Subset Technique in Konya, Turkey. *Environ. Monit. Assess.* **2021**, *193*, 174. [CrossRef]
11. Parker, A.L.; Filmer, M.S.; Featherstone, W.E. First Results from Sentinel-1A InSAR over Australia: Application to the Perth Basin. *Remote Sens.* **2017**, *9*, 299. [CrossRef]
12. Marbouti, M.; Praks, J.; Antropov, O.; Rinne, E.; Leppäranta, M. A Study of Landfast Ice with Sentinel-1 Repeat-Pass Interferometry over the Baltic Sea. *Remote Sens.* **2017**, *9*, 833. [CrossRef]
13. Ferretti, A.; Prati, C.; Rocca, F. Permanent Scatterers in SAR Interferometry. *IEEE Trans. Geosci. Remote Sens.* **2001**, *39*, 13. [CrossRef]
14. Hooper, A.; Zebker, H.; Segall, P.; Kampes, B. A New Method for Measuring Deformation on Volcanoes and Other Natural Terrains Using InSAR Persistent Scatterers: A NEW PERSISTENT SCATTERERS METHOD. *Geophys. Res. Lett.* **2004**, *31*, 110. [CrossRef]
15. Baali, F.; Rouabhia, A.; Kherici, N.; Djabri, L.; Bouchaou, L.; Hani, A. Underground water quality and contamination risk. The case of the basin of Chéria (NE Algeria). *Estud. Geol.* **2007**, *63*, 127–133. [CrossRef]
16. Fehdi, C.; Nouioua, I.; Belfar, D.; Djabri, L.; Salameh, E. Detection of Underground Cavities by Combining Electrical Resistivity Imaging and Ground Penetrating Radar Surveys: A Case Study from Draa Douamis Area (North East of Algeria). In *H2Karst Research in Limestone Hydrogeology*; Springer: Berlin/Heidelberg, Germany, 2014; pp. 69–82.
17. Merghadi, A.; Abderrahmane, B.; Tien Bui, D. Landslide Susceptibility Assessment at Mila Basin (Algeria): A Comparative Assessment of Prediction Capability of Advanced Machine Learning Methods. *ISPRS Int. J. Geo-Inf.* **2018**, *7*, 268. [CrossRef]

18. Wang, X.; Zhang, Q.; Zhao, C.; Qu, F.; Zhang, J. A Novel Method of Generating Deformation Time-Series Using Interferometric Synthetic Aperture Radar and Its Application in Mexico City. *Remote Sens.* **2018**, *10*, 1741. [CrossRef]
19. Luo, W.; Dou, J.; Fu, Y.; Wang, X.; He, Y.; Ma, H.; Wang, R.; Xing, K. A Novel Hybrid LMD–ETS–TCN Approach for Predicting Landslide Displacement Based on GPS Time Series Analysis. *Remote Sens.* **2022**, *15*, 229. [CrossRef]
20. Fiaschi, S.; Di Martire, D.; Tessitore, S.; Achilli, V.; Ahmed, A.; Borgstrom, S.; Calcaterra, D.; Fabris, M.; Ramondini, M.; Serpelloni, E. Monitoring of Land Subsidence in Ravenna Municipality Using Two Different DInSAR Techniques: Comparison and Discussion of the Results. *Ecology* **2015**, *23*, 38–50.
21. Ito, H.; Susaki, J.; Anahara, T. Integrating Multi-Temporal SAR Images and GPS Data to Monitor Three-Dimensional Land Subsidence. *ISPRS Ann. Photogramm. Remote Sens. Spat. Inf. Sci.* **2019**, *4*, 9–16. [CrossRef]
22. Merghadi, A.; Yunus, A.P.; Dou, J.; Whiteley, J.; ThaiPham, B.; Bui, D.T.; Avtar, R.; Abderrahmane, B. Machine Learning Methods for Landslide Susceptibility Studies: A Comparative Overview of Algorithm Performance. *Earth-Sci. Rev.* **2020**, *207*, 103225. [CrossRef]
23. Dou, J.; Yunus, A.P.; Merghadi, A.; Wang, X.; Yamagishi, H. A Comparative Study of Deep Learning and Conventional Neural Network for Evaluating Landslide Susceptibility Using Landslide Initiation Zones. In *Understanding and Reducing Landslide Disaster Risk*; Guzzetti, F., Mihalić Arbanas, S., Reichenbach, P., Sassa, K., Bobrowsky, P.T., Takara, K., Eds.; Springer: Cham, Switzerland, 2021; pp. 215–223, ISBN 978-3-030-60226-0.
24. Dou, J.; Yunus, A.P.; Tien Bui, D.; Sahana, M.; Chen, C.-W.; Zhu, Z.; Wang, W.; Pham, B.T. Evaluating GIS-Based Multiple Statistical Models and Data Mining for Earthquake and Rainfall-Induced Landslide Susceptibility Using the LiDAR DEM. *Remote Sens.* **2019**, *11*, 638. [CrossRef]
25. Hamdi, L.; Defaflia, N.; Fehdi, C.; Merghadi, A. InSAR Investigation on DRAA-Douamis Sinkholes in Cheria Northeastern of Algeria. In Proceedings of the IGARSS 2020-2020 IEEE International Geoscience and Remote Sensing Symposium, Waikoloa, HI, USA, 26 September–2 October 2020; IEEE: Piscataway, NJ, USA, 2020; pp. 1034–1037.
26. Braitenberg, C.; Pivetta, T.; Barbolla, D.F.; Gabrovšek, F.; Devoti, R.; Nagy, I. Terrain Uplift Due to Natural Hydrologic Overpressure in Karstic Conduits. *Sci. Rep.* **2019**, *9*, 3934. [CrossRef]
27. Borsa, A.A.; Agnew, D.C.; Cayan, D.R. Ongoing Drought-Induced Uplift in the Western United States. *Science* **2014**, *345*, 1587–1590. [CrossRef] [PubMed]
28. Barbour, A.J.; Wyatt, F.K. Modeling Strain and Pore Pressure Associated with Fluid Extraction: The Pathfinder Ranch Experiment: BARBOUR AND WYATT. *J. Geophys. Res. Solid Earth* **2014**, *119*, 5254–5273. [CrossRef]
29. Schmidt, D.A.; Bürgmann, R. Time-Dependent Land Uplift and Subsidence in the Santa Clara Valley, California, from a Large Interferometric Synthetic Aperture Radar Data Set: SANTA CLARA VALLEY INSAR TIME SERIES. *J. Geophys. Res. Solid Earth* **2003**, *108*, B9. [CrossRef]
30. Huang, J.; Ji, M.; Xie, Y.; Wang, S.; He, Y.; Ran, J. Global Semi-Arid Climate Change over Last 60 Years. *Clim. Dyn.* **2016**, *46*, 1131–1150. [CrossRef]
31. Kottek, M.; Grieser, J.; Beck, C.; Rudolf, B.; Rubel, F. World Map of the Köppen-Geiger Climate Classification Updated. *Meteorol. Z.* **2006**, *15*, 259–263. [CrossRef]
32. Dai, A. Increasing Drought under Global Warming in Observations and Models. *Nat. Clim. Chang.* **2013**, *3*, 52–58. [CrossRef]
33. Yuan, D.; Zhang, L.; Yan, R.; Wu, L.; Feng, Y.; Feng, L. Application of Optimized Grey-Markov Model to Land Subsidence Monitoring with InSAR. *IEEE Access* **2022**, *10*, 96720–96730. [CrossRef]
34. Yan, H.; Dai, W.; Liu, H.; Gao, H.; Neely, W.R.; Xu, W. Fusion of Spatially Heterogeneous GNSS and InSAR Deformation Data Using a Multiresolution Segmentation Algorithm and Its Application in the Inversion of Slip Distribution. *Remote Sens.* **2022**, *14*, 3293. [CrossRef]
35. Struhár, J.; Rapant, P.; Kačmařík, M.; Hlaváčová, I.; Lazecký, M. Monitoring Non-Linear Ground Motion above Underground Gas Storage Using GNSS and PSInSAR Based on Sentinel-1 Data. *Remote Sens.* **2022**, *14*, 4898. [CrossRef]
36. Ren, H.; Feng, X. Calculating Vertical Deformation Using a Single InSAR Pair Based on Singular Value Decomposition in Mining Areas. *Int. J. Appl. Earth Obs. Geoinf.* **2020**, *92*, 102115. [CrossRef]
37. Ji, P.; Lv, X.; Wang, R. Deriving 3-D Surface Deformation Time Series with Strain Model and Kalman Filter from GNSS and InSAR Data. *Remote Sens.* **2022**, *14*, 2816. [CrossRef]
38. Umarhadi, D.A.; Widyatmanti, W.; Kumar, P.; Yunus, A.P.; Khedher, K.M.; Kharrazi, A.; Avtar, R. Tropical Peat Subsidence Rates Are Related to Decadal LULC Changes: Insights from InSAR Analysis. *Sci. Total Environ.* **2022**, *816*, 151561. [CrossRef]
39. Umarhadi, D.A.; Avtar, R.; Widyatmanti, W.; Johnson, B.A.; Yunus, A.P.; Khedher, K.M.; Singh, G. Use of Multifrequency (C-band and L-band) SAR Data to Monitor Peat Subsidence Based on Time-series SBAS InSAR Technique. *Land Degrad. Dev.* **2021**, *32*, 4779–4794. [CrossRef]
40. Beccaro, L.; Tolomei, C.; Gianardi, R.; Sepe, V.; Bisson, M.; Colini, L.; De Ritis, R.; Spinetti, C. Multitemporal and Multisensor InSAR Analysis for Ground Displacement Field Assessment at Ischia Volcanic Island (Italy). *Remote Sens.* **2021**, *13*, 4253. [CrossRef]

remote sensing

MDPI

Article

Toward a Real-Time Analysis of Column Height by Visible Cameras: An Example from Mt. Etna, in Italy

Alvaro Aravena [1], Giuseppe Carparelli [2], Raffaello Cioni [2], Michele Prestifilippo [3] and Simona Scollo [3,*]

[1] Facultad de Ciencias Básicas, Universidad Católica del Maule, Talca 3480112, Chile
[2] Dipartimento di Scienze della Terra, Universita degli Studi di Firenze, 50121 Florence, Italy
[3] Istituto Nazionale di Geofisica e Vulcanologia, Osservatorio Etneo, 95125 Catania, Italy
* Correspondence: simona.scollo@ingv.it

Abstract: Volcanic plume height is one the most important features of explosive activity; thus, it is a parameter of interest for volcanic monitoring that can be retrieved using different remote sensing techniques. Among them, calibrated visible cameras have demonstrated to be a promising alternative during daylight hours, mainly due to their low cost and low uncertainty in the results. However, currently these measurements are generally not fully automatic. In this paper, we present a new, interactive, open-source MATLAB tool, named 'Plume Height Analyzer' (PHA), which is able to analyze images and videos of explosive eruptions derived from visible cameras, with the objective of automatically identifying the temporal evolution of eruption columns. PHA is a self-customizing tool, i.e., before operational use, the user must perform an iterative calibration procedure based on the analysis of images of previous eruptions of the volcanic system of interest, under different eruptive, atmospheric and illumination conditions. The images used for the calibration step allow the computation of ad hoc expressions to set the model parameters used to recognize the volcanic plume in new images, which are controlled by their individual characteristics. Thereby, the number of frames used in the calibration procedure will control the goodness of the model to analyze new videos/images and the range of eruption, atmospheric, and illumination conditions for which the program will return reliable results. This also allows improvement of the performance of the program as new data become available for the calibration, for which PHA includes ad hoc routines. PHA has been tested on a wide set of videos from recent explosive activity at Mt. Etna, in Italy, and may represent a first approximation toward a real-time analysis of column height using visible cameras on erupting volcanoes.

Keywords: eruption column height; image analysis; Etna volcano; visible cameras; MATLAB

Citation: Aravena, A.; Carparelli, G.; Cioni, R.; Prestifilippo, M.; Scollo, S. Toward a Real-Time Analysis of Column Height by Visible Cameras: An Example from Mt. Etna, in Italy. *Remote Sens.* **2023**, *15*, 2595. https://doi.org/10.3390/rs15102595

Academic Editors: Stefano Morelli, Veronica Pazzi and Mirko Francioni

Received: 4 March 2023
Revised: 1 May 2023
Accepted: 10 May 2023
Published: 16 May 2023

1. Introduction

Multiple volcanic hazards are associated with tephra dispersal [1–3], which encourages volcanological observatories to permanently improve their monitoring systems with the aim of tracking the main features of an explosive eruption [4–7]. Eruption column height is one of the most important source parameters for volcanic monitoring purposes [8,9]. In fact, this parameter is reported in the VONA (Volcano Observatory Notices for Aviation) messages issued in real-time by volcano observatories when an ash-producing event occurs and/or when there is a change in volcanic behavior [10]. The VONA messages are usually sent by fax or email by the observatory to the pertinent Area Control Centre, Meteorological Watch Office, and Volcanic Ash Advisory Centre [10]. Plume height estimation is also essential to evaluate the mass eruption rate of an explosive event [11–14], and represents a critical factor in forecasting volcanic ash dispersion [15–17] through numerical modeling [18–22]. Moreover, the level reached by the volcanic plume is essential in some gas plumes and aerosol retrievals by satellite [4]. Eruption column height can be obtained using different remote sensing techniques, including satellite [23–25], thermal or visible

video cameras [4,26,27], radar [28–31], and Lidar [32–34]. However, in some circumstances, discrepancies among results from different instruments can occur [35,36]. Satellite systems, for example, may fail when the volcanic plume is not optically thick enough [4], whereas the quality of radar retrievals could depend on different factors such as the volcanic particle size [37].

Recent studies have demonstrated that the use of calibrated visible cameras seem promising and is becoming a useful tool from a volcano monitoring perspective [4]. Cameras in the visible band are able to detect volcanic plumes during daylight hours. It is a very low-cost system when compared to others and allows, in case of an eruption, measurement of the plume height directly from the images [4]. However, plume height estimation from visible cameras is often not automatic and needs an operator to manually sign the height variation with time. Although the error estimations may be less than 5% [4], automatic retrievals of volcanic plume from low-cost visible cameras could reduce the time analysis and lessen the hazard during explosive eruptions. In fact, if the plume height is retrieved automatically, its value could be used in data assimilation procedures needed for a reliable forecast of ash dispersal. Nowadays, while image-processing algorithms have been developed to detect, track, and extract the main parameters of convective plumes from thermal cameras [38,39], automatic procedures to analyze volcanic plume height from visible cameras are scarce [6] and they are not yet implemented for monitoring purposes. In this sense, it is worth noting that, currently, data assimilation techniques of volcanic plume dispersal are mainly based on satellite data [40,41] and we retain that the use of both satellite and ground-based data could really improve the results of volcanic ash dispersal forecasts [42].

Mount Etna (Sicily, Italy) is one of the most active volcanoes in the world, characterized by both effusive and explosive events that can be enclosed in a range that spans from long lasting, low intensity manifestations to paroxysmal phases with a short duration [43,44]. These eruptions may produce a high quantity of volcanic particles and, depending on the atmospheric conditions, fine ash can reach long distances from the summit craters [45]. Moreover, such particles represent a risk for the population and buildings of the neighboring areas, as well as for air traffic, airports, and other critical infrastructures [8,46]. For this reason, during the last ten years, many tools have been developed at the Istituto Nazionale di Geofisica e Vulcanologia, Osservatorio Etneo (INGV-OE) with the aim of detecting the main features of volcanic plumes and the prevention of hazard from tephra fallout [4,8,47]. In this sense, considering that column height estimates from calibrated visible cameras were added by the volcanologist on duty in the VONA messages during the recent Etna activity in 2021–2022, the automatic estimation of this value is a desirable task at INGV-OE, and results can be extended to other observatories around the world. In this paper, we present an interactive, open-source MATLAB tool designed to analyze images of volcanic eruptions derived from visible cameras, and to automatically recognize the temporal evolution of the volcanic plume height. Even though PHA is not an operative instrument for monitoring purposes yet, the code presented here may represent a first approximation toward a real-time analysis of column height using visible cameras on erupting volcanic systems.

This paper is organized as follows: in Section 2, we briefly describe the camera network of INGV-OE (Section 2.1) and the methodology used to detect the volcanic plume and automatically estimate the column height (Section 2.2). In Section 3, we show the main results focusing our attention on some test cases and on the construction of a code that is able to analyze images with different eruption, atmospheric, and illumination conditions. Finally, in Sections 4 and 5, we discuss the main findings, limitations, and future advances associated with this program.

2. Materials and Methods

2.1. Camera Network of INGV-OE and Dataset

The surveillance network of Etna, whose data are managed by the INGV-OE, includes seismic and infrasonic stations, tiltmeters, GPS (global positioning systems), strainmeters, UV scanners, and thermal and visible cameras [48], among other instruments installed for monitoring purposes. In particular, the visible camera network of INGV-OE includes two low-cost visible cameras: EBVH (Etna Bronte Visible High-definition camera) and ECV (Etna Catania Visible camera), which sit in the west flank of Etna near the town of Bronte and in the southern flank of Etna in Catania, respectively. These cameras (model VIVOTEK IP8172P) present a maximum resolution of 2560 × 1920, with a field-of-view of 33°–93° (vertical), 24°–68° (horizontal), and 40°–119° (diagonal). The cameras are calibrated in terms of location and orientation [49]. With this information, assuming that the plume has a negligible depth and is confined to a vertical plane that rotates according to the wind direction, it is possible to manually estimate the height associated with each pixel of the images and thus calculate the plume height from the record of visible cameras [4], with uncertainties of the order of 0.5 km. Additional details can be found in Scollo et al. [4,49]. Specifically, the dataset considered in this work consists of videos recorded by the ECV static camera for different explosive eruptions (Table 1). This dataset includes both eruptions with optimal visibility conditions and eruptions where column height is not detectable, even manually (Table 1).

Table 1. Dataset of videos of camera ECV considered in this work. These events are sourced from the South East Crater (SEC).

ID	Date	Time (UTC)	Frames	Observations
V01	10 April 2011	08:00–08:15	450	Optimal atmospheric conditions. The outline of the plume is diffuse.
V02	10 April 2011	10:30–10:45	450	Favorable atmospheric conditions.
V03	12 May 2011	03:30–03:45	450	Favorable atmospheric conditions. The outline of the plume is diffuse. The images are particularly dark.
V04	12 May 2011	05:00–05:15	450	Favorable atmospheric conditions. The outline of the plume is diffuse during a portion of the video.
V05	9 July 2011	14:00–14:30	900	Unfavorable atmospheric conditions. The outline of the plume is diffuse during a portion of the video.
V06	25 July 2011	05:00–05:15	450	Partially favorable atmospheric conditions (presence of small clouds near the plume).
V07	25 July 2011	06:45–07:00	450	Weak plume with most of the ash spreading laterally [1]. Optimal atmospheric conditions.
V08	20 August 2011	07:00–07:30	900	Partially unfavorable atmospheric conditions.
V08b	20 August 2011	07:00–08:00	61	Partially unfavorable atmospheric conditions.
V09	29 August 2011	04:00–04:15	450	Poor visibility. The outline of the plume is diffuse.
V10	29 August 2011	04:30–04:45	450	Plume height is beyond the measurement limit during the whole video. The images are particularly reddish.
V11	8 September 2011	06:00–06:15	450	The outline of the plume is diffuse. Favorable atmospheric conditions.
V12	8 September 2011	07:30–07:45	450	Favorable atmospheric conditions.
V13	15 November 2011	10:00–10:15	450	No visibility [2].
V14	15 November 2011	12:15–12:30	450	Unfavorable atmospheric conditions. Plume height is beyond the measurement limit during the whole video.
V15	5 January 2012	05:45–06:00	450	The images are particularly dark. Plume height is beyond the measurement limit during the whole video

Table 1. *Cont.*

ID	Date	Time (UTC)	Frames	Observations
V16	5 January 2012	13:00–13:15	450	Weak plume with most of the ash spreading laterally [1].
V17	18 March 2012	05:00–05:15	450	Weak plume with most of the ash spreading laterally [1].
V18	18 March 2012	08:00–08:15	450	Optimal atmospheric conditions.
V18b	18 March 2012	08:00–09:00	61	Optimal atmospheric conditions.
V19	28 February 2013	10:00–10:15	450	Poor visibility. A small portion of the plume is recognizable [2].
V20	28 February 2013	10:30–10:45	450	Poor visibility. A small portion of the plume is recognizable [2].
V21	3 April 2013	13:30–13:45	450	Partially favorable atmospheric conditions (presence of small clouds near the plume).
V21b	3 April 2013	13:00–14:00	61	Partially favorable atmospheric conditions (presence of small clouds near the plume).
V22	3 April 2013	16:00–16:15	450	Weak plume with most of the ash spreading laterally [1]. The outline of the plume is diffuse.
V23	12 April 2013	10:45–11:00	450	Favorable atmospheric conditions.
V24	12 April 2013	16:00–16:15	450	Weak plume with most of the ash spreading laterally [1]. The outline of the plume is diffuse.
V25	18 April 2013	08:00–08:15	450	Weak plume with most of the ash spreading laterally [1]. The outline of the plume is diffuse.
V26	18 April 2013	10:30–13:45	5850	The video includes a period with plume height beyond the measurement limit, while the outline of the plume is diffuse in the final part.
V27	27 April 2013	14:30–14:45	450	Weak plume with most of the ash spreading laterally [1].
V28	27 April 2013	17:45–18:00	450	The images are particularly dark.
V29	19 April 2020	06:00–10:00	7200	Favorable atmospheric conditions.
V30	12 March 2021	06:35–12:10	361	The video includes a period with plume height beyond the measurement limit.

[1] Video employed to complement the set of calibration images used for the construction of an operative calibration file, but it was discarded for the analysis of plume height versus time because this parameter is not considered informative in this case. [2] Video employed to complement the set of calibration images used for the construction of an operative calibration file, but it was discarded for the analysis of plume height versus time due to visibility limitations.

2.2. Method for the Detection of Plume Height: The Program PHA

PHA (Plume Height Analyzer) is an open-source MATLAB tool that is able to analyze images and videos of volcanic eruptions (derived from visible cameras), with the objective of detecting the volcanic plume and calculation of the temporal evolution of plume height. The Image Processing Toolbox of MATLAB is required for launching the program PHA, whose graphical interface includes six sections (see Table 2). PHA is a self-customizing model, which means that the user must perform an iterative calibration procedure based on the analysis of images of previous eruptions before the model can be used to automatically detect plume height from new images. The underlying, final goal of this approach is to create a 'universal' functional algorithm that would automatically work for new eruptions (without further calibration), thus dealing with different eruption, atmospheric, and illumination conditions. Such a functionality would open the doors for us to implement real-time procedures to compute the column height of ongoing eruptions from the analysis of visible cameras.

Table 2. Summary of functions present in the PHA program.

Section	Function	Description
Fixed mask	Load	Load a previously created fixed mask.
Fixed mask	Create	The program displays a graphical interface, where the user can draw a fixed mask on a reference image (selected by the user). This information is then saved in the folder MaskFiles.
Fixed mask	Plot	Plot the reference image and fixed mask.
Vent position	Load	Load a previously created vent position.
Vent position	Create	The program displays a graphical interface, where the user can select the vent position on a reference image (selected by the user). This information is then saved in the folder VentFiles.
Vent position	Plot	Plot the reference image, vent position and fixed mask.
Pixel to height	Load	Load a previously created pixel-height conversion matrix.
Pixel to height	Create	Three modalities to create a pixel-height conversion matrix are available: -Constant, vertical gradient: the user is asked to indicate the height associated with the vent and with the top of the reference image. -Bilinear interpolation: a graphical interface is displayed, and the user is asked to select a set of pixels of the image and indicate their heights. The resulting conversion matrix is computed by fitting this information as a function of pixel position, using a bilinear interpolation. -Second-order interpolation: a graphical interface is displayed, and the user is asked to select a set of pixels of the image and indicate their heights. The resulting conversion matrix is computed by fitting this information as a function of pixel position, using a second-order interpolation. The resulting pixel-height conversion matrix is saved in the folder PixelHeightFiles.
Pixel to height	Plot	Plot the reference image and the isolines of height, derived from the pixel-height conversion matrix.
Calibration: Lab mask	Load	Load a previously created calibration function.
Calibration: Lab mask	Create	An interactive, iterative procedure is launched, which samples frames from a calibration dataset provided by the user (a single video, a folder containing videos, or a folder containing images) and shows the application of different threshold values in the Lab mask (see Section 2.2.2). The user is asked to indicate the best conservative threshold value. Once the iteration is finished by the user, the program computes the functions used to calculate the Lab mask threshold as a function of the image properties (see Section 2.2.2). The resulting function is saved in the folder CalibrationFiles/LabMask.
Calibration: Lab mask	Improve	This routine reproduces the same process associated with the creation of a Lab mask calibration, but the information is added to an existent Lab mask calibration. Since the performance of this mask is strongly controlled by the amount of data that the calibration includes, this function allows to improve the program performance for a given static camera.
Calibration: Lab mask	Merge	This routine allows to merge the data contained in two or more existent Lab mask calibrations and creates a new, likely better calibration function.
Calibration: Lab mask	Test	An iterative procedure is launched that shows the application of the Lab mask, whose threshold is computed with the loaded calibration function, on a set of frames selected by the user (a single video, a folder containing videos, or a folder containing images).

Table 2. *Cont.*

Section	Function	Description
Calibration: Lab mask	Compare	The user is asked to select two or more calibration functions (in order to compare them) and a set of frames (a single video or a folder of images). Two modalities are available: -Plot Threshold: the program calculates the Lab mask thresholds of the selected frames considering the different calibration functions. Then, this information is plotted. -Show images: an iterative procedure is launched that shows the application of different Lab masks, whose thresholds are computed using the selected calibration functions, on the set of frames indicated by the user.
Calibration: Default Parameters	Load	Load a previously created set of default parameters. Even though the results presented in this paper consider the same set of default parameters, this section allows to increase the applicability field of this code.
Calibration: Default Parameters	Create	A window is displayed, where the user can change some of the constant parameters used in the code (e.g., maximum number of clusters in Lab mask function). Even though the results presented in this paper consider the same set of default parameters, this section allows to increase the applicability field of this code.
Analysis	Single video	This function allows analyzing a single video. The user is asked to provide the frame step adopted to analyze the video and the time interval between two consecutives frames in the video. The output is a plot of the temporal evolution of plume height, and this information can be saved in the folder Results.
Analysis	Folder with images	This function allows analyzing a folder containing images. The user is asked to provide the time interval between two consecutives images. The output is a plot of the temporal evolution of plume height, and this information can be saved in the folder Results.
Analysis	Analyze manually	This function allows to select manually the pixel associated with the maximum height on a set of frames (a single video or a folder of images). The output is a plot of the temporal evolution of plume height, and this information can be saved in the folder Results.
Results	Single plot	This function allows plotting the results of previously analyzed videos/folders with images. The input of this function is the output file saved by any of the three functions of the section Analysis.
Results	Compare plots	This function allows comparing the results of previously analyzed videos/folders with images. The inputs of this function are the output files saved by any of the three functions of the section Analysis.

For each frame analyzed (e.g., Figure 1a), the general procedure to compute the plume height consists of a series of successive steps (Figure 1):

(a) Application of a fixed mask to identify and discard the zones of the images associated with infrastructure (e.g., buildings, antennas, etc.) and volcano topography (Figure 1b, see Section 2.2.1).
(b) Subsequent use of a mask to identify and discard the zones of the images associated with the sky. This mask is mainly based on the analysis of the images in Lab scale (Figure 1c, see Section 2.2.2) and requires the development of the model calibration.
(c) The application of three successive procedures to identify and discard clouds, including those in contact with the plume (Figure 1d–f).
(d) A procedure to evaluate the internal variability of the non-masked zone of the images and eventually exclude the low-variability zones.
(e) Finally, considering a pixel-to-height conversion matrix (Figure 2), the highest pixel belonging to the plume is identified.

Figure 1. Illustrative example of the application of the procedures used to identify the plume in the program PHA. (**a**) Original image. (**b**) Application of the fixed mask. (**c**) Application of the Lab mask. (**d**–**f**) Application of the different algorithms aimed at discarding the clouds from the image.

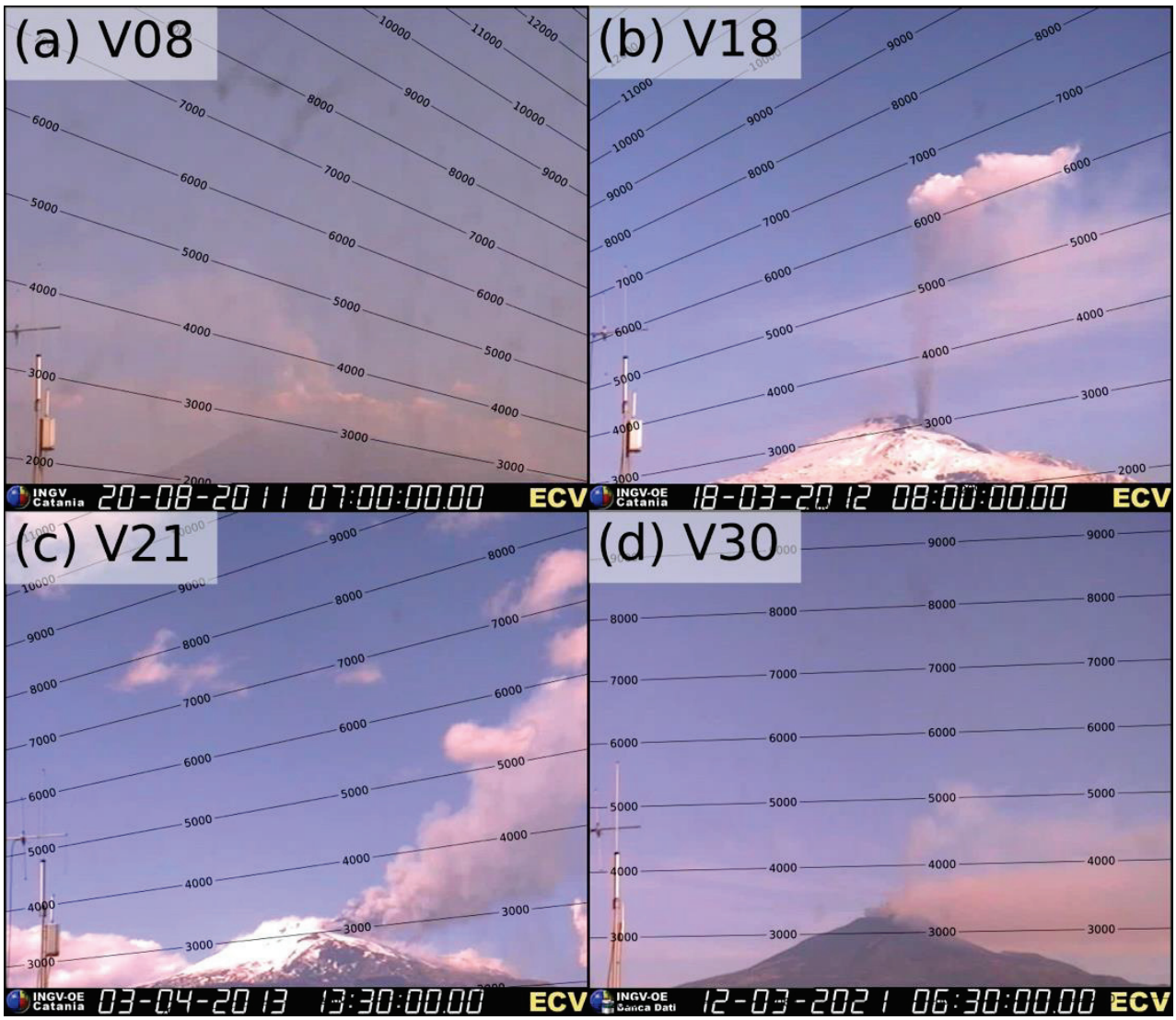

Figure 2. Examples of the pixel-height conversion matrix used in this work. They are based on the dominant wind field observed during four events of Mount Etna (see titles and Table 1) [4]. Winds blowing to the E (to the right in the images) translate into height isocurves dipping to the W, while when winds blow to the W (to the left in the images), the resulting height isocurves dip to the E. Data are presented in m a.s.l.

In this section, we present in detail each one of the described steps, together with all the interactive functions that PHA includes for their development (see Table 2).

2.2.1. Fixed Mask

Given a static camera, a fixed mask is introduced (Figure 1b) in order to discard all the pixels of the images that are associated with infrastructure and volcano topography. This is important to avoid processing pixels whose properties are not associated with the eruption and/or atmospheric characteristics. Since this process must be performed only once for each static camera, the best way to define this mask is manually. For this, PHA includes ad hoc functions that allow creating interactively, saving, loading, and plotting the fixed mask (Table 2).

2.2.2. Lab Mask

We have observed that the third channel of an image in Lab scale (i.e., the color dimension *b*) generally discriminates well between clear sky pixels and other zones of the processed frames (e.g., volcanic plume and clouds; Figure 2c). The suitability of this channel to recognize sky pixels under optimal illumination conditions is similar to that observed by considering the subtraction of the red and the blue channels of the image in RGB scale, which is used in the software PlumeTraP [6], while it is slightly better during sunrise and sunset. For most frames of the studied videos, we have observed that a threshold value for the third channel of the image in Lab scale can be set in order to create a mask to split the image in two regions (hereafter, the Lab mask). However, it is not possible to set a single threshold value that works for a large set of images. Instead, it depends on specific image characteristics, which are in turn controlled by atmospheric factors as well as eruption and illumination conditions. Due to this, we developed an iterative procedure (hereafter, the Lab calibration) to calculate a function that, for each analyzed frame, provides the threshold (T) used to compute the Lab mask. This calibration can be performed using a reference video, a folder of videos, or a folder of images, and consists of an iterative procedure where different frames are sampled and analyzed, and the user is asked to indicate the best conservative mask (i.e., not masking the plume) from a choice of nine alternatives (Figure 3). Let us consider a calibration procedure based on N frames. For each frame ($i = 1, \ldots, N$), and considering the portion of the images not masked by the fixed mask, the algorithm saves the following information:

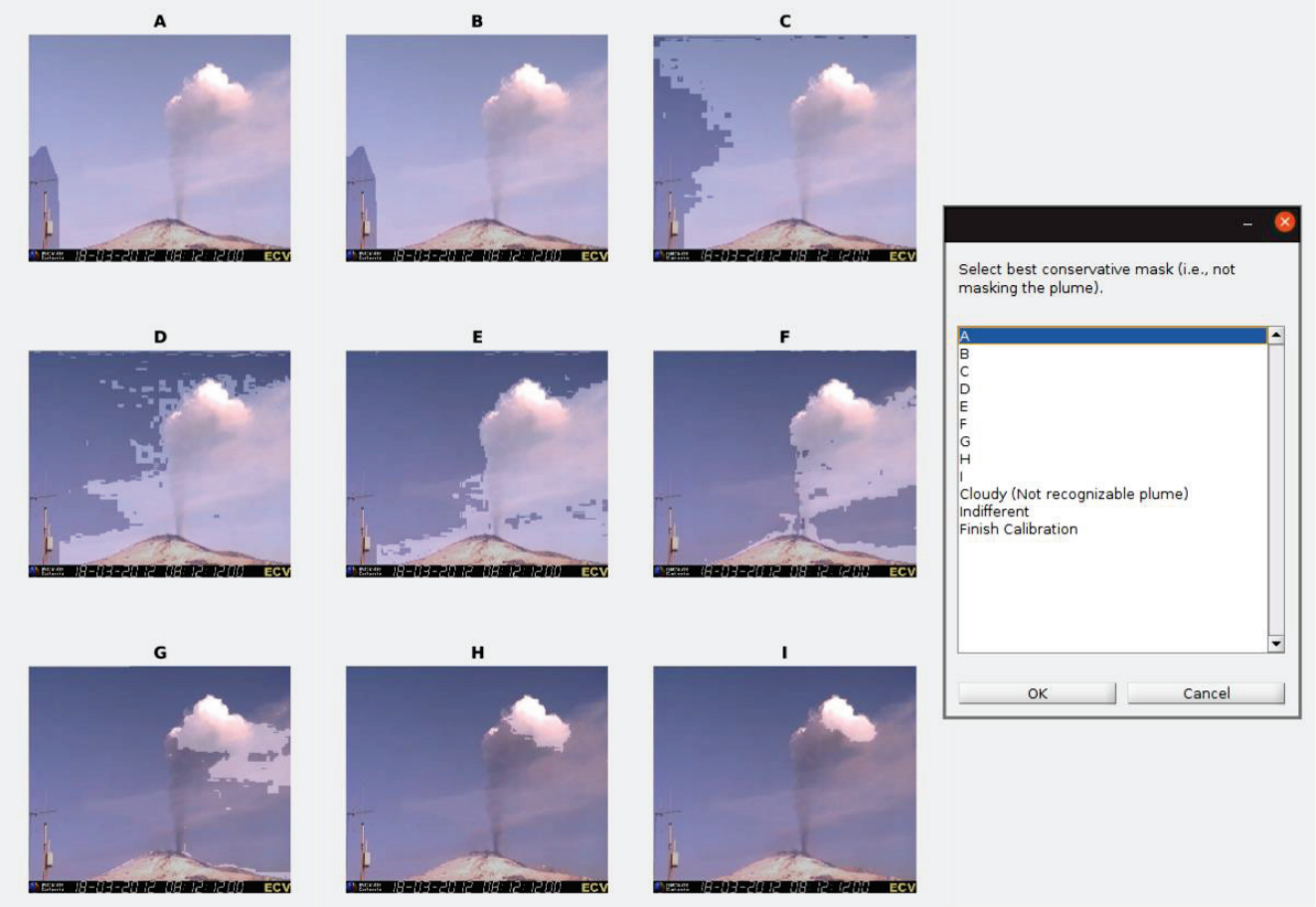

Figure 3. Illustrative example of the iterative procedure used to define the threshold value of the Lab mask, necessary to recognize the pixels belonging to the volcanic plume as a function of the image properties. In these images, the lightened areas correspond to pixels potentially considered as part of the ash plume. In this case, the recommended choice is E or F.

- Mean value of L (Lab scale, L_i).
- Mean value of a (Lab scale, a_i).
- Mean value of b (Lab scale, b_i).
- Mean value of R (RGB scale, R_i).
- Mean value of G (RGB scale, G_i).
- Mean value of B (RGB scale, B_i).
- Threshold (T_i).

The properties of the i-th calibration image are thus given by $X_i = \{L_i, a_i, b_i, R_i, G_i, B_i\}$ and the information provided by the user, by selecting the best conservative mask, is given by T_i. Using X_i and distance-based criteria, calibration images are automatically clustered. The number of clusters (M) clearly depends on N: the larger the set of calibration images, the higher the number of clusters. The use of weighted, distance-based clustering techniques allows automatically generating classes of images characterized by common eruption, atmospheric, and illumination conditions. In this procedure, the *distance* between the different frames is computed by adopting the vector X_i associated with each of them to define their *positions*. For each cluster, a specific function is derived to calculate the threshold (T) used in the Lab mask:

$$T = F_j(X) = F_j(\{R, G, B, L, a, b\})$$

where j is a subscript referring to the cluster (i.e., $j = 1, \ldots, M$). F_j is defined using a polynomial fit computed by adopting the subset of calibration images that defines the j–th cluster. The order of this polynomial fit depends on the amount of data available in this cluster (first order regression for clusters with 20 data or less, and second order regression for clusters with more than 20 data). We also assume that $F_j(X)$ is bounded by the minimum and maximum thresholds within the calibration images.

Thus, when a new image is analyzed, characterized by the vector X_n, the code finds its cluster by computing the minimum distance between X_n and X_i ($i = 1, \ldots, N$), and then it adopts the function F_j associated with this specific cluster to calculate $F_j(X_n)$. On the other hand, a calibration function defined by the nearest calibration frame (in terms of the image characteristics, that is, in terms of the vector X_i) is also present in PHA. To present conservative results, in this work we use the more conservative choice between both the alternatives for each frame analyzed.

The number of iterations determines the spectrum of images that the code will be able to analyze correctly. Since this is a critical factor in the effectiveness of the presented procedure, PHA includes a set of functions that allows creating and interactively improving the calibration data, as well as for loading, comparing, and testing them (Table 2). We remark that the only relevant correction needed by the Lab mask is associated with dark zones of the plume during sunrise and sunset, but this is automatically solved with no need of calibration. Additionally, note that this iterative procedure allows the user to indicate the images where the plume is not recognizable, which permits the code to automatically identify the images where the estimation of plume height is not possible using visible cameras (e.g., cloudy conditions, night images).

2.2.3. Cloud Identification

At this point, in general, the algorithm has masked all but the plume and clouds. Three successive procedures are then employed to discard the pixels associated with clouds:

(a) We trace a large number of segments between border points of the image (above the vent position) including both horizontal and inclined segments. When a line intersecting a completely masked zone is identified (i.e., with no plume or clouds), the entire region above this line is masked, reducing the computation time and discarding pixels associated with clouds (Figure 1d).

(b) Then, all the not masked pixels are clustered considering a distance-based criterion, and only the nearest cluster to the volcanic vent is conserved for the following steps (Figure 1e).
(c) Finally, the perimeter of the non-masked region is studied to identify lobe-like geometries. When the distance (calculated through a line) between two points in the non-masked region border is much lower than the distance calculated through the perimeter of this region, these points are assumed to define a lobe-like geometry, and this part of the non-masked zone is discarded. In this way, clouds superposed to the plume tend to be discarded (Figure 1f).

Since this procedure needs the volcanic vent position as an input parameter, PHA includes a set of functions that allow to interactively set the position of the vent (note that the definition of vent position must be performed only once for each static camera). The program allows plotting and loading this information as well (Table 2).

2.2.4. Internal Variability of Non-Masked Zone

At this point, the algorithm has identified a set of pixels that represent a good candidate for the volcanic plume. However, sometimes the limits of the plume are diffuse, and thus we need an additional criterion. Since color variability tends to be higher in the plume, we adopted a threshold to consider the portion of the mask characterized by a large color variability. A fixed threshold value has works for all the videos studied here, and thus calibration is not needed. In any case, PHA includes proper functions to set different values of threshold when it is required (e.g., for other volcanoes or other static cameras).

2.2.5. Pixel to Height Conversion

In order to calculate plume height, we need a procedure that is able to relate pixels to plume height. This is represented by a conversion matrix with the same dimensions of the images, indicating the height associated with each pixel of the image. In this way, the model is able to evaluate the height of all the pixels belonging to the plume and determine the plume height (i.e., the maximum height associated with a plume pixel). While PHA offers different alternatives to create a conversion matrix (see Table 2), in this work we use specific conversion matrixes associated with the wind fields observed during some of the eruptions described here (see Section 2.1 and Figure 2). The frames studied present a maximum measurement height of the order of 10 km a.s.l. due to limitations in the field view, which is influenced by wind direction and intensity as well. Whereas winds blowing to the E (to the right in the images) translate into height isocurves dipping to the W, when winds blow to the W (to the left in the images), the height isocurves dip to the E. On the other hand, winds blowing to the south (i.e., directly towards the ECV camera) produce more spaced height isocurves (i.e., reduction in the measurement limit) and winds blowing to the north translate into less spaced height isocurves (i.e., increment of the measurement limit). Specific details about the geometric considerations needed to define these pixel-to-height conversion matrixes can be found in Scollo et al. [4,49].

2.2.6. Results

Once the information of each frame is computed, PHA plots the temporal evolution of height plume, excluding results considered outliers within the temporal series. Results are also saved in MATLAB files that can be imported, plotted, and compared later using the program PHA.

3. Test Examples and Results

3.1. Internal Calibrations

As a first step, we show examples of internal calibrations, i.e., we use a few frames of single videos to create a calibration file and then we apply it to analyze the same videos. We focus on three short videos with different degrees of complexity (V18, V08 and V21; see Table 1) and a long-lasting video with significant changes in eruption and illumination

conditions (V30; see Table 1). Note that all the calibration files and results described in this paper are included in the Git repository https://github.com/AlvaroAravena/PHA (accessed on 12 January 2023).

3.1.1. V18 (18 March 2012)

This eruption is part of the 25 low-explosivity events observed at Etna between January 2011 and April 2012 [50]. V18 is characterized by extremely favorable illumination and atmospheric conditions. We performed three independent calibrations using only 5 frames out of 450 recorded over a 15 min period (calibration files V18_a-c).

In Figure 4, we show the evolution of the Lab threshold estimated using these three calibrations on the 450 frames of V18. We can note that the application of the different calibration files produces reasonably similar decreasing trends for the Lab threshold. Then, we used the same set of calibration files to analyze V18 with the pixel-to-height conversion matrix presented in Figure 2b (see Section 2.2.5). We highlight that, due to the optimal illumination and atmospheric conditions of V18, an even smaller number of calibration frames seems enough to produce reproducible numerical results and similar to manual estimates, as observed in Figure S1a in the Supplementary Material.

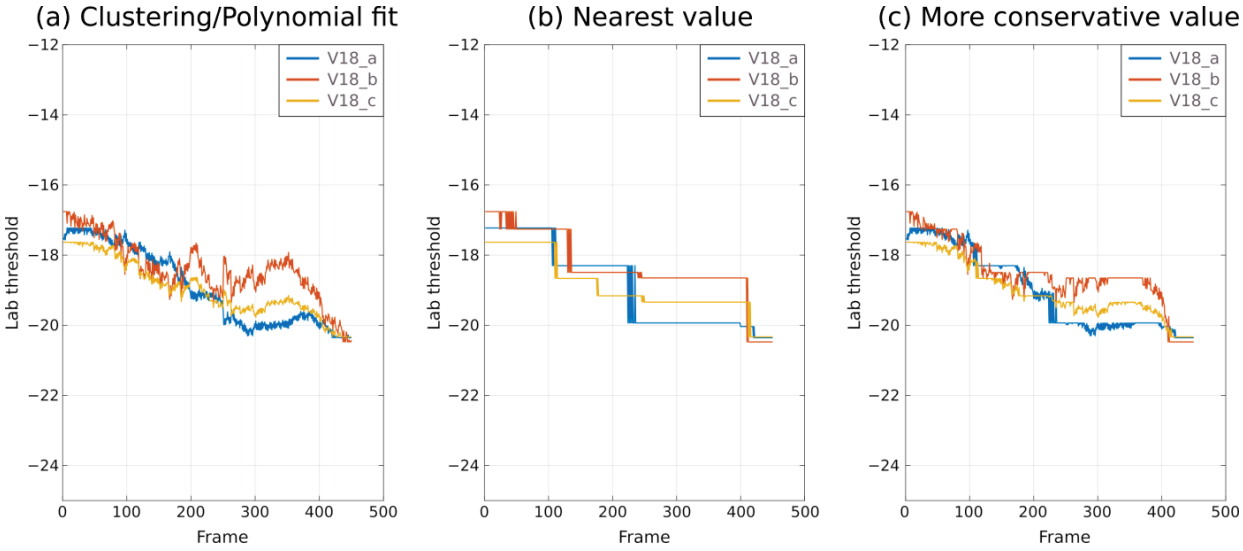

Figure 4. Threshold values for the Lab mask as a function of frame number of the video V18, computed using three different calibrations based on five frames extracted from V18 (see legends). In the different panels, we present the application of different fit strategies to define the threshold for the Lab mask. Results derived from the application of clustering and polynomial fit are presented in panel a, results in panel b are associated with a criterion of nearest value, and panel c presents, for each frame, the more conservative choice between panels a and b (i.e., the minimum value). Note that PHA (see Table 2) can generate this figure automatically.

The temporal evolutions of column height, calculated using the different calibration files, are strongly consistent between them (Figure 5a), showing percentage differences of the order of 0.2% during the video (maximum value of 1.0%). Note that similar average percentage differences are computed when numerical results are compared with manual estimates (Figure S1a). The results indicate a continuous increase in column height from ~6700 m up to ~8200 during these 15 min, with oscillations with a period of about 5 min (see Supplementary Videos S1–S3 in the Supplementary Material). The regularity in the evolution of plume height highlights the precision of this program under favorable atmospheric and illumination conditions.

We dispose of an additional set of 61 frames for a longer period (1 h) of the same eruption (V18b). Since a significant change in the eruption and illumination conditions

occurs, the previous calibrations are not able to capture the characteristics of the complete video (note that it was recorded at 8 a.m.). In fact, these calibrations only work for the first ~35 frames of the video. Instead, we created three new, independent calibrations based on 5 frames out of 61 recorded over a period of 1 h (calibration files V18b_a–c). Results are consistent between them and show an increasing trend of plume height from ~6700 up to more than the measurement limit (Figure 5b and Supplementary Videos S4–S6). In this case, our calibrations produce average percentage differences of the order of 0.3% (0.5% before reaching the measurement limit), with a maximum value of 4.1%.

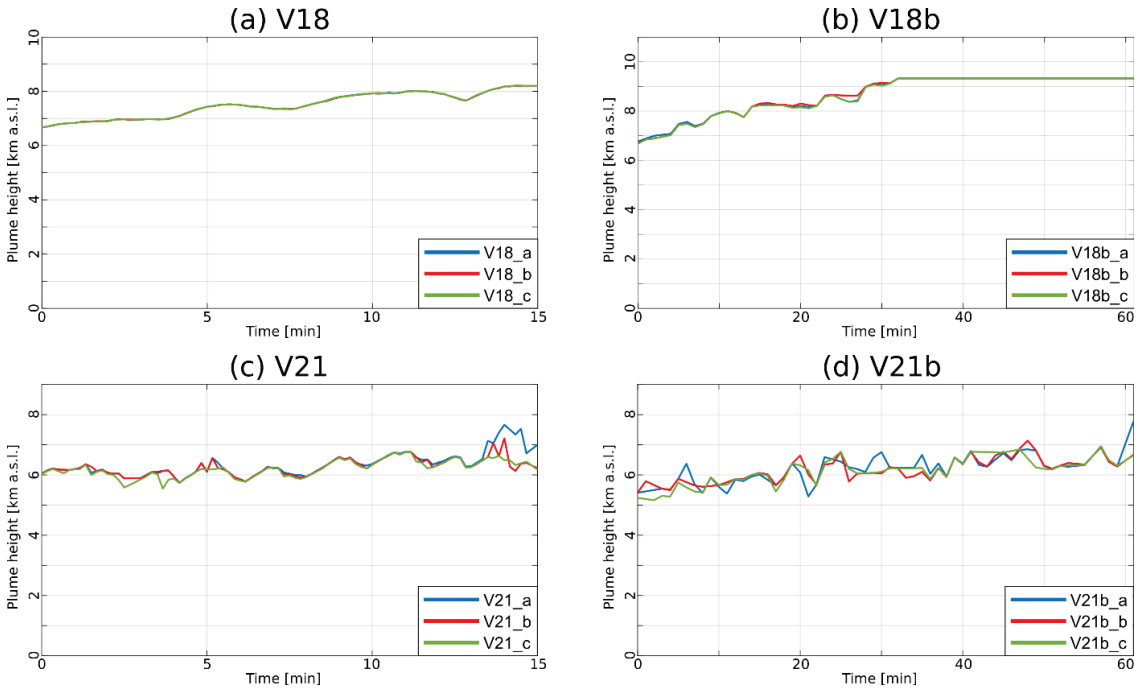

Figure 5. Plume height as a function of time for some reference videos (see titles) of Mt. Etna (see Table 1) using different files of internal calibration (see legends and Section 3.1). The measurement limit in panel b is 9326 m a.s.l.

3.1.2. V21 (3 April 2013)

V21 is a video characterized by favorable illumination conditions and partially favorable atmospheric conditions due to the presence of several clouds that often cover part of the eruption plume. In this case as well, we performed three independent calibrations with only 5 frames out of 450 (calibration files V21_a–c), and then they were used to analyze the same video. The pixel-to-height conversion matrix is presented in Figure 2c (see Section 2.2.5). The evolution of plume height calculated using the different calibration files is similar (Figure 5c), showing oscillations between ~5800 and ~6800 m a.s.l. The only significant differences between numerical results are observed in a few, specific frames near the end of the video (differences of the order of 1000 m or less), when small clouds disturb the plume identification for two of the calibrations (see Supplementary Videos S7–S9). On average, the percentage differences of plume height associated with these calibrations are of the order of 1.3%. When compared with manual estimates, the average percentage differences of plume height are instead of the order of 3.0% (Figure S1b). Interestingly, Figure S1b shows a regular decrease in the average percentage difference with respect to manual estimates when the number of frames used for the Lab calibration increases, suggesting that a calibration based on >8 frames would produce a significantly better performance.

An additional video with 61 frames over a longer period of the same eruption was analyzed using three different calibrations based on only 5 frames (calibration files V21b_a–c). A general trend of plume height increase can be observed (from ~5300 to ~6900 m a.s.l.;

Figure 5d). The main discrepancies between the curves are product of the interference of small clouds and the plume (instead, large clouds are typically recognized and discarded; see Supplementary Videos S10–S12). The percentage differences between the results obtained with these independent 5-frames-based calibrations are of the order of 2.8% (average value), with a maximum value of 11.5%. Interestingly, the calibrations constructed using a period of 15 min (i.e., calibration files V21_a–c) are able to capture well the characteristics of the complete video V21b (Supplementary Figure S2), reflecting that the illumination conditions are nearly constant during the 1 h video V21b (note that it was recorded at 1 p.m.).

3.1.3. V08 (20 August 2011)

V08 is also included in the sequence of 25 low-explosivity events observed at Etna between January 2011 and April 2012 [50]. This video presents partially unfavorable illumination and atmospheric conditions, with permanent presence of a strata of low-altitude clouds. We constructed three independent calibrations with 5 frames each (out of 900 frames), which were used to analyze the same video (calibration files V08_a-c). On the other hand, the matrix of pixel-to-height conversion of this video is presented in Figure 2a (see Section 2.2.5). The results produced by PHA, highly consistent between them, are characterized by a continuous increase in plume height up to reach the image top and thus exceed the measurement limit (Figure 6a). The increase in plume height occurs rapidly, at a rate of ~600 m/min, from ~4200 to ~9800 m a.s.l. Some of the calibrations differ in specific frames during the waxing phase due to the diffuse limits of the plume in this period (see Supplementary Videos S13–S15), while they capture well the general tendency of plume height. In this case, on average, the percentage differences of plume height are of the order of 0.3% (1.1% before reaching the measurement limit), with a maximum value of 11.5%. With respect to manual estimates, the average percentage differences are of the order of 3.0%, and we also observe a regular decrease in the average percentage difference with respect to manual estimates when the number of frames used for the Lab calibration increases (Figure S1c). Results suggest that, for this video, an internal calibration based on 5 frames is enough to produce reliable data of column height.

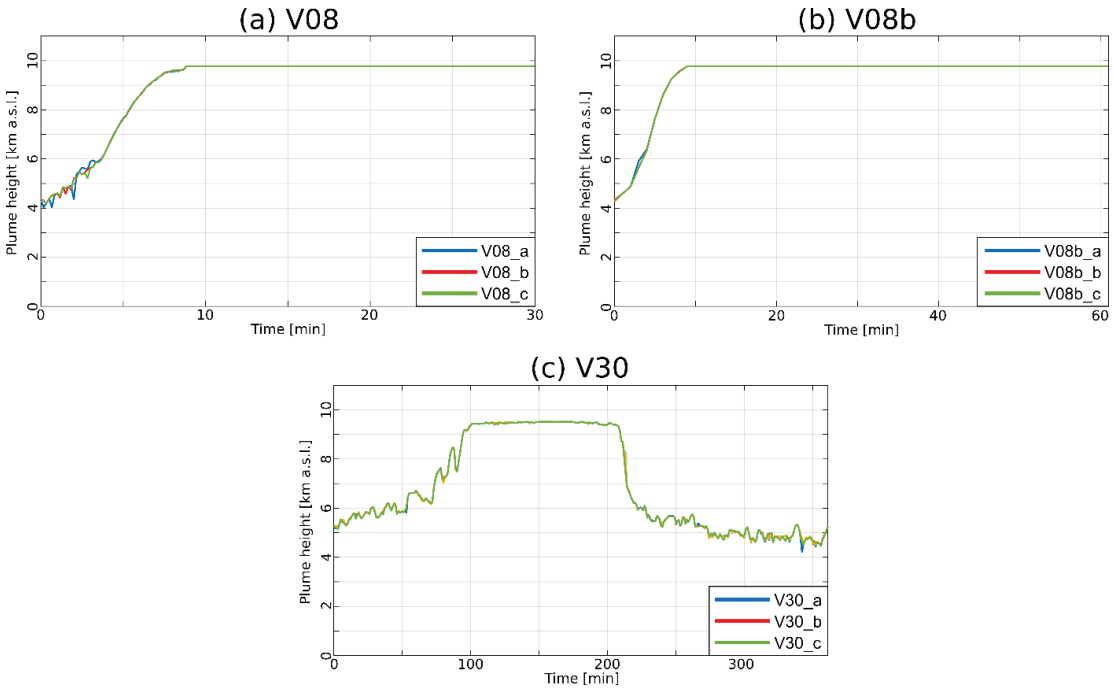

Figure 6. Plume height as a function of time for some reference videos (see titles) of Mt. Etna (see Table 1) using different files of internal calibration (see legends and Section 3.1). The measurement limit in panels a and b is 9774 m a.s.l. and that of panel c is 9517 m a.s.l.

The same set of calibrations was able to analyze the frames of the video V08b (Table 1), which comprises a longer period of the same eruption (Figure 6b). Results associated with the different calibration files (see Supplementary Videos S16–S18) are strongly consistent and capture well the characteristics of the waxing phase described in the previous paragraph.

3.1.4. V30 (12 March 2021)

V30 is a ~6-h-lasting video with strong changes in the illumination and eruption conditions, comprising well-defined waxing and waning phases. Consequently, a larger number of calibration frames must be considered in order to create a functional calibration file. We constructed three independent 10-frames-based calibrations (out of 361 frames), which were used to analyze the same video (Figure 6c and Supplementary Videos S19–S21). Our results, obtained by adopting the pixel-to-height conversion matrix presented in Figure 2d, show a waxing phase from a plume height of ~5200 m a.s.l. to a value beyond the measurement limit, with an average rate of plume height increase in the order of 40 m/min, much smaller than that observed in V08. Note, however, that the waxing phase can be divided in two steps with different variation rates of plume height (Figure 6c). The waning phase, from beyond the measurement limit up to a plume height of ~5500 m a.s.l., occurred at a rate of ~120 m/min and, after that, plume height decreases slowly up to ~4700 m a.s.l. The results obtained using the different calibrations are strongly similar, with average differences of the order of 2.0%, while average percentage differences of the order of 7.0% are obtained when numerical results are compared with manual estimates (Figure S1d). Note that at least 10 calibration frames are needed to obtain average percentage differences (with respect to manual measurements) below 10% (Figure S1d).

3.2. Operational Calibration

We have shown that PHA permits to analyze videos of volcanic eruptions by means of a fast calibration process. Although this may be useful for research and operative purposes by itself, an autonomous operative use of PHA requires that the program can recognize the characteristics of new images and estimate proper calibration parameters. In other words, in order to advance toward the implementation of a real-time column height estimation procedure using visible cameras on erupting volcanoes, we need a calibration file that considers a large set of eruption, illumination, and atmospheric conditions. To do this, PHA includes a set of functions that allows to create, merge, and improve calibrations by adding new data, permitting to refine the performance of the program as new data becomes available for the calibration as well (see Table 2).

To show the capability of the program to deal with a large calibration file and to recognize different conditions simultaneously, we merged a set of calibration files constructed using different videos (Table 1). Our dataset includes: (a) 5 frames for short-lasting videos with a capture period of 1 min (V08b, V18b, and V21b), (b) 10 frames for long-lasting videos with a capture period of 1 min (V30), (c) 40 frames for long-lasting videos with a capture period of 2 s (V26 and V29), and (d) 10 frames for short-lasting videos with a capture period of 2 s (all the other videos), totaling 375 frames. The application of a common calibration file for a large set of videos has shown that:

(a) For eruptions with favorable atmospheric conditions and when the outline of the plume is well defined (V02, V10, V12, V15, V18, V18b, V23, V28, V29, and V30), PHA is able to trace accurately plume height and in some cases small-scale oscillations of this parameter can be identified as well (Figure 7). Comparisons with manual estimates of plume height are presented in Figure 7, where we can observe remarkably consistent trends.

(b) For eruptions with unfavorable atmospheric conditions (e.g., small clouds interfering the visual field; V06, V08, V08b, V14, V21, and V21b), the program is able to recognize well the range of values of plume height and general tendencies, but small-scale oscillations are not traced and occasional mistakes in punctual frames are observed. However, we stress that they are typically below the intrinsic uncertainty of plume

height estimations based on visible cameras [4], as observed in Figure 8, where we present comparisons with manual estimates.

(c) Finally, for eruptions with plumes characterized by diffuse outlines (V01, V03, V04, V05, V09, V11 and V26), PHA is able to trace well the range of values of plume height and recognizes large-scale tendencies. However, the results present a typically oscillating behavior around the manual estimates (Figure 9) and occasional mistakes in specific frames are observed as well.

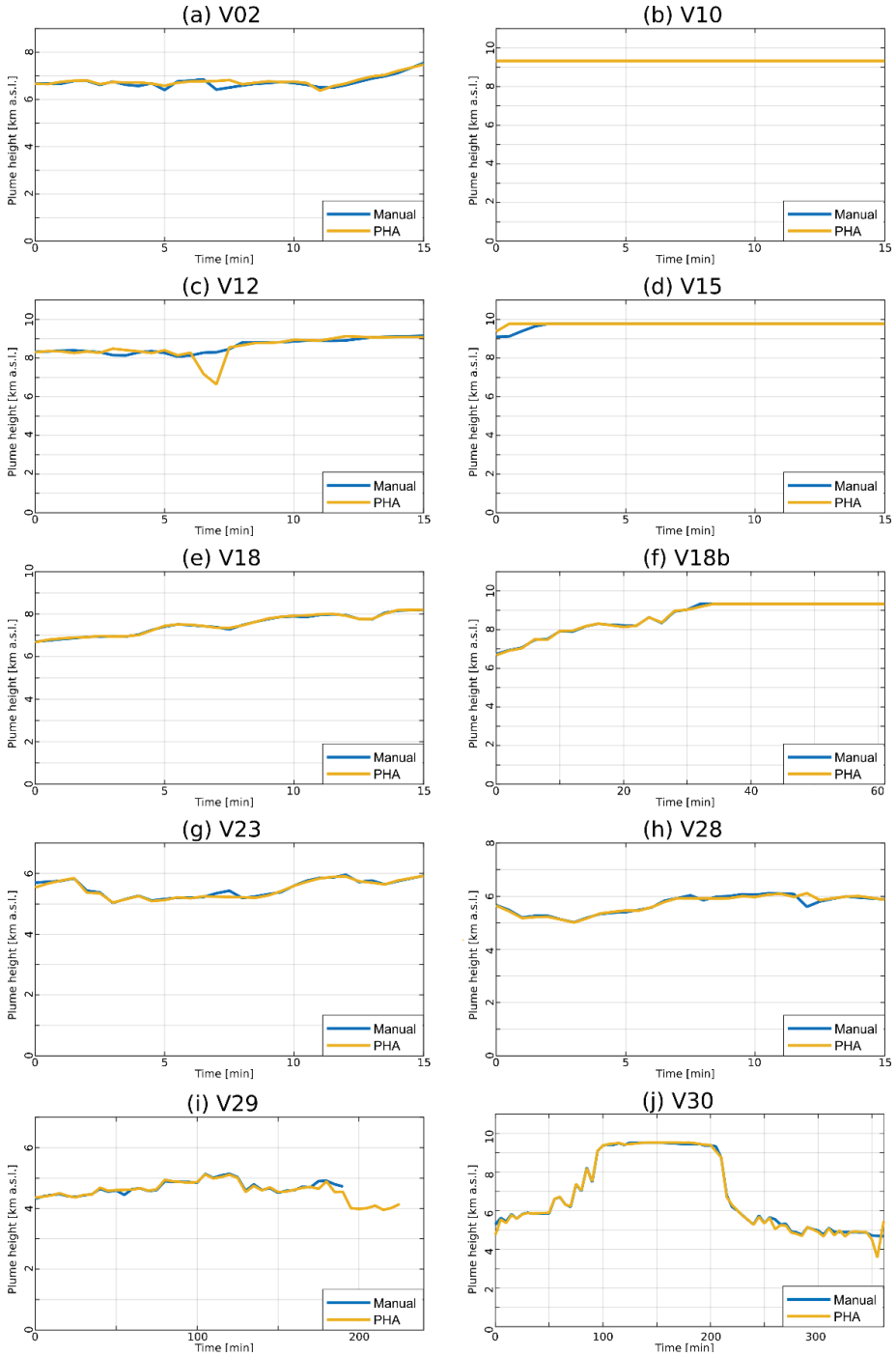

Figure 7. Plume height as a function of time for some reference videos (see titles) of Mt. Etna (see Table 1), using a common calibration file (see Section 3.2). These videos are characterized by favorable atmospheric and illumination conditions, and the plumes present a well-defined outline.

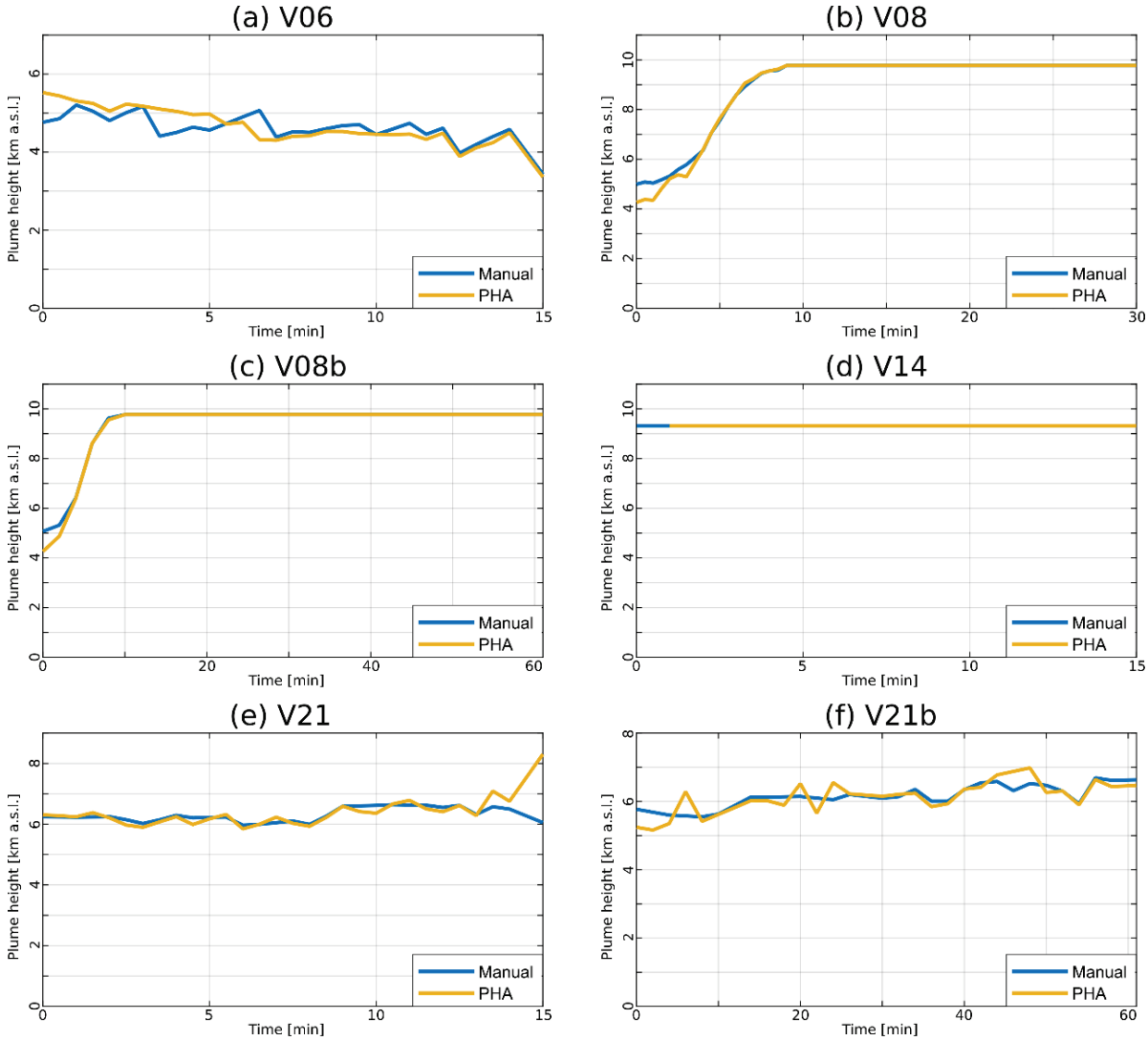

Figure 8. Plume height as a function of time for some reference videos (see titles) of Mt. Etna (see Table 1), using a common calibration file (see Section 3.2). These videos are characterized by unfavorable atmospheric conditions (e.g., presence of clouds interfering with the visual field), and the plumes present a well-defined outline.

In general terms, results are consistent with manual measurements, showing that PHA, when an enough large number of frames are present in the calibration file, is able to deal with different eruption, atmospheric, and illumination conditions. The average percentage difference between manual and automatic measurements of column height is 2.70%, with a median of 0.59% and 90th and 95th percentiles of 8.55% and 13.73%, respectively. Regarding the absolute difference between the two estimates of column height, the average value is 166.8 m, with a median of 34.5 m and with 90th and 95th percentiles of 548.0 m and 925.1 m, respectively.

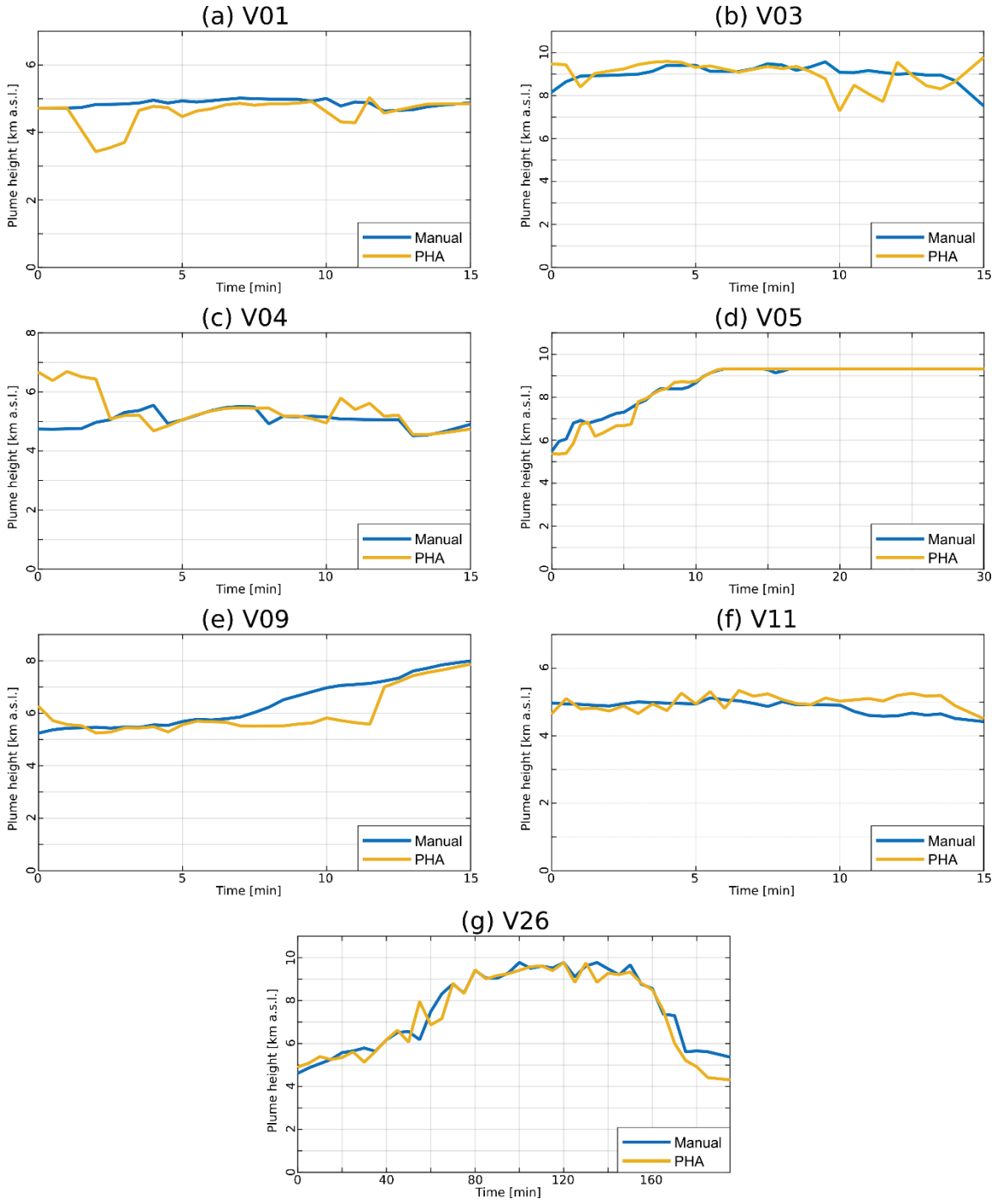

Figure 9. Plume height as a function of time for some reference videos (see titles) of Mt. Etna (see Table 1), using a common calibration file (see Section 3.2). These videos are characterized by plumes with diffuse outlines.

4. Discussion

4.1. The Program PHA

In this paper, we have presented the program PHA, which is a novel, open-source MATLAB tool designed to analyze images from visible cameras of volcanic plumes, with the aim of automatically recognizing the plume and estimate its maximum height as a function of time. Due to the intrinsic variability of the images captured during volcanic eruptions, which is a consequence of changes in eruption, illumination, and atmospheric

conditions, PHA was conceived as a self-customizing tool. This means that, before operational use, an iterative calibration procedure must be performed, based on the analysis of previous eruptions of the volcanic system of interest, possibly occurred under different environmental and volcanic conditions. The algorithm created to identify the volcanic plume largely relies on the analysis of the third channel of the images in Lab scale, which allows recognizing and discarding pixels associated with the sky, and the application of a series of procedures aimed at discarding clouds and determining high-color gradient zones in the plume.

By means of a series of illustrative applications of PHA on some events at Mt. Etna, Italy, we showed that a bounded number of frames can be used to calibrate the model and create a functional tool that is able to process data from past eruptions and trace the plume height automatically, with reproducible and accurate results when compared with manual measurements (see Section 3.1). However, to create a program that is able to recognize in real-time the characteristics of new images and estimate proper calibration parameters, a calibration with a large set of images with different characteristics in terms of illumination, atmospheric conditions, and eruption parameters, is needed. PHA includes a large set of interactive functionalities to facilitate the construction of a truly operative tool in the context of volcano monitoring, with functions to create, improve, and merge the data of different calibration files. In this paper, these functions were used to create a calibration file based on 375 images captured by the ECV visible camera of Etna. This calibration file has been shown to be useful to analyze videos of 23 events of Mt. Etna. Results are remarkably consistent with manual estimations when illumination and atmospheric conditions are favorable, while some occasional mistakes are still present when illumination and atmospheric conditions are not optimal. However, even in this case, the program permits to recognize large-scale, time-dependent tendencies of the eruptions, with differences between PHA and manual estimates typically below the intrinsic uncertainty of these measurements [4]. This first attempt shows that PHA is potentially useful to construct a tool that is able to analyze automatically visible camera images of Mt. Etna, with important applications for monitoring purposes, and may represent a significant approximation toward a real-time analysis of column height using visible cameras on erupting volcanoes.

4.2. Limitations, Strengths, and Future Advances of PHA

This tool presents the intrinsic limitations of images of visible cameras: reliable results can be obtained exclusively during daylight hours and with a small to moderate presence of clouds. They also present a bounded visual field, which translated into the presence of measurement limits as those observed in the ECV visible camera of Mt. Etna (see Figures 5–9). On the other hand, due to the frequent presence of clouds in the summit of stratovolcanoes, this tool cannot be directly used to recognize the onset of an explosive eruption. In fact, the current version of the code does not include an automatic procedure to detect the absence of an ash plume and, in such a case, it will only indicate that the plume height, if present, is less than the minimum measurement limit.

Additionally, a calibration step is strictly needed before its use and, even if this tool can be set to analyze a posteriori the record of visible cameras from any explosive volcanic eruption, the availability of large datasets of past eruptions is necessary to construct an operative tool in real-time for monitoring purposes. Thus, this type of application is only feasible in volcanoes with frequent and well-monitored volcanic activity such as Etna, where the need of having a rapid, reliable tool to detect and measure volcanic plumes represents an impelling necessity.

Even though PHA is still not an operative instrument at INGV-OE, the results presented in this paper are encouraging in terms of the applicability of a customizable tool to estimate plume height as a function of time for monitoring purposes. To further improve the performance of PHA, the inclusion of additional videos of past eruptions is needed, as well as more code reliability testing and analysis of videos from other volcanoes with enough eruptions recorded. Additionally, the structure of the code allows for the refine-

ment of the model by including new variables that are able to characterize the calibration frames (i.e., increasing the dimensions of the vector X_i; see Section 2.2.2); thus improving the characteristics of the fit used to calculate the calibration-derived inputs. We emphasize that this code can also be adapted to analyze images from thermal cameras, which uncovers additional development opportunities for this code in the future.

5. Conclusive Remarks

A new open-source MATLAB tool named Plume Height Analyzer' (PHA) able to analyze images from visible cameras of volcanic plumes and automatically estimate its maximum height as a function of time is presented in this paper. Although the tool uses an iterative calibration procedure based on the analysis of previous eruptions of a given volcano and should be tested under different environmental and volcanic conditions, it may represent a first approximation toward a real-time analysis of column height using visible cameras on erupting volcanoes.

Supplementary Materials: The following supporting information can be downloaded at: https://www.mdpi.com/article/10.3390/rs15102595/s1. Figure S1: Average percentage difference with respect to manual measurements of column height for a set of results obtained with the program PHA, as a function of the number of frames used for the construction of the calibration files adopted (internal calibration). For each video (see titles), we created fifteen independent calibration files with different numbers of calibration frames (from 2 to 10 in panels a-c, from 4 to 20 in panel d). In each panel, we present the mean value (filled circles) and standard deviation (bars) associated with the application of three independent calibration files, created using different numbers of calibration frames (see x-axis). Figure S2: Plume height as a function of time for video V21b of Etna (see Table 1) using different files of internal calibration (see legends and Section 3.1). Video S1: Video V18 analyzed using the calibration file V18_a. Video S2: Video V18 analyzed using the calibration file V18_b. Video S3: Video V18 analyzed using the calibration file V18_c. Video S4: Video V18b analyzed using the calibration file V18b_a. Video S5: Video V18b analyzed using the calibration file V18b_b. Video S6: Video V18b analyzed using the calibration file V18b_c. Video S7: Video V21 analyzed using the calibration file V21_a. Video S8: Video V21 analyzed using the calibration file V21_b. Video S9: Video V21 analyzed using the calibration file V21_c. Video S10: Video V21b analyzed using the calibration file V21b_a. Video S11: Video V21b analyzed using the calibration file V21b_b. Video S12: Video V21b analyzed using the calibration file V21b_c. Video S13: Video V08 analyzed using the calibration file V08_a. Video S14: Video V08 analyzed using the calibration file V08_b. Video S15: Video V08 analyzed using the calibration file V08_c. Video S16: Video V08b analyzed using the calibration file V08_a. Video S17: Video V08b analyzed using the calibration file V08_b. Video S18: Video V08b analyzed using the calibration file V08_c. Video S19: Video V30 analyzed using the calibration file V30_a. Video S20: Video V30 analyzed using the calibration file V30_b. Video S21: Video V30 analyzed using the calibration file V30_c.

Author Contributions: Conceptualization, R.C. and S.S; methodology, A.A., G.C., R.C., M.P. and S.S; software, A.A. and G.C.; writing—original draft preparation, A.A. and G.C.; Writing—review and editing, A.A., G.C., R.C., M.P. and S.S. All authors have read and agreed to the published version of the manuscript.

Funding: This work was also in the framework of the INGV Project "Pianeta Dinamico" (D53J19000170001), funded by MUR ("Ministero dell'Università e della Ricerca, Fondo finalizzato al rilancio degli investimenti delle amministrazioni centrali dello Stato e allo sviluppo del Paese, legge 145/2018").

Data Availability Statement: The data used in this paper belong to INGV and can be made available upon request to the authors.

Acknowledgments: The program PHA is available online via the webpage https://www.github.com/AlvaroAravena/PHA (accessed on 12 January 2023).

Conflicts of Interest: The authors declare no conflict of interest.

References

1. Bonadonna, C.; Connor, C.B.; Houghton, B.F.; Connor, L.; Byrne, M.; Laing, A.; Hincks, T.K. Probabilistic modeling of tephra dispersal: Hazard assessment of a multiphase rhyolitic eruption at Tarawera, New Zealand. *J. Geophys. Res. Solid Earth* **2005**, *110*, 2896. [CrossRef]
2. Wilson, T.M.; Stewart, C.; Sword-Daniels, V.; Leonard, G.S.; Johnston, D.M.; Cole, J.W.; Wardman, J.; Wilson, G.; Barnard, S.T. Volcanic ash impacts on critical infrastructure. *Phys. Chem. Earth Parts A/B/C* **2012**, *45*, 5–23. [CrossRef]
3. Craig, H.; Wilson, T.; Stewart, C.; Outes, V.; Villarosa, G.; Baxter, P. Impacts to agriculture and critical infrastructure in Argentina after ashfall from the 2011 eruption of the Cordón Caulle volcanic complex: An assessment of published damage and function thresholds. *J. Appl. Volcanol.* **2016**, *5*, 7. [CrossRef]
4. Scollo, S.; Prestifilippo, M.; Bonadonna, C.; Cioni, R.; Corradini, S.; Degruyter, W.; Rossi, E.; Silvestri, M.; Biale, E.; Carparelli, G.; et al. Near-Real-Time Tephra Fallout Assessment at Mt. Etna, Italy. *Remote Sens.* **2019**, *11*, 2987. [CrossRef]
5. Perttu, A.; Taisne, B.; De Angelis, S.; Assink, J.D.; Tailpied, D.; Williams, R.A. Estimates of plume height from infrasound for regional volcano monitoring. *J. Volcanol. Geotherm. Res.* **2020**, *402*, 106997. [CrossRef]
6. Simionato, R.; Jarvis, P.A.; Rossi, E.; Bonadonna, C. PlumeTraP: A New MATLAB-Based Algorithm to Detect and Parametrize Volcanic Plumes from Visible-Wavelength Images. *Remote Sens.* **2022**, *14*, 1766. [CrossRef]
7. Vásconez, F.; Moussallam, Y.; Harris, A.J.; Latchimy, T.; Kelfoun, K.; Bontemps, M.; Macías, C.; Hidalgo, S.; Córdova, J.; Battaglia, J.; et al. VIGIA: A thermal and visible imagery system to track volcanic explosions. *Remote Sens.* **2022**, *14*, 3355. [CrossRef]
8. Scollo, S.; Prestifilippo, M.; Spata, G.; D'Agostino, M.; Coltelli, M. Monitoring and forecasting Etna volcanic plumes. *Nat. Hazards Earth Syst. Sci.* **2009**, *9*, 1573–1585. [CrossRef]
9. White, J.T.; Connor, C.B.; Connor, L.; Hasenaka, T. Efficient inversion and uncertainty quantification of a tephra fallout model. *J. Geophys. Res. Solid Earth* **2017**, *122*, 281–294. [CrossRef]
10. Lechner, P.; Tupper, A.; Guffanti, M.; Loughlin, S.; Casadevall, T. *Volcanic Ash and Aviation—The Challenges of Real-Time, Global Communication of a Natural Hazard*; Advances in Volcanology Series; Springer: Cham, Switzerland, 2017; pp. 51–64. [CrossRef]
11. Sparks, R. The dimensions and dynamics of volcanic eruption columns. *Bull. Volcanol.* **1986**, *48*, 3–15. [CrossRef]
12. Mastin, L.G.; Guffanti, M.; Servranckx, R.; Webley, P.; Barsotti, S.; Dean, K.; Durant, A.; Ewert, J.W.; Neri, A.; Rose, W.I.; et al. A multidisciplinary effort to assign realistic source parameters to models of volcanic ash-cloud transport and dispersion during eruptions. *J. Volcanol. Geotherm. Res.* **2009**, *186*, 10–21. [CrossRef]
13. Degruyter, W.; Bonadonna, C. Improving on mass flow rate estimates of volcanic eruptions. *Geophys. Res. Lett.* **2012**, *39*, 2566. [CrossRef]
14. Mereu, L.; Scollo, S.; Garcia, A.; Sandri, L.; Bonadonna, C.; Marzano, F.S. A New Radar-Based Statistical Model to Quantify Mass Eruption Rate of Volcanic Plumes. *Geophys. Res. Lett.* **2023**, *50*, e2022GL100596. [CrossRef]
15. Tupper, A.; Textor, C.; Herzog, M.; Graf, H.; Richards, M. Tall clouds from small eruptions: The sensitivity of eruption height and fine ash content to tropospheric instability. *Nat. Hazards* **2009**, *51*, 375–401. [CrossRef]
16. Denlinger, R.P.; Pavolonis, M.; Sieglaff, J. A robust method to forecast volcanic ash clouds. *J. Geophys. Res. Atmos.* **2012**, *117*. [CrossRef]
17. Bonadonna, C.; Folch, A.; Loughlin, S.; Puempel, H. Future developments in modelling and monitoring of volcanic ash clouds: Outcomes from the first IAVCEI-WMO workshop on Ash Dispersal Forecast and Civil Aviation. *Bull. Volcanol.* **2012**, *74*, 1–10. [CrossRef]
18. Searcy, C.; Dean, K.; Stringer, W. PUFF: A high-resolution volcanic ash tracking model. *J. Volcanol. Geotherm. Res.* **1998**, *80*, 1–16. [CrossRef]
19. Stohl, A.; Forster, C.; Frank, A.; Seibert, P.; Wotawa, G. The Lagrangian particle dispersion model FLEXPART version 6.2. *Atmos. Chem. Phys.* **2005**, *5*, 2461–2474. [CrossRef]
20. Costa, A.; Macedonio, G.; Folch, A. A three-dimensional Eulerian model for transport and deposition of volcanic ashes. *Earth Planet. Sci. Lett.* **2006**, *241*, 634–647. [CrossRef]
21. Tadini, A.; Roche, O.; Samaniego, P.; Guillin, A.; Azzaoui, N.; Gouhier, M.; de' Michieli Vitturi, M.; Pardini, P.; Eychenne, J.; Bernard, B.; et al. Quantifying the uncertainty of a coupled plume and tephra dispersal model: PLUME-MOM/HYSPLIT simulations applied to Andean volcanoes. *J. Geophys. Res. Solid Earth* **2020**, *125*, e2019JB018390. [CrossRef]
22. Aravena, A.; Bevilacqua, A.; Neri, A.; Gabellini, P.; Ferrés, D.; Escobar, D.; Aiuppa, A.; Cioni, R. Scenario-based probabilistic hazard assessment for explosive events at the San Salvador Volcanic complex, El Salvador. *J. Volcanol. Geotherm. Res.* **2023**, *438*, 107809. [CrossRef]
23. Rose, W.I.; Bluth, G.J.S.; Ernst, G.G. Integrating retrievals of volcanic cloud characteristics from satellite remote sensors: A summary. *Philos. Trans. R. Soc. Lond. Ser. A Math. Phys. Eng. Sci.* **2000**, *358*, 1585–1606. [CrossRef]
24. Piscini, A.; Corradini, S.; Marchese, F.; Merucci, L.; Pergola, N.; Tramutoli, V. Volcanic ash cloud detection from space: A comparison between the RSTASH technique and the water vapour corrected BTD procedure. *Geomat. Nat. Hazards Risk* **2011**, *2*, 263–277. [CrossRef]
25. Prata, F.; Lynch, M. Passive Earth Observations of Volcanic Clouds in the Atmosphere. *Atmosphere* **2019**, *10*, 199. [CrossRef]
26. Andò, B.; Pecora, E. An advanced video-based system for monitoring active volcanoes. *Comput. Geosci.* **2006**, *32*, 85–91. [CrossRef]
27. Prata, A.J.; Bernardo, C. Retrieval of volcanic ash particle size, mass and optical depth from a ground-based thermal infrared camera. *J. Volcanol. Geotherm. Res.* **2009**, *186*, 91–107. [CrossRef]

28. Harris, D.M.; Rose, W.I.; Roe, R.; Thompson, M.R.; Lipman, P.; Mullineaux, D. Radar observations of ash eruptions. *USA Geol. Surv. Prof. Pap.* **1981**, *1250*, 323–333.
29. Vulpiani, G.; Ripepe, M.; Valade, S. Mass discharge rate retrieval combining weather radar and thermal camera observations. *J. Geophys. Res. Solid Earth* **2016**, *121*, 5679–5695. [CrossRef]
30. Marzano, F.S.; Picciotti, E.; Montopoli, M.; Vulpiani, G. Inside volcanic clouds: Remote sensing of ash plumes using microwave weather radars. *Bull. Am. Meteorol. Soc.* **2013**, *94*, 1567–1586. [CrossRef]
31. Montopoli, M. Velocity profiles inside volcanic clouds from three-dimensional scanning microwave dual-polarization Doppler radars. *J. Geophys. Res. Atmos.* **2016**, *121*, 7881–7900. [CrossRef]
32. Wiegner, M.; Gasteiger, J.; Groß, S.; Schnell, F.; Freudenthaler, V.; Forkel, R. Characterization of the Eyjafjallajökull ash-plume: Potential of lidar remote sensing. *Phys. Chem. Earth Parts A/B/C* **2012**, *45*, 79–86. [CrossRef]
33. Scollo, S.; Boselli, A.; Coltelli, M.; Leto, G.; Pisani, G.; Spinelli, N.; Wang, X. Monitoring Etna volcanic plumes using a scanning LiDAR. *Bull. Volcanol.* **2012**, *74*, 2383–2395. [CrossRef]
34. Sicard, M.; Córdoba-Jabonero, C.; Barreto, A.; Welton, E.J.; Gil-Díaz, C.; Carvajal-Pérez, C.V.; Torres, C. Volcanic eruption of Cumbre Vieja, La Palma, Spain: A first insight to the particulate matter injected in the troposphere. *Remote Sens.* **2022**, *14*, 2470. [CrossRef]
35. Tupper, A.; Wunderman, R. Reducing discrepancies in ground and satellite-observed eruption heights. *J. Volcanol. Geotherm. Res.* **2009**, *186*, 22–31. [CrossRef]
36. Corradini, S.; Montopoli, M.; Guerrieri, L.; Ricci, M.; Scollo, S.; Merucci, L.; Marzano, F.S.; Pugnaghi, S.; Prestifilippo, M.; Ventress, L.J.; et al. A multi-sensor approach for volcanic ash cloud retrieval and eruption characterization: The 23 November 2013 Etna lava fountain. *Remote Sens.* **2016**, *8*, 58. [CrossRef]
37. Marzano, F.S.; Vulpiani, G.; Rose, W.I. Microphysical characterization of microwave radar reflectivity due to volcanic ash clouds. *IEEE Trans. Geosci. Remote Sens.* **2006**, *44*, 313–327. [CrossRef]
38. Bombrun, M.; Jessop, D.; Harris, A.; Barra, V. An algorithm for the detection and characterisation of volcanic plumes using thermal camera imagery. *J. Volcanol. Geotherm. Res.* **2018**, *352*, 26–37. [CrossRef]
39. Wood, K.; Thomas, H.; Watson, M.; Calway, A.; Richardson, T.; Stebel, K.; Naismith, A.; Berthoud, L.; Lucas, J. Measurement of three dimensional volcanic plume properties using multiple ground based infrared cameras. *ISPRS J. Photogramm. Remote Sens.* **2019**, *154*, 163–175. [CrossRef]
40. Osores, S.; Ruiz, J.; Folch, A.; Collini, E. Volcanic ash forecast using ensemble-based data assimilation: An ensemble transform Kalman filter coupled with the FALL3D-7.2 model (ETKF-FALL3D version 1.0). *Geosci. Model Dev.* **2020**, *13*, 1–22. [CrossRef]
41. Pardini, F.; Corradini, S.; Costa, A.; Ongaro, T.E.; Merucci, L.; Neri, A.; Stelitano, D.; de'Michieli Vitturi, M. Ensemble-Based Data Assimilation of Volcanic Ash Clouds from Satellite Observations: Application to the 24 December 2018 Mt. Etna Explosive Eruption. *Atmosphere* **2020**, *11*, 359. [CrossRef]
42. Lu, S.; Lin, H.X.; Heemink, A.; Segers, A.; Fu, G. Estimation of volcanic ash emissions through assimilating satellite data and ground-based observations. *J. Geophys. Res. Atmos.* **2016**, *121*, 10971–10994. [CrossRef]
43. Branca, S.; del Carlo, P. Types of eruptions of Etna volcano AD 1670–2003: Implications for short-term eruptive behaviour. *Bull. Volcanol.* **2005**, *67*, 732–742. [CrossRef]
44. De Beni, E.; Behncke, B.; Branca, S.; Nicolosi, I.; Carluccio, R.; D'Ajello Caracciolo, F.; Chiappini, M. The continuing story of Etna's New Southeast Crater (2012–2014): Evolution and volume calculations based on field surveys and aerophotogrammetry. *J. Volcanol. Geotherm. Res.* **2015**, *303*, 175–186. [CrossRef]
45. Kampouri, A.; Amiridis, V.; Solomos, S.; Gialitaki, A.; Marinou, E.; Spyrou, C.; Georgoulias, A.K.; Akritidis, D.; Papagiannopoulos, N.; Mona, L.; et al. Investigation of Volcanic Emissions in the Mediterranean: "The Etna–Antikythera Connection". *Atmosphere* **2021**, *12*, 40. [CrossRef]
46. Scollo, S.; Coltelli, M.; Bonadonna, C.; Del Carlo, P. Tephra hazard assessment at Mt. Etna (Italy). *Nat. Hazards Earth Syst. Sci.* **2013**, *13*, 3221–3233. [CrossRef]
47. Alparone, S.; Andronico, D.; Lodato, L.; Sgroi, T. Relationship between tremor and volcanic activity during the Southeast Crater eruption on Mount Etna in early 2000. *J. Geophys. Res. Solid Earth* **2003**, *108*, 2241. [CrossRef]
48. Calvari, S.; Biale, E.; Bonaccorso, A.; Cannata, A.; Carleo, L.; Currenti, G.; Di Grazia, G.; Ganci, G.; Iozzia, A.; Pecora, E.; et al. Explosive paroxysmal events at Etna volcano of different magnitude and intensity explored through a multidisciplinary monitoring system. *Remote Sens.* **2022**, *14*, 4006. [CrossRef]
49. Scollo, S.; Prestifilippo, M.; Pecora, E.; Corradini, S.; Merucci, L.; Spata, G.; Coltelli, M. Eruption column height estimation of the 2011-2013 Etna lava fountains. *Ann. Geophys.* **2014**, *57*, 2. [CrossRef]
50. Behncke, B.; Branca, S.; Corsaro, R.A.; De Beni, E.; Miraglia, L.; Proietti, C. The 2011–2012 summit activity of Mount Etna: Birth, growth and products of the new SE crater. *J. Volcanol. Geotherm. Res.* **2014**, *270*, 10–21. [CrossRef]

land

MDPI

Article

Spatial and Temporal Characteristics of Dust Storms and Aeolian Processes in the Southern Balkash Deserts in Kazakhstan, Central Asia

Gulnura Issanova [1,2,3], Azamat Kaldybayev [3], Yongxiao Ge [1,2,4,*], Jilili Abuduwaili [1,2,4] and Long Ma [1,2,4]

[1] State Key Laboratory of Desert and Oasis Ecology, Key Laboratory of Ecological Safety and Sustainable Development in Arid Lands, Xinjiang Institute of Ecology and Geography Chinese Academy of Sciences, Urumqi 830011, China
[2] CAS Research Centre for Ecology and Environment of Central Asia, Urumqi 830011, China
[3] Faculty of Geography and Environmental Sciences, Al-Farabi Kazakh National University, Almaty 050040, Kazakhstan
[4] University of Chinese Academy of Sciences, Beijing 100049, China
* Correspondence: geyx@ms.xjb.ac.cn

Abstract: Sand and dust storms are hazardous to the environment and have a significant role in desertification. Under the influence of climate change and human activities, dust storms and aeolian processes have been common phenomena in the Southern Balkash deserts in Kazakhstan, Central Asia. However, knowledge gaps on spatial and temporal characteristics of dust storms and aeolian process in the Southern Balkash deserts still exist. Therefore, in present study, meteorological observations and numerous cartographic materials were used to identify the powerful sources with the highest frequency of dust storms and aeolian processes in the Southern Balkash deserts. The result showed that the Southern Balkash deserts were covered mainly by transverse parabolic sands (48%), dome dunes (24%), and transverse dome dunes (23%), where the aeolian processes occurred to a significant degree. Significant and strong degrees of aeolian processes occurred in most of the Southern Balkash deserts. The eastern part of the Taukum and the northern part of the Zhamankum and Karakum deserts were prone to aeolian processes to a substantial degree. The Moiynkum, Bestas, Saryesikatyrau, and Taukum deserts had the most frequent storms, occuring, on average, 17 to 43 days/per year. The occurrence of dust storms has been of a stable decreasing trend since the 1990s, except for 2008–2009. Aeolian dust in the Southern Balkash deserts flowed mainly from the western and southwestern to the eastern and northeastern. The results of the present study shed light on the temporal and spatial characteristics of dust storms and aeolian processes in the Southern Balkash deserts. This is of great importance in helping to monitor and predict dust storms and motion patterns of aeolian dust in this region.

Keywords: aeolian process; sand and dust storms; soil deflation; desert; Kazakhstan; Central Asia

Citation: Issanova, G.; Kaldybayev, A.; Ge, Y.; Abuduwaili, J.; Ma, L. Spatial and Temporal Characteristics of Dust Storms and Aeolian Processes in the Southern Balkash Deserts in Kazakhstan, Central Asia. *Land* **2023**, *12*, 668. https://doi.org/10.3390/land12030668

Academic Editors: Stefano Morelli, Veronica Pazzi and Mirko Francioni

Received: 7 February 2023
Revised: 8 March 2023
Accepted: 8 March 2023
Published: 12 March 2023

1. Introduction

Central Asia, located in the northern hemisphere's temperate desert belt, is covered mainly by drylands and is one of the most important sources of global aeolian dust and aerosol [1,2]. Sand and dust storms are becoming more common events in the arid and semi-arid regions of Central Asia, particularly around the desert zone, as global temperatures rise [3–5]. Deserts in Kazakhstan and Central Asia are characterized by a continental climate with long dry summers, strong winds, a scarcity of vegetation cover, a lack of moisture in the soil, relatively low air humidity, frequent waterlogging of the soil, and atmospheric droughts [6,7]. The strong winds can carry sand/dust and form dunes, mounds, and ridges, since winds can remove sand particles of different sizes and move them during deflation over long distances [8–11]. Desertification because of soil deflation has affected desert and semi-desert regions in Kazakhstan and Central Asia [12,13].

The vast "dust belt", which is the primary permanent source of storms in Central Asia, extends from the west to the southern deserts: the Caspian Sea deserts, the Kyzylkum, Aralkum deserts (Aral Sea region), and Southern Balkash deserts [14]. Sandy and clayey deserts, with an area of about 30 million ha, are mostly spread in this zone [15]. Sandy deserts occupy about one-third of the entire desert zone. The largest include the Kyzylkum, the Karakum, the Aralkum, the Moiynkum, the Saryesikatyrau (Southern Balkash deserts), and the sands of the Caspian lowlands (Naryn deserts). The deserts arose tens of thousands of years ago on the site of former (ephemeral) rivers, playas, and saline lakes [16] and are located mainly in the lowlands [17,18]. They are often the primary and active sources of aeolian processes as sand and dust storms of high frequencies [19–28].

Many terminal lakes in arid Central Asia have turned into deserts as a result of climate change and human activity, including a new salt desert in the playa of the Ebinur Lake basin, the newly formed Aralkum desert in the Aral Sea basin, and the world's earliest Aral-Sea-type disaster (Lop Nur) in the Tarim Basin [29–31]. Since the 1970s, a substantial decrease in the Ile river runoff has led to a reduction in the Balkash Lake's water depth, which accelerated the desertification process and had devastating effects on the diverse flora and fauna that depend on it [32]. Sand and dust storms are one of the main signs and causes of desertification in this region. Degradation and desertification are pervasive in the Southern Balkash deserts at present [20,33]. They have occurred mainly because of anthropogenic activities such as irrigation and electric energy production, which results in changes in the level of the Balkash Lake. The regulation of water resources and irrigation has led to the reduction of groundwater level, increasing water mineralization, and intensive soil salinization, consequently causing the growth of solonchak desert areas and the drying of ponds, leading to the promotion of aeolian processes such as dust/salt storms [25] and plant changes toward more xerophyte types [34–36]. This is due, in particular, to the problem of the irrational use and management of water resources in connection with the exploitation of resources, and the construction of technical structures in the Balkash Lake basin that attracts great attention all over the world to the processes of desertification [37,38]. Currently, most of the research work focuses on the change in water resources [39–41], water hydrochemistry [42,43], and paleoenvironmental change [44,45]. Dust activities caused by environmental changes in the Balkash Lake basin have also attracted some attention. Gholami et al. [46] identified the high susceptibility areas in Central Asia, including Karakum, Aralkum, Kyzylkum, and arid lands around Balkash Lake by introducing a new integrated modeling approach. Nobakht et al. [47] presented a new inventory of dust emission sources in Central Asia using a dust enhancement technique. They found that the higher frequency of dust storms observed in the Aral Sea region and Balkash-Zhetysu (Zhungar) regions was due to land damage. Unfortunately, little attention was paid to the detailed information on dust storms and aeolian processes in the Southern Balkash deserts. Thus, knowledge of the spatial and temporal characteristics of dust storms and aeolian processes in the Southern Balkash deserts is scarce. To bridge the knowledge gaps, the present study aims to provide new insights into the dust storms and aeolian processes in the Southern Balkash deserts in Kazakhstan, Central Asia.

Therefore, the primary purpose of this study was to analyze the temporal and spatial characteristics of dust storms and aeolian processes in the Southern Balkash deserts in order to know the modern soil deflation processes' intensity in the desert. The novelty of this study is reflected by the presentation of the latest information on the spatial and temporal distribution of dust storms and the aeolian process. Firstly, the geology and geomorphology of the Southern Balkash deserts were presented to introduce the background information, and then we expounded the spatial and temporal characteristics of dust storms in the Southern Balkash deserts. Finally, wind regimes and wind direction, the nexus between soil texture and dust storm intensity, and the aeolian processes in the Southern Balkash deserts were elaborated in the present study.

2. Materials and Methods

2.1. Overview of the Study Area

The Southern Balkash deserts, with a vast area of about 70,000 km^2, belong to sandy deserts according to features of the formation of the deserts of the study region [12]. It is located in southeast Kazakhstan within the shallow Balkash-Alakol depression and in the Balkash lowland, an accumulative plain gently sloping toward the north with a minimum absolute elevationof 340 m. It is divided in the north by the southern slopes of the Saryarka; in the west and south by the Shu-Ile watershed plateau; and in the southeast by the ridges of the Zhetysu Alatau (Figure 1). The desert is located in the zone of gray soils (serozems) interspersed with locally developed, mainly takyr-like solonchak, and meadow-boggy soils. The vegetation cover here is represented by wormwood and feather grass. Additionally, large areas are occupied by sandy desert soils developed in massifs of semi-fixed aeolian sands, where white *haloxylon*, *calligonum*, *krascheninnikovia*, and wormwood are found. Takyr-like soils are formed in drainless basins of dried-up lakes and are predominantly saline.

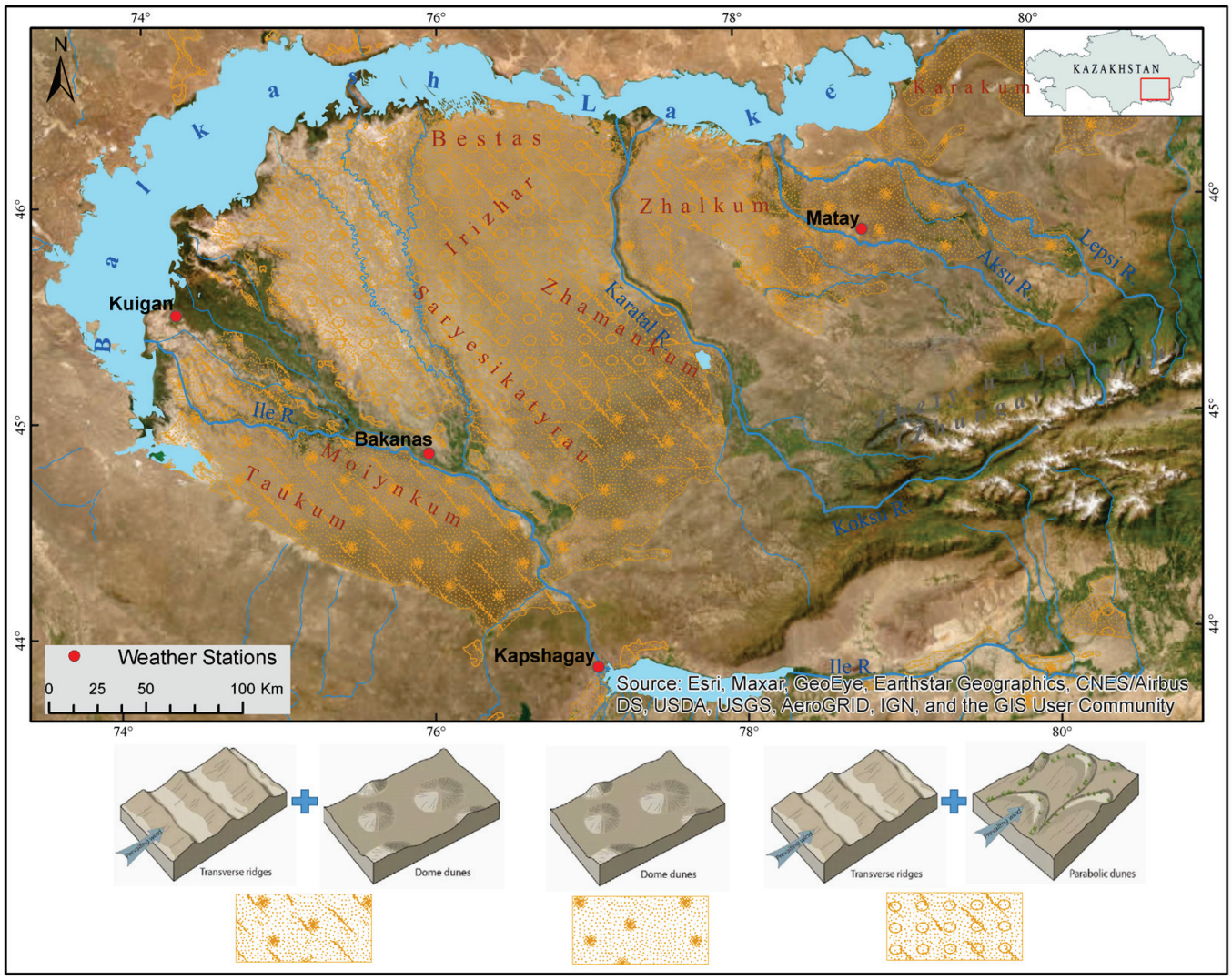

Figure 1. Desert sands and their geomorphological types in the Southern Balkash deserts.

The climate of the deserts is continental and arid [48]. The Southern Balkash is described by large daily and annual fluctuations in air temperature and has a high solar radiation level and a long dry summer period. The air temperature in January is an average of −16 °C in the northern part, the southern part of the plain territory is −5 °C, and the

mean temperature is about 20–25 °C; in July. In summer, the precipitation completely evaporates on the plain. The most significant monthly precipitation falls in spring (April–May) and the least falls in February and August–September [20]. The water balance of Balkash Lake mainly depends on the flow of the rivers of the Southern Balkash region, mainly from the Ile River. The Ile River crosses the desert, flowing into the lake. Some rivers flowing down the slopes of the Zhetysu Alatau also cross the Saryesikatyrau desert, flowing into Balkash Lake. Other smaller rivers are lost in the sands (Figure 1).

2.2. Dust Storm and Wind Data

"Dataset on dust storm climatology and wind regime for Kazakhstan" issued by KazHydromet (Kazakhstan) provides the dust storm and wind regime data from all the meteorological stations within Kazakhstan, which offers great advantages for dust activity studies. In the present study, the average monthly number of days in the dust storm data of four stations from the above dataset, namely the Bakanas, Kuigan, Matay, and Kapshagay, was used to characterize the variation of dust storm and wind directions in the Southern Balkash deserts. Statistical methods were used to analyze the long-term dynamics and seasonal frequency of dust storms by the average number of dusty days for 1971–2020 and in different months for 1966–2003, respectively. The wind rose of the four meteorological stations was built according to the wind direction data from 1966 to 2003 derived from the "Dataset on dust storm climatology and wind regime for Kazakhstan".

The spatial distribution of wind speed was based on gridded mean wind speed data from Global Wind Atlas version 3.1. It is developed, owned, and operated by the Technical University of Denmark (DTU) and contains all new data on wind resources around the world. As such, it can be used to identify global, national, regional, and local high-wind areas. Global Wind Atlas has made high-resolution climate and wind statistical data available to users through their geoportal (http://globalwindatlas.com/, accessed on 15 September 2021). The resolution of gridded data is 1 km [49]. The mean wind speed calculated at a height of 100 m and every 250 m on land surfaces was used in the present study.

2.3. Archive Cartographic Materials

Numerous archive cartographic materials with information on soil texture [50] and plant communities [51] were selected to investigate the sources of aeolian processes and dust storms in the Southern Balkash deserts in Kazakhstan.

Firstly, the archive cartographic materials were vectorized. Then, the spatial distribution of dust storms was analyzed using geostatistical methods in Arc Map. As a result, on the vectorized cartographic map, the present study defined the relationship between the origin of dust storms and soil texture with plant communities, identified the sources of sand and dust storms shown on the map, and estimated the area of storms of different degrees.

Initial topographic information and the geomorphological types of sands were obtained from Soviet topographic maps at 1:500,000 scales. The degree of manifestation of aeolian processes and the degree of desertification were derived from the maps of the National Atlas of Kazakhstan [52]. The overlaying of thematic layers in a GIS environment was performed to analyze the regional distribution of and the spatial relationship bewteen sands and aeolian processes.

3. Results and Discussion

3.1. Geology and Geomorphology of the Southern Balkash Deserts

The Southern Balkash depressions were located in the deserts that took shape in the Neogene. Paleogene deposits are found mainly on the periphery. Paleogene and Neogene formations lie like a mantle on the leveled surface of the Paleozoic. In the Quaternary period, the active formation of the relief was accompanied by the accumulation and redistribution of deposits. This process developed against intense tectonic movements and climate fluctuations, which caused great diversity in the genesis of Quaternary deposits and signifi-

cant differences in their thicknesses [53]. Modern aeolian deposits are widespread in the Southern Balkash depression. Their composition is feldspar-quartz. Granites, amphiboles, mica, chlorite, and epidote are found in trace levels in the sands; apatite, hematite, pyroxene, and sphene are less prevalent [54]. According to the geomorphology of the sands, the transverse parabolic sands (48%) are dominant in the region, and they cover Saryesikatyrau, Bestas, Zhamankum, and Irizhar sands. Dome dunes (24%) cover the eastern sands, including the Karakum and the southern part of the Saryesikatyrau. Transverse-dome dunes cover the Taukum and Moiynkum deserts with an area of 23% to form the territory of the Southern Balkash deserts (Figure 1).

The ridges of the Bestas sands extend in a northwesterly direction. Their height is 6–8 m, their width is several tens of meters, and their length is up to 200 m; rarely are ridges 8–20 m high. The ridges are slightly soddy and covered with a characteristic powder—coarse sand [55]. The height of the ridges and mounds of the Moiynkum sands is 2–6 m, occasionally reaching 15 m. The direction of the strike of the ridges is north and northwest. The slopes are gentle. The structure of the ridges is the same as that in the Bestas sands. The sands are well-fixed by vegetation. The southern shore of Balkash Lake, along the entire lake, adjoins the coastal lacustrine-saline plain with an area of more than 27 thousand km^2. The greatest width reaches 30 km. Dense crusts of salts on the surface and vast regions of solonetzes and plump solonchaks can be sources of salt aerosols. The aeolian relief is represented by chains of coastal dunes and dunes up to 8 m high and sometimes form complex star-shaped dunes that are 10–15 m high [56].

3.2. Spatial and Temporal Characteristics of Dust Storms in the Southern Balkash Deserts

Sand and dust storms occurring at different frequencies and for different durations are common in arid and semi-arid regions in Kazakhstan and Central Asia, which develop intensive soil deflation and contribute to the spread of desertification. According to analyses of observation data from weather stations, storms are typical almost all over Kazakhstan with its continental climate, the high wind speed ($\geq$6 m/s) regime, frequent soil and atmospheric droughts, and the scarcity of vegetation cover [57]. The broad diversity characterizes the spatial distribution of the storms in the Southern Balkash deserts.

The Southern Balkash deserts in Kazakhstan are regions with the most frequent storms. (Figure 2). Dust storms, occurring at a frequency of more than 20 days, are common in the coastal areas of the Balkash Lake and Ile River basin, primarily in Moiynkum, Bestas, and western Saryesi-katyrau sands. In addition, the Taukum, Zhalkum, Irizhar, and Saryesikatyrau deserts are subject to dust storms at a frequency of 10–20 days per year. Mountainous areas were comparatively less prone to dust storms. The frequency of their occurrence was <10 days/year (Figure 2). The annual amount of days with deflationary processes in the form of storms reached 30–90 days in the Moiynkum and Taukum deserts, decreasing to 10–20 days in the foothills of the Zhetysu (Zhungar) Alatau [36].

The Bakanas region showed a large number of storms because of takyr-like soils containing clay particles and many silty sand sediments that are prone to the soil deflation process. In addition, this region was affected by human activity, particularly irrigation agriculture and the water supply for electric energy production from water reservoirs [58]. The overall dynamics of the storms have shown an increasing trend since the 1970s up to 1988 (Figure 3) and can be explained by the establishment of the Kapshagay water reservoir in the 1970s. The Balkash Lake area has shrunk to 4700 km^2 due to intensive water use from the Ile, Karatal, and Lepsi rivers [20]. Consequently, a significant part of the coastal area was exposed to salinity and soil degradation. Due to the regulation and reduction of the river flows of the Ile and Karatal, many lakes are drying, including the salt lakes in the deltas [58]. As a result, new sources of dust/sand storms, leading to high concentrations of salt in atmospheric streams, have appeared in the deserts of the Southern Balkash. These salts provoke the deterioration of pasture conditions, and the reduction of biodiversity, salinity, and desertification in general.

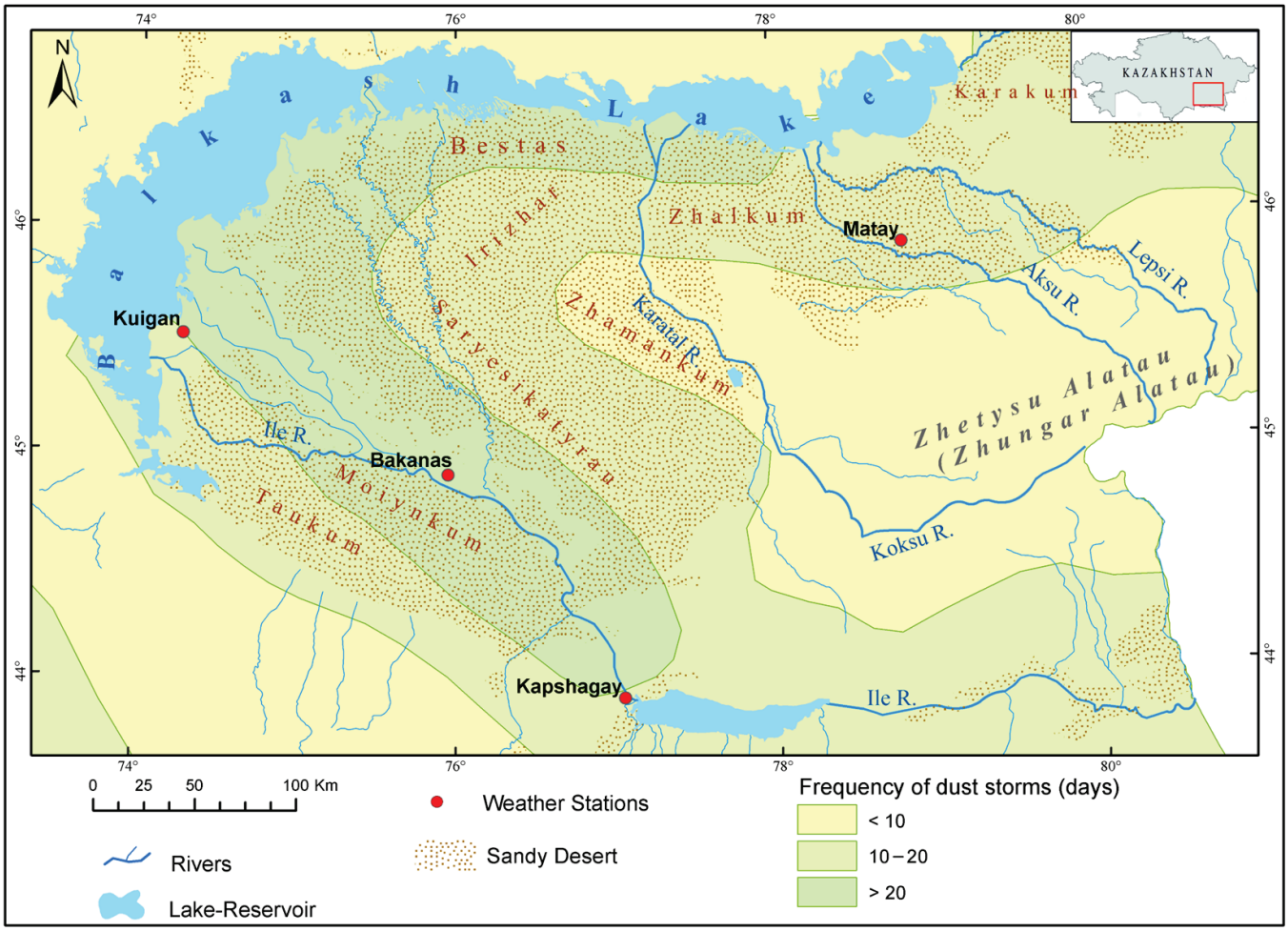

Figure 2. Spatial distribution of dust storms in the Southern Balkash deserts.

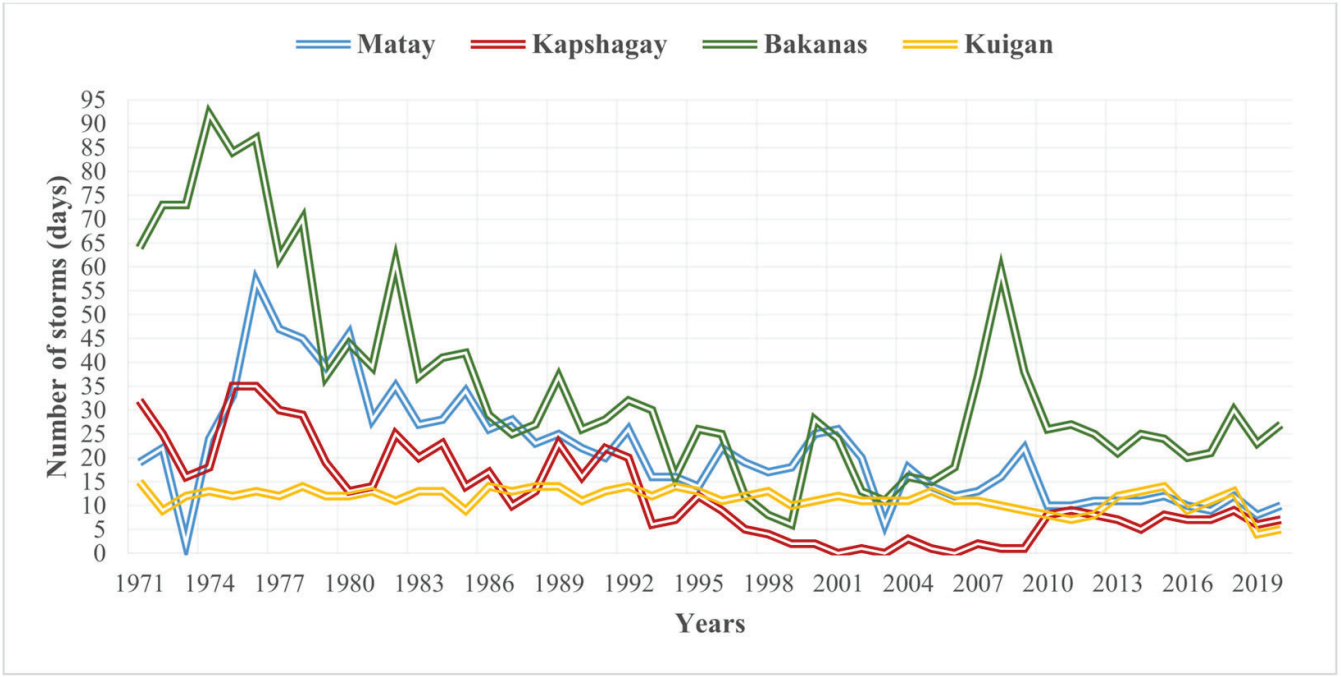

Figure 3. Long-term dynamics of sand and dust storms in the Southern Balkash deserts.

The geographical location and climatic features of Kazakhstan are variable with its large territory. Consequently, storm activities differ with annual and inter-annual variability. For example, the spring and summer seasons are more favorable to storm outbreaks. According to the data analysis of storms in the Southern Balkash deserts, two peaks were detected from 1966 to 2003: in April–June and July–September (Figure 4).

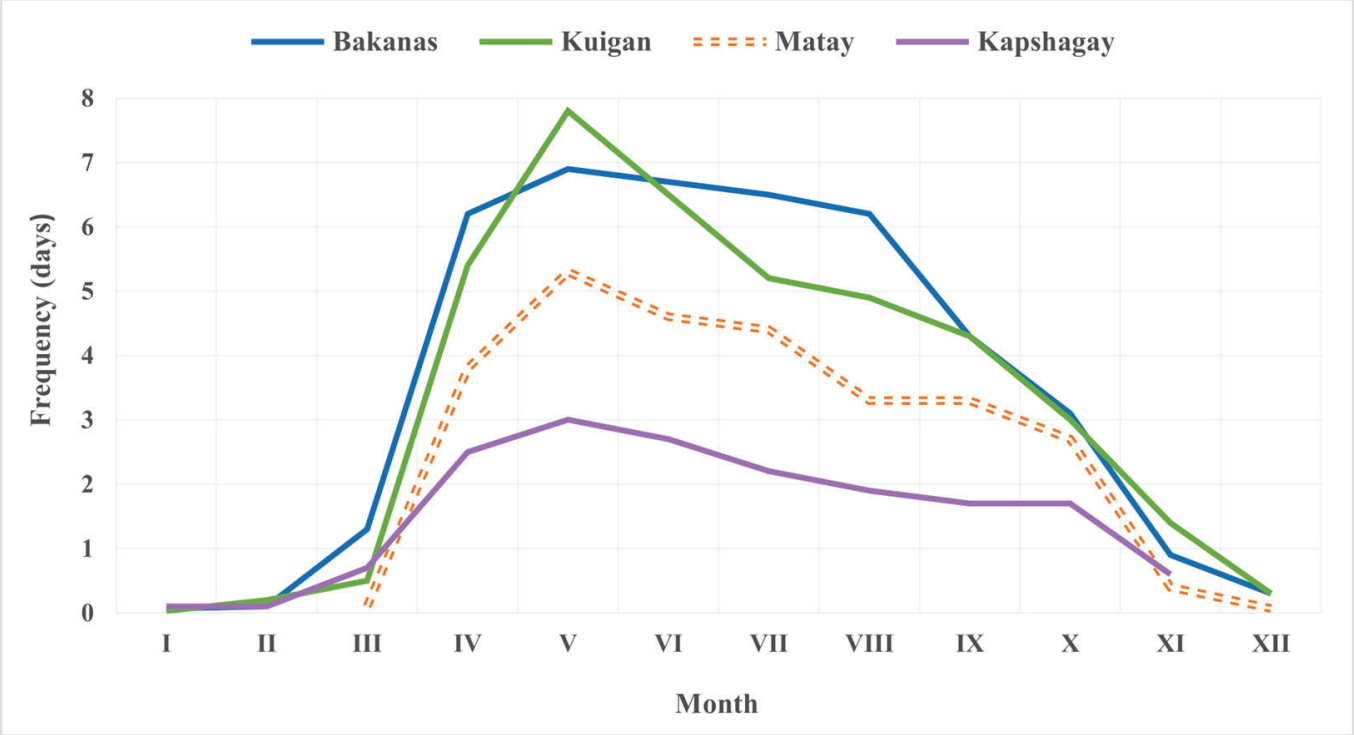

Figure 4. Seasonal frequency of storms for the period 1966–2003 in the Southern Balkash deserts.

Because of the sharp rise in temperature and high wind speed in the spring [59], the surface of southern deserts deteriorates in theintensive evaporation of humidity, which, together with strong winds, contributes to the development of dust and sand storm phenomena. As a result, the southern deserts of the Balkash (meteorological stations: Bakanas, Kuigan, and Matay) are one of the main areas of Kazakhstan where regular storms occur, especially in the period from April to August and April–September (Figure 4). The average annual duration of storms for the period 1966–2003 was 43 days at the Bakanas meteorological station, 40 days at the Kuigan station, and 28 and 17 days per year at the Matay and Kapshagay stations, respectively.

3.3. Wind Regime and Wind Direction in the Southern Balkash Deserts

In Kazakhstan, the wind regime mostly has a continental character. It is conditioned mainly by local barik-circulation conditions, depending on orographic features, sun exposure, and topography [60]. The wind speed is variable within Kazakhstan, and it is high mainly in the desert zone. Almost 50% of the territory of Kazakhstan has an annual wind speed of an average of 4–5 m/s. It can reach a speed of $\geq$6 m/s in the Caspian Sea's coastal areas, mountain passes, and corridors in the south and southeast of Kazakhstan. In the Southern Balkash deserts, wind speed ranges from 0.5 m/s in the mountainous areas to 8 m/s toward the deserts (Figure 5). The maximum wind speeds occur in the spring—summer period, meaning that deflation processes are intense at this time [61,62].

The aeolian process in deserts is a regular phenomenon, and the wind regime is related to baric topography and climatic conditions. Wind regime defines the speed and direction of the movement of wind in a particular desert area [12,20]. In the Southern Balkash deserts, the western winds are dominant and controlled by the general circulation of air

masses in southeastern Kazakhstan [36,56]. Consequently, the sand movement directions are northeast, southeast, and east (the Bakanas, Matay, and Kuigan stations) (Figure 5). The direction and speed of the movement of active dunes mainly depend on the relief, and local orographic conditions play their role in the appearance of winds. Therefore, wind of a westerly direction is observed at the Kapshagay station. This is due to a well-known local easterly mountain and valley, "Shelek", and the wind and orographic condition of the region. It is created by transferring cold air from the part of the Ile Alatau that is a glacierized zone in the headwaters of the Shelek River to the Ile River valley (Figure 5). The mean annual wind speed is 8–10 m/s [63]. The character of mountain-valley winds depends on the height of the local topography, the slope exposure, and the gorge directions.

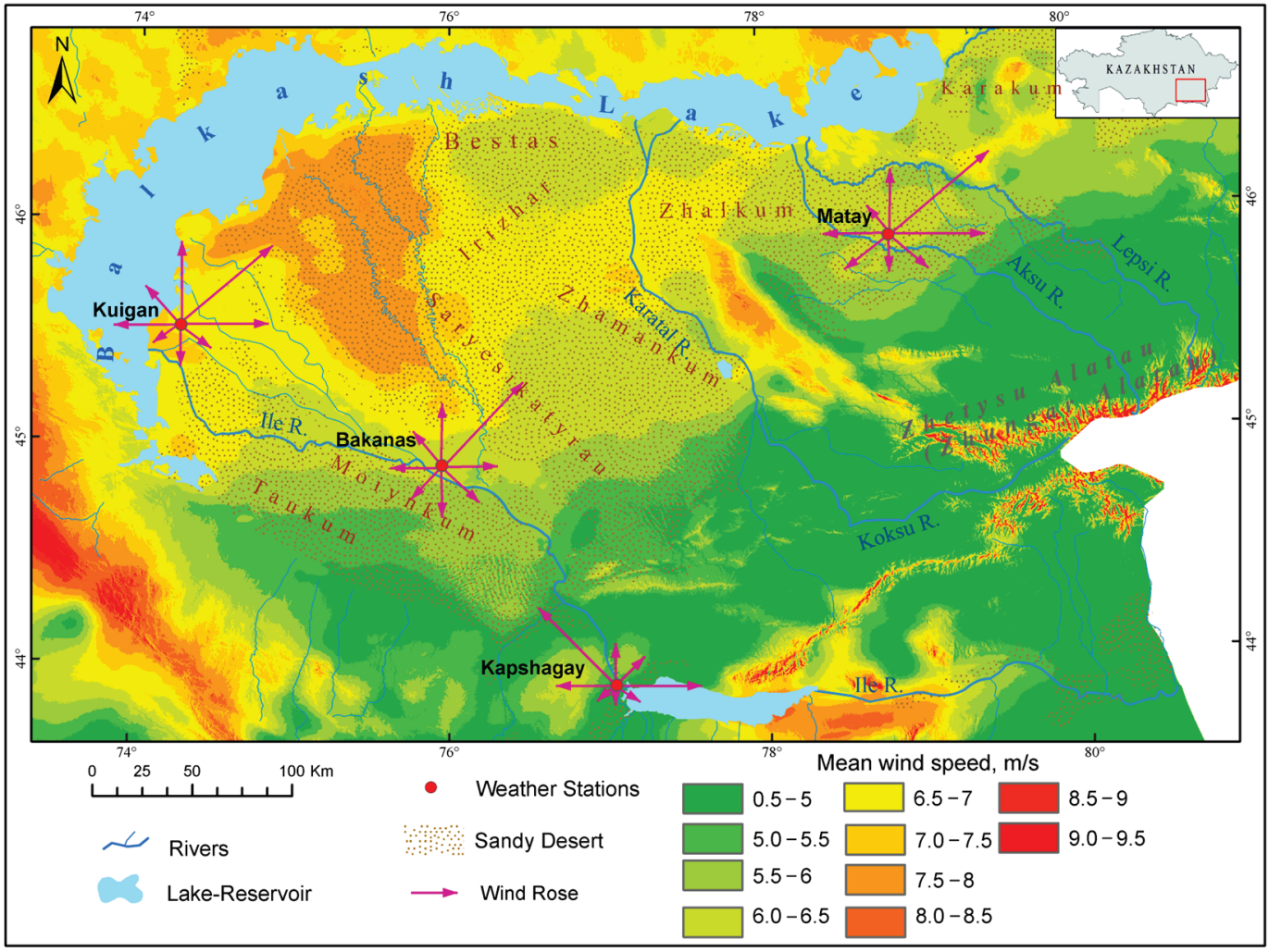

Figure 5. Spatial wind speed and its directions in the Southern Balkash deserts.

Considering this, the direction of the wind could either coincide or not coincide with the regular nature of the winds of the surrounding plains, i.e., they can either increase or decrease the overall strength of the wind [20]. In addition, local air circulation in the region prevails over the general atmospheric circulation [64,65]. That is why the local winds are often vital in the region and steadily blowing. They are noted in the surrounding area of mountain spurs and gorges [12].

Strong winds can erode and move a large number of small particles, deposit them elsewhere, and form dunes in a desert or on a beach. Consequently, wind is one of the main relief-forming factors in a sandy desert. Additionally, strong winds cause dust and sand storms in the Taukum, Moiynkum, and Saryesikatyrau deserts, and sand with different-

sized particles can transport from the surface and accumulate elsewhere. In deserts, winds cross the threshold speed of 6 m/s cause sand deflation [66–68]. Windy, dry weather with a wind speed of 6 m/s was observed on 60 to 127 days/year in the Southern Balkash deserts; such weather occurred on 80–100 days per year in most areas of the Saryesikatyrau and Taukum sands; the occurrence of this weather reached up to 100–120 days/year in the southern shore of Balkash Lake [67,68].

3.4. The Relationship between Strong and Very Strong Dust Storm Origin and Soil Texture

A strong dust storm in Kazakhstan occurs when the wind speed is 10–14 m/s with visibility from 500 m to 1000 m [69]. They last from 3 to 12 h. Storms lasting 12 h with a wind speed of >15 m/s and a visibility decrease to ≥50 m are extreme storms [57,70]. Severe and extreme dust storms last 3.1−4 days and largely cover the Ile River valley, the eastern half of the Moiynkum desert, and the Saryesikatyrau desert (Figure 6). These are agricultural areas with wind speeds surpassing >8 m/s and predominantly light-composed soils (soil particle size > 250 microns), as well as the dryness of sandy deserts with minimal vegetation cover, result in powerful dust storms [56]. The dust storms covering the areas in the Southern Balkash deserts can be considered in three groups of the following frequencies: 3.1–4 days (20%), 1.1–3 days (48%), and one day(32%) in the whole region of deserts.

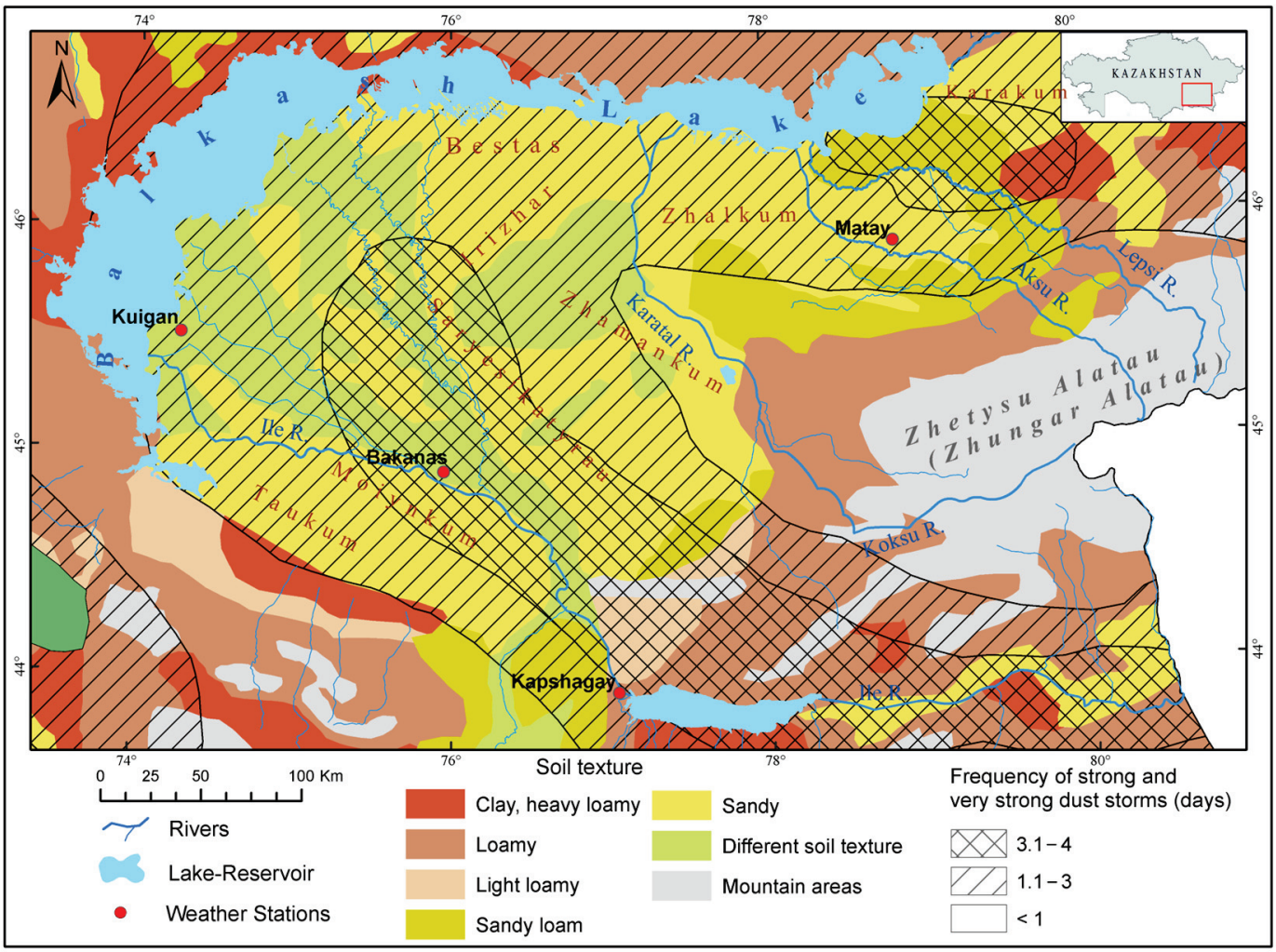

Figure 6. The relationship between the origin of strong and very strong dust storms and soil texture.

Soil texture is a critical soil feature defining the soil surface's resistance to wind erosion or soil deflation. Soil textures include lightly and heavily loamy, loamy, sandy loam, sandy,

clay, and soils of various compositions (Figure 6). As is well-known, the potential and active sources of dust storms are distributed in soils with a light texture (sandy loam and sandy) that are prone to soil deflation (Figure 6).

The sources of strong and very strong dust storms with frequencies of 1.1–3 days and 3.1–4 days per year are found mainly in areas with high wind speed and light-textured soils (Figure 6). Furthermore, such places are located in regions of sandy deserts with sparse vegetation or sometimes barren dunes. In addition, the parts were used intensively for agricultural purposes and industrial development. Moreover, the light-textured soils or sands with a psammophytic plant community are the source for the outbreak of aerosols of different sizes in the atmosphere can be clearly noticed by monitoring from space satellites [59,71].

Since the plant community plays its role in forming dust/sand storms, according to the edaphic deserts map analysis of Middle Asia, the psammophytic vegetation is vulnerable to dust and sand storms. Therefore, the Edaphic deserts with psammophytic plant communities are distributed in vast sandy massifs such as the Kyzylkum, Moiynkum, Aral Karakum, Southern Balkash deserts (Saryesiktyrau and Taukum) [51].

3.5. Aeolian Processes in the Southern Balkash Deserts

The aeolian process, closely related to weathering processes, is widely developed and distributed in the arid zone, particularly in deserts. It first appeared in the second half of the Middle Quaternary era [53] and continue to this day: deflationary basins are being worked out; sandy mounds, dunes, and rows are winding up; and the most considerable total thickness of aeolian deposits in the Southern Balkash deserts reaches 25–30 m [72,73].

Aeolian processes are actively manifested in the sandy and sandy loam deposits of the Southern Balkash deserts, which are locally weakly fixed by vegetation. Silty sands and light sandy loams are intensively blown and contribute to the formation of large massifs of scattered sands in the Southern Balkash deserts. The sandy massifs of the Southern Balkash deserts, such as the Taukum, Saryesikatyrau, and Moiynkum deserts, have an elongated direction due to the northwestern and northeastern winds and aeolian processes that partly took part in their formation. According to the composed map, the degree of the occurrence of the aeolian process is significant and strong in most of the Southern Balkash deserts (Figure 7). In the Taukum sandy massifs, aeolian processes are most active in spring [56], and its eastern part is prone to them to a strong degree (Figure 7). As well as the northern part of the Zhamankum sands (the left bank of the Karatal river) and Karakum sands (eastern coast of the Balkash Lake) are subject to the aeolian process to a strong degree (Figure 7).

The accumulation of aeolian deposits is associated with local, regional, and global atmospheric processes (strong winds, heavy rains, etc.), and the deposits can be found everywhere [74]. Heavy rains contribute to the movement of a significant amount of fine earth on the slopes. Erosion furrows are formed at 5–10 cm in deep and inter-ridge depressions, and dry channels are formed at 10–20 cm. Deflation and aeolian accumulation quickly destroy these forms of aeolian relief [75]. The intensity of the manifestation of aeolian accumulation processes is clearly pronounced within the modern lacustrine sloping swampy plain. The plain comprises lacustrine-marsh deposits, partly fine-grained silty sands overlain by aeolian sands. They were formed due to the wind processing of sandy beaches and the inflow from the central parts of the Taukum sandy massif. Intense deflation zones are confined to the elevated southeastern part of the Taukum (Figure 7). Under the influence of southwestern and northeastern winds, sand is continuously blown and accumulates in depressions between ridges. Local deflation processes occur in fixed transverse-dome dunes in the Taukum and on the border of the Saryesikatyrau and Moiynkum sands.

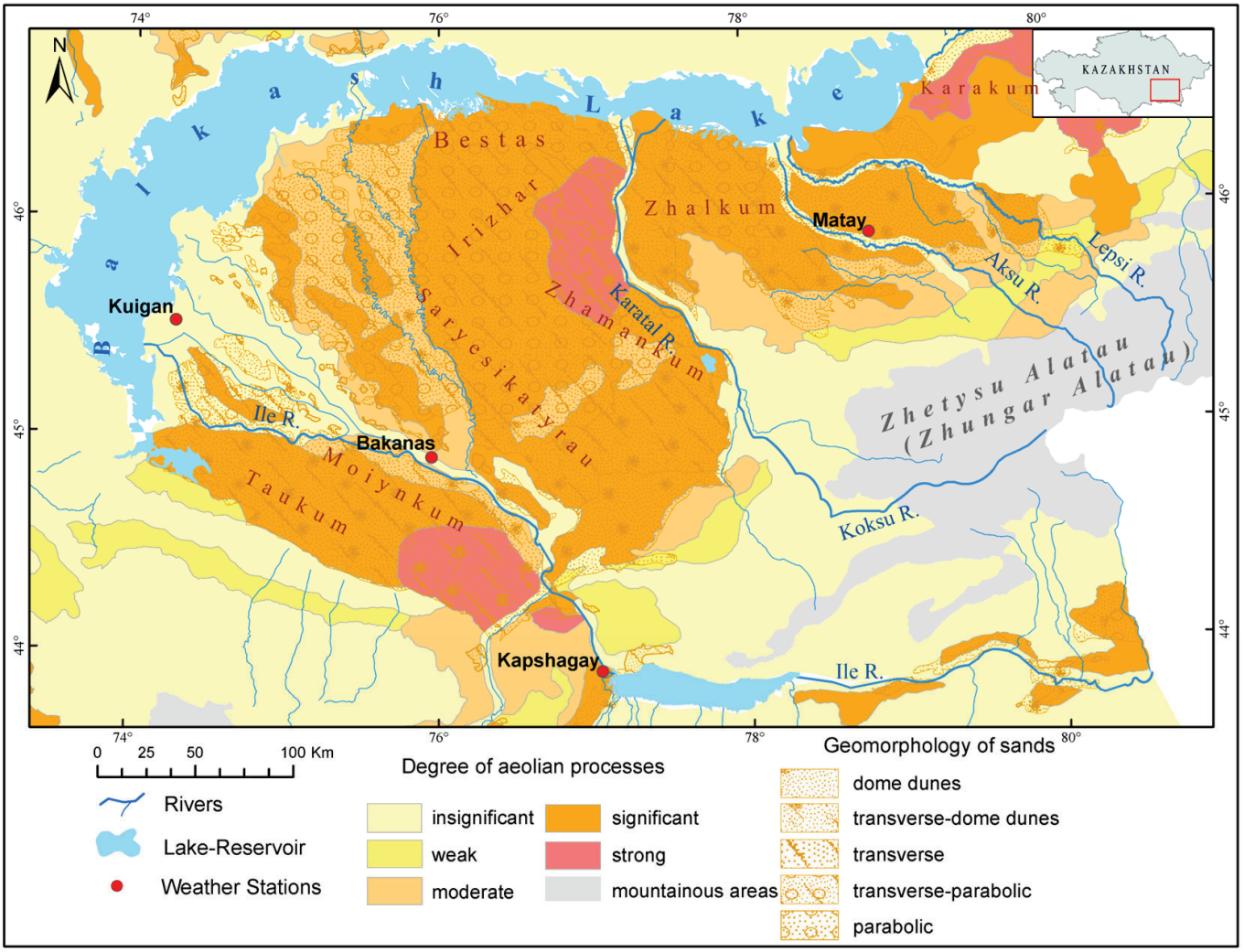

Figure 7. Regional division (zoning) of the aeolian processes in the Southern Balkash deserts.

4. Conclusions

In the present study, a dataset on dust storm climatology and wind regime and archive cartographic materials, coupled with classical statistical methods and geostatistical methods, were used to study the spatial and temporal characteristics of dust storms and aeolian processes in the Southern Balkash deserts in Kazakhstan, Central Asia. The main results and conclusions were drawn as follows.

Transverse-parabolic sands (48%) dominate the Southern Balkash deserts, and dome dunes (24%) cover the eastern sands, including the Karakum and the southern part of the Saryesikatyrau. Transverse-dome dunes cover 23% of the territory of the Southern Balkash deserts.

Dust storms with a frequency of >20 days are distributed in the Balkash Lake and Ile River valley coastal areas. The Bakanas region shows a large number of storms because of takyr-like soils containing clay particles and many silty sand sediments that are prone to the soil deflation process. The Moiynkum, Bestas, Saryesikatyrau, and Taukum deserts are the areas with the most frequent sand and dust storms (17 to 43 days/per year). The occurrence of and and dust storms has steadily decreased since the 1990s, except for 2008–2009. Seasonally, two peaks (April–June and July–September) of sand and dust storms were detected between 1966 and 2003.

The sources of strong and very strong dust storms in the Southern Balkash deserts, with a frequency of 1.1–3 days and 3.1–4 days per year, are found primarily in areas with a high wind speed and light-textured soils. The degree of the occurrence of aeolian processes

is significant and strong in most Southern Balkash deserts. Aeolian dust flows mainly from the western and southwestern directions to the eastern and northeastern directions.

This study can be considered the first attempt at revealing the temporal and spatial characteristics of dust storms and aeolian processes in the Southern Balkash deserts, which allows an assessment of the intensity of modern soil deflation processes and predicts the possibility of sand movement in the Southern Balkash deserts. In the future, we will continue to carry out research on the impact of wind erosion on desertification, dust emission flux, and the prevention of desertification in the Southern Balkash deserts by conducting an observation and model simulation. This will be of great importance to the monitoring and early warning of dust storms and sustainable development in this region.

Author Contributions: Conceptualization and methodology, G.I.; software, G.I. and A.K.; formal analysis, G.I., Y.G. and A.K.; investigation, G.I. and A.K.; data curation and writing—original draft preparation, writing—review and editing, G.I., Y.G. and L.M.; visualization, G.I., Y.G. and A.K.; supervision, project administration, and funding acquisition, Y.G. and J.A. All authors have read and agreed to the published version of the manuscript.

Funding: This research was sponsored by the Youth Innovation Promotion Association of CAS (2023459), National Natural Science Foundation of China (42171014), Natural Science Foundation of Xinjiang Uygur Autonomous Region (2022D01A153, 2022D01A352), the Postdoctoral Fellowship provided by Al-Farabi Kazakh National University, and the Foundation of State Key Laboratory of Desert and Oasis Ecology, Xinjiang Institute of Ecology and Geography Chinese Academy of Sciences.

Data Availability Statement: The data presented in this study are available on request from the corresponding author.

Acknowledgments: Our gratitude goes to M. Stambekov for partly providing weather station data on dust storms in the present study. The authors would like to thank the editors for their assistance with the manuscript, as well as the reviewers for their positive and informative comments and suggestions, which significantly improved the manuscript.

Conflicts of Interest: The authors declare no conflict of interest.

References

1. Shen, H.; Abuduwaili, J.; Samat, A.; Ma, L. A review on the research of modern aeolian dust in Central Asia. *Arab. J. Geosci.* **2016**, *9*, 625. [CrossRef]
2. Orlovsky, N.S.; Orlovsky, L.; Indoitu, R. Severe dust storms in Central Asia. *Arid Ecosyst.* **2013**, *3*, 227–234. [CrossRef]
3. Cao, H.; Liu, J.; Wang, G.; Yang, G.; Luo, L. Identification of sand and dust storm source areas in Iran. *J. Arid Land* **2015**, *7*, 567–578. [CrossRef]
4. Hu, Q.; Han, Z. Northward Expansion of Desert Climate in Central Asia in Recent Decades. *Geophys. Res. Lett.* **2022**, *49*, e2022GL098895. [CrossRef]
5. Monforte, P.; Ragusa, M.A. Temperature Trend Analysis and Investigation on a Case of Variability Climate. *Mathematics* **2022**, *10*, 2202. [CrossRef]
6. Indoitu, R.; Orlovsky, L.; Orlovsky, N. Dust storms in Central Asia: Spatial and temporal variations. *J. Arid Environ.* **2012**, *85*, 62–70. [CrossRef]
7. Lioubimtseva, E.; Cole, R.; Adams, J.; Kapustin, G. Impacts of climate and land-cover changes in arid lands of Central Asia. *J. Arid Environ.* **2005**, *62*, 285–308. [CrossRef]
8. Al-Dousari, A.M.; Al-Awadhi, J.; Ahmed, M. Dust fallout characteristics within global dust storm major trajectories. *Arab. J. Geosci.* **2013**, *6*, 3877–3884. [CrossRef]
9. Galayeva, O.; Semenov, O. Sand transportation by wind in the Aral Sea region. *Hydrometeorol. Ecol.* **2011**, *3*, 73–85.
10. Goudie, A. Dust storms and their geomorphological implications. *J. Arid Environ.* **1978**, *1*, 291–311. [CrossRef]
11. Middleton, N.; Kang, U. Sand and dust storms: Impact mitigation. *Sustainability* **2017**, *9*, 1053. [CrossRef]
12. Babaev, A.G. *Desert Problems and Desertification in Central Asia: The Researchers of the Desert Institute*; Springer Science & Business Media: Berlin/Heidelberg, Germany, 2012.
13. Parakshina, E.; Saparov, A.; Mirzakeev, E. Soil Erosion in Kazakhstan. *Almaty Poligraphy-Serv.* **2010**. (In Russian)
14. Middleton, N.J. Desert dust hazards: A global review. *Aeolian Res.* **2017**, *24*, 53–63. [CrossRef]
15. Medeu, A.R. *Republic of Kazakhstan: Environment and Ecology*; The Institute of Geography ltd., National science and technology centre «Parasat»: Almaty, Kazakhstan, 2010; p. 520. (In Russian)
16. Karami, S.; Hamzeh, N.H.; Kaskaoutis, D.G.; Rashki, A.; Alam, K.; Ranjbar, A. Numerical simulations of dust storms originated from dried lakes in central and southwest Asia: The case of Aral Sea and Sistan Basin. *Aeolian Res.* **2021**, *50*, 100679. [CrossRef]

17. Prospero, J.M.; Ginoux, P.; Torres, O.; Nicholson, S.E.; Gill, T.E. Environmental characterization of global sources of atmospheric soil dust identified with the Nimbus 7 Total Ozone Mapping Spectrometer (TOMS) absorbing aerosol product. *Rev. Geophys.* **2002**, *40*, 1002. [CrossRef]
18. Zhou, C.; Gui, H.; Hu, J.; Ke, H.; Wang, Y.; Zhang, X. Detection of New Dust Sources in Central/East Asia and Their Impact on Simulations of a Severe Sand and Dust Storm. *J. Geophys. Res. Atmos.* **2019**, *124*, 10232–10247. [CrossRef]
19. Al-Dabbas, M.A.; Ayad Abbas, M.; Al-Khafaji, R.M. Dust storms loads analyses—Iraq. *Arab. J. Geosci.* **2012**, *5*, 121–131. [CrossRef]
20. Issanova, G.; Abuduwaili, J.; Oleg, S. Deflation processes and their role in desertification of the southern Pre-Balkhash deserts. *Arab. J. Geosci.* **2014**, *7*, 4513–4521.
21. Orlovsky, L.; Orlovsky, N.; Durdyev, A. Dust storms in Turkmenistan. *J. Arid Environ.* **2005**, *60*, 83–97. [CrossRef]
22. Orlovsky, L.; Tolkacheva, G.; Orlovsky, N.; Mamedov, B. Dust storms as a factor of atmospheric air pollution in the Aral Sea basin. *WIT Trans. Ecol. Environ.* **2004**, *74*, 353–362.
23. Squires, V.R. Dust and sandstorms: An early warning of impending disaster. In *Global Alarm: Dust and Sandstorms from World's Drylands*; United Nations: New York, NY, USA, 2001; pp. 15–28.
24. Groll, M.; Opp, C.; Aslanov, I. Spatial and temporal distribution of the dust deposition in Central Asia–results from a long term monitoring program. *Aeolian Res.* **2013**, *9*, 49–62. [CrossRef]
25. Indoitu, R.; Kozhoridze, G.; Batyrbaeva, M.; Vitkovskaya, I.; Orlovsky, N.; Blumberg, D.; Orlovsky, L. Dust emission and environmental changes in the dried bottom of the Aral Sea. *Aeolian Res.* **2015**, *17*, 101–115. [CrossRef]
26. O'Hara, S.L.; Wiggs, G.F.; Mamedov, B.; Davidson, G.; Hubbard, R.B. Exposure to airborne dust contaminated with pesticide in the Aral Sea region. *Lancet* **2000**, *355*, 627–628. [CrossRef]
27. Opp, C.; Groll, M.; Aslanov, I.; Lotz, T.; Vereshagina, N. Aeolian dust deposition in the southern Aral Sea region (Uzbekistan): Ground-based monitoring results from the LUCA project. *Quat. Int.* **2017**, *429*, 86–99. [CrossRef]
28. Orlovsky, L.; Orlovsky, N. White Sand Storms in Central Asia. In *Global Alarm: Dust and Sand Storms from the World's Drylands*; United Nations: New York, NY, USA, 2001; pp. 169–201.
29. Mischke, S.; Liu, C.; Zhang, J.; Zhang, C.; Zhang, H.; Jiao, P.; Plessen, B. The world's earliest Aral-Sea type disaster: The decline of the Loulan Kingdom in the Tarim Basin. *Sci. Rep.* **2017**, *7*, 43102. [CrossRef] [PubMed]
30. Ge, Y.; Abuduwaili, J.; Ma, L.; Wu, N.; Liu, D. Potential transport pathways of dust emanating from the playa of Ebinur Lake, Xinjiang, in arid northwest China. *Atmos. Res.* **2016**, *178–179*, 196–206. [CrossRef]
31. Wu, N.; Ge, Y.; Abuduwaili, J.; Issanova, G.; Saparov, G. Insights into Variations and Potential Long-Range Transport of Atmospheric Aerosols from the Aral Sea Basin in Central Asia. *Remote Sens.* **2022**, *14*, 3201. [CrossRef]
32. Isbekov, K.B.; Tsoy, V.N.; Crétaux, J.F.; Aladin, N.V.; Plotnikov, I.S.; Clos, G.; Berge-Nguyen, M.; Assylbekova, S.Z. Impacts of water level changes in the fauna, flora and physical properties over the Balkhash Lake watershed. *Lakes Reserv. Sci. Policy Manag. Sustain. Use* **2019**, *24*, 195–208. [CrossRef]
33. Iskakov, N.A.; Medeu, A.R. *Republic of Kazakhstan: Natural Resources and Conditions*; Ministry for Environmental Protection: Almaty, Kazakhstan, 2006; Volume 1. (In Russian)
34. Kovda, V.A. *Problems of Desertification and Soil Salinization in Arid Territories of the World*; Nauka: Moscow, Russia, 2008; p. 415. (In Russian)
35. Matinfar, H.R.; Alavi Panah, S.K.; Zand, F.; Khodaei, K. Detection of soil salinity changes and mapping land cover types based upon remotely sensed data. *Arab. J. Geosci.* **2013**, *6*, 913–919. [CrossRef]
36. Skotselias, I.I. Actual hydrometeorological problems of Balkhash Lake and Pre-Balkhash region. Saint Petersburg. *Gidrometeoizdat* **1995**. (In Russian)
37. Sills, J.; Ussenaliyeva, A. Save Kazakhstan's shrinking Lake Balkhash. *Science* **2020**, *370*, 303. [CrossRef]
38. Sills, J.; Aladin, N.V.; Høeg, J.T.; Plotnikov, I. Small Aral Sea brings hope for Lake Balkhash. *Science* **2020**, *370*, 1283.
39. Duan, W.; Zou, S.; Chen, Y.; Nover, D.; Fang, G.; Wang, Y. Sustainable water management for cross-border resources: The Balkhash Lake Basin of Central Asia, 1931–2015. *J. Clean. Prod.* **2020**, *263*, 121614. [CrossRef]
40. Myrzakhmetov, A.; Dostay, Z.; Alimkulov, S.; Tursunova, A.; Sarsenova, I. Level regime of Balkhash Lake as the indicator of the state of the environmental ecosystems of the region. *Paddy Water Environ.* **2022**, *20*, 315–323. [CrossRef]
41. Cherednichenko, A.V.; Cherednichenko, A.V.; Cherednichenko, V.S.; Storozhenko, N.D.; Kozhachmetova, E.P.; Kupchishin, A.I.; Abdrahimov, R.G. Dynamic of Balkhash lake level under climate change conditions. *IOP Conf. Ser. Earth Environ. Sci.* **2019**, *321*, 012012. [CrossRef]
42. Shen, B.; Wu, J.; Zhan, S.; Jin, M.; Saparov, A.S.; Abuduwaili, J. Spatial variations and controls on the hydrochemistry of surface waters across the Ili-Balkhash Basin, arid Central Asia. *J. Hydrol.* **2021**, *600*, 126565. [CrossRef]
43. Shen, B.; Wu, J.; Zhan, S.; Jin, M. Spatial Distributions, Sources and Risk Assessment of Toxic Elements in Waters of a Central Asian Basin. *Water Resour. Manag.* **2022**, *36*, 6187–6203. [CrossRef]
44. Mischke, S.; Zhang, C.; Plessen, B. Lake Balkhash (Kazakhstan): Recent human impact and natural variability in the last 2900 years. *J. Great Lakes Res.* **2020**, *46*, 267–276. [CrossRef]
45. Sala, R.; Deom, J.-M.; Aladin, N.V.; Plotnikov, I.S.; Nurtazin, S. Geological History and Present Conditions of Lake Balkhash. In *Large Asian Lakes in a Changing World: Natural State and Human Impact*; Mischke, S., Ed.; Springer International Publishing: Cham, Switzerland, 2020; pp. 143–175.

46. Gholami, H.; Mohammadifar, A.; Malakooti, H.; Esmaeilpour, Y.; Golzari, S.; Mohammadi, F.; Li, Y.; Song, Y.; Kaskaoutis, D.G.; Fitzsimmons, K.E.; et al. Integrated modelling for mapping spatial sources of dust in central Asia—An important dust source in the global atmospheric system. *Atmos. Pollut. Res.* **2021**, *12*, 101173. [CrossRef]
47. Nobakht, M.; Shahgedanova, M.; White, K. New Inventory of Dust Emission Sources in Central Asia and Northwestern China Derived From MODIS Imagery Using Dust Enhancement Technique. *J. Geophys. Res. Atmos.* **2021**, *126*, e2020JD033382. [CrossRef]
48. Issanova, G.; Abuduwaili, J. Introduction and Status of Storms in Central Asia and their Environmental Problems. In *Aeolian proceses as Dust Storms in the Deserts of Central Asia and Kazakhstan*; Springer Singapore: Singapore, 2017; pp. 1–27.
49. Badger, J.; Hahmann, A.; Larsén, X.G.; Badger, M.; Kelly, M.; Olsen, B.T.; Mortensen, N.G. *The Global Wind Atlas: An EUDP Project Carried out by DTU Wind Energy*; DTU Orbit: Copenhagen, Denmark, 2015.
50. Issanova, G.; Abuduwaili, J.; Kaldybayev, A.; Semenov, O.; Dedova, T. Dust storms in Kazakhstan: Frequency and division. *J. Geol. Soc. India* **2015**, *85*, 348–358. [CrossRef]
51. Akzhygitova, N.; Breckle, S.; Winkler, G.; Volkova, E.; Wucherer, W.; Kurochkina, L.; Makulbekova, G.; Ogar, N.; Rachkovskaya, E.; Safronova, I. *Botanical Geography of Kazakhstan and Middle Asia (Desert Region)*; Komarov Botanical Institute of the Russian Academy of Sciences: Saint Petersburg, Russia, 2003.
52. National Atlas of Kazakhstan (NAKZ). *Environment and ecology.* **2010**, *3*. (In Russian)
53. Muhs, D.R. The geologic records of dust in the Quaternary. *Aeolian Res.* **2013**, *9*, 3–48. [CrossRef]
54. Nikitin, S.A. Sands of the Western Balkash. In Proceedings of the Dokuchaev Soil Institute, Part 11, 1935; pp. 147–226. (In Russian)
55. Dedova, T.V.; Semenov, O.F.; Tuseeva, N.B. Division of Kazakhstan territory by the repetition of very strong dust storms and based on meteorological observations, remote sensing images and GIS. In *Republic of Kazakhstan: Environment and Ecology*; Iskakov, T.B., Medeu, A.R., Eds.; Almaty, Kazakhstan, 2006. (In Russian)
56. Semenov Oleg, E. *Introduction to Experimental Meteorology and Climatology of Sand Storms*, 2nd ed.; Fizmatkniga: Moscow, Russia, 2020; 448p.
57. Kudekov, T. Modern ecological condition of Balkhash Lake basin. *Kaganat Almaty* **2002**, *388*. (In Russian)
58. Belgibayev, I. Desertification and some ecological problems of Southern Pre-Balkhash region. In Proceedings of the Materials of Scientific-Practice Conference "Problems of Hydrometeorology and Ecology", Almaty, Kazakhstan, 5 July 2001; pp. 242–249. (In Russian)
59. Shi, L.; Zhang, J.; Yao, F.; Zhang, D.; Guo, H. Temporal variation of dust emissions in dust sources over Central Asia in recent decades and the climate linkages. *Atmos. Environ.* **2020**, *222*, 117176. [CrossRef]
60. Issanova, G.; Abuduwaili, J. *Aeolian Processes as Dust Storms in the Deserts of Central Asia And Kazakhstan*; Springer: Berlin/Heidelberg, Germany, 2017.
61. Wang, W.; Samat, A.; Ge, Y.; Ma, L.; Tuheti, A.; Zou, S.; Abuduwaili, J. Quantitative Soil Wind Erosion Potential Mapping for Central Asia Using the Google Earth Engine Platform. *Remote Sens.* **2020**, *12*, 3430. [CrossRef]
62. Xi, X.; Sokolik, I.N. Seasonal dynamics of threshold friction velocity and dust emission in Central Asia. *J. Geophys. Res. Atmos.* **2015**, *120*, 1536–1564. [CrossRef]
63. Murzaev, E. *Middle Asia. The Natural Geographical Characteristics*; Publication of the Academy of Sciences USSR: Moscow, Russia, 1958; p. 646. (In Russian)
64. Sidorov, V. *Climatology and Meteorology*; Ural State Technical University: Ekaterinburg, Russia, 2006; p. 146. (In Russian)
65. Uteshev, A.S.; Semenov, O.E. *Climate and Wind Erosion of the Soil*; Kainar, Almaty, 1967. (In Russian)
66. Bagnold, R.A. The transport of sand by wind. *Geogr. J.* **1937**, *89*, 409–438. [CrossRef]
67. Fediushina, L. The distribution of wind erosion weather in the territory of Almaty and Zhambyl regions. *Tr. KazNIGMI* **1972**, *49*, 64–75. (In Russian)
68. Fediushina, L. The distribution of dust storms in the territory of Almaty and Zhambyl regions. *Tr. KazNIGMI* **1972**, *49*, 76–83. (In Russian)
69. Dar, M.A.; Ahmed, R.; Latif, M.; Azam, M. Climatology of dust storm frequency and its association with temperature and precipitation patterns over Pakistan. *Nat. Hazards* **2022**, *110*, 655–677. [CrossRef]
70. Romanov, N. Dust storms in Central Asia. *Tajikistan Tashkent* **1960**, 198. (In Russian)
71. Maman, S.; Blumberg, D.G.; Tsoar, H.; Mamedov, B.; Porat, N. The Central Asian ergs: A study by remote sensing and geographic information systems. *Aeolian Res.* **2011**, *3*, 353–366. [CrossRef]
72. Platonova, L.I. Geomorphological structure and Quaternary deposits of the western part of the Ili depression. *Doctor Almaty* **1962**. (In Russian)
73. Fin'ko, E.A. *Morphostructural Analysis in the Study of Modern Tectonic Movements: A Case Study of Eastern and Southern Kazakhstan*; Nedra: Moscow, Russia, 1973. (In Russian)
74. Evseeva, N.; Kvasnikova, Z. Recent eolian processes in the south-eastern West Siberia. *Geomorfol. Geomorphol. RAS* **2010**, *3*, 40–46. (In Russian) [CrossRef]
75. Namazbayeva, A.E. Eolian morphogenesis in the Taukum desert. In Proceedings of the International Conference "Zhandaev Readings", Almaty, Kazakhstan, 2001; pp. 152–156. (In Russian)

sustainability

MDPI

Article

A Multiscale Normalization Method of a Mixed-Effects Model for Monitoring Forest Fires Using Multi-Sensor Data

Lanbo Feng [1], Huashun Xiao [1,*], Zhigao Yang [2] and Gui Zhang [3]

[1] School of Forestry, Central South University of Forestry and Technology, Changsha 410004, China; Cahrmisty@163.com
[2] National Forest Fire Prevention Virtual Simulation Experimental Teaching Center, Changsha 410004, China; zgyang@126.com
[3] Key Laboratory of Digital Dongting Lake of Hunan Province, Changsha 410004, China; csfu3s@163.com
* Correspondence: hsxiao@126.com

Abstract: This paper points out the shortcomings of existing normalization methods, and proposes a brightness temperature inversion normalization method for multi-source remote sensing monitoring of forest fires. This method can satisfy both radiation normalization and observation angle normalization, and reduce the discrepancies in forest fire monitoring between multi-source sensors. The study was based on Himawari-8 data; the longitude, latitude, solar zenith angle, solar azimuth angle, emissivity, slope, aspect, elevation, and brightness temperature values were collected as modeling parameters. The mixed-effects brightness temperature inversion normalization (MEMN) model based on FY-4A and Himawari-8 satellite sensors is fitted by multiple stepwise regression and mixed-effects modeling methods. The results show that, when the model is tested by Himawari-8 data, the coefficient of determination (R^2) reaches 0.8418, and when it is tested by FY-4A data, R^2 reaches 0.8045. At the same time, through comparison and analysis, the accuracy of the MEMN method is higher than that of the random forest normalization method (RF) ($R^2 = 0.7318$), the pseudo-invariant feature method (PIF) ($R^2 = 0.7264$), and the automatic control scatter regression method (ASCR) ($R^2 = 0.6841$). The MEMN model can not only reduce the discrepancies in forest fire monitoring owing to different satellite sensors between FY-4A and Himawari-8, but also improve the accuracy and timeliness of forest fire monitoring.

Keywords: Himawari-8; FY-4A; forest fires monitoring; brightness temperature inversion; normalization; mixed-effects model

Citation: Feng, L.; Xiao, H.; Yang, Z.; Zhang, G. A Multiscale Normalization Method of a Mixed-Effects Model for Monitoring Forest Fires Using Multi-Sensor Data. *Sustainability* **2022**, *14*, 1139. https://doi.org/10.3390/su14031139

Academic Editors: Stefano Morelli, Veronica Pazzi and Mirko Francioni

Received: 21 December 2021
Accepted: 11 January 2022
Published: 20 January 2022

1. Introduction

Forest fires have the characteristics of strong suddenness, strongly destructive, high risk, and frequent occurrence. Factors such as human activities, the terrain conditions, changes in land use, and climate will all have a certain impact on the probability of fire [1]. They are one of the most difficult and devastating natural disasters with which to deal. Fire influences both forest structure and function [2].

Current remote sensing approaches to forest fire monitoring and detection in China can be grouped as follows: (a) air-monitoring systems, (b) ground-monitoring systems, and (c) space-monitoring systems. Among them, air-monitoring refers to the use of manned aircraft or unmanned aerial vehicles (UAVs) to monitor forest fires. Its advantages are that it can obtain high-quality internal information data of the fire site when the fire occurs, effectively provide the trend of fire spread after a fire, and guide firefighting operations. However, manned aerial vehicles are operated by human pilot(s) and are typically large and expensive. Using a manned aerial vehicle puts the life of the pilot in harm's way, threatened by a hazardous environment and operator fatigue. Aircraft systems may sustain with higher payloads and speed, but hovering in one place and maintaining high and low speeds are the challenges [3]. At the same time, UAVs cannot monitor a wide range of

areas in real time in all-weather conditions. Its main application is to guide firefighting after a fire occurs [4]. Ground-monitoring refers to the manual monitoring of forest fires by establishing ground observation towers or using ground measuring instruments [5]. Its advantages are low cost, accurate positioning, and real-time detection, but ground-based measurement instruments may suffer from limited surveillance ranges and are not suitable for very large areas such as forests [6]. Space-monitoring refers to remote sensing monitoring of forest fires using satellites. It has the shortcomings of low spatial resolution and it is unable to capture detailed fire data to guide firefighting. However, its advantages are particularly obvious, and one of these advantages that its monitoring range is particularly wide. With the rapid development of remote sensing technology, the high temporal resolution of static satellites makes the timeliness of satellite monitoring particularly high, and satellite monitoring can quickly locate the approximate fire point. Effective monitoring of fire points can quickly guide the subsequent forest fire fighting. Satellite remote sensing monitoring can greatly reduce the environmental damage and resource loss caused by forest fires. Therefore, satellite remote sensing monitoring is an important part of the integrated monitoring system for forest fires in the space, air, and ground of China. The brightness temperature is a key parameter to monitor forest fires by satellite. The monitoring of abnormally high brightness temperature points is an important basis for determining the occurrence of fires.

At present, there are a large number of satellites monitoring forest fires and there are abundant sources of remote sensing data. The conversion from the digital number (DN) of a satellite image to radiance is affected by many factors, including illumination geometry, sensor calibration, and atmospheric condition, among others. As multi-temporal images are often acquired at different times under different atmospheric conditions, solar illumination, sensor calibration, and view angles, radiometric correction is required to remove radiometric distortions [7–10]. The main methods to effectively correct the radiation deviation at this stage are as follows: the random forest normalization method, pseudo-invariant feature method, multiple change detection relative radiation normalization method, and automatic scattergram-controlled regression method, among others. Zhao W [11] proposes a practical normalization method based on random forest. The results show that the spatial pattern of normalized LST data can be significantly improved. Unlike the previous normalization method, the proposed method is only based on satellite observations without other auxiliary data. Therefore, this method shows good potential for normalizing the time effects of wide-angle polar-orbiting satellite observations. The PIF relative radiation normalization method is used to study the radiation normalization of inter-phase remote sensing data. De Carvalho O et al. [12] proposed a new technique for accurately selecting PIF. New sequential methods enable one to select, by different attributes, a number of invariant targets over the brightness range of the images, and to improve the accuracy of PIF radiation normalization. Elvidge et al. [13] proposed the automatic scatter control and regression (ASCR) method. The relevant literature shows that the ASCR method is simple to operate, efficient in execution, and can reduce clouds and shadows; its radiation normalization effect is also significantly better for various commonly used statistical methods. However, owing to ASCR requirements, the area contains a large area of water and land features, so this method should be used in areas with less water bodies or in multi-temporal images. When the water body has undergone major changes, the accuracy of the calculation results will be difficult to guarantee, and cannot reflect the advantages of ASCR. Aiming at the shortcomings of the existing method, Himawari-8 and FY-4A are unified to the same or similar radiative benchmarks, then the mixed-effects brightness temperature inversion normalization model is established by considering the fixed and random effects of the model.

The MEMN method not only meets the requirements of radiation normalization, but also eliminates the influence of solar azimuth angle and solar zenith angle, meeting the requirements of observation angle normalization. At the same time, the MEMN method can reduce the influence of the studied satellites owing to the difference in sensor sensitivity,

the difference in solar zenith angle and solar azimuth angle, and the satellite in-orbit state characteristics, among others, and improves the accuracy of forest fire monitoring. The normalized model based on geostationary satellite parameters with high temporal resolution can greatly improve the timeliness of forest fire monitoring. It can be used for the normalized analysis of remote sensing data from a variety of satellites, which greatly increases the application range of remote sensing data. The MEMN method will become a key technology for accurate monitoring of forest fires by satellite.

2. Materials and Methods

2.1. Data Introduction

Forest fire monitoring requires particularly high timeliness of remote sensing images, Himawari-8 satellite carries the world's advanced AHI (advanced Himawari imager). The temporal resolution of the entire observation is 10 min once, so Himawari-8 was selected as the normalized reference image. FY-4A is a Chinese-made geostationary satellite, but its spatial resolution and time resolution are relatively low compared with Himawari-8, so it makes sense to choose FY-4A as the satellite to be calibrated. Topographic factors such as slope, aspect, and elevation are collected from the digital elevation model (DEM) of SRTM with 90 m resolution; in the JAXA Himawari Monitor, the official website of Himawari-8, clear sky images with low cloud content are selected, and all data used in the experiment are remotely sensed images of the same moment. The Himawari-8 data were downloaded from the Japan Meteorological Agency (JMA, Tokyo, Japan) in the Himawari standard format (HSD), and the FY-4A AGRI 4 km data were downloaded from the National Satellite Meteorological Satellite (NSM) website, which were interpolated to obtain the same standard 2 km spatial data as Himawari-8. The purpose of interpolation of FY-4A from 4 km to 2 km is to make the pixels contained in each grid complete pixels in statistical data, so as to eliminate the deviation caused by statistical data. This is because the principle of grid statistics in this paper is to count the maximum, minimum, and mean values of all the complete pixels contained in the grid. In the subsequent analysis, the grid size is set to 7×7, that is, the size of each grid is 14 km $\times$ 14 km. If the FY-4A data of 4 km spatial resolution are used for statistics, each grid will contain the number of incomplete FY-4A pixels, and the statistical results of the data will cause certain errors. Thus, we interpolate FY-4A from 4 km to 2 km. The solar zenith angle and solar azimuth angle parameters were collected from the FY-4A L1_GEO data.

The theoretical basis for satellite remote sensing fire point detection is that infrared radiation is significantly enhanced when the material is in a high temperature combustion state, and the fire point image element temperature is usually about 800 K. The temperature radiation peak is located near 4 μm [14–17]. Therefore, the band near the central wavelength of 4 μm (seventh channel of Himawari-8 and eighth channel of FY-4A) was selected for bright temperature inversion. In this study, Hunan Province in China was selected as the study area (Figure 1).

2.2. Data Pre-Processing

Taking into account the differences in the coordinate systems and spatial resolutions of the above-mentioned different types of data sources, the source data are transformed and processed first: (1) Convert the FY-4A AGRI 4 km data to the WGS84 coordinate system, and interpolate its spatial resolution at the same time to 2 km, thus matching the Himawari-8 data. (2) Considering that the Himawari-8 HSD data are an uncalibrated full-disk observations, it needs to be radiometrically calibrated [18,19], involving band clipping to obtain the brightness temperature inversion and the band required to collect the solar zenith angle and solar azimuth angle.

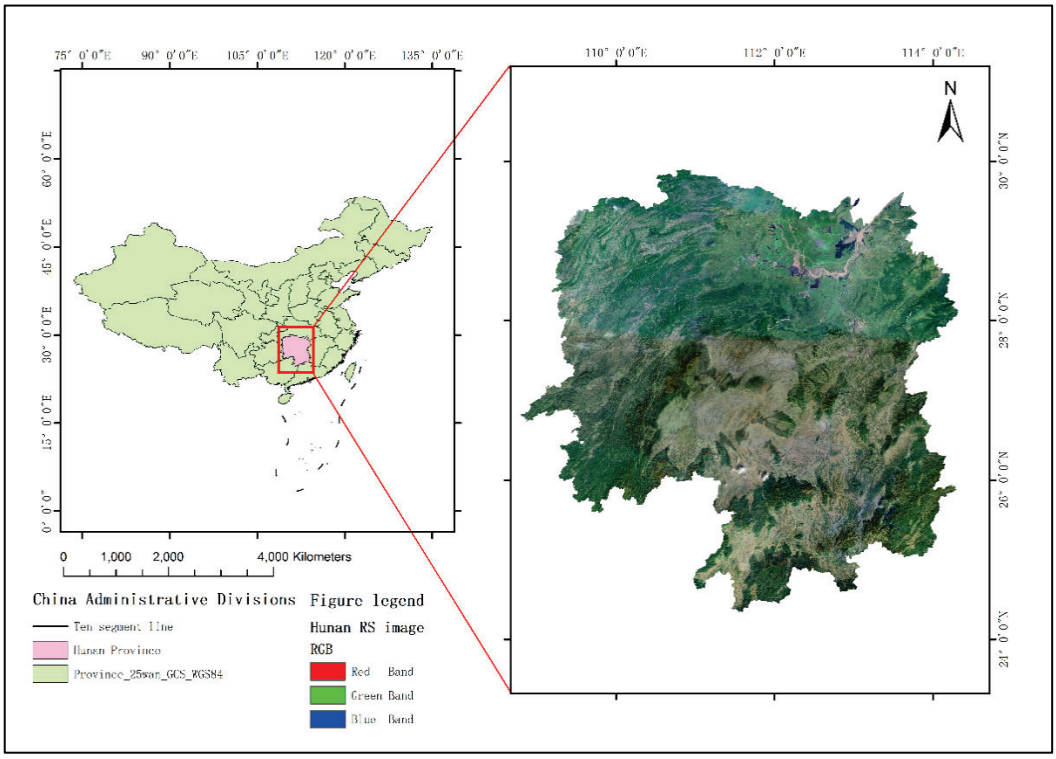

Figure 1. The map of the study area.

On the basis of the above-mentioned data preprocessing, in order to eliminate data collection errors caused by irregular sample selection and inconsistent spatial resolution, a collection data grid is established. The values of slope, aspect, and elevation parameters were obtained by calculating the SRTM DEM by ArcGIS. At the same time, the cloud cover data [20,21], emissivity parameters [22–25], and land cover types [26–28] are obtained by raster calculation.

2.3. Determination of Model Parameters

The factors that may influence the results of brightness temperature values during the brightness temperature inversion were analyzed. The correction coefficients of the data were obtained from the header file of Himawari-8 data: the parameters solar zenith angle (SOZ) and solar azimuth angle (SOA) were obtained by geometric correction and radiometric correction; the parameters black body temperature (TBB) and surface specific emissivity (emissivity) were obtained by brightness temperature inversion; and DEM data were preprocessed to obtain the parameters of slope, aspect, and elevation, as well as the longitude and latitude of each sample pixel.

The following were selected: longitude, latitude, solar zenith angle, solar azimuth angle, slope, aspect, elevation, and emissivity as the independent variables for modeling, and TBB was selected as the dependent variable to build the MEMN model. The correlation analysis of each variable was performed, and the results are shown in Figure 2.

2.4. Data Collection

When collecting parameters such as latitude, longitude, slope, aspect, elevation, solar zenith angle, solar azimuth angle, emissivity, brightness temperature, and so on, the remote sensing data for collecting parameter values are derived from different sensors, and their spatial resolutions are also different. In order to reduce the error, a grid data acquisition method is proposed. Based on the principle of grid analysis, the grid is established by ArcGIS software. Each grid contains the same number of pixels, the legal pixel is the pixel at the centroid point of each grid, and the maximum pixel value in each grid is collected as

the result value of the legal pixel. The maximum pixel value refers to the pixel in which the maximum brightness temperature value is located in each grid area. The parameters used for statistics are as follows: brightness temperature value, emissivity value, solar altitude angle, solar azimuth angle, slope, slope direction, and elevation. The legal pixel value is the pixel at the centroid point of each 7 × 7 grid, which is used for statistics such as longitude and latitude. Therefore, the grid size setting determines the data collection results. According to the analysis of the multiple linear regression result and scatter plot analysis based on the study data, it is found that the relationship between emissivity and brightness temperature is linear, and that emissivity is the best factor for fitting the linear basic model of brightness temperature. Therefore, we start to set different sizes of grids to count the brightness temperature and emissivity, and choose the most linearly related grid as the grid to count all the modeling factor parameters. When selecting the grid size, we set the grid to different sizes, analyze the linear correlation between emissivity and brightness temperature under each size condition, and set the grid size under the highest linear correlation condition as the final collection grid size used in the data. It can be seen from Figure 3 that, when the grid is set to 7 × 7 (each grid contains 7 × 7 pixels), the linear correlation between surface emissivity and brightness temperature is the highest. Therefore, the 7 × 7 grid is selected as the grid for data collection.

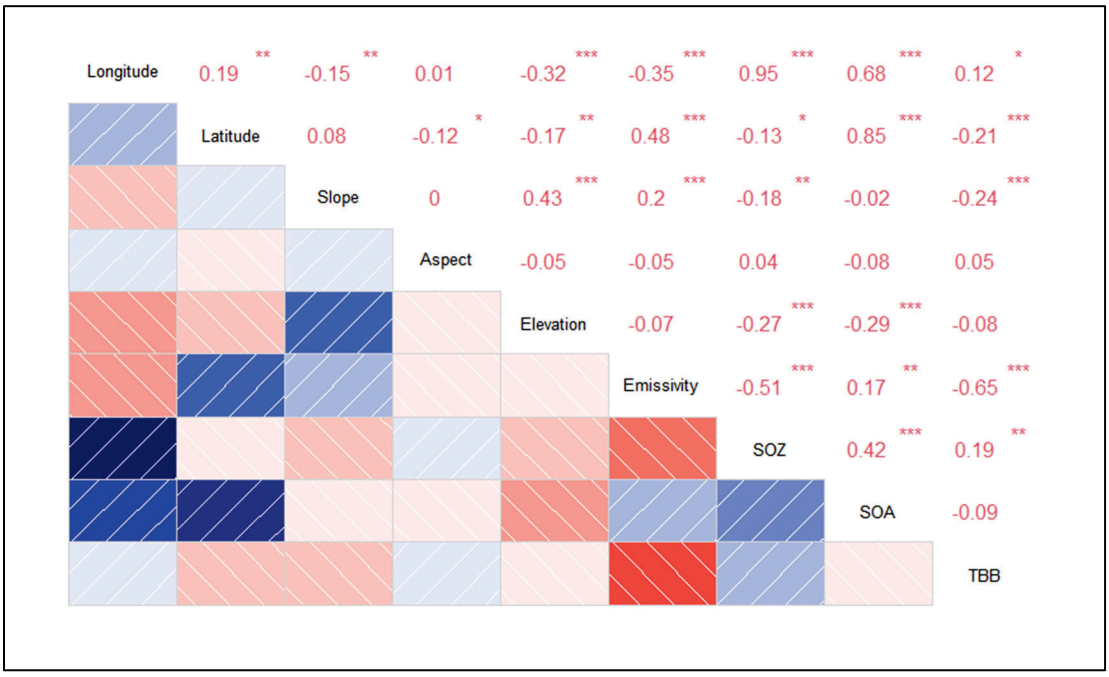

Figure 2. The values in the graph indicate the degree of autocorrelation among the factors; the higher absolute value indicates higher correlation, where * represents the significance of the significant factors, each * is a 5% significance level, and more * means more significance. The diagonal line of the grid in the figure indicates the trend of correlation; the diagonal line to the left indicates negative correlation and the diagonal line to the right indicates positive correlation.

2.5. Classification of Model Parameters

The site of factors such as elevation, slope, and aspect is mainly based on the classification standard of site factors of "Technical Regulations for Forest Resources Planning and Design Investigation (GB/T26426-2010)". On this basis, the elevation is graded per hundred meters. All parameters are graded as in Table 1.

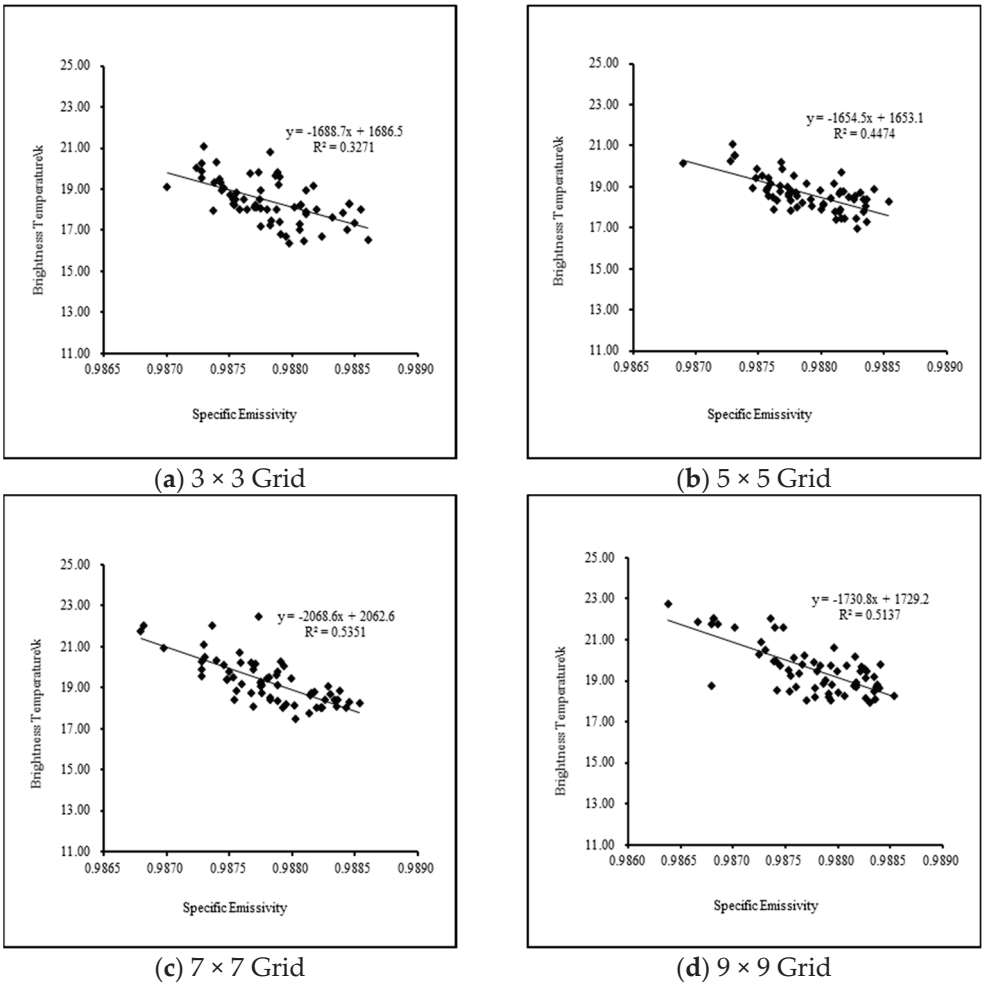

(**a**) 3 × 3 Grid (**b**) 5 × 5 Grid

(**c**) 7 × 7 Grid (**d**) 9 × 9 Grid

Figure 3. The linear relationship between the statistical values of the brightness temperature and the calculated values of the surface specific emissivity, which is the main correlation of the underlying model, can be seen by analyzing the statistical values for different grid size conditions. The two possess the most relevant linear relationship when the grid of the statistics is set to Figure 2c.

Table 1. Parameter grading of the hybrid model.

Site Factors	**Grade Division**							
Elevation	Level 1 per 100 m							
Slope gradient	[0,5] I	[6,15] II	[16,25] III	[26,35] IV	[36,45] V	≥46 VI		
Slope aspect	(337.5, 22.5] North slope	(22.5, 67.5] Northeast slope	(67.5, 112.5] East slope	(112.5, 157.5] Southeast slope	(157.5, 202.5] South slope	(202.5, 247.5] Southwest slope	(247.5, 292.5] West slope	(292.5, 337.5] Northwest slope

2.6. Normalized Modeling

(1) Multiple linear regression. Multiple linear regression analysis can avoid the multicollinearity of variables or the random influence of independent variables on dependent variables, so as to extract the independent variables of the main influencing factors to explain the change of dependent variables [29,30].

(2) Linear mixed-effects model (LME) expression. According to the number of random effect factors, the linear mixed-effects model (LME) is divided into two basic forms: single-level and multi-level. This study is a relational model constructed based on a multi-level linear model that contains two random effect factors. The general expression of the mixed effect model is as follows [31,32]:

$$y = X\beta + Z\alpha + \varepsilon \quad (1)$$

In Formula (1), y is the vector of observations; β is the fixed-effects parameter vector; α is the random effects parameter vector; the matrices X and Z are design matrices corresponding to fixed and random effects, respectively (through analysis, this research identifies emissivity as a fixed effect and identifies slope, aspect, elevation, and solar azimuth angle as random effects); and ε is the error vector.

2.7. Model Accuracy Evaluation

The evaluation of the regression prediction model is an indispensable step in the model building process. The evaluation of model accuracy is carried out using the Akaike information criterion (*AIC*), Bayesian information criterion (*BIC*), mean absolute error (*MAE*), coefficient of determination (R^2), and root mean square error (*RMSE*). These formulas are shown respectively as follows:

$$AIC = -2\ln(\mathrm{L}) + 2\mathrm{K} \tag{2}$$

$$BIC = -2\ln(\mathrm{L}) + \ln(\mathrm{n})\mathrm{k} \tag{3}$$

$$MAE = \sum_{i+1}^{n} |y_i - \hat{y}i|/n \tag{4}$$

$$R^2 = 1 - \sum_{i+1}^{n} \left(y_i - \hat{y}i\right)^2 / \sum_{i+1}^{n} (y_i - \overline{y})^2 \tag{5}$$

$$RMSE = \sqrt{\sum_{i+1}^{n} (y_i - \overline{y}_i)^2 / (n-1)} \tag{6}$$

In Formulas (2)–(6), y_i is the measured value of the i-th sample, $\hat{y}_i$ is the estimated value of the i-th sample, $\overline{y}$ is the average measured value, n is the number of samples, K is the number of model parameters, and L is the maximum likelihood function value of the model. Among them, the smaller the value of *AIC* and *BIC*, the better the fitting effect of the model. The closer the values of *MAE* and *RMSE* are to 0, and the closer the value of R^2 is to 1, and the higher the accuracy of the model [33].

3. Results

3.1. Multiple Linear Regression

According to the correlation analysis, it is known that longitude, latitude, emissivity, slope, aspect, elevation, solar azimuth angle, and solar zenith angle can be used as modeling factors. Among them, latitude, longitude, emissivity, and TBB are highly correlated. After analysis, the factors with a good fitting effect are selected as the independent variables of the basic model. After classification, K-means clustering, and factors' combination, the remaining factors with a good fitting effect can be selected as random effects to join the basic model. In order to determine the independent variables of the basic model, multiple linear stepwise regression analysis of multiple independent variable factors of the basic model is used, and the results are shown in Tables 2 and 3.

Table 2. Multiple regression model analysis of variance.

Factor Group	Sum of Squares	Freedom	Mean Square	F Value	Pr > F
Longitude	7.1550	1	7.1550	7.5492	0.006372 **
Latitude	29.8800	1	29.8800	31.5249	4.534×10^{-8} **
Emissivity	220.2950	1	220.2950	232.4239	$<2.2 \times 10^{-16}$ ***
Residuals	280.5530	296	0.9480		

Note: * represents the level of significance of the significant factor, and a higher number of * indicates a more significant factor.

Table 3. Multiple regression model fitting results.

Parameters	Values	Standard Value	Value T	Pr > F	R^2
(Intercept)	2.300×10^3	1.509×10^2	15.238	$<2 \times 10^{-16}$ ***	0.4731
Longitude	-2.594×10^{-1}	5.606×10^{-2}	−4.627	5.55×10^{-6} ***	
Latitude	3.305×10^{-2}	7.204×10^{-3}	4.588	6.61×10^{-6} ***	
Emissivity	-2.280×10^3	1.496×10^2	−15.245	$<2 \times 10^{-16}$ ***	

Note: * represents the level of significance of the significant factor, and a higher number of * indicates a more significant factor.

Latitude, longitude, and emissivity are factors that have significant effects on TBB, which can be used as independent variables to fit the basic model. In stepwise regression analysis, when longitude and latitude are used as the fixed factors of the basic model, the accuracy of the basic model is low. At the same time, when longitude and latitude are used as fixed factors to fit the mixed-effects model, the accuracy of the model is only slightly improved, and it is not convenient for the practical application of the model. In order to simplify the model form, it can be seen from Tables 2 and 3 that the value of F and value of T of emissivity are obviously optimal. Therefore, without considering the longitude and latitude as the fixed factor of the basic model and the random effect of the mixed-effects model, the emissivity is determined to be the independent variable of the basic model for fitting.

3.2. Determination of the Basic Model

Fitting the basic model, the results are shown in Table 4.

Table 4. Results of the basic model fit.

Parameters	Values	Down Limit	Up Limit	Fitting Data		
				R^2	MAE	RMSE
a	−1747.4422	−1978.5302	1516.3542	0.4244	0.7907	1.0142
b	1745.5010	1517.2530	1973.7489			

The specific form of the basic model is determined by Table 4 as follows:

$$TBB = -1747.44 \times EMS + 1745.50 \quad (7)$$

In Formula (7), TBB is the value of brightness temperature and EMS is the emissivity value of the main correlation factor.

3.3. Fitting the Mixed-Effects Model

Taking into account the slope, aspect, elevation, solar zenith angle, and solar azimuth angle will affect the true brightness temperature value. Based on the fixed linear model, slope, aspect, elevation, solar zenith angle, and solar azimuth angle are taken as random effects to introduce different combination positions of model parameters a and b. The mixed-effects model is fitted after introduction, and the results are summarized in Table 5.

According to the evaluation indexes in Table 5, it can be known that, when fitting the site type (LDLX) combined with slope, aspect, and elevation, and SOA and SOZ as random effects into the fixed model, the accuracy of the model is improved. The amount of AIC and BIC decreased. Among them, M2, M6, and M10 are the model results and evaluation when the random effects LDLX, SOZ, and SOA are added to parameter b of the fixed model, respectively. Obviously, when LDLX and SOA are used as random effects, the accuracy of the model is improved greatly, and when SOZ is used as a random effect, the accuracy of the model is improved slightly. Among them, M4, M8, and M12 are the model results and evaluation when the random effects ldlx, soz, and soa (LDLX, SOZ, and SOA

are clustered by the K-means method) are added as random effects to parameter b of the fixed model. It can be seen that, when ldlx and soa are used as random effects, the accuracy of the model is greatly improved, and soz is the result of singular fitting. After the analysis, soz is not considered as a random effect, and ldlx and soz are determined as random effects of the MEMN model.

Table 5. Linear mixed effects model parameter estimates.

Random Factor	Model	Parameter Combination	R^2	*AIC*	*BIC*	*RMSE*	*MAE*
LDLX	M1	a	0.5181	865.8	880.6	0.9314	0.7206
	M2	b	0.5181	865.8	880.6	0.9314	0.7205
ldlx	M3	a	0.6640	754.4	769.2	0.7752	0.5794
	M4	b	0.6640	754.4	769.2	0.7752	0.5794
SOZ	M5	a	0.4452	867.8	882.6	0.9959	0.7751
	M6	b	0.4454	867.8	882.6	0.9957	0.7749
soz	M7	a			Singular fit		
	M8	b			Singular fit		
SOA	M9	a	0.5194	867.0	881.8	0.9306	0.7289
	M10	b	0.5196	867.0	881.8	0.9305	0.7288
soa	M11	a	0.7942	632.7	647.6	0.6067	0.4381
	M12	b	0.7942	632.7	647.6	0.6067	0.4381
Ldlx + soa	M13	a + a	0.8418	590.4	609.0	0.5321	0.3977
	M14	b + b	0.8418	590.4	609.0	0.5321	0.3977
	M15	b + a	0.8418	590.4	609.0	0.5321	0.3977
	M16	a + b	0.8418	590.4	609.0	0.5321	0.3977

Note: The parameter combinations a and b refer to the mixed-effects model construction by adding random effects to each parameter separately.

According to Table 5, we selected M14 as the optimal model. Analysis of the evaluation indicators of the M14 model shows that the coefficient of determination R^2 increased from 0.4244 to 0.8418, an increase of 98.35%; the MAE decreased from 0.7907 to 0.3977, a decrease of 49.37%; and the $RMSE$ decreased from 1.0142 to 0.5321, a decrease of 47.52%. The R^2 displays a significant improvement, and MAE and $RMSE$ are significantly reduced. Therefore, the determined model form is as follows:

$$TBB_{ij} = \mathrm{a} \times EMS_{ij} + \left(\mathrm{b} + b_i + b_j\right) + \varepsilon_{ij} \quad (8)$$

In the formula, TBB_{ij} is the brightness temperature value of the *i*-th grade site type and *j*-th grade solar azimuth angle. EMS_{ij} is the emissivity value for the *i*-th grade site type and the j-th grade solar azimuth angle. b_i is the random effect parameter of the site effect, and b_j is the random effect parameter of the solar azimuth angle effect. $b_i \sim N(0, \psi 1)$,$\psi 1$ is the design matrix of the random effect parameter of the site; and $b_j \sim N(0, \psi 2)$,$\psi 2$ is the design matrix of the random effect parameters of the solar azimuth angle. e_{ij} is the error term of the *i*-th grade site type and *j*-th grade solar azimuth angle.

It can be seen from Figure 4 that, compared with the basic model, the prediction value of the mixed-effects model is less discrete, and the residuals of the mixed-effects model are more concentrated on both sides of the X axis. To sum up, the model based on the random effects of ldlx and soa groups can display greatly improved accuracy.

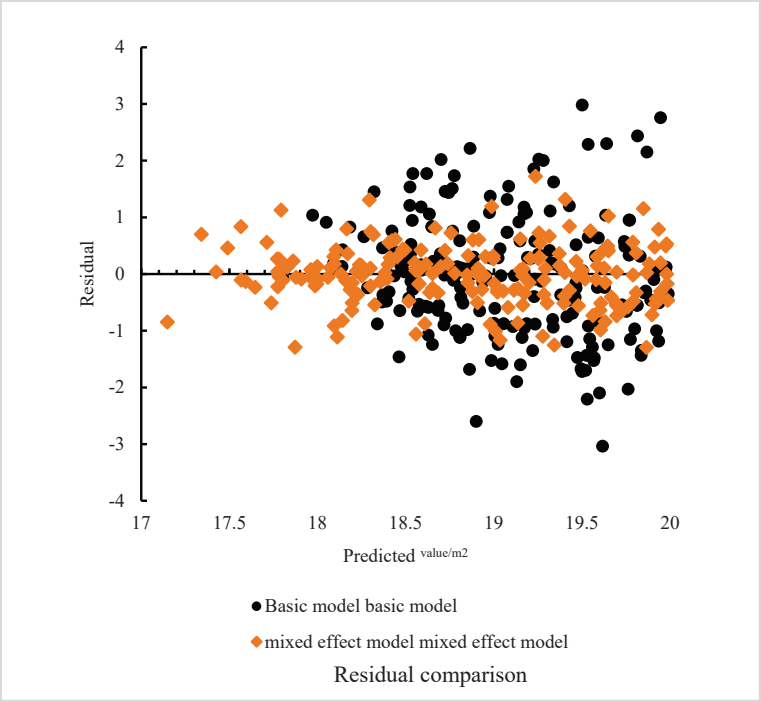

Figure 4. The orange diamond indicates the dispersion of the mixed-effects model predictions, and the black circle indicates the dispersion of the basic model predictions.

3.4. Comparison of the Accuracy of Normalization Methods

The data used in the model evaluation are the Himawari-8 and FY-4A image data at 06:30 (UTC) on 10 December 2019 in Hunan Province in China. The measured values of factors such as emissivity, solar zenith angle, slope, aspect, elevation, and brightness temperature are collected. The predictive values of brightness temperature are calculated by the *MEMN* model and the *RF* model in the literature [6]. The accuracy between the two models was compared and evaluated based on three indicators: coefficient of determination (R^2), mean absolute error (*MAE*), and root mean square error (*RMSE*).

The radiance of the reference image Himawari-8 (Figure 5a) is quite different from the image FY-4A (Figure 5b), which is the image to be corrected. The normalized image (Figure 5c) is obtained after normalization by the RF method. At the same time, the normalized image (Figure 5d) is obtained by the MEMN method.

The pixel values of normalized images were statistically analyzed. Figure 6 is the linear correlation comparison chart between the MEMN method and RF method. Table 6 shows the comparison of the model accuracy evaluation index of two methods. It can be seen that the accuracy of the MEMN method is better than that of the RF method.

Table 6. Comparison of evaluation indicators for different normalization methods.

Brightness Temperature Inversion Normalization Method	R^2	*MAE*	*RMSE*
MEMN Method	0.8045	0.4657	0.5648
RF Method	0.7318	0.5583	0.6817
PIF Method	0.7264	0.5603	0.7155
ASCR Method	0.6841	0.6193	0.7882

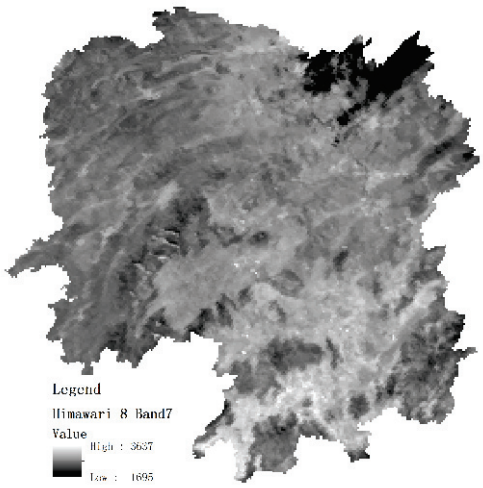

(**a**) Refer to Himawari-8 B7 image

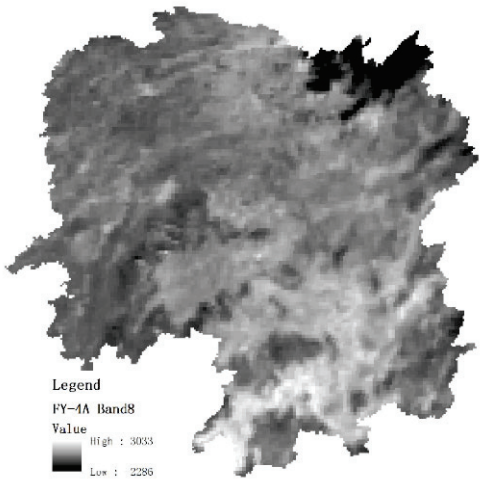

(**b**) To be corrected FY-4A B8 image

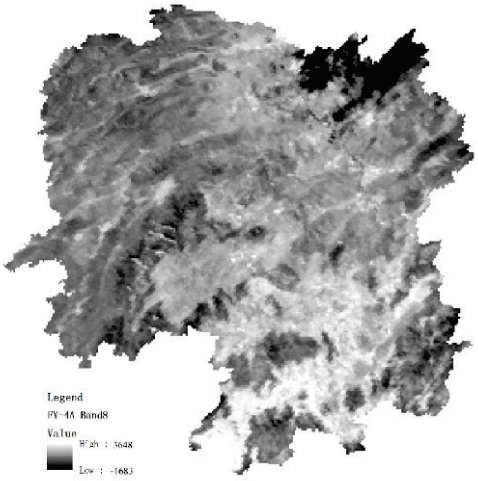

(**c**) Radiation Normalized Image By MEMN

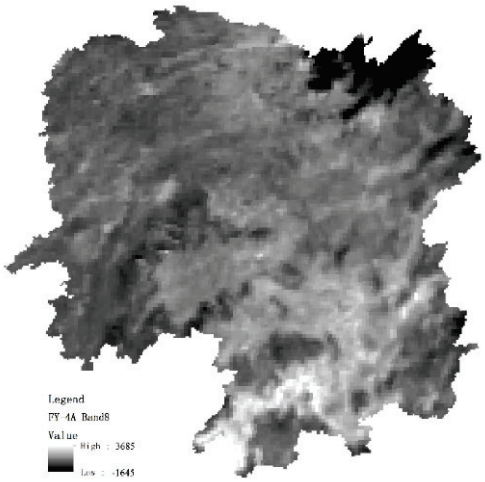

(**d**) Normalized Image By RF

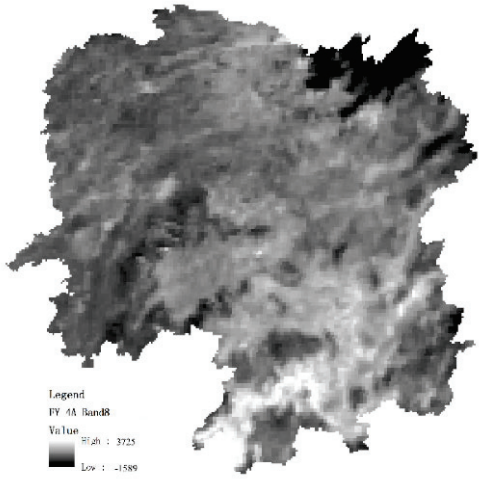

(**e**) Radiation Normalized Image By PIF

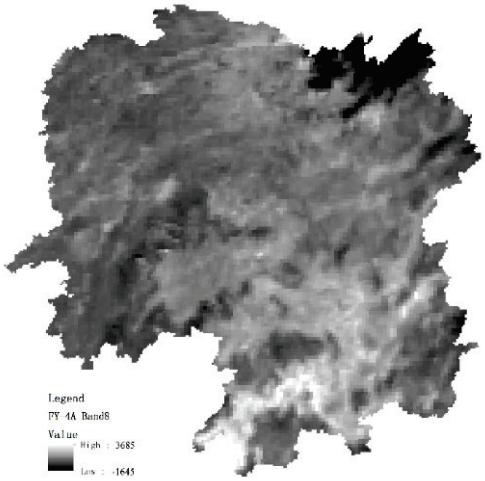

(**f**) Normalized Image By ASCR

Figure 5. Original image and normalization results of different methods (mid-wave infrared channel).

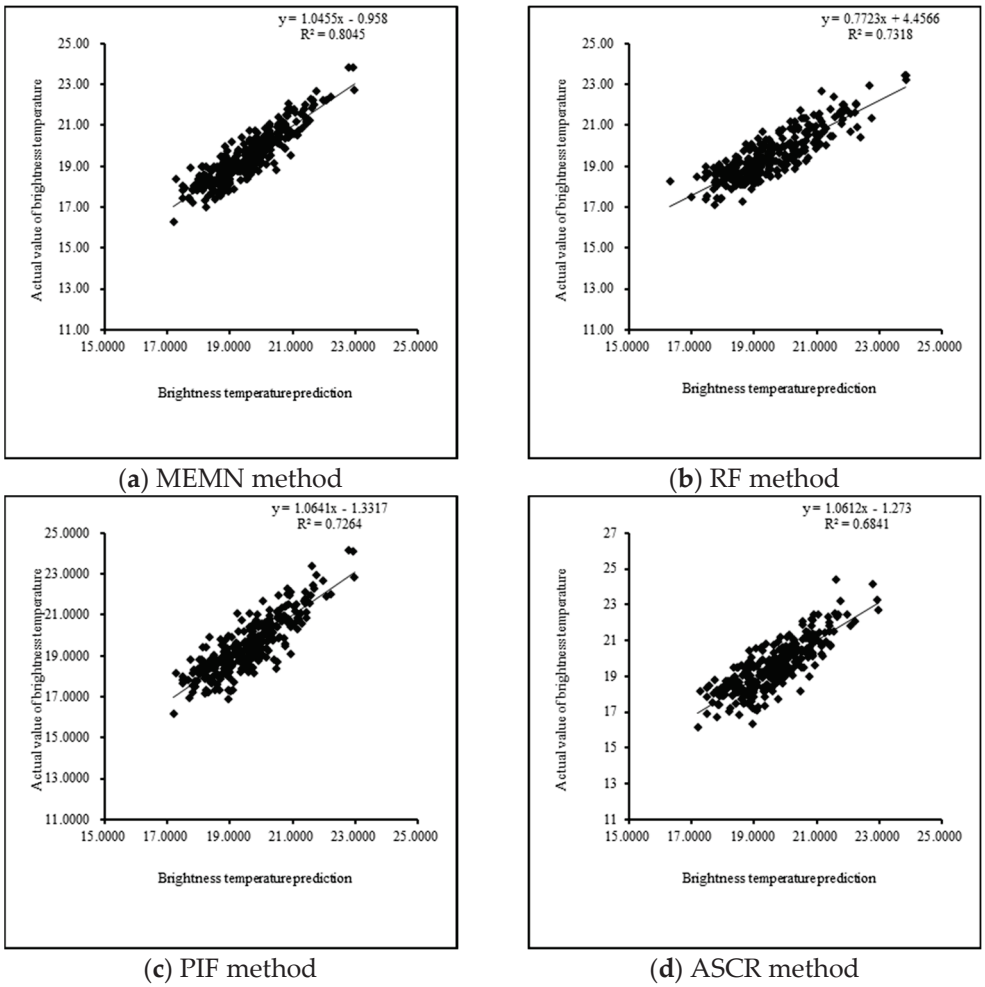

Figure 6. Comparison of the accuracy of the mixed-effects model normalization method with the random forest normalization method.

3.5. The Results of Fire Detection Verification

In order to verify the improvement of the effect of the MEMN method on the fire monitoring of the original image, we selected the FY-4A raw data, the Himawari-8 raw data, and the data processed by the MEMN method to identify the fire in Hunan Province at a certain time using the corresponding fire discrimination algorithm, and compared it with the fire situation published in China at that time to verify the accuracy. The results are analyzed in Figure 7. Figure 7a shows the fire point determined by the forest and grassland fire information sharing platform in China. Figure 7b shows the fire point of FY-4A raw data determined by the decision tree fire point recognition algorithm [34] based on FY-4A B8 and FY-4A B12. Figure 7c shows the fire point of Himawari-8 raw data determined by the LSA SAF Meteosat fire point recognition algorithm [35] based on Himawari-8 B7 and Himawari-8 B14. Figure 7d shows the fire point of FY-4A and Himawari-8, which is normalized by the MEMN method and then determined by the fire point recognition algorithm.

Table 7 show that, compared with the number of fires in Hunan Province on 10 December 2019 counted by the National Forest Grassland Fire Prevention and Extinguishing Information Sharing Platform, the fire detection rate of forest fires in FY-4 A original remote sensing image is 54.5%, and the fire detection rate of forest fires in Himawari-8 original remote sensing image is 72.7%. The fire detection rate of forest fires in remote sensing images normalized by the MEMN method is 90.9%. The MEMN normalization method has greatly improved the accuracy of forest fire monitoring.

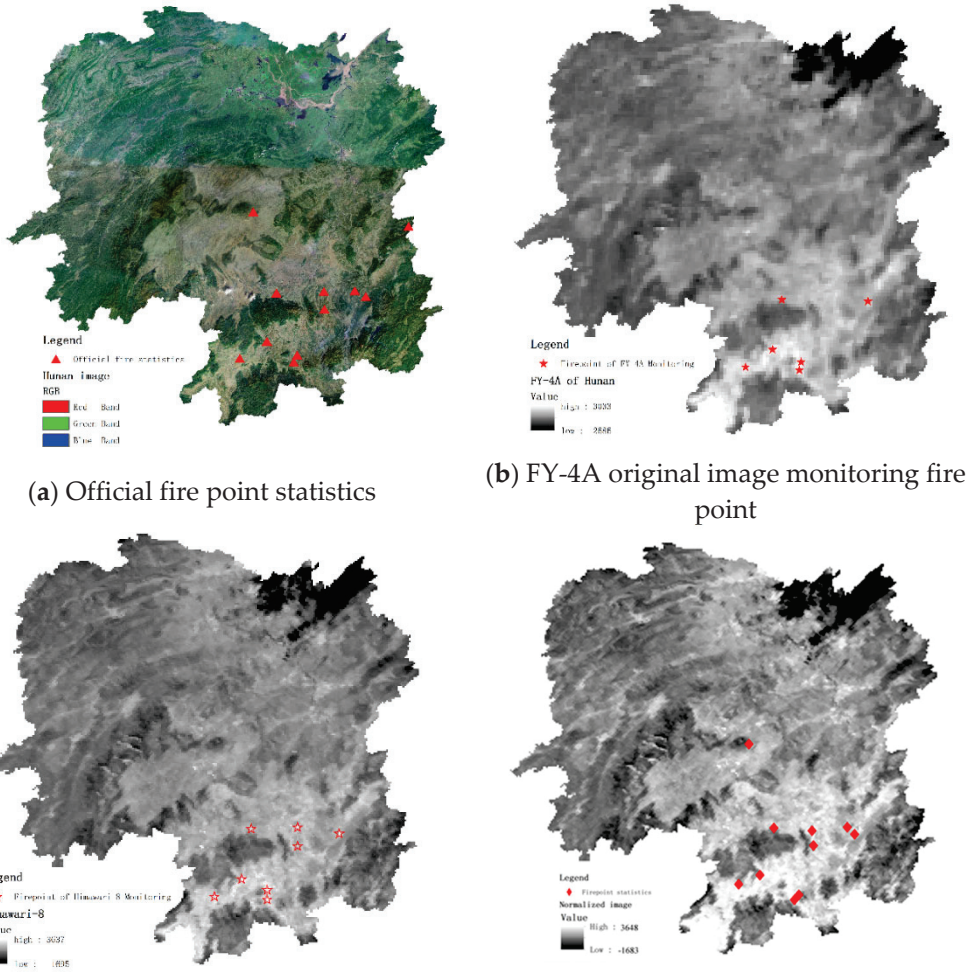

(**a**) Official fire point statistics

(**b**) FY-4A original image monitoring fire point

(**c**) Himawari-8 original image monitoring fire point

(**d**) MEMN normalized image monitoring fire point

Figure 7. Comparison of the fire point monitoring results of different images.

Table 7. Comparative analysis of the fire detection rate.

	Actual Number of Fire Points	Number Detected	Fire Detection Rate
FY-4A original image	11	6	54.5%
Himawari-8 original image	11	8	72.7%
MEMN normalized image	11	10	90.9%

4. Discussions

Aiming to address the problems that the single normalization scale leads to insufficient accuracy of multi-source sensor forest fire monitoring and the low temporal resolution of polar orbit satellite sensor leads to a lack of timeliness in forest fire monitoring, this article extracts and analyzes the influencing factors of brightness temperature in Hunan Province in China, introduces the regression prediction method of the mixed-effects model, constructs the normalized brightness temperature inversion model based on Himawari-8 and FY-4A, and verifies the model. The main conclusions are as follows.

(1) The MEMN model based on Himawari-8 solves the problems of the single factor and weak adaptability of model parameters in traditional methods such as the RF method, PIF method, and ASCR method. The grid data acquisition method is used to solve the problem of irregular sample selection and determine the modeling parameter values of each sample. Then, the basic model was fitted by multiple stepwise regres-

sion: $TBB = -1747.44 \times EMS + 1745.50$. Finally, the random effects site type (ldlx) and solar azimuth angle (soa) are added to the foundation after classification, clustering, and combination. Then, the MEMN model based on Himawari-8 is established: $TBB_{ij} = \mathrm{a} \times EMS_{ij} + \left(\mathrm{b} + b_i + b_j\right) + \varepsilon_{ij}$. The results of the accuracy evaluation and applicability test show that the MEMN model based on Himawari-8 has higher accuracy, and the determination coefficient is 0.8418 after introducing the random effect group of site type (ldlx) and solar azimuth angle (soa).

(2) Taking the normalized model of Himawari-8 as a reference and using the data collected by FY-4A to evaluate the accuracy of the model, the result showed that R^2 reached 0.7542. Comparing the results calculated by the random forest normalization method of the literature [6] to the data of the same period, the indicators of the MEMN method are better than those of the RF method. This result means that the MEMN method based on Himawari-8 is more applicable to the FY-4A sensor, and the normalized effect is better.

(3) The MEMN method has the following advantages. First, it considers more parameters, more standardized sample selection, and relatively high accuracy. Second, it can meet the requirements of observation angle normalization and radiation normalization at the same time. Finally, the model has good ability to divide the terrain and radiation errors equally, as well as to reduce the infrared radiation difference between different satellite sensors.

The key technology of this study is to combine the mixed-effects model with the normalization method. After analysis, the radiation normalization parameter is regarded as the fixed effect of the mixed-effects model, and the observation angle normalization parameter is regarded as the random effect, so as to realize the image normalization research that meets the two scales at the same time. The results have certain theoretical significance for the improvement of the normalization method, and have practical value for improving the accuracy and timeliness of forest fire monitoring.

5. Conclusions

In this paper, two geostationary satellite normalization models with different spatial resolution and time resolution are constructed, and the effect is ideal. This model is suitable for the normalization between single-phase cross-sensors. The construction of the normalized model of a multi-temporal cross-sensor and multi-temporal single sensor is still to be studied and analyzed. It is possible to combine the multi-temporal cross-sensor and multi-temporal single sensor. The construction of the mixed-effects model of the sensor is the main research direction in the next step.

Author Contributions: Z.Y. conceived and designed the study. L.F. wrote the first draft, performed the data analysis, and collected all the study data. H.X. and G.Z. provided critical insights in editing the manuscript. All authors have read and agreed to the published version of the manuscript.

Funding: This work was supported in part by the Science and Technology Innovation Platform and Talent Plan Project of Hunan Province under Grant 2017TP1022, in part by the Emergency Management Science and Technology Project of Hunan Province under Grant 2020YJ007, in part by the Natural Science Foundation of Hunan Province under Grant 2020JJ4938, and in part by the Scientific Research Project of Hunan Provincial Education Department under Grant 20A506.

Institutional Review Board Statement: Not applicable.

Informed Consent Statement: Not applicable.

Data Availability Statement: The data presented in this study are available on request from the corresponding author.

Conflicts of Interest: The authors declare no conflict of interest.

References

1. Wang, S.; Li, H.; Niu, S. Empirical research on climate warming risks for forest fires: A case study of grade I forest fire danger zone, Sichuan Province, China. *Sustainability* **2021**, *13*, 7773. [CrossRef]
2. Wotton, B.M.; Nock, C.A.; Flannigan, M.D. Forest fire occurrence and climate change in Canada. *Int. J. Wildland Fire* **2010**, *19*, 253–271. [CrossRef]
3. Singhal, G.; Bansod, B.; Mathew, L. Unmanned Aerial Vehicle Classification, Applications and Challenges: A review. *ICAFOF*. 2018. Available online: https://www.preprints.org/manuscript/201811.0601/v1 (accessed on 1 December 2021).
4. Yuan, C.; Zhang, Y.; Liu, Z. A survey on technologies for automatic forest fire monitoring, detection, and fighting using unmanned aerial vehicles and remote sensing techniques. *Can. J. For. Res.* **2015**, *45*, 783–792. [CrossRef]
5. Yang, X.; Chen, R.; Zhang, F.; Zhang, L.; Fan, X.; Ye, Q.; Fu, L. Pixel-level automatic annotation for forest fire image. *Eng. Appl. Artif. Intell.* **2021**, *104*, 104353. [CrossRef]
6. Dhall, A.; Dhasade, A.; Nalwade, A.; Raj, M.V.K.; Kulkarni, V. A survey on systematic approaches in managing forest fires. *Appl. Geogr.* **2020**, *121*, 102266. [CrossRef]
7. Yong, H.; Liu, L.; Liu, L.; Jiao, Q. Comparison of absolute and relative radiometric normalization use Landsat time series images. In *MIPPR 2011: Remote Sensing Image Processing, Geographic Information Systems, and Other Applications*; SPIE: Bellingham, WA, USA, 2011; Volume 8006, p. 800616. [CrossRef]
8. Yuan, D.; Elvidge, C.D. Comparison of relative radiometric normalization techniques. *ISPRS J. Photogramm. Remote Sens.* **1996**, *51*, 117–126. [CrossRef]
9. Tuia, D.; Marcos, D.; Camps-Valls, G. Multi-temporal and multi-source remote sensing image classification by nonlinear relative normalization. *ISPRS J. Photogramm. Remote Sens.* **2016**, *120*, 1–12. [CrossRef]
10. Hutengs, C.; Vohland, M. Downscaling land surface temperatures at regional scales with random forest regression. *Remote Sens. Environ.* **2016**, *178*, 127–141. [CrossRef]
11. Zhao, W.; Wu, H.; Yin, G.; Duan, S.B. Normalization of the temporal effect on the MODIS land surface temperature product using random forest regression. *ISPRS J. Photogramm. Remote Sens.* **2019**, *152*, 109–118. [CrossRef]
12. De Carvalho, J.O.A.; Guimarães, R.F.; Silva, N.C.; Gillespie, A.R.; Gomes, R.A.T.; Silva, C.R.; De Carvalho, A.P.F. Radiometric normalization of temporal images combining automatic detection of pseudo-invariant features from the distance and similarity spectral measures, density scatterplot analysis, and robust regression. *Remote Sens.* **2013**, *5*, 2763–2794. [CrossRef]
13. Elvidge, C.; Yuan, D.; Weerackoon, R.D.; Lunetta, R. Relative radiometric normalization of landsat multispectral scanner (MSS) data using an automatic scattergram-controlled regression. *ISPRS J. Photogramm. Remote Sens.* **1995**, *61*, 1255–1260.
14. Kaufman, Y.J.; Justice, C.O.; Flynn, L.P.; Kendall, J.D.; Prins, E.M.; Giglio, L.; Ward, D.E.; Menzel, W.P.; Setzer, A.W. Potential global fire monitoring from EOS-MODIS. *J. Geophys. Res.* **1998**, *103*, 32215–32238. [CrossRef]
15. Giglio, L.; Schroeder, W.; Justice, C.O. The collection 6 MODIS active fire detection algorithm and fire products. *Remote Sens. Environ.* **2016**, *178*, 31–41. [CrossRef]
16. Dozier, J. A method for satellite identification of surface temperature fields of subpixel resolution. *Remote Sens. Environ.* **1981**, *11*, 221–229. [CrossRef]
17. Matson, M.; Dozier, J. Identification of sub-resolution high temperature sources using a thermal IR sensor. *Photogram. Eng. Remote Sens.* **1998**, *47*, 1311–1318.
18. Yi, Q.; Huang, J.; McVicar, T.R.; West, S.; Khan, M.; Steven, A.D.L. Estimating surface solar irradiance from geostationary Himawari-8 over Australia: A physics-based method with calibration. *Sol. Energy* **2021**, *220*, 119–129. [CrossRef]
19. Okuyama, A.; Takahashi, M.; Date, K.; Hosaka, K.; Murata, H.; Tabata, T.; Yoshino, R. Validation of Himawari-8/AHI radiometric calibration based on two years of in-orbit data. *J. Meteorol. Soc. Jpn.* **2018**, *96*, 91–109. [CrossRef]
20. Ward, J.G.; Merceret, F.J. An automated cloud-edge detection algorithm using cloud physics and radar data. *J. Atmos. Ocean. Technol.* **2004**, *21*, 762–765. [CrossRef]
21. Liu, C.; Yang, S.; Di, D.; Yang, Y.; Zhou, C.; Hu, X.; Sohn, B.J. A Machine Learning-Based Cloud Detection Algorithm for the Himawari-8 Spectral Image. *Adv. Atmos. Sci.* **2021**, 1–14. Available online: https://link.springer.com/article/10.1007/s00376-021-0366-x (accessed on 1 December 2021). [CrossRef]
22. Zhang, R.; Qu, J.J.; Liu, Y.; Hao, X.; Huang, C.; Zhan, X. Detection of burned areas from mega-fires using daily and historical MODIS surface reflectance. *Int. J. Remote Sens.* **2015**, *36*, 1167–1187. [CrossRef]
23. Mitraka, Z.; Chrysoulakis, N.; Kamarianakis, Y.; Partsinevelos, P.; Tsouchlaraki, A. Improving the estimation of urban surface emissivity based on sub-pixel classification of high resolution satellite imagery. *Remote Sens. Environ.* **2012**, *117*, 125–134. [CrossRef]
24. Ma, X.L.; Wan, Z.; Moeller, C.C.; Menzel, W.P.; Gumley, L.E. Simultaneous retrieval of atmospheric profiles, land-surface temperature, and surface emissivity from Moderate-Resolution Imaging Spectroradiometer thermal infrared data: Extension of a two-step physical algorithm. *Appl. Opt.* **2002**, *41*, 909–924. [CrossRef]
25. Zhou, S.; Cheng, J. An improved temperature and emissivity separation algorithm for the advanced Himawari imager. *IEEE Trans. Geosci. Remote Sens.* **2020**, *58*, 7105–7124. [CrossRef]
26. Friedl, M.A.; Sulla-Menashe, D.; Tan, B.; Schneider, A.; Ramankutty, N.; Sibley, A.; Huang, X. MODIS collection 5 global land cover: Algorithm refinements and characterization of new datasets. *Remote Sens. Environ.* **2010**, *114*, 168–182. [CrossRef]
27. Foody, G.M. Status of land cover classification accuracy assessment. *Remote Sens. Environ.* **2002**, *80*, 185–201. [CrossRef]

28. Liu, Q.; Kampffmeyer, M.; Jenssen, R.; Salberg, A.-B. Dense dilated convolutions' merging network for land cover classification. *IEEE Trans. Geosci. Remote Sens.* **2020**, *58*, 6309–6320. [CrossRef]
29. Bandyopadhyay, G.; Chattopadhyay, S. Single hidden layer artificial neural network models versus multiple linear regression model in forecasting the time series of total ozone. *Int. J. Environ. Sci. Technol.* **2007**, *4*, 141–149. [CrossRef]
30. Šoškić, M.; Plavšić, D.; Trinajstić, N. Link between orthogonal and standard multiple linear regression models. *J. Chem. Inf. Comput. Sci.* **1996**, *36*, 829–832. [CrossRef]
31. Lindstrom, M.J.; Bates, D. Nonlinear mixed effects models for repeated measures data. *Biometrics* **1990**, *46*, 673–687. [CrossRef]
32. Pinheiro, J.C.; Bates, D.M. *Mixed-Effects Models in S and S-PLUS*; Springer: New York, NY, USA, 2002; ISBN 978-1-4419-0317-4.
33. Scaranello, M.A.D.S.; Alves, L.; Vieira, S.A.; De Camargo, P.B.; Joly, C.A.; Martinelli, L. Height-diameter relationships of tropical Atlantic moist forest trees in southeastern Brazil. *Sci. Agric.* **2012**, *69*, 26–37. [CrossRef]
34. Wang, L.; Guo, N.; Wang, W.; Zuo, H. Optimization of the local split-window algorithm for FY-4A land surface temperature retrieval. *Remote Sens.* **2019**, *11*, 2016. [CrossRef]
35. Wooster, M.J.; Roberts, G.; Freeborn, P.H.; Xu, W.; Govaerts, Y.; Beeby, R.; He, J.; Lattanzio, A.; Fisher, D.; Mullen, R. LSA SAF Meteosat FRP products—Part 1: Algorithms, product contents, and analysis. *Atmos. Chem. Phys.* **2015**, *15*, 13217–13239. [CrossRef]

remote sensing

MDPI

Technical Note

Tropical Cyclone Impact and Forest Resilience in the Southwestern Pacific

Baptiste Delaporte [1,2], Thomas Ibanez [3], Marc Despinoy [2,*], Morgan Mangeas [1] and Christophe Menkes [1]

[1] ENTROPIE, IRD, University of New Caledonia, University of La Reunion, CNRS, Ifremer, Labex Corail, 98800 Noumea, New Caledonia, France; baptiste.delaporte@protonmail.com (B.D.); morgan.mangeas@ird.fr (M.M.); christophe.menkes@ird.fr (C.M.)
[2] ESPACE-DEV (UMR 228), University of New Caledonia, University of Montpellier, IRD, University of Antilles, University of French Guyana, University of La Réunion, 98800 Noumea, New Caledonia, France
[3] AMAP, University of Montpellier, CIRAD, CNRS, INRAE, IRD, 34398 Montpellier, France; thomas.ibanez@ird.fr
* Correspondence: marc.despinoy@ird.fr

Abstract: Tropical cyclones (TCs) can have profound effects on the dynamics of forest vegetation that need to be better understood. Here, we analysed changes in forest vegetation induced by TCs using the normalized difference vegetation index (NDVI). We used an accurate historical database of TC tracks and intensities, together with the Willoughby cyclone model to reconstruct the 2D surface wind speed structure of TCs and analyse how TCs affect forest vegetation. We used segmented linear models to identify significant breakpoints in the relationship between the reconstructed maximum sustained wind speed (Wmax) and the observed changes in NDVI. We tested the hypothesis that the rate of change in damage caused by TCs to forest and recovery time would increase according to Wmax thresholds as defined in the widely used Saffir–Simpson hurricane wind scale (SSHWS). We showed that the most significant breakpoint was located at 50 m/s. This breakpoint corresponds to the transition between categories 2 and 3 TCs in the SSHWS. Below this breakpoint, damages caused to forest vegetation and the time needed to recover from these damages were negligable. We found a second breakpoint, with a sharp increase in damages for winds >75 m/s. This suggested that extremely intense tropical cyclones, which might be more frequent in the future, can cause extreme damages to forest vegetation. Nevertheless, we found high variation in the observed damages and time needed to recover for a given Wmax. Further studies are needed to integrate other factors that might affect the exposure and resistance to TCs as well as forests' capacity to recover from these disturbances.

Keywords: tropical cyclones; damages; forests; maximum sustained wind speed; normalized difference vegetation index; recovery time; Saffir–Simpson hurricane wind scale; South Pacific Islands

Citation: Delaporte, B.; Ibanez, T.; Despinoy, M.; Mangeas, M.; Menkes, C. Tropical Cyclone Impact and Forest Resilience in the Southwestern Pacific. *Remote Sens.* **2022**, *14*, 1245. https://doi.org/10.3390/rs14051245

Academic Editors: Stefano Morelli, Veronica Pazzi and Mirko Francioni

Received: 24 January 2022
Accepted: 25 February 2022
Published: 3 March 2022

1. Introduction

Tropical cyclones (TCs), also referred to as hurricanes in the North Atlantic and Northeast Pacific and typhoons in the Northwest Pacific, generate high speed winds and heavy rainfalls over large areas. Immediate impacts of TCs on forests can be particularly devastating with damages ranging from defoliation to extensive trunk snapping or tree uprooting. Most studies focused on the local- or landscape–scale damages caused by a single TC (e.g., [1–9]). Analyses of the impacts of multiple TCs on larger regional or global scales are needed to better understand how forests respond to these large–scale disturbances in the context of changing TCs intensity [10].

Increasingly available and accurate remote–sensed vegetation index time series and TC trajectories and characteristics databases now allow to analyse the impacts of TCs on forests and their recovery at large spatio–temporal scales (e.g., [11–13]). Maximum sustained wind

speed (Wmax) appears to be a key parameter to predict changes in vegetation indices. Yet, the direct relationship between local Wmax and the observed vegetation indices dynamics has, to our knowledge, not been explored. We suggest that this could be tackled using simple cyclone models that allow reconstructing the 2D wind speed structure (e.g., [14]) from TC characteristics available in TC databases.

The Saffir–Simpson Hurricane Wind Scale (SSHWS, [15]) is one of the most commonly used TC classifications. It uses Wmax to anticipate the potential damages caused by TCs. SSHWS ranges from category 1 TCs (Wmax between 33 and 42 m/s) which are predicted to mostly damage foliage, to category 5 TCs (Wmax $\geq$ 70 m/s) which are predicted to cause extensive snapping or uprooting of shrubs and trees (Table 1). On top of that classification, category 3 or higher TCs (Wmax $\geq$ 50 m/s) are considered as major TCs that can cause devastating to catastrophic damages (https://www.nhc.noaa.gov/aboutsshws.php, accessed on 22 February 2022). Yet, to our knowledge, the potential damages anticipated by the SSHWS have not been confronted concerning actual damages on a regional scale and on multiple storms over a long time period.

Table 1. Saffir–Simpson hurricane wind scale (SSHWS).

Category	Sustained Wind Speed (m/s)
ine 5 (major)	$\geq$70
4 (major)	58–70
3 (major)	50–58
2	43–49
1	33–42
Tropical Storm (TS)	18–32
Tropical Depression (TD)	<17

Here, we used high–resolution historical database of TC tracks and intensities (IBTrACS, [16]), together with the Willoughby cyclone model [17] to reconstruct the 2D surface wind speed structure of TCs to analyse how TCs affect forest vegetation. Our analyses cover six archipelagos of the south–west Pacific region over the 2000–2020 period. Our understanding of the impacts of TCs on forests in the islands of this region is relatively poor as most studies in this region have been conduced in Australia and on a global scale most studies have focused on the most intense cyclones in the North Atlantic Basin and to a lesser extent in the North West Pacific Basin [18]. We expect that damage caused by TCs to forests and the time needed to recover from these damages would increase with increasing Wmax. We test the hypothesis that the rate of change in damage caused by TCs to forests and the recovery time would increase according to Wmax thresholds as defined in the SSHWS. More particularly, we expect that winds generated by major, category 3 or higher, TCs would result in particularly intense damages.

2. Materials and Methods

2.1. Study Area

The study area encompasses 76 islands in six archipelagos (New Caledonia, Vanuatu, Fiji, Samoa, Tonga, Wallis and Futuna) located in the South West Pacific basin in longitude 152.3° E–162.5° W and latitude 10.0° S–30.0° S. Small islands, i.e., those less than 5 km long and/or wide were omitted. In this region, TCs mostly occur between November and May during austral summer [19]. On average, 6–8 tropical storms occur in the South West Pacific Basin between November and May with a peak of activity in February–March [20]. There are 2 to 5 tropical storms per decade on land for the considered islands with maximum cyclone densities west of Vanuatu and north of New Caledonia extending into the Coral Sea, between 10° S and 25° S fading off toward Samoa [21].

2.2. Forest Vegetation

Changes in forest vegetation induced by TCs were analysed using the Normalized Difference Vegetation Index (NDVI), one of the most widely used satellite–based vegetation indices [22]. Chlorophyll pigments contained in leaves are responsible for photosynthesis and absorb red light (RED), whereas healthy leaf tissues reflect strongly in the near infrared region (NIR) of the light spectrum. The NDVI is computed as the normalized ratio between RED and NIR reflected by the vegetation and captured by the sensor of the satellite (Equation (1)). The *NDVI* ranges from -1 to 1 and is positively correlated with the density and health of the vegetation (i.e., the higher the *NDVI*, the denser or healthier the vegetation) with negative *NDVI* values corresponding to water areas.

$$NDVI = \frac{\rho(NIR) - \rho(Red)}{\rho(NIR) + \rho(Red)} \in [-1:1] \quad (1)$$

We used the NDVI from the MOD13Q1 products supplied by the MODIS (Moderate Resolution Imaging Spectroradiometer) sensor that was launched by NASA onboard the Terra satellite in 1999. The MOD13Q1 products have provided NDVI values every 16 days since February 2000 at a 250 m pixel spatial resolution. We extracted NDVI of forested areas using the "tree cover, broadleaved, evergreen, closed to open (>15%)" vegetation class from the global land cover map produced by the European Spatial Agency (https://www.esa.int/Applications/Observing_the_Earth/Space_for_our_climate/ESA_global_land_cover_map_available_online, accessed on 22 February 2022) and resampled at 250 m to match the NDVI resolution. Prior to the analyses, all pixels covered by clouds or water were removed using the pixel reliability files provided by MOD13Q1.

2.3. Tropical Cyclones

We used the Saffir–Simpson hurricane wind scale (SSHWS, Table 1, [15]) to classify TC intensities. TC trajectories and characteristics were extracted from the IBTrACS database ([16], https://www.ncdc.noaa.gov/ibtracs/, accessed on 22 February 2022). This database provides the positions of each TC center and their maximum 10 min–sustained wind speed (Wmax) every 6 h. We only considered cyclones reaching category 1 or higher (Wmax $\geq$ 33 m/s). A total of 74 TCs with Wmax $\geq$ 33 m/s crossed the studied area between 2000 and 2020 (Figure 1).

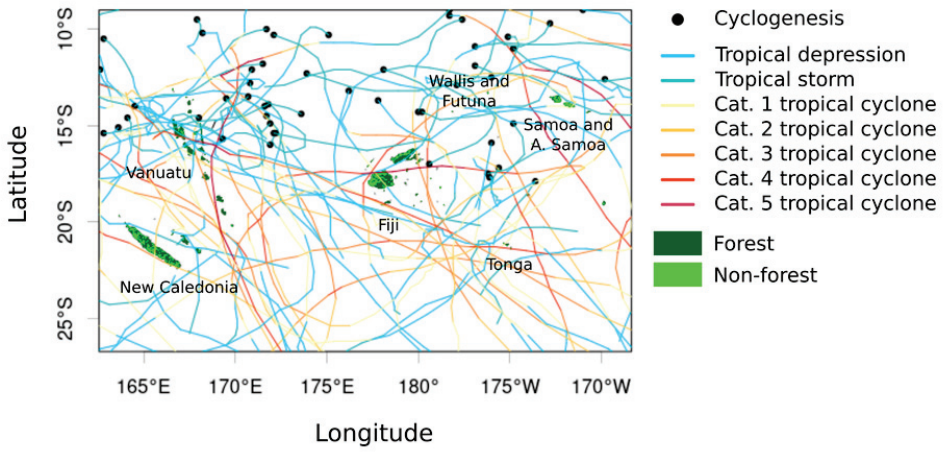

Figure 1. Trajectories of all tropical cyclones reaching category 1 or higher (i.e., Wmax $\geq$ 33 m/s) at some point on their tracks between 2000 and 2020 in the South West Pacific Basin.

Following Vincent et al. [23], we then used the Willoughby cyclone model [17] to reconstruct the 2D idealized surface wind speed structure generated by each TC over the 20 year period studied (2000–2020). The Willoughby model (Equation (2)) allows to

reconstruct at a given time (t) the 2D surface wind speed structure of a TC based on both the latitude of its center (Φ) and the maximum sustained wind speed (*Wmax*) as provided by the IBTrACS database.

$$\begin{cases} (a) & RMW & = & 46.4e^{-0.0155Wmax+0.0169|\phi|} \\ (b) & nn & = & 2.1340+0.0077Wmax-0.4522ln(RMW)-0.0038|\phi| \\ (c) & XX1 & = & 287.6-1.942Wmax+7.799ln(RMW)-1.819|\phi| \\ (d) & XX2 & = & 25 \\ (e) & AA & = & 0.5913+0.0029Wmax-0.1361ln(RMW)-0.0042|\phi| \\ (f) & Wr & = & Wmax|(\frac{r}{RMW})^{nn}| \quad if \quad r \leq RMW \\ (g) & Wr & = & Wmax((1-AA)e^{-|\frac{r-RMW}{XX1}|}+AAe^{-|\frac{r-RMW}{XX2}|}) \\ & & & if \quad r \geq RMW \end{cases} \quad (2)$$

In Equation (2) *RMW* is the radius of maximum wind (i.e., the distance *r* from the center where wind speed reaches *Wmax*), *Wr* is the radial wind speed generated at distance *r* from the center of the TC.

The Willoughby model generates an exponential increase in wind speed from the center of the TC (the "eye") to the RMW where winds reach their maximum speed (Wmax, Figure 2). Beyond RMW, wind speed decreases exponentially as a function of Wmax and Φ. According to this model, the most powerful TC over the studied area and study period (i.e., the category 5 TC Winston in 2016) generated winds ≥ 17 m/s up to 250 km off the TC center. Because TCs can move fast, we performed a linear interpolation of the original six–hour Φ and Wmax provided by the IBTrACS database to reconstruct the 2D surface wind speed structure of each TC every 15 min at a 250 m spatial resolution. Finally, we computed for each TC the maximum speed of winds that affected each pixel.

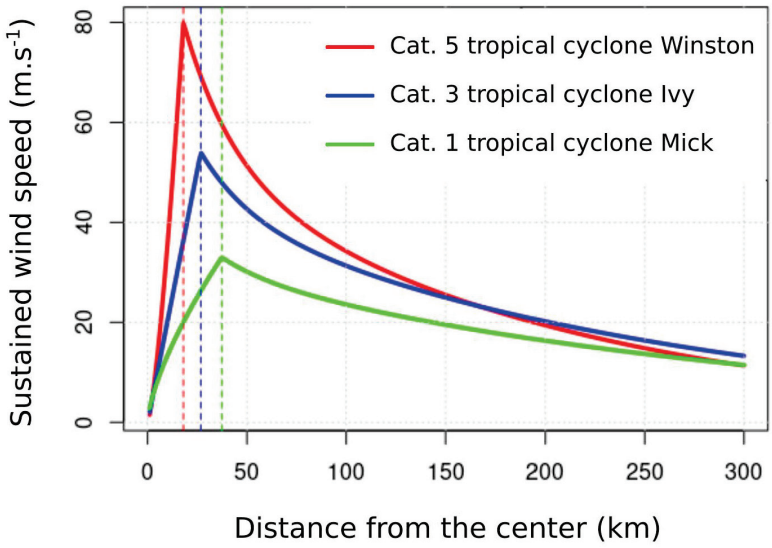

Figure 2. Example of 2D surface wind speed structure reconstructed using the Willoughby model (Equation (2) (f and g)) for category 1 tropical cyclone Mick (3–5 December 2009), category 3 tropical cyclone Ivy (21–28 February 2004), and category 5 tropical cyclone Winston (7 February–3 March 2016). Vertical dotted lines represent RMW, the distance r from the center of the tropical cyclone where winds reach their maximum speed (Wmax.)

2.4. Analysis

We analysed the damages caused by TCs to forest vegetation and the recovery time from these damages. For each forest pixel exposed to wind generated by a category 1 or greater TC, we computed the damage caused by the cyclone passages as the relative changes in NDVI:

$$\Delta NDVI_{ti} = [(NDVI_{ti} - NDVI_{t0})/NDVI_{t0}] \times 100 \quad (3)$$

where $NDVI_{t0}$ is the NDVI value measured just before the passage of the TC at t_0, $NDVI_{ti}$ is the NDVI value measured at t_i just after the passage of the TC with i starting at the first NDVI acquisition date after the passage of the TC and then every 16 days over the following year.

Recovery times from these damages were estimated as TR, the time t_i needed to recover at least 95% of the pre–cyclone NDVI value ($NDVI_{t0}$). Many $\Delta NDVI_{ti}$ values were missing because of the lack of acquisition or because of the presence of clouds. We filled in missing values using the linear interpolation function na.approx from the zoo R package.

We then used two types of model to predict damages ($\Delta NDVI_{t1}$) and recovery time (TR) as a function of the maximum sustained wind speed (W_{max}): (i) Segmented linear models with fixed W_{max} breakpoints corresponding to the boundaries of the categories of the Saffir–Simpson hurricane wind scale (hereafter, SSHWS model), and (ii) segmented linear models with free number and location of W_{max} breakpoints (hereafter, optimized model). For the optimized models, we tested different numbers of breakpoints ranging from 1 to 5 breakpoints and then kept the models that minimized the Bayesian information criterion (BIC), i.e., the models that exhibited the best compromise between the number of parameters and likelihood. Segmented linear models were adjusted using the segmented function of the segmented R package [24] and BIC values were computed using the BIC function available in the R base package. We tested the significance of the presence of breakpoints (i.e., the presence of a non-constant regression parameter in the linear predictor) using the davies.test function [24].

Reconstructed W_{max} and observed $\Delta NDVI_{t1}$ are available online (http://preditropic.ird.nc, accessed on 22 February 2022). Moreover, it let the user forecast the $\Delta NDVI_{t1}$ following a simulated TC based on the optimized model.

3. Results

According to the 2D reconstruction of the wind speed structure of TCs, almost all forest pixels (95.6%) located in the studied area were exposed at least once to maximum sustained wind speed $\geq$ 33 m/s over the last 20 years (Table 2). A third of these forest pixels (33.1%) were exposed at least three times to such wind speeds (Table 2). Most intense TCs are relatively infrequent. Only 29 TCs reached categories 4 or 5 and less than a quarter (21.3%) of the forest pixels were exposed at least once to maximum sustained wind speed $\geq$ 58 m/s (category 4). This proportion fell down to 5% when we only considered category 5 cyclone winds (i.e., $\geq$70 m/s, Table 2).

For both damages and recovery time, optimized segmented linear models (for which the number and position of breakpoints were optimized) performed much better than SSHWS segmented linear models (for which the number and position of breakpoints were fixed following the SSHWS), with ΔBIC = -28.35 and -44.33, respectively (Tables 3 and 4). In both cases the optimized models identified two significant breakpoints. The first breakpoints, located at 50.00 m/s for damages as swhown in Figure 3a and 50.48 m/s for recovery time as shown in Figure 3c, corresponded to the transition between category 2 and 3 TCs. Below 50.00 m/s observed damages were negligible ($\lesssim$1% decrease in NDVI on average) and the corresponding recovery time was less than two weeks.

Table 2. Coverage of forest pixels exposed to different intensity and frequency of TCs between 2000 and 2020. For instance, in the first row we can read that most forest pixels (95.6%) were exposed to at least one category 1 or higher TC and in the third row that a third of forest pixels (33.1%) were exposed to at least three category 1 or higher TCs.

Maximum Sustained Wind Speed	Frequency	Coverage (%)
≥33 m/s (Cat. 1 or higher)	At least once	95.6
	At least twice	71.0
	At least 3 times	33.1
	At least 4 times	9.9
	At least 5 times	1.0
	At least 6 times	0.0
≥43 m/s (Cat. 2 or higher)	At least once	73.4
	At least twice	22.3
	At least 3 times	2.0
	At least 4 times	0.0
≥50 m/s (Cat. 3 or higher)	At least once	43.1
	At least twice	3.9
	At least 3 times	0.0
≥58 m/s (Cat. 4 or higher)	At least once	21.3
	At least twice	0.3
	At least 3 times	0.0
≥70 m/s (Cat. 5)	At least once	5.4
	At least twice	0.0

Table 3. Summary and performances of the segmented linear models explaining the variation in the damages (ΔNDVIt1) as a function of Wmax. In the SSHWS model the breakpoints were fixed using the Saffir–Simpson hurricane wind scale boundaries. In the optimized model the location and number of breakpoints were optimized.

Model	BIC	Beakpoints	Davies Tests		Slope
			Best at	*p*-Value	
SSHWS	252.07	43.00	34.00	<0.001	0.02
		50.00	49.78	<0.001	−0.24
		58.00	69.00	0.08	−0.90
		70.00	75.00	<0.001	−1.13
					−1.78
Optimized	223.72	50.00	51.78	<0.001	−0.08
		75.70	74.22	<0.001	−1.05
					−7.45

Table 4. Summary and performances of the segmented linear models explaining the variation recovery time (TR) as a function of Wmax. In the SSHWS model the breakpoints were fixed using the Saffir–Simpson hurricane wind scale boundaries. In the optimized model the location and number of breakpoints were optimized.

Model	BIC	Beakpoints	Davies Tests		Slope
			Best at	*p*-Value	
SSHWS	376.03	43.00	34.00	0.008	0.49
		50.00	51.22	<0.001	−0.10
		58.00	69.00	<0.001	4.14
		70.00	77.00	<0.001	3.64
					6.35
Optimized	331.73	50.48	52.22	<0.001	0.42
		76.64	77.00	<0.001	3.80
					51.56

For Wmax greater than 50 m/s, observed damages to forest vegetation started to increase with an average at ∼1% of NDVI loss for each 1 m/s increase in Wmax (Figure 3a). This increase in damages resulted in a sharper increase in recovery time with an average rate of almost four days per 1 m/s increase in Wmax (Figure 3c). Another breakpoint was identified within the category 5 TC category at 75 m/s (75.70 m/s for damages and 76.64 m/s for recovery time). Above this breakpoint, damages and recovery times sharply increased. On average >40% decrease in NDVI and >150 days of recovery time were observed for the strongest winds (78 m/s).

We observed high deviations around these trends. Standard deviation for the observed damages was about 20% and tended to slightly decrease with increasing wind speed (Figure 3b). Standard deviation in recovery time was about 30–35 days below 50.00 m/s, but then sharply increased reaching on average ∼90 days for category 5 TCs (Figure 3d). Furthermore, over 20% of the studied pixels did not recover after one year.

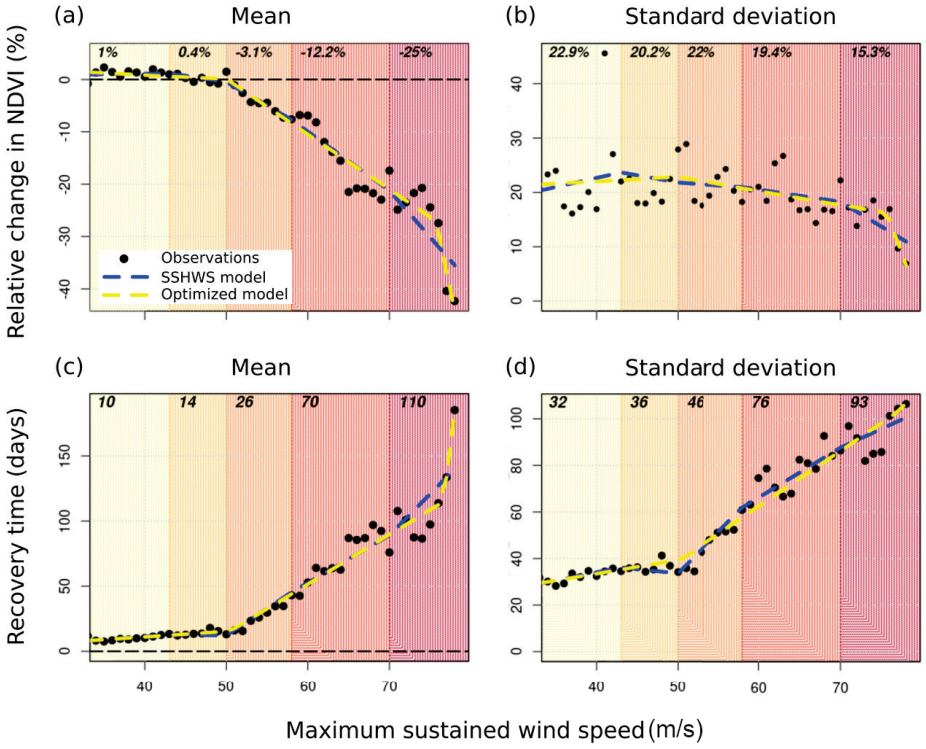

Figure 3. Mean and standard deviation of relative change in NDVI ($\Delta NDVI_{t1}$) (**a**,**b**) and recovery time (TR) (**c**,**d**) as a function of maximum sustained wind speed (W_{max}). Values in bold represent the average for each TC category (SSHWS). Blue lines correspond to piecewise linear regressions with breakpoints based on the SSHWS TC classification and yellow lines correspond to piecewise linear regressions with optimized breakpoints minimizing the Bayesian Information Criterion.

One important outcome of our modelling is the production of spatial maps of damage and recovery time. An example is illustrated in Figure 4 which shows the observed and best-modelled (optimized model) damages and recovery caused by the category 5 TC Winston (2016) on Viti Levu (Fiji).

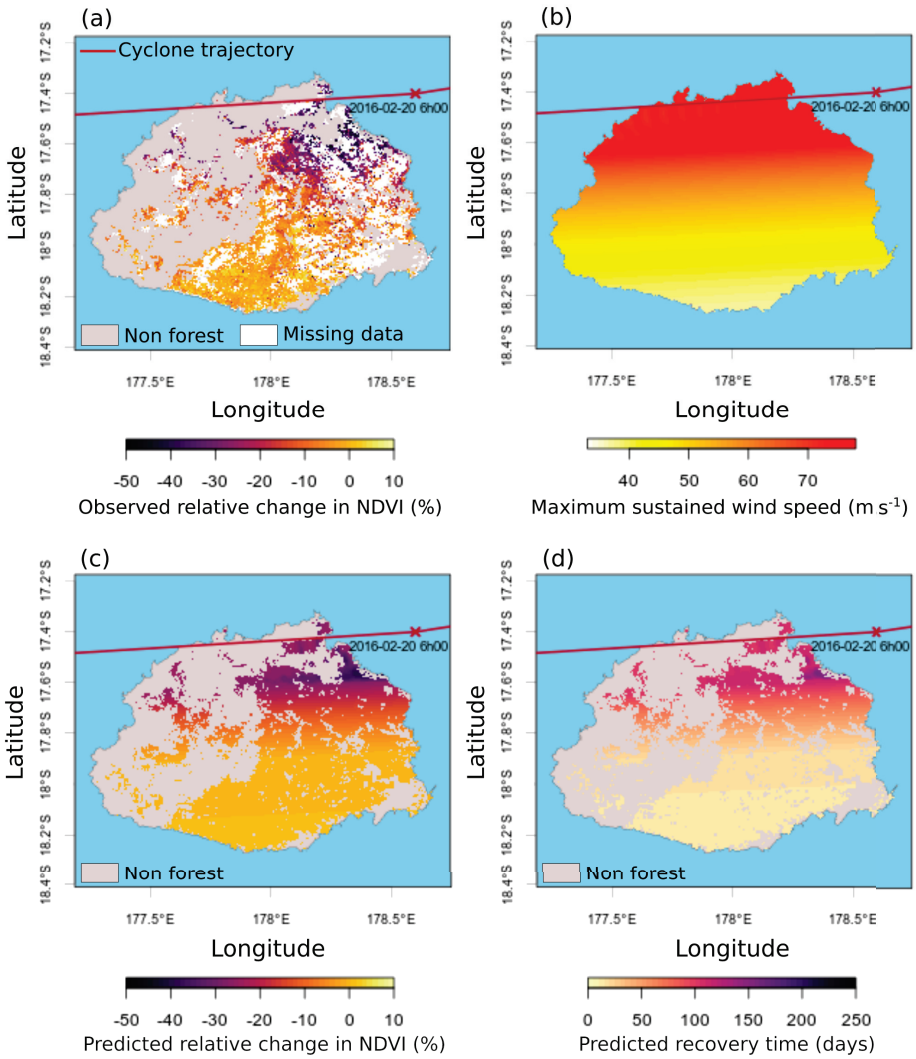

Figure 4. Example of relative change in NDVI observed after tropical cyclone Winston on Viti Levu in Fiji (**a**), reconstructed maximum sustained wind speed (**b**), predicted changes in NDVI (**c**) using the optimized models, and predicted recovery time (**d**). Winston severely impacted Viti Levu with wind gusts up to 78 m/s between 19 and 20 February 2016.

4. Discussion

Our results partly support the use of the Saffir–Simpson hurricane wind scale (SSHWS) to anticipate the damages caused by TCs to forest vegetation. Simpson [15] suggested that winds < 50 m/s mostly resulted in minor defoliation and we indeed found that such winds resulted in negligible damages to forest vegetation ($\lesssim$1% decrease in NDVI). Our modelling showed that the most significant breakpoint was located at 50 m/s. This breakpoint corresponded to the transition between category 2 and 3 TCs identified by Simpson [15] above which trees start to experience major damages including extensive defoliation, branch breaking, tree uprooting, and bole snapping. This is in agreement with field observation in the south-west Pacific. For instance, forest plots located on Tutuila (American Samoa) and exposed to winds of 12–14 m/s generated by TC Heta (2003–2004) exhibited < 5% uprooting or bole snapping for trees larger than 10 cm [25]. Forest plots located on a neighboring island (Ta'u) exposed to reconstructed wind of 60–62 m/s from the TC Olaf (2005) exhibited from 20% to almost 100% uprooting or bole snapping for trees larger than 10 cm depending on the species [5]. Intermediate damages were observed on the

island of Vava'u (Tonga) with about 20% uprooting or bole snapping for trees larger than 10 cm in forest plots affected by reconstructed wind of 51 m/s from TC Waka (2001) [26].

Model optimization highlighted another significant breakpoint located around 75 m.s, i.e., within the highest category of the SSHWS (that begins at 70 m/s for category 5). When this breakpoint was reached, sharp increases in both the damages caused by TCs and the recovery time were observed. These high intensity winds (>75 m/s) resulted on average in a reduction in NDVI greater than 40%. While this breakpoint relies only on a few points, it feeds the debate about updating TC intensity scales to better fit increasing TC intensity (e.g., [27,28]). Indeed, such extremely intense TCs occurred during the last decade and may reflect the possible intensification of these disturbances under human–induced global warming (e.g., [10,29]). For instance, after typhoon Haiyan (2013), one of the most intense TCs ever recorded worldwide, severely impacted the Philippines, Lin et al. [30] suggested creating a new category 6 for TCs generating winds $\geq$ 80 m/s. However, based on the most recent analyses [10], it is not clear that increased TC intensities have indeed occurred during the past 40 years (1979–2017) in the Western Pacific. On the same line, while Winston (2016) generated sustained wind speed > 80 m/s in the South Pacific, i.e, one of the strongest winds on record in the South Pacific, it remains to be explored whether such intensity records may increase in the future under global warming.

Reconstructed maximum wind speed was a good predictor of observed mean damages caused by TCs and mean recovery time. However, we observed large variations around mean trends. These large variations may be partly explained by the topography of the studied mountainous islands. Indeed, wind exposure varies greatly with topographical position, which result in very patchy damages in topographically complex areas [3,8,31]. The TC regime could also play a role in the effects of these disturbances on forests. Forests that have been historically exposed to frequent intense TCs are likely to be acclimated or adapted to these disturbances and thus could be more resistant to TCs than forests that have been historically rarely exposed to these disturbances [13]. Different levels of resistance of different forest types also probably explain the large variation in observed damages for a given maximum sustained wind speed. For instance, for a given wind speed, damages are expected to be lower in dry forests than in wet forests because dry forests are shorter [32] and composed of species that have on average harder wood than in wet forests [33]. Indeed, shorter tree height and higher wood density can provide higher mechanical resistance to wind and are often associated with less important cyclone–induced damages [5,18,34]. Finally, large variation in the observed damages for a given maximum sustained wind speed could be explained by different TC translation speeds with slower TCs (longer residence time) which should be more destructive than faster ones [35].

Variation in recovery time substantially increased with maximum sustained damage, especially after category 3–5 TCs. Below category 3 cyclones, damages mostly consisted in defoliation and recovery in production of new leaves. However, category 3 and more cyclones caused greater damages such as branch breaking, uprooting, and bole snapping. Several processes allowed recovery from these damages, including growth of surviving trees, growth of new trees from seed or sapling banks, and growth of new trees from new colonization events. Resprouting of surviving trees, i.e., the production of new vegetative growth from above or below ground dormant buds, is often observed after disturbances by TCs [36–38]. Resprouting capacity probably varies depending on habitat type and species composition. For instance, dry forest species might be better resprouters than wet forest species [39]. The rapidity of the establishment of new trees should be affected by the amount of forest and its spatial configuration. For the same level of damages, we expect that recovery time would be shorter in more forested and less fragmented landscapes compared to less forested and more fragmented ones. However, we cannot know whether the recovery in NDVI was due to the growth of trees or other growth forms. Likewise, we cannot know whether the recovery in NDVI was due to the growth of native species or to the establishment of non–native, potentially invasive, species. Invasion by non–native plant

species following disturbance by TCs [40] which can slow down or block forest recovery is also more likely in more fragmented areas [41].

5. Conclusions

We found that damages caused to forest vegetation by TCs based on NDVI changes were negligible for winds <50 m/s, i.e., for category 1–2 TCs (SSHWS). This is consistent with recent conclusions reached by Peereman et al. [13] on global mangroves. Above this breakpoint, reduction in NDVI increased linearly with increasing wind speed which likely resulted from increasing major damages to vegetation, including branch breaking, tree uprooting, and bole snapping. A second breakpoint, with a sharp increase in damages for winds > 75 m/s suggested that extremely intense TCs can cause extreme damages to forest vegetation. While reconstructed maximum sustained wind speed was a good predictor of damages and recovery time, we observed large variations in the resistance and recovery of vegetation for a given wind speed. We hypothesize that these variations can be further explored by integrating other spatial factors such as topographical exposure, forest types, TC regime, and landscape structure as well as more detailed surface wind structures that are not represented in analytical models. Such enhanced wind structures may come from the recent advances on very intense wind retrievals from satellite imagery [42]. Whether the frequency of intense TCs will increase compared to weaker cyclones under climate change needs further investigations, especially in the South Pacific [10] and will require further advances in climate cyclone modelling in the future scenario [43]. Finally, we found that >20% of the studied forest pixels did not fully recover their pre–cyclone NDVI values after one year. Further studies are needed to assess whether or not these areas can recover to a forest state in a longer time period or whether they may shift toward non–forest states.

Author Contributions: Writing—original draft preparation, B.D.; writing—review and editing, T.I., C.M., M.D. and M.M.; supervision, C.M., M.M., M.D. and T.I.; project administration, M.D. and C.M.; funding acquisition, M.D.; Conceptualization, B.D., C.M., M.D. and M.M.; methodology, B.D., M.M., C.M., T.I. and M.D.; software, B.D.; validation, T.I. and C.M.; formal analysis, C.M., T.I. and M.M.; resources, T.I.; data curation, M.D. All authors have read and agreed to the published version of the manuscript.

Funding: That work was funded by the French Pacific Funds and T.I. was partly supported by Hermon Slade fundation (HSF 19105).

Conflicts of Interest: The authors declare no conflict of interest.

Abbreviations

The following abbreviations are used in this manuscript:

ESA	European Space Agency
IBTrACS	International Best Track Archive for Climate Stewardship
NASA	National Aeronautics and Space Administration
NDVI	Normalized Difference Vegetation Index
NIR	Near Infrared Region
MOD13Q1	MODIS vegetation index product (NDVI and EVI)
RMW	Radius of Maximum Wind
SSHWS	Saffir–Simpson Hurricane Wind Scale
TC	Tropical Cyclone

References

1. Lugo, A.E.; Applefield, M.; Douglas, J.P.; Macdonald, R.B. The impact of Hurricane David on the forests of Dominica. *Can. J. For. Res. Can. Rech. For.* **1983**, 13, 201–211. [CrossRef]
2. Basnet, K.; Likens, G.E.; Scatena, F.N.; Lugo, A.E. Hurricane Hugo: Damage to a Tropical Rain Forest in Puerto Rico. *J. Trop. Ecol.* **1992**, *8*, 47–55. [CrossRef]
3. Boose, E.R.; Foster, D.R.; Fluet, M. Hurricane Impacts to Tropical and Temperate Forest Landscapes. *Ecol. Monogr.* **1994**, 64, 369–400. [CrossRef]

4. Metcalfe, D.J.; Bradford, M.G.; Ford, A.J. Cyclone damage to tropical rain forests: Species- and community-level impacts. *Austral Ecol.* **2008**, *33*, 432–441. [CrossRef]
5. Webb, E.L.; van de Bult, M.; Fa'aumu, S.; Webb, R.C.; Tualaulelei, A.; Carrasco, L.R. Factors Affecting Tropical Tree Damage and Survival after Catastrophic Wind Disturbance. *Biotropica* **2014**, *46*, 32–41. [CrossRef]
6. Ni, Y.; Wang, T.; Cao, H.; Li, Y.; Bin, Y.; Zhang, R.; Wang, Y.; Lian, J.; Ye, W. An old-growth subtropical evergreen broadleaved forest suffered more damage from Typhoon Mangkhut than an adjacent secondary forest. *For. Ecol. Manag.* **2021**, *496*, 119433. [CrossRef]
7. Peereman, J.; Hogan, J.A.; Lin, T.-C. Assessing typhoon-induced canopy damage using vegetation indices in the Fushan Experimental Forest, Taiwan. *Remote Sens.* **2020**, *12*, 1654. [CrossRef]
8. Turton, S.M. Landscape-scale impacts of Cyclone Larry on the forests of northeast Australia, including comparisons with previous cyclones impacting the region between 1858 and 2006. *Austral Ecol.* **2008**, *33*, 409–416. [CrossRef]
9. Rutledge, B.T.; Cannon, J.B.; McIntyre, R.K.; Holl, A.M.; Jack, S.B. Tree, stand, and landscape factors contributing to hurricane damage in a coastal plain forest: Post-hurricane assessment in a longleaf pine landscape. *For. Ecol. Manag.* **2021**, *481*, 118724. [CrossRef]
10. Kossin, J.P.; Knapp, K.R.; Olander, T.L.; Velden, C.S. Global increase in major tropical cyclone exceedance probability over the past four decades. *Proc. Natl. Acad. Sci. USA* **2020**, *117*, 11975–11980. [CrossRef]
11. Gang, C.; Pan, S.; Tian, H.; Wang, Z.; Xu, R.; Bian, Z.; Pan, N.; Yao, Y.; Shi, H. Satellite observations of forest resilience to hurricanes along the northern Gulf of Mexico. *For. Ecol. Manag.* **2020**, *472*, 118243. [CrossRef]
12. De Beurs, K.M.; McThompson, N.S.; Owsley, B.C.; Henebrrefy, G.M. Hurricane damage detection on four major Caribbean islands. *Remote Sens. Environ.* **2019**, *229*, 1–13. [CrossRef]
13. Peereman, J.; Hogan, J.A.; Lin, T.-C. Disturbance frequency, intensity and forest structure modulate cyclone-induced changes in mangrove forest canopy cover. *Glob. Ecol. Biogeogr.* **2021**, *31*, 37–50. [CrossRef]
14. Boose, E.R.; Serrano, M.I.; Foster, D.R. Landscape and regional impacts of hurricanes in Puerto Rico. *Ecol. Monogr.* **2004**, *74*, 335–352. [CrossRef]
15. Simpson, R.H. The hurricane disaster potential scale. *Weatherwise* **1974**, *27*, 169–186.
16. Knapp, K.R.; Kruk, M.C.; Levinson, D.H.; Diamond, H.J.; Neumann, C.J. The International Best Track Archive for Climate Stewardship (IBTrACS). *Bull. Am. Meteorol. Soc.* **2010**, *91*, 363–376. [CrossRef]
17. Willoughby, H.E.; Darling, R.W.R.; Rahn, M.E. Parametricrepresentation of the primary hurricane vortex. Part II: A new family of sectionally continuous profiles. *Mon. Weather Rev.* **2006**, *134*, 1102–1120. [CrossRef]
18. Lin, T.-C.; Hogan, J.A.; Chang, C.-T. Tropical Cyclone Ecology: A Scale-Link Perspective. *Trends Ecol. Evol.* **2020**, *35*, P594–P604. [CrossRef]
19. Menkes, C.E.; Lengaigne, M.; Marchesiello, P.; Jourdain, N.C.; Vincent, E.M.; Lefèvre, J.; Chauvin, F.; Royer, J.-F. Comparison of tropical cyclogenesis indices on seasonal to interannual timescales. *Clim. Dyn.* **2012**, *38*, 301–321. [CrossRef]
20. Jourdain, N.C.; Marchesiello, P.; Menkes, C.E.; Lefevre, J.; Vincent, E.M.; Lengaigne, M.; Chauvin, F. Mesoscale Simulation of Tropical Cyclones in the South Pacific: Climatology and Interannual Variability. *J. Clim.* **2011**, 24, 3–25. [CrossRef]
21. Payri, C.E.; Allain, V.; Aucan, J.; David, C.; David, V.; Dutheil, C.; Loubersac, L.; Menkes, C.; Pelletier, B.; Pestana, G.; Samadi, S. Chapter 27—New Caledonia. In *World Seas: An Environmental Evaluation*, 2nd ed.; Sheppard, C., Ed.; Academic Press: New Caledonia, France, 2019; pp. 593–618. [CrossRef]
22. Huang, S.; Tang, L.; Hupy, J.P.; Wang, Y.; Shao, G. A commentary review on the use of normalized difference vegetation index (NDVI) in the era of popular remote sensing. *J. For. Res.* **2021**, *32*, 1–6. [CrossRef]
23. Vincent, E.M.; Lengaigne, M.; Menkes, C.E.; Jourdain, N.C.; Marchesiello, P.; Madec, G. Interannual variability of the South Pacific Convergence Zone and implications for tropical cyclone genesis. *Clim. Dyn.* **2012**, *36*, 1881–1896. [CrossRef]
24. Muggeo, V.M.R. segmented: An R Package to Fit Regression Models with Broken-Line Relationships. *R News* **2008**, *8*, 20–25. Available online: https://cran.r-project.org/doc/Rnews/ (accessed on 22 February 2022).
25. Webb, E.L.; Seamon, J.O.; Fa'aumu, S. Frequent, low-amplitude disturbances drive high tree turnover rates on a remote, cyclone-prone Polynesian island. *J. Biogeogr.* **2011**, *38*, 1240–1252. [CrossRef]
26. Franklin, J.; Drake, D.R.; McConkey, K.R.; Tonga, F.; Smith, L.B. The effects of Cyclone Waka on the structure of lowland tropical rain forest in Vava'u, Tonga. *J. Trop. Ecol.* **2004**, *20*, 409–420. [CrossRef]
27. Kantha, L.Classification of hurricanes: Lessons from Katrina, Ike, Irene, Isaac and Sandy. *Ocean Eng.* **2013**, *70*, 124–128. [CrossRef]
28. Bloemendaal, N.; de Moel, H.; Mol, J.M.; Bosma, P.R.M.; Polen, A.N.; Collins, J.M. Adequately reflecting the severity of tropical cyclones using the new Tropical Cyclone Severity Scale. *Environ. Res. Lett.* **2021**, 16, *16*, 014048. [CrossRef]
29. Walsh, K.J.E.; McBride, J.L.; Klotzbach, P.J.; Balach, ran, S.; Camargo, S.J.; Holl, G.; Knutson, T.R.; Kossin, J.P.; Lee, T.; Sobel, A.; Sugi, M. Tropical cyclones and climate change. *Wiley Interdiscip. Rev. Clim. Chang.* **2016**, *7*, 65–89. [CrossRef]
30. Lin, I.-I.; Pun, I.-F.; Lien, C.-C. "Category-6" supertyphoon Haiyan in global warming hiatus: Contribution from subsurface ocean warming. *Geophys. Res. Lett.* **2014**, *41*, 8547–8553. [CrossRef]
31. Bellingham, P.J.; Kapos, V.; Varty, N.; Healey, J.R.; Tanner, E.V.J.; Kelly, D.L.; Dalling, J.W.; Burns, L.S.; Lee, D.; Sidrak, G. Hurricanes need not cause high mortality: The effects of Hurricane Gilbert on forests in Jamaica. *J. Trop. Ecol.* **1992**, *8*, 217–223. [CrossRef]

32. Ibanez, T.; Keppel, G.; Menkes, C.; Gillespie, T.W.; Lengaigne, M.; Mangeas, M.; Rivas-Torres, G.; Birnbaum, P. Globally consistent impact of tropical cyclones on the structure of tropical and subtropical forests. *J. Ecol.* **2019**, *107*, 279–292. [CrossRef]
33. Ibanez, T.; Chave, J.; Barrabé, L.; Elodie, B.; Boutreux, T.; Trueba, S.; V.; Rot, H.; Birnbaum, P. Community variation in wood density along a bioclimatic gradient on a hyper-diverse tropical island. *J. Veg. Sci.* **2017**, *28*, 19–33. [CrossRef]
34. Curran, T.J.; Gersbach, L.N.; Edwards, W.; Krockenberger, A.K. Wood density predicts plant damage and vegetative recovery rates caused by cyclone disturbance in tropical rainforest tree species of North Queensland, Australia. *Austral Ecol.* **2008**, *33*, 442–450. [CrossRef]
35. Liu, L.; Wang, Y.; Zhan, R.; Xu, J.; Duan, Y. Increasing Destructive Potential of Landfalling Tropical Cyclones over China. *J. Clim.* **2020**, *33*, 3731–3743. [CrossRef]
36. Walker, L. Tree Damage and Recovery from Hurricane Hugo in Luquillo Experimental Forest, Puerto-Rico. *Biotropica* **1991**, *23*, 379–385. [CrossRef]
37. Bellingham, P.J.; Tanner, E.V.J.; Healey, J.R. Sprouting of Trees in Jamaican Montane Forests, after a Hurricane. *J. Ecol.* **1994**, *8*, 747–758. [CrossRef]
38. Van Bloem, S.J.; Murphy, P.G.; Lugo, A.E. A link between hurricane-induced tree sprouting, high stem density and short canopy in tropical dry forest. *Tree Physiol.* **2007**, *27*, 475–480. [CrossRef] [PubMed]
39. Poorter, L.; Kitajima, K.; Mercado, P.; Chubiña, J.; Melgar, I.; Prins, H.H.T. Resprouting as a persistence strategy of tropical forest trees: Relations with carbohydrate storage and shade tolerance. *Ecology* **2010**, *91*, 2613–2627. [CrossRef]
40. Murphy, H.T.; Metcalfe, D.J. The perfect storm: Weed invasion and intense storms in tropical forests. *Austral Ecol.* **2016**, *41*, 864–874. [CrossRef]
41. Catterall, C.P.; McKenna, S.; Kanowski, J.; Piper, S.D. Do cyclones and forest fragmentation have synergistic effects? A before-after study of rainforest vegetation structure at multiple sites. *Austral Ecol.* **2008**, *33*, 471–484. [CrossRef]
42. Al-Khaldi, M.M.; Johnson, J.T.; Kang, Y.; Katzberg, S.J.; Bringer, A.; Kubatko, E.; Wood, D. Track-Based Cyclone Maximum Wind Retrievals Using the Cyclone Global Navigation Satellite System (CYGNSS) Mission Full DDMs. *IEEE J. Sel. Top. Appl. Earth Obs. Remote Sens.* **2020**, *13*, 21–29. [CrossRef]
43. Dutheil, C.; Lengaigne, M.; Bador, M.; Vialard, J.; Lefèvre, J.; Jourdain, N.C.; Jullien, S.; Peltier, A.; Sultan, B.; Menkes, C. Impact of projected sea surface temperature biases on tropical cyclones projections in the South Pacific. *Sci. Rep.* **2020**, *10*, 12. [CrossRef]

MDPI
St. Alban-Anlage 66
4052 Basel
Switzerland
www.mdpi.com

MDPI Books Editorial Office
E-mail: books@mdpi.com
www.mdpi.com/books

Academic Open
Access Publishing

mdpi.com

ISBN 978-3-7258-0326-2